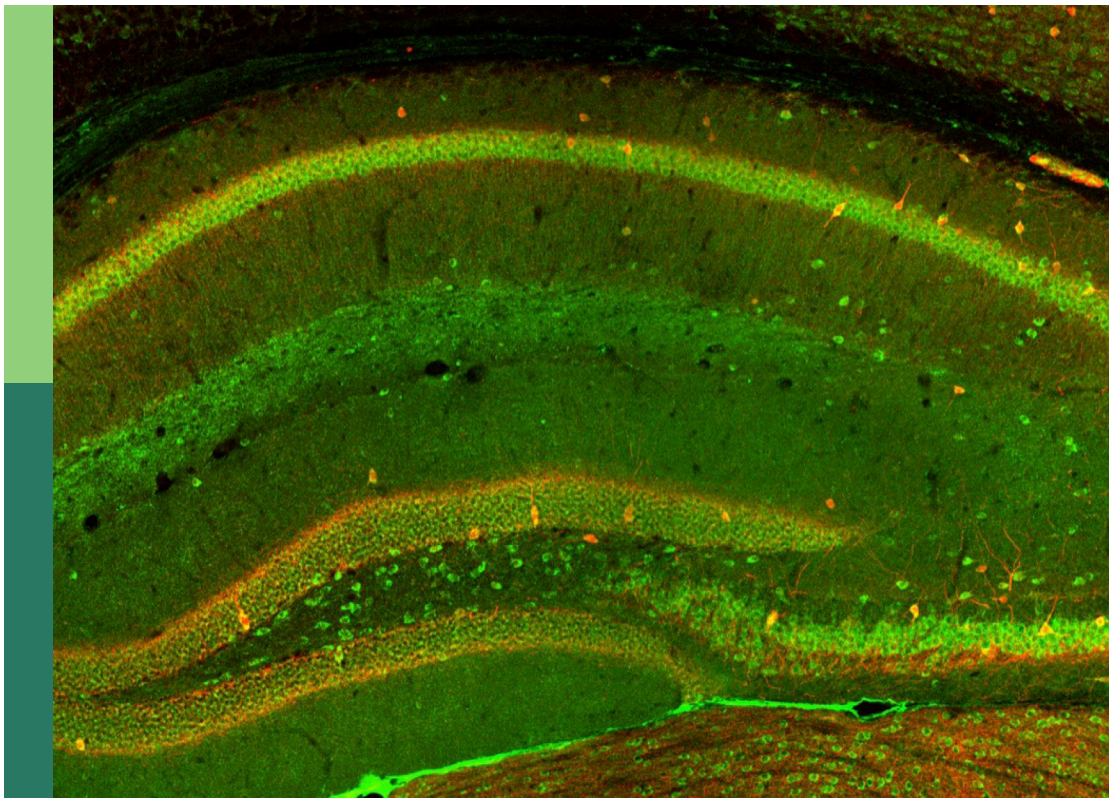
frontiers | Research Topics

Cellular and synaptic mechanisms in the auditory system in health and disease

Edited by
Christian Keine and Bernhard Englitz

Published in
Frontiers in Cellular Neuroscience
Frontiers in Synaptic Neuroscience



FRONTIERS EBOOK COPYRIGHT STATEMENT

The copyright in the text of individual articles in this ebook is the property of their respective authors or their respective institutions or funders. The copyright in graphics and images within each article may be subject to copyright of other parties. In both cases this is subject to a license granted to Frontiers.

The compilation of articles constituting this ebook is the property of Frontiers.

Each article within this ebook, and the ebook itself, are published under the most recent version of the Creative Commons CC-BY licence. The version current at the date of publication of this ebook is CC-BY 4.0. If the CC-BY licence is updated, the licence granted by Frontiers is automatically updated to the new version.

When exercising any right under the CC-BY licence, Frontiers must be attributed as the original publisher of the article or ebook, as applicable.

Authors have the responsibility of ensuring that any graphics or other materials which are the property of others may be included in the CC-BY licence, but this should be checked before relying on the CC-BY licence to reproduce those materials. Any copyright notices relating to those materials must be complied with.

Copyright and source acknowledgement notices may not be removed and must be displayed in any copy, derivative work or partial copy which includes the elements in question.

All copyright, and all rights therein, are protected by national and international copyright laws. The above represents a summary only. For further information please read Frontiers' Conditions for Website Use and Copyright Statement, and the applicable CC-BY licence.

ISSN 1664-8714
ISBN 978-2-8325-7294-8
DOI 10.3389/978-2-8325-7294-8

Generative AI statement
Any alternative text (Alt text) provided alongside figures in the articles in this ebook has been generated by Frontiers with the support of artificial intelligence and reasonable efforts have been made to ensure accuracy, including review by the authors wherever possible. If you identify any issues, please contact us.

About Frontiers

Frontiers is more than just an open access publisher of scholarly articles: it is a pioneering approach to the world of academia, radically improving the way scholarly research is managed. The grand vision of Frontiers is a world where all people have an equal opportunity to seek, share and generate knowledge. Frontiers provides immediate and permanent online open access to all its publications, but this alone is not enough to realize our grand goals.

Frontiers journal series

The Frontiers journal series is a multi-tier and interdisciplinary set of open-access, online journals, promising a paradigm shift from the current review, selection and dissemination processes in academic publishing. All Frontiers journals are driven by researchers for researchers; therefore, they constitute a service to the scholarly community. At the same time, the *Frontiers journal series* operates on a revolutionary invention, the tiered publishing system, initially addressing specific communities of scholars, and gradually climbing up to broader public understanding, thus serving the interests of the lay society, too.

Dedication to quality

Each Frontiers article is a landmark of the highest quality, thanks to genuinely collaborative interactions between authors and review editors, who include some of the world's best academicians. Research must be certified by peers before entering a stream of knowledge that may eventually reach the public - and shape society; therefore, Frontiers only applies the most rigorous and unbiased reviews. Frontiers revolutionizes research publishing by freely delivering the most outstanding research, evaluated with no bias from both the academic and social point of view. By applying the most advanced information technologies, Frontiers is catapulting scholarly publishing into a new generation.

What are Frontiers Research Topics?

Frontiers Research Topics are very popular trademarks of the *Frontiers journals series*: they are collections of at least ten articles, all centered on a particular subject. With their unique mix of varied contributions from Original Research to Review Articles, Frontiers Research Topics unify the most influential researchers, the latest key findings and historical advances in a hot research area.

Find out more on how to host your own Frontiers Research Topic or contribute to one as an author by contacting the Frontiers editorial office: frontiersin.org/about/contact

Cellular and synaptic mechanisms in the auditory system in health and disease

Topic editors
Christian Keine — University of Oldenburg, Germany
Bernhard Englitz — Radboud University, Netherlands

Citation
Keine, C., Englitz, B., eds. (2026). *Cellular and synaptic mechanisms in the auditory system in health and disease*. Lausanne: Frontiers Media SA.
doi: 10.3389/978-2-8325-7294-8

Table of contents

05 Editorial: Cellular and synaptic mechanisms in the auditory system in health and disease
Bernhard Englitz and Christian Keine

09 Genetic tools for studying cochlear inhibition
Eleftheria Slika and Paul Albert Fuchs

17 Cyclic AMP signaling promotes regeneration of cochlear synapses after excitotoxic or noise trauma
Sriram Hemachandran, Ning Hu, Catherine J. Kane and Steven H. Green

31 Age-related upregulation of dense core vesicles in the central inferior colliculus
Jeffrey G. Mellott, Syllissa Duncan, Justine Busby, Laila S. Almassri, Alexa Wawrzyniak, Milena C. Iafrate, Andrew P. Ohl, Elizabeth A. Slabinski, Abigail M. Beaver, Diana Albaba, Brenda Vega, Amir M. Mafi, Morgan Buerke, Nick J. Tokar and Jesse W. Young

52 Molecular and functional profiling of cell diversity and identity in the lateral superior olive, an auditory brainstem center with ascending and descending projections
Ayse Maraslioglu-Sperber, Erika Pizzi, Jonas O. Fisch, Kathrin Kattler, Tamara Ritter and Eckhard Friauf

93 Age-related changes in olivocochlear efferent innervation in gerbils
Friederike Steenken, Asli Pektaş and Christine Köppl

110 Cholinergic modulation in the vertebrate auditory pathway
Chao Zhang and R. Michael Burger

123 Unraveling the molecular landscape of lead-induced cochlear synaptopathy: a quantitative proteomics analysis
Pankaj Bhatia, Shomaila Mehmood, Nicole Doyon-Reale, Rita Rosati, Paul M. Stemmer and Samson Jamesdaniel

137 Noise-induced cochlear synaptopathy in C57BL/6N mice as a function of trauma strength: ribbons are more vulnerable than postsynapses
Kerstin Blum, Pauline Schepsky, Philip Derleder, Philipp Schätzle, Fahmi Nasri, Philipp Fischer, Jutta Engel and Simone Kurt

152 Loss of C1q alters the auditory brainstem response
Sima M. Chokr, Ashley Bui-Tran and Karina S. Cramer

167 Obliteration of a glycinergic projection to the medial geniculate in an animal model of autism
Yusra Mansour and Randy Kulesza

184 Does age protect against loss of tonotopy after acute deafness in adulthood?
Nicole Rosskothen-Kuhl, Sarah Green and Till F. Jakob

200 Maintenance of a central high frequency synapse in the absence of synaptic activity
Sascha Lessle, Lena Ebbers, Yvette Dörflinger, Simone Hoppe, Michaela Kaiser, Hans Gerd Nothwang and Christoph Körber

217 Noise-induced ribbon synapse loss in the mouse basal cochlear region does not reduce inner hair cell exocytosis
David Oestreicher, Alfonso Mauro Malpede, Annalena Reitmeier, Carolin Paula Bräuer, Laura Schoch, Nicola Strenzke and Tina Pangrsic

230 The spatial buildup of nonlinear compression in the cochlea
Kostas Kondylidis, Anna Vavakou and Marcel van der Heijden

243 Cellular and synaptic specializations for sub-millisecond precision in the mammalian auditory brainstem
Christian Keine and Bernhard Englitz

273 Robust inhibitory glycinergic transmission and the effect of bafilomycin, folimycin and EIPA: lessons from the auditory brainstem
Erika Pizzi, Lina N. Hofmann, Abhyudai Singh and Eckhard Friauf

frontiers | Frontiers in Cellular Neuroscience

TYPE Editorial
PUBLISHED 23 October 2025
DOI 10.3389/fncel.2025.1717740

Check for updates

OPEN ACCESS

EDITED AND REVIEWED BY
Arianna Maffei,
Stony Brook University, United States

*CORRESPONDENCE
Christian Keine
christian.keine@uol.de

RECEIVED 02 October 2025
ACCEPTED 09 October 2025
PUBLISHED 23 October 2025

CITATION
Englitz B and Keine C (2025) Editorial: Cellular and synaptic mechanisms in the auditory system in health and disease.
Front. Cell. Neurosci. 19:1717740.
doi: 10.3389/fncel.2025.1717740

COPYRIGHT
© 2025 Englitz and Keine. This is an open-access article distributed under the terms of the Creative Commons Attribution License (CC BY). The use, distribution or reproduction in other forums is permitted, provided the original author(s) and the copyright owner(s) are credited and that the original publication in this journal is cited, in accordance with accepted academic practice. No use, distribution or reproduction is permitted which does not comply with these terms.

Editorial: Cellular and synaptic mechanisms in the auditory system in health and disease

Bernhard Englitz[1] and Christian Keine[2,3]*

[1]Computational Neuroscience Lab, Donders Center for Neuroscience, Radboud University, Nijmegen, Netherlands, [2]Division of Physiology, School of Medicine and Health Sciences, Carl von Ossietzky Universität Oldenburg, Oldenburg, Germany, [3]Research Center Neurosensory Science, Carl von Ossietzky Universität, Oldenburg, Germany

KEYWORDS

auditory system, hearing, synaptic transmission, cellular mechanisms, synapse

Editorial on the Research Topic
Cellular and synaptic mechanisms in the auditory system in health and disease

Introduction

The auditory system enables animals to navigate and interpret their acoustic environment through sophisticated neural computations. This process begins with the conversion of sound waves into electrical signals in the cochlea and culminates in complex encoding of location and context in central brain regions. Each stage relies on specialized cellular and synaptic mechanisms. Understanding these mechanisms, their development, changes with experience and age and susceptibility to disease, is key to comprehending both normal hearing and auditory dysfunction. This Research Topic explores the cellular and synaptic specializations underlying hearing, focusing on the resilience of synaptic transmission, developmental and age-related changes, and the modulatory influences that fine-tune auditory circuits. By bringing together diverse methods and perspectives across different processing stages, the studies in the present Research Topic contribute to a refined picture of the molecular and cellular machinery required for proper auditory function and its vulnerabilities, advancing the state of the art.

Specialization in the auditory system

The peripheral auditory system employs sophisticated preprocessing to optimize neural encoding. In the cochlea, the vast dynamic range of audible sounds is compressed by three orders of magnitude for inner hair cell transduction (Rhode, 2007). Kondylidis et al., using optical coherence tomography, demonstrate that this compression occurs progressively along the basilar membrane in an intensity-dependent manner, optimizing the signal for neural transduction.

As signals ascends to the brainstem, they are further processed by synapses adapted for speed and temporal precision. As reviewed by Keine and Englitz, these synapses share common features, including large presynaptic terminals, fast-gating AMPA receptors, and a repertoire of voltage-gated ion channels that enable high-frequency synaptic transmission.

This high-frequency firing, however, places immense metabolic demands on the system, particularly for replenishing synaptic vesicles (SV). Addressing this challenge,

Pizzi et al. explore the metabolic cost of this precision at an inhibitory brainstem synapse critical for sound localization. Their findings reveal that even the fundamental process of SV refilling requires auxiliary mechanisms beyond the canonical vesicular ATPase proton pump to keep pace with the relentless demand. This suggests that sustaining high-frequency signaling requires unique, and perhaps still undiscovered, molecular solutions.

Ototoxicity, aging and hearing loss

Despite its sophisticated design, the auditory system is vulnerable to trauma and aging (Howarth and Shone, 2006; Kujawa and Liberman, 2009; Gold and Bajo, 2014). Cochlear synaptopathy, or 'hidden hearing loss', involves damage to the synapse between inner hair cells (IHC) and spiral ganglion neurons occurring before hair cell loss. This explains why individuals with normal audiograms may struggle to hear in noisy environments.

Environmental toxins pose another significant threat, particularly for children and pregnant women (Tiwari et al., 2012; Olufemi et al., 2022). Bhatia et al. provide compelling evidence that chronic lead exposure induces cochlear synaptopathy and synapse loss without affecting outer hair cells (OHC). Through proteomic analysis, they identified proteins involved in the synaptic vesicle cycle as key targets of lead-induced ototoxicity.

Noise trauma, a common insult, can inflict similar damages and is particularly prominent in elderly individuals (Cunningham and Tucci, 2017). Oestreicher et al. show that even a single moderate noise exposure causes significant and persistent loss of IHC ribbon synapses in the high-frequency area of the cochlea. Intriguingly, they found that the remaining synapses compensated this loss by increasing their neurotransmitter release, indicating the presence of a potent compensatory mechanism and suggesting that ribbon counts alone may not fully predict synaptic output.

Further exploring the dose-dependent damage of acoustic trauma leading to cochlear synaptopathy, Blum et al. demonstrate that presynaptic ribbons are more susceptible to noise trauma than their postsynaptic partners, identifying the presynaptic element as the more fragile component of this first auditory synapse.

These studies naturally lead to the question of therapeutic intervention. Hemachandran et al. explored the potential to promote cochlear synapse regeneration after excitotoxic or noise-induced damage. They demonstrate both *in vitro* and *in vivo* that stimulating cyclic AMP signaling effectively promotes the regeneration of IHC ribbon synapses and restores partial function. This work identifies the cAMP/PKA pathway as a promising target for minimally invasive therapies aimed at reversing cochlear synaptopathy.

Complementing this outlook, the mini-review by Slika and Fuchs summarizes the powerful genetic tools, from viral vectors to CRISPR, now being used to study and potentially manipulate the olivocochlear efferent system for therapeutic gain.

Development, maintenance, and plasticity

A central question in developmental neuroscience is the interplay between genetically encoded programs and activity-dependent refinement in shaping neural circuits. Challenging long-held assumptions about activity-dependence (Hubel and Wiesel, 1964; Blankenship et al., 2009; Kirkby et al., 2013; Wang and Bergles, 2015), Lessle et al. investigate the maintenance of the calyx of Held, a giant presynaptic terminal in the medial nucleus of the trapezoid body (MNTB) known for its temporal fidelity (von Gersdorff and Borst, 2002; Borst and Soria van Hoeve, 2012; Joris and Trussell, 2018). By selectively silencing neurotransmission after synapse maturation, they found that its fundamental structure, including active zone number and postsynaptic AMPAR composition, remained remarkably intact even after weeks of inactivity. This suggests the existence of a robust, genetically encoded program for maintaining this highly specialized synapse, largely independent of ongoing activity.

This inherent stability, however, is fine-tuned by other factors during development. While MNTB neurons typically receive a single calyx of Held input in adults, multiple calyces make contact to MNTB neurons during development (Hoffpauir et al., 2006; Rodríguez-Contreras et al., 2008; Holcomb et al., 2013; Sierksma et al., 2017). Chokr et al. explored the role of the classical complement cascade, a part of the innate immune system, in pruning and elimination of immature calyceal inputs. They found that C1q, the initiating molecule of this cascade, is expressed by microglia during the period of synapse elimination. While its absence did not prevent pruning, it resulted in a subtle but significant speed-up of auditory signal transmission, pointing to a nuanced role for immune-related molecules in fine-tuning auditory processing.

Developmental insults can have profound and lasting consequences on the auditory system. Mansour and Kulesza investigated the consequences of *in utero* exposure to valproic acid (VPA), an animal model relevant to autism spectrum disorder (ASD), which is often associated with auditory dysfunction (Moore et al., 2000; Bromley et al., 2013; Hernández-Díaz et al., 2024; Pack et al., 2024; Bolton et al., 2012; Christensen et al., 2013; Ramezani et al., 2019; Mansour et al., 2021). Their work reveals the near-complete obliteration of a specific glycinergic projection from the MNTB to the auditory thalamus, highlighting the vulnerability of specific auditory pathways to developmental disruptions and pointing to potential thalamic processing deficits in this ASD model.

The balance between structural stability and plasticity continues into adulthood and is profoundly impacted by aging (Ingham et al., 1998; Syka, 2002; Ouda et al., 2015). Rosskothen-Kuhl et al. address how the age at the onset of deafness influences central auditory organization. Using Fos mapping after cochlear implant stimulation, they demonstrate that rats deafened as young adults show rapid degradation of brainstem tonotopy, resembling neonatally deafened animals. In contrast, rats deafened as adults largely preserved their tonotopic organization. This suggests that the reduced plasticity of the aging brain, while limiting adaptation, may also confer some resilience that protects established neural circuits from maladaptive reorganization following injury.

While age-related changes in IHC and spiral ganglion neurons are well documented, relatively little is known about the impact of age on the efferent system (Adams and Schulte, 1997; Suryadevara et al., 2001; Bovee et al., 2024). Steenken et al. provide a detailed analysis of age-related changes in the olivocochlear efferent system

of the gerbil cochlea. While confirming an overall decline in efferent terminals, they found that innervation density remained largely intact, implying a parallel degeneration of efferents and their targets. Another key finding was the increased prevalence of "orphaned" OHCs (lacking efferent input) in aged animals, suggesting that medial olicocochlear degeneration may precede OHC loss.

The degradation of the peripheral auditory system during aging or following cochlear damage is often compensated by downregulation of inhibition in the central auditory system (Caspary et al., 2008; Richardson et al., 2012; Caspary and Llano, 2018). Mellott et al. focus on the inferior colliculus (IC), a major integration hub, uncovering a significant age-related upregulation of dense core vesicles (DCVs), particularly during middle age. As DCVs contain neuromodulators and neurotrophins, this finding suggests an increase in modulatory capacity, possibly to compensate for the declining peripheral input or GABAergic inhibition. Notably, terminals containing DCVs appeared to be preferentially spared from age-related synapse loss.

Molecular and neuromodulatory complexity

A deeper understanding of auditory circuit function requires dissecting its immense molecular and chemical diversity. Using the power of next-generation RNA sequencing (Macaulay and Voet, 2014; Svensson et al., 2018), Marasliogl-Sperber et al. provide a high-resolution molecular and functional profile of neurons in the mouse lateral superior olive (LSO). They successfully correlate transcriptomic signatures with electrophysiological properties, delineating the two principal neuron types: ascending principal neurons (pLSOs) and descending lateral olivocochlear (LOC) neurons. The identification of hundreds of differentially expressed genes, including novel markers and specific ion channel subunits, offers a powerful resource for dissecting LSO circuitry and function.

Beyond the primary excitatory and inhibitory transmitters, neurons in the auditory system are influenced by neuromodulators that shape their function (Burger and Kopp-Scheinpflug, 2022). The review by Zhang and Burger focusses the rapidly growing knowledge on cholinergic modulation throughout the auditory pathway, with an emphasis on brainstem and midbrain nuclei. They detail the diverse array of nicotinic and muscarinic receptors and their multifaceted roles in shaping fundamental auditory computations, from gain control and noise protection to synaptic plasticity, underscoring the dynamic chemical landscape that governs our perception of sound.

Conclusion and future directions

Collectively, this diverse set of 16 studies helps to advance our understanding of the auditory brainstem from a simple series of relays into a highly dynamic and sophisticated processing hub. The Research Topic highlights a theme: The very specializations that enable reliable signal transmission with sub-millisecond precision go alongside profound vulnerabilities. Yet, this fragility is counterbalanced by numerous protective, modulatory, and plastic mechanisms that are themselves shaped by development, insult, and age.

The path forward is illuminated by the innovative approaches showcased in this Research Topic. The high-resolution molecular atlases generated by techniques like single-cell sequencing are invaluable for designing targeted pharmacological or genetic interventions. Similarly, a deeper understanding of the brain's own compensatory strategies could lead to therapies that move beyond simple acoustic amplification, aiming instead to protect and restore synaptic fidelity. The surprising resilience of giant synapses to inactivity, the nuanced roles of neuro-immune interactions, and the paradoxical effects of aging on plasticity all open new avenues of investigation. Ultimately, this Research Topic might help to move beyond treating the downstream consequences of hearing loss and instead learn to preserve, repair, and even enhance the remarkable artwork of precision that is found in the auditory system.

Author contributions

BE: Writing – review & editing. CK: Writing – original draft, Writing – review & editing.

Funding

The author(s) declare that financial support was received for the research and/or publication of this article. This work was supported by intramural funding to CK (Carl von Ossietzky Universität Oldenburg; FP 2024-099). The funders had no role in design or preparation of this manuscript.

Acknowledgments

We would like to thank the 74 authors who have contributed their effort to this Research Topic.

Conflict of interest

The authors declare that the research was conducted in the absence of any commercial or financial relationships that could be construed as a potential conflict of interest.

Generative AI statement

The author(s) declare that no Gen AI was used in the creation of this manuscript.

Any alternative text (alt text) provided alongside figures in this article has been generated by Frontiers with the support of artificial intelligence and reasonable efforts have been made to ensure accuracy, including review by the authors wherever possible. If you identify any issues, please contact us.

Publisher's note

All claims expressed in this article are solely those of the authors and do not necessarily represent those of their affiliated organizations, or those of the publisher, the editors and the reviewers. Any product that may be evaluated in this article, or claim that may be made by its manufacturer, is not guaranteed or endorsed by the publisher.

References

Adams, J. C., and Schulte, B. A. (1997). Histopathologic observations of the aging gerbil cochlea. *Hear. Res.* 104, 101–111. doi: 10.1016/S0378-5955(96)00184-0

Blankenship, A. G., Blankenship, A. G., Feller, M. B., and Feller, M. B. (2009). Mechanisms underlying spontaneous patterned activity in developing neural circuits. *Nat. Rev. Neurosci.* 11, 18–29. doi: 10.1038/nrn2759

Bolton, P. F., Golding, J., Emond, A., and Steer, C. D. (2012). Autism spectrum disorder and autistic traits in the Avon Longitudinal Study of Parents and Children: precursors and early signs. *J. Am. Acad. Child Adolesc. Psychiatry* 51, 249–260.e25. doi: 10.1016/j.jaac.2011.12.009

Borst, J. G. G,. and Soria van Hoeve, J. (2012). The calyx of Held synapse: from model synapse to auditory relay. *Annu. Rev. Physiol.* 74, 199–224. doi: 10.1146/annurev-physiol-020911-153236

Bovee, S., Klump, G. M., Pyott, S. J., Sielaff, C., and Köppl, C. (2024). Cochlear ribbon synapses in aged gerbils. *Int. J. Mol. Sci.* 25:2738. doi: 10.3390/ijms25052738

Bromley, R. L., Mawer, G. E., Briggs, M., Cheyne, C., Clayton-Smith, J., García-Fiñana, M., et al. (2013). The prevalence of neurodevelopmental disorders in children prenatally exposed to antiepileptic drugs. *J. Neurol. Neurosurg. Psychiatry* 84, 637–643. doi: 10.1136/jnnp-2012-304270

Burger, R. M., and Kopp-Scheinpflug, C. (2022). Editorial: neuromodulatory function in auditory processing. *Front. Neural Circuits* 16:898646. doi: 10.3389/fncir.2022.898646

Caspary, D. M., Ling, L., Turner, J. G., and Hughes, L. F. (2008). Inhibitory neurotransmission, plasticity and aging in the mammalian central auditory system. *J. Exp. Biol.* 211, 1781–1791. doi: 10.1242/jeb.013581

Caspary, D. M., and Llano, D. A. (2018). "Aging processes in the subcortical auditory system," in *The Oxford Handbook of the Auditory Brainstem* (Oxford: Oxford University Press), 639–680.

Christensen, J., Grønborg, T. K., Sørensen, M. J., Schendel, D., Parner, E. T., Pedersen, L. H., et al. (2013). Prenatal valproate exposure and risk of autism spectrum disorders and childhood autism. *JAMA* 309, 1696–1703. doi: 10.1001/jama.2013.2270

Cunningham, L. L., and Tucci, D. L. (2017). Hearing loss in adults. *N. Engl. J. Med.* 377, 2465–2473. doi: 10.1056/NEJMra1616601

Gold, J. R., and Bajo, V. M. (2014). Insult-induced adaptive plasticity of the auditory system. *Front. Neurosci.* 8:110. doi: 10.3389/fnins.2014.00110

Hernández-Díaz, S., Straub, L., Bateman, B. T., Zhu, Y., Mogun, H., Wisner, K. L., et al. (2024). Risk of autism after prenatal topiramate, valproate, or lamotrigine exposure. *N. Engl. J. Med.* 390, 1069–1079. doi: 10.1056/NEJMoa2309359

Hoffpauir, B. K., Grimes, J. L., Mathers, P. H., and Spirou, G. A. (2006). Synaptogenesis of the calyx of Held: rapid onset of function and one-to-one morphological innervation. *J. Neurosci.* 26, 5511–5523. doi: 10.1523/JNEUROSCI.5525-05.2006

Holcomb, P. S., Hoffpauir, B. K., Hoyson, M. C., Jackson, D. R., Deerinck, T. J., Marrs, G. S., et al. (2013). Synaptic inputs compete during rapid formation of the calyx of held: a new model system for neural development. *J. Neurosci.* 33, 12954–12969. doi: 10.1523/JNEUROSCI.1087-13.2013

Howarth, A., and Shone, G. R. (2006). Ageing and the auditory system. *Postgrad. Med. J.* 82, 166–171. doi: 10.1136/pgmj.2005.039388

Hubel, D. H., and Wiesel, T. N. (1964). Effects of monocular deprivation in kittens. *Naunyn. Schmiedebergs. Arch. Pharmacol.* 248, 492–497. doi: 10.1007/BF00348878

Ingham, N. J., Thornton, S. K., Comis, S. D., and Withington, D. J. (1998). The auditory brainstem response of aged guinea pigs. *Acta Otolaryngol.* 118, 673–680. doi: 10.1080/00016489850183160

Joris, P. X., and Trussell, L. O. (2018). The calyx of Held: a hypothesis on the need for reliable timing in an intensity-difference encoder. *Neuron* 100, 534–549. doi: 10.1016/j.neuron.2018.10.026

Kirkby, L. A., Sack, G. S., Firl, A., and Feller, M. B. (2013). A role for correlated spontaneous activity in the assembly of neural circuits. *Neuron* 80, 1129–1144. doi: 10.1016/j.neuron.2013.10.030

Kujawa, S. G., and Liberman, M. C. (2009). Adding insult to injury: cochlear nerve degeneration after "temporary" noise-induced hearing loss. *J. Neurosci.* 29, 14077–14085. doi: 10.1523/JNEUROSCI.2845-09.2009

Macaulay, I. C., and Voet, T. (2014). Single cell genomics: advances and future perspectives. *PLoS Genet.* 10:e1004126. doi: 10.1371/journal.pgen.1004126

Mansour, Y., Burchell, A., and Kulesza, R. J. (2021). Central auditory and vestibular dysfunction are key features of autism spectrum disorder. *Front. Integr. Neurosci.* 15:743561. doi: 10.3389/fnint.2021.743561

Moore, S. J., Turnpenny, P., Quinn, A., Glover, S., Lloyd, D. J., Montgomery, T., et al. (2000). A clinical study of 57 children with fetal anticonvulsant syndromes. *J. Med. Genet.* 37, 489–497. doi: 10.1136/jmg.37.7.489

Olufemi, A. C., Mji, A., and Mukhola, M. S. (2022). Potential health risks of lead exposure from early life through later life: implications for public health education. *Int. J. Environ. Res. Public Health* 19:16006. doi: 10.3390/ijerph192316006

Ouda, L., Profant, O., and Syka, J. (2015). Age-related changes in the central auditory system. *Cell Tissue Res.* 361, 337–358. doi: 10.1007/s00441-014-2107-2

Pack, A. M., Oskoui, M., Williams Roberson, S., Donley, D. K., French, J., Gerard, E. E., et al. (2024). Teratogenesis, perinatal, and neurodevelopmental outcomes after in utero exposure to antiseizure medication: practice guideline from the AAN, AES, and SMFM: practice guideline from the AAN, AES, and SMFM. *Neurology* 102:e209279. doi: 10.1212/WNL.0000000000209279

Ramezani, M., Lotfi, Y., Moossavi, A., and Bakhshi, E. (2019). Auditory brainstem response to speech in children with high functional autism spectrum disorder. *Neurol. Sci.* 40, 121–125. doi: 10.1007/s10072-018-3594-9

Rhode, W. S. (2007). Basilar membrane mechanics in the 6-9 kHz region of sensitive chinchilla cochleae. *J. Acoust. Soc. Am.* 121, 2792–2804. doi: 10.1121/1.2718397

Richardson, B. D., Brozoski, T. J., Ling, L. L., and Caspary, D. M. (2012). Targeting inhibitory neurotransmission in tinnitus. *Brain Res.* 1485, 77–87. doi: 10.1016/j.brainres.2012.02.014

Rodríguez-Contreras, A., van Hoeve, J. S. S., Habets, R. L. P., Locher, H., and Borst, J. G. G. (2008). Dynamic development of the calyx of Held synapse. *Proc. Natl. Acad. Sci. U. S. A.* 105, 5603–5608. doi: 10.1073/pnas.0801395105

Sierksma, M. C., Tedja, M. S., and Borst, J. G. G. (2017). *In vivo* matching of postsynaptic excitability with spontaneous synaptic inputs during formation of the rat calyx of Held synapse. *J. Physiol.* 595, 207–231. doi: 10.1113/JP272780

Suryadevara, A. C., Schulte, B. A., Schmiedt, R. A., and Slepecky, N. B. (2001). Auditory nerve fibers in young and quiet-aged gerbils: morphometric correlations with endocochlear potential. *Hear. Res.* 161, 45–53. doi: 10.1016/S0378-5955(01)00340-9

Svensson, V., Vento-Tormo, R., and Teichmann, S. A. (2018). Exponential scaling of single-cell RNA-seq in the past decade. *Nat. Protoc.* 13, 599–604. doi: 10.1038/nprot.2017.149

Syka, J. (2002). Plastic changes in the central auditory system after hearing loss, restoration of function, and during learning. *Physiol. Rev.* 82, 601–636. doi: 10.1152/physrev.00002.2002

Tiwari, A. K. M., Mahdi, A. A., Zahra, F., Sharma, S., and Negi, M. P. S. (2012). Evaluation of low blood lead levels and its association with oxidative stress in pregnant anemic women: a comparative prospective study. *Indian J. Clin. Biochem.* 27, 246–252. doi: 10.1007/s12291-012-0202-2

von Gersdorff, H., and Borst, J. G. G. (2002). Short-term plasticity at the calyx of Held. *Nat. Rev. Neurosci.* 3, 53–64. doi: 10.1038/nrn705

Wang, H. C., and Bergles, D. E. (2015). Spontaneous activity in the developing auditory system. *Cell Tissue Res.* 361, 65–75. doi: 10.1007/s00441-014-2007-5

frontiers | Frontiers in Cellular Neuroscience

TYPE Mini Review
PUBLISHED 15 March 2024
DOI 10.3389/fncel.2024.1372948

Check for updates

OPEN ACCESS

EDITED BY
Christian Keine,
University of Oldenburg, Germany

REVIEWED BY
Tejbeer Kaur,
Rutgers, The State University of New Jersey - Busch Campus, United States
Charles Liberman,
Harvard University, United States
Nicola Strenzke,
University Medical Center Göttingen, Germany

*CORRESPONDENCE
Paul Albert Fuchs
✉ pfuchs1@jhmi.edu

RECEIVED 18 January 2024
ACCEPTED 28 February 2024
PUBLISHED 15 March 2024

CITATION
Slika E and Fuchs PA (2024) Genetic tools for studying cochlear inhibition.
Front. Cell. Neurosci. 18:1372948.
doi: 10.3389/fncel.2024.1372948

COPYRIGHT
© 2024 Slika and Fuchs. This is an open-access article distributed under the terms of the Creative Commons Attribution License (CC BY). The use, distribution or reproduction in other forums is permitted, provided the original author(s) and the copyright owner(s) are credited and that the original publication in this journal is cited, in accordance with accepted academic practice. No use, distribution or reproduction is permitted which does not comply with these terms.

Genetic tools for studying cochlear inhibition

Eleftheria Slika and Paul Albert Fuchs*

The Center for Hearing and Balance, Otolaryngology-Head and Neck Surgery, Johns Hopkins, University School of Medicine Baltimore, Baltimore, MD, United States

Efferent feedback to the mammalian cochlea includes cholinergic medial olivocochlear neurons (MOCs) that release ACh to hyperpolarize and shunt the voltage change that drives electromotility of outer hair cells (OHCs). Via brainstem connectivity, MOCs are activated by sound in a frequency- and intensity-dependent manner, thereby reducing the amplification of cochlear vibration provided by OHC electromotility. Among other roles, this efferent feedback protects the cochlea from acoustic trauma. Lesion studies, as well as a variety of genetic mouse models, support the hypothesis of efferent protection from acoustic trauma. Genetic knockout and gain-of-function knockin of the unique α9α10-containing nicotinic acetylcholine receptor (nAChR) in hair cells show that acoustic protection correlates with the efficacy of cholinergic inhibition of OHCs. This protective effect was replicated by viral transduction of the gain-of-function α9L9'T nAChR into α9-knockout mice. Continued progress with "efferent gene therapy" will require a reliable method for visualizing nAChR expression in cochlear hair cells. To that end, mice expressing HA-tagged α9 or α10 nAChRs were generated using CRISPR technology. This progress will facilitate continued study of the hair cell nAChR as a therapeutic target to prevent hearing loss and potentially to ameliorate associated pathologies such as hyperacusis.

KEYWORDS

cochlea, efferent, hair cell, trauma, synaptopathy, gene therapy

Introduction

Molecular therapy for inner ear disease is gaining traction through gene replacement for monogenic deafness, as well as small molecule therapies to ameliorate metabolic or ototoxic damage (Lustig and Akil, 2019; Ma et al., 2019). Confounding any therapeutic approach is the continued susceptibility to acoustic overexposure, which can further weaken hair cells and neuronal contacts. Thus, an intriguing strategy is the complementary enhancement of olivocochlear inhibition to minimize acoustic damage. Acoustic protection via cholinergic inhibition of cochlear outer hair cells has been well established by lesion experiments and genetic manipulation in animals but remains to be determined in humans where such methods are not possible (Fuente, 2015). Two strategies have been proposed based on the unique nicotinic AChR (nAChR) of the hair cell: small molecules that can serve as positive allosteric modulators (Elgoyhen et al., 2009) and genetic alteration of the nicotinic AChR of the hair cell (Taranda et al., 2009; Boero et al., 2018, 2020). This mini-review will describe recent advances to facilitate the study of cochlear nAChRs. The ultimate therapeutic goal is not "gene rescue" in the usual sense, but rather the addition of a gain-of-function receptor variant to enhance the native neuronal mechanism for stronger acoustic protection. An appealing aspect of this approach is that olivocochlear efferent neurons are themselves driven by sound in a

frequency- and intensity-dependent manner so that the therapeutic effect will be matched to the nature of the threat.

The inner ear is innervated by afferent and efferent neurons that comprise a negative feedback loop (Spoendlin, 1985). In the mammalian cochlea, myelinated type I afferents are excited by glutamate release from inner hair cells (IHCs) to provide all aspects of acoustic sensitivity to the brain (Meyer and Moser, 2010). Sparser, unmyelinated, acoustically insensitive type II afferents ramify among outer hair cells. This was described by Brown (1987) and has been reviewed in Zhang and Coate (2017). Medial olivocochlear efferents (MOCs), driven by afferent connections through the brainstem, release acetylcholine (ACh) to inhibit outer hair cells (OHCs) (Guinan, 1996), while lateral olivocochlear efferents (LOCs) contact type I afferent dendrites, producing a mix of excitation and inhibition (Reijntjes and Pyott, 2016). Inhibition of OHCs by MOCs reduces electromechanical amplification of cochlear vibration, causing maximal loss of sensitivity for IHCs to type I cochlear afferent signaling at the characteristic frequency. This mechanism has been reviewed in Guinan (2010) and Fuchs and Lauer (2019). The frequency- and intensity-dependent acoustic excitation of MOC efferents (Robertson and Gummer, 1985; Liberman and Brown, 1986) thus provides cochlear gain control that is tuned to the acoustic environment. MOC inhibition shifts the dynamic range of afferents and may improve the detection of signals in noise, temporal resolution, and aspects of selective attention, reviewed in Guinan (2010) and Fuchs and Lauer (2019). While definitive evidence for these roles in signal processing is limited, there is agreement that efferent feedback can protect the inner ear from acoustic trauma. This has been shown by lesion studies reviewed in Fuente (2015) and electrical stimulation of MOC efferents (Rajan and Johnstone, 1988; Rajan, 2001).

Genetically altered mice for studying efferent inhibition

The discovery of the genes encoding the subunits of the hair cell nAChR, α9, and α10 (Elgoyhen et al., 1994, 2001) led to the development of mouse models in which these subunits could be knocked out, demonstrating their essential roles (Vetter et al., 2007) and making these animals more prone to acoustic trauma (Lauer and May, 2011; Maison et al., 2013). Equally informative was the subsequent production of point mutation, gain-of-function hair cell nAChR mice (α9L9'T), in which efferent inhibition was greatly enhanced, and noise-induced threshold shifts in ABR and DPOAE were substantially reduced (Taranda et al., 2009). Complementary loss and gain-of-function mouse models have since been used to show that after identical acoustic overexposure, threshold shifts (ABR and DPOAE) are greater in the α9-knockout mice than in wildtype littermates, while the nAChR gain-of-function mice suffered no hearing loss due to these measures (Figure 1; Boero et al., 2018). These studies revealed a similar outcome for measures of noise-induced afferent denervation of IHCs, "synaptopathy." The amplitude of ABR wave 1 (a measure of the number of afferents responding to a saturating loud sound) was reduced after noise exposure in wildtype mice and α9 knockouts but unchanged compared to pre-exposure magnitude in the α9L9'T gain-of-function transgenic mice.

Commensurate with the changes in ABR wave 1 amplitude, wildtype, and α9-knockout mice lost IHC synapses (paired CtBP2 and GluA2 immunolabel) 7 days after noise damage. Remarkably, α9 gain-of-function IHCs had a small but significant *increase* in the number of IHC ribbon synapses in all cochlear regions compared to controls (average ABR wave 1 amplitude also was larger, but not statistically significant).

A reduction of age-related hearing loss (presbycusis) was demonstrated by comparison of ABR and DPOAE thresholds in mice 6 and 12 months old (Boero et al., 2020). These were elevated 15 dB on average in wildtype mice but unchanged in the α9 gain-of-function mice. Similarly, ABR wave 1 amplitude diminished from 6 to 12 months in wildtype mice but was unchanged in α9 transgenic gain-of-function mice. The α9 gain-of-function mice also had more IHC ribbon synapses at 12 months of age than did the wildtype littermates. Thus, enhanced efferent feedback mitigated both OHC- and IHC-specific pathologies.

nAChR viral transduction in the mouse cochlea

The correlation between α9 nAChR function and acoustic protection in the genetically modified mice supports the hair cell nAChR as a target to prevent hearing loss in humans. First, however, as for any gene therapy, a number of barriers must be overcome to establish feasibility, reproducibility, and safety. How will the gene product be delivered? Is it expressed at significant levels and localized appropriately? How long does it persist? To begin to address these questions, a series of experiments were carried out using viral carriers to express α9 nAChR subunits in the mouse cochlea. The first foray introduced α9L9'T to "rescue" α9-knockout mice (Zhang et al., 2023), with the aim of replicating the marked differences in acoustic protection observed between knockout and knockin mice (Figure 1).

The modified AAV2.7 m8 (Dalkara et al., 2013) was shown previously to drive widespread expression of green fluorescent protein (GFP) in hair cells and supporting cells of the mouse cochlea (Isgrig et al., 2019). Thus, this virus was constructed commercially to carry the mouse α9L9'T nAChR into the inner ear of homozygous α9-knockout mice (C57BL/6 J genetic background) at postnatal day 0–2 (Zhang et al., 2023). A posterior semi-circular canal approach was used to inject 1–2 μL of virus at ~10^{13} viral copies per ml. Two to three weeks later, the virally produced α9-containing nAChRs were visualized by labeling with Cy3-conjugated RgIA5727, a modified peptide isolated from cone snail venom that binds selectively to α9-containing nAChRs of hair cells (Fisher et al., 2021). Cy3-RgIA5727 puncta were found on the synaptic pole of the majority of OHCs examined at 3 weeks post-injection.

Cohorts of control and experimental mice had hearing tested at 3 weeks of age (ABR thresholds), then exposed to loud sound (2 h @90 dB, 2–20 kHz), and re-tested 1 and 14 days later (clicks and pure tones at 8, 12, 16, 24, and 32 kHz). α9L9'T-injected mice were compared to littermates injected with a virus expressing green fluorescent protein (GFP) and to uninjected littermates (Figure 2). The acoustic trauma protocol caused equivalent upward shifts for click and pure-tone thresholds (hearing loss) 1 day later in uninjected or

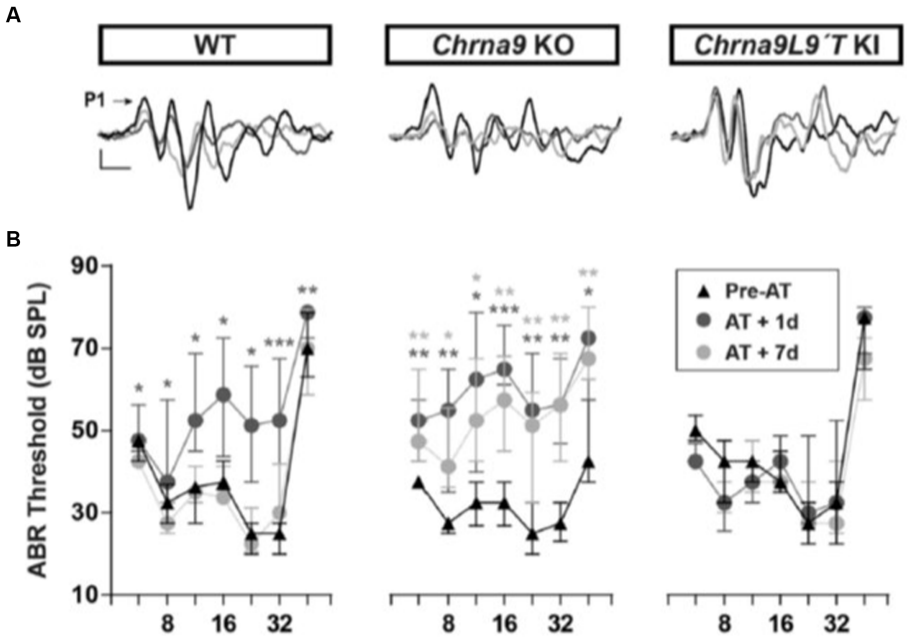


FIGURE 1
ABR measurements before and after acoustic trauma (AT). **(A)** Representative ABR traces from WT, Chrna9 KO, and Chrna9L9T KI mice at P21 before trauma (Pre-AT, black trace), 1 day after AT (AT1d, dark gray trace), and AT7d (light gray trace). The arrow indicates peak 1 amplitude. Calibration: vertical, 0.4 μV; horizontal, 1 ms. **(B)** ABR thresholds in WT ($n = 12$), Chrna9 KO ($n = 14$), and Chrna9L9T KI ($n = 15$) mice at P21 before AT, 1 day after AT, and 7 days after AT. Median and interquartile ranges are shown, and the comparisons were made using the Friedman tests followed by a *post-hoc* test. Dark gray asterisks represent the statistical significance of AT +1d values compared with Pre-AT, and light gray asterisks represent AT +7d values compared with Pre-AT controls. *$p < 0.05$; **$p < 0.01$; ***$p < 0.001$ (Boero et al., 2018; Figures 2A,B; https://www.jneurosci.org/content/38/34/7440).

GFP-injected mice (22 dB shift averaged across all tones and click), while α9L9'T-injected mice experienced approximately half that average shift (12 dB), significant only for the higher frequencies (16, 24, and 32 kHz). In all cohorts, thresholds returned to normal 14 days after trauma.

In addition to measures of threshold that reflect the function of OHCs, IHCs to afferent signaling were examined by measuring the amplitude of wave 1 of the ABR evoked by saturating, loud clicks and tones. All cohorts experienced a 50% drop in wave 1 amplitude 1 day after acoustic trauma; 14 days later, wave 1 showed no recovery in uninjected and GFP-injected mice, but statistically complete recovery in α9L9'T-injected mice. Thus, both OHC damage (threshold shift) and afferent denervation (synaptopathy) in α9-knockout mice were protected to some degree by viral expression of the gain-of-function α9L9'T nAChR.

Visualizing nAChRs in hair cells with fluorophore-conjugated conotoxin peptide RgIA

Immunolocalization of nAChRs generally, and in the cochlea particularly, has been hampered by the difficulty of producing robust immunolabeling of the receptor. To circumvent this limitation, viral expression of nAChRs was visualized in α9-null mice using a fluorescently tagged biotoxin. Venom from carnivorous cone snails contains a host of biologically active compounds (Olivera et al., 1991) among them a highly selective and potent α9 antagonist, RgIA (Ellison et al., 2006). This has been chemically modified to conjugate with a Cy3 fluorophore. Cy3-RgIA5727 was shown to retain its blocking ability and to label cochlear hair cells at the location of efferent synapses on older outer or younger inner hair cells (Fisher et al., 2021). This labeling is essentially irreversible, making this a promising tool for identifying α9-containing nAChRs in the wide variety of tissues where they have been proposed to act (Liu et al., 2019; Hone and McIntosh, 2023). One limitation however is that Cy3-RgIA5727 only binds in unfixed tissue. In addition, the Cy3 moiety makes the compound sticky so that densely packed tissues tend to accumulate the label and resist washout (e.g., Kolliker's organ region of immature cochleas) (Fisher et al., 2021).

Visualizing HA-tagged nAChRs in CRISPRed mice

While Cy3-RgIA5727 was a boon for studying "rescued" α9-null mice and could be useful to localize α9 nAChRs in other tissues, the ultimate goal is to carry out efferent gene therapy on wild-type mice. As Cy3-RgIA5727 will label nAChRs whether native or of viral origin, another tool is needed. Thus, the CRISPR-Cas9 technique was used to produce mice with an HA tag on either the α9 or the α10 subunit of the hair cell nAChR (Vyas et al., 2020). These α9HA, or α10HA mice had no discernible change in hearing (normal ABR thresholds and waveforms), no obvious vestibular deficits (e.g., circling) and growth and breeding appeared normal. When fixed and processed cochlear tissues of adult mice were examined with fluorescence microscopy, HA

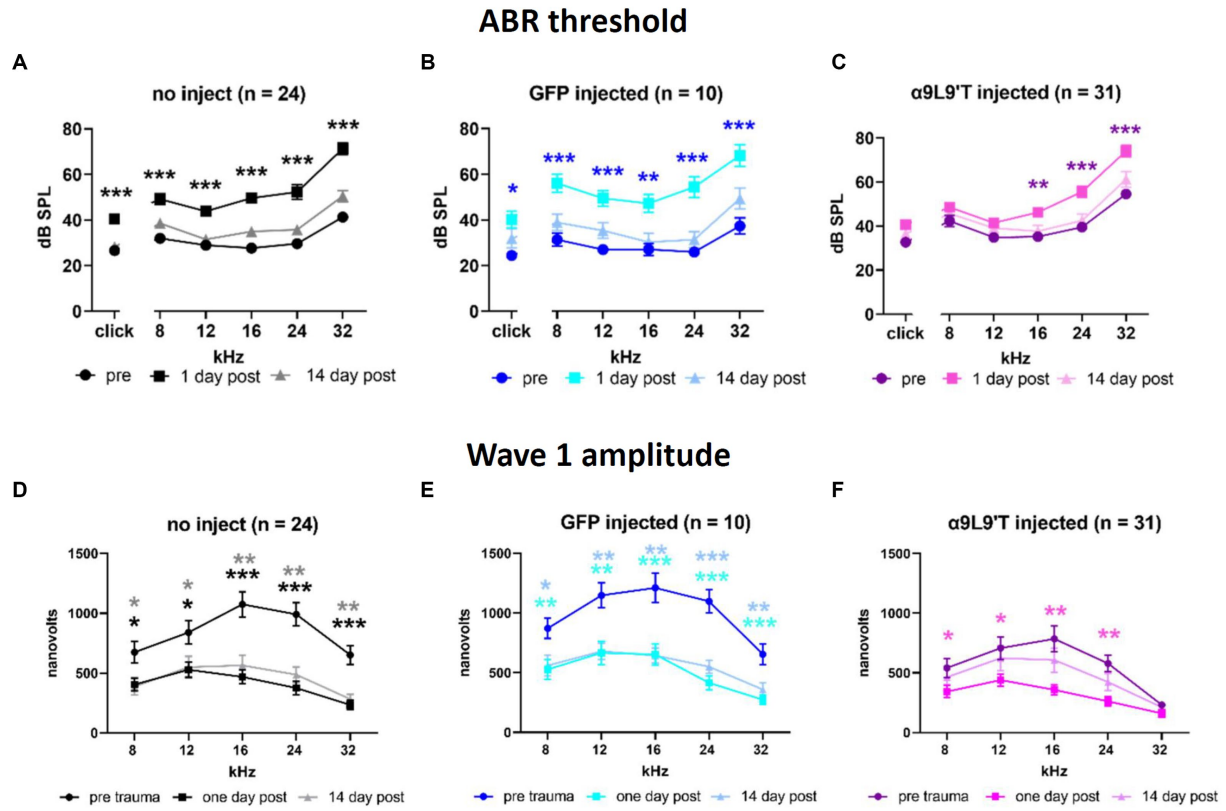


FIGURE 2
Effect of noise exposure on **(A)** uninjected C67BL/6J mice, **(B)** mice injected with virus-bearing GFP, and **(C)** mice injected with the α9L9'T-bearing virus ABR thresholds collected prior to 1 and 14days after acoustic trauma for all cohorts. The amplitude of wave 1 for saturating loud click and tone ABRs for **(D)** uninjected, **(E)** GFP-injected, and **(F)** α9L9'T-injected mice (same cohorts as in upper panels). Darker asterisks denote pre- to 1-day post. Lighter asterisks denote pre- to 14days post. No significant differences between pre- and 14-day post in α9L9'T-injected mice were observed **(F)**. Statistical significance from multiple unpaired *t*-tests with Welch correction, $*p<0.05$, $**p<0.01$, $***p<0.001$ [Reprinted with permission from Zhang et al., 2023].

immunolabel was aligned with SV2-immunolabeled efferent terminals of outer hair cells throughout the cochleas of both α9HA and α10HA mice. Labeling was equivalent in hetero- and homozygotes. In early postnatal mice (P7-P8) when inner hair cells have inhibitory cholinergic synapses, HA immunolabel of inner hair cells was juxtaposed to ChAT-immunolabeled efferent processes, though not at older ages (P20) when the efferent synapses have retracted. In addition to the dense synaptic location of the HA immunolabel, lower level, diffuse cytoplasmic immunoreactivity occurred in young inner hair cells and near the cuticular plate in older outer hair cells. Type II vestibular hair cells also express α9-containing nAChRs (Yu et al., 2020). An ongoing study is examining the distribution of HA-tagged α9-containing nAChRs in these CRISPRed mouse lines, as well as following viral injection of HA-tagged α9L9'T in wild-type mice.

The 9 amino acid HA peptide and an 11 or 12 amino acid spacer were attached to the carboxy tail of either subunit (after transmembrane region 4). This location is predicted to be extracellular, so potentially could interact with other segments, particularly the longer extracellular ligand-binding amino-terminal. To examine the possibility of functional changes, tight-seal whole-cell recordings were made from inner and outer hair cells from apical segments of cochleas from P9 to P11 aged mice (efferent innervation is present on both populations of hair cells at this time and place). Heterozygous and homozygous α9HA and α10HA mice were studied. Electrical stimulation evoked synaptic release while hair cell membrane potential was altered to determine the ionic constituents of the postsynaptic current. In addition, the probability of synaptic release was measured during these long 1-Hz shock trains (that do not cause facilitation) (Ballestero et al., 2011). In all cases, postsynaptic currents included calcium-dependent potassium current as well as cation current through the nAChR, replicating the well-established inhibitory mechanism. Synaptic transmission to inner and outer hair cells of heterozygous α9HA and α10HA mice was quantitatively indistinguishable from that of wild type. However, in homozygous mice (both α9HA and α10HA), the probability of release was significantly lower onto outer hair cells than in heterozygotes (and wildtype). Perhaps related to this, efferent synaptic terminals onto the outer hair cells of homozygous mice (α9HA and α10HA) were significantly smaller (although equal in number) than those onto the outer hair cells of heterozygous mice (Supplementary material in Vyas et al., 2020). It is not certain how presynaptic release efficacy could be altered by HA-tagged postsynaptic receptors, although retrograde facilitation has been observed at these synapses (Kong et al., 2013), perhaps pointing to a change in nAChR binding or gating

efficiency. Whatever the cause, future functional studies should employ heterozygous HA mice that have normal synaptic transmission and robust synaptic immunolabeling. The more diffuse cytoplasmic HA labeling also recommends caution if seeking HA-nAChR expression in other tissues. The preferential synaptic localization of the HA label in hair cells and its developmental regulation confirm the biological reality of this expression in cochlear hair cells. Some confirmatory evidence should be sought for other, novel expression patterns.

Discussion

Substantial progress has been made in detailing the morphology, neurochemistry, and cellular physiology of hair cell inhibition. The efferent projection to the inner ear was identified by Rasmussen in the early 20th century (Rasmussen, 1946). Details of that innervation, including the identity of acetylcholine as a principal neurotransmitter, have been well documented and reviewed in Klinke and Galley (1974). Galambos showed that electrical stimulation of the efferent axons reduced the amplitude of the acoustically evoked compound action potential (Galambos, 1956), while Wiederhold and Kiang confirmed this effect at the level of single cochlear afferents (Wiederhold and Kiang, 1970). Intracellular recordings by Russell in fish (Flock and Russell, 1973, 1976) and frogs (Ashmore and Russell, 1982) provided the first direct evidence for hair cell hyperpolarization by efferent input. This was elaborated by studies in the turtle inner ear that detailed effects on acoustic sensitivity and tuning (Art et al., 1982, 1985; Art et al., 1984; Art and Fettiplace, 1984). Voltage-clamp recording from single isolated chicken hair cells revealed a two-channel mechanism for cholinergic inhibition (Fuchs and Murrow, 1992a,b): calcium influx through a ligand-gated nAChR that drives a far larger increase in calcium-dependent potassium current. This two-channel mechanism of cholinergic inhibition appears to be universal for vertebrate hair cells whether in the cochlea, vestibule, or lateral line. Also universal, efferent terminals are aligned with a near-membrane postsynaptic cistern (Smith and Sjostrand, 1961; Saito, 1980; Fuchs et al., 2014) that may be integral to postsynaptic calcium homeostasis (Lioudyno et al., 2004; Fuchs, 2014; Zachary et al., 2018; Moglie et al., 2021).

The two-channel hypothesis was cemented by the discovery of novel nicotinic receptor subunits, α9 and α10 that comprise the hair cell nAChR (Elgoyhen et al., 1994, 2001). These are distantly related to the muscle and neuronal alpha subunits but differ pharmacologically. In particular, nicotine inhibits, rather than activates, and the most potent small molecule antagonist is strychnine (Elgoyhen et al., 2009). Knockout and gain-of-function knock-in mice have since demonstrated a strong correlation between the function of the hair cell nAChR, and protection from acoustic trauma (Taranda et al., 2009; Boero et al., 2018, 2020). Thus, the ability of efferent feedback to protect from acoustic trauma is well established in animal models, although the significance of this effect for humans remains unsettled. Standard techniques for quantifying efferent feedback, contralateral sound to suppress DPOAEs, show smaller effects in human trials than in animal experiments (Collet et al., 1990; Chambers et al., 2012), consistent with less dense efferent innervation in the human cochlea (Liberman and Liberman, 2019). Nonetheless, the experimental evidence from animals is sufficiently strong to consider the hair cell nAChR as a therapeutic target for the prevention of noise-induced hearing loss, particularly for those at risk of early-onset age-related hearing loss in the military, workplace, or other loud sound environments. Indeed, enhanced efferent function and expanded innervation driven by the gain-of-function nAChR (Murthy et al., 2009; Boero et al., 2018) could have an outsized impact in humans by increasing the modest efferent innervation that declines with age (Liberman and Liberman, 2019). Viral transfection in the mouse cochlea can persist for at least 1 year (Bankoti et al., 2021). Ongoing gene therapy trials (e.g., otoferlin; Qi et al., 2024) will determine this for humans.

An unresolved issue concerns the complex development of efferent innervation of the cochlea. In the first two postnatal weeks in rodents, IHCs express α9-containing nAChRs and are inhibited by ACh release from efferent neurons (Glowatzki and Fuchs, 2000; Simmons, 2002). This transient innervation of IHCs is thought to be important in modulating ribbon synapse maturation and spontaneous afferent firing that shapes central connectivity, reviewed in Rutherford et al. (2021), Frank and Goodrich (2018), and Di Guilmi et al. (2019); 2 weeks postnatally, those IHCs synapses are lost. In contrast, efferent contacts on OHCs begin to function late in the first postnatal week, beginning in the cochlear base and extending to the apex in the second postnatal week (Rohmann et al., 2015), consistent with the basal-to-apical maturation of OHC function (Beurg et al., 2018; Jeng et al., 2020). Thus, both IHCs and OHCs of genetically modified mice could be impacted by altered expression of α9-containing nAChRs. However, it takes 2–3 weeks post-injection for maximal viral expression (Isgrig et al., 2019; Zhang et al., 2023), so early postnatal injection of the gain-of-function α9L9'T may not affect IHC development. Nonetheless, improving the efficacy of viral delivery in adult animals (Zhu et al., 2021) will eliminate development as a confounding factor and will expand future clinical applications.

A second consideration is whether viral transduction will be effective after synaptic maturation is complete. Viral injections in early postnatal mice may benefit by integration of introduced α9 subunits into still-developing synapses. It is conceivable that integration will be suppressed in stabilized adult synapses. However, adult nAChRs do turn over. At the mature neuromuscular junction, bungarotoxin-labeled nAChRs have a half-life of 6–8 days, which is considerably shorter (~2 days) in developing or denervated muscle (Berg and Hall, 1975; Pumplin and Fambrough, 1982; Salpeter and Harris, 1983). This motivates continued study of the pattern and lifetime of viral expression in adult cochleas.

Viral constructs utilized to date employ a strong generic promoter. While useful for the present experiments, such robust expression may not be the best therapeutic strategy. A previous study on the neuronal gain-of-function nAChRs described excitotoxicity due to increased calcium loads (Drenan and Lester, 2012). While this does not happen to hair cells in the knockin mouse lines where expression is under native promoter control, it is conceivable that expression under the strong viral promoter could be disadvantageous. Even in the α9L9'T-knockin mice, there were some unexpected changes. Efferent terminals on OHCs of the α9L9'T mice had reduced quantum content (compensated by increased facilitation ratios) compared to

wild-type synapses (Wedemeyer et al., 2018). This could be a beneficial homeostatic adaptation, but other viral constructs, and more extensive studies, including discriminative hearing tasks, are needed to further the ultimate goal of therapeutic translation. For example, OHC-targeted gene therapy with cell-specific promoters could limit off-target effects or overexpression. Additional promise is offered by epigenetic modulation to increase viral transduction (Layman et al., 2015; Chen et al., 2016; Deng et al., 2019).

Author contributions

ES: Data curation, Formal analysis, Investigation, Methodology, Visualization, Writing – original draft, Writing – review & editing. PF: Conceptualization, Formal analysis, Funding acquisition, Project administration, Resources, Supervision, Visualization, Writing – original draft, Writing – review & editing.

Funding

The author(s) declare that financial support was received for the research, authorship, and/or publication of this article. This study was supported by R01 DC001508 from the National Institutes for Deafness and Communication Disorders and by the David M. Rubenstein Professorship and Fund for Hearing Research at Johns Hopkins University School of Medicine.

Acknowledgments

We thank F. Chakir for mouse-keeping and genotyping, H. Hiel and M. Wood for histology 323 and microscopy support, and K. Burke and A. M. Lauer for guidance on phenotyping.

Conflict of interest

The authors declare that the research was conducted in the absence of any commercial or financial relationships that could be construed as a potential conflict of interest.

Publisher's note

All claims expressed in this article are solely those of the authors and do not necessarily represent those of their affiliated organizations, or those of the publisher, the editors and the reviewers. Any product that may be evaluated in this article, or claim that may be made by its manufacturer, is not guaranteed or endorsed by the publisher.

References

Art, J. J., Crawford, A. C., Fettiplace, R., and Fuchs, P. A. (1982). Efferent regulation of hair cells in the turtle cochlea. *Proc. R. Soc. Lond. B Biol. Sci.* 216, 377–384.

Art, J. J., Crawford, A. C., Fettiplace, R., and Fuchs, P. A. (1985). Efferent modulation of hair cell tuning in the cochlea of the turtle. *J. Physiol.* 360, 397–421. doi: 10.1113/jphysiol.1985.sp015624

Art, J. J., and Fettiplace, R. (1984). Efferent desensitization of auditory nerve fibre responses in the cochlea of the turtle *Pseudemys scripta elegans*. *J. Physiol.* 356, 507–523. doi: 10.1113/jphysiol.1984.sp015480

Art, J. J., Fettiplace, R., and Fuchs, P. A. (1984). Synaptic hyperpolarization and inhibition of turtle cochlear hair cells. *J. Physiol.* 356, 525–550. doi: 10.1113/jphysiol.1984.sp015481

Ashmore, J. F., and Russell, I. J. (1982). Effect of electrical stimulation on hair cells of the frog sacculus. *J. Physiol.* 329:25.

Ballestero, J., de San Martin, J. Z., Goutman, J., Elgoyhen, A. B., Fuchs, P. A., and Katz, E. (2011). Short-term synaptic plasticity regulates the level of olivocochlear inhibition to auditory hair cells. *J. Neurosci.* 31, 14763–14774. doi: 10.1523/JNEUROSCI.6788-10.2011

Bankoti, K., Generotti, C., Hwa, T., Wang, L., O'Malley, B. W. Jr., and Li, D. (2021). Advances and challenges in adeno-associated viral inner-ear gene therapy for sensorineural hearing loss. *Mol Ther Methods Clin Dev* 21, 209–236. doi: 10.1016/j.omtm.2021.03.005

Berg, D. K., and Hall, Z. W. (1975). Loss of alpha-bungarotoxin from junctional and extrajunctional a receptors in rat diaphragm muscle *in vivo* and in organ culture. *J. Physiol.* 252, 771–789. doi: 10.1113/jphysiol.1975.sp011169

Beurg, M., Cui, R., Goldring, A. C., Ebrahim, S., Fettiplace, R., and Kachar, B. (2018). Variable number of TMC1-dependent mechanotransducer channels underlie tonotopic conductance gradients in the cochlea. *Nat. Commun.* 9:2185. doi: 10.1038/s41467-018-04589-8

Boero, L. E., Castagna, V. C., Di Guilmi, M. N., Goutman, J. D., Elgoyhen, A. B., and Gomez-Casati, M. E. (2018). Enhancement of the medial Olivocochlear system prevents hidden hearing loss. *J. Neurosci.* 38, 7440–7451. doi: 10.1523/JNEUROSCI.0363-18.2018

Boero, L. E., Castagna, V. C., Terreros, G., Moglie, M. J., Silva, S., Maass, J. C., et al. (2020). Preventing presbycusis in mice with enhanced medial olivocochlear feedback. *Proc. Natl. Acad. Sci. USA* 117, 11811–11819. doi: 10.1073/pnas.2000760117

Brown, M. C. (1987). Morphology of labeled afferent fibers in the guinea pig cochlea. *J. Comp. Neurol.* 260, 591–604. doi: 10.1002/cne.902600411

Chambers, A. R., Hancock, K. E., Maison, S. F., Liberman, M. C., and Polley, D. B. (2012). Sound-evoked olivocochlear activation in unanesthetized mice. *J. Assoc. Res. Otolaryngol.* 13, 209–217. doi: 10.1007/s10162-011-0306-z

Chen, J., Hill, K., and Sha, S. H. (2016). Inhibitors of histone deacetylases attenuate noise-induced hearing loss. *J. Assoc. Res. Otolaryngol.* 17, 289–302. doi: 10.1007/s10162-016-0567-7

Collet, L., Kemp, D. T., Veuillet, E., Duclaux, R., Moulin, A., and Morgon, A. (1990). Effect of contralateral auditory stimuli on active cochlear micro-mechanical properties in human subjects. *Hear. Res.* 43, 251–261. doi: 10.1016/0378-5955(90)90232-E

Dalkara, D., Byrne, L. C., Klimczak, R. R., Visel, M., Yin, L., Merigan, W. H., et al. (2013). *In vivo*-directed evolution of a new adeno-associated virus for therapeutic outer retinal gene delivery from the vitreous. *Sci. Transl. Med.* 5:189ra76.

Deng, X., Liu, Z., Li, X., Zhou, Y., and Hu, Z. (2019). Generation of new hair cells by DNA methyltransferase (DNMT) inhibitor 5-azacytidine in a chemically-deafened mouse model. *Sci. Rep.* 9:7997. doi: 10.1038/s41598-019-44313-0

Di Guilmi, M. N., Boero, L. E., Castagna, V. C., Rodriguez-Contreras, A., Wedemeyer, C., Gomez-Casati, M. E., et al. (2019). Strengthening of the efferent Olivocochlear system leads to synaptic dysfunction and tonotopy disruption of a central auditory nucleus. *J. Neurosci.* 39, 7037–7048. doi: 10.1523/JNEUROSCI.2536-18.2019

Drenan, R. M., and Lester, H. A. (2012). Insights into the neurobiology of the nicotinic cholinergic system and nicotine addiction from mice expressing nicotinic receptors harboring gain-of-function mutations. *Pharmacol. Rev.* 64, 869–879. doi: 10.1124/pr.111.004671

Elgoyhen, A. B., Johnson, D. S., Boulter, J., Vetter, D. E., and Heinemann, S. (1994). Alpha 9: an acetylcholine receptor with novel pharmacological properties expressed in rat cochlear hair cells. *Cell* 79, 705–715. doi: 10.1016/0092-8674(94)90555-X

Elgoyhen, A. B., Katz, E., and Fuchs, P. A. (2009). The nicotinic receptor of cochlear hair cells: a possible pharmacotherapeutic target? *Biochem. Pharmacol.* 78, 712–719. doi: 10.1016/j.bcp.2009.05.023

Elgoyhen, A. B., Vetter, D. E., Katz, E., Rothlin, C. V., Heinemann, S. F., and Boulter, J. (2001). alpha10: a determinant of nicotinic cholinergic receptor function in mammalian vestibular and cochlear mechanosensory hair cells. *Proc. Natl. Acad. Sci. USA* 98, 3501–3506. doi: 10.1073/pnas.051622798

Ellison, M., Haberlandt, C., Gomez-Casati, M. E., Watkins, M., Elgoyhen, A. B., McIntosh, J. M., et al. (2006). Alpha-RgIA: a novel conotoxin that specifically and

potently blocks the alpha9alpha10 nAChR. *Biochemistry* 45, 1511–1517. doi: 10.1021/bi0520129

Fisher, F., Zhang, Y., Vincent, P. F. Y., Gajewiak, J., Gordon, T. J., Glowatzki, E., et al. (2021). Cy3-RgIA-5727 labels and inhibits alpha9-containing nAChRs of Cochlear hair cells. *Front. Cell. Neurosci.* 15:697560. doi: 10.3389/fncel.2021.697560

Flock, A., and Russell, I. (1973). Efferent nerve fibres: postsynaptic action on hair cells. *Nat. New Biol.* 243, 89–91.

Flock, A., and Russell, I. (1976). Inhibition by efferent nerve fibres: action on hair cells and afferent synaptic transmission in the lateral line canal organ of the burbot *Lota lota*. *J. Physiol.* 257, 45–62. doi: 10.1113/jphysiol.1976.sp011355

Frank, M. M., and Goodrich, L. V. (2018). Talking back: development of the olivocochlear efferent system. *Wiley Interdiscip. Rev. Dev. Biol.* 7:e324. doi: 10.1002/wdev.324

Fuchs, P. A. (2014). A 'calcium capacitor' shapes cholinergic inhibition of cochlear hair cells. *J. Physiol.* 592, 3393–3401. doi: 10.1113/jphysiol.2013.267914

Fuchs, P. A., and Lauer, A. M. (2019). Efferent inhibition of the cochlea. *Cold Spring Harb Perspect Med* 9:a033530. doi: 10.1101/cshperspect.a033530

Fuchs, P. A., Lehar, M., and Hiel, H. (2014). Ultrastructure of cisternal synapses on outer hair cells of the mouse cochlea. *J. Comp. Neurol.* 522, 717–729. doi: 10.1002/cne.23478

Fuchs, P. A., and Murrow, B. W. (1992a). Cholinergic inhibition of short (outer) hair cells of the chick's cochlea. *J. Neurosci.* 12, 800–809. doi: 10.1523/JNEUROSCI.12-03-00800.1992

Fuchs, P. A., and Murrow, B. W. (1992b). A novel cholinergic receptor mediates inhibition of chick cochlear hair cells. *Proc. Biol. Sci.* 248, 35–40.

Fuente, A. (2015). The olivocochlear system and protection from acoustic trauma: a mini literature review. *Front. Syst. Neurosci.* 9:94. doi: 10.3389/fnsys.2015.00094

Galambos, R. (1956). Suppression of auditory nerve activity by stimulation of efferent fibers to cochlea. *J. Neurophysiol.* 19, 424–437. doi: 10.1152/jn.1956.19.5.424

Glowatzki, E., and Fuchs, P. A. (2000). Cholinergic synaptic inhibition of inner hair cells in the neonatal mammalian cochlea. *Science* 288, 2366–2368. doi: 10.1126/science.288.5475.2366

Guinan, J. J. (1996). "Physiology of olivocochlear efferents" in *The cochlea*. eds. P. Dallos, N. Arthur Popper and R. Richard Fay (New York: Springer)

Guinan, J. J. Jr. (2010). Cochlear efferent innervation and function. *Curr. Opin. Otolaryngol. Head Neck Surg.* 18, 447–453. doi: 10.1097/MOO.0b013e32833e05d6

Hone, A. J., and McIntosh, J. M. (2023). Nicotinic acetylcholine receptors: therapeutic targets for novel ligands to treat pain and inflammation. *Pharmacol. Res.* 190:106715. doi: 10.1016/j.phrs.2023.106715

Isgrig, K., McDougald, D. S., Zhu, J., Wang, H. J., Bennett, J., and Chien, W. W. (2019). AAV2.7m8 is a powerful viral vector for inner ear gene therapy. *Nat. Commun.* 10:427. doi: 10.1038/s41467-018-08243-1

Jeng, J. Y., Ceriani, F., Hendry, A., Johnson, S. L., Yen, P., Simmons, D. D., et al. (2020). Hair cell maturation is differentially regulated along the tonotopic axis of the mammalian cochlea. *J. Physiol.* 598, 151–170. doi: 10.1113/JP279012

Klinke, R., and Galley, N. (1974). Efferent innervation of vestibular and auditory receptors. *Physiol. Rev.* 54, 316–357. doi: 10.1152/physrev.1974.54.2.316

Kong, J. H., Zachary, S., Rohmann, K. N., and Fuchs, P. A. (2013). Retrograde facilitation of efferent synapses on cochlear hair cells. *J. Assoc. Res. Otolaryngol.* 14, 17–27. doi: 10.1007/s10162-012-0361-0

Lauer, A. M., and May, B. J. (2011). The medial olivocochlear system attenuates the developmental impact of early noise exposure. *J. Assoc. Res. Otolaryngol.* 12, 329–343. doi: 10.1007/s10162-011-0262-7

Layman, W. S., Williams, D. M., Dearman, J. A., Sauceda, M. A., and Zuo, J. (2015). Histone deacetylase inhibition protects hearing against acute ototoxicity by activating the Nf-kappaB pathway. *Cell Death Discov* 1:15012. doi: 10.1038/cddiscovery.2015.12

Liberman, M. C., and Brown, M. C. (1986). Physiology and anatomy of single olivocochlear neurons in the cat. *Hear. Res.* 24, 17–36. doi: 10.1016/0378-5955(86)90003-1

Liberman, L. D., and Liberman, M. C. (2019). Cochlear efferent innervation is sparse in humans and decreases with age. *J. Neurosci.* 39, 9560–9569. doi: 10.1523/JNEUROSCI.3004-18.2019

Lioudyno, M., Hiel, H., Kong, J. H., Katz, E., Waldman, E., Parameshwaran-Iyer, S., et al. (2004). A "synaptoplasmic cistern" mediates rapid inhibition of cochlear hair cells. *J. Neurosci.* 24, 11160–11164. doi: 10.1523/JNEUROSCI.3674-04.2004

Liu, Q., Li, M., Whiteaker, P., Shi, F. D., Morley, B. J., and Lukas, R. J. (2019). Attenuation in nicotinic acetylcholine receptor alpha9 and alpha10 subunit double Knock-out mice of experimental autoimmune encephalomyelitis. *Biomol. Ther.* 9:827. doi: 10.3390/biom9120827

Lustig, L., and Akil, O. (2019). Cochlear gene therapy. *Cold Spring Harb Perspect Med* 9:a033191. doi: 10.1101/cshperspect.a033191

Ma, Y., Wise, A. K., Shepherd, R. K., and Richardson, R. T. (2019). New molecular therapies for the treatment of hearing loss. *Pharmacol. Ther.* 200, 190–209. doi: 10.1016/j.pharmthera.2019.05.003

Maison, S. F., Usubuchi, H., and Liberman, M. C. (2013). Efferent feedback minimizes cochlear neuropathy from moderate noise exposure. *J. Neurosci.* 33, 5542–5552. doi: 10.1523/JNEUROSCI.5027-12.2013

Meyer, A. C., and Moser, T. (2010). Structure and function of cochlear afferent innervation. *Curr. Opin. Otolaryngol. Head Neck Surg.* 18, 441–446. doi: 10.1097/MOO.0b013e32833e0586

Moglie, M. J., Wengier, D. L., Elgoyhen, A. B., and Goutman, J. D. (2021). Synaptic contributions to Cochlear outer hair cell ca(2+) dynamics. *J. Neurosci.* 41, 6812–6821. doi: 10.1523/JNEUROSCI.3008-20.2021

Murthy, V., Taranda, J., Elgoyhen, A. B., and Vetter, D. E. (2009). Activity of nAChRs containing alpha9 subunits modulates synapse stabilization via bidirectional signaling programs. *Dev. Neurobiol.* 69, 931–949. doi: 10.1002/dneu.20753

Olivera, B. M., Rivier, J., Scott, J. K., Hillyard, D. R., and Cruz, L. J. (1991). Conotoxins. *J. Biol. Chem.* 266, 22067–22070. doi: 10.1016/S0021-9258(18)54531-2

Pumplin, D. W., and Fambrough, D. M. (1982). Turnover of acetylcholine receptors in skeletal muscle. *Annu. Rev. Physiol.* 44, 319–335. doi: 10.1146/annurev.ph.44.030182.001535

Qi, J., Tan, F., Zhang, L., Lu, L., Zhang, S., Zhai, Y., et al. (2024). AAV-mediated gene therapy restores hearing in patients with DFNB9 deafness. *Adv Sci (Weinh)*:e2306788. doi: 10.1002/advs.202306788

Rajan, R. (2001). Noise priming and the effects of different cochlear centrifugal pathways on loud-sound-induced hearing loss. *J. Neurophysiol.* 86, 1277–1288. doi: 10.1152/jn.2001.86.3.1277

Rajan, R., and Johnstone, B. M. (1988). Binaural acoustic stimulation exercises protective effects at the cochlea that mimic the effects of electrical stimulation of an auditory efferent pathway. *Brain Res.* 459, 241–255. doi: 10.1016/0006-8993(88)90640-3

Rasmussen, G. L. (1946). The olivary peduncle and other fiber projections of the superior olivary complex. *J. Comp. Neurol.* 84, 141–219. doi: 10.1002/cne.900840204

Reijntjes, D. O. J., and Pyott, S. J. (2016). The afferent signaling complex: regulation of type I spiral ganglion neuron responses in the auditory periphery. *Hear. Res.* 336, 1–16. doi: 10.1016/j.heares.2016.03.011

Robertson, D., and Gummer, M. (1985). Physiological and morphological characterization of efferent neurones in the guinea pig cochlea. *Hear. Res.* 20, 63–77. doi: 10.1016/0378-5955(85)90059-0

Rohmann, K. N., Wersinger, E., Braude, J. P., Pyott, S. J., and Fuchs, P. A. (2015). Activation of BK and SK channels by efferent synapses on outer hair cells in high-frequency regions of the rodent cochlea. *J. Neurosci.* 35, 1821–1830. doi: 10.1523/JNEUROSCI.2790-14.2015

Rutherford, M. A., von Gersdorff, H., and Goutman, J. D. (2021). Encoding sound in the cochlea: from receptor potential to afferent discharge. *J. Physiol.* 599, 2527–2557. doi: 10.1113/JP279189

Saito, K. (1980). Fine structure of the sensory epithelium of the guinea pig organ of Corti: afferent and efferent synapses of hair cells. *J. Ultrastruct. Res.* 71, 222–232. doi: 10.1016/S0022-5320(80)90108-2

Salpeter, M. M., and Harris, R. (1983). Distribution and turnover rate of acetylcholine receptors throughout the junction folds at a vertebrate neuromuscular junction. *J. Cell Biol.* 96, 1781–1785. doi: 10.1083/jcb.96.6.1781

Simmons, D. D. (2002). Development of the inner ear efferent system across vertebrate species. *J. Neurobiol.* 53, 228–250. doi: 10.1002/neu.10130

Smith, C. A., and Sjostrand, F. S. (1961). Structure of the nerve endings on the external hair cells of the guinea pig cochlea as studied by serial sections. *J. Ultrastruct. Res.* 5, 523–556. doi: 10.1016/S0022-5320(61)80025-7

Spoendlin, H. (1985). Anatomy of cochlear innervation. *Am. J. Otolaryngol.* 6, 453–467. doi: 10.1016/S0196-0709(85)80026-0

Taranda, J., Maison, S. F., Ballestero, J. A., Katz, E., Savino, J., Vetter, D. E., et al. (2009). A point mutation in the hair cell nicotinic cholinergic receptor prolongs cochlear inhibition and enhances noise protection. *PLoS Biol.* 7:e18. doi: 10.1371/journal.pbio.1000018

Vetter, D. E., Katz, E., Maison, S. F., Taranda, J., Turcan, S., Ballestero, J., et al. (2007). The alpha10 nicotinic acetylcholine receptor subunit is required for normal synaptic function and integrity of the olivocochlear system. *Proc. Natl. Acad. Sci. USA* 104, 20594–20599. doi: 10.1073/pnas.0708545105

Vyas, P., Wood, M. B., Zhang, Y., Goldring, A. C., Chakir, F. Z., Fuchs, P. A., et al. (2020). Characterization of HA-tagged alpha9 and alpha10 nAChRs in the mouse cochlea. *Sci. Rep.* 10:21814. doi: 10.1038/s41598-020-78380-5

Wedemeyer, C., Vattino, L. G., Moglie, M. J., Ballestero, J., Maison, S. F., Di Guilmi, M. N., et al. (2018). A gain-of-function mutation in the alpha9 nicotinic acetylcholine receptor alters medial Olivocochlear efferent short-term synaptic plasticity. *J. Neurosci.* 38, 3939–3954. doi: 10.1523/JNEUROSCI.2528-17.2018

Wiederhold, M. L., and Kiang, N. Y. (1970). Effects of electric stimulation of the crossed olivocochlear bundle on single auditory-nerve fibers in the cat. *J. Acoust. Soc. Am.* 48, 950–965. doi: 10.1121/1.1912234

Yu, Z., McIntosh, J. M., Sadeghi, S. G., and Glowatzki, E. (2020). Efferent synaptic transmission at the vestibular type II hair cell synapse. *J. Neurophysiol.* 124, 360–374. doi: 10.1152/jn.00143.2020

Zachary, S., Nowak, N., Vyas, P., Bonanni, L., and Fuchs, P. A. (2018). Voltage-gated calcium influx modifies cholinergic inhibition of inner hair cells in the immature rat cochlea. *J. Neurosci.* 38, 5677–5687. doi: 10.1523/JNEUROSCI.0230-18.2018

Zhang, K. D., and Coate, T. M. (2017). Recent advances in the development and function of type II spiral ganglion neurons in the mammalian inner ear. *Semin. Cell Dev. Biol.* 65, 80–87. doi: 10.1016/j.semcdb.2016.09.017

Zhang, Y., Hiel, H., Vincent, P. F. Y., Wood, M. B., Elgoyhen, A. B., Chien, W., et al. (2023). Engineering olivocochlear inhibition to reduce acoustic trauma. *Mol Ther Methods Clin Dev* 29, 17–31. doi: 10.1016/j.omtm.2023.02.011

Zhu, J., Choi, J. W., Ishibashi, Y., Isgrig, K., Grati, M., Bennett, J., et al. (2021). Refining surgical techniques for efficient posterior semicircular canal gene delivery in the adult mammalian inner ear with minimal hearing loss. *Sci. Rep.* 11:18856. doi: 10.1038/s41598-021-98412-y

frontiers | Frontiers in Cellular Neuroscience

TYPE Original Research
PUBLISHED 17 April 2024
DOI 10.3389/fncel.2024.1363219

Check for updates

OPEN ACCESS

EDITED BY
Bernhard Englitz,
Radboud University, Netherlands

REVIEWED BY
Athanasia Warnecke,
Hannover Medical School, Germany
Soledad Levano,
University of Basel, Switzerland
Toru Miwa,
Osaka City University, Japan

*CORRESPONDENCE
Steven H. Green
✉ steven-green@uiowa.edu

RECEIVED 30 December 2023
ACCEPTED 27 March 2024
PUBLISHED 17 April 2024

CITATION
Hemachandran S, Hu N, Kane CJ and Green SH (2024) Cyclic AMP signaling promotes regeneration of cochlear synapses after excitotoxic or noise trauma. *Front. Cell. Neurosci.* 18:1363219. doi: 10.3389/fncel.2024.1363219

COPYRIGHT
© 2024 Hemachandran, Hu, Kane and Green. This is an open-access article distributed under the terms of the Creative Commons Attribution License (CC BY). The use, distribution or reproduction in other forums is permitted, provided the original author(s) and the copyright owner(s) are credited and that the original publication in this journal is cited, in accordance with accepted academic practice. No use, distribution or reproduction is permitted which does not comply with these terms.

Cyclic AMP signaling promotes regeneration of cochlear synapses after excitotoxic or noise trauma

Sriram Hemachandran, Ning Hu, Catherine J. Kane and Steven H. Green*

Department of Biology, University of Iowa, Iowa City, IA, United States

Introduction: Cochlear afferent synapses connecting inner hair cells to spiral ganglion neurons are susceptible to excitotoxic trauma on exposure to loud sound, resulting in a noise-induced cochlear synaptopathy (NICS). Here we assessed the ability of cyclic AMP-dependent protein kinase (PKA) signaling to promote cochlear synapse regeneration, inferred from its ability to promote axon regeneration in axotomized CNS neurons, another system refractory to regeneration.

Methods: We mimicked NICS *in vitro* by applying a glutamate receptor agonist, kainic acid (KA) to organotypic cochlear explant cultures and experimentally manipulated cAMP signaling to determine whether PKA could promote synapse regeneration. We then delivered the cAMP phosphodiesterase inhibitor rolipram via implanted subcutaneous minipumps in noise-exposed CBA/CaJ mice to test the hypothesis that cAMP signaling could promote cochlear synapse regeneration *in vivo*.

Results: We showed that the application of the cell membrane-permeable cAMP agonist 8-cpt-cAMP or the cAMP phosphodiesterase inhibitor rolipram promotes significant regeneration of synapses *in vitro* within twelve hours after their destruction by KA. This is independent of neurotrophin-3, which also promotes synapse regeneration. Moreover, of the two independent signaling effectors activated by cAMP – the cAMP Exchange Protein Activated by cAMP and the cAMP-dependent protein kinase – it is the latter that mediates synapse regeneration. Finally, we showed that systemic delivery of rolipram promotes synapse regeneration *in vivo* following NICS.

Discussion: *In vitro* experiments show that cAMP signaling promotes synapse regeneration after excitotoxic destruction of cochlear synapses and does so via PKA signaling. The cAMP phosphodiesterase inhibitor rolipram promotes synapse regeneration *in vivo* in noise-exposed mice. Systemic administration of rolipram or similar compounds appears to provide a minimally invasive therapeutic approach to reversing synaptopathy post-noise.

KEYWORDS

cyclic AMP-dependent protein kinase, cochlea, spiral ganglion neuron, auditory nerve, synapse, regeneration, synaptopathy, noise

Introduction

The spiral ganglion neurons (SGNs) in the cochlea transmit auditory sensation from the sensory hair cells to the brain reviewed in Nayagam et al. (2011). About 95% of the SGNs synapse on inner hair cells (IHCs). Exposure to high-intensity sound can destroy these synapses as well as the cochlear hair cells themselves. However, even at sound levels too low to permanently impair hair cell function, the synapses are vulnerable. Such noise-induced loss of cochlear synapses, also termed noise-induced cochlear "synaptopathy" (NICS), is apparent when counting IHC synapses in histological preparations of cochleae from noise-exposed animals in which the hair cells survive (Kujawa and Liberman, 2009; Lin et al., 2011). The SGNs themselves survive for many weeks after loss of their peripheral synapses (Kujawa and Liberman, 2006).

NICS can be detected in live noise-exposed animals by changes in the auditory brainstem response (ABR). After noise exposure, there is a temporary elevation of auditory threshold (temporary threshold shift, TTS) assessed by ABR and, if the noise is loud enough to cause hair cell loss, there will be a permanent elevation of auditory threshold (permanent threshold shift, PTS) (Ryan et al., 2016). If there is synapse loss only and no hair cell loss, the ABR threshold generally recovers after the TTS and there is no PTS. However, the amplitude of wave-I of the ABR, the wave corresponding to spike activity in the SGNs, is permanently reduced (Kujawa and Liberman, 2009; Lin et al., 2011). Thus, a permanent reduction of ABR wave-I amplitude without PTS after noise exposure suggests NICS without hair cell loss.

Several studies have shown NICS to be due to excitotoxic damage to the synapses caused by excessive release of glutamate from IHCs exposed to high-intensity sound. Intracochlear perfusion with glutamatergic agonists causes swelling and degeneration of postsynaptic boutons on the IHCs, resembling the consequences of noise exposure (Pujol et al., 1985; Puel et al., 1998). Compromising glutamate reuptake by knockout of the glutamate transporter GLAST exacerbates NICS (Hakuba et al., 2000); conversely, synapse loss after noise exposure can be mitigated by selective blockade of glutamate receptors (Puel et al., 1994; Hu et al., 2020) or by prevention of glutamate release from IHCs by VGluT3 knockout (Kim et al., 2019). Similarly, exposure of organotypic cochlear explants cultures to the glutamate receptor agonist kainic acid (KA) *in vitro* causes synapse degeneration resembling that which occurs after noise exposure *in vivo* (Wang and Green, 2011). This provides an *in vitro* model to facilitate the assessment of compounds that can prevent synaptopathy or promote regeneration of synapses after excitotoxic trauma. Indeed, the regeneration of synapses in the cochlea is limited even though the damaged axon terminals remain immediately adjacent to the base of the IHCs (Moverman et al., 2023). It is striking that the axons are unable to grow past this small gap, and reestablish synaptic contact with the hair cells. The use of the *in vitro* model of cochlear synaptopathy showed that neurotrophic factors, BDNF or NT-3, that promote axon regeneration in other neural systems effectively promoted regeneration of IHC-SGN synapses (Wang and Green, 2011). Indeed, NT-3 has been successfully used to promote synapse regeneration after NICS *in vivo* (Wan et al., 2014; Sly et al., 2016; Suzuki et al., 2016).

Delivery of NT-3 or other peptides intracochlearly requires invasive measures. Thus, comparably effective agents that are small molecules, which can be delivered systemically and reach the cochlea through the circulation, are prime candidates for post-noise therapy. Here we use *in vitro* and *in vivo* models of cochlear synaptopathy to investigate, as such candidates, compounds that stimulate signaling by the second messenger 3′,5′-cyclic adenosine monophosphate (cAMP). Cyclic AMP is an important second messenger that, among many intracellular functions, promotes axon growth (Roisen et al., 1972; Pichichero et al., 1973) and has been shown to promote axon regeneration within the central nervous system (CNS) (Hannila and Filbin, 2008), otherwise recalcitrant to axonal regeneration. By promoting growth cone advance, cAMP, acting via cyclic AMP-dependent protein kinase (PKA), is a crucial determinant in decisions within axonal growth cones as to whether external cues are attractive or repulsive (McFarlane, 2000). Reduced PKA activity can result in cues that are typically chemoattractants, including neurotrophins, to become chemorepulsive (Wang and Zheng, 1998; Gallo et al., 2002) while increased PKA activity can prevent repulsion of axon growth by chemorepulsive cues (Song et al., 1997, 1998; Cai et al., 2001). This ability of PKA activity to overcome cues that inhibit axon growth allows agents that activate PKA to elicit axon growth on chemorepulsive surfaces such as CNS myelin (Song et al., 1998; Cai et al., 1999, 2001; Bandtlow, 2003) and is therefore of great interest with regard to promotion of axon regeneration in injured spinal cord (Qiu et al., 2002; Hannila and Filbin, 2008; Chan et al., 2014). Moreover, the ability of neurotrophic factors to promote axon regeneration has been shown to require PKA activity (Cai et al., 1999; Gallo et al., 2002) and synergize with PKA activity (Lu et al., 2004).

Here, we hypothesize that, like axonal regeneration in the CNS, the poor regeneration of synapses after NICS is due to a chemorepulsive inhibitory cue that can be overcome by activation of PKA in SGNs. We show that two cell membrane-permeable compounds that can activate PKA signaling – a cAMP agonist and an inhibitor of 3′,5′-cyclic nucleotide phosphodiesterase 4 (PDE4) expressed in the inner ear (Degerman et al., 2017; Mittal et al., 2017) – both promote synaptic regeneration *in vitro* and the latter can promote synapse regeneration after NICS *in vivo* when delivered systemically.

Materials and methods

Animals

For experiments using organotypic cochlear cultures, we used Sprague-Dawley rat pups from our breeding colony. Animals exposed to noise were 12–14-week-old male and female CBA/CaJ mice from our breeding colony. All of the animals were housed under a regular 12-h day/night cycle with continuous access to water and food. Noise exposures were at about the same time

Abbreviations: ABR, auditory brainstem response; KA, kainic acid; NICS, noise-induced cochlear synaptopathy; P, postnatal day; PDE, phosphodiesterase; PND, post-noise day; PSD, postsynaptic density; PTS, permanent threshold shift; PKA, cyclic AMP-dependent protein kinase; TTS, temporary threshold shift.

of day for all mice. All experimental procedures were approved by the University of Iowa Institutional Animal Care and Use Committee and were performed following the relevant guidelines and regulations of the University of Iowa Institutional Animal Care and Use Committee and is reported in accordance with ARRIVE guidelines.[1]

Noise exposure and experimental groups

The mice were exposed to noise using a paradigm similar to that described by Kujawa and Liberman (2009): 100 dB SPL, octave-band noise, 8–16 kHz for 2 h. The noise was generated with a RZ6 multi I/O processor, a high-frequency power amplifier (IPR-1600 DSP, Peavey Electronics Corporation, Meridian, MS, United States), a high-frequency loudspeaker (Beyma driver CP21F 1 inch HF slot tweeter, Valencia, Spain) in a custom-made sound-proof chamber with the high-frequency speaker built into its top. The noise exposure was controlled using RpvdsEx software (Version 5.6, Tucker-Davis Technologies, Inc., Alachua, FL, United States).

Two mice awake and unrestrained, each in a small iron-wire cage, were positioned head-to-head below the center of the speaker. The noise level was monitored with a 1/4 inch condenser microphone (Model 7017, ACO Pacific, Inc., Belmont, CA, United States) placed at the center of the space between the two animals at the approximate level of the animals' ears. The variation of noise levels between the animals' ears and over the time of exposure was <1 dB.

In general, we have two criteria for exclusion of animals based on ABR (see below). (1) Temporary threshold shift <30 dB at 16 kHz, which would suggest a possibility that the noise exposure was not sufficient to cause synaptopathy. (2) Permanent threshold shift, defined as detectable threshold elevation at post-noise day 14, which would suggest that the noise damage was not limited to synaptopathy.

Systemic administration of rolipram

One day after the noise exposure, the mice were divided into two experimental groups: a DMSO control group and a Rolipram-treated group. All mice were anesthetized during the procedure using continuous inhalation of a 0.5%–5% isoflurane/oxygen mixture. The fur was shaved from the incision site at the lower neck area and the site was cleaned and antiseptic applied. An incision ∼1 cm in length was made and a subcutaneous tunnel then made from the incision site down to the lower back. Because rolipram has been reported to be eliminated rapidly after injection (Krause and Kühne, 1988), we chose to continuously infuse rolipram from an implanted minipump. A sterilized minipump was inserted into the subcutaneous tunnel. The minipumps used in this study were Alzet type 2002 minipumps (3 × 0.7 cm in size) designed for use in small animals such as adult mice. They have a flow rate of 0.5 μl/h and a capacity to deliver contents for 2 weeks. The incision was closed using absorbable suture. A local analgesia was applied to the incision site and an iodine-containing antiseptic applied directly to the wound area after suturing the skin. After recovery, the mouse was returned to the animal facility and its condition checked daily post-surgery. The minipumps were filled with either control vehicle only (DMSO) or with rolipram (Sigma; catalog #557330) dissolved in DMSO to deliver 4.4 mg/kg/day. The mice were injected intraperitoneally with 4.4 mg/kg rolipram immediately after implantation of the minipump to elevate rolipram concentration immediately while the minipump was more gradually ramping up rolipram concentration. This specific dose for the *in vivo* studies was estimated based on the results of the *in vitro* dose response study described in section "Results" and was within the range of rolipram dosages used in previous *in vivo* studies (Siuciak et al., 2007; Kraft et al., 2013).

Reported side-effects in some patients receiving PDE inhibitors have included nausea or vomiting (Spina, 2008). However, we did not observe any such signs of distress in the mice receiving rolipram at this dosage and they showed normal weight gain. At the time of euthanasia (14–16 weeks of age), the mean (± SD) weight for rolipram-treated mice was 26.7 ± 3.3 g, not significantly different from DMSO-only control mice, 29.2 ± 7.5 g.

Measurement of auditory brainstem response

Our procedure for measuring ABR has been described in detail previously (Hu et al., 2020) and is briefly summarized here. Responses were recorded from anesthetized mice from 90 dB SPL to 10 dB below the threshold level in 10 dB steps, and repeated in 5 dB steps near-threshold, the lowest stimulus level that evokes an identifiable ABR wave-I. The wave-I amplitude was measured between the first positive maximum to the following negative minimum. Wave-I amplitudes as a function of stimulus intensity were fitted by a two-order polynomial function for group comparisons. A RZ6 multi I/O processor with BioSigRZ software, a RA4PA 4 channel preamplifier, and a MF1 speaker (Tucker-Davis Technologies, Inc.) were used to deliver the acoustic stimuli and record the response signal. The acoustic stimuli were delivered to the external auditory meatus of the mouse from the MF1 speaker via a custom-made insertion tube. These consisted of 5 ms tone-pips presented at a rate of 21/s, alternating polarities, at frequencies of 8, 16, and 32 kHz. An active needle electrode was placed at the midline of the vertex of the skull, a reference electrode at the ipsilateral mastoid, and a ground electrode in the lower back. The acquisition time was 12 ms, at a sampling rate of 25,000/s with a band-pass filter 300–3,000 Hz, averaged over 128–1,024 sweeps.

Synapse counts in cochlear wholemounts

After the ABR measure on PND14, mice were deeply anesthetized using an intraperitoneal injection of 80–100 mg/kg ketamine/10–12.5 mg/kg xylazine. While under surgical plane of anesthesia, the mice were exsanguinated by intracardial perfusion, first with ice-cold saline, then with 4% paraformaldehyde fixative,

1 https://arriveguidelines.org

followed by decapitation. Processing of the tissue for synapse counts in whole-mount preparations was essentially as we have previously described (Hu et al., 2020). The temporal bones were removed and dissected quickly in ice-cold PBS. Most of the bony structure around the cochlea was carefully removed to expose the cochlea, which was fixed in 4% paraformaldehyde for 12 min, washed with ice-cold PBS, and transferred to 0.12 mM EDTA for decalcification at 4°C for 48 h. After decalcification, the cochlea was permeabilized with 1% Triton X-100 in PBS for 1 h at room temperature, washed three times with 1% Triton X-100 in PBS, and blocked in PBS with 0.1% Triton X-100, 5% horse serum, 0.1% bovine serum albumin (blocking buffer) for 60 min at room temperature.

Immunofluorescent labeling used the following primary antibodies in blocking buffer at 4°C for 24 h: myosin 6 and/or myosin 7a (Sigma), 1:400, to label the hair cells; anti-CtBP2 mouse IgG1 (BD Transduction Labs), 1:400, to label the presynaptic ribbons; and anti-PSD95 (Thermo-Scientific), 1:400, to label the postsynaptic densities (PSDs) on the SGN postsynaptic boutons. Further fixation after primary antibodies was for 2 h in 4% PFA. Fluorescent secondary antibodies used were Alexa Fluor 488-goat anti-Mouse IgG1, Alexa Fluor 546 goat anti-Mouse IgG2a, and Alexa Fluor 633 goat anti-rabbit in blocking buffer incubated at 4°C for 24 h in blocking buffer.

After immunolabeling the cochlea was cut into 5–6 pieces and mounted on a glass coverslip and imaged using a Leica SPE confocal microscope. First, a low magnification image was acquired to measure the lengths of the pieces and align them to the mouse tonotopic map according to Muller's length-frequency equation (Muller et al., 2005). Using the Muller equation, the 8, 16, and 32 kHz locations of the cochlea were identified and imaged at higher magnification with a 63× / 1.3 NA oil objective and additional 3× electronic magnification to obtain clear images of synapses. For counting purposes, we operationally define a synapse as a colocalized presynaptic ribbon and PSD. All synapses on all hair cells wholly included in the field were counted and the synapse number divided by the number of IHCs in the field to obtain synapses/IHC. The counts were made, using ImageJ, in 3D image stacks in which the optical sections in the *x*-*y* plane ("*z*-sections") were captured at a spacing of 0.3 μm along the *z*-axis. The representative images shown in the figures in this paper are the maximum intensity *Z*-projections of such stacks although, for counting, we used the original image stacks, not the *Z*-projections. An ImageJ macro was used to assign a random eight-digit number to all images so the person counting was unaware of the experimental group.

Cochlear organotypic culture

Organotypic cochlear explant cultures were used for synapse counts following excitotoxic trauma *in vitro*. Our procedure for preparation of organotypic cochlear explant cultures has been described in detail previously (Wang and Green, 2011) and is briefly summarized here. After euthanasia by decapitation, the cochleae of postnatal day 5 (P5) rat pups of both sexes were removed and dissected in ice-cold PBS. The middle turn of the cochlea was used for these experiments to reduce variability due to physiological differences along the tonotopic axis and because this region corresponds to the region of the cochlea targeted by the octave-band noise exposure *in vivo*. After separating the membranous labyrinth from the modiolus, the non-sensory regions were removed using fine forceps, leaving just the organ of Corti and the corresponding part of the spiral ganglion intact. Each explant was transferred to a separate well of a multichambered coverglass system (Lab-Tek; catalog #155411) where it was positioned on a glass coverslip coated with polyornithine (100 μg/ml; Sigma; catalog #P3655) and laminin (20 μg/ml; Gibco; catalog #23017015). The explants were cultured in DMEM/N2/20% fetal bovine serum (Gibco; catalog #11965092/Gibco; catalog #17502048/Gibco; catalog #26140079) at 37°C, 6.5% CO_2.

The explant was left undisturbed for ∼16 h to allow it to firmly attach to the coverslip. We have previously described (Wang and Green, 2011) 2 h treatment with 0.5 mM kainic acid (KA; Tocris; catalog #0222) to cause excitotoxic trauma. After the washout of the KA, the explants were maintained for up to 72 h, as indicated in the individual figures, in control culture medium or in culture medium with experimental agents added. Experimental agents used in this study were 8-cpt-cAMP (1 mM; Sigma; catalog #c3912), a stable cell membrane-permeable cAMP agonist; 8-cpt-2-O-Me-cAMP (100 μM; Sigma; catalog #c8988) a stable cell membrane-permeable cAMP agonist selective for the exchange protein activated by cAMP (EPAC) pathway; rolipram (2.4 μM; Sigma; catalog #557330), a PDE4 inhibitor; 50 ng/ml Neurotrophin-3 (NT-3, Cell Signaling; catalog #5273); 2 μg/ml TrkC-IgG, a selective NT-3 antagonist was produced in our lab (Wang and Green, 2011); H-89 (20 μM; Sigma; catalog #371963-M) a PKA inhibitor. Inhibitors, TrkC-IgG or H89, were added to the cultures 15 min prior to the addition of other experimental agents to ensure that these inhibitors were already in place.

After experimental treatment for the appropriate duration, the cultures were fixed using 4% paraformaldehyde for 7 min, then permeabilized with 1% Triton X-100. Immunolabeling of hair cells, PSDs, and presynaptic ribbons, followed by confocal imaging, randomization, and synapse counting, were done as described above for cochlear wholemount preparations.

Results

cAMP induces synapse regeneration *in vitro* via cAMP-dependent protein kinase signaling

As an *in vitro* model for NICS, we have previously shown that exposing organotypic cochlear explant cultures to the excitotoxin kainic acid results in loss of afferent synapses on IHCs (Wang and Green, 2011). The PSDs are nearly all gone by the end of a 2 h exposure to excitotoxins although presynaptic ribbons remain. We used this model system to show that neurotrophins NT-3 and BDNF promote synapse regeneration *in vitro* (Wang and Green, 2011) and here use it to ask whether cAMP signaling can promote synapse regeneration and, if so, by which signaling pathway. As described in section "Materials and methods," the cochleae are cultured overnight, exposed to 0.5 mM KA for 2 h, cultured for a further 3 days in experimental or control media, then fixed and

imaged to assess synapse regeneration. Representative images are shown in **Figure 1** for control cultures and cultures maintained with modulators of cAMP signaling after excitotoxic destruction of synapses.

Figure 1A shows images of a representative control culture not exposed to KA (No KA control) that can be contrasted with comparable images of a KA-treated culture, 3 days post-KA, shown in **Figure 1B**. KA treatment causes a near-complete loss of PSDs (visualized by PSD95 immunoreactivity), although the presynaptic ribbons (visualized by CtBP2 immunoreactivity) persist even 3 days post-KA, as we have previously shown (Wang and Green, 2011). As shown in **Figure 1C**, maintaining the cultures in the cell-permeant cAMP agonist, 8-cpt-cAMP (1 mM) during the 3-day post-KA period restores a significant number of PSDs. The regenerated PSDs colocalize with the synaptic ribbons implying that these are synapses. For KA-treated cultures, the number of synapses (operationally defined as colocalized PSDs and ribbons) in cultures maintained in 8-cpt-cAMP is significantly greater than in cultures with no added 8-cpt-cAMP (**Figure 1G**).

Intracellular signaling initiated by cAMP utilizes at least two distinct cAMP-responsive effectors, both of which can be activated by 8-cpt-cAMP: the Exchange Protein Activated by cAMP (EPAC) (Robichaux and Cheng, 2018) and cAMP-dependent protein kinase (protein kinase A, PKA) (Taylor et al., 2013). Having implicated cAMP signaling, we asked which of these alternative effectors is utilized to effect cochlear synapse regeneration. As shown in **Figures 1D, G**, the EPAC-selective cAMP agonist, 8-cpt-2-O-Me-cAMP, fails to promote synapse regeneration. Maintenance of KA-exposed cochlear explants in 8-cpt-2-O-Me-cAMP results in synapse numbers significantly lower than maintenance in 8-cpt-cAMP and not significantly different from control KA-exposed cochlear explants. This implies that cAMP promotes regeneration via the PKA pathway rather than the EPAC pathway. To test that directly, we added the PKA inhibitor H-89 to cultures maintained in 8-cpt-cAMP. H-89 abrogated the effect of 8-cpt-cAMP on synapse regeneration, as can be seen by the lack of PSDs in **Figure 1D** and the quantified data in **Figure 1G**.

We next assessed the effect on synapse regeneration of an alternative means of activating PKA: raising intracellular cAMP levels by inhibiting cyclic AMP phosphodiesterase (PDE), the enzyme that metabolizes cAMP. A particular isoform of PDE, PDE type 4 (PDE4), is ubiquitously and highly expressed in nervous tissue (Bolger et al., 1993; Omori and Kotera, 2007) so is likely to play a major role in the metabolism of cAMP in neurons. PDE4 is selectively inhibited by the compound rolipram (Weishaar et al., 1985), which has been previously used as neuroprotective agent to promote SGN survival *in vitro* (Hegarty et al., 1997; Bok et al., 2003; Kranz et al., 2014; Glueckert et al., 2015).

We tested rolipram at 0.8, 2.4, and 8 μM for ability to promote synapse regeneration. Rolipram effectively promoted a significant recovery of synapses post-KA (**Figure 1F**). The quantified data in **Figure 1G** shows that 2.4 or 8 μM rolipram were approximately equally effective in promoting synapse regeneration, comparable to 1 mM 8-cpt-cAMP with synapse numbers restored to 60%—0% of the No-KA control. Rolipram at 0.8 μM was effective but significantly less so than at 2.4 μM. These results are consistent with a reported $ED_{50} \approx 0.8$ μM for the particular rolipram stereoisomer that we used (Underwood et al., 1994).

Rolipram-induced synapse regeneration is maximal within 12 h

In the preceding experiments, a 3 day period was allowed for synapse regeneration because we had previously allowed a 3 day period for neurotrophin-induced regeneration (Wang and Green, 2011). To investigate whether cAMP-induced regeneration might occur more quickly than this, we compared cultures maintained up to 16 h post-KA in control medium to cultures maintained post-KA in medium containing 2.4 μM rolipram. We fixed the cultures 8, 12, or 16 h after washout of KA and representative images of these cultures are shown in **Figures 2A–E**. Cultures maintained without rolipram post-KA show no evidence of synapse regeneration (**Figure 2F**) but cultures maintained in rolipram show synapse regeneration within 8 h post-KA, which reaches its maximum extent by 12 h post-KA.

Rolipram-induced cochlear synapse regeneration does not require NT-3

Our previous study of cochlear synapse regeneration (Wang and Green, 2011) showed that NT-3, the major neurotrophin expressed in the mature organ of Corti (Bailey and Green, 2014), is necessary for cochlear synapse regeneration *in vitro*. Specifically, sequestration of endogenous NT-3 using TrkC-IgG significantly diminished the ability of BDNF to promote synapse regeneration when added to the culture medium. Here we asked whether NT-3 signaling is necessary for promotion of synapse regeneration by cAMP.

Sequestration of endogenous NT-3 would similarly diminish the ability of cAMP signaling to promote synapse regeneration. Possible reasons for this might include synergism between cAMP and NT-3 signaling or cAMP promoting synapse regeneration by stimulating NT-3 synthesis or secretion. We used the same strategy as in Wang and Green (2011) to block NT-3 signaling: addition of TrkC-IgG fusion protein, which binds NT-3 with high affinity and specificity, to the culture wells. The effectiveness of TrkC-IgG can be seen by comparing **Figures 3A, B**, which shows that synapse regeneration normally promoted by NT-3 is prevented by TrkC-IgG. In contrast, synapse regeneration promoted by rolipram is apparently not reduced by TrkC-IgG (**Figures 3C, D**). These data indicate that neurotrophins and cAMP use approximately equally effective, but distinct, signaling pathways to promote synapse formation.

Rolipram promotes synapse regeneration *in vivo* following noise exposure

Having shown that rolipram can promote synapse regeneration *in vitro* following excitotoxic trauma, we next asked whether rolipram can, likewise, promote synapse regeneration *in vivo* following NICS. The design of the experiment is diagrammed in **Figure 4A**. The rolipram administration began 1 day after the noise exposure (post-noise day 1, PND1) to avoid any possible effects on NICS itself and to restrict this study to the effects

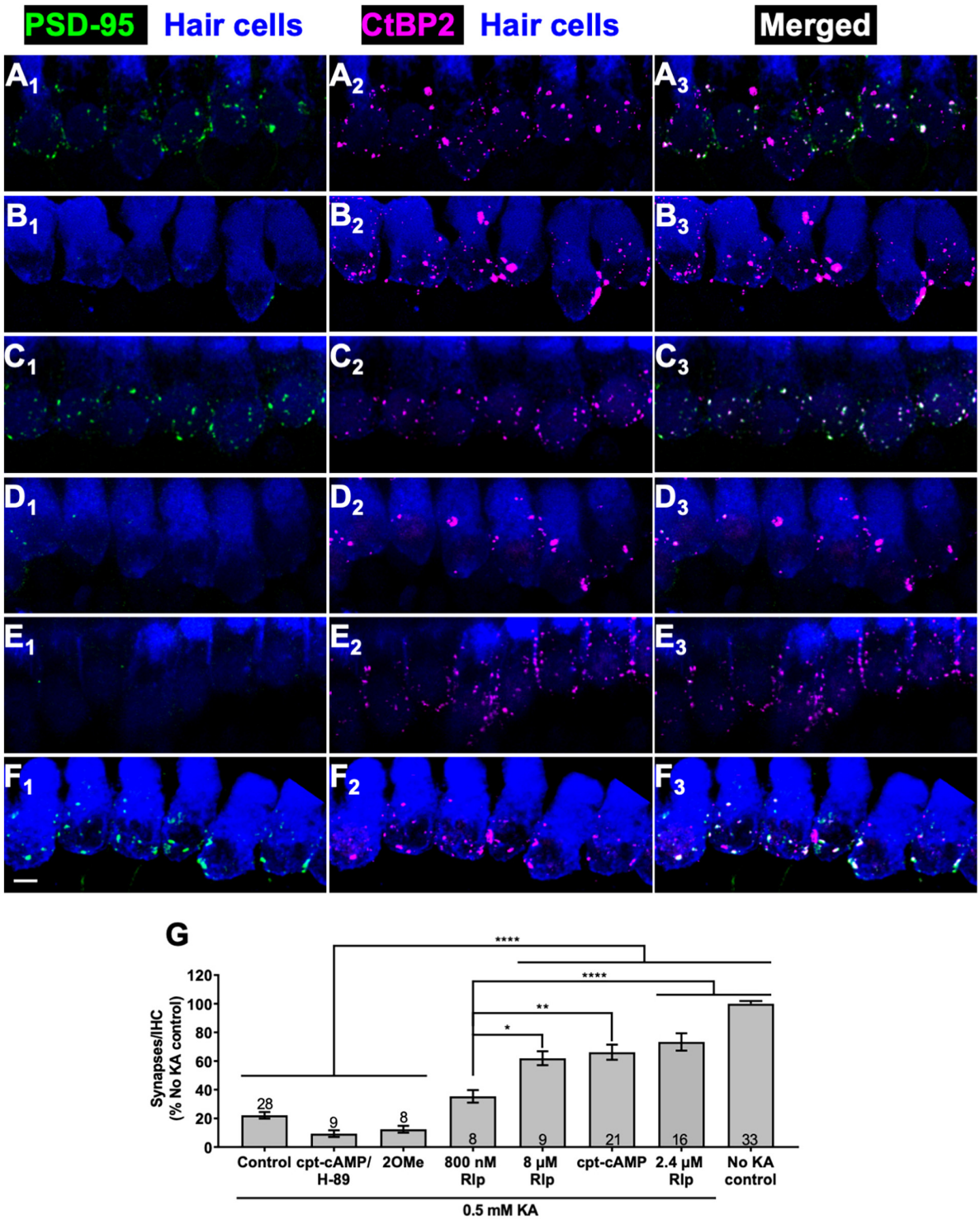


FIGURE 1
Cyclic AMP-dependent protein kinase signaling promotes synapse regeneration. **(A–F)** Examples of organotypic cochlear cultures: middle region of P5 rat cochleae exposed to 0.5 mM KA for 2 h and fixed after an additional 72 h post-KA exposed to the indicated experimental treatments: **(A)** no kainate exposure control; **(B–F)** 0.5 mM kainate; **(B)** control, no added factors; **(C)** 1 mM cpt-cAMP; **(D)** 1 mM cpt-cAMP with 20 μM H-89; **(E)** 0.5 mM 100 μM 8-cpt 2MeO cAMP; **(F)** 2.4 μM rolipram. In this figure and all following figures showing confocal images, what is shown in each image is a projection of the 3D volume to a single plane (*Z*-projection), the actual synapse counts were done on the original 3D confocal image stacks. The explants were labeled to detect postsynaptic densities (PSDs, anti-PSD95), presynaptic ribbons (anti-CtBP2), and hair cells (anti-myosin VI). Column 1 shows PSDs (green) and hair cell labeling (blue); column 2 shows ribbons (magenta) and hair cell labeling (blue); column 3 shows merged hair cell, ribbon and PSD labeling to show colocalization of PSDs and ribbons. Scale is the same for all images; scale bar, 20 μm (panel F_1). **(G)** Synapses/IHC present 72 h after a 2 h exposure to KA, relative to cultures not exposed to KA (expressed as a percentage). Shown are means ± SEM for the indicated number of organotypic cochlear explant cultures. Significance of differences among conditions for each value of kainate was determined by ANOVA with Tukey's multiple comparisons test: $*p < 0.05$, $**p < 0.01$, $****p < 0.0001$. After KA, cultures were maintained in medium containing CPT-cAMP (1 mM), CPT-cAMP (1 mM) and PKA inhibitor H89 (20 μM), EPAC-selective activator 8-pCPT-2-O-Me-cAMP (100 μM), or PDE4 inhibitor rolipram (Rlp) at the three concentrations indicated.

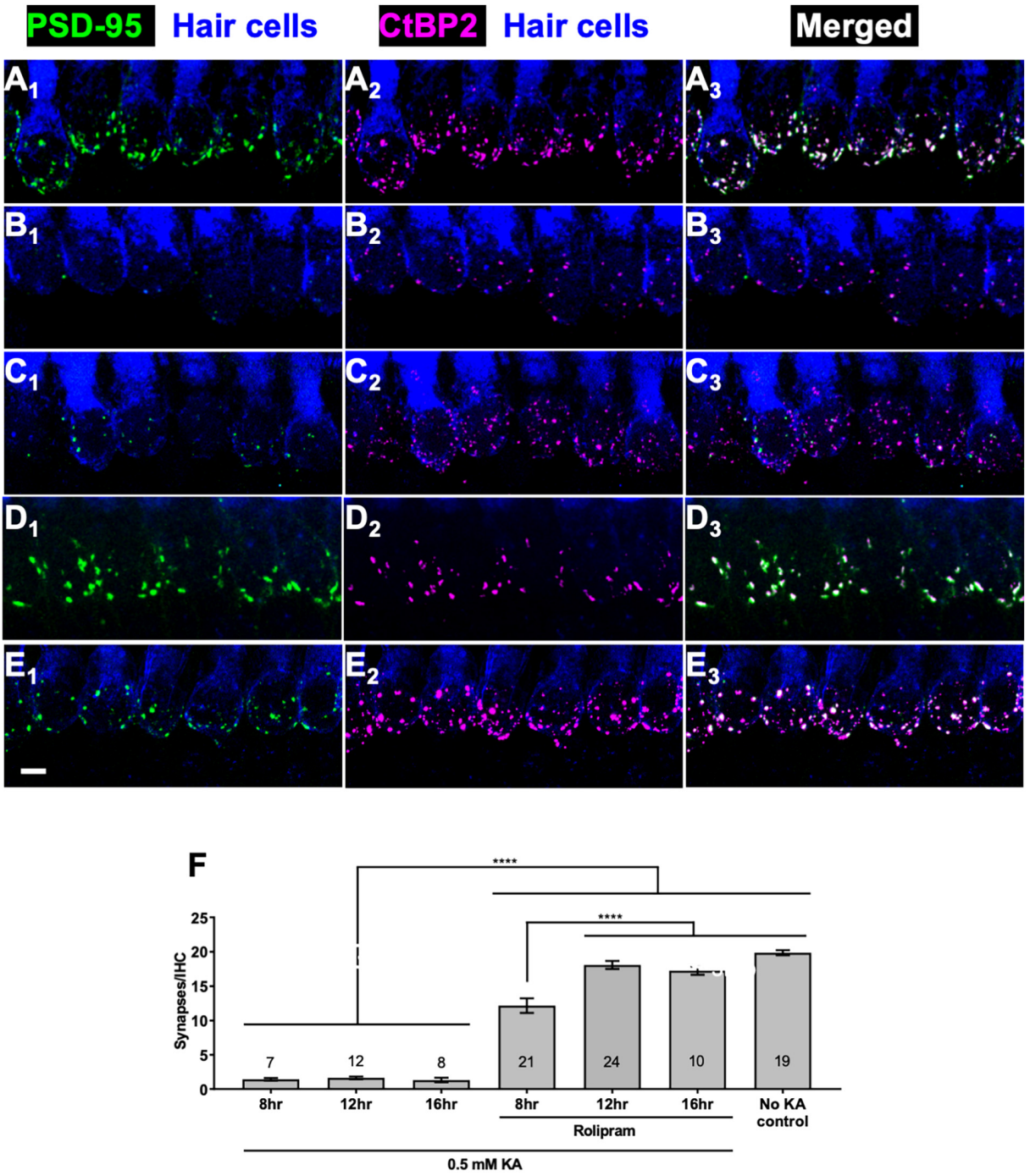


FIGURE 2
Rolipram promotes synapse regeneration within 12 h. Explants were labeled to detect SGN peripheral axons, postsynaptic densities, presynaptic ribbons, and hair cells and representative images displayed as described in Figure 1. **(A)** No KA control; **(B–E)** 2 h exposure to 0.5 mM KA followed by 16 h in control medium with no added factors **(B)** or in medium with 2.4 μM rolipram for 8 h **(C)** or 12 h **(D)** or 16 h **(E)**. All panels are at the same magnification. Scale is the same for all images; scale bar, 20 μm (panel E_1). **(F)** Quantitation of synapses/IHC present 8, 12, or 16 h after a 2 h exposure to KA for cultures maintained with or without rolipram (2.4 μM). Shown are means ± SEM for the indicated number of organotypic cochlear explant cultures. The significance of differences among conditions was determined by ANOVA with Tukey's multiple comparisons tests: ****$p < 0.0001$.

of rolipram on post-noise synapse regeneration. The rolipram concentration was rapidly established by an injection on PND1 and then maintained continuously by an implanted minipump until PND14 when the mouse was euthanized. The rolipram in the minipump was dissolved in DMSO and the control mice were treated identically to the rolipram-treated mice except that the minipump was filled with DMSO only.

Auditory brainstem response was measured three times for each mouse (Figure 4). First, the ABR was measured 2–6 days (typically 5 days) prior to noise exposure to establish a baseline

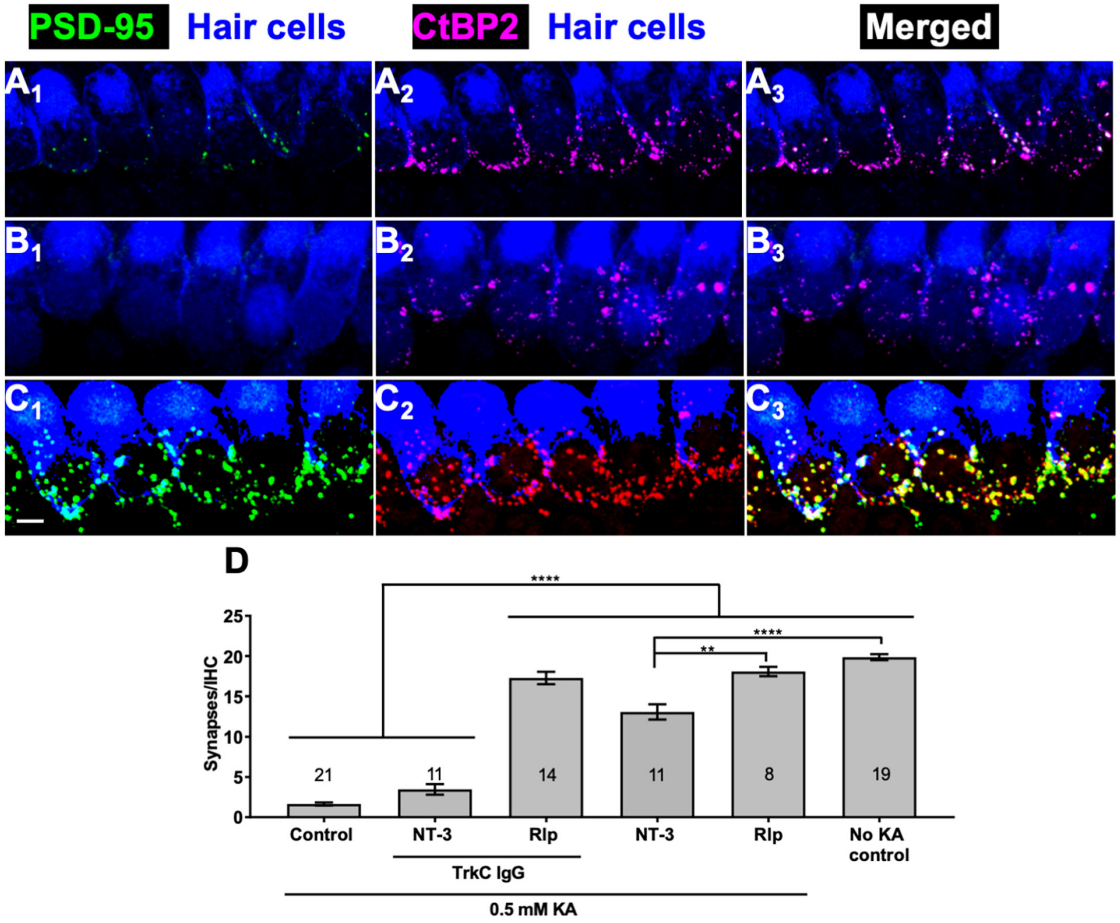


FIGURE 3
Rolipram-induced synapse regeneration does not require endogenous NT-3. TrkC-IgG was used to block TrkC signaling. Explants were labeled to detect postsynaptic densities, presynaptic ribbons, and hair cells and representative images displayed as described in **Figure 1**. Synapses were allowed to regenerate for 12 h after KA exposure in the indicated conditions. **(A)** NT-3 (50 ng/ml); **(B)** NT-3 (50 ng/ml), and TrkC-IgG (2 μg/ml); **(C)** rolipram (Rlp, 2.4 μM) and TrkC-IgG (2 μg/ml). All panels are at the same magnification. Scale is the same for all images; scale bar, 20 μm (lower left panel C_1). **(D)** Quantification of synapses/IHC present 12 h after a 2 h exposure to KA for cultures maintained with NT-3 (50 ng/ml) or rolipram (2.4 μM) and with or without TrkC-IgG (2 μg/ml). Shown are means ± SEM for the indicated number of organotypic cochlear explant cultures. The significance of differences among conditions was determined by ANOVA with Tukey's multiple comparisons test: $^{**}p < 0.01$, $^{****}p < 0.0001$.

for each mouse to which post noise measures could be compared. Second, ABR was measured 1 day after noise exposure (post-noise day 1, PND1), immediately prior to the surgery to implant the minipump, to assess the effectiveness of the noise exposure. The average TTS at PND1 in our studies was 10 dB at 8 kHz, 40 dB at 16 kHz, and 50 dB at 32 kHz. Mice with a TTS <30 dB at 16 and 32 kHz were excluded from the study because of the possibility that the noise exposure was insufficient to cause synaptopathy. A final ABR measure was performed on post-noise day 14 (PND14) immediately prior to euthanasia. One purpose of the PND14 measure was to establish the lack of a PTS, i.e., that the mice used in this study had normal (same as prenoise baseline) auditory thresholds. Synaptopathy alone cannot cause significant threshold elevation (see discussion in Lin et al., 2011) so threshold elevation at PND14 implies hearing impairment due to noise damage other than synaptopathy, presumably, hair cell loss. As this study focuses exclusively on hearing impairment due to synaptopathy, ears with threshold elevation >10 dB at PND14, relative to the pre noise ABR, were excluded. The ABR measure at PND14 was also used for the quantitation of wave-I amplitude. With no PTS, a significant reduction in wave-I amplitude relative to the pre noise ABR measure implies synaptopathy. As shown in **Figures 4B–D**, the mice in this study showed a significant TTS at PND1 and a lack of significant PTS at PND14, relative to their pre noise ABR measures.

Immediately after the PND14 ABR measure, the mice were sacrificed and the cochleae dissected for histology so the synapses could be directly counted. **Figure 5** shows representative images of afferent synapses labeled in the cochlea preparations from rolipram-treated and control mice at three cochlea locations: 8, 16, and 32 kHz. Noise damage to synapses is more intense at higher frequencies (Kujawa and Liberman, 2009) so, because the noise exposure was an 8–16 kHz octave band, synapse loss at the 8 kHz location was minor (**Figures 5A, G**) but there was significant synapse loss in control (DMSO only) mice at the 16 and 32 kHz locations (**Figures 5C, E, G**). In contrast, mice receiving rolipram did not exhibit significant synapse loss (**Figures 5D, F, G**). Because the rolipram was administered after the noise exposure, we do

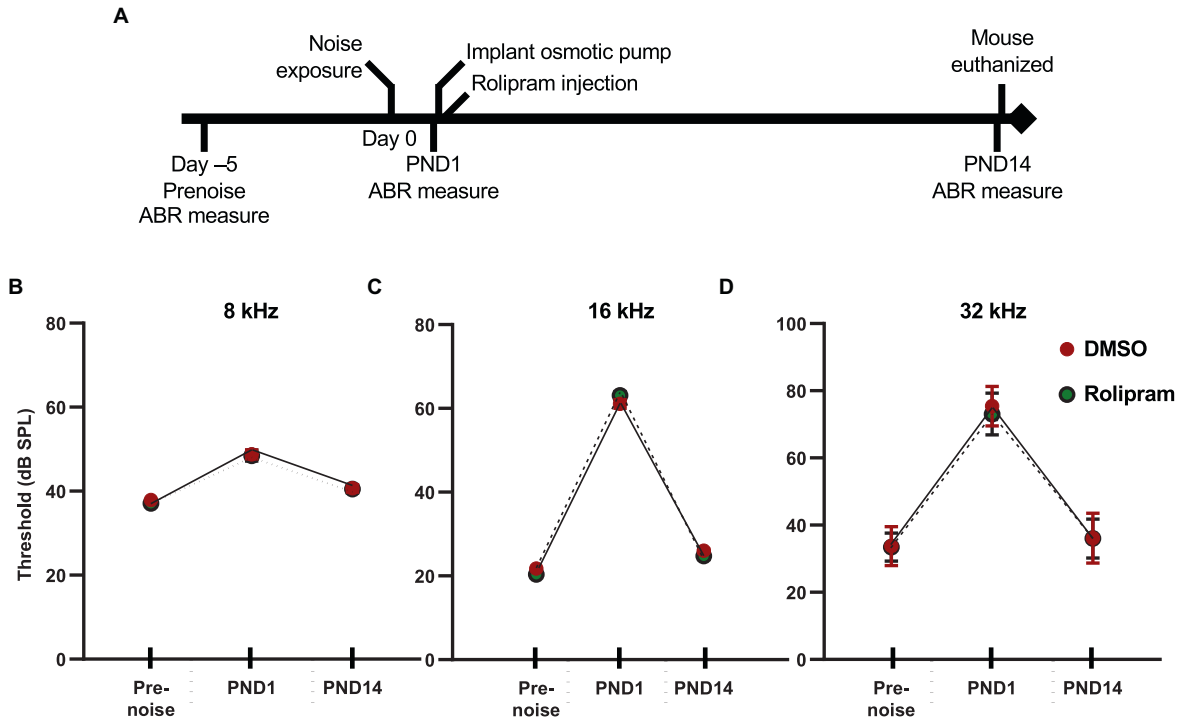


FIGURE 4
In vivo assessment of rolipram: timeline of ABR measures and corresponding auditory thresholds. **(A)** Timeline for the noise exposure experiments shows times relative to noise exposure (day 0) for three ABR measures: (1) prenoise, to verify normal hearing and establish a baseline for each individual mouse for normalization of post-noise measures; (2) postnoise day 1 (PND1), to measure temporary threshold shift (TTS) and verify effective noise exposure; and (3) postnoise day 14 (PND14) to ensure lack of permanent threshold shift and to measure wave-I amplitude. **(B–D)** Measures of ABR thresholds (mean ± SD) at, respectively, 8, 16, and 32 kHz for each of the three timepoints shown in panel **(A)** for noise-exposed mice implanted with subcutaneous minipumps delivering systemically only DMSO (DMSO, $n = 23$) or rolipram in DMSO (rolipram, $n = 24$). These data show a similar threshold elevation (>40 dB for 16 and 32 kHz tone pips) between prenoise and 1 day postnoise (TTS), and subsequent return to prenoise threshold by post-noise day 14. There was no significant difference in these measures between DMSO and rolipram, indicating that rolipram affects neither the TTS nor recovery from the TTS.

not infer that rolipram was protective against noise damage but, rather, that rolipram promoted synapse regeneration after noise. This is consistent with the observation of cAMP-promoted synapse regeneration following excitotoxic destruction of synapses *in vitro*.

Rolipram partially restores ABR wave-I amplitude following noise exposure

We next asked whether the restored synapses *in vivo* were functional. Because synapse loss results in a reduction in ABR wave-I amplitude, a physiological indication of functional recovery would be increased wave-I amplitude in rolipram-treated mice relative to control mice. This was tested at PND14, by which time auditory thresholds had recovered in the noise-exposed mice. The ABR was recorded at 8, 16, and 32 kHz. The ABR wave-I amplitude at PND14 for 8 kHz stimuli (Figures 6A, B) did not show a significant change from the pre noise amplitude, consistent with the lack of significant change in synapse number, nor was there any affect of rolipram (Figure 6G).

The ABR for 16 kHz tones, as expected, showed a significant decline in wave-I amplitude at PND14 in control mice relative to the pre noise measure (Figure 6C). Rolipram treatment resulted in a partial recovery of wave-I amplitude (Figure 6D) that was significant at sound intensities >60 dB SPL (Figure 6H). Similarly, at 32 kHz, the wave-I amplitude at PND14 had declined relative to the pre noise level in control mice (Figure 6E), a decline that partially recovered in rolipram-treated mice (Figures 6F, I). Rolipram appears to promote a complete or near-complete structural recovery and a partial functional recovery of cochlear synapses by PND14.

Chronic rolipram does not itself affect the ABR or synapse numbers

We considered the possibility that rolipram simply promotes axon sprouting in the cochlea whether or not there has been synapse loss. Such a general effect on axon sprouting could appear to be specifically rolipram-induced synapse regeneration but is rather attributable to a very different process. We therefore tested the possibility that rolipram generally induces sprouting by delivering rolipram to non-noise-exposed mice for 2 weeks using a minipump, following the identical protocol as had been used for the noise-exposed mice. Because the mice were not noise-exposed, we could include both male and female mice. As shown in Figure 7, synapse number is not significantly affected by a 2 week exposure to rolipram. Also, ABR wave-I amplitude is unaffected by

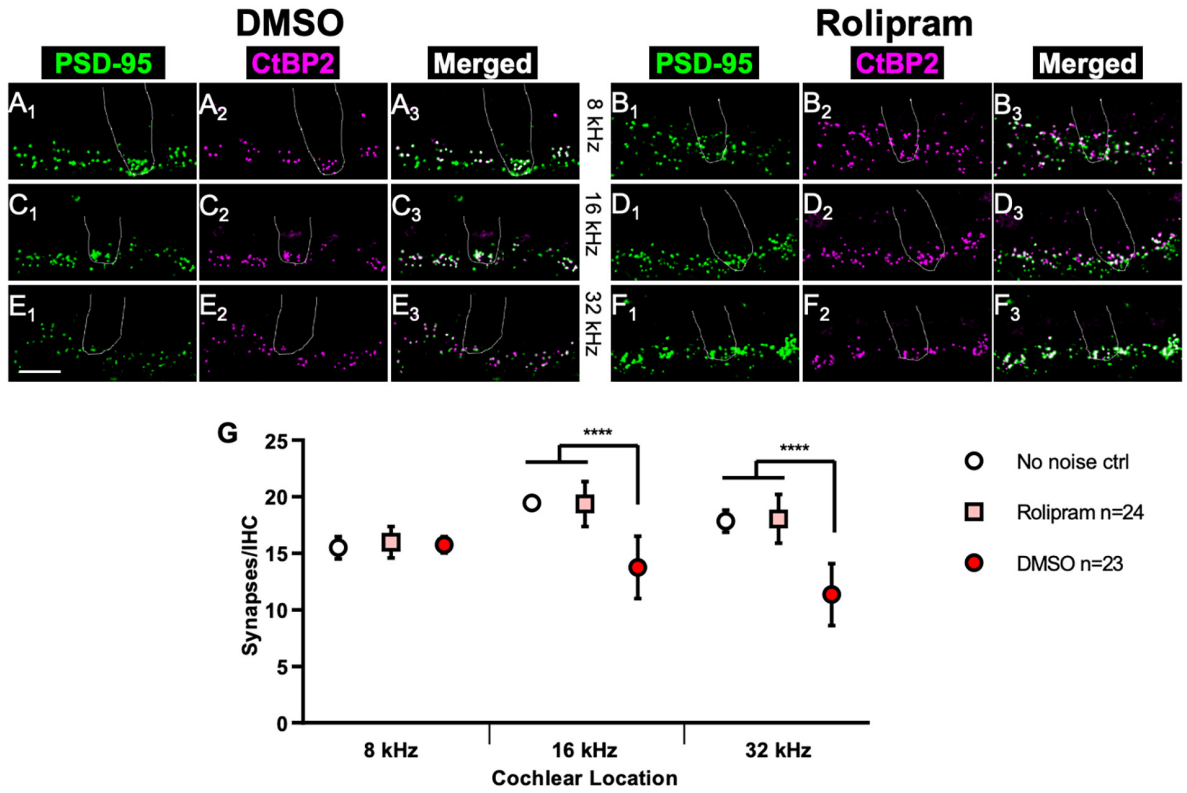


FIGURE 5
Mice treated with rolipram during noise exposure exhibit reduced synapse loss. **(A–F)** Dissected cochlear wholemount preparations were labeled (see section "Materials and methods") to detect postsynaptic densities (green) and presynaptic ribbons (magenta), using the same antibodies as for Figure 1. Shown are representative examples at three cochlear locations, 8 kHz **(A,B)**, 16 kHz **(C,D)**, and 32 kHz **(E,F)** from mice in which either control DMSO **(A,C,E)** or DMSO with 4.4 mg/Kg/day rolipram **(B,D,F)** was delivered starting after the noise exposure. The location of a hair cell is shown by the dotted outline in each panel. Scale is the same for all images; scale bar, 10 μm (lower left panel E_1). **(G)** Quantification of synapses/IHC for noise-exposed mice treated with control DMSO vehicle only and noise-exposed mice treated with rolipram in DMSO. Shown are means ± SEM for the indicated number of ears. The significance of differences among the three experimental groups was determined by ANOVA with Tukey's multiple comparisons test: ****$p < 0.0001$. Synapses/IHC for control non-noise-exposed ears (No noise ctrl) is from Hu et al. (2020).

this same chronic exposure to rolipram. These data imply that the apparent rescue of synapse number observed in rolipram-treated mice is not due to sprouting of undamaged axons but, rather, to repair/regeneration of damaged synapses.

Discussion

Studies of noise-exposed mice and guinea pigs have shown that cochlear afferent synapses on the IHCs are susceptible to noise damage even at noise exposures too low to destroy the hair cells themselves (Kujawa and Liberman, 2009; Lin et al., 2011; Sergeyenko et al., 2013; Liberman, 2017). Studies of postmortem human cochleae have correspondingly shown reduced numbers of synapses on surviving hair cells (Viana et al., 2015) and the primary death of SGNs (Makary et al., 2011). In humans, this loss of synapses has been implicated in diminished speech-in-noise comprehension (Shaheen et al., 2015), and tinnitus (Schaette and McAlpine, 2011). Therefore, means to promote synapse regeneration may be valuable for reducing hearing impairment. We have shown that treatment with neurotrophic factors promotes cochlear synapse regeneration *in vitro* following synapse destruction by excitotoxic trauma (Wang and Green, 2011). This approach has been successfully extended to show synapse regeneration by NT-3 *in vivo* in mice after NICS (Wan et al., 2014; Sly et al., 2016; Suzuki et al., 2016).

Here, we take a different approach to synapse regeneration. The distal axons of the SGNs fail to regenerate their terminals and synapses, in spite of the proximity of the hair cells. We hypothesize that there might be an inhibitory signal for SGN axons analogous to inhibition of axon regeneration in the CNS. Consistent with that hypothesis, is that a function-blocking antibody to a chemorepellent axon guidance factor, RGMa, promotes synapse regeneration after noise exposure (Nevoux et al., 2021).

For axon regeneration in the CNS, the ability of neurotrophic factors to promote regeneration was found to be PKA-dependent (Cai et al., 1999). Moreover, treatment with agents that activated cAMP signaling was also capable of promoting axon regeneration (Qiu et al., 2002) via PKA (Aglah et al., 2008). While the possibility of an inhibitory signal in cochlea has not been tested directly, nevertheless, it suggested that activators of PKA might promote regeneration of cochlear synapses. Indeed, our experiments with cultured organotypic cochlear explants showed that the ability of 8-cpt-cAMP, a cell membrane-permeable cAMP mimetic, to promote synapse regeneration likewise requires PKA activity. A possible advantage over neurotrophic factors is that activators

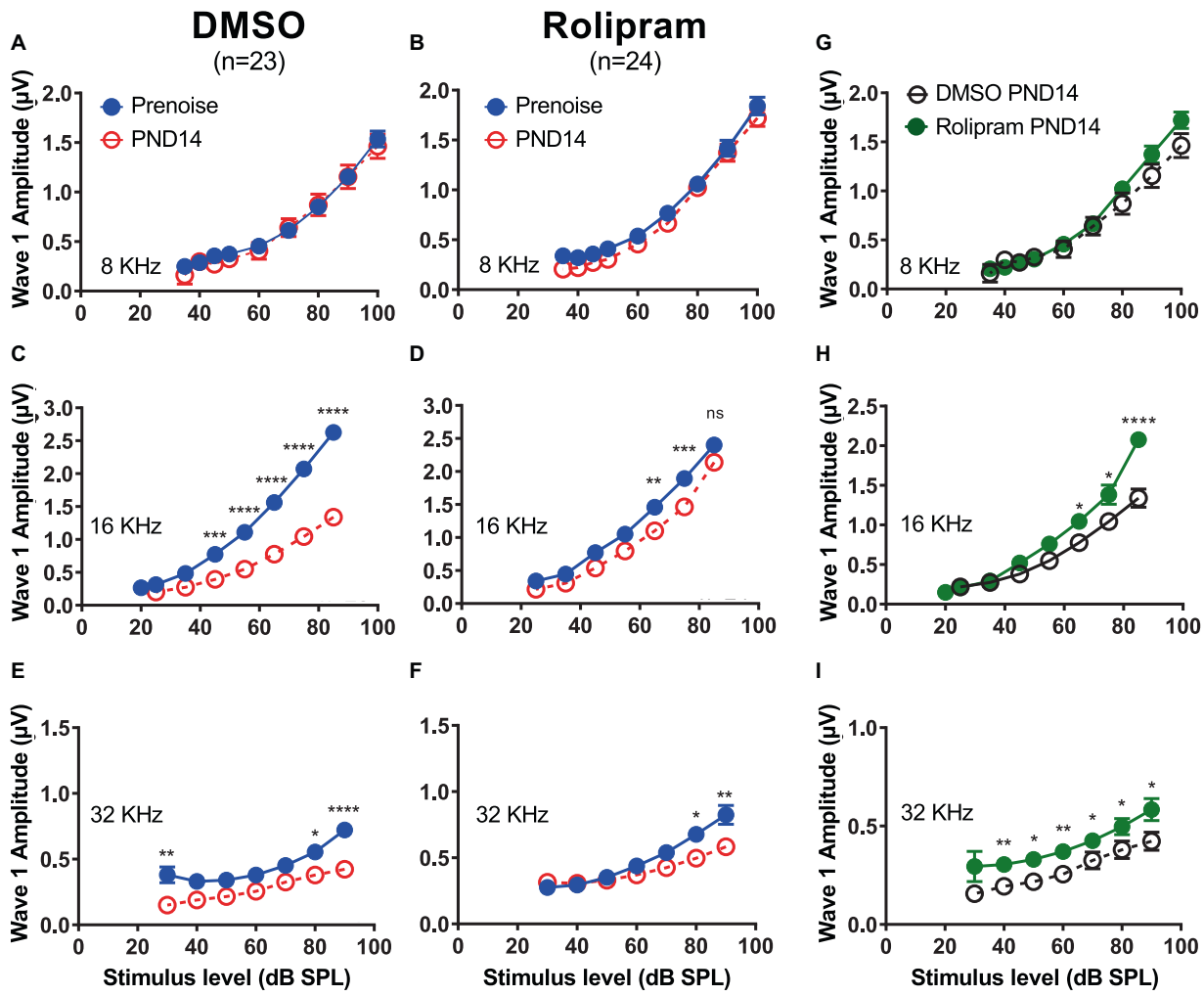


FIGURE 6
Mice treated with rolipram during noise exposure exhibit reduced decline in wave-I amplitude. **(A–F)** Measurements of ABR wave-I amplitude as a function of stimulus intensity ("growth curves") made, on the same mice, prenoise (empty circle) and 14 days postnoise (PND14, filled circle) for 8 kHz **(A,B)**, 16 kHz **(C,D)**, and 32 kHz **(E,F)** tone pips, at indicated stimulus levels, for mice in which either control DMSO **(A,C,E)** or DMSO with rolipram **(D–F)** was delivered starting after the noise exposure. Shown are means ± SEM for the indicated number of ears. The curves were constructed by fitting the data (by least squares) to a second-order polynomial. Significance of amplitude differences between prenoise and PND14 measures at each stimulus level is as shown: *$p < 0.05$, **$p < 0.01$, ***$p < 0.001$, ****$p < 0.0001$. Repeated measure two-way ANOVA with Sidak's multiple comparisons test for all suprathreshold stimulus levels and prenoise vs. PND14. **(G–I)** Direct comparison of PND14 wave-I amplitude between control DMSO and Rolipram groups. Significant differences between prenoise and PND14 were found at 16 and 32 kHz.

of cAMP signaling can be administered orally or systemically by injection, which would make them more amenable to therapeutic use (Chan et al., 2014). One such activator of PKA signaling is the PDE4 inhibitor rolipram, which can promote axon regeneration in the CNS (Nikulina et al., 2004; Hannila and Filbin, 2008). We showed here that rolipram is also effective in promoting cochlear synapse regeneration *in vitro*. Therefore, we assessed the ability of rolipram to promote regeneration of cochlear synapses *in vivo*.

Rolipram is a drug capable of being rapidly absorbed orally and can cross the blood-brain barrier (Krause and Kühne, 1988; Krause et al., 1990) making it a viable candidate for systemic, as opposed to intracochlear, administration. In this study, we used implanted osmotic pumps to continuously deliver the rolipram, providing a constant concentration in the mice. When assessed by PND14, the rolipram-treated mice showed a complete or near-complete restoration of synapses in those cochlear regions in which synapses had been lost in the control mice. Because delivery of rolipram was initiated a day after noise exposure, by which time synapses have degenerated (Liberman et al., 2015), the implication is that rolipram did not prevent the degeneration but promoted regeneration of synapses that had already degenerated. Nevertheless, ABR wave-I amplitude recovered significantly but not to pre-noise levels. Further investigation will be required to determine the reason(s) for this.

The second messenger cAMP has many functions in intracellular signaling and, for example, has been implicated in axonal growth through its effect on microtubule assembly (Roisen et al., 1972). Nevertheless, our studies of cultured SGNs (Hegarty et al., 1997) have shown that cAMP signaling does not promote neurite growth but, rather, inhibits neurite growth promoted by neurotrophic factors. We have also shown that

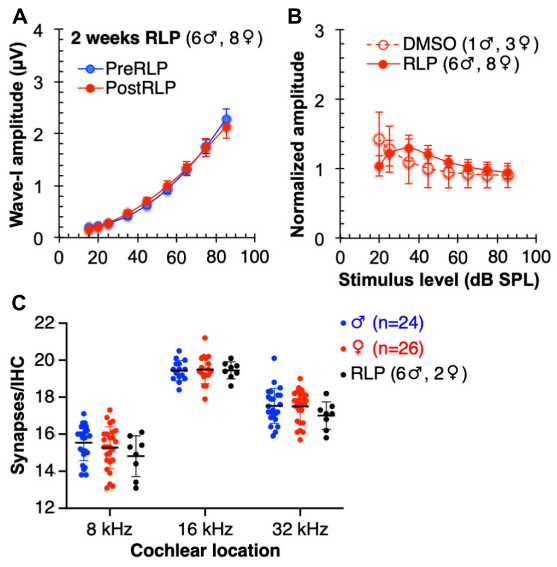


FIGURE 7
Mice chronically treated with rolipram for 2 weeks exhibit no significant changes in ABR wave-I amplitude or synapse number. **(A)** Direct comparison of wave-I amplitude measured, at 16 kHz, 1 day prior to rolipram (RLP) treatment (PreRLP) and after 2 weeks of rolipram treatment (PostRLP), assessed as summarized for **Figure 6**. Shown are means ± SEM. The curves were constructed by fitting the data (by least squares) to a second-order polynomial. An *F*-test was used to ask whether the pre-rolipram and 14 day rolipram data were better fit by a single curve (null hypothesis) or, alternatively, by two different curves. The conclusion (alpha = 0.05) was to accept the null hypothesis, indicating no significant difference caused by 2 weeks of rolipram exposure. **(B)** ABR wave-I amplitude was determined prior to, and after 2 weeks, of continuous rolipram treatment (RLP) or control vehicle only (DMSO). The amplitude after treatment was normalized to the amplitude prior to treatment. Shown is the mean normalized amplitude at each stimulus level for the indicated number of mice. **(C)** Quantification of synapses/IHC for male and female mice and mice treated with rolipram for 14 days (RLP). Shown are means ± SEM for the indicated number of ears at three cochlear locations, 8, 16, and 32 kHz. There was no significant difference between males and females and no significant effect of rolipram on synapse number (two-way ANOVA).

synaptically targeted PKA can limit synapse formation in the brain (Lu et al., 2011). Therefore, we do not necessarily infer from the experiments summarized above that PKA signaling directly promotes synapse regeneration. However, cyclic AMP signaling has been shown to prevent or reverse the effect of chemorepellent substrate factors, facilitating chemoattraction (Song et al., 1998; Hannila and Filbin, 2008). Thus, we can suggest an alternative hypothesis that molecules intrinsic to the cochlea prevent synapse regeneration but cAMP, signaling via PKA, counteracts this inhibition. Our observations and those of Nevoux et al. (2021) are consistent with, and support such a hypothesis, but do not identify a specific inhibitory signal or rule out all alternative hypotheses. Regardless of the mechanism by which this is accomplished, rolipram does appear to be effective in promoting recovery from noise-induced cochlear synaptopathy.

Restoration of cochlear synapses by PDE4 inhibitors such as rolipram has potential advantages over the restoration of cochlear synapses by agents, such as neurotrophic factors, that must be delivered directly to the cochlea or, transtympanically, to the round window (Suzuki et al., 2016). These latter routes of delivery are more invasive and do not appear to have been effective in all subjects (Suzuki et al., 2016). Moreover, high levels of NT-3 in the cochlea may damage otherwise healthy elements (Lee et al., 2016). Rolipram and related compounds have already been suggested as possible therapeutics because of their ability to be administered systemically or even orally and stimulate cAMP signaling (Nicholson et al., 1991). They have been used, for example, to treat depression (Wachtel, 1983; Horowski, 1985) and the related PDE4 inhibitor roflumilast has FDA approval for treatment of symptoms of chronic obstructive pulmonary disorder by oral delivery (Wedzicha et al., 2016). A possible concern is that rolipram has been reported to induce endolymphatic hydrops (Degerman et al., 2017, 2019). However, this occurred when rolipram was administered in combination with vasopressin, and with a 4-week exposure time. In our experiments, synapse recovery occurred within 2 weeks of treatment with rolipram alone. Two weeks of exposure to rolipram had no effect on hearing as assessed by ABR (**Figure 7**). The similar compound roflumilast has been used as a therapeutic with endolymphatic hydrops not reported as an adverse reaction (Wedzicha et al., 2016).

Conclusion

In summary, we show here that agents, including the cAMP phosphodiesterase inhibitor rolipram, that stimulate cAMP signaling promote cochlear synapse regeneration in an *in vitro* model of cochlear synaptopathy, doing so via cAMP-dependent protein kinase signaling. We further show that rolipram, delivered systemically by injection, is effective in restoring cochlear synapses *in vivo* in noise-exposed mice, without adverse effect on hearing. These results suggest that small-molecule activators of cAMP signaling, which can be delivered systemically, can have therapeutic value in the treatment of NICS.

Data availability statement

The raw data supporting the conclusions of this article will be made available by the authors, without undue reservation.

Ethics statement

The animal study was approved by the University of Iowa Institutional Animal Care and Use Committee. The study was conducted in accordance with the local legislation and institutional requirements.

Author contributions

SH: Conceptualization, Data curation, Formal analysis, Investigation, Methodology, Writing – original draft, Writing – review & editing. NH: Conceptualization, Data curation, Formal analysis, Investigation, Methodology, Project administration,

Writing – review & editing. CK: Data curation, Formal analysis, Methodology, Writing – review & editing. SHG: Conceptualization, Data curation, Formal analysis, Funding acquisition, Investigation, Project administration, Supervision, Writing – original draft, Writing – review & editing.

Funding

The author(s) declare financial support was received for the research, authorship, and/or publication of this article. This study was supported by NIH grant DC017722 and DoD grant W81XWH-14-1-0494 (SHG).

Acknowledgments

We thank Julia Hetherton for essential technical support. An earlier version of this manuscript was posted on Research Square (Hemachandran et al., 2022).

Conflict of interest

The authors declare that the research was conducted in the absence of any commercial or financial relationships that could be construed as a potential conflict of interest.

The author(s) declared that they were an editorial board member of Frontiers, at the time of submission. This had no impact on the peer review process and the final decision.

Publisher's note

All claims expressed in this article are solely those of the authors and do not necessarily represent those of their affiliated organizations, or those of the publisher, the editors and the reviewers. Any product that may be evaluated in this article, or claim that may be made by its manufacturer, is not guaranteed or endorsed by the publisher.

References

Aglah, C., Gordon, T., and Posse de Chaves, E. I. (2008). cAMP promotes neurite outgrowth and extension through protein kinase A but independently of Erk activation in cultured rat motoneurons. *Neuropharmacology* 55, 8–17. doi: 10.1016/j.neuropharm.2008.04.005

Bailey, E. M., and Green, S. H. (2014). Postnatal expression of neurotrophic factors accessible to spiral ganglion neurons in the auditory system of adult hearing and deafened rats. *J. Neurosci.* 34, 13110–13126. doi: 10.1523/JNEUROSCI.1014-14.2014

Bandtlow, C. E. (2003). Regeneration in the central nervous system. *Exp. Gerontol.* 38, 79–86.

Bok, J., Zha, X. M., Cho, Y. S., and Green, S. H. (2003). An extranuclear locus of cAMP-dependent protein kinase action is necessary and sufficient for promotion of spiral ganglion neuronal survival by cAMP. *J. Neurosci.* 23, 777–787. doi: 10.1523/JNEUROSCI.23-03-00777.2003

Bolger, G., Michaeli, T., Martins, T., St John, T., Steiner, B., Rodgers, L., et al. (1993). A family of human phosphodiesterases homologous to the dunce learning and memory gene product of Drosophila melanogaster are potential targets for antidepressant drugs. *Mol. Cell Biol.* 13, 6558–6571. doi: 10.1128/mcb.13.10.6558-6571.1993

Cai, D., Qiu, J., Cao, Z., McAtee, M., Bregman, B. S., and Filbin, M. T. (2001). Neuronal cyclic AMP controls the developmental loss in ability of axons to regenerate. *J. Neurosci.* 21, 4731–4739.

Cai, D., Shen, Y., De Bellard, M., Tang, S., and Filbin, M. T. (1999). Prior exposure to neurotrophins blocks inhibition of axonal regeneration by MAG and myelin via a cAMP-dependent mechanism. *Neuron* 22, 89–101. doi: 10.1016/s0896-6273(00)80681-9

Chan, K. M., Gordon, T., Zochodne, D. W., and Power, H. A. (2014). Improving peripheral nerve regeneration: From molecular mechanisms to potential therapeutic targets. *Exp. Neurol.* 261, 826–835.

Degerman, E., In 't Zandt, R., Pålbrink, A., Eliasson, L., Cayé-Thomasen, P., and Magnusson, M. (2017). Inhibition of phosphodiesterase 3, 4, and 5 induces endolymphatic hydrops in mouse inner ear, as evaluated with repeated 9.4T MRI. *Acta Oto-Laryngol.* 137, 8–15. doi: 10.1080/00016489.2016.1211320

Degerman, E., In 't Zandt, R., Pålbrink, A., and Magnusson, M. (2019). Endolymphatic hydrops induced by different mechanisms responds differentially to spironolactone: A rationale for understanding the diversity of treatment responses in hydropic inner ear disease. *Acta Otolaryngol.* 139, 685–691. doi: 10.1080/00016489.2019.1616819

Gallo, G., Ernst, A. F., McLoon, S. C., and Letourneau, P. C. (2002). Transient PKA activity is required for initiation but not maintenance of BDNF-mediated protection from nitric oxide-induced growth-cone collapse. *J. Neurosci.* 22, 5016–5023.

Glueckert, R., Pritz, C. O., Roy, S., Dudas, J., and Schrott-Fischer, A. (2015). Nanoparticle mediated drug delivery of rolipram to tyrosine kinase B positive cells in the inner ear with targeting peptides and agonistic antibodies. *Front. Aging Neurosci.* 7:71. doi: 10.3389/fnagi.2015.00071

Hakuba, N., Koga, K., Gyo, K., Usami, S.-I., and Tanaka, K. (2000). Exacerbation of noise-induced hearing loss in mice lacking the glutamate transporter GLAST. *J. Neurosci.* 20, 8750–8753. doi: 10.1523/JNEUROSCI.20-23-08750.2000

Hannila, S. S., and Filbin, M. T. (2008). The role of cyclic AMP signaling in promoting axonal regeneration after spinal cord injury. *Exp. Neurol.* 209, 321–332.

Hegarty, J. L., Kay, A. R., and Green, S. H. (1997). Trophic support of cultured spiral ganglion neurons by depolarization exceeds and is additive with that by neurotrophins or cAMP and requires elevation of [Ca2+]i within a set range. *J. Neurosci.* 17, 1959–1970. doi: 10.1523/JNEUROSCI.17-06-01959.1997

Hemachandran, S., Hu, N., and Green, S. H. (2022). Cyclic AMP signaling promotes regeneration of cochlear synapses after excitotoxic or noise trauma. *ResearchSquare* doi: 10.21203/rs.21203.rs-2184223/v21 84221

Horowski, R. (1985). Clinical effects of the neurotropic selective cAMP phosphodiesterase inhibitor rolipram in depressed patients: Global evaluation of the preliminary reports. *Curr. Ther. Res.*

Hu, N., Rutherford, M. A., and Green, S. H. (2020). Protection of cochlear synapses from noise-induced excitotoxic trauma by blockade of Ca^{2+}-permeable AMPA receptors. *Proc. Natl. Acad. Sci. U. S. A.* 3:1914247117. doi: 10.1073/pnas.1914247117

Kim, K. X., Payne, S., Yang-Hood, A., Li, S. Z., Davis, B., Carlquist, J., et al. (2019). Vesicular glutamatergic transmission in noise-induced loss and repair of cochlear ribbon synapses. *J. Neurosci.* 39, 4434–4447. doi: 10.1523/JNEUROSCI.2228-18.2019

Kraft, P., Schwarz, T., Göb, E., Heydenreich, N., Brede, M., Meuth, S. G., et al. (2013). The phosphodiesterase-4 inhibitor rolipram protects from ischemic stroke in mice by reducing blood–brain-barrier damage, inflammation and thrombosis. *Exp. Neurol.* 247, 80–90. doi: 10.1016/j.expneurol.2013.03.026

Kranz, K., Warnecke, A., Lenarz, T., Durisin, M., and Scheper, V. (2014). Phosphodiesterase type 4 inhibitor rolipram improves survival of spiral ganglion neurons in vitro. *PLoS One* 9:e92157. doi: 10.1371/journal.pone.0092157

Krause, W., and Kühne, G. (1988). Pharmacokinetics of rolipram in the rhesus and cynomolgus monkeys, the rat and the rabbit. Studies on species differences. *Xenobiotica* 18, 561–571. doi: 10.3109/00498258809041693

Krause, W., Kuhne, G., and Sauerbrey, N. (1990). Pharmacokinetics of (+)-rolipram and (-)-rolipram in healthy volunteers. *Eur. J. Clin. Pharmacol.* 38, 71–75.

Kujawa, S. G., and Liberman, M. C. (2006). Acceleration of age-related hearing loss by early noise exposure: Evidence of a misspent youth. *J. Neurosci.* 26, 2115–2123. doi: 10.1523/JNEUROSCI.4985-05.2006

Kujawa, S. G., and Liberman, M. C. (2009). Adding insult to injury: Cochlear nerve degeneration after "temporary" noise-induced hearing loss. *J. Neurosci.* 29, 14077–14085. doi: 10.1523/JNEUROSCI.2845-09.2009

Lee, M. Y., Kurioka, T., Nelson, M. M., Prieskorn, D. M., Swiderski, D. L., Takada, Y., et al. (2016). Viral-mediated Ntf3 overexpression disrupts innervation and hearing in nondeafened guinea pig cochleae. *Mol. Ther. Methods Clin. Dev.* 3:16052. doi: 10.1038/mtm.2016.52

Liberman, L. D., Suzuki, J., and Liberman, M. C. (2015). Dynamics of cochlear synaptopathy after acoustic overexposure. *J. Assoc. Res. Otolaryngol.* 16, 205–219. doi: 10.1007/s10162-015-0510-3

Liberman, M. C. (2017). Noise-induced and age-related hearing loss: New perspectives and potential therapies. *F1000Res* 6:927. doi: 10.12688/f1000research.11310.1

Lin, H. W., Furman, A. C., Kujawa, S. G., and Liberman, M. C. (2011). Primary neural degeneration in the guinea pig cochlea after reversible noise-induced threshold shift. *J. Assoc. Res. Otolaryngol.* 12, 605–616. doi: 10.1007/s10162-011-0277-0

Lu, P., Yang, H., Jones, L. L., Filbin, M. T., and Tuszynski, M. H. (2004). Combinatorial therapy with neurotrophins and cAMP promotes axonal regeneration beyond sites of spinal cord injury. *J. Neurosci.* 24, 6402–6409. doi: 10.1523/JNEUROSCI.1492-04.2004

Lu, Y., Zha, X. M., Kim, E. Y., Schachtele, S., Dailey, M. E., Hall, D. D., et al. (2011). A kinase anchor protein 150 (AKAP150)-associated protein kinase A limits dendritic spine density. *J. Biol. Chem.* 286, 26496–26506. doi: 10.1074/jbc.M111.254912

Makary, C. A., Shin, J., Kujawa, S. G., Liberman, M. C., and Merchant, S. N. (2011). Age-related primary cochlear neuronal degeneration in human temporal bones. *J. Assoc. Res. Otolaryngol.* 12, 711–717.

McFarlane, S. (2000). Attraction vs. repulsion: The growth cone decides. *Biochem. Cell Biol.* 78, 563–568.

Mittal, R., Bencie, N., Shaikh, N., Mittal, J., Liu, X. Z., and Eshraghi, A. A. (2017). Role of cyclic nucleotide phosphodiesterases in inner ear and hearing. *Front. Physiol.* 8:908. doi: 10.3389/fphys.2017.00908

Moverman, D. J., Liberman, L. D., Kraemer, S., Corfas, G., and Liberman, M. C. (2023). Ultrastructure of noise-induced cochlear synaptopathy. *Sci. Rep.* 13:19456.

Muller, M., von Hunerbein, K., Hoidis, S., and Smolders, J. W. (2005). A physiological place-frequency map of the cochlea in the CBA/J mouse. *Hear. Res.* 202, 63–73. doi: 10.1016/j.heares.2004.08.011

Nayagam, B. A., Muniak, M. A., and Ryugo D. K. (2011). The spiral ganglion: connecting the peripheral and central auditory systems. *Hear. Res.* 278, 2–20.

Nevoux, J., Alexandru, M., Bellocq, T., Tanaka, L., Hayashi, Y., Watabe, T., et al. (2021). An antibody to RGMa promotes regeneration of cochlear synapses after noise exposure. *Sci. Rep.* 11:2937. doi: 10.1038/s41598-021-81294-5

Nicholson, C. D., Challiss, R. J., and Shahid, M. (1991). Differential modulation of tissue function and therapeutic potential of selective inhibitors of cyclic nucleotide phosphodiesterase isoenzymes. *Trends Pharmacol. Sci.* 12, 19–27. doi: 10.1016/0165-6147(91)90484-a

Nikulina, E., Tidwell, J. L., Dai, H. N., Bregman, B. S., and Filbin, M. T. (2004). The phosphodiesterase inhibitor rolipram delivered after a spinal cord lesion promotes axonal regeneration and functional recovery. *Proc. Natl. Acad. Sci. U. S. A.* 101, 8786–8790.

Omori, K., and Kotera, J. (2007). Overview of PDEs and their regulation. *Circ. Res.* 100, 309–327.

Pichichero, M., Beer, B., and Clody, D. E. (1973). Effects of dibutyryl cyclic AMP on restoration of function of damaged sciatic nerve in rats. *Science* 182, 724–725. doi: 10.1126/science.182.4113.724

Puel, J. L., Pujol, R., Tribillac, F., Ladrech, S., and Eybalin, M. (1994). Excitatory amino acid antagonists protect cochlear auditory neurons from excitotoxicity. *J. Comp. Neurol.* 341, 241–256. doi: 10.1002/cne.903410209

Puel, J. L., Ruel, J., Gervais d'Aldin, C., and Pujol, R. (1998). Excitotoxicity and repair of cochlear synapses after noise-trauma induced hearing loss. *Neuroreport* 9, 2109–2114.

Pujol, R., Lenoir, M., Robertson, D., Eybalin, M., and Johnstone, B. M. (1985). Kainic acid selectively alters auditory dendrites connected with cochlear inner hair cells. *Hear. Res.* 18, 145–151. doi: 10.1016/0378-5955(85)90006-1

Qiu, J., Cai, D., Dai, H., McAtee, M., Hoffman, P. N., Bregman, B. S., et al. (2002). Spinal axon regeneration induced by elevation of cyclic AMP. *Neuron* 34, 895–903.

Robichaux, W. G. III, and Cheng, X. (2018). Intracellular cAMP sensor EPAC: Physiology, pathophysiology, and therapeutics development. *Physiol. Rev.* 98, 919–1053. doi: 10.1152/physrev.00025.2017

Roisen, F. J., Murphy, R. A., Pichichero, M. E., and Braden, W. G. (1972). Cyclic adenosine monophosphate stimulation of axonal elongation. *Science* 175, 73–74.

Ryan, A. F., Kujawa, S. G., Hammill, T., Le Prell, C., and Kil, J. (2016). Temporary and permanent noise-induced threshold shifts: A review of basic and clinical observations. *Otol. Neurotol.* 37, e271–e275. doi: 10.1097/mao.0000000000001071

Schaette, R., and McAlpine, D. (2011). Tinnitus with a normal audiogram: Physiological evidence for hidden hearing loss and computational model. *J. Neurosci.* 31, 13452–13457. doi: 10.1523/JNEUROSCI.2156-11.2011

Sergeyenko, Y., Lall, K., Liberman, M. C., and Kujawa, S. G. (2013). Age-related cochlear synaptopathy: An early-onset contributor to auditory functional decline. *J. Neurosci.* 33, 13686–13694. doi: 10.1523/JNEUROSCI.1783-13.2013

Shaheen, L. A., Valero, M. D., and Liberman, M. C. (2015). Towards a diagnosis of cochlear neuropathy with envelope following responses. *J. Assoc. Res. Otolaryngol.* 16, 727–745. doi: 10.1007/s10162-015-0539-3

Siuciak, J. A., Chapin, D. S., McCarthy, S. A., and Martin, A. N. (2007). Antipsychotic profile of rolipram: Efficacy in rats and reduced sensitivity in mice deficient in the phosphodiesterase-4B (PDE4B) enzyme. *Psychopharmacology* 192, 415–424. doi: 10.1007/s00213-007-0727-x

Sly, D. J., Campbell, L., Uschakov, A., Saief, S. T., Lam, M., and O'Leary, S. J. (2016). Applying neurotrophins to the round window rescues auditory function and reduces inner hair cell synaptopathy after noise-induced hearing loss. *Otol. Neurotol.* 37, 1223–1230. doi: 10.1097/MAO.0000000000001191

Song, H., Ming, G., He, Z., Lehmann, M., McKerracher, L., Tessier-Lavigne, M., et al. (1998). Conversion of neuronal growth cone responses from repulsion to attraction by cyclic nucleotides. *Science* 281, 1515–1518. doi: 10.1126/science.281.5382.1515

Song, H. J., Ming, G. L., and Poo, M. M. (1997). cAMP-induced switching in turning direction of nerve growth cones. *Nature* 388, 275–279. doi: 10.1038/40864

Spina, D. (2008). PDE4 inhibitors: Current status. *Br. J. Pharmacol.* 155, 308–315. doi: 10.1038/bjp.2008.307

Suzuki, J., Corfas, G., and Liberman, M. C. (2016). Round-window delivery of neurotrophin 3 regenerates cochlear synapses after acoustic overexposure. *Sci. Rep.* 6:24907. doi: 10.1038/srep24907

Taylor, S. S., Zhang, P., Steichen, J. M., Keshwani, M. M., and Kornev, A. P. (2013). PKA: Lessons learned after twenty years. *Biochim. Biophys. Acta* 1834, 1271–1278. doi: 10.1016/j.bbapap.2013.03.007

Underwood, D. C., Kotzer, C. J., Bochnowicz, S., Osborn, R. R., Luttmann, M. A., Hay, D. W., et al. (1994). Comparison of phosphodiesterase III, IV and dual III/IV inhibitors on bronchospasm and pulmonary eosinophil influx in guinea pigs. *J. Pharmacol. Exp. Ther.* 270, 250–259.

Viana, L. M., O'Malley, J. T., Burgess, B. J., Jones, D. D., Oliveira, C. A., Santos, F., et al. (2015). Cochlear neuropathy in human presbycusis: Confocal analysis of hidden hearing loss in post-mortem tissue. *Hear. Res.* 327, 78–88. doi: 10.1016/j.heares.2015.04.014

Wachtel, H. (1983). Potential antidepressant activity of rolipram and other selective cyclic adenosine 3′, 5′-monophosphate phosphodiesterase inhibitors. *Neuropharmacology* 22, 267–272.

Wan, G., Gomez-Casati, M. E., Gigliello, A. R., Liberman, M. C., and Corfas, G. (2014). Neurotrophin-3 regulates ribbon synapse density in the cochlea and induces synapse regeneration after acoustic trauma. *Elife* 3:e03564. doi: 10.7554/eLife.03564

Wang, Q., and Green, S. H. (2011). Functional role of neurotrophin-3 in synapse regeneration by spiral ganglion neurons on inner hair cells after excitotoxic trauma in vitro. *J. Neurosci.* 31, 7938–7949. doi: 10.1523/JNEUROSCI.1434-10.2011

Wang, Q., and Zheng, J. Q. (1998). cAMP-mediated regulation of neurotrophin-induced collapse of nerve growth cones. *J. Neurosci.* 18, 4973–4984. doi: 10.1523/JNEUROSCI.18-13-04973.1998

Wedzicha, J. A., Calverley, P. M., and Rabe, K. F. (2016). Roflumilast: A review of its use in the treatment of COPD. *Int. J. Chron. Obstruct. Pulmon. Dis.* 11, 81–90. doi: 10.2147/copd.s89849

Weishaar, R. E., Cain, M. H., and Bristol, J. A. (1985). A new generation of phosphodiesterase inhibitors: Multiple molecular forms of phosphodiesterase and the potential for drug selectivity. *J. Med. Chem.* 28, 537–545. doi: 10.1021/jm5000 1a001

frontiers | Frontiers in Cellular Neuroscience

TYPE Original Research
PUBLISHED 01 May 2024
DOI 10.3389/fncel.2024.1396387

Check for updates

OPEN ACCESS

EDITED BY
Christian Keine,
University of Oldenburg, Germany

REVIEWED BY
Tara Sankar Roy,
North DMC Medical College and Hindu Rao Hospital, India
Aaron Benson Wong,
Erasmus University Medical Center, Netherlands

*CORRESPONDENCE
Jeffrey G. Mellott
✉ jmellott@neomed.edu

RECEIVED 05 March 2024
ACCEPTED 11 April 2024
PUBLISHED 01 May 2024

CITATION
Mellott JG, Duncan S, Busby J, Almassri LS, Wawrzyniak A, Iafrate MC, Ohl AP, Slabinski EA, Beaver AM, Albaba D, Vega B, Mafi AM, Buerke M, Tokar NJ and Young JW (2024) Age-related upregulation of dense core vesicles in the central inferior colliculus.
Front. Cell. Neurosci. 18:1396387.
doi: 10.3389/fncel.2024.1396387

COPYRIGHT
© 2024 Mellott, Duncan, Busby, Almassri, Wawrzyniak, Iafrate, Ohl, Slabinski, Beaver, Albaba, Vega, Mafi, Buerke, Tokar and Young. This is an open-access article distributed under the terms of the Creative Commons Attribution License (CC BY). The use, distribution or reproduction in other forums is permitted, provided the original author(s) and the copyright owner(s) are credited and that the original publication in this journal is cited, in accordance with accepted academic practice. No use, distribution or reproduction is permitted which does not comply with these terms.

Age-related upregulation of dense core vesicles in the central inferior colliculus

Jeffrey G. Mellott[1,2]*, Syllissa Duncan[1], Justine Busby[1], Laila S. Almassri[1,2], Alexa Wawrzyniak[1], Milena C. Iafrate[1], Andrew P. Ohl[1], Elizabeth A. Slabinski[1], Abigail M. Beaver[1], Diana Albaba[1], Brenda Vega[1], Amir M. Mafi[3], Morgan Buerke[4], Nick J. Tokar[1] and Jesse W. Young[1]

[1]Department of Anatomy and Neurobiology, Northeast Ohio Medical University, Rootstown, OH, United States, [2]University Hospitals Hearing Research Center, Northeast Ohio Medical University, Rootstown, OH, United States, [3]The Ohio State University College of Medicine, Columbus, OH, United States, [4]Department of Psychology, Louisiana State University, Baton Rouge, LA, United States

Presbycusis is one of the most prevalent disabilities in aged populations of industrialized countries. As we age less excitation reaches the central auditory system from the periphery. To compensate, the central auditory system [e.g., the inferior colliculus (IC)], downregulates GABAergic inhibition to maintain homeostatic balance. However, the continued downregulation of GABA in the IC causes a disruption in temporal precision related to presbycusis. Many studies of age-related changes to neurotransmission in the IC have therefore focused on GABAergic systems. However, we have discovered that dense core vesicles (DCVs) are significantly upregulated with age in the IC. DCVs can carry neuropeptides, co-transmitters, neurotrophic factors, and proteins destined for the presynaptic zone to participate in synaptogenesis. We used immuno transmission electron microscopy across four age groups (3-month; 19-month; 24-month; and 28-month) of Fisher Brown Norway rats to examine the ultrastructure of DCVs in the IC. Tissue was stained post-embedding for GABA immunoreactivity. DCVs were characterized by diameter and by the neurochemical profile (GABAergic/non-GABAergic) of their location (bouton, axon, soma, and dendrite). Our data was collected across the dorsolateral to ventromedial axis of the central IC. After quantification, we had three primary findings. First, the age-related increase of DCVs occurred most robustly in non-GABAergic dendrites in the middle and low frequency regions of the central IC during middle age. Second, the likelihood of a bouton having more than one DCV increased with age. Lastly, although there was an age-related loss of terminals throughout the IC, the proportion of terminals that contained at least one DCV did not decline. We interpret this finding to mean that terminals carrying proteins packaged in DCVs are spared with age. Several recent studies have demonstrated a role for neuropeptides in the IC in defining cell types and regulating inhibitory and excitatory neurotransmission.

Given the age-related increase of DCVs in the IC, it will be critical that future studies determine whether (1) specific neuropeptides are altered with age in the IC and (2) if these neuropeptides contribute to the loss of inhibition and/or increase of excitability that occurs during presbycusis and tinnitus.

KEYWORDS

inferior colliculus, GABA, synapse, aging, dense core vesicles

1 Introduction

The auditory system plays a crucial role in our everyday lives by enabling communication, sound localization, and information processing. Conversely, auditory system dysfunction leads to impaired communication, difficulty participating in noisy social environments, and an overall decrease in quality of life. As the aging population continues to grow, there is an increased demand for understanding the mechanisms underlying hearing loss, which affects nearly three-quarters of individuals aged 70 years or older (Goman and Lin, 2016). The functional decline of the auditory system with age often begins with the degradation of the peripheral auditory system, which leads to a decrease in excitation sent to the central auditory system (Knipper et al., 2022; Rumschlag et al., 2022). The central auditory system compensates for this decreased excitation by downregulating GABAergic inhibition; this is believed to be an attempt at restoring homeostatic levels of activity (Caspary et al., 2008; Richardson et al., 2012; Caspary and Llano, 2018). Unfortunately the gradual loss of GABA into old age leads to functional deficits and increased central neural gain (Caspary et al., 2008; Auerbach et al., 2014, 2019). Age-related downregulation of GABAergic inhibition is well documented in the inferior colliculus (IC), an auditory midbrain structure that serves as the hub of the central auditory system (Wenstrup, 2005; Caspary et al., 2008; Syka, 2020). The IC is organized into three subdivisions [central (ICc), lateral cortex (IClc), and dorsal cortex (ICd)] and processes information from multiple ascending and descending auditory projections (see reviews: Oliver, 2005; Syka, 2020). Neurons and inputs within the lemniscal ICc are arranged into isofrequency lamina, which are organized tonotopically along the ventromedial (high frequencies) to dorsolateral (low frequencies) axis (Oliver and Morest, 1984; Oliver, 2005; Malmierca et al., 2008; Syka, 2020).

Considering that mammalian presbycusis is frequency specific, it is important to understand age-related molecular and ultrastructural changes in relation to the tonotopic axis (Walton et al., 1998; Cai et al., 2018; Parthasarathy et al., 2018; Koehler et al., 2023). In our ongoing investigations of the aging synaptic ultrastructure in the IC, we observed a dramatic increase of dense core vesicles (DCVs) in the aged IC. In the current study, we quantify and characterize this increase in DCVs. DCVs are membrane-bound organelles that contain dense granular cores; they are one of two types of organelles that secrete chemical signals throughout the nervous system, with classic clear synaptic vesicles being the other (Sorra et al., 2006; Persoon et al., 2018). Unlike synaptic vesicles which are found in large pools at active zones and carry classic neurotransmitters, DCVs are rarer, and they tend to package biogenic amines, neuromodulators, presynaptic machinery, neuropeptides, neurotrophic factors, and hormones (Peters et al., 1991; Michael et al., 2006; Sorra et al., 2006; Merighi, 2018). A number of important neuromodulators involved in auditory midbrain function are transported by DCVs, including serotonin, neuropeptide Y (NPY), vasoactive intestinal peptide (VIP), brain-derived neurotrophic factor (BDNF), and fibroblast growth factors (Pelletier et al., 1981; Sato et al., 2001; Dieni et al., 2012; Schofield and Hurley, 2018; Goyer et al., 2019; Silveira et al., 2020, 2023). DCVs are transported via both dendritic and axonal trafficking, where microtubule dependent kinesin-1 motors (KIF1) and motor dynein mediate trafficking into dendrites and axons (Zheng et al., 2008; Lipka et al., 2016). It is unclear whether DCVs are preferentially released at axons or dendrites (Kennedy and Ehlers, 2011; Persoon et al., 2018). To our knowledge, very little is understood about the populations of DCVs in the auditory midbrain, including what proteins they contain and their trafficking patterns.

The goal of the present study is to determine whether DCVs are upregulated in the aging ICc. Specifically, we examined three tissue blocks taken across the ventromedial-dorsolateral ICc axis. For the sake of conciseness, alignment with our previous studies, and convention as the tonotopic axis is well established, we refer to the ventromedial-most ICc block as representing the high frequency region, the middle block as representing the middle frequency region, and dorsolateral-most block as representing lower frequencies. We used immuno transmission electron microscopy to analyze DCVs in GABAergic and non-GABAergic boutons, axons, and dendrites of Fischer Brown Norway (FBN) rats across four (3–4 months "young"; 19–20 months "early middle-age"; 24 months "late middle-age"; and 28–29 months "old") age groups. We discovered that: (1) DCVs were markedly increased in non-GABAergic dendrites during middle age. Many of these DCVs were located near postsynaptic densities. (2) The probability of a GABAergic or non-GABAergic bouton having more than one DCV increased with age. (3) Despite the age-related loss of boutons throughout the IC, the percentage of non-GABAergic and GABAergic boutons that had at least one DCV did not decline with age. We conclude that synapses lost in the IC in aging may not be synapses that co-release neuropeptides. Ultimately, it appears that the many possible proteins packaged by DCVs may have a significant role in the processing of acoustic signals in the aging IC.

Abbreviations: DCV, dense core vesicle; FBN, Fischer Brown Norway; GABA, gamma-aminobutyric acid; GAD, glutamic acid decarboxylase; IC, inferior colliculus; ICc, central nucleus of the inferior colliculus; ICd, dorsal cortex of the inferior colliculus; IClc, lateral cortex of the inferior colliculus; LD, large dendrite; MD, medium dendrite; SD, small dendrite.

TABLE 1 Summary of ICc DCV in GABA-negative profiles.

	# of animals	Area analyzed (μm^2)	# of DCV	Average diameter (nm)	# of DCV in bouton	# of DCV in axon	# of DCV in dendrite
3–4 month							
High frequency	5	16,000 (3,200/animal)	175	69.2	75	16	84
Middle frequency	5	16,000 (3,200/animal)	184	66.2	89	11	83
Low frequency	5	16,000 (3,200/animal)	194	69.2	100	13	81
19–20 month							
High frequency	5	16,000 (3,200/animal)	356	65.3	162	9	185
Middle frequency	5	16,000 (3,200/animal)	311	69.7	113	20	188
Low frequency	5	16,000 (3,200/animal)	267	70.5	110	23	142
24 month							
High frequency	5	16,000 (3,200/animal)	438	68.8	162	27	244
Middle frequency	5	16,000 (3,200/animal)	428	71.1	160	39	225
Low frequency	5	16,000 (3,200/animal)	382	70.9	133	23	226
28 month							
High frequency	5	16,000 (3,200/animal)	399	62.4	147	24	222
Middle frequency	5	16,000 (3,200/animal)	351	65.2	146	14	190
Low frequency	5	16,000 (3,200/animal)	326	64.7	133	26	165
Summary of ICc DCV in GABAergic profiles							
3–4 month							
High frequency	5	16,000 (3,200/animal)	85	69.8	49	9	24
Middle frequency	5	16,000 (3,200/animal)	110	70.9	42	18	44
Low frequency	5	16,000 (3,200/animal)	97	74.2	62	10	24
19–20 month							
High frequency	5	16,000 (3,200/animal)	110	65.3	64	7	39
Middle frequency	5	16,000 (3,200/animal)	116	71.6	65	9	34
Low frequency	5	16,000 (3,200/animal)	102	67.4	50	12	34
24 month							
High frequency	5	16,000 (3,200/animal)	163	71	68	9	82
Middle frequency	5	16,000 (3,200/animal)	165	73.8	86	14	61
Low frequency	5	16,000 (3,200/animal)	148	69.3	86	9	50
28 month							
High frequency	5	16,000 (3,200/animal)	188	61.2	76	18	84
Middle frequency	5	16,000 (3,200/animal)	158	68.2	89	9	51
Low frequency	5	16,000 (3,200/animal)	125	65.1	53	19	39

2 Materials and methods

2.1 Animals

All procedures were conducted in accordance with the Northeast Ohio Medical University Institutional Animal Care and Use Committee and NIH guidelines. Results are described from 20 male FBN rats [National Institute of Aging; Bethesda, MD, USA; RRID:SCR_007317 (housed by Charles River Laboratories, Wilmington, MA, USA)] across four age groups (5 animals per age group): 3–4 months "young"; 19–20 months "early middle-age"; 24 months "late middle-age"; and 28–29 months "old" (**Tables 1**–**3**). For a details regarding ambient sound levels, please see Cai et al. (2018). Efforts were made to minimize the number of animals and their suffering.

2.2 Perfusion and sectioning

Each animal was deeply anesthetized with isoflurane and perfused transcardially with Tyrode's solution, followed by 250 ml of 2% glutaraldehyde and 2% paraformaldehyde [with one

TABLE 2 Excitatory bouton breakdown.

	Total boutons	Bouton loss from 3 months	Total DCVs	# of boutons w/1 DCV	# of boutons w/2 DCV	# of boutons w/3 DCV	# of boutons w/4 DCV	# of boutons w/5 DCV	# of boutons w/>5 DCV	# of boutons w/at least 1 DCV	% boutons w/at least 1 DCV
3–4 months											
High frequency											
B72; R23	224		13	8	1	1	–	–	–	10	
B96; R41	207		9	5	2	–	–	–	–	7	
B123; R42	202		10	7	–	1	–	–	–	8	
B129; R116	194		22	12	3	–	1	–	–	16	
B132; R117	240		21	10	4	1	–	–	–	15	
Total	1,067	N/A	75	42	10	3	1	0	0	56	5.24%
Middle frequency											
B73; R23	208		13	4	3	1	–	–	–	8	
B97; R41	215		12	10	2	–	–	–	–	12	
B124; R42	219		19	11	1	2	–	–	–	14	
B130; R116	185		25	13	3	2	–	–	–	18	
B133; R117	204		20	14	1	–	1	–	–	16	
Total	1,031	N/A	89	52	10	5	1	0	0	68	6.60%
Low frequency											
B74; R23	217		17	13	–	–	1	–	–	14	
B98; R41	225		8	6	1	–	–	–	–	7	
B125; R42	192		21	10	1	3	–	–	–	14	
B131; R116	231		36	21	3	3	–	–	–	27	
B134; R117	237		18	7	4	1	–	–	–	12	
Total	1,096	N/A	100	57	9	7	1	0	0	74	6.80%
19–20 months											
High frequency											
B78; R63	184		41	15	5	4	1	–	–	25	
B81; R98	197		24	15	1	1	1	–	–	18	
B84; R99	204		33	14	3	3	1	–	–	21	
B105; R84	187		35	16	4	2	–	1	–	23	
B142; R96	209		29	14	3	3	–	–	–	23	
Total	981	9.10%	162	74	16	13	3	1	0	110	11.20%

(Continued)

10.3389/fncel.2024.1396387

TABLE 2 (Continued)

	Total boutons	Bouton loss from 3 months	Total DCVs	# of boutons w/1 DCV	# of boutons w/2 DCV	# of boutons w/3 DCV	# of boutons w/4 DCV	# of boutons w/5 DCV	# of boutons w/>5 DCV	# of boutons w/at least 1 DCV	% boutons w/at least 1 DCV
Middle frequency											
B79; R63	186		23	5	6	2	–	–	–	13	
B82; R98	196		19	7	2	1	–	1	–	11	
B103; R83	218		39	8	5	2	3	–	–	18	
B106; R84	154		5	5	–	–	–	–	–	5	
B141; R96	201		27	15	6	–	–	–	–	21	
Total	955	7.40%	113	40	19	5	3	1	0	68	7.12%
Low frequency											
B80; R63	202		36	9	4	4	1	1	–	19	
B86; R99	207		27	5	4	2	2	–	–	13	
B104; R83	179		20	10	5	–	–	–	–	15	
B107; R84	200		11	6	1	1	–	–	–	8	
B143; R96	221		16	9	2	1	–	–	–	12	
Total	1,009	8%	110	39	16	8	3	1	0	67	6.60%
24 months											
High frequency											
B111; R101	158		23	5	3	–	3	–	–	11	
B114; R102	156		28	9	4	2	–	1	–	16	
B117; R100	170		27	11	4	–	2	–	–	17	
B135; R109	143		25	6	2	5	–	–	–	13	
B138; R110	187		59	16	6	4	3	–	1 (7)	29	
Total	814	23.80%	162	47	19	11	8	1	1	86	11%
Middle frequency											
B112; R101	202		25	4	5	2	–	1	–	12	
B115; R102	179		53	25	2	2	2	2	–	33	
B118; R100	132		31	5	2	2	4	–	–	13	
B121; R108	166		19	10	–	3	–	–	–	13	
B136; R109	137		32	7	2	5	–	–	1 (6)	15	
Total	816	20.90%	160	51	11	14	6	3	1	86	10.50%

(Continued)

10.3389/fncel.2024.1396387

TABLE 2 (Continued)

	Total boutons	Bouton loss from 3 months	Total DCVs	# of boutons w/1 DCV	# of boutons w/2 DCV	# of boutons w/3 DCV	# of boutons w/4 DCV	# of boutons w/5 DCV	# of boutons w/>5 DCV	# of boutons w/at least 1 DCV	% boutons w/at least 1 DCV
Low frequency											
B113; R101	167		19	9	1	1	–	1	–	12	
B116; R102	217		47	10	8	3	3	–	–	24	
B119; R100	176		7	5	1	–	–	–	–	6	
B122; R108	203		36	4	4	5	1	1	–	15	
B137; R109	160		24	12	3	2	–	–	–	17	
Total	923	15.80%	133	40	17	11	4	2	0	74	8.02%
28–29 months											
High frequency											
B87; R29	134		12	6	1	–	1	–	–	8	
B90; R46	154		48	5	6	7	–	2	–	20	
B93; R79	147		11	8	–	1	–	–	–	9	
B99; R45	134		33	7	7	4	–	–	–	18	
B126; R47	181		43	9	9	1	2	1	–	22	
Total	750	29.70%	147	35	23	13	3	3	0	77	10.30%
Middle frequency											
B88; R99	156		10	6	2	–	–	–	–	8	
B91; R46	173		29	5	3	4	–	–	1 (6)	13	
B94; R79	150		36	13	4	2	1	1	–	21	
B100; R45	158		42	4	4	5	2	–	1 (7)	16	
B127; R47	138		29	15	5	–	1	–	–	21	
Total	775	24.80%	146	43	18	11	4	1	2	79	10.20%
Low frequency											
B89; R99	167		12	5	2	1	–	–	–	8	
B92; R46	190		44	11	1	2	5	1		20	
B95; R79	189		34	12	4	2	2	–		20	
B101; R45	180		27	7	6	3	–	1	–	17	
B128; R47	177		16	14	1	–	–	–	–	15	
Total	903	17.60%	133	49	14	8	7	2	0	80	8.70%

"BXX" designates the block number. "RXX" designates the animal.

10.3389/fncel.2024.1396387

TABLE 3 GABAergic bouton breakdown.

	Total boutons	Bouton loss from 3 months	Total DCVs	# of boutons w/1 DCV	# of boutons w/2 DCV	# of boutons w/3 DCV	# of boutons w/4 DCV	# of boutons w/5 DCV	# of boutons w/>5 DCV	# of boutons w/at least 1 DCV	% of boutons w/at least 1 DCV
3–4 months											
High frequency											
B72; R23	188		8	6	2	–	–	–	–	8	
B96; R41	216		6	3	–	1	–	–	–	4	
B123; R42	180		7	4	–	1	–	–	–	5	
B129; R116	212		14	3	4	1	–	–	–	8	
B132; R117	219		14	7	2	1	–	–	–	10	
Total	1,015	N/A	49	23	8	4	0	0	0	35	3.50%
Middle frequency											
B73; R23	187		4	4	–	–	–	–	–	4	
B97; R41	170		7	5	1	–	–	–	–	6	
B124; R42	159		13	5	–	1	–	–	–	6	
B130; R116	208		14	3	2	1	1	–	–	7	
B133; R117	193		4	4	–	–	–	–	–	4	
Total	917	N/A	42	21	3	2	1	0	0	27	2.90%
Low frequency											
B74; R23	238		10	8	1	–	–	–	–	9	
B98; R41	204		8	7	1	–	–	–	–	8	
B125; R42	164		15	10	1	1	–	–	–	12	
B131; R116	172		21	11	5	–	–	–	–	16	
B134; R117	209		8	6	1	–	–	–	–	7	
Total	987	N/A	62	42	9	1	0	0	0	52	5.30%
19–20 months											
High frequency											
B78; R63	155		25	8	4	3	–	–	–	15	
B81; R98	171		13	6	–	1	1	–	–	8	
B84; R99	201		14	5	3	1	–	–	–	9	
B105; R84	196		7	7	–	–	–	–	–	7	
B142; R96	222		5	–	1	1	–	–	–	2	
Total	945	6.90%	64	26	8	6	1	0	0	41	4.30%

(Continued)

10.3389/fncel.2024.1396387

TABLE 3 (Continued)

	Total boutons	Bouton loss from 3 months	Total DCVs	# of boutons w/1 DCV	# of boutons w/2 DCV	# of boutons w/3 DCV	# of boutons w/4 DCV	# of boutons w/5 DCV	# of boutons w/>5 DCV	# of boutons w/at least 1 DCV	% of boutons w/at least 1 DCV
Middle frequency											
B79; R63	217		13	8	1	1	–	–	–	10	
B82; R98	187		8	6	1	–	–	–	–	7	
B103; R83	154		18	10	2	–	1	–	–	13	
B106; R84	159		11	8	–	1	–	–	–	9	
B141; R96	133		15	5	2	2	–	–	–	9	
Total	850	7.30%	65	37	6	4	1	0	0	48	5.60%
Low frequency											
B80; R63	140		10	8	1	–	–	–	–	9	
B86; R99	168		17	7	1	3	–	–	–	11	
B104; R83	174		7	3	2	–	–	–	–	5	
B107; R84	203		12	8	–	–	1		–	9	
B143; R96	210		4	4	–	–	–	–	–	4	
Total	895	9.30%	50	30	4	3	1	0	0	38	4.20%
24 months											
High frequency											
B111; R101	199		13	10	–	1	–	–	–	11	
B114; R102	162		5	3	1	–	–	–	–	4	
B117; R100	129		7	6	1	–	–	–	–	7	
B135; R109	170		8	5		1	–	–	–	6	
B138; R110	172		35	8	4	5	1	–	–	18	
Total	832	18%	68	32	6	7	1	0	0	46	5.50%
Middle frequency											
B112; R101	124		16	5	4	2				11	
B115; R102	187		24	8	4	1		1		14	
B118; R100	144		19	9	2	2				13	
B121; R108	127		11	5	3					8	
B136; R109	142		16	10	1		1			12	
Total	724	21%	86	37	14	5	1	1	0	58	8.01%

(Continued)

10.3389/fncel.2024.1396387

TABLE 3 (Continued)

	Total boutons	Bouton loss from 3 months	Total DCVs	# of boutons w/1 DCV	# of boutons w/2 DCV	# of boutons w/3 DCV	# of boutons w/4 DCV	# of boutons w/5 DCV	# of boutons w/>5 DCV	# of boutons w/at least 1 DCV	% of boutons w/at least 1 DCV
Low frequency											
B113; R101	170		16	11	1	1	–	–	–	13	
B116; R102	139		15	9	3	–	–	–	–	12	
B119; R100	155		16	4	3	2	–	–	–	9	
B122; R108	181		15	5	5	–	–	–	–	10	
B137; R109	156		24	12	4	–	1	–	–	17	
Total	801	18.90%	86	41	16	3	1	0	0	61	7.60%
28–29 months											
High frequency											
B87; R29	135		8	6	1	–	–	–	–	7	
B90; R46	172		18	7	4	1	–	–	–	12	
B93; R79	136		9	6	–	1	–	–	–	7	
B99; R45	159		15	8	2	1	–	–	–	11	
B126; R47	165		26	11	2	1	2	–	–	16	
Total	767	24.40%	76	38	9	4	2	0	0	53	6.90%
Middle frequency											
B88; R99	138		5	5	–	–	–	–	–	5	
B91; R46	130		22	7	2	2	–	1	–	12	
B94; R79	129		11	7	–	–	1	–	–	8	
B100; R45	130		22	13	1	1	1	–	–	16	
B127; R47	153		29	8	6	3	–	–	1 (6)	18	
Total	680	25.80%	89	40	9	6	2	1	1	59	8.70%
Low frequency											
B89; R99	168		9	3	3	–	–	–	–	6	
B92; R46	142		7	4	–	1	–	–	–	5	
B95; R79	144		3	3	–	–	–	–	–	3	
B101; R45	159		7	7	–	–	–	–	–	7	
B128; R47	182		27	4	8	1	1	–	–	14	
Total	795	19.50%	53	21	11	2	1	0	0	35	4.40%

"BXX" designates the block number. "RXX" designates the animal.

10.3389/fncel.2024.1396387

exception; case R79, Blocks 93,94, and 95 (Tables 1, 2) was perfused and stored with 3% glutaraldehyde and 1% paraformaldehyde] in 0.1 M phosphate buffer at a pH 7.4. The brain was removed and stored at 4°C in 2% glutaraldehyde and 2% paraformaldehyde in 0.1 M phosphate buffer. The following day the brain was prepared for processing by removing the cerebellum and cortex and blocking the remaining piece with transverse cuts posterior to the cochlear nucleus and anterior to the thalamus. The tissue was then cut into 50 μm thick transverse section with a Vibratome (VT1000S, Leica Microsystems, Buffalo Grove, IL, USA). The tissue was collected in six series. Series were processed as described below or stored in freezing buffer for future processing.

2.3 Tissue processing for EM

A series of tissue was post-fixed in 1% osmium tetroxide for 30 min, dehydrated in a series of alcohols (50%, 70%, 95%, 100% and 2× propylene oxide; each run was 10 min), embedded in Durcupan resin (Sigma-Aldrich; Millipore Sigma, Burlington, MA, USA) and flat-mounted between sheets of Aclar Embedding Film (Ted Pella, Inc., Redding, CA, USA) at 60°C for 48–72 h. Mid-rostrocaudal IC sections (between interaural levels 0.24 and 0.36 mm; Paxinos and Watson, 1998) were examined with brightfield stereomicroscopy. Trapezoidal blocks, with a 0.75 mm base and 0.5–0.6 mm height, were extracted across the ventromedial-dorsolateral axis of the ICc (Figure 1). Three "blocks" of tissue were taken from each animal processed in the study. The ventromedial-dorsomedial axis of the rat ICc, after fixation, is approximately 2 mm. To better avoid our dorsolateral-most block including lateral or dorsal cortex of the IC, the total length of tissue taken across the axis was ∼1.8 mm (0.6 mm height per block). Initial borders of the ICc were delineated according to the rat anatomical atlas of the brain (Paxinos and Watson, 1998). Osmium fixation revealing the conspicuous lateral lemniscal fibers, libraries of decarboxylase (GAD) immunoreactivity in EM prepared tissue, adjacent sections reacted for Nissl, and our experience with EM in the IC further guided our block trimming to best ensure tissue was from ICc (Nakamoto et al., 2013; Mellott et al., 2014; Mafi et al., 2022). More specific details on the trimming process can be found in Mafi et al. (2022). Tissue blocks were glued to a cylindric resin base with cyanoacrylate (Krazy Glue, Columbus, OH, USA). IC sections with removed tissue blocks were then imaged for record keeping and representative comparison between cases. We refer to the ventromedial-most ICc block as representing the high frequency region, the middle-most block representing the middle frequency region, and dorsolateral-most block representing lower frequencies (Figure 1). We did not record from the ICc; however we adopt this naming convention for the sake of conciseness, brevity, and convention as the tonotopic axis is well established.

Ultrathin sections were taken at a thickness of 50 nm with an ultramicrotome (UC6 Ultramicrotome, Leica Microsystems, Buffalo Grove, IL, USA). For each block of tissue, every twelfth section was collected onto a 200 or 300-mesh Formvar coated nickel mesh grid (Electron Microscopy Science, Hatfield, PA, USA) to ensure a singular synapse was not collected across two grids and analyzed twice. A total of eight grids, each with a single ultrathin section of layer of the ICc, were collected per block of tissue. Briefly, see Nakamoto et al. (2013) and Mellott et al. (2014), sections dried for 3 h and were then placed overnight into anti-GABA antibody (rabbit anti-GABA, Sigma, St. Louis, MO, USA) diluted 1:500 in 0.05 M Tris-buffered saline with 0.1% Triton X-100, pH 7.6 (TBST), washed in TBST pH 7.6, then washed in TBST pH 8.2, and placed into a secondary antibody conjugated to 15 nm gold particles (goat anti-rabbit, diluted 1:25 in TBST pH 8.2; Ted Pella Inc., Redding, CA, USA). Lastly, sections were washed in TBST pH 7.6, washed in Nanopure water, stained with uranyl acetate (2% aqueous) and Reynold's lead citrate (Reynolds, 1963), and dried.

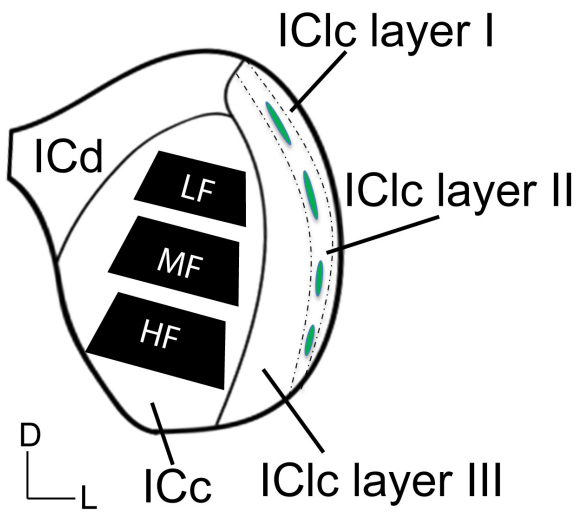


FIGURE 1
Schematic illustrating three subdivisions of the inferior colliculus in the coronal plane. The black trapezoids indicate the regions of ICc across the ventromedial-dorsolateral axis where tissue was extracted from in each case. Dashed lines demonstrate the approximate borders between the three layers of the lateral cortex of the inferior colliculus (ICIc). Green ovals indicate the approximate locations of the GABAergic modules that are often found and define anatomical features of the second ICIc layer. D, dorsal; L, lateral; HF, high frequency region; ICc, central inferior colliculus; ICd, dorsal cortex of the IC; ICIc layer I, the first layer of the lateral cortex of the IC; ICIc layer II, the second layer of the ICIc; ICIc layer III, the third layer of the ICIc; LF, low frequency region; MF, middle frequency region.

2.4 EM imaging

Sixty blocks of tissue from 20 male FBN rats with superior ultrastructure were chosen for imaging and quantification. We use a 5-point scale to grade the intactness and quality of ultrastructure in each case. Only tissue with a score of 4 or 5 was quantified. Our 5-point scale reflects a combination of successful fixation, immunogold processing and absence of electron dense artifacts. Nine of the 15 cases were scored as a "5" and the remaining six cases were a "4." Scores of 4 and 5 yield clear ultrastructure with easily identifiable profiles that are readily resolved. The distinction between a 4 and a 5 is commonly due to a fold in the tissue or excess precipitate, which we avoid when imaging. Tissue scored as a 3 yields ultrastructure that can be qualitatively analyzed; however membrane integrity is not preserved such

that quantitative data can be consistently extracted. All images presented are from a case scored as a 4/5. Tissue scored as a 1 or 2 has severe defects in the pre- and postsynaptic membranes such that synaptic profiles are difficult to interpret. Ultrastructure of the ICc was imaged with a transmission electron microscope (JEM-1400Plus, JEOL, Peabody, MA, USA) at an accelerating voltage of 80 kV and at a magnification of 50,000. Based on experience, a magnification of 50,000 ensures that all inhibitory synapses in the inferior colliculus are visible. Tissue was digitally imaged and rendered with an Orius 100 keV or Rio9 side mount camera (Gatan, Pleasanton, CA, USA). Images of ultrastructure were taken with Gatan Microscopy Suite Software (GMS3, Gatan, Pleasanton, CA, USA) integrated and calibrated with SerialEM Tomography software (Mastronarde, 2003). SerialEM is a gold standard for analytical applications in biological TEM and allowed us to image and analyze and add data at higher rate of efficiency. For each tissue block, we collected 400 μm^2 (22,214 × 22,214 pixels) montages across 8 grids for a total of 3,200 μm^2. All attempts were made such that each montage was collected from the center of each ultrathin section. Montages were analyzed by individuals blind to the age and ICc region imaged. Adobe Photoshop (Adobe Systems, Inc., San Jose, CA, USA) was used to add scale bars, crop images, adjust intensity levels and colorize monochrome images.

2.5 Analysis of inhibitory and excitatory profiles

We recorded each DCV that was present in a bouton, axon, and dendrite. Our classification of ultrastructure is largely based on the criteria defined by Peters et al. (1991) and our previous work (Mellott et al., 2014; Nakamoto et al., 2014; Mafi et al., 2022). Briefly, boutons have a "pool" of vesicles with clear centers and generally an absence of a cytoskeleton. We never observed a bouton with a DCV without clear vesicles. Dendrites were identified through a combination of criteria (irregular contours, spines, presence of synaptic inputs, and free ribosomes). Axons were commonly myelinated, and axons do not commonly contain free ribosomes in their cytoplasm. Identifying small unmyelinated axons from small dendrites provides some difficulty (Peters et al., 1991). Generally speaking, small axons in the IC travel as bundles through the neuropil while dendrites travel in irregular patterns and are not typically in bundles. Additionally, the presence of ribosomes can help identify dendrites. When identifying a presynaptic terminal with a DCV we first note if the postsynaptic density is symmetric or asymmetric. We then classified each profile (bouton, axon, and dendrite) as non-GABAergic or GABAergic based on the accumulation of gold particles as compared to background (Nakamoto et al., 2013; Mellott et al., 2014; Mafi et al., 2022). In our previous report on the aging ultrastructure of the IC, we found that immunogold labeling was reduced in the aged tissue (Mafi et al., 2022). To maintain consistency between studies, older structures that were characterized as GABAergic had to have a density of gold particles that was at least three times greater than background. Although the goal of the current study was not synaptic analysis, when a DCV was identified in a bouton forming a synapse, we characterized the synapse as either excitatory or GABAergic for qualitative analysis. Synapses were classified by: (1) vesicle shape [pleomorphic vesicles (inhibitory) or round vesicles (excitatory)] and, (2) postsynaptic densities forming symmetric (pre- and postsynaptic membranes were of similar thickness; inhibitory) or asymmetric (postsynaptic densities were conspicuously thicker than the presynaptic densities; excitatory) junctions (Rockel and Jones, 1973; Paloff and Usunoff, 1992; Helfert et al., 1999; Nakamoto et al., 2013). Detailed descriptions characterizing IC ultrastructure with post-embedding immunogold techniques to label GABAergic profiles can be found in Nakamoto et al. (2013) and Mafi et al. (2022).

2.6 Data analysis

We examined 48,000 μm^2 of ICc across five blocks of 3–4-month-old tissue, 48,000 μm^2 of ICc across five blocks of 19–20-month-old tissue, 48,000 μm^2 of ICc across five blocks of 24-month-old tissue, and 48,000 μm^2 of ICc across five blocks of 28–29-month-old tissue with ImageJ (Schneider et al., 2012; **Table 1**). As boutons and synapses are known to be reduced in the aging IC, we quantified each bouton in each tissue block of each case to better understand age-related changes to the presence of DCVs in boutons (Helfert et al., 1999; Mafi et al., 2022).

Variation in number of DCVs by ultrastructural location according to age group, was analyzed using one-way analysis of variance (ANOVA) models for each region. Six separate ANOVAs were run with age as the independent variable and number of DCVs as the outcome. Tukey's Honest Significant Difference (HSD) was run for pairwise *post-hoc* tests of differences between consecutive age groups (i.e., 3–4 months versus 19–20 months, 19–20 months versus 24 months, 24 months versus 28–29 months) and pairwise values were adjusted using the false discovery rate procedure (Benjamini and Hochberg, 1995), a method that simultaneously limits experiment-wise alpha inflation and minimizes the correlated loss of statistical power. All statistical tests were performed in R (version 3.6.3 for Mac OS X; R Core Team, 2020), supplemented by the add-on packages *nlme compareGroups* (Subirana et al., 2014).

3 Results

We examined the ultrastructural location of DCVs in non-GABAergic and GABAergic terminals, axons, and dendrites across four age groups (3–4 months, 19–20 months, 24 months, and 28–29 months) in the central inferior colliculus (ICc). We analyzed 3,811 DCVs in excitatory profiles and 1,567 DCVs in inhibitory profiles across 192,000 μm^2 of tissue (**Table 1**). DCVs were most commonly located in non-GABAergic profiles at each age (**Table 1**). The most robust age-related increases of DCVs also occurred in non-GABAergic profiles (**Table 1**). We first describe DCV ultrastructure across the ventromedial-dorsolateral axis of the ICc. We then present data regarding age-related increases of DCVs in the dendrites of IC cells. Lastly, we qualitatively describe the frequency of DCVs in non-GABAergic and GABAergic boutons in the aging IC.

10.3389/fncel.2024.1396387

3.1 DCVs can be found across the ICc, regardless of age

Regardless of age and ventromedial-dorsolateral location, DCVs were found in dendrites, terminals, and axons in the ICc (Figure 2). We observed DCVs in both GABAergic and non-GABAergic presynaptic terminals in the ICc (Figures 2A, C, H, J–L). DCVs were also found in GABAergic and non-GABAergic dendrites (Figures 2D–G, I). Often, DCVs located in dendrites were near the postsynaptic density (Figures 2D, F, G, I). We did not observe DCVs at dendrodendritic synapses; it appears that dendrodendritic synapses in the rat IC are rare. At 28–29 months DCVs were found in presynaptic terminals forming non-prototypical synapses [e.g., GABAergic synapse forming an apparent asymmetric synapse (Figure 2J), non-GABAergic synapse with a subsynaptic body (Figure 2L)]. However, it was rare to observe a DCV bound to the pre- or postsynaptic membrane (Figure 2).

3.2 DCVs increase with age in non-GABAergic dendrites in low- and middle-frequency areas of the ICc

The total number of DCVs in non-GABAergic dendrites at 3–4 months across the high (ventromedial), middle and low (dorsolateral) frequency regions was 84, 83, and 81, respectively (Table 1). By 19–20 months these values doubled across the IC and increased further at 24 months (Table 1). When DCVs were observed in dendrites, they were typically singular and not near other DCVs. However at older ages in the low and middle frequency regions, while still uncommon, we observed DCVs near each other (Figure 3). In the low frequency region, the number of DCVs significantly increased from 83 to 226 at 24 months ($^*p$ = 0.004; Figure 4A). In the middle frequency region, the number of DCVs significantly increased from 83 to 255 at 24 months ($^*p$ = 0.025; Figure 4A). However the age-related increase of DCVs was not found to be significant at 19–20 months and 28–29 months (Figure 4A). In the high frequency region, despite an increase in the number of DCVs with age, our models did not detect a significant increase with age (Figure 4A).

3.3 DCVs do not significantly increase with age in GABAergic dendrites in the ICc

Although the total raw number of DCVs increased at older ages in the GABAergic dendrites, we found no significant change from 3 to 4 months in the high frequency region, middle frequency region and low frequency region (Figure 4B). A contributing factor to the non-significant findings appears to be the variability of DCV pools in the aging GABAergic dendrites. During aging we observed a few aged GABAergic dendrites in cross-section with dozens of DCVs (Figure 5). Thus, it appears that a few select neurons in the ICc may retrogradely transport neurotrophins and/or neuropeptides at great quantities during aging.

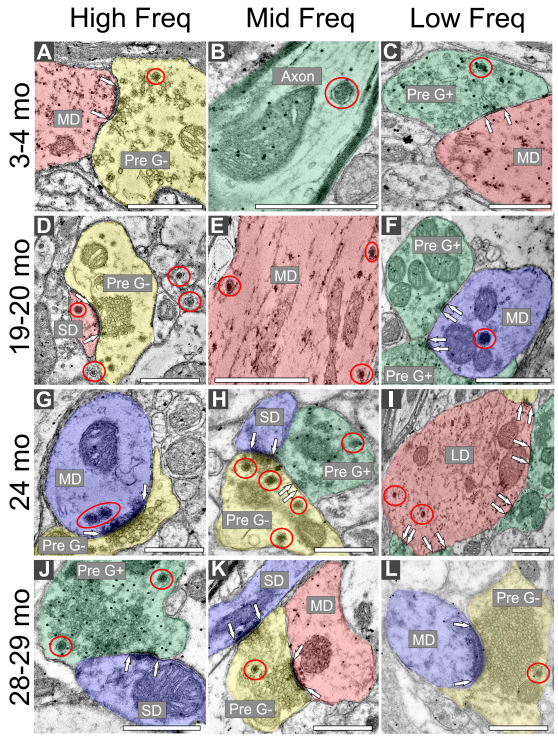


FIGURE 2
Electron micrographs across four age groups showing dense core vesicle (DCV) ultrastructure across the ventromedial-dorsolateral axis of the central inferior colliculus (ICc). GABAergic presynaptic (Pre G+) terminals are pseudocolored green. GABAergic postsynaptic targets are pseudocolored red. GABA-negative presynaptic (Pre G−) terminals are pseudocolored yellow. GABA-negative postsynaptic targets are pseudocolored blue. Black dots demonstrate immunogold labeling of GABA. Synapses are indicated by pairs of white arrows. **(A–C)** Electron micrographs showing examples of DCVs in 3–4 month old tissue across the ventromedial-dorsolateral axis of the ICc. **(D–F)** Electron micrographs showing examples DCVs in 19–20 month old tissue across the ventromedial-dorsolateral axis of the ICc. **(G–I)** Electron micrographs showing examples DCVs in 24 month old tissue across the ventromedial-dorsolateral axis of the ICc. **(J–L)** Electron micrographs showing examples DCVs in 28 month old tissue across the ventromedial-dorsolateral axis of the ICc. DCVs are circled in red. LD, large dendrite; MD, medium dendrite; SD, small dendrite. Scale bars, 500 nm.

3.4 Non-GABAergic boutons with DCVs are more likely to be spared in aging

Approximately 6% of non-GABAergic boutons had one or more DCVs at 3–4 months of age (Table 2). The majority of these boutons had just one DCV, regardless of location in the ICc (Figure 6 and Table 2). At later ages, it became more common to find non-GABAergic boutons with at least one DCV, and boutons with multiple DCVs also increased (Figures 6, 7 and Table 2). These boutons with multiple DCVs commonly made synapses onto non-GABAergic dendrites (Figure 7). The most conspicuous increase of DCVs occurred in the high frequency ICc at 19–20 months, and the high and middle frequency regions at 24 months (Figure 6 and Table 2). At 3–4 months of age, the low frequency ICc had the greatest raw number (100) of DCVs (Table 2). However, by 19–20 months

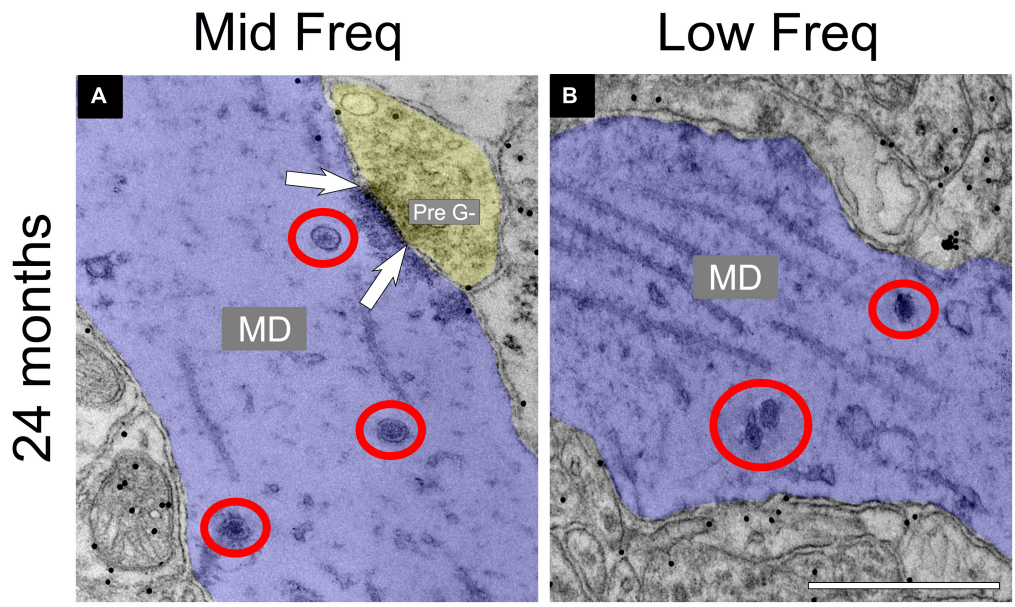


FIGURE 3
Electron micrographs at 24 months showing dense core vesicle (DCV) ultrastructure in the middle and low frequency regions of the central inferior colliculus (ICc). GABA-negative dendrites are pseudocolored blue. A GABA-negative presynaptic (Pre G–) terminal is pseudocolored yellow. Black dots demonstrate immunogold labeling of GABA. Synapses are indicated by pairs of white arrows. **(A)** Electron micrograph showing a group of DCVs in a non-GABAergic dendrite at 24 months in the middle frequency region of the ICc. **(B)** Electron micrograph showing a group of DCVs in a non-GABAergic dendrite at 24 months in the low frequency region of the ICc. DCVs are circled in red. MD, medium dendrite. Scale bars, 500 nm.

the number of DCVs in the high frequency/ventromedial region had more than doubled (75–162), and the percentage of non-GABAergic boutons with at least one DCV increased from 5.24% to 11.2% (Table 2). At 24 months, the number of DCVs in the middle frequency region of the ICc doubled (68–160), and the percentage of boutons with at least one DCV increased from 6.6% to 10.5% (Table 2). Increases in the number of DCVs in the low frequency region were less robust between 3–4 months and 24/28–29 months (100–133), and the percentage of boutons having at least one DCV between 3–4 months and 28 months increased slightly (6.8%–8.7%; Table 2). Overall, these increases were largely driven by an increasing population of non-GABAergic boutons having four or more DCVs (Figure 7 and Table 2).

As boutons and synapses are known to be downregulated in the aging IC, we quantified each non-GABAergic bouton in our experiments to better understand what proportion of boutons contain DCVs during aging. At 3–4 months we found a consistent number of boutons across the ventromedial-dorsolateral axis of the ICc (high-1,067; middle-1,031; low-1,096: Table 2). In the high frequency region at 19–20 month, 24 months, and 28–29 months there was a 9.1%, 23.8%, and 29.7% reduction of non-GABAergic boutons, respectively (Table 2). In the middle frequency region at 19–20 months, 24 months, and 28–29 months there was a 7.4%, 20.9%, and 24.8% reduction of non-GABAergic boutons, respectively (Table 2). Lastly, in the low frequency region at 19–20 months, 24 months, and 28–29 months there was a 8.0%, 15.8%, and 17.6% reduction of non-GABAergic boutons, respectively (Table 2). Taken together with the data mentioned above, our findings suggest that non-GABAergic cells/boutons that package DCVs are more likely to be spared during aging than non-GABAergic cells/boutons that do not package DCVs.

3.5 GABAergic boutons with DCVs are more likely to be spared in aging

Similar to non-GABAergic boutons, at any age and/or ICc location GABAergic boutons that contained DCVs typically had just one (Figure 8). GABAergic boutons with multiple DCVs occurred more routinely during aging in the middle and low frequency regions (Figure 8). However, at older ages, the proportion of GABAergic boutons with just one DCV increased in the high frequency ICc (Figure 8). As with the non-GABAergic population, during aging there was a greater raw number of DCVs in GABAergic boutons and a higher number of GABAergic boutons with at least one DCV in the high and middle frequency regions of the ICc (Figure 8 and Table 3). The raw number of DCVs in GABAergic boutons and number of GABAergic boutons with at least one DCV peaked at 24 months, but was lowest at 28 months (Figure 8 and Table 3).

We also quantified each GABAergic bouton in our experiments. Unsurprisingly, there was an overall reduction of GABAergic boutons at each age and at each ICc region (Table 3). The percentage of GABAergic boutons across the ICc with a DCV was only ~4% at 3–4 months and increased during aging, with greater variability in the low frequency ICc (Table 3). Taken together we come to the same conclusion as we have with the non-GABAergic population: GABAergic cells/boutons that package DCVs are more likely to be spared during aging than GABAergic cells/boutons that do not package DCVs.

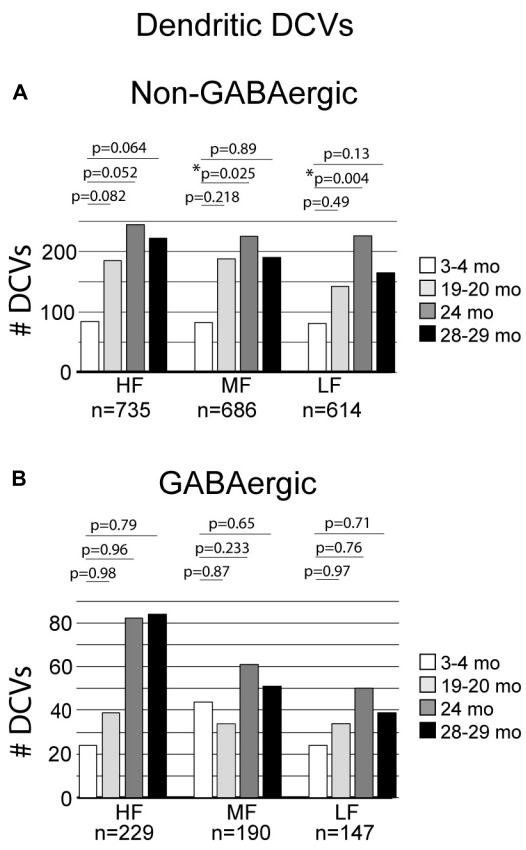


FIGURE 4
Bar graphs summarizing the number of DCVs found in non-GABAergic and GABAergic dendrites. **(A)** Pairwise differences demonstrated a significant increase of DCVs in non-GABAergic dendrites in the middle frequency region between 3–4 and 24 months (*p = 0.025). Pairwise differences also revealed a significant increase of DCVs in non-GABAergic dendrites in the low frequency region at 24 months (*p = 0.004). **(B)** Pairwise differences demonstrated no significant age-related differences in the number of DCVs from 3 to 4 months across GABAergic dendrites in the high frequency region (19–20 months, p = 0.98; 24 months, p = 0.96; 28–29 months, p = 0.79), middle frequency region (19–20 months, p = 0.87; 24 months, p = 0.233; 28–29 months, p = 0.65), and low frequency region (19–20 months, p = 0.97; 24 months, p = 0.76; 28–29 months, [p = 0.71]). Each age group had five cases.

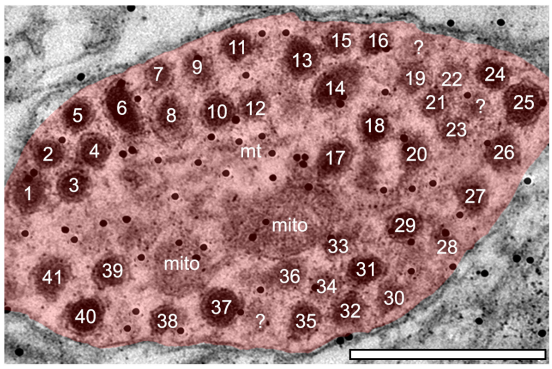


FIGURE 5
Electron micrograph of a medium sized GABAergic dendrite at 24-months from the ventromedial (high frequency region) of the central IC with over 40 DCVs. Although rare, GABAergic dendrites packed with DCVs could be found in the aged IC. Black dots demonstrate immunogold labeling of GABA. mito, mitochondria; ?, likely DCV. Scale bar, 500 nm.

4 Discussion

The current study describes populations of DCVs in the aging ICc. Our findings demonstrate that DCVs are infrequent in the young rat ICc. This agrees with studies conducted in cat (Paloff and Usunoff, 1992). However, our data demonstrate that DCVs increase with aging in the rat ICc. Specifically we found the greatest increase of DCVs at 24 months in non-GABAergic dendrites throughout the middle and dorsolateral portions of the ICc's ventromedial-dorsolateral tonotopic axis (corresponding to mid- and low-frequency representation). This is interesting as the FBN rat has been shown to lose low frequency hearing around 24 months of age (Keithley et al., 1992; Caspary et al., 2005; Cai et al., 2018). While the raw number of DCVs in boutons did not significantly change during aging, there was (1) an increase in the number of boutons with multiple DCVs, and (2) the percentage of all boutons that had at least one DCV increased with age. Given that we broadly found a ~25% loss of boutons across the ICc, which reflects findings by Helfert et al. (1999), we interpret our data to imply that presynaptic boutons in the ICc which are lost with age are not likely releasing contents that would be packaged by a DCV. As this is the first report of age-related changes to DCVs in the IC, future studies will hopefully determine what neuropeptides, neurotrophins and/or presynaptic proteins are undergoing age-related changes in the IC.

4.1 Technical considerations

The FBN rat is a recommended aging model by the National Institute on Aging as it has a longer median lifespan than other strains of mice and rats (Lipman et al., 1996; Lipman, 1997). Of note, the FBN rat is routinely used as a characterized model for aging, in particular for studies of the central auditory system (Caspary et al., 2008; Cai et al., 2018; Caspary and Llano, 2018; Robinson et al., 2019; Mafi et al., 2020, 2021, 2022; Kommajosyula et al., 2021). We have chosen to use four age groups in this study. Our 3–4 month and 28–29 month groups are standard ages for "young" and "old," when there are no hearing deficits and very well characterized hearing loss, respectively. The use of two middle ages, a 19–20 month group and 24 month group, reflect ages when hearing deficits are not commonly reported and when hearing thresholds are significantly elevated, respectively (Cai et al., 2018). However, we acknowledge that the hearing thresholds of the FBN rats in the current study were not measured and we do not know if a 19 month old rat had perfect hearing or if a 24 month old rat had poor hearing.

In the current study we equate parts of the ICc with tonotopic regions (e.g., low-frequency region). We did not characterize IC cells with electrophysiological techniques in the current study. We took the ventromedial-dorsomedial axis of the ICc tissue and divided it into thirds. While we do not know the characteristic frequencies represented in each tissue block, as the tonotopic axis of the IC is well established, we have no reason to believe that

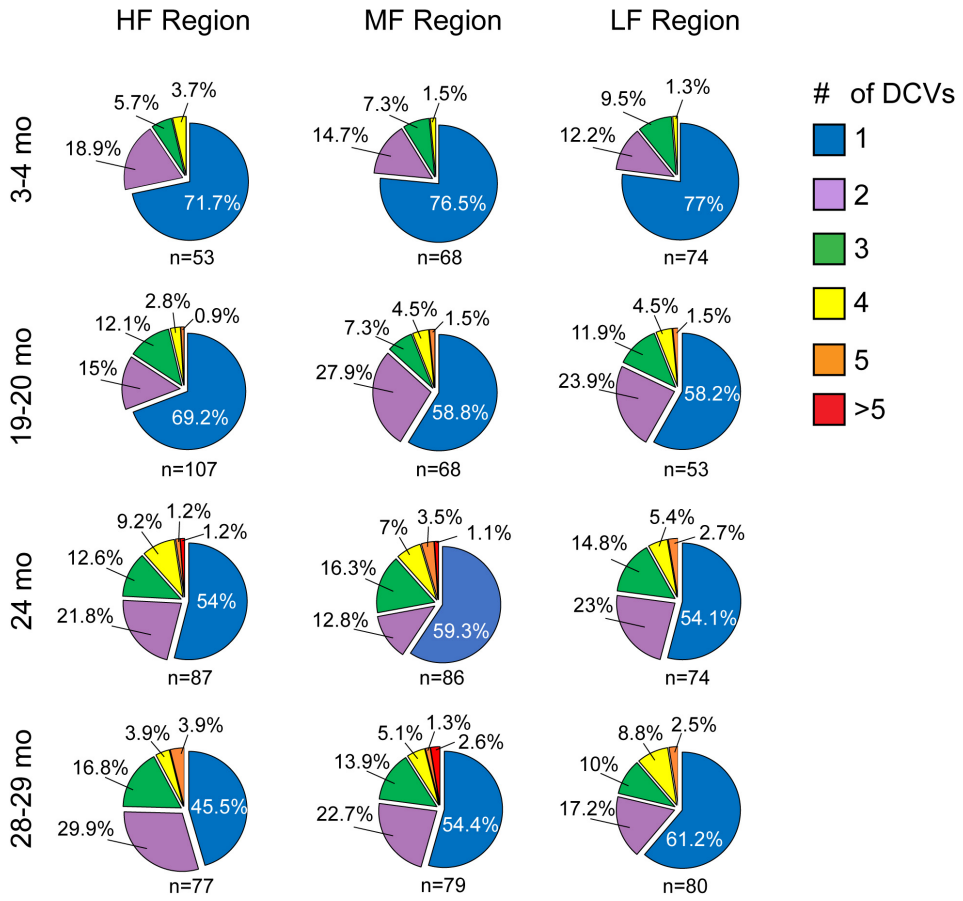


FIGURE 6
Pie charts showing the distribution of non-GABAergic boutons that had at least one DCV across four age groups from tissue representing the high, middle, and low frequency regions of the ICc. Regardless of ICc region, when a bouton had a DCV at 3–4 months, having just one was the most common (blue). We did not observe a 3–4 month non-GABAergic bouton with five or more. At the three later ages it became more common for non-GABAergic boutons that had a DCV to have three (green), four (yellow), five (orange), or more (red). The *n*'s represent the number of boutons that had at least one DCV. HF, high frequency; MF, middle frequency; LF, low frequency.

our ventromedial most block does not represent higher frequencies compared to the other two blocks; and the dorsolateral most block would represent the lowest frequencies. Another consideration in the interpretation of our data is that, although a common view of the IC's tonotopic map is one of a continuous gradient, the rat IC tonotopic map may be organized in a stepwise manner (Malmierca et al., 2008). Thus, our middle-most ICc blocks may represent frequencies closer to one end of the tonotopic map than the other.

We only immunolabeled for GABA, thus we cannot know the neurochemical profile of boutons that were not GABAergic. In terms of non-GABAergic boutons that formed symmetric synapses, we presume these are in part glycinergic. That said, the IC receives input from many neuromodulators, and the morphology of their postsynaptic densities are not well classified (Schofield and Hurley, 2018). We hope that this study will serve as a foundation to examine the ultrastructure of neuromodulators and neurotransmitters that are packaged by DCVs in the aging IC.

4.2 DCVs in the inferior colliculus

The first ultrastructural description of DCVs in the IC was in cat (Jones and Rockel, 1973; Rockel and Jones, 1973; Paloff et al., 1989). Decades later, boutons containing DCVs were characterized in greater detail and defined a unique type of ICc bouton (Paloff and Usunoff, 1992). The current study broadly agrees with the findings from these original studies: (1) DCVs occurred in boutons with pools of smaller clear vesicles, (2) DCVs were not clustered toward the synapse or membrane, (3) boutons with DCVs commonly had 0–1 mitochondria, (4) DCVs are not uniformly found throughout the ICc, and (5) DCVs are generally uncommon in the ICc (Paloff and Usunoff, 1992). Our findings are further in line with Paloff and Usunoff (1992) in that we found presynaptic terminals with a DCV(s) terminating on a soma to be exceedingly rare (observed only once in our analysis of 192,000 μm^2 of tissue). However,

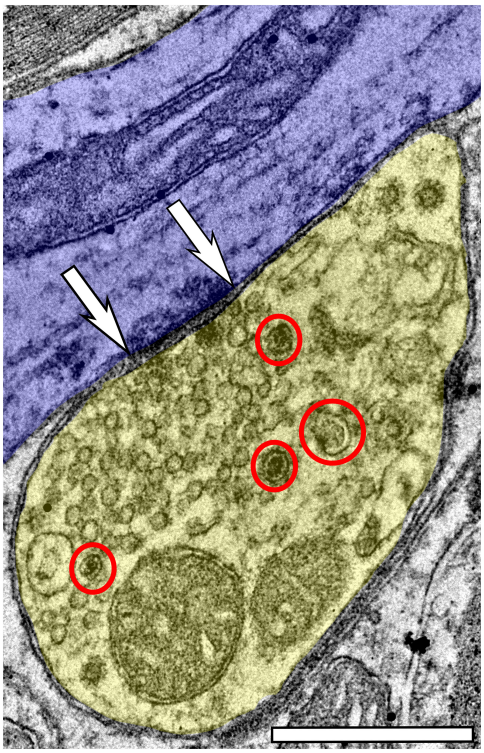


FIGURE 7
Electron micrograph of a non-GABAergic terminal from the dorsolateral (low frequency region) of the ICc at 28–29 months with at least four DCVs forming an asymmetric synapse onto a non-GABAergic medium dendrite. DCVs are circled in red. Scale bar, 500 nm.

Rockel and Jones (1973) found that boutons carrying DCVs more routinely terminate on cell bodies.

The current study (in rat) differs from the previous studies (in cat) in two ways. First, work in the cat has demonstrated that when DCVs are present in presynaptic boutons, there may be over one to two dozen (Rockel and Jones, 1973; Paloff and Usunoff, 1992). The current study in rats, and mice (unpublished observations), rarely revealed more than three DCVs in a single bouton. Previous reports of the rat IC ultrastructure also imply that DCVs, let alone pools of them, are rare (Ribak and Roberts, 1986; Roberts and Ribak, 1987). Even though Roberts and Ribak revealed and described the rat IC ultrastructure in considerable detail, only one DCV is visible throughout their images (Ribak and Roberts, 1986; Roberts and Ribak, 1987). Our data also appears to be in agreement with prior studies in rat hippocampus that quantified DCVs, as presynaptic terminals containing DCVs commonly had only a few (Sorra et al., 2006; Tao et al., 2018). Taken together, we believe that the pool size of DCVs in presynaptic terminals is likely species dependent.

Second, we found that the number of DCVs found in dendrites was nearly equal to the number of DCVs found in axons/boutons at young age (**Table 1**). Furthermore, specifically during middle-age in the dorsolateral half of the ICc, there was a significant age-related increase of DCVs in the ICc dendrites. Previous reports focus on DCVs pools in the IC do not describe a consistent population of DCVs throughout the dendrites of the ICc (Rockel and Jones, 1973; Paloff and Usunoff, 1992). It is unknown if these reports simply did not analyze dendrites for DCVs or if there is a species difference between cats and the current studies that largely utilize rodent and cell culture. However, in the mammalian central nervous system, DCVs pools can be found equally distributed between the dendrites and axons/terminals of a given cell (Persoon et al., 2018). However, DCVs in the axons and boutons are often focused on as their release probability is much higher than the ones in the dendrites (Persoon, et al., 2018). It is important to note DCV fusion events in dendrites are not as tightly time locked to a cell firing and require sustained Ca^{2+} (Xia et al., 2009). Fusion mechanism aside, dendritic exocytosis is a critical function for retrograde signaling, synapse growth and plasticity, and cellular morphology and DCVs play a prominent role in the dendritic release of many neuropeptides and neurotrophins (Regehr et al., 2009; Kennedy and Ehlers, 2011; Ramamoorthy et al., 2011).

A major finding of the current study was that while there was a loss (~25%) of boutons at old age, the percentage of boutons with DCVs did not change with age. Similar to the dendritic population, the more robust increases occurred in the GABA-negative boutons. We found that non-GABAergic and GABAergic boutons with DCVs made synapses onto both GABAergic and excitatory dendrites (we presume non-GABAergic dendrites in the IC are excitatory as only GABAergic and glutamatergic cells have been demonstrated in the IC, Merchán et al., 2005; Oliver, 2005) at any age. Thus, the contents of DCVs in the aging IC are likely affecting both inhibitory and excitatory circuits.

4.3 Functional implications

Broadly, DCVs are divided into small (~40–80 nm) and large (~90–200 nm) groups (Peters et al., 1991; Paloff and Usunoff, 1992; Edwards, 1998; Sorra et al., 2006; Trueta and De-Miguel, 2012; Merighi, 2018; Tao et al., 2018). Smaller DCVs tend to package biogenic amines, neuromodulators, and presynaptic machinery, while larger DCVs tend to package neuropeptides, hormones and neurotrophic factors (Peters et al., 1991; Michael et al., 2006; Sorra et al., 2006; Merighi, 2018). The exact diameter that defines a small versus a large DCV appears to be a sliding scale based on location (peripheral or central nervous system) and species, and what ultimately determines the size of a DCV is not well known (Merighi, 2018; Lin et al., 2022). Regardless of diameter, there appears to be considerable differences in the locations, releasing mechanisms, stimulation rates for release, and packaged content of DCVs between the peripheral and central nervous systems, nuclei within in the central nervous system, and between cultured and *in vivo* studies (Hökfelt, 2010; Kennedy and Ehlers, 2011; Persoon et al., 2018). In the central nervous system, much of our knowledge regarding DCVs is obtained from the hippocampus, hypothalamus, and neuromodulatory nuclei (e.g. Raphe and Locus Coeruleus: Sorra et al., 2006; Trueta and De-Miguel, 2012). As this is the first report on the aging DCV population in the IC, further studies are needed to reveal the functional relevance of our data. That said, we would like to comment on a few functions that an age-related increase of DCVs may reflect.

4.3.1 Hearing loss and neuromodulation

GABAergic inhibition is reduced in the aging IC (Caspary et al., 2008; Syka, 2020). This downregulation of GABA

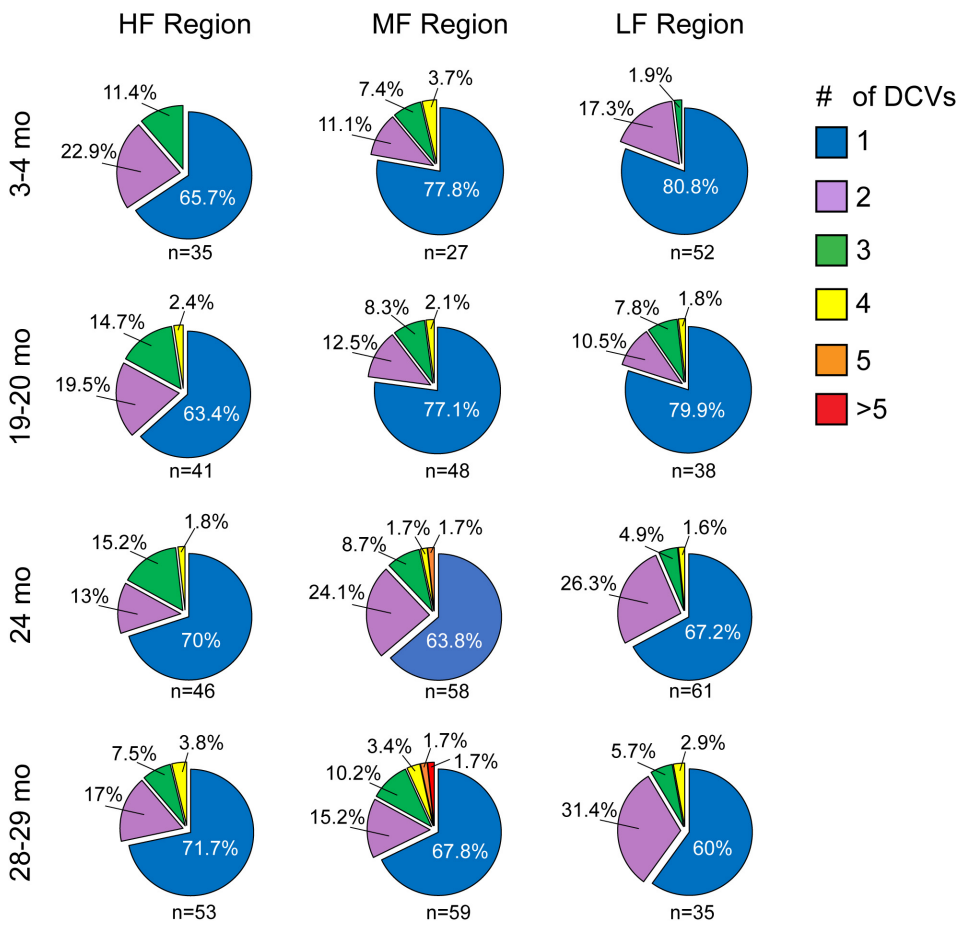


FIGURE 8
Pie charts showing the distribution of GABAergic boutons that had at least one DCV across four age groups from tissue representing the high, middle, and low frequency regions of the ICc. Regardless of ICc region, when a bouton had a DCV at 3–4 months, having just one was the most common (blue). We did not observe a 3–4 month GABAergic bouton with five or more. At the three later ages there was a slight increase in the number of GABAergic boutons with four (yellow) or more (orange and red) DCVs. The *n*'s represent the number of boutons that had at least one DCV. HF, high frequency; MF, middle frequency; LF, low frequency.

may be a compensatory homeostatic response to the loss of peripheral excitation (Caspary et al., 2008; Richardson et al., 2012; Caspary and Llano, 2018). Later in life the ongoing decline in GABAergic neurotransmission likely contributes to disrupted temporal precision and increases in central gain that underlie conditions such as presbycusis, tinnitus, and hyperacusis (Palombi and Caspary, 1996; Frisina, 2001; Brozoski et al., 2002; Walton et al., 2002; Norena, 2011; Parthasarathy and Bartlett, 2011; Auerbach et al., 2019).

Although a number of neuromodulators are released in the IC (e.g., serotonin, dopamine, acetylcholine, and noradrenaline), their roles in the aging IC across middle and old ages have not been thoroughly explored (Klepper and Herbert, 1991; Paloff and Usunoff, 2000; Hurley and Pollak, 2005a; Motts and Schofield, 2009; Hurley and Sullivan, 2012; Schofield and Hurley, 2018; Noftz et al., 2020, 2021). In the context of the current study, serotonin neurotransmission may be a promising avenue to pursue in future studies. First, serotonin is known to be packaged in DCVs in the central nervous system (Bruns et al., 2000; Trueta and De-Miguel, 2012; Kim et al., 2021). Second, serotonin has a myriad of functions in the IC (Hurley and Pollak, 1999, 2001, 2005b; Hurley et al., 2002). Third, it is known that aging and hearing loss affects serotonergic neurotransmission (Tadros et al., 2007; Hall et al., 2012; Shim et al., 2012). It is notable that in each of these studies, serotonin and its receptors increased in the aging IC and during hearing loss. Perhaps the increase of DCVs is correlated with increases of serotonin neurotransmission in the aging IC.

Recent studies in the IC have identified a novel class of GABAergic cells that express the neuropeptide/neuromodulator NPY (Silveira et al., 2020, 2023; Anair et al., 2022). Generally speaking, NPY in the brain provides neuroprotective effects during healthy and pathological aging (Chen et al., 2019; Pain et al., 2022). Interestingly, NPY can be trafficked down dendrites, released postsynaptically, and act on presynaptic and postsynaptic receptors

(Ramamoorthy et al., 2011; Yi et al., 2018). Future studies will use immunoEM to determine if NPY is also trafficked by DCVs in the dendrites of GABAergic IC cells. Given that NPY significantly regulates local excitation in the IC, it will be critical to determine how the balance of excitation and inhibition is affected by NPY neurotransmission in the aging IC. Our data show increased DCVs in middle and low frequency IC in a model of presbycusis, so it will be interesting to determine whether serotonin or NPY effects change across the tonotopic axis.

4.3.2 Brain-derived growth factor and plasticity

Another potential peptide contained in IC DCVs is BDNF, a neurotrophin released by DCVs throughout the brain to regulate functions such as synaptic transmission, plasticity, neurite growth, and gene regulation (Kennedy and Ehlers, 2011; Dieni et al., 2012). In the auditory system, BDNF is critical for development and normal acoustic function (Wissel et al., 2006; Singer et al., 2014; Chumak et al., 2016). In the IC, BDNF has been tied to development, acoustic trauma, and dendritic integrity (Hafidi et al., 1996; Sato et al., 2001; Sharma et al., 2009; Meltser and Canlon, 2010). Further studies will need to determine if BDNF DCVs are trafficked to IC axons, dendrites or both as the cellular location of BDNF DCVs differ across reports (Dean et al., 2009; Matsuda et al., 2009; Kennedy and Ehlers, 2011; Dieni et al., 2012; Persoon et al., 2018).

Fibroblast growth factors are another likely protein packaged by IC DCVs. Compellingly, levels of fibroblast growth factor receptor 2 (FGF-2) spike during middle age when hearing deficits are not common, and while there is a decrease at old age, FGF-2 levels are still elevated compared to young brains (Sato et al., 2001). This pattern is very similar to trends in the current study, where DCVs in excitatory dendrites maximally increase at middle age and then decline into old age, yet are still more numerous than at young age. Given that (1) FGF-2 contributes to dendritic arborization and synaptic plasticity, (2) DCVs often carry contents such growth factors that play a role in synaptogenesis, and (3) the aged IC has a loss of dendrites and synapses, the IC may undergo a number of plastic events during middle age (Helfert et al., 1999; Sorra et al., 2006; Li et al., 2020). Further supporting the theory of increased plasticity with aging in the IC, perineuronal nets (organized extracellular matrix that have substantial roles in neural plasticity) increase with aging in the IC (Fader et al., 2016; Bosiacki et al., 2019; Mafi et al., 2020, 2021; Almassri et al., 2023). Taken altogether, the increase of DCVs in the aging IC may contribute to elements of dendritic and synaptic plasticity.

Data availability statement

The original contributions presented in this study are included in the article/supplementary material, further inquiries can be directed to the corresponding author.

Ethics statement

The animal study was approved by the Northeast Ohio Medical University Institutional Animal Care and Use Committee. The study was conducted in accordance with the local legislation and institutional requirements.

Author contributions

JM: Conceptualization, Data curation, Funding acquisition, Investigation, Methodology, Project administration, Resources, Supervision, Validation, Visualization, Writing – original draft, Writing – review & editing. SD: Data curation, Formal analysis, Investigation, Writing – review & editing. JB: Data curation, Formal analysis, Investigation, Writing – review & editing. LA: Writing – original draft, Writing – review & editing. AW: Data curation, Formal analysis, Investigation, Supervision, Writing – review & editing. MI: Formal analysis, Investigation, Writing – review & editing. AO: Investigation, Methodology, Supervision, Writing – review & editing. ES: Data curation, Formal analysis, Investigation, Writing – review & editing. AB: Data curation, Investigation, Writing – review & editing. DA: Data curation, Investigation, Writing – review & editing. BV: Data curation, Investigation, Writing – review & editing. AM: Data curation, Formal analysis, Investigation, Methodology, Writing – review & editing. MB: Data curation, Formal analysis, Investigation, Methodology, Software, Writing – review & editing. NT: Investigation, Project administration, Supervision, Writing – review & editing. JY: Data curation, Formal analysis, Software, Supervision, Writing – review & editing.

Funding

The author(s) declare financial support was received for the research, authorship, and/or publication of this article. This work was supported by the NIH/NIDCD grant R01 DC017708 and National Institute on Aging rodent colony.

Acknowledgments

We gratefully acknowledge Dr. Nichole Beebe for critical feedback on an earlier draft of the manuscript.

Conflict of interest

The authors declare that the research was conducted in the absence of any commercial or financial relationships that could be construed as a potential conflict of interest.

Publisher's note

All claims expressed in this article are solely those of the authors and do not necessarily represent those of their affiliated organizations, or those of the publisher, the editors and the reviewers. Any product that may be evaluated in this article, or claim that may be made by its manufacturer, is not guaranteed or endorsed by the publisher.

References

Almassri, L. S., Ohl, A. P., Iafrate, M. C., Wade, A. D., Tokar, N. J., Mafi, A. M., et al. (2023). Age-related upregulation of perineuronal nets on inferior collicular cells that project to the cochlear nucleus. *Front. Aging Neurosci.* 15:1271008. doi: 10.3389/fnagi.2023.1271008

Anair, J. D., Silveira, M. A., Mirjalili, P., Beebe, N. L., Schofield, B. R., and Roberts, M. T. (2022). Inhibitory NPY neurons provide a large and heterotopic commissural projection in the inferior colliculus. *Front. Neural Circ.* 16:871924. doi: 10.3389/fncir.2022.871924

Auerbach, B. D., Radziwon, K., and Salvi, R. (2019). Testing the central gain model: Loudness growth correlates with central auditory gain enhancement in a rodent model of hyperacusis. *Neuroscience* 407, 93–107. doi: 10.1016/j.neuroscience.2018.09.036

Auerbach, B. D., Rodrigues, P. V., and Salvi, R. J. (2014). Central gain control in tinnitus and hyperacusis. *Front. Neurol.* 5:206. doi: 10.3389/fneur.2014.00206

Benjamini, Y., and Hochberg, Y. (1995). Controlling the false discovery rate: A practical and powerful approach to multiple testing. *J. R. Stat. Soc. Ser. B* 57, 289–300.

Bosiacki, M., Gąssowska-Dobrowolska, M., Kojder, K., Fabiańska, M., Jeżewski, D., Gutowska, I., et al. (2019). Perineuronal nets and their role in synaptic homeostasis. *Int. J. Mol. Sci.* 20:4108. doi: 10.3390/ijms20174108

Brozoski, T. J., Bauer, C. A., and Caspary, D. M. (2002). Elevated fusiform cell activity in the dorsal cochlear nucleus of chinchillas with psychophysical evidence of tinnitus. *J. Neurosci.* 22, 2383–2390.

Bruns, D., Riedel, D., Klingauf, J., and Jahn, R. (2000). Quantal release of serotonin. *Neuron* 28, 205–220. doi: 10.1016/s0896-6273(00)00097-0

Cai, R., Montgomery, S. C., Graves, K. A., Caspary, D. M., and Cox, B. C. (2018). The FBN rat model of aging: Investigation of ABR waveforms and ribbon synapse changes. *Neurobiol. Aging* 62, 53–63.

Caspary, D. M., Ling, L., Turner, J. G., and Hughes, L. F. (2008). Inhibitory neurotransmission, plasticity and aging in the mammalian central auditory system. *J. Exp. Biol.* 211, 1781–1791.

Caspary, D. M., and Llano, D. A. (2018). "Aging process in the subcortical auditory system," in *The Oxford Handbook of the Auditory Brainstem*, ed. K. Kandler (Oxford: Oxford Press), 1–45. doi: 10.1093/oxfordhb/9780190849061.013.16

Caspary, D. M., Schatteman, T. A., and Hughes, L. F. (2005). Age-related changes in the inhibitory response properties of dorsal cochlear nucleus output neurons: Role of inhibitory inputs. *J. Neurosci.* 25, 10952–10959.

Chen, X., Du, Y., and Chen, L. (2019). Neuropeptides exert neuroprotective effects in Alzheimer's Disease. *Front. Mol. Neurosci.* 11:493. doi: 10.3389/fnmol.2018.00493

Chumak, T., Rüttiger, L., Lee, S. C., Campanelli, D., Zuccotti, A., Singer, W., et al. (2016). BDNF in lower brain parts modifies auditory fiber activity to gain fidelity but increases the risk for generation of central noise after injury. *Mol. Neurobiol.* 53, 5607–5627. doi: 10.1007/s12035-015-9474-x

Dean, C., Liu, H., Dunning, F., Chang, P., Jackson, M., and Chapman, E. (2009). Synaptotagmin-IV modulates synaptic function and long-term potentiation by regulating BDNF release. *Nat. Neurosci.* 12, 767–776.

Dieni, S., Matsumoto, T., Dekkers, M., Rauskolb, S., Ionescu, M. S., Deogracias, R., et al. (2012). BDNF and its pro-peptide are stored in presynaptic dense core vesicles in brain neurons. *J. Cell Biol.* 196, 775–788. doi: 10.1083/jcb.201201038

Edwards, R. H. (1998). Neurotransmitter release: Variations on a theme. *Curr. Biol.* 8, R883–R885. doi: 10.1016/s0960-9822(07)00551-9

Fader, S. M., Imaizumi, K., Yanagawa, Y., and Lee, C. C. (2016). Wisteria floribunda agglutinin-labeled perineuronal nets in the mouse inferior colliculus, thalamic reticular nucleus and auditory cortex. *Brain Sci* 6:13. doi: 10.3390/brainsci6020013

Frisina, R. D. (2001). Subcortical neural coding mechanisms for auditory temporal processing. *Hear. Res.* 158, 1–27.

Goman, A. M., and Lin, F. R. (2016). Prevalence of hearing loss by severity in the United States. *Am. J. Public Health* 106, 1820–1822. doi: 10.2105/AJPH.2016.303299

Goyer, D., Silveira, M. A., George, A. P., Beebe, N. L., Edelbrock, R. M., Malinski, P. T., et al. (2019). A novel class of inferior colliculus principal neurons labeled in vasoactive intestinal peptide-Cre mice. *eLife* 8:e43770. doi: 10.7554/eLife.43770

Hafidi, A., Moore, T., and Sanes, D. H. (1996). Regional distribution of neurotrophin receptors in the developing auditory brainstem. *J. Comp. Neurol.* 367, 454–464.

Hall, I. C., Sell, G. L., Chester, E. M., and Hurley, L. M. (2012). Stress-evoked increases in serotonin in the auditory midbrain do not directly result from elevations in serum corticosterone. *Behav. Brain Res.* 226, 41–49. doi: 10.1016/j.bbr.2011.08.042

Helfert, R. H., Sommer, T. J., Meeks, J., Hofstetter, P., and Hughes, L. F. (1999). Age-related synaptic changes in the central nucleus of the inferior colliculus of Fischer-344 rats. *J. Comp. Neurol.* 406, 285–298.

Hökfelt, T. (2010). Looking at neurotransmitters in the microscope. *Prog. Neurobiol.* 90, 101–118. doi: 10.1016/j.pneurobio.2009.10.005

Hurley, L. M., and Pollak, G. D. (1999). Serotonin differentially modulates responses to tones and frequency-modulated sweeps in the inferior colliculus. *J. Neurosci.* 19, 8071–8082. doi: 10.1523/JNEUROSCI.19-18-08071.1999

Hurley, L. M., and Pollak, G. D. (2001). Serotonin effects on frequency tuning of inferior colliculus neurons. *J. Neurophysiol.* 85, 828–842. doi: 10.1152/jn.2001.85.2.828

Hurley, L. M., and Pollak, G. D. (2005a). Serotonin shifts first-spike latencies of inferior colliculus neurons. *J. Neurosci.* 25, 7876–7886. doi: 10.1523/JNEUROSCI.1178-05.2005

Hurley, L. M., and Pollak, G. D. (2005b). Serotonin modulates responses to species-specific vocalizations in the inferior colliculus. *J. Comp. Physiol. A Neuroethol. Sens. Neural Behav. Physiol.* 191, 535–546. doi: 10.1007/s00359-005-0623-y

Hurley, L. M., and Sullivan, M. R. (2012). From behavioral context to receptors: Serotonergic modulatory pathways in the IC. *Front. Neural Circ.* 6:58. doi: 10.3389/fncir.2012.00058

Hurley, L. M., Thompson, A. M., and Pollak, G. D. (2002). Serotonin in the inferior colliculus. *Hear. Res.* 168, 1–11. doi: 10.1016/s0378-5955(02)00365-9

Jones, E. G., and Rockel, A. J. (1973). Observations on complex vesicles, neurofilamentous hyperplasia and increased electron density during terminal degeneration in the inferior colliculus. *J. Comp. Neurol.* 147, 93–118. doi: 10.1002/cne.901470105

Keithley, E. M., Ryan, A. F., and Feldman, M. L. (1992). Cochlear degeneration in aged rats of four strains. *Hear. Res.* 59, 171–178.

Kennedy, M. J., and Ehlers, M. D. (2011). Mechanisms and function of dendritic exocytosis. *Neuron* 69, 856–875. doi: 10.1016/j.neuron.2011.02.032

Kim, H., Kim, J., Lee, H., Shin, E., Kang, H., Jeon, J., et al. (2021). Baiap3 regulates depressive behaviors in mice via attenuating dense core vesicle trafficking in subsets of prefrontal cortex neurons. *Neurobiol. Stress* 16:100423. doi: 10.1016/j.ynstr.2021.100423

Klepper, A., and Herbert, H. (1991). Distribution and origin of noradrenergic and serotonergic fibers in the cochlear nucleus and inferior colliculus of the rat. *Brain Res.* 557, 190–201.

Knipper, M., Singer, W., Schwabe, K., Hagberg, G. E., Li Hegner, Y., Rüttiger, L., et al. (2022). Disturbed balance of inhibitory signaling links hearing loss and cognition. *Front. Neural Circ.* 15:785603. doi: 10.3389/fncir.2021.785603

Koehler, C. C., Almassri, L. S., Tokar, N., Mafi, A. M., O'Hara, M. J., Young, J. W., et al. (2023). Age-related changes of GAD1 mRNA expression in the central inferior colliculus. *Transl. Med. Aging* 70, 20-32

Kommajosyula, S. P., Bartlett, E. L., Cai, R., Ling, L., and Caspary, D. M. (2021). Corticothalamic projections deliver enhanced responses to medial geniculate body as a function of the temporal reliability of the stimulus. *J. Physiol.* 599, 5465–5484. doi: 10.1113/JP282321

Li, S., Lu, Y., Ding, D., Ma, Z., Xing, X., Hua, X., et al. (2020). Fibroblast growth factor 2 contributes to the effect of salidroside on dendritic and synaptic plasticity after cerebral ischemia/reperfusion injury. *Aging* 12, 10951–10968. doi: 10.18632/aging.103308

Lin, Z., Li, Y., Hang, Y., Wang, C., Liu, B., Li, J., et al. (2022). Tuning the size of large dense-core vesicles and quantal neurotransmitter release via secretogranin II liquid-liquid phase separation. *Adv. Sci.* 9:e2202263. doi: 10.1002/advs.202202263

Lipka, J., Kapitein, L. C., Jaworski, J., and Hoogenraad, C. C. (2016). Microtubule-binding protein doublecortin-like kinase 1 (DCLK1) guides kinesin-3-mediated cargo transport to dendrites. *EMBO J.* 35, 302–318. doi: 10.15252/embj.201592929

Lipman, R. D. (1997). Pathobiology of aging rodents: Inbred and hybrid models. *Exp. Gerontol.* 32, 215–228. doi: 10.1016/s0531-5565(96)00037-x

Lipman, R. D., Chrisp, C. E., Hazzard, D. G., and Bronson, R. T. (1996). Pathologic characterization of brown Norway, brown Norway Fischer 344, and Fischer 344 brown Norway rats with relation to age. *J. Gerontol. A Biol. Sci. Med. Sci.* 51, B54–B59.

Mafi, A., Tokar, N., Russ, M., Barat, O., and Mellott, J. (2022). Age-related ultrastructural changes in the lateral cortex of the inferior colliculus. *Neurobiol. Aging* 120, 43–59.

Mafi, A. M., Hofer, L. N., Russ, M. G., Young, J. W., and Mellott, J. G. (2020). The density of perineuronal nets increases with age in the inferior colliculus in the Fischer Brown Norway rat. *Front. Aging Neurosci.* 11:27. doi: 10.3389/fnagi.2020.00027

Mafi, A. M., Russ, M. G., Hofer, L. N., Pham, V. Q., Young, J. W., and Mellott, J. G. (2021). Inferior collicular cells that project to the auditory thalamus are increasingly surrounded by perineuronal nets with age. *Neurobiol. Aging* 105, 1–15. doi: 10.1016/j.neurobiolaging.2021.04.001

Malmierca, M. S., Izquierdo, M. A., Cristaudo, S., Hernández, O., Pérez-González, D., Covey, E., et al. (2008). A discontinuous tonotopic organization in the inferior colliculus of the rat. *J. Neurosci.* 28, 4767–4776. doi: 10.1523/JNEUROSCI.0238-08.2008

Mastronarde, D. (2003). SerialEM: A program for automated tilt series acquisition on tecnai microscopes using prediction of specimen position. *Microsc. Microanal.* 9, 1182–1183. doi: 10.1017/S1431927603445911

Matsuda, N., Lu, H., Fukata, Y., Noritake, J., Gao, H., Mukherjee, S., et al. (2009). Differential activity-dependent secretion of brain-derived neurotrophic factor from axon and dendrite. *J. Neurosci.* 29, 14185–14198.

Mellott, J. G., Bickford, M. E., and Schofield, B. R. (2014). Descending projections from auditory cortex to excitatory and inhibitory cells in the nucleus of the brachium of the inferior colliculus. *Front. Syst. Neurosci.* 8:188. doi: 10.3389/fnsys.2014.00188

Meltser, I., and Canlon, B. (2010). The expression of mitogen-activated protein kinases and brain-derived neurotrophic factor in inferior colliculi after acoustic trauma. *Neurobiol. Disease* 40, 325–330. doi: 10.1016/j.nbd.2010.06.006

Merchán, M., Aguilar, L. A., Lopez-Poveda, E. A., and Malmierca, M. S. (2005). The inferior colliculus of the rat: Quantitative immunocytochemical study of GABA and glycine. *Neuroscience* 136, 907–925.

Merighi, A. (2018). Costorage of high molecular weight neurotransmitters in large dense core vesicles of mammalian neurons. *Front. Cell. Neurosci.* 12:272. doi: 10.3389/fncel.2018.00272

Michael, D. J., Cai, H., Xiong, W., Ouyang, J., and Chow, R. H. (2006). Mechanisms of peptide hormone secretion. *Trends Endocrinol. Metab.* 17, 408–415.

Motts, S. D., and Schofield, B. R. (2009). Sources of cholinergic input to the inferior colliculus. *Neuroscience* 160, 103–114.

Nakamoto, K. T., Mellott, J. G., Killius, J., Storey-Workley, M. E., Sowick, C. S., and Schofield, B. R. (2013). Analysis of excitatory synapses in the guinea pig inferior colliculus: A study using electron microscopy and GABA immunocytochemistry. *Neuroscience* 237, 170–183. doi: 10.1016/j.neuroscience.2013.01.061

Nakamoto, K. T., Mellott, J. G., Killius, J., Storey-Workley, M. E., Sowick, C. S., and Schofield, B. R. (2014). Ultrastructural characterization of GABAergic and excitatory synapses in the inferior colliculus. *Front. Neuroanat.* 8:108. doi: 10.3389/fnana.2014.00108

Noftz, W. A., Beebe, N. L., Mellott, J. G., and Schofield, B. R. (2020). Cholinergic projections from the pedunculopontine tegmental nucleus contact excitatory and inhibitory neurons in the inferior colliculus. *Front. Neural Circ.* 14:43. doi: 10.3389/fncir.2020.00043

Noftz, W. A., Beebe, N. L., Mellott, J. G., and Schofield, B. R. (2021). Dense cholinergic projections to auditory and multisensory nuclei of the intercollicular midbrain. *Hear. Res.* 411:108352. doi: 10.1016/j.heares.2021.108352

Norena, A. J. (2011). An integrative model of tinnitus based on a central gain controlling neural sensitivity. *Neurosci. Biobehav. Rev.* 35, 1089–1109.

Oliver, D. L. (2005). "Neuronal organization in the inferior colliculus," in *The Inferior Colliculus*, eds J. Winer and C. Schreiner (New York, NY: Springer), 69–114.

Oliver, D. L., and Morest, D. K. (1984). The central nucleus of the inferior colliculus in the cat. *J. Comp. Neurol.* 222, 237–264. doi: 10.1002/cne.902220207

Pain, S., Brot, S., and Gaillard, A. (2022). Neuroprotective effects of neuropeptide Y against neurodegenerative disease. *Curr. Neuropharmacol.* 20, 1717–1725. doi: 10.2174/1570159X19666210906120302

Paloff, A. M., and Usunoff, K. G. (1992). The fine structure of the inferior colliculus in the cat II. synaptic organization. *J. Hirnforsch.* 33, 77–106.

Paloff, A. M., and Usunoff, K. G. (2000). Tyrosine hydroxylase-like immunoreactive synaptic boutons in the inferior colliculus of the cat. *Ann. Anat.* 182, 423–426. doi: 10.1016/S0940-9602(00)80047-3

Paloff, A. M., Usunoff, K. G., Hinova-Palova, D. V., and Ivanov, D. P. (1989). The fine structure of the inferior colliculus in the cat. I. Neuronal perikarya in the central nucleus. *J. Hirnforschung* 30, 69–90.

Palombi, P. S., and Caspary, D. M. (1996). GABA inputs control discharge rate primarily within frequency receptive fields of inferior colliculus neurons. *J. Neurophysiol.* 75, 2211–2219. doi: 10.1152/jn.1996.75.6.2211

Parthasarathy, A., and Bartlett, E. L. (2011). Age-related auditory deficits in temporal processing in F-344 rats. *Neuroscience* 192, 619–630. doi: 10.1016/j.neuroscience.2011.06.042

Parthasarathy, A., Herrmann, B., and Bartlett, E. L. (2018). Aging alters envelope representations of speech-like sounds in the inferior colliculus. *Neurobiol. Aging* 73, 30–40.

Paxinos, G., and Watson, C. (1998). *The Rat Brain in Stereotaxic Coordinates*. San Diego, CA: Academic Press.

Pelletier, G., Steinbusch, H. W., and Verhofstad, A. A. (1981). Immunoreactive substance P and serotonin present in the same dense-core vesicles. *Nature* 293, 71–72. doi: 10.1038/293071a0

Persoon, C. M., Moro, A., Nassal, J. P., Farina, M., Broeke, J. H., Arora, S., et al. (2018). Pool size estimations for dense-core vesicles in mammalian CNS neurons. *EMBO J.* 37:e99672. doi: 10.15252/embj.201899672

Peters, A., Palay, S. L., and Webster, H. (1991). in *The Fine Structure of the Nervous System: Neurons and Their Supporting Cells*, ed. S. Palay (Oxford: Oxford University Press).

R Core Team (2020). *R: A Language and Environment for Statistical Computing*. Vienna: R Foundation for Statistical Computing.

Ramamoorthy, P., Wang, Q., and Whim, M. D. (2011). Cell type-dependent trafficking of neuropeptide Y-containing dense core granules in CNS neurons. *J. Neurosci.* 31, 14783–14788. doi: 10.1523/JNEUROSCI.2933-11.2011

Regehr, W. G., Carey, M. R., and Best, A. R. (2009). Activity-dependent regulation of synapses by retrograde messengers. *Neuron* 63, 154–170.

Reynolds, E. (1963). The use of lead citrate at high pH as an electron-opaque stain in electron microscopy. *J. Cell Biol.* 17, 208–212.

Ribak, C. E., and Roberts, R. C. (1986). The ultrastructure of the central nucleus of the inferior colliculus of the Sprague-Dawley rat. *J. Neurocytol.* 15, 421–438. doi: 10.1007/BF01611726

Richardson, B. D., Brozoski, T. J., Ling, L. L., and Caspary, D. M. (2012). Targeting inhibitory neurotransmission in tinnitus. *Brain Res.* 1485, 77–87.

Roberts, R. C., and Ribak, C. E. (1987). An electron microscopic study of GABAergic neurons and terminals in the central nucleus of the inferior colliculus of the rat. *J. Neurocytol.* 16, 333–345. doi: 10.1007/BF01611345

Robinson, L. C., Barat, O., and Mellott, J. G. (2019). GABAergic and glutamatergic cells in the inferior colliculus dynamically express the $GABA_AR$ γ_1 subunit during aging. *Neurobiol. Aging* 80, 99–110. doi: 10.1016/j.neurobiolaging.2019.04.007

Rockel, A., and Jones, E. (1973). Observations on the fine structure of the central nucleus of the inferior colliculus of the cat. *J. Comp. Neurol.* 147, 61–92.

Rumschlag, J. A., McClaskey, C. M., Dias, J. W., Kerouac, L. B., Noble, K. V., Panganiban, C., et al. (2022). Age-related central gain with degraded neural synchrony in the auditory brainstem of mice and humans. *Neurobiol. Aging* 115, 50–59. doi: 10.1016/j.neurobiolaging.2022.03.014

Sato, T., Wilson, T. S., Hughes, L. F., Konrad, H. R., Nakayama, M., and Helfert, R. H. (2001). Age-related changes in levels of tyrosine kinase B receptor and fibroblast growth factor receptor 2 in the rat inferior colliculus: Implications for neural senescence. *Neuroscience* 103, 695–702. doi: 10.1016/s0306-4522(01)00022-7

Schneider, C., Rasband, W., and Eliceiri, K. (2012). NIH Image to ImageJ: 25 years of image analysis. *Nat. Methods* 9, 671–675. doi: 10.1038/nmeth.2089

Schofield, B. R., and Hurley, L. (2018). "Circuits for modulation of auditory function," in *The Mammalian Auditory Pathways Springer Handbook of Auditory Research*, eds D. L. Oliver, N. B. Cant, R. R. Fay, and A. N. Popper (Cham: Springer International Publishing), 235–267.

Sharma, V., Nag, T. C., Wadhwa, S., and Roy, T. S. (2009). Temporal distribution of mRNA expression levels of various genes in the developing human inferior colliculus. *Neurosci. Lett.* 461, 229–234. doi: 10.1016/j.neulet.2009.06.049

Shim, H. J., Lee, L. H., Huh, Y., Lee, S. Y., and Yeo, S. G. (2012). Age-related changes in the expression of NMDA, serotonin, and GAD in the central auditory system of the rat. *Acta Oto-laryngol.* 132, 44–50. doi: 10.3109/00016489.2011.622785

Silveira, M. A., Anair, J. D., Beebe, N. L., Mirjalili, P., Schofield, B. R., and Roberts, M. T. (2020). Neuropeptide Y expression defines a novel class of GABAergic projection neuron in the inferior colliculus. *J. Neurosci.* 40, 4685–4699. doi: 10.1523/JNEUROSCI.0420-20.2020

Silveira, M. A., Drotos, A. C., Pirrone, T. M., Versalle, T. S., Bock, A., and Roberts, M. T. (2023). Neuropeptide Y signaling regulates recurrent excitation in the auditory midbrain. *J. Neurosci.* 43, 7626–7641. doi: 10.1523/JNEUROSCI.0900-23.2023

Singer, W., Panford-Walsh, R., and Knipper, M. (2014). The function of BDNF in the adult auditory system. *Neuropharmacology* 76(Pt C), 719–728. doi: 10.1016/j.neuropharm.2013.05.008

Sorra, K. E., Mishra, A., Kirov, S. A., and Harris, K. M. (2006). Dense core vesicles resemble active-zone transport vesicles and are diminished following synaptogenesis in mature hippocampal slices. *Neuroscience* 141, 2097–2106. doi: 10.1016/j.neuroscience.2006.05.033

Subirana, I., Sanz, H., and Vila, J. (2014). Building bivariate tables: The compareGroups Package for R. *J. Stat. Softw.* 57, 1–16. doi: 10.18637/jss.v057.i12

Syka, J. (2020). "Age-related changes in the auditory brainstem and inferior colliculus," in *Aging and Hearing*, eds K. S. Helfer, E. L. Bartlett, A. N. Popper, and R. R. Fay (Switzerland: Springer), 67–96.

Tadros, S. F., D'Souza, M., Zettel, M. L., Zhu, X., Lynch-Erhardt, M., and Frisina, R. D. (2007). Serotonin 2B receptor: Upregulated with age and hearing loss in mouse auditory system. *Neurobiol. Aging* 28, 1112–1123. doi: 10.1016/j.neurobiolaging.2006.05.021

Tao, C. L., Liu, Y. T., Zhou, Z. H., Lau, P. M., and Bi, G. Q. (2018). Accumulation of dense core vesicles in hippocampal synapses following chronic inactivity. *Front. Neuroanat.* 12:48. doi: 10.3389/fnana.2018.00048

Trueta, C., and De-Miguel, F. F. (2012). Extrasynaptic exocytosis and its mechanisms: A source of molecules mediating volume transmission in the nervous system. *Front. Physiol.* 3:319. doi: 10.3389/fphys.2012.00319

Walton, J. P., Frisina, R. D., and O'Neill, W. E. (1998). Age-related alteration in processing of temporal sound features in the auditory midbrain of the CBA mouse. *J. Neurosci.* 18, 2764–2776.

Walton, J. P., Simon, H., and Frisina, R. D. (2002). Age-related alterations in the neural coding of envelope periodicities. *J. Neurophysiol.* 88, 565–578. doi: 10.1152/jn.2002.88.2.565

Wenstrup, J. J. (2005). "The tectothalamic system," in *The Inferior Colliculus*, eds J. A. Winer and C. E. Schreiner (New York, NY: Springer), 200–230. doi: 10.1007/0-387-27083-3_7

Wissel, K., Wefstaedt, P., Miller, J. M., Lenarz, T., and Stöver, T. (2006). Differential brain-derived neurotrophic factor and transforming growth factor-beta expression in the rat cochlea following deafness. *Neuroreport* 17, 1297–1301. doi: 10.1097/01.wnr.0000233088.92839.23

Xia, X., Lessmann, V., and Martin, T. F. (2009). Imaging of evoked dense-core-vesicle exocytosis in hippocampal neurons reveals long latencies and kiss and- run fusion events. *J. Cell Sci.* 122, 75–82.

Yi, M., Li, H., Wu, Z., Yan, J., Liu, Q., Ou, C., et al. (2018). A promising therapeutic target for metabolic diseases: Neuropeptide Y receptors in humans. *Cell Physiol. Biochem.* 1, 88–107. doi: 10.1159/000486225

Zheng, Y., Wildonger, J., Ye, B., Zhang, Y., Kita, A., Younger, S. H., et al. (2008). Dynein is required for polarized dendritic transport and uniform microtubule orientation in axons. *Nat. Cell Biol.* 10, 1172–1180. doi: 10.1038/ncb1777

frontiers | Frontiers in Cellular Neuroscience

TYPE Original Research
PUBLISHED 23 May 2024
DOI 10.3389/fncel.2024.1354520

Check for updates

OPEN ACCESS

EDITED BY
Christian Keine,
University of Oldenburg, Germany

REVIEWED BY
Karl Kandler,
University of Pittsburgh, United States
Yong Lu,
Northeast Ohio Medical University, United States
Barbara Jane Morley,
Boys Town National Research Hospital, United States

*CORRESPONDENCE
Eckhard Friauf
✉ eckhard.friauf@bio.uni-kl.de

†These authors have contributed equally to this work

‡PRESENT ADDRESSES
Ayse Maraslioglu-Sperber,
Department of Otolaryngology – Head & Neck Surgery, Stanford University School of Medicine, Stanford, CA, United States
Tamara Ritter,
Cell and Neurobiology Group, Institute of Anatomy, University Medical Center of the Johannes Gutenberg-University Mainz, Mainz, Germany

RECEIVED 12 December 2023
ACCEPTED 15 March 2024
PUBLISHED 23 May 2024

CITATION
Maraslioglu-Sperber A, Pizzi E, Fisch JO, Kattler K, Ritter T and Friauf E (2024) Molecular and functional profiling of cell diversity and identity in the lateral superior olive, an auditory brainstem center with ascending and descending projections. *Front. Cell. Neurosci.* 18:1354520. doi: 10.3389/fncel.2024.1354520

COPYRIGHT
© 2024 Maraslioglu-Sperber, Pizzi, Fisch, Kattler, Ritter and Friauf. This is an open-access article distributed under the terms of the Creative Commons Attribution License (CC BY). The use, distribution or reproduction in other forums is permitted, provided the original author(s) and the copyright owner(s) are credited and that the original publication in this journal is cited, in accordance with accepted academic practice. No use, distribution or reproduction is permitted which does not comply with these terms.

Molecular and functional profiling of cell diversity and identity in the lateral superior olive, an auditory brainstem center with ascending and descending projections

Ayse Maraslioglu-Sperber[1†‡], Erika Pizzi[1†], Jonas O. Fisch[1], Kathrin Kattler[2], Tamara Ritter[1‡] and Eckhard Friauf[1*]

[1]Animal Physiology Group, Department of Biology, University of Kaiserslautern-Landau, Kaiserslautern, Germany, [2]Genetics/Epigenetics Group, Department of Biological Sciences, Saarland University, Saarbrücken, Germany

The lateral superior olive (LSO), a prominent integration center in the auditory brainstem, contains a remarkably heterogeneous population of neurons. Ascending neurons, predominantly principal neurons (pLSOs), process interaural level differences for sound localization. Descending neurons (lateral olivocochlear neurons, LOCs) provide feedback into the cochlea and are thought to protect against acoustic overload. The molecular determinants of the neuronal diversity in the LSO are largely unknown. Here, we used patch-seq analysis in mice at postnatal days P10-12 to classify developing LSO neurons according to their functional and molecular profiles. Across the entire sample ($n = 86$ neurons), genes involved in ATP synthesis were particularly highly expressed, confirming the energy expenditure of auditory neurons. Two clusters were identified, pLSOs and LOCs. They were distinguished by 353 differentially expressed genes (DEGs), most of which were novel for the LSO. Electrophysiological analysis confirmed the transcriptomic clustering. We focused on genes affecting neuronal input–output properties and validated some of them by immunohistochemistry, electrophysiology, and pharmacology. These genes encode proteins such as osteopontin, Kv11.3, and Kvβ3 (pLSO-specific), calcitonin-gene-related peptide (LOC-specific), or Kv7.2 and Kv7.3 (no DEGs). We identified 12 "Super DEGs" and 12 genes showing "Cluster similarity." Collectively, we provide fundamental and comprehensive insights into the molecular composition of individual ascending and descending neurons in the juvenile auditory brainstem and how this may relate to their specific functions, including developmental aspects.

KEYWORDS

patch-seq, lateral superior olive (LSO), olivocochlear system, Single-cell RNA sequencing, biophysical properties, sound localization

Introduction

Brain areas are composed of highly heterogenous cell populations with diverse structure and function. An extensive knowledge about individual cell types is required to better understand the functional organization of neural systems at different levels. Over the past two decades, next-generation RNA sequencing (RNA-seq) has paved new roads to investigate the

molecular determinants of cellular diversity (Macaulay and Voet, 2014; Svensson et al., 2018). In the present study, we took advantage of recent advances in RNA-seq technologies and employed patch-seq, a powerful multi-modal single-cell approach, to decipher the biophysical and transcriptomic determinants of neuronal heterogeneity in the lateral superior olive (LSO). The LSO is a conspicuous brainstem nucleus receiving and analyzing binaural input. It contains neurons in the ascending and the descending pathway, namely principal neurons (pLSOs) and lateral olivocochlear neurons (LOCs). pLSOs are involved in sound localization, whereas LOCs enable the central auditory system (CAS) to directly control the cochlear periphery (reviews: Friauf et al., 2019; Yin et al., 2019; Owrutsky et al., 2021).

pLSOs amount to almost $\frac{3}{4}$ of all LSO neurons (Helfert and Schwartz, 1986, 1987; Franken et al., 2018), whose number slightly exceeds 1,600 in mice (Hirtz et al., 2011). By performing a subtraction-like process of excitatory and inhibitory input signals from the ipsi- and contralateral ear, respectively, pLSOs detect interaural level differences (Tollin, 2003). The main inputs are in strict tonotopic register and are glutamatergic, respectively, glycinergic with modulatory GABAergic inputs (Fischer et al., 2019). Collectively, these inputs are tuned for fast and precise synaptic transmission, even during sustained high-frequency stimulation (Krächan et al., 2017; Müller et al., 2022). pLSOs in mice have fusiform somata with a surface area of ~130 μm^2 (Williams et al., 2022). For juvenile mice, an input resistance (R_{in}) of 96 MΩ, a resting potential (V_{rest}) of −64 mV, and a membrane capacitance (C_m) of 11 pF have been reported (Sterenborg et al., 2010). Another study found 70 MΩ, −57 mV and 22 pF for mouse LSO neurons in general (Leao et al., 2006). A striking feature of pLSO neurons is a prominent inward current (I_h) which is mediated through hyperpolarization-activated and cyclic nucleotide-modulated (HCN) channels (Leao et al., 2006; Sterenborg et al., 2010).

Two subpopulations of pLSOs can be distinguished by their intrinsic firing pattern *in vitro* (rats: Barnes-Davies et al., 2004). In mice, the first subtype, termed single spiking (Sterenborg et al., 2010) or onset-burst pLSOs (Haragopal and Winters, 2023), fires 1–5 action potentials (APs) of short latency during prolonged depolarization. The second pLSO subtype fires throughout the duration of the stimulus and has been termed multiple firing (Sterenborg et al., 2010) or multi-spiking (Haragopal and Winters, 2023).

pLSO neurons send ipsilateral, glycinergic projections to the intermediate nucleus and the dorsal nucleus of the lateral lemniscus (INLL, DNLL) as well as the central nucleus of the inferior colliculus (CNIC) (Figure 1A; Friauf et al., 2019; Mellott et al., 2022). pLSOs also give rise to contralateral, mainly glutamatergic projections terminating in the DNLL and CNIC (Saint Marie et al., 1989; Saint Marie and Baker, 1990; Glendenning et al., 1992; Fredrich et al., 2009; Abraham et al., 2010). As recently reported, both projection types contribute relatively equally to the pLSO output in mice (Haragopal et al., 2023).

LOCs are the second major neuron type in the LSO. They form one of the two branches of efferent projections of the auditory system, the second branch being composed of medial olivocochlear neurons (MOCs, reviews: Brown, 2011; Guinan, 2011). Ontogenetically, LOCs and MOCs have a motoneuronal nature (Karis et al., 2001; Simmons, 2002). The efferent auditory system comprises ~470 neurons (mice), with LOCs exceeding MOCs by ~2-fold (Campbell and Henson, 1988). In mice, LOC somata are round and have a surface area of ~100 μm^2 (Williams et al., 2022); (Suthakar and Ryugo, 2021, report ~140 μm^2). Most LOC somata are intrinsic to the LSO and intermingled with pLSO somata (mice); few somata reside in a shell region surrounding the LSO (Wu et al., 2020; Williams et al., 2022).

Axons of LOCs are thin and unmyelinated (Brown, 2011). Virtually all (99%) project into the ipsilateral cochlea (Guinan, 2018). The axons make *en passant* synapses primarily on radial "dendrites" of type I auditory neurons, beneath the basal pole of inner hair cells (Warr et al., 1997; Simmons, 2002). A minority of LOCs contact inner hair cells directly (Liberman, 1990; Sobkowicz and Slapnick, 1994; Sobkowicz et al., 1997). Furthermore, LOCs may project to the ventral cochlear nucleus (Ryan et al., 1990) and have axon collaterals terminating in the LSO itself and slightly outside (Brown, 1993). In line with the unmyelinated nature of their axons, peripheral effects of LOC activity are slower than MOC effects and occur over minutes. LOCs likely modulate auditory nerve fiber activity in a reflex manner (Guinan, 2011) and protect the cochlea against noise-induced hearing loss (Darrow et al., 2007; Fuchs and Lauer, 2019).

Like pLSOs, LOCs receive excitatory and inhibitory inputs, yet with longer latencies and slower kinetics (review: Friauf et al., 2019). They differ from pLSOs in several biophysical properties. For instance, they display a regular firing pattern in response to depolarizing current pulses injected *in vitro*, whereby the first AP occurs with a substantial and variable delay (25–180 ms; Adam et al., 1999). In contrast to pLSOs, LOCs lack I_h currents, but they exhibit prominent low-threshold and rapidly activating and inactivating transient outward K^+ currents. By counteracting depolarizing effects of excitatory synapses, these currents are key determinants of synaptic integration and repetitive AP activity (Rothman and Manis, 2003; Manis, 2008). In accordance with their relatively small somata (Williams et al., 2022), mouse LOCs have an exceptionally low C_m (6 pF) (Sterenborg et al., 2010). The authors also reported a very high R_{in} (~300 MΩ) and a relatively positive V_{rest} (−43 mV). Low C_m values in LOCs were also obtained by Fujino et al. (1997) and Leijon and Magnusson (2014) (mouse, 15 pF; rat, 40 pF).

The neurochemistry of LOCs is complex. They are predominantly cholinergic but also contain various other transmitters (reviews: Brown, 2011; Sewell, 2011). In mice, GABAergic markers have been described in all cochlear LOC fibers (Maison et al., 2003). A smaller, non-cholinergic fraction of LOCs is dopaminergic (Eybalin et al., 1993; Gil-Loyzaga, 1995; Safieddine et al., 1997; Darrow et al., 2006). Besides these classical transmitters, several neuromodulators have been described, including calcitonin-gene-related peptide (CGRP) (Kresse et al., 1995; Maison et al., 2003; Wu et al., 2018; summaries: Robertson and Mulders, 2000; Le Prell et al., 2021), urocortin (Vetter et al., 2002; Kaiser et al., 2011), and opioid peptides such as dynorphin (Le Prell et al., 2014) or enkephalins (Eybalin, 1993; Safieddine et al., 1997). A cholinergic LOC may co-contain CGRP and opioids, and various opioids can co-localize as well (Altschuler et al., 1988; Safieddine et al., 1997; Frank et al., 2023). Therefore, LOCs belong to the growing category of multi-transmitter neurons. Taken together, LOCs, despite being only a few, dynamically fine-tune auditory nerve activity via the release of excitatory and inhibitory transmitters (Groff and Liberman, 2003). The functions of LOCs in hearing, however, are virtually unknown (Romero and Trussell, 2022). They are much less explored than MOCs, and many issues are still under investigation (Kitcher et al., 2022). For example, direct evidence that LOCs respond to sound is still missing (Fuchs and Lauer, 2019).

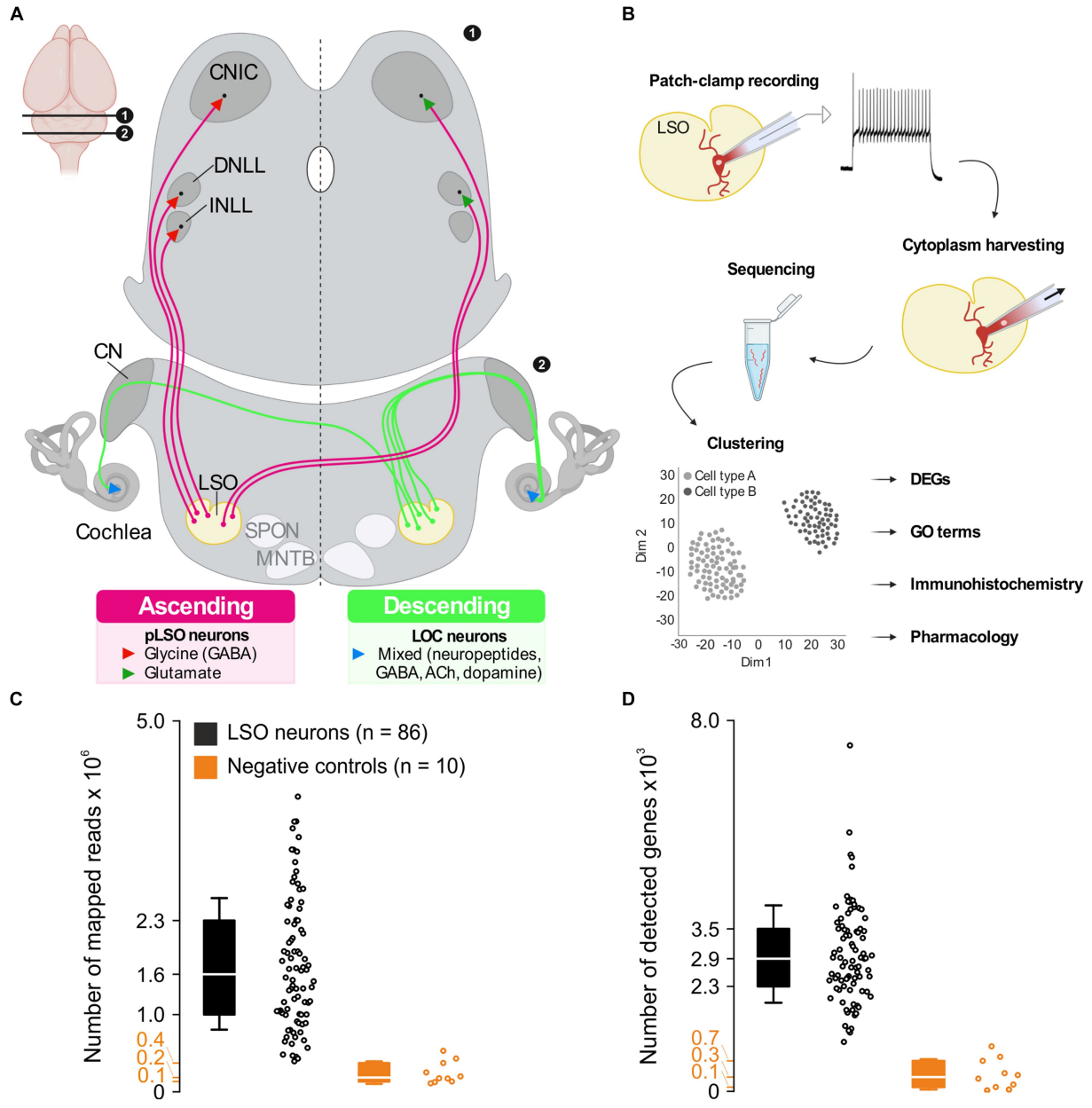


FIGURE 1
A priori quality checks result in 86 LSO patch-seq neurons of sufficient quality. **(A)** Ascending projections (left) and descending projections (right) of LSO neurons. Inset (top left) depicts position of coronal sections in the brain. **(B)** Patch-seq workflow. Whole-cell patch-clamp experiments were performed to assess electrophysiological properties, followed by cytoplasm harvesting. The cytoplasm was used for cDNA library synthesis and sequencing. After processing sequencing reads, unsupervised clustering was done to identify neuron types, and further analyses were performed to characterize these neuron types. **(C)** Number of mapped reads from 86 LSO neurons of sufficient quality and 10 neurons from negative controls (black and orange, respectively). **(D)** As **(C)**, but for detected genes. CN, cochlear nuclear complex; CNIC, central nucleus of the inferior colliculus; DNLL, dorsal nucleus of the lateral lemniscus; INLL, intermediate nucleus of the lateral lemniscus; LSO, lateral superior olive; MNTB, medial nucleus of the trapezoid body; SPON, superior paraolivary nucleus. See also Supplementary Figures S1, S2. In these and all subsequent box plots, center line marks median (Q2), box limits mark first and third quartile (Q1 and Q3), and whiskers represent standard deviation (SD).

Previous research has primarily focused on the electrophysiological properties and differentiation of neurons in the LSO. Some studies explored the molecular determinants influencing these electrophysiological properties but used now outdated techniques such as serial analysis of gene expression (SAGE) (Koehl et al., 2004; Nothwang et al., 2006) or microarrays (Ehmann et al., 2013; Xiao et al., 2013). These methods have not been able to achieve single cell resolution, which is critical in heterogeneous nuclei such as the LSO. Recently, Frank et al. (2023) presented transcriptomic single-cell transcriptomic results for LOC neurons but not for pLSO neurons. Here, we combined electrophysiology and transcriptomics using the patch-seq technique to assess functional and molecular diversity in individual LSO neurons of juvenile mice. We functionally characterized cell types in brain slices, harvested the cytoplasm and performed genome-wide expression profiling. Our goal was to identify molecular determinants of cellular heterogeneity and similarity in the

LSO. We identified two clusters, pLSOs and LOCs. Differential expression was found for 353 genes, including known and novel cell type-specific markers. In particular, Kv channel subunits were intensively analyzed. Our comprehensive study identified complex molecular fingerprints at the single-cell level, paving the way for a variety of follow-up studies.

Methods

Animals and ethical approval

Animal breeding and experiments were approved by the regional councils of the Land Rhineland-Palatinate according to the German Animal Protection Law (TSchG §4/3) and followed the guidelines for the welfare of laboratory animals. C57BL/6 J mice were bred in the animal facilities of the University of Kaiserslautern, and both sexes were analyzed at postnatal day (P) 11 ± 1, i.e., around hearing onset.

Brainstem slices preparation and electrophysiology

RNase-free solutions were prepared, and equipment was cleaned as described (Cadwell et al., 2017). Coronal brainstem slices were prepared (Hirtz et al., 2011) and *in vitro* electrophysiology was performed as described (Müller et al., 2019). Briefly, slices were perfused with ASCF (in mM: 125 NaCl, 2.5 KCl, 1 $MgCl_2$, 1.25 NaH_2PO_4, 2 sodium pyruvate, 3 *myo*-inositol, 0.44 L-ascorbic acid, 25 $NaHCO_3$, 10 D-glucose, 2 $CaCl_2$, pH 7.4 when oxygenated with carbogen). Whole-cell patch-clamp recordings from LSO neurons were performed at 36.5 ± 1°C. Patch pipettes were filled with internal solution (in mM: 140 potassium gluconate, 10 HEPES, 5 EGTA, 1 $MgCl_2$, 2 Na_2ATP, 0.3 Na_2GTP). The internal solution contained 0.8% RNase inhibitor (Invitrogen). The liquid junction potential was 15.4 mV and was corrected online.

Current clamp

V_{rest} values are an average over a 30-s period (sample frequency 5 kHz, otherwise 50 kHz). The initial phase of the hyperpolarizing response to a −200-pA, 200-ms current pulse was fitted mono-exponentially (OriginPro 9.1, OriginLab) to determine the membrane time constant (τ_m). Current pulses with increasing amplitude (−200–1,000 pA, in 50-pA steps, 200 ms) were used to approximate rheobase, determine AP latency at rheobase, firing pattern (150 pA above rheobase) and voltage sag (at −200 pA). Triangular current pulses (rise to peak 1.5 ms, decay to baseline 3.5 ms, 10 repeats) were injected to determine AP amplitude, threshold, halfwidth, and peak latency. AP halfwidth was measured at 50% of the AP peak amplitude from baseline.

Voltage clamp

A 200-ms negative voltage step from the holding potential (V_{hold}; −70 mV) to −75 mV was applied to determine series resistance (R_s) and R_{in} (sampled at 20 kHz). Membrane currents were recorded for 1 min at V_{hold}. Peak amplitudes of spontaneous postsynaptic currents (sPSCs) and their kinetics (10–90% rise time, 100–37% decay time constant τ_{decay}) were determined at V_{hold} and analyzed using Mini Analysis 6 (Synaptosoft). With a Cl-reversal potential of −112 mV, inhibitory sIPSCs were outward currents. Thus, they could be easily distinguished from excitatory sEPSCs which were inward currents. For each neuron, 100 sIPSCs and 100 sEPSCs were averaged. Data analysis was performed using custom-written IgorPro 6 and IgorPro 8 routines (WaveMetrics), and Clampfit 10 (Molecular Devices). Data visualization was performed using IgorPro, OriginPro 9.1, and CorelDRAW Graphics Suite 2019 (Corel Corporation).

Cytoplasm harvesting

Electrophysiological characterization was limited to ~10–15 min to minimize mRNA degradation. Total RNA was then extracted into the patch pipette by gently aspirating the neuronal cytoplasm. Shrinkage of the soma and entry of the nucleus into the pipette were visually monitored under DIC optics (Supplementary Figures S1A1–A3). After successful harvesting, atmospheric pressure was restored and the pipette was slowly removed from the soma (Supplementary Figure S1B). In case of contamination of the pipette by extracellular material, absence of a membrane patch at the tip of the pipette, or soma swelling, samples were discarded (Supplementary Figures S1C1,C2,D1,D2). The contents of the pipette were collected in a reaction tube containing 2 µL lysis buffer, 0.2% Triton-X, ERCC RNA Spike-In Mix (Invitrogen, 1:400,000 dilution) and RNase inhibitor. Samples were stored at −80°C and processed further *en bloc* (library preparation and sequencing). From a total of 263 patched neurons, 103 were retained for further analysis. Ultimately, 86 neurons passed the RNA quality control (see below). One negative control was collected per experimental day. A pipette filled with internal solution was moved so that its tip touched the slice. It was then withdrawn, and the contents of the pipette were processed as for harvested cells.

Library preparation and sequencing

Double-stranded cDNA was generated as described, with minor modifications (Picelli et al., 2013). Briefly, 1 µL of 10 mM dNTPs and 0.5 µL of Oligo-dT primer (Supplementary Table S1) were added to each sample, and samples were incubated at 72°C for 3 min and immediately placed on ice. Reverse transcription was performed using 0.5 µL SuperScript II RT (200 U/µL, Invitrogen) supplemented with 0.25 µL RNasin (40 U/µL, Promega), 2 µL Superscript II first-strand buffer (5x), 0.48 µL 100 mM DTT, 2 µL 5 M betaine, 0.12 µL 0.5 M $MgCl_2$, 0.1 µL 100 µM template-switching oligonucleotide and 0.25 µL nuclease-free water. Incubation was performed at 42°C for 90 min, followed by 10 cycles at 50°C for 2 min and another incubation step at 42°C for 2 min. Enzyme inactivation was achieved by incubation at 70°C for 15 min. cDNA was pre-amplified by adding 12.5 µL KAPA HiFi HotStart ReadyMix PCR Kit (Roche), 0.25 µL IS PCR primer and 2.25 µL nuclease-free water with these thermocycling conditions: 98°C for 3 min, 18 cycles at 98°C for 20 s, 67°C for 15 s, 72°C for 6 min and final elongation at 72°C for 5 min. cDNA was purified using 0.8 X Ampure XP Beads (Beckman Coulter) and elution in 7 µL RNase free water. Quality control of randomly selected cells was assessed on an Agilent Bioanalyzer using the HS DNA Kit. On average, 450 pg. of cDNA was used as input for dual-indexed Nextera XT library

preparation (Illumina). A total of 9 cycles of library amplification were performed according to the manufacturer's recommendations. All individual single-cell libraries were pooled in equal amounts prior to purification of 100 µL pooled libraries with 1X Ampure XP Beads (Beckman Coulter) and final elution in 15 µL RNase-free water.

Library quality control and next generation sequencing

Prior to sequencing, the library pool was quantified using the Qubit dsDNA HS Assay Kit (Invitrogen), and the fragment size distribution was checked using the High Sensitivity DNA Kit (Agilent) on an Agilent 2100 Bioanalyzer. The library pool was additionally quantified with the PerfeCTa NGS Quantification Kit (Quanta Biosciences) and normalized for clustering on a cBot (Illumina). Libraries were sequenced on a HiSeq2500 (Illumina) using dual index reads with 88 bp read length.

Processing and analysis of single-cell RNA-seq data

Initial quality control of the raw data was performed using FastQC.[1] Reads were trimmed using Trim Galore! (v0.4.2)[2] to remove 3′ ends with base quality below 20 and adapter sequences. Reads were aligned to the mouse genome mm10 using STAR (Dobin et al., 2013, v2.5.2a) with a 2-pass mapping strategy per sample. PCR duplicates were detected using MarkDuplicate from the Picard tools (version 1.115).[3] Reads aligned to mm10 were summarized to Gencode annotation vM2 (Harrow et al., 2012) using featureCounts (Liao et al., 2014, v1.5.0-p3) and counting primary alignments only (Li and Dewey, 2011, v1.3.1).

For quality control, filtering, and normalization of single-cell RNA-seq (scRNA-seq) data, we used the *SingleCellExperiment* R package (version 1.8.0, Amezquita et al., 2020) and the *scran* package (version 1.14.6; Lun et al., 2016) on Bioconductor. The deconvolution method was used to remove cell-specific library size biases, and size factors were calculated for each library using the *ComputeSumFactors* function. Of 103 aspirated cells, 17 (~16%) were discarded due to poor sequencing quality, leaving 86 neurons. Poor quality cells had >3 median absolute differences below the median for number of counts or number of transcripts. Genes with an average of at least one count in at least 5% of the neurons qualified for downstream analysis, resulting in 11,659 expressed genes. Transcripts per million (TPM) values were calculated by normalizing for gene length and sequencing depth (Zheng et al., 2020). The top 500 highly expressed genes were selected for Kyoto Encyclopedia of Genes and Genomes (KEGG) enrichment analysis using gene set enrichment analysis (GSEA) performed with DAVID 2021 (Huang et al., 2009; Sherman et al., 2022).

Clustering was performed using SC3 (Kiselev et al., 2017) and Seurat (Satija et al., 2015). Principal component analysis (PCA) was performed using the Seurat function *RunPCA* (Lun et al., 2016). Normalized $\log_2$-transformed highly variable gene (HVG) counts were used as input. t-Distributed Stochastic Neighbor Embedding (tSNE) (Kobak and Berens, 2019) plots were generated with *RunTSNE*.

DEGs were detected using the *findMarkers* function from the *scran* package, which uses a *t*-test by default. A gene was defined as a DEG if the normalized count showed a ≥2-fold upregulation ($\log_2$FC ≥ 1) and a false discovery rate (FDR) ≤ 0.05 ($-\log_{10}$FDR ≤ 1.3). DEGs were ranked by their Area Under the Receiver-Operating Characteristic curve (AUROC). DEGs were also selected for Gene Ontology (GO) enrichment analysis using GSEA performed with DAVID 2021. GO terms were condensed using REVIGO (Jiang and Conrath algorithm) (Supek et al., 2011). UpSet plots were generated using the UpSetR package (v.1.4.0) (Conway et al., 2017).

Super DEGs and cluster similarity

DEG analysis is a widely used method for assessing differences between samples. However, at least one pitfall is associated with very low expression levels. A gene may qualify as a DEG even if the average expression level in the two samples is very low (e.g., *Scn4b*|Navβ4, DEG#173 in pLSO, showed 1.5 vs. 0.0 TPM; Supplementary Figure S8A and Supplementary Table S6). To account for this caveat, we applied a more stringent approach and condensed the DEGs that showed an expression level of ≥10 TPM in ≥1 cluster. If the normalized counts differed ≥4-fold ($\log_2$FC ≥ 2), these DEGs were defined as "Super DEGs." In addition, we used the same "≥10 TPM in ≥1 cluster" criterion to determine "Cluster similarity," defined as ≤2-fold difference between clusters ($\log_2$FC ≤ 1). We further assessed Cluster similarity by using the overlapping index (OI), a means to quantify the similarity of datasets in terms of their distributions (*cf.* chapter" Super DEGs and Cluster similarity between pLSOs and LOCs"; OI = 0 → no overlap, OI = 1 → perfect overlap; Pastore and Calcagni, 2019).

To make the data sets more explorable, we have added the file in Supplementary Table S6. It lists the complex gene expression profiles for each neuron and allows the user to interactively change the selection criteria, such as the TPM threshold, and to assess how the changes affect the percentage of cells expressing a gene.

Data availability statement

The single-cell RNA sequencing data generated during this research project has been submitted to NCBI GEO and can be accessed using the accession number GSE241761.

Immunohistochemistry

Lethally anesthetized mice (7% chloral hydrate, 0.01 mL/g body weight or 10% ketamine, 220 µg/g body weight plus 2% xylazine, 24 µg/g body weight) were transcardially perfused with 100 mM phosphate-buffered saline (PBS, pH 7.4) at room temperature (RT), followed by ice-cold 4% paraformaldehyde (PFA) for 20 min. Brains were removed from the skull, postfixed for 2 h in 4% PFA (4°C) and stored in 30% sucrose-PBS at 4°C overnight. For Kv7.2, Kv7.3, and osteopontin, brain fixation was performed with Zamboni solution. 30-µm-thick brainstem slices were cut with a sliding microtome (HM 400 R, MICROM) and transferred to 15% sucrose-PBS, followed by

1 https://www.bioinformatics.babraham.ac.uk/projects/fastqc/
2 http://www.bioinformatics.babraham.ac.uk/projects/trim_galore/
3 http://broadinstitute.github.io/picard/

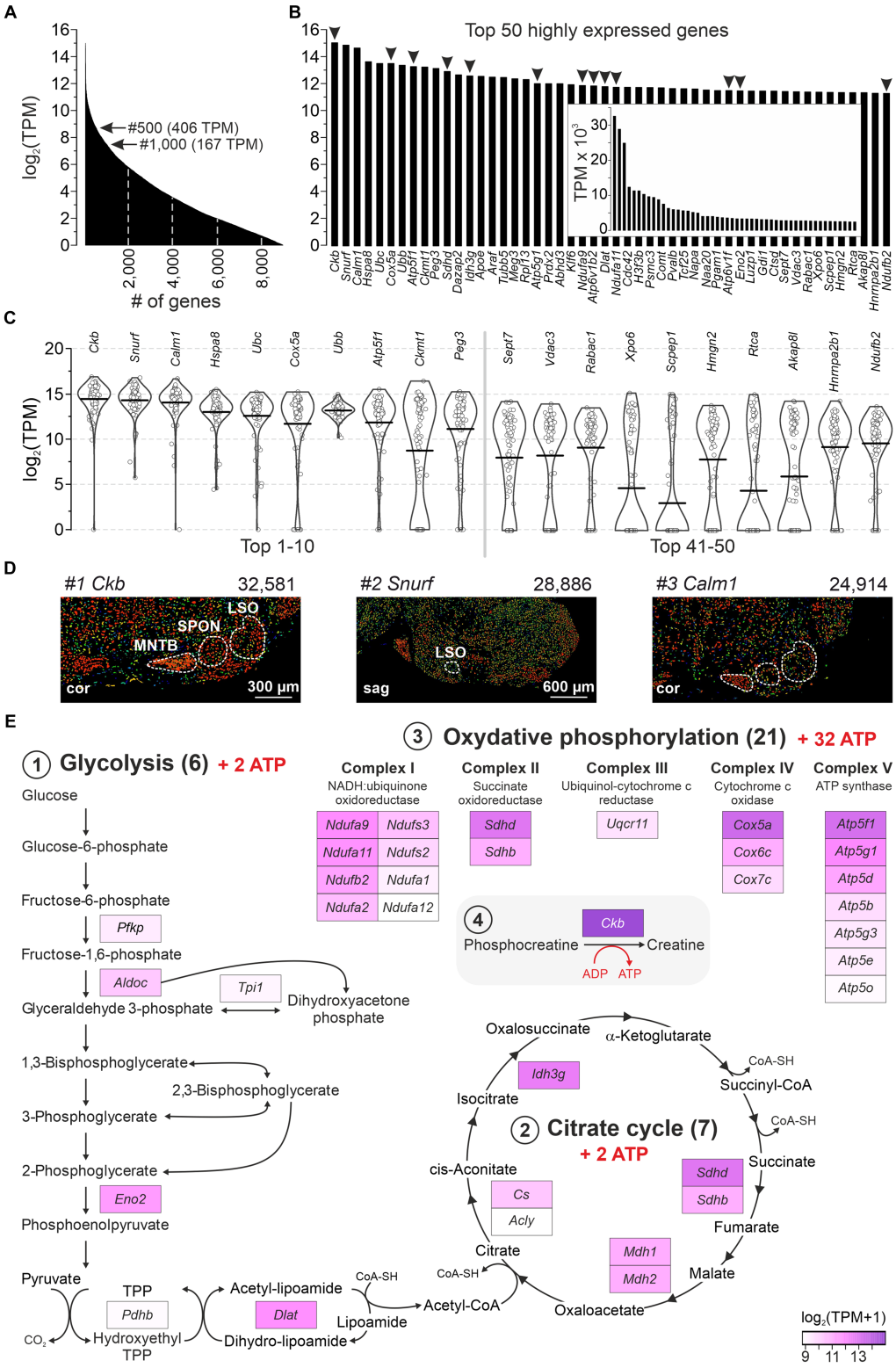


FIGURE 2
A majority of highly expressed genes reveal high energy demands for LSO neurons. **(A)** Expression levels of 9,082 genes with mean TPM ≥ 1 ($\log_2$). Arrows point to genes #500 and #1,000. **(B)** Top 50 highly expressed genes ranked by expression level. Arrowheads mark 13 genes involved in ATP synthesis (*cf.* **E**). **(C)** Violin plots for transcripts #1–10 and #41–50 from **(B)** (1 dot per neuron). Horizontal bars correspond to mean values. **(D)** *In situ* hybridization images of the SOC for the top three highly expressed genes (*Ckb, Snurf, Calm1;* modified images from AMBA; for URLs, see Supplementary Table S7). Expression mask image displays highlight cells that have the highest probability of gene expression (from low/blue to high/red). TPM values are also provided. **(E)** GSEA of the 500 most highly expressed genes (≥ 406 TPM). Three KEGG pathways: (1) Glycolysis (M00001, M00307), (2) Citrate cycle (M00009), (3) OxPhos (mmu00190). (4) ATP synthesis-related *Ckb* (#1). cor, coronal; sag, sagittal (see also Supplementary Table S2).

three rinses in PBS (30 min, RT). Incubation and rinsing steps were performed free-floating unless otherwise noted. For Kvβ3, a heat-induced epitope retrieval protocol was used prior to antibody treatment. For this, slices were immersed in 10 mM sodium citrate buffer (pH 6.0) plus 0.05% Tween 20 (Roth) and heated at 95°C for 20–40 min. They were then returned to RT, followed by three rinses in PBS (5 min, RT).

Fluorescence labeling

Sections were incubated in blocking solution (0.3% Triton X-100, 10% goat serum [donkey serum for osteopontin], 3% BSA in KCl-free PBS) for 2 h at RT. Antibodies to osteopontin (1:250, goat, R&D Systems), vGLUT1 (1:500, guinea pig, Synaptic Systems), GlyT2 (1:250, mouse, Synaptic Systems), CGRP (1:500, guinea pig, Synaptic Systems), Kv7.2 (1:500, rabbit, Synaptic Systems), Kv7.3 (1:500, rabbit, Synaptic Systems), Kv11.3 (1:250, rabbit, Alomone) and Kvβ3 (1:200, rabbit, Biomol) were applied overnight at 4°C in carrier solution (0.3% Triton-X-100, 1% goat serum [donkey serum for osteopontin], 1% BSA in KCl-free PBS) solution followed by three rinses in PBS (30 min, RT). The sections were then incubated for 90 min in the dark with secondary antibodies (1,500, goat anti-guinea pig AlexaFluor 488, goat anti-rabbit AlexaFluor 568, Thermo Fisher Scientific; goat anti-rabbit AlexaFluor 488, Invitrogen; goat anti-mouse AlexaFluor 568, donkey anti-goat AlexaFluor 488, Molecular Probes; donkey anti-goat AlexaFluor 568, Invitrogen). After three PBS rinses (30 min, RT), sections were mounted on gelatin-coated slides and coverslipped with mounting medium containing 2.5% 1,4-diazabicyclo [2.2.2] octane (Sigma-Aldrich). Images were captured with a TCS SP5 X confocal microscope equipped with an HCX PL APO Lambda blue 63x oil objective (Leica Microsystems).

3,3′-diaminobenzidine labeling

To block endogenous peroxidase, sections were incubated for 30 min in 10% methanol, 3% H_2O_2 KCl-free PBS, rinsed in PBS (three times 10 min, RT), and transferred to blocking solution for 2 h at RT. Primary antibodies against CGRP or osteopontin were applied overnight at 4°C, followed by three rinses in PBS (30 min, RT). The sections were then incubated with biotinylated secondary antibodies (1:100, goat anti-guinea pig, Rockland; 1:100, donkey anti-goat, Jackson) in carrier solution for 90 min at RT and rinsed in PBS (three times 10 min, RT). NeutrAvidin-HRP (1,500, Invitrogen) was applied in carrier solution overnight at 4°C. After three rinses in PBS (30 min, RT), the sections were incubated in DAB solution (0.7 mg/mL, SigmaFast DAB tablets) for 5 min, followed by H_2O_2 solution (0.7 mg/mL, SigmaFast urea hydrogen peroxide tablets) for 17 min and rinsed in PBS (three times 10 min, RT). Finally, the sections were mounted on slides and images were captures using a light microscope equipped with Plan-Neofluar objectives (Axioscope 2; 2.5x/0.12; 20x/0.5; 40x/0.75;100x/1.3 oil objective, Carl Zeiss) or an F-View 2 camera (Olympus Soft Imaging Solutions).

Calculation of the number of fluorescent cells

The number of immunolabeled cell bodies was determined using the ImageJ Cell Counter plugin. Three LSO sections per animal ($N = 4$) were divided into a medial and a lateral half, in which three arbitrarily placed squares (edge length 100 µm) defined the 30,000-µm^2 region of interest from which somata were counted. A total of 24 regions of interest were analyzed.

Pharmacology

The Kv7.2/3 agonist retigabine (N-(2-amino-4-(4-fluorobenzylamino)phenyl) carbamic acid ethyl ester; Sigma-Aldrich) was dissolved in water and stored at 4°C. On the day of the experiment, this stock solution (100 mM) was diluted, and retigabine (30 µM) was applied 10 min before and throughout the electrophysiological measurements. To analyze drug effects, we used the same current step protocol as described above in the electrophysiology section, but sampled at 20 kHz.

Statistics

Statistical analyses were performed using Excel (Microsoft) or GraphPad Prism 9 (GraphPad Software). Data were tested for normal distribution using the Kolmogorov–Smirnov test. If normally distributed, they were compared in a 2-tailed Student's *t*-test. Otherwise, a Mann–Whitney-U test (unpaired data) or a Wilcoxon signed-rank test (paired data) was used. The Šidák correction was used for multiple comparisons.

Allen mouse brain atlas for *in situ* hybridization images

For selected genes, we compared the expression level to *in situ* hybridization results from the AMBA.[4] We primarily analyzed P56 sections. They were chosen because >40% of the genes of interest were missing data at P14. P14 images in the AMBA were mainly sagittal views and less informative. Therefore, they were analyzed for comparison purposes only. The images show slightly modified coronal or sagittal sections (Supplementary Figures S4, S5). They represent gene expression energy values per 200-µm voxel. To allow direct navigation to an image of interest, we have provided the hyperlinks in Supplementary Table S7.

Results

A priori checks revealed 86 patch-seq LSO neurons of sufficient quality

The LSO is a brainstem nucleus containing neuron types with ascending and descending projections (Figure 1A). To gain a comprehensive understanding about the molecular and physiological complexity of this prominent nucleus, we performed patch-seq experiments in acute slices (Figure 1B). We recorded from 263 patch-clamped LSO neurons and harvested the cytoplasm in 103 cases (see Methods for exclusion criteria). Of these 103, 86 passed the quality controls and displayed 1.6×10^6 mapped reads (median; interquartile range (IQR) 1.3×10^6; Figure 1C). Negative controls yielded an 8-fold lower number (median: 0.2×10^6; IQR: 0.2×10^6). The mean mapping rate exceeded 80% and was thus >2-fold higher than in negative controls (Supplementary Figure S2A). The largest proportion of reads

4 https://mouse.brain-map.org/

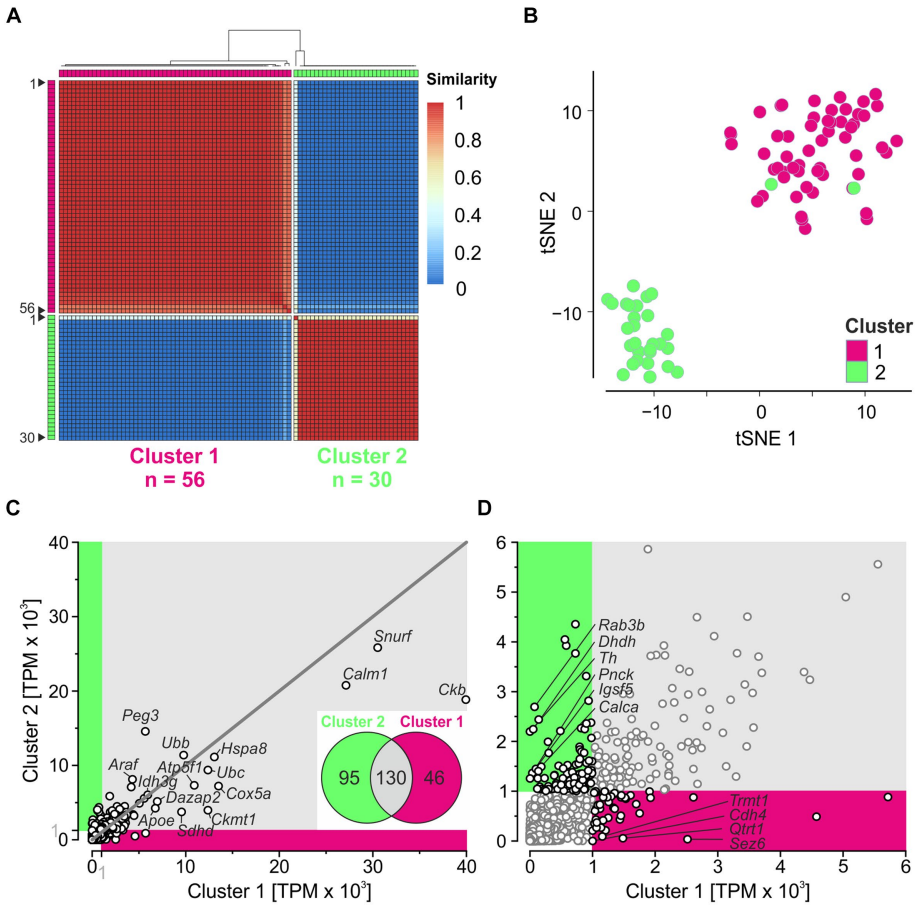


FIGURE 3
Unsupervised clustering reveals two major clusters. **(A)** Consensus matrix obtained for two clusters. Matrix shows how often each pair of neurons ($n = 86$) is assigned to the same cluster (1 = 100%). **(B)** tSNE plot based on PCs 1–10. **(C)** Correlation analysis of global expression profiles for 11,659 genes. Magenta and green sections include non-intersecting genes with mean TPM ≥1,000 in cluster 1 and cluster 2, respectively. The top 15 highly expressed genes (*cf.* Figure 2B) are provided with names. Dots on the 45-degree line imply same gene expression levels in both clusters. Inset: Venn diagram showing the number of intersecting (Cluster 1 ∩ Cluster 2; $n = 130$) and non-intersecting genes (Cluster 1\Cluster 2) ∪ (Cluster 2\Cluster 1; $n = 46 + 95 = 141$). **(D)** Close-up of non-intersecting genes with ≥1,000 TPM (black dots). For genes with <100 TPM in the complementary cluster, names are provided ($n = 4, 6$) (see also Supplementary Figure S3).

mapped to exons (45%), an almost 3-fold higher value than in negative controls (Supplementary Figures S2C,D). The median percentage of ribosomal RNA was 3.8% (IQR: 4.5%; Supplementary Figure S2B). With one exception, no single value exceeded 15%, indicating sufficient rRNA depletion (Dobin and Gingeras, 2015). The number of detected genes per neuron or negative control correlated with the number of reads mapped. A mean of 2,863 genes were found per neuron (median: 2.9×10^3; IQR: 1.2×10^3; Figure 1D) and 310 genes in negative controls, a >9-fold lower value (median; IQR: 565; Figure 1D). The number of mapped reads, number of detected genes, mapping rate, and rRNA rate were consistent with published patch-seq datasets (Cadwell et al., 2017, 2020), demonstrating a high library quality.

Highest gene expression levels imply high energy demands in LSO neurons

A major advantage of the single-cell patch-seq approach, which is absent from bulk analyses (Koehl et al., 2004; Nothwang et al., 2006; Ehmann et al., 2013; Xiao et al., 2013; Moritz et al., 2015; Kolson et al., 2016), is the ability to focus on neurons instead of globally addressing different cell types (including glia or blood endothelium). We took advantage of this and examined the most abundant transcripts in the 86 LSO neurons. Within the cohort of 9,082 genes with ≥1 TPM, 185 and 60 showed TPM values >1,024 and > 2,048, respectively (Figure 2A). The 50 most highly expressed genes are shown in Figure 2B (32,581–2,460 TPM, inset). For 20 of them, bee swarm and violin plots are depicted in Figure 2C. Three genes showed exceptionally high expression levels, namely *Ckb*, *Snurf*, and *Calm1* (Figure 2B; mean TPM: 32,581, 28,886, 24,914). They encode brain-type creatine kinase B (CKB), SNRPN upstream open reading frame protein (SNURF; SNRPN = small nuclear ribonucleoprotein polypeptide N), and calmodulin 1 (CALM1 aka CaM), respectively. Our findings are corroborated by *in situ* hybridization results from the AMBA which show high signal intensities in the major nuclei of the superior olivary complex (SOC) (Figure 2D). Further information on *Ckb*, *Snurf*, and *Calm1* is provided in the Discussion.

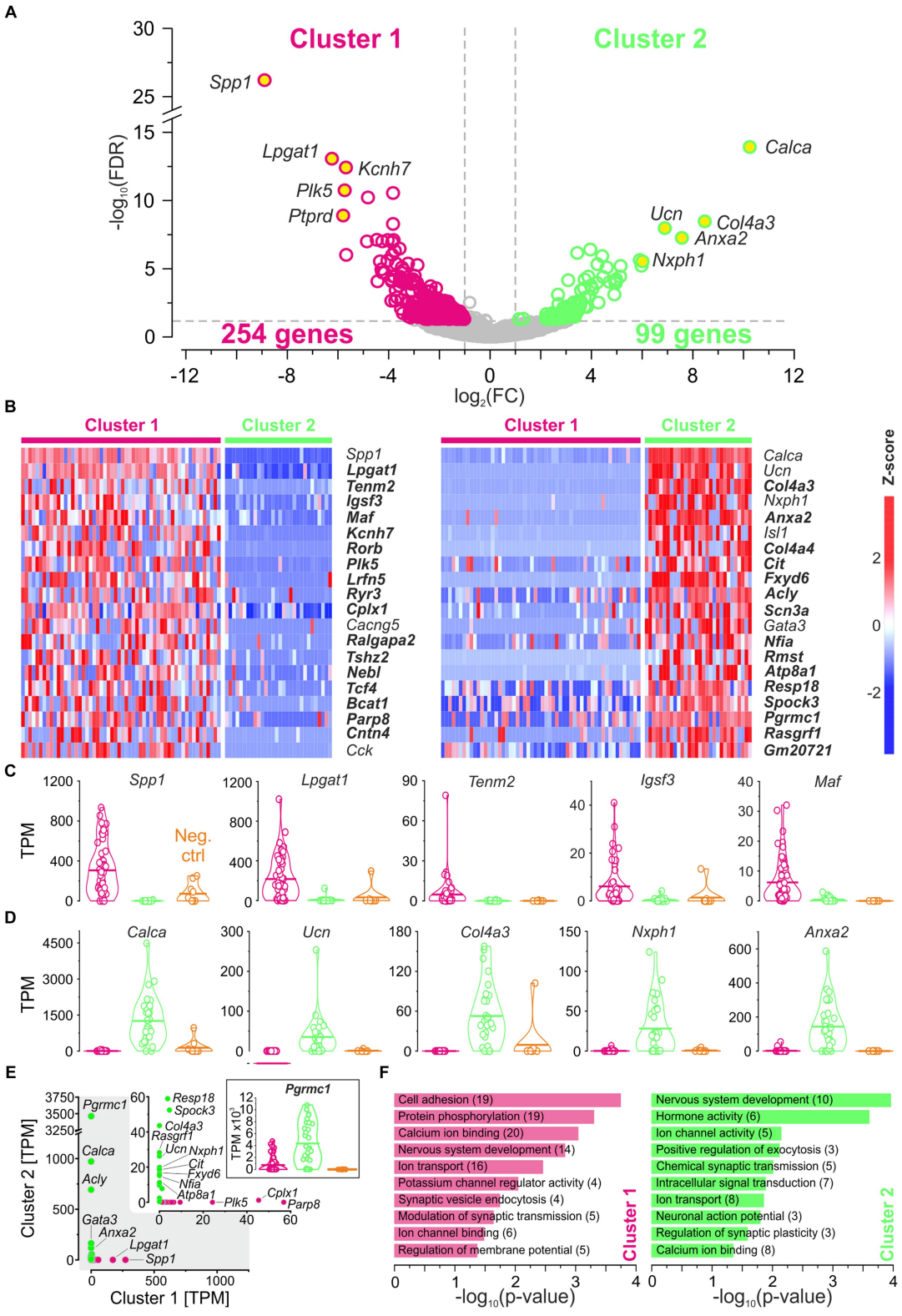


FIGURE 4
DEGs affiliate cluster 1 with pLSOs and cluster 2 with LOCs. **(A)** Volcano plot depicting DEGs for each cluster. DEGs#1–5, as ranked by FC values, are provided with names (yellow dots). Dashed gray lines depict cut-off levels (FC = 2; FDR = 0.05). **(B)** Heat maps of z-scores for the top 20 DEGs in each cluster. Thirty-two newly detected genes are marked in bold. **(C)** Violin plots for DEGs#1–5 in cluster 1 (magenta). Horizontal bars depict mean values. Values from cluster 2 (green) and negative controls (orange) are shown for comparison. **(D)** As **(C)**, but for cluster 2. **(E)** Scatter plot comparing the median expression levels of DEGs#1–20 from cluster 1 and 2. Inset is a close-up for ≤60 TPM. Genes with >10 TPM are provided with names (5 in cluster 1, 15 in cluster 2). Violin plot for *Pgrmc1*, DEG#18 in cluster 2. **(F)**, Selected enriched GO terms for DEGs in cluster 1 (magenta) and in cluster 2 (green). Number of genes in brackets (see also Supplementary Tables S3, S4).

Glucose consumption is a signature of brain activity (Ashrafi and Ryan, 2017) and is particularly high in the CAS (Sokoloff, 1981). As 13 of the 50 most highly expressed genes in our sample encode enzymes involved in catabolism, we examined pathways of energy demand and ATP production in more detail. We analyzed gene enrichment in pathways that completely combust glucose to CO_2 and H_2O: (1) Glycolysis (including Pyruvate oxidation), (2) Citrate cycle, and (3) Oxidative phosphorylation (OxPhos; Supplementary Table S2). The analysis included 162 genes, including *Ckb* (4). Among the top 500 highly expressed genes, 7% (33) belonged into these pathways and were distributed across the four categories (Figure 2E). When normalized to the set of 162, the frequency was 20%. Taken together, these numbers emphasize and specify the genes involved in ATP generation and highlight the importance of energy metabolism in the LSO.

Gene enrichment analysis revealed seven genes among the top 500 that encode v-ATPase subunits (*Atp6ap1*, *Atp6v1b2*, *Atp6v6v11*, *Atp6v0c*, *Atp6v0d1*, *Atpv1e1*, *Atp6v1d*; 3,589–438 TPM; #24 to #460). Twenty-three v-ATPase genes have been described (Alexander et al., 2011). v-ATPases are associated with lysosomes and primary-active proton pumps which play an important role in driving transmitter loading into synaptic vesicles (Egashira et al., 2015). Our results indicate that LSO neurons were in a metabolically active state.

scRNA-seq reveals two clusters of LSO neurons

To identify neuron types in the LSO, we applied unsupervised clustering. We determined the consensus matrix for 2–10 clusters using SC3 and calculated the average silhouette width for each number of clusters (widths vary from 0 to 1; a width close to 1 represents the optimal number of clusters). We obtained the largest width (0.98) with two clusters (Supplementary Figures S3A,B). Fifty-six of the 86 neurons (~2/3) belonged to cluster 1, and 30 (~1/3) belonged to cluster 2 (Figure 3A). Similarity values were close to 1 for each neuron in its own cluster and close to 0 in the other cluster, except for neuron #1 in cluster 2. We checked for consistent results using the alternative tool Seurat, which assigned 59 neurons to cluster 1 and 27 neurons to cluster 2 (Supplementary Figure S3C). Fifty-six neurons in cluster 1 overlapped between SC3 and Seurat, while 27 neurons overlapped in cluster 2. The substantial overlap demonstrated consistency between the two tools. For three clusters, the results were less consistent and the overlap between SC3 and Seurat was small (Supplementary Figure S3D). Taken together, these results confirm the best results with two clusters.

To visualize the clustering results, we performed a PCA based on HVG (Methods and Supplementary Figure S3E). PC1 explained 11% of the variance and separated both clusters, except for two neurons belonging to cluster 2. Because PC1 plus PC2 together explained only 17% of the variance, we generated a tSNE plot using PC1–PC10. Again, the neurons were clearly separated into two clusters, except for two neurons (Figure 3B; see also Supplementary Figure S3E). Overall, these results demonstrate two major clusters for our sample, regardless of the clustering method used. Below, we explore the two clusters obtained by SC3.

After dividing the 86 patch-seq neurons into two clusters, we assessed the expression level of 11,659 genes (Figure 3C). Two hundred and seventy-one genes exceeded TPM ≥ 1,000 in at least one cluster. Approximately 50% of the genes overlapped (130/271; inset), indicating considerable similarity between the two clusters. Each of the 13 genes involved in ATP synthesis shown in Figure 2B ended up in the intersection, suggesting high metabolic demands in both clusters. Among the 141 non-intersecting genes with ≥1,000 TPM (46 in cluster 1; 95 in cluster 2), only four and six, respectively, showed <100 TPM in the complementary cluster (Figure 3D). This again indicates homogeneity between the two clusters for many transcripts.

Search for molecular signatures in each cluster

The above comparisons revealed considerable similarities between the clusters. To identify differences, we focused on DEGs (see Methods for definition). As documented in a volcano plot, 353 DEGs were identified, of which 254 were upregulated in cluster 1 and 99 in cluster 2 (Figure 4A; Supplementary Table S3). To identify the top DEGs, the DEGs were ranked by the AUROC value. In Figure 4B, the expression of the top 40 DEGs, 20 in each cluster, is visualized in heatmaps (56 neurons in cluster 1, 30 in cluster 2). Below and in Supplementary results, we provide some background information for each of these top 40 DEGs.

Cluster 1, DEGs#1–6

#1—Spp1: osteopontin

DEG#1 in cluster 1 was *Spp1* (Figures 4B,C,E). *Spp1* codes for the secreted phosphoprotein 1 = osteopontin (OPN), a cell adhesion molecule with multiple functions (Denhardt and Guo, 1993). Its expression is reported to be high in >20 brainstem regions, and OPN mRNA has been described in some LSO neurons of P14 rats (see Figure 3C in Lee et al., 2001). Our results from P11 mice are consistent with this pattern (see Figures 5A,B). In the rat cochlear nuclear complex, *Spp1* expression resulted in 5-14-fold higher mRNA levels in the two ventral nuclei than in the dorsal nucleus (see Figure 5 in Friedland et al., 2006). *Spp1* contributes to neuronal development (Jiang et al., 2019), including axon myelination (Selvaraju et al., 2004; Nam et al., 2019; Cappellano et al., 2021) and axon regeneration after injury (Duan et al., 2015). It has been suggested that OPN is involved in the formation and/or maintenance of axons with high conduction velocity (Higo et al., 2010). Notably, pLSO and MNTB neurons are myelinated (as are neurons in the ventral cochlear nuclei and motoneurons), whereas LOCs are not. The AMBA shows high to intermediate expression levels for *Spp1* in the LSO at P14 and at P56 (Supplementary Figure S4). Corresponding immunohistochemical views of the OPN protein pattern are shown in Figures 5A,B. For *Spp1* and subsequent genes, the expression level and numerical details are provided in Supplementary Table S3. In summary, our *Spp1*|OPN results support the idea that pLSOs belong to cluster 1, whereas LOCs do not.

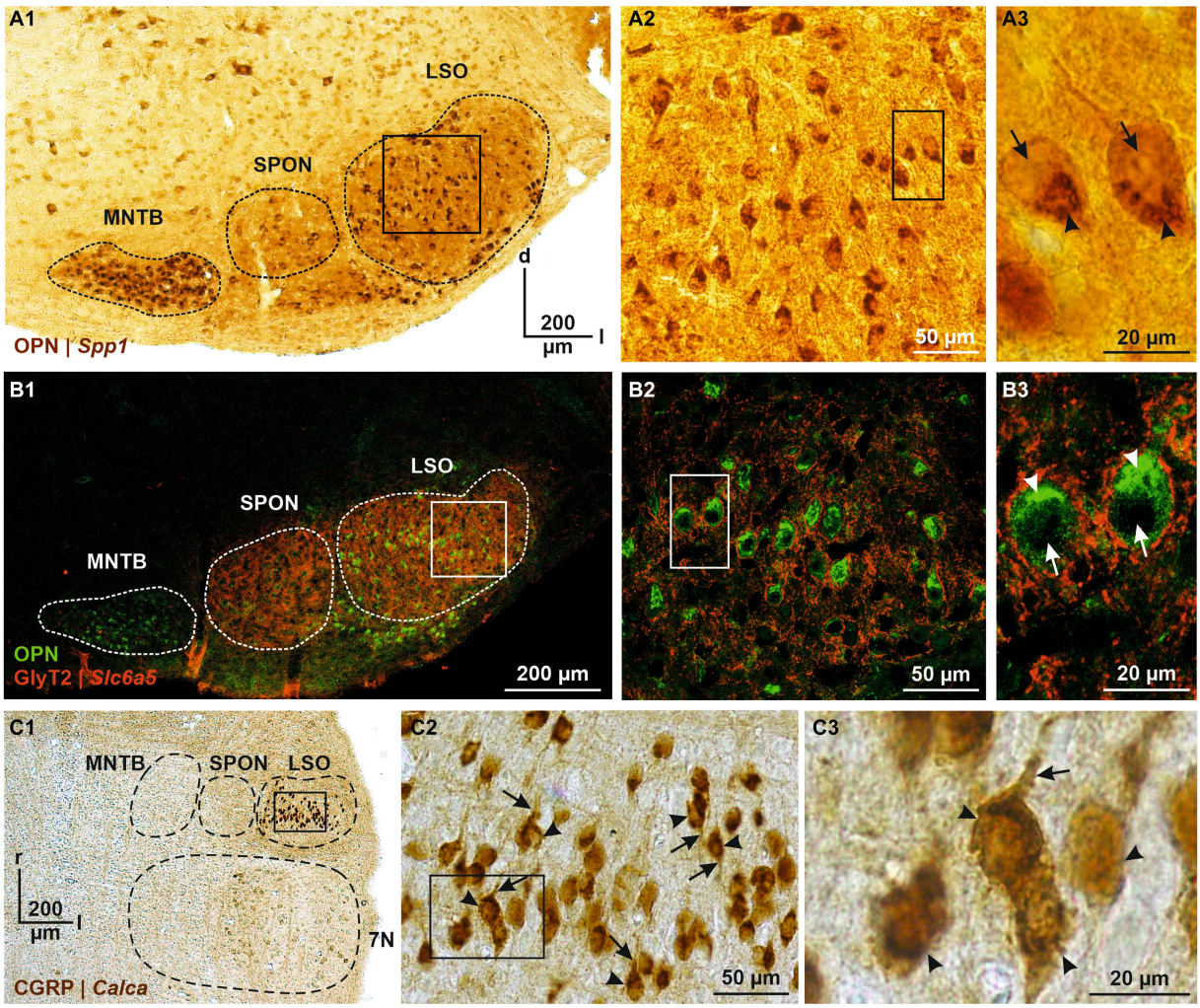


FIGURE 5
Immunohistochemical analysis of OPN and CGRP, encoded by DEG#1 in cluster 1 and cluster 2 (*Spp1* and *Calca*, respectively). **(A1)** OPN immunoreactivity in the SOC (**A1**, coronal brainstem section) and LSO **(A2)**. DAB-stained coronal brainstem slice at P12. Close-up of two representative neurons in **(A3)**. **(B)** As **(A)**, but double labeling for OPN (green) and GlyT2 (red). In **(A3,B3)**, cytoplasmic immunosignals are marked by arrowheads and nuclei by arrows. **(C)** CGRP immunoreactivity in the SOC (**C1**, horizontal brainstem section) and LSO **(C2)**. DAB-stained horizontal brainstem slice at P12. Close-ups of four representative neurons in **(C3)**. In **(C2,C3)**, somatic and dendritic immunosignals are marked by arrowheads and arrows, respectively. Borders of MNTB, SPON, 7 N, and LSO are indicated by dashed black or white lines. d, dorsal; l, lateral; r, rostral; 7 N, facial nucleus.

#2—*Lpgat1*: lysosphatidylglyceral acyltransferase 1

DEG#2 in cluster 1 was *Lpgat1* (Figures 4B,C,E). This gene codes for lysophosphatidylglycerol acyltransferase 1 (LPGAT1), an enzyme associated with the endoplasmic reticulum and involved in lipid metabolism (Yang et al., 2004). LPGAT1 regulates triacylglycerol synthesis which is critical to maintain the integrity of mitochondrial membranes (Wei et al., 2020). In the vestibular organ of chickens, the protein has been exclusively identified in hair cells (Herget et al., 2013). The AMBA shows high *Lpgat1* expression in the LSO at P56 (Supplementary Figure S4, no AMBA data available for P14).

#3—*Tenm2:* teneurin transmembrane protein 2

DEG#3 in cluster 1 was *Tenm2* (Figures 4B,C). *Tenm2* belongs to the teneurin family that comprises four members (*Tenm1-4*). It codes for teneurin transmembrane protein 2 (TEN2, aka TENM2), an axon guidance and adhesion molecule that interacts across the synaptic cleft with presynaptic latrophilin1, thus mediating Ca^{2+} signaling and synapse formation (Vysokov et al., 2016). Teneurin proteins are abundant throughout the central nervous system and play a role in regulating synaptic partner matching (Hong et al., 2012; Leamey and Sawatari, 2014). A distinct role of *Tenm2* in the generation of binocular projections has been demonstrated in the mouse visual system, and *Tenm2* knockout resulted in specific wiring deficits in the retinogeniculate pathway (Young et al., 2013). In the auditory system, high *Tenm2* expression is present in spiral ganglion neurons of the Ib subtype, whereas type II neurons highly express *Tenm3* (Petitpré et al., 2018). As to date, information about *Tenm2* in the CAS is missing. The AMBA shows a few cells with low *Tenm2* expression in the LSO at P56 (Supplementary Figure S4, no AMBA data available for P14).

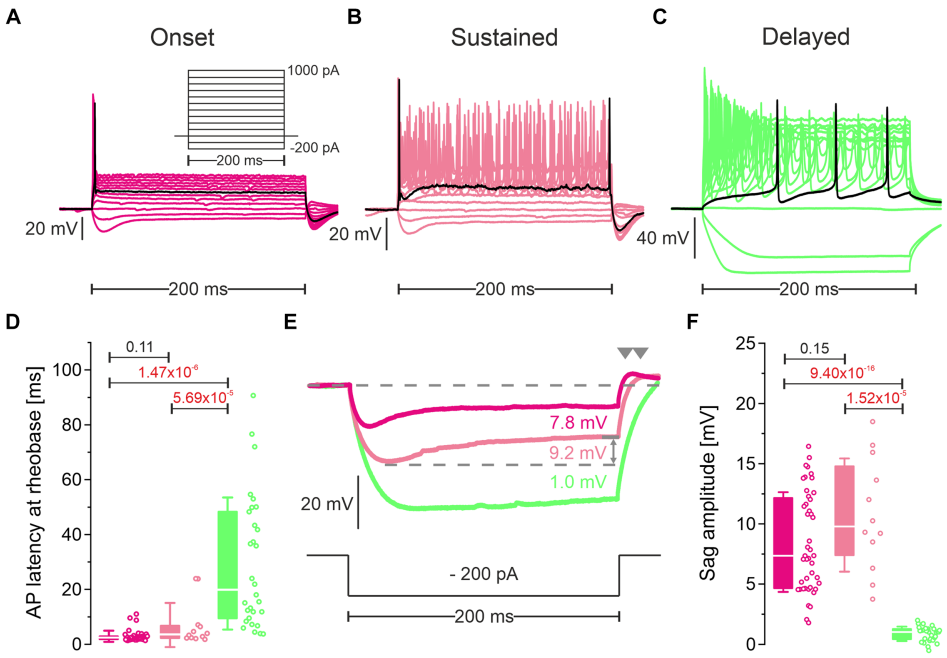


FIGURE 6
Cluster 1 neurons and cluster 2 neurons differ in their firing pattern and their response to hyperpolarization. **(A–C)** Representative voltage traces in response to rectangular current pulses (inset in **A**; −200 to +1,000 pA, 100 pA increments, 200 ms duration) of an onset firing cluster 1 neuron (pLSO—Onset; **(A)**, a sustained firing cluster 1 neuron (pLSO—Sustained; **(B)**, and a delayed firing cluster 2 neuron (LOC—Delayed; **(C)**. Black traces depict responses at rheobase. Notice different voltage scaling. **(D)** Statistics for the peak latency of the first AP at rheobase. Open dots depict single neurons. Numbers above bars represent *p*-values (in red if significant). **(E)** Voltage traces in response to a – 200-pA|200-ms current pulse highlighting sag behavior. Same color code as in **(A–C)**. Sag amplitudes were quantified as indicated by the gray double arrow. Rebound behavior after the hyperpolarizing current pulse is marked by gray arrowheads. **(F)** As **(D)**, but for sag amplitude (see also Supplementary Table S5).

#4—*Igsf3:* immunoglobulin superfamily member 3

DEG#4 in cluster 1 was *Igsf3* (Figures 4B,C). It belongs to the Ig superfamily whose members are major regulators of many developmental processes, such as differentiation, axogenesis, dendritogenesis, and synaptogenesis. Like the other three members of the little studied EWI Ig subfamily, IGSF3 (aka EWI-3) contains a Glu-Trp-Ile (EWI) motif. IGSF3 is a neuron-specific membrane protein that is produced in various neuronal populations when neural circuits are formed (Usardi et al., 2017). It is transiently found in cerebellar granule cells before their final maturation and highly concentrated in axon terminals. The AMBA shows only two cells expressing *Igsf3* in the LSO at P56 (Supplementary Figure S4, no AMBA data available for P14).

#5—*MAF:* MAF bZIP transcription factor

DEG#5 in cluster 1 was *Maf* (Figures 4B,C). The *Maf* family encodes b leucine zipper (bZIP)-containing transcription factors which act as homo-or hetero-dimers. Depending on the binding site and binding partner, the encoded proteins are transcriptional activators or repressors. cMAF controls eye and lens development (Ring et al., 2000) and directs the development of low-threshold touch receptors (Wende et al., 2012). Pacinian corpuscles, which are essential to detect small-amplitude high-frequency vibrations, become severely atrophied in *c-Maf* mutants. Several genes encoding K^+ channels are downregulated in such mutants (*Kcna1, Kcng4, Kcnh5, Kcnq4*). In the cerebral cortex, c-MAF regulates the potential of GABAergic interneurons to acquire a somatostatin-positive identity, shortly after these neurons become postmitotic (Mi et al., 2018). The AMBA shows high expression levels for *Maf* in the LSO at P14 and at P28 (Supplementary Figure S4).

#6—*Kcnh7:* potassium voltage-gated channel subfamily H member 7

DEG#6 in cluster 1 was *Kcnh7* (Figure 4B). Kv11.3, the encoded protein, is the third member in the family of ERG channels (ether-a-go-go-related). Our study demonstrates no gene expression for Kv11.2 and only low expression for Kv11.1 (*cf.* chapter "Potassium channels"). Consistent with our results, the AMBA shows low to intermediate *Kcnh7* expression in the LSO at P14 and P56 and few cells with high signal intensity at P56 (Supplementary Figure S4). Below, we further analyze *Kcnh7*|Kv11.3 on the protein level (*cf.* chapter "Immunohistochemical analysis of Kv11.3 and Kvβ3"), and we refer to the Discussion for an elaborate treatise.

#7–20

Information on DEGs#7–20 is provided in Supplementary results.

Cluster 2, DEGs#1–6

#1—*Calca*: calcitonin gene-related peptide

DEG#1 in cluster 2 was *Calca* (Figures 4B,D,E). *Calca* codes for CGRP, the calcitonin gene-related peptide. As elaborated in the

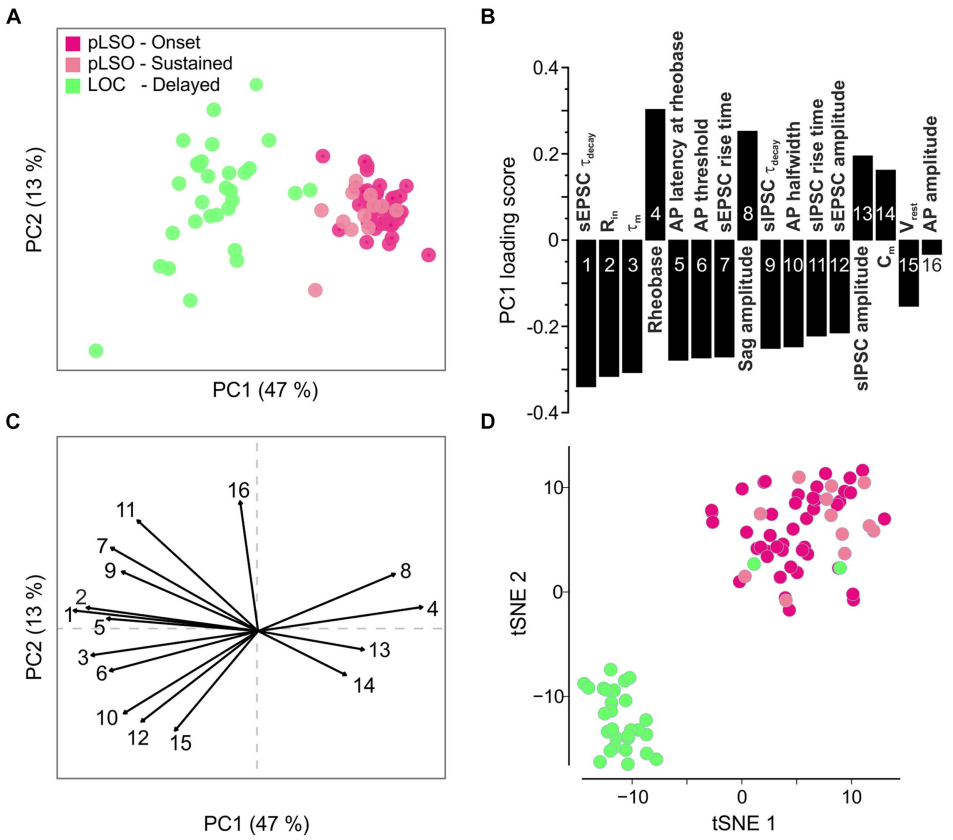


FIGURE 7
Principal component analysis (PCA) of electrophysiological features confirms the two clusters identified via transcriptomics. **(A)** PCA plot based on 16 electrophysiological features. **(B)** Loading scores for PC1 shown in **(A)**. **(C)** Vector factor map showing the features depicted in **(B)** and their contribution to PC1 and PC2. **(D)** Same tSNE plot as in Figure 3B, but color-coded according to the firing pattern (see also Supplementary Figures S6, S7).

Introduction, CGRP is present in LOCs but absent from pLSOs. Therefore, our DEG results provide initial hints that cluster 2 may comprise LOCs. To assess whether the protein follows mRNA, we performed immunohistochemical analysis of CGRP and demonstrated intense labeling in the LSO (Figure 5C), therewith confirming previous results (Safieddine and Eybalin, 1992; Robertson and Mulders, 2000). AMBA shows LSO cells with high gene expression at P14 and intermediate to high expression at P56 (Supplementary Figure S5).

#2—Ucn: urocortin

The tentative conclusion that cluster 2 comprises LOCs was reinforced by our findings on DEG#2, which was *Ucn* (Figures 4B,D,E). *Ucn* codes for urocortin, one of three members in the urocortin family composed of stress-related corticotropin-releasing hormone neuropeptides. In rats, urocortin was demonstrated in a small subset of LSO neurons (Vaughan et al., 1995; Kaiser et al., 2011). It is reportedly absent from other auditory nuclei (Bittencourt et al., 1999). *Ucn* expression appears to be specific for LOCs, and urocortin is abundant in their axon terminals in the cochlea (Vetter et al., 2002; Kaiser et al., 2011). Consistent with our results, AMBA shows LSO cells with high gene expression levels at P14. Interestingly, *Ucn* expression P56 is almost absent (Supplementary Figure S5). As LOCs modulate the excitability of auditory nerve fibers, urocortin may balance physiological reactions to acoustic stress via high affinity binding to corticotropin-releasing factor receptor CRFR1 during development (Graham and Vetter, 2011).

#3—Col4a3: collagen type IV alpha 3 chain

DEG#3 in cluster 2 was *Col4a3* (Figures 4B,D,E). *Col4a3* codes for the α3 domain of type IV collagen. Type IV collagens are the major structural component of basement membranes, including the strial capillary basement membranes in the inner ear. *Col4a3* mutations affect the structure and function of the cochlea and result in syndromic deafness (Mochizuki et al., 1994; Angeli et al., 2012; Kolla et al., 2020). Thus, *Col4a3* is considered a deafness gene (Müller and Barr-Gillespie, 2015). As to date, the literature is virtually devoid of reports on *Col4a3* in combination with neurons. Type IV collagens inhibit cell proliferation and astroglial differentiation while promoting neuronal differentiation (Ali et al., 1998). In this context, it is of some interest that DEG#7 in cluster 2 was *Col4a4*, which encodes the α4 domain of type IV collagen (Figure 4B). AMBA shows low *Col4a3* expression in a few cells in the LSO at P56 (Supplementary Figure S5, no AMBA data available for P14). However, *Col4a3* was identified very recently as a marker for LOCs in a study that employed single-nucleus sequencing in mice (Frank et al., 2023). Our results confirm these findings.

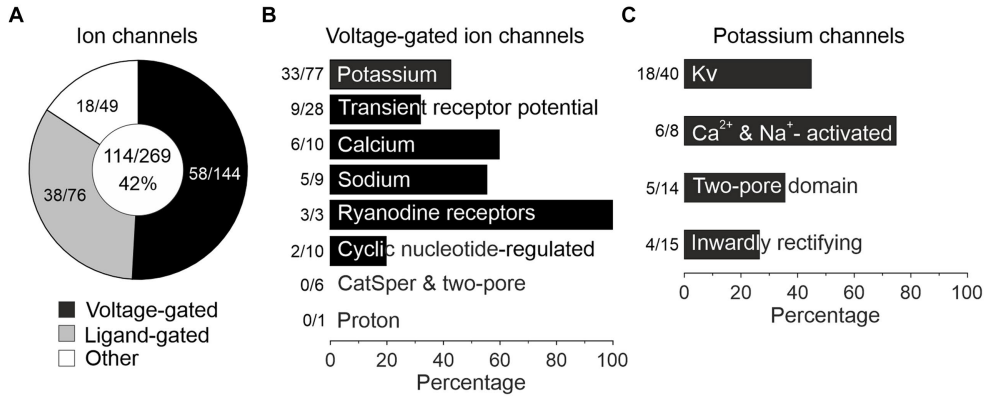


FIGURE 8
pLSOs and LOCs express a wide array of ion channels. **(A)** Forty-two percent (114/269) of ion channel genes (voltage-gated, ligand-gated, other) listed in the IUPHAR/BPS Guide to Pharmacology are expressed in the LSO. **(B)** Across the eight family members of voltage-gated ion channels, genes encoding potassium channels are most highly represented (43%; 33/77 genes). **(C)** The majority of potassium channel genes encode Kv channels (45%, 18/40).

#4—Nxph1: neurexophilin 1

DEG#4 in cluster 2 was *Nxph1* (Figures 4B,D,E). *Nxph1* codes for the neuronal glycoprotein neurexophilin1. Four isoforms of neurexophilin (Nxph1-Nnxph4) form a conserved family of neuropeptide-like molecules that interact with neurexins, crucial presynaptic cell-adhesion molecules (Missler and Südhof, 1998; Ding et al., 2020). Nxph1 is a specific ligand for α-neurexin 1 (aka NRXN1α) and essential for transsynaptic activation. Neurexins (NRXN1-3) consist of an α-and a β-protein and play important roles in synaptic plasticity and synapse maturation. By binding to the postsynaptic ligand, they can directly influence ligand-binding receptors, thereby altering a neuron's excitatory or inhibitory ability. A restricted *Nxph1* expression was described in subpopulations of inhibitory neurons (Petrenko et al., 1996; summary: Born et al., 2014). Conjunctively, these transsynaptic cell adhesion molecules coordinate synapse formation, restructuring, and elimination in both directions. From in the Petrenko paper, one can deduce that LSO neurons express neurexophilin. AMBA shows a low to intermediate expression level in the LSO at P56 (Supplementary Figure S5, no AMBA data available for P14).

#5—Anxa2: annexin A2

Anxa2, DEG#5 in cluster 2 (Figures 4B,D,E), is one of 13 annexin A genes expressed in vertebrates. Members of this subfamily are soluble proteins that are recruited to membranes in the presence of elevated Ca^{2+} where they bind phospholipids. Among the multiple roles of annexins are membrane aggregation, exocytosis, and endocytosis regulation. *Anxa2* is highly expressed in nociceptors where AnxA2 regulates TRPA1-dependent acute and inflammatory pain (Avenali et al., 2014). Gene expression was also demonstrated in surrounding cells in the developing mouse cochlea (Scheffer et al., 2015). To our knowledge, relevant papers on auditory neurons do not exist (Pubmed search: "Anxa2 auditory" or "Annexin A2 auditory"; 2023–10-22). AMBA shows only a few LSO cells with low *Anxa2* expression at P14 and P56 (Supplementary Figure S5).

#6—Isl1: insulin gene enhancer protein ISL1

Isl1 (aka *Islet-1*), DEG#6 of cluster 2 (Figure 4B), is a homeobox gene encoding the insulin gene enhancer protein ISL1. The gene product, a transcription factor, promotes motoneuron development (Ericson et al., 1992) and affects efferents to the inner ear. *Isl1* expression has been reported in olivocochlear efferents (Frank and Goodrich, 2018). Our patch-seq results are consistent with these reports. As the inner ear efferents originate in a progenitor zone for motoneurons, it is not surprising that factors assigning a motoneuron identity (e.g., ISL1 and ChAT) overlap considerably between such efferents and facial motoneurons. In fact, inner ear efferents represent a subset of motoneurons, although they form no synapses with muscle fibers (Frank and Goodrich, 2018). AMBA shows few LSO cells with intermediate to high *Isl1* expression at P56 (Supplementary Figure S5, no AMBA data available for P14).

#7–20

Information on DEGs#7–20 is provided in Supplementary results.

Summary for DEGs#1–20 of each cluster

Taken together, DEGs#1–20 in cluster 1 plus cluster2 contain eight genes (20%) whose expression was previously described in the LSO (cluster 1: *Spp1*, *Cacng5*, *Cck*; cluster 2: *Calca*, *Ucn*, *Nxph1*, *Isl1*, *Gata3*). We now attribute their expression to neurons. The results for the remaining 80% of the genes are new. Each of the three known DEGs in cluster 1 can be associated with pLSOs. Similarly, four genes from cluster 2 can be associated with LOCs (*Calca*, *Ucn*, *Isl1*, *Gata3*). Thus, the transcriptomic results provide substantial and consistent evidence to conclude that cluster 1 and cluster 2 contain pLSOs and LOCs, respectively. If our conclusion is correct (see below), we identified 17 novel marker genes for pLSOs and 15 for LOCs (highlighted in bold in Figure 4B).

Figure 4B shows 40 DEGs ranked by the z-score. Corresponding expression levels are detailed in violin plots (Figures 4C,D), highlighting significant expression differences. We also plotted the corresponding TPM values for both clusters (Figure 4E and inset). The highest expression in cluster 2 was seen for *Pgrmc1* (3,462 TPM). However, this DEG did not end up higher than #18 (Figure 4B), because 50% of cluster 1 neurons also expressed it, at

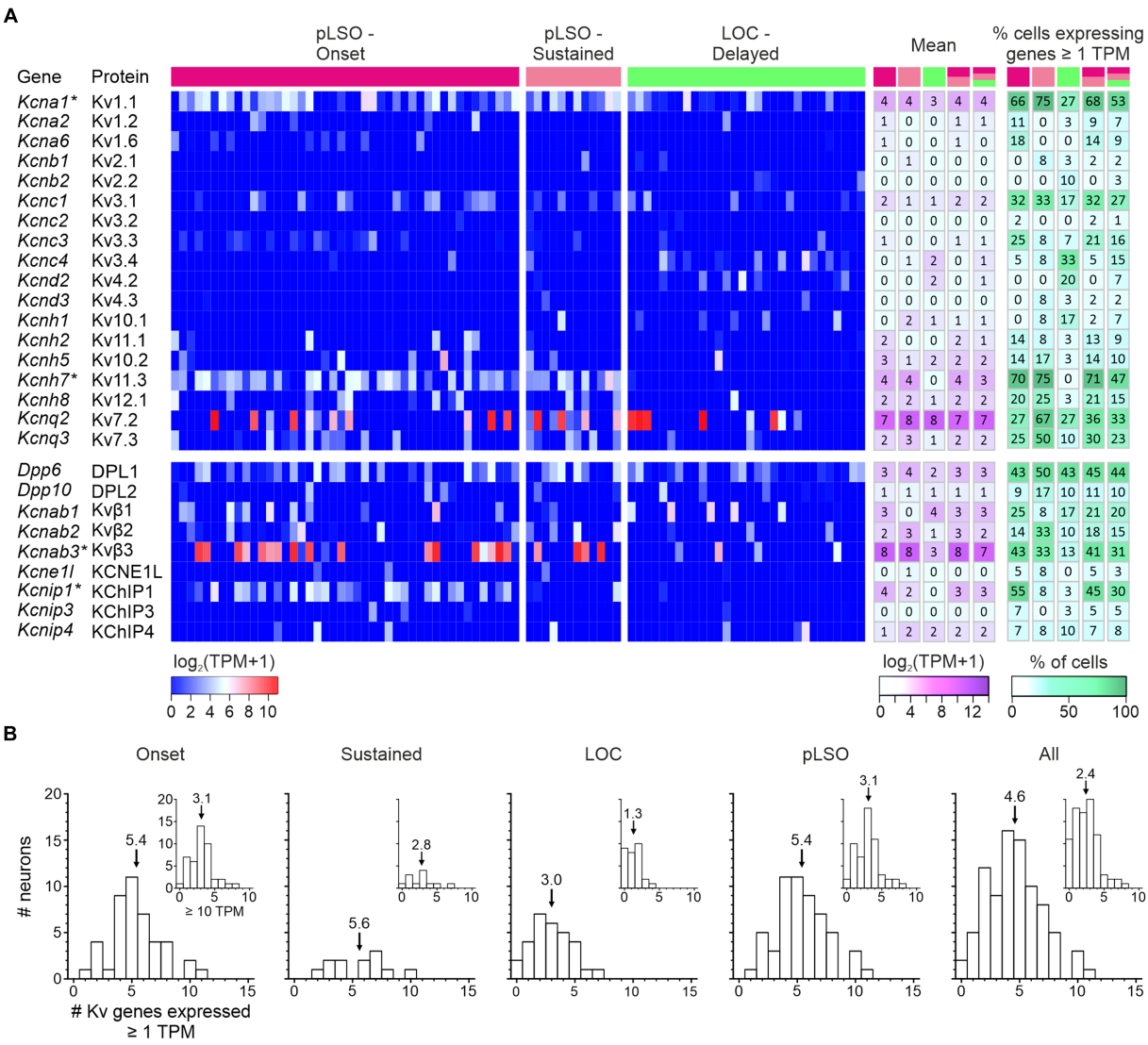


FIGURE 9
Expression of genes encoding voltage-gated potassium (Kv) α subunits and regulatory subunits ($n = 18, 9$). **(A)** Heat maps show expression levels [$\log_2$(TPM + 1)] for single neurons (three cohorts). To the right, the mean and the percentage of cells expressing a given gene are depicted for five cohorts (pLSO—Onset, pLSO—Sustained, LOC—Delayed, pLSO, all neurons; $n = 44, 12, 30, 56, 86$). DEGs are marked with asterisks. **(B)** Frequency histograms show distribution of gene expression for five cohorts (criteria: ≥ 1 TPM; ≥ 10 TPM for insets). Mean values are marked by arrows (see also Supplementary Table S6).

levels up to 4,763 TPM (framed inset in Figure 4E). In cluster 1, TPM values were relatively low, and the highest value was found for *Spp1* (273; 0 in cluster 2). Overall, 20 of the 40 DEGs showed TPM values ≤10 (15 in cluster 1; 5 in cluster 2). For these, we did not provide names (Figure 4E and inset, gene names provided only if >10 TPM).

We compared our data with AMBA's P14 and P56 data, covering 17 of the top 40 DEGs at P14 (42.5%) and 38 DEGs at P28/P56 (95%). A developmental assessment revealed virtually no change in the expression profile of six DEGs in pLSO neurons, while two transcription factors (*Rorb*, *Tcf4*) and *Cacng5* appeared to be downregulated with age. Among the marker genes for LOC neurons, seven genes (*Calca, Ucn, Cit, Fxyd6, Gata3, Nfia, Atp8a1*) showed lower levels at P56, with only two showing no change, indicating developmental downregulation.

Search for functional groups among DEGs

Next, we analyzed the 353 DEGs according to GO annotations. Several GO terms were enriched (Figure 4F; Supplementary Table S4). More specifically, the terms "Nervous system development," "Calcium ion binding," and "Ion transport" appeared in both clusters. Within the GO term "Hormone activity," which was unique for cluster 2, *Calca* and *Ucn* (DEG#1 and #2) encode CGRP and urocortin, established neurotransmitters for LOCs (*cf.* Introduction). The third gene in this GO term was *Uts2b* (DEG#25), which encodes the neuromodulator urotensin 2B (Supplementary Table S3). Urotensin 2B is involved in motoneuron function and stimulates ACh release (Huitron-Resendiz et al., 2005; Nothacker and Clark, 2005). The fourth "Hormone activity" gene was *Calcb* (DEG#34). It is a paralog of *Calca* and codes for the calcitonin related polypeptide β-CGRP (formerly known as CGRP-II;

Alexander et al., 2021). β-CGRP enables calcitonin receptor binding activity and participates in regulating the cytosolic Ca^{2+} concentration. Recently, *Calcb* expression has been associated with a subset of LOCs (Frank et al., 2023). The fifth gene in the GO term was *Igf1* (DEG#58), which encodes the insulin growth factor 1 (IGF-I). IGF-I is involved in differentiation and maturation of neurons and synapses (Nieto-Estévez et al., 2016). Finally, the sixth "Hormone activity" gene was *Vgf* (DEG#77), which encodes the neurosecretory protein VGF (= VGF nerve growth factor inducible). VGF is a neuropeptide precursor involved in neurogenesis and metabolic regulation.

Collectively, the results from the unsupervised clustering analysis clearly affiliate the two clusters with pLSOs and LOCs.

Immunohistochemical detection of proteins complies with gene expression (*Spp1*|OPN and *Calca*|CGRP)

We identified *Spp1*|OPN as DEG#1 in cluster 1 (presumably pLSOs) and *Calca*|CGRP as DEG#1 in cluster 2 (presumably LOCs). To assess correspondence between gene expression and protein abundance, we performed immunohistochemical experiments. Immunosignals for OPN were intense in the LSO and other SOC nuclei (Figures 5A1,B1). They were spread throughout the LSO and were associated with somata and proximal dendrites of cells reminiscent of pLSOs, because of their fusiform shape and size (Figures 5A2,A3,B2,B3). Labeling was particularly strong in a cup-shaped structure within the cytoplasm and virtually absent from the cells' nucleus. Double labeling with glycine transporter type 2 (GlyT2), used to mark the perisomatic zone, demonstrated cytoplasmic OPN localization, rather than an association with the plasma membrane (Figures 5A3,B3). Conjunctively, the results demonstrate a correspondence between high *Spp1* expression and a high OPN abundance, implying a close correlation between mRNA and protein level. Moreover, OPN appears to be associated with pLSOs.

Because of the elaborate demonstration of CGRP in coronal sections (references in Introduction), we characterized the protein in horizontal sections (Figure 5C). CGRP immunosignals were strong in the LSO, as for OPN. In contrast, they were virtually absent from other SOC nuclei (Figure 5C1). Labeled somata were located along the tonotopic axis (from lateral to medial), and their size was a bit smaller than for OPN-positive somata (Figures 5C2,C3). Immunopositive dendrites were oriented perpendicular to the tonotopic axis, as described for LOCs (Friauf et al., 2019). Cytoplasmic labeling was more homogeneous than for OPN. Together, the *Calca*|CGRP findings imply a close relationship between gene expression and protein abundance. They also provide additional evidence that cluster 2 comprises LOCs. In the following, we will exploit the electrophysiological properties of our patch-seq neurons to assess whether cluster 1 comprises pLSOs, whereas cluster 2 comprises LOCs.

Electrophysiology: pLSOs form cluster 1, LOCs form cluster 2

A great advantage of the patch-seq method is its potential to characterize electrophysiological parameters prior to scRNA-seq. We determined 16 physiological features prior to cytoplasm harvesting. Because of the comprehensive knowledge about such features and the differences between pLSOs and LOCs (Sterenborg et al., 2010), we assessed whether the two clusters are also distinguishable by electrophysiological parameters.

One important biophysical feature is the firing pattern. Among cluster 1 neurons, we observed two types of firing pattern. At rheobase, ~80% (44/56) neurons displayed a single AP with a short latency (Figures 6A,D; Supplementary Figure S6B; Supplementary Table S5.1). We refer to them as "pLSO—Onset." The remaining 20% of cluster 1 neurons fired ~2 APs near rheobase (Figure 6B; Supplementary Figure S6B). The latency of the first AP was longer than for Onset neurons (7.0 ms vs. 2.9 ms; Supplementary Table S5.1). We refer to these neurons as "pLSO—Sustained." Cluster 2 neurons displayed a delay-type repetitive firing pattern that clearly distinguished them from cluster 1 neurons (Figure 6C, Supplementary Figure S6B; Supplementary Table 5.1). Near rheobase, ~4 APs were generated, and the latency of the first AP (29.4 ms) was several-fold longer than for Onset and Sustained neurons. These neurons are named "LOC—Delayed." A delay-type repetitive firing pattern is characteristic for LOCs, identified as such via retrograde labeling from the cochlea (Fujino et al., 1997). The authors correlated the firing pattern to A-currents.

The approximated rheobase values differed statistically between the three neuron types (Supplementary Figure S6A). With increasing current pulse amplitudes, pLSO-Onset neurons kept firing only few APs (Supplementary Figure S6B). In contrast, Sustained neurons increased their firing rate linearly, whereas Delayed neurons peaked and declined thereafter. These findings are in accordance with previous studies on pLSOs and LOCs in gerbils (Sanes, 1990; Walcher et al., 2011), rats (Kandler and Friauf, 1995; Fujino et al., 1997; Adam et al., 1999, 2001), and mice (Sterenborg et al., 2010; Walcher et al., 2011; Haragopal and Winters, 2023). Therefore, they provide independent physiological evidence that cluster 1 consists of pLSOs whereas cluster 2 is composed of LOCs.

pLSOs and LOCs can be distinguished by a sag behavior of the membrane potential in response to hyperpolarizing current steps. We found prominent sag behavior in Onset and Sustained neurons, but a virtual absence in Delayed neurons (Figures 6E,F). These findings confirm published results. pLSOs specifically show a depolarizing rebound behavior after the termination of hyperpolarizing current pulses (Kandler and Friauf, 1995; Walcher et al., 2011). Indeed, we found a rebound behavior in Onset and Sustained neurons, but not in the Delayed type (Figure 6E).

We further compared V_{rest}, R_{in}, τ_m, C_m as well as the AP peak amplitude, halfwidth, and threshold across the three neuron types. Of these seven biophysical features, R_{in} and τ_m were significantly higher in Sustained neurons than in Onset neurons, whereas six parameters differed between Delayed neurons and each pLSO subtype (rheobase, V_{rest}, R_{in}, τ_m, AP halfwidth, AP threshold; Supplementary Figures S6C–G,I,J). The AP amplitude did not differ significantly between the three groups (Supplementary Figures S6G,H). In a last step, we assessed six synaptic parameters, namely the peak amplitude, the rise time, and the τ_{decay} of sEPSCs and sIPSCs. Whereas none of the six parameters was statistically distinguishable between Onset and Sustained

neurons, Delayed neurons differed significantly in 9/12 cases when compared to the two subtypes of pLSOs (Supplementary Figure S7).

Overall, the electrophysiological results, together with our findings on DEGs, provide sufficient evidence to conclude that pLSOs belong to cluster 1, whereas LOCs belong to cluster 2. Moreover, the differences between the two subtypes in cluster 1 are too small to warrant a subcategorization into two subclusters.

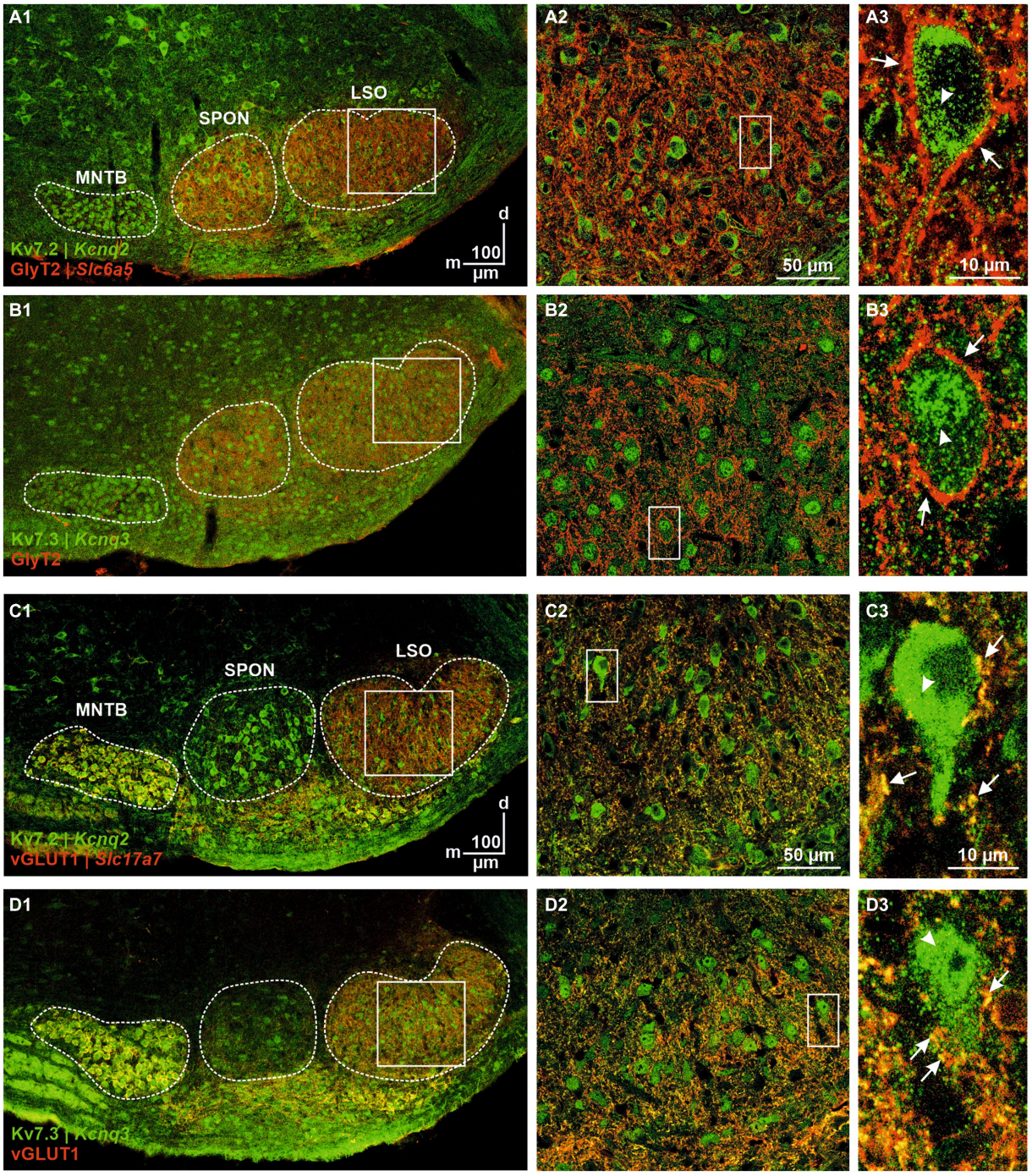


FIGURE 10
Immunohistochemical analysis of Kv7.2 and Kv7.3. **(A)** Kv7.2- (green) and GlyT2-immunolabeling (red) of the SOC **(A1)** and LSO **(A2)**. Coronal brainstem slice at P12. Close-up of a representative neuron in **(A3)**. Punctate glycinergic terminals surrounding the soma are marked by arrows; cytoplasmic Kv7.2 immunosignals are marked by an arrowhead. **(B)** As **(A)**, but for Kv7.3. **(C)** Kv7.2- (green) and vGLUT1-immunolabeling (red) of the SOC **(C1)** and LSO **(C2)**. Coronal brainstem slice at P12. Close-up of a representative neuron in **(C3)**. Punctate glutamatergic terminals surrounding the soma are marked by arrows; cytoplasmic Kv7.2 immunosignals are marked by an arrowhead. **(D)** As **(C)**, but for Kv7.3.

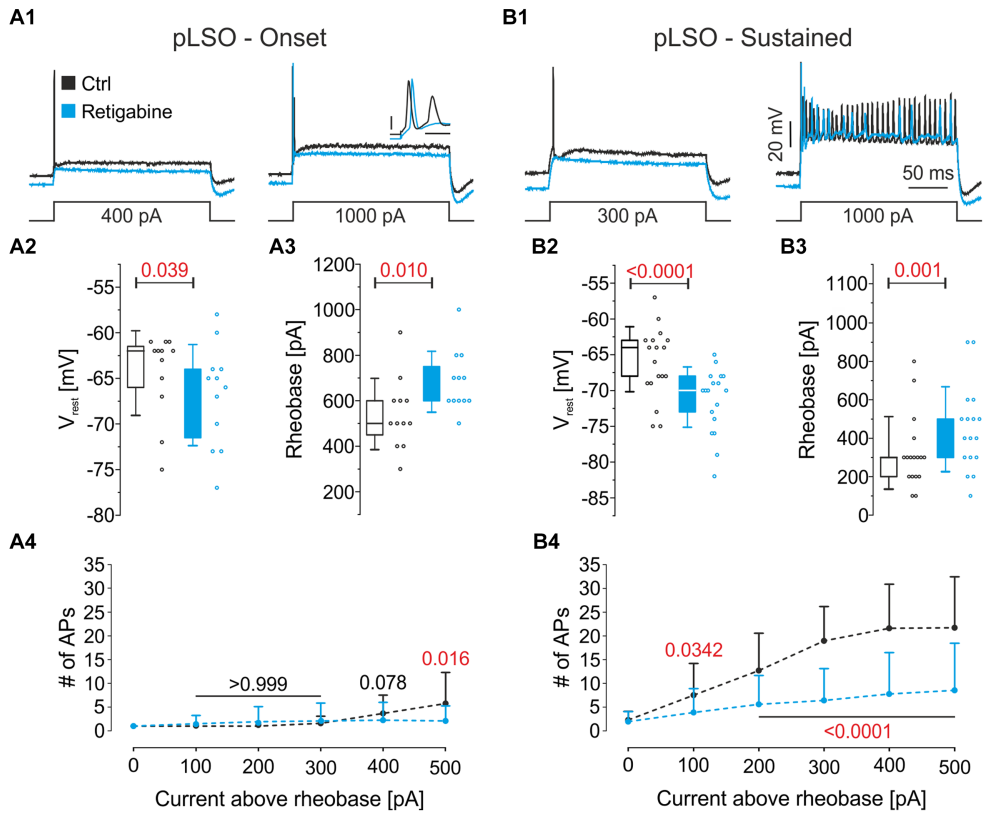


FIGURE 11
Pharmacological analysis of Kv7.2 and Kv7.3. **(A1)** Representative voltage traces from a pLSO—Onset neuron before (black) and after application of the Kv7.2/3 agonist retigabine (30 μM; light blue). Traces are in response to rectangular current pulses (left: control rheobase; right: 1,000 pA; 200 ms). Inset: close-up of the first 4 ms (scale bars: 20 mV; 2 ms). **(A2,A3)** Statistics for V_{rest} and rheobase in pLSO—Onset neurons. Open dots depict single neurons. **(A4)** Mean number of APs elicited as a function of the current amplitude above rheobase in pLSO—Onset neurons. Bars depict SD. Numbers depict *p*-values (in red when significant). **(B)** As **(A)**, but for pLSO—Sustained neurons (see also Supplementary Table S5).

Transcriptional pLSO and LOC clusters comply with electrophysiological differences

The above electrophysiological characterization comprised 16 features. To reduce the dimensionality of the multivariate data and to search for potentially novel subclusters present in our electrophysiological data sets, we performed a PCA based on the 16 electrophysiological features. In such analyses, novel subclusters may arise due to a combination of differences that need not be significant, but together reveal distinct cell types. The results were in accordance with—and thus confirmed—the two clusters of LSO neurons identified via mRNA sequencing. The two subtypes of pLSOs (Onset and Sustained) clustered together (Figure 7A). The PCA also showed higher heterogeneity for cluster 2 than for cluster 1 where virtually all neurons were spotted in close vicinity to each other.

PC1 explained almost 50% of the cluster formation (Figure 7A). To determine the contribution of each feature to PC1, we evaluated the loading scores (Figure 7B). Four of the 16 features described time-related PSC characteristics (feature 1, 7, 9, 11). Thus, specific kinetics of both excitatory and inhibitory ligand-gated receptors appear to be a solid physiological means to distinguish pLSOs from LOCs (faster values in pLSOs). Moreover, R_{in}, feature 2 on the loading score, may also be used to distinguish the two major types of LSO neurons rapidly and easily during electrophysiological characterization (*cf.* Supplementary Figure 6D). The lowest influence on PC1 was provided by the AP amplitude, followed by V_{rest} (Figure 7B; Supplementary Figures S6C,H). A vector factor map analysis showed a positive correlation of rheobase, sag amplitude, sIPSC amplitude, and C_m with PC1, whereas all other features were negatively correlated (Figures 7B,C). Interestingly, PC2 was mainly influenced by the AP amplitude and V_{rest}, with both vectors being almost antiparallel to one another.

To assess a linkage of the three types of firing pattern with the gene expression pattern, we reused the tSNE plot from Figure 3B and mapped the data from the electrophysiological clusters onto the corresponding neurons (Figure 7D). Remarkably, there was absolute congruency between the transcriptional cluster assignment and the electrophysiological parameters. Hence, we feel safe to conclude that cluster 1 represents pLSOs and cluster 2 LOCs. Within the pLSOs, we identified two subtypes by their biophysical differences.

pLSOs and LOCs express different sets of ion channel genes

Auditory brainstem neurons possess a plethora of morphological and functional features as well as molecular specializations that enable

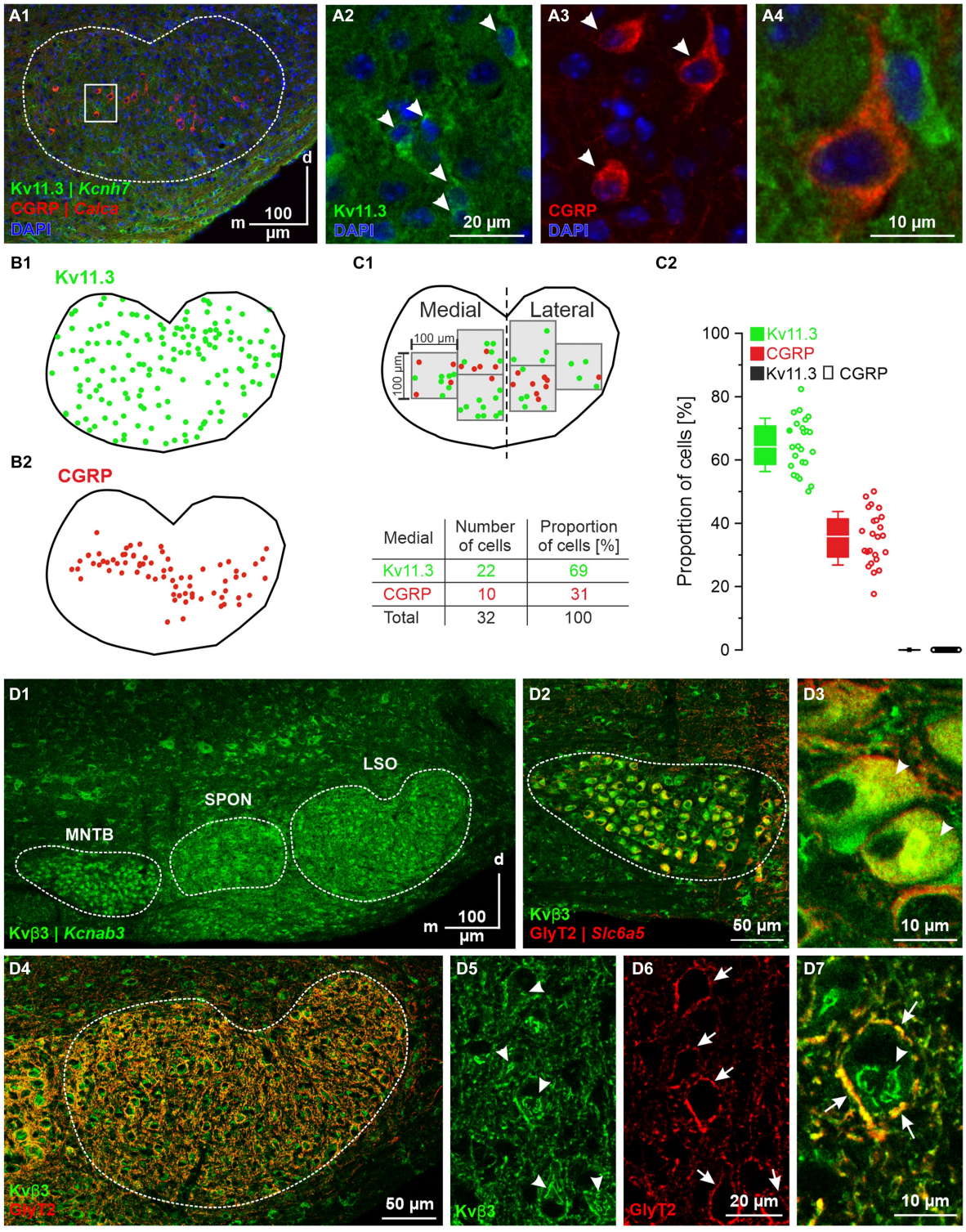


FIGURE 12
Immunohistochemical analysis of Kv11.3 and Kvβ3. **(A1–A4)** Kv11.3- (green) and CGRP-immunolabeling (red) in the LSO. Coronal brainstem slice at P12. Close-ups of representative neurons in **(A2–A4)**. Cell nuclei are DAPI-stained (blue). **(B1)** Distribution of Kv11.3-immunopositive somata (overlay from three sections). **(B2)** As **(B1)**, but for CGRP. **(C1)** Region of interest (3 squares, edge length: 100 µm) in the medial and lateral half of an LSO section in which immunopositive somata were counted. Table exemplarily shows number of somata obtained in the medial half. **(C2)** Statistics of the quantification shown in **(C1)**. The two solid dots relate to the example in **(C1)**. Kv11.3 ∩ CGRP depicts absence of double labeled somata. **(D1)** Kvβ3-immunolabeling (green) in the SOC. Coronal brainstem slice at P12. **(D2)** Kvβ3- and GlyT2-immunosignals (red) in the MNTB. **(D3)** Close-up of two representative MNTB neurons. Arrowheads mark cytoplasmic Kvβ3 signals. **(D4)** Double labeling for Kvβ3 and GlyT2 in the LSO. **(D5)** Five representative Kvβ3 immunopositive LSO neurons (marked by arrowheads). **(D6)** Perisomatic GlyT2-immunosignals (marked by arrows). Same neurons as in **(D5)**. **(D7)** Close-up of a double-labeled LSO neuron. Arrowhead marks cytoplasmic Kvβ3 signals; arrows mark presumptive MNTB axon terminals surrounding the soma. d, dorsal; m, medial.

them to reliably process information in an ultrafast and temporally precise way (Oertel, 1997; Trussell, 1997, 1999; Golding and Oertel, 2012). Among morphological features are the well-known presynaptic terminals of the calyx-or endbulb-type (Held, 1893). Functional features include AP firing behavior and synaptic fidelity. Molecular specializations comprise an elaborate repertoire of voltage-gated ion channels (Hardman and Forsythe, 2009; Oertel, 2009; Reijntjes and Pyott, 2016). Of the 269 mouse genes for ion channels listed in the International Union of Basic and Clinical Pharmacology/British Pharmacological Society Guide to Pharmacology (IUPHAR/BPS GTP) (Alexander et al., 2021), our sample expressed 42% (114/269; Figure 8A; Supplementary Table S6 for cohort-related results). More specifically, 40% of voltage-gated ion channel genes were expressed (58/144; Figure 8A). For ligand-gated and other ion channels, values were 50 and 36%, respectively (38/76 and 18/49). Dividing the category "Voltage-gated ion channels" into eight subdivisions revealed expression of 43% of the potassium channels, by far the highest number (33/77; Figure 8B). Together, the results illustrate a broad repertoire of ion channels in LSO neurons, particularly potassium channels.

Potassium channels

As potassium channels are crucial determinants of multiple physiological properties (V_{rest}, AP threshold, firing rate, AP duration, postsynaptic potential duration, timing), and because of the immense interest auditory brainstem neurons have received concerning those channels, we focused on this subcategory (Figure 8C). Among 33 expressed K^+ channel genes, 18 encode pore-forming Kv αsubunits (18/40 = 45%), six Ca^{2+}- or Na^+-activated (KCa or KNa) channels (6/8 = 75%), five two-pore domain K2P channels (5/14 = 36%), and four inwardly rectifying Kir channels (4/15 = 27%).

Transcript levels for the 18 Kv α subunits and the spread across single neurons are shown in Figure 9A and Supplementary Table S6. The panel also depicts expression for nine genes encoding "Potassium voltage-gated channel regulatory subunits" (of 14 listed,[5] Gray et al., 2015). Overall, the LSO neurons expressed a high number of Kv genes (50%; 27/54). For five genes, the mean TPM values exceeded 10 (i.e., $\log_2[TPM + 1] > 3.5$) in at least one cluster (white-magenta heat map in Figure 9A; Supplementary Table S6). These genes were: pLSOs: *Kcnab3*|Kvβ3, *Kcnq2*|Kv7.2, *Kcna1*|Kv1.1, *Kcnh7*|Kv11.3; LOCs: *Kcnq2*|Kv7.2, *Kcnab1*|Kvβ1. Across all LSO neurons, the by far highest TPM values were seen for *Kcnq2* and *Kcnab3* (mean: 166 and 141). Four Kv genes qualified as DEGs in pLSOs (marked by asterisks in Figure 9A; pLSOs: *Kcna1*|Kv1.1, DEG#92; *Kcnh7*|Kv11.3, DEG#6; *Kcnab3*|Kvβ3, DEG#146; *Kcnip1*|KChIP1, DEG#67). We also determined the percentage of neurons expressing a given gene (white-green heat map in Figure 9A). *Kcna1*|Kv1.1 and *Kcnh7*|Kv11.3 were expressed by ~70% of cluster 1 neurons. For cluster 2, the percentage was relatively low: ~40% of the neurons expressed *Dpp6*|DPL1, the highest value observed (Figure 9A). Cluster 1 neurons displayed similarly high values for this gene.

We wondered how many Kv genes a single LSO neuron may express and assessed the heat maps vertically (threshold ≥1 TPM). On average, a single neuron expressed 17% of the Kv genes expressed in the whole sample (4.6/27; range: 0–11; Figure 9B). More specifically, values for the four cohorts were: 5.4 Onset; 5.6 Sustained; 3.0 LOCs (= cluster 2); 5.4 pLSOs (= cluster 1). Thus, pLSOs appear to express a 1.8-fold higher number of Kv genes than LOCs, implying higher complexity in the ascending LSO branch for this ion channel family. Taken together, pLSOs and LOCs show a broad and complex repertoire of Kv transcripts for α and regulatory subunits. Even within a cohort, molecular individuality seems to be a prominent feature. It appears that the complexity of the Kv channel profile in pLSOs is higher than in LOCs. Fifteen percent of the 27 Kv channel genes are DEGs, with no exception in pLSOs, emphasizing the importance of Kv channels particularly in this neuron type. To validate the gene expression results, we performed immunohistochemistry for four Kv subunits (next chapter). In one case, we also performed a series of pharmacological experiments.

Immunohistochemical and pharmacological analysis of Kv7.2 and Kv7.3

Kv7.2 (aka KCNQ2) immunoreactivity was detectable in all major SOC nuclei, and labeling was predominantly somatic (Figures 10A1,A2). GlyT2 colabeling helped to identify pLSOs by their soma shape and the punctate perisomatic and peridendritic pattern described before (Figure 10A3; Friauf et al., 2019). Kv7.2 immunosignals were strong in the cytoplasm, whereas a neurons' nucleus was virtually immunonegative. We also analyzed Kv7.3 immunoreactivity (Figure 10B). The overall pattern resembled that seen for Kv7.2, except that labeling was more prominent in the nucleus than in the cytoplasm (Figure 10B3). For both Kv7 subunits, we observed no co-localization with GlyT2 in the LSO (Figures 10A2,A3,B2,B3), indicating that Kv7.2 and Kv7.3 are not present in glycinergic axon terminals. In contrast, immunosignals for Kv7.2 and Kv7.3 co-localized with vGLUT1-immunopositive axon terminals contacting LSO neurons at the soma and in the neuropil (Figures 10C,D). Together, these results suggest that the two Kv7 subunits are specific for glutamatergic synapses and absent from glycinergic terminals. This difference between the ipsilateral excitatory and the contralateral inhibitory input may be of physiological relevance for transmitter release in the context of sound localization and should be addressed in future studies.

To address functional Kv7.2/7.3 channels in pLSOs, we performed pharmacological experiments in which retigabine was applied while assessing biophysical properties from pLSOs. The drug is a Kv7.2/3 agonist that shifts channel activation toward more negative potentials (Main et al., 2000; Wickenden et al., 2000). In both pLSO subtypes, Onset and Sustained, retigabine hyperpolarized V_{rest} by ~4 mV (Figures 11A1,A2,B1,B2; Supplementary Table S5.2). Moreover, it increased the rheobase by ~30%, thus reducing multiple-firing behavior (Figures 11A1,A3,A4,B1,B3,B4). In summary, the immunohistochemical and pharmacological analyses validated our patch-seq data and obtained some interesting results concerning transmitter-type association. To our knowledge, this study is the first detailed report on Kv7.2 and Kv7.3 proteins in the LSO (*cf.* Cooper et al., 2001; for Kv7.5, see Caminos et al., 2007).

5 http://www.genenames.org

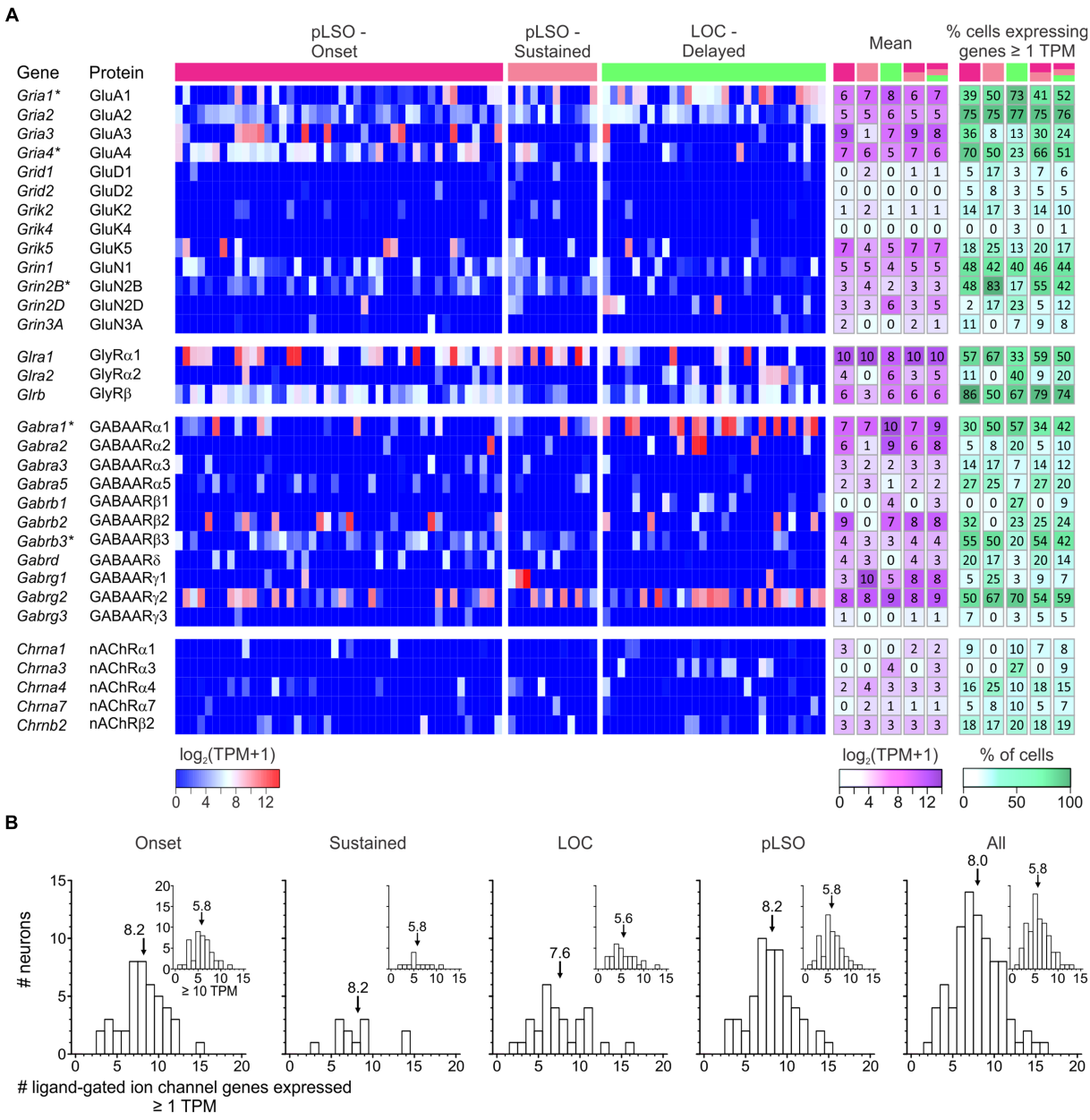


FIGURE 13
Expression of genes encoding ligand-gated ion channels ($n = 32$). **(A)** Heat maps show expression levels [$\log_2$(TPM + 1)] for single neurons (three cohorts). To the right, the mean and the percentage of cells expressing a given gene are depicted for five cohorts (pLSO—Onset, pLSO—Sustained, LOC—Delayed, pLSO, all neurons; $n = 44, 12, 30, 56, 86$). DEGs are marked with asterisks. **(B)** Frequency histograms show distribution of gene expression for five cohorts (criteria: ≥ 1 TPM; ≥ 10 TPM for insets). Mean values are marked by arrows (see also Supplementary Table S6).

Immunohistochemical analysis of Kv11.3 and Kvβ3

We also validated expression for *Kcnh7*|Kv11.3 (DEG#6). It was expressed by ~70% of the pLSOs, whereas LOCs completely lacked expression (*cf.* Figure 9A). Double-immunofluorescent labeling of SOC sections for Kv11.3 and CGRP demonstrated Kv11.3 immunosignals throughout the LSO, whereas CGRP-positive cells were restricted to the center of the LSO, stretching along the tonotopic axis (Figures 12A1,B1,B2). For both proteins, immunosignals were localized in the somata and proximal dendrites (Figures 12A2–A4; see also Figure 5C3). In central aspects of the LSO, Kv11.3-positive somata outnumbered CGRP-positive ones ~2-fold (65% vs. 35%; Figure 12C2). Kv11.3 signals did not overlap with CGRP signals (Figures 12C1,C2), confirming the mRNA results and demonstrating exquisite cell-type specificity.

We finally performed immunohistochemical validation experiments for *Kcnab3*|Kvβ3 (DEG#146 in pLSOs). Kvβ3 immunolabeling was heavy in MNTB, SPON and LSO (Figure 12D1). The somata of MNTB neurons displayed intense immunosignals in the cytoplasm, but not in the nuclei. An opposite pattern occurred in LSO and SPON neurons (Figures 12D2–D7).

LSO and SPON neurons displayed perisomatic labeling, suggesting the presence of Kvβ3-positive MNTB axon terminals. Indeed, double labeling demonstrated co-distribution of perisomatic Kvβ3 signals with GlyT2 signals, confirming presynaptic Kvβ3 in inhibitory synapses.

Ca^{2+} and Na^{+}-activated, two-pore domain, and inwardly rectifying Kv channels

Besides the Kv channels, three other classes of potassium channels are known (Figure 8C). They are encoded by 37 genes, and we found expression for 15 of them (Supplementary Table S6). In LOCs, *Kcnn3*|KCa2.3 and *Kcnj3*|Kir3.1 expression was high and moderate, respectively (427 vs. 30 TPM). pLSOs showed a high expression for *Kcnn1*|KCa2.1 and a moderate one for *Kcnj3*|Kir3.1 (134 vs. 18 TPM). None of the genes was a DEG. KCa2.1 and KCa2.3 form small-conductance, Ca^{2+}-activated K^{+} channels (SK channels) that have high Ca^{2+} affinity and mediate the SK currents (Bond et al., 2005; Faber, 2009; Adelman et al., 2012). They are a major contributor to the afterhyperpolarization phase of APs and regulate AP firing, including AP precision (Engel et al., 1999; Hallworth et al., 2003). Their Ca^{2+} sensitivity is provided by CaM (Saimi and Kung, 2002), for which our study shows the third highest expression level among 11,659 genes (Figure 2B; Supplementary Table S3.2). SK2 channels in outer hair cells are activated via Ca^{2+} influx through ionotropic ACh receptors activated by cholinergic MOC neurons, ultimately resulting in hyperpolarization, and turning down the cochlear amplifier (Housley and Ashmore, 1991; Guinan, 2011; Maison et al., 2013). To our knowledge, nothing is known about the role of KCa2 channels in auditory brainstem neurons.

Voltage-gated sodium (Nav) channels

Nav channels play a fundamental role in generating, shaping, and conducting APs (Catterall et al., 2005; de Lera Ruiz and Kraus, 2015; Hull and Isom, 2018). LSO neurons in total expressed nine Nav genes (Supplementary Figure S8A; Supplementary Table S6), of which five encoded α subunits and four regulatory β subunits (13 genes are listed altogether: Nav1.1—Nav1.9 plus Navβ1—Navβ4). Thus, 69% (9/13) of Nav genes were expressed in our sample. Mean expression levels of ≥10 TPM in at least one cluster were seen for four genes (pLSOs: *Scn1a*|Nav1.1, *Scn8a*|Nav1.6, *Scn1b*|Navβ1; LOCs: *Scn1a*|Nav1.1, *Scn3a*|Nav1.3, *Scn8a*|Nav1.6, *Scn1b*|Navβ1). Across all neurons, highest expression occurred for *Scn1b*|Navβ1, followed by *Scn8a*|Nav1.6, and *Scn1a*|Nav1.1 (mean TPM: 92, 47, 16). Three genes qualified as DEGs (pLSOs: *Scn4b*|Navβ4, DEG#173; LOCs: *Scn2a*|Nav1.2, DEG#49; *Scn3a*|Nav1.3, DEG#11). *Scn4b* transcripts were found in 25% of pLSOs and in not at all in LOCs. *Scn2a* was expressed by ~60% of LOCs and ~ 20% of pLSOs. Likewise, *Scn3a* was expressed by ~70% of LOCs and 20% of pLSOs.

At the single cell level, an average neuron expressed 33% (3.0/9) Nav genes displayed in the whole sample (range: 0–7; Supplementary Figure S8B). Corresponding values for the four cohorts were: 2.9 Onset; 2.9 Sustained; 3.2 LOCs [= cluster 2]; 2.9 pLSOs [= cluster 1]. Thus, ~3 Nav genes appear to be expressed per LSO neuron, regardless of the subtype, indicating similar numerical complexity. Nevertheless, the fact that 33% of the genes are DEGs, together with the broad percent range, implies a considerable amount of molecular individuality at the cellular level.

Voltage-gated calcium (Cav) channels

Of 10 listed genes encoding Cav channel α subunits, six were expressed by the LSO neurons (Supplementary Figure S9A; Supplementary Table S6). In the group of regulatory subunits (α2δ, β, γ), we found expression for 12/16 genes. Collectively, LSO neurons expressed ~70% of the listed Cav genes (18/26). Therefore, gene expression for Cav channels was more elaborate than for Kv channels, but very similar to Nav channels (Kv: 50%; Nav: 69%). In general, expression levels were also considerably higher than for Kv or Nav subunits. Across all LSO neurons, mean TPM values exceeded 200 for Cav2.3, Cav2.2, and Cavβ4 (639, 372, 218), values not seen for Kv and Nav channels. Whereas mean TPM values ≥10 in at least one cluster occurred for five Kv and four Nav genes, 11 Cav genes fulfilled these criteria. On the α subunit side, these were *Cacna1b*|Cav2.2, *Cacna1d*|Cav1.3, *Cacna1e*|Cav2.3, and *Cacna1g*|Cav3.1. Across all LSO neurons, by far the highest mean TPM value was observed for Cav2.3, followed by Cav2.2 (1,491 and 372). For α2δ subunits, genes with ≥10 TPM were *Cacna2d2*|Cavα2δ2 and *Cacna2d3*|Cavα2δ3. For the β subunits, we identified *Cacnb1*|Cavβ1, *Cacnb3*|Cavβ3 and *Cacnb4*|Cavβ4, and for the γ subunits, we found *Cacng2*|Cavγ2 and *Cacng4*|Cavγ4. Only two Cav genes were DEGs, one gene per cluster (LOCs: *Cacna1e*|Cav2.3, DEG#26; pLSOs: *Cacng5*|Cavγ5, DEG#12). Concerning the percentage of cells, Cav2.3 was expressed by ~70% of the LOC cohort and Cavγ5 by ~65% of the pLSO cohort.

An average LSO neuron expressed 25% Cav genes (4.5/18; α plus regulatory subunits; range: 1–9; Supplementary Figure S9B). Corresponding values for the four cohorts were: 4.5 Onset; 5.4 Sustained; 4.3 LOCs [= cluster 2]; 4.7 pLSOs [= cluster 1]. The numbers indicate a similar complexity across clusters. In summary, a large fraction of Cav genes is expressed in our LSO sample (~70%). The expression profile differs substantially between pLSOs and LOCs as well as between the two pLSO subtypes. However, the similar number of expressed genes per neuron indicates similar complexity across cohorts.

Transient receptor potential channels

Mammalian TRP channels form a superfamily comprising six families (Venkatachalam and Montell, 2007; Talavera et al., 2008). The patch-seq LSO neurons expressed ~$\frac{1}{3}$ of the listed TRP genes (9/28; Supplementary Figure S10A; Supplementary Table S6). Five of them displayed a mean of ≥10 TPM in at least one cluster, namely *Mcoln1*|TRPML1, *Pkd2l2*|TRPP5, *Trpm2*|TRPM2, *Trpm7*|TRPM7, and *Trpv2*|TRPV2. For three genes, TPM values were ≥ 100 in at least one cohort (TRPML1, TRPP5, TRPM2). The highest level (374 TPM) was observed for TRPML1 in Sustained neurons. None of the TRP genes was a DEG, implying only minor differences between both clusters. We found only very low transcript levels, if any, for TRPC channels. This slightly contrasts with earlier findings of mGluR-activated TRP-like channels that mediate Ca^{2+} influx in the developing

LSO upon high-frequency stimulation (Ene et al., 2003, 2007). The authors concluded that these Ca^{2+} channels are likely TRPC channels.

An average LSO neuron expressed 1.4 TRP genes (5% of 28 listed; range: 0–5; Supplementary Figure S10B). Corresponding values for the four cohorts were: 1.2 Onset; 1.8 Sustained; 1.6 LOCs [= cluster 2]; 1.3 pLSOs [= cluster 1]. In summary, ~1/3 of all TRP genes (9/28) were expressed in our sample. There is a remarkable similarity between the two pLSO subgroups which was not evident for Kv, Nav, or Cav channels.

Cyclic nucleotide-regulated channels

CNR channels translate concentration changes of cyclic nucleotides into electrical signals (Craven and Zagotta, 2006; Napolitano et al., 2021). They are closely homologous to Kv channels and form two families, HCN channels and cyclic nucleotide-gated (CNG) channels (Craven and Zagotta, 2006). In contrast to Kv, Nav or Cav channels, CNG channels are poorly ion selective and only weakly voltage dependent. CNG channels are tetramers formed by CNGA and CNGB subunits, whereas HCN channels are tetramers formed by four subunits (HCN1–4). The latter open with hyperpolarization, are weakly K^+ selective, and are regulated by cyclic nucleotides, e.g., cAMP. Of 10 *Cng/Hcn* genes listed in the IUPHAR/BPS GTP (Alexander et al., 2021), LSOs exclusively expressed HCN channels (20%, 2/10; Supplementary Figure S11A; Supplementary Table S6). None qualified for a DEG. Mean expression levels for *Hcn2*|HCN2 were low (< 5 TPM); only *Hcn1*|HCN1 displayed a mean of ≥10 TPM. The highest percentage of neurons expressing a HCN gene was 50% in Onset neurons (white-green heatmap). The other cohorts displayed substantially lower values, particularly for HCN2.

An average LSO neuron expressed 20% of the HCN genes (0.4/2; range: 0–2; Supplementary Figure S11B). Corresponding values for the four cohorts were: 0.6 Onset; 0.1 Sustained; 0.3 LOCs; 0.5 pLSOs. Collectively, gene expression for HCN channels was not high in the LSO. However, HCN channel-mediated voltage sags have been described in pLSO—Onset and Sustained neurons (Leao et al., 2006). Our recordings confirm voltage sags in both pLSO types, but we find HCN channel expression only in Onset neurons. It is plausible that mRNA levels for HCN channels (and protein turnover) are too low in Sustained neurons to be detected. This is supported by a study indicating that HCN channels are sequestered within endosomes which can serve as an alternative reservoir for HCN surface expression, independent of their biosynthesis (Hardel et al., 2008).

Ligand-gated ionotropic receptors (GluA, GluD, GluK, GluN, GlyR, GABAAR, nAChR)

LSO neurons receive fast synaptic input through multiple neurotransmitter systems targeting ligand-gated ion channels. Our electrophysiological data showed that the kinetics of excitatory and inhibitory sPSCs are solid means to distinguish pLSOs from LOCs (Figures 7B,C). To further assess this difference on the transcript level, we analyzed gene expression for subunits of six major channel types: glutamatergic AMPA, NMDA, kainate, and "orphan" receptors (GluA, GluN, GluK, GluD), glycine receptors (GlyRs), γ-amino-butyric acid receptors (GABAARs), and nicotinic acetylcholine receptors (nAChRs). We found expression for 55% of the receptor subunit genes (32/58 listed in IUPHAR/BPS GTP; Figure 13A). Thirteen (67%) of them code for ionotropic glutamate receptors, three for GlyRs, 11 for GABAARs, and five for nAChR subunits (Figure 13A; Supplementary Table S6; listed are 18, 5, 19, and 16). For 19 genes, the mean expression was ≥10 TPM in at least one cluster (15 in pLSOs, 17 in LOCs).

Across all 86 neurons, the highest expression occurred for *Glra1*|GlyRα_1 (756 TPM), followed by *Gabra1*|GABAARα_1, *Gabrg2*|GABAARγ2, *Gria3*|GluA3, and *Gabrb2*|GABAARβ2. In comparison, GluK5, GluN, or nAChR gene expression was substantially lower (90 TPM for GluK5, the highest value). Expression for four glutamate receptor subunits of the GluD and GluK subtype was generally low, and it was absent for 5 of 18 genes listed. Slightly higher expression levels were seen for nAChRs. Five genes turned out to be DEGs (pLSOs: *Gria4*|GluA4 DEG#40, *Grin2b*|GluN2B DEG#36, *Gabrb3*|GABAARβ3 DEG#72; LOCs: *Gria1*|GluA1 DEG#68, *Gabra1*|GABAARα1 DEG#89). The diversity emphasizes the importance of diverse ligand-gated ionotropic receptors in LSO neurons and points to specific functions, even within a cluster. This is highlighted by the percentage of pLSOs expressing a DEG:66% for *Gria4,* 55% for *Grin2b*, and 54% for *Gabrb3* (Figure 13A, white-green heatmap; 23, 17, and 20% for LOCs). Values in LOCs were 73% for *Gria1* and 57% for *Gabra1* (41 and 34% for pLSOs).

Concerning the question of how many genes encoding ligand-gated receptor subunits are expressed in a single LSO neuron, the mean number was 8.0 (range: 2–14; Figure 13B). Corresponding values for the four cohorts were: 8.2 Onset; 8.2 Sustained; 7.6 LOCs; 8.2 pLSOs, implying similar transcript complexity. Taken together, more than 50% of the subunits in ligand-gated ion channels are detectable at the mRNA level. The high number of DEGs (5 in 58) demonstrates clear differences between pLSOs and LOCs.

G protein-coupled receptors (mGluR, GABABR, mAChR)

G protein-coupled receptors (GPCRs) constitute the largest family of cell-surface proteins involved in signal transmission (Rosenbaum et al., 2009). Upon agonist binding, they activate specific heterotrimeric G proteins which results in the modulation of distinct downstream effector proteins, including ion channels. The receptors are characterized by the presence of seven membrane-spanning segments in a monomer. We focused on three major types of GPCRs being activated by glutamate, GABA, or acetylcholine. For metabotropic glutamate receptors (mGluRs), there are three groups comprising eight members (group I: mGluR1, mGluR5; group II: mGluR2, mGluR3; group III: mGluR4, 6–8). Whereas group I receptors are primarily present at postsynaptic sites, group II and III mGluRs localize predominantly presynaptically. Metabotropic GABA receptors have two members (GABABR1 and GABABR2), whereas metabotropic ACh receptors (mAChRs) have five (M1—M5, encoded by *Chrm1—Chrm5*).

LSO neurons in general expressed 67% of the named GPCR genes (10/15; Supplementary Figure S12A; Supplementary Table S6). Four genes displayed a mean expression of ≥10 TPM in at least one cluster

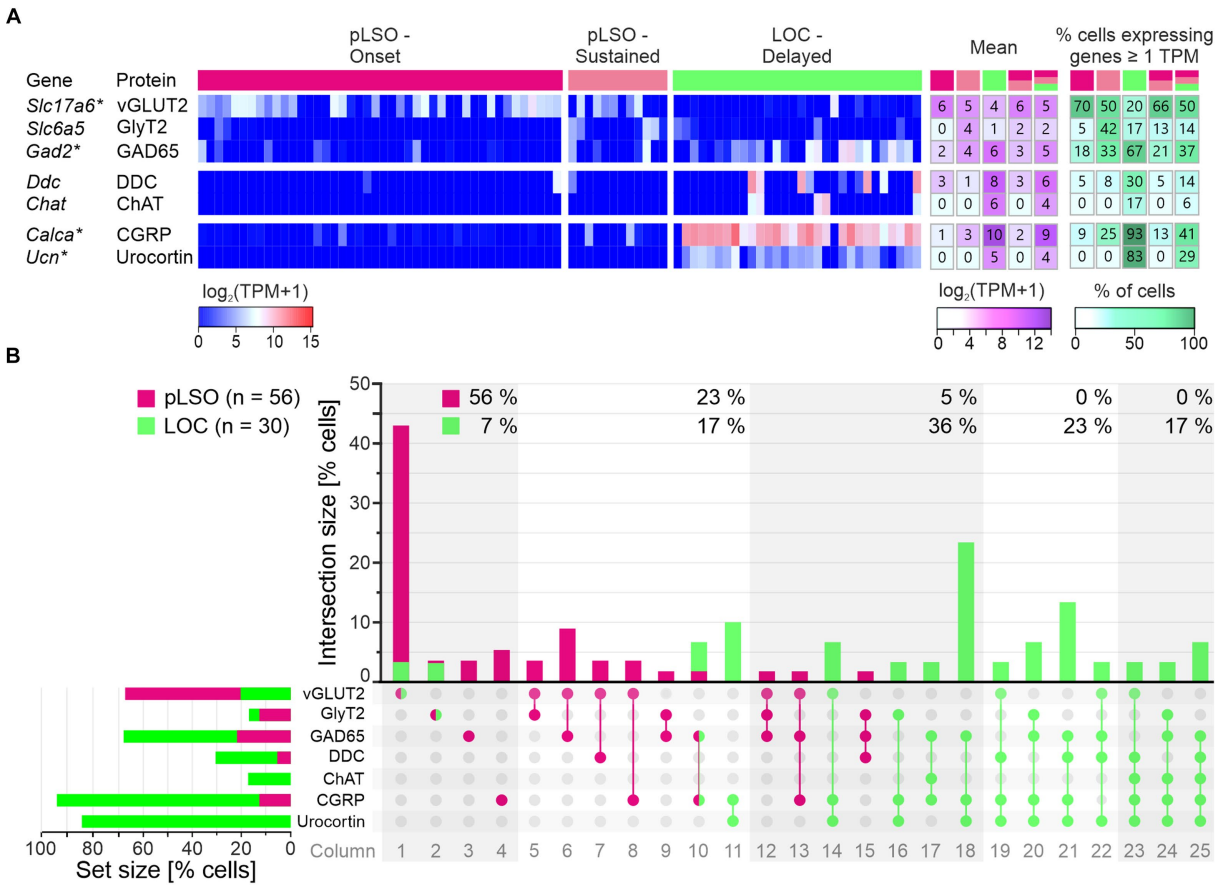


FIGURE 14
Expression of neurotransmitter-associated genes ($n = 7$). **(A)** Heat maps show expression levels [$\log_2$(TPM + 1)] for single neurons (three cohorts). To the right, the mean and the percentage of cells expressing a given gene are depicted for five cohorts (pLSO—Onset, pLSO—Sustained, LOC—Delayed, pLSO, all neurons; $n = 44, 12, 30, 56, 86$). DEGs are marked with asterisks. **(B)** UpSet plot shows percentage of neurons expressing genes for neurotransmitter-associated proteins in pLSOs (magenta) and LOCs (green). Vertical bars show the percentage of neurons expressing one or a combination of genes (Intersection size; 100% relates to 56 pLSOs and to 30 LOCs). Values at the top represent the sum of the gray/white shaded areas, indicating the percentage of concurrent expression of either one, two, three, four or five neurotransmitter-associated genes. Note that we did not find neurotransmitter-associated gene expression in all pLSOs. Dots (and connecting lines) mark where the overlap occurs. Horizontal bars (Set size) show the percentage of neurons expressing a given gene (see also Supplementary Table S6).

(GABABR1, mGluR1, mGluR3, mGluR8). By far the highest expression was seen for mGluR3 (all LSO: 521 TPM). In contrast, mGluR4 transcripts were almost absent, and those for mGluR2 and mGluR6 were undetected. Within GABABRs, transcripts prevailed for GABABR1 (25 TPM). Among the mAChRs, expression was absent for three genes and low for M2 and M4. Nevertheless, *Chrm2*|M2 was DEG#93 for LOCs (the only DEG in the CPCG group; TPM: 5 vs. 0). It was expressed by 27% of LOCs and 2% of pLSOs.

An average LSO neuron expressed 2.0 GPCR genes (range: 0–6; Supplementary Figure S12B). Corresponding values in the cohorts were: 1.5 Onset; 2.3 Sustained; 2.6 LOCs; 1.7 pLSOs. Together, the results demonstrate a higher GPCR complexity in LOCs.

Neurotransmitter-associated genes (excitatory, inhibitory, modulating)

LSO neurons display a high degree of transmitter diversity (*cf.* Figure 1A). To explore the diversity at the single-cell level, we analyzed gene expression of a subset of neurotransmitter-associated molecules, including neuropeptides to explore neurotransmitter phenotype. Figure 14A and Supplementary Table S6 illustrate seven neurotransmitter-associated genes expressed in the LSO (*Slc17a6*|vGLUT2; *Slc6a5*|GlyT2; *Gad2*|GAD65; *Ddc*|DOPA decarboxylase = DDC; *Chat*|choline acetyltransferase = ChAT; *Calca*|CGRP; *Ucn*|urocortin). The highest expression was seen for CGRP (LOCs: 1,256 TPM), followed by DDC (LOCs: 231 TPM), GAD65 (LOCs: 87 TPM), and vGLUT2 (pLSOs: 59 TPM). Four genes qualified for DEGs (LOCs: *Calca*|CGRP DEG#1; *Ucn*|urocortin DEG#2; *Gad2*|GAD65 DEG#32; pLSOs: *Slc17a6*|vGLUT2 DEG#26). Transcripts for vGLUT2, indicative of a glutamatergic phenotype, were found in 66% of the pLSOs, and transcripts indicative of a glycinergic and GABAergic phenotype in 13 and 21%, respectively (Figure 14A, white-green heatmap). Thus, the predominant transmitter in pLSOs seems to be glutamate. The opposite appears to hold for LOCs, as 67% of them showed transcripts for GAD65 and 17% for GlyT2, whereas only 20% were associated with a glutamatergic phenotype (sum >100% because of multi-transmitter neurons; see below). Our results also indicate an excitatory, rather than an inhibitory, phenotype for most Onset neurons (70% vGLUT2, only 5% GlyT2 and 18% GAD65),

whereas Sustained neurons appear to substantially utilize inhibitory transmitters (42% GlyT2 plus 33% GABA vs. 50% vGLUT2). Reportedly, membrane properties of excitatory pLSOs favor integrative level coding, whereas those of inhibitory pLSOs favor time coding (Haragopal and Winters, 2023).

As the above results implied multi-transmitter properties, we analyzed our samples in more detail. In total, the 86 LSO neurons displayed 25 combinations of neurotransmitter-associated gene expression (Figure 14B, columns 1–25; see also Supplementary Table S6). Of those, 13 combinations were seen in pLSOs and 15 combinations in LOCs. A single transmitter phenotype was obvious in 56% of the pLSOs (columns 1–4). Forty-three percent of the pLSOs appeared to be purely glutamatergic (column 1), whereas 23% co-expressed one to two neurotransmitter-associated genes in addition to vGLUT2 (columns 5–8, 12, 13). Thus, glutamate was by far the predominant transmitter type in pLSOs (66%; see Set size diagram). The remaining 34% were vGLUT2 negative (columns 2–4, 9, 10, 15). Seven pLSOs (12.5%) expressed the CGRP gene, which was a bit surprising because the neuropeptide is usually affiliated with LOCs. Transcripts for ChAT and urocortin were completely absent from the pLSO cohort. The maximum number of neurotransmitter-associated genes expressed in an individual pLSO was three (columns 12, 13, 15; 9% of the neurons).

LOCs displayed a substantially higher degree of multi-transmitter properties than pLSOs. Seventeen percent of them co-expressed five genes (Figure 14B, columns 23–25). Forty percent of the LOCs co-expressed >3 genes (columns 19–25), whereas no pLSO did so. On the other side, only 7% of the LOCs displayed a single-transmitter phenotype (Figure 14B, columns 1, 2; vs. 56% pLSOs). The dominant subtype of LOCs (23%) co-expressed genes coding for GABA, CGRP, and urocortin (column 18). Across all combinations, 93 and 83% of the LOCs showed transcripts for CGRP and urocortin, respectively (see Set size diagram). This pair of neuropeptides is clearly a hallmark of LOCs. Transcripts for GAD65 occurred in 67% of the LOCs. They were always associated

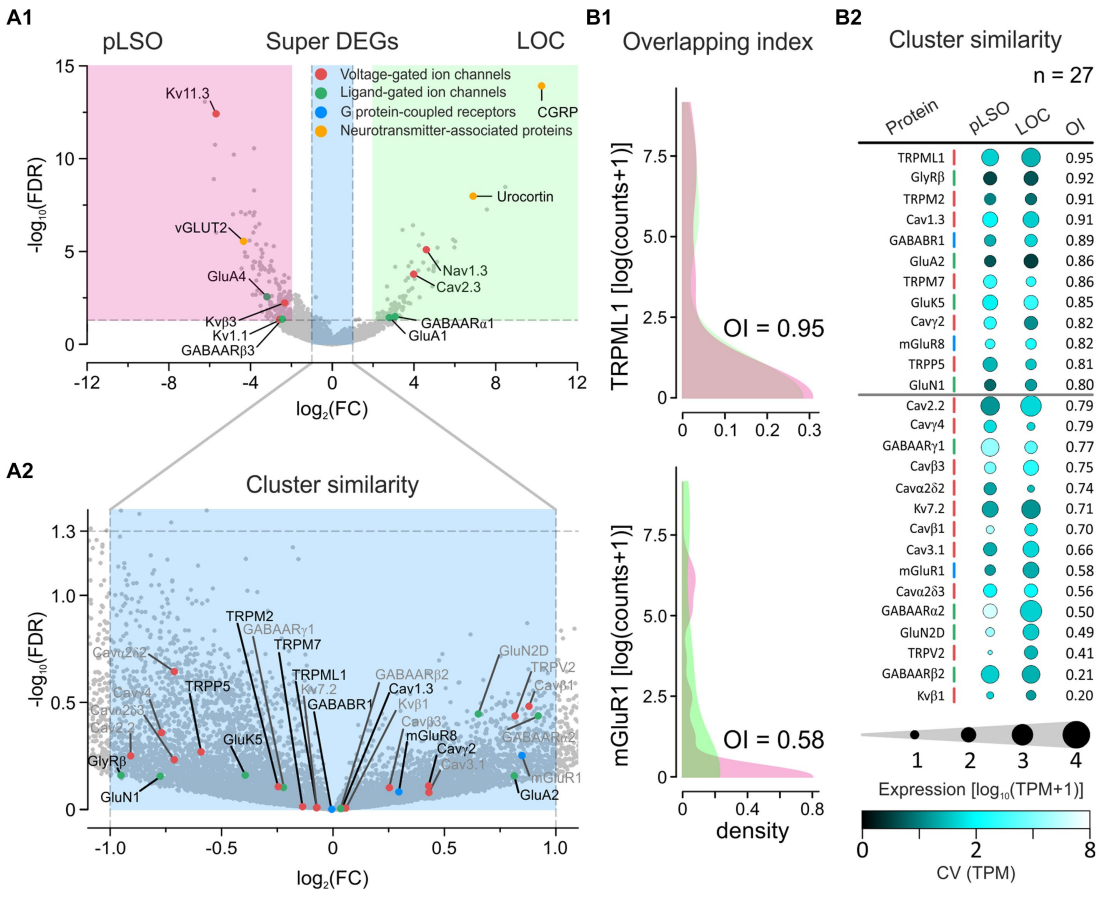


FIGURE 15
Super DEGs and cluster similarity. **(A1)** Volcano plot depicting "Super DEGs" involved in neurotransmission (set from Figure 4A). Four categories were assessed, together comprising 114 genes: Voltage-gated ion channels, Ligand-gated ion channels, G protein-coupled receptors, Neurotransmitter-associated proteins. Criteria for cluster specificity: expression level ≥ 10 TPM in at least one cluster, FC ≥ 4, red and green sector. For the 12 Super DEGs, the protein name is provided. **(A2)** Volcano plot depicting "Cluster similarity" (criteria: expression level ≥ 10 TPM in at least one cluster, FC ≤ 2; blue sector). For the 27 genes demonstrating cluster similarity, the protein name is provided [in gray if overlapping index (OI) < 0.8]. **(B1)** Density distributions for two example genes and the resulting OI. Distribution for pLSOs in magenta, for LOCs in green. **(B2)** Ranking the 27 genes by their OI. In the balloon plot, the dot size indicates TPM and the color code the coefficient of variance (CV). High OIs occur if dot size and colors are similar between clusters. Congruent density distributions yield an OI of 1.0. Colored vertical bars mark the same category shown in **(A1,A2)**. The horizontal line depicts the arbitrary threshold of 0.8 (see also Supplementary Table S6).

with co-expression, in 10 neurons for three to four additional genes (columns 20–22, 24, 25). Thirty percent of LOCs expressed *Ddc*|DDC, indicative of a dopaminergic phenotype (vs. 6% of pLSOs). *Ddc* expression was always associated with three to four other transcripts, in each case for CGRP and urocortin. At a frequency of 17% (3 neurons), LOCs expressed *Chat*, a surprisingly low number (see Discussion for explanation). *Chat* expression was invariably flanked by CGRP transcripts and in some cases also with GAD65 (columns 17, 24, 25) and/or urocortin transcripts (columns 23–25).

An average LSO neuron expressed 1.9 neurotransmitter-associated genes (range: 0–5; Supplementary Table S6). Corresponding values for the four cohorts were: 1.1 pLSO—Onset; 1.6 pLSO—Sustained; 3.3 LOCs; 1.2 pLSOs. The almost 3-fold higher value in LOCs compared to pLSOs further highlights the complex transmitter repertoire in the LOC system. Collectively, the results on neurotransmitters add further facets to the overall picture that pLSOs and LOCs differ considerably in their transmitter repertoire. Altogether, the UpSet plot in Figure 14B shows that only 3 of the 25 combinations are shared between the two clusters (columns 1, 2, 10). This implies a very clear distinction between pLSOs and LOCs concerning their transmitter repertoire. pLSOs are characteristic in that they express mainly glutamatergic or GABAergic genes. In contrast, LOCs display multi-transmitter properties, most frequently GABA plus two neuropeptides.

Super DEGs and cluster similarity between pLSOs and LOCs

In a final analysis, we assessed "Super DEGs" and "Cluster similarity" (details in Methods). We restricted the analysis to the field of neurotransmission, namely voltage-gated ion channels, ligand-gated ion channels, GPCRs, and neurotransmitter-associated proteins (Figure 15). The input comprised 114 genes, of which 18 were DEGs. About 10% of the genes (12/114) were Super DEGs (6 in each cluster; Figure 15A1). Five of them encode subunits of voltage-gated ion channels (pLSOs: Kv11.3, Kvβ3, Kv1.1; LOCs: Nav1.3, Cav2.3), four encode subunits of ligand-gated ion channels (pLSOs: GluA4, GABAARβ3; LOCs: GABAARα1, GluA1), and three genes encode neurotransmitter-related proteins (pLSOs: vGLUT2; LOCs: CGRP, urocortin). No Super DEG was revealed for GPCRs.

Cluster similarity was found for ~25% of the genes (27/114; Figure 15A2). We further quantified this finding by determining an overlapping index (OI) (Pastore and Calcagni, 2019). OI values ranged from 0.95 to 0.2 and allowed to rank the genes. When the stringency was increased (by setting the OI threshold to 0.8), 12 genes remained. Six of them encode subunits of voltage-gated ion channels (Cav1.3, Cavγ2, TRPML1, TRPM2, TRPM7, TRPP5), four encode subunits of ligand-gated ion channels (GlyRβ, GluA2, GluK5, GluN1), two encode GPCRs (GABABR1, mGluR8), and none encodes neurotransmitter-related proteins.

Taken together, ~80% (90/114) of the genes involved in neurotransmission are neither Super DEGs nor do they fulfill the stringent criteria for Cluster similarity. The remaining 24 genes categorize equally to Super DEGs and Cluster similarity (12 + 12). Moreover, the 12 Super DEGs are equally split between pLSOs and LOCs. Thus, we crystallized three manageable sets of neurotransmitter-associated genes whose expression pattern differs between pLSOs and LOCs or, on the other hand, is closely similar.

Discussion

Brain function depends on the action of individual neurons. Neurons are relatively easy to track when a brain region consists of a homogeneous population of neurons (e.g., a motor nucleus). The scenario is much more complex and complicates analysis when the area of interest is a heterogeneous nucleus, such as the LSO. Here we characterized different neuron types of the juvenile mouse LSO using the patch-seq method to identify transcriptional differences and similarities. By choosing a juvenile age (at the onset of hearing), we were able to capture genes that are relevant for maturation. We obtained five main results (graphically summarized in Figure 16). (1) LSO neurons show high gene expression for ATP synthesizing proteins (Figure 2). (2) There are two prominent clusters: pLSOs and LOCs, the major types involved in the ascending (afferent) and descending (efferent) auditory pathways, respectively (Figure 3). (3) pLSOs and LOCs differ in 353 DEGs (254 + 99; Figure 4A). (4) Among the top 40 DEGs (20 in each cluster), 80% were hitherto undescribed (17 in pLSOs; 15 in LOCs; bold in Figure 4B). (5) Among the 114 listed genes involved in neurotransmission, 12 (~10%) are Super DEGs, of which three encode Kv channel subunits typical for pLSOs (Figure 15). Another 12 show Cluster similarity, highlighting the overlap of neurotransmission-related molecules between the two neuron types.

Extraordinarily high expression for three genes: *Ckb, Snurf, Calm1*

The three most highly expressed genes showed expression levels of ~25,000 TPM and more, >2-fold higher than the fourth gene (Figure 2). The related proteins are brain-type creatine kinase B (CKB), SNRPN upstream open reading frame protein (SNURF; SNRPN = small nuclear ribonucleoprotein polypeptide N), and calmodulin 1 (CALM1 also known as CaM).

CKB is involved in energy homeostasis. The cytosolic enzyme transfers phosphate between ATP and various phosphogens, for example creatine, thus generating phosphocreatine and ADP and establishing a readily available ATP-buffering system. It is not surprising that *Ckb* expression correlates very well with gene expression for Na^+/K^+-ATPase α1 and α3 subunits (Jiao et al., 2021; NB: α3 is exclusive to neurons). The CKB-mediated buffer system appears to play a pivotal role in the hair bundle of vestibular hair cells (Shin et al., 2007). Reduced CKB activity is associated with hearing impairment in mice with Huntington disease (Lin et al., 2011). Interactions of CKB with the potassium-chloride transporter KCC2 have been demonstrated (Inoue et al., 2004, 2006; Li et al., 2007; Salin-Cantegrel et al., 2008). The interactions facilitate KCC2-mediated Cl-extrusion from neurons and maintain the low intracellular Cl-concentration required for effective inhibitory neurotransmission, i.e., hyperpolarization (for LSO, Balakrishnan et al., 2003). As robust inhibitory input to LSO neurons is crucial for sound localization, high CKB abundance is not surprising. Indeed, high *Ckb* expression in the LSO is also shown in the AMBA (Figure 2D), thus validating our data.

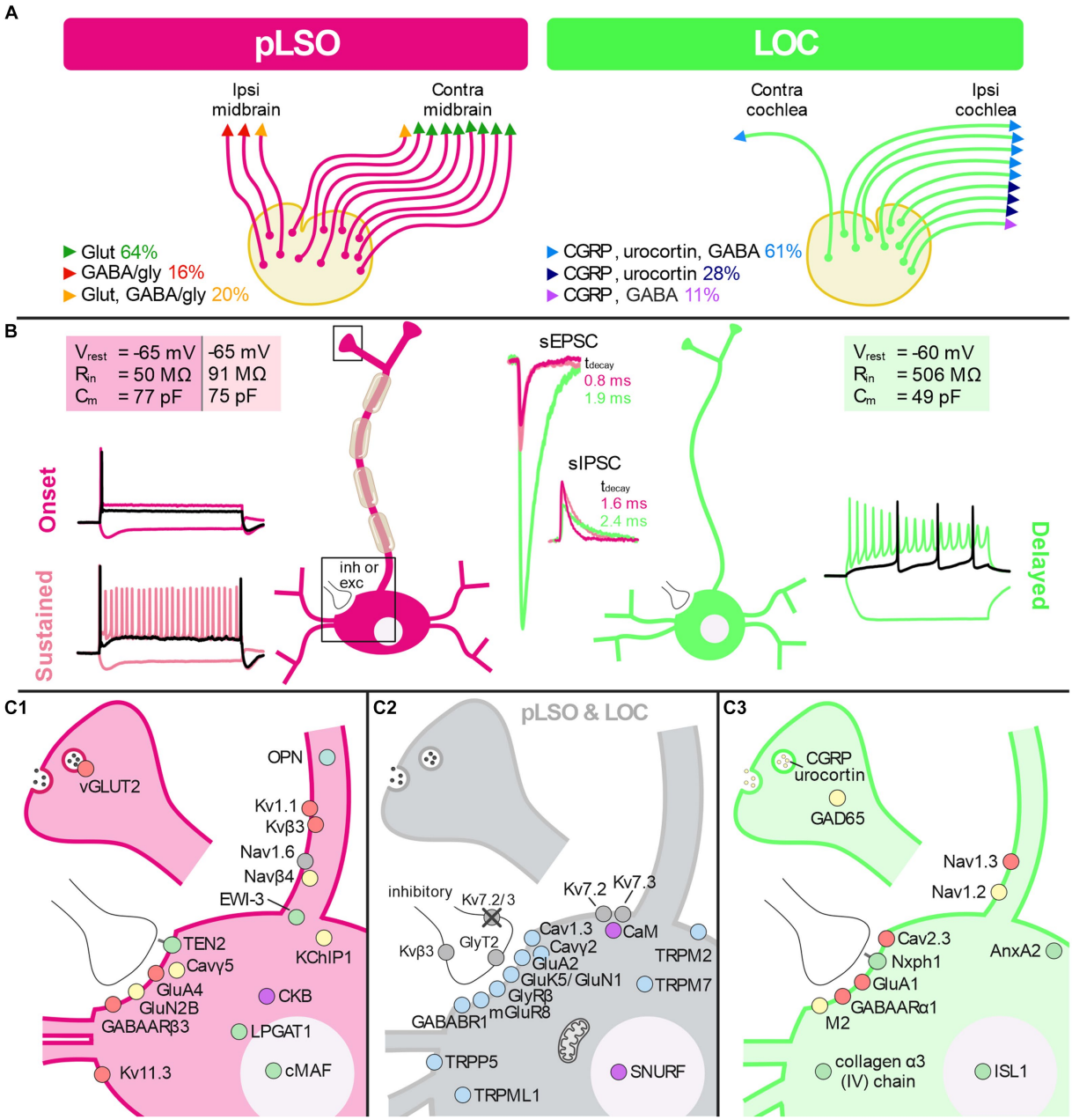


FIGURE 16
Graphical summary of the major results from the present study. Schemata depict differences and similarities between pLSOs and LOCs. **(A)** Gene expression for the three classical transmitters glutamate, glycine, and GABA demonstrates an excitatory phenotype in 64%, an inhibitory in 16%, and a mixed excitatory + inhibitory in 20% of pLSOs. In LOCs, the prevailing three transmitter profiles are CGRP + urocortin + GABA, CGRP + urocortin, and CGRP + GABA (61, 29, 11%). Overall, the transmitter repertoire of LOCs is more complex (see also Figure 13 and Supplementary Table S6). **(B)** Each subtype of pLSOs (onset or sustained firing) has a slightly lower V_{rest}, a drastically lower R_{in}, and a slightly higher C_m than LOCs. Moreover, each subgroup displays sag behavior. LOCs show a delayed firing pattern and no sag behavior. pLSOs have fusiform somata and thick, myelinated axons, whereas LOCs have round somata and thin, unmyelinated axons. Postsynaptic currents (sEPSCs and sIPSCs) show considerably faster kinetics in pLSOs than in LOCs (notice τ_{decay}) (see also Figure 6 and Supplementary Figures S6, S7). **(C)** Cluster-specific genes (pLSO vs. LOC) as well as genes displaying inter-cluster similarity (pLSO and LOC). For the sake of clarity, the three panels depict only selected gene products (pLSO: 17, both: 18, LOC: 13). **(C1)** For pLSOs, we plotted the end products of six Super DEGs (red), five top DEGs (green), four DEGs involved in neurotransmission (yellow), the top one highly expressed gene (purple), and Nav1.6 (gray) (see also Figures 2–4, 5–9, 11–15). **(C2)** Across both neuron types, we plotted the end products of 12 genes demonstrating Cluster similarity (light blue), top two and top three highly expressed genes (purple), and four proteins for which we obtained confirmative results via immunohistochemistry or pharmacology (gray). The mitochondrion represents genes involved in ATP synthesis (see Figure 2E; see also Figures 2, 9–15). **(C3)** For LOCs, we plotted the end products of six Super DEGs, six top DEGs, and three DEGs involved in neurotransmission (same color code as in **(C1)**, see also Figures 4, 5, 12–15). The scenario in **(C1–C3)** is hypothetic as schemata show proteins at their presumptive location. glut, glutamate; gly, glycine; inh, inhibitory; exc, excitatory.

SNURF is a 71 amino acid-long polypeptide encoded by the two-gene locus "*snurf/snrpn*." This locus also encodes the small nuclear ribonucleoprotein (associated) polypeptide N (SNRPN) (Ozçelik et al., 1992). Across seven tissues, SNRPN is most abundant in the brain (rat; McAllister et al., 1988). Extensive alternative splicing and promoter usage occurs for SNURF and

SNRPN, and the full-length nature of several transcripts remains to be determined. Like other imprinted genes, the *SNURF/SNRPN* domain is involved in neurodevelopment (Ribeiro Ferreira et al., 2019). Developmentally related changes of DNA methylation have been described for the mouse gene (Miyazaki et al., 2009). Loss of imprinted gene expression leads to disorders, e.g., severe intellectual disability (Nicholls et al., 1998). Presumably, SNURF plays a role in pre-mRNA splicing, and in line with this, SNURF is localized to the cell's nucleus. Despite decades of research, the biological role of SNURF is not fully understood (Basak and Basak, 2022). A Pubmed search ("snurf brain" and "snurf neuron"; 2023–10-22) revealed 14 and nine results, respectively. None was associated with papers on the auditory system, the brainstem, or the cortex. Taken together, our study discovered *Snurf* as a novel gene that probably plays an important role in the CAS. The intermediate expression level for *Snurf* in the LSO and other auditory brainstem regions, as demonstrated in the AMBA, strengthens our conclusion.

CaM is one of three calmodulin proteins in the family of EF-hand Ca^{2+}-binding proteins. These ubiquitous proteins exhibit a high degree of evolutionary conservation (Wren et al., 2019). CaM-Ca^{2+} complexes mediate the control of many structurally different proteins, such as voltage-gated ion channels (e.g., Cav1.3: Johny et al., 2013; Cav2.1: Lee et al., 2002; Jiang et al., 2008; KCa2: Bildl et al., 2004; Kv7.1: Sachyani et al., 2014; Kv7.2: Alaimo and Villarroel, 2018; Nav1.5: Gabelli et al., 2014). CaM appears to be the most relevant transducer of Ca^{2+} signals (Levitan, 1999; Faas et al., 2011). Moreover, irrespective of the intracellular Ca^{2+} concentration, CaM is constitutively tethered to Kv7.2/3 channels and presumably plays a key role in Kv7 channel folding and trafficking (Wen and Levitan, 2002; review: Soldovieri et al., 2011). Notably, the present study demonstrates substantial gene expression for Kv7.2 and Kv7.3 (Figures 9, 10), pointing to such an interaction.

In the CAS, mostly analyzed at calyx of Held synapses, CaM controls several forms of synaptic plasticity (Nakamura et al., 2008; Lee et al., 2010; Lipstein et al., 2013). *Calm1* expression increases significantly upon tone rearing in auditory cortex interneurons, implying a role in experience-and activity-dependent circuit refinement during the tonotopic critical period (Kalish et al., 2020). We are not aware of a CaM study in the LSO. Based on our results, we suggest investigating interactions between CaM and Kv7.2/3 channels in pLSOs. Consistent with our findings, the AMBA shows intermediate to high expression levels in the LSO (Figure 2D).

Energy metabolism: ATP synthesis

Besides *Ckb*, 32 other genes among the top 500 were involved in ATP synthesis (Figure 2). The prevalence of transcripts for catabolic pathways is consistent with classic reports of high energy consumption in auditory brainstem neurons that fire APs at particularly high rates (e.g., Sokoloff, 1981). Previous reports on the LSO have focused on a few metabolic proteins (Trattner et al., 2013; Brosel et al., 2018). Our study is the first to comprehensively address LSO neurons and link ATP demand to a variety of specific enzymes. In a recent scRNA-seq study in the mouse cochlea, 33 genes among the top 500 in class I spiral ganglion neurons were associated with energy metabolism (Petitpré et al., 2018). Nine of them overlapped with the 33 genes detected in LSO neurons, all of them in the OxPhos group (*Ndufa11*, *Ndufs2*, *Ndufs3*, *Sdhb*, *Sdhd*, *Cox5a*, *Atp5b*, *Atp5f1*, *Atp5g3*). The overlap of ~30% indicates similarity between the two groups of auditory neurons, but also considerable dissimilarity, as previously shown for mitochondrial molecules (Fecher et al., 2019). In this lineage, only 3 of the 33 genes were DEGs (cluster 1: *Pfkp*, DEG#21, *Ckb*, DEG#254; cluster 2: *Acly*, DEG#10), suggesting a similar efficiency of ATP synthesis in pLSOs and LOCs. An attractive hypothesis is that ATP may also be used as an extracellular messenger by maturing LSO neurons (Dietz et al., 2012; Babola et al., 2020).

There is considerable controversy over whether neurons use lactate—rather than glucose—to fuel oxidative phosphorylation (Pellerin and Magistretti, 2012; Nortley and Attwell, 2017; Li and Sheng, 2021). Lactate would be released from glial cells via the astrocyte-neuron lactate shuttle. Neuronal computation is energetically expensive, with most of the energy used to reverse ion entry that has generated synaptic potentials and APs (Harris et al., 2012; Meyer et al., 2022). LSO neurons generate APs at unusually high rates of several hundred Hertz (Brosel et al., 2018). We examined transcripts for key enzymes and obtained evidence that LSO neurons do not primarily use lactate as a carbon source for ATP generation. The expression of *Slc16A2*, which encodes the neuronal monocarboxylate transporter MCT2, was absent from our sample. In contrast, the expression of *Slc2a3,* which encodes the neuronal glucose transporter GLUT3, was high (gene #201, 955 TPM). Expression levels of other genes (neuronal *Ldha*|lactate dehydrogenase A, #5,658, 4 TPM; astrocytic *Glo1*|lactoylglutahione lyase, #1,521, 82 TPM; *Glo2* = *Hagh*|hydroxyacylglutathione hydrolase, #119, 1,225 TPM; astrocytic *Slc16A1*|MCT1, #6,252, 3 TPM) confirm our conclusion that lactate-fueled OxPhos is not the major ATP producer in LSO neurons. This does not mean that LSO neurons exclusively utilize glucose (Brosel et al., 2018), and developmental changes may also be considered (Lujan et al., 2021). Collectively, our results support the conclusion of an extraordinary ATP demand in LSO neurons and suggest glucose—rather than lactate—as the primary energy source.

The two clusters cover ~90% of the LSO neurons

Our patch-seq LSO neurons clearly separated into two clusters, with 65% belonging to pLSOs and 35% to LOCs. Literature data suggest that pLSOs and LOCs together comprise ~90% of all LSO neurons (~70% + ~20%). In addition to pLSOs and LOCs, several other neuron types have been described morphologically. No categorization data are available for mice, but five types have been described in gerbils and cats and seven in rats (Helfert and Schwartz, 1987; Rietzel and Friauf, 1998). A prominent subtype are the LSO marginal cells, so named because of the location of the somata along the edges of the LSO (review: Friauf et al., 2019). Marginal cells appear to comprise only ~5% of the population, regardless of the species analyzed (Ollo and Schwartz, 1979; Helfert and Schwartz, 1986, 1987; Rietzel and Friauf, 1998). Small neurons tend to be underrepresented in patch-clamp recordings, and we did not specifically target small

somata or for somata located in the marginal zones of the LSO. Nevertheless, we are confident that we did not miss any major cell type.

Based on our results, we also find it unlikely that pLSOs and LOCs form further subclusters, although we did find differences in membrane properties between pLSOs —Onset and Sustained neurons. Interestingly, Onset and Sustained neurons have been described in both vGLUT2-positive and vGLUT2-negative pLSOs (they are presumably excitatory and inhibitory, respectively; Haragopal and Winters, 2023). This complicates the identification of distinct expression profiles for excitatory and inhibitory pLSO subclusters. Nevertheless, activity-dependent maturation could manifest differences in the expression profile and result in different membrane properties between Onset and Sustained pLSOs.

Super DEGs in pLSOs

Kcnh7|Kv11.3 was DEG#6 in pLSOs (Figure 9A). The gene encodes ERG3, a pore-forming subunit of ether-a-gogo-related channels. ERG channels have a predominantly somatic location, are most active after intense electrical activity, and effectively modulate neuronal excitability, thereby complementing Kv1 channels (Hardman and Forsythe, 2009). The channels are inward rectifiers with unusual gating kinetics. They open at relatively negative membrane potentials, thus affecting the depolarization phase of an AP, and they inactivate very rapidly. The highest conductance is generated during repolarization (Shepard et al., 2007; Bauer and Schwarz, 2018), when the fast recovery from inactivation takes place (Bauer and Schwarz, 2018). Several studies showed a role of ERG channels in the nervous system (Sacco et al., 2003; Niculescu et al., 2013). In ventral cochlear nucleus neurons, they play a role in setting AP threshold and AP frequency (Yildirim and Bal, 2018). In the mouse MNTB, where ERG1 and ERG3 subunits are predominant, ERG currents modulate Kv1 currents and limit AP generation around AP threshold voltages (Hardman and Forsythe, 2009).

Kcna1|Kv1.1 was DEG#92 in pLSOs (Figure 9A). Kv α subunits have received extensive attention in the auditory brainstem, and immunoreactivity has been demonstrated in several species in somata, dendrites, and axon terminals (mouse: Wang et al., 1994; Brew et al., 2003; rat: Barnes-Davies et al., 2004; gerbil: Nabel et al., 2019); three bat species: (Rosenberger et al., 2003; Pätz et al., 2022). Kv1.1 channels were most intensively analyzed. They carry a rapidly activated, low-threshold, and sustained K^+ current (I_{KL}) that determines the 1st AP latency as well as the AP waveform (Kole et al., 2007; Fischl et al., 2016). MNTB neurons in Kv1.1 knockout mice display a reduced I_{KL} and are hyperexcitable (Brew et al., 2003). In line with this, pharmacological blockade of Kv1.1 channels in pLSOs with α-dendrotoxin (NB: blocks also Kv1.2 and Kv1.6; Oak and Yi, 2014) convert a single-firing to a multiple-firing pattern (Barnes-Davies et al., 2004). Kv1.1 knockout mice display behavioral deficits in sound localization (Robbins and Tempel, 2012; Karcz et al., 2015), and their LSO neurons show a weaker capability of encoding interaural level differences (Karcz et al., 2011). pLSOs clearly differ from LOCs regarding Kv1.1 channels. The results provide further evidence for the importance of temporal integration of excitation and inhibition during sound localization, especially in the ascending branch of the LSO.

The Kvβ3-encoding gene *Kcnab3* was DEG#146 in pLSOs. Three Kvβ isoforms have been described in the brain (Heinemann et al., 1995; Rhodes et al., 1996). They have oxidoreductase activity and interact with the pore-forming α subunits of Kv1 and Kv4 channels (Dwenger et al., 2022). The assembly generally increases whole cell Kv current and modifies voltage sensitivity (Pongs and Schwarz, 2010). We are not aware of a study on Kvβ3 in the auditory system. Our results show high protein abundance in the major SOC nuclei and co-distribution of Kvβ3 and GlyT2 in axon terminals terminating on pLSO somata, most likely originating from MNTB neurons (Figure 12D).

Slc17a6|vGLUT2 was DEG#26 in pLSOs. Vesicular glutamate transporters are involved in the storage and release of glutamate. Our patch-seq results for genes expressing vGLUT confirm *in situ* hybridization results showing the absence of vGLUT1 and the presence of vGLUT2 in mouse LSO somata (Ito et al., 2011). They are also consistent with the detection of vGLUT2 in the LSO of rat, mouse, and owl monkey at the protein level (Blaesse et al., 2005; Haragopal and Winters, 2023) and at the mRNA level (Hackett et al., 2011). The association of vGLUT2 with pLSOs is consistent with findings in rats that vGLUT2-positive LSO neurons project into the contralateral inferior colliculus (IC; virtually no ipsilateral projection), thus representing ascending neurons (Ito and Oliver, 2010). Moreover, concerning the three classical fast neurotransmitters (glutamate, glycine, GABA; expressed by 44 pLSOs in different combinations), we show a surprisingly high 4:1 ratio between a purely excitatory and a purely inhibitory phenotype (64% vs. 16%; Figure 16; Supplementary Table S6). The remaining 20% show a mixed phenotype (predominantly glutamate plus GABA; notice rounding effect). Thus, the present results indicate a dominant glutamatergic phenotype in mouse pLSOs, whereas glycinergic and/or GABAergic neurons are much less abundant. A mixed phenotype (glutamate plus glycine) has also been described for the projections of LSO neurons into the IC of rats (Fredrich et al., 2009). The authors found that all ipsilaterally projecting neurons were glycinergic, with 60% of them also staining for glutamate. Similar to mice, ¾ of the LSO neurons in gerbils are excitatory (Mellott et al., 2022). In contrast, excitatory and inhibitory LSO neurons appear to be balanced in cats (Glendenning et al., 1992) and guinea pigs (Helfert et al., 1989). We propose that species differences underlie the different ratios.

Gria4|GluA4 was DEG#40 in pLSOs. In contrast, GluA1 subunits appear to be a marker for LOCs (DEG#68). Kinetics of glutamatergic ionotropic receptors can be in the submillisecond range (Geiger et al., 1997), and the fastest kinetics are obtained when GluA4 subunits are present (auditory brainstem: Geiger et al., 1995; Yang et al., 2011; Rubio et al., 2017). By contrast, GluA1-containing receptors are slow-gating. At calyx of Held synapses, GluA4 is the main determinant for the fast synaptic responses and indispensable for driving high-fidelity neurotransmission and conveying precise temporal information (Yang et al., 2011). GluA4 is also expressed in auditory nerve synapses (Rubio and Wenthold, 1997), and its loss impairs the acoustic startle response (García-Hernández and Rubio, 2021). These results emphasize the importance of this subunit in the CAS.

AMPAR-mediated EPSCs in the LSO are characterized by sub-millisecond decay times (0.77 ms) that are slowed upon acoustic trauma, which is mirrored by mRNA decreases for GluA4, yet increases for GluA1 (Pilati et al., 2016). In this line, our transcriptomic results imply different kinetics at glutamate receptors between pLSOs

and LOCs. Indeed, our electrophysiological findings demonstrate considerably faster EPSC kinetics in pLSOs (Supplementary Figures S7D,E; Supplementary Table S5.1; Figure 16). The involvement of pLSOs in sound localization requires sub-millisecond precision in signal integration. According to our data, hyper-precise kinetics are not present in LOCs, which seem to protect the auditory nerve fibers from excitotoxic effects of acoustic overexposure, a process occurring in minutes (Accardi, 2014). Notably, pLSOs have myelinated axons, whereas LOC axons are unmyelinated (Brown, 2011).

The sixth Super DEG in pLSOs, *Gabrb3*, codes for GABAARβ3, the β3 subunit of $GABA_A$ receptors (DEG#72). $GABA_A$ receptors are heteropentamers, most often consisting of subunits from three different families in a 2:2:1 fashion (2α+2β+1 of either γ, δ, ε, π). The most common arrangement is $2\alpha_1 2\beta_2\gamma_2$. Intermediate levels of *Gabrb3* mRNA were identified in the LSO of rats and mice (Campos et al., 2001; Fischer et al., 2019), and immunosignals for β3 subunits have been described in the rat LSO (Pirker et al., 2000). Our patch-seq results confirm the expression in pLSOs. *Gabrb3* loss results in severe cochlear histopathology, providing evidence for a functional GABAergic innervation of the cochlea (Maison et al., 2006). The physiological role of β3 has not yet been analyzed in the CAS. The same holds for GABAARα1, whose encoding gene was a Super DEG in LOCs. In a mammalian expression system, receptors containing the α1 subunit responded to GABA application with long-duration openings that were organized in multi-opening bursts, in contrast to brief-duration, isolated openings of receptors containing α6 subunits (Fisher, 2004). The author suggested that GABA acts as a high efficacy agonist at the former receptor type. Consequently, LOCs may be more efficiently inhibited by GABA than pLSOs (see also Fischer et al., 2019). Interestingly, a given pLSO neuron or LOC neuron displays an almost inverse expression pattern for β3 or α1 GABAAR subunits (Figure 13A), indicating substantial architectural and functional differences.

Super DEGs in LOCs

For LOCs, the Super DEGs *Calca* and *Ucn*, encoding the neuropeptides CGRP and urocortin, respectively, were DEG#1 and DEG#2 (Figure 4B). There is clear evidence that CGRP is a molecular marker for LOCs (mouse: Maison et al., 2003; Wu et al., 2018). Reportedly, CGRP is not associated with pLSOs, and our results confirm this, although we found few CGRP transcripts in 13% of these neurons (< 2 TPM; Figure 14A). Our results document the impressively complex multi-transmitter properties of LOCs at the single-cell level. The cohort displays 12 multi-transmitter variants, more than 90% (28/30) of the neurons express at least two of the seven transmitter genes analyzed, and up to five neurotransmitter genes can be co-expressed by a single neuron (Figure 14B). The dominant combination is GABA + CGRP + urocortin, which was observed in 61% of the LOCs (Figure 16; Supplementary Table S6). In 10 neurons, it was flanked by the expression of a fourth or even a fifth gene. Urocortin demonstrates an even higher cell-type specificity than CGRP, as gene expression was completely absent from pLSOs (Figure 14A). Taken together, our patch-seq results demonstrate high transmitter complexity for LOCs at single-cell resolution. They also imply functional diversity within this relatively small population of efferent neurons.

Scn3a|Nav1.3 (DEG#11 in LOCs) encodes an α subunit of Nav1.3 channels generally less common than Nav1.1, Nav1.2, and Nav1.6 channels in the central nervous system (Scott et al., 2010). Nav1.3 channels are more abundant in the fetal than the adult brain (Liao et al., 2023). Nav1.3 currents recover rapidly from inactivation, which results in low AP thresholds and high AP frequencies (Cummins et al., 2001; Liao et al., 2023). However, the distinct expression of *Scn3a*|Nav1.3 in LOCs does not explain the higher AP threshold compared to pLSOs (Supplementary Figure S6J). AMBA shows no *Scn3a* expression in the LSO at P56, and P14 data was not available (Supplementary Figure S5).

As gene expression for Nav1.3 subunits was low in pLSOs, we assessed other Nav genes and found the highest expression level for *Scn8a*|Nav1.6, followed by *Scn1a*|Nav1.1 (66 and 18 TPM; Supplementary Figure S8A; Supplementary Table S6). The LOC cohort displayed considerably lower Nav1.6 expression (12 TPM; < 5-fold). Nav1.6 subunits are abundant in the nervous system and occur in various excitatory and inhibitory neurons. They form dense clusters at axon initial segments and nodes of Ranvier where they are the dominant Nav subtype (Caldwell et al., 2000; Chen et al., 2008; Zybura et al., 2021). For example, they are the major isoform at Calyx of Held-MNTB axon terminals where the abundance increases during development (Leao et al., 2005). In the auditory nerve, Nav1.6 and Nav1.1 are placed at the AP generator site, together with the submembraneous scaffolding protein ankyrin (Kim and Rutherford, 2016). As demonstrated in several brain regions, Nav1.6 channels contribute to peak Na^+ currents and repetitive AP firing (references summarized in Chen et al., 2008). They display persistent and resurgent Na^+ currents, lower the AP threshold and mediate repetitive spiking (Zybura et al., 2021). Together, the above findings suggest an important role for Nav1.6 channels in initiation and propagation of high-frequency AP bursts in LSO neurons, particularly in myelinated, mature pLSOs.

Cacna1e, coding for Cav2.3, was DEG#26 in LOCs. Previously, we identified mRNA for Cav2.3 in LSO neurons (Jurkovicova-Tarabova et al., 2012). Cav2.3 is the α1 subunit of R-type Cav channels (Catterall, 2011). Together with PQ-and N-type channels (containing Cav2.1 and Cav2.2 subunits, respectively), R-type channels mediate presynaptic Ca^{2+} influx and neurotransmitter release (Ricoy and Frerking, 2014; Held et al., 2020). Among the 18 Cav genes expressed in the LSO cohort, *Cacna1e*|Cav2.3 demonstrated the highest value by far (mean TPMs: LOCs 1,491; pLSOs 182; Supplementary Figure S9A; Supplementary Table S6). High TPM values also occurred for Cav2.2 in both neuron types (pLSOs 414; LOCs 363). Together, we reason that LOCs likely prioritize Cav2.3 subunits over Cav2.2 subunits, whereas pLSOs favor the reverse order. On the other hand, *Cacna1a*|Cav2.1 expression seems be negligible in both groups (6.1 vs. 2.2 TPM). The functional impact of this needs to be determined.

Cluster similarity

Our Cluster similarity scoring finally revealed 12 genes, four of which code for TRP channels, another four for glutamate receptor molecules, two for Cav channels and one each for glycine and GABA receptor subunits (Figure 15). Among the four TRP channels were two TRPM channels (melastatin) as well as one TRPML (mucolipin), and one TRPP (polycystin) channel (TRPM2, TRPM7, TRPML1, TRPP5).

TRP channels are cation channels that generally cause cell depolarization. However, they can also be associated with intracellular organelles and function as intracellular Ca^{2+} release channels (Gees et al., 2010). They play a crucial role in sensory physiology, possibly contributing to hearing (Venkatachalam and Montell, 2007). TRP channels have been poorly studied in the CAS. In the mouse ventral cochlear nucleus, activation of TRPM2 channels shifts V_{rest} to more positive values (Bal et al., 2020). The authors reasoned that TRPM2 channels, which are induced by oxidative stress, may play a modulatory role in setting the excitability level of stellate cells. To our knowledge, there is no study on TRPM or TRPPP channels in the SOC. Our results show that pLSOs and LOCs are similar in their TRP channel composition, as also evidenced by the absence of any DEG in this group. These results pave the way for further investigations. Of note is the relatively low percentage of neurons expressing a given TRP gene (highest value: 50% for TRPM7 in LOCs), indicating heterogeneity within a given cluster. This issue of inter-cellular heterogeneity is of interest for future studies.

Regarding Cluster similarity for glutamate receptor molecules, ~15% (4/26; including 18 ionotropic and 8 metabotropic) met the criteria, namely GluA2, GluK5, GluN1, and mGluR8. This corresponds to one gene in each major class (AMPA; kainate, NMDA, metabotropic; Figures 15A2,B). Regardless of subtype, ~75% of the LSO neurons showed GluA2 transcripts, the highest proportion across all 32 ligand-gated ion channels (Figure 13A). The Cluster similarity observed for GluA2 contrasts with the Super DEGs GluA1 and GluA4. Edited GluA2 subunits render AMPA receptors Ca^{2+} impermeable and are abundant in the brain. AMPA receptors lacking GluA2 are Ca^{2+}-permeable, allowing them to serve as signaling molecules via Ca^{2+} influx, in addition to mediating excitatory neurotransmission (Man, 2011).

Kainate receptor subunits, including GluK5, have been identified in the SOC by immunohistochemistry and pharmacological analysis (Petralia et al., 1994; Löhrke and Friauf, 2002; Vitten et al., 2004). Notably, GluK5 subunits have high agonist affinity and fast kinetics (Dhingra et al., 2022). In summary, there is consistent evidence that both types of LSO neurons are equipped with fast gating glutamate receptors, and pLSOs even more so than LOCs.

Our results on GluN1 confirm immunohistochemical findings in the LSO (Nakagawa et al., 2000) and attribute the subunit to both pLSOs and LOCs. Glycine, a co-agonist at NMDA receptors, binds to GluN1 subunits, whereas glutamate binds to GluN2. Consequently, NMDA receptors require both subunits to be functional. Our study shows similar expression for both isoforms (GluN2B and GluN2D), and the majority of pLSOs express GluN2B, especially the Sustained neurons (Figure 13A). Our GluN2B results are consistent with a pharmacological report suggesting a correspondence of the NMDA receptor subunit with the period of major circuit refinement at MNTB-LSO synapses (Case and Gillespie, 2011). In particular, GluN2B subunits confer relatively long decay kinetics to NMDA receptors, and the developmental shortening of EPSCs likely results from a subunit substitution of GluN2A for GluN2B.

For genes involved in inhibitory neurotransmission, Cluster similarity was demonstrated for the ionotropic GlyR subunit GlyRβ and the metabotropic GABABR1 (Figures 13A2,B2, 14A; Supplementary Figure S12A). For GlyRβ, we found expression in 79% of the pLSOs and 67% of the LOCs. The 79% value was the highest observed in the pLSO cohort. The presence of GlyRβ transcripts is expected, as this subunit is a mandatory component of heteropentameric GlyRs and essential for their postsynaptic localization (Weltzien et al., 2012). The higher TPM values for the adult GlyRα1 compared to the fetal GlyRα2 (Figure 13A) indicate that most of the replacement of the fetal by the adult α subunits (Dutertre et al., 2012) has occurred by the time mice begin to hear, at least in pLSOs (α3 and α4 transcripts were not detected in our sample).

GABABR1 is one of two GPCR molecules activated by GABA (review: Bassetti, 2022). The level for GABABR1 transcripts was moderate in our LSO sample (~25 TPM), >10-fold higher than the very low *Gabbr2*|GABABR2 expression (~1 TPM; Supplementary Figure S12A; Supplementary Table S6). Since GABABRs are obligatory heterodimers composed of GABABR1 and GABABR2 subunits (review: Frangaj and Fan, 2018), the difference in expression is surprising. Based on our transcript results, we cannot localize the GABABR subunits to presynaptic or postsynaptic sites. We have recently shown that postsynaptic GABABRs mediate hyperpolarization in a modulatory manner in mouse pLSOs (Fischer et al., 2019). GABABR signaling has previously been shown to mediate long-lasting depression at inhibitory gerbil MNTB-LSO synapses (Kotak et al., 2001). This form of synaptic depression declines with age and may contribute to the use-dependent reorganization of MNTB axon arbors.

In the Cav channel group (Zamponi et al., 2015), we observed Cluster similarity for two subunits, Cav1.3 and Cavγ2. Cav1.3 plays an important role in the auditory system. It is involved in deafness (Platzer et al., 2000) and in the development of auditory brainstem structures, including the LSO (Hirtz et al., 2011, 2012). Functional Cav1.3 channels have been described in pLSOs (Jurkovicova-Tarabova et al., 2012). Therefore, the present results at the mRNA level are consistent with previous findings at the protein level.

Cavγ2, also known as stargazin or TARPγ2 (most literature refers to stargazin), is one of eight Cavγ isoforms in a functionally diverse family (Chen et al., 2007; Bissen et al., 2019). Six of the eight Cavγ isoforms belong to the TARP subfamily, including Cavγ2 (and Cavγ5). TARP stands for "Transmembrane AMPAR regulatory protein," implying an interaction with AMPA receptors and not a mandatory role as a true Cav subunit. TARP/AMPAR complexes promote the correct trafficking of AMPARs and their targeting to the synaptic surface (review: Jacobi and von Engelhardt, 2017). TARPγ2-containing AMPARs have been localized in presynaptic axon terminals where they modulate GABA release (Rigby et al., 2015). The expression profile of Cavγ2 (and the other AMPAR regulatory subunits) and the functional characterization in the auditory brainstem await future studies. In this context, it is worth noting that *Cacng5*|Cavγ5 was DEG#12 in pLSOs.

Kcnq2|Kv7.2 was not on the top 12 list of genes showing Cluster similarity (its position was 18; Figure 15B2). Nevertheless, we analyzed Kv7.2 in combination with Kv7.3 by means of immunohistochemistry and pharmacology. Kv7.2 and Kv7.3 are primarily found in the brain (Baculis et al., 2020). They are the major molecular correlate of low-threshold, non-inactivating Kv channels that mediate the M current, which is hyperpolarizing and critical for preventing neuronal hyperactivity (Wang et al., 1998; Robbins, 2001; Brown and Passmore, 2009). In the calyx of Held terminals, Kv7 channels, most likely Kv7.5 homomers, control release probability through changes in V_{rest} (Huang and Trussell, 2011). In adition, they function to facilitate reliable

high-frequency synaptic signaling (Zhang et al., 2022). Our results suggest a similar function for Kv7.2 and Kv7.3 channels in pLSOs. Whether the channels are localized in pLSO axon terminals and involved in modulating transmitter release requires further analysis.

Species differences

There is increasing evidence that a variety of characteristics vary considerably among species in the SOC, including the LSO. Species-specific effects (e.g., low-frequency vs. high-frequency hearing) on structure and function are well known (Heffner and Heffner, 1992; Grothe, 2000; Fritzsch et al., 2013) and are evident in the SOC. First, there is considerable variation in the arrangement, shape, and relative size of individual SOC nuclei (Friauf et al., 2019). Second, there are species differences in the location of olivocochlear neurons in the SOC (Aschoff and Ostwald, 1987; Brown, 2011). Third, there are species differences in the quantitative contribution of LOCs and MOCs to olivocochlear fibers (Perrot and Collet, 2014). Fourth, interspecies differences may explain the inconsistencies between reports on the transmitter repertoire of LOCs (Guinan, 2011). Fifth, discrepancies in the excitatory/inhibitory transmitter ratio have been reported for pLSO neurons (Williams et al., 2022). In the heterogeneous LSO, these differences have created multi-scale, long-standing, and persistent puzzles (Guinan, 2011; Williams et al., 2022). Consequently, general statements about the LSO when pooled from different species must be interpreted with caution. We have taken this into account for the summary cartoon (Figure 16), which shows results from mice only.

Validating the patch-seq results

For a few genes, we exemplarily validated our transcriptomic results on the protein level (Figures 5, 10, 11, 12). Furthermore, we compared them with those of a very recent study using single-nucleus sequencing of LOCs (Frank et al., 2023). The comparison revealed considerable similarity between the genes detected, thus strengthening each study. For example, both studies found expression of Col4a3 and B3galt1 in LOC neurons.

Methodological considerations

We do not want to hide the fact that the patch-seq method has its limitations. The general limitations of scRNA-seq also apply to the patch-seq variant. Contamination from the extracellular solution can lead to false positives and affect the quality of the results. To minimize this problem, we performed stringent quality controls (see Methods). The low throughput (we patched 263 neurons but collected only 103) reflects our caution in cell harvesting to minimize contamination. In addition, we took advantage of the fact that extracting the cytosol and the nucleus significantly increases the RNA yield and improves the quality of the transcriptomic data. Finally, by including negative controls and carefully monitoring the harvesting process, we were able to gain insight into potential sources of contamination. Our observations indicate that the effects of contaminants on the transcriptomic profiles were generally small. For example, ChAT expression and urocortin expression were absent in the pLSO cohort. Nevertheless, we attribute some of the results on CGRP (in 12.5% of pLSOs) and HCN (in 17% of LOCs) to contamination (see Figure 14; Supplementary Figure S11). To allow a *post hoc* reaction to the effects of the contamination problem, we have designed the gene tables in such a way that the readers can interactively change the TPM thresholds and thus adjust the stringency of the filtering criteria to their personal needs (*cf.* Supplementary Table S6).

The age of the animals is another factor influencing contamination. In patch-seq experiments in adult tissue, where a dense perineuronal network of glial cells is present, the risk of contamination is higher. This was one of the reasons why we used young mice (P10-P12) in the present study. By limiting the sampling to this age, we also obtained a unique database for the cell identity of the developing LSO neurons. Given that numerous electrophysiological, biochemical and anatomical studies have used and continue to use this age in the LSO, we believe that our database will be of great value to the research community.

Other challenges arise from the fact that, due to biological and technical limitations, only a fraction of mRNA is captured, leading to zero inflation and false-negative results. We believe that some of our results, such as not detecting HCN in all pLSOs, are affected by zero inflation.

Comparisons of results at the transcript level with those at the protein level are confronted with an imperfect correlation between the transcriptome and the corresponding proteome (Nie et al., 2007; Schwanhäusser et al., 2011; Liu et al., 2016). The mapping between high-throughput measurements at the level of the transcriptome and the corresponding proteome is complex (Gunawardana et al., 2015). Conclusions based on the transcriptome alone should therefore be treated with caution, and gene expression levels should only be used as a proxy for protein levels (Liu et al., 2016).

We assume that some of our unexpected results have biological causes, in addition to the artifacts mentioned above. For example, the lack of ChAT expression that we observed in most LOCs is consistent with the low *in situ* hybridization signals detected in AMBA LSO P14 sections. However, neurons in the facial nucleus and other motor nuclei are strongly labeled in the AMBA. It is possible that gene expression for ChAT is low in the LSO while protein abundance is high. Taken together, it is advisable for future studies to first extend the transcriptomic findings to the protein level in order to determine whether the described mRNA level is manifested in protein abundance and to localize the proteins in the neurons before starting functional analyses.

Conclusion and outlook

Our study provides a comprehensive catalog of marker genes for the two major neuron types in the juvenile LSO. It also provides fundamental and comprehensive insights into the molecular composition of the ascending and descending microcircuits associated with the LSO and how this may relate to their function, including cell type-specific maturation. Our study suggests several areas for further investigation. It is also worthwhile to use our extensive data sets in a correlative manner. For example, it would be worthwhile to analyze which gene or gene network affects which physiological parameter (e.g., Kv genes and AP properties). For this purpose, we have added several supplementary files with data for each neuron in our sample (Supplementary Table S3, S6). In addition, the

regulatory subunits of ion channels should be analyzed more thoroughly (Yan and Tomita, 2012). Due to space limitations, this was not done in the present study. In particular, the abundance of proteins interacting with AMPARs (Jackson and Nicoll, 2011; Cull-Candy and Farrant, 2021; Jacobi and von Engelhardt, 2021), kainate receptors (Palacios-Filardo et al., 2016), GABARs (Nakamura et al., 2016; Yamasaki et al., 2017), and GlyRs (Liu and Wong-Riley, 2013) deserves special attention. Our multidimensional single-cell expression data provide a valuable foundation for research in this direction. Regulatory subunits contribute to the diversity and function of these macromolecular signaling complexes. This is also true for the voltage-gated ion channels (Figure 9; Supplementary Figures S8–S11). It is very likely that SOC neurons, with their temporally precise, robust, and resilient neurotransmission behavior, contain highly specialized signaling molecules that differ at the single-cell level.

Data availability statement

The data is available on NCBI GEO under the accession number GSE241761.

Ethics statement

The animal study was approved by the German Animal Protection Law (TSchG §4/3). The study was conducted in accordance with the local legislation and institutional requirements.

Author contributions

AM-S: Writing – review & editing, Writing – original draft, Visualization, Validation, Investigation, Formal analysis, Conceptualization. EP: Writing – review & editing, Visualization, Validation, Investigation, Formal analysis, Conceptualization. JF: Writing – review & editing, Visualization, Software, Formal analysis. KK: Writing – review & editing, Investigation, Conceptualization. TR: Writing – review & editing, Visualization, Investigation, Formal analysis. EF: Writing – original draft, Supervision, Resources, Project administration, Funding acquisition, Conceptualization, Writing – review & editing.

Funding

The authors declare financial support was received for the research, authorship, and/or publication of this article. This project has received funding from the Deutsche Forschungsgemeinschaft DFG (Fr 1784/23–1).

Acknowledgments

We thank Tina Kehrwald and Jennifer Winkelhoff for technical assistance, Jörn Walter for providing access to the HiSeq 2500 sequencing system, and Ekkehard Neuhaus for granting us access to the TCS SP5 X confocal microscope. We would also thank Abhyudai Singh for pointing out the overlapping index. Finally, many thanks to Felix Felmy for his comments on an early version of the manuscript.

Conflict of interest

The authors declare that the research was conducted in the absence of any commercial or financial relationships that could be construed as a potential conflict of interest.

Publisher's note

All claims expressed in this article are solely those of the authors and do not necessarily represent those of their affiliated organizations, or those of the publisher, the editors and the reviewers. Any product that may be evaluated in this article, or claim that may be made by its manufacturer, is not guaranteed or endorsed by the publisher.

Supplementary material

The Supplementary material for this article can be found online at: https://www.frontiersin.org/articles/10.3389/fncel.2024.1354520/full#supplementary-material

References

Abraham, N. M., Egger, V., Shimshek, D. R., Renden, R., Fukunaga, I., Sprengel, R., et al. (2010). Synaptic inhibition in the olfactory bulb accelerates odor discrimination in mice. *Neuron* 65, 399–411. doi: 10.1016/j.neuron.2010.01.009

Accardi, A. (2014). Unveiling the secret lives of glutamate transporters: VGLUTs engage in multiple transport modes. *Neuron* 84, 1110–1112. doi: 10.1016/j.neuron.2014.12.008

Adam, T. J., Finlayson, P. G., and Schwarz, D. W. (2001). Membrane properties of principal neurons of the lateral superior olive. *J. Neurophysiol.* 86, 922–934. doi: 10.1152/jn.2001.86.2.922

Adam, T. J., Schwarz, D. W. F., and Finlayson, P. G. (1999). Firing properties of chopper and delay neurons in the lateral superior olive of the rat. *Exp. Brain Res.* 124, 489–502. doi: 10.1007/s002210050645

Adelman, J. P., Maylie, J., and Sah, P. (2012). Small-conductance Ca^{2+}-activated K^+ channels: form and function. *Annu. Rev. Physiol.* 74, 245–269. doi: 10.1146/annurev-physiol-020911-153336

Alaimo, A., and Villarroel, A. (2018). Calmodulin: a multitasking protein in Kv7.2 potassium channel functions. *Biomol. Ther.* 8:57. doi: 10.3390/biom8030057

Alexander, S. P., Christopoulos, A., Davenport, A. P., Kelly, E., Mathie, A., Peters, J. A., et al. (2021). The concise guide to pharmacology 2021/22: G protein-coupled receptors. *Br. J. Pharmacol.* 178 Suppl 1, S27–S156. doi: 10.1111/bph.15538

Alexander, S. P., Mathie, A., and Peters, J. A. (2011). Guide to receptors and channels (GRAC), 5th edition. *Br. J. Pharmacol.* 164 Suppl 1, S1–S324. doi: 10.1111/j.1476-5381.2011.01649_1.x

Ali, S. A., Pappas, I. S., and Parnavelas, J. G. (1998). Collagen type IV promotes the differentiation of neuronal progenitors and inhibits astroglial differentiation in cortical cell cultures. *Dev. Brain Res.* 110, 31–38. doi: 10.1016/s0165-3806(98)00091-1

Altschuler, R. A., Reeks, K. A., Fex, J., and Hoffman, D. W. (1988). Lateral olivocochlear neurons contain both enkephalin and dynorphin immunoreactivities: immunocytochemical co-localization studies. *J. Histochem. Cytochem.* 36, 797–801. doi: 10.1177/36.7.2898496

Amezquita, R. A., Lun, A. T. L., Becht, E., Carey, V. J., Carpp, L. N., Geistlinger, L., et al. (2020). Orchestrating single-cell analysis with Bioconductor. *Nat. Methods* 17, 137–145. doi: 10.1038/s41592-019-0654-x

Angeli, S., Lin, X., and Liu, X. Z. (2012). Genetics of hearing and deafness. *Anat. Rec.* 295, 1812–1829. doi: 10.1002/ar.22579

Aschoff, A., and Ostwald, J. (1987). Different origins of cochlear efferents in some bat species, rats, and guinea-pigs. *J. Comp. Neurol.* 264, 56–72. doi: 10.1002/cne.902640106

Ashrafi, G., and Ryan, T. A. (2017). Glucose metabolism in nerve terminals. *Curr. Opin. Neurobiol.* 45, 156–161. doi: 10.1016/j.conb.2017.03.007

Avenali, L., Narayanan, P., Rouwette, T., Cervellini, I., Sereda, M., Gomez-Varela, D., et al. (2014). Annexin A2 regulates TRPA1-dependent nociception. *J. Neurosci.* 34, 14506–14516. doi: 10.1523/JNEUROSCI.1801-14.2014

Babola, T. A., Kersbergen, C. J., Wang, H. C., and Bergles, D. E. (2020). Purinergic signaling in cochlear supporting cells reduces hair cell excitability by increasing the extracellular space. *eLife* 9:e52160. doi: 10.7554/eLife.52160

Baculis, B. C., Zhang, J., and Chung, H. J. (2020). The role of K,7 channels in neural plasticity and behavior. *Front. Physiol.* 11:568667. doi: 10.3389/fphys.2020.568667

Bal, R., Ozturk, G., Etem, E. O., Eraslan, E., and Ozaydin, S. (2020). Modulation of the excitability of stellate neurons in the ventral cochlear nucleus of mice by TRPM2 channels. *Eur. J. Pharmacol.* 882:173163. doi: 10.1016/j.ejphar.2020.173163

Balakrishnan, V., Becker, M., Löhrke, S., Nothwang, H. G., Güresir, E., and Friauf, E. (2003). Expression and function of chloride transporters during development of inhibitory neurotransmission in the auditory brainstem. *J. Neurosci.* 23, 4134–4145. doi: 10.1523/JNEUROSCI.23-10-04134.2003

Barnes-Davies, M., Barker, M. C., Osmani, F., and Forsythe, I. D. (2004). Kv1 currents mediate a gradient of principal neuron excitability across the tonotopic axis in the rat lateral superior olive. *Eur. J. Neurosci.* 19, 325–333. doi: 10.1111/j.0953-816x.2003.03133.x

Basak, S., and Basak, A. (2022). Proteins and proteases of Prader-Willi syndrome: a comprehensive review and perspectives. *Biosci. Rep.* 42:BSR20220610. doi: 10.1042/bsr20220610

Bassetti, D. (2022). Keeping the balance: $GABA_B$ receptors in the developing brain and beyond. *Brain Sci.* 12:419. doi: 10.3390/brainsci12040419

Bauer, C. K., and Schwarz, J. R. (2018). Ether-à-go-go K^+ channels: effective modulators of neuronal excitability. *J. Physiol.* 596, 769–783. doi: 10.1113/JP275477

Bildl, W., Strassmaier, T., Thurm, H., Andersen, J., Eble, S., Oliver, D., et al. (2004). Protein kinase CK2 is coassembled with small conductance Ca^{2+}-activated K^+ channels and regulates channel gating. *Neuron* 43, 847–858. doi: 10.1016/j.neuron.2004.08.033

Bissen, D., Foss, F., and Acker-Palmer, A. (2019). AMPA receptors and their minions: auxiliary proteins in AMPA receptor trafficking. *Cell. Mol. Life Sci.* 76, 2133–2169. doi: 10.1007/s00018-019-03068-7

Bittencourt, J. C., Vaughan, J., Arias, C., Rissman, R. A., Vale, W. W., and Sawchenko, P. E. (1999). Urocortin expression in rat brain: evidence against a pervasive relationship of urocortin-containing projections with targets bearing type 2 CRF receptors. *J. Comp. Neurol.* 415, 285–312. doi: 10.1002/(SICI)1096-9861(19991220)415:3<285::AID-CNE1>3.0.CO;2-0

Blaesse, P., Ehrhardt, S., Friauf, E., and Nothwang, H. G. (2005). Developmental pattern of three vesicular glutamate transporters in the rat superior olivary complex. *Cell Tissue Res.* 320, 33–50. doi: 10.1007/s00441-004-1054-8

Bond, C. T., Maylie, J., and Adelman, J. P. (2005). SK channels in excitability, pacemaking and synaptic integration. *Curr. Opin. Neurobiol.* 15, 305–311. doi: 10.1016/j.conb.2005.05.001

Born, G., Breuer, D., Wang, S., Rohlmann, A., Coulon, P., Vakili, P., et al. (2014). Modulation of synaptic function through the α-neurexin-specific ligand neurexophilin-1. *Proc. Natl. Acad. Sci. U. S. A.* 111, E1274–E1283. doi: 10.1073/pnas.1312112111

Brew, H. M., Hallows, J. L., and Tempel, B. L. (2003). Hyperexcitability and reduced low threshold potassium currents in auditory neurons of mice lacking the channel subunit Kv1.1. *J. Physiol.* 548, 1–20. doi: 10.1113/jphysiol.2002.035568

Brosel, S., Grothe, B., and Kunz, L. (2018). An auditory brainstem nucleus as a model system for neuronal metabolic demands. *Eur. J. Neurosci.* 47, 222–235. doi: 10.1111/ejn.13789

Brown, D. A., and Passmore, G. M. (2009). Neural KCNQ (Kv7) channels. *Br. J. Pharmacol.* 156, 1185–1195. doi: 10.1111/j.1476-5381.2009.00111.x

Brown, M. C. (1993). Fiber pathways and branching patterns of biocytin-labeled olivocochlear neurons in the mouse brainstem. *J. Comp. Neurol.* 337, 600–613. doi: 10.1002/cne.903370406

Brown, M. C. (2011). "Anatomy of Olivocochlear neurons" in *Auditory and vestibular Efferents*. eds. D. K. Ryugo, R. R. Fay and A. N. Popper (New York, NY: Springer)

Cadwell, C. R., Scala, F., Fahey, P. G., Kobak, D., Mulherkar, S., Sinz, F. H., et al. (2020). Cell type composition and circuit organization of clonally related excitatory neurons in the juvenile mouse neocortex. *eLife* 9:e52951. doi: 10.7554/eLife.52951

Cadwell, C. R., Scala, F., Li, S., Livrizzi, G., Shen, S., Sandberg, R., et al. (2017). Multimodal profiling of single-cell morphology, electrophysiology, and gene expression using patch-seq. *Nat. Protoc.* 12, 2531–2553. doi: 10.1038/nprot.2017.120

Caldwell, J. H., Schaller, K. L., Lasher, R. S., Peles, E., and Levinson, S. R. (2000). Sodium channel $Na_v1.6$ is localized at nodes of Ranvier, dendrites, and synapses. *Proc. Natl. Acad. Sci. U. S. A.* 97, 5616–5620. doi: 10.1073/pnas.090034797

Caminos, E., Garcia-Pino, E., Martinez-Galan, J. R., and Juiz, J. M. (2007). The potassium channel KCNQ5/Kv7.5 is localized in synaptic endings of auditory brainstem nuclei of the rat. *J. Comp. Neurol.* 505, 363–378. doi: 10.1002/cne.21497

Campbell, J. P., and Henson, M. M. (1988). Olivocochlear neurons in the brainstem of the mouse. *Hear. Res.* 35, 271–274. doi: 10.1016/0378-5955(88)90124-4

Campos, M. L., De Cabo, C., Wisden, W., Juiz, J. M., and Merlo, D. (2001). Expression of GABA(a) receptor subunits in rat brainstem auditory pathways: cochlear nuclei, superior olivary complex and nucleus of the lateral lemniscus. *Neuroscience* 102, 625–638. doi: 10.1016/s0306-4522(00)00525-x

Cappellano, G., Vecchio, D., Magistrelli, L., Clemente, N., Raineri, D., Barbero Mazzucca, C., et al. (2021). The Yin-Yang of osteopontin in nervous system diseases: damage versus repair. *Neural Regen. Res.* 16, 1131–1137. doi: 10.4103/1673-5374.300328

Case, D. T., and Gillespie, D. C. (2011). Pre-and postsynaptic properties of glutamatergic transmission in the immature inhibitory MNTB-LSO pathway. *J. Neurophysiol.* 106, 2570–2579. doi: 10.1152/jn.00644.2010

Catterall, W. A. (2011). Voltage-gated calcium channels. *Cold Spring Harb. Perspect. Biol.* 3:a003947. doi: 10.1101/cshperspect.a003947

Catterall, W. A., Goldin, A. L., and Waxman, S. G. (2005). International Union of Pharmacology. XLVII. Nomenclature and structure-function relationships of voltage-gated sodium channels. *Pharmacol. Rev.* 57, 397–409. doi: 10.1124/pr.57.4.4

Chen, R. S., Deng, T. C., Garcia, T., Sellers, Z. M., and Best, P. M. (2007). Calcium channel g subunits: a functionally diverse protein family. *Cell Biochem. Biophys.* 47, 178–186. doi: 10.1007/s12013-007-0002-0

Chen, Y., Yu, F. H., Sharp, E. M., Beacham, D., Scheuer, T., and Catterall, W. A. (2008). Functional properties and differential neuromodulation of $Na_v1.6$ channels. *Mol. Cell. Neurosci.* 38, 607–615. doi: 10.1016/j.mcn.2008.05.009

Conway, J. R., Lex, A., and Gehlenborg, N. (2017). UpSetR: an R package for the visualization of intersecting sets and their properties. *Bioinformatics* 33, 2938–2940. doi: 10.1093/bioinformatics/btx364

Cooper, E. C., Harrington, E., Jan, Y. N., and Jan, L. Y. (2001). M channel KCNQ2 subunits are localized to key sites for control of neuronal network oscillations and synchronization in mouse brain. *J. Neurosci.* 21, 9529–9540. doi: 10.1523/JNEUROSCI.21-24-09529.2001

Craven, K. B., and Zagotta, W. N. (2006). CNG and HCN channels: two peas, one pod. *Annu. Rev. Physiol.* 68, 375–401. doi: 10.1146/annurev.physiol.68.040104.134728

Cull-Candy, S. G., and Farrant, M. (2021). Ca^{2+}-permeable AMPA receptors and their auxiliary subunits in synaptic plasticity and disease. *J. Physiol.* 599, 2655–2671. doi: 10.1113/jp279029

Cummins, T. R., Aglieco, F., Renganathan, M., Herzog, R. I., Dib-Hajj, S. D., and Waxman, S. G. (2001). Nav1.3 sodium channels: rapid repriming and slow closed-state inactivation display quantitative differences after expression in a mammalian cell line and in spinal sensory neurons. *J. Neurosci.* 21, 5952–5961. doi: 10.1523/jneurosci.21-16-05952.2001

Darrow, K. N., Maison, S. F., and Liberman, M. C. (2007). Selective removal of lateral olivocochlear efferents increases vulnerability to acute acoustic injury. *J. Neurophysiol.* 97, 1775–1785. doi: 10.1152/jn.00955.2006

Darrow, K. N., Simons, E. J., Dodds, L., and Liberman, M. C. (2006). Dopaminergic innervation of the mouse inner ear: evidence for a separate cytochemical group of cochlear efferent fibers. *J. Comp. Neurol.* 498, 403–414. doi: 10.1002/cne.21050

De Lera Ruiz, M., and Kraus, R. L. (2015). Voltage-gated sodium channels: structure, function, pharmacology, and clinical indications. *J. Med. Chem.* 58, 7093–7118. doi: 10.1021/jm501981g

Denhardt, D. T., and Guo, X. J. (1993). Osteopontin: a protein with diverse functions. *FASEB J.* 7, 1475–1482. doi: 10.1096/fasebj.7.15.8262332

Dhingra, S., Yadav, J., and Kumar, J. (2022). Structure, function, and regulation of the kainate receptor. *Subcell. Biochem.* 99, 317–350. doi: 10.1007/978-3-031-00793-4_10

Dietz, B., Jovanovic, S., Wielsch, B., Nerlich, J., Rübsamen, R., and Milenkovic, I. (2012). Purinergic modulation of neuronal activity in developing auditory brainstem. *J. Neurosci.* 32, 10699–10712. doi: 10.1523/JNEUROSCI.0372-12.2012

Ding, X., Meng, S., Zhou, J., Yang, J., Li, H., and Zhou, W. (2020). Translational inhibition of a-neurexin 2. *Sci. Rep.* 10:3403. doi: 10.1038/s41598-020-60289-8

Dobin, A., Davis, C. A., Schlesinger, F., Drenkow, J., Zaleski, C., Jha, S., et al. (2013). STAR: ultrafast universal RNA-seq aligner. *Bioinformatics* 29, 15–21. doi: 10.1093/bioinformatics/bts635

Dobin, A., and Gingeras, T. R. (2015). Mapping RNA-seq reads with STAR. *Curr. Protoc. Bioinformatics* 51:11.14.1. doi: 10.1002/0471250953.bi1114s51

Duan, X., Qiao, M., Bei, F., Kim, I. J., He, Z., and Sanes, J. R. (2015). Subtype-specific regeneration of retinal ganglion cells following axotomy: effects of osteopontin and mTOR signaling. *Neuron* 85, 1244–1256. doi: 10.1016/j.neuron.2015.02.017

Dutertre, S., Becker, C. M., and Betz, H. (2012). Inhibitory glycine receptors: an update. *J. Biol. Chem.* 287, 40216–40223. doi: 10.1074/jbc.R112.408229

Dwenger, M. M., Raph, S. M., Baba, S. P., Moore, J. B. T., and Nystoriak, M. A. (2022). Diversification of potassium currents in excitable cells via Kvβ proteins. *Cells* 11:2230. doi: 10.3390/cells11142230

Egashira, Y., Takase, M., and Takamori, S. (2015). Monitoring of vacuolar-type H^+ ATPase-mediated proton influx into synaptic vesicles. *J. Neurosci.* 35, 3701–3710. doi: 10.1523/jneurosci.4160-14.2015

Ehmann, H., Hartwich, H., Salzig, C., Hartmann, N., Clement-Ziza, M., Ushakov, K., et al. (2013). Time-dependent gene expression analysis of the developing superior olivary complex. *J. Biol. Chem.* 288, 25865–25879. doi: 10.1074/jbc.M113.490508

Ene, F. A., Kalmbach, A., and Kandler, K. (2007). Metabotropic glutamate receptors in the lateral superior olive activate TRP-like channels: age-and experience-dependent regulation. *J. Neurophysiol.* 97, 3365–3375. doi: 10.1152/jn.00686.2006

Ene, F. A., Kullmann, P. H. M., Gillespie, D. C., and Kandler, K. (2003). Glutamatergic calcium responses in the developing lateral superior olive: receptor types and their specific activation by synaptic activity patterns. *J. Neurophysiol.* 90, 2581–2591. doi: 10.1152/jn.00238.2003

Engel, J., Schultens, H. A., and Schild, D. (1999). Small conductance potassium channels cause an activity-dependent spike frequency adaptation and make the transfer function of neurons logarithmic. *Biophys. J.* 76, 1310–1319. doi: 10.1016/s0006-3495(99)77293-0

Ericson, J., Thor, S., Edlund, T., Jessell, T. M., and Yamada, T. (1992). Early stages of motor neuron differentiation revealed by expression of homeobox gene Islet-1. *Science* 256, 1555–1560. doi: 10.1126/science.1350865

Eybalin, M. (1993). Neurotransmitters and neuromodulators of the mammalian cochlea. *Physiol. Rev.* 73, 309–373. doi: 10.1152/physrev.1993.73.2.309

Eybalin, M., Charachon, G., and Renard, N. (1993). Dopaminergic lateral efferent innervation of the guinea-pig cochlea: immunoelectron microscopy of catecholamine-synthesizing enzymes and effect of 6-hydroxydopamine. *Neuroscience* 54, 133–142. doi: 10.1016/0306-4522(93)90389-w

Faas, G. C., Raghavachari, S., Lisman, J. E., and Mody, I. (2011). Calmodulin as a direct detector of Ca^{2+} signals. *Nat. Neurosci.* 14, 301–304. doi: 10.1038/Nn.2746

Faber, E. S. (2009). Functions and modulation of neuronal SK channels. *Cell Biochem. Biophys.* 55, 127–139. doi: 10.1007/s12013-009-9062-7

Fecher, C., Trovo, L., Muller, S. A., Snaidero, N., Wettmarshausen, J., Heink, S., et al. (2019). Cell-type-specific profiling of brain mitochondria reveals functional and molecular diversity. *Nat. Neurosci.* 22, 1731–1742. doi: 10.1038/s41593-019-0479-z

Fischer, A. U., Müller, N. I. C., Deller, T., Del Turco, D., Fisch, J. O., Griesemer, D., et al. (2019). GABA is a modulator, rather than a classical transmitter, in the medial nucleus of the trapezoid body-lateral superior olive sound localization circuit. *J. Physiol.* 597, 2269–2295. doi: 10.1113/jp277566

Fischl, M. J., Burger, R. M., Schmidt-Pauly, M., Alexandrova, O., Sinclair, J. L., Grothe, B., et al. (2016). Physiology and anatomy of neurons in the medial superior olive of the mouse. *J. Neurophysiol.* 116, 2676–2688. doi: 10.1152/jn.00523.2016

Fisher, J. L. (2004). The a1 and a6 subunit subtypes of the mammalian $GABA_A$ receptor confer distinct channel gating kinetics. *J. Physiol.* 561, 433–448. doi: 10.1113/jphysiol.2003.051839

Frangaj, A., and Fan, Q. R. (2018). Structural biology of $GABA_B$ receptor. *Neuropharmacology* 136, 68–79. doi: 10.1016/j.neuropharm.2017.10.011

Frank, M. M., and Goodrich, L. V. (2018). Talking back: development of the olivocochlear efferent system. *Wiley Interdiscip. Rev. Dev. Biol.* 7:e324. doi: 10.1002/wdev.324

Frank, M. M., Sitko, A. A., Suthakar, K., Cadenas, L. T., Hunt, M., Yuk, M. C., et al. (2023). Experience-dependent flexibility in a molecularly diverse central-to-peripheral auditory feedback system. *eLife* 12:e83855. doi: 10.7554/eLife.83855

Franken, T. P., Joris, P. X., and Smith, P. H. (2018). Principal cells of the brainstem's interaural sound level detector are temporal differentiators rather than integrators. *eLife* 7:e33854. doi: 10.7554/eLife.33854

Fredrich, M., Reisch, A., and Illing, R. B. (2009). Neuronal subtype identity in the rat auditory brainstem as defined by molecular profile and axonal projection. *Exp. Brain Res.* 195, 241–260. doi: 10.1007/s00221-009-1776-7

Friauf, E., Krächan, E. G., and Müller, N. I. C. (2019). "Lateral superior olive" in *The Oxford handbook of the auditory brainstem*. ed. K. Kandler (New York, NY: Oxford University Press)

Friedland, D. R., Popper, P., Eernisse, R., and Cioffi, J. A. (2006). Differentially expressed genes in the rat cochlear nucleus. *Neuroscience* 142, 753–768. doi: 10.1016/j.neuroscience.2006.06.060

Fritzsch, B., Pan, N., Jahan, I., Duncan, J. S., Kopecky, B. J., Elliott, K. L., et al. (2013). Evolution and development of the tetrapod auditory system: an organ of corti-centric perspective. *Evol. Dev.* 15, 63–79. doi: 10.1111/ede.12015

Fuchs, P. A., and Lauer, A. M. (2019). Efferent inhibition of the cochlea. *Cold Spring Harb. Perspect. Med.* 9:a033530. doi: 10.1101/cshperspect.a033530

Fujino, K., Koyano, K., and Ohmori, H. (1997). Lateral and medial olivocochlear neurons have distinct electrophysiological properties in the rat brain slice. *J. Neurophysiol.* 77, 2788–2804. doi: 10.1152/jn.1997.77.5.2788

Gabelli, S. B., Boto, A., Kuhns, V. H., Bianchet, M. A., Farinelli, F., Aripirala, S., et al. (2014). Regulation of the $Na_v1.5$ cytoplasmic domain by calmodulin. *Nat. Commun.* 5:5126. doi: 10.1038/ncomms6126

García-Hernández, S., and Rubio, M. E. (2021). Role of GluA4 in the acoustic and tactile startle responses. *Hear. Res.* 414:108410. doi: 10.1016/j.heares.2021.108410

Gees, M., Colsoul, B., and Nilius, B. (2010). The role of transient receptor potential cation channels in Ca^{2+} signaling. *Cold Spring Harb. Perspect. Biol.* 2:a003962. doi: 10.1101/cshperspect.a003962

Geiger, J. R., Melcher, T., Koh, D. S., Sakmann, B., Seeburg, P. H., Jonas, P., et al. (1995). Relative abundance of subunit mRNAs determines gating and Ca^{2+} permeability of AMPA receptors in principal neurons and interneurons in rat CNS. *Neuron* 15, 193–204. doi: 10.1016/0896-6273(95)90076-4

Geiger, J. R. P., Lubke, J., Roth, A., Frotscher, M., and Jonas, P. (1997). Submillisecond AMPA receptor-mediated signaling at a principal neuron-interneuron synapse. *Neuron* 18, 1009–1023. doi: 10.1016/S0896-6273(00)80339-6

Gil-Loyzaga, P. E. (1995). Neurotransmitters of the olivocochlear lateral efferent system: with an emphasis on dopamine. *Acta Otolaryngol.* 115, 222–226. doi: 10.3109/00016489509139296

Glendenning, K. K., Baker, B. N., Hutson, K. A., and Masterton, R. B. (1992). Acoustic chiasm V: inhibition and excitation in the ipsilateral and contralateral projections of LSO. *J. Comp. Neurol.* 319, 100–122. doi: 10.1002/cne.903190110

Golding, N. L., and Oertel, D. (2012). Synaptic integration in dendrites: exceptional need for speed. *J. Physiol.* 590, 5563–5569. doi: 10.1113/jphysiol.2012.229328

Graham, C. E., and Vetter, D. E. (2011). The mouse cochlea expresses a local hypothalamic-pituitary-adrenal equivalent signaling system and requires corticotropin-releasing factor receptor 1 to establish normal hair cell innervation and cochlear sensitivity. *J. Neurosci.* 31, 1267–1278. doi: 10.1523/JNEUROSCI.4545-10.2011

Gray, K. A., Yates, B., Seal, R. L., Wright, M. W., and Bruford, E. A. (2015). Genenames.org: the HGNC resources in 2015. *Nucleic Acid Res.* 43, D1079–D1085. doi: 10.1093/nar/gku1071

Groff, J. A., and Liberman, M. C. (2003). Modulation of cochlear afferent response by the lateral olivocochlear system: activation via electrical stimulation of the inferior colliculus. *J. Neurophysiol.* 90, 3178–3200. doi: 10.1152/jn.00537.2003

Grothe, B. (2000). The evolution of temporal processing in the medial superior olive, an auditory brainstem structure. *Prog. Neurobiol.* 61, 581–610. doi: 10.1016/s0301-0082(99)00068-4

Guinan, J. J. (2011). "Physiology of the medial and lateral olivocochlear systems" in *Auditory and vestibular efferents*. eds. D. K. Ryugo, R. R. Fay and A. N. Popper (New York, NY: Springer)

Guinan, J. J. (2018). Olivocochlear efferents: their action, effects, measurement and uses, and the impact of the new conception of cochlear mechanical responses. *Hear. Res.* 362, 38–47. doi: 10.1016/j.heares.2017.12.012

Gunawardana, Y., Fujiwara, S., Takeda, A., Woo, J., Woelk, C., and Niranjan, M. (2015). Outlier detection at the transcriptome-proteome interface. *Bioinformatics* 31, 2530–2536. doi: 10.1093/bioinformatics/btv182

Hackett, T. A., Takahata, T., and Balaram, P. (2011). *VGLUT1* and *VGLUT2* mRNA expression in the primate auditory pathway. *Hear. Res.* 274, 129–141. doi: 10.1016/j.heares.2010.11.001

Hallworth, N. E., Wilson, C. J., and Bevan, M. D. (2003). Apamin-sensitive small conductance calcium-activated potassium channels, through their selective coupling to voltage-gated calcium channels, are critical determinants of the precision, pace, and pattern of action potential generation in rat subthalamic nucleus neurons in vitro. *J. Neurosci.* 23, 7525–7542. doi: 10.1523/jneurosci.23-20-07525.2003

Haragopal, H., Mellott, J. G., Dhar, M., Kanel, A., Mafi, A., Tokar, N., et al. (2023). Tonotopic distribution and inferior colliculus projection pattern of inhibitory and excitatory cell types in the lateral superior olive of mice. *J. Comp. Neurol.* 531, 1381–1388. doi: 10.1002/cne.25515

Haragopal, H., and Winters, B. D. (2023). Principal neuron diversity in the murine lateral superior olive supports multiple sound localization strategies and segregation of information in higher processing centers. *Commun. Biol.* 6:432. doi: 10.1038/s42003-023-04802-5

Hardel, N., Harmel, N., Zolles, G., Fakler, B., and Klöcker, N. (2008). Recycling endosomes supply cardiac pacemaker channels for regulated surface expression. *Cardiovasc. Res.* 79, 52–60. doi: 10.1093/cvr/cvn062

Hardman, R. M., and Forsythe, I. D. (2009). Ether-à-go-go-related gene K^+ channels contribute to threshold excitability of mouse auditory brainstem neurons. *J. Physiol.* 587, 2487–2497. doi: 10.1113/jphysiol.2009.170548

Harris, J. J., Jolivet, R., and Attwell, D. (2012). Synaptic energy use and supply. *Neuron* 75, 762–777. doi: 10.1016/j.neuron.2012.08.019

Harrow, J., Frankish, A., Gonzalez, J. M., Tapanari, E., Diekhans, M., Kokocinski, F., et al. (2012). GENCODE: the reference human genome annotation for the ENCODE project. *Genome Res.* 22, 1760–1774. doi: 10.1101/gr.135350.111

Heffner, R. S., and Heffner, H. E. (1992). "Evolution of sound localization in mammals" in *The evolutionary biology of hearing*. eds. A. N. Popper, R. R. Fay and D. B. Webster (New York, NY: Springer)

Heinemann, S. H., Rettig, J., Wunder, F., and Pongs, O. (1995). Molecular and functional characterization of a rat brain K_vb3 potassium channel subunit. *FEBS Lett.* 377, 383–389. doi: 10.1016/0014-5793(95)01377-6

Held, H. (1893). Die zentrale Gehörleitung. *Arch. Anat. Physiol. Anat. Abt.* 17, 201–248.

Held, R. G., Liu, C., Ma, K., Ramsey, A. M., Tarr, T. B., De Nola, G., et al. (2020). Synapse and active zone assembly in the absence of presynaptic Ca^{2+} channels and Ca^{2+} entry. *Neuron* 107, 667–683.e9. doi: 10.1016/j.neuron.2020.05.032

Helfert, R. H., Bonneau, J. M., Wenthold, R. J., and Altschuler, R. A. (1989). GABA and glycine immunoreactivity in the guinea pig superior olivary complex. *Brain Res.* 501, 269–286. doi: 10.1016/0006-8993(89)90644-6

Helfert, R. H., and Schwartz, I. R. (1986). Morphological evidence for the existence of multiple neuronal classes in the cat lateral superior olivary nucleus. *J. Comp. Neurol.* 244, 533–549. doi: 10.1002/cne.902440409

Helfert, R. H., and Schwartz, I. R. (1987). Morphological features of five neuronal classes in the gerbil lateral superior olive. *Am. J. Anat.* 179, 55–69. doi: 10.1002/aja.1001790108

Herget, M., Scheibinger, M., Guo, Z., Jan, T. A., Adams, C. M., Cheng, A. G., et al. (2013). A simple method for purification of vestibular hair cells and non-sensory cells, and application for proteomic analysis. *PLoS One* 8:e66026. doi: 10.1371/journal.pone.0066026

Higo, N., Sato, A., Yamamoto, T., Nishimura, Y., Oishi, T., Murata, Y., et al. (2010). SPP1 is expressed in corticospinal neurons of the macaque sensorimotor cortex. *J. Comp. Neurol.* 518, 2633–2644. doi: 10.1002/cne.22356

Hirtz, J. J., Boesen, M., Braun, N., Deitmer, J. W., Kramer, F., Lohr, C., et al. (2011). Ca_v1.3 calcium channels are required for normal development of the auditory brainstem. *J. Neurosci.* 31, 8280–8294. doi: 10.1523/JNEUROSCI.5098-10.2011

Hirtz, J. J., Braun, N., Griesemer, D., Hannes, C., Janz, K., Löhrke, S., et al. (2012). Synaptic refinement of an inhibitory topographic map in the auditory brainstem requires functional Ca_v1.3 calcium channels. *J. Neurosci.* 32, 14602–14616. doi: 10.1523/JNEUROSCI.0765-12.2012

Hong, W., Mosca, T. J., and Luo, L. (2012). Teneurins instruct synaptic partner matching in an olfactory map. *Nature* 484, 201–207. doi: 10.1038/nature10926

Housley, G. D., and Ashmore, J. F. (1991). Direct measurement of the action of acetylcholine on isolated outer hair cells of the guinea pig cochlea. *Proc. Biol. Sci.* 244, 161–167. doi: 10.1098/rspb.1991.0065

Huang, D. W., Sherman, B. T., and Lempicki, R. A. (2009). Systematic and integrative analysis of large gene lists using DAVID bioinformatics resources. *Nat. Protoc.* 4, 44–57. doi: 10.1038/nprot.2008.211

Huang, H., and Trussell, L. O. (2011). KCNQ5 channels control resting properties and release probability of a synapse. *Nat. Neurosci.* 14, 840–847. doi: 10.1038/nn.2830

Huitron-Resendiz, S., Kristensen, M. P., Sanchez-Alavez, M., Clark, S. D., Grupke, S. L., Tyler, C., et al. (2005). Urotensin II modulates rapid eye movement sleep through activation of brainstem cholinergic neurons. *J. Neurosci.* 25, 5465–5474. doi: 10.1523/JNEUROSCI.4501-04.2005

Hull, J. M., and Isom, L. L. (2018). Voltage-gated sodium channel β subunits: the power outside the pore in brain development and disease. *Neuropharmacology* 132, 43–57. doi: 10.1016/j.neuropharm.2017.09.018

Inoue, K., Ueno, S., and Fukuda, A. (2004). Interaction of neuron-specific K^+-cl-cotransporter, KCC2, with brain-type creatine kinase. *FEBS Lett.* 564, 131–135. doi: 10.1016/S0014-5793(04)00328-X

Inoue, K., Yamada, J., Ueno, S., and Fukuda, A. (2006). Brain-type creatine kinase activates neuron-specific K+-cl- co-transporter KCC2. *J. Neurochem.* 96, 598–608. doi: 10.1111/j.1471-4159.2005.03560.x

Ito, T., Bishop, D. C., and Oliver, D. L. (2011). Expression of glutamate and inhibitory amino acid vesicular transporters in the rodent auditory brainstem. *J. Comp. Neurol.* 519, 316–340. doi: 10.1002/cne.22521

Ito, T., and Oliver, D. L. (2010). Origins of glutamatergic terminals in the inferior colliculus identified by retrograde transport and expression of VGLUT1 and VGLUT2 genes. *Front. Neuroanat.* 4:135. doi: 10.3389/fnana.2010.00135

Jackson, A. C., and Nicoll, R. A. (2011). The expanding social network of ionotropic glutamate receptors: TARPs and other transmembrane auxiliary subunits. *Neuron* 70, 178–199. doi: 10.1016/j.neuron.2011.04.007

Jacobi, E., and von Engelhardt, J. (2017). Diversity in AMPA receptor complexes in the brain. *Curr. Opin. Neurobiol.* 45, 32–38. doi: 10.1016/j.conb.2017.03.001

Jacobi, E., and von Engelhardt, J. (2021). Modulation of information processing by AMPA receptor auxiliary subunits. *J. Physiol.* 599, 471–483. doi: 10.1113/jp276698

Jiang, R., Prell, C., and Lönnerdal, B. (2019). Milk osteopontin promotes brain development by up-regulating osteopontin in the brain in early life. *FASEB J.* 33, 1681–1694. doi: 10.1096/fj.201701290RR

Jiang, X., Lautermilch, N. J., Watari, H., Westenbroek, R. E., Scheuer, T., and Catterall, W. A. (2008). Modulation of Ca_V2.1 channels by Ca^{2+}/calmodulin-dependent protein kinase II bound to the C-terminal domain. *Proc. Natl. Acad. Sci. U. S. A.* 105, 341–346. doi: 10.1073/pnas.0710213105

Jiao, S., Johnson, K., Moreno, C., Yano, S., and Holmgren, M. (2021). Comparative description of the mRNA expression profile of Na^+/K^+-ATPase isoforms in adult mouse nervous system. *J. Comp. Neurol.* 530, 627–647. doi: 10.1002/cne.25234

Johny, M. B., Yang, P. S., Bazzazi, H., and Yue, D. T. (2013). Dynamic switching of calmodulin interactions underlies Ca^{2+} regulation of Ca_V1.3 channels. *Nat. Commun.* 4:1717. doi: 10.1038/ncomms2727

Jurkovicova-Tarabova, B., Griesemer, D., Pirone, A., Sinnegger-Brauns, M. J., Striessnig, J., and Friauf, E. (2012). Repertoire of high voltage-activated Ca^{2+} channels in the lateral superior olive: functional analysis in wild-type, Ca_v $1.3^{-/-}$, and Ca_v1.2DHP$^{-/-}$ mice. *J. Neurophysiol.* 108, 365–379. doi: 10.1152/jn.00948.2011

Kaiser, A., Alexandrova, O., and Grothe, B. (2011). Urocortin-expressing olivocochlear neurons exhibit tonotopic and developmental changes in the auditory brainstem and in the innervation of the cochlea. *J. Comp. Neurol.* 519, 2758–2778. doi: 10.1002/cne.22650

Kalish, B. T., Barkat, T. R., Diel, E. E., Zhang, E. J., Greenberg, M. E., and Hensch, T. K. (2020). Single-nucleus RNA sequencing of mouse auditory cortex reveals critical period triggers and brakes. *Proc. Natl. Acad. Sci. U. S. A.* 117, 11744–11752. doi: 10.1073/pnas.1920433117

Kandler, K., and Friauf, E. (1995). Development of electrical membrane properties and discharge characteristics of superior olivary complex neurons in fetal and postnatal rats. *Eur. J. Neurosci.* 7, 1773–1790. doi: 10.1111/j.1460-9568.1995.tb00697.x

Karcz, A., Allen, P. D., Walton, J., Ison, J. R., and Kopp-Scheinpflug, C. (2015). Auditory deficits of Kcna1 deletion are similar to those of a monaural hearing impairment. *Hear. Res.* 321, 45–51. doi: 10.1016/j.heares.2015.01.003

Karcz, A., Hennig, M. H., Robbins, C. A., Tempel, B. L., Rübsamen, R., and Kopp-Scheinpflug, C. (2011). Low-voltage activated Kv1.1 subunits are crucial for the processing of sound source location in the lateral superior olive in mice. *J. Physiol.* 589, 1143–1157. doi: 10.1113/jphysiol.2010.203331

Karis, A., Pata, I., Van Doorninck, J. H., Grosveld, F., De Zeeuw, C. I., De Caprona, D., et al. (2001). Transcription factor GATA-3 alters pathway selection of olivocochlear neurons and affects morphogenesis of the ear. *J. Comp. Neurol.* 429, 615–630. doi: 10.1002/1096-9861(20010122)429:4<615::aid-cne8>3.0.co;2-f

Kim, K. X., and Rutherford, M. A. (2016). Maturation of Na_V and K_V channel topographies in the auditory nerve spike initiator before and after developmental onset of hearing function. *J. Neurosci.* 36, 2111–2118. doi: 10.1523/jneurosci.3437-15.2016

Kiselev, V. Y., Kirschner, K., Schaub, M. T., Andrews, T., Yiu, A., Chandra, T., et al. (2017). SC3: consensus clustering of single-cell RNA-seq data. *Nat. Methods* 14, 483–486. doi: 10.1038/nmeth.4236

Kitcher, S. R., Pederson, A. M., and Weisz, C. J. C. (2022). Diverse identities and sites of action of cochlear neurotransmitters. *Hear. Res.* 419:108278. doi: 10.1016/j.heares.2021.108278

Kobak, D., and Berens, P. (2019). The art of using t-SNE for single-cell transcriptomics. *Nat. Commun.* 10:5416. doi: 10.1038/s41467-019-13056-x

Koehl, A., Schmidt, N., Rieger, A., Pilgrim, S. M., Letunic, I., Bork, P., et al. (2004). Gene expression profiling of the rat superior olivary complex using serial analysis of gene expression. *Eur. J. Neurosci.* 20, 3244–3258. doi: 10.1111/j.1460-9568.2004.03791.x

Kole, M. H., Letzkus, J. J., and Stuart, G. J. (2007). Axon initial segment Kv1 channels control axonal action potential waveform and synaptic efficacy. *Neuron* 55, 633–647. doi: 10.1016/j.neuron.2007.07.031

Kolla, L., Kelly, M. C., Mann, Z. F., Anaya-Rocha, A., Ellis, K., Lemons, A., et al. (2020). Characterization of the development of the mouse cochlear epithelium at the single cell level. *Nat. Commun.* 11:2389. doi: 10.1038/s41467-020-16113-y

Kolson, D. R., Wan, J., Wu, J., Dehoff, M., Brandebura, A. N., Qian, J., et al. (2016). Temporal patterns of gene expression during calyx of Held development. *Dev. Neurobiol.* 76, 166–189. doi: 10.1002/dneu.22306

Kotak, V. C., Dimattina, C., and Sanes, D. H. (2001). $GABA_B$ and Trk receptor signaling mediates long-lasting inhibitory synaptic depression. *J. Neurophysiol.* 86, 536–540. doi: 10.1152/jn.2001.86.1.536

Krächan, E. G., Fischer, A. U., Franke, J., and Friauf, E. (2017). Synaptic reliability and temporal precision are achieved via high quantal content and effective replenishment: auditory brainstem versus hippocampus. *J. Physiol.* 595, 839–864. doi: 10.1113/JP272799

Kresse, A., Jacobowitz, D. M., and Skofitsch, G. (1995). Detailed mapping of CGRP mRNA expression in the rat central nervous system: comparison with previous immunocytochemical findings. *Brain Res. Bull.* 36, 261–274. doi: 10.1016/0361-9230(94)00201-b

Le Prell, C. G., Hughes, L. F., and Bledsoe, S. C. Jr. (2014). Dynorphin release by the lateral olivocochlear efferents may inhibit auditory nerve activity: a cochlear drug delivery study. *Neurosci. Lett.* 571, 17–22. doi: 10.1016/j.neulet.2014.04.024

Le Prell, C. G., Hughes, L. F., Dolan, D. F., and Bledsoe, S. C. Jr. (2021). Effects of calcitonin-gene-related-peptide on auditory nerve activity. *Front. Cell Dev. Biol.* 9:752963. doi: 10.3389/fcell.2021.752963

Leamey, C. A., and Sawatari, A. (2014). The teneurins: new players in the generation of visual topography. *Semin. Cell Dev. Biol.* 35, 173–179. doi: 10.1016/j.semcdb.2014.08.007

Leao, K. E., Leao, R. N., Sun, H., Fyffe, R. E., and Walmsley, B. (2006). Hyperpolarization-activated currents are differentially expressed in mice brainstem auditory nuclei. *J. Physiol.* 576, 849–864. doi: 10.1113/jphysiol.2006.114702

Leao, R. M., Kushmerick, C., Pinaud, R., Renden, R., Li, G. L., Taschenberger, H., et al. (2005). Presynaptic Na^+ channels: locus, development, and recovery from inactivation at a high-fidelity synapse. *J. Neurosci.* 25, 3724–3738. doi: 10.1523/JNEUROSCI.3983-04.2005

Lee, A., Westenbroek, R. E., Haeseleer, F., Palczewski, K., Scheuer, T., and Catterall, W. A. (2002). Differential modulation of $Ca_v2.1$ channels by calmodulin and Ca^{2+}-binding protein 1. *Nat. Neurosci.* 5, 210–217. doi: 10.1038/nn805

Lee, J. S., Ho, W. K., and Lee, S. H. (2010). Post-tetanic increase in the fast-releasing synaptic vesicle pool at the expense of the slowly releasing pool. *J. Gen. Physiol.* 136, 259–272. doi: 10.1085/jgp.201010437

Lee, M. Y., Choi, J. S., Lim, S. W., Cha, J. H., Chun, M. H., and Chung, J. W. (2001). Expression of osteopontin mRNA in developing rat brainstem and cerebellum. *Cell Tissue Res.* 306, 179–185. doi: 10.1007/s004410100456

Leijon, S., and Magnusson, A. K. (2014). Physiological characterization of vestibular efferent brainstem neurons using a transgenic mouse model. *PLoS One* 9:e98277. doi: 10.1371/journal.pone.0098277

Levitan, I. B. (1999). It is calmodulin after all! Mediator of the calcium modulation of multiple ion channels. *Neuron* 22, 645–648. doi: 10.1016/S0896-6273(00)80722-9

Li, B., and Dewey, C. N. (2011). RSEM: accurate transcript quantification from RNA-Seq data with or without a reference genome. *BMC Bioinformatics* 12:323. doi: 10.1186/1471-2105-12-323

Li, H., Khirug, S., Cai, C., Ludwig, A., Blaesse, P., Kolikova, J., et al. (2007). KCC2 interacts with the dendritic cytoskeleton to promote spine development. *Neuron* 56, 1019–1033. doi: 10.1016/j.neuron.2007.10.039

Li, S., and Sheng, Z. H. (2021). Energy matters: presynaptic metabolism and the maintenance of synaptic transmission. *Nat. Rev. Neurosci.* 23, 4–22. doi: 10.1038/s41583-021-00535-8

Liao, S., Liu, T., Yang, R., Tan, W., Gu, J., and Deng, M. (2023). Structure and function of sodium channel Nav1.3 in neurological disorders. *Cell. Mol. Neurobiol.* 43, 575–584. doi: 10.1007/s10571-022-01211-w

Liao, Y., Smyth, G. K., and Shi, W. (2014). featureCounts: an efficient general purpose program for assigning sequence reads to genomic features. *Bioinformatics* 30, 923–930. doi: 10.1093/bioinformatics/btt656

Liberman, M. C. (1990). Effects of chronic cochlear de-efferentation on auditory-nerve response. *Hear. Res.* 49, 209–223. doi: 10.1016/0378-5955(90)90105-x

Lin, Y. S., Chen, C. M., Soong, B. W., Wu, Y. R., Chen, H. M., Yeh, W. Y., et al. (2011). Dysregulated brain creatine kinase is associated with hearing impairment in mouse models of Huntington disease. *J. Clinical. Invest.* 121, 1519–1523. doi: 10.1172/JCI43220

Lipstein, N., Sakaba, T., Cooper, B. H., Lin, K. H., Strenzke, N., Ashery, U., et al. (2013). Dynamic control of synaptic vesicle replenishment and short-term plasticity by Ca^{2+}-calmodulin-Munc13-1 signaling. *Neuron* 79, 82–96. doi: 10.1016/j.neuron.2013.05.011

Liu, Q., and Wong-Riley, M. T. (2013). Postnatal development of glycine receptor subunits alpha1, alpha2, alpha3, and beta immunoreactivity in multiple brain stem respiratory-related nuclear groups of the rat. *Brain Res.* 1538, 1–16. doi: 10.1016/j.brainres.2013.09.028

Liu, Y., Beyer, A., and Aebersold, R. (2016). On the dependency of cellular protein levels on mRNA abundance. *Cell* 165, 535–550. doi: 10.1016/j.cell.2016.03.014

Löhrke, S., and Friauf, E. (2002). Developmental distribution of the glutamate receptor subunits KA2, GluR6/7, and delta 1/2 in the rat medial nucleus of the trapezoid body. A quantitative image analysis. *Cell Tissue Res.* 308, 19–33. doi: 10.1007/s00441-002-0533-z

Lujan, B. J., Singh, M., Singh, A., and Renden, R. B. (2021). Developmental shift to mitochondrial respiration for energetic support of sustained transmission during maturation at the calyx of Held. *J. Neurophysiol.* 126, 976–996. doi: 10.1152/jn.00333.2021

Lun, A. T., Mccarthy, D. J., and Marioni, J. C. (2016). A step-by-step workflow for low-level analysis of single-cell RNA-seq data with Bioconductor. *F1000Res* 5:2122. doi: 10.12688/f1000research.9501.2

Macaulay, I. C., and Voet, T. (2014). Single cell genomics: advances and future perspectives. *PLoS Genet.* 10:e1004126. doi: 10.1371/journal.pgen.1004126

Main, M. J., Cryan, J. E., Dupere, J. R., Cox, B., Clare, J. J., and Burbidge, S. A. (2000). Modulation of KCNQ2/3 potassium channels by the novel anticonvulsant retigabine. *Mol. Pharmacol.* 58, 253–262. doi: 10.1124/mol.58.2.253

Maison, S. F., Adams, J. C., and Liberman, M. C. (2003). Olivocochlear innervation in the mouse: immunocytochemical maps, crossed versus uncrossed contributions, and transmitter colocalization. *J. Comp. Neurol.* 455, 406–416. doi: 10.1002/cne.10490

Maison, S. F., Pyott, S. J., Meredith, A. L., and Liberman, M. C. (2013). Olivocochlear suppression of outer hair cells in vivo: evidence for combined action of BK and SK2 channels throughout the cochlea. *J. Neurophysiol.* 109, 1525–1534. doi: 10.1152/jn.00924.2012

Maison, S. F., Rosahl, T. W., Homanics, G. E., and Liberman, M. C. (2006). Functional role of GABAergic innervation of the cochlea: phenotypic analysis of mice lacking $GABA_A$ receptor subunits a1, a2, a5, a6, b2, b3, or d. *J. Neurosci.* 26, 10315–10326. doi: 10.1523/jneurosci.2395-06.2006

Man, H. Y. (2011). GluA2-lacking, calcium-permeable AMPA receptors--inducers of plasticity? *Curr. Opin. Neurobiol.* 21, 291–298. doi: 10.1016/j.conb.2011.01.001

Manis, P. B. (2008). "Biophysical specializations of neurons that encode timing" in *The senses: a comprehensive reference*. eds. P. Dallos and D. Oertel (Oxford: Elsevier)

Mcallister, G., Amara, S. G., and Lerner, M. R. (1988). Tissue-specific expression and cDNA cloning of small nuclear ribonucleoprotein-associated polypeptide N. *Proc. Natl. Acad. Sci. USA* 85, 5296–5300. doi: 10.1073/pnas.85.14.5296

Mellott, J. G., Dhar, M., Mafi, A., Tokar, N., and Winters, B. D. (2022). Tonotopic distribution and inferior colliculus projection pattern of inhibitory and excitatory cell types in the lateral superior olive of Mongolian gerbils. *J. Comp. Neurol.* 530, 506–517. doi: 10.1002/cne.25226

Meyer, D. J., Diaz-Garcia, C. M., Nathwani, N., Rahman, M., and Yellen, G. (2022). The Na^+/K^+ pump dominates control of glycolysis in hippocampal dentate granule cells. *eLife* 11:e81645. doi: 10.7554/eLife.81645

Mi, D., Li, Z., Lim, L., Li, M., Moissidis, M., Yang, Y., et al. (2018). Early emergence of cortical interneuron diversity in the mouse embryo. *Science* 360, 81–85. doi: 10.1126/science.aar6821

Missler, M., and Südhof, T. C. (1998). Neurexophilins form a conserved family of neuropeptide-like glycoproteins. *J. Neurosci.* 18, 3630–3638. doi: 10.1523/jneurosci.18-10-03630.1998

Miyazaki, K., Mapendano, C. K., Fuchigami, T., Kondo, S., Ohta, T., Kinoshita, A., et al. (2009). Developmentally dynamic changes of DNA methylation in the mouse Snurf/Snrpn gene. *Gene* 432, 97–101. doi: 10.1016/j.gene.2008.11.019

Mochizuki, T., Lemmink, H. H., Mariyama, M., Antignac, C., Gubler, M. C., Pirson, Y., et al. (1994). Identification of mutations in the a3(IV) and a4(IV) collagen genes in autosomal recessive Alport syndrome. *Nat. Genet.* 8, 77–82. doi: 10.1038/ng0994-77

Moritz, C. P., Eckstein, E., Tenzer, S., and Friauf, E. (2015). Neuroproteomics in the auditory brainstem: candidate proteins for ultrafast and precise information processing. *Mol. Cell. Neurosci.* 64, 9–23. doi: 10.1016/j.mcn.2014.08.006

Müller, N. I. C., Paulussen, I., Hofmann, L. N., Fisch, J. O., Singh, A., and Friauf, E. (2022). Development of synaptic fidelity and action potential robustness at an inhibitory sound localization circuit: effects of otoferlin-related deafness. *J. Physiol.* 600, 2461–2497. doi: 10.1113/JP280403

Müller, N. I. C., Sonntag, M., Maraslioglu, A., Hirtz, J. J., and Friauf, E. (2019). Topographic map refinement and synaptic strengthening of a sound localization circuit require spontaneous peripheral activity. *J. Physiol.* 597, 5469–5493. doi: 10.1113/jp277757

Müller, U., and Barr-Gillespie, P. G. (2015). New treatment options for hearing loss. *Nat. Rev. Drug Discov.* 14, 346–365. doi: 10.1038/nrd4533

Nabel, A. L., Callan, A. R., Gleiss, S. A., Kladisios, N., Leibold, C., and Felmy, F. (2019). Distinct distribution patterns of potassium channel sub-units in somato-dendritic compartments of neurons of the medial superior olive. *Front. Cell. Neurosci.* 13:38. doi: 10.3389/fncel.2019.00038

Nakagawa, H., Sato, K., Shiraishi, Y., Kuriyama, H., and Altschuler, R. A. (2000). NMDAR1 isoforms in the rat superior olivary complex and changes after unilateral cochlear ablation. *Brain Res. Dev. Brain Res.* 77, 246–257. doi: 10.1016/s0169-328x(00)00059-0

Nakamura, T., Yamashita, T., Saitoh, N., and Takahashi, T. (2008). Developmental changes in calcium/calmodulin-dependent inactivation of

calcium currents at the rat calyx of Held. *J. Physiol.* 586, 2253–2261. doi: 10.1113/jphysiol.2007.142521

Nakamura, Y., Morrow, D. H., Modgil, A., Huyghe, D., Deeb, T. Z., Lumb, M. J., et al. (2016). Proteomic characterization of inhibitory synapses using a novel pHluorin-tagged gamma-aminobutyric acid receptor, type a ($GABA_A$), a2 subunit knock-in mouse. *J. Biol. Chem.* 291, 12394–12407. doi: 10.1074/jbc.M116.724443

Nam, S. M., Seo, J. S., Nahm, S. S., and Chang, B. J. (2019). Effects of ascorbic acid on osteopontin expression and axonal myelination in the developing cerebellum of lead-exposed rat pups. *Int. J. Environ. Res. Public Health* 16:983. doi: 10.3390/ijerph16060983

Napolitano, L. M. R., Torre, V., and Marchesi, A. (2021). CNG channel structure, function, and gating: a tale of conformational flexibility. *Pflugers Arch.* 473, 1423–1435. doi: 10.1007/s00424-021-02610-6

Nicholls, R. D., Saitoh, S., and Horsthemke, B. (1998). Imprinting in Prader-Willi and Angelman syndromes. *Trends Genet.* 14, 194–200. doi: 10.1016/s0168-9525(98)01432-2

Niculescu, D., Hirdes, W., Hornig, S., Pongs, O., and Schwarz, J. R. (2013). Erg potassium currents of neonatal mouse Purkinje cells exhibit fast gating kinetics and are inhibited by mGluR1 activation. *J. Neurosci.* 33, 16729–16740. doi: 10.1523/JNEUROSCI.5523-12.2013

Nie, L., Wu, G., Culley, D. E., Scholten, J. C., and Zhang, W. (2007). Integrative analysis of transcriptomic and proteomic data: challenges, solutionsa and applications. *Crit. Rev. Biotechnol.* 27, 63–75. doi: 10.1080/07388550701334212

Nieto-Estévez, V., Defterali, Ç., and Vicario-Abejón, C. (2016). IGF-I: a key growth factor that regulates neurogenesis and synaptogenesis from embryonic to adult stages of the brain. *Front. Neurosci.* 10:52. doi: 10.3389/fnins.2016.00052

Nortley, R., and Attwell, D. (2017). Control of brain energy supply by astrocytes. *Curr. Opin. Neurobiol.* 47, 80–85. doi: 10.1016/j.conb.2017.09.012

Nothacker, H. P., and Clark, S. (2005). From heart to mind. The urotensin II system and its evolving neurophysiological role. *FEBS J.* 272, 5694–5702. doi: 10.1111/j.1742-4658.2005.04983.x

Nothwang, H. G., Koehl, A., and Friauf, E. (2006). Comparative gene expression analysis reveals a characteristic molecular profile of the superior olivary complex. *Anat Rec A Discov Mol Cell Evol Biol* 288A, 409–423. doi: 10.1002/ar.a.20301

Oak, M. H., and Yi, E. (2014). Voltage-gated K^+ channels contributing to temporal precision at the inner hair cell-auditory afferent nerve fiber synapses in the mammalian cochlea. *Arch. Pharm. Res.* 37, 821–833. doi: 10.1007/s12272-014-0411-8

Oertel, D. (1997). Encoding of timing in the brain stem auditory nuclei of vertebrates. *Neuron* 19, 959–962. doi: 10.1016/s0896-6273(00)80388-8

Oertel, D. (2009). A team of potassium channels tunes up auditory neurons. *J. Physiol.* 587, 2417–2418. doi: 10.1113/jphysiol.2009.173575

Ollo, C., and Schwartz, I. R. (1979). The superior olivary complex in C57BL/6 mice. *Am. J. Anat.* 155, 349–373. doi: 10.1002/aja.1001550306

Owrutsky, Z. L., Benichoux, V., and Tollin, D. J. (2021). "Binaural hearing by the mammalian auditory brainstem: joint coding of interaural level and time differences by the lateral superior olive" in *Binaural hearing*. eds. R. Y. Litovsky, M. J. Goupell, R. R. Fay and A. N. Popper (Cham: Springer)

Ozçelik, T., Leff, S., Robinson, W., Donlon, T., Lalande, M., Sanjines, E., et al. (1992). Small nuclear ribonucleoprotein polypeptide N (SNRPN), an expressed gene in the Prader-Willi syndrome critical region. *Nat. Genet.* 2, 265–269. doi: 10.1038/ng1292-265

Palacios-Filardo, J., Aller, M. I., and Lerma, J. (2016). Synaptic targeting of kainate receptors. *Cereb. Cortex* 26, 1464–1472. doi: 10.1093/cercor/bhu244

Pastore, M., and Calcagni, A. (2019). Measuring distribution similarities between samples: a distribution-free overlapping index. *Front. Psychol.* 10:1089. doi: 10.3389/fpsyg.2019.01089

Pätz, C., Console-Meyer, L., and Felmy, F. (2022). Structural arrangement of auditory brainstem nuclei in the bats Phyllostomus discolor and *Carollia perspicillata*. *J. Comp. Neurol.* 530, 2762–2781. doi: 10.1002/cne.25355

Pellerin, L., and Magistretti, P. J. (2012). Sweet sixteen for ANLS. *J. Cereb. Blood Flow Metab.* 32, 1152–1166. doi: 10.1038/jcbfm.2011.149

Perrot, X., and Collet, L. (2014). Function and plasticity of the medial olivocochlear system in musicians: a review. *Hear. Res.* 308, 27–40. doi: 10.1016/j.heares.2013.08.010

Petitpré, C., Wu, H., Sharma, A., Tokarska, A., Fontanet, P., Wang, Y., et al. (2018). Neuronal heterogeneity and stereotyped connectivity in the auditory afferent system. *Nat. Commun.* 9:3691. doi: 10.1038/s41467-018-06033-3

Petralia, R. S., Wang, Y. X., and Wenthold, R. J. (1994). Histological and ultrastructural localization of the kainate receptor subunits, KA2 and GluR6/7, in the rat nervous system using selective antipeptide antibodies. *J. Comp. Neurol.* 349, 85–110. doi: 10.1002/cne.903490107

Petrenko, A. G., Ullrich, B., Missler, M., Krasnoperov, V., Rosahl, T. W., and Südhof, T. C. (1996). Structure and evolution of neurexophilin. *J. Neurosci.* 16, 4360–4369. doi: 10.1523/jneurosci.16-14-04360.1996

Picelli, S., Bjorklund, A. K., Faridani, O. R., Sagasser, S., Winberg, G., and Sandberg, R. (2013). Smart-seq2 for sensitive full-length transcriptome profiling in single cells. *Nat. Methods* 10, 1096–1098. doi: 10.1038/nmeth.2639

Pilati, N., Linley, D. M., Selvaskandan, H., Uchitel, O., Hennig, M. H., Kopp-Scheinpflug, C., et al. (2016). Acoustic trauma slows AMPA receptor-mediated EPSCs in the auditory brainstem, reducing GluA4 subunit expression as a mechanism to rescue binaural function. *J. Physiol.* 594, 3683–3703. doi: 10.1113/JP271929

Pirker, S., Schwarzer, C., Wieselthaler, A., Sieghart, W., and Sperk, G. (2000). $GABA_A$ receptors: immunocytochemical distribution of 13 subunits in the adult rat brain. *Neuroscience* 101, 815–850. doi: 10.1016/s0306-4522(00)00442-5

Platzer, J., Engel, J., Schrott-Fischer, A., Stephan, K., Bova, S., Chen, H., et al. (2000). Congenital deafness and sinoatrial node dysfunction in mice lacking class D L-type Ca^{2+} channels. *Cell* 102, 89–97. doi: 10.1016/s0092-8674(00)00013-1

Pongs, O., and Schwarz, J. R. (2010). Ancillary subunits associated with voltage-dependent K^+ channels. *Physiol. Rev.* 90, 755–796. doi: 10.1152/physrev.00020.2009

Reijntjes, D. O. J., and Pyott, S. J. (2016). The afferent signaling complex: regulation of type I spiral ganglion neuron responses in the auditory periphery. *Hear. Res.* 336, 1–16. doi: 10.1016/j.heares.2016.03.011

Rhodes, K. J., Monaghan, M. M., Barrezueta, N. X., Nawoschik, S., Bekele-Arcuri, Z., Matos, M. F., et al. (1996). Voltage-gated K^+ channel b subunits: expression and distribution of Kvb1 and Kvb2 in adult rat brain. *J. Neurosci.* 16, 4846–4860. doi: 10.1523/jneurosci.16-16-04846.1996

Ribeiro Ferreira, I., Dos Santos, D., Cunha, W., Henrique Ferreira Gomes, L., Azevedo Cintra, H., Lopes Cabral Guimaraes Fonseca, L., et al. (2019). A rapid and accurate methylation-sensitive high-resolution melting analysis assay for the diagnosis of Prader Willi and Angelman patients. *Mol. Genet. Genomic Med.* 7:e637. doi: 10.1002/mgg3.637

Ricoy, U. M., and Frerking, M. E. (2014). Distinct roles for Cav2.1-2.3 in activity-dependent synaptic dynamics. *J. Neurophysiol.* 111, 2404–2413. doi: 10.1152/jn.00335.2013

Rietzel, H. J., and Friauf, E. (1998). Neuron types in the rat lateral superior olive and developmental changes in the complexity of their dendritic arbors. *J. Comp. Neurol.* 390, 20–40. doi: 10.1002/(SICI)1096-9861(19980105)390:1%3C20::AID-CNE3%3E3.0.CO;2-S

Rigby, M., Cull-Candy, S. G., and Farrant, M. (2015). Transmembrane AMPAR regulatory protein γ-2 is required for the modulation of GABA release by presynaptic AMPARs. *J. Neurosci.* 35, 4203–4214. doi: 10.1523/jneurosci.4075-14.2015

Ring, B. Z., Cordes, S. P., Overbeek, P. A., and Barsh, G. S. (2000). Regulation of mouse lens fiber cell development and differentiation by the Maf gene. *Development* 127, 307–317. doi: 10.1242/dev.127.2.307

Robbins, C. A., and Tempel, B. L. (2012). Kv1.1 and Kv1.2: similar channels, different seizure models. *Epilepsia* 53 Suppl 1, 134–141. doi: 10.1111/j.1528-1167.2012.03484.x

Robbins, J. (2001). KCNQ potassium channels: physiology, pathophysiology, and pharmacology. *Pharmacol. Ther.* 90, 1–19. doi: 10.1016/s0163-7258(01)00116-4

Robertson, D., and Mulders, W. H. (2000). Distribution and possible functional roles of some neuroactive peptides in the mammalian superior olivary complex. *Microsc. Res. Tech.* 51, 307–317. doi: 10.1002/1097-0029(20001115)51:4<307::AID-JEMT2>3.0.CO;2-4

Romero, G. E., and Trussell, L. O. (2022). Central circuitry and function of the cochlear efferent systems. *Hear. Res.* 425:108516. doi: 10.1016/j.heares.2022.108516

Rosenbaum, D. M., Rasmussen, S. G., and Kobilka, B. K. (2009). The structure and function of G-protein-coupled receptors. *Nature* 459, 356–363. doi: 10.1038/nature08144

Rosenberger, M. H., Fremouw, T., Casseday, J. H., and Covey, E. (2003). Expression of the Kv1.1 ion channel subunit in the auditory brainstem of the big brown bat, *Eptesicus fuscus*. *J. Comp. Neurol.* 462, 101–120. doi: 10.1002/cne.10713

Rothman, J. S., and Manis, P. B. (2003). The roles potassium currents play in regulating the electrical activity of ventral cochlear nucleus neurons. *J. Neurophysiol.* 89, 3097–3113. doi: 10.1152/jn.00127.2002

Rubio, M. E., Matsui, K., Fukazawa, Y., Kamasawa, N., Harada, H., Itakura, M., et al. (2017). The number and distribution of AMPA receptor channels containing fast kinetic GluA3 and GluA4 subunits at auditory nerve synapses depend on the target cells. *Brain Struct. Funct.* 222, 3375–3393. doi: 10.1007/s00429-017-1408-0

Rubio, M. E., and Wenthold, R. J. (1997). Glutamate receptors are selectively targeted to postsynaptic sites in neurons. *Neuron* 18, 939–950. doi: 10.1016/s0896-6273(00)80333-5

Ryan, A. F., Keithley, E. M., Wang, Z. X., and Schwartz, I. R. (1990). Collaterals from lateral and medial olivocochlear efferent neurons innervate different regions of the cochlear nucleus and adjacent brainstem. *J. Comp. Neurol.* 300, 572–582. doi: 10.1002/cne.903000410

Sacco, T., Bruno, A., Wanke, E., and Tempia, F. (2003). Functional roles of an ERG current isolated in cerebellar Purkinje neurons. *J. Neurophysiol.* 90, 1817–1828. doi: 10.1152/jn.00104.2003

Sachyani, D., Dvir, M., Strulovich, R., Tria, G., Tobelaim, W., Peretz, A., et al. (2014). Structural basis of a Kv7.1 potassium channel gating module: studies of the intracellular c-terminal domain in complex with calmodulin. *Structure* 22, 1582–1594. doi: 10.1016/j.str.2014.07.016

Safieddine, S., and Eybalin, M. (1992). Triple immunofluorescence evidence for the coexistence of acetylcholine, enkephalins and calcitonin gene-related peptide within efferent (olivocochlear) neurons of rats and guinea-pigs. *Eur. J. Neurosci.* 4, 981–992. doi: 10.1111/j.1460-9568.1992.tb00124.x

Safieddine, S., Prior, A. M., and Eybalin, M. (1997). Choline acetyltransferase, glutamate decarboxylase, tyrosine hydroxylase, calcitonin gene-related peptide and opioid peptides coexist in lateral efferent neurons of rat and guinea-pig. *Eur. J. Neurosci.* 9, 356–367. doi: 10.1111/j.1460-9568.1997.tb01405.x

Saimi, Y., and Kung, C. (2002). Calmodulin as an ion channel subunit. *Annu. Rev. Physiol.* 64, 289–311. doi: 10.1146/annurev.physiol.64.100301.111649

Saint Marie, R. L., and Baker, R. A. (1990). Neurotransmitter-specific uptake and retrograde transport of [3H]glycine from the inferior colliculus by ipsilateral projections of the superior olivary complex and nuclei of the lateral lemniscus. *Brain Res.* 524, 244–253. doi: 10.1016/0006-8993(90)90698-b

Saint Marie, R. L., Morest, D. K., and Brandon, C. J. (1989). The form and distribution of GABAergic synapses on the principal cell types of the ventral cochlear nucleus of the cat. *Hear. Res.* 42, 97–112. doi: 10.1016/0378-5955(89)90120-2

Salin-Cantegrel, A., Shekarabi, M., Holbert, S., Dion, P., Rochefort, D., Laganière, J., et al. (2008). HMSN/ACC truncation mutations disrupt brain-type creatine kinase-dependant activation of K^+/cl^- co-transporter 3. *Hum. Mol. Genet.* 17, 2703–2711. doi: 10.1093/hmg/ddn172

Sanes, D. H. (1990). An in vitro analysis of sound localization mechanisms in the gerbil lateral superior olive. *J. Neurosci.* 10, 3494–3506. doi: 10.1523/JNEUROSCI.10-11-03494.1990

Satija, R., Farrell, J. A., Gennert, D., Schier, A. F., and Regev, A. (2015). Spatial reconstruction of single-cell gene expression data. *Nat. Biotechnol.* 33, 495–502. doi: 10.1038/nbt.3192

Scheffer, D. I., Shen, J., Corey, D. P., and Chen, Z. Y. (2015). Gene expression by mouse inner ear hair cells during development. *J. Neurosci.* 35, 6366–6380. doi: 10.1523/JNEUROSCI.5126-14.2015

Schwanhäusser, B., Busse, D., Li, N., Dittmar, G., Schuchhardt, J., Wolf, J., et al. (2011). Global quantification of mammalian gene expression control. *Nature* 473, 337–342. doi: 10.1038/nature10098

Scott, L. L., Mathews, P. J., and Golding, N. L. (2010). Perisomatic voltage-gated sodium channels actively maintain linear synaptic integration in principal neurons of the medial superior olive. *J. Neurosci.* 30, 2039–2050. doi: 10.1523/JNEUROSCI.2385-09.2010

Selvaraju, R., Bernasconi, L., Losberger, C., Graber, P., Kadi, L., Avellana-Adalid, V., et al. (2004). Osteopontin is upregulated during in vivo demyelination and remyelination and enhances myelin formation in vitro. *Mol. Cell. Neurosci.* 25, 707–721. doi: 10.1016/j.mcn.2003.12.014

Sewell, W. F. (2011). "Pharmacology and neurochemistry of olivocochlear efferents" in *Auditory and vestibular efferents*. eds. D. K. Ryugo, R. R. Fay and A. N. Popper (New York, NY: Springer)

Shepard, P. D., Canavier, C. C., and Levitan, E. S. (2007). Ether-a-go-go-related gene potassium channels: what's all the buzz about? *Schizophr. Bull.* 33, 1263–1269. doi: 10.1093/schbul/sbm106

Sherman, B. T., Hao, M., Qiu, J., Jiao, X., Baseler, M. W., Lane, H. C., et al. (2022). DAVID: a web server for functional enrichment analysis and functional annotation of gene lists (2021 update). *Nucleic Acid Res.* 50, W216–W221. doi: 10.1093/nar/gkac194

Shin, J. B., Streijger, F., Beynon, A., Peters, T., Gadzala, L., Mcmillen, D., et al. (2007). Hair bundles are specialized for ATP delivery via creatine kinase. *Neuron* 53, 371–386. doi: 10.1016/j.neuron.2006.12.021

Simmons, D. D. (2002). Development of the inner ear efferent system across vertebrate species. *J. Neurobiol.* 53, 228–250. doi: 10.1002/neu.10130

Sobkowicz, H. M., and Slapnick, S. M. (1994). The efferents interconnecting auditory inner hair cells. *Hear. Res.* 75, 81–92. doi: 10.1016/0378-5955(94)90059-0

Sobkowicz, H. M., Slapnick, S. M., Nitecka, L. M., and August, B. K. (1997). Compound synapses within the GABAergic innervation of the auditory inner hair cells in the adolescent mouse. *J. Comp. Neurol.* 377, 423–442. doi: 10.1002/(sici)1096-9861(19970120)377:3<423::Aid-cne9>3.0.Co;2-4

Sokoloff, L. (1981). Localization of functional activity in the central nervous system by measurement of glucose utilization with radioactive deoxyglucose. *J. Cereb. Blood Flow Metab.* 1, 7–36. doi: 10.1038/jcbfm.1981.4

Soldovieri, M. V., Miceli, F., and Taglialatela, M. (2011). Driving with no brakes: molecular pathophysiology of Kv7 potassium channels. *Physiology* 26, 365–376. doi: 10.1152/physiol.00009.2011

Sterenborg, J. C., Pilati, N., Sheridan, C. J., Uchitel, O. D., Forsythe, I. D., and Barnes-Davies, M. (2010). Lateral olivocochlear (LOC) neurons of the mouse LSO receive excitatory and inhibitory synaptic inputs with slower kinetics than LSO principal neurons. *Hear. Res.* 270, 119–126. doi: 10.1016/j.heares.2010.08.013

Supek, F., Bosnjak, M., Skunca, N., and Smuc, T. (2011). REVIGO summarizes and visualizes long lists of gene ontology terms. *PLoS One* 6:e21800. doi: 10.1371/journal.pone.0021800

Suthakar, K., and Ryugo, D. K. (2021). Projections from the ventral nucleus of the lateral lemniscus to the cochlea in the mouse. *J. Comp. Neurol.* 529, 2995–3012. doi: 10.1002/cne.25143

Svensson, V., Vento-Tormo, R., and Teichmann, S. A. (2018). Exponential scaling of single-cell RNA-seq in the past decade. *Nat. Protoc.* 13, 599–604. doi: 10.1038/nprot.2017.149

Talavera, K., Nilius, B., and Voets, T. (2008). Neuronal TRP channels: thermometers, pathfinders and life-savers. *TINS* 31, 287–295. doi: 10.1016/j.tins.2008.03.002

Tollin, D. J. (2003). The lateral superior olive: a functional role in sound source localization. *Neuroscientist* 9, 127–143. doi: 10.1177/1073858403252228

Trattner, B., Gravot, C. M., Grothe, B., and Kunz, L. (2013). Metabolic maturation of auditory neurones in the superior olivary complex. *PLoS One* 8:e67351. doi: 10.1371/journal.pone.0067351

Trussell, L. O. (1997). Cellular mechanisms for preservation of timing in central auditory pathways. *Curr. Opin. Neurobiol.* 7, 487–492. doi: 10.1016/s0959-4388(97)80027-x

Trussell, L. O. (1999). Synaptic mechanisms for coding timing in auditory neurons. *Annu. Rev. Physiol.* 61, 477–496. doi: 10.1146/annurev.physiol.61.1.477

Usardi, A., Iyer, K., Sigoillot, S. M., Dusonchet, A., and Selimi, F. (2017). The immunoglobulin-like superfamily member IGSF3 is a developmentally regulated protein that controls neuronal morphogenesis. *Dev. Neurobiol.* 77, 75–92. doi: 10.1002/dneu.22412

Vaughan, J., Donaldson, C., Bittencourt, J., Perrin, M. H., Lewis, K., Sutton, S., et al. (1995). Urocortin, a mammalian neuropeptide related to fish urotensin I and to corticotropin-releasing factor. *Nature* 378, 287–292. doi: 10.1038/378287a0

Venkatachalam, K., and Montell, C. (2007). TRP channels. *Annu. Rev. Biochem.* 76, 387–417. doi: 10.1146/annurev.biochem.75.103004.142819

Vetter, D. E., Li, C., Zhao, L., Contarino, A., Liberman, M. C., Smith, G. W., et al. (2002). Urocortin-deficient mice show hearing impairment and increased anxiety-like behavior. *Nat. Genet.* 31, 363–369. doi: 10.1038/ng914

Vitten, H., Reusch, M., Friauf, E., and Löhrke, S. (2004). Expression of functional kainate and AMPA receptors in developing lateral superior olive neurons of the rat. *J. Neurobiol.* 59, 272–288. doi: 10.1002/neu.10326

Vysokov, N. V., Silva, J. P., Lelianova, V. G., Ho, C., Djamgoz, M. B., Tonevitsky, A. G., et al. (2016). The mechanism of regulated release of lasso/Teneurin-2. *Front. Mol. Neurosci.* 9:59. doi: 10.3389/fnmol.2016.00059

Walcher, J., Hassfurth, B., Grothe, B., and Koch, U. (2011). Comparative posthearing development of inhibitory inputs to the lateral superior olive in gerbils and mice. *J. Neurophysiol.* 106, 1443–1453. doi: 10.1152/jn.01087.2010

Wang, H., Kunkel, D. D., Schwartzkroin, P. A., and Tempel, B. L. (1994). Localization of Kv1.1 and Kv1.2, two K channel proteins, to synaptic terminals, somata, and dendrites in the mouse brain. *J. Neurosci.* 14, 4588–4599. doi: 10.1523/JNEUROSCI.14-08-04588.1994

Wang, H. S., Pan, Z., Shi, W., Brown, B. S., Wymore, R. S., Cohen, I. S., et al. (1998). KCNQ2 and KCNQ3 potassium channel subunits: molecular correlates of the M-channel. *Science* 282, 1890–1893. doi: 10.1126/science.282.5395.1890

Warr, W. B., Boche, J. B., and Neely, S. T. (1997). Efferent innervation of the inner hair cell region: origins and terminations of two lateral olivocochlear systems. *Hear. Res.* 108, 89–111. doi: 10.1016/s0378-5955(97)00044-0

Wei, Z., Zhao, J., Niebler, J., Hao, J. J., Merrick, B. A., and Xia, M. (2020). Quantitative proteomic profiling of mitochondrial toxicants in a human cardiomyocyte cell line. *Front. Genet.* 11:719. doi: 10.3389/fgene.2020.00719

Weltzien, F., Puller, C., O'sullivan, G. A., Paarmann, I., and Betz, H. (2012). Distribution of the glycine receptor ß-subunit in the mouse CNS as revealed by a novel monoclonal antibody. *J. Comp. Neurol.* 520, 3962–3981. doi: 10.1002/cne.23139

Wen, H., and Levitan, I. B. (2002). Calmodulin is an auxiliary subunit of KCNQ2/3 potassium channels. *J. Neurosci.* 22, 7991–8001. doi: 10.1523/jneurosci.22-18-07991.2002

Wende, H., Lechner, S. G., Cheret, C., Bourane, S., Kolanczyk, M. E., Pattyn, A., et al. (2012). The transcription factor c-Maf controls touch receptor development and function. *Science* 335, 1373–1376. doi: 10.1126/science.1214314

Wickenden, A. D., Yu, W., Zou, A., Jegla, T., and Wagoner, P. K. (2000). Retigabine, a novel anti-convulsant, enhances activation of KCNQ2/Q3 potassium channels. *Mol. Pharmacol.* 58, 591–600. doi: 10.1124/mol.58.3.591

Williams, I. R., Filimontseva, A., Connelly, C. J., and Ryugo, D. K. (2022). The lateral superior olive in the mouse: two systems of projecting neurons. *Front. Neural Circuits* 16:1038500. doi: 10.3389/fncir.2022.1038500

Wren, L. M., Jiménez-Jáimez, J., Al-Ghamdi, S., Al-Aama, J. Y., Bdeir, A., Al-Hassnan, Z. N., et al. (2019). Genetic mosaicism in calmodulinopathy. *Circ. Genom. Precis. Med.* 12, 375–385. doi: 10.1161/circgen.119.002581

Wu, J. S., Vyas, P., Glowatzki, E., and Fuchs, P. A. (2018). Opposing expression gradients of calcitonin-related polypeptide alpha (Calca/Cgrpa) and tyrosine hydroxylase (Th) in type II afferent neurons of the mouse cochlea. *J. Comp. Neurol.* 526, 425–438. doi: 10.1002/cne.24341

Wu, J. S., Yi, E., Manca, M., Javaid, H., Lauer, A. M., and Glowatzki, E. (2020). Sound exposure dynamically induces dopamine synthesis in cholinergic LOC efferents for feedback to auditory nerve fibers. *eLife* 9:e52419. doi: 10.7554/eLife.52419

Xiao, L., Michalski, N., Kronander, E., Gjoni, E., Genoud, C., Knott, G., et al. (2013). BMP signaling specifies the development of a large and fast CNS synapse. *Nat. Neurosci.* 16, 856–864. doi: 10.1038/nn.3414

Yamasaki, T., Hoyos-Ramirez, E., Martenson, J. S., Morimoto-Tomita, M., and Tomita, S. (2017). GARLH family proteins stabilize $GABA_A$ receptors at synapses. *Neuron* 93, 1138–1152.e6. doi: 10.1016/j.neuron.2017.02.023

Yan, D., and Tomita, S. (2012). Defined criteria for auxiliary subunits of glutamate receptors. *J. Physiol.* 590, 21–31. doi: 10.1113/jphysiol.2011.213868

Yang, Y., Cao, J., and Shi, Y. (2004). Identification and characterization of a gene encoding human LPGAT1, an endoplasmic reticulum-associated lysophosphatidylglycerol acyltransferase. *J. Biol. Chem.* 279, 55866–55874. doi: 10.1074/jbc.M406710200

Yang, Y. M., Aitoubah, J., Lauer, A. M., Nuriya, M., Takamiya, K., Jia, Z., et al. (2011). GluA4 is indispensable for driving fast neurotransmission across a high-fidelity central synapse. *J. Physiol.* 589, 4209–4227. doi: 10.1113/jphysiol.2011.208066

Yildirim, C., and Bal, R. (2018). ERG channels regulate excitability in stellate and bushy cells of mice ventral cochlear nucleus. *J. Membr. Biol.* 251, 711–722. doi: 10.1007/s00232-018-0048-5

Yin, T. C. T., Smith, P. H., and Joris, P. X. (2019). Neural mechanisms of binaural processing in the auditory brainstem. *Compr. Physiol.* 9, 1503–1575. doi: 10.1002/cphy.c180036

Young, T. R., Bourke, M., Zhou, X., Oohashi, T., Sawatari, A., Fässler, R., et al. (2013). Ten-m2 is required for the generation of binocular visual circuits. *J. Neurosci.* 33, 12490–12509. doi: 10.1523/jneurosci.4708-12.2013

Zamponi, G. W., Striessnig, J., Koschak, A., and Dolphin, A. C. (2015). The physiology, pathology, and pharmacology of voltage-gated calcium channels and their future therapeutic potential. *Pharmacol. Rev.* 67, 821–870. doi: 10.1124/pr.114.009654

Zhang, Y., Li, D., Darwish, Y., Fu, X., Trussell, L. O., and Huang, H. (2022). KCNQ channels enable reliable presynaptic spiking and synaptic transmission at high frequency. *J. Neurosci.* 42, 3305–3315. doi: 10.1523/jneurosci.0363-20.2022

Zheng, Z., Chen, E., Lu, W., Mouradian, G., Hodges, M., Liang, M., et al. (2020). Single-cell rranscriptomic analysis. *Compr. Physiol.* 10, 767–783. doi: 10.1002/cphy.c190037

Zybura, A., Hudmon, A., and Cummins, T. R. (2021). Distinctive properties and powerful neuromodulation of $Na_v1.6$ sodium channels regulates neuronal excitability. *Cells* 10:1595. doi: 10.3390/cells10071595

Glossary

AMBA	Allen Mouse Brain Atlas
AP	action potential
AUROC	Area Under the Receiver-Operating Characteristic
CAS	central auditory system
C_m	membrane capacitance
CNIC	central nucleus of the inferior colliculus
CNS	central nervous system
DAB	3,3′-Diaminobenzidine
τ_{decay}	decay time constant
DEG	differentially expressed gene
DNLL	dorsal nucleus of the lateral lemniscus
FC	fold-change
FDR	false discovery rate
GSEA	Gene Set Enrichment Analysis
GO	Gene Ontology
HVG	highly variable genes
IC	inferior colliculus
INLL	intermediate nucleus of the lateral lemniscus
IQR	interquartile range
IUPHAR/BPS GTP	International Union of Basic and Clinical Pharmacology/British Pharmacological Society Guide to Pharmacology
KEGG	Kyoto Encyclopedia of Genes and Genomes
LOC	lateral olivocochlear neuron
LSO	lateral superior olive
MOC	medial olivocochlear neuron
MNTB	medial nucleus of the trapezoid body
OI	overlapping index
OxPhos	oxidative phosphorylation
P	postnatal day
PBS	phosphate-buffered saline
PCA	principal component analysis
PFA	paraformaldehyde
pLSO	LSO principal neuron
R_{in}	input resistance
R_s	series resistance
RT	room temperature
scRNA-seq	single cell RNA-sequencing
sEPSC	spontaneous excitatory postsynaptic current
sIPSC	spontaneous inhibitory postsynaptic current
SOC	superior olivary complex
SPON	superior paraolivary nucleus
τ_m	membrane time constant
TPM	transcripts per million
tSNE	t-distributed stochastic neighbor embedding
V_{hold}	holding potential
V_{rest}	resting membrane potential

frontiers | Frontiers in Synaptic Neuroscience

TYPE Original Research
PUBLISHED 03 June 2024
DOI 10.3389/fnsyn.2024.1422330

Check for updates

OPEN ACCESS

EDITED BY
Bernhard Englitz,
Radboud University, Netherlands

REVIEWED BY
Adam Hockley,
University of Salamanca, Spain
Paul Albert Fuchs,
Johns Hopkins University, United States
Catherine J. C. Weisz,
National Institutes of Health (NIH),
United States

*CORRESPONDENCE
Christine Köppl
✉ Christine.Koeppl@uol.de

RECEIVED 23 April 2024
ACCEPTED 20 May 2024
PUBLISHED 03 June 2024

CITATION
Steenken F, Pektaş A and Köppl C (2024) Age-related changes in olivocochlear efferent innervation in gerbils.
Front. Synaptic Neurosci. 16:1422330.
doi: 10.3389/fnsyn.2024.1422330

COPYRIGHT
© 2024 Steenken, Pektaş and Köppl. This is an open-access article distributed under the terms of the Creative Commons Attribution License (CC BY). The use, distribution or reproduction in other forums is permitted, provided the original author(s) and the copyright owner(s) are credited and that the original publication in this journal is cited, in accordance with accepted academic practice. No use, distribution or reproduction is permitted which does not comply with these terms.

Age-related changes in olivocochlear efferent innervation in gerbils

Friederike Steenken[1,2], Asli Pektaş[1] and Christine Köppl[1,2,3]*

[1]Department of Neuroscience, School of Medicine and Health Science, Carl von Ossietzky Universität Oldenburg, Oldenburg, Germany, [2]Cluster of Excellence "Hearing4all", Carl von Ossietzky Universität Oldenburg, Oldenburg, Germany, [3]Research Centre Neurosensory Science, Carl von Ossietzky Universität Oldenburg, Oldenburg, Germany

Introduction: Age-related hearing difficulties have a complex etiology that includes degenerative processes in the sensory cochlea. The cochlea comprises the start of the afferent, ascending auditory pathway, but also receives efferent feedback innervation by two separate populations of brainstem neurons: the medial olivocochlear and lateral olivocochlear pathways, innervating the outer hair cells and auditory-nerve fibers synapsing on inner hair cells, respectively. Efferents are believed to improve hearing under difficult conditions, such as high background noise. Here, we compare olivocochlear efferent innervation density along the tonotopic axis in young-adult and aged gerbils (at ~50% of their maximum lifespan potential), a classic animal model for age-related hearing loss.

Methods: Efferent synaptic terminals and sensory hair cells were labeled immunohistochemically with anti-synaptotagmin and anti-myosin VIIa, respectively. Numbers of hair cells, numbers of efferent terminals, and the efferent innervation area were quantified at seven tonotopic locations along the organ of Corti.

Results: The tonotopic distribution of olivocochlear innervation in the gerbil was similar to that previously shown for other species, with a slight apical cochlear bias in presumed lateral olivocochlear innervation (inner-hair-cell region), and a broad mid-cochlear peak for presumed medial olivocochlear innervation (outer-hair-cell region). We found significant, age-related declines in overall efferent innervation to both the inner-hair-cell and the outer-hair-cell region. However, when accounting for the age-related losses in efferent target structures, the innervation density of surviving elements proved unchanged in the inner-hair-cell region. For outer hair cells, a pronounced increase of orphaned outer hair cells, i.e., lacking efferent innervation, was observed. Surviving outer hair cells that were still efferently innervated retained a nearly normal innervation.

Discussion: A comparison across species suggests a basic aging scenario where outer hair cells, type-I afferents, and the efferents associated with them, steadily die away with advancing age, but leave the surviving cochlear circuitry largely intact until an advanced age, beyond 50% of a species' maximum lifespan potential. In the outer-hair-cell region, MOC degeneration may precede outer-hair-cell death, leaving a putatively transient population of orphaned outer hair cells that are no longer under efferent control.

KEYWORDS

hearing, auditory, cochlea, inner ear, aging, sensory, hair cells, immunohistochemistry

1 Introduction

Age-related hearing loss is one of the most prevalent sensory disorders, affecting nearly one third of the world's population aged 65 years or older (Liberman, 2017; WHO, 2021). In our society, which is demographically growing older, an increase of patients with hearing problems is expected (WHO, 2021).

The Mongolian gerbil (*Meriones unguiculatus*) is a classic animal model for studying age-related hearing loss. It has a relatively short lifespan, and low-frequency hearing similar to that of humans (Ryan, 1976). It is easy to maintain (Cheal, 1986), and shows similarities to human age-related pathologies that are associated with hearing loss (reviews in Gates and Mills, 2005; Heeringa and Köppl, 2019). Gerbils are typically classified as "old" when they reach 36 months of age, which corresponds to 50% of their maximal lifespan potential, comparable to a human aged 61 years (reviewed by Castaño-González et al., 2024). Age-related morphological changes in the gerbil cochlea include loss of afferent synapses on inner hair cells (IHC; Gleich et al., 2016; Steenken et al., 2021; Bovee et al., 2024), loss of spiral ganglion neurons (Keithley et al., 1989; Suryadevara et al., 2001), hair-cell loss (Tarnowski et al., 1991; Adams and Schulte, 1997), and a lowered endocochlear potential (Schulte and Schmiedt, 1992; Schmiedt et al., 2002). Age-related changes to the efferent innervation of the gerbil cochlea have only been explored in a developmental context (Rontal and Echteler, 2003; Kaiser et al., 2011). Thus, even the efferent innervation in the young-adult gerbil is poorly characterized and its potential degeneration with advancing age remains unexplored.

Efferent fibers that innervate the cochlea originate in two spatially distinct subsets of neurons – medial olivocochlear (MOC) and lateral olivocochlear (LOC; review in Guinan, 2018) – although species-specific variations in their precise locations occur (reviewed in Brown, 2011; Lauer et al., 2022). The cell bodies of MOC neurons are located within the medial superior olivary complex and their myelinated axons innervate the outer hair cells (OHC) of either the contralateral or the ipsilateral ear, or rarely both (reviewed in Kimura and Wersall, 1962; Warr and Guinan, 1979; Guinan, 2011). In the mature ear, MOC neurons are primarily cholinergic and, to a lesser extent, use gamma-aminobutyric acid (reviews in Eybalin, 1993; Elgoyhen et al., 2019; Kitcher et al., 2022). The binding of acetylcholine promotes Ca^{2+} influx, which increases the opening of Ca^{2+}-dependent K^+ channels, and leads to hyperpolarization of OHC (Elgoyhen et al., 2019). Thus, MOC efferents exert cochlear gain control by reducing the voltage-driven electromotility of OHC (Brown and Nuttall, 1984; Cooper and Guinan, 2006). Furthermore, in young-adult mice, MOC fibers form *en passant* terminals on type-I auditory-nerve fibers within the inner spiral bundle (Hua et al., 2021), with as yet unknown function. MOC efferents may affect the progression of cochlear aging. Expression of a modified α9α10 cholinergic nicotinic postsynaptic receptor complex in OHC of mice, which provided enhanced olivocochlear inhibition, slowed the loss of spiral ganglion neurons and preserved hearing function (Boero et al., 2020). Conversely, lesioning olivocochlear neurons in the brainstem aggravated hearing loss and cochlear ribbon-synapse loss, although this was less clearly a specific MOC effect, and may have been compounded by LOC loss (Liberman et al., 2014).

LOC neurons of the second major efferent subsystem reside in and around the lateral superior olivary nucleus. The majority of LOC neurons innervates the ipsilateral ear (Warr and Guinan, 1979; Robertson, 1985). Their unmyelinated fibers cross the outer spiral lamina and synapse onto the unmyelinated processes of type-I afferents that run up toward and terminate on IHC (Warr and Guinan, 1979). While the majority of LOC neurons are cholinergic, they have been observed to also express other neurotransmitters and neuromodulators, including dopamine, calcitonin gene-related peptide, gamma-aminobutyric acid, glycine, and opioid peptides such as enkephalin (Eybalin, 1993; Kitcher et al., 2022). The function of the LOC system is more elusive due to the difficulties of directly assessing its physiological function (recent review in Lauer et al., 2022). However, the variety of neurotransmitters suggests functional variety. For example, dopamine is suggested to play a role in cochlear neuroprotection (Eybalin et al., 1993; D'Aldin et al., 1995; Oestreicher et al., 1997; Darrow et al., 2007). The LOC system may also regulate the spontaneous activity of type-I afferents (Ruel et al., 2006) and maintain the binaural balance needed for sound localization (Groff and Liberman, 2003; Darrow et al., 2006).

For the gerbil, an age-related loss of MOC and LOC neurons located in the brainstem, of 31 and 24%, respectively, has already been shown (Radtke-Schuller et al., 2015). Findings in human and mouse indicated species-specific changes in the peripheral terminals of aging olivocochlear efferents: In humans, LOC innervation density was unaffected, while MOC innervation was reduced with age (Liberman and Liberman, 2019). Age-related changes in CBA/CaJ mice yielded mixed results. While one study found a loss of innervation density for both MOC and LOC efferents (Grierson et al., 2022), a different study found even increased MOC innervation in apical regions, and mixed results for LOC cochlear innervation (Kobrina et al., 2020).

Here, we immunohistochemically labeled efferent terminals and hair cells in cochleae of young-adult and old gerbils. We quantified the signal at seven tonotopic locations along the organ of Corti and confirmed a typical pattern of LOC and MOC innervation density across the tonotopic axis. Both the presumed LOC and the presumed MOC innervation were significantly reduced in the cochleae of old gerbils. However, when correcting for the age-related losses in efferent target structures, such as loss in afferent fibers (Steenken et al., 2021) and OHC loss (Tarnowski et al., 1991; Adams and Schulte, 1997), the surviving cochlear circuitry appeared surprisingly intact.

2 Materials and methods

2.1 Animals

Results from a total of 26 cochleae from 20 Mongolian gerbils (*Meriones unguiculatus*) are reported here (Table 1). Young-adult gerbils (5 males, 7 females) were between 3 and 8 months old. Old gerbils (6 males, 2 females) were 36 to 41 months of age, corresponding to just over 50% of the species' maximal lifespan potential (reviewed by Castaño-González et al., 2024). All experiments were in compliance with the relevant laws supervised by the Landesamt für Verbraucherschutz und Lebensmittelsicherheit (LAVES) of Lower Saxony. To minimize noise-induced hearing damage, animals lived their entire lives in a controlled, quiet environment with an average sound level of 48 and 55 dBA, outside and during working hours, respectively.

2.2 Tissue collection

Gerbils were euthanized with an overdose of sodium-pentobarbital ("Narcoren," Merial GmbH, Hallbergmoos, Germany,

10.3389/fnsyn.2024.1422330

TABLE 1 Cochleae and cochlear positions examined in individual gerbils.

Animal ID	Side(s)	Age (months)	Sex	LOC, equivalent frequency locations	MOC, equivalent frequency locations
AHG61	R, L	41	m	0.5, 1, 2, 4, 8, 16, 32	0.5, 1, 2, 4, 8, 16, 32
AHG62	L	41	m	0.5, 1, 2, 4, 8, 16, 32	0.5, 8, 16
AHG64	R, L	36	m	0.5, 1, 2, 4, 8, 16, 32	2, 4, 8, 16, 32
AHG65	L	36	f	2, 8, 32	
AHG74	L	37	m	0.5, 1, 2, 4, 8, 16, 32	1, 2, 4, 8, 32
AHG75	R,L	36	f	0.5, 1, 2, 4, 8, 16, 32	1, 2, 4, 8, 16
BPG27	R	38	m	0.5, 1, 2, 4, 8, 16, 32	2, 8, 16
BPG36	R,L	36	m	0.5, 1, 2, 4, 8, 16, 32	1, 2, 16, 32
BPG11	R	4	m	1, 2, 4, 8, 16, 32	2, 8, 16
BPG16	L	8	m	0.5, 1, 4, 8, 16, 32	2, 8
BPG18	R,L	4	m	0.5, 1, 2, 4, 8, 16, 32	0.5, 1, 2, 4, 8, 16, 32
BPG19	L	3	m	0.5, 1, 2, 4, 8, 16, 32	0.5, 1, 2, 8, 32
BPG20	L	3	m	0.5, 1, 2, 4, 8, 16, 32	0.5, 1, 2, 4, 8, 16, 32
BPG21	R	6	f	0.5, 1, 2, 4, 8, 16, 32	0.5, 1, 2, 4, 8, 16, 32
BPG22	R,L	6	f	0.5, 1, 2, 4, 8, 16, 32	2, 4, 8, 32
BPG24	R	7	f	0.5, 1, 2, 4, 8, 16, 32	4, 8, 32
BPG31	R	5	f	0.5, 1, 2, 4, 8, 16, 32	0.5, 1, 2, 4, 8, 16
BPG32	R	6	f	1, 2, 4, 8, 16, 32	2, 4, 8, 16, 32
BPG33	R	6	f	0.5, 1, 2, 4, 8, 16, 32	0.5, 1, 2, 4, 8, 16, 32
BPG34	R	6	f	0.5, 1, 2, 4, 8, 16, 32	2, 4, 8, 16, 32

480 mg/kg body weight). When breathing stopped, gerbils were decapitated, and the bullae were rapidly dissected out of the head. The cochlea was accessed by breaking away the bone of the bulla, and the apex carefully opened by scratching the bone with fine forceps. The round-window membrane was perforated with the tip of the needle of an insulin syringe and the oval window opened by removing the stapes with forceps. Next, 450 µL 4% paraformaldehyde in phosphate buffered saline (PBS) was gently introduced through the oval window with an insulin syringe. Cochleae were post-fixed on ice in ice-cold fixative in falcon tubes, for 1 h, with brief manual agitation every 15 min.

2.3 Histology

Cochleae were decalcified in 0.5 M ethylenediaminetetraacetic acid for 2 days on a shaker at 8°C. After removing excess tissue, cochleae were permeabilized in 1% Triton X in PBS, on a shaker at room temperature for 1 h. Next, cochleae were washed in 0.2% Triton X in PBS 3 times for 5 min and subsequently incubated in blocking solution (3% bovine serum albumin in 0.2% Triton X PBS), for 1 h, on a shaker at room temperature. Primary antibodies included anti-synaptotagmin-1 (DSHB mAb48 (asv48)) IgG2b monoclonal mouse, Developmental Studies Hybridoma Bank, Iowa City, IA, USA; RRID: AB_2199314, diluted 1:200 (concentrate) or 1:20 (supernatant)) to label efferent terminals, and anti-MyosinVIIa (IgG polyclonal rabbit, Proteus Biosciences, Ramona, CA, USA; cat. No. 25e6790; RRID: AB_10015251; diluted 1:400) to label cochlear hair cells. Antibodies were diluted in blocking solution, and cochleae were incubated for 1 day at 37°C.

Cochleae were then washed 5 times for 5 min in 0.2% Triton X PBS. Secondary antibodies that specifically targeted the primary antibodies were then applied for 1 day at 37°C; these were AF488 goat anti-mouse (monoclonal secondary antibody IgG2b; Invitrogen, Thermo Fisher Scientific, Waltham, MA, USA; cat. no A-21141; RRID:AB_2535778; diluted 1:1000), and donkey anti-rabbit-AF647 (polyclonal secondary antibody; Life Technologies-Molecular Probes; cat. no. A-31573; RRID: AB_162544; diluted 1:1000). Cochleae were then washed twice for 5 min in 0.2% Triton X PBS, and 3 times for 5 min in PBS before they were micro-dissected into 6–10 pieces under a stereo microscope (Steenken et al., 2022). Pieces were mounted on slides using Vectashield Mounting Medium (Vector Laboratories, Burlingame, CA, USA, H-10 0 0).

2.4 Image acquisition

Images of cochlear pieces were acquired with a Nikon epi-fluorescence microscope system (Nikon Eclipse Ni-Ei with associated NIS Elements software, Version 4.30, 64-bit, Nikon, Minato, Tokyo, Japan). Cochlear length was assessed by measuring along the IHC row of each cochlear piece and specific cochlear locations that corresponded to selected frequencies (0.5 kHz, 1 kHz, 2 kHz, 4 kHz, 8 kHz, 16 kHz, 32 kHz) were identified relative to the length of the individual cochlea (Müller, 1996). High-resolution confocal stacks were acquired with a Leica TCS SP8 microscope system (Leica Microsystem CMS GmbH, Wetzlar, Germany) using an oil-immersion objective (40x, numerical aperture 1.3). Fluorescence tags were excited by different lasers [488-nm (Optically pumped semiconductor laser),

and 638-nm (Diode)], and released photons were counted via a hybrid detector. Stacks were recorded in sequential scanning mode for the two channels, with a pixel resolution of $X,Y = 63.1$ nm and $Z = 0.37$ µm. Crosstalk between the channels was excluded with control specimens that were labeled with only one of the two antibodies. All confocal stacks were deconvolved (Huygens Essentials, Version 15.10, SVI, Hilversum, Netherlands) with default settings (maximum iteration: 80; signal to noise ratio: 10; quality threshold: 0.01), using a theoretical point-spread function.

2.5 Image analysis

All image analysis was carried out with ImageJ (FIJI, Schindelin et al., 2012). First, a defined region of interest (ROI) was cropped to only include either the IHC or OHC region. Thus, a median area of 7981.6 µm^2 and containing 8.5–15.5 IHCs was analyzed for LOC terminals. Likewise, a median area of 6446.5 µm^2 and containing 32–54 OHCs was analyzed for MOC terminals. Second, the fluorescent channels were separated. The channel with the MyoVIIa-label, displaying IHCs or OHCs, was used to manually count hair cells. The channel with the synaptotagmin label was used for all analyses of efferent innervation.

To quantify efferent innervation area, we followed a procedure according to Liberman and Liberman (2019). First, a z-projection using maximum (IHC region) or average (OHC region) pixel intensity was computed. The choice of average pixel intensity for the MOC analysis was governed by higher background levels in the OHC region, which was thus more effectively suppressed. After carefully comparing different auto-thresholding algorithms to best detect the labeled structures in these z-projections, we chose "Moments" for LOC, and "Li" for MOC. These were then applied to produce a binary image (examples shown in Figures 1B,C,E,F). Finally, the efferent innervation area was derived by multiplying the total ROI area with the fraction of synaptotagmin-labeled area within the ROI. For the OHC region, the area of synaptotagmin label was also determined separately for each OHC row. For this, particle detection ("particle analyzer" plugin in ImageJ) was applied and the areas of all detected particles in a given row of OHC were summed. Particles were only included if they were larger than 2 µm^2, holes were filled, and objects on edges were included. Note that this procedure had been intended to yield a count of terminals which, however, was discarded as unreliable. Ultimately, only the sum of the detected particle areas was used. The result of this slightly modified procedure for measuring innervation area in individual OHC rows, when summed, was not significantly different from the total innervation area in the OHC region determined by the simpler procedure above (see Supplementary Figure S1) (mixed model ANOVA: $F(1,170) = 0.92$; $p = 0.34$). All area measurements were normalized per hair cell, by dividing total area by the HC count in the relevant ROI.

After adjusting brightness and contrast automatically, counts of individual MOC terminals were obtained manually, in 3D, from each image stack displaying both labeled channels. As for area, these counts were normalized per OHC by dividing the terminal count by the HC count in the relevant ROI. In addition, OHCs without terminals (orphaned OHCs), and terminals that were not associated with an OHC (orphaned terminals) were quantified separately.

Estimated counts of LOC terminals were also obtained in 3D by an automated procedure applied to the synaptotagmin signal of each image stack. First, the image stack was binarized by applying the auto-threshold filter "moments." Next, the "3D objects counter" plugin in ImageJ, with a specified minimum object size of 100 voxels, was used to quantify LOC terminals. Objects at the edges were excluded. Here, too, the counts were normalized per IHC, by dividing the "objects counter" result by the HC count in the relevant ROI. The numbers of cochleae that were analyzed for each specific metric are listed in Table 2.

2.6 Statistical analysis

Only one ear from each animal was initially analyzed. However, if a particular tonotopic location could not be evaluated, the same location was supplemented using if possible the other ear of the same individual. Reasons to exclude locations were: loss of HCs due to the dissection process, or abundant and unspecific background staining. In some cases, the structural integrity of OHC rows was compromised, thus that the analysis of total innervation area was feasible, but the allocation into distinct rows was impossible.

Statistical tests were carried out in Matlab (version 2022b, Mathworks, Natick, MA, USA) and IBM SPSS Statistics for Windows (version 29.0, IBM Corp, Armonk, NY, USA). Data from several tonotopic locations of individual animals do not represent independent samples. Therefore, linear mixed-model analyses of variance (ANOVA) were used to test for differences in efferent innervation, with age group and cochlear location as fixed factors. These were followed by post-hoc t-tests. Data describing findings in young-adult gerbils were tested with linear mixed-model ANOVAs and subsequent multiple comparisons (MATLAB function "multcompare" with default Tukey–Kramer correction).

3 Results

We used an antibody against synaptotagmin 1 to label efferent terminals. Synaptotagmin 1 is a calcium sensor attached to vesicles and as such controls fusion events to the presynaptic membrane (Wolfes and Dean, 2020). In mature C57Bl/6J mice, synaptotagmin 1 can be found in presynaptic efferent terminals on type-I fibers below IHCs (Reisinger et al., 2011; the OHC region was not investigated). In the gerbil cochlea, it labeled large structures terminating onto OHCs and smaller structures in close vicinity to the basal pole of IHCs (Figures 1A,D). This pattern is similar to that found below IHCs of C57BL6/J mice labeled with an antibody against synaptic vesicle protein 2 (Dondzillo et al., 2021), or at OHCs and below IHC in CBA/CaJ mice labeled with the same antibody (Kobrina et al., 2020). The same pattern was apparent below IHCs and at OHCs in CBA/CaJ mice labeled with an antibody against vesicular acetylcholine transporter (VAT; Grierson et al., 2022), as well as in the IHC and OHC area in the gerbil labeled with an antibody against synapsin (Barone et al., 2019). Based on these observations, we assume that anti-synaptotagmin comprehensively labeled all olivocochlear efferent presynaptic endings in our gerbils. It was, however, not possible to distinguish between LOC and MOC efferent terminals based on the

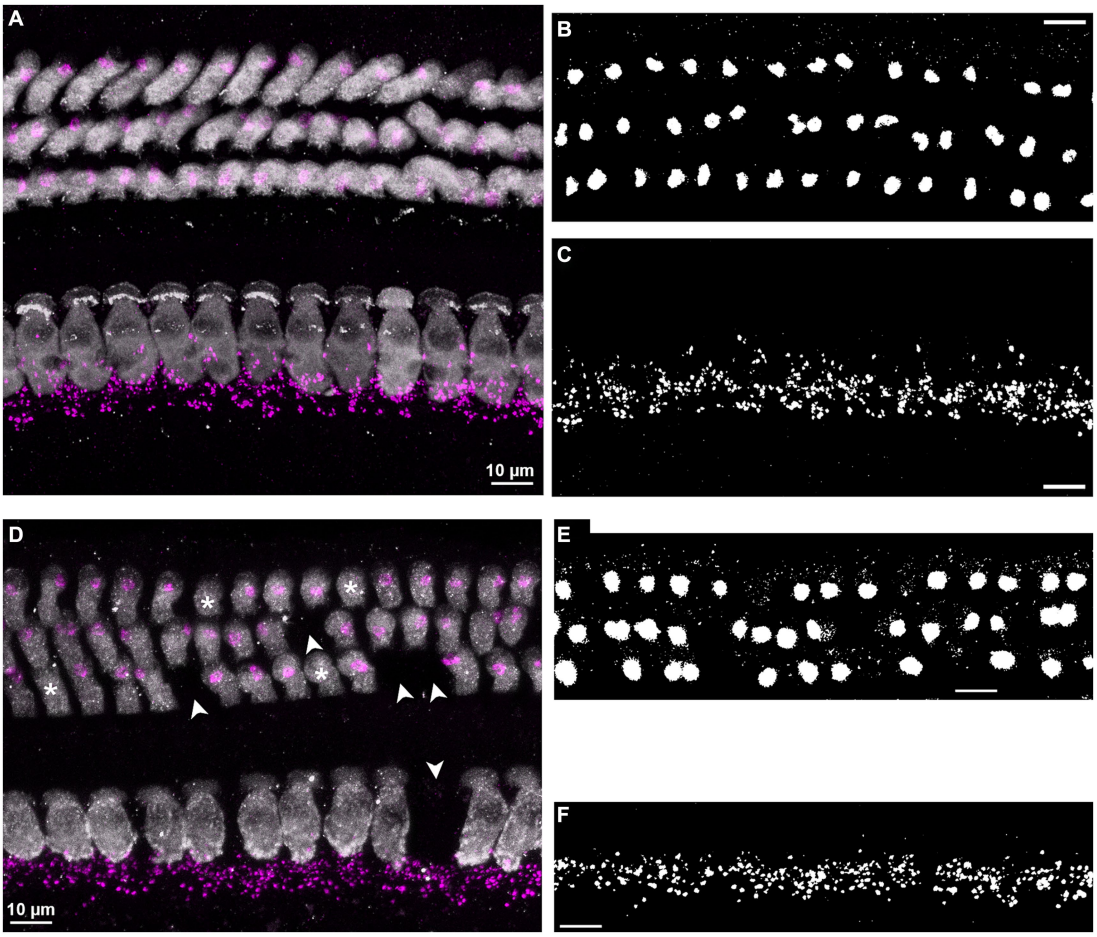


FIGURE 1
Examples of immunolabel and image analysis. **(A–C)** Illustrate an example from a young-adult female gerbil, aged 5 months, from a cochlear location corresponding to 8 kHz. **(D–F)** Illustrate an example from an old male, aged 41 months, from a cochlear location corresponding to 16 kHz. All scale bars correspond to 10 µm. **(A,D)** Confocal images, showing the entire organ of Corti, with IHCs (bottom) and OHCs (top). Hair cells (gray) and efferent terminals (magenta) were labeled with antibodies against myosin VIIa and synaptotagmin-1, respectively, and the synaptotagmin label was sharpened by deconvolution. The confocal stacks were collapsed into a 2D image by applying maximum intensity z-projection. Note that in the old individual **(D)**, several hair cells were missing (arrowheads) and 4 OHCs were orphaned, that is, were not associated with efferent terminals (asterisks). **(B,E)** The synaptotagmin channel only, after cropping the OHC area, applying average-intensity z-projection, and auto-thresholding with the algorithm "Li," to binarize the labeled signal (presumably MOC synapses) within this region. **(C,F)** Same as in panels **(B,E)**, for the IHC area, but with maximum-intensity z-projection and auto-thresholding algorithm "moments."

TABLE 2 **Not every cochlear location, and every metric, could be evaluated in all 12 young-adult gerbils and 8 old gerbils.**

Cochlear frequency	IHC (young/old)	OHC (young/old)	IHC innervation area (young/old)	IHC terminals (young/old)	OHC innervation area (young/old)	OHC terminals (young/old)
0.5	10/7	6/2	10/7	10/7	6/2	5/1
1	12/7	6/4	12/7	12/7	6/4	6/3
2	11/8	11/6	11/8	11/8	11/6	11/5
4	12/7	9/4	12/7	10/7	9/4	9/4
8	12/8	12/6	12/8	12/8	12/6	12/5
16	12/7	8/6	12/7	12/7	8/6	8/6
32	12/8	9/3	12/8	12/8	9/3	9/3

This table details the number of young-adult and old gerbils that contributed data, separately for each cochlear location (given in column 1), and each metric (columns 2–7): number of IHC, number of OHC, efferent innervation areas in proximity to IHC and OHC, and terminal numbers innervating the area around IHCs and OHCs.

anti-synaptotagmin label. Therefore for our analysis we classified all labeled structures in the OHC area as presumed MOC terminals and, likewise, all terminals within the IHC area as presumed LOC efferents, although we are aware that a minority of terminals innervating the IHC region might be formed by MOC fibers (Zachary and Fuchs, 2015; Hua et al., 2021).

3.1 Tonotopic variation of efferent innervation in young-adult gerbils

Since no quantitative data are available on cochlear efferent innervation in gerbils, we first established the typical pattern in young adults. Tonotopic variation of innervation was examined for seven locations along the cochlea, in total covering 75% of its length and equivalent best frequencies from 0.5 to 32 kHz (Müller, 1996). Two different metrics were obtained: (1) Area of synaptotagmin label in 2D projections, normalized per HC, and (2) numbers of terminals (OHC region, presumed MOC) or estimated numbers of terminals (IHC region, presumed LOC) counted in 3D, also normalized per HC.

LOC innervation area per IHC varied significantly along the length of the cochlea, with a peak at 1 to 2 kHz (Figure 2A; mixed-model ANOVA: $F(6,74) = 3.52$; $p = 0.004$). However, post-hoc Tukey–Kramer-corrected t-tests showed that this peak was not significantly different from all other locations. Thus, the LOC innervation area per IHC was nearly uniform along the entire cochlea. In contrast, the estimated number of terminals per IHC varied more clearly along the cochlea (Figure 2B; mixed-model ANOVA: $F(6,72) = 5.37$, $p < 0.0005$). The highest number of LOC terminals was found around and near IHC of the apical 1 kHz-location (mean: 36.96/median: 39.19 terminals per IHC). This number then decreased almost monotonically toward the most basal location evaluated (mean: 23.29/median: 24.0 terminals per IHC).

MOC efferent innervation area per OHC varied significantly and was maximal at mid- to high-frequency, basal locations (Figure 3A; mixed-model ANOVA: $F(6,54) = 3.48$, $p = 0.0055$, and Tukey–Kramer corrected t-tests). At the extreme apex, the innervation area was smaller compared to most mid-frequency cochlear positions. The number of terminals per OHC was also differentially distributed along the cochlea (Figure 3C; mixed-model ANOVA: $F(6,53) = 7.85$, $p < 0.0005$). Very similar to innervation area, OHC at the extreme apex received the lowest numbers of efferent terminals, and the numbers peaked broadly at the mid-frequencies, between 2 and 16 kHz.

Interestingly, the mean below 1 at 0.5 kHz suggests that not all OHCs were efferently innervated at this location. Indeed, direct examination revealed orphaned OHCs in all young-adult cochleae at the extreme apex, less frequently at the 1 kHz location, and only very rarely at more basal locations (Figure 4C). Such orphans appeared randomly in all three rows of OHC. Figures 3B,D show revised versions of efferent innervation area / OHC and terminal number / OHC, where orphaned OHCs were ignored for the normalization. This eliminated any significant tonotopic variation for the labeled area / innervated OHC (Figure 3B; mixed-model-ANOVA: $F(6,53) = 1.93$, $p = 0.0925$) while the number of terminals per innervated OHC remained lower for apical cochlear locations compared to mid-cochlear locations (Figure 3D; mixed-model ANOVA: $F(6,50) = 4.92$, $p = 0.0005$).

Next, we explored whether the efferent innervation varied between the three rows of OHC, but found no differences. Neither the efferent innervation area, corrected for orphaned OHCs, (n-way-ANOVA: $F(2,132) = 0{,}74$, $p = 0.48$), nor the terminal number on innervated OHCs varied between the rows (n-way ANOVA: $F(2,150) = 11.38$, $p = 0.39$). Finally, we also screened for orphaned terminals, that is, terminals not apposed to an OHC. This was observed only once in young-adult cochleae.

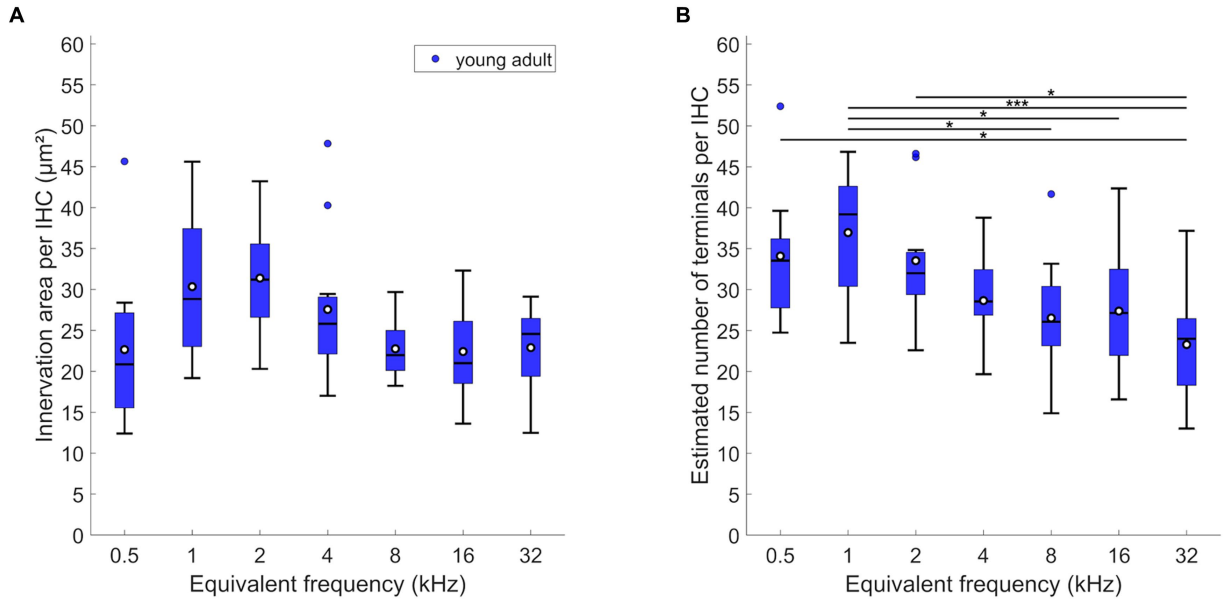


FIGURE 2
LOC innervation in young-adult gerbils. Data are displayed as **(A)** innervation area or **(B)** number of terminals per IHC. Box plots show the median (horizontal line), the 25th and 75th percentiles (upper and lower boundaries of the box), the data range without outliers (whiskers), and outliers (colored circles, defined as a value larger than three scaled median absolute deviations from the median). Means are also depicted, as white circles within each box. Note that not every cochlear location (expressed as equivalent frequency) included data from all 12 young-adult gerbils (see Tables 1, 2 for details). Asterisks denote significant differences between the cochlear frequencies connected by the respective line below (Tukey–Kramer-corrected post-hoc tests; *$p < 0.05$, ***$p < 0.001$).

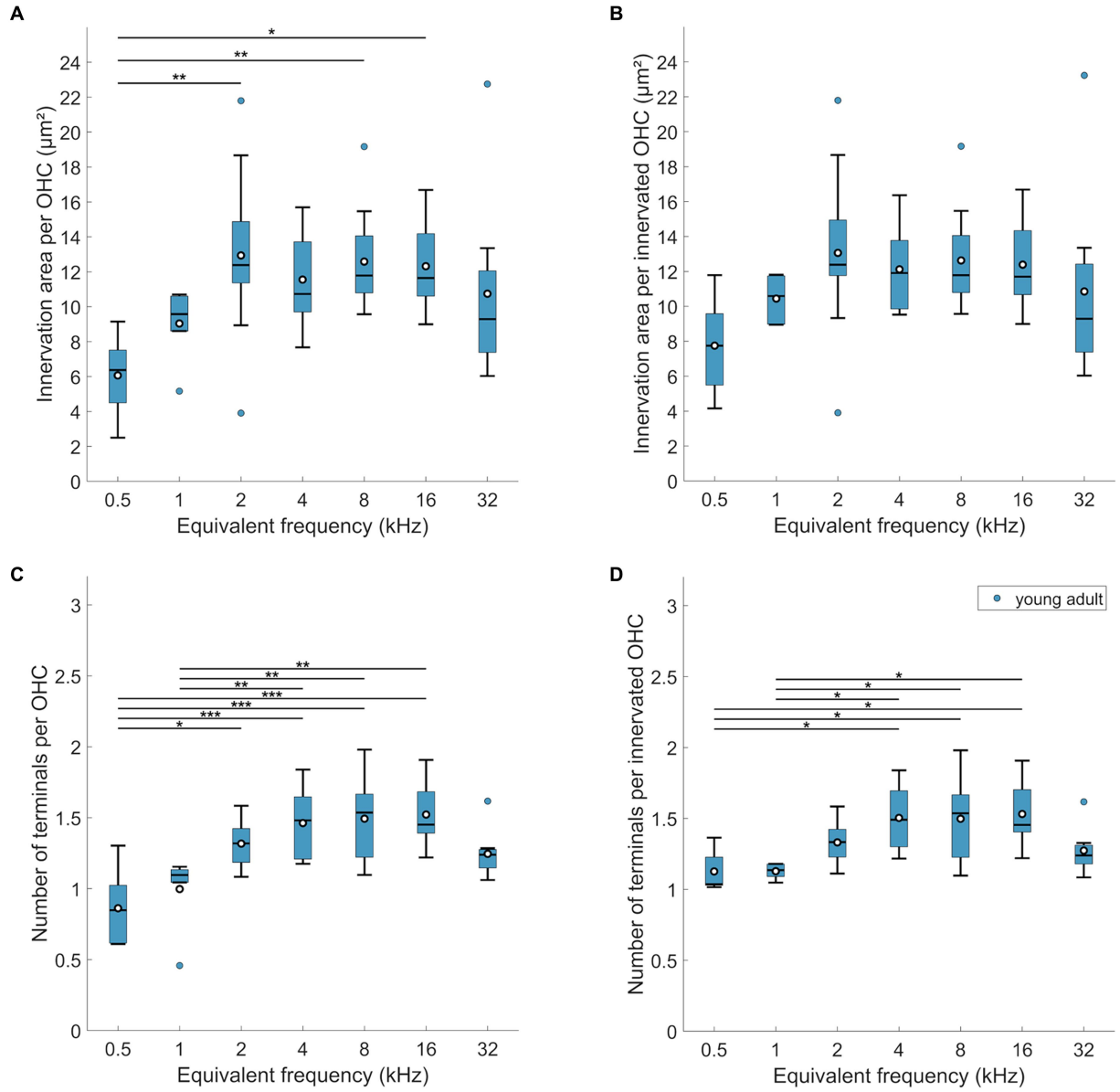


FIGURE 3
MOC innervation in young-adult gerbils. Data are displayed as **(A,B)** innervation area or **(C,D)** number of terminals, and were normalized either per OHC **(A,C)** or per innervated OHC, that is, corrected for orphaned OHCs **(B,D)**. Box plots show the median (horizontal line), the 25th and 75th percentiles (upper and lower boundaries of the box), the data range without outliers (whiskers), and outliers (colored circles). Means are also depicted, as white circles within each box. Note that not every cochlear frequency included data from all 12 young-adult gerbils (see Tables 1, 2). Asterisks denote significant differences between the cochlear frequencies connected by the respective line below (Tukey–Kramer-corrected post-hoc tests; *$p < 0.05$, **$p < 0.01$, ****$p < 0.001$).

3.2 Age-related loss of efferent target structures

The core interest of our research was focused on age-related changes of the efferent cochlear innervation that might indicate changes in efferent function. We thus aimed to differentiate between overall losses in efferent label and confounding losses of efferent target structures that are already known to occur in quiet-aged gerbils (Tarnowski et al., 1991; Steenken et al., 2021). To this end, the age-related loss of both IHCs and OHCs was quantified in our gerbil sample.

3.2.1 Age-related loss of IHC and afferent fiber terminals

For IHC, no age-related loss was apparent (Figure 4A; n-way ANOVA: $F(1,119) = 3{,}11$, $p = 0.08$). The mean number of IHCs contained within the analyzed ROIs (representing 130 µm along the cochlear apex-base axis) was 12.49 (std + −1; median: 12.5) in young-adult gerbils and 12.19 (std + −1.34; median: 12) IHCs in old gerbils.

The main target of LOC efferents are not the IHC directly, but the type-I afferents coursing up to and connecting to the IHC. We did not investigate the age-related loss of afferents for the sample reported here. However, the loss of afferent synaptic connections was recently

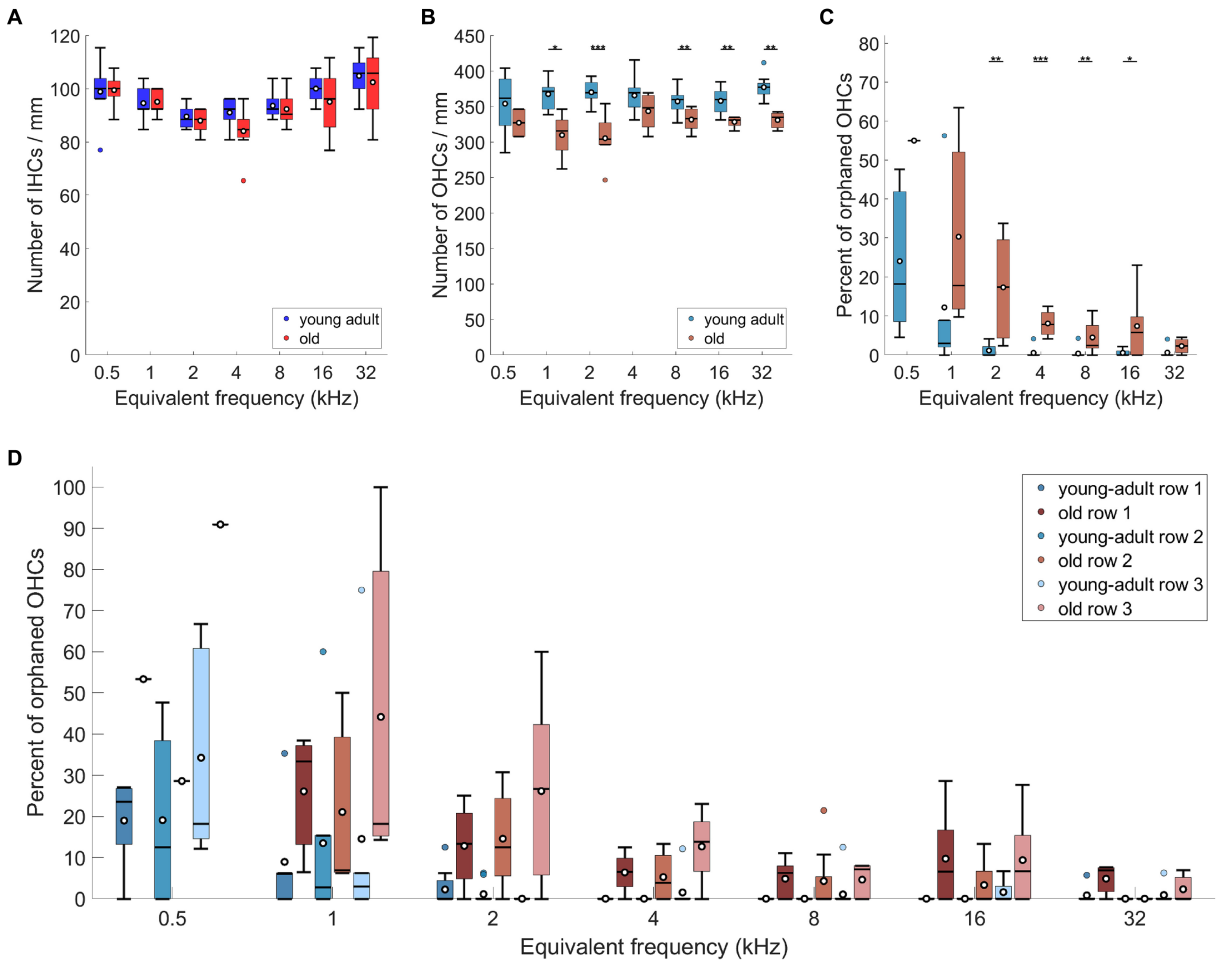


FIGURE 4
Age-related losses of hair cells and increase of orphaned OHCs. **(A)** Number of IHCs, **(B)** number of OHCs, both per mm of cochlear length, **(C)** percentage of non-innervated, i.e., orphaned OHCs, and **(D)** percentage of orphaned OHCs, separately for the three rows of OHCs. Box plots show the median (horizontal line), the 25th and 75th percentiles (upper and lower boundaries of the box), the data range without outliers (whiskers), and outliers (colored circles). Means are also depicted, as white circles within each box. Boxes in blue display data from young-adult gerbils, boxes in red represent old gerbils, and different shades of red and blue distinguish data from the IHC region, the OHC region, and the three rows of OHC, as indicated in the legends. Note that not every cochlear frequency included data for all 12 young-adult gerbils and 8 old gerbils (see Tables 1, 2). Asterisks denote significant differences between the age groups indicated by the respective line below (post-hoc tests; *p<0.05, **p<0.01, ***p<0.001).

quantified for the same tonotopic locations in other samples from our gerbil colony (Steenken et al., 2021; Bovee et al., 2024). The implications of this for the novel results reported here will therefore be addressed in the discussion.

3.2.2 Age-related loss of OHC and increase in orphaned OHC

Regarding OHC, young-adult gerbils had on average 47.34 (std+−3.02; median: 48) OHCs contained within the analyzed ROIs (representing 130 µm along the apex-base axis). This number was significantly reduced in old gerbils (Figure 4B; n-way ANOVA: $F(1,78)=48.84$, $p<0.0005$), with only 42.11 (std+−3.39; median: 42.5) OHCs contained in the same-sized ROIs. On average, this represents a fairly small loss of 11% OHC. Post-hoc tests at specific cochlear locations revealed that the age-related loss was significant for 5 of the 7 locations evaluated, sparing only the extreme apex (0.5 kHz) and a mid-cochlear region (4 kHz).

Since young-adult gerbils typically displayed a minor fraction of orphaned OHCs (devoid of efferent innervation) in the cochlear apex, we explored whether this phenomenon increased and/or spread over larger cochlear regions with age. Compared to young-adult gerbils, old gerbils showed an overall significant increase in the percentage of orphaned OHCs (Figure 4C; n-way ANOVA: $F(1,70)=21.76$, $p<0.0005$). Frequency also had a significant effect (n-way ANOVA: $F(6,70)=10.07$, $p<0.0005$), confirming larger numbers of orphaned OHCs in the apex; these decreased toward the base. When comparing the numbers at specific cochlear locations (post-hoc tests), an age-related increase was significant for mid-cochlear frequencies (2–16 kHz), suggesting a spread of the phenomenon toward more basal locations in old cochleae (Figure 4C). An increase in orphans was observed for all three rows of OHC (Figure 4D), with a significant overall difference between the rows (n-way ANOVA: $F(2,222)=8.92$, $p=0.0002$). Posthoc Tukey–Kramer-corrected t-tests, however, did

not confirm significant differences between specific rows. The large significant effect in the ANOVA model appeared to be dominated by the very small data set ($n = 1$) obtained for old gerbils at the cochlear location corresponding to 0.5 kHz. When this location was omitted in the ANOVA model, the difference became less significant (n-way ANOVA: $F(2,208) = 3.56$, $p = 0.03$). In both ANOVAs, no interaction was apparent between rows and age or frequency. Finally, orphaned terminals (without an OHC close by) were occasionally observed, but remained rare (a total of 6 across all cochlear locations evaluated in all gerbils, of which 5 were found in old cochleae).

3.3 Age-related changes of efferents in IHC region (presumed LOC)

In comparison to young adults, old gerbils showed a significant decrease in the LOC innervation area per IHC (Figure 5A; n-way ANOVA: $F(1,119) = 29.09$; $p < 0.0005$). Over all tonotopic locations, the age-related loss amounted to 24%. As already seen for young adults alone, there was a significant effect of frequency (n-way ANOVA: $F(6,119) = 4.87$, $p < 0.0005$), suggesting tonotopic variation in LOC innervation. However, no interaction was found between frequency and age, indicating similar tonotopic variation in young-adult and old gerbils, and a uniform loss of innervation area along the aging cochlea. Post-hoc comparisons confirmed significant age-related losses for 4 of the 7 cochlear locations evaluated (Figure 5A).

Compared to young adults, old animals also showed significantly fewer efferent terminals per IHC (Figure 5B; n-way ANOVA: $F(1,116) = 35.81$, $p < 0.0005$). Furthermore, an effect of frequency was confirmed (n-way ANOVA: $F(6,116) = 9.26$, $p < 0.0005$), but there was no significant interaction between age and frequency, suggesting a uniform loss of terminals per IHC along the cochlea. Over all tonotopic locations, the age-related loss amounted to 23%. Post-hoc comparisons revealed that the age-related loss was significant for most cochlear locations (5 out of 7 evaluated; Figure 5B).

In summary, old gerbils had lost around 23% of their presumed LOC innervation. This loss appeared nearly uniform along the tonotopic axis. The two metrics evaluated here, labeled area and estimated number of terminals, yielded nearly identical results.

3.4 Age-related changes of efferents in the OHC region (presumed MOC)

The MOC innervation area per OHC, corrected for orphaned OHCs, showed a significant age effect (Figure 6A; n-way ANOVA: $F(1,77) = 4.4$, $p = 0.0392$). Over all tonotopic locations, the age-related loss amounted to 12%. However, post-hoc comparisons for each cochlear location revealed that only the 1 kHz-location showed a significant age-related reduction of MOC innervation area per OHC. Frequency also had a significant effect (n-way ANOVA: $F(6,77) = 4.83$, $p < 0.0005$), but there was no significant interaction between age and frequency. Thus, the tendency toward smaller innervation area in the apex, already observed in young adults, remained unchanged in old gerbils (Figure 3B).

Manual counts of terminals per innervated OHC revealed a significant overall loss of terminal number in old gerbils (Figure 6B; n-way ANOVA: $F(1,70) = 4.25$, $p = 0.043$). Over all tonotopic locations, this age-related loss amounted to 9%. However, similar to innervation area, most cochlear locations did not reveal significant age-related losses with location-specific post-hoc tests. Here, only the 16 kHz-location showed a significant decline in the number of

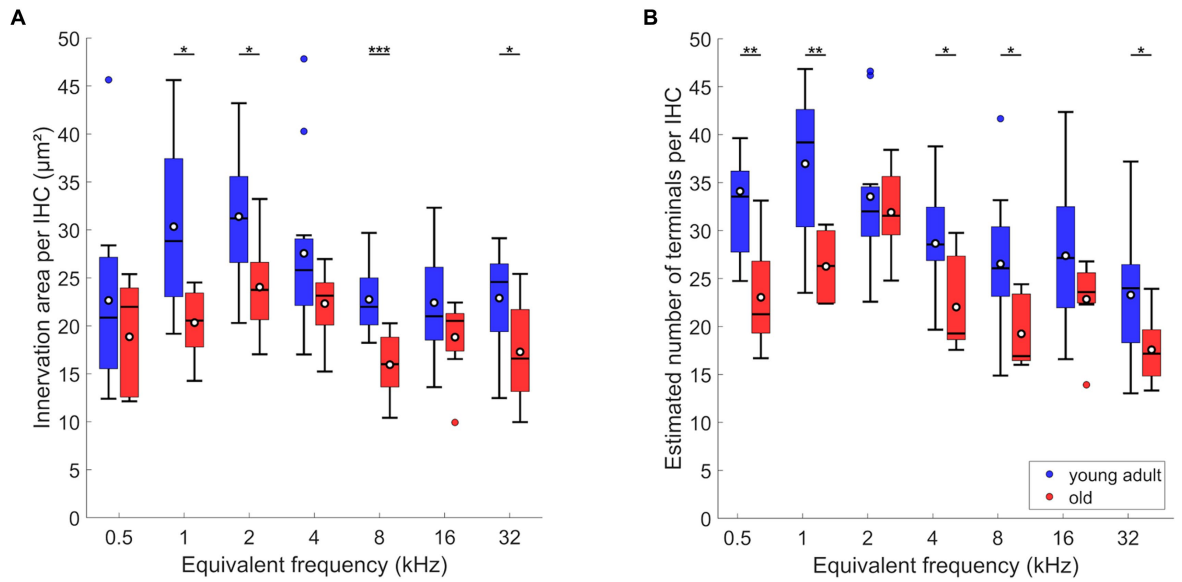


FIGURE 5
Age-related changes of efferents in IHC region. **(A)** Innervation area and **(B)** number of terminals per IHC. Box plots show the median (horizontal line), the 25th and 75th percentiles (upper and lower boundaries of the box), the data range without outliers (whiskers), and outliers (colored circles). Means are also depicted, as white circles within each box. Boxes in blue display data from young-adult gerbils, boxes in red represent old gerbils. Note that not every cochlear frequency included data for all 12 young-adult gerbils and 8 old gerbils (see Tables 1, 2). Asterisks denote significant differences between the age groups indicated by the respective line below (post-hoc tests; *$p < 0.05$, **$p < 0.01$, ***$p < 0.001$).

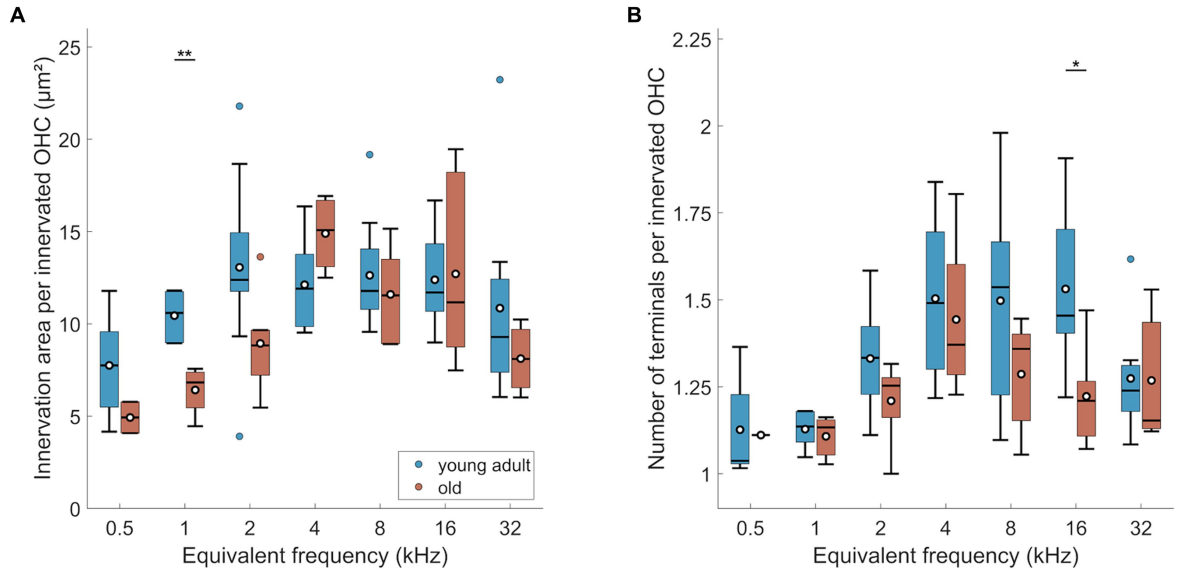


FIGURE 6
Age-related changes of efferents in OHC region. **(A)** Innervation area and **(B)** number of terminals per innervated OHC. Box plots show the median (horizontal line), the 25th and 75th percentiles (upper and lower boundaries of the box), the data range without outliers (whiskers), and outliers (colored circles). Means are also depicted, as white circles within each box. Boxes in blue display data from young-adult gerbils, boxes in red represent old gerbils. Note that not every cochlear frequency included data for all 12 young-adult gerbils and 8 old gerbils (see Tables 1, 2). Asterisks denote significant differences between the age groups indicated by the respective line below (post-hoc tests; $*p < 0.05$, $**p < 0.01$, $***p < 0.001$).

terminals (Figure 6B). As already shown for young-adult gerbils alone, the number of terminals per OHC was also frequency dependent (n-way ANOVA: $F(6,70) = 3.8$, $p = 0.0025$), with lower numbers of terminals per innervated OHC in the apex. An interaction between age and frequency was absent, indicating a trend toward loss of terminal numbers all along the cochlea.

To explore whether the three OHC rows are differentially affected by age, the efferent innervation area (Figure 7A) and the number of terminals per OHC (Figure 7B) were assessed separately for each row. Innervation area was not affected by row number (Figure 7A; n-way-ANOVA: $F(2,206) = 0.66$, $p = 0.516$). Likewise, terminal number per OHC was not different between the rows (Figure 7B; n-way-ANOVA: $F(2,221) = 1.6$, $p = 0.204$).

In summary, we observed a tendency for mild losses in MOC innervation of surviving OHC, of around 10%. There was no evidence for differential losses along the tonotopic axis or between the three rows of OHC. Thus, the typical mid- to high-frequency bias of MOC innervation density was retained in old gerbils. Both metrics that were evaluated here, labeled area and number of terminals, agreed in their principal results.

4 Discussion

The present study quantified the olivocochlear innervation at seven tonotopic locations along the organ of Corti of gerbils, with the primary aim to probe for age-related changes between young adults and aged individuals. We found that innervation area and number of terminals of presumed LOC cochlear efferents were significantly reduced in the cochleae of old gerbils. This loss might be confounded by an equivalent loss in afferent fibers (Steenken et al., 2021), such that the surviving afferents retain a near-normal efferent innervation. Contrary to IHC, an age-related OHC loss was found, as previously reported (Tarnowski et al., 1991; Adams and Schulte, 1997). Furthermore, an increased number of non-efferently innervated OHCs, i.e., orphaned OHCs, was apparent in old gerbils. The loss of putative MOC efferents on surviving and still innervated OHCs was mild but significant. We found no difference in efferent innervation between the three rows of OHCs, and no differential age-related loss.

4.1 Efferent innervation patterns in young adults

In the young-adult gerbil, the presumed LOC innervation in the IHC region showed a tendency to peak apically, around 1–2 kHz equivalent best frequency, and decrease nearly monotonically toward the cochlear base. The presumed MOC innervation of OHCs tended to peak broadly and more basally, in regions between 2 and 16 kHz equivalent best frequency. These tonotopic patterns appear to be quite typical across species.

LOC innervation density tends to show a bias toward the cochlear apex, if any. An apical bias was observed in rat (Vetter et al., 1991) and human (Liberman and Liberman, 2019) and, less pronounced, in cat (Liberman et al., 1990) and gerbil (this study). In young-adult CBA/CaJ mice, LOC innervation is nearly uniform along the tonotopic gradient (Maison et al., 2003; Kobrina et al., 2020; Grierson et al., 2022). In the brainstem of gerbils, both Kaiser et al. (2011) and Radtke-Schuller et al. (2015) found more LOC neurons in the medial, high-frequency limb of the lateral superior olive that houses the LOC neurons that innervate basal, high-frequency regions of the cochlea (Sanes et al., 1989). This apparent disagreement with our cochlear data, where the efferent innervation of IHCs tended to be significantly denser in apical cochlear regions (Figure 2), suggests a more extensive branching pattern of LOC peripheral axons in the cochlear apex.

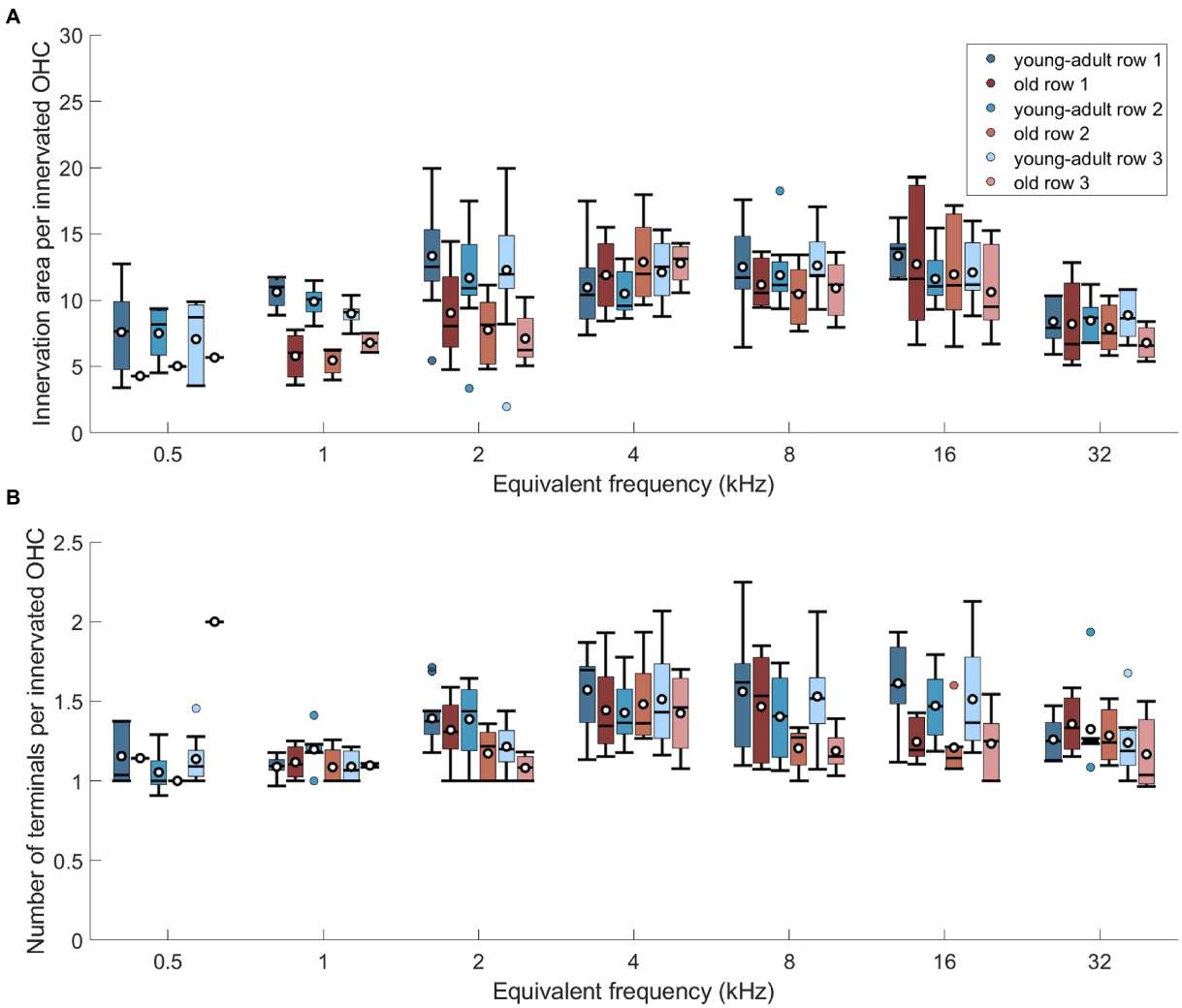


FIGURE 7
No differential, age-related changes of efferents across the 3 rows of OHCs. **(A)** Innervation area per innervated OHC at seven cochlear frequencies displayed separately for the three rows of OHC, for both age groups. **(B)** Same as in panel **(A)**, but for number of terminals per innervated OHC. Box plots show the median (horizontal line), the 25th and 75th percentiles (upper and lower boundaries of the box), the data range without outliers (whiskers), and the outliers (colored circles). Means are also depicted, as white circles within each box. Boxes in blue display data from young-adult gerbils, boxes in red represent old gerbils, and different shades distinguish the three rows of OHC. Note that not every cochlear frequency included data for all 12 young-adult gerbils and 8 old gerbils (see Tables 1, 2). Post-hoc tests revealed no significant differences between the rows at any cochlear frequency.

MOC innervation tends to peak broadly in mid-cochlear regions, which then also coincides broadly with the range of most sensitive hearing in the behavioral audiogram of a given species, as previously shown for cat (Fay, 1988; Liberman et al., 1990), human (Zwicker and Fastl, 1990; Liberman and Liberman, 2019), CBA/CaJ mouse (Maison et al., 2003; Radziwon et al., 2009; Grierson et al., 2022) and guinea pig (Heffner et al., 1971; Kujawa and Liberman, 1997; Liberman and Liberman, 2019). This was confirmed here for the gerbil, whose behavioral sensitivity is best between 1 and 20 kHz (Ryan, 1976). The number of presumed MOC terminals on gerbil OHC – between 1 and 2 – is similar to that shown for CBA/CaJ mice, also using immunolabeling (Maison et al., 2003; Grierson et al., 2022), but appears low compared to the counts from electron-microscopic reconstructions in cat (0–9; Liberman et al., 1990) and guinea pig (4–13; Hashimoto and Kimura, 1988). Mouse and gerbil are also the only species where no trend of decreasing MOC innervation area across the OHC rows was evident (Maison et al., 2003; this study). In the cat, a decrease in both efferent area and terminal number from OHC row 1 to row 3 was quantified (Liberman et al., 1990), and similar qualitative observations were reported for guinea pig, rhesus monkey, and human (Hashimoto and Kimura, 1988; Liberman and Liberman, 2019). Together, this suggests that compared to the other species investigated so far there are fewer MOC terminals on individual OHCs of gerbil and mouse, but an even distribution among the OHC rows.

A perhaps surprising finding in our study was that even in young-adult gerbils, orphaned OHC with no efferent terminals were regularly seen in the cochlear apex. The phenomenon of orphaned OHC has also been reported (but not quantified) for young-adult rhesus

monkeys and humans, where it was associated with a general trend of decreasing MOC innervation density from row 1 to row 3 (Liberman and Liberman, 2019).

4.2 Age-related changes to bulk efferent innervation in IHC region (presumed LOC)

For two different metrics of efferent innervation, we showed a significant and nearly uniform loss of about 23% in the IHC region of old gerbils. This agrees remarkably well with counts of presumed LOC neurons in and around the lateral superior olive in the brainstem of gerbils (Radtke-Schuller et al., 2015). There, an overall loss of 24% was found in gerbils that were of similar old age to those in the present study (2.5–3.5 years), compared to young adults. The loss of LOC neurons was disproportionally higher in the medial, high-frequency limb of the LSO (Radtke-Schuller et al., 2015). This does not agree with our observation of a uniform loss across the tonotopic axis. However, subtle differences between the gerbil samples (our gerbils were raised in a controlled, quiet environment), or as yet unknown differences in the cochlear branching patterns of LOC axons in the cochlear apex versus the base (as suggested above, see section 4.1), could conceivably account for this difference.

Similar, extensive reductions in bulk metrics of IHC efferent innervation have not so far been observed in aging individuals of other species. An exception are C57BL/6 mice (Stamataki et al., 2006; Lauer et al., 2012; Jeng et al., 2021), a strain that is well known for its accelerated auditory aging phenotype (e.g., Spongr et al., 1997) and thus difficult to compare across species. For comparing equivalent ages across species, we refer here to their respective maximum lifespan potential (reviewed in Castaño-González et al., 2024). In humans, no significant change was found in LOC innervation, quantified as ChAT-immunolabeled area per IHC (very similar to one of our metrics in gerbil). This was in individuals up to 86 years (Liberman and Liberman, 2019), equivalent to 70% of the human maximal lifespan potential, that is, even beyond the lifespan range explored here for gerbils. Aging CBA/CaJ mice showed no consistent changes in immunolabeled area per IHC (Kobrina et al., 2020) or only losses limited to a narrow frequency range around 32 kHz, for immunolabeled volume (Grierson et al., 2022). This agreed with only minor losses, of 13%, in the overall numbers of LOC brainstem neurons (Vicencio-Jimenez et al., 2021). The mice evaluated in those studies were between 18 and 30 months old, equivalent to about 50–80% of their maximal lifespan potential.

We note that the efferent innervation metrics compared above were all normalized per surviving IHC. Age-related loss of IHC is typically minor, especially in individuals that lived in a controlled, quiet environment. However, a controlled environment is not always feasible. The extent of age-related IHC loss varies between studies, and is often region-specific within the cochlea (e.g., human: Liberman and Liberman, 2019; Wu et al., 2019; CBA/CaJ mice: Spongr et al., 1997; Sergeyenko et al., 2013; Parthasarathy and Kujawa, 2018; Kobrina et al., 2020; Grierson et al., 2022). This should therefore be controlled for when comparing innervation metrics across studies. In our sample, the number of IHCs was not significantly different between young-adult and old gerbils (Figure 4A), in agreement with previous observations in quiet-aged gerbils of similar age (Tarnowski et al., 1991; Adams and Schulte, 1997).

4.3 Confounding age-related loss of type-I afferents

An important confounding factor that was not addressed in the current sample, and not in any of the studies discussed above (see section 4.2), is the concomitant loss of type-I afferents, the primary target of LOC efferent innervation. For gerbils, the loss of afferent synaptic connections, assessed as co-localized puncta immunolabeled for pre-synaptic ribbons and post-synaptic glutamate receptor patches, was recently quantified, for the same 7 tonotopic locations, in another sample from our colony, and for the same age groups (Steenken et al., 2021). Compared to young adults, old gerbils showed significant losses of afferent synapses, of, on average, around 20% (Steenken et al., 2021). Medians of these published data, for each tonotopic location, are re-plotted in Figure 8A. It is well established that type-I afferent fibers very rarely branch and typically form only a single synapse with a single IHC (reviewed in Moser et al., 2006). Thus, a loss of synaptic connections means an equivalent loss of afferent fibers in the immediate proximity of IHC. Using this assumption, Figures 8B,C show estimates of the efferent innervation per afferent fiber under each IHC, derived by dividing the median values shown in Figures 5A,B by the medians shown in Figure 8A. A formal statistical test is not feasible, because the quantification of afferent and efferent innervation derived from different individuals. However, the age-related differences in Figures 8B,C appear to be negligible.

For aging gerbils, we thus conclude that LOC neurons and their peripheral terminals in the cochlea degenerate together with their principal targets, the type-I afferent peripheral dendrites. This suggests that the efferent innervation of surviving targets in the IHC region of aging gerbils is still intact – at least numerically. More subtle changes, such as the intriguing shift toward a higher proportion of axosomatic efferent synapses on aging IHCs that was observed in C57BL/6J mice (Lauer et al., 2012; Zachary and Fuchs, 2015; Jeng et al., 2021) remain possible, and should be explored in future studies. Of note, the small efferent terminals in the IHC area are notoriously difficult to resolve individually in immunolabeled material. The absolute numbers of presumed LOC terminals that were estimated in the present study are thus almost certainly underestimates. High-resolution electron microscopic data from young-adult cat (Liberman et al., 1990) and mouse (Hua et al., 2021) have shown typical numbers of 5–20 efferent terminals on one afferent terminal dendrite.

As discussed above (see section 4.2), in humans and CBA/CaJ mice, there is little evidence for age-related degeneration of LOC neurons and their peripheral terminals. This is despite drastic age-related losses in afferent synapses or peripheral dendrites to the IHCs. For CBA/CaJ mice of comparably old ages to those evaluated for LOC bulk innervation, a mean loss of between 20 and 50% of afferent synapses (depending on cochlear location and precise age) has been shown (Sergeyenko et al., 2013; Kobrina et al., 2020). In humans, the age-related loss of peripheral afferent dendrites was even more drastic, at 45–65%, again depending on cochlear location and precise age (Wu et al., 2019). Thus, in mice and humans, the loss of afferent targets does not appear to result in an equivalent loss of LOC innervation, in contrast to our observations in the gerbil. It remains to be clarified whether these species-specific differences might be explained by different time courses of afferent retraction and

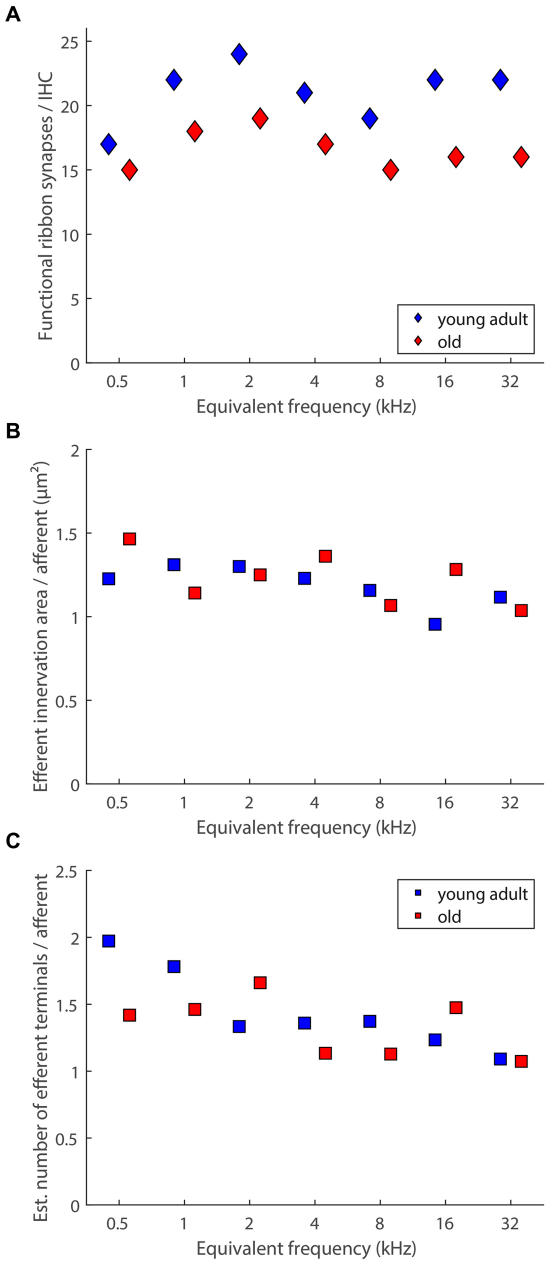


FIGURE 8
Age-related loss of presumed LOC innervation explained by loss of its primary target (afferent innervation). **(A)** Medians of functional ribbon synapses per IHC (replotted from Steenken et al., 2021, their Figure 3). **(B)** An estimate of efferent innervation area per afferent dendrite connecting to IHCs, derived by dividing the median values shown in Figure 5A by the data in panel **(A)**. **(C)** An estimate of the number of efferent terminals on each afferent dendrite connecting to IHCs, derived by dividing the median values shown in Figure 5B by the data in panel **(A)**.

degeneration. Degeneration of the spiral ganglion cell body occurs significantly later than the detachment of the peripheral dendrite from the IHC ribbon synapse, such that counts at different locations yield significantly different results for the same chronological age (Makary et al., 2011; Sergeyenko et al., 2013; Wu et al., 2019). Thus, if the retraction of the primary dendrite happened relatively more quickly in gerbil, a delay between observed afferent synapse loss and observed LOC loss might be less noticeable. Interestingly, a spatial re-distribution of presumed LOC terminals occurred in aging CBA/CaJ mice, such that many shifted to a position further below the IHC's basal pole (Grierson et al., 2022), which could reflect afferent dendrites retracting together with the efferent terminals attached to them. A minority was also seen further up on the IHC than typically observed in young adults (Grierson et al., 2022), which could reflect the exploration of new targets by orphaned LOC branches, and possibly axosomatic re-connections (see also section 4.5). Higher-resolution ultrastructural studies are needed to resolve the dynamics of potential efferent retraction and re-distribution that are associated with age-related changes to their targets.

4.4 Age-related changes to efferent innervation in OHC region (presumed MOC)

The overall density of MOC terminals per OHC declined only mildly in old gerbils, by about 10%, and was not consistently significant for most cochlear locations (Figure 6). Comparisons with previous studies are problematic in detail and highlight that for evaluating MOC innervation in particular, it is crucial to be aware of subtle methodological differences when comparing species or ages. Furthermore, C57BL/6 mice, with their accelerated auditory aging phenotype, are again a special case (Fu et al., 2010; Jeng et al., 2020) and are excluded from our species comparison. Two separate confounding factors need to be considered. First, OHC loss in aged cochleae tends to be more severe than IHC loss, and more variable between species and studies, even for comparable lifespan stages. The loss of OHCs in our quiet-aged gerbils was, on average, a moderate 11%, which is consistent with previous gerbil studies, despite slightly different tonotopic patterns of this loss (Tarnowski et al., 1991; Adams and Schulte, 1997). In humans and mice, more drastic OHC losses were observed that were typically most pronounced at the apical and basal extremes of the cochlea (Spongr et al., 1997; Sergeyenko et al., 2013; Liberman and Liberman, 2019; Kobrina et al., 2020; Wu et al., 2020; Grierson et al., 2022). If a specific evaluation of the efferent innervation status is aimed for, it is thus imperative to normalize MOC innervation metrics to the number of surviving OHCs. After doing so, age-related declines are typically moderate or cannot be clearly demonstrated. In humans of comparably old ages to the gerbils of the present study, VAT-immunolabeled area per surviving OHC was not significantly different to younger adults, but it did significantly decline in even older individuals, aged up to 70% of the human maximum lifespan potential (Liberman and Liberman, 2019). In C3H/HeJ mice (a strain with a similar auditory-aging phenotype to CBA/CaJ), no loss in the number of efferent synapses per surviving OHC was evident (Jeng et al., 2020), but the mice were still comparatively young, only up to 40% of their maximum lifespan potential. In CBA/CaJ mice of much more advanced ages, up to 80% of their maximum lifespan potential, the loss of VAT-immunolabeled area per surviving OHC was borderline significant when compared to young adults (Grierson et al., 2022).

Furthermore, conclusions may differ, depending on the metric used to evaluate efferent innervation. Both Kobrina et al. (2020) and Grierson et al. (2022) observed a more pronounced age-related decline in their CBA/CaJ mice when MOC innervation was quantified as the

number of terminals per surviving OHC (instead of immunolabeled area). Very interestingly, in both studies the numbers of efferent terminals per OHC fell below 1 at the most apical locations which strongly suggests that orphaned OHC, without any efferent innervation, occurred. This was pronounced in the apical regions of our old gerbils and was quantified here for the first time. Efferent innervation metrics were then normalized per innervated OHC in Figures 3B,D, 6, 7. If we instead normalized per surviving OHC (see Supplementary Figure S2), the overall difference between young-adult and old ears was larger and more clearly significant (18% loss in innervation area per OHC, n-way ANOVA: $F(1,78) = 8.08$, $p = 0.0057$; and 16% loss in terminal number per OHC, n-way ANOVA: $F(1,73) = 16.04$, $p < 0.0005$). Orphaned OHC have been anecdotally reported in young-adult rhesus monkeys and humans (Liberman and Liberman, 2019) as well as in old mice of several strains (Fu et al., 2010; Jeng et al., 2020; Grierson et al., 2022). It is currently unclear whether this phenomenon is particularly pronounced in gerbils or whether it has simply received little attention in other species.

Age-related OHC loss and an increase in orphaned OHCs also need to be considered when comparing age-related losses in the numbers of brainstem MOC neurons to peripheral metrics of OHC efferent innervation. For both old gerbils (Radtke-Schuller et al., 2015) and old CBA/CaJ mice (Vicencio-Jimenez et al., 2021), MOC neuron numbers were reduced by, on average, 31 and 36%, respectively, compared to young adults. These numbers are in the same ballpark as OHC losses (mice: Kobrina et al., 2020; Grierson et al., 2022) or OHC losses and orphaned OHCs combined (gerbil: this study), and are thus consistent with the more moderate reductions observed for the efferent innervation of surviving OHC.

We conclude that the extent of age-related changes in the efferent innervation of surviving OHCs varies between studies, and that some of this variation may be due to the as yet underappreciated phenomenon of orphaned OHCs (i.e., OHCs without efferent innervation). In the gerbil, the proportion of orphaned OHCs clearly increased with age, and spread further basally along the cochlea. Surviving OHCs that were still efferently innervated showed a tendency for only a small reduction in efferent innervation. This is consistent with previous suggestions that the loss of MOC innervation might precede OHC death (Jacobson et al., 2003; Zhu et al., 2007; Fu et al., 2010; Grierson et al., 2022).

4.5 Implications for efferent function in the aging cochlea

Counts of olivocochlear neurons in the brainstem clearly showed a substantial age-related decline of both LOC and MOC (Radtke-Schuller et al., 2015; Vicencio-Jimenez et al., 2021). Most interestingly, the olivocochlear efferents were differentially more vulnerable to neurodegeneration than either vestibular efferents and trigeminal motor neurons (which share a common descent with olivocochlear efferents), or brainstem neurones of the ascending auditory pathway (Radtke-Schuller et al., 2015; Vicencio-Jimenez et al., 2021). This implicates a specific trigger for age-related, auditory efferent loss. Data on peripheral innervation, such as those reported here, suggest that this loss occurs, to a large extent, in parallel with the loss of efferent target structures in the cochlea, primarily OHCs and type-I afferents. A likely aging scenario is thus that OHCs and type-I afferents die steadily with advancing age, taking their efferents with them. The surviving cochlear circuitry, however, remains, at least numerically, intact. This, in turn, predicts that it should be difficult to attribute age-related cochlear functional deficits specifically to a decline in efferent function.

For LOC, current evidence does not clearly support any specific sequence of age-related degeneration. Data from mice and humans that showed a more extensive loss of afferent, compared to efferent, synapses at comparable ages (see section 4.3) might suggest that the type-I afferents disconnect from the IHC first. For the gerbil, where we found no such discrepancy, this would then imply that LOC terminals degenerate quickly (perhaps more quickly than in mice and humans) together with their respective afferent dendrite, leaving the LOC circuitry that remains on the surviving afferents intact. On the other hand, there is evidence for subtle re-modeling of the LOC circuitry in aging cochleae that may not be obvious in common metrics of efferent innervation density. New axosomatic efferent contacts with IHC may be formed (Lauer et al., 2012) by LOC branches (Jeng et al., 2021), leading to the intriguing hypothesis that age-related loss of afferent synapses and dendrites may induce some of the thus orphaned LOC efferent branches to move up onto the IHC. Axosomatic efferent synapses on aging IHC have been shown to be functional, and inhibitory (Zachary and Fuchs, 2015). It currently remains unclear whether this is a general phenomenon across species, or even across mouse strains (Jeng et al., 2021), and whether it could be functionally adaptive. Understanding of LOC function and any potential age-related deficits is still in its infancy, and awaits the development of specific assays (reviewed in Lauer et al., 2022).

Indirect assays of MOC function, via their known suppression of otoacoustic emissions, showed age-related declines in both mice and humans, consistent with neurodegeneration (Kim et al., 2002; Jacobson et al., 2003; Zhu et al., 2007). Importantly, the decline began before there was any evidence of OHC degeneration, suggesting that the change was specific to the MOC efferent system. This hypothesis is supported by observations of mild losses of MOC innervation on surviving OHCs, and possibly an age-related increase in orphaned OHCs (see section 4.4) that, together, imply a sequence of degeneration, with efferents retracting first and OHCs dying shortly after. However, whether this truly causes a specific efferent dysfunction remains to be shown. Several technical issues with the rather indirect DPOAE suppression assay, as well as reduced afferent input to the neural feedback loops involved, due to age-related degeneration of type-I afferent neurons, remain valid concerns (reviewed in Guinan, 2018; Fuchs and Lauer, 2019). More direct measures of OHC functional aging revealed subtle changes in OHC size and membrane properties that, however, caused no functional deficits (Jeng et al., 2020). In summary, although there is (mainly anatomical) evidence that MOC degeneration may be the primary age-related event, closely followed by OHC death, any specific functional deficit associated with the initial MOC loss remains to be demonstrated. This hypothesized deficit should be larger, the longer is the delay between MOC loss and OHC death, leaving a more or less significant, transient population of orphaned OHCs that are no longer under efferent control.

Data availability statement

The raw data supporting the conclusions of this article will be made available by the authors, without undue reservation.

Ethics statement

The animal study was approved by Niedersächsisches Landesamt für Verbraucherschutz und Lebensmittelsicherheit (LAVES), Oldenburg, Germany. The study was conducted in accordance with the local legislation and institutional requirements.

Author contributions

FS: Data curation, Formal analysis, Investigation, Methodology, Supervision, Validation, Visualization, Writing – original draft, Writing – review & editing. AP: Formal analysis, Investigation, Methodology, Validation, Writing – original draft, Writing – review & editing. CK: Conceptualization, Data curation, Funding acquisition, Methodology, Project administration, Resources, Supervision, Validation, Writing – original draft, Writing – review & editing.

Funding

The author(s) declare financial support was received for the research, authorship, and/or publication of this article. This work was supported by the Deutsche Forschungsgemeinschaft (DFG, German Research Foundation) under Germany's Excellence Strategy – EXC 2177/1 – Project ID 390895286.

Acknowledgments

We acknowledge the Fluorescence Microscopy Service Unit, Carl von Ossietzky Universität Oldenburg, for the use of their imaging facilities. We thank Sonja Pyott for advice on immunostaining procedures, Inga Peters for help with specimen preparation and image analysis, and Amarins Heeringa for help with statistics and figure preparation. English language service was provided by stels-ol.

Conflict of interest

The authors declare that the research was conducted in the absence of any commercial or financial relationships that could be construed as a potential conflict of interest.

Publisher's note

All claims expressed in this article are solely those of the authors and do not necessarily represent those of their affiliated organizations, or those of the publisher, the editors and the reviewers. Any product that may be evaluated in this article, or claim that may be made by its manufacturer, is not guaranteed or endorsed by the publisher.

Supplementary material

The Supplementary material for this article can be found online at: https://www.frontiersin.org/articles/10.3389/fnsyn.2024.1422330/full#supplementary-material

References

Adams, J. C., and Schulte, B. A. (1997). Histopathologic observations of the aging gerbil cochlea. *Hear. Res.* 104, 101–111. doi: 10.1016/S0378-5955(96)00184-0

Barone, C. M., Douma, S., Reijntjes, D. O. J., Browe, B. M., Köppl, C., Klump, G., et al. (2019). Altered cochlear innervation in developing and mature naked and Damaraland mole rats. *J. Comp. Neurol.* 527, 2302–2316. doi: 10.1002/cne.24682

Boero, L. E., Castagna, V. C., Terreros, G., Moglie, M. J., Silva, S., Maass, J. C., et al. (2020). Preventing presbycusis in mice with enhanced medial olivocochlear feedback. *Proc. Natl. Acad. Sci. U. S. A.* 117, 11811–11819. doi: 10.1073/pnas.2000760117

Bovee, S., Klump, G. M., Pyott, S. J., Sielaff, C., and Köppl, C. (2024). Cochlear ribbon synapses in aged gerbils. *Int. J. Mol. Sci.* 25:2738. doi: 10.3390/ijms25052738

Brown, M. C. (2011). "Anatomy of Olivocochlear neurons" in *Auditory and vestibular efferents*. eds. D. Ryugo, R. R. Fay and A. N. Popper (New York, NY: Springer Science+Business Media, LLC), 17–37.

Brown, M. C., and Nuttall, A. L. (1984). Efferent control of cochlear inner hair cell responses in the guinea-pig. *J. Physiol.* 354, 625–646. doi: 10.1113/jphysiol.1984.sp015396

Castaño-González, K., Köppl, C., and Pyott, S. J. (2024). The crucial role of diverse animal models to investigate cochlear aging and hearing loss. *Hear. Res.* 445:108989. doi: 10.1016/j.heares.2024.108989

Cheal, M. L. (1986). The gerbil: a unique model for research on aging. *Exp. Aging Res.* 12, 3–21. doi: 10.1080/03610738608259430

Cooper, N. P., and Guinan, J. J. (2006). Efferent-mediated control of basilar membrane motion. *J. Physiol. Lond.* 576, 49–54. doi: 10.1113/jphysiol.2006.114991

D'Aldin, C., Puel, J. L., Leducq, R., Crambes, O., Eybalin, M., and Pujol, R. (1995). Effects of a dopaminergic agonist in the guinea pig cochlea. *Hear. Res.* 90, 202–211. doi: 10.1016/0378-5955(95)00167-5

Darrow, K. N., Maison, S., and Liberman, M. C. (2006). Cochlear efferent feedback balances interaural sensitivity. *Nat. Neurosci.* 9, 1474–1476. doi: 10.1038/nn1807

Darrow, K. N., Maison, S. F., and Liberman, M. C. (2007). Selective removal of lateral olivocochlear efferents increases vulnerability to acute acoustic injury. *J. Neurophysiol.* 97, 1775–1785. doi: 10.1152/jn.00955.2006

Dondzillo, A., Takeda, H., and Gubbels, S. P. (2021). Sex difference in the efferent inner hair cell synapses of the aging murine cochlea. *Hear. Res.* 404:108215. doi: 10.1016/j.heares.2021.108215

Elgoyhen, A. B., Wedemeyer, C., and Di Guilmi, M. N. (2019). "Efferent innervation to the cochlea" in *The Oxford handbook of the auditory brainstem*. ed. K. Kandler (Oxford: Oxford University Press), 58–94.

Eybalin, M. (1993). Neurotransmitters and neuromodulators of the mammalian cochlea. *Physiol. Rev.* 73, 309–373. doi: 10.1152/physrev.1993.73.2.309

Eybalin, M., Charachon, G., and Renard, N. (1993). Dopaminergic lateral efferent innervation of the guinea-pig cochlea: Immunoelectron microscopy of catecholamine-synthesizing enzymes and effect of 6-hydroxydopamine. *Neuroscience* 54, 133–142. doi: 10.1016/0306-4522(93)90389-W

Fay, R. R. (1988). *Hearing in vertebrates: a psychophysics databook. 1st* Edn Winnetka, Illinois, USA: Hill-Fay Associates.

Fu, B., Le Prell, C. G., Simmons, D., Lei, D., Schrader, A., Chen, A. B., et al. (2010). Age-related synaptic loss of the medial olivocochlear efferent innervation. *Mol. Neurodegener.* 5:53. doi: 10.1186/1750-1326-5-53

Fuchs, P. A., and Lauer, A. M. (2019). Efferent inhibition of the cochlea. *Cold Spring Harb. Perspect. Med.* 9:a033530. doi: 10.1101/cshperspect.a033530

Gates, G. A., and Mills, J. H. (2005). Presbycusis. *Lancet* 366, 1111–1120. doi: 10.1016/S0140-6736(05)67423-5

Gleich, O., Semmler, P., and Strutz, J. (2016). Behavioral auditory thresholds and loss of ribbon synapses at inner hair cells in aged gerbils. *Exp. Gerontol.* 84, 61–70. doi: 10.1016/j.exger.2016.08.011

Grierson, K. E., Hickman, T. T., and Liberman, M. C. (2022). Dopaminergic and cholinergic innervation in the mouse cochlea after noise-induced or age-related synaptopathy. *Hear. Res.* 422:108533. doi: 10.1016/j.heares.2022.108533

Groff, J. A., and Liberman, M. C. (2003). Modulation of cochlear afferent response by the lateral olivocochlear system: activation via electrical stimulation of the inferior colliculus. *J. Neurophysiol.* 90, 3178–3200. doi: 10.1152/jn.00537.2003

Guinan, J. J. (2011). "Physiology of the medial and lateral olivocochlear systems" in *Auditory and vestibular efferents*. eds. D. Ryugo, R. R. Fay and A. N. Popper (New York, NY: Springer Science+Business Media, LLC), 39–81.

Guinan, J. J. Jr. (2018). Olivocochlear efferents: their action, effects, measurement and uses, and the impact of the new conception of cochlear mechanical responses. *Hear. Res.* 362, 38–47. doi: 10.1016/j.heares.2017.12.012

Hashimoto, S., and Kimura, R. S. (1988). Computer-aided three-dimensional reconstruction and morphometry of the outer hair cells of the guinea pig cochlea. *Acta Otolaryngol.* 105, 64–74. doi: 10.3109/00016488809119447

Heeringa, A. N., and Köppl, C. (2019). The aging cochlea: towards unraveling the functional contributions of strial dysfunction and synaptopathy. *Hear. Res.* 376, 111–124. doi: 10.1016/j.heares.2019.02.015

Heffner, R., Heffner, H., and Masterton, B. (1971). Behavioral measurements of absolute and frequency-difference thresholds in Guinea pig. *J. Acoust. Soc. Am.* 49, 1888–1895. doi: 10.1121/1.1912596

Hua, Y., Ding, X., Wang, H., Wang, F., Lu, Y., Neef, J., et al. (2021). Electron microscopic reconstruction of neural circuitry in the cochlea. *Cell Rep.* 34:108551. doi: 10.1016/j.celrep.2020.108551

Jacobson, M., Kim, S., Romney, J., Zhu, X., and Frisina, R. D. (2003). Contralateral suppression of distortion-product Otoacoustic emissions declines with age: a comparison of findings in CBA mice with human listeners. *Laryngoscope* 113, 1707–1713. doi: 10.1097/00005537-200310000-00009

Jeng, J. Y., Carlton, A. J., Johnson, S. L., Brown, S. D. M., Holley, M. C., Bowl, M. R., et al. (2021). Biophysical and morphological changes in inner hair cells and their efferent innervation in the ageing mouse cochlea. *J. Physiol.* 599, 269–287. doi: 10.1113/JP280256

Jeng, J. Y., Johnson, S. L., Carlton, A. J., De Tomasi, L., Goodyear, R. J., De Faveri, F., et al. (2020). Age-related changes in the biophysical and morphological characteristics of mouse cochlear outer hair cells. *J. Physiol.* 598, 3891–3910. doi: 10.1113/JP279795

Kaiser, A., Alexandrova, O., and Grothe, B. (2011). Urocortin-expressing olivocochlear neurons exhibit tonotopic and developmental changes in the auditory brainstem and in the innervation of the cochlea. *J. Comp. Neurol.* 519, 2758–2778. doi: 10.1002/cne.22650

Keithley, E. M., Ryan, A. F., and Woolf, N. K. (1989). Spiral ganglion cell density in young and old gerbils. *Hear. Res.* 38, 125–133. doi: 10.1016/0378-5955(89)90134-2

Kim, S. H., Frisina, D. R., and Frisina, R. D. (2002). Effects of age on contralateral suppression of distortion product otoacoustic emissions in human listeners with normal hearing. *Audiol. Neuro Otol.* 7, 348–357. doi: 10.1159/000066159

Kimura, R. S., and Wersall, J. (1962). Termination of the olivocochlear bundle in relation to the outer hair cells of the organ of Corti in guinea pig. *Acta Otolaryngol.* 55, 11–32. doi: 10.3109/00016486209127336

Kitcher, S. R., Pederson, A. M., and Weisz, C. J. C. (2022). Diverse identities and sites of action of cochlear neurotransmitters. *Hear. Res.* 419:108278. doi: 10.1016/j.heares.2021.108278

Kobrina, A., Schrode, K. M., Screven, L. A., Javaid, H., Weinberg, M. M., Brown, G., et al. (2020). Linking anatomical and physiological markers of auditory system degeneration with behavioral hearing assessments in a mouse (*Mus musculus*) model of age-related hearing loss. *Neurobiol. Aging* 96, 87–103. doi: 10.1016/j.neurobiolaging.2020.08.012

Kujawa, S. G., and Liberman, M. C. (1997). Conditioning-related protection from acoustic injury: effects of chronic Deefferentation and sham surgery. *J. Neurophysiol.* 78, 3095–3106. doi: 10.1152/jn.1997.78.6.3095

Lauer, A. M., Fuchs, P. A., Ryugo, D. K., and Francis, H. W. (2012). Efferent synapses return to inner hair cells in the aging cochlea. *Neurobiol. Aging* 33, 2892–2902. doi: 10.1016/j.neurobiolaging.2012.02.007

Lauer, A. M., Jimenez, S. V., and Delano, P. H. (2022). Olivocochlear efferent effects on perception and behavior. *Hear. Res.* 419:108207. doi: 10.1016/j.heares.2021.108207

Liberman, M. C. (2017). Noise-induced and age-related hearing loss: new perspectives and potential therapies. *F1000Res* 6:927. doi: 10.12688/f1000research.11310.1

Liberman, M. C., Dodds, L. W., and Pierce, S. (1990). Afferent and efferent innervation of the cat cochlea: quantitative analysis with light and electron microscopy. *J. Comp. Neurol.* 301, 443–460. doi: 10.1002/cne.903010309

Liberman, L. D., and Liberman, M. C. (2019). Cochlear efferent innervation is sparse in humans and decreases with age. *J. Neurosci. Off. J. Soc. Neurosci.* 39, 9560–9569. doi: 10.1523/JNEUROSCI.3004-18.2019

Liberman, M. C., Liberman, L. D., and Maison, S. F. (2014). Efferent feedback slows cochlear aging. *J. Neurosci.* 34, 4599–4607. doi: 10.1523/JNEUROSCI.4923-13.2014

Maison, S. F., Adams, J. C., and Liberman, M. C. (2003). Olivocochlear innervation in the mouse: immunocytochemical maps, crossed versus uncrossed contributions, and transmitter colocalization. *J. Comp. Neurol.* 455, 406–416. doi: 10.1002/cne.10490

Makary, C. A., Shin, J., Kujawa, S. G., Liberman, M. C., and Merchant, S. N. (2011). Age-related primary cochlear neuronal degeneration in human temporal bones. *J. Assoc. Res. Otolaryngol.* 12, 711–717. doi: 10.1007/s10162-011-0283-2

Moser, T., Brandt, A., and Lysakowski, A. (2006). Hair cell ribbon synapses. *Cell Tissue Res.* 326, 347–359. doi: 10.1007/s00441-006-0276-3

Müller, M. (1996). The cochlear place-frequency map of the adult and developing mongolian gerbil. *Hear. Res.* 94, 148–156. doi: 10.1016/0378-5955(95)00230-8

Oestreicher, E., Arnold, W., Ehrenberger, K., and Felix, D. (1997). Dopamine regulates the glutamatergic inner hair cell activity in guinea pigs. *Hear. Res.* 107, 46–52. doi: 10.1016/S0378-5955(97)00023-3

Parthasarathy, A., and Kujawa, S. G. (2018). Synaptopathy in the aging cochlea: characterizing early-neural deficits in auditory temporal envelope processing. *J. Neurosci. Off. J. Soc. Neurosci.* 38, 7108–7119. doi: 10.1523/JNEUROSCI.3240-17.2018

Radtke-Schuller, S., Seeler, S., and Grothe, B. (2015). Restricted loss of olivocochlear but not vestibular efferent neurons in the senescent gerbil (*Meriones unguiculatus*). *Front. Aging Neurosci.* 7:4. doi: 10.3389/fnagi.2015.00004

Radziwon, K. E., June, K. M., Stolzberg, D. J., Xu-Friedman, M. A., Salvi, R. J., and Dent, M. L. (2009). Behaviorally measured audiograms and gap detection thresholds in CBA/CaJ mice. *J. Comp. Physiol. A Neuroethol. Sens. Neural Behav. Physiol.* 195, 961–969. doi: 10.1007/s00359-009-0472-1

Reisinger, E., Bresee, C., Neef, J., Nair, R., Reuter, K., Bulankina, A., et al. (2011). Probing the functional equivalence of Otoferlin and Synaptotagmin 1 in exocytosis. *J. Neurosci.* 31, 4886–4895. doi: 10.1523/JNEUROSCI.5122-10.2011

Robertson, D. (1985). Brainstem location of efferent neurones projecting to the guinea pig cochlea. *Hear. Res.* 20, 79–84. doi: 10.1016/0378-5955(85)90060-7

Rontal, D. A., and Echteler, S. M. (2003). Developmental segregation in the efferent projections to auditory hair cells in the gerbil. *J. Comp. Neurol.* 467, 509–520. doi: 10.1002/cne.10931

Ruel, J., Wang, J., Dememes, D., Gobaille, S., Puel, J. L., and Rebillard, G. (2006). Dopamine transporter is essential for the maintenance of spontaneous activity of auditory nerve neurones and their responsiveness to sound stimulation. *J. Neurochem.* 97, 190–200. doi: 10.1111/j.1471-4159.2006.03722.x

Ryan, A. (1976). Hearing sensitivity of the mongolian gerbil, *Meriones unguiculatus*. *J. Acoust. Soc. Am.* 59, 1222–1226. doi: 10.1121/1.380961

Sanes, D. H., Merickel, M., and Rubel, E. W. (1989). Evidence for an alteration of the tonotopic map in the gerbil cochlea during development. *J. Comp. Neurol.* 279, 436–444. doi: 10.1002/cne.902790308

Schindelin, J., Arganda-Carreras, I., Friese, E., Kaynig, V., Pietzsch, T., Preibisch, S., et al. (2012). Fiji: an open-source platform for biological-image analysis. *Nat. Methods* 9, 676–682. doi: 10.1038/nmeth.2019

Schmiedt, R. A., Lang, H., Okamura, H., and Schulte, B. A. (2002). Effects of furosemide applied chronically to the round window: a model of metabolic Presbyacusis. *J. Neurosci.* 22, 9643–9650. doi: 10.1523/JNEUROSCI.22-21-09643.2002

Schulte, B. A., and Schmiedt, R. A. (1992). Lateral wall Na, K-ATPase and endocochlear potentials decline with age in quiet-reared gerbils. *Hear. Res.* 61, 35–46. doi: 10.1016/0378-5955(92)90034-K

Sergeyenko, Y., Lall, K., Liberman, M. C., and Kujawa, S. G. (2013). Age-related cochlear synaptopathy: an early-onset contributor to auditory functional decline. *J. Neurosci. Off. J. Soc. Neurosci.* 33, 13686–13694. doi: 10.1523/JNEUROSCI.1783-13.2013

Spongr, V., Flood, D. G., Frisina, R. D., and Salvi, R. J. (1997). Quantitative measures of hair cell loss in CBA and C57BL/6 mice throughout their life spans. *J. Acoust. Soc. Am.* 101, 3546–3553. doi: 10.1121/1.418315

Stamataki, S., Francis, H. W., Lehar, M., May, B. J., and Ryugo, D. K. (2006). Synaptic alterations at inner hair cells precede spiral ganglion cell loss in aging C57BL/6J mice. *Hear. Res.* 221, 104–118. doi: 10.1016/j.heares.2006.07.014

Steenken, F., Bovee, S., and Köppl, C. (2022). Immunolabeling and counting ribbon synapses in young adult and aged gerbil cochleae. *J. Vis. Exp.* 182:e63874. doi: 10.3791/63874

Steenken, F., Heeringa, A. N., Beutelmann, R., Zhang, L., Bovee, S., Klump, G. M., et al. (2021). Age-related decline in cochlear ribbon synapses and its relation to different metrics of auditory-nerve activity. *Neurobiol. Aging* 108, 133–145. doi: 10.1016/j.neurobiolaging.2021.08.019

Suryadevara, A. C., Schulte, B. A., Schmiedt, R. A., and Slepecky, N. B. (2001). Auditory nerve fibers in young and quiet-aged gerbils: morphometric correlations with endocochlear potential. *Hear. Res.* 161, 45–53. doi: 10.1016/S0378-5955(01)00340-9

Tarnowski, B. I., Schmiedt, R. A., Hellstrom, L. I., Lee, F. S., and Adams, J. C. (1991). Age-related changes in cochleas of mongolian gerbils. *Hear. Res.* 54, 123–134. doi: 10.1016/0378-5955(91)90142-V

Vetter, D. E., Adams, J. C., and Mugnaini, E. (1991). Chemically distinct rat olivocochlear neurons. *Synapse* 7, 21–43. doi: 10.1002/syn.890070104

Vicencio-Jimenez, S., Weinberg, M. M., Bucci-Mansilla, G., and Lauer, A. M. (2021). Olivocochlear changes associated with aging predominantly affect the medial olivocochlear system. *Front. Neurosci.* 15:704805. doi: 10.3389/fnins.2021.704805

Warr, W. B., and Guinan, J. J. (1979). Efferent innervation of the organ of corti: two separate systems. *Brain Res.* 173, 152–155. doi: 10.1016/0006-8993(79)91104-1

WHO (2021). *World report on hearing*. Geneva: World Health Organization.

Wolfes, A. C., and Dean, C. (2020). The diversity of synaptotagmin isoforms. *Curr. Opin. Neurobiol.* 63, 198–209. doi: 10.1016/j.conb.2020.04.006

Wu, P. Z., Liberman, L. D., Bennett, K., de Gruttola, V., O'Malley, J. T., and Liberman, M. C. (2019). Primary neural degeneration in the human cochlea: evidence for hidden hearing loss in the aging ear. *Neuroscience* 407, 8–20. doi: 10.1016/j.neuroscience.2018.07.053

Wu, P. Z., O'Malley, J. T., de Gruttola, V., and Liberman, M. C. (2020). Age-related hearing loss is dominated by damage to inner ear sensory cells, not the cellular battery that powers them. *J. Neurosci. Off. J. Soc. Neurosci.* 40, 6357–6366. doi: 10.1523/JNEUROSCI.0937-20.2020

Zachary, S. P., and Fuchs, P. A. (2015). Re-emergent inhibition of Cochlear inner hair cells in a mouse model of hearing loss. *J. Neurosci. Off. J. Soc. Neurosci.* 35, 9701–9706. doi: 10.1523/JNEUROSCI.0879-15.2015

Zhu, X. X., Vasilyeva, O. N., Kim, S., Jacobson, M., Romney, J., Waterman, M. S., et al. (2007). Auditory efferent feedback system deficits precede age-related hearing loss: contralateral suppression of otoacoustic emissions in mice. *J. Comp. Neurol.* 503, 593–604. doi: 10.1002/cne.21402

Zwicker, E., and Fastl, H. (1990). *Psychoacoustics: facts and models*. New York: Springer-Verlag.

frontiers | Frontiers in Cellular Neuroscience

TYPE Review
PUBLISHED 19 June 2024
DOI 10.3389/fncel.2024.1414484

Check for updates

OPEN ACCESS

EDITED BY
Bernhard Englitz,
Radboud University, Netherlands

REVIEWED BY
Michael Thomas Roberts,
University of Michigan, United States
Jeffrey Garrett Mellott,
Northeast Ohio Medical University,
United States

*CORRESPONDENCE
R. Michael Burger
✉ rmb206@lehigh.edu

RECEIVED 09 April 2024
ACCEPTED 06 June 2024
PUBLISHED 19 June 2024

CITATION
Zhang C and Burger RM (2024) Cholinergic modulation in the vertebrate auditory pathway.
Front. Cell. Neurosci. 18:1414484.
doi: 10.3389/fncel.2024.1414484

COPYRIGHT
© 2024 Zhang and Burger. This is an open-access article distributed under the terms of the Creative Commons Attribution License (CC BY). The use, distribution or reproduction in other forums is permitted, provided the original author(s) and the copyright owner(s) are credited and that the original publication in this journal is cited, in accordance with accepted academic practice. No use, distribution or reproduction is permitted which does not comply with these terms.

Cholinergic modulation in the vertebrate auditory pathway

Chao Zhang[1] and R. Michael Burger[2]*

[1]Cold Spring Harbor Laboratory, Cold Spring Harbor, NY, United States, [2]Department of Biological Sciences, Lehigh University, Bethlehem, PA, United States

Acetylcholine (ACh) is a prevalent neurotransmitter throughout the nervous system. In the brain, ACh is widely regarded as a potent neuromodulator. In neurons, ACh signals are conferred through a variety of receptors that influence a broad range of neurophysiological phenomena such as transmitter release or membrane excitability. In sensory circuitry, ACh modifies neural responses to stimuli and coordinates the activity of neurons across multiple levels of processing. These factors enable individual neurons or entire circuits to rapidly adapt to the dynamics of complex sensory stimuli, underscoring an essential role for ACh in sensory processing. In the auditory system, histological evidence shows that acetylcholine receptors (AChRs) are expressed at virtually every level of the ascending auditory pathway. Despite its apparent ubiquity in auditory circuitry, investigation of the roles of this cholinergic network has been mainly focused on the inner ear or forebrain structures, while less attention has been directed at regions between the cochlear nuclei and midbrain. In this review, we highlight what is known about cholinergic function throughout the auditory system from the ear to the cortex, but with a particular emphasis on brainstem and midbrain auditory centers. We will focus on receptor expression, mechanisms of modulation, and the functional implications of ACh for sound processing, with the broad goal of providing an overview of a newly emerging view of impactful cholinergic modulation throughout the auditory pathway.

KEYWORDS

acetylcholine, modulation, auditory, sound, nicotinic, muscarinic

Introduction

The vast richness of sound sensation endows us with the ability to communicate, enjoy music, and navigate the world. These auditory experiences rely on an impossibly complex neural architecture that spans every major division of the central nervous system. Despite decades of research investigating the myriad components of this pathway, fundamental discoveries regarding its basic organizational and functional features continue to emerge with astonishing frequency. In recent years, new evidence has shown that modulatory circuitry is overlaid upon, and integrated within these circuits, adding further complexity to the fundamental neural computations that enable hearing in animals. This review focuses on recent work investigating cholinergic modulation along this pathway. These studies demonstrate that cholinergic circuits appear to influence auditory function at all levels and in a diversity of ways, from sound transduction in the inner ear to the auditory cortex (Figure 1).

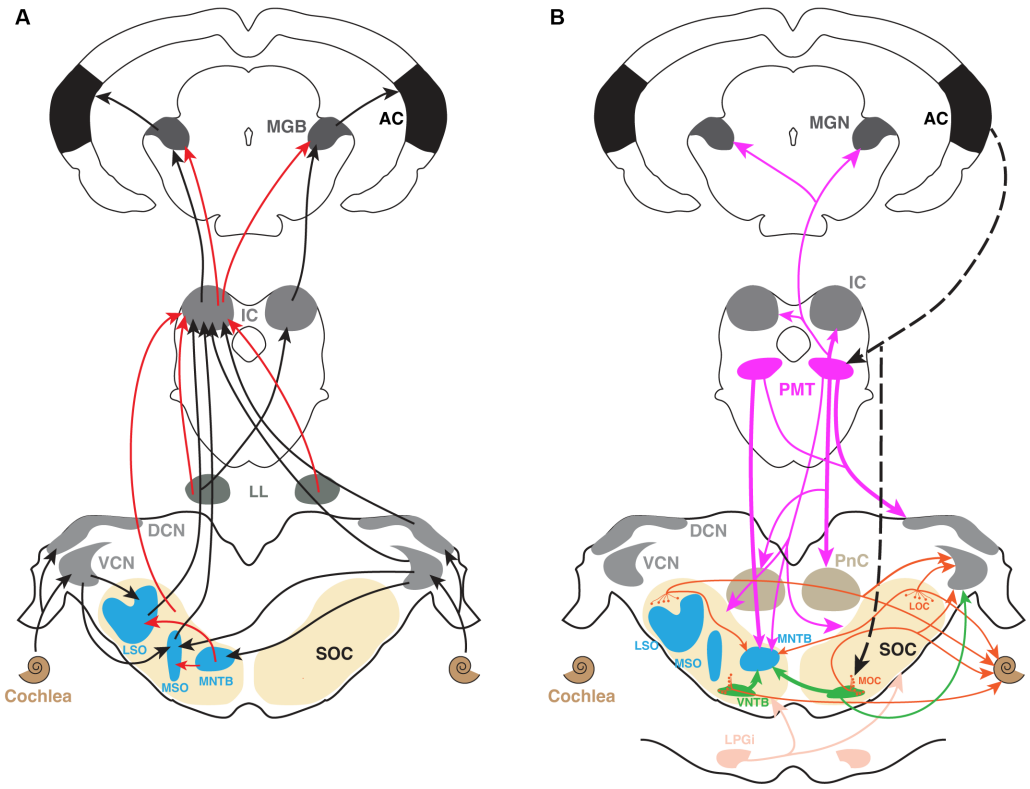


FIGURE 1
The mammalian ascending auditory pathway and its interactions with a complex cholinergic network. **(A)** The major components of the ascending auditory pathway from cochlea to the auditory cortex. *Black arrows* indicate excitation while *red arrows* indicate inhibition. The superior olive and its constituent nuclei are shown in *beige* and *blue*, respectively. **(B)** A summary of the known cholinergic connectivity within the auditory system. The colors of the arrows match the colors of the different cholinergic sources. Thickness of the arrows from the same source indicates the relative strength of cholinergic outputs based on anatomical descriptions. AC, auditory cortex; DCN, dorsal cochlear nucleus; IC, inferior colliculus; LL, lateral lemniscus; LOC, lateral olivecochlear; LPGi, lateral paragigantocellular nucleus; LSO, lateral superior olive; MGN, medial geniculate nucleus; MNTB, medial nucleus of trapezoid body; MOC, medial olivecochlear; MSO, medial superior olive; PMT, pontomesencephalic tegmentum; PnC, pontine reticular nucleus; SOC, superior olivary complex; VCN, ventral cochlear nucleus; VNTB, ventral nucleus of trapezoid body.

General organization of the ascending auditory pathway

Sound is first transduced into electrical signals in the hair cells of the inner ear before processing through a rich and interconnected network of auditory centers from the ear to cortex in vertebrates. Afferent auditory nerve fibers encode and relay this information to several distinct neuron types in the cochlear nucleus (CN) of the brain (Osen, 1969a, 1970; Young and Brownell, 1976; Rhode et al., 1983; Oertel et al., 2002; Maclaine and Llano, 2020). The mammalian cochlear nucleus complex is composed of two major divisions, the ventral (VCN) and dorsal cochlear nuclei (DCN) (Osen, 1969b). The VCN receives primary excitatory innervation from the inner ear via auditory nerve, therefore serving as the entry point of acoustic information into the brain (Arnesen and Osen, 1978; Oertel et al., 1990). The DCN is a cerebellum-like structure that receives both auditory nerve input as well as input from VCN and other brain regions (Osen, 1969b; Moore and Osen, 1979; Hackney et al., 1990; Oertel and Cao, 2020). The major outputs from the CN branch to form terminals in both ipsilateral and contralateral brainstem nuclei as well as the contralateral midbrain (Harrison and Irving, 1966; Bruce Warr, 1995; Davis, 2005). In the brainstem, the superior olivary complex (SOC) receives bilateral input from both CNs, and performs numerous fundamental auditory computations including those related to sound localization (Stotler, 1953; Kiss and Majorossy, 1983; Glendenning et al., 1985, 1991; Thompson and Schofield, 2000). The SOC is composed of both primary SOC nuclei and periolivary nuclei. The primary SOC comprises the medial nucleus of trapezoid body (MNTB), medial superior olive (MSO) and lateral superior olive (LSO). These nuclei have been intensively studied for their physiological properties as major centers of binaural computations for sound-localization (Goldberg and Brown, 1969; Yin and Chan, 1990; Grothe and Sanes, 1993; Pollak et al., 2003; Burger and Rubel, 2008; Grothe and Pecka, 2014; Risoud et al., 2018). SOC nuclei output to lateral lemniscus (LL) ipsilaterally and inferior colliculus (IC) bilaterally (Adams, 1979; Glendenning et al., 1981; Schofield, 1991; Oliver et al., 1995; Malmierca and Merchán, 2004; Henkel, 2018). Lemniscal nuclei in turn project to both ipsilateral and contralateral inferior colliculus (IC) in the midbrain (Harrison and Howe, 1974; Schofield, 2002). In this way, the IC is a major integration center of auditory circuitry, serving as the point of convergence for nearly all afferent pathways emanating from lower nuclei (Pollak et al., 1986; Zook and Casseday, 1987; Ito et al., 2016; Maclaine and Llano, 2020). The IC projects to the ipsilateral thalamic medial geniculate nucleus (MGN) (Tachibana et al., 1979; Kudo and Niimi, 1980; Rouiller and de Ribaupierre, 1985; Mellott et al., 2019), from which the acoustic

information is then conveyed to the primary auditory cortex (AC) (Oliver and Hall, 1978; Brugge and Howard, 2002). Two subdivisions of AC, the primary and secondary AC (A1, A2, respectively) receive auditory input from MGN, thus completing the major afferent circuitry (Strutz, 1987; Bizley, 2017).

A pervasive cholinergic network influences the ascending auditory pathway

ACh was first chemically identified by Baeyer (1867). Its recognition as a neurotransmitter by Dale (1914) and Loewi and Navratil (1926), initiated over a century of studies on this biochemically important molecule. Upon released into the synaptic cleft, ACh binds to one of many ionotropic or metabotropic acetylcholine receptors (AChRs) that influences the physiology of neurons is a wide variety of ways. Cholinergic function has been extensively studied in high ordered auditory neurons, like those of the thalamus and cortex. For example, the forebrain nucleus basalis (NB) serves as the main cholinergic source projecting widely to neocortex. Using *in vivo* recording, Froemke et al. (2007) discovered that NB-originating cholinergic input is capable of shaping the frequency tuning of auditory cortex (A1) neurons, by simultaneously increasing excitatory input and dampening inhibitory input. In a complimentary study, Leach et al. (2013) conducted behavioral studies on ferrets and discovered that loss of NB cholinergic circuitry reduces the accuracy of localizing brief sounds, and prevents adaptation to chronic occlusion of one ear, thereby significantly impairing sound-localization ability. ACh has also been suggested to modulate several important AC computational functions including spatial receptive fields (Froemke et al., 2007; Metherate, 2011), frequency selectivity (Ashe et al., 1989; McKenna et al., 1989; Metherate and Weinberger, 1989, 1990), tuning curves (Froemke et al., 2007; Metherate et al., 2012), rate-level functions (RLF) (McKenna et al., 1988; Metherate et al., 1990; Metherate and Weinberger, 1990; Kawai et al., 2007), sound-evoked firing patterns (Metherate et al., 1992), intra-cortical communication (Froemke et al., 2007; James et al., 2019) and cognitive function (Metherate, 2004; Liang et al., 2006, 2008; Leach et al., 2013). In the thalamus, ACh has been suggested to influence the firing pattern and encoding efficacy of MGN neurons (Mooney et al., 2004; Varela and Sherman, 2007; Hamada et al., 2010; Sottile et al., 2017; Richardson et al., 2021). Overall, the cholinergic modulation on AC and auditory thalamus strongly suggested the critical role of ACh in mediating higher-ordered sensory processing. For a thorough review of this work see (Metherate and Hsieh, 2004; Richardson et al., 2021; Kunnath et al., 2023).

More recently, work in the auditory brainstem has extended this general view of cholinergic modulation to lower ordered central processing. Studies on cholinergic function by our lab and others reveals that ACh makes major contributions to fundamental neural computations that enable or enhance features such as signal detection in noise and sound intensity encoding in several brainstem and midbrain regions. Here we will describe findings from our recent studies and those of other laboratories on cholinergic modulation that are building a new appreciation of its pervasive and complex functionality to light.

A diversity of acetylcholine receptors mediate intrinsic properties of neurons

There are two broad categories of AChRs, muscarinic and nicotinic, named for the agonistic effects of the fungal toxin muscarine or the plant toxin nicotine on the receptors (Servent et al., 2011). Muscarinic receptors (mAChRs) comprise a diverse class of metabotropic G-protein coupled receptors (GPCRs) (Ishii and Kurachi, 2006). Among the five major subtypes of mAChR, referred to as M1-M5; M1, M3 and M5 subtypes engage Gq proteins and trigger IP3 and calcium signaling pathways upon receptor activation (Roeren et al., 1988; Caulfield and Birdsall, 1998; Eglen, 2006). In contrast, M2 and M4 subtypes employ Gi proteins to down-regulate adenylyl cyclase, and subsequently decrease protein kinase A activity (Dell'Acqua et al., 1993). Through both pathways, mAChRs can function to indirectly influence the activity of ion channels in the cytoplasmic membrane and influence neural signaling. Typically, M1, M3, and M5 receptor activation imparts a net excitatory effect, while M2 and M4 activation drives inhibitory/suppressive effects (Figure 2).

Globally, the excitatory mAChRs effects derive from suppressive modulation of potassium channels (Brown, 2018). These potassium channels include voltage dependent Kv7 (KCNQ) (Brown and Adams, 1980; Womble and Moises, 1992), leak K2p (KCNP) (Madison et al., 1987; Womble and Moises, 1992; Coggan et al., 1994), G-protein-coupled inward rectifiers (GIRK) (Uchimura and North, 1990), and Ca^{++} activated potassium SK family channels that are responsible for the slow afterhyperpolarization current I_{AHP} (Madison et al., 1987; Coggan et al., 1994). mAChR-dependent block of K,7-mediated outward M-current (I_M) enhances excitability by producing membrane depolarization, increasing input resistance and reducing action potential threshold. In the auditory system, the Kv7 expression has been documented in several regions. Anatomical evidence suggested the prevalence of Kv7.5 in synaptic endings of the rat auditory brainstem nuclei, including CN, LSO, MSO, SPN, MNTB, LL, and IC (Caminos et al., 2007; Garcia-Pino et al., 2010). Kv7.2, 7.3 and 7.4 were anatomically identified in mammalian IC (Wang et al., 1998; Kharkovets et al., 2000). Kv7.4 was also found in cochlear hair cells, CN and LL (Kharkovets et al., 2000). The presence of Kv7 in these regions strongly suggests the co-expression of mAChRs. Other than Kv7-mediated modulation of excitation, blockage of voltage-insensitive leak K^+ channels by muscarinic receptors was observed to excite T stellate cells of VCN (Fujino and Oertel, 2001). On the other hand, muscarinic receptors have also been shown to hyperpolarize neurons and thereby decrease neuron excitability, by activating GIRK channels in Golgi cells of DCN (Irie et al., 2006) and in caudal pontine reticular nucleus (Bosch and Schmid, 2006). In addition, post-synaptic M1/M3 mAChRs activation has been shown to influence synaptic plasticity by converting long-term potentiation (LTP) into long-term depression (LTD) in mouse principal DCN neurons (Zhao and Tzounopoulos, 2011). This effect is likely due to an interplay between the cholinergic system and another potent modulator, the endocannabinoid system. It is suggested that upon activation of these mAChRs, the postsynaptic GPCR-coupled intracellular cascade enhanced modulation by parallel endocannabinoid signaling impinging on the same DCN neuron.

Nicotinic receptors (nAChRs) are ionotropic cation channels (Itier and Bertrand, 2001; Hammond, 2015) composed of 5 subunits. These channels are variably selective for Na^+, K^+ and Ca^{2+} depending

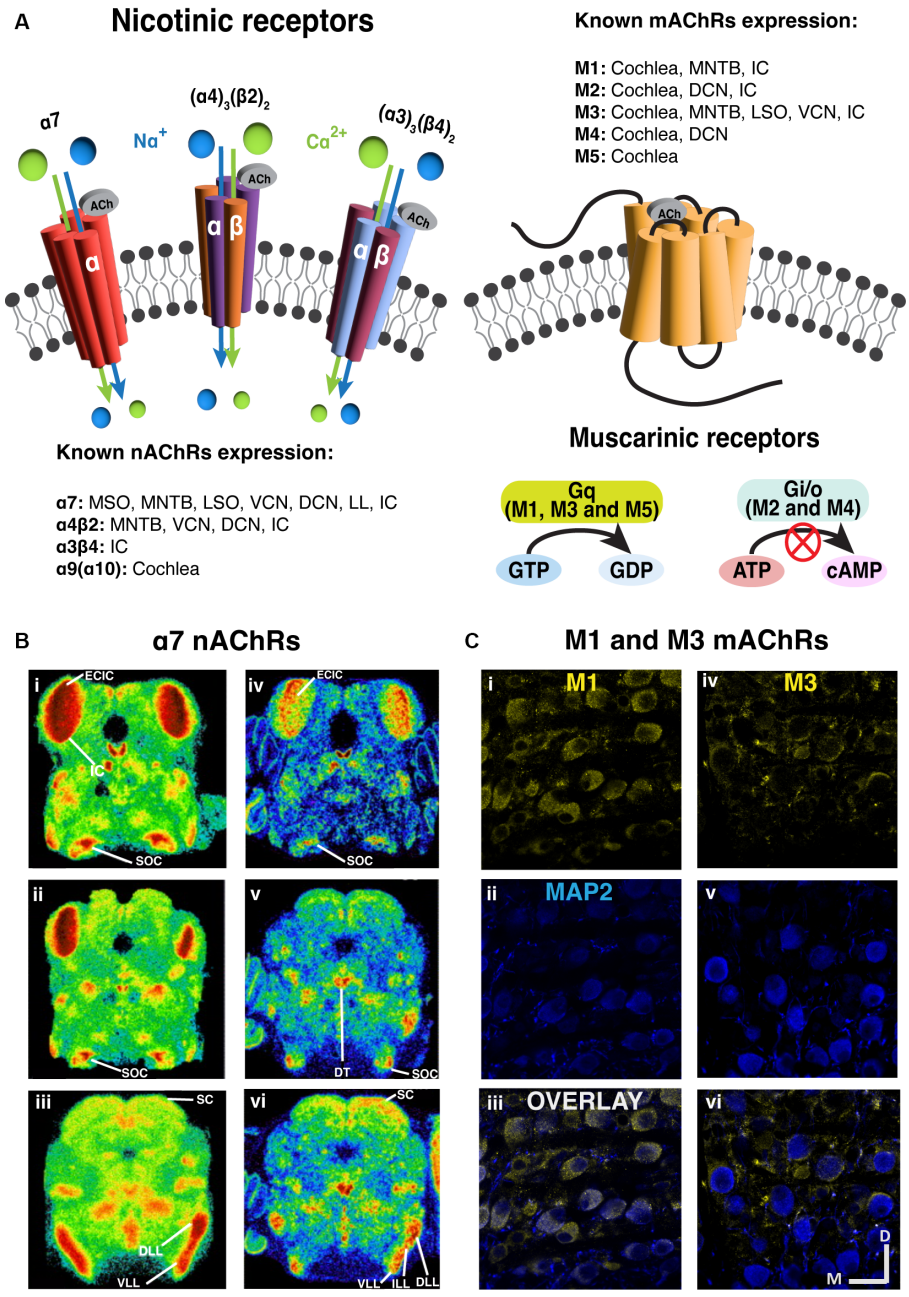


FIGURE 2
Prevalent expression of nicotinic and muscarinic acetylcholine receptors along the brainstem auditory pathway. **(A)** The structure and signaling pathways of ionotropic nicotinic and metabotropic muscarinic cholinergic receptors in the CNS. Three representative nAChRs, α7, (α4)3(β2)2 and (α3)3(β4)2 subtypes are shown, showing that most nAChRs are ligand gated ion channels. On the other hand, most mAChRs are G protein-coupled receptors (GPCR). M1, M3 and M5 subtypes are Gq-coupling excitatory receptors, while M2 and M4 are Gi/o-coupling inhibitory receptors. **(B)** The expression of α7 nAChRs are prevalent in the auditory brainstem [adapted from Happe and Morley (2004), with permission from Elsevier; license # 5762610422615]. Left panels **(i–iii)**: Representative images of mouse α7 mRNA *in situ* hybridization at several levels of the auditory brainstem at P10. Right panels **(iv–vi)**: Representative images of rat 125I-α-bungarotoxin binding at several levels of the auditory brainstem at P10. **(C)** Immunohistochemical labeling shows that both M1 and M3 mAChRs expression in the gerbil medial nucleus of trapezoid body [MNTB, adapted from Weimann et al. (2024), with permission from the Journal of Neuroscience under CC-BY license]. M1 expression yellow label **(i–iii)** appears to be somatic while M3 labeling yellow label **(iv–vi)** suggests presynaptic localization. The microtubule associated protein 2 (MAP2) was labeled in blue. DCN, dorsal cochlear nucleus; DLL, dorsal lateral lemniscus; DT, dorsal tegmental; ECIC, external cortex of inferior colliculus; IC, inferior colliculus; ILL, intermediate lateral lemniscus; LL, lateral lemniscus; LSO, lateral superior olive; MNTB, medial nucleus of trapezoid body; MOC, medial olivecochlear; MSO, medial superior olive; SC, superior colliculus; SOC, superior olivary complex; VCN, ventral cochlear nucleus; VLL, ventral lateral lemniscus.

on subunit composition (Beker et al., 2003; Weber et al., 2005), where alpha-7 subunit containing channels exhibit prominent Ca^{2+} permeability. The influx of Ca^{2+} through alpha-7 subunit containing receptors has been shown to increase neurotransmitter release when these receptors are expressed in pre-synaptic terminals (Shen and Yakel, 2009; Uteshev, 2012). Generally, when ionotropic nAChRs are

excitatory and expressed post-synaptically, their activation leads to cation influx and depolarization (Changeux and Paas, 2009; Akers et al., 2020).

Cholinergic neurons are both extrinsic and intrinsic to the auditory system

The complexity of afferent auditory circuitry is complemented by a similarly complex network of cholinergic circuitry throughout the system. Some of these cholinergic projections arise from cholinergic or neuromodulatory nuclei outside of the canonical auditory centers, while other cholinergic neurons are intrinsic to the auditory pathway itself. Sources of ACh that project to AC have been identified primarily in the basal forebrain, while several regions between the cochlear nucleus and thalamus receive major cholinergic projections from the midbrain pontomesencephalic tegmentum (PMT) (Shute and Lewis, 1967; Hallanger et al., 1987; Schofield et al., 2011; Figure 1B). Furthermore, cholinergic cells have been identified in the SOC of rats (Sherriff and Henderson, 1994), guinea pigs (Motts et al., 2008), gerbils (Beebe et al., 2021; Zhang et al., 2021), mouse (Beebe et al., 2023) and human (Mizukawa et al., 1986; Heckers et al., 1992). Among the periolivary nuclei, the ventral nucleus of trapezoid body (VNTB) has been identified as a major cholinergic source to CN in rats (Gomez-Nieto et al., 2008), guinea pigs (Mellott et al., 2011), gerbils (Beebe et al., 2021), and mice (Beebe et al., 2023). Moreover, the lateral paragigantocellular nucleus (LPGi) has been recently identified as a novel cholinergic source that projects bilaterally to CN (Beebe et al., 2023) and SOC (Beebe et al., 2021). The LPGi has previously been associated with autonomic functions and sensory gating (Stornetta et al., 2013; Schofield and Hurley, 2018), and it has numerous connections with auditory structures (Andrezik et al., 1981; Kamiya et al., 1988). Additionally, neurons in VNTB and PMT have been shown to be driven by sound (Koyama et al., 1994; Reese et al., 1995a,b). Together these findings suggest that ACh release is triggered by numerous cholinergic sources upon sound presentation, and that this circuitry is poised to influence sound processing throughout the brain. Functionally, the involvement of a potent, sound-driven neuromodulator along the afferent pathway may render auditory neurons capable of dynamically adjusting excitability or synaptic transmission. These modulatory inputs maybe engaged to rapidly accommodate the demands of complex stimulus variations in intensity, spectral content, location and temporal structure. We will highlight some results that support this newly emerging broader view of cholinergic modulation.

Cholinergic function is diverse along the ascending auditory pathway

Cochlea and auditory nerve

The auditory periphery includes a cochlear amplification function mediated by electromotile outer hair cells (OHC) that increases acoustic gain and enhances cochlear output over a range of stimulus intensities (Guinan, 1996; Darrow et al., 2006, 2007). Efferent cholinergic projections protect the auditory periphery from sound-induced damage via suppression of the cochlear amplification system (Wolpert et al., 2014; Guinan, 2018). Cholinergic olivo-cochlear neurons include medial olivo-cochlear (MOC) and lateral olivo-cochlear (LOC) neurons. The anatomy and physiology of these efferent circuits has been reviewed in detail (Ciuman, 2010; Künzel and Wagner, 2017; Fuchs and Lauer, 2019; Romero and Trussell, 2022). The efferent synaptic inhibition at cochlear hair cells has been shown to involve α9α10-containing nicotinic receptors (Elgoyhen et al., 1994, 2001; Taranda et al., 2009). The activation of α9α10 nAChRs leads to increased Ca2+ influx, which subsequently activates Ca2+ dependent small conductance potassium SK2 channel (Dulon et al., 1998; Glowatzki and Fuchs, 2000; Oliver et al., 2000). This, in turn, leads to hyperpolarization of the cell membrane and hence, gain reduction (Roux et al., 2011). The main outcome of activating ACh release of this circuit is the suppression of sound-evoked responses, as demonstrated in Figure 3. This suppression leads to an elevated baseline cochlear threshold, and opposes acoustic injury caused by intense noise. In addition to this nicotinic effect, all five subtypes of muscarinic receptors are also found in the cochlea (Khan et al., 2002; Maison et al., 2010). Double deletion of M2/M4 mAChRs was shown to attenuate auditory responses of IHCs, which the authors suggest could decrease their vulnerability to acoustic injury (Maison et al., 2010). The muscarinic component is also suggested to act on cellular calcium-involving cascades to regulate the electromotility of OHC (Kalinec et al., 2000), presumably through shortening OHC and increasing motility amplitude (Kakehata et al., 1993; Dallos et al., 1997).

The effect of the olivo-cochlear reflex on the input–output encoding function of auditory fibers is well-known and has been thoroughly reviewed (Guinan, 1996; Künzel and Wagner, 2017). It has also been suggested that activation of the olivo-cochlear reflex could improve signal detection from noisy backgrounds by transiently enhancing acoustic gain in auditory fibers (Winslow and Sachs, 1988; Kawase et al., 1993). In terms of gain enhancement, one obvious benefit of modulation is to amplify responses to low input level sounds. The amplification of specific sound responses may have a particularly important function when acoustic information requires elevated neural sensitivity to ensure signal encoding. For example, in stimulus conditions where adapting neural responses to sound fall below threshold, temporary postsynaptic gain modulation may offset adaptive processes and preserve responses to reduced input amplitudes. We will highlight a few of the numerous examples type of modulation beyond the auditory periphery where cholinergic release has been documented to enhance or suppress responses at low stimulus intensities (Habbicht and Vater, 1996; Zhang et al., 2021).

Acetylcholine in central nuclei: the cochlear nucleus

The coexistence of muscarinic and nicotinic AChRs in the CN was first described in 1966 (Comis and Whitfield, 1968). They showed that the administration of either atropine, a muscarinic antagonist or dihydro-β-erythroidine (DHβE), a nicotinic antagonist reversed the ACh-induced threshold lowering in cat CN. Anatomical evidence further supported the cholinergic innervation of the CN in cats (Osen and Roth, 1969; Godfrey et al., 1977). Rodent anatomical studies have documented the presence of ACh-related markers in CN of rats (Godfrey and Matschinsky, 1981; Godfrey et al., 1987; Sherriff and

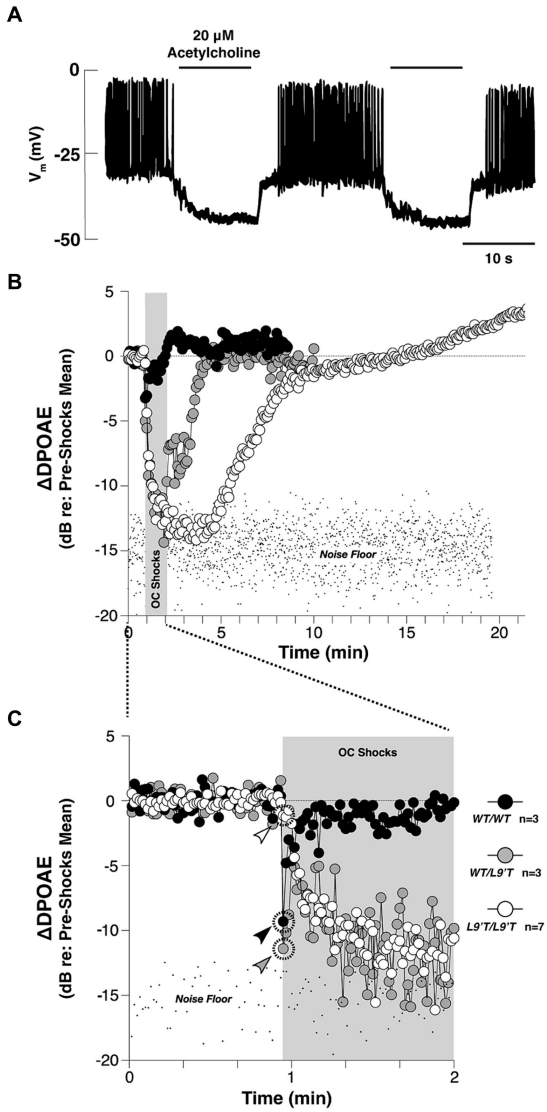


FIGURE 3
The cholinergic efferent feedback circuit suppresses hair cell activity and otoacoustic emissions from in the auditory periphery.
(A) Cholinergic inhibition of Ca^{2+} action potentials in the rat inner hair cells (IHC) during whole-cell current clamp. Application of 20 µM ACh hyperpolarized the membrane potential by ~15 mV, and thereby abolished the generation of Ca^{2+} action potentials of the IHC in response to 120 pA injection current [Adapted from Glowatzki and Fuchs (2000); with permission from American Association for the Advancement of Science; license # 5752590513900].
(B) Olivocochlear (OC)-mediated suppression of cochlear distortion product otoacoustic emission (DPOAE) is mediated by α9-containing nAChRs [adapted from Taranda et al. (2009), with permission from PLOS Biology under CC-BY license]. The DPOAEs were measured from anesthetized mice before, during and after 70-s of shock trains delivered to the OC bundle indicated by the *gray bars*. The mutant nAChRs are more sensitive to ACh than the wild-type nAChRs. Compared to the wild-type, mutant mice showed slowed, enhanced and prolonged OC-mediated suppression. **(C)** The onset period of the OC train shown in **(B)**. Arrowheads in **(C)** indicate the first point after shock-train onset for each genotype. In both **(B,C)**, note that the suppression with hypersensitized nAChRs were so strong that the DPOAE amplitudes were driven below the background noise floor.

Henderson, 1994; Yao and Godfrey, 1995, 1996; Happe and Morley, 1998), chinchilla (Rasmussen, 1960, 1965), mice (Martin, 1981), guinea pigs (Mellott et al., 2011; Schofield et al., 2011) and gerbils (Gillet et al., 2018). Specifically, both mAChRs and nAChRs have been identified in the CN of rats (Morley et al., 1977; Hunt and Schmidt, 1978; Yao and Godfrey, 1995, 1996; Happe and Morley, 1998) and gerbils (Gillet et al., 2018).

Functionally, ACh has been shown to enhance acoustic gain in the CN. *In vivo* studies in the VCN demonstrated that ACh enhanced the tone-evoked response of VCN neurons (Caspary et al., 1983; Goyer et al., 2016). This effect steepened the slope in dynamic range of the RLF and as a result, the difference in firing rates evoked by adjacent intensities was magnified. This suggested an elevated sensitivity and enhanced neural discriminability between similar intensities. Specifically, in the spherical bushy cells (SBCs) of gerbil VCN, this effect is likely mediated by the activation of fast inward current associated with α7 subunit containing nAChRs (Figure 4; Goyer et al., 2016). Indeed, studies have shown that signal detection in noisy backgrounds is also improved in T stellate cells of VCN, through a transiently enhanced sensitivity to tones via a cholinergic input putatively evoked during the olivocochlear reflex (Fujino and Oertel, 2001).

Additional studies in other divisions of the CN have similarly shown that cholinergic activation suppressed sound-evoked responses. This was observed in DCN (Comis and Whitfield, 1968; Caspary et al., 1983); likely through M2 and/or M4 mAChRs (Chen et al., 1995). This suppression effect has been suggested to be involved in noise protection at the level of CN. As the synaptic targets of auditory nerve fibers, the diverse populations of CN neurons give rise to several parallel processing streams that ascend the auditory system. Among these types it has been suggested that the hyperactivity of fusiform cells indicates tinnitus. Intense sound-induced hyperactivity has been shown to be suppressed by carbachol in fusiform cells of DCN (Kaltenbach and Zhang, 2007; Manzoor et al., 2013). Additionally, intense tone exposure has been shown to upregulate the choline acetyltransferase activity in the hamster CN (Jin et al., 2006), suggesting another potentially protective mechanism mediated by intrinsic cholinergic circuitry.

Acetylcholine in central nuclei: the superior olive

Several studies have identified markers of cholinergic signaling in the Superior Olive across a number of mammalian species. For example, mAChRs have been found in cat medial superior olive (MSO) through conventional autoradiographic receptor-binding of quinuclidinyl benzilate (QNB) (Glendenning and Baker, 1988). M3 muscarinic receptors were also found in LSO of both rat and guinea pig (Safieddine et al., 1996). In 2004, Happe and Morley demonstrated α7 nAChRs expression in rat SOC from radioactive mRNA *in situ* hybridization and from α-bungarotoxin binding (Happe and Morley, 2004). Similarly to that shown in CN, intense tones increased ChAT activity in the SOC (Godfrey et al., 2013), raising the possibility that the cholinergic network broadly protects against hearing damage throughout the system.

Since many principal SOC neurons are functionally well-understood, the region provides fertile ground to empirically evaluate the contribution of cholinergic mechanisms to fundamental neural computations. Remarkably, physiological investigations of cholinergic modulation in the SOC were lacking until Huang and Trussell (2011) showed that blocking Kv7.5 elevated resting membrane potential of the presynaptic terminals in the Calyx of Held, regulating transmitter

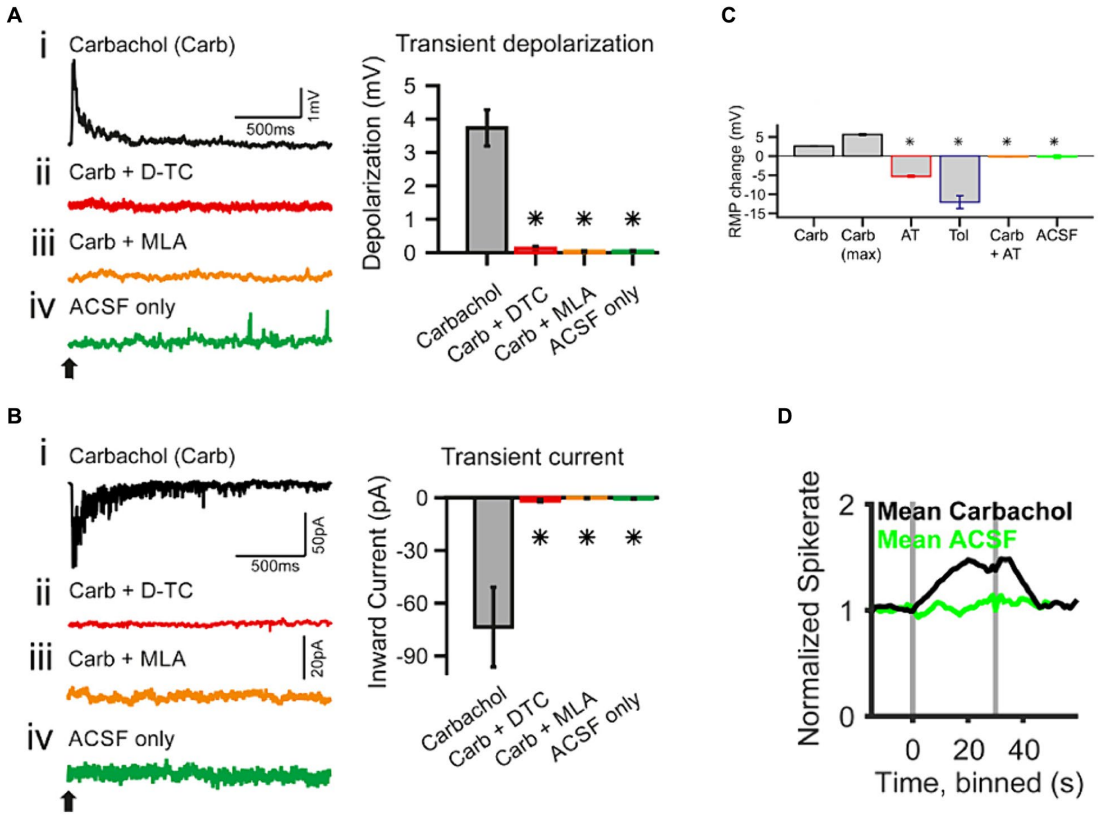


FIGURE 4
Whole-cell patch-clamp recording in spherical bushy cells (SBC) of the cochlear nucleus shows acetylcholine raises spiking probability [adapted from Goyer et al. (2016), with permission from eNeuro under BB-CY license]. **(A)** Transient effects of carbachol-mediated nAChR activation. The traces are current-clamp recordings with puff application of 500 μM carbachol (Carb; application time is marked by a *black arrow*). **(Ai–Aiv)** The transient depolarization elicited by the carbachol puff **(i)** was abolished when the slice had been superfused with 50 μM d-tubocurarine (D-TC), a general nAChR blocker **(ii)**; or with 20 nM methyllycaconitine (MLA), a specific α7 nAChR blocker **(iii)**; and with the puffing only the vehicle (ACSF) yielded no effect **(iv)**. **(B)** The traces are voltage-clamp recordings at −60 mV holding potential with carbachol application (application time marked by a black arrow). **(Bi–Biv)** SBCs showed a transient inward current upon carbachol application **(i)**, which was abolished in the presence of nicotinic blockers, D-TC **(ii)** and MLA **(iii)**; further, no current was observed upon puff application of the vehicle only **(iv)**. The population data for both type of recordings is shown on the right of each individual example. **(C)** Acetylcholine sets the SBC resting membrane potential (RMP) through muscarinic receptors. AT, atropine, muscarinic antagonist, 20 μM; Tol, tolterodine, muscarinic antagonist, 100 nM. **(D)** *In vivo* single unit recordings show that the spontaneous spike probability of SBC is increased by activating cholinergic signaling through iontophoresis of 5–500 mM carbachol (gray bars indicate the onset and offset of carbachol application). *$p < 0.05$.

release. This finding suggested the involvement of muscarinic signaling due to the well-known modulatory coupling of mAChRs to Kv7 channel gating. Recently, we identified a postsynaptic mAChR mechanism in gerbil MNTB neurons that is limited to a developmental period up to and surrounding hearing onset (~ postnatal day 12) (Weimann et al., 2024). We showed that the postsynaptic activation mAChRs enhances MNTB excitability through suppression of a Kv7 conductance. This effect declines over the first week following hearing onset but appears to be partially offset by an emerging nicotinic response by around P18. In a separate *in vivo* study, we showed that by adulthood, nicotinic AChR activation fine-tunes sound intensity encoding performance of MNTB in a stimulus dependent manner. This effect is mediated by activation of both α7 and α4β2 nAChRs subtypes (Zhang et al., 2021). Further, Zhang et al. (2021) showed that the nAChR-induced increase in tonic firing improved MNTB neurons' sensitivity to tones and discriminability between similar intensities. By using *in vivo* extracellular recording with pharmacological manipulations of nAChRs, this study also showed that activation of α7 or α4β2 nAChRs preferentially enhanced pure-tone evoked responses, relative to noise-driven responses (Figure 5). As a result, the ability of MNTB to detect pure-tones embedded in broadband noise was improved by cholinergic activation.

Acetylcholine in central nuclei: the inferior colliculus

Similarly to lower auditory regions, ACh in the midbrain Inferior Colliculus (IC) produces excitatory effects on sound-evoked responses through both nicotinic and muscarinic receptors (Watanabe and Simada, 1973). Cholinergic modulation in IC was initially studied in the cat by monitoring *in vivo* extracellular spontaneous neural responses in IC (Curtis and Koizumi, 1961). Histologically, radioactive receptor-binding techniques have been used to confirm expression of metabotropic mAChRs in the IC of rat (Rotter et al., 1979), and cat (Glendenning and Baker, 1988), and ionotropic nAChRs in rat (Clarke et al., 1985; Morley and Happe, 2000). Furthermore, Sottile et al. (2017) showed that the β2-containing nAChRs are expressed in the rat GABAergic IC neurons, while the α4β2 nAChRs are expressed in

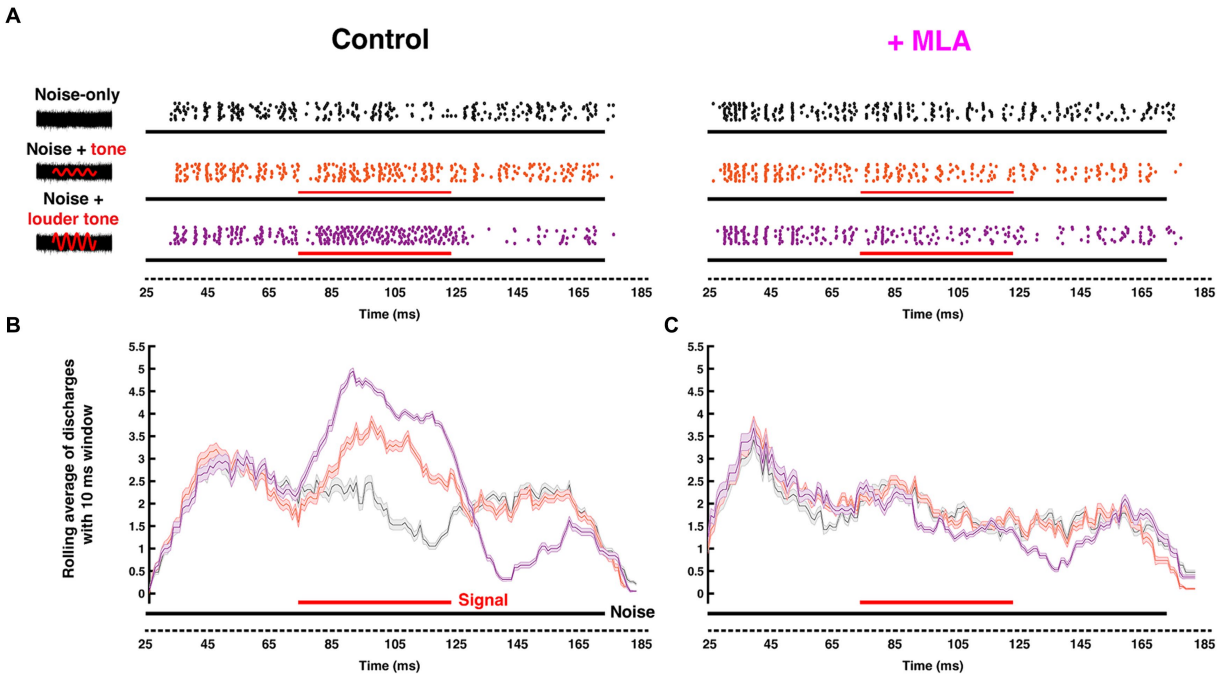


FIGURE 5
Endogenous cholinergic activity enhances signal detection of computational neurons in the gerbil auditory brainstem [Reproduced from Zhang et al. (2021), with permission from the Journal of Neuroscience under CC-BY license]. **(A)** Left: Schematic representation of the stimuli delivered to the ear canal of anesthetized gerbil. The stimuli include a 50 ms *CF* pure tone signal (*red*) of variable intensity embedded within a simultaneous 150-ms-wide-band frozen noise (*black*) presented at a fixed intensity. Amplitudes of the red sinusoidal curves schematically represent the variable selected tone intensities. Right: The corresponding raster plots with increasing signal/noise ratio, with each dot represent an action potential recorded from MNTB using *in vivo* extracellular recording with piggy-back multi-barrel electrodes, loaded with 20 mM methyllycaconitine (MLA), an α7-nAChR-specific antagonist. **(B,C)** Moving average (with a 10 ms shifting binning window) of action potentials fired before **(B)** and after **(C)** MLA administration. Solid black and red bars along the time axis represent the durations of noise and pure tone stimuli, respectively, where thickness indicates intensity. The neuron's ability to differentiate pure-tone signal from wide-band noise was abolished after blocking α7 nAChRs.

non-GABAergic IC neurons. This finding was later substantiated by the Schofield group in a study showing that the cholinergic cells in the PMT contact both GABAergic and glutamatergic IC neurons (Noftz et al., 2020). Notably, a physiological study of α3β4 nAChRs in the auditory system characterized the influence of these receptors in the mouse IC (Rivera-Perez et al., 2021). Interestingly, Rivera-Perez et al. showed that activation of α3β4 nAChRs prolonged inward current and therefore extended the depolarization period for excitation, in contrast to the generally observed phenomenon that nAChR activation promotes short-duration depolarizations of cell membrane. Furthermore, extracellular recordings in the bat IC showed that cholinergic signaling affects the RLFs of IC neurons in a heterogenous fashion exhibiting either increased or in some cases, decreased, gain (Habbicht and Vater, 1996). In some neurons, the excitatory, upward shift of RLF was observed, with an elevated firing rate for both baseline intensity responses and over the dynamic range by the same magnitude. In other cases, the complementary effect was seen with a suppressive, downward shift of the RLF. There were also several cases where ACh elevated the auditory threshold of IC neurons and therefore, resulted in a parallel shift of the RLF (Figure 6). Together this constellation of varied effects appeared to extend modulatory capacity to influence encoding sensitivity to acoustic input.

One key finding demonstrated a more targeted and specific modulation of response gain in the IC. An innovative and foundational study by Ayala and Malmierca (2015) showed that ACh also contributes to stimulus-specific adaptation (SSA) in rat IC. They repetitively presented two separate tones while monitoring single-neuron activity *in vivo*. One tone (*f1*) was repeated at a high repetition rate, while the *'test tone'(f2)* was presented only rarely. During 75 ms bouts of sound presentation, *f1* was presented with 90% probability of occurrence while *f2* was presented rarely at just 10% probability. Both tones were presented near the neuron's characteristic frequency (*CF*), and each evoked similar firing patterns. SSA typically manifested as a decreased response to the repetitive tone (*f1*) while the test tone (*f2*) response was unaffected (Figure 6C). The SSA magnitude was assessed by comparing the rare-tone evoked responses to those of the repetitive tones over the course of each trial. Interestingly, for neurons showing moderate SSA to the repetitive tone (*f1*), ACh preferentially enhanced these adapted responses relative to test tone responses. Ayala and Malmierca (2015) then showed that this differential influence was generally attributable to mAChR activation. Significantly, this study demonstrated that ACh has the capacity to enhance auditory encoding in a highly specific manner by differentially modulating single neuron responses to very similar stimuli.

Another important finding of cholinergic effects in IC revealed its role in plasticity of stimulus feature selectivity. Ji and Suga (2009) characterized a shift of best frequency (BF) tuning in IC neurons of bats induced by acoustic conditioning. Their study showed that applying mAChRs antagonist abolished this BF shift (Ji and Suga, 2009), but activating mAChRs significantly *augmented* the BF shift (Ji et al., 2001). Gao and Suga (2000) suggested that the corticofugal efferent feedback to IC, exhibits cholinergic plasticity that, in turn, contributes to the magnitude of cortical neuron BF plasticity. This

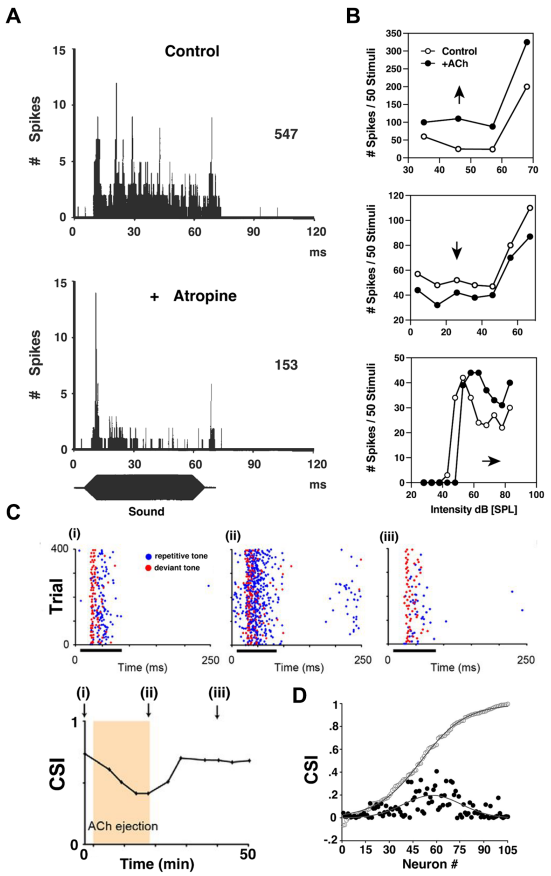


FIGURE 6
ACh influences input–output functions and stimulus-specific adaptation in the inferior colliculus. **(A)** Post-stimulus time histogram (PSTH) of discharges recorded from a bat IC neuron before (upper) and after (lower) atropine administration using multi-barrel electrodes. Blocking mAChRs of IC significantly decreased the tonic firing of the IC neurons during sound presentation. **(B)** The heterogeneity of cholinergic effects on bat IC neurons, reflected by the rate-level functions (RLFs) from three single units before and after ACh application. Upper: an upward shift of RLF indicates increased output (Spike count) without changing threshold; Middle: a downward shift of RLF indicates decrease output without affecting threshold; Lower: a parallel shift before saturation phase indicates an elevated threshold, and lowered maximum and saturation levels indicate decreased firing capabilities. [**A**,**B** are adapted and reproduced from Habbicht and Vater (1996); with permission from Elsevier; license # 5762610950216]. **(C)** Dot rasters of one rat IC neuron demonstrating stimulus-specific adaptation (SSA) under baseline **(i)**, ACh **(ii)**, and recovery **(iii)** conditions [adapted from Ayala and Malmierca (2015), with permission from the Journal of Neuroscience under BB-CY license]. During the experiment, the subject was presented with a standard, repetitive sound (blue) and a rare, deviant tone (red). The SSA was observable as a decrease in response to the standard *f1* tone *blue markers, left panel*, but not to a rare *f2* test tone *red markers*. The degree of SSA was quantified by the common SSA index (CSI, lower panel). The arrows in lower panel indicate the time point at which rasters are collected in panel **(i)–(iii)**. This particular neuron exhibits moderate levels of SSA, and the level of SSA was profoundly affected by ACh ejection due to elevated firing rate *middle panel*. On a population level shown in **(D)**, the strength of the effect of ACh depended on the baseline CSI. The baseline cumulative CSI values (open circles) among all IC neurons and the absolute response difference observed during ACh application (black circles, expressed in positive values) suggest that the SSA in IC neurons is broadly modulated by ACh, but is particularly strong for neurons in the moderate range of SSA magnitudes.

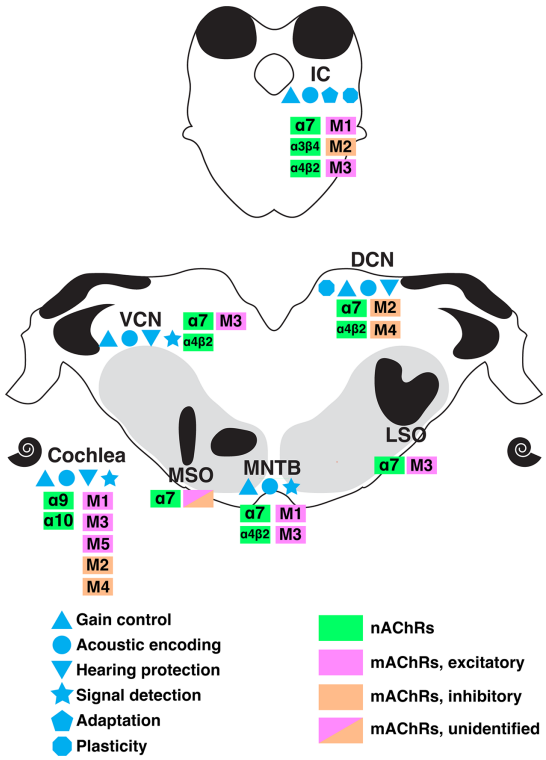


FIGURE 7
A summary of the currently understood distribution of cholinergic receptor subtypes, expression patterns, and functional roles along the ascending auditory pathway as indicated by colors and symbols shown. DCN, dorsal cochlear nucleus; IC, inferior colliculus; LSO, lateral superior olive; MNTB, medial nucleus of trapezoid body; MSO, medial superior olive; VCN, ventral cochlear nucleus.

finding implicates cholinergic circuitry in associative learning. Taken together, both Ayala and Malmierca (2015) as well as the Suga laboratory studies demonstrated that ACh can mediate very subtle stimulus-specific effects that extend its modulatory potential well beyond simple gain control mechanisms.

Conclusion

Cholinergic circuitry has long been implicated in higher order functions such as attention and sensory gating, particularly in forebrain structures. However, recent emerging work has convincingly showed that ACh is also intricately involved in serving even the most basic functions of sensory encoding throughout the auditory pathway including lower order processing regions. In this review, we summarized a wide range of physiologically important cholinergic impacts on neural computation in the brainstem auditory system. These functions include acoustic gain control, sound encoding, noise protection, signal-in-noise detection and intensity adaptation. Figure 7 summarizes the known receptor expression patterns and functional roles for cholinergic modulation in the lower auditory system as evidenced in the literature to date. M1-M5 mAChRs and α7, α4β2, α9α10, α3β4-containing nAChRs have been demonstrated to mediate these wide ranging and impactful computational functions. The variety of acetylcholine receptors expressed in these nuclei further suggests the prevalence and significance of neuromodulation at early

stage of sound processing. Overall, these findings underscore a general view that sound processing depends on a sophisticated coordination of synaptic inputs from overlapping afferent, efferent, and modulatory circuitry. It is clear from the emerging work highlighted here, that there remains much more to be discovered regarding modulatory influences on auditory computations than is currently understood.

Author contributions

CZ: Writing – original draft, Writing – review & editing. RB: Writing – original draft, Writing – review & editing.

Funding

The author(s) declare that financial support was received for the research, authorship, and/or publication of this article. This work was supported by National Institutes of Health/National Institute on Deafness and Other Communication Disorders Grant R15 DC016461.

Conflict of interest

The authors declare that the research was conducted in the absence of any commercial or financial relationships that could be construed as a potential conflict of interest.

Publisher's note

All claims expressed in this article are solely those of the authors and do not necessarily represent those of their affiliated organizations, or those of the publisher, the editors and the reviewers. Any product that may be evaluated in this article, or claim that may be made by its manufacturer, is not guaranteed or endorsed by the publisher.

References

Adams, J. C. (1979). Ascending projections to the inferior colliculus. *J. Comp. Neurol.* 183, 519–538. doi: 10.1002/cne.901830305

Akers, A. T., Cooper, S. Y., Baumgard, Z. J., Casinelli, G. P., Avelar, A. J., and Henderson, B. J. (2020). Upregulation of nAChRs and changes in excitability on VTA dopamine and GABA neurons correlates to changes in nicotine-reward-related behavior. 7, ENEURO.0189–ENEU20.2020. doi: 10.1523/ENEURO.0189-20.2020

Andrezik, J. A., Chan-Palay, V., and Palay, S. L. (1981). The nucleus paragigantocellularis lateralis in the rat. Demonstration of afferents by the retrograde transport of horseradish peroxidase. *Anat Embryol (Berl)* 161, 373–390. doi: 10.1007/BF00316049

Arnesen, A. R., and Osen, K. K. (1978). The cochlear nerve in the cat: topography, cochleotopy, and fiber spectrum. *J. Comp. Neurol.* 178, 661–678. doi: 10.1002/cne.901780405

Ashe, J. H., McKenna, T. M., and Weinberger, N. M. (1989). Cholinergic modulation of frequency receptive fields in auditory cortex: II. Frequency-specific effects of anticholinesterases provide evidence for a modulatory action of endogenous ACh. *Synapse* 4, 44–54. doi: 10.1002/syn.890040106

Ayala, Y. A., and Malmierca, M. S. (2015). Cholinergic modulation of stimulus-specific adaptation in the inferior colliculus. *J. Neurosci.* 35, 12261–12272.

Baeyer, A. (1867). I. Ueber das Neurin. *Justus Liebigs Ann. Chem.* 142, 322–326. doi: 10.1002/jlac.18671420311

Beebe, N. L., Herrera, Y. N., Noftz, W. A., Roberts, M. T., and Schofield, B. R. (2023). Characterization of three cholinergic inputs to the cochlear nucleus. *J. Chem. Neuroanat.* 131:102284. doi: 10.1016/j.jchemneu.2023.102284

Beebe, N. L., Zhang, C., Burger, R. M., and Schofield, B. R. (2021). Multiple sources of cholinergic input to the superior Olivary complex. *Front. Neural. Circuits* 15:715369. doi: 10.3389/fncir.2021.715369

Beker, F., Weber, M., Fink, R. H., and Adams, D. J. (2003). Muscarinic and nicotinic ACh receptor activation differentially mobilize Ca2+ in rat intracardiac ganglion neurons. *J. Neurophysiol.* 90, 1956–1964. doi: 10.1152/jn.01079.2002

Bizley, J. K. (2017). "Chapter 26 - audition" in *Conn's Translational Neuroscience*. ed. P. M. Conn (San Diego: Academic Press), 579–598.

Bosch, D., and Schmid, S. (2006). Activation of muscarinic cholinergic receptors inhibits giant neurones in the caudal pontine reticular nucleus. *Eur. J. Neurosci.* 24, 1967–1975. doi: 10.1111/j.1460-9568.2006.05085.x

Brown, D. A. (2018). Regulation of neural ion channels by muscarinic receptors. *Neuropharmacology* 136, 383–400. doi: 10.1016/j.neuropharm.2017.11.024

Brown, D. A., and Adams, P. R. (1980). Muscarinic suppression of a novel voltage-sensitive K+ current in a vertebrate neurone. *Nature* 283, 673–676. doi: 10.1038/283673a0

Bruce Warr, W. (1995). "Parallel ascending pathways from the Cochlear nucleus: neuroanatomical evidence of functional specialization" in *Contributions to sensory physiology*. ed. W. D. Neff (Elsevier), 1–38.

Brugge, J. F., and Howard, M. A. (2002). "Hearing" in *Encyclopedia of the human brain*. ed. V. S. Ramachandran (New York: Academic Press), 429–448.

Burger, R. M., and Rubel, E. (2008). The senses: a comprehensive reference. *Ed. D. Oertel.* 613–630.

Caminos, E., Garcia-Pino, E., Martinez-Galan, J. R., and Juiz, J. M. (2007). The potassium channel KCNQ5/Kv7.5 is localized in synaptic endings of auditory brainstem nuclei of the rat. *J. Comp. Neurol.* 505, 363–378. doi: 10.1002/cne.21497

Caspary, D. M., Havey, D. C., and Faingold, C. L. (1983). Effects of acetylcholine on cochlear nucleus neurons. *Exp. Neurol.* 82, 491–498. doi: 10.1016/0014-4886(83)90419-3

Caulfield, M. P., and Birdsall, N. J. (1998). International Union of Pharmacology. XVII. Classification of muscarinic acetylcholine receptors. *Pharmacol. Rev.* 50, 279–290

Changeux, J. P., and Paas, Y. (2009). "Nicotinic acetylcholine receptors" in *Encyclopedia of neuroscience*. ed. L. R. Squire (Oxford: Academic Press), 1129–1133.

Chen, K., Waller, H. J., and Godfrey, D. A. (1995). Muscarinic receptor subtypes in rat dorsal cochlear nucleus. *Hear. Res.* 89, 137–145. doi: 10.1016/0378-5955(95)00131-6

Ciuman, R. R. (2010). The efferent system or olivocochlear function bundle - fine regulator and protector of hearing perception. *Int. J. Biomed. Sci.* 6, 276–288. doi: 10.59566/IJBS.2010.6276

Clarke, P. B., Schwartz, R. D., Paul, S. M., Pert, C. B., and Pert, A. (1985). Nicotinic binding in rat brain: autoradiographic comparison of [3H]acetylcholine, [3H]nicotine, and [125I]-alpha-bungarotoxin. *J. Neurosci.* 5, 1307–1315. doi: 10.1523/JNEUROSCI.05-05-01307.1985

Coggan, J. S., Purnyn, S. L., Knoper, S. R., and Kreulen, D. L. (1994). Muscarinic inhibition of two potassium currents in guinea-pig prevertebral neurons: differentiation by extracellular cesium. *Neuroscience* 59, 349–361. doi: 10.1016/0306-4522(94)90601-7

Comis, S. D., and Whitfield, I. C. (1968). Influence of centrifugal pathways on unit activity in the cochlear nucleus. *J. Neurophysiol.* 31, 62–68. doi: 10.1152/jn.1968.31.1.62

Curtis, D. R., and Koizumi, K. (1961). Chemical transmitter substances in brain stem of cat. *J. Neurophysiol.* 24, 80–90. doi: 10.1152/jn.1961.24.1.80

Dale, H. H. (1914). The action of certain esters and ethers of choline, and their relation to MUSCARINE. *J. Pharmacol. Exp. Ther.* 6, 147–190.

Dallos, P., He, D. Z., Lin, X., Sziklai, I., Mehta, S., and Evans, B. N. (1997). Acetylcholine, outer hair cell electromotility, and the cochlear amplifier. *J. Neurosci.* 17, 2212–2226. doi: 10.1523/JNEUROSCI.17-06-02212.1997

Darrow, K. N., Maison, S. F., and Liberman, M. C. (2006). Cochlear efferent feedback balances interaural sensitivity. *Nat. Neurosci.* 9, 1474–1476. doi: 10.1038/nn1807

Darrow, K. N., Maison, S. F., and Liberman, M. C. (2007). Selective removal of lateral olivocochlear efferents increases vulnerability to acute acoustic injury. *J. Neurophysiol.* 97, 1775–1785. doi: 10.1152/jn.00955.2006

Davis, K. A. (2005). Contralateral effects and binaural interactions in dorsal cochlear nucleus. *J. Assoc. Res. Otolaryngol.* 6, 280–296. doi: 10.1007/s10162-005-0008-5

Dell'Acqua, M. L., Carroll, R. C., and Peralta, E. G. (1993). Transfected m2 muscarinic acetylcholine receptors couple to G alpha i2 and G alpha i3 in Chinese hamster ovary cells. Activation and desensitization of the phospholipase C signaling pathway. *J. Biol. Chem.* 268, 5676–5685. doi: 10.1016/S0021-9258(18)53372-X

Dulon, D., Luo, L., Zhang, C., and Ryan, A. F. (1998). Expression of small-conductance calcium-activated potassium channels (SK) in outer hair cells of the rat cochlea. *Eur. J. Neurosci.* 10, 907–915. doi: 10.1046/j.1460-9568.1998.00098.x

Eglen, R. M. (2006). Muscarinic receptor subtypes in neuronal and non-neuronal cholinergic function. *Auton. Autacoid Pharmacol.* 26, 219–233. doi: 10.1111/j.1474-8673.2006.00368.x

Elgoyhen, A. B., Johnson, D. S., Boulter, J., Vetter, D. E., and Heinemann, S. (1994). Alpha 9: an acetylcholine receptor with novel pharmacological properties expressed in rat cochlear hair cells. *Cell* 79, 705–715. doi: 10.1016/0092-8674(94)90555-X

Elgoyhen, A. B., Vetter, D. E., Katz, E., Rothlin, C. V., Heinemann, S. F., and Boulter, J. (2001). alpha10: a determinant of nicotinic cholinergic receptor function in mammalian vestibular and cochlear mechanosensory hair cells. *Proc. Natl. Acad. Sci. U. S. A.* 98, 3501–3506. doi: 10.1073/pnas.051622798

Froemke, R. C., Merzenich, M. M., and Schreiner, C. E. (2007). A synaptic memory trace for cortical receptive field plasticity. *Nature* 450, 425–429. doi: 10.1038/nature06289

Fuchs, P. A., and Lauer, A. M. (2019). Efferent inhibition of the cochlea. *Cold Spring Harb. Perspect. Med.* 9:a033530. doi: 10.1101/cshperspect.a033530

Fujino, K., and Oertel, D. (2001). Cholinergic modulation of stellate cells in the mammalian ventral cochlear nucleus. *J. Neurosci.* 21, 7372–7383. doi: 10.1523/JNEUROSCI.21-18-07372.2001

Gao, E., and Suga, N. (2000). Experience-dependent plasticity in the auditory cortex and the inferior colliculus of bats: role of the corticofugal system. *Proc. Natl. Acad. Sci. U. S. A.* 97, 8081–8086.

Garcia-Pino, E., Caminos, E., and Juiz, J. M. (2010). KCNQ5 reaches synaptic endings in the auditory brainstem at hearing onset and targeting maintenance is activity-dependent. *J. Comp. Neurol.* 518, 1301–1314. doi: 10.1002/cne.22276

Gillet, C., Goyer, D., Kurth, S., Griebel, H., and Kuenzel, T. (2018). Cholinergic innervation of principal neurons in the cochlear nucleus of the Mongolian gerbil. *J. Comp. Neurol.* 526, 1647–1661. doi: 10.1002/cne.24433

Glendenning, K. K., and Baker, B. N. (1988). Neuroanatomical distribution of receptors for three potential inhibitory neurotransmitters in the brainstem auditory nuclei of the cat. *J. Comp. Neurol.* 275, 288–308. doi: 10.1002/cne.902750210

Glendenning, K. K., Brunso-Bechtold, J. K., Thompson, G. C., and Masterton, R. B. (1981). Ascending auditory afferents to the nuclei of the lateral lemniscus. *J. Comp. Neurol.* 197, 673–703. doi: 10.1002/cne.901970409

Glendenning, K. K., Hutson, K. A., Nudo, R. J., and Masterton, R. B. (1985). Acoustic chiasm II: anatomical basis of binaurality in lateral superior olive of cat. *J. Comp. Neurol.* 232, 261–285. doi: 10.1002/cne.902320210

Glendenning, K. K., Masterton, R. B., Baker, B. N., and Wenthold, R. J. (1991). Acoustic chiasm. III: nature, distribution, and sources of afferents to the lateral superior olive in the cat. *J. Comp. Neurol.* 310, 377–400. doi: 10.1002/cne.903100308

Glowatzki, E., and Fuchs, P. A. (2000). Cholinergic synaptic inhibition of inner hair cells in the neonatal mammalian cochlea. *Science* 288, 2366–2368. doi: 10.1126/science.288.5475.2366

Godfrey, D. A., Kaltenbach, J. A., Chen, K., and Ilyas, O. (2013). Choline acetyltransferase activity in the hamster central auditory system and long-term effects of intense tone exposure. *J. Neurosci. Res.* 91, 987–996. doi: 10.1002/jnr.23227

Godfrey, D. A., and Matschinsky, F. M. (1981). Quantitative distribution of choline acetyltransferase and acetylcholinesterase activities in the rat cochlear nucleus. *J. Histochem. Cytochem.* 29, 720–730. doi: 10.1177/29.6.7252132

Godfrey, D. A., Park-Hellendall, J. L., Dunn, J. D., and Ross, C. D. (1987). Effects of trapezoid body and superior olive lesions on choline acetyltransferase activity in the rat cochlear nucleus. *Hear. Res.* 28, 253–270. doi: 10.1016/0378-5955(87)90053-0

Godfrey, D. A., Williams, A. D., and Matschinsky, F. M. (1977). Quantitative histochemical mapping of enzymes of the cholinergic system in cat cochlear nucleus. *J. Histochem. Cytochem.* 25, 397–416. doi: 10.1177/25.6.69653

Goldberg, J. M., and Brown, P. B. (1969). Response of binaural neurons of dog superior olivary complex to dichotic tonal stimuli: some physiological mechanisms of sound localization. *J. Neurophysiol.* 32, 613–636. doi: 10.1152/jn.1969.32.4.613

Gomez-Nieto, R., Rubio, M. E., and Lopez, D. E. (2008). Cholinergic input from the ventral nucleus of the trapezoid body to cochlear root neurons in rats. *J. Comp. Neurol.* 506, 452–468. doi: 10.1002/cne.21554

Goyer, D., Kurth, S., Gillet, C., Keine, C., Rubsamen, R., and Kuenzel, T. (2016). Slow cholinergic modulation of spike probability in ultra-fast time-coding sensory neurons. *eNeuro* 3, ENEURO.0186–ENEU16.2016. doi: 10.1523/ENEURO.0186-16.2016

Grothe, B., and Pecka, M. (2014). The natural history of sound localization in mammals--a story of neuronal inhibition. *Front. Neural Circuits* 8:116. doi: 10.3389/fncir.2014.00116

Grothe, B., and Sanes, D. H. (1993). Bilateral inhibition by glycinergic afferents in the medial superior olive. *J. Neurophysiol.* 69, 1192–1196. doi: 10.1152/jn.1993.69.4.1192

Guinan, J. J. (1996). "Physiology of Olivocochlear Efferents" in *The cochlea*. eds. P. Dallos, A. N. Popper and R. R. Fay (New York, NY: Springer New York), 435–502.

Guinan, J. J. (2018). Olivocochlear efferents: their action, effects, measurement and uses, and the impact of the new conception of cochlear mechanical responses. *Hear. Res.* 362, 38–47. doi: 10.1016/j.heares.2017.12.012

Habbicht, H., and Vater, M. (1996). A microiontophoretic study of acetylcholine effects in the inferior colliculus of horseshoe bats: implications for a modulatory role. *Brain Res.* 724, 169–179. doi: 10.1016/0006-8993(96)00224-7

Hackney, C. M., Osen, K. K., and Kolston, J. (1990). Anatomy of the cochlear nuclear complex of guinea pig. *Anat Embryol* 182, 123–149. doi: 10.1007/BF00174013

Hallanger, A. E., Levey, A. I., Lee, H. J., Rye, D. B., and Wainer, B. H. (1987). The origins of cholinergic and other subcortical afferents to the thalamus in the rat. *J. Comp. Neurol.* 262, 105–124. doi: 10.1002/cne.902620109

Hamada, S., Houtani, T., Trifonov, S., Kase, M., Maruyama, M., Shimizu, J., et al. (2010). Histological determination of the areas enriched in cholinergic terminals and M2 and M3 muscarinic receptors in the mouse central auditory system. *Anat. Rec. (Hoboken)* 293, 1393–1399. doi: 10.1002/ar.21186

Hammond, C. (2015). "Chapter 8 - the ionotropic nicotinic acetylcholine receptors" in *Cellular and molecular neurophysiology*. ed. C. Hammond. *4th* ed (Boston: Academic Press), 173–197.

Happe, H. K., and Morley, B. J. (1998). Nicotinic acetylcholine receptors in rat cochlear nucleus: [125I]-alpha-bungarotoxin receptor autoradiography and in situ hybridization of alpha 7 nAChR subunit mRNA. *J. Comp. Neurol.* 397, 163–180. doi: 10.1002/(SICI)1096-9861(19980727)397:2<163::AID-CNE2>3.0.CO;2-Z

Happe, H. K., and Morley, B. J. (2004). Distribution and postnatal development of alpha 7 nicotinic acetylcholine receptors in the rodent lower auditory brainstem. *Brain Res. Dev. Brain Res.* 153, 29–37. doi: 10.1016/j.devbrainres.2004.07.004

Harrison, J. M., and Howe, M. E. (1974). "Anatomy of the descending auditory system (mammalian)" in *Auditory system: Anatomy physiology*. eds. H. W. Ades, A. Axelsson, I. L. Baird, G. V Békésy, R. L. Boord and C. CBGet al. (Berlin, Heidelberg: Springer Berlin Heidelberg), 363–388.

Harrison, J. M., and Irving, R. (1966). Ascending connections of the anterior ventral cochlear nucleus in the rat. *J. Comp. Neurol.* 126, 51–63. doi: 10.1002/cne.901260105

Heckers, S., Geula, C., and Mesulam, M. M. (1992). Cholinergic innervation of the human thalamus: dual origin and differential nuclear distribution. *J. Comp. Neurol.* 325, 68–82. doi: 10.1002/cne.903250107

Henkel, C. K. (2018). "Chapter 21 - the auditory system" in *Fundamental neuroscience for basic and clinical applications*. eds. D. E. Haines and G. A. Mihailoff. *5th* ed (Elsevier), 306–319.e301.

Huang, H., and Trussell, L. O. (2011). KCNQ5 channels control resting properties and release probability of a synapse. *Nat. Neurosci.* 14, 840–847.

Hunt, S., and Schmidt, J. (1978). Some observations on the binding patterns of alpha-bungarotoxin in the central nervous system of the rat. *Brain Res.* 157, 213–232. doi: 10.1016/0006-8993(78)90025-2

Irie, T., Fukui, I., and Ohmori, H. (2006). Activation of GIRK channels by muscarinic receptors and group II metabotropic glutamate receptors suppresses Golgi cell activity in the cochlear nucleus of mice. *J. Neurophysiol.* 96, 2633–2644. doi: 10.1152/jn.00396.2006

Ishii, M., and Kurachi, Y. (2006). Muscarinic acetylcholine receptors. *Curr. Pharm. Des.* 12, 3573–3581. doi: 10.2174/138161206778522056

Itier, V., and Bertrand, D. (2001). Neuronal nicotinic receptors: from protein structure to function. *FEBS Lett.* 504, 118–125. doi: 10.1016/S0014-5793(01)02702-8

Ito, T., Bishop, D. C., and Oliver, D. L. (2016). Functional organization of the local circuit in the inferior colliculus. *Anat. Sci. Int.* 91, 22–34. doi: 10.1007/s12565-015-0308-8

James, N. M., Gritton, H. J., Kopell, N., Sen, K., and Han, X. (2019). Muscarinic receptors regulate auditory and prefrontal cortical communication during auditory processing. *Neuropharmacology* 144, 155–171. doi: 10.1016/j.neuropharm.2018.10.027

Ji, W., Gao, E., and Suga, N. (2001). Effects of acetylcholine and atropine on plasticity of central auditory neurons caused by conditioning in bats. *J. Neurophysiol.* 86, 211–225. doi: 10.1152/jn.2001.86.1.211

Ji, W., and Suga, N. (2009). Tone-specific and nonspecific plasticity of inferior colliculus elicited by pseudo-conditioning: role of acetylcholine and auditory and somatosensory cortices. *J. Neurophysiol.* 102, 941–952. doi: 10.1152/jn.00222.2009

Jin, Y. M., Godfrey, D. A., Wang, J., and Kaltenbach, J. A. (2006). Effects of intense tone exposure on choline acetyltransferase activity in the hamster cochlear nucleus. *Hear. Res.* 216-217, 168–175. doi: 10.1016/j.heares.2006.02.002

Kakehata, S., Nakagawa, T., Takasaka, T., and Akaike, N. (1993). Cellular mechanism of acetylcholine-induced response in dissociated outer hair cells of guinea-pig cochlea. *J. Physiol.* 463, 227–244. doi: 10.1113/jphysiol.1993.sp019592

Kalinec, F., Zhang, M., Urrutia, R., and Kalinec, G. (2000). Rho GTPases mediate the regulation of cochlear outer hair cell motility by acetylcholine. *J. Biol. Chem.* 275, 28000–28005. doi: 10.1074/jbc.M004917200

Kaltenbach, J. A., and Zhang, J. (2007). Intense sound-induced plasticity in the dorsal cochlear nucleus of rats: evidence for cholinergic receptor upregulation. *Hear. Res.* 226, 232–243. doi: 10.1016/j.heares.2006.07.001

Kamiya, H., Itoh, K., Yasui, Y., Ino, T., and Mizuno, N. (1988). Somatosensory and auditory relay nucleus in the rostral part of the ventrolateral medulla: a morphological study in the cat. *J. Comp. Neurol.* 273, 421–435. doi: 10.1002/cne.902730311

Kawai, H., Lazar, R., and Metherate, R. (2007). Nicotinic control of axon excitability regulates thalamocortical transmission. *Nat. Neurosci.* 10, 1168–1175. doi: 10.1038/nn1956

Kawase, T., Delgutte, B., and Liberman, M. C. (1993). Antimasking effects of the olivocochlear reflex. II. Enhancement of auditory-nerve response to masked tones. *J. Neurophysiol.* 70, 2533–2549. doi: 10.1152/jn.1993.70.6.2533

Khan, K. M., Drescher, M. J., Hatfield, J. S., Khan, A. M., and Drescher, D. G. (2002). Muscarinic receptor subtypes are differentially distributed in the rat cochlea. *Neuroscience* 111, 291–302. doi: 10.1016/S0306-4522(02)00020-9

Kharkovets, T., Hardelin, J. P., Safieddine, S., Schweizer, M., El-Amraoui, A., Petit, C., et al. (2000). KCNQ4, a K+ channel mutated in a form of dominant deafness, is expressed in the inner ear and the central auditory pathway. *Proc. Natl. Acad. Sci. USA* 97, 4333–4338. doi: 10.1073/pnas.97.8.4333

Kiss, A., and Majorossy, K. (1983). Neuron morphology and synaptic architecture in the medial superior olivary nucleus. Light- and electron microscope studies in the cat. *Exp. Brain Res.* 52, 315–327. doi: 10.1007/BF00238026

Koyama, Y., Jodo, E., and Kayama, Y. (1994). Sensory responsiveness of "broad-spike" neurons in the laterodorsal tegmental nucleus, locus coeruleus and dorsal raphe of awake rats: implications for cholinergic and monoaminergic neuron-specific responses. *Neuroscience* 63, 1021–1031. doi: 10.1016/0306-4522(94)90569-X

Kudo, M., and Niimi, K. (1980). Ascending projections of the inferior colliculus in the cat: an autoradiographic study. *J. Comp. Neurol.* 191, 545–556. doi: 10.1002/cne.901910403

Kunnath, A. J., Gifford, R. H., and Wallace, M. T. (2023). Cholinergic modulation of sensory perception and plasticity. *Neurosci. Biobehav. Rev.* 152:105323. doi: 10.1016/j.neubiorev.2023.105323

Künzel, T., and Wagner, H. (2017). Cholinergic top-down influences on the auditory brainstem. *e-Neuroforum* 23, 35–44. doi: 10.1515/nf-2016-A107

Leach, N. D., Nodal, F. R., Cordery, P. M., King, A. J., and Bajo, V. M. (2013). Cortical cholinergic input is required for normal auditory perception and experience-dependent plasticity in adult ferrets. *J. Neurosci.* 33, 6659–6671. doi: 10.1523/JNEUROSCI.5039-12.2013

Liang, K., Poytress, B. S., Chen, Y., Leslie, F. M., Weinberger, N. M., and Metherate, R. (2006). Neonatal nicotine exposure impairs nicotinic enhancement of central auditory processing and auditory learning in adult rats. *Eur. J. Neurosci.* 24, 857–866. doi: 10.1111/j.1460-9568.2006.04945.x

Liang, K., Poytress, B. S., Weinberger, N. M., and Metherate, R. (2008). Nicotinic modulation of tone-evoked responses in auditory cortex reflects the strength of prior auditory learning. *Neurobiol. Learn. Mem.* 90, 138–146. doi: 10.1016/j.nlm.2008.02.006

Loewi, O., and Navratil, E. (1926). Über humorale Übertragbarkeit der Herznervenwirkung. *Pflugers Arch. Gesamte Physiol. Menschen Tiere* 214-214, 678–688. doi: 10.1007/BF01741946

Maclaine, K. D., and Llano, D. A. (2020). "2.45 - the aging central auditory system" in *The senses: A comprehensive reference*. ed. B. Fritzsch. *2nd* ed (Oxford: Elsevier), 884–895.

Madison, D. V., Lancaster, B., and Nicoll, R. A. (1987). Voltage clamp analysis of cholinergic action in the hippocampus. *J. Neurosci.* 7, 733–741. doi: 10.1523/JNEUROSCI.07-03-00733.1987

Maison, S. F., Liu, X. P., Vetter, D. E., Eatock, R. A., Nathanson, N. M., Wess, J., et al. (2010). Muscarinic signaling in the cochlea: presynaptic and postsynaptic effects on efferent feedback and afferent excitability. *J. Neurosci.* 30, 6751–6762. doi: 10.1523/JNEUROSCI.5080-09.2010

Malmierca, M. S., and Merchán, M. A. (2004). "CHAPTER 31 - auditory system" in *The rat nervous system*. ed. G. Paxinos. *3rd* ed (Burlington: Academic Press), 997–1082.

Manzoor, N. F., Chen, G., and Kaltenbach, J. A. (2013). Suppression of noise-induced hyperactivity in the dorsal cochlear nucleus following application of the cholinergic agonist, carbachol. *Brain Res.* 1523, 28–36. doi: 10.1016/j.brainres.2013.05.025

Martin, M. R. (1981). Acetylcholinesterase-positive fibers and cell bodies in the cochlear nuclei of normal and reeler mutant mice. *J. Comp. Neurol.* 197, 153–167. doi: 10.1002/cne.901970112

McKenna, T. M., Ashe, J. H., Hui, G. K., and Weinberger, N. M. (1988). Muscarinic agonists modulate spontaneous and evoked unit discharge in auditory cortex of cat. *Synapse* 2, 54–68. doi: 10.1002/syn.890020109

McKenna, T. M., Ashe, J. H., and Weinberger, N. M. (1989). Cholinergic modulation of frequency receptive fields in auditory cortex: I Frequency-specific effects of muscarinic agonists. *Synapse* 4, 30–43. doi: 10.1002/syn.890040105

Mellott, J. G., Beebe, N. L., and Schofield, B. R. (2019). Bilateral projections to the thalamus from individual neurons in the inferior colliculus. *J. Comp. Neurol.* 527, 1118–1126. doi: 10.1002/cne.24600

Mellott, J. G., Motts, S. D., and Schofield, B. R. (2011). Multiple origins of cholinergic innervation of the cochlear nucleus. *Neuroscience* 180, 138–147. doi: 10.1016/j.neuroscience.2011.02.010

Metherate, R. (2004). Nicotinic acetylcholine receptors in sensory cortex. *Learn. Mem.* 11, 50–59. doi: 10.1101/lm.69904

Metherate, R. (2011). Functional connectivity and cholinergic modulation in auditory cortex. *Neurosci. Biobehav. Rev.* 35, 2058–2063. doi: 10.1016/j.neubiorev.2010.11.010

Metherate, R., Ashe, J. H., and Weinberger, N. M. (1990). Acetylcholine modifies neuronal acoustic rate-level functions in guinea pig auditory cortex by an action at muscarinic receptors. *Synapse* 6, 364–368. doi: 10.1002/syn.890060409

Metherate, R., Cox, C. L., and Ashe, J. H. (1992). Cellular bases of neocortical activation: modulation of neural oscillations by the nucleus basalis and endogenous acetylcholine. *J. Neurosci.* 12, 4701–4711. doi: 10.1523/JNEUROSCI.12-12-04701.1992

Metherate, R., and Hsieh, C. Y. (2004). Synaptic mechanisms and cholinergic regulation in auditory cortex. *Prog. Brain Res.* 145, 143–156. doi: 10.1016/S0079-6123(03)45010-3

Metherate, R., Intskirveli, I., and Kawai, H. D. (2012). Nicotinic filtering of sensory processing in auditory cortex. *Front. Behav. Neurosci.* 6:44. doi: 10.3389/fnbeh.2012.00044

Metherate, R., and Weinberger, N. M. (1989). Acetylcholine produces stimulus-specific receptive field alterations in cat auditory cortex. *Brain Res.* 480, 372–377. doi: 10.1016/0006-8993(89)90210-2

Metherate, R., and Weinberger, N. M. (1990). Cholinergic modulation of responses to single tones produces tone-specific receptive field alterations in cat auditory cortex. *Synapse* 6, 133–145. doi: 10.1002/syn.890060204

Mizukawa, K., McGeer, P. L., Tago, H., Peng, J. H., McGeer, E. G., and Kimura, H. (1986). The cholinergic system of the human hindbrain studied by choline acetyltransferase immunohistochemistry and acetylcholinesterase histochemistry. *Brain Res.* 379, 39–55. doi: 10.1016/0006-8993(86)90253-2

Mooney, D. M., Zhang, L., Basile, C., Senatorov, V. V., Ngsee, J., Omar, A., et al. (2004). Distinct forms of cholinergic modulation in parallel thalamic sensory pathways. *Proc. Natl. Acad. Sci. U. S. A.* 101, 320–324. doi: 10.1073/pnas.0304445101

Moore, J. K., and Osen, K. K. (1979). The cochlear nuclei in man. *Am. J. Anat.* 154, 393–417. doi: 10.1002/aja.1001540306

Morley, B. J., and Happe, H. K. (2000). Cholinergic receptors: dual roles in transduction and plasticity. *Hear. Res.* 147, 104–112. doi: 10.1016/S0378-5955(00)00124-6

Morley, B. J., Lorden, J. F., Brown, G. B., Kemp, G. E., and Bradley, R. J. (1977). Regional distribution of nicotinic acetylcholine receptor in rat brain. *Brain Res.* 134, 161–166. doi: 10.1016/0006-8993(77)90935-0

Motts, S. D., Slusarczyk, A. S., Sowick, C. S., and Schofield, B. R. (2008). Distribution of cholinergic cells in guinea pig brainstem. *Neuroscience* 154, 186–195. doi: 10.1016/j.neuroscience.2007.12.017

Noftz, W. A., Beebe, N. L., Mellott, J. G., and Schofield, B. R. (2020). Cholinergic projections from the Pedunculopontine tegmental nucleus contact excitatory and inhibitory neurons in the inferior colliculus. *Front. Neural. Circuits* 14:43. doi: 10.3389/fncir.2020.00043

Oertel, D., and Cao, X.-J. (2020). "2.27 - the ventral Cochlear nucleus" in *The senses: A comprehensive reference*. ed. B. Fritzsch. *2nd* ed (Oxford: Elsevier), 517–532.

Oertel, D., Fay, R. R., and Popper, A. N. (2002). *Integrative functions in the mammalian auditory pathway*. Springer Nature.

Oertel, D., Wu, S. H., Garb, M. W., and Dizack, C. (1990). Morphology and physiology of cells in slice preparations of the posteroventral cochlear nucleus of mice. *J. Comp. Neurol.* 295, 136–154. doi: 10.1002/cne.902950112

Oliver, D. L., Beckius, G. E., and Shneiderman, A. (1995). Axonal projections from the lateral and medial superior olive to the inferior colliculus of the cat: a study using electron microscopic autoradiography. *J. Comp. Neurol.* 360, 17–32. doi: 10.1002/cne.903600103

Oliver, D. L., and Hall, W. C. (1978). The medial geniculate body of the tree shrew, *Tupaia glis*. II. Connections with the neocortex. *J. Comp. Neurol.* 182, 459–493. doi: 10.1002/cne.901820306

Oliver, D., Klocker, N., Schuck, J., Baukrowitz, T., Ruppersberg, J. P., and Fakler, B. (2000). Gating of Ca2+−activated K+ channels controls fast inhibitory synaptic transmission at auditory outer hair cells. *Neuron* 26, 595–601. doi: 10.1016/S0896-6273(00)81197-6

Osen, K. K. (1969a). Cytoarchitecture of the cochlear nuclei in the cat. *J. Comp. Neurol.* 136, 453–483. doi: 10.1002/cne.901360407

Osen, K. K. (1969b). The intrinsic organization of the cochlear nuclei. *Acta Otolaryngol.* 67, 352–359. doi: 10.3109/00016486909125462

Osen, K. K. (1970). Course and termination of the primary afferents in the cochlear nuclei of the cat. An experimental anatomical study. *Arch. Ital. Biol.* 108, 21–51

Osen, K. K., and Roth, K. (1969). Histochemical localization of cholinesterases in the cochlear nuclei of the cat, with notes on the origin of acetylcholinesterase-positive afferents and the superior olive. *Brain Res.* 16, 165–185. doi: 10.1016/0006-8993(69)90092-4

Pollak, G. D., Burger, R. M., and Klug, A. (2003). Dissecting the circuitry of the auditory system. *Trends Neurosci.* 26, 33–39. doi: 10.1016/S0166-2236(02)00009-7

Pollak, G. D., Wenstrup, J. J., and Fuzessery, Z. M. (1986). Auditory processing in the mustache bat's inferior colliculus. *Trends Neurosci.* 9, 556–561. doi: 10.1016/0166-2236(86)90176-1

Rasmussen, G. (1960). Efferent fibers of the cochlear nerve and cochlear nucleus. *Neural Mechanisms Auditory Vestibular Systems* 8, 105–115.

Rasmussen, G. (1965). Efferent connections of the cochlear nucleus. *Sensori Neural Hearing Processes Disord.*, 61–75.

Reese, N. B., Garcia-Rill, E., and Skinner, R. D. (1995a). Auditory input to the pedunculopontine nucleus: II Unit responses. *Brain Res Bull* 37, 265–273. doi: 10.1016/0361-9230(95)00001-U

Reese, N. B., Garcia-Rill, E., and Skinner, R. D. (1995b). The pedunculopontine nucleus--auditory input, arousal and pathophysiology. *Prog. Neurobiol.* 47, 105–133. doi: 10.1016/0301-0082(95)00023-O

Rhode, W. S., Oertel, D., and Smith, P. H. (1983). Physiological response properties of cells labeled intracellularly with horseradish peroxidase in cat ventral cochlear nucleus. *J. Comp. Neurol.* 213, 448–463. doi: 10.1002/cne.902130408

Richardson, B. D., Sottile, S. Y., and Caspary, D. M. (2021). Mechanisms of GABAergic and cholinergic neurotransmission in auditory thalamus: impact of aging. *Hear. Res.* 402:108003. doi: 10.1016/j.heares.2020.108003

Risoud, M., Hanson, J. N., Gauvrit, F., Renard, C., Lemesre, P. E., Bonne, N. X., et al. (2018). Sound source localization. *Eur. Ann. Otorhinolaryngol. Head Neck Dis.* 135, 259–264. doi: 10.1016/j.anorl.2018.04.009

Rivera-Perez, L. M., Kwapiszewski, J. T., and Roberts, M. T. (2021). alpha3beta4 (*) nicotinic acetylcholine receptors strongly modulate the excitability of VIP neurons in the mouse inferior colliculus. *Front. Neural Circuits* 15:709387. doi: 10.3389/fncir.2021.709387

Roeren, T., LeVeen, R. F., and Nugent, L. (1988). Photoplethysmographic documentation of improved microcirculation after pentoxifylline therapy. *Angiology* 39, 929–933. doi: 10.1177/000331978803901101

Romero, G. E., and Trussell, L. O. (2022). Central circuitry and function of the cochlear efferent systems. *Hear. Res.* 425:108516. doi: 10.1016/j.heares.2022.108516

Rotter, A., Birdsall, N. J., Field, P. M., and Raisman, G. (1979). Muscarinic receptors in the central nervous system of the rat. II. Distribution of binding of [3H] propylbenzilylcholine mustard in the midbrain and hindbrain. *Brain Res.* 180, 167–183. doi: 10.1016/0165-0173(79)90003-1

Rouiller, E. M., and de Ribaupierre, F. (1985). Origin of afferents to physiologically defined regions of the medial geniculate body of the cat: ventral and dorsal divisions. *Hear. Res.* 19, 97–114. doi: 10.1016/0378-5955(85)90114-5

Roux, I., Wersinger, E., McIntosh, J. M., Fuchs, P. A., and Glowatzki, E. (2011). Onset of cholinergic efferent synaptic function in sensory hair cells of the rat cochlea. *J. Neurosci.* 31, 15092–15101. doi: 10.1523/JNEUROSCI.2743-11.2011

Safieddine, S., Bartolami, S., Wenthold, R. J., and Eybalin, M. (1996). Pre- and postsynaptic M3 muscarinic receptor mRNAs in the rodent peripheral auditory system. *Brain Res. Mol. Brain Res.* 40, 127–135

Schofield, B. R. (1991). Superior paraolivary nucleus in the pigmented guinea pig: separate classes of neurons project to the inferior colliculus and the cochlear nucleus. *J. Comp. Neurol.* 312, 68–76. doi: 10.1002/cne.903120106

Schofield, B. R. (2002). Ascending and descending projections from the superior olivary complex in guinea pigs: different cells project to the cochlear nucleus and the inferior colliculus. *J. Comp. Neurol.* 453, 217–225. doi: 10.1002/cne.10402

Schofield, B., and Hurley, L. (2018). Circuits for modulation of auditory function. The mammalian auditory pathways: Synaptic organization and microcircuits. 235–267. doi: 10.1007/978-3-319-71798-2_9

Schofield, B. R., Motts, S. D., and Mellott, J. G. (2011). Cholinergic cells of the pontomesencephalic tegmentum: connections with auditory structures from cochlear nucleus to cortex. *Hear. Res.* 279, 85–95. doi: 10.1016/j.heares.2010.12.019

Servent, D., Blanchet, G., Mourier, G., Marquer, C., Marcon, E., and Fruchart-Gaillard, C. (2011). Muscarinic toxins. *Toxicon* 58, 455–463. doi: 10.1016/j.toxicon.2011.08.004

Shen, J. X., and Yakel, J. L. (2009). Nicotinic acetylcholine receptor-mediated calcium signaling in the nervous system. *Acta Pharmacol. Sin.* 30, 673–680. doi: 10.1038/aps.2009.64

Sherriff, F. E., and Henderson, Z. (1994). Cholinergic neurons in the ventral trapezoid nucleus project to the cochlear nuclei in the rat. *Neuroscience* 58, 627–633. doi: 10.1016/0306-4522(94)90086-8

Shute, C. C., and Lewis, P. R. (1967). The ascending cholinergic reticular system: neocortical, olfactory and subcortical projections. *Brain* 90, 497–520. doi: 10.1093/brain/90.3.497

Sottile, S. Y., Ling, L., Cox, B. C., and Caspary, D. M. (2017). Impact of ageing on postsynaptic neuronal nicotinic neurotransmission in auditory thalamus. *J. Physiol.* 595, 5375–5385. doi: 10.1113/JP274467

Stornetta, R. L., Macon, C. J., Nguyen, T. M., Coates, M. B., and Guyenet, P. G. (2013). Cholinergic neurons in the mouse rostral ventrolateral medulla target sensory afferent areas. *Brain Struct. Funct.* 218, 455–475. doi: 10.1007/s00429-012-0408-3

Stotler, W. A. (1953). An experimental study of the cells and connections of the superior olivary complex of the cat. *J. Comp. Neurol.* 98, 401–431. doi: 10.1002/cne.900980303

Strutz, J. (1987). Anatomy of the central auditory pathway. Demonstration with horseradish peroxidase in the guinea pig. *HNO* 35, 407–415

Tachibana, M., Rothman, J. M., and Guth, P. S. (1979). Somatostatin along the auditory pathway. *Hear. Res.* 1, 365–368. doi: 10.1016/0378-5955(79)90006-6

Taranda, J., Maison, S. F., Ballestero, J. A., Katz, E., Savino, J., Vetter, D. E., et al. (2009). A point mutation in the hair cell nicotinic cholinergic receptor prolongs cochlear inhibition and enhances noise protection. *PLoS Biol.* 7:e18. doi: 10.1371/journal.pbio.1000018

Thompson, A. M., and Schofield, B. R. (2000). Afferent projections of the superior olivary complex. *Microsc. Res. Tech.* 51, 330–354. doi: 10.1002/1097-0029(20001115)51:4<330::AID-JEMT4>3.0.CO;2-X

Uchimura, N., and North, R. A. (1990). Muscarine reduces inwardly rectifying potassium conductance in rat nucleus accumbens neurones. *J. Physiol.* 422, 369–380. doi: 10.1113/jphysiol.1990.sp017989

Uteshev, V. V. (2012). alpha7 nicotinic ACh receptors as a ligand-gated source of ca(2+) ions: the search for a ca(2+) optimum. *Adv. Exp. Med. Biol.* 740, 603–638. doi: 10.1007/978-94-007-2888-2_27

Varela, C., and Sherman, S. M. (2007). Differences in response to muscarinic activation between first and higher order thalamic relays. *J. Neurophysiol.* 98, 3538–3547. doi: 10.1152/jn.00578.2007

Wang, H. S., Pan, Z., Shi, W., Brown, B. S., Wymore, R. S., Cohen, I. S., et al. (1998). KCNQ2 and KCNQ3 potassium channel subunits: molecular correlates of the M-channel. *Science* 282, 1890–1893. doi: 10.1126/science.282.5395.1890

Watanabe, T., and Simada, Z. (1973). Pharmacological properties of cat's collicular auditory neurons. *Jpn. J. Physiol.* 23, 291–308. doi: 10.2170/jjphysiol.23.291

Weber, M., Motin, L., Gaul, S., Beker, F., Fink, R. H., and Adams, D. J. (2005). Intravenous anaesthetics inhibit nicotinic acetylcholine receptor-mediated currents and Ca2+ transients in rat intracardiac ganglion neurons. *Br. J. Pharmacol.* 144, 98–107. doi: 10.1038/sj.bjp.0705942

Weimann, S. R., Zhang, C., and Burger, R. M. (2024). A developmental switch in cholinergic mechanisms of modulation in the medial nucleus of the trapezoid body. *J. Neurosci.* 44:e0356232023. doi: 10.1523/JNEUROSCI.0356-23.2023

Winslow, R. L., and Sachs, M. B. (1988). Single-tone intensity discrimination based on auditory-nerve rate responses in backgrounds of quiet, noise, and with stimulation of the crossed olivocochlear bundle. *Hear. Res.* 35, 165–189. doi: 10.1016/0378-5955(88)90116-5

Wolpert, S., Heyd, A., and Wagner, W. (2014). Assessment of the noise-protective action of the olivocochlear efferents in humans. *Audiol. Neurootol.* 19, 31–40. doi: 10.1159/000354913

Womble, M. D., and Moises, H. C. (1992). Muscarinic inhibition of M-current and a potassium leak conductance in neurones of the rat basolateral amygdala. *J. Physiol.* 457, 93–114. doi: 10.1113/jphysiol.1992.sp019366

Yao, W., and Godfrey, D. A. (1995). Immunohistochemistry of muscarinic acetylcholine receptors in rat cochlear nucleus. *Hear. Res.* 89, 76–85. doi: 10.1016/0378-5955(95)00123-7

Yao, W., and Godfrey, D. A. (1996). Autoradiographic distribution of muscarinic acetylcholine receptor subtypes in rat Cochlear nucleus. *Audit. Neurosci.* 2, 241–255

Yin, T. C., and Chan, J. C. (1990). Interaural time sensitivity in medial superior olive of cat. *J. Neurophysiol.* 64, 465–488. doi: 10.1152/jn.1990.64.2.465

Young, E. D., and Brownell, W. E. (1976). Responses to tones and noise of single cells in dorsal cochlear nucleus of unanesthetized cats. *J. Neurophysiol.* 39, 282–300. doi: 10.1152/jn.1976.39.2.282

Zhang, C., Beebe, N. L., Schofield, B. R., Pecka, M., and Burger, R. M. (2021). Endogenous cholinergic signaling modulates sound-evoked responses of the medial nucleus of the trapezoid body. *J. Neurosci.* 41, 674–688. doi: 10.1523/JNEUROSCI.1633-20.2020

Zhao, Y., and Tzounopoulos, T. (2011). Physiological activation of cholinergic inputs controls associative synaptic plasticity via modulation of endocannabinoid signaling. *J. Neurosci.* 31, 3158–3168. doi: 10.1523/JNEUROSCI.5303-10.2011

Zook, J. M., and Casseday, J. H. (1987). Convergence of ascending pathways at the inferior colliculus of the mustache bat, *Pteronotus parnellii*. *J. Comp. Neurol.* 261, 347–361. doi: 10.1002/cne.902610303

frontiers | Frontiers in Cellular Neuroscience

TYPE Original Research
PUBLISHED 22 July 2024
DOI 10.3389/fncel.2024.1408208

Check for updates

OPEN ACCESS

EDITED BY
Christian Keine,
University of Oldenburg, Germany

REVIEWED BY
Matthew William Kelley,
National Institutes of Health (NIH),
United States
Tina Pangrsic,
University Medical Center Göttingen, Germany

*CORRESPONDENCE
Samson Jamesdaniel
✉ sjamesdaniel@wayne.edu

RECEIVED 27 March 2024
ACCEPTED 03 July 2024
PUBLISHED 22 July 2024

CITATION
Bhatia P, Mehmood S, Doyon-Reale N, Rosati R, Stemmer PM and Jamesdaniel S (2024) Unraveling the molecular landscape of lead-induced cochlear synaptopathy: a quantitative proteomics analysis.
Front. Cell. Neurosci. 18:1408208.
doi: 10.3389/fncel.2024.1408208

COPYRIGHT
© 2024 Bhatia, Mehmood, Doyon-Reale, Rosati, Stemmer and Jamesdaniel. This is an open-access article distributed under the terms of the Creative Commons Attribution License (CC BY). The use, distribution or reproduction in other forums is permitted, provided the original author(s) and the copyright owner(s) are credited and that the original publication in this journal is cited, in accordance with accepted academic practice. No use, distribution or reproduction is permitted which does not comply with these terms.

Unraveling the molecular landscape of lead-induced cochlear synaptopathy: a quantitative proteomics analysis

Pankaj Bhatia[1], Shomaila Mehmood[1], Nicole Doyon-Reale[1], Rita Rosati[1], Paul M. Stemmer[1] and Samson Jamesdaniel[1,2]*

[1]Institute of Environmental Health Sciences, Wayne State University, Detroit, MI, United States, [2]Department of Family Medicine and Public Health Sciences, Wayne State University, Detroit, MI, United States

Introduction: Exposure to heavy metal lead can cause serious health effects such as developmental neurotoxicity in infants, cognitive impairment in children, and cardiovascular and nephrotoxic effects in adults. Hearing loss is one of the toxic effects induced by exposure to lead. Previous studies demonstrated that exposure to lead causes oxidative stress in the cochlea and disrupts ribbon synapses in the inner hair cells.

Methods: This study investigated the underlying mechanism by evaluating the changes in the abundance of cochlear synaptosomal proteins that accompany lead-induced cochlear synaptopathy and hearing loss in mice. Young-adult CBA/J mice were given lead acetate in drinking water for 28 days.

Results: Lead exposure significantly increased the hearing thresholds, particularly at the higher frequencies in both male and female mice, but it did not affect the activity of outer hair cells or induce hair cell loss. However, lead exposure decreased wave-I amplitude, suggesting lead-induced cochlear synaptopathy. In agreement, colocalization of pre- and post-synaptic markers indicated that lead exposure decreased the number of paired synapses in the basal turn of the cochlea. Proteomics analysis indicated that lead exposure increased the abundance of 352 synaptic proteins and decreased the abundance of 394 synaptic proteins in the cochlea. Bioinformatics analysis indicated that proteins that change in abundance are highly enriched in the synaptic vesicle cycle pathway.

Discussion: Together, these results suggest that outer hair cells are not the primary target in lead-induced ototoxicity, that lead-induced cochlear synaptopathy is more pronounced in the basal turn of the cochlea, and that synaptic vesicle cycle signaling potentially plays a critical role in lead-induced cochlear synaptopathy.

KEYWORDS

cochlear synaptopathy, lead-induced ototoxicity, hearing loss, cochlear synaptosomes, synaptic vesicle cycle

1 Introduction

Environmental contamination with heavy metal lead is a growing concern because lead exposure affects human health, particularly that of children, and pregnant and lactating women, who are more vulnerable to its toxic effects (Choi et al., 2008; Tiwari et al., 2012;

Olufemi et al., 2022). According to the World Health Organization, out of the 2 million deaths worldwide that are related to chemical exposure, nearly half of the deaths are linked to lead exposure (WHO, 2023a). Some of the common sources of lead exposure include mining, industrial pollutants, paints, contaminated foods, and water (Guidotti et al., 2007; Obeng-Gyasi, 2019; Kumar et al., 2020). Lead enters the body through multiple routes, accumulates over time, and causes severe health problems. Even at lower concentrations, lead can negatively impact health (Wani et al., 2015). The nervous system is particularly susceptible to the toxic effects of lead. Chronic exposure to lead is associated with an increased risk of neurodegenerative disorders, such as Alzheimer's and Parkinson's disease (Wang et al., 2020). The lead-induced neurotoxicity is characterized by disruptions in synaptic transmission, oxidative stress, and inflammation within the central nervous system (Hossain et al., 2016; Mahmoud and Sayed, 2016; Mohanraj et al., 2022). Workers exposed to inorganic lead experience reduced sensory and motor conduction velocities, indicating damage to the peripheral nervous system (Zheng et al., 2011). Even asymptomatic workers with chronic exposure to lead have subclinical damage to peripheral nerves (Seppäläinen and Hernberg, 1980; Bilińska et al., 2005).

In addition to the other well-known neurotoxic effects, lead exposure is linked to adverse auditory effects, including hearing loss (Park et al., 2010; Jamesdaniel et al., 2018; Zhang et al., 2019). Lead crosses the blood–brain barrier, injures the astrocytes in rat hippocampus, and potentially affects the central auditory pathway leading to auditory deficits (Selvín-Testa et al., 1991; Castellanos and Fuente, 2016; Shvachiy et al., 2023). Additionally, chronic lead exposure can damage the peripheral auditory pathway (Holdstein et al., 1986; Zou et al., 2003), because it adversely impacts axonal integrity and myelin organization (Brubaker et al., 2009), which can result in reduced nerve conduction velocity and impaired signal transmission efficiency (Takeuchi et al., 2021; Aktürk et al., 2022). Chronic exposure to lead for 60 days significantly reduced the count of spiral ganglion neurons, delayed the latency of auditory brainstem response (ABR) wave I, and caused hearing loss (Zhang et al., 2019). Lead exposure is also reported to modify neuronal structural proteins, increase phosphorylation of neurofilament proteins in auditory brainstem nuclei, cause neuritic beading in axons, impair axonal transport, and affect brainstem conduction time and temporal auditory processing (Jones et al., 2008). However, the molecular mechanism by which lead exposure causes auditory dysfunction is not fully understood.

Oxidative stress appears to play a central role in mediating the ototoxic effects of lead. Lead exposure in rats triggered oxidative stress within the cochlea, leading to degenerative changes in spiral ganglion neurons and subsequent hearing loss (Xue-wen et al., 2011; Hu et al., 2019). Chronic lead exposure also downregulated several cochlear genes that encode critical antioxidant enzymes (Jamesdaniel et al., 2018). Another recent study showed that lead exposure increased nitrative stress in the spiral ganglion cells and disrupted the ribbon synapses resulting in cochlear synaptopathy (Rosati et al., 2022). To gain further insights into the molecular landscape of lead-induced cochlear synaptopathy, the current study investigated the lead-induced changes in cochlear synaptosomal proteins by high throughput proteomics analyses. Cochlear synaptosomal proteins extracted from lead-exposed mice were analyzed by tandem mass spectrometry and critical targets and molecular pathways associated with lead-induced cochlear synaptopathy were identified by bioinformatics analyses.

2 Experimental procedures

2.1 Experimental design and statistical rationale

Auditory deficits and proteomics profile of cochlear synaptosomes were analyzed in mice exposed to lead (Figure 1A). The electrophysiology experiments were done in four to eight biological replicates, immunohistochemistry and immunoblotting experiments were done in a minimum of three biological replicates, and the mass spectrometry experiments were conducted using four to six biological replicates in each group.

2.2 Animals

Five-week-old male and female CBA/J mice (Jackson Laboratories, Bar Harbor, ME, United States) were used in this study. The animals were provided with food and water *ad libitum* and maintained in accordance with the standard guidelines of the National Institutes of Health. The University Institutional Animal Care and Use Committee reviewed and approved the experimental protocol (IACUC-22-01-4298).

2.3 Lead exposure

After baseline hearing tests, mice with normal hearing were randomly divided into two sets. Control mice were provided regular drinking water over a 28-day period, while the mice in the lead exposure group were provided with drinking water containing lead acetate (2 mM; Cat # 316512, Sigma-Aldrich, St. Louis, MO, USA) for 28 days. After the post-exposure hearing tests on the 29th day, the animals were euthanized, and blood and cochlea samples were collected. The animals' appearance and behavior were monitored throughout the study, and their body weight was measured every other week.

2.4 Inductively coupled plasma mass spectrometry

To analyze the blood lead levels, 75-µl of blood was mixed with an equal volume of 0.1% Triton X-100 and then diluted with 300 mL of 2% nitric acid. The mixture was incubated for 1–2 h and then centrifuged. The sample was diluted again with 2% nitric acid for a final 50-fold dilution. A standard curve was generated using lead concentrations ranging from 0.05 to 200 ppb. The analysis was conducted using an Agilent 7,700X Series inductively coupled plasma mass spectrometer (ICP-MS).

2.5 Auditory brainstem responses and distortion product otoacoustic emissions

Auditory brainstem responses (ABR) and distortion product otoacoustic emissions (DPOAE) were recorded using Tucker Davis Technologies (TDT) System III hardware. The BioSigRZ software

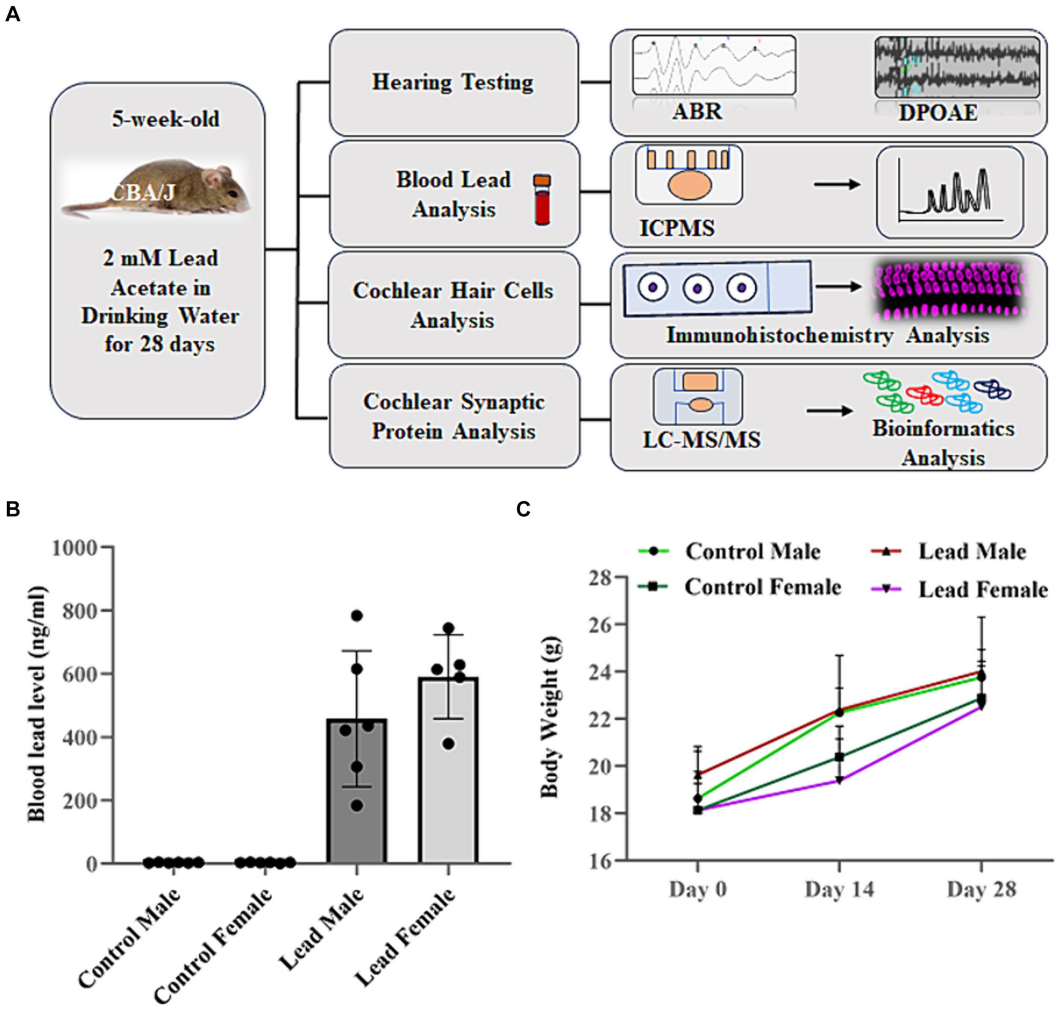


FIGURE 1
Overview of research design. **(A)** CBA/J mice were exposed to lead in drinking water for 28 days. Lead body burden was analyzed by assessing the blood lead levels 1 day after the last exposure. Hearing loss was assessed by measuring the shift in ABR thresholds while the outer hair cell activity was assessed by measuring DPOAE amplitudes. Hair cell loss and ribbon synaptic disruption was assessed by immunohistochemical analysis of cochlear sensory epithelium. The lead-induced changes in abundance of synaptosomal proteins and associated signaling pathways were assessed by LC–MS/MS and bioinformatics analysis, respectively. **(B)** ICPMS analysis indicated that lead exposure increased the blood lead levels in male and female mice (457.60 ± 87.8 ng/mL in males and 590.72 ± 59.28 ng/mL in females). Animals in the control groups consumed normal water, while those in the lead groups consumed water containing 2 mM lead acetate for 28 days. The results are expressed as mean ± standard error mean, $n = 5–6$.
(C) Measurement of body weight on day 0, 14, and day 28 indicated that exposure to lead did not alter the normal weight gain of CBA/J mice. The results are expressed as mean ± standard deviation, $n = 6$. ABR, auditory brainstem response; DPOAE, distortion product otoacoustic emissions; ICPMS, inductively coupled plasma mass spectrometry; LC–MS/MS, liquid chromatography tandem mass spectrometry.

(v5.7.6.) was used to present sound stimuli. Mice were anesthetized with isoflurane (4% induction, 1.5% maintenance with 1 L/min O_2) and placed on a temperature-controlled heating pad maintained at 38°C inside the soundproof chamber (ECKEL-AB-4230, Morrisburg, Ontario). For recording ABRs, the electrodes were placed subcutaneously at the vertex of the skull (active), mastoid region under the left ear (reference), and the right ear (ground). The sound stimuli of clicks and tone bursts at frequencies of 4, 8, 16, 24, or 32 kHz were delivered into the external auditory meatus. The ABR waveforms were obtained by averaging 512 stimulus presentations, delivered at 21/s. The sound intensity varied in 5-dB intervals starting from 90 dB Sound Pressure Level (SPL). The hearing threshold was determined by identifying the lowest intensity of stimuli that elicited Wave I peak. The amplitude (difference between the voltage levels of the peak and the trough) and the latency (the time elapsed from the onset of the stimulus to the peak of the first wave) of Wave I were measured using 90-dB SPL stimuli.

DPOAEs were measured using two primary tones, f1 and f2, at an f2/f1 ratio of 1.2. The L2–L1 was held at +10 dB for L1 levels ranging from 80 dB SPL to 20 dB SPL in 10 dB increments. The Tucker-Davis Technology (TDT) RZ6 system was used to generate the stimulus, while and f1 and f2 were delivered by using multifield magnetic speakers (TDT, Alachua, FL, United States). The frequency of f2 varied from 4 kHz to 40 kHz. SPLs at the cubic difference frequency (2f1–f2) were measured using the ER10B + probe microphone (Etymotic Research, Inc., Elk Grove Village, IL, United States), along with

hardware and software from TDT. Distortion product data were collected every 20.971 ms and averaged 512 times while a 100-kHz band surrounding 2f1–f2 was used for measuring the noise floor.

2.6 Immunohistochemistry of cochlear surface preparations

After euthanizing the mice, the temporal bones were quickly extracted on ice-cold PBS, the blood in the cochlea was flushed out by perfusing with 4% paraformaldehyde in PBS (7.4 pH) through the oval window, and the cochlear tissue was fixed for 24 h. Then the cochlea was decalcified in 100 mM ethylenediaminetetraacetic acid disodium salt (EDTA) solution in PBS (7.4 pH) for 48–72 h. Fully decalcified tissue was micro-dissected in ice-cold PBS solution under a stereomicroscope (Olympus model # SZH-ILLK) and the cochlear sensory epithelium was separated from the bony capsule and the lateral wall. Then the sensory epithelium was cut into apex, middle, and basal sections.

For the immunolabeling, each cochlear section was first incubated in a blocking solution containing 10% normal goat serum for 2 h at room temperature. Then the tissue was incubated with primary antibodies overnight and then with secondary antibodies for 2 h at 4°C. The primary antibodies used in this study were: rabbit anti-glutamate receptor 2 (GluR2), clone 6C4 (1:200, IgG, Millipore # MAB397), mouse anti-C-terminal-binding protein-2 (CtBP2) (1:400, IgG1, BD Biosciences # 612044), and mouse anti-myosin VIIa monoclonal antibody (1:500, IgG2a, Santa Cruz biotechnology # 74516). The secondary antibodies used were goat anti-rabbit Alexa Fluor (AF) 647 (1:500, IgG, Thermo Fisher Scientific # 21244), goat anti-mouse AF 568 (1:500, IgG1, Thermo Fisher Scientific # 21124), and goat anti-mouse AF 488 (1:500, IgG2a, Thermofisher Scientific # 21131). The ProLong Gold antifade with DAPI was used for mounting the tissue, and a coverslip was secured from the side using Biotium CoverGrip Coverslip Sealant (Fisher Scientific # NC0154994).

2.7 Confocal microscopy and image processing

All images were captured using a Zeiss confocal microscope LSM 800 and analyzed using Zeiss Zen Blue 3.7 and ImageJ/Fiji software (v 1.46r). Immunolabeling of OHCs and IHCs were captured using 40x plan apochromatic objective and 1.3 numerical aperture. The immunolabeling of presynaptic ribbons (CtBP2) and postsynaptic ribbons (GluR2) were captured using a 63x-magnification objective lens with an effective numerical aperture of 1.4. Z-stacks of 10–15 slices for hair cells and 20–25 slices for CtBP2 and GluR2 puncta were compressed to make maximum intensity projection. The localization of CtBP2 and GluR2 puncta were examined to assess the pairing of the synapses using Zen software (v 3.7). Hair cell counts were quantified in 100 µm segments of the apex (4–8 kHz), middle (16–24 kHz), and basal (32 kHz) regions of the cochlea, and the ribbon synapses were counted in 6-IHCs and averaged to get ribbon synapses/IHC. The number of paired synaptic ribbons was counted using the 3D Object Counter of ImageJ software.

2.8 Cochlear synaptosomal protein extraction

Cochlear tissue was dissected and the synaptosomal proteins were extracted from the entire cochlea by homogenizing the tissue in Syn-PER reagent (Thermo Scientific # 87793, Rockford, IL, USA) following the manufacturer's protocol. Briefly, the homogenate was centrifuged at 1200 × *g* for 10 min at 4°C, and the supernatant was transferred to a new tube and centrifuged at 15,000 × *g* for 20 min at 4°C. Then, the supernatant was discarded, and the synaptosome pellets were resuspended in Syn-PER reagent. This step was repeated, and the supernatant was carefully discarded to obtain the pellets containing synaptosome proteins.

2.9 Immunoblotting

The enrichment of the synaptosomal proteins was verified by immunoblotting with anti-SNAP-25. A total of 5 µg of proteins from the synaptosomal fraction, non-synaptosomal fraction (supernatant), and the total cochlear homogenate were separated on 4–20% gradient SDS-Page gels, transferred to PVDF membranes, and probed with goat polyclonal SNAP-25 antibody (1:500, IgG, ThermoFisher Scientific # PA1-9102, Waltham, MA, USA). The bands were developed using a chemiluminescence detection reagent (Thermo Fisher Scientific # 34076), and the bands were visualized using FluorChem E System (ProteinSimple, San Jose, CA, USA). Mouse monoclonal β-Actin Antibody (1:500, IgG1κ, Santa Cruz Biotechnology # sc-47778, CA, USA) was used for normalization.

2.10 Liquid chromatography tandem mass spectrometry

Synaptosomal pellets were resuspended in water and then combined with an equivalent volume of 2.5% Lithium Dodecyl Sulfate (Sigma L9781, St. Louis, MO, USA) in 40 mM Triethylammonium bicarbonate buffer (TEAB, Honeywell Fluka, 60–044-974, Suwanee, GA, USA). The samples were homogenized in a Bullet Blender (Next Advance, BT12LT, Baltimore, MD, USA) utilizing a single 3.2 mm stainless steel bead in each tube (Next Advance, SSB32, Baltimore, MD, USA) for 1 min, incubated for 5 min at 95°C to deactivate enzymes then filtered through 0.8 mL Pierce spin columns to decrease the viscosity. Samples were reduced by adding 5 mM DL-Dithiothreitol (DTT, Sigma, D5545, St. Louis, MO, USA) and incubated for 30 min at 37°C. Then the samples were alkylated by adding 15 mM Iodoacetamide (IAA) (Sigma, I1149, St. Louis, MO, USA) and further incubated for 30 min at room temperature in the dark. The alkylation process was halted by adding 5 mM DTT, the samples were acidified by adding 10% of the initial volume of 12% phosphoric acid and precipitated by addition of 5 volumes of methanol (MeOH) and incubating overnight at −20°C. Finally, the samples were centrifuged at 4,000 × *g* for 5 min to separate the pellets, which were then washed with 80% MeOH and 1% TEAB, and the washed pellets were air-dried and resuspended in 50 µL of 40 mM TEAB. Digestion was achieved using trypsin (Promega) at a ratio of 1:25 (w/w), and the samples were incubated at 47°C for 1 h, followed by 3 h at 37°C. The resultant peptides were solubilized in 20 µL of 0.1% formic acid (FA), and 10 µL

of this solution was utilized for proteomics analysis. Final analysis was performed on the samples using a Thermo Scientific Vanquish-Neo chromatography system with an Acclaim PepMap 100 trap column (100 µm × 2 cm, C18, 5 µm, 100 Å), and Thermo Scientific Easy-Spray PepMap RSLC C18 75 um x25 cm column. A gradient starting at 4% acetonitrile and finishing at 30% acetonitrile 100 min later was used for all samples. LC–MS/MS with Data Independent Acquisition (DIA) was performed on an Orbitrap Eclipse MS system. MS1 spectra were acquired at 120,000 resolutions in the 400 to 1,600 Da mass range with an AGC of 1e6. MS2 spectra were acquired using variable windows with a resolution set at 15,000.

2.11 Bioinformatics analysis

Spectronaut-18 software (Biognosys; v18) was used to quantitatively profile the proteomic changes and identify the differentially abundant synaptosomal proteins. A fold change of ±1.5 was chosen as a criterion for selecting proteins of interest. Official gene symbols of high and low-abundant proteins were used for GO annotation and KEGG (Kyoto Encyclopedia of Genes and Genomes) pathway enrichment analysis. Shiny GO v0.80 bioinformatics tool (Ge et al., 2020) was used with FDR = 0.05, to identify the signaling pathways regulated by genes of differentially expressed proteins. The top 30 biological processes (BP), and KEGG pathways associated with lead-induced changes in the abundance of cochlear synaptosomal proteins were identified by the bioinformatics analysis. The Search Tool for the Retrieval of Interacting Genes (STRING) database Version 12.0 was used for protein–protein interaction (PPI) analysis (Szklarczyk et al., 2016).

2.12 Statistical analysis

Data were analyzed using Microsoft Excel's Data Analysis Toolkit (Office Professional Plus 2016, Microsoft, Redmond, WA, USA) and GraphPad Prism (v10, La Jolla, CA, USA). Volcano plots were generated using Spectronaut software. Statistical analysis employed a two-tailed unpaired t-test, with significance set at $p < 0.05$. The outcomes are presented as mean ± standard deviation or standard error mean.

3 Results

3.1 Lead exposure via drinking water increased blood lead levels

Exposure of mice to drinking water containing 2 mM lead acetate for 28 days significantly increased the blood lead levels. Figure 1B shows the average blood lead levels in control and lead-exposed mice. The blood lead load in lead-exposed male and female mice was 457.60 ± 87.78 ng/mL and 495.68 ± 106.66 ng/mL, respectively, and was significantly higher than the blood lead levels detected in control male (2.78 ± 0.36 ng/mL) and female (2.54 ± 0.55 ng/mL) mice. This indicated that the 28-day exposure used in this study increased the lead body burden in mice. However, this lead exposure did not alter the body weight of the animals (Figure 1C).

3.2 Hearing thresholds are altered by lead exposure

ABRs were recorded to evaluate the effect of lead exposure on hearing thresholds. ABRs indicated that while the control mice had normal hearing across all frequencies, lead exposure significantly increased the hearing thresholds across multiple frequencies. In males, the hearing thresholds were elevated in ABRs elicited with pure-tone stimuli at 8, 16, 24, and 32 kHz, and click, while in females, the hearing thresholds were elevated in ABRs elicited with pure-tone stimuli at 4, 16, 24, and 32 kHz, and click. These results indicated that lead exposure for 28 days induced significant hearing loss in mice. The lead-induced shift in hearing thresholds was more pronounced in ABRs elicited with pure-tone stimuli at higher frequencies (24 and 32 kHz) and click, and the shifts were similar in both male and female mice. Although a two-tailed parametric *t*-test showed a significant difference in the shifts between 8 and 32 kHz ($p = 0.0318$), suggesting that the higher frequency regions may be more vulnerable to lead-induced ototoxicity, the ANOVA test did not show a significant difference. The hearing threshold shifts also indicated that both sexes are equally susceptible to lead-induced hearing impairment (Figures 2A–C). As we did not record the ABR a few days or weeks after the cessation of lead treatment, we do not have the data to show if the hearing loss will recover.

3.3 Outer hair cells are not affected by lead exposure

DPOAEs were recorded to evaluate the effect of lead exposure on OHC activity. The DP amplitudes measured in both male and female mice with f2 stimuli at 4, 8, 16, 24, 32, and 40 kHz indicated that the DPOAEs were similar in both control and lead-exposed mice (Figure 3A). This suggested that the OHC activity is not affected by lead exposure. Additionally, the effect of lead exposure on hair cell viability was assessed by immunohistochemistry analysis of cochlear surface preparations. Evaluation of myosin-VIIa immunostaining indicated that there was no hair cell loss in the apical, middle, and basal regions of the cochlea in both control and lead-exposed mice (Figure 3B). This suggested that lead exposure did not affect the viability of hair cells in the cochlea. Furthermore, the quantification of OHCs and IHCs confirmed no loss of hair cells in the apex, middle, and basal regions of the cochlea after lead exposure (Figures 3C,D).

3.4 Cochlear synaptic transmission is affected after lead exposure

The amplitude and latency of ABR wave-I were evaluated to assess the effect of lead exposure on cochlear synaptic transmission. Measurement of ABR wave-I amplitude recorded with pure-tone and click stimuli at 90 dB SPL indicated that lead exposure induced a significant reduction in wave-I amplitudes across multiple frequencies (24, and 32 kHz) when compared to the control group (Figures 4A–C). The decrease in wave-I amplitude was more pronounced at higher frequencies (24 and 32 kHz) than at lower frequencies (4, 8, and 16 kHz). However, the ABR wave-I latency was similar in both the control and lead-exposed groups, suggesting that wave-I latency is not affected by the 28-day lead exposure

(Figures 4D–F). Together, these results suggest that the lead exposure paradigm used in this study decreases the number of firing neurons within the cochlea and thereby affects the cochlear synaptic transmission.

3.5 Lead exposure disrupted the pairing of cochlear ribbon synapses

The cochlear ribbon synapses were evaluated by immunohistochemistry analysis of presynaptic ribbon (CtBP2) and postsynaptic receptor (GluR2) markers to determine the effect of lead exposure on the pairing of synapses. Lead exposure decreased the number of CtBP2 and GluR2 puncta located at the presynaptic and postsynaptic sides of the IHC synapse, respectively (Figures 5A–C). The absence of CtBP2 staining in the nuclei of IHCs in our images is probably due to the orientation of the tissue on the slide and the variations in the focal plane that were specifically used to capture high-quality images of ribbon synapse. The localization of the CtBP2 and GluR2 puncta was examined to quantify the number of paired synapses (Figure 5D), which indicated that the paired synapse count was significantly decreased in the middle and basal turn of the cochlea in lead-exposed mice (Figure 5E). Further, the lead-induced decrease in pair synaptic count was more pronounced in the basal region of the cochlea. These results suggest that the lead-induced reduction in the number of paired synapses contributes to the hearing impairment observed after lead exposure. Additionally, the basal region appears to be more susceptible to lead-induced ototoxicity.

3.6 Lead exposure altered the abundance of cochlear synaptosomal proteins

The changes in the abundance of cochlear synaptosomal proteins were evaluated to identify potential targets of lead-induced disruption of cochlear ribbon synapses and cochlear synaptic transmission. Immunoblotting with SNAP25 indicated the enrichment of synaptosomal proteins in the analyzed samples (Figure 6A). Although we have verified the enrichment of some other synaptosomal proteins in our samples using western blots in previous studies also (Shahab et al., 2024), we did not verify that all the proteins detected in the mass spectrometry analysis are from the synaptosomal compartment. Analysis of the mass spectrometry data using Spectronaut software identified a total of 4,947 proteins. The *p*-value histogram of the identified proteins indicated an anti-conservative graph in which the data followed the null distribution (Figure 6B). Further analyses of the data applying the criteria of $p < 0.05$ and fold change ±1.5, identified 746 differentially abundant proteins. Of these, the abundance of 352 proteins was increased while the abundance of 394 proteins was decreased after lead exposure (Figure 6C).

3.7 Synaptic vesicle cycle machinery is affected in lead-induced cochlear synaptopathy

The Shiny GO enrichment analysis of proteins whose abundance was increased after lead exposure indicated that BPs such as sodium ion export across the plasma membrane, clathrin-dependent endocytosis, and synaptic vesicle endocytosis were significantly enriched (Figures 7A,B). The KEGG pathways enrichment analysis revealed that the synaptic vesicle cycle is a highly enriched KEGG pathway (Figures 7C,D), and included proteins encoded by genes such as *Snap25*, *Vamp2*, *Slc1a2* that are associated with the vesicle-mediated transport. The network analysis of significantly enriched KEGG pathways indicated that the synaptic vesicle cycle pathway did not interact with the other enriched KEGG pathways (Figure 7C). The protein–protein-interaction (PPI) analysis of differentially expressed proteins in the synaptic vesicle cycle pathway, identified 22 nodes (proteins) and 39 edges (lines connecting nodes), with a PPI-enrichment value of $<1.0 \times 10^{-16}$ (Figure 7D). The illustration of

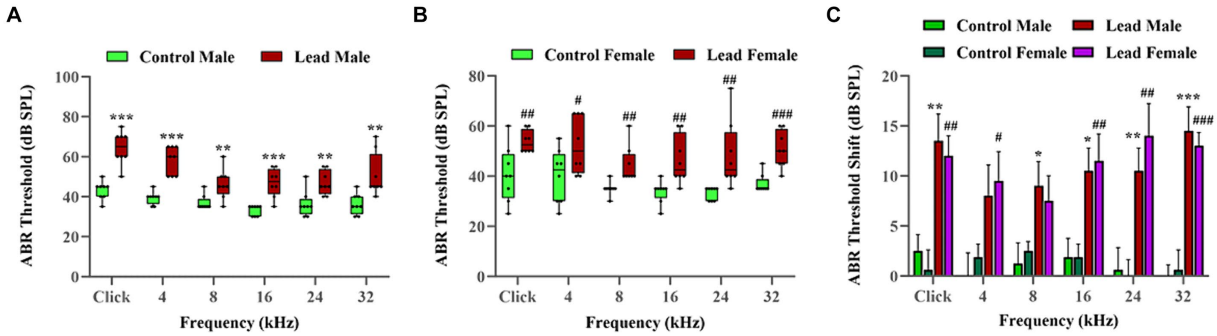


FIGURE 2
Lead-induced changes in the hearing thresholds. **(A,B)** Lead exposure elevated the ABR thresholds in both male and female mice, respectively. The hearing thresholds recorded using the left ear are illustrated. The results are expressed as mean ± standard error mean; $n = 8$. **(C)** The ABRs indicated that lead exposure induced a significant shift in the hearing thresholds (ranging from 8.00 to 14.50 dB in male mice and 7.50 to 14.00 dB in female mice) across multiple frequencies. Further analysis using *t*-tests indicate that the lead-induced threshold shifts at high frequencies (32 kHz) are significant ($p < 0.05$) compared to those at lower frequencies (8 kHz). The ABR threshold shifts represent the difference in thresholds measured at a young age (5 weeks) and 4 weeks later. The results are expressed as mean ± standard error mean; $n = 8$–10. * Indicates $p < 0.05$, ** $p < 0.01$, and *** $p < 0.001$ vs. control male; # indicates $p < 0.05$, ## $p < 0.01$, and ### $p < 0.001$ vs. control female. ABR, auditory brainstem response.

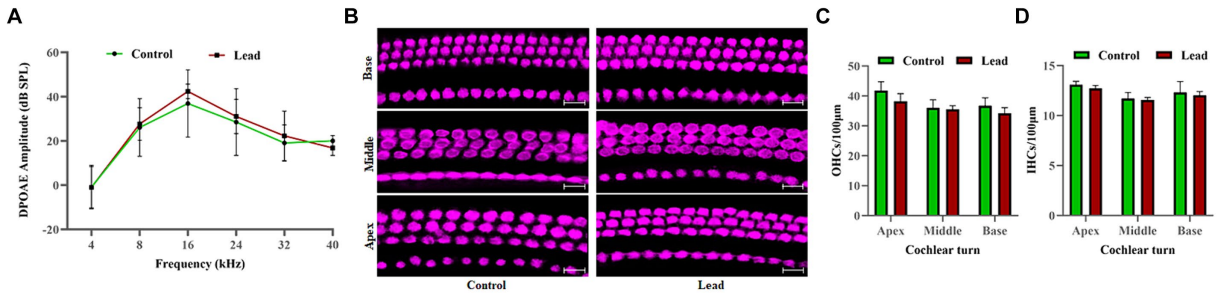


FIGURE 3
Effect of lead exposure on the hair cells. **(A)** The DPOAEs recorded using 4, 8, 16, 24, 32, and 40 kHz f2 stimuli indicated that the DPOAE amplitudes elicited using 70 dB SPL (L1) stimuli were similar in both control and lead exposed animals. The results are expressed as mean ± standard deviation; $n = 4–8$. **(B)** Immunohistochemical analysis with anti-myosin VIIa indicated that lead exposure did not affect the viability of both the OHCs and IHCs in the apex, middle, and basal regions of the organ of Corti. **(C,D)** OHCs and IHCs counts were carried out, and the mean number of cells per 100 µm section of the apex, middle, and basal region of the cochlea were displayed. Images are representative of three biological replicates. Scale bar = 20 µm. DPOAE, distortion product otoacoustic emissions; OHCs, outer hair cells; IHCs, inner hair cells.

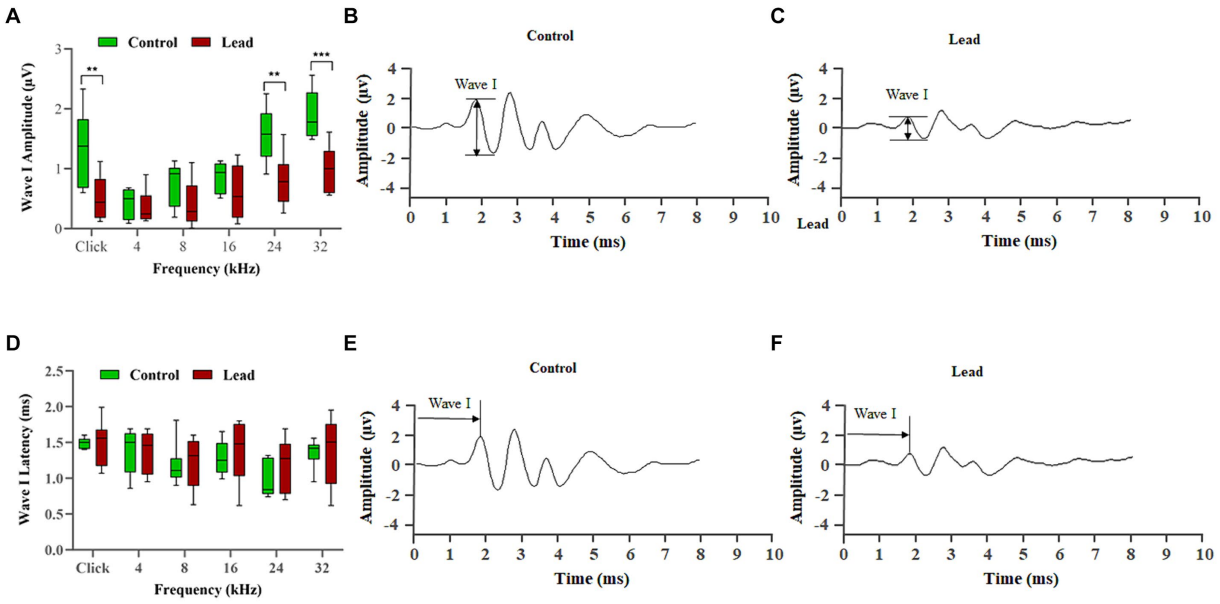


FIGURE 4
Effect of lead on the signal transmission in cochlear nerve fibers. **(A–C)** Lead exposure significantly reduced the amplitude of ABR wave I elicited using click and 24, and 32 kHz stimulus frequencies suggesting a decrease in the number of neurons firing in response to a stimulus. The lead-induced changes were greater at the higher frequencies, indicating that the basal region is more susceptible to lead-induced toxicity. The results are expressed as mean ± standard error mean; $n = 8$. ** Indicates $p < 0.01$, and ***$p < 0.001$ vs. control male. **(D–F)** Lead exposure did not alter the latency of ABR wave I, which suggests that the speed of neural conduction is not affected. Data collected from the left ear is illustrated. The results are expressed as mean ± standard error mean; $n = 8$. ABR, auditory brainstem response.

the synaptic vesicle cycle KEGG pathway highlights the differentially expressed proteins (red) that play a critical role in this signaling pathway (Figure 8).

Additionally, bioinformatics analysis of proteins whose abundance was decreased after lead exposure indicated that BPs such as NADH regeneration, canonical glycolysis, and glucose catabolic process to pyruvate were significantly enriched (Supplementary Figures S1A,B). The KEGG pathways enrichment analysis revealed that 2-Oxocarboxylic acid metabolism, pyruvate metabolism and nitrogen metabolism pathways were highly enriched (Supplementary Figures S1C,D). The network analysis of significantly enriched KEGG pathways indicated that the interaction between these pathways was limited (Supplementary Figures S1C. The protein–protein-interaction (PPI) analysis of differentially abundant proteins in the 2-Oxocarboxylic acid metabolism pathway, identified 8 nodes and 14 edges, with a PPI-enrichment value of $<1.0 \times 10^{-16}$ (Supplementary Figure S1D).

4 Discussion

Environmental exposure to ototoxicants is partly responsible for inducing disabling hearing loss, which is estimated to affect 1 in every 10 people by 2050 (WHO, 2023b). Heavy metal lead, which is

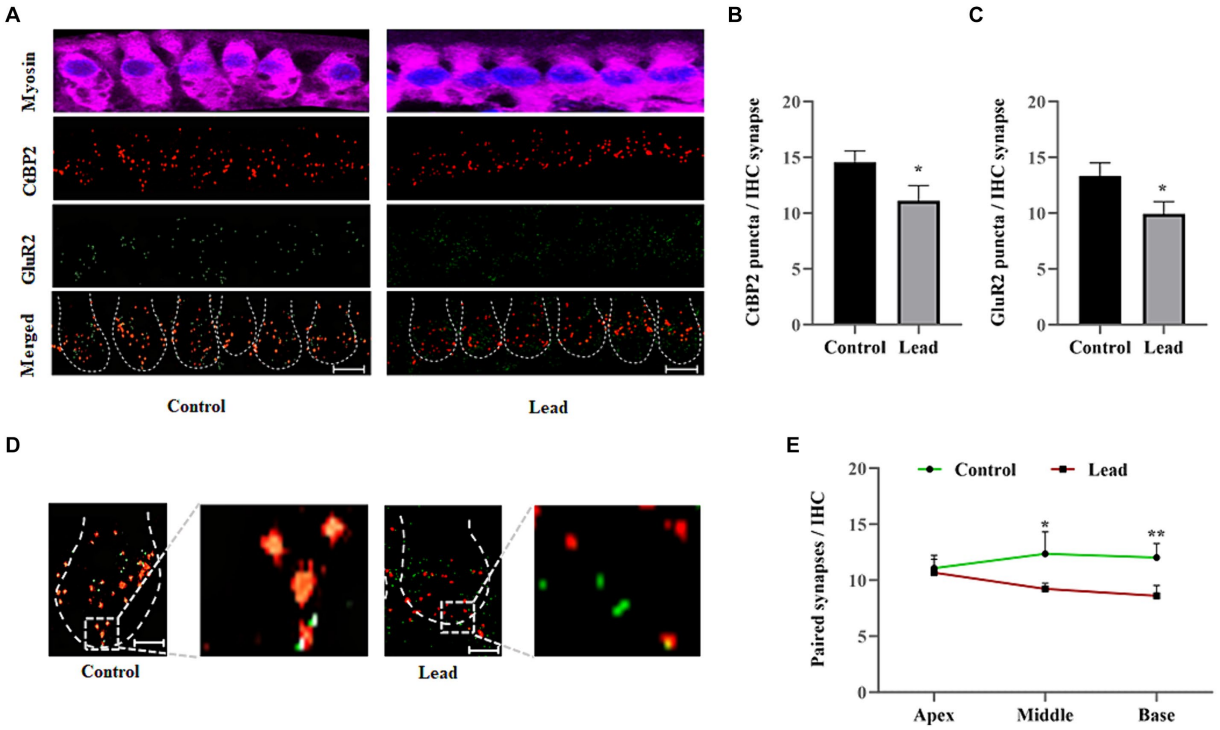


FIGURE 5
Lead-induced changes in the cochlear ribbon synapses. **(A)** Immunohistochemical staining of ribbon synapses in the basal turn of the cochlea indicated that lead exposure affected the presynaptic ribbons and postsynaptic receptors. The presynaptic ribbons were stained with anti-CtBP2 (red) and postsynaptic receptors were stained with anti-GluR2 (green). The images are representative of three biological replicates, scale bar = 10 μm. **(B,C)** Quantification of the CtBP2 and GluR2 puncta per inner hair cell synapse indicated that lead exposure significantly decreased the number of puncta. The data represent the basal turn of the organ of Corti. The results are expressed as mean ± standard deviation; $n = 3$. * Indicates $p < 0.05$ vs. control. **(D)** The pairing of the presynaptic ribbons with postsynaptic receptors was examined by documenting the yellow stained puncta (clearly visible in the zoomed image), which indicated paired ribbon synapses. The images are representative of three biological replicates, scale bar = 10 μm. **(E)** Quantification of the paired synapses per IHC indicated a significant decrease in the basal cochlear turn after lead exposure. The results are expressed as mean ± standard deviation; $n = 3–6$. * Indicates $p < 0.05$ and **$p < 0.01$ vs. control. CtBP2, C-terminal-binding protein-2; GluR2, glutamate receptor 2; IHC, inner hair cell.

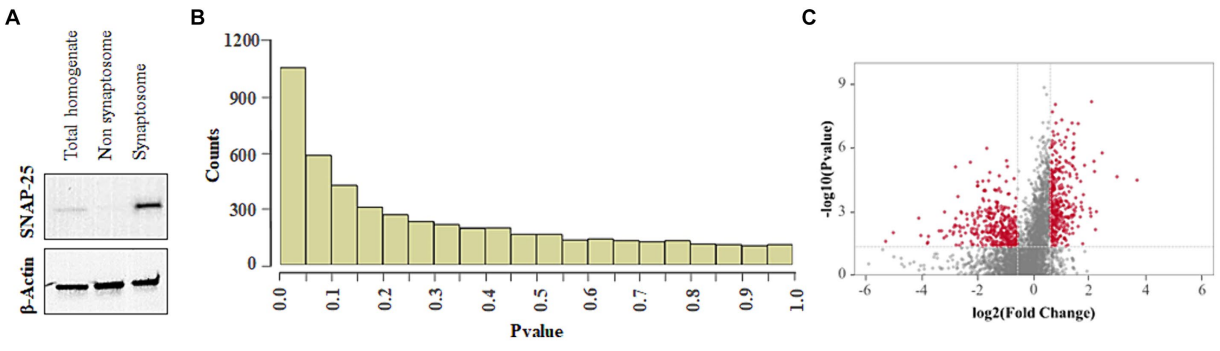


FIGURE 6
Effect of lead on cochlear synaptosomal proteins. **(A)** Immunoblot indicates the enrichment of SNAP-25 in the synaptosomal fraction. The images are representative of three biological replicates. **(B)** *p*-value histogram of lead-induced changes in the abundance of cochlear synaptosomal proteins indicates an anti-conservative graph where the data follows the null distribution. **(C)** Volcano plot illustrates the fold changes of 4,947 cochlear synaptosomal proteins identified using mass spectrometry analysis. The plot indicates that lead exposure increased the abundance of 352 synaptic proteins (red dots on the right side) and decreased the abundance of 394 synaptic proteins (red dots on the left side). A Fold change of ±1.5 was used as a criterion for selecting high and low-abundant proteins. The horizontal red line represents $p < 0.05$. Results are expressed as the mean of four biological replicates.

ubiquitous, affects auditory function after high-level exposures. Although the ototoxic effects of lead have been well documented, the underlying mechanisms are yet to be fully understood. This study provided evidence that outer hair cells are not the primary targets in lead-induced hearing loss. The immunostaining of the cochlear ribbon synapses indicated that the basal turn is more susceptible to lead-induced ototoxicity (Rosati et al., 2022). Furthermore, the mass spectrometry analyses identified critical synaptosomal proteins whose abundance is significantly altered by lead exposure while the bioinformatics analyses identified signaling pathways that are potentially associated with lead-induced cochlear synaptopathy.

Exposure of mice to lead in water for 28 days significantly increased their blood lead levels, which served as an indicator of the body burden. Consistent with previous studies (Jamesdaniel et al., 2018; Hu et al., 2019) lead exposure induced hearing loss in mice. Moreover, the lead-induced shift in hearing thresholds was similar in male and female mice suggesting that both sexes are susceptible to lead-induced ototoxicity. However, the otoacoustic emissions, even at higher frequencies, indicated that the activity of OHCs, which amplify and fine-tune sound signals within the cochlea (Goutman et al., 2015; Ashmore, 2019), were not affected by this lead exposure, which is consistent with the absence of auditory deficits after lead exposure observed in some studies (Carlson and Neitzel, 2018). Moreover, immunostaining of OHCs, which are highly susceptible to damage from noise and other ototoxic drugs, indicated that this lead exposure did not induce hair cell loss, even in the basal turn of the cochlea. These results indicate that lead exposure at concentrations that do not affect OHCs, can induce hearing impairment in mice and suggest that

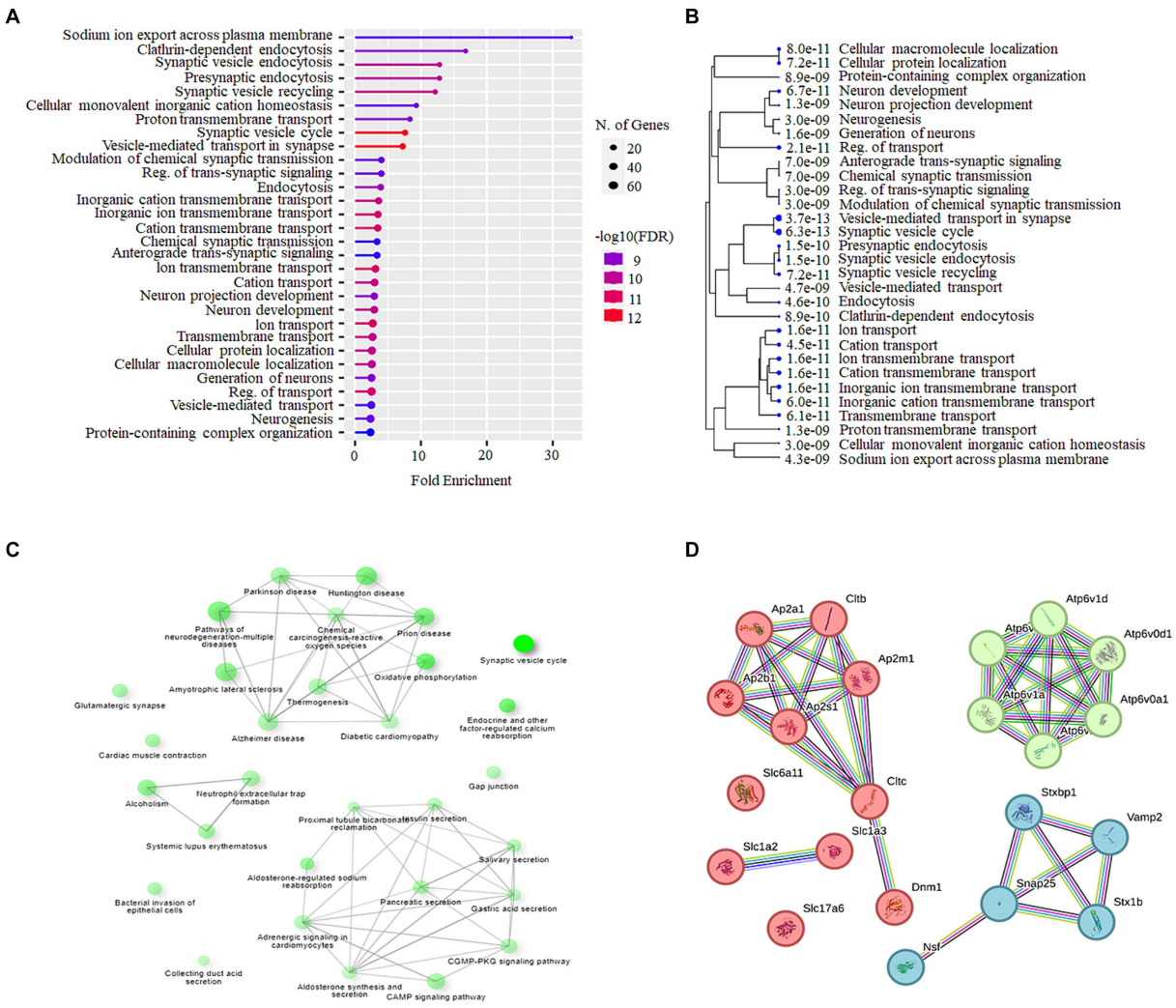


FIGURE 7
Bioinformatics analysis of cochlear synaptosomal proteins whose abundance was increased after lead exposure. **(A)** The GO analysis using the Shiny GO platform revealed the BPs enriched in the data set. The dot plot illustrates the fold enrichment, FDR, and the total number of proteins associated with these BPs. **(B)** The hierarchical clustering tree illustrates the clustering of significantly enriched BPs (p-value cutoff = 0.05). **(C)** The network analysis of enriched KEGG pathways shows the number of proteins in the pathway (indicated by the size of the node) and the percentage of overlapping proteins (indicated by the thickness of the edges). **(D)** The STRING interaction analysis of proteins associated with the synaptic vesicle cycle pathway illustrates the type of interaction with the highest confidence (0.900). Three main clusters, cluster 1 represented by red nodes, cluster 2 represented by green nodes and cluster 3 represented by light blue nodes were detected. GO, Gene Ontology; BPs, Biological processes; FDR, False discovery rate; STRING, Search Tool for the Retrieval of Interacting Genes.

cochlear hair cell loss or death is not the primary target in lead-induced hearing impairment.

As lead exposure resulted in hearing loss without affecting the OHCs, other potential cochlear targets, such as the ribbon synapses, were examined. The ribbon synapses are crucial in transmitting signals from the IHCs to the auditory neurons and serve as the primary excitatory afferent synapses within the auditory pathway (Becker et al., 2018; Gao et al., 2020). The precise release of neurotransmitters at these synapses governs the firing pattern of the auditory nerve, which determines sound intensity and timing (Fuchs, 2005; Johnson et al., 2019). Therefore, any disruption in these ribbon synapses may contribute to the development of cochlear synaptopathy (Wei et al., 2020). The ABR wave I amplitudes are considered as an indicator of ribbon-synapse functionality (Yuan et al., 2020). A noticeable decrease in the amplitude of ABR wave-I was observed in lead-exposed animals compared to the control group. This suggested a reduction in the number of neurons responding to sound stimuli leading to cochlear synaptopathy. Moreover, consistent with previous studies (Rosati et al., 2022), lead exposure significantly decreased the expression of CtBP2 and GluR2, which are pre-and post-synaptic protein markers in IHC synapses, particularly in the basal turn of the Organ of Corti. The number of paired synapses was also significantly decreased in the basal turn after lead exposure suggesting lead-induced ribbon synaptic disruption and cochlear synaptopathy. As the decreases in both the ABR wave-I amplitude and the number of paired ribbon synapses were more pronounced in the basal region of the cochlea, these findings suggest that the basal region of the cochlea is more susceptible to lead-induced toxicity. Our data showed that the hair cells are intact, while there are significant differences in synaptic ribbon counts and a significant decrease in the number of paired synapses. Though we did not assess SGN counts, in a previous study, we reported lead-induced nitrative stress in SGNs (Rosati et al., 2022). Others have reported that lead exposure results in degenerative changes in SGNs (Hu et al., 2019), demyelination of neurons, and neurotoxic effects on both central and peripheral nerves (Seppäläinen and Hernberg, 1980; Bilińska et al., 2005; Zheng et al., 2011). Therefore, we assume that the ABR threshold shift is due to potential damage to the ribbon synapses, SGNs, and the cochlear nerves.

The connection between ribbon synapse disruption and hearing loss is well-established (Liu et al., 2016; Feng et al., 2020; Liu et al., 2022). A prior study demonstrated that lead exposure decreases the expression levels of presynaptic marker CtBP2 and postsynaptic marker GluR2, and disrupts the ribbon synapses in the cochlea

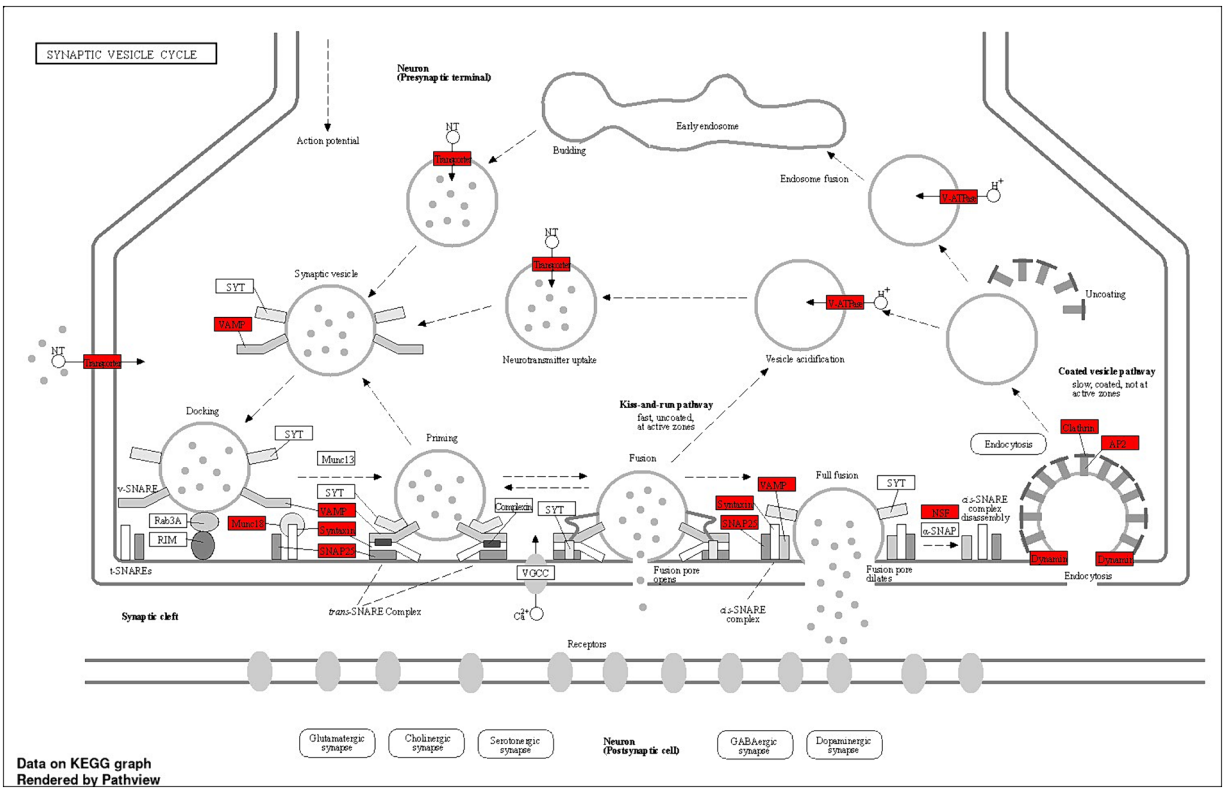


FIGURE 8
Schematic summary of the synaptic vesicle cycle pathway, illustrating key steps and proteins involved, including differentially expressed proteins. The dotted lines indicate the synaptic vesicle cycle, from neurotransmitter filling to release, followed by endocytosis. Budding: Neurotransmitters are actively transported into the synaptic vesicle, initiating the filling process. Docking: Vesicles filled with neurotransmitters dock at the active zone of the presynaptic membrane. Priming: Fully filled vesicles undergo priming, becoming competent for Ca^{2+}–triggered fusion-pore opening. Fusion: Synaptotagmin-1 (SYT1) facilitates the release of neurotransmitters from the vesicles into the synaptic cleft. Endocytosis: Vesicles recycle via clathrin/Ap2-mediated endocytosis, returning to the presynaptic membrane for reuse. Some vesicles may also recycle through endosomes. Snap25, Vamp, clathrin, and Ap2 are among the key proteins involved in the synaptic vesicle cycle pathway, whose abundance has been observed to increase after lead exposure. This suggests that synaptic vesicle cycle signaling potentially plays a critical role in lead-induced ototoxicity.

(Rosati et al., 2022). In the current study, the proteomics changes underlying lead-induced disruption of ribbon synapses were analyzed to help identify crucial targets and signaling pathways associated with lead-induced cochlear synaptopathy. In addition, bioinformatics analysis of the cochlear synaptosomal proteins whose abundance was significantly altered by lead exposure was performed to identify the BPs and signaling pathways that are associated with lead-induced cochlear synaptopathy. As the extracted synaptic protein fraction is likely to contain both afferent and efferent synaptic material along with other possible contaminants, the observations of this study are relevant to the hair cell synapses and, to some extent, to efferent synapses.

Analysis of proteins whose abundance was increased after lead exposure indicated the enrichment of many BPs, including sodium ion export across plasma membrane, clathrin-dependent endocytosis, and synaptic vesicle endocytosis. These BPs play a key role in not only hair cell function, but also in vesicle recycling at presynaptic terminals, and the transport/release of neurotransmitters crucial for auditory neurotransmission. Lead-induced changes in these processes can lead to hearing impairment (Jin et al., 2009; Trune, 2010; Grabner and Moser, 2018; Wei et al., 2020). Analysis of associated KEGG pathways indicated that the synaptic vesicle cycle pathway is highly enriched (fold enrichment of 17.6) and included 22 proteins. This pathway plays a crucial role in the cochlear ribbon synapses and potential changes in the abundance of proteins that regulate this signaling can affect the transmission of auditory signals. Analysis of proteins whose abundance was decreased after lead exposure indicated the enrichment of many biological processes, including NADH regeneration, canonical glycolysis and glucose catabolic process to pyruvate. NAD^+ metabolism and glucose hypometabolism are implicated in age-related hearing loss (Kim et al., 2014; Zainul Abidin et al., 2021). Moreover, NAD^+ metabolism is also associated with protection against noise-induced hearing loss (Brown et al., 2014). NADH treatment rescued mitochondrial dysfunction, reduced cell apoptosis, and prevented hearing loss (Qiu et al., 2024). Factors that affect these processes can compromise cochlear function, and therefore, lead-induced changes in the synaptic proteins associated with these processes can contribute to hearing impairment. Analysis of associated KEGG pathways indicated that the 2-Oxocarboxylic acid metabolism pathway is highly enriched (fold enrichment of 22.2), although the potential link between the 8 proteins included in this pathway and hearing function is not known.

Neurotransmission through the chemical synapses relies on the synaptic vesicle cycle machinery, particularly on a continuous supply of receptors and proteins required for synaptic signaling (Watson et al., 2023). The synaptic vesicles play a vital role in neurotransmitter uptake, storage, and release during synaptic transmission (Volknandt, 1995). A substantial and rapidly releasable pool of synaptic vesicles is important for efficiently and accurately transmitting auditory information (Wei et al., 2020). So, lead-induced disruption of the synaptic proteins can significantly affect the transmission of signals. Among the cochlear synaptic proteins whose abundance was increased after lead exposure and are part of the synaptic vesicle cycle pathway, proteins encoded by genes such as *Ap2a1, Ap2m1, Slc17a6, Nsf, Slc1a2, Slc1a3, Snap25, Stxbp1, Vamp2, Ap2s1, Slc6a11, Stx1b, Ap2b1,* have been previously reported to be associated with auditory function. Specifically, *Ap2a1*, *Ap2m1*, *Ap2s1*, and *Ap2b1* are implicated in clathrin-mediated endocytosis (Di Rubbo et al., 2013; Lacruz et al., 2013) and IHC-specific deletion of *Ap2m1* induces profound hearing impairment in mice (Jung et al., 2015). *Slc17a6*, *Slc1a2*, *Slc1a3*, and *Slc6a11* can potentially influence synaptic transmission in the cochlear nucleus (CN) region of auditory system because *Slc17a6* and *Slc1a3* are upregulated in noise-induced and age-related hearing loss (Tadros et al., 2007; Manohar et al., 2016) and *Slc1a2* has been reported to play a crucial role in noise-induced cochlear synaptopathy by regulating glutamate clearance (Lavinsky et al., 2018). Moreover, *Nsf* is necessary for maintaining synaptic contacts between hair cells and afferent neurons (Mo and Nicolson, 2011) while SNARE proteins, including *Snap25*, *Stxbp1*, *Stx1b*, and *Vamp2*, mediate membrane fusion during vesicle trafficking and neurotransmitter release, which are crucial for normal exocytosis in neurons (Sollner et al., 1993; Salpietro et al., 2019; Cali et al., 2022). *Snap25* is essential for normal hearing function, ensuring IHC exocytosis, and ribbon synapse maintenance because mice with *Snap25* inactivation after hearing onset experience a significant level of hearing loss due to defective exocytosis, ribbon degeneration, and IHC loss (Calvet et al., 2022). *Vamp2* has been reported to play a role in the cochlear neuron development in nonhuman primates (Hosoya et al., 2021). Further, many of these proteins are linked to vesicle-mediated transport, fusion, clathrin coating assembly, and synaptic transmission, suggesting that the lead-induced changes in their abundance can influence neurotransmission across cochlear ribbon synapses. As the changes in these proteins can contribute to the lead-induced decrease in the ABR wave-I amplitudes, these proteins are likely to be crucial targets of lead-induced cochlear synaptopathy. Although we did not verify the changes in the abundance of proteins by alternate methods in this study, we have validated some of the changes detected by mass spectrometry analysis by using western blots in our recent study (Shahab et al., 2024). As the changes in the synaptosomal proteins may also reflect the general malfunction of protein expression regulation, further studies are needed to gain mechanistic insights into how these changes regulate lead-induced cochlear synaptopathy.

Collectively, the findings of this study demonstrate that lead-induced ototoxicity primarily targets cochlear synaptic function, particularly in the basal turn of the cochlea, even though other causes, such as damage to the spiral ganglions and demyelination of the cochlear nerve can also lead to reduced hearing sensitivity. The lead-induced cochlear synaptopathy is associated with changes in the abundance of many synaptosomal proteins, and the increase in the abundance of proteins encoded by genes such as *Snap25 and Vamp2 has* been associated with hearing loss in other studies. Conversely, the changes in the abundance of many other proteins, including those encoded by genes such as *Aco1, Bcat2* lack a direct link to hearing loss. While their involvement in cochlear stress response is unexplored, our findings pave the way for future research, to shed light on their involvement in the molecular mechanisms underlying lead-induced cochlear damage.

Data availability statement

The datasets presented in this study can be found in online repositories. The mass spectrometry proteomics data have been deposited to the ProteomeXchange Consortium via the PRIDE partner repository with the dataset identifier PXD050415.

Ethics statement

The animal study was approved by Institutional Animal Care and Use Committee, Wayne State University. The study was conducted in accordance with the local legislation and institutional requirements.

Author contributions

PB: Data curation, Formal analysis, Investigation, Methodology, Writing – original draft. SM: Formal analysis, Resources, Visualization, Writing – original draft. ND-R: Investigation, Writing – original draft. RR: Formal analysis, Investigation, Methodology, Visualization, Writing – original draft. PS: Resources, Supervision, Writing – review & editing. SJ: Conceptualization, Funding acquisition, Project administration, Resources, Supervision, Writing – review & editing.

Funding

The author(s) declare that financial support was received for the research, authorship, and/or publication of this article. This research was supported by a Department of Defense Grant (W81XWH2210827) to SJ. We acknowledge the assistance of the Wayne State University Proteomics Core that is supported through NIH grants P30ES020957, P30CA022453, and S10OD030484.

Acknowledgments

We acknowledge the assistance of the Wayne State University Lumigen Instrumentation Core for blood lead level measurement.

Conflict of interest

The authors declare that the research was conducted in the absence of any commercial or financial relationships that could be construed as a potential conflict of interest.

Publisher's note

All claims expressed in this article are solely those of the authors and do not necessarily represent those of their affiliated organizations, or those of the publisher, the editors and the reviewers. Any product that may be evaluated in this article, or claim that may be made by its manufacturer, is not guaranteed or endorsed by the publisher.

Supplementary material

The Supplementary material for this article can be found online at: https://www.frontiersin.org/articles/10.3389/fncel.2024.1408208/full#supplementary-material

References

Aktürk, T., Çeliker, G., and Saçmacı, H. (2022). Impact of occupational lead exposure on nerve conduction study data. *Int. J. Neurosci.* 132, 306–312. doi: 10.1080/00207454.2021.1873784

Ashmore, J. (2019). Outer hair cells and electromotility. *Cold Spring Harb. Perspect. Med.* 9:a033522. doi: 10.1101/cshperspect.a033522

Becker, L., Schnee, M. E., Niwa, M., Sun, W., Maxeiner, S., Talaei, S., et al. (2018). The presynaptic ribbon maintains vesicle populations at the hair cell afferent fiber synapse. *eLife* 7:e30241. doi: 10.7554/eLife.30241

Bilińska, M., Antonowicz-Juchniewicz, J., Koszewicz, M., Kaczmarek-Wdowiak, B., and Kreczyńska, B. (2005). Distribution of conduction velocity in the ulnar nerve among lead-exposed workers. *Med. Pr.* 56, 139–146

Brown, K. D., Maqsood, S., Huang, J. Y., Pan, Y., Harkcom, W., Li, W., et al. (2014). Activation of SIRT3 by the NAD+ precursor nicotinamide riboside protects from noise-induced hearing loss. *Cell Metab.* 20, 1059–1068. doi: 10.1016/j.cmet.2014.11.003

Brubaker, C. J., Schmithorst, V. J., Haynes, E. N., Dietrich, K. N., Egelhoff, J. C., Lindquist, D. M., et al. (2009). Altered myelination and axonal integrity in adults with childhood lead exposure: a diffusion tensor imaging study. *Neurotoxicology* 30, 867–875. doi: 10.1016/j.neuro.2009.07.007

Cali, E., Rocca, C., Salpietro, V., and Houlden, H. (2022). Epileptic phenotypes associated with SNAREs and related synaptic vesicle exocytosis machinery. *Front. Neurol.* 12:806506. doi: 10.3389/fneur.2021.806506

Calvet, C., Peineau, T., Benamer, N., Cornille, M., Lelli, A., Plion, B., et al. (2022). The SNARE protein SNAP-25 is required for normal exocytosis at auditory hair cell ribbon synapses. *iScience* 25:105628. doi: 10.1016/j.isci.2022.105628

Carlson, K., and Neitzel, R. L. (2018). Hearing loss, lead (Pb) exposure, and noise: a sound approach to ototoxicity exploration. *J. Toxicol. Environ. Health B Crit. Rev.* 21, 335–355. doi: 10.1080/10937404.2018.1562391

Castellanos, M. J., and Fuente, A. (2016). The adverse effects of heavy metals with and without noise exposure on the human peripheral and central auditory system: a literature review. *Int. J. Environ. Res. Public Health* 13:1223. doi: 10.3390/ijerph13121223

Choi, J., Tanaka, T., Koren, G., and Ito, S. (2008). Lead exposure during breastfeeding. *Can. Fam. Physician* 54, 515–516

Di Rubbo, S., Irani, N. G., Kim, S. Y., Xu, Z. Y., Gadeyne, A., Dejonghe, W., et al. (2013). The clathrin adaptor complex AP-2 mediates endocytosis of brassinosteroid insensitive1 in Arabidopsis. *Plant Cell* 25, 2986–2997. doi: 10.1105/tpc.113.114058

Feng, S., Yang, L., Hui, L., Luo, Y., Du, Z., Xiong, W., et al. (2020). Long-term exposure to low-intensity environmental noise aggravates age-related hearing loss via disruption of cochlear ribbon synapses. *Am. J. Transl. Res.* 12, 3674–3687

Fuchs, P. A. (2005). Time and intensity coding at the hair cell's ribbon synapse. *J. Physiol.* 566, 7–12. doi: 10.1113/jphysiol.2004.082214

Gao, L., Kita, T., Katsuno, T., Yamamoto, N., Omori, K., and Nakagawa, T. (2020). Insulin-like growth factor 1 on the maintenance of ribbon synapses in mouse cochlear explant cultures. *Front. Cell. Neurosci.* 14:571155. doi: 10.3389/fncel.2020.571155

Ge, S. X., Jung, D., and Yao, R. (2020). ShinyGO: a graphical gene-set enrichment tool for animals and plants. *Bioinformatics* 36, 2628–2629. doi: 10.1093/bioinformatics/btz931

Goutman, J. D., Elgoyhen, A. B., and Gómez-Casati, M. E. (2015). Cochlear hair cells: the sound sensing machines. *FEBS Lett.* 589, 3354–3361. doi: 10.1016/j.febslet.2015.08.030

Grabner, C. P., and Moser, T. (2018). Individual synaptic vesicles mediate stimulated exocytosis from cochlear inner hair cells. *Proc. Natl. Acad. Sci.* 115, 12811–12816. doi: 10.1073/pnas.1811814115

Guidotti, T. L., Calhoun, T., Davies-Cole, J. O., Knuckles, M. E., Stokes, L., Glymph, C., et al. (2007). Elevated lead in drinking water in Washington, DC, 2003-2004: the public health response. *Environ. Health Perspect.* 115, 695–701. doi: 10.1289/ehp.8722

Holdstein, Y., Pratt, H., Goldsher, M., Rosen, G., Shenhav, R., Linn, S., et al. (1986). Auditory brainstem evoked potentials in asymptomatic lead-exposed subjects. *J. Laryngol. Otol.* 100, 1031–1036. doi: 10.1017/S0022215100100519

Hosoya, M., Fujioka, M., Murayama, A. Y., Ozawa, H., Okano, H., and Ogawa, K. (2021). Neuronal development in the cochlea of a nonhuman primate model, the common marmoset. *Dev. Neurobiol.* 81, 905–938. doi: 10.1002/dneu.22850

Hossain, S., Bhowmick, S., Jahan, S., Rozario, L., Sarkar, M., Islam, S., et al. (2016). Maternal lead exposure decreases the levels of brain development and cognition-related proteins with concomitant upsurges of oxidative stress, inflammatory response and apoptosis in the offspring rats. *Neurotoxicology* 56, 150–158. doi: 10.1016/j.neuro.2016.07.013

Hu, S. S., Cai, S. Z., and Kong, X. Z. (2019). Chronic lead exposure results in auditory deficits and disruption of hair cells in postweaning rats. *Oxidative Med. Cell. Longev.* 2019, 1–8. doi: 10.1155/2019/4289169

Jamesdaniel, S., Rosati, R., Westrick, J., and Ruden, D. M. (2018). Chronic lead exposure induces cochlear oxidative stress and potentiates noise-induced hearing loss. *Toxicol. Lett.* 292, 175–180. doi: 10.1016/j.toxlet.2018.05.004

Jin, Z., Uhlen, I., Wei-Jia, K., and Mao-Li, D. (2009). Cochlear homeostasis and its role in genetic deafness. *J. Otol.* 4, 15–22. doi: 10.1016/S1672-2930(09)50003-7

Johnson, S. L., Safieddine, S., Mustapha, M., and Marcotti, W. (2019). Hair cell afferent synapses: function and dysfunction. *Cold Spring Harb. Perspect. Med.* 9:a033175. doi: 10.1101/cshperspect.a033175

Jones, L. G., Prins, J., Park, S., Walton, J. P., Luebke, A. E., and Lurie, D. I. (2008). Lead exposure during development results in increased neurofilament phosphorylation, neuritic beading, and temporal processing deficits within the murine auditory brainstem. *J. Comp. Neurol.* 506, 1003–1017. doi: 10.1002/cne.21563

Jung, S., Maritzen, T., Wichmann, C., Jing, Z., Neef, A., Revelo, N. H., et al. (2015). Disruption of adaptor protein 2μ (AP-2μ) in cochlear hair cells impairs vesicle reloading of synaptic release sites and hearing. *EMBO J.* 34, 2686–2702. doi: 10.15252/embj.201591885

Kim, H. J., Oh, G. S., Choe, S. K., Kwak, T. H., Park, R., and So, H. S. (2014). NAD(+) metabolism in age-related hearing loss. *Aging Dis.* 5, 150–159. doi: 10.14336/AD.2014.0500150

Kumar, A., Kumar, A., MMS, C. P., Chaturvedi, A. K., Shabnam, A. A., Subrahmanyam, G., et al. (2020). Lead toxicity: health hazards, influence on food chain, and sustainable remediation approaches. *Int. J. Environ. Res. Public Health* 17:2179. doi: 10.3390/ijerph17072179

Lacruz, R. S., Brookes, S. J., Wen, X., Jimenez, J. M., Vikman, S., Hu, P., et al. (2013). Adaptor protein complex 2-mediated, clathrin-dependent endocytosis, and related gene activities, are a prominent feature during maturation stage amelogenesis. *J. Bone Miner. Res.* 28, 672–687. doi: 10.1002/jbmr.1779

Lavinsky, J., Salehi, P., Wang, J., and Friedman, R. (2018). Genome-wide association study for noise-induced cochlear synaptopath. *bioRxiv*. 311407. doi: 10.1101/311407

Liu, K., Ji, F., Yang, G., Hou, Z., Sun, J., Wang, X., et al. (2016). SMAD4 defect causes auditory neuropathy via specialized disruption of cochlear ribbon synapses in mice. *Mol. Neurobiol.* 53, 5679–5691. doi: 10.1007/s12035-015-9454-1

Liu, Z., Luo, Y., Guo, R., Yang, B., Shi, L., Sun, J., et al. (2022). Head and neck radiotherapy causes significant disruptions of cochlear ribbon synapses and consequent sensorineural hearing loss. *Radiother. Oncol.* 173, 207–214. doi: 10.1016/j.radonc.2022.05.023

Mahmoud, Y., and Sayed, S. (2016). Effects of L-cysteine on lead acetate induced neurotoxicity in albino mice. *Biotech. Histochem.* 91, 327–332. doi: 10.3109/10520295.2016.1164897

Manohar, S., Dahar, K., Adler, H. J., Dalian, D., and Salvi, R. (2016). Noise-induced hearing loss: neuropathic pain via Ntrk1 signaling. *Mol. Cell. Neurosci.* 75, 101–112. doi: 10.1016/j.mcn.2016.07.005

Mo, W., and Nicolson, T. (2011). Both pre-and postsynaptic activity of Nsf prevents degeneration of hair-cell synapses. *PLoS One* 6:e27146. doi: 10.1371/journal.pone.0027146

Mohanraj, N., Joshi, N. S., Poulose, R., Patil, R. R., Santhoshkumar, R., Kumar, A., et al. (2022). A proteomic study to unveil lead toxicity-induced memory impairments invoked by synaptic dysregulation. *Toxicol. Rep.* 9, 1501–1513. doi: 10.1016/j.toxrep.2022.07.002

Obeng-Gyasi, E. (2019). Sources of lead exposure in various countries. *Rev. Environ. Health* 34, 25–34. doi: 10.1515/reveh-2018-0037

Olufemi, A. C., Mji, A., and Mukhola, M. S. (2022). Potential health risks of Lead exposure from early life through later life: implications for public health education. *Int. J. Environ. Res. Public Health* 19:16006. doi: 10.3390/ijerph192316006

Park, S. K., Elmarsafawy, S., Mukherjee, B., Spiro, A. 3rd, Vokonas, P. S., Nie, H., et al. (2010). Cumulative lead exposure and age-related hearing loss: the VA normative aging study. *Hear. Res.* 269, 48–55. doi: 10.1016/j.heares.2010.07.004

Qiu, Y., Wang, H., Pan, H., Ding, X., Guan, J., Zhuang, Q., et al. (2024). NADH improves AIF dimerization and inhibits apoptosis in iPSCs-derived neurons from patients with auditory neuropathy spectrum disorder. *Hear. Res.* 441:108919. doi: 10.1016/j.heares.2023.108919

Rosati, R., Birbeck, J. A., Westrick, J., and Jamesdaniel, S. (2022). Lead exposure induces nitrative stress and disrupts ribbon synapses in the cochlea. *Front. Mol. Neurosci.* 15:934630. doi: 10.3389/fnmol.2022.934630

Salpietro, V., Malintan, N. T., Llano-Rivas, I., Spaeth, C. G., Efthymiou, S., Striano, P., et al. (2019). Mutations in the neuronal vesicular SNARE VAMP2 affect synaptic membrane fusion and impair human neurodevelopment. *Am. J. Hum. Genet.* 104, 721–730. doi: 10.1016/j.ajhg.2019.02.016

Selvín-Testa, A., Lopez-Costa, J. J., Nessi de Aviñon, A. C., and Pecci Saavedra, J. (1991). Astroglial alterations in rat hippocampus during chronic lead exposure. *Glia* 4, 384–392. doi: 10.1002/glia.440040406

Seppäläinen, A. M., and Hernberg, S. (1980). Subclinical lead neuropathy. *Am. J. Ind. Med.* 1, 413–420. doi: 10.1002/ajim.4700010319

Shahab, M., Rosati, R., Stemmer, P. M., Dombkowski, A., and Jamesdaniel, S. (2024). Quantitative profiling of cochlear synaptosomal proteins in cisplatin-induced synaptic dysfunction. *Hear. Res.* 447:109022. doi: 10.1016/j.heares.2024.109022

Shvachiy, L., Amaro-Leal, Â., Outeiro, T. F., Rocha, I., and Geraldes, V. (2023). Intermittent Lead exposure induces behavioral and cardiovascular alterations associated with neuroinflammation. *Cells* 12:818. doi: 10.3390/cells12050818

Sollner, T., Whiteheart, S. W., Brunner, M., Erdjument-Bromage, H., Geromanos, S., Tempst, P., et al. (1993). SNAP receptors implicated in vesicle targeting and fusion. *Nature* 362, 318–324. doi: 10.1038/362318a0

Szklarczyk, D., Morris, J. H., Cook, H., Kuhn, M., Wyder, S., Simonovic, M., et al. (2016). The STRING database in 2017: quality-controlled protein–protein association networks, made broadly accessible. *Nucleic Acids Res.* 45, D362–D368. doi: 10.1093/nar/gkw937

Tadros, S. F., D'Souza, M., Zettel, M. L., Zhu, X., Waxmonsky, N. C., and Frisina, R. D. (2007). Glutamate-related gene expression changes with age in the mouse auditory midbrain. *Brain Res.* 1127, 1–9. doi: 10.1016/j.brainres.2006.09.081

Takeuchi, H., Taki, Y., Nouchi, R., Yokoyama, R., Kotozaki, Y., Nakagawa, S., et al. (2021). Lead exposure is associated with functional and microstructural changes in the healthy human brain. *Commun. Biol.* 4:912. doi: 10.1038/s42003-021-02435-0

Tiwari, A. K., Mahdi, A. A., Zahra, F., Sharma, S., and Negi, M. P. (2012). Evaluation of low blood Lead levels and its association with oxidative stress in pregnant anemic women: a comparative prospective study. *Indian J. Clin. Biochem.* 27, 246–252. doi: 10.1007/s12291-012-0202-2

Trune, D. R. (2010). Ion homeostasis in the ear: mechanisms, maladies, and management. *Curr. Opin. Otolaryngol. Head Neck Surg.* 18, 413–419. doi: 10.1097/MOO.0b013e32833d9597

Volknandt, W. (1995). The synaptic vesicle and its targets. *Neuroscience* 64, 277–300. doi: 10.1016/0306-4522(94)00408-W

Wang, T., Zhang, J., and Xu, Y. (2020). Epigenetic basis of lead-induced neurological disorders. *Int. J. Environ. Res. Public Health* 17:4878. doi: 10.3390/ijerph17134878

Wani, A. L., Ara, A., and Usmani, J. A. (2015). Lead toxicity: a review. *Interdiscip. Toxicol.* 8, 55–64. doi: 10.1515/intox-2015-0009

Watson, E. T., Pauers, M. M., Seibert, M. J., Vevea, J. D., and Chapman, E. R. (2023). Synaptic vesicle proteins are selectively delivered to axons in mammalian neurons. *eLife* 12:e82568. doi: 10.7554/eLife.82568

Wei, M., Wang, W., Liu, Y., Mao, X., Chen, T. S., and Lin, P. (2020). Protection of cochlear ribbon synapses and prevention of hidden hearing loss. *Neural Plast.* 2020, 1–11. doi: 10.1155/2020/8815990

WHO (2023a) International Lead poisoning prevention week 23–29 October 2023. Available at: https://www.who.int/campaigns/international-lead-poisoning-prevention-week/2023/about

WHO (2023b). Deafness and hearing loss February 2023. Available at: https://www.who.int/news-room/fact-sheets/detail/deafness-and-hearing-loss

Xue-Wen, W., Da-Lian, D., Hong, S., Hong, L., Hai-yan, J., and Salvi, R. (2011). Lead neurotoxicity in rat cochlear organotypic cultures. *J. Otol.* 6, 43–50. doi: 10.1016/S1672-2930(11)50021-2

Yuan, X., Liu, H., Li, Y., Li, W., Yu, H., and Shen, X. (2020). Ribbon synapses and hearing impairment in mice after in utero sevoflurane exposure. *Drug Des. Devel. Ther.* 14, 2685–2693. doi: 10.2147/DDDT.S253031

Zainul Abidin, F. N., Scelsi, M. A., Dawson, S. J., and Altmann, A. (2021). Glucose hypometabolism in the auditory pathway in age related hearing loss in the ADNI cohort. *Neuroimage Clin.* 32:102823. doi: 10.1016/j.nicl.2021.102823

Zhang, Y., Jiang, Q., Xie, S., Wu, X., Zhou, J., and Sun, H. (2019). Lead induced ototoxicity and neurotoxicity in adult guinea pig. *Biomed. Res. Int.* 2019, 1–8. doi: 10.1155/2019/3626032

Zheng, G., Tian, L., Liang, Y., Broberg, K., Lei, L., Guo, W., et al. (2011). δ-Aminolevulinic acid dehydratase genotype predicts toxic effects of lead on workers' peripheral nervous system. *Neurotoxicology* 32, 374–382. doi: 10.1016/j.neuro.2011.03.006

Zou, C., Zhao, Z., Tang, L., Chen, Z., and Du, L. (2003). The effect of lead on brainstem auditory evoked potentials in children. *Chin. Med. J.* 116, 565–568

10.3389/fncel.2024.1408208

Glossary

ABR	auditory brainstem response
BP	biological process
CtBP2	C-terminal-binding protein-2
DPOAE	distortion product otoacoustic emission
DTT	DL-Dithiothreitol
EDTA	ethylenediaminetetraacetic acid disodium salt
FA	formic acid
GluR2	Glutamate receptor 2
GO	Gene Ontology
IAA	Iodoacetamide
ICP-MS	inductively coupled plasma mass spectrometry
IHC	inner hair cells
KEGG	Kyoto Encyclopedia of Genes and Genomes
LC–MS/MS	Liquid Chromatography Tandem Mass Spectrometry
MeOH	methanol
NAD	Nicotinamide adenine dinucleotide
NADH	reduced nicotinamide adenine dinucleotide
OHCs	outer hair cells
PBS	phosphate buffered saline
PPI	protein–protein interaction
SNAP-25	Synaptosomal-Associated Protein 25
STRING	Search Tool for the Retrieval of Interacting Genes
TDT	Tucker Davis Technologies
TEAB	Triethylammonium bicarbonate buffer

frontiers | Frontiers in Cellular Neuroscience

TYPE Original Research
PUBLISHED 01 October 2024
DOI 10.3389/fncel.2024.1465216

Check for updates

OPEN ACCESS

EDITED BY
Christian Keine,
University of Oldenburg, Germany

REVIEWED BY
Jianxin Bao,
Duke University, United States
Christine Koeppl,
University of Oldenburg, Germany
Allison B. Coffin,
Washington State University, United States

*CORRESPONDENCE
Jutta Engel
✉ jutta.engel@uni-saarland.de
Simone Kurt
✉ simone.kurt@uni-saarland.de

†These authors have contributed equally to this work and share first authorship

‡These authors have contributed equally to this work

RECEIVED 15 July 2024
ACCEPTED 12 September 2024
PUBLISHED 01 October 2024

CITATION
Blum K, Schepsky P, Derleder P, Schätzle P, Nasri F, Fischer P, Engel J and Kurt S (2024) Noise-induced cochlear synaptopathy in C57BL/6 N mice as a function of trauma strength: ribbons are more vulnerable than postsynapses.
Front. Cell. Neurosci. 18:1465216.
doi: 10.3389/fncel.2024.1465216

COPYRIGHT
© 2024 Blum, Schepsky, Derleder, Schätzle, Nasri, Fischer, Engel and Kurt. This is an open-access article distributed under the terms of the Creative Commons Attribution License (CC BY). The use, distribution or reproduction in other forums is permitted, provided the original author(s) and the copyright owner(s) are credited and that the original publication in this journal is cited, in accordance with accepted academic practice. No use, distribution or reproduction is permitted which does not comply with these terms.

Noise-induced cochlear synaptopathy in C57BL/6 N mice as a function of trauma strength: ribbons are more vulnerable than postsynapses

Kerstin Blum[1,2†], Pauline Schepsky[1†], Philip Derleder[1], Philipp Schätzle[1], Fahmi Nasri[1†], Philipp Fischer[1], Jutta Engel[1,2*‡] and Simone Kurt[1,2*‡]

[1]Center for Integrative Physiology and Molecular Medicine (CIPMM), School of Medicine, Department of Biophysics, Saarland University, Homburg, Germany, [2]Center for Gender-specific Biology and Medicine (CGBM), School of Medicine, Saarland University, Homburg, Germany

Noise-induced cochlear synaptopathy is characterized by irreversible loss of synapses between inner hair cells (IHCs) and spiral ganglion neurons (SGNs) despite normal hearing thresholds. We analyzed hearing performance and cochlear structure in C57BL/6N mice exposed to 100, 106, or 112dB SPL broadband noise (8–16kHz) for 2h. Auditory brainstem responses (ABRs) were assessed before, directly after, and up to 28days post-trauma. Finally, the number, size, and pairing of IHC presynaptic (CtBP2-positive) ribbons and postsynaptic AMPA receptor scaffold (Homer1-positive) clusters were analyzed along the cochlea. Four weeks after the 100dB SPL trauma, a permanent threshold shift (PTS) was observed at 45kHz, which after the higher traumata extended toward middle to low frequencies. Loss in ABR wave I amplitudes scaled with trauma strength indicating loss of functional IHC synaptic connections. Latencies of wave I mostly increased with trauma strength. No trauma-related OHC loss was found. The number of synaptic pairs was reduced in the midbasal and basal cochlear region in all trauma conditions, with ribbon loss amounting up to 46% of control. Ribbons surviving the trauma were paired, whereas 4–6 unpaired postsynapses/IHC were found in the medial, midbasal, and basal regions irrespective of trauma strength, contrasting findings in CBA/CaJ mice. Our data confirm the susceptibility of ribbon synapses and ABR wave I amplitudes to a noise trauma of 100dB SPL or larger. Notably, peripheral dendrites bearing IHC postsynapses were less vulnerable than presynaptic ribbons in C57BL/6N mice.

KEYWORDS

noise trauma, cochlear synaptopathy, hidden hearing loss, hair cell, ribbon, postsynapse, auditory nerve, ABR

Introduction

In the adult mammalian cochlea, sound-induced displacement of hair bundles causes depolarization of IHCs and opening of $Ca_v1.3$ Ca^{2+} channels (Platzer et al., 2000; Brandt et al., 2003). These channels cluster at 15–30 active zones at the basolateral synaptic pole, which are composed of a single presynaptic ribbon innervated by an afferent dendrite of one SGN (Fuchs et al., 2003; Khimich et al., 2005). Sound-evoked release of glutamate activates glutamate receptors at the afferent boutons and may trigger action potentials in the individual nerve fiber. Research in rodent and primate models has shown that ribbon synapses of IHCs can degenerate after exposure to

moderate noise (octave-band noise, 100 dB SPL, 2 h) in the high-frequency region accompanied by a temporary threshold shift (TTS) but without a permanent elevation of hearing thresholds (PTS), which was termed noise-induced hidden hearing loss (NIHHL) (Kujawa and Liberman, 2006, 2009; Hickox et al., 2017). This phenomenon probably also exists in humans (Schaette and McAlpine, 2011; Hickox et al., 2017; Wu et al., 2021).

A functional assay for NIHHL in rodents is the reduction of ABR wave I amplitude, indicating fewer functional nerve fibers contributing to the ABR signal (Kujawa and Liberman, 2009). On the ultrastructural level, an immediate and irreversible reduction of presynaptic ribbons was found in CBA/CaJ mice, which led to the term "cochlear synaptopathy" (Kujawa and Liberman, 2009; Liberman et al., 2015; Liberman and Kujawa, 2017). Similar synaptic damage has been observed in age-related hearing loss in mice (Kujawa and Liberman, 2015; Liberman and Kujawa, 2017; Jeng et al., 2020a).

Whereas ribbon loss in CBA/CaJ mice was irreversible (Kujawa and Liberman, 2009), recent studies revealed partial regeneration of ribbons in C57BL/6J mice (Shi et al., 2015; Kaur et al., 2019; Manickam et al., 2023) and full regeneration in guinea pigs (Shi et al., 2013; Song et al., 2016; Hickman et al., 2020, 2021). Repair of ribbon synapses requires the action of resident macrophages in the cochlea (Kaur et al., 2019; Manickam et al., 2023).

Noise causes elevated influx of Ca^{2+} through $Ca_v1.3$ channels IHCs, which couple IHC membrane potential changes to exocytosis of glutamate (Frank et al., 2009). Excess Ca^{2+} may be toxic to ribbons and cause their degeneration (Kim et al., 2019). Postsynaptically, glutamate excitotoxicity is the accepted reason for swelling, possible detachment, and degeneration of afferent dendrites (Puel et al., 1994; Kujawa and Liberman, 2009; Wang and Green, 2011; Kim et al., 2019).

The ~18 afferent fibers contacting one IHC differ in anatomical and physiological properties and show either high (HSR), medium (MSR), or low spontaneous firing rates (LSRs) (Liberman, 1982). According to molecular differences, HSR fibers correspond to type Ia, MSR fibers to Ib, and LSR fibers to Ic fibers [nomenclature according to Shrestha et al. (2018), with a proportion of Ia: Ib: Ic of approximately 46%: 28%: 26% (Petitpré et al., 2018; Shrestha et al., 2018; Sun et al., 2018)]. HSR fibers are activated at the hearing threshold, LSR fibers at loud tones, and MSR fibers in between; for review, see Moser et al. (2023). It has been suggested that LSR fibers are particularly sensitive to hidden hearing loss and noise-induced cochlear synaptopathy (Furman et al., 2013; Song et al., 2016). Cochlear synaptopathy is also observed after a PTS trauma (Hickox et al., 2017; Valero et al., 2017).

The mouse strain used in this study, C57BL/6N, has been widely used for the generation of knockout mice by 'The International Knockout Mouse Consortium' (Mianné et al., 2016). Our aim was to analyze the effects of the classical NIHHL trauma (TTS only; 8–16 kHz, 2 h, 100 dB SPL) on hearing and cochlear synaptopathy-related symptoms in C57BL/6N mice and how the outcome was altered by traumata of 106 dB SPL or ml 112 dB SPL, which both cause permanent hearing loss.

Materials and methods

Animals

C57BL/6N mice were purchased from Charles River, Sulzfeld, Germany, and bred in the animal facility of the Centre for Integrative Physiology and Molecular Medicine Homburg, with regular back-crossing to prevent the generation of an in-house substrain. The mice were housed in individually ventilated cages in the temperature-controlled facility with free access to food and water and a 12-h dark/light cycle. Mice of either sex were used for the experiments. The animal care, use, and experimental protocols followed the national and institutional guidelines and were reviewed and approved by the Animal Welfare Commissioner and the Regional Board of Animal Experimentation of Saarland. All experiments were performed in accordance with the European Communities Council Directive (86/609/EEC).

Auditory brainstem response (ABR) measurements

Mice were anesthetized by injecting a mixture of Fentanyl (0.05 mg/kg body weight, Fentanyl Hameln® - 50 µg/ml, Hameln Pharma Plus GmbH, Hameln, Germany), Midazolam (5 mg/kg body weight, Midazolam Hameln® - 5 mg/ml, Hameln Pharma Plus GmbH, Hameln, Germany), and Medetomidine (0.5 mg/kg body weight, Domitor® - 1 mg/ml, Orion Corporation, Espoo, Finland) intraperitoneally (i.p.) (Deichelbohrer et al., 2017; Julien-Schraermeyer et al., 2020). Surgical tolerance tested with a negative toe pinch reflex was obtained after 15 min for approximately 75 min. If necessary, one-third of the initial dose of anesthetics was injected i.p. to achieve sufficient anesthetic depth. The antidote dosage was a mixture of Naloxone (1.2 mg/kg body weight, Naloxone Inresa® 0.4 mg, Inresa Arzneimittel GmbH, Freiburg, Germany), Flumazenil (0.5 mg/kg body weight, Flumazenil Inresa® – 0.5 mg i.v., Inresa Arzneimittel GmbH, Freiburg, Germany) and Atipamezole (2.5 mg/kg body weight, Antisedan® – 5 mg/ml, Orion Corporation, Espoo, Finland) (Deichelbohrer et al., 2017; Julien-Schraermeyer et al., 2020). The antidote was applied subcutaneously immediately after the end of the ABR measurement. Because of frequent anesthesia, animals were monitored for severity and distress daily for the first 10 days of the experiment according to a score sheet. The score sheet recorded the general condition, wellbeing, spontaneous activity, clinical findings, and body weight. There was a tendency of some weight loss on the day after trauma, which however was not significant. No further deviations were observed. After the final ABR recording, some of the mice were euthanized by cervical dislocation under anesthesia (see above) and used for immunohistochemistry.

ABRs to free field clicks (100 µs) and pure tones (3 ms, 1 ms ramp) were recorded with subdermal silver wire electrodes (diameter: 0.25 mm, purity: 99.99%, Good Fellow, Hamburg, Germany) at the ear (positive), the vertex (negative), and the back of the animal (reference) using the Audiology Lab setup plus software (Otoconsult, Frankfurt, Germany). After amplification by a factor of 10^5, the signals were averaged for 256 repetitions at each sound pressure level presented (click: 0–80 dB SPL, pure tones: 0–100 dB SPL in steps of 5 dB).

Noise trauma

Anesthetized animals aged 7–9 weeks were placed in a custom-made sound-proof booth directly underneath the center of a speaker

(Stage Line PA Horn Tweeter MHD-220 N/RD, MONACOR INTERNATIONAL GmbH & Co. KG, Bremen) positioned 12 cm above the animal's head. Body temperature was maintained with a temperature-controlled heating pad (Otoconsult, Frankfurt, Germany). The speaker's output was measured with a condenser microphone (Brüel & Kjær 4135; Brüel & Kjær, Bremen, Germany) placed at the position of the animal's head and below the speaker. The microphone output was read in dB SPL with a measuring amplifier (Brüel & Kjær 2636; Brüel & Kjær). The speaker's frequency spectrum was checked with a spectrum analyzer (Ono Sokki Multi-purpose FFT Analyzer CF-5220; Ono Sokki Technology, Yokohama, Japan). In the 8–16 kHz frequency range of presented noise levels (100, 106, or 112 dB SPL, root-mean-square [SPLrms]), the frequency response was flat (± 2 dB), and no distortion products could be detected. Noise exposure was performed binaurally with octave-band noise (8–16 kHz) at either 100, 106, or 112 dB SPL for 2 h. Noise exposure was interrupted every 30 min for maximally 2 min to check the toe pinch reflex, breathing rate, and to apply additional anesthesia (one third of the initial dose) if required.

Hearing thresholds and analysis of ABR waveforms

Click ABRs and frequency-dependent (f-ABRs) were recorded 2 days before trauma (day-2), directly after the trauma (day 0), and on days 1, 2, 3, 5, 7, 14, 21, and 28 after trauma (Figure 1A). Hearing thresholds were determined by the lowest sound pressure that produced visually distinct evoked potentials by assessing the traces from above threshold to near threshold for each animal and ear. If for a given ear a threshold of the audiogram could not yet be identified at 100 dB SPL, the auditory threshold was defined as 105 dB SPL. For days-2, 0, and 28 after trauma, amplitudes and latencies of ABR wave I were analyzed. The peak-to-peak amplitude of ABR wave I was defined as $I = I_n - I_p$, with I_n being the amplitude of the negative peak at time = t_n and I_p the amplitude of the following positive peak at t_p. Wave I amplitudes as a function of the stimulus level (growth functions) were plotted for all ears. The latency of wave I was defined as t_n with respect to the time of stimulus onset, $t = 0$.

Immunohistochemistry

Mice were euthanized by cervical dislocation under anesthesia with isoflurane. If not stated otherwise, chemicals were purchased from Sigma-Aldrich (St. Louis, MO, USA). Immunolabeling was performed on whole-mounts of the organ of Corti of 12-week-old mice. Cochlea were dissected from the temporal bone in ice-cold PBS (Gibco, Carlsbad, CA, USA). The scalae of each cochlea were injected with ice-cold Zamboni's fixative (Morphisto, Offenbach, Germany), followed by immersion in the fixative for 20 min on ice. After replacing the fixative with PBS, the cochlear spiral was carefully dissected into two parts, one containing the apical and medial region covering approximately 45% length of the basilar membrane, and one covering the midbasal and basal part (Figure 1B).

Specimens were permeabilized and blocked with PBS containing 3% BSA and 0.5% Triton-X 100 and incubated in reaction buffer (3% BSA, 0.2% Triton-X in PBS) containing the respective primary antibodies at 4°C overnight. Specimens were labeled with antibodies against CtPB2/Ribeye (mouse monoclonal, BD Transduction Laboratories, Franklin Lakes, NJ, USA; 1:500) and Homer1 (rabbit polyclonal, Synaptic Systems, Germany; 1:1000). Primary antibodies were labeled with Alexa 488-anti mouse secondary antibodies (goat or donkey polyclonal, Fisher Scientific, Carlsbad, CA, USA; 1:500) or Cy3-anti rabbit (goat polyclonal, Jackson Immuno Research Laboratories, Ely, UK; 1:1500) at room temperature for 70 min. Specimens were stained with DAPI at 1:333 in PBS, washed, carefully placed under microscope control, and embedded with VECTASHIELD® H1000 (Vector Laboratories, Newark, CA, USA).

For all immunolabeling experiments, both ears of four animals were analyzed. Specimens were immunolabeled in two or more independent experiments for each condition (control, 100 dB SPL, 106 dB SPL, and 112 dB SPL trauma group). Fluorescence images were acquired using a confocal laser scanning microscope LSM710 with the acquisition software ZEN 2012 SP1, Version 8.1.10.484 (both Carl Zeiss Microscopy GmbH, Jena, Germany). Overview images of 607 µm × 607 µm (1,024 pixel × 1,024 pixel) were obtained using a 20x objective (ZEISS Plan-Apochromat, 0.8 NA), whereas *z*-stacks of optical slices with 70 nm × 70 nm pixel size and 0.32 µm slice thickness were obtained using a 63x oil objective (ZEISS Plan-Apochromat), 1.4 NA, with a pinhole of 1 airy unit. For the quantification of the number and size of ribbons and Homer1 spots, images of 948 × 546 pixels

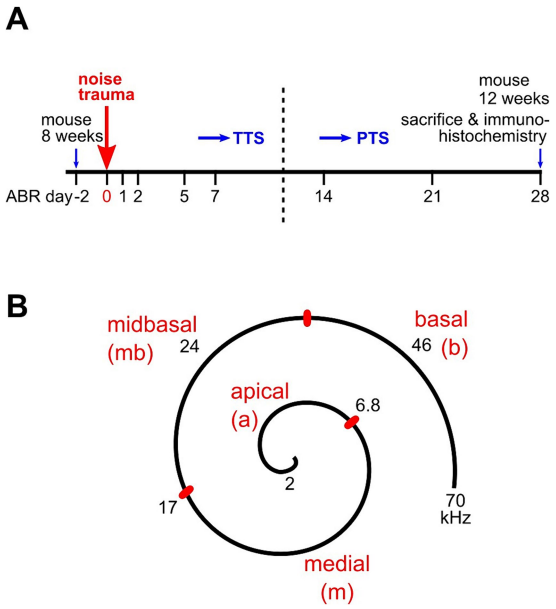


FIGURE 1
Experimental design of hearing measurements, trauma application, and cochlear assignment. **(A)** ABR thresholds were initially recorded in mice aged 7–8 weeks at day-2 for each animal. At day 0, the animal received a 2 h band noise trauma, 8–16 kHz, of either 100 dB, 106 dB, or 112 dB SPL. Days of further ABR measurements are indicated. ABRs of the no trauma control group were recorded on days-2 and 28 only. After a final ABR recording on day 28, animals were euthanized and 4 of them were processed for immunohistochemistry (see Methods). **(B)** Sketch with the assignment of auditory frequencies to regions of the cochlear spiral in the mouse. Adapted from Müller et al. (2005) and Engel et al. (2006).

(64.26 µm × 37.01 µm) covering the basolateral poles of usually 8 IHCs on average were acquired at equal laser and gain settings. Images of at least 3 stacks of each part of the organ of Corti were acquired, and the origin of any 8-IHC stack within that part and with regard to its original cochlear tonotopic location was noted by using the overview image of the slide.

Image processing

Images were processed with Fiji (Schindelin et al., 2012). After calculating the maximum intensity projections (MIPs) of z-stacks, the channel of interest was background-subtracted. If IHCs were positioned very steeply in the organ of Corti, which led to overlay and optical fusion of synapses, these z-stacks were excluded. A thresholded binary image was created (0 below, 1 above threshold) with thresholds of 6–16% of the maximum intensity of the green (CtBP2) and of 5–16% of the red (Homer1) color channel, depending on the individual conditions due to effects of the bony lamina spiralis or of supporting cells on the fluorescence signals, especially in the high-frequency regions of the cochlea. After discarding clusters smaller than 0.05 µm^2, the number and area of clusters were analyzed by Fiji's particle count routine. After blinding the data files, the unpaired ribbons and unpaired Homer1 clusters were counted manually. The numbers of pre-and postsynapses were normalized by the number of IHCs in the frame, respectively.

Auditory frequency ranges were assigned to pieces of the organ of Corti according to the murine frequency map (Müller et al., 2005) as follows: 2–6.8 kHz, apical; > 6.8–17 kHz, medial; > 17–32 kHz, midbasal; > 32 kHz, basal (Figure 1B).

Statistical analysis

Data for ABR thresholds were averaged for each animal; they are presented as mean ± standard deviation (SD) for n animals per experimental group. For click and frequency ABRs, differences of the means were tested for statistical significance by the Kruskal–Wallis test (non-parametric) with $\alpha = 0.05$ and Bonferroni test (post-hoc test) using Statistica 13.0 (StatSoft, Hamburg, Germany).

Immunohistochemical data were analyzed using SPSS Statistics Vs. 25.0.0.1 (International Business Machines Corp., Armonk, NY, U.S.A.). Quantitative immunohistochemical data are presented as mean ± SD or as box-and-whisker-plots for small regions of IHCs (usually 8 IHCs per z-stack) of the apical, medial, midbasal, and basal cochlear part, respectively, with images obtained from independent experiments and 4 mice of each trauma group. The homogeneity of variances was tested with the Brown–Forsythe test. In case of equal variances, one-way ANOVA was used; otherwise, the Kruskal–Wallis test. For each cochlear region, data were tested pairwise for the control and a trauma group, respectively, as well as between trauma groups with the Bonferroni post-hoc test. Box-and-whisker plots use boxes to represent the 25th–75th percentiles, horizontal bar to represent the median (the mean is sometimes indicated by a square), and whiskers to represent the 10th–90th percentiles. For better comprehension, the numbers of ribbons, postsynapses, unpaired ribbons or unpaired postsynapses were normalized by the number of IHCs in the particular region, respectively.

Results

Noise trauma of increasing strength increases the permanent threshold shift in the high-frequency range and, in addition, causes PTS in middle and lower frequencies

We subjected C57BL/6 N mice to the classical noise trauma (band noise from 8 to 16 kHz for 2 h, 100 dB SPL). This trauma had been found to cause loss of synaptic ribbons and nerve fibers despite the lack of PTS in CBA/CaJ mice, which opened the field of noise-induced cochlear synaptopathy (Kujawa and Liberman, 2009). In addition, we also tested the effects of more intense noise (106 dB SPL and 112 dB SPL) on TTS and PTS, and on the fate of ribbons and postsynapses. In this study, we only show ABR data for days -2, 0, and 28. On day -2, click ABR thresholds were equal for the four experimental groups, including a control group that did not receive a trauma at day 0 except for one single frequency (2.8 kHz; Figure 2A). Click ABR thresholds increased monotonically with trauma strength at day 0, and declined 4 weeks after the trauma. Four weeks after trauma, click thresholds had returned to control values for the 100 dB SPL trauma but were still elevated for the 106 dB SPL and the 112 dB SPL trauma, respectively. Analysis of f-ABR thresholds before, directly after, and 4 weeks after the trauma (Figures 2B–D and Table 1) provides a frequency-specific view of TTS and PTS and the effects of trauma strength. f-ABR thresholds, which were nearly undistinguishable at day-2 (Figure 2B), strongly increased in the mid- to high-frequency region on the day of the trauma, indicating a TTS in the frequency band of the noise and above (Figure 2C and Table 1). For comparison, the threshold curve of the untreated control group is indicated by open symbols and a broken line. At day 28, the group exposed to 100 dB SPL had recovered with respect to the age-matched control group except for 45.2 kHz. The group exposed to 106 dB SPL, however, showed a PTS of 19 dB and 25 dB at 16 kHz and 22.6 kHz, respectively, whereas the 112 dB SPL trauma group exhibited a PTS in the entire range between 11.3 and 32 kHz, which was as large as 23 dB at 11.3 kHz and 36 dB at 16 kHz. For statistical analysis, see Table 1.

In summary, the 100 dB SPL trauma recapitulated a TTS trauma in our mouse background as described in Kujawa and Liberman (2009) for CBA/CaJ mice except for 45 kHz. Increasing the trauma strength to 106 and 112 dB SPL resulted in a stronger PTS with a wider range of affected frequencies as a monotonic function of trauma strength.

Increased noise trauma leads to a stronger reduction of ABR wave I amplitudes

Substantial failure of information transmission at IHC synapses due to the destruction of ribbons, peripheral dendrites, or both is not necessarily reflected by an increase in hearing thresholds (Kujawa and Liberman, 2009; Hickox et al., 2017). It is, however, reflected by the frequency-specific amplitude of ABR wave I, a readout for functional synapses between IHC ribbons and nerve fibers (Figure 3). Here,

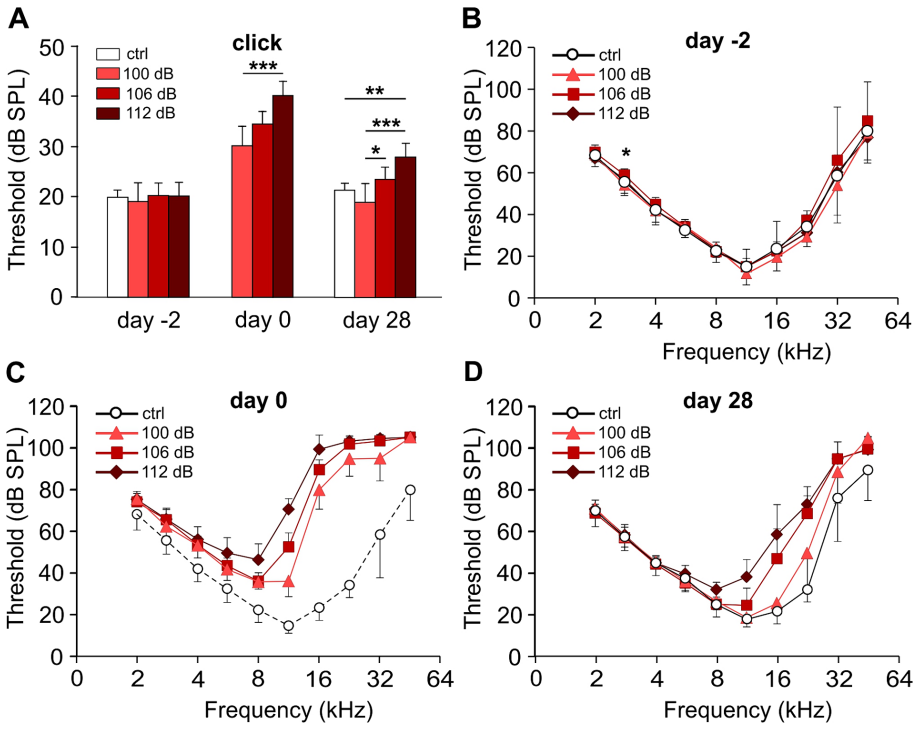


FIGURE 2
Hearing performance of the control and of the trauma groups before, directly after, and 28 days after noise trauma. Click ABR and pure-tone audiograms of the trauma groups before (day-2), directly after (day 0), and 28 days after the noise trauma (band noise, 8–16 kHz for 2 h) of either 100, 106, or 112 dB SPL and of the control group at days-2 and 28. **(A)** Click ABR thresholds (mean ± SD.) for the untreated control (ctrl) and the three trauma groups at days-2, 0, and 28. **(B–D)** Pure-tone audiograms showing mean f-ABR thresholds (±SD., only one direction is shown) recorded at day-2 **(B)**, after trauma (day 0, **C**), and at day 28 **(D)**. Data of the control group from day-2 are indicated in panel **(C)**, connected by dashed lines for comparison. The permanent threshold shift with respect to the untreated control 4 weeks after trauma was evaluated for each trauma strength and frequency **(D)**. Kruskal–Wallis test, with Bonferroni correction for multiple comparisons; **(A, B)** $*p < 0.05$; $**p < 0.01$; $***p < 0.001$; statistical analysis for **(C,D)**, see Table 1 for clarity. Number of animals: day-2: control, 7; 100 dB, 9; 106 dB, 20; 112 dB, 10; day 0: 100 dB, 8; 106 dB, 20; 112 dB, 10; day 28: control, 7; 100 dB, 8; 106 dB, 20; 112 dB, 10.

growth functions of averaged ABR peak-to-peak wave I amplitudes are shown for the frequencies 11.3, 16, 22.6, and 32 kHz in the untreated control group (Figure 3A) and for the three traumata (Figures 3B–D) at day 28, respectively. These growth functions indirectly also reflect the thresholds (starting point of a growth curve with respect to the level at the x-axis). Four weeks after trauma, the 100 dB SPL trauma led to (an irreversible) reduction of the growth functions at 22 kHz and 32 kHz only, whereas 106 dB SPL trauma additionally reduced the growth function at 16 kHz. Expectedly, the 112 dB SPL trauma showed the largest reduction of the growth functions for all four frequencies analyzed, including wave I amplitudes at 11 kHz.

Increasing the noise trauma leads to the elevation of ABR wave I latencies

The reduction of ABR wave I amplitudes (Figure 3) indicates a gradual loss of functional synaptic connections and afferent nerve fibers as a function of trauma strength in the mid- to high-frequency range. Next, we determined the latencies of wave I for the frequencies 11, 16, 22, and 32 kHz (Figure 4). It should be noted that under control conditions (i.e., without noise trauma), latencies increase with decreasing frequency as the traveling wave needs time to excite the basilar membrane at characteristic frequencies closer to the cochlear apex. Level-dependent ABR wave I latency functions were determined for the control and the three trauma groups (Figure 4). The shorter the latency at a fixed frequency and given level, the more HSR fibers are synchronously active (Bourien et al., 2014). Hence, noise trauma-induced loss of synaptic connections might increase latencies at a given level. At 11 kHz, there is a tendency for increased latencies after the 106 and the 112 dB trauma (Figure 4A). Latencies further deviate from the latency of the control group at 16 and 22 kHz (Figures 4B,C). Note a non-systematic level-dependent shape of the latency functions after the 112 dB SPL trauma at both 16 and 22 kHz, which will be addressed in the Discussion. At 32 kHz, latencies could hardly be measured at all (Figure 4D).

Noise traumata did not cause outer hair cell loss

We examined how outer hair cells (OHCs) and IHC synapses led to the malfunction of type I auditory nerve fibers (ANFs). OHCs amplify the vibrations of the basilar membrane and reduce the threshold for the mechanical activation of IHCs below ~50 dB SPL

TABLE 1 Effect of trauma strength on f-ABR thresholds at day 0 (TTS) and day 28 (PTS).

Day 0											
Group	vs. group (dB SPL)	2 kHz	2.8 kHz	4 kHz	5.6 kHz	8 kHz	11.3 kHz	16 kHz	22.6 kHz	32 kHz	45.2 kHz
ctrl	100										**
	106		*	*	**	**	**	***	***	***	***
	112		*	**	***	***	***	***	***	***	**
100 dB SPL	106										
	112						***	**			
106 dB SPL	112					*	*				

Day 28											
Group	vs. group (dB SPL)	2 kHz	2.8 kHz	4 kHz	5.6 kHz	8 kHz	11.3 kHz	16 kHz	22.6 kHz	32 kHz	45.2 kHz
ctrl	100										*
	106							**	**		
	112						***	***	***		
100 dB SPL	106							*			
	112						***	**	*		
106 dB SPL	112					*					

Statistical analysis of inter-group comparisons of differences in f-ABR thresholds, see Figures 2C,D; Kruskal–Wallis test, with Bonferroni correction for multiple comparisons; *$p < 0.05$; ** $p < 0.01$; *** $p < 0.001$.

(Fettiplace, 2017). If part of the OHCs in a cochlear region are non-functional, the thresholds for activation of IHCs will be increased, which finally will also be reflected in altered ABR wave I growth functions. A previous study in CBA/CaJ mice showed massive OHC degeneration in the high-frequency region after a noise trauma of 100 dB SPL and an increase in distortion product otoacoustic emission (DPOAE) thresholds (Liberman et al., 2015). Although we did not analyze the function of OHCs by, e.g., measuring DPOAEs, we determined their presence by counting OHC nuclei in the apical, medial, midbasal, and basal region (*cf.* Figure 1B and see Methods) in DAPI-stained specimens that were also used for the analysis of IHC pre-and postsynapses. OHC numbers were assessed in regions of 10 slots (potential OHC place) × 3 rows. Figure 5A shows an example from a midbasal turn 4 weeks after the trauma of 100 dB SPL, with missing OHC nuclei encircled in red. Analyzing the percentage of OHC loss as a function of cochlear location and trauma strength (Figure 5B) revealed average numbers of <1% OHC loss in the apical and medial turn and of 1–3% with some variation in the midbasal and basal region, which did not depend on trauma strength, with the following *p*-values: 0.976 (apical), 0.142 (medial), 0.186 (midbasal), and 0.616 (basal part; Kruskal–Wallis test). Due to difficulties of preserving the delicate, narrow stretch of OHCs from the basal turn during dissection and labeling as well as the difficulties of imaging close to the bone there are no data for the basal turn in the 100 dB SPL trauma. In summary, there was no trauma-dependent excess loss of OHCs, even in the midbasal and basal cochlear regions. Although we cannot rule out that OHCs from noise trauma-exposed mice were less capable of active amplification 4 weeks after trauma, we conclude that the trauma-induced increase of hearing thresholds and the decrease of ABR wave I amplitudes were not caused by cellular OHC loss.

Immunolabeling of ribbons and postsynapses

Classical noise-induced synaptopathy studies have focused on the detailed analysis of immunolabeled synaptic ribbons. Reduction of nerve fiber counts in CBA/CaJ mice pointed to a pronounced vulnerability of part of the ANF type I in the mid- to high-frequency regions to a 100 dB SPL trauma (Kujawa and Liberman, 2009). More recently, also postsynapses have been examined in rodents (Liberman et al., 2015; Kaur et al., 2019; Kim et al., 2019; Hickman et al., 2020; Manickam et al., 2023). Because of the variable performance of anti-GluR2/3 antibodies, we used Homer1 immunolabeling to characterize the number and size of postsynaptic receptor clusters in MIPs of cochlear whole-mounts. Homer1 is a scaffold of ionotropic glutamate receptors (Iasevoli et al., 2014) and is closely opposed to glutamate receptor clusters in afferents type I (Martinez-Monedero et al., 2016; Reijntjes et al., 2020). In the following experiments, we, therefore, used Homer1 as a proxy for the postsynapses and an indicator for a nerve fiber terminal close to the IHC basal pole.

Cochlear synaptopathy was characterized in mice euthanized 4 weeks after the respective trauma (day 28) and compared with aged-matched no trauma control mice. Imaging optical stacks of pieces of cochlear whole-mounts co-labeled for the ribbon marker CtBP2 and the postsynaptic marker Homer1 was performed in stretches comprising eight neighboring IHCs in all cochlear regions. Example MIPs of the midbasal region for no trauma control and for the different trauma strengths are shown in Figure 6. In general, pre-and postsynapses were closely apposed, often indicated by a white overlap of their fluorescence signals. Each trauma caused unpaired pre-and postsynapses, with a larger number of unpaired

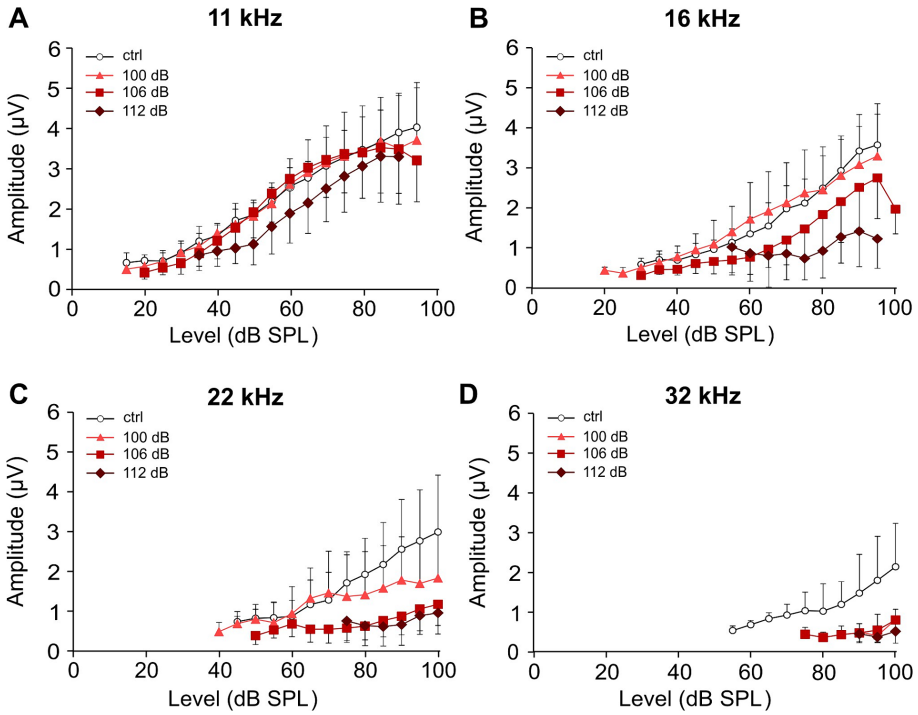


FIGURE 3
Effect of increasing strength of the noise trauma on growth functions of ABR wave I amplitudes 4 weeks after trauma. **(A–D)** Growth functions of the average peak-to-peak amplitudes of ABR wave I (±SD., only one direction is shown) for the control group (no trauma) and the groups exposed to 100 dB SPL, 106 dB SPL, and 112 dB SPL at 11 kHz **(A)**, 16 kHz **(B)**, 22 kHz **(C)**, and 32 kHz **(D)** at day 28. Note that because of the occurrence of permanent threshold increases, less amplitude values could be extracted for higher frequencies and higher trauma levels. The minimum number of data required for presenting a mean value was set to three in each condition.

postsynapses. We quantified the number of pre-and postsynapses per IHC for the apical, medial, midbasal, and basal cochlear regions for the aged-matched no trauma control and the three traumata of 100 dB SPL, 106 dB SPL, and 112 dB SPL (Figure 7). A significant decrease of the average number of ribbons was observed in the medial region (for 100 dB and 112 dB) as well as in the midbasal and basal regions (for all three traumata, respectively; Figure 7A). Four weeks after the 100 dB SPL trauma, ribbon number declined from 17.5 ± 2.0 to 14.6 ± 2.7, corresponding to 83.5% in the medial region, from 17.1 ± 2.3 to 10.4 ± 2.8 or 61.0%, in the midbasal region, and from 14.8 ± 2.0 to 8.0 ± 1.7 or 53.9%, in the basal region. Notably, increasing the trauma to 106 dB SPL or 112 dB SPL did not aggravate the ribbon loss, suggesting that all vulnerable ribbons were fully destroyed by the 100 dB SPL trauma. Regarding the postsynapses, a significant loss was only observed in the midbasal region for the 100 dB SPL trauma (from 17.3 ± 2.5 to 14.0 ± 2.6 or 81.1%) and the 106 dB SPL trauma (to 13.6 ± 2.6 or 80.0%; Figure 7B). Surprisingly, the 112 dB SPL trauma did not cause a significant decline of Homer1 clusters. Similarly, in the basal cochlear region, there was no significant decline in the number of postsynaptic clusters for any of the traumata.

Taken together, presynapses were more vulnerable than postsynapses to an acoustic trauma ranging from 100 dB SPL to 112 dB SPL in the mid- to high-frequency regions of the cochlea.

We also analyzed the effects of acoustic trauma on the sizes of pre-and postsynapses as judged from their area in MIPs (Figure 8). The average area of ribbons significantly increased with trauma even in the apical region (for 112 dB SPL), medial region (for both, 106 and 112 dB SPL), midbasal region (for all trauma strengths), and basal region (for both 106 and 112 dB SPL; Figure 8A). Unlike the loss of ribbons, the increase in the size appeared to scale with trauma strength. We also observed an increase in the postsynaptic area except for the basal region (Figure 8B). The increase in the size of Homer1 clusters was not as large as in the case of ribbons but appeared to scale with trauma strength, as it was very prominent and highly significant for the highest trauma applied (112 dB SPL) in the apical, medial, and midbasal regions (Figure 8B).

Finally, we determined the number of unpaired ribbons/IHC and of unpaired postsynapses/IHC as a function of trauma strength and cochlear location (Figure 9). Though the number of unpaired ribbons/IHC was quite variable after trauma, the median number ranged between 0.13 and 0.75 for control or any trauma condition along the cochlear axis (Figure 9A). Unpaired ribbons thus were a rare finding for all conditions (no trauma control, traumata of 100 dB SPL, 106 dB SPL, and 112 dB SPL) in the entire cochlea (Figure 9A). In contrast, trauma increased the number of unpaired ('orphan') postsynapses in the medial, midbasal, and basal regions irrespective of trauma strength. Whereas in control mice the median number of unpaired postsynapses ranged between 0.75 and 1.38, the 100 dB SPL trauma caused 1.75 (apical region) to 5.75 orphan postsynapses per IHC (basal region, Figure 9B). Notably, increasing the trauma strength to 106 or 112 dB SPL did not further increase the number of orphan postsynapses. It should be noted that the loss of ribbons was generally larger than the number of orphan postsynapses. The 100 dB SPL trauma, e.g., caused loss of 6.7 ribbons per IHC (Figure 7A) and generated 4.2 orphan

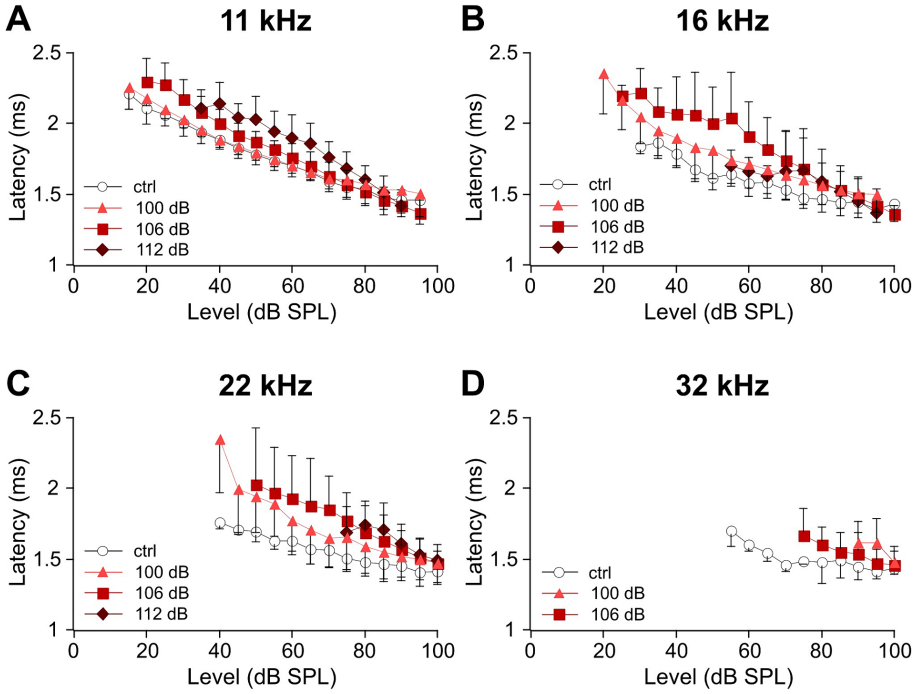


FIGURE 4
Sound level-dependent latencies of ABR wave I increase with trauma strength for the mid-to-high auditory frequencies. **(A–D)** Average level-dependent latencies of ABR wave I measured at the negative peak I (see Methods) are displayed for the unexposed control and the three trauma groups at day 28 after trauma for the frequencies 11 kHz **(A)**, 16 kHz **(B)**, 22 kHz **(C)**, and 32 kHz **(D)**. Note that because of the permanent threshold shift, fewer values were obtained for higher frequencies and higher trauma levels. The minimum number of data required for presenting a mean value was set to three in each condition.

postsynapses per IHC (Figure 9B), indicating that on average only 2-3 postsynapses (i.e., nerve terminals) had degenerated per IHC.

Taken together, the mildest trauma applied (100 dB SPL) caused a large reduction of the number of ribbons in the medial (by 26%), midbasal (39%) and basal cochlear region (46%) and a small reduction of the number of postsynapses in the midbasal cochlear region (by 19%), both of which were not aggravated by a further increase in trauma strength to 106 dB SPL or even to 112 dB SPL. As a consequence, a substantial number of postsynapses in the mid- to high-frequency region was left without a presynaptic partner in each trauma (orphan postsynapses). In contrast, unpaired ribbons were rare—the median value was well below one per IHC in both control and trauma conditions, underlining the specific noise-induced vulnerability of IHC synaptic ribbons.

Discussion

Using C57BL/6 N mice, we have shown that a 100 dB SPL, 8–16 kHz, 2 h noise trauma causes a TTS ranging from 8 to 45 kHz and a PTS restricted to 45 kHz compared with age-matched control animals (without trauma) at day 28. Increasing the trauma level to 106 and 112 dB SPL aggravated the degree of both TTS and PTS and enlarged the permanently affected frequency range toward lower frequencies, respectively. All traumata reduced the amplitudes of ABR wave I in the 16 kHz–32 kHz region. On the ultrastructural level, a loss of the number of synaptic ribbons in the medial, midbasal, and basal regions was observed after the 100 dB SPL trauma that did not further increase with trauma strength. The reduction of postsynaptic Homer1 clusters was less severe for all traumata. As a consequence, 4–6 unpaired (orphan) postsynapses per IHC were present in the mid- to high-frequency region, a phenomenon that did not scale with trauma strength.

Noise-induced changes in hearing thresholds

Here, we used a mouse line (C57BL/6 N) that shows early onset of high-frequency hearing loss starting at the age of 3–6 months, which is caused by a cadherin 23 splice variant that has a slight but progressive impact on tip link stability (Zhou et al., 2006; Kane et al., 2012; Jeng et al., 2020b). Within the time course of our experiments, from 2 to 3 months of age, this effect was negligible in the control group (without trauma). Four weeks after trauma, the click thresholds were unaffected for both the 100 dB SPL and the 106 dB SPL trauma, respectively, yet significantly increased after the 112 dB SPL trauma (Figure 2A). HHL per definition describes the loss of functional IHC synapses/nerve fibers without a permanent threshold elevation. Across ABR test frequencies, we observed a threshold elevation at 45 kHz 4 weeks after the 100 dB SPL trauma compared with unexposed age-matched control animals, indicating that in the highest frequency range the hearing loss was overt rather than hidden. Depending on trauma strength, duration, and frequency characteristics, various cochlear structures can

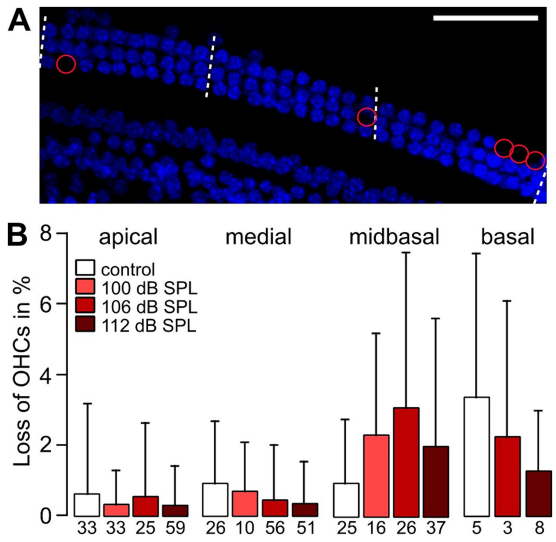


FIGURE 5
Average loss of OHCs in high-frequency cochlear regions is small and is not related to trauma strength. **(A)** Example MIPs of confocal stacks of the midbasal part of a whole-mount organ of Corti from a 12-week-old mouse that had been exposed to a 2 h noise trauma from 8 to 16 kHz of 100 dB SPL 4 weeks after trauma. The number of OHC nuclei (DAPI-stained, blue) was counted in regions of nominally 10 OHCs per row in length (i.e., nominally 30 OHCs for the three OHC rows) as indicated by the dashed lines. Missing nuclei are indicated by red circles. **(B)** Percentage of OHC loss in regions of 3 × 10 OHCs (mean + SD) for the control and the trauma groups as a function of cochlear location. Numbers below the bars indicate the number of regions of OHC counts providing the space for 30 OHCs obtained from 4 different mice. Scale bar: 50 µm.

be permanently affected. It was until the discovery of hidden hearing loss that OHCs were regarded as the most sensitive structures in the cochlea (Wang et al., 2002; Liberman and Kujawa, 2017; Natarajan et al., 2023). In CBA/CaJ mice, massive OHC loss was observed after the classical 100 dB SPL trauma (8–16 kHz, 2 h) in the basal region (Liberman et al., 2015). In this study, trauma strength did not correlate with the cellular loss of OHCs 4 weeks after the trauma (Figure 5) but the possibility of a trauma-related *functional* OHC impairment, which would feed less energy into the cochlea, should be considered. A noise-induced functional impairment of OHCs may have been responsible for our high-frequency PTS of the 100 dB SPL trauma, possibly caused by the cadherin 23 malfunction (Zhou et al., 2006; Kane et al., 2012; Jeng et al., 2020b) or other OHC susceptibility genes (Lavinsky et al., 2021a; Shuster et al., 2021).

The degree of both TTS and PTS and the range of affected frequencies were monotonic functions of trauma strengths (Figures 2C,D and Table 1), similar to findings in CBA/CaJ mice exposed to the same trauma paradigm with either 100, 106, 112, or 116 dB SPL (Wang et al., 2002). Four weeks after the 112 dB SPL trauma, a small but significant PTS remained down to 11.3 kHz, the center of the noise frequency band (Figure 2D). Using a less intense noise trauma, the PTS is usually shifted by half an octave toward high-frequency (basal) regions because of cochlear mechanics (Cody and Johnstone, 1981). In our 112 dB SPL trauma experiments, basilar membrane movements were so large that the PTS extended down to 11.3 kHz.

Noise-induced changes of ABR wave I amplitudes and latencies

Growth functions of ABR wave I amplitudes reflect level-dependent synchronous firing of ANFs. With increasing level of the stimulus, the fiber types Ia, Ib, and Ic should be activated in this sequence, and reduced growth functions indicate a loss of functional nerve fibers (Moser et al., 2023). In this study, ABR growth functions were reduced for frequencies ≥22 kHz (for the 100 dB SPL trauma), ≥ 16 kHz (for the 106 dB SPL trauma), and ≥11 kHz (for the 112 dB SPL trauma) 4 weeks after trauma (Figure 3) indicating an increasing loss of functional fibers with trauma strength.

We further show latency functions of wave I for four selected frequencies, which indicate that at a given frequency latencies mostly rose with increasing trauma strength (Figure 4). In a healthy cochlea, both amplitude and latency of compound action potentials of the auditory nerve, the basis of the ABR signal, are dominated by HSR fibers (Bourien et al., 2014). Cochleae of different mouse lines treated with a similar HHL trauma showed a reduction in synaptic pairs by ~50% (Kujawa and Liberman, 2009; Suthakar and Liberman, 2021). These numbers are too high for exclusive functional type Ic fiber loss. Indeed, noise-induced loss of type Ia fibers has been recently demonstrated in CBA/CaJ mice (Suthakar and Liberman, 2021).

Factors affecting the consequences of noise trauma

Recently, genetic studies on hearing performance and the vulnerability to noise trauma have been performed for a large number of mouse inbred strains (Boussaty et al., 2020; Jeng et al., 2020a, 2020b; Lavinsky et al., 2021b; Milon et al., 2021; Early et al., 2022). In genetic noise studies, neither CBA/CaJ nor C57BL/6 N mice were included, only the line C57BLKS/J, which is closely related to the C57BL/6 J strain (Lavinsky et al., 2021b). It should be kept in mind that the C57BL/6 N line was separated from C57BL/6 J mice in 1951 (Kane et al., 2012). With regard to the stability of wave I amplitude, C57BLKS/J mice were found to be rather resistant to noise trauma from 2 to 10 kHz at 108 dB SPL (Lavinsky et al., 2021b). The C57BL/6 N line is the basis for genetic mouse models generated by 'The International Knockout Mouse Consortium' (Mianné et al., 2016) and is therefore important for ourselves and others (Jeng et al., 2020a, 2020b).

Apart from genetic differences, a second factor that may affect the outcome of noise trauma experiments is anesthesia, which may alter the middle ear reflex or cochlear efferent reflexes (Ohlemiller et al., 2016). There are few studies in which the effects of noise trauma in awake mice were compared with those of anesthetized mice (Reijntjes et al., 2018; Jongkamonwiwat et al., 2020). One study did not find a difference in TTS or PTS in f-ABR as well as in the number of ribbons/IHC in all cochlear regions for C57BL/6 J and FVB mice (Reijntjes et al., 2018). Another study observed a larger TTS in anesthetized FVB mice after 7–14 days, which came down to the same PTS thresholds as in awake mice for 94, 100, and 105 dB SPL traumata, respectively (Jongkamonwiwat et al., 2020). Both groups used ketamine-based anesthesia, whereas we used fully antagonizable fentanyl-based anesthesia to limit its duration in frequent ABR measurements.

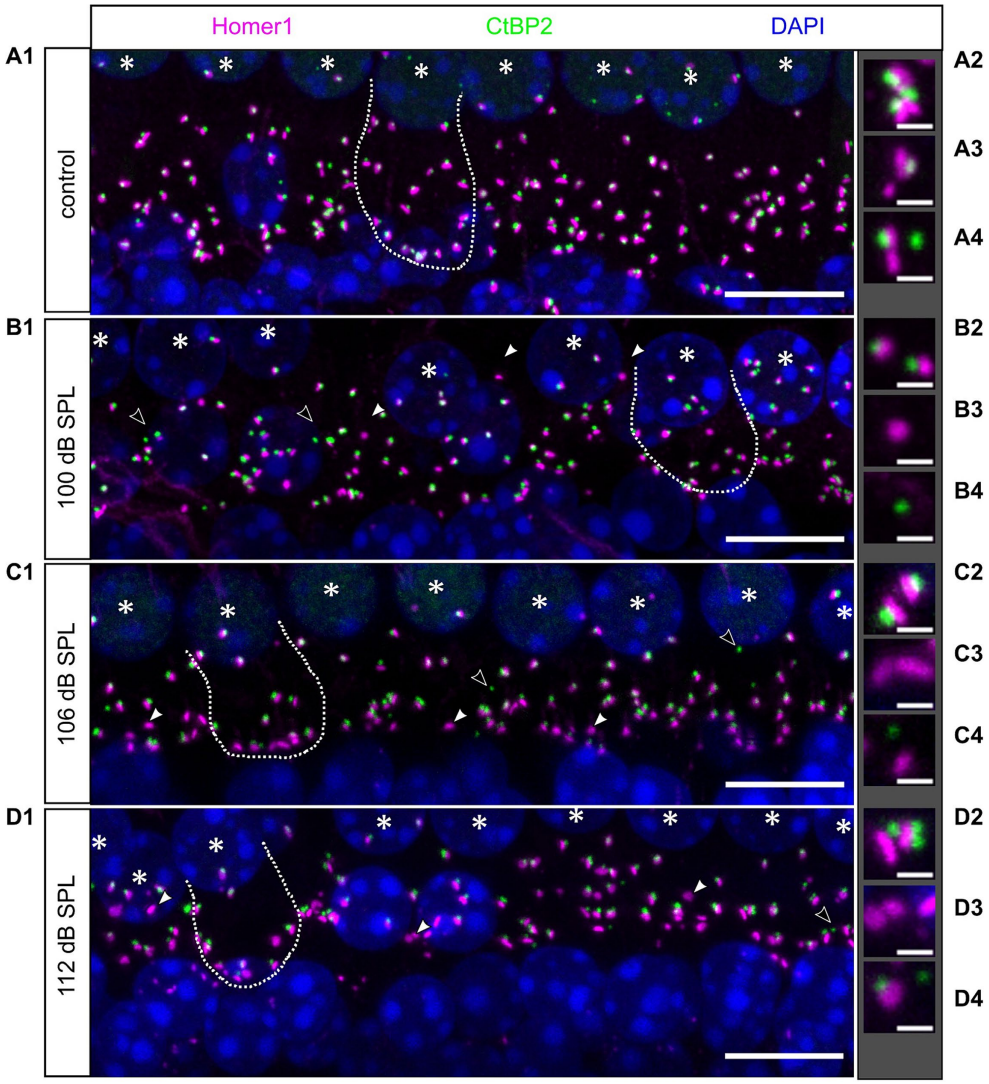


FIGURE 6
Effects of noise traumata of 100, 106, and 112 dB SPL on IHC synapses 4 weeks after trauma as evaluated by immunolabeling for CtBP2 and Homer1. MIPs of confocal stacks of whole-mount organs of Corti showing the basolateral pole of eight IHCs each immunolabeled for presynaptic ribbons (CtBP2, green) and postsynaptic glutamate receptors using Homer1 (magenta). **(A1)** Specimen of an unexposed 12-week-old control mouse. **(B1–D1)** Example specimen of mice that had been exposed to a noise trauma at 8 weeks of age of 100 dB SPL **(B1)**, 106 dB SPL **(C1)**, and 112 dB SPL **(D1)** at day 28 after trauma. Unpaired ribbons are indicated by open arrowheads and unpaired postsynaptic spots by closed arrowheads. Nuclei are stained in blue with DAPI; IHC nuclei are additionally indicated by white stars. An outline of one IHC is indicated by a white dotted line in each panel. The thumbnails to the right **(A2–A4,B2–B4,C2–C4,D2–D4)** show enlargements of paired synapses or unpaired synaptic components selected from the respective main panels **(A1–D1)**. Scale bars: 10 µm in main panels, 1 µm for thumbnails.

Cochlear synaptopathy—IHC ribbons are more vulnerable than AN fibers

A noise trauma that causes overt rather than hidden hearing loss (i.e., PTS) includes cochlear synaptopathy (Wu et al., 2020, 2021), but so far, little systematic quantification as a function of trauma strength has been performed. Noise-induced cochlear synaptopathy is defined as the loss of paired IHC synapses at a certain time after a noise trauma, leading to the reduction of auditory information channels between IHCs and the central auditory system. At the level of a single IHC-SGN synapse, it can present as (i) selective loss of the ribbon, (ii) selective loss of the postsynapse, (iii) loss of both ribbon and postsynapse, or (iv) detachment of ribbon and postsynapse without degeneration. In all four constellations, the transmission of information along the specific AN fiber will be prevented. The accepted hypothesis is that acoustic overstimulation of IHCs causes glutamate excitotoxicity in the postsynapses of type I (predominantly Ic, i.e., LSR) fibers causing swelling, bursting, and retraction of the terminal dendrite from the IHC (Ruel et al., 2007; Liberman and Kujawa, 2017; Valero et al., 2017; Kim et al., 2019; Hu et al., 2020). On the other hand, synaptic ribbons are vulnerable to acoustic overstimulation, too—with loss of up to 50–60% on the day after exposure to 100 dB SPL in the 32 kHz region in CBA/CaJ mice (Kujawa and Liberman, 2009; Liberman et al., 2015). Studies using mouse lines such as C57BL/6J showed some degree of ribbon regeneration (Shi et al., 2015; Kaur et al.,

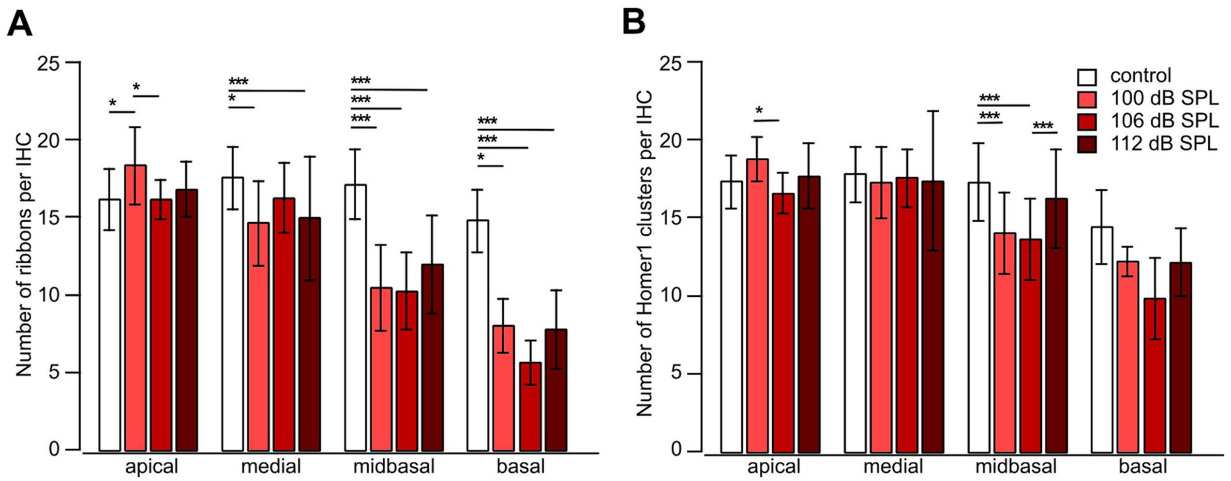


FIGURE 7
Noise trauma strongly reduces the number of presynaptic ribbons but less so the number of postsynaptic Homer1 clusters in the mid-to high-frequency range 4 weeks after trauma. **(A,B)** Number of presynaptic ribbons per IHC **(A)** and number of postsynaptic Homer1 clusters per IHC **(B)** as a function of trauma strength and cochlear location. Data are given as mean ± SD; numbers of regions comprising usually 8 IHCs: control (no trauma): apical 19, medial 37, midbasal 82, basal 12; 100 dB SPL: apical 8, medial 10, midbasal 15, basal 4; 106 dB SPL: apical 18, medial 33, midbasal 65, basal 4; 112 dB SPL: apical 46, medial 51, midbasal 48, basal 10, from 4 mice in total. One-way ANOVA for apical ribbons and medial postsynapses, Kruskal–Wallis test otherwise, with Bonferroni correction for multiple comparisons; *$p < 0.05$; **$p < 0.01$; ***$p < 0.001$.

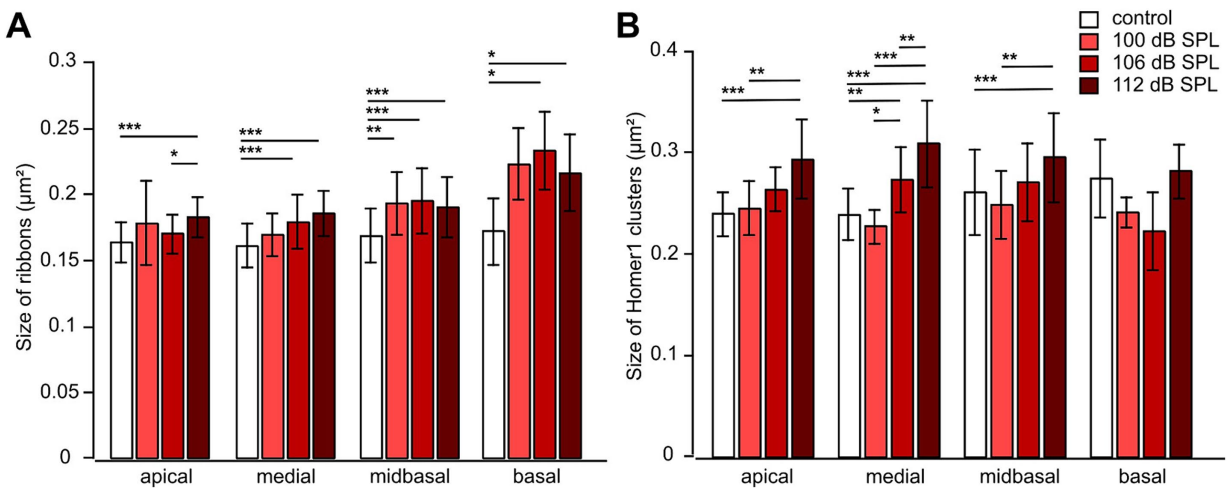


FIGURE 8
Noise trauma increases the sizes of both presynaptic ribbons and Homer1 clusters 4 weeks after trauma. **(A,B)** Mean area ± SD of presynaptic ribbons **(A)** and mean area ± SD of postsynaptic Homer1 clusters **(B)** Figure 6 as a function of trauma strength and cochlear location. Data are given as mean ± SD; numbers of regions comprising usually 8 IHCs: control (no trauma): apical 19, medial 37, midbasal 82, basal 12; 100 dB SPL: apical 8, medial 10, midbasal 15, basal 4; 106 dB SPL: apical 18, medial 33, midbasal 65, basal 4; 112 dB SPL: apical 46, medial 51, midbasal 48, basal 10, from 4 mice in total. Kruskal–Wallis test with Bonferroni correction for multiple comparisons, * $p < 0.05$; ** $p < 0.01$; *** $p < 0.001$.

2019; Kim et al., 2019), whereas in guinea pigs, most ribbons regenerated after noise trauma (Shi et al., 2013, 2016; Hickman et al., 2020, 2021).

We used the postsynaptic marker Homer1, which is a scaffold for glutamate receptors (Iasevoli et al., 2014) because anti-Homer1 antibody labeling, which indicates the existence and position of the afferent bouton, is very robust (Martinez-Monedero et al., 2016; Reijntjes et al., 2020). An unexpected finding of this study is that more ribbons than postsynapses were lost 4 weeks after trauma leading to 3–6 unpaired postsynapses per IHC in the medial, midbasal, and basal regions. This reveals that despite the presumed excitotoxic swelling of afferent boutons, more boutons than ribbons survived 4 weeks after trauma, indicating that IHC synaptic ribbons rather than AN fibers are the most vulnerable structures in C57BL/6 N mice. We cannot tell whether the trauma-induced orphan terminals would have retracted and degenerated over many months after their partner ribbon had died, as observed in CBA/CaJ mice (Kujawa and Liberman, 2009) because the analysis of the long-term survival of SGN was not the aim of our study. Moreover, C57BL/6 N mice are not suitable for following hearing into old age. Nevertheless, it will be interesting to look at the

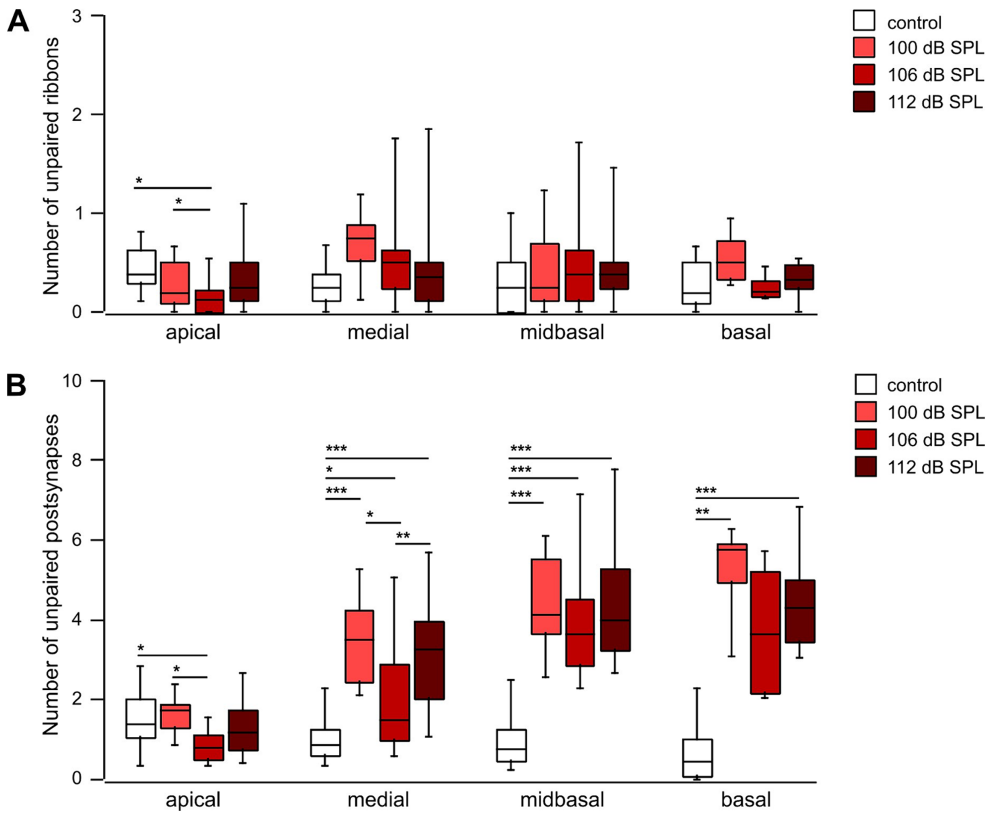


FIGURE 9
Postsynapses are less vulnerable to noise trauma than presynaptic ribbons **(A,B)** Box-and-whisker plots of the number of unpaired ribbons per IHC **(A)** and of orphan postsynapses per IHC (Homer1 clusters, **B**) as a function of cochlear location 4 weeks after trauma of the respective strength. Regions with usually 8 IHCs that went into the analysis of Figures 7, 8 were further analyzed for the number of unpaired pre-and postsynapses. Age-matched groups that did not receive any trauma, but were tested for their hearing function at days -2 and 28, served as controls. One-way ANOVA for unpaired ribbons of the midbasal and basal region; Kruskal–Wallis test otherwise, Bonferroni correction for multiple comparisons, * $p < 0.05$; ** $p < 0.01$; *** $p < 0.001$.

fate of synapses at time points closer to the trauma (e.g., on days 1, 3, 7, and 14), which we plan in the future.

The striking vulnerability of part of synaptic ribbons poses new questions as to (i) which ribbons are primarily affected and (ii) what is the mechanism of degeneration. Answering these questions may foster therapies for treating noise-induced cochlear synaptopathy in humans by addressing a novel target, the *presynaptic ribbons*. So far, treatment aimed at the regeneration of ANF by intracochlear application of neurotrophin 3 in a mouse model (Suzuki et al., 2016; Ji et al., 2024).

The finding that surviving ribbons on average had a larger size (Figure 7) may suggest either compensation for the substantial loss in ribbon number (hence in functional connections to the brain) by increased ribbon sizes or a process of dysregulation. An increase in ribbon size has been found in previous studies (Liberman et al., 2015; Kim et al., 2019; Reijntjes et al., 2020), which suggests some presynaptic plasticity on the IHC side. This leads to the question as to why IHCs are able to change the size of surviving or newly built ribbons rather than replacing dead ribbons with new ones at those sites that oppose orphan boutons. Electron microscopic studies revealed a structural phenotype in presynaptic regions of noise-damaged IHCs, specifically a dysregulation of the vesicle recycling pathway (Bullen et al., 2019; Moverman et al., 2023). The range of dysregulation may span from nearly normal functioning ribbons with slightly changed sizes to failure of membrane recycling, preventing the build-up of new ribbons replacing damaged ones.

Noise-induced changes pointing to plasticity or dysregulation are also present in postsynapses, as shown by a trauma-induced increase in size (Figure 8B; Bullen et al., 2019) and upregulation of PSD-95 (Bao et al., 2004). A recent analysis of noise-induced transcriptomic changes in whole cochlea and specific cell types such as OHCs and SGN type Ia found activation of the immune response and many cell-type specific changes, especially the ATF3/ATF4 stress-response pathway (Milon et al., 2021).

Another unexpected finding was the fact that the loss of ribbons in the most affected (midbasal) region 4 weeks after the 100 dB SPL trauma could not be aggravated by further increasing trauma strength, as was the number of orphan postsynapses (for the medial, midbasal, and basal regions). In other words, the 100 dB SPL trauma that did not change ABR thresholds (except the threshold at 45 kHz in this study) was large enough to damage all the vulnerable ribbons such that higher traumata did not add further damage to the synapses.

In humans, evidence is accumulating that an increase in sensorineural hearing thresholds might almost always be accompanied by a considerable degree of cochlear synaptopathy. In the aging process, loss of information channels from IHCs to the central

nervous system is likely a major cause for poor speech recognition abilities, especially in background noise, and is exacerbated by the individual noise history (Bakay et al., 2018; Wu et al., 2019, 2021). Accepting that the IHC synapse is the most vulnerable structure in the cochlea endangered by both noise and aging, which leads to severe communication problems on top of increasing hearing thresholds, requires more effort in both protection measures and in developing therapeutic strategies targeting IHC synapses, especially presynaptic ribbons.

Data availability statement

The raw data supporting the conclusions of this article will be made available by the authors, without undue reservation.

Ethics statement

The animal study was approved by Animal Welfare Commissioner and the Regional Board of Animal Experimentation of Saarland. The study was conducted in accordance with the local legislation and institutional requirements.

Author contributions

KB: Methodology, Supervision, Writing – original draft, Writing – review & editing. Data curation, Formal analysis, Investigation, Validation, Visualization. PaS: Formal analysis, Investigation, Methodology, Visualization, Validation, Writing – original draft. PD: Formal analysis, Investigation, Visualization, Writing – original draft. PhS: Formal analysis, Investigation, Visualization, Validation, Writing – original draft, Writing – review & editing. FN: Formal analysis, Investigation, Visualization, Writing – original draft. PF: Formal analysis, Investigation, Visualization, Writing – original draft. JE: Conceptualization, Funding acquisition, Methodology, Project administration, Resources, Supervision, Writing – original draft, Writing – review & editing. SK: Conceptualization, Data curation, Formal analysis, Funding acquisition, Investigation, Methodology, Project administration, Resources, Supervision, Validation, Visualization, Writing – original draft, Writing – review & editing.

Funding

The author(s) declare that financial support was received for the research, authorship, and/or publication of this article. This study was supported by DFG SFB 894 (A8 to JE), DFG PP1608 (to SK and JE), and Saarland University.

Acknowledgments

We thank Kerstin Fischer for excellent technical assistance and Stefan Münkner for providing macros for image analysis with FIJI.

Conflict of interest

The authors declare that the research was conducted in the absence of any commercial or financial relationships that could be construed as a potential conflict of interest.

Publisher's note

All claims expressed in this article are solely those of the authors and do not necessarily represent those of their affiliated organizations, or those of the publisher, the editors and the reviewers. Any product that may be evaluated in this article, or claim that may be made by its manufacturer, is not guaranteed or endorsed by the publisher.

References

Bakay, W. M. H., Anderson, L. A., Garcia-Lazaro, J. A., McAlpine, D., and Schaette, R. (2018). Hidden hearing loss selectively impairs neural adaptation to loud sound environments. *Nat. Commun.* 9:4298. doi: 10.1038/s41467-018-06777-y

Bao, J., Lin, H., Ouyang, Y., Lei, D., Osman, A., Kim, T.-W., et al. (2004). Activity-dependent transcription regulation of PSD-95 by neuregulin-1 and Eos. *Nat. Neurosci.* 7, 1250–1258. doi: 10.1038/nn1342

Bourien, J., Tang, Y., Batrel, C., Huet, A., Lenoir, M., Ladrech, S., et al. (2014). Contribution of auditory nerve fibers to compound action potential of the auditory nerve. *J. Neurophysiol.* 112, 1025–1039. doi: 10.1152/jn.00738.2013

Boussaty, E. C., Gillard, D., Lavinsky, J., Salehi, P., Wang, J., Mendonça, A., et al. (2020). The genetics of variation of the wave 1 amplitude of the mouse auditory brainstem response. *JARO J. Assoc. Res. Otolaryngol.* 21, 323–336. doi: 10.1007/s10162-020-00762-3

Brandt, A., Striessnig, J., and Moser, T. (2003). CaV1.3 channels are essential for development and presynaptic activity of cochlear inner hair cells. *J. Neurosci.* 23, 10832–10840. doi: 10.1523/JNEUROSCI.23-34-10832.2003

Bullen, A., Anderson, L., Bakay, W., and Forge, A. (2019). Localized disorganization of the cochlear inner hair cell synaptic region after noise exposure. *Biol. Open* 8:bio038547. doi: 10.1242/bio.038547

Cody, A. R., and Johnstone, B. M. (1981). Acoustic trauma: single neuron basis for the "half-octave shift". *J. Acoust. Soc. Am.* 70, 707–711. doi: 10.1121/1.386906

Deichelbohrer, M., Wu, M.-F., Seitz, B., Hüttenberger, D., Laschke, M. W., Foth, H.-J., et al. (2017). Bacterial keratitis: photodynamic inactivation reduced experimental inflammation. *Exp. Ther. Med.* 14, 4509–4514. doi: 10.3892/etm.2017.5109

Early, S., Du, E., Boussaty, E., and Friedman, R. (2022). Genetics of noise-induced hearing loss in the mouse model. *Hear. Res.* 425:108505. doi: 10.1016/j.heares.2022.108505

Engel, J., Braig, C., Ruttiger, L., Kuhn, S., Zimmermann, U., Blin, N., et al. (2006). Two classes of outer hair cells along the tonotopic axis of the cochlea. *Neuroscience* 143, 837–849. doi: 10.1016/j.neuroscience.2006.08.060

Fettiplace, R. (2017). Hair cell transduction, tuning and synaptic transmission in the mammalian cochlea. *Compr. Physiol.* 7, 1197–1227. doi: 10.1002/cphy.c160049

Frank, T., Khimich, D., Neef, A., and Moser, T. (2009). Mechanisms contributing to synaptic Ca2+ signals and their heterogeneity in hair cells. *Proc Natl Acad Sci U A* 106, 4483–4488. doi: 10.1073/pnas.0813213106

Fuchs, P. A., Glowatzki, E., and Moser, T. (2003). The afferent synapse of cochlear hair cells. *Curr. Opin. Neurobiol.* 13, 452–458. doi: 10.1016/s0959-4388(03)00098-9

Furman, A. C., Kujawa, S. G., and Liberman, M. C. (2013). Noise-induced cochlear neuropathy is selective for fibers with low spontaneous rates. *J. Neurophysiol.* 110, 577–586. doi: 10.1152/jn.00164.2013

Hickman, T. T., Hashimoto, K., Liberman, L. D., and Liberman, M. C. (2020). Synaptic migration and reorganization after noise exposure suggests regeneration in a mature mammalian cochlea. *Sci. Rep.* 10:19945. doi: 10.1038/s41598-020-76553-w

Hickman, T. T., Hashimoto, K., Liberman, L. D., and Liberman, M. C. (2021). Cochlear synaptic degeneration and regeneration after noise: effects of age and neuronal subgroup. *Front. Cell. Neurosci.* 15:281. doi: 10.3389/fncel.2021.684706

Hickox, A. E., Larsen, E., Heinz, M. G., Shinobu, L., and Whitton, J. P. (2017). Translational issues in cochlear synaptopathy. *Hear. Res.* 349, 164–171. doi: 10.1016/j.heares.2016.12.010

Hu, N., Rutherford, M. A., and Green, S. H. (2020). Protection of cochlear synapses from noise-induced excitotoxic trauma by blockade of ca^{2+}-permeable AMPA receptors. *Proc. Natl. Acad. Sci.* 117, 3828–3838. doi: 10.1073/pnas.1914247117

Iasevoli, F., Tomasetti, C., Buonaguro, F., and de Bartolomeis, A. (2014). The glutamatergic aspects of schizophrenia molecular pathophysiology: role of the postsynaptic density, and implications for treatment. *Curr. Neuropharmacol.* 12, 219–238. doi: 10.2174/1570159X12666140324183406

Jeng, J.-Y., Ceriani, F., Olt, J., Brown, S. D. M., Holley, M. C., Bowl, M. R., et al. (2020a). Pathophysiological changes in inner hair cell ribbon synapses in the ageing mammalian cochlea. *J. Physiol.* 598, 4339–4355. doi: 10.1113/JP280018

Jeng, J.-Y., Johnson, S. L., Carlton, A. J., Tomasi, L. D., Goodyear, R. J., Faveri, F. D., et al. (2020b). Age-related changes in the biophysical and morphological characteristics of mouse cochlear outer hair cells. *J. Physiol.* 598, 3891–3910. doi: 10.1113/JP279795

Ji, L., Borges, B. C., Martel, D. T., Wu, C., Liberman, M. C., Shore, S. E., et al. (2024). From hidden hearing loss to supranormal auditory processing by neurotrophin 3-mediated modulation of inner hair cell synapse density. *PLoS Biol.* 22:e3002665. doi: 10.1371/journal.pbio.3002665

Jongkamonwiwat, N., Ramirez, M. A., Edassery, S., Wong, A. C. Y., Yu, J., Abbott, T., et al. (2020). Noise exposures causing hearing loss generate Proteotoxic stress and activate the Proteostasis network. *Cell Rep.* 33:108431. doi: 10.1016/j.celrep.2020.108431

Julien-Schraermeyer, S., Illing, B., Tschulakow, A., Taubitz, T., Guezguez, J., Burnet, M., et al. (2020). Penetration, distribution, and elimination of remofuscin/soraprazan in Stargardt mouse eyes following a single intravitreal injection using pharmacokinetics and transmission electron microscopic autoradiography: implication for the local treatment of Stargardt's disease and dry age-related macular degeneration. *Pharmacol. Res. Perspect.* 8:e00683. doi: 10.1002/prp2.683

Kane, K. L., Longo-Guess, C. M., Gagnon, L. H., Ding, D., Salvi, R. J., and Johnson, K. R. (2012). Genetic background effects on age-related hearing loss associated with Cdh23 variants in mice. *Hear. Res.* 283, 80–88. doi: 10.1016/j.heares.2011.11.007

Kaur, T., Clayman, A. C., Nash, A. J., Schrader, A. D., Warchol, M. E., and Ohlemiller, K. K. (2019). Lack of Fractalkine receptor on macrophages impairs spontaneous recovery of ribbon synapses after moderate noise trauma in C57BL/6 mice. *Front. Neurosci.* 13:620. doi: 10.3389/fnins.2019.00620

Khimich, D., Nouvian, R., Pujol, R., Tom Dieck, S., Egner, A., Gundelfinger, E. D., et al. (2005). Hair cell synaptic ribbons are essential for synchronous auditory signalling. *Nature* 434, 889–894. doi: 10.1038/nature03418

Kim, K. X., Payne, S., Yang-Hood, A., Li, S.-Z., Davis, B., Carlquist, J., et al. (2019). Vesicular glutamatergic transmission in noise-induced loss and repair of Cochlear ribbon synapses. *J. Neurosci.* 39, 4434–4447. doi: 10.1523/JNEUROSCI.2228-18.2019

Kujawa, S. G., and Liberman, M. C. (2006). Acceleration of age-related hearing loss by Early noise exposure: evidence of a misspent youth. *J. Neurosci.* 26, 2115–2123. doi: 10.1523/JNEUROSCI.4985-05.2006

Kujawa, S. G., and Liberman, M. C. (2009). Adding insult to injury: cochlear nerve degeneration after "temporary" noise-induced hearing loss. *J. Neurosci.* 29, 14077–14085. doi: 10.1523/JNEUROSCI.2845-09.2009

Kujawa, S. G., and Liberman, M. C. (2015). Synaptopathy in the noise-exposed and aging cochlea: primary neural degeneration in acquired sensorineural hearing loss. *Hear. Res.* 330, 191–199. doi: 10.1016/j.heares.2015.02.009

Lavinsky, J., Kasperbauer, G., Bento, R. F., Mendonça, A., Wang, J., Crow, A. L., et al. (2021a). Noise exposure and distortion product otoacoustic emission suprathreshold amplitudes: a genome-wide association study. *Audiol. Neurotol.* 26, 445–453. doi: 10.1159/000514143

Lavinsky, J., Mendonça, A., Bressan, M., da Silva, V. A. R., Kasperbauer, G., Wang, J., et al. (2021b). Large-scale phenotyping of ABR P1-N1 amplitudes before and after exposure to noise in 69 strains of mice. *Mamm. Genome* 32, 427–434. doi: 10.1007/s00335-021-09913-0

Liberman, M. C. (1982). Single-neuron labeling in the cat auditory nerve. *Science* 216, 1239–1241.

Liberman, M. C., and Kujawa, S. G. (2017). Cochlear synaptopathy in acquired sensorineural hearing loss: manifestations and mechanisms. *Hear. Res.* 349, 138–147. doi: 10.1016/j.heares.2017.01.003

Liberman, L. D., Suzuki, J., and Liberman, M. C. (2015). Dynamics of cochlear synaptopathy after acoustic overexposure. *J. Assoc. Res. Otolaryngol.* 16, 205–219. doi: 10.1007/s10162-015-0510-3

Manickam, V., Gawande, D. Y., Stothert, A. R., Clayman, A. C., Batalkina, L., Warchol, M. E., et al. (2023). Macrophages promote repair of inner hair cell ribbon synapses following noise-induced Cochlear Synaptopathy. *J. Neurosci.* 43, 2075–2089. doi: 10.1523/JNEUROSCI.1273-22.2023

Martinez-Monedero, R., Liu, C., Weisz, C., Vyas, P., Fuchs, P. A., and Glowatzki, E. (2016). GluA2-containing AMPA receptors distinguish ribbon-associated from Ribbonless afferent contacts on rat Cochlear hair cells. *eNeuro* 3:ENEURO.0078-16.2016. doi: 10.1523/ENEURO.0078-16.2016

Milon, B., Shulman, E. D., So, K. S., Cederroth, C. R., Lipford, E. L., Sperber, M., et al. (2021). A cell-type-specific atlas of the inner ear transcriptional response to acoustic trauma. *Cell Rep.* 36:109758. doi: 10.1016/j.celrep.2021.109758

Mianné, J., Chessum, L., Kumar, S., Aguilar, C., Codner, G., Hutchison, M., et al. (2016). Correction of the auditory phenotype in C57BL/6N mice via CRISPR/Cas9-mediated homology directed repair. *Genome Med.* 8: 16. doi: 10.1186/s13073-016-0273-4

Moser, T., Karagulyan, N., Neef, J., and Jaime Tobón, L. M. (2023). Diversity matters — extending sound intensity coding by inner hair cells via heterogeneous synapses. *EMBO J.* 42:e114587. doi: 10.15252/embj.2023114587

Moverman, D. J., Liberman, L. D., Kraemer, S., Corfas, G., and Liberman, M. C. (2023). Ultrastructure of noise-induced cochlear synaptopathy. *Sci. Rep.* 13:19456. doi: 10.1038/s41598-023-46859-6

Müller, M., von Hunerbein, K., Hoidis, S., and Smolders, J. W. (2005). A physiological place-frequency map of the cochlea in the CBA/J mouse. *Hear. Res.* 202, 63–73. doi: 10.1016/j.heares.2004.08.011

Natarajan, N., Batts, S., and Stankovic, K. M. (2023). Noise-induced hearing loss. *J. Clin. Med.* 12:2347. doi: 10.3390/jcm12062347

Ohlemiller, K. K., Jones, S. M., and Johnson, K. R. (2016). Application of mouse models to research in hearing and balance. *J. Assoc. Res. Otolaryngol.* 17, 493–523. doi: 10.1007/s10162-016-0589-1

Petitpré, C., Wu, H., Sharma, A., Tokarska, A., Fontanet, P., Wang, Y., et al. (2018). Neuronal heterogeneity and stereotyped connectivity in the auditory afferent system. *Nat. Commun.* 9:3691. doi: 10.1038/s41467-018-06033-3

Platzer, J., Engel, J., Schrott-Fischer, A., Stephan, K., Bova, S., Chen, H., et al. (2000). Congenital deafness and sinoatrial node dysfunction in mice lacking class D L-type Ca2+ channels. *Cell* 102, 89–97.

Puel, J.-L., Pujol, R., Tribillac, F., Ladrech, S., and Eybalin, M. (1994). Excitatory amino acid antagonists protect cochlear auditory neurons from excitotoxicity. *J. Comp. Neurol.* 341, 241–256. doi: 10.1002/cne.903410209

Reijntjes, D. O. J., Köppl, C., and Pyott, S. J. (2020). Volume gradients in inner hair cell-auditory nerve fiber pre-and postsynaptic proteins differ across mouse strains. *Hear. Res.* 390:107933. doi: 10.1016/j.heares.2020.107933

Reijntjes, D. O. J., Schubert, N. M. A., Pietrus-Rajman, A., van Dijk, P., and Pyott, S. J. (2018). Changes in spontaneous movement in response to silent gaps are not robust enough to indicate the perception of tinnitus in mice. *PLoS One* 13:e0202882. doi: 10.1371/journal.pone.0202882

Ruel, J., Wang, J., Rebillard, G., Eybalin, M., Lloyd, R., Pujol, R., et al. (2007). Physiology, pharmacology and plasticity at the inner hair cell synaptic complex. *Hear. Res.* 227, 19–27. doi: 10.1016/j.heares.2006.08.017

Schaette, R., and McAlpine, D. (2011). Tinnitus with a normal audiogram: physiological evidence for hidden hearing loss and computational model. *J. Neurosci.* 31, 13452–13457. doi: 10.1523/JNEUROSCI.2156-11.2011

Schindelin, J., Arganda-Carreras, I., Frise, E., Kaynig, V., Longair, M., Pietzsch, T., et al. (2012). Fiji: an open-source platform for biological-image analysis. *Nat. Methods* 9, 676–682. doi: 10.1038/nmeth.2019

Shi, L., Chang, Y., Li, X., Aiken, S., Liu, L., and Wang, J. (2016). Cochlear Synaptopathy and noise-induced hidden hearing loss. *Neural Plast.* 2016:6143164. doi: 10.1155/2016/6143164

Shi, L., Liu, L., He, T., Guo, X., Yu, Z., Yin, S., et al. (2013). Ribbon synapse plasticity in the cochleae of Guinea pigs after noise-induced silent damage. *PLoS One* 8:e81566. doi: 10.1371/journal.pone.0081566

Shi, L., Liu, K., Wang, H., Zhang, Y., Hong, Z., Wang, M., et al. (2015). Noise induced reversible changes of cochlear ribbon synapses contribute to temporary hearing loss in mice. *Acta Otolaryngol.* 135, 1093–1102. doi: 10.3109/00016489.2015.1061699

Shrestha, B. R., Chia, C., Wu, L., Kujawa, S. G., Liberman, M. C., and Goodrich, L. V. (2018). Sensory neuron diversity in the inner ear is shaped by activity. *Cell* 174, 1229–1246.e17. doi: 10.1016/j.cell.2018.07.007

Shuster, B., Casserly, R., Lipford, E., Olszewski, R., Milon, B., Viechweg, S., et al. (2021). Estradiol protects against noise-induced hearing loss and modulates auditory physiology in female mice. *Int. J. Mol. Sci.* 22:12208. doi: 10.3390/ijms222212208

Song, Q., Shen, P., Li, X., Shi, L., Liu, L., Wang, J., et al. (2016). Coding deficits in hidden hearing loss induced by noise: the nature and impacts. *Sci. Rep.* 6:25200. doi: 10.1038/srep25200

Sun, S., Babola, T., Pregernig, G., So, K., Nguyen, M., Palermo, A., et al. (2018). Hair cell Mechanotransduction regulates spontaneous activity and spiral ganglion subtype specification in the auditory system. *Cell* 174, 1247–1263. doi: 10.1016/j.cell.2018.07.008

Suthakar, K., and Liberman, M. C. (2021). Auditory-nerve responses in mice with noise-induced cochlear synaptopathy. *J. Neurophysiol.* 126, 2027–2038. doi: 10.1152/jn.00342.2021

Suzuki, J., Corfas, G., and Liberman, M. C. (2016). Round-window delivery of neurotrophin 3 regenerates cochlear synapses after acoustic overexposure. *Sci. Rep.* 6:24907. doi: 10.1038/srep24907

Valero, M. D., Burton, J. A., Hauser, S. N., Hackett, T. A., Ramachandran, R., and Liberman, M. C. (2017). Noise-induced cochlear synaptopathy in rhesus monkeys (*Macaca mulatta*). *Hear. Res.* 353, 213–223. doi: 10.1016/j.heares.2017.07.003

Wang, Q., and Green, S. H. (2011). Functional role of neurotrophin-3 in synapse regeneration by spiral ganglion neurons on inner hair cells after excitotoxic trauma in vitro. *J. Neurosci.* 31, 7938–7949. doi: 10.1523/JNEUROSCI.1434-10.2011

Wang, Y., Hirose, K., and Liberman, M. C. (2002). Dynamics of noise-induced cellular injury and repair in the mouse cochlea. *J. Assoc. Res. Otolaryngol.* 3, 248–268. doi: 10.1007/s101620020028

Wu, P. Z., Liberman, L. D., Bennett, K., de Gruttola, V., O'Malley, J. T., and Liberman, M. C. (2019). Primary neural degeneration in the human cochlea: evidence for hidden hearing loss in the aging ear. *Neuroscience* 407, 8–20. doi: 10.1016/j.neuroscience.2018.07.053

Wu, P., O'Malley, J. T., de Gruttola, V., and Liberman, M. C. (2020). Age-related hearing loss is dominated by damage to inner ear sensory cells, not the cellular battery that powers them. *J. Neurosci.* 40, 6357–6366. doi: 10.1523/JNEUROSCI.0937-20.2020

Wu, P.-Z., O'Malley, J. T., de Gruttola, V., and Liberman, M. C. (2021). Primary neural degeneration in noise-exposed human Cochleas: correlations with outer hair cell loss and word-discrimination scores. *J. Neurosci.* 41, 4439–4447. doi: 10.1523/JNEUROSCI.3238-20.2021

Zhou, X., Jen, P. H., Seburn, K. L., Frankel, W. N., and Zheng, Q. Y. (2006). Auditory brainstem responses in 10 inbred strains of mice. *Brain Res.* 1091, 16–26. doi: 10.1016/j.brainres.2006.01.107

frontiers | Frontiers in Cellular Neuroscience

TYPE Original Research
PUBLISHED 02 October 2024
DOI 10.3389/fncel.2024.1464670

Check for updates

OPEN ACCESS

EDITED BY
Christian Keine,
University of Oldenburg, Germany

REVIEWED BY
Hainan Lang,
Medical University of South Carolina, United States
Guoqiang Wan,
Nanjing University, China

*CORRESPONDENCE
Karina S. Cramer
✉ cramerk@uci.edu

RECEIVED 14 July 2024
ACCEPTED 30 August 2024
PUBLISHED 02 October 2024

CITATION
Chokr SM, Bui-Tran A and Cramer KS (2024) Loss of C1q alters the auditory brainstem response.
Front. Cell. Neurosci. 18:1464670.
doi: 10.3389/fncel.2024.1464670

COPYRIGHT
© 2024 Chokr, Bui-Tran and Cramer. This is an open-access article distributed under the terms of the Creative Commons Attribution License (CC BY). The use, distribution or reproduction in other forums is permitted, provided the original author(s) and the copyright owner(s) are credited and that the original publication in this journal is cited, in accordance with accepted academic practice. No use, distribution or reproduction is permitted which does not comply with these terms.

Loss of C1q alters the auditory brainstem response

Sima M. Chokr, Ashley Bui-Tran and Karina S. Cramer*

Department of Neurobiology and Behavior, University of California Irvine, Irvine, CA, United States

Neural circuits in the auditory brainstem compute interaural time and intensity differences used to determine the locations of sound sources. These circuits display features that are specialized for these functions. The projection from the ventral cochlear nucleus (VCN) to the medial nucleus of the trapezoid (MNTB) body travels along highly myelinated fibers and terminates in the calyx of Held. This monoinnervating synapse emerges during development as multiple inputs are eliminated. We previously demonstrated that elimination of microglia with a colony stimulating factor-1 inhibitor results in impaired synaptic pruning so that multiple calyceal terminals reside on principal cells of MNTB. This inhibitor also resulted in impaired auditory brainstem responses (ABRs), with elevated thresholds and increased peak latencies. Loss of the microglial fractalkine receptor, CX3CR1, decreased peak latencies in the ABR. The mechanisms underlying these effects are not known. One prominent microglial signaling pathway involved in synaptic pruning and plasticity during development and aging is the C1q-initiated compliment cascade. Here we investigated the classical complement pathway initiator, C1q, in auditory brainstem maturation. We found that C1q expression is detected in the MNTB by the first postnatal week. C1q levels increased with age and were detected within microglia and surrounding the soma of MNTB principal neurons. Loss of C1q did not affect microglia-dependent calyceal pruning. Excitatory and inhibitory synaptic markers in the MNTB and LSO were not altered with C1q deletion. ABRs showed that C1q KO mice had normal hearing thresholds but shortened peak latencies. Altogether this study uncovers the developmental time frame of C1q expression in the sound localization pathway and shows a subtle functional consequence of C1q knockdown.

KEYWORDS

auditory brainstem, microglia, medial nucleus of the trapezoid body (MNTB), neural development, complement

Introduction

Specialized auditory circuits that allow us to process and localize sound with precision rely on carefully orchestrated neurodevelopmental mechanisms. Neural circuit assembly requires axon guidance, synapse strengthening and pruning, and neuroglial communication. Circuit precision is heavily linked with the correct number of synapses, which is ensured through synapse tagging, glial cell contact, and engulfment of the unwanted synaptic connections. During auditory circuit development, synaptic pruning is selective, ensuring robust and accurate means to process and react to a given stimulus. Mechanisms by which high frequency sound sources are localized with precision include a thickly myelinated contralateral connection between the ventral cochlear nucleus (VCN) and the medial nucleus of the

trapezoid body (MNTB). This enveloping synapse is referred to as the calyx of Held. The MNTB is a relay nucleus that provides inhibitory input to the lateral superior olive (LSO) which simultaneously receives excitatory input from spherical bushy cells from the ipsilateral VCN. These bilateral inputs result in an excitatory/inhibitory (E/I) ratio that aids in localization of sound sources (Boudreau and Tsuchitani, 1968; Gjoni et al., 2018; Grothe et al., 2010; Karcz et al., 2011; Magnusson et al., 2008; Tollin, 2003).

During development, multiple protocalyces, or immature calyces, are eliminated resulting in a single calyx innervating a single MNTB cell (Hoffpauir et al., 2006; Holcomb et al., 2013; Morest, 1969; Rodríguez-Contreras et al., 2008; Sätzler et al., 2002). Young, immature calyces are morphologically and electrophysiologically distinct from more mature and elaborate calyces (Hoffpauir et al., 2006; Rodríguez-Contreras et al., 2008; Sierksma et al., 2017). Presumably, the protcalyces that display weaker activity are detected and eliminated. However, this mechanism has yet to be unraveled (Kronander et al., 2019; Sierksma et al., 2020; Sierksma et al., 2017). Some developmental studies have pointed to microglia, the brain's immune cells, as potential candidates for synaptic pruning and circuit formation (Bilimoria and Stevens, 2015; Erblich et al., 2011; Favuzzi et al., 2021; Hoshiko et al., 2012; Kettenmann et al., 2013; Matcovitch-Natan et al., 2016; Milinkeviciute et al., 2019; Paolicelli et al., 2011; Schafer et al., 2012). In the brainstem, loss of microglia through pharmacological inhibition of the colony stimulating factor 1 receptor (CSF1R), essential for microglial survival and proliferation, impairs calyceal elimination, resulting in higher instances of polyinnervated MNTB cells in mature animals (Milinkeviciute et al., 2019). Treatment cessation and microglial return restores the 1:1 synapse-cell ratio (Milinkeviciute et al., 2021b). Functionally, loss of microglia leads to auditory brainstem response (ABR) deficits, as shown by higher hearing thresholds and increased peak latencies (Milinkeviciute et al., 2021b). Microglial repopulation largely rescues these functional deficits as well (Milinkeviciute et al., 2021b). Long-term CSF1R inhibition prevents pruning recovery, elevates inhibitory protein levels, and sustains and worsens ABR threshold and latency deficits (Chokr et al., 2022). Investigation of a major signaling pathway, through the microglial fractalkine receptor (CX3CR1), revealed that congenital depletion of CX3CR1 does not affect calyceal pruning. However, CX3CR1 mutants have decreased ABR peak latencies, lack tonotopic size gradients in the MNTB, and do not display age-related decrease of inhibitory proteins, suggesting defects in inhibitory synaptic pruning (Milinkeviciute et al., 2021a). Together, these studies support a role for microglia in the formation of sound localization circuitry. However, our understanding of the mechanisms by which microglia regulate pruning and circuit maturity remains deficient.

Previous studies have demonstrated that that synapses are removed during neural development through microglia-secreted complement protein C1q-tagging and opsonization (Cong et al., 2022; Fonseca et al., 2017; Fonseca et al., 2004; Presumey et al., 2017; Stevens et al., 2007). The complement system is traditionally recognized for its role in immune defense and inflammation but in the brain has multifaceted functions in neurodevelopment and degeneration (Zhang et al., 2023). C1q is the initiator protein for the classical complement cascade. Once bound to pathogen or debris, a protease cascade is triggered where either complement protein C3 leads to macrophage/microglia-mediated excision or C3 triggers the terminal activation of the complement pathway which leads to lysis (Schafer et al., 2012; Stevens et al., 2007; Zhang et al., 2023). C1q is known as an "eat me" signal for synapse elimination, which in the context of neural development is pivotal to ensure circuit accuracy and achievement of the E/I balance (Dejanovic et al., 2022). However, the effects of this signal are heterogeneous throughout brain regions and time frames. In the visual cortex, loss of C1q does not affect synapse density or microglial phagocytosis (Cong et al., 2022; Zhang et al., 2023). In an epilepsy model, C1q has a neuroprotective role and prevents synaptic pruning, its consequences appearing in seizures from improper E/I ratios (Chu et al., 2010).

Our understanding of C1q in auditory system development is lacking, despite implications on regulation of E/I ratios, an essential component for accurate auditory processing. In the cochlea, complement C1q Like 1 (C1QL1), a secreted component of C1Q-related protein, is expressed in adult inner and outer hair cells (Liu et al., 2018; Liu et al., 2014; Qi et al., 2021). C1QL1 is expressed in outer hair cells in a tonotopic gradient along the cochlea (Biswas et al., 2021). Loss of C1QL1 reduces the number of nerve fibers innervating hair cells, progresses loss of outer hair cells, leads to increased hearing thresholds, and increases peak 1 latency in the ABR (Qi et al., 2021).

The role of C1q in auditory brainstem development has not been investigated. Here, we studied the effects of C1q in development of auditory brainstem circuitry. We used a C1q knockout (KO) model to test whether loss of C1q affects calyceal pruning levels, synaptic protein expression, and auditory function. We found that, like microglial markers, C1q expression is detected as early as postnatal day (P) 8 and increases by P14, just after hearing onset. C1q expression was detected both in a colocalized fashion with vesicular glutamate transporter 1/2 (VGLUT1/2) protein surrounding MNTB cells and in a net-like pattern throughout the MNTB independent of VGLUT1/2 puncta. Super-resolution imaging revealed that C1q surrounds MNTB neurons in close proximity to VGLUT1/2-positive calyceal synapses. We also found that C1q is present within microglial somata and processes. Loss of C1q did not affect calyceal pruning or calyx size. Neither excitatory nor inhibitory synaptic protein levels were affected in the MNTB or LSO. Auditory brainstem responses showed that C1q KO mice had normal hearing thresholds, but faster peak latencies along the ascending auditory pathway. These data support that C1q regulates some functional aspects of auditory circuit development, but it is not responsible for regulating E/I synapses in the superior olivary complex.

Methods

Animals

We used C57/BL6 mice of both sexes at postnatal day (P) 8 ($n = 12$), P14 ($n = 18$), and P28 ($n = 27$). To investigate the effects of C1q depletion, we used ($n = 41$, P28) C1qa knock-out mice (C1q KO) (Jackson lab ID: 031675) (Fonseca et al., 2017). C1q KO was routinely confirmed during colony maintenance with qPCR (Fonseca et al., 2017). For C1q localization studies in relation to microglia, we used $CX3CR1^{+/GFP}$ mice at P8 ($n = 3$) and P14 ($n = 10$) (Jung et al., 2000). All animal procedures were performed in accordance with the Institutional Animal Care and Use Committee at the University of California, Irvine (UCI). Mice were reared in a standard day/light

cycle and received food and water *ad libitum*. Mice were housed in groups with no more than 5 adult mice per cage. Litters remained with the nursing dam until at least P21.

Neuronal tracing

Calyceal pruning was assessed using a dye-insertion method as previously described (Chokr et al., 2022; Milinkeviciute et al., 2021a; Milinkeviciute et al., 2021b; Milinkeviciute et al., 2019). Briefly, P28 mice were transcardially perfused with oxygenated artificial cerebrospinal fluid (aCSF; 130 mM NaCl, 3 mM KCl, 1.2 mM KH2PO4, 20 mM NaHCO3, 3 mM HEPES, 10 mM glucose, 2 mM CaCl2, 1.3 mM MgSO4 infused with 95% O2 and 5% CO2). Brains were extracted and transferred to oxygenated solution for approximately 30 min and were then transferred to an aCSF filled petri dish. A glass micropipette was filled with rhodamine dextran (RDA; MW 3000, Invitrogen; in solution of 6.35% RDA with 0.4% Triton-X100 in PBS). The pipette was inserted in the midline to aim for the ventral acoustic stria and RDA was electroporated at 5 pulses/s at 55 V for 50 ms using an Electro Square Porator (ECM830; BTX). These pulses result in a sparse dye labeling of globular bushy cell axons and their calyceal terminals. Brains were transferred back to the oxygenated aCSF and the dye was allowed to travel for approximately 2 h. The tissue was then transferred to 4% paraformaldehyde solution refrigerated overnight, and then transferred to a 30% sucrose solution in 0.1 M PBS until cryosectioning. Brainstems were coronally cryosectioned at 20 µm in a series of 5 alternating slides. Tissue sections containing RDA-labeled calyces were immunohistochemically stained for vesicular glutamate transporter 1/2 (VGLUT1/2).

Determination of mono- or polyinnervation

RDA-filled calyces were imaged using confocal microscopy (Leica SP8, 40X oil objective, zoom: 2.37, pinhole: 0.43). *Z*-stack images of Nissl, RDA, and VGLUT1/2 were acquired at a resolution of 1024 × 1024, with a *z*-step size of 0.32 µm. Gain and offset were adjusted accordingly if the intensity was noticeably different in comparison with other sections on the same slide.

Image stacks were reconstructed and analyzed using Imaris software (version 10.0; Bitplane). Calyces were assessed for quality by ensuring that each calyx was fully visible within the *z*-stack and had a visible preterminal axon segment. Calyces were reconstructed using the surface module with 0.125–0.3 surface detail to capture an accurate depiction of calyx processes shape. Calyceal surface area and volume were measured.

Mono- or polyinnervation status of the MNTB neuron was determined by visualizing the RDA-filled calyx with a Nissl-stained MNTB cell. MNTB cells contacted by an RDA-filled calyx, without VGLUT1/2 immunolabeling surrounding non-calyceal spaces, were designated as monoinnervated. Cells were classified as polyinnervated if VGLUT1/2 labeling surrounded non-calyceal spaces around the cell. Neurons were only considered polyinnervated if the non-calyceal VGLUT1/2 immunolabel surrounded ~25% or more of the MNTB cell (Milinkeviciute et al., 2019). We compared the percentage of mono- versus polyinnervated neurons in control and C1q KO mice.

Immunolabeling

Brain sections were stained for complement protein C1q and vesicular glutamate transporter 1/2 (VGLUT1/2), vesicular glutamate transporter 2 (VGLUT2), or glycine transporter 2 (GLYT2). Mounted brain sections were outlined with hydrophobic PAP pen barrier and kept on a slide warmer for 10 min until dry. Sections were rinsed with 0.1 M phosphate buffer saline (PBS) for 10 min then incubated in 0.1% sodium dodecyl sulfate in PBS for antigen retrieval (5 min) and rinsed with PBS. Next, sections were incubated in blocking solution containing 5% normal goat serum (NGS; Vector Laboratories S-1000) and 0.3% Triton X-100 (Acros 9,002-93-1) in 0.1 M PBS for 1 h at room temperature, followed by overnight incubation in blocking solution containing the vesicular glutamate transporter 1/2 (VGLUT1/2), VGLUT2 antibody (1,200 dilution, Synaptic Systems, 135,503 or 135,418), or GLYT2 antibody (1,200 dilution, Synaptic Systems, 272,003). Tissue probed for C1q was incubated in anti-mouse C1q (rabbit monoclonal, clone 27.1) culture supernatant as described in Fonseca et al. (2017), Li et al. (2008), and Stephan et al. (2013) with 0.3% Triton X-100 and 0.5% bovine serum albumin. The tissue was then rinsed with PBS and incubated for 90 min in blocking buffer containing goat anti-rabbit tagged with an Alexa (Invitrogen) fluorophore (1,500 dilution, anti-rabbit 647, A21244, anti-rabbit 555, A21428 or anti-guinea pig A11073). Sections were then washed with PBS and incubated in blue fluorescent Nissl stain (NeuroTrace 435/455, Life Technologies N21479) diluted 1:200 in 0.3% Triton X-100 in 0.1 M PBS. Sections were rinsed with PBS and coverslipped with Glycergel mounting medium (Dako C0563). Statistical analyses for immunolabeling results are presented in Table 1.

Fluorescent imaging and analysis

Immunolabeled sections were visualized and imaged with a Zeiss Axioskop-2 microscope, an Axiocam camera, and Zen image analysis software. We analyzed the auditory nuclei on both sides of the midline. For each animal in our analysis, at least three sections were included per primary antibody stain. Images were exported and analyzed using FIJI imaging software. The corresponding Nissl image was used to guide outlines for the nuclei using the ROI function, and these outlines were then used to calculate percent coverage in the ROI of the channel containing the primary antibody stain as previously described (Milinkeviciute et al., 2021b; Milinkeviciute et al., 2019).

Super-resolution microscopy

Super-resolution images of GFP-microglia, RDA-labeled calyces, and C1q staining were obtained with the ZEISS Elyra 7 with Lattice SIM^2 microscope. Stained sections were imaged with a 63× oil immersion lens with 2.0 laser power settings. Following confirmation of C1q presence throughout each selected microglia, approximately 6–9 µm *Z*-stack images were obtained in 0.3 µm increments. These imaging settings led to a 60 nm resolution, allowing us to obtain accurate spatial settings of C1q protein relative to microglial somas and branches. Images were then processed through the Zeiss black software with SIM^2 settings set to "Standard Fixed." Once processed, images were converted to IMARIS compatible files. We used the

TABLE 1 Immunolabeling analyses.

C1q coverage across tonotopic axis			
2-way Anova			
Source of variation	**p value**	**F (DFn, DFd)**	
Interaction	<0.0001	F (2, 66) = 45.67	
Age	0.1332	F (1, 66) = 2.311	
MNTB region	0.0089	F (2, 66) = 5.072	
Šídák's multiple comparisons test	**p value**	**t**	**DF**
P8:Medial vs. P8:Central	0.9995	0.8576	66
P8:Medial vs. P8:Lateral	<0.0001	5.702	66
P8:Medial vs. P14:Medial	<0.0001	5.52	66
P8:Central vs. P8:Lateral	0.0001	4.844	66
P8:Central vs. P14:Central	>0.9999	0.2072	66
P8:Lateral vs. P14:Lateral	<0.0001	7.946	66
P14:Medial vs. P14:Central	<0.0001	6.615	66
P14:Medial vs. P14:Lateral	<0.0001	9.169	66
P14:Central vs. P14:Lateral	0.1776	2.554	66
Polyinnervation ratio			
Mann–Whitney test	**p value**		
WT vs. C1q KO	0.9365		
Descriptive statistics	WT	C1q KO	
Mean	0.2801	0.2133	
Std. Deviation	0.1564	0.03613	
Std. Error of Mean	0.07818	0.01616	
Calyx surface area			
Mann–Whitney test	**p value**		
WT vs. C1q KO	0.6468		
Descriptive statistics	WT	C1q KO	
Mean	575.2	551.3	
Std. Deviation	225.5	234.4	
Std. Error of Mean	47.03	45.11	
Calyx volume			
Mann–Whitney test	**p value**		
WT vs. C1q KO	0.4252		
Descriptive statistics	WT	C1q KO	
Mean	240.9	211	
Std. Deviation	116.5	109.2	
Std. Error of Mean	24.3	22.29	
VGLUT 1/2 MNTB coverage total			
Mann–Whitney test	**p value**		
WT vs. C1q KO	0.1143		
Descriptive statistics	WT	C1q KO	
Mean	0.04362	0.08103	
Std. Deviation	0.01032	0.04266	
Std. Error of Mean	0.005159	0.01742	

(Continued)

TABLE 1 (Continued)

VGLUT1/2 MNTB coverage across tonotopic axis			
2-way Anova			
Source of variation	**p value**	**F (DFn, DFd)**	
Interaction	0.4335	F (2, 24) = 0.8656	
Tonotopic region	0.0125	F (2, 24) = 5.291	
Genotype	0.0132	F (1, 24) = 7.159	
Tukey's multiple comparisons test	**P value**	**q**	**DF**
Medial			
WT vs. C1q KO	0.6248	0.7006	24
Central			
WT vs. C1q KO	0.0326	3.209	24
Lateral			
WT vs. C1q KO	0.0737	2.645	24
WT			
Medial vs. Central	0.4475	1.74	24
Medial vs. Lateral	0.6919	1.166	24
Central vs. Lateral	0.9135	0.5741	24
C1q KO			
Medial vs. Central	0.0052	4.935	24
Medial vs. Lateral	0.0451	3.601	24
Central vs. Lateral	0.619	1.334	24
VGLUT1/2 LSO coverage total			
Mann–Whitney test	**p value**		
WT vs. C1q KO	0.1167		
Descriptive statistics	WT	C1q KO	
Mean	0.4606	0.4091	
Std. Deviation	0.03059	0.04696	
Std. Error of Mean	0.01766	0.01775	
2-way Anova			
Source of variation	**p value**	**F (DFn, DFd)**	
Interaction	0.5658	F (2, 16) = 0.5903	
Tonotopic region	<0.0001	F (1.574, 12.59) = 44.95	
Genotype	0.1138	F (1, 8) = 3.151	
Tukey's multiple comparisons test	**p value**	**q**	**DF**
Medial			
WT vs. C1q KO	0.8061	0.3622	6.23
Central			
WT vs. C1q KO	0.2362	2.019	3.497
Lateral			
WT vs. C1q KO	0.0248	3.909	7.913
WT			
Medial vs. Central	0.0067	23.11	2
Medial vs. Lateral	0.0853	6.26	2

(Continued)

TABLE 1 (Continued)

Central vs. Lateral	0.1994	3.828	2
C1q KO			
Medial vs. Central	0.0004	11.95	6
Medial vs. Lateral	0.0946	3.62	6
Central vs. Lateral	0.0051	7.289	6
GLYT2 MNTB coverage total			
Mann–Whitney test	**p value**		
WT vs. C1q KO	>0.9999		
Descriptive statistics	WT	C1q KO	
Mean	0.01765	0.02799	
Std. Deviation	0.01247	0.02849	
Std. Error of Mean	0.005577	0.01274	

GLYT2 MNTB coverage across tonotopic axis			
2-way Anova			
Source of variation	**p value**	**F (DFn, DFd)**	
Interaction	0.5303	$F(2, 16) = 0.6602$	
Tonotopic region	0.1395	$F(1.962, 15.69) = 2.245$	
Genotype	0.455	$F(1, 8) = 0.6164$	
Tukey's multiple comparisons test	**p value**	**q**	**DF**
Medial			
WT vs. C1q KO	0.4129	1.286	4.163
Central			
WT vs. C1q KO	0.4635	1.101	6.548
Lateral			
WT vs. C1q KO	0.8432	0.2904	6.934
WT			
Medial vs. Central	0.4304	1.954	4
Medial vs. Lateral	0.0597	4.756	4
Central vs. Lateral	0.9268	0.5303	4
C1q KO			
Medial vs. Central	0.4172	1.998	4
Medial vs. Lateral	0.966	0.3558	4
Central vs. Lateral	0.3427	2.272	4
GLYT2 LSO coverage total			
Mann–Whitney test	**p value**		
WT vs. C1q KO	>0.9999		
Descriptive statistics	WT	C1q KO	
Mean	0.2994	0.294	
Std. Deviation	0.03702	0.05418	
Std. Error of Mean	0.01851	0.02423	

GLYT2 LSO coverage across tonotopic axis			
2-way Anova			

(Continued)

TABLE 1 (Continued)

Source of variation	**p value**	**F (DFn, DFd)**	
Interaction	0.5518	$F(2, 14) = 0.6206$	
Tonotopic region	<0.0001	$F(1.146, 8.025) = 50.73$	
Genotype	0.7912	$F(1, 7) = 0.07569$	
Tukey's multiple comparisons test	**p value**	**q**	**DF**
Medial			
WT vs. C1q KO	0.7618	0.4466	6.676
Central			
WT vs. C1q KO	0.7159	0.5361	6.981
Lateral			
WT vs. C1q KO	0.4895	1.032	6.883
WT			
Medial vs. Central	0.0152	9.155	3
Medial vs. Lateral	0.25	2.884	3
Central vs. Lateral	0.0056	12.98	3
C1q KO			
Medial vs. Central	0.0687	4.538	4
Medial vs. Lateral	0.0917	4.103	4
Central vs. Lateral	0.0001	25.63	4

IMARIS 10.0 software for background subtraction and representative image editing.

Auditory brainstem responses

Auditory brainstem responses (ABRs) were tested on 7 control and 11 C1q KO mice of both sexes at P28. Mice used for ABRs were selected at random and used for synaptic protein assessment following collection. We used the same ABR recording methods as previously described (Chokr et al., 2022; Milinkeviciute et al., 2021b). Mice were anesthetized with an intramuscular injection of ketamine (75 mg/kg, KetaVed, VEDCO) and xylazine (15 mg/kg, AnaSed, NADA #139-236). Body temperature was maintained at 35°C via a far infrared warming pad (Kent Scientific, RT-0501) and sterile ocular lubricant (Puralube Vet Ointment, 006PHM02-1-8) was applied on the eyes. We inserted three pin electrodes subcutaneously with the positive, negative, and ground electrodes at the vertex, right cheek, and back near the right leg, respectively. The electrodes were connected to Tucker-Davis Technologies (TDT) RA4PA 4-channel Medusa amplifier, which was connected to a TDT RA16 Medusa Base Station. The ABR was performed in a sound-attenuating chamber (102 × 98 × 81 cm, Industrial Acoustics Company). Click and pure tone stimuli were generated using the TDT SigGen software version 4.4. Sound was presented with the TDT MF1 Multi-Function Speaker through an ear tube inserted in the animal's left ear, with stimuli repeated 500 times at a rate of 21 stimuli per second. The stimuli were emitted using the TDT RP2.1 enhanced real time processor and the sound level was controlled with the TDT PA5 programmable attenuator. The recorded responses were amplified by the TDT SA1

stereo power amp and filtered through BioSig software version 4.4. Each sample ABR was recorded for 12 ms in response to 100 µs click or 3 ms pure tone stimuli (4, 8, 12, 16, 24, 32 kHz) and decreasing sound intensities (5 dB SPL steps from 80 to 10 dB SPL). An averaged response was computed at each sound level and was used for ABR analysis.

ABR analysis

Averaged ABR recordings were assessed for hearing threshold, peak latency, interpeak latency, and peak amplitude. We defined hearing threshold as the lowest sound intensity at which peak I level (µV) was ≥4 standard deviations above the noise level (Bogaerts et al., 2009; Chokr et al., 2022; Milinkeviciute et al., 2021b). Peaks were manually detected and labeled by a blinded observer using BioSig, and data were exported for analysis. Peak latency was determined as the time from stimulus onset to the apex of the peak. Interpeak latency was calculated as the difference of absolute peak time between peaks I–II, II–III, III–IV, I–III, and I–IV. Peak amplitude was determined as the change in microvolts between the preceding trough and the apex of the subsequent peak. All ABR mean, standard error, and statistics are presented in Supplementary Table S1.

Statistics

Multiple litters were used for each experimental group. Littermate controls were not used for experiments that included the congenital mutation as the breeders for C1q KO were mutants. Quantitative results are presented as the mean ± SEM. All statistical analyses were performed using Prism Software (v9.3.1; GraphPad Software). Comparisons between genotype or age group were made with a Welch's *t* test, a Mann–Whitney test, or a two-way ANOVA with Sidak's multiple comparisons test unless otherwise indicated. Statistical significance was accepted at $p < 0.05$. Details of statistical analyses are presented in Table 1 and Supplementary Table S1.

Results

C1q is present in MNTB during circuit refinement

Microglia appear in the auditory brainstem as early as P0 in the ventral cochlear nucleus (VCN) and by P6 in the medial nucleus of the trapezoid body (MNTB) (Dinh et al., 2014). Microglia are the primary source of C1q in the brain and C1q increases with age throughout the brain (Fonseca et al., 2017; Stephan et al., 2013). In other brain regions, C1q plays a developmental role in synapse protection, elimination, and ultimately circuit formation. Whether C1q is present in the brainstem during a period of circuit refinement was unknown. Here, we characterized C1q expression before and after hearing onset in wildtype mice.

We assessed whether C1q is present during microglia-dependent circuit formation. At postnatal day (P) 8, C1q was expressed throughout the MNTB with an average areal coverage ratio of 0.2331 ± 0.02521 ($n = 12$) (Figures 1A,B). At P8, C1q surrounded MNTB cells and appeared in clusters resembling microglia (Figure 1A). At P14, C1q coverage ratios (0.3268 ± 0.0157, $n = 18$) significantly increased with age ($p = 0.0019$, Mann Whitney U = 37) and patterns appeared more uniformly diffuse (Figures 1A,B). Before hearing onset, C1q expression across the tonotopic axis significantly diminished in coverage from the medial (0.3594 ± 0.0013) and central (0.3037 ± 0.0223) regions to low frequency lateral regions (0.1193 ± 0.0103), respectively (Medial-Central $p = 0.995$, $t = 0.8576$, df = 66, Medial-Lateral $p < 0.0001$, $t = 5.702$, df = 66, Central-Lateral $p = 0.0001$, $t = 4.844$, df = 66) (Figure 1B). This expression gradient shifted at P14. C1q expression was significantly lower in medial regions (0.1761 ± 0.0019), remained comparable in central regions (0.3237 ± 0.0091) and increased in lateral regions (0.3829 ± 0.0097) (Medial-Central $p < 0.0001$, $t = 6.615$, df = 66, Medial-Lateral $p < 0.0001$, $t = 2.554$, df = 66, Central-Lateral $p = 0.1776$, $t = 2.554$, df = 66) (Figure 1B). We also found that these expression values differed with age, where medial C1q expression was significantly diminished after hearing onset ($p < 0.0001$, $t = 5.520$, df = 66) and lateral C1q expression was significantly elevated after hearing onset ($p < 0.0001$, $t = 7.946$, df = 66) (Figure 1B). C1q KO mice lacked any C1q expression in the brainstem (Figure 1A). Therefore, we determined that C1q is present in the MNTB during a period of microglia-dependent pruning and circuit refinement, and that tonotopic C1q expression patterns shift after hearing onset.

We further investigated C1q expression by obtaining super-resolution images of C1q before and after hearing onset, and in the mature animal. Microglia are the primary source of C1q in the brain but whether microglia express C1q during development was not known. At P8, we found that C1q is mostly present within microglial cells in the VCN, LSO, and MNTB, with remarkably less expression in the surrounding area (Figure 1C). In microglia with larger soma or less branching, indicating younger microglia, C1q levels appeared denser (Figure 1C). After hearing onset, C1q appeared present both within and outside of microglia, with higher density in microglia with larger somas (Figure 1C). Further, we found that at P28, C1q was present in close proximity to calyces visualized with rhodamine-dye (RDA) and VGLUT2 co-labeling (Figure 1D). These data indicated the anatomical location of C1q during MNTB development and lead us to investigate whether calyceal pruning involves C1q.

C1q removal does not impair calyceal monoinnervation

We found that C1q levels in wildtype animals are elevated just after hearing onset, a period of microglia-dependent calyceal refinement. Therefore, we tested whether loss of microglial C1q tagging affects the establishment of calyceal monoinnervation of MNTB neurons. We sparsely labeled calyces using rhodamine dye (RDA) injections in the ventral acoustic stria and immunolabeled VGLUT1/2 on those sections to detect calyces in the MNTB. Principal cells that were almost exclusively surrounded by an RDA-labeled calyx were determined as monoinnervated, while cells surrounded by an RDA calyx and at least 25% VGLUT1/2 labeling were determined polyinnervated (see Materials and Methods). Confocal images were reconstructed and analyzed on IMARIS software.

We assessed calyces for innervation and size in 4 control and 5 C1q KO mice at P28. Both groups showed mono- and polyinnervated MNTB cells (Figures 2A,B). We determined the percentage of mono- vs. polyinnervated cells in each animal (WT 0.28 ± 0.07% of cells, C1q

10.3389/fncel.2024.1464670

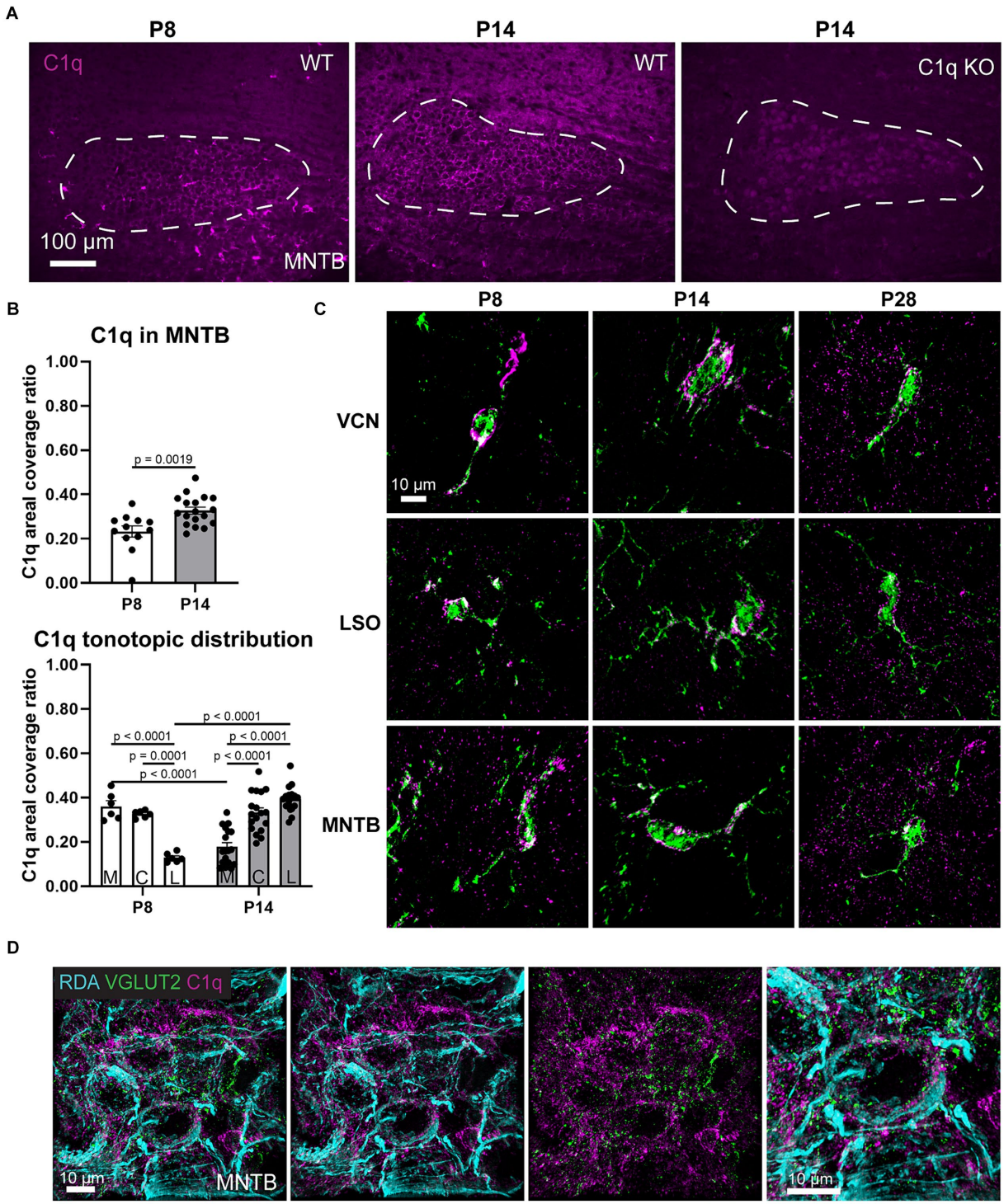


FIGURE 1
C1q is expressed in the developing auditory brainstem. **(A)** At P8, C1q (magenta) can be detected in the MNTB and appears in clusters resembling glia. P14 C1q expression appears dispersed throughout the MNTB. There was no immunoreactivity in C1q KO mice. **(B)** C1q levels significantly increase after hearing onset. At P8, C1q levels are higher in medial regions and at P14, C1q levels are higher in lateral regions. **(C)** Super-resolution images visualizing C1q expression (magenta) within GFP-microglia (green). C1q can be detected throughout the microglial somas and branches. In the mature animal (P28) C1q protein was also detected outside of microglial cells. **(D)** Rhodamine-dye labeled calyces (cyan) with C1q (magenta) and excitatory synapse marker VGLUT2 (green). C1q tags calyces and surrounds the non-calyceal regions around MNTB cells.

KO 0.21 ± 0.02% of cells) and found that C1q deletion does not affect calyceal elimination during development ($p = 0.3790$, $t = 0.9289$, df = 7, Welch's t-test) (Figure 2C). Next, we measured the calyx surface area of RDA labeled calyces in WT (572.3 ± 47.03 µm^2) and C1q KO (551.3 ± 45.11 µm^2). We found that C1q elimination does not affect calyx surface area ($p = 0.7154$, $t = 0.3667$, df = 48, Welch's t-test)

(Figure 2D). Calyx volume was also assessed in both groups (WT 240.9 ± 24.30 μm^3, C1q KO 211.0 ± 22.29 μm^3). We did not see effects of C1q removal on calyx volume ($p = 0.3688$, $t = 0.9079$, df = 45, Welch's t-test; Figure 2E). Altogether we found that removal of the microglial C1q signaling pathway did not affect the robust establishment of monoinnervation in the MNTB.

Loss of C1q does not alter excitatory or inhibitory synaptic protein expression

Pharmacological elimination of microglia disrupted excitatory calyceal pruning (Chokr et al., 2022; Milinkeviciute et al., 2019). Congenital elimination of CX3CR1 impaired inhibitory synapse elimination (Milinkeviciute et al., 2021a). In the lateral geniculate nucleus, loss of C1q leads to an abnormal E/I synapse ratio (Presumey et al., 2017; Stevens et al., 2007). However, some aspects of neural development and synaptic strengthening do not depend on C1q (Welsh et al., 2020). Therefore, we tested whether C1q KO mice exhibit an changes in excitatory and inhibitory presynaptic protein levels. We assessed excitatory protein expression by immunolabeling VGLUT1/2 puncta in coronal brainstem sections. In the MNTB, VGLUT1/2 areal coverage ratios were comparable between wildtype (0.04362 ± 0.01) and C1q KO (0.08103 ± 0.02) ($p = 9.1143$, Mann–Whitney test) (Figures 3A,B). VGLUT1/2 expression across the MNTB tonotopic showed a significant interaction between tonotopic region and genotype ($p = 0.0147$, 2-way ANOVA, F (2, 16) = 5.559) (Figure 3B). However, multiple comparison analysis did not indicate genotype differences in any of the regions (medial $p = 0.7722$, central $p = 0.1612$, lateral $p = 0.2403$) (Figure 3B). The LSO predominantly receives excitatory input from the ipsilateral VCN. We tested whether loss of C1q affects VGLUT1/2 expression in the LSO. We found that VGLUT1/2 levels were comparable between WT (0.4606 ± 0.017) and C1q KO mice (0.4091 ± 0.012) ($p = 0.1167$, Mann–Whitney test). Tonotpic VGLUT1/2 expression did not differ based on genotype ($p = 0.5658$, 2-way ANOVA, F (2, 16) = 0.5903) (Figures 3A,B).

We previously found that loss of microglial fraktalkine receptor led to increased GLYT2 levels in the MNTB (Milinkeviciute et al., 2021a). Here, we tested whether C1q regulates inhibitory synapse levels in the superior olivary complex. We found that C1q KO did not alter GLYT2 expression in the MNTB ($p > 0.9999$, Mann–Whitney test) in the MNTB (Figures 3C,D). GLYT2 levels across the MNTB tonotopic axis were similar between WT and C1q KO mice ($p = 0.5303$, F (2, 16) = 0.6602, 2-way ANOVA) (Figure 3D). GLYT2 levels were also similar in the LSO ($p > 0.9999$, Mann–Whitney test) and did not differ based on tonotopic region ($p = 0.5518$, F (2, 14) = 0.6206, 2-way ANOVA) (Figure 3D). Together, these data show that congenital loss of C1q did not affect excitatory or inhibitory synapse levels in the superior olivary complex.

C1q depletion alters the auditory brainstem responses

The ABR waveform reflects overall activity in the cochlea, spiral ganglion cells, and VIIIth nerve (peak I), cochlear nucleus (peak II), superior olivary complex which includes MNTB and LSO (peak III), and lateral lemniscus (peak IV) (Henry, 1979; Jewett, 1970; Jewett and Williston, 1971). Mice that underwent pharmacological microglia depletion showed significant hearing loss and abnormal auditory brainstem function, as detected by their elevated ABR thresholds, delayed peak latencies, and reduced peak amplitudes (Chokr et al.,

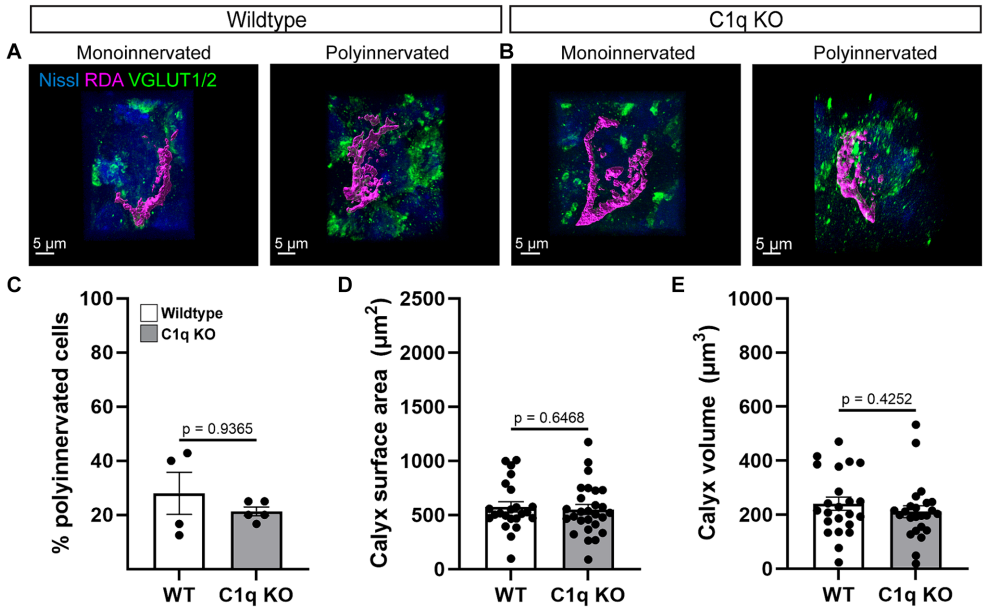


FIGURE 2
C1q deletion does not affect calyceal pruning. **(A,B)** Rhodamine-dye (RDA) labeled calyces (magenta) were 3D reconstructed and visualized with a Nissl (blue) and VGLUT1/2 (green) colabel. Mono- and polyinnervated cells were detected in both genotypes. **(C)** C1q deletion did not alter pruning. **(D)** Calyx surface areas in C1q KO were comparable with controls. **(E)** Calyx volumes in C1q KO were similar to control sizes.

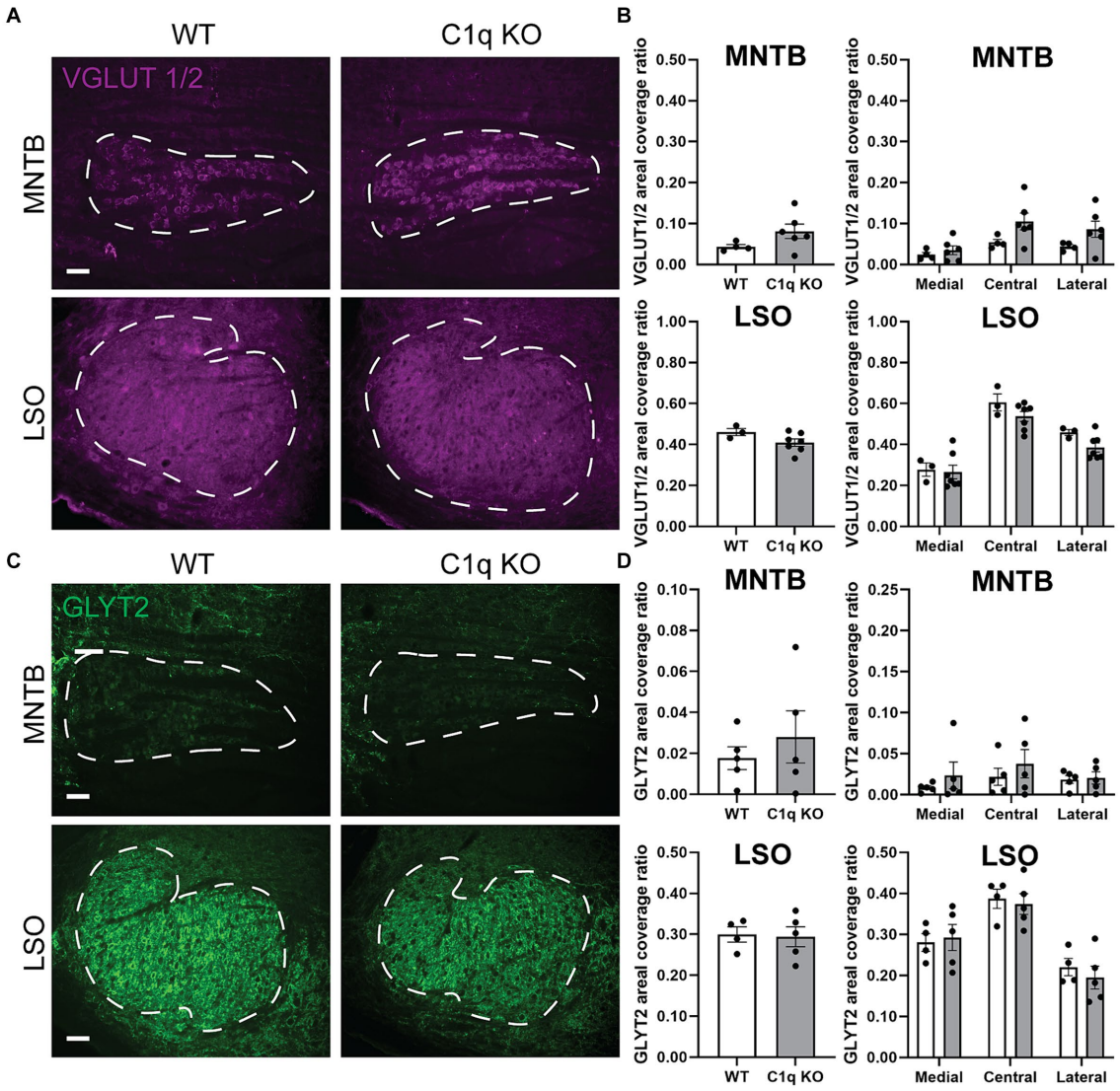


FIGURE 3
Excitatory and inhibitory presynaptic proteins are not altered with C1q knockout. **(A)** Immunolabeling of excitatory protein marker VGLUT1/2 (magenta) in WT and C1q KO mice in the MNTB and LSO, respectively. **(B)** C1q deletion did not alter VGLUT levels in the MNTB or LSO. **(C)** Immunolabeling of the inhibitory synapse marker GLYT2 (green) in WT and C1q KO mice in the MNTB and LSO, respectively. **(D)** GLYT2 levels were not affected by C1q knockout.

2022; Milinkeviciute et al., 2021b). Some recovery in the ABR was detected following microglial return (Milinkeviciute et al., 2021b). Mice that lack the C1QL1 protein in the cochlea also have extensive hearing loss as shown by their elevated hearing thresholds and delayed peak 1 latencies (Qi et al., 2021). Here, we assessed whether loss of microglia-secreted C1q affects the mouse hearing profile. Seven wildtype (WT) and 11 C1q KO (KO) mice of both sexes at P28 were used for ABR comparisons. All ABR statistical analyses indicating peak amplitude, latency, and interpeak latency differences are shown in Supplementary Table S1. Statistical significance is reported below as $p < 0.05$.

Click and pure tone (4, 8, 12, 16, 24, and 32 kHz) stimuli were presented to the left ear at decreasing intensities (80–10 dB SPL, 5 dB SPL increments). Hearing threshold in response to both click and pure tones and was defined as the lowest intensity at which peak I level (μV) was greater than or equal to 4 standard deviations from noise (Milinkeviciute et al., 2021b). Click thresholds in C1q KO mice were comparable to age-matched controls ($p = 0.3559$, Mann Whitney $U = 24$) (Figure 4A). C1q KO mice appeared to have significantly lower hearing thresholds at 16 kHz ($p = 0.0148$, $t = 4.107$, df = 9.272) (Figure 4B). All other tested frequencies were comparable to controls (4 kHz $p = 0.7397$, $t = 1.429$, df = 6.241; 8 kHz $p = 0.7170$, $t = 6.818$, df = 6.528; 12 kHz $p = 0.1104$, $t = 3.085$, df = 9.272, 24 kHz $p = 0.8767$, $t = 1.093$, df = 12.74; 32 kHz $p = 0.3223$, $t = 2.100$, df = 9.763) (Figure 4B). Sample traces in Figure 4C illustrate these values. These data show that C1q KO mouse hearing thresholds are largely comparable to age-matched controls with the exception of diminished thresholds at a central frequency.

We tested the effects of C1q removal on ABR peak amplitudes. Peak amplitude was defined as the difference in level (μV) between the apex of the peak and its preceding trough. All statistical analyses are detailed in Supplementary Table S1. C1q KO mice showed

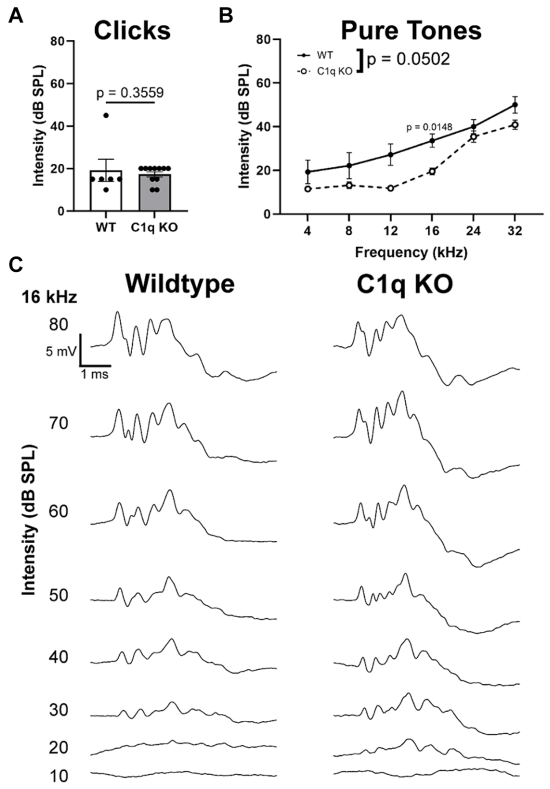


FIGURE 4
Hearing thresholds in C1q KO mice and controls. **(A)** Hearing thresholds did not differ between controls and C1q KO mice in response to click stimuli. **(B)** C1q KO mice had slightly decreased hearing thresholds compared to age-matched controls. **(C)** Sample traces for wildtype and C1q KO mice.

normal peak I amplitudes at every frequency tested (Supplementary Table S1; Figure 5A). At peak II, C1q KO mice showed decreased peak amplitude at 8 kHz, but the other frequencies tested did not show any differences (Supplementary Table S1; Figure 5B). At the level of the SOC, peak III amplitudes in C1q KO were comparable to controls at every frequency level (Supplementary Table S1; Figure 5C). Peak IV amplitudes, which reflect the projections of SOC activity to the LL along the ascending auditory pathway, showed significantly elevated peak amplitudes at 4, 12, 16, and 24 kHz (Supplementary Table S1; Figure 5D). Taken together, C1q KO mice showed largely unaffected peak amplitudes in the earlier peaks until peak IV, where peak amplitudes appeared larger than those of age-matched controls. Increases in amplitude may reflect deficits in auditory processing (Abadi et al., 2016; Schaette and McAlpine, 2011).

Loss of microglia leads to delayed peak latencies, especially at the lower frequencies, whereas the elimination of microglial fractalkine signaling decreases peak latencies, especially at the higher frequencies (Chokr et al., 2022; Milinkeviciute et al., 2021a; Milinkeviciute et al., 2021b). Here, we assessed whether loss of C1q affects peak latencies along the ascending auditory pathway. C1q KO mice showed significantly decreased peak I latencies at 4, 8, and 12 kHz, the mid to high frequencies were not affected (Supplementary Table S1; Figure 6A). At peak II, C1q KO mice showed significantly reduced peak latencies at 12 and 16 kHz, the other frequencies were not affected (Supplementary Table S1; Figure 6B). Peak III latencies were significantly reduced at 4, 12, and 16 kHz in the C1q KO mice (Supplementary Table S1; Figure 6C). At peak IV, peak latencies in C1q KO were significantly reduced at 4 and 8 kHz, compared to age-matched controls (Supplementary Table S1; Figure 6D). Overall, it appears that peak latencies are shortened in C1q KO mice, particularly for the lower frequencies.

We assessed central latency effects by measuring interpeak latencies in C1q KO and their age-matched wild type controls. Interpeak latency was defined as the difference in time (ms) between the apex of the peak and the apex of the preceding peak. C1q KO mice had significantly decreased peak I–II latency at 16 kHz, while the other frequencies tested were not affected (Supplementary Table S1; Figure 7A). Latencies between peaks II–III were unaffected in C1q KO mice at all frequencies (Supplementary Table S1; Figure 7B). Interpeak latency was shortened between peaks III–IV at 16 kHz, while the other frequencies remained unaffected by C1q depletion (Supplementary Table S1; Figure 7C). Next, we assessed overall interpeak latencies effects by examining latency differences between peaks I–III and I–IV. At 4 kHz, peak I–III interpeak latencies were significantly shortened in C1q KO mice (Supplementary Table S1; Figure 7D). Peak I–IV latencies were unaffected at all frequency levels (Supplementary Table S1). Together, the interpeak latencies appear disrupted at some low to mid frequency regions.

Discussion

In this study we investigated the role of the classic complement cascade initiator, C1q, in the context of auditory brainstem development. We found that C1q is present throughout the brainstem before and after hearing onset. C1q expression increases by P14, a period of microglia-regulated circuit refinement. We observed that microglia contain C1q within their soma and processes, and C1q expression is more prominent surrounding MNTB cells after hearing onset. Further, C1q closely surrounds VGLUT2 puncta, indicating its calyceal interactions. Loss of C1q, however, does not affect monoinnervation in the MNTB. C1q ablation does not alter the E/I protein ratio in the auditory brainstem. C1q KO mice appeared to have mostly normal ABR hearing thresholds. However, we found that loss of C1q leads to decreased peak latencies, particularly in the lower frequencies tested.

Dispersion of C1q protein in the developing brain

In C57/BL6 mice C1q levels increase during development, followed by a sharp increase in older animals (Reichwald et al., 2009; Rupprecht et al., 2021; Stephan et al., 2013). Throughout the brain, C1q expression rises between P6 to 15 and P15 to 30 (Stephan et al., 2013). In the developing lateral geniculate nucleus (LGN), it was found that C1q peaks in expression in the first two postnatal weeks, in contrast with C1q downregulation in adulthood (Stevens et al., 2007). C1q increases are predominantly found at the synapse and can influence synaptic plasticity outside of the classical complement cascade (Stephan et al., 2013; Stevens et al., 2007). Here, we found that

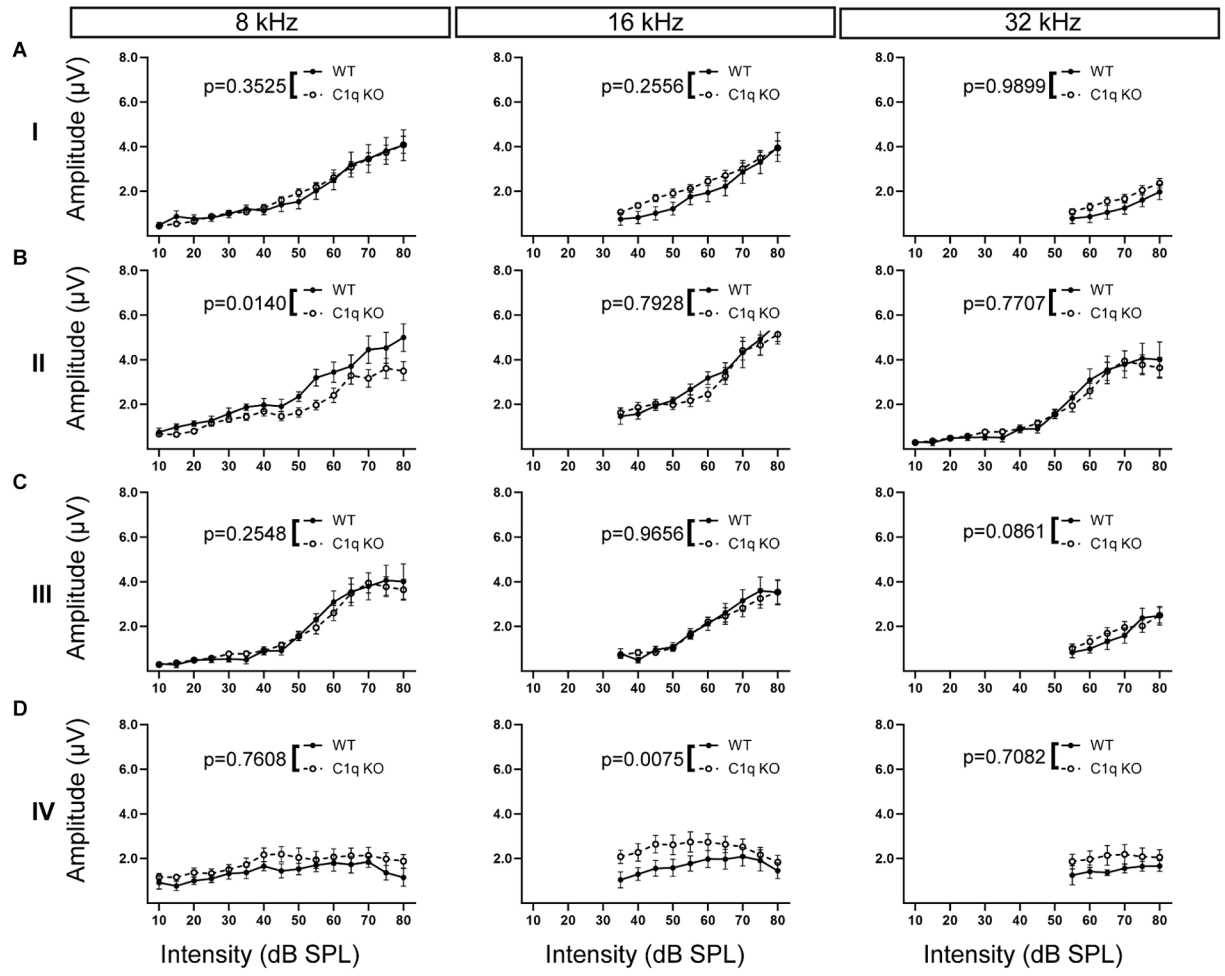


FIGURE 5
ABR peak amplitudes in C1q KO mice. **(A)** Peak I amplitudes in C1q KO mice were comparable to controls. **(B)** C1q KO mice had slightly diminished peak II amplitude at low frequencies but the mid to high frequencies were not altered. **(C)** Peak III amplitude was not altered from C1q deletion. **(D)** C1q KO peak IV amplitude was elevated in mid frequencies, but other frequencies were comparable to controls.

C1q levels in the MNTB increase with age. We also found a gradient shift where at P8, earlier developing high frequency regions have higher C1q expression, and at P14 low frequency regions have higher C1q expression. Developing microglia contain C1q clusters within their soma and processes, and non-microglial C1q is more apparent at older ages. These findings imply that C1q follows a developmental sequence during auditory circuit optimization.

C1q roles are heterogeneous depending on brain region and age. Hippocampal development entails C1q and C3-mediated synaptic pruning (Paolicelli et al., 2011). C1q KO mice have deficiencies in retinogeniculate refinement, and LGN neurons remain polyinnervated with C1q removal (Stevens et al., 2007). During a period of robust activity-dependent pruning in the postnatal retinogeniculate system, microglia engulf retinal ganglion cells in a C3-dependent way (Schafer et al., 2012). C1q is not required for the development of a spine population implicated in ocular dominance plasticity in the binocular primary visual cortex (Welsh et al., 2020). Dendritic morphology is not dependent on C1q removal in this model system and firing rates of V1b in C1q KO mice are normal (Welsh et al., 2020). Using a monocular deprivation (MD) paradigm, C1q protein levels in the primary visual cortex were not experience-dependent, and MD did not reduce spine numbers on L2/3 pyramidal neurons in C1q knock-out mice (Welsh et al., 2020). In a model of demyelinating disease, C1q depletion rescues the number and function of synapses (Vukojicic et al., 2019). Here, we observed C1q expression surrounding MNTB cells and in close proximity to calyx-associated excitatory puncta. We did not find changes in calyx elimination following C1q removal or in our assessment of synaptic protein expression. Our findings further emphasize that C1q has heterogeneous roles in synapse elimination. It should be noted that C1q docking in calyceal regions may have synapse protection roles that should be investigated.

C1q modulates auditory signal transmission

Microglia play a pivotal role in auditory brainstem formation and loss of microglia through CSF1R inhibition results in hearing impairments such as higher ABR thresholds and delayed peak

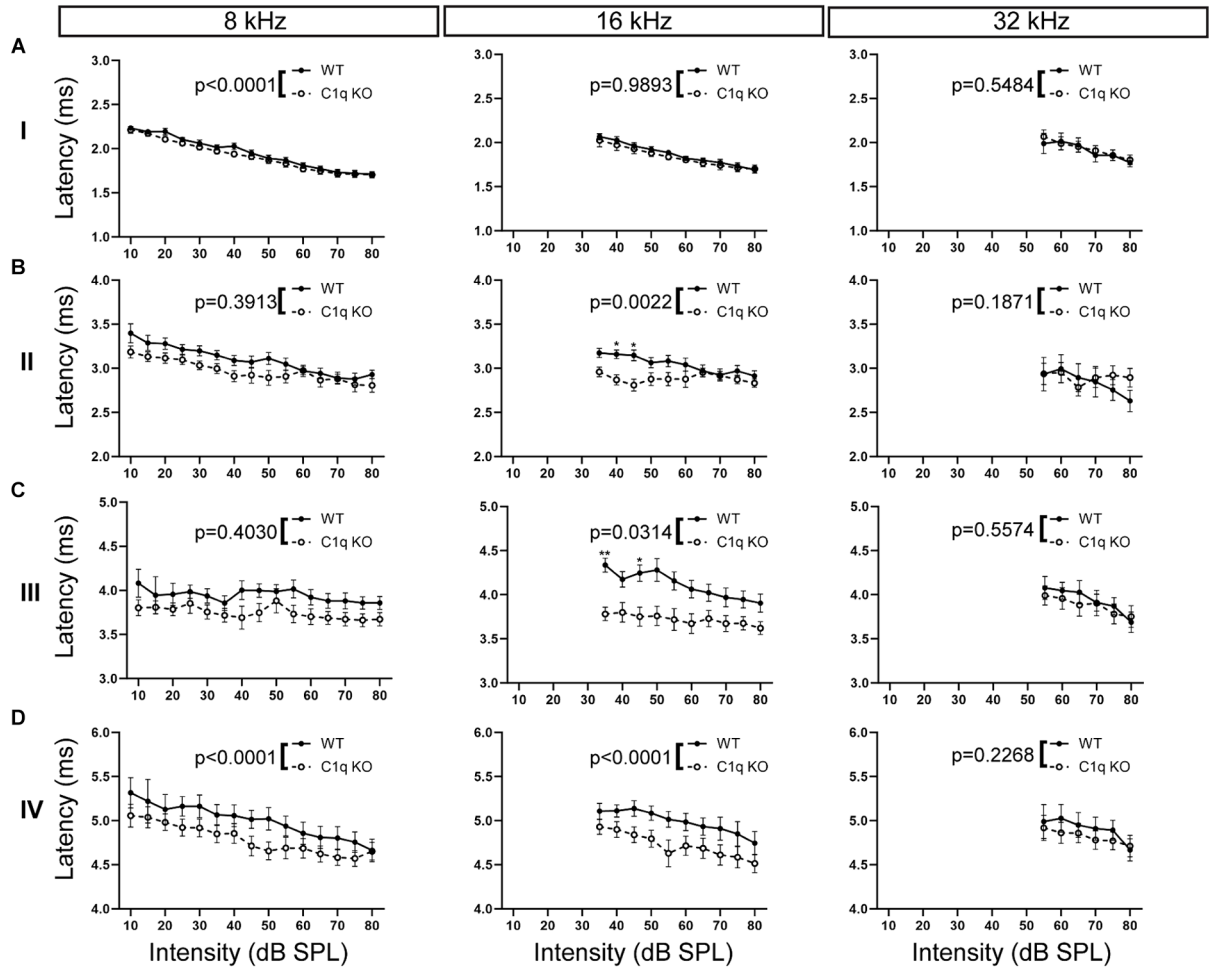


FIGURE 6
ABR peak latencies are decreased in C1q KO mice. **(A)** Peak I latencies were comparable in each frequency tested. **(B)** Peak II latency was shortened in the central frequencies in C1q KO mice. **(C)** Peak III latencies were diminished in mid frequencies in C1q KO mice. **(D)** C1q KO mice had shortened peak latencies at low and middle frequencies compared to age-matched controls.

latencies (Chokr et al., 2022; Milinkeviciute et al., 2021b). Interestingly, disruption of CX3CR1, a major microglial signaling pathway, results in shortened peak latencies (Milinkeviciute et al., 2021a).

Connections in the brainstem are highly myelinated, and disruptions in myelination can affect the ABR (Ito et al., 2004; Long et al., 2018; Sinclair et al., 2017; Xing et al., 2012). C1q may activate myelin by binding to myelin oligodendrocyte glycoprotein, potentially playing a role in demyelinating diseases (Johns and Bernard, 1997). Indeed, in a cuprizone-induced demyelination mouse model, C1q protein levels are elevated (Gao et al., 2022). C1q KO prevents white matter loss (Leah et al., 2020). C1q KO mice have increased spontaneous and evoked epileptiform activity, and increased excitatory connectivity, which can be detected through frequent behavioral seizures (Chu et al., 2010). C1q inhibition is a potent therapeutic target for demyelinating diseases and conditions with disrupted E/I balance such as epilepsy or schizophrenia (Dalakas et al., 2020; Lansita et al., 2017; Maes et al., 2021; McGonigal et al., 2016). Our ABR results show elevated peak amplitudes and decreased peak latencies, which are consistent with phenotypes that model increased myelination and a disrupted E/I balance. We postulate that although elevated peak amplitudes and decreased peak latencies can be a sign of an improved ABR profile, it is possible that these changes may indicate hyperactivity and excitability in the ascending auditory pathway. Detailed electrophysiological studies that investigate the effects of microglial signaling pathways on myelination in the sound localization pathway are currently lacking. These findings unravel a new avenue to explore the interplay of C1q and myelin in the context of auditory brainstem development and function.

Conclusion

We showed here that C1q is present in the developing auditory brainstem. C1q protein is predominantly within microglia prior to hearing onset and increases in expression and surrounds MNTB cells after hearing onset. C1q molecules also surround calyceal excitatory puncta but loss of C1q does not affect calyceal pruning or the E/I synaptic ratio in the MNTB or LSO. Auditory brainstem responses revealed that loss of C1q shortens signal transmission, a phenotype suggesting altered myelination or neural strength.

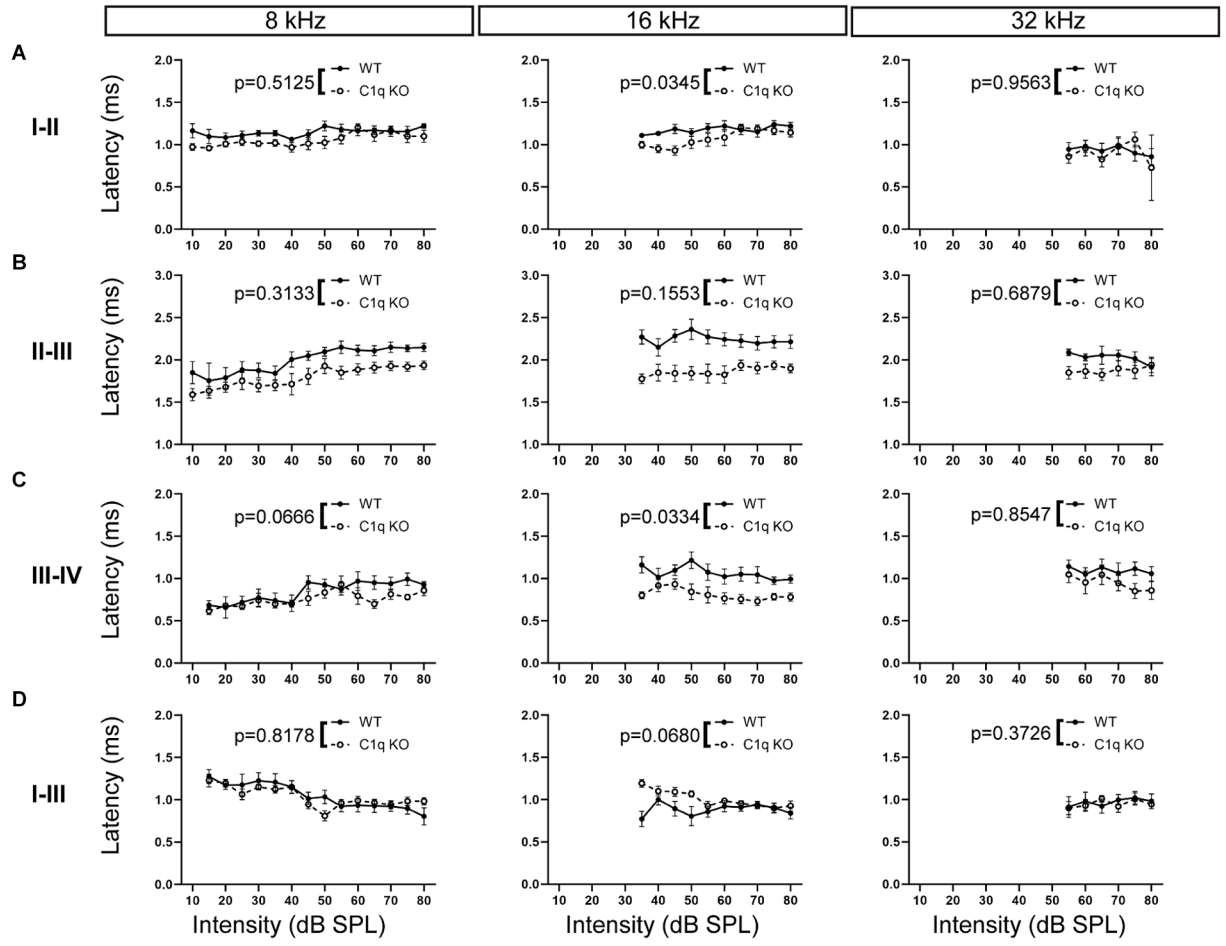


FIGURE 7
ABR interpeak latencies in C1q KO mice and age-matched controls. **(A)** C1q deletion diminished peak I–II interpeak latency at 16 kHz, while other frequencies were unaffected. **(B)** Peak II–III interpeak latencies were comparable to controls across all frequency levels. **(C)** Peak III–IV latency was diminished at 16 kHz. **(D)** Peak I–III interpeak latency was unaltered from C1q deletion.

Data availability statement

The original contributions presented in the study are included in the article/Supplementary material, further inquiries can be directed to the corresponding author.

Ethics statement

The animal study was approved by UC Irvine Institutional Animal Care and Use Committee. The study was conducted in accordance with the local legislation and institutional requirements.

Author contributions

SC: Data curation, Formal analysis, Investigation, Methodology, Validation, Visualization, Writing – original draft, Writing – review & editing. AB-T: Formal analysis, Investigation, Writing – review & editing. KC: Conceptualization, Formal analysis, Funding acquisition, Investigation, Methodology, Resources, Supervision, Writing – review & editing.

Funding

The author(s) declare that financial support was received for the research, authorship, and/or publication of this article. This research was supported by NIH NIDCD DC010796 and NIH T32 DC010775.

Acknowledgments

The authors would like to thank Dr. Andrea Tenner and Shu-Hui Chu for providing the C1q monoclonal antibody and for their intellectual contributions. We would also like to thank Dr. Adeela Syed from the Optical Biology Core at UC Irvine for providing technical assistance in acquiring super-resolution images on the Zeis Elyra 7 microscope.

Conflict of interest

The authors declare that the research was conducted in the absence of any commercial or financial relationships that could be construed as a potential conflict of interest.

Publisher's note

All claims expressed in this article are solely those of the authors and do not necessarily represent those of their affiliated organizations, or those of the publisher, the editors and the reviewers. Any product that may be evaluated in this article, or claim that may be made by its manufacturer, is not guaranteed or endorsed by the publisher.

Supplementary material

The Supplementary material for this article can be found online at: https://www.frontiersin.org/articles/10.3389/fncel.2024.1464670/full#supplementary-material

References

Abadi, S. P., Khanbabaee, G. M., and Sheibani, K. M. (2016). Auditory brainstem response wave amplitude characteristics as a diagnostic tool in children with speech delay with unknown causes. *Iran J Med Sci* 41, 415–421

Bilimoria, P. M., and Stevens, B. (2015). Microglia function during brain development: new insights from animal models. *Brain Res.* 1617, 7–17. doi: 10.1016/j.brainres.2014.11.032

Biswas, J., Pijewski, R. S., Makol, R., Miramontes, T. G., Thompson, B. L., Kresic, L. C., et al. (2021). C1ql1 is expressed in adult outer hair cells of the cochlea in a tonotopic gradient. *PLoS One* 16:e0251412. doi: 10.1371/journal.pone.0251412

Bogaerts, S., Clements, J. D., Sullivan, J. M., and Oleskevich, S. (2009). Automated threshold detection for auditory brainstem responses: comparison with visual estimation in a stem cell transplantation study. *BMC Neurosci.* 10:104. doi: 10.1186/1471-2202-10-104

Boudreau, J. C., and Tsuchitani, C. (1968). Binaural interaction in the cat superior olive S segment. *J. Neurophysiol.* 31, 442–454. doi: 10.1152/jn.1968.31.3.442

Chokr, S. M., Milinkeviciute, G., Jimenez, G. A., Abubakr, H., and Cramer, K. S. (2022). Long-term microglia depletion impairs synapse elimination and auditory brainstem function. *Sci. Rep.* 12:18521. doi: 10.1038/s41598-022-23250-5

Chu, Y., Jin, X., Parada, I., Pesic, A., Stevens, B., Barres, B., et al. (2010). Enhanced synaptic connectivity and epilepsy in C1q knockout mice. *Proc. Natl. Acad. Sci. USA* 107, 7975–7980. doi: 10.1073/pnas.0913449107

Cong, Q., Soteros, B. M., Huo, A., Li, Y., Tenner, A. J., and Sia, G. M. (2022). C1q and SRPX2 regulate microglia mediated synapse elimination during early development in the visual thalamus but not the visual cortex. *Glia* 70, 451–465. doi: 10.1002/glia.24114

Dalakas, M. C., Alexopoulos, H., and Spaeth, P. J. (2020). Complement in neurological disorders and emerging complement-targeted therapeutics. *Nat. Rev. Neurol.* 16, 601–617. doi: 10.1038/s41582-020-0400-0

Dejanovic, B., Wu, T., Tsai, M.-C., Graykowski, D., Gandham, V. D., Rose, C. M., et al. (2022). Complement C1q-dependent excitatory and inhibitory synapse elimination by astrocytes and microglia in Alzheimer's disease mouse models. *Nat. Aging* 2, 837–850. doi: 10.1038/s43587-022-00281-1

Dinh, M. L., Koppel, S. J., Korn, M. J., and Cramer, K. S. (2014). Distribution of glial cells in the auditory brainstem: normal development and effects of unilateral lesion. *Neuroscience* 278, 237–252. doi: 10.1016/j.neuroscience.2014.08.016

Erblich, B., Zhu, L., Etgen, A. M., Dobrenis, K., and Pollard, J. W. (2011). Absence of colony stimulation factor-1 receptor results in loss of microglia, disrupted brain development and olfactory deficits. *PLoS One* 6:e26317. doi: 10.1371/journal.pone.0026317

Favuzzi, E., Huang, S., Saldi, G. A., Binan, L., Ibrahim, L. A., Fernández-Otero, M., et al. (2021). GABA-receptive microglia selectively sculpt developing inhibitory circuits. *Cell* 184:5686. doi: 10.1016/j.cell.2021.10.009

Fonseca, M. I., Chu, S. H., Hernandez, M. X., Fang, M. J., Modarresi, L., Selvan, P., et al. (2017). Cell-specific deletion of C1qa identifies microglia as the dominant source of C1q in mouse brain. *J. Neuroinflammation* 14:48. doi: 10.1186/s12974-017-0814-9

Fonseca, M. I., Zhou, J., Botto, M., and Tenner, A. J. (2004). Absence of C1q leads to less neuropathology in transgenic mouse models of Alzheimer's disease. *J. Neurosci.* 24, 6457–6465. doi: 10.1523/JNEUROSCI.0901-04.2004

Gao, Z., Zhang, C., Feng, Z., Liu, Z., Yang, Y., Yang, K., et al. (2022). C1q inhibits differentiation of oligodendrocyte progenitor cells via Wnt/β-catenin signaling activation in a cuprizone-induced mouse model of multiple sclerosis. *Exp. Neurol.* 348:113947. doi: 10.1016/j.expneurol.2021.113947

Gjoni, E., Zenke, F., Bouhours, B., and Schneggenburger, R. (2018). Specific synaptic input strengths determine the computational properties of excitation-inhibition integration in a sound localization circuit. *J. Physiol.* 596, 4945–4967. doi: 10.1113/JP276012

Grothe, B., Pecka, M., and McAlpine, D. (2010). Mechanisms of sound localization in mammals. *Physiol. Rev.* 90, 983–1012. doi: 10.1152/physrev.00026.2009

Henry, K. R. (1979). Auditory nerve and brain stem volume-conducted potentials evoked by pure-tone pips in the CBA/J laboratory mouse. *Audiology* 18, 93–108. doi: 10.3109/00206097909072623

Hoffpauir, B. K., Grimes, J. L., Mathers, P. H., and Spirou, G. A. (2006). Synaptogenesis of the calyx of held: rapid onset of function and one-to-one morphological innervation. *J. Neurosci.* 26, 5511–5523. doi: 10.1523/JNEUROSCI.5525-05.2006

Holcomb, P. S., Hoffpauir, B. K., Hoyson, M. C., Jackson, D. R., Deerinck, T. J., Marrs, G. S., et al. (2013). Synaptic inputs compete during rapid formation of the calyx of held: a new model system for neural development. *J. Neurosci.* 33, 12954–12969. doi: 10.1523/JNEUROSCI.1087-13.2013

Hoshiko, M., Arnoux, I., Avignone, E., Yamamoto, N., and Audinat, E. (2012). Deficiency of the microglial receptor CX3CR1 impairs postnatal functional development of thalamocortical synapses in the barrel cortex. *J. Neurosci.* 32, 15106–15111. doi: 10.1523/JNEUROSCI.1167-12.2012

Ito, T., Tokuriki, M., Shibamori, Y., Saito, T., and Nojyo, Y. (2004). Cochlear nerve demyelination causes prolongation of wave I latency in ABR of the myelin deficient (md) rat. *Hear. Res.* 191, 119–124. doi: 10.1016/j.heares.2003.12.019

Jewett, D. L. (1970). Volume-conducted potentials in response to auditory stimuli as detected by averaging in the cat. *Electroencephalogr. Clin. Neurophysiol.* 28, 609–618. doi: 10.1016/0013-4694(70)90203-8

Jewett, D. L., and Williston, J. S. (1971). Auditory-evoked far fields averaged from the scalp of humans. *Brain* 94, 681–696. doi: 10.1093/brain/94.4.681

Johns, T. G., and Bernard, C. C. (1997). Binding of complement component Clq to myelin oligodendrocyte glycoprotein: a novel mechanism for regulating CNS inflammation. *Mol. Immunol.* 34, 33–38. doi: 10.1016/s0161-5890(97)00005-9

Jung, S., Aliberti, J., Graemmel, P., Sunshine, M. J., Kreutzberg, G. W., Sher, A., et al. (2000). Analysis of fractalkine receptor CX(3)CR1 function by targeted deletion and green fluorescent protein reporter gene insertion. *Mol. Cell. Biol.* 20, 4106–4114. doi: 10.1128/MCB.20.11.4106-4114.2000

Karcz, A., Hennig, M. H., Robbins, C. A., Tempel, B. L., Rübsamen, R., and Kopp-Scheinpflug, C. (2011). Low-voltage activated Kv1.1 subunits are crucial for the processing of sound source location in the lateral superior olive in mice. *J. Physiol.* 589, 1143–1157. doi: 10.1113/jphysiol.2010.203331

Kettenmann, H., Kirchhoff, F., and Verkhratsky, A. (2013). Microglia: new roles for the synaptic stripper. *Neuron* 77, 10–18. doi: 10.1016/j.neuron.2012.12.023

Kronander, E., Clark, C., and Schneggenburger, R. (2019). Role of BMP signaling for the formation of auditory brainstem nuclei and large auditory relay synapses. *Dev. Neurobiol.* 79, 155–174. doi: 10.1002/dneu.22661

Lansita, J. A., Mease, K. M., Qiu, H., Yednock, T., Sankaranarayanan, S., and Kramer, S. (2017). Nonclinical development of ANX005: a humanized anti-C1q antibody for treatment of autoimmune and neurodegenerative diseases. *Int. J. Toxicol.* 36, 449–462. doi: 10.1177/1091581817740873

Leah, C. G., Heidi, E. K., Ileana, S., and Gareth, R. H. (2020). Deficiency of complement component C1Q prevents cerebrovascular damage and white matter loss in a mouse model of chronic obesity. *eneuro* 7:e57. doi: 10.1523/ENEURO.0057-20.2020

Li, M., Ager, R. R., Fraser, D. A., Tjokro, N. O., and Tenner, A. J. (2008). Development of a humanized C1q a chain knock-in mouse: assessment of antibody independent beta-amyloid induced complement activation. *Mol. Immunol.* 45, 3244–3252. doi: 10.1016/j.molimm.2008.02.022

Liu, H., Chen, L., Giffen, K. P., Stringham, S. T., Li, Y., Judge, P. D., et al. (2018). Cell-specific transcriptome analysis shows that adult pillar and Deiters' cells express genes encoding machinery for specializations of Cochlear hair cells. *Front. Mol. Neurosci.* 11:356. doi: 10.3389/fnmol.2018.00356

Liu, H., Pecka, J. L., Zhang, Q., Soukup, G. A., Beisel, K. W., and He, D. Z. (2014). Characterization of transcriptomes of cochlear inner and outer hair cells. *J. Neurosci.* 34, 11085–11095. doi: 10.1523/JNEUROSCI.1690-14.2014

Long, P., Wan, G., Roberts, M. T., and Corfas, G. (2018). Myelin development, plasticity, and pathology in the auditory system. *Dev. Neurobiol.* 78, 80–92. doi: 10.1002/dneu.22538

Maes, M., Vojdani, A., Sirivichayakul, S., Barbosa, D. S., and Kanchanatawan, B. (2021). Inflammatory and oxidative pathways are new drug targets in multiple episode schizophrenia and leaky gut, Klebsiella pneumoniae, and C1q immune complexes are additional drug targets in first episode schizophrenia. *Mol. Neurobiol.* 58, 3319–3334. doi: 10.1007/s12035-021-02343-8

Magnusson, A. K., Park, T. J., Pecka, M., Grothe, B., and Koch, U. (2008). Retrograde GABA signaling adjusts sound localization by balancing excitation and inhibition in the brainstem. *Neuron* 59, 125–137. doi: 10.1016/j.neuron.2008.05.011

Matcovitch-Natan, O., Winter, D. R., Giladi, A., Vargas Aguilar, S., Spinrad, A., Sarrazin, S., et al. (2016). Microglia development follows a stepwise program to regulate brain homeostasis. *Science* 353:aad8670. doi: 10.1126/science.aad8670

McGonigal, R., Cunningham, M. E., Yao, D., Barrie, J. A., Sankaranarayanan, S., Fewou, S. N., et al. (2016). C1q-targeted inhibition of the classical complement pathway prevents injury in a novel mouse model of acute motor axonal neuropathy. *Acta Neuropathol. Commun.* 4:23. doi: 10.1186/s40478-016-0291-x

Milinkeviciute, G., Chokr, S. M., Castro, E. M., and Cramer, K. S. (2021a). CX3CR1 mutation alters synaptic and astrocytic protein expression, topographic gradients, and response latencies in the auditory brainstem. *J. Comp. Neurol.* 529, 3076–3097. doi: 10.1002/cne.25150

Milinkeviciute, G., Chokr, S. M., and Cramer, K. S. (2021b). Auditory brainstem deficits from early treatment with a CSF1R inhibitor largely recover with microglial repopulation. *eNeuro* 8:ENEURO.0318. doi: 10.1523/ENEURO.0318-20.2021

Milinkeviciute, G., Henningfield, C. M., Muniak, M. A., Chokr, S. M., Green, K. N., and Cramer, K. S. (2019). Microglia regulate pruning of specialized synapses in the auditory brainstem. *Front Neural Circuits* 13:55. doi: 10.3389/fncir.2019.00055

Morest, D. K. (1969). The differentiation of cerebral dendrites: a study of the post-migratory neuroblast in the medial nucleus of the trapezoid body. *Z. Anat. Entwicklungsgesch.* 128, 271–289. doi: 10.1007/BF00522528

Paolicelli, R. C., Bolasco, G., Pagani, F., Maggi, L., Scianni, M., Panzanelli, P., et al. (2011). Synaptic pruning by microglia is necessary for normal brain development. *Science* 333, 1456–1458. doi: 10.1126/science.1202529

Presumey, J., Bialas, A. R., and Carroll, M. C. (2017). Complement system in neural synapse elimination in development and disease. *Adv. Immunol.* 135, 53–79. doi: 10.1016/bs.ai.2017.06.004

Qi, Y., Xiong, W., Yu, S., Du, Z., Qu, T., He, L., et al. (2021). Deletion of C1ql1 causes hearing loss and abnormal auditory nerve fibers in the mouse cochlea. *Front. Cell. Neurosci.* 15:713651. doi: 10.3389/fncel.2021.713651

Reichwald, J., Danner, S., Wiederhold, K. H., and Staufenbiel, M. (2009). Expression of complement system components during aging and amyloid deposition in APP transgenic mice. *J. Neuroinflammation* 6:35. doi: 10.1186/1742-2094-6-35

Rodríguez-Contreras, A., van Hoeve, J. S., Habets, R. L., Locher, H., and Borst, J. G. (2008). Dynamic development of the calyx of held synapse. *Proc. Natl. Acad. Sci. USA* 105, 5603–5608. doi: 10.1073/pnas.0801395105

Rupprecht, C., Rupprecht, R., and Rammes, G. (2021). C1q, a small molecule with high impact on brain development: putative role for aging processes and the occurrence of Alzheimer's disease. *Eur. Arch. Psychiatry Clin. Neurosci.* 271, 809–812. doi: 10.1007/s00406-021-01273-9

Sätzler, K., Söhl, L. F., Bollmann, J. H., Borst, J. G. G., Frotscher, M., Sakmann, B., et al. (2002). Three-dimensional reconstruction of a Calyx of held and its postsynaptic principal neuron in the medial nucleus of the trapezoid body. *J. Neurosci.* 22, 10567–10579. doi: 10.1523/JNEUROSCI.22-24-10567.2002

Schaette, R., and McAlpine, D. (2011). Tinnitus with a Normal audiogram: physiological evidence for hidden hearing loss and computational model. *J. Neurosci.* 31, 13452–13457. doi: 10.1523/JNEUROSCI.2156-11.2011

Schafer, D. P., Lehrman, E. K., Kautzman, A. G., Koyama, R., Mardinly, A. R., Yamasaki, R., et al. (2012). Microglia sculpt postnatal neural circuits in an activity and complement-dependent manner. *Neuron* 74, 691–705. doi: 10.1016/j.neuron.2012.03.026

Sierksma, M. C., Slotman, J. A., Houtsmuller, A. B., and Borst, J. G. G. (2020). Structure–function relation of the developing calyx of held synapse in vivo. *J. Physiol.* 598, 4603–4619. doi: 10.1113/JP279976

Sierksma, M. C., Tedja, M. S., and Borst, J. G. G. (2017). In vivo matching of postsynaptic excitability with spontaneous synaptic inputs during formation of the rat calyx of held synapse. *J. Physiol.* 595, 207–231. doi: 10.1113/JP272780

Sinclair, J. L., Fischl, M. J., Alexandrova, O., Heβ, M., Grothe, B., Leibold, C., et al. (2017). Sound-evoked activity influences myelination of brainstem axons in the trapezoid body. *J. Neurosci.* 37, 8239–8255. doi: 10.1523/JNEUROSCI.3728-16.2017

Stephan, A. H., Madison, D. V., Mateos, J. M., Fraser, D. A., Lovelett, E. A., Coutellier, L., et al. (2013). A dramatic increase of C1q protein in the CNS during normal aging. *J. Neurosci.* 33, 13460–13474. doi: 10.1523/JNEUROSCI.1333-13.2013

Stevens, B., Allen, N. J., Vazquez, L. E., Howell, G. R., Christopherson, K. S., Nouri, N., et al. (2007). The classical complement cascade mediates CNS synapse elimination. *Cell* 131, 1164–1178. doi: 10.1016/j.cell.2007.10.036

Tollin, D. J. (2003). The lateral superior olive: a functional role in sound source localization. *Neuroscientist* 9, 127–143. doi: 10.1177/1073858403252228

Vukojicic, A., Delestrée, N., Fletcher, E. V., Pagiazitis, J. G., Sankaranarayanan, S., Yednock, T. A., et al. (2019). The classical complement pathway mediates microglia-dependent remodeling of spinal motor circuits during development and in SMA. *Cell Rep.* 29, 3087–3100.e3087. doi: 10.1016/j.celrep.2019.11.013

Welsh, C. A., Stephany, C.-É., Sapp, R. W., and Stevens, B. (2020). Ocular dominance plasticity in binocular primary visual cortex does not require C1q. *J. Neurosci.* 40, 769–783. doi: 10.1523/JNEUROSCI.1011-19.2019

Xing, Y., Samuvel, D. J., Stevens, S. M., Dubno, J. R., Schulte, B. A., and Lang, H. (2012). Age-related changes of myelin basic protein in mouse and human auditory nerve. *PLoS One* 7:e34500. doi: 10.1371/journal.pone.0034500

Zhang, W., Chen, Y., and Pei, H. (2023). C1q and central nervous system disorders. *Front. Immunol.* 14:1145649. doi: 10.3389/fimmu.2023.1145649

frontiers | Frontiers in Cellular Neuroscience

TYPE Original Research
PUBLISHED 17 October 2024
DOI 10.3389/fncel.2024.1465255

Check for updates

OPEN ACCESS

EDITED BY
Christian Keine,
University of Oldenburg, Germany

REVIEWED BY
Sarthak Singhal,
University of California, San Diego, United States
Michael Thomas Roberts,
University of Michigan, United States
Sara Reis,
University of Porto, Portugal

*CORRESPONDENCE
Randy Kulesza
✉ rkulesza@lecom.edu

RECEIVED 16 July 2024
ACCEPTED 07 October 2024
PUBLISHED 17 October 2024

CITATION
Mansour Y and Kulesza R (2024) Obliteration of a glycinergic projection to the medial geniculate in an animal model of autism. *Front. Cell. Neurosci.* 18:1465255. doi: 10.3389/fncel.2024.1465255

COPYRIGHT
© 2024 Mansour and Kulesza. This is an open-access article distributed under the terms of the Creative Commons Attribution License (CC BY). The use, distribution or reproduction in other forums is permitted, provided the original author(s) and the copyright owner(s) are credited and that the original publication in this journal is cited, in accordance with accepted academic practice. No use, distribution or reproduction is permitted which does not comply with these terms.

Obliteration of a glycinergic projection to the medial geniculate in an animal model of autism

Yusra Mansour[1] and Randy Kulesza[2]*

[1]Department of Otolaryngology—Head and Neck Surgery, Detroit, MI, United States, [2]Department of Anatomy, Lake Erie College of Osteopathic Medicine, Erie, PA, United States

Auditory dysfunction affects the vast majority of people with autism spectrum disorder (ASD) and can range from deafness to hypersensitivity. *In utero* exposure to the antiepileptic valproic acid (VPA) is associated with significant risk of an ASD diagnosis in humans and timed *in utero* exposure to VPA is utilized as an animal model of ASD. VPA-exposed rats have significantly fewer neurons in their auditory brainstem, thalamus and cortex, reduced ascending projections to the midbrain and thalamus and reduced descending projections from the cortex to the auditory midbrain. Consistent with these anatomical changes, VPA-exposed animals also have abnormal auditory brainstem responses. We have recently described a significant ascending projection from calbindin-positive neurons in the medial nucleus of the trapezoid body (MNTB) to the ventral division of the medial geniculate (vMG) in rats that bypasses the central nucleus of the inferior colliculus (CNIC). Since we found that axonal projections to the vMG in VPA-exposed rats are reduced beyond what is predicted from neuron loss alone, we hypothesize that VPA exposure would result in a significant reduction in the MNTB projection to the vMG. We examined this hypothesis by quantifying the proportion of retrogradely-labeled neurons in the MNTB of control and VPA-exposed animals after injections of retrograde tracers in the CNIC and vMG in control and VPA-exposed animals. Our results indicate that in control animals, the MNTB forms the largest projection from the superior olivary complex to the MG and that this projection is nearly abolished by *in utero* VPA exposure.

KEYWORDS

hearing, brainstem, autism, development, neurodevelopmental disorders

Introduction

Autism spectrum disorder (ASD) is a developmental disability characterized by social, communication and behavioral difficulties (Allen, 1988; Wing, 1997; American Psychiatric Association, 2013; CDC.gov, 2024). Approximately one in 36 children will be diagnosed with ASD and this is four times more common in males (CDC.gov, 2024). There are several key signs and symptoms of ASD, but the vast majority of subjects have some degree of auditory dysfunction (Greenspan and Wieder, 1997; Tomchek and Dunn, 2007; Bolton et al., 2012; reviewed in Mansour et al., 2021a) and this can range across individuals from deafness to hypersensitivity to sounds (Roper et al., 2003; Alcántara et al., 2004; Khalfa et al., 2001; Szelag et al., 2004; Teder-Sälejärvi et al., 2005; Gravel et al., 2006; Tharpe et al., 2006; Russo et al., 2009). Indeed, many individuals with ASD have longer latency auditory brainstem responses (ABR) (Ornitz, 1969; Student and Sohmer, 1978; Rosenblum et al., 1980; Sohmer, 1982; Tanguay et al., 1982; Gillberg et al., 1983; Sersen et al., 1990; Thivierge et al., 1990; Wong and

Wong, 1991; Maziade et al., 2000; Kwon et al., 2007; Roth et al., 2012; Azouz et al., 2014; Tas et al., 2007; Miron et al., 2018; Ramezani et al., 2019; Delgado et al., 2023). Consistent with hearing impairments from a developmental etiology, we have identified significant and consistent auditory brainstem hypoplasia in the brainstem of individuals with ASD (Kulesza and Mangunay, 2008; Kulesza et al., 2011; Lukose et al., 2015; Mansour and Kulesza, 2020). Specifically, in our study of the superior olivary complex (SOC) in a cohort of 28 subjects with ASD ranging from 4 to 39 years of age, we found significantly fewer neurons and surviving neurons were significantly smaller across nearly all constituent nuclei, including the medial nucleus of the trapezoid body (MNTB). In addition, several of these subjects had marked gliosis in and around the medial superior olive (MSO) and/or islands of ectopic neurons posterior and lateral to the SOC (Lukose et al., 2015).

In utero exposure to the antiepileptic drug valproic acid (VPA) is associated with elevated risk of an ASD diagnosis in humans (Moore et al., 2000; Williams et al., 2001; Rasalam et al., 2005; Koren et al., 2006; Bromley et al., 2013; Christensen et al., 2013; Hernández-Díaz et al., 2024; Pack et al., 2024). Accordingly, timed *in utero* exposure to VPA is a biologically relevant and validated animal model of ASD (rodents: Rodier et al., 1996; Mabunga et al., 2015; primates: Zhao et al., 2019). Consistent with the neuropathological changes we identified in the SOC of human subjects with ASD, animals exposed to VPA *in utero* have significantly fewer neurons in the ventral cochlear nuclei (VCN), SOC, nuclei of the lateral lemniscus (NLL), central nucleus of the inferior colliculus (CNIC), and medial geniculate (MG; Lukose et al., 2011; Zimmerman et al., 2018; Mansour et al., 2019). VPA-exposed animals also have fewer neurons across all layers of the auditory cortex with smaller pyramidal and non-pyramidal neurons in auditory association areas (Kosmer and Kulesza, 2024). Besides having fewer neurons throughout the auditory brainstem and forebrain, VPA-exposed animals have reduced ascending projections to the CNIC (Zimmerman et al., 2020) and MG (Mansour et al., 2021b) and reduced descending projections from layer VI of auditory cortex to the CNIC (Kosmer and Kulesza, 2024). VPA-exposed animals have fewer calbindin (CB) immunoreactive neurons in several locations, including the octopus cell area in the VCN, MNTB (Zimmerman et al., 2018), dorsal nucleus of the lateral lemniscus (DNLL; Mansour et al., 2019), primary auditory cortex (Kosmer and Kulesza, 2024), and cerebellum (Main and Kulesza, 2017) and fewer CB+ puncta in vestibular nuclei (Mansour et al., 2022). VPA-exposed animals have significantly more cFOS+ neurons in the VCN, MNTB and CNIC after exposure to pure tone stimuli, consistent with disruption of inhibitory circuits (Dubiel and Kulesza, 2016). Finally, VPA-exposed animals have abnormal auditory brainstem responses, including elevated thresholds, and longer latency responses for wave III, IV and V, consistent with auditory brainstem dysfunction (Malhotra and Kulesza, 2023).

The rat MNTB is composed primarily of glycinergic, CB+ principal neurons that receive input from globular bushy cells (GBCs) in the contralateral VCN via the calyx of Held (Morest, 1968a,b; Ottersen and Storm-Mathisen, 1984; Friauf and Ostwald, 1988; Arai et al., 1991; Résibois and Rogers, 1992; Lohmann and Friauf, 1996; Smith et al., 1991). MNTB principal neurons project within the ipsilateral SOC to the medial and lateral superior olives (MSO and LSO, respectively; Spangler et al., 1985; Helfert et al., 1989), and the superior paraolivary nucleus (SPON; Kuwabara et al., 1991; Banks and Smith, 1992; Sommer et al., 1993; Kulesza, 2007; see Figure 1, control). The MNTB also sends a descending projection to the GBC area of the ipsilateral VCN (Schofield, 1994) and ascending projections to both the ventral and intermediate nuclei of the lateral lemniscus (VNLL, INLL; Spangler et al., 1985; Sommer et al., 1993; Smith et al., 1998; Kelly et al., 2009; Saldaña et al., 2009; see Figure 1, control). Injections of retrograde tracers into nuclei further rostral in the brainstem such as the DNLL and CNIC indicate that only rare MNTB neurons project to these targets (rat: Beyerl, 1978; Druga and Syka, 1984; Coleman and Clerici, 1987; Kelly et al., 1998, 2009; Saldaña et al., 2009; guinea pig: Schofield and Cant, 1992; cat: Adams, 1979; Brunso-Bechtold et al., 1981; gerbil: Nordeen et al., 1983; Cant and Benson, 2006; mole: Kudo et al., 1990). However, we have recently demonstrated a projection from the MNTB to the ipsilateral MG that bypasses the CNIC in Sprague–Dawley rats (Burchell et al., 2022). Specifically, approximately 40% of MNTB neurons project to the ipsilateral ventral division of the MG (vMG; Burchell et al., 2022). Because VPA exposure results in significantly reduced ascending projections from the SOC to the MG, we hypothesized that *in utero* VPA exposure will result in a significant reduction in this ascending glycinergic projection from the MNTB to the MG. We examined this hypothesis in a library of retrograde tracer injections into the CNIC and MG from control and VPA-exposed animals (Zimmerman et al., 2020; Mansour et al., 2021b).

Methods

All handling and surgical procedures were approved by the LECOM Institutional Animal Care and Use Committee (protocols #16-02, 19–04, 20–02 & 21–03) and conducted in accordance with the National Institute of Health Guide for the Care and Use of Laboratory Animals. Sprague–Dawley rats were maintained on a 12 h light/dark cycle with *ad libitum* access to food and water. *In utero* exposure to VPA was performed per our previous work in this model (Figure 2A; Main and Kulesza, 2017; Zimmerman et al., 2018; Mansour et al., 2019; Zimmerman et al., 2020; Mansour et al., 2021b; Mansour and Kulesza, 2021; Mansour et al., 2022; Malhotra and Kulesza, 2023; Kosmer and Kulesza, 2024). All dams were fed 3.1 g of peanut butter on embryonic days (E) 7–12. Dams in the VPA group were fed peanut butter mixed with 800 mg/kg of VPA on E10 and E12 (Figure 2A). Both control and VPA-exposed dams were permitted to deliver pups without interference and pups were weaned on postnatal day (P) 21. Only male pups were included in the study because gender-specific effects of VPA exposure are established (Schneider et al., 2008). We conducted this study under the assumption that all male pups in a given litter were equally impacted by VPA exposure; our previous studies provide data consistent with this strategy (Main and Kulesza,

Abbreviations: ASD, Autism spectrum disorder; CB + Calbindin positive; CNIC, Central nucleus of the inferior colliculus; dMG, Dorsal nucleus of the medial geniculate; DMW, Dorsal medial wedge; DNLL, Dorsal nucleus of the lateral lemniscus; E, Embryonic; FB, Fast blue; FG, Fluorogold; GBC, Globular bushy cell; INLL, Intermediate nucleus of the lateral lemniscus; LSO, Lateral superior olive; MG, Medial geniculate; mMG, Medial nucleus of the medial geniculate; MNTB, Medial nucleus of the trapezoid body; MSO, Medial superior olive; P, Postnatal; PBS, Phosphate buffered saline; SOC, Superior olivary complex; SPON, Superior paraolivary nucleus; VCN, Ventral cochlear nucleus; vMG, Ventral nucleus of the medial geniculate; VNLL, Ventral nucleus of the lateral lemniscus; VPA, Valproic acid.

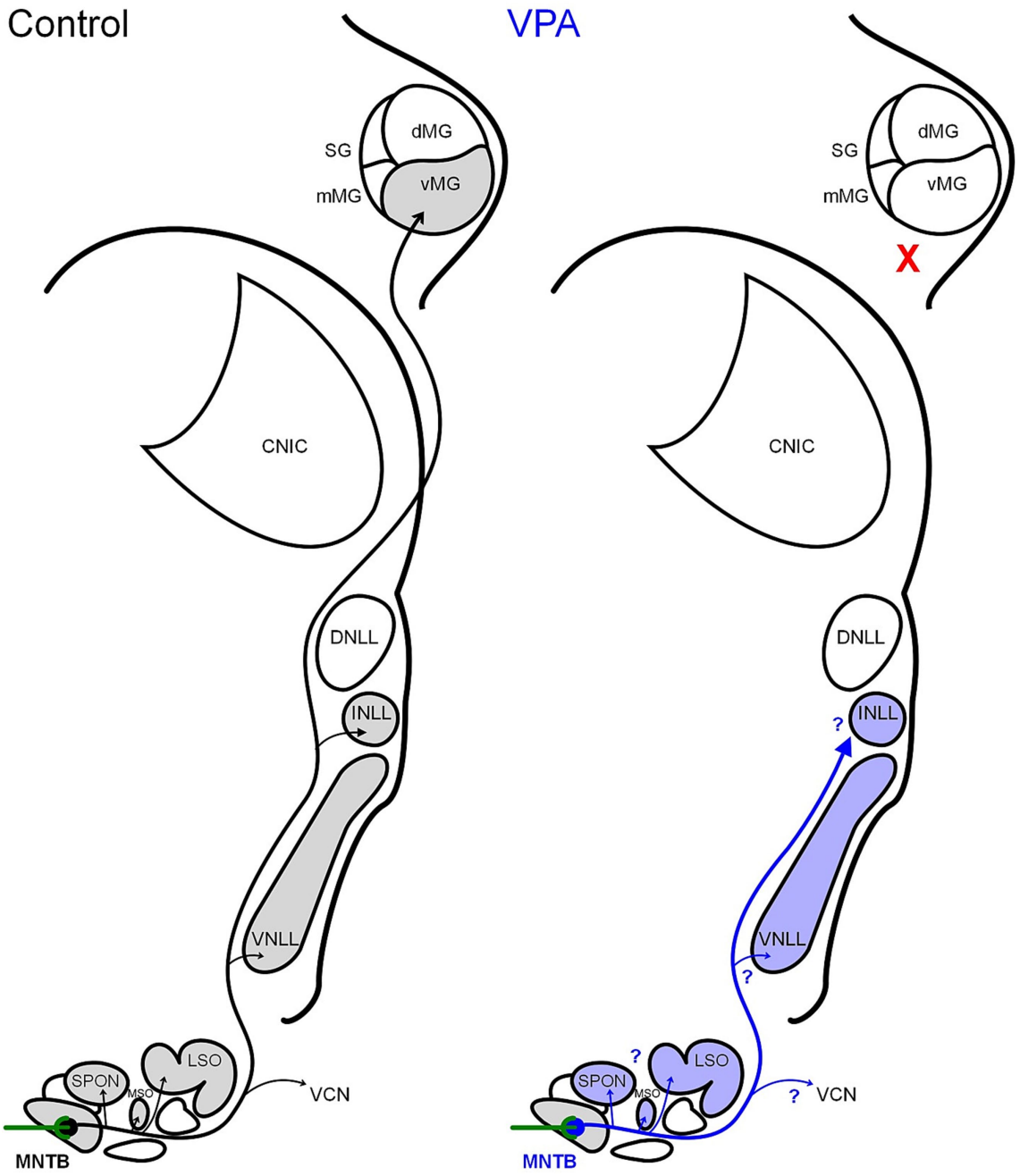


FIGURE 1
Schematic of MNTB projections. In control animals, the MNTB receives its main input from the contralateral VCN via the calyx of Held and projects within the SOC, to the ipsilateral VCN, to the VNLL, INLL, and MG. Our tract tracing results indicate that VPA exposure abolishes the MNTB projection to the MG. Currently, it is unclear if VPA exposure impacts other projections from the MNTB.

2017; Zimmerman et al., 2018; Mansour et al., 2019; Zimmerman et al., 2020; Mansour et al., 2021b; Mansour and Kulesza, 2021).

Animals receiving tracer injections were anesthetized with vaporized isoflurane (5% isoflurane in oxygen for induction, 2–3% for maintenance at 1.2 L/min). When animals were unresponsive to toe pinch, they were fitted with an anesthesia mask and secured in a stereotaxic frame with non-rupture ear bars. Body temperature was maintained with an electric heating pad. The animal's scalp was cleaned with iodine solution and injected with 0.25% bupivacaine; eyes were covered with ophthalmic ointment or closed and covered over with the anesthesia mask. A midline incision was made over the parietal and occipital bones and the dorsal aspect of the brain was approached via stereotaxic craniotomy. All injections were made with a tracer-dedicated 1 µL Hamilton KH Neuros syringe (32-gauge, four points).

We studied projections from the MNTB to the CNIC in injection site-matched cases from seven control and eight VPA-exposed animals (Figure 2B). In all animals, the CNIC was approached 0.2 mm rostral to lambda, 1.5 mm to the right of the midline. A depth measurement was taken from the surface of the dura mater and deposits of 100 nL

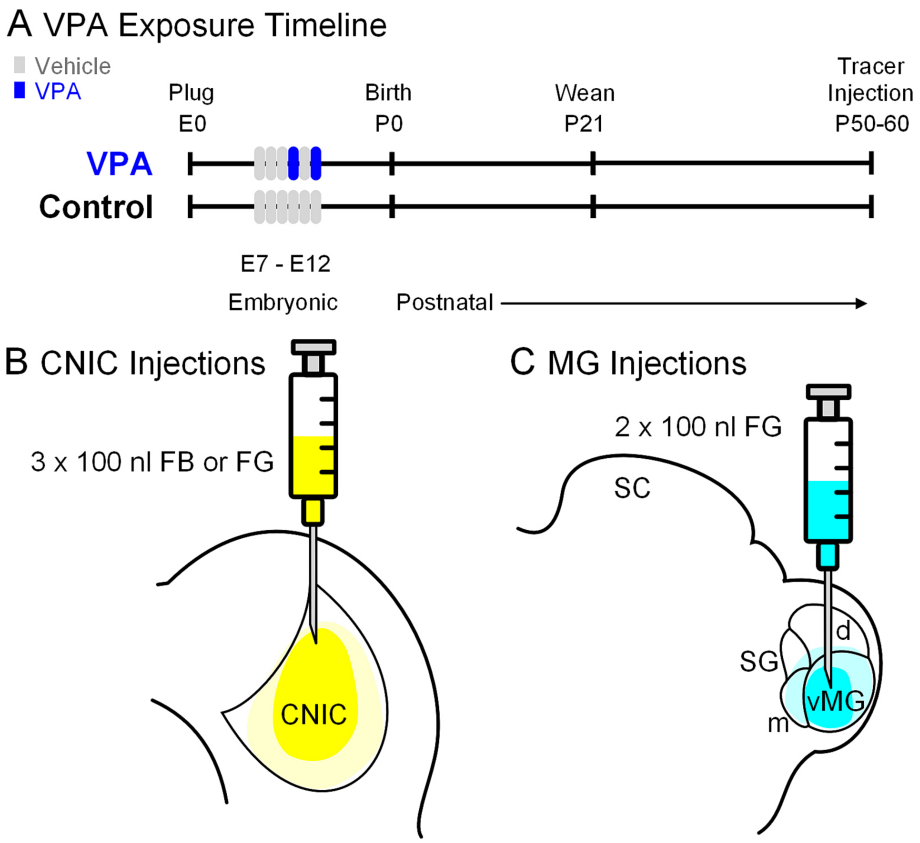


FIGURE 2
Experimental paradigm. Panel **(A)** shows the timing of VPA exposure, weaning and tracer injections. The experimental timeline (embryonic day 0; E0) started with identification of a vaginal plug. Pregnant females in the control group were fed peanut butter (vehicle) from E7 through E12; those in the experimental group received peanut butter on E7-9 and E11 and peanut butter + VPA on E10 and E12. Pups were weaned on P21 and stereotaxic injections of retrograde tracers were made between P50-60. Three injections (100 nL each) were made into the CNIC **(B)**. In a separate group of animals, two injections (100 nL each) were made into the MG **(C)**.

of Fast Blue (FB; 2.5% in water; Polysciences) or Fluorogold (FG, 4% in saline; Fluochrome) were made at depths of −3.6, − 3.2, and − 2.6 mm for a total injected volume of 300 nL.

We studied projections from the MNTB to the MG in injection site-matched cases from six control and six VPA-exposed animals (Figure 2C). The stereotaxic coordinates were the same for all control and VPA-exposed animals: 5.6 mm caudal to bregma and 3.4 mm to the right of the midline (as indicated by Paxinos and Watson, 2007). Injections of FG were made as described above. A depth measurement was taken from the surface of the dura mater and deposits of 100 nL of FG were made at depths of −5.8 and − 5.0 mm for a total injected volume of 200 nL.

The syringe was left in place for 10 min after the final injection to permit diffusion of the tracer. After the syringe was removed, the scalp wound was injected with lidocaine and sutured. Animals were removed from anesthesia and placed in their home cage and monitored until they were able to stand on all fours. Six-days following the surgery, animals were anesthetized with isoflurane and perfused through the ascending aorta first with 0.9% saline and then 4% paraformaldehyde (PFA) in phosphate buffered saline (pH 7.4; "fixative"). Brains were dissected from the skull and the right side (ipsilateral to the tracer injection) was marked with a syringe needle and post-fixed for at least 24 h. Twenty-four hours before frozen sectioning, brains were transferred into cryoprotectant (30% sucrose in fixative). Brains were sectioned in the coronal plane at a thickness of 50 µm and sections were collected in PBS from the cochlear nucleus through the injection site in the CNIC or MG in three wells. Injection sites were recovered from well 3; sections from well 2 were counter stained with Neurotrace Red (NT; Invitrogen), mounted onto glass slides from cresyl gelatin, coverslipped with Entellan (Millipore Sigma) and photographed with an Olympus CKX41 microscope with epifluorescence and a DP71 camera. The rostrocaudal borders of the MNTB, SPON and dorsalmedial wedge (DMW) were as previously delineated (Kulesza et al., 2002; Mansour et al., 2021b; Burchell et al., 2022). For each section including the MNTB, two images were collected—one of NT (using a rhodamine filter cube) and one of FB/FG labeling (using a UV filter cube) using a 20 × objective. Each pair of images was combined using the z-stack feature in Fiji (Schindelin et al., 2012) to form a single layer image containing overlayed NT and FB/FG labeling.

Counts of FB/FG + MNTB neurons were made from 4 to 6 stacked images per animal. The overlayed FB/FG and NTR images were imported into Fiji and analyzed with the cell counting feature. In these images, neurons were considered FB or FG + if they had blue or yellow fluorescent labeling within a cell body contour. Neurons were

TABLE 1 Neuron loss and projection changes in VPA-exposed animals.

	Number of neurons in nucleus[a,b,d]		MG neurons per total number of neurons in nucleus[a,b,c]			Total number of neurons projecting to MG[c]		MG neurons per projecting neurons in nucleus[c]			Projection Change[c]
	A	B	C	D	E	F	G	H	I	J	K
Calculation			46,796/A	23,403/B	D/C	A*%FG+	B*%FG+	46,796/F	23,403/G	I/H	E-J
	Control	VPA	Control	VPA	VPA/C	Control	VPA	Control	VPA	VPA/C	VPA/C
vMG + mMG	46,796	23,403									
						(36.7%)	(1.6%)				
IL MNTB	6,591	5,300	7.10	4.41	0.62	2,419	84.8	19.34	275.97	12.56	**−11.94**
IL LSO	2,586	1,935	18.10	12.09	0.67	173.26	75.47	270.09	310.09	1.15	−0.48
CL LSO	2,586	1,935	18.10	12.09	0.67	57.67	157.70	811.48	148.40	0.18	+0.49
IL MSO	1,201	517	38.96	45.27	1.16	148.56	38.93	314.99	601.15	1.91	−0.75
IL SPON	2,265	1,302	20.66	17.97	0.87	450.96	155.20	103.77	150.79	1.45	−0.58
IL DMW	2,407	1,803	19.44	12.98	0.67	883.37	485.91	52.97	48.16	0.91	−0.24
CL DMW	2,407	1,803	19.44	12.98	0.67	403.17	98.26	116.07	238.17	2.05	−1.38
IL VNTB	3,244	2,606	34.13	22.5	0.66	389.28	260.6	120.21	89.80	0.74	−0.08
CL VNTB	3,244	2,606	34.13	22.5	0.66	32.44	26.06	1,442.54	898.04	0.62	0.04
CL VCN	23,111	15,280	2.02	1.53	0.76	7,164.41	825.12	6.53	28.36	4.34	−3.59

[a]Zimmerman et al. (2018).
[b]Mansour et al. (2019).
[c]Mansour and Kulesza (2020).
[d]Mansour and Kulesza (2021).

considered negative if the cell body demonstrated NT labeling and lacked any blue/yellow fluorescence. At least 80 MNTB neurons were analyzed in each overlayed image and counts from these 4–6 images were averaged, resulting in a single percentage of FB/FG + MNTB neurons per animal. In Table 1, we re-examine previously published data from our study of ascending projections to the MG from the rat SOC (Mansour et al., 2021b) to demonstrate the relative size of the MNTB projection to the MG. Morphology of NTR and FB/FG-labeled MNTB neurons was quantified as previously described (Zimmerman et al., 2018).

GraphPad Prism (10.1, San Diego, CA) was used to generate descriptive statistics and conduct all statistical comparisons. Data that fit a normal distribution are presented in the text as mean ± standard deviation (SD); data that did not fit a normal distribution are presented as the median with the 95% confidence interval of the median. Specifically, the number of neurons projecting to the CNIC and MG were compared with Mann–Whitney (one-tailed) and neuronal morphology was compared with ANOVA with Tukey's multiple comparison test. Differences were considered statistically significant if p values were < 0.05.

Results

Projections to the CNIC

After injections of FB or FG into the CNIC (Figures 3, 4), only 2.2% (95% CI: 0–5.62%) of neurons in the ipsilateral MNTB were retrogradely labeled in control animals (Figure 5A). In VPA-exposed animals, 1.49% (0–7.14%) of neurons in the ipsilateral MNTB were labeled (Figure 5B). This difference was not significant [$U(7,8) = 22.5$, $p = 0.54$; Figure 6A]. Contralateral to the injection site, no retrogradely labeled MNTB neurons were found in control or VPA-exposed animals (Figure 5A).

Projections to the MG

After injections of FG into the MG (Figures 7, 8), 36.7% (20–50%) of neurons in the ipsilateral MNTB were retrogradely labeled in control animals (Figures 9A,B). In VPA-exposed animals, only 1.6% (1.3–2.9%) of neurons in the ipsilateral MNTB were labeled (Figures 9C,D). This difference was significant [$U(6,6) = 0$, $p = 0.001$; Figure 6B]. Contralateral to the injection site, only 0.43% (0–0.55%) MNTB neurons were retrogradely labeled in control animals and 0.18% (0–0.59%) MNTB neurons were labeled in VPA-exposed animals. This difference was not significant [$U(6,6) = 14$, $p = 0.57$; Figure 6B]. In control animals, MNTB neurons had a cross-sectional area of $182.5 \pm 65.37\ \mu m^2$. MNTB neurons retrogradely labeled from the MG had a cross-sectional area of $177.6 \pm 70.23\ \mu m^2$. This difference was not significant ($p = 0.98$; Figure 6C). In VPA-exposed animals, MNTB neurons had a cross-sectional area of $125.1 \pm 50.93\ \mu m^2$ and those retrogradely labeled from the MG had a cross sectional area of $126.1 \pm 43.88\ \mu m^2$. This difference was not significant ($p > 0.99$; Figure 6C). Consistent with our previous reports, MNTB neurons in control animals are significantly larger than those in VPA-exposed animals [$F(3, 144) = 10.84$, $p < 0.0001$]. Retrogradely, labeled neurons in the MNTB of control animals were significantly larger than those in VPA-exposed animals ($p = 0.035$; Figure 6C).

Proportion of SOC neurons projecting to the MG

Our previous studies indicate the rat MNTB contains 6,591 neurons in control animals and 5,300 neurons in VPA exposed animals (Table 1, columns A and B; Zimmerman et al., 2018). This equates to a 20% loss of neurons in the MNTB after VPA exposure. Our tract tracing experiments indicate that 36.7% of MNTB neurons in control and only 1.6% of MNTB neurons in VPA-exposed animals project to the ipsilateral MG. Based on these values, we estimate that in control animals 2,419 MNTB neurons project to the ipsilateral MG (Table 1, column F). However, after VPA exposure, this drops to only about 85 total neurons (Table 1, column G) and constitutes a loss of 96% of the MNTB projection to the MG.

In control animals, the vMG and mMG combined include 46,796 neurons, but only 23,403 neurons in VPA-exposed animals (Mansour et al., 2021b; Table 1, columns A and B). This equates to a 50% loss of neurons in the vMG and mMG after VPA exposure. Accordingly, there are nearly 15 times as many MG neurons per MNTB neuron projecting to the MG in VPA-exposed animals (Table 1, column H and I). This drastic change led us to ask if the MNTB projection to the MG was more severely impacted by VPA exposure than other SOC nuclei. Figure 6D shows linear correlation lines comparing the projection to the MG from the MSO and LSO combined and the MNTB alone. In control animals about 320 neurons from the ipsilateral MSO and LSO combined project to the MG while approximately 2,400 MNTB neurons make this projection. In VPA-exposed animals, only about 114 neurons from the MSO and LSO project to the MG, while only about 85 MNTB neurons make this projection (Figure 6F). Figure 5E shows linear correlation lines comparing the projection to the MG from the SPON and the MNTB. In control animals, approximately 450 SPON neurons project to the MG and only about 160 SPON neurons in VPA-exposed animals make this projection (Table 1, columns F and G) (Figure 6E). Together, this suggests that VPA exposure results in a ~65% decrease in the projection from the MSO and LSO and a 66% decrease in the projection from the SPON to the MG (Figure 6F). However, VPA exposure results in a 96% decrease in the projection from the MNTB to the MG (Figure 6F; Table 1, column F and G).

Finally, we asked if *in utero* VPA exposure altered the contributions of the SOC nuclei to the olivogeniculate projection (Mansour et al., 2021b). The proportional contributions of each SOC nucleus to the olivogeniculate projection are shown in Figure 5G. The control pie chart is based on distribution of 4,075 neurons; the VPA pie chart is based on distribution of only 840 neurons. The largest projection to the MG is from the medial SOC in control animals: 91% of the olivogeniculate projection comes from the SPON, DMW and MNTB. This proportion changes drastically after VPA exposure. In VPA-exposed animals, the SPON, DMW and MNTB contribute only 75% of the MG projection and the MSO and LSO contribute ~25%. In control animals, the largest single contributor to the olivogeniculate project is the MNTB (53%, Figure 6G). While in VPA-exposed animals the DMW is the largest single contributor (53%) followed by the LSO (21%, Figure 6G).

Since all auditory brainstem nuclei have fewer neurons after VPA exposure (except the VNTB: Mansour and Kulesza, 2021), we calculated a projection change. This calculation compares neuron loss and projection loss (Table 1, column K). A negative value indicates loss of projections beyond what is predicted by VPA-induced neuron loss. The MNTB has a projection change of −11.94 and the VCN has a projection change of −3.59, indicating these are the most severely affected of the brainstem nuclei.

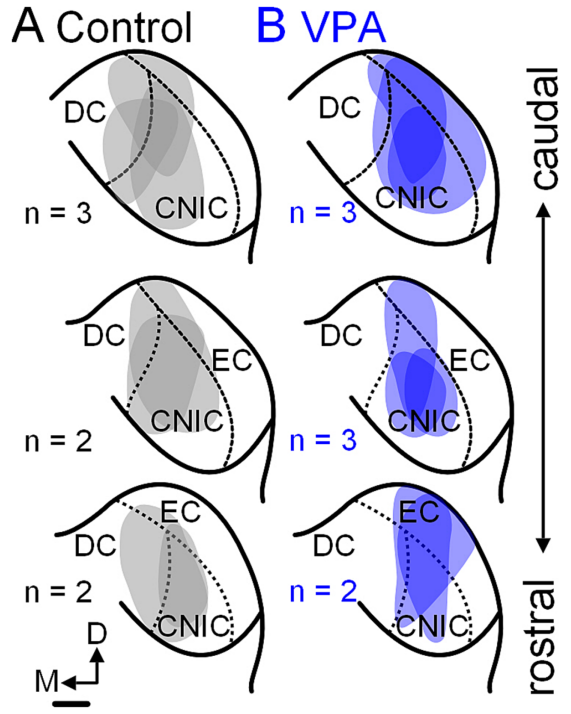


FIGURE 3
Tracer injection sites in the CNIC. Injection sites for the seven control animals are shown in panel **(A)** and those for the eight VPA-exposed animals are shown in panel **(B)**. These cases were selected to match injections site size and rostrocaudal distribution of injections between control and VPA-exposed animals. The scale bar is equal to 500 μm. D, Dorsal; DC, Dorsal cortex; EC, External cortex; and M, Medial.

Discussion

This study provides the first detailed examination of the impact of *in utero* exposure to the antiepileptic VPA on a novel, glycinergic projection from the MNTB to the auditory thalamus. It is important here to recall our finding that VPA exposure results in significantly smaller brains and brainstems (Zimmerman et al., 2018; Mansour et al., 2019). Accordingly, VPA animals received proportionally larger tracer deposits in the CNIC and MG and in theory this should result in more retrogradely labeled neurons, but this was not the case. *In utero* VPA exposure results in hypoplasia and dysmorphology in the auditory brainstem and thalamus, abnormal patterns of CB immunolabeling, reduced ascending projections to the CNIC and MG, abnormal auditory brainstem responses and imbalanced excitatory/inhibitory inputs to brainstem neurons (Zimmerman et al., 2018; Mansour et al., 2019; Zimmerman et al., 2020; Alhelo and Kulesza, 2022). Similar morphological changes have been found in the SOC of human subjects with ASD, including significantly fewer neurons in the MNTB (Kulesza and Mangunay, 2008; Kulesza et al., 2011; Lukose et al., 2015). Therefore, our findings may provide insight into structural and functional changes in the auditory pathway of subjects with ASD and other neurodevelopment disorders.

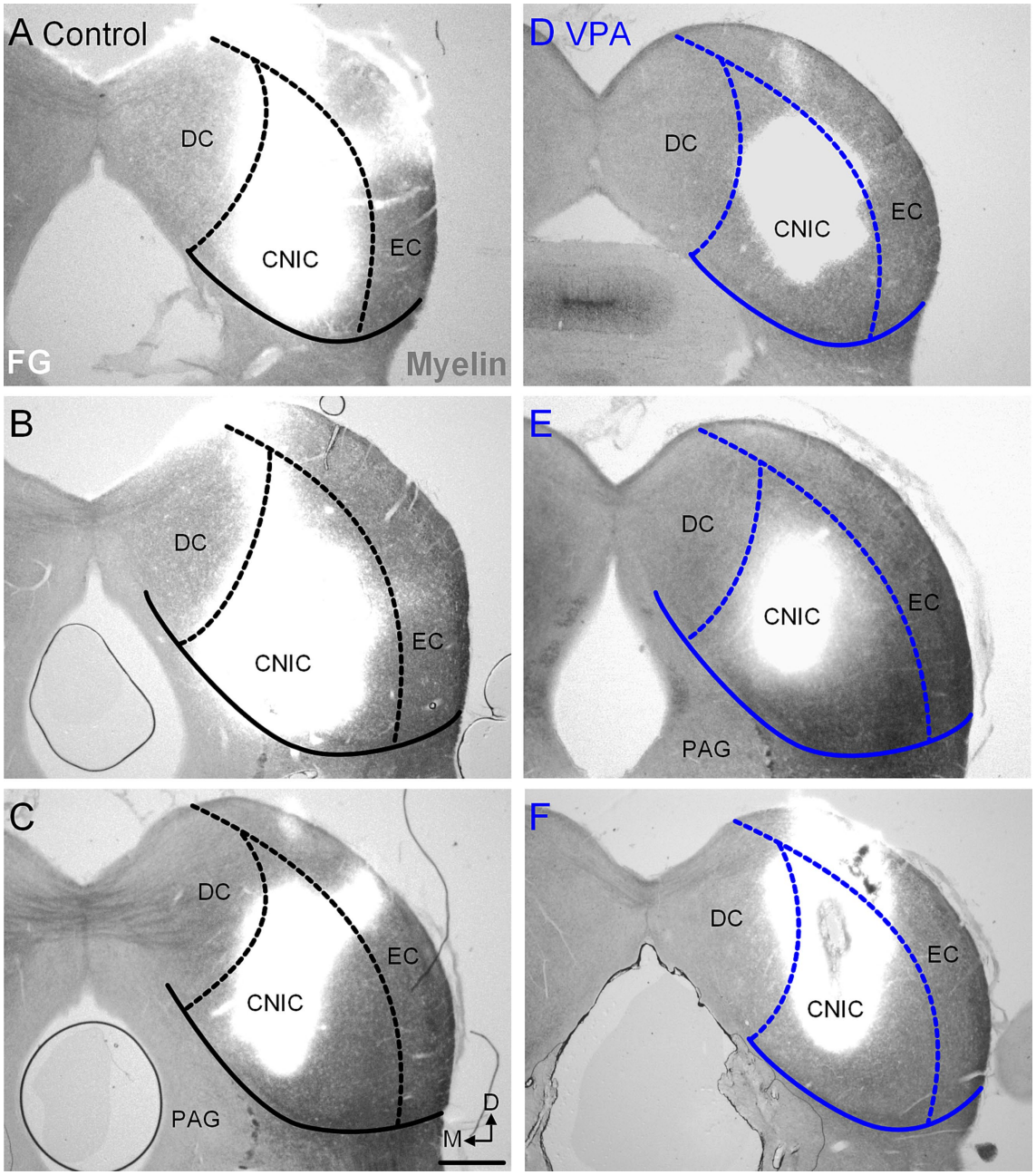


FIGURE 4
Injection sites in the CNIC. Representative examples of recovered injections sites in the CNIC are provided for control **(A–C)** and VPA-exposed animals **(D–F)**. The images were taken with simultaneous illumination with white light and a mercury lamp with a UV filter cube. Myeloarchitecture is shown in gray and the tracer injection in white. The scale bar is equal to 500 µm. D, Dorsal; DC, Dorsal cortex; EC, External cortex; M, Medial.

Connectivity of the MNTB

The MNTB receives a fast and precise glutamatergic input from GBCs in the contralateral VCN via the calyx of Held (Harrison and Irving, 1964; Morest, 1968a,b; Kuwabara et al., 1991; Smith et al., 1991). Consequently, evoked responses from MNTB principal neurons maintain the precision of the auditory nerve and GBCs. Principal MNTB neurons use glycine as a neurotransmitter (Moore and Caspary, 1983; Wenthold et al., 1987) and project to surrounding nuclei in the ipsilateral SOC (Moore and Caspary, 1983; Kuwabara and Zook, 1992; Sommer et al., 1993; Smith et al., 1998), the ipsilateral VCN (guinea pig: Schofield, 1994), and VNLL and INLL (Spangler et al., 1985; Sommer et al., 1993; Smith et al., 1998; Kelly et al., 2009; Saldaña et al., 2009). Glycinergic input from the MNTB to the MSO and LSO plays essential roles in coding sound source localization (Zarbin et al., 1981; Moore and Caspary, 1983; Kuwabara and Zook, 1992; Grothe and Sanes, 1993; Kapfer et al., 2002). In the SPON, MNTB inputs form temporally precise rebound responses that code the offset of tone-pips and rapid fluctuations in the stimulus envelope (Kulesza et al., 2003; Kadner et al., 2006). The projection from the MNTB to the MG is a recent discovery—it was first described in guinea pigs (Schofield et al.,

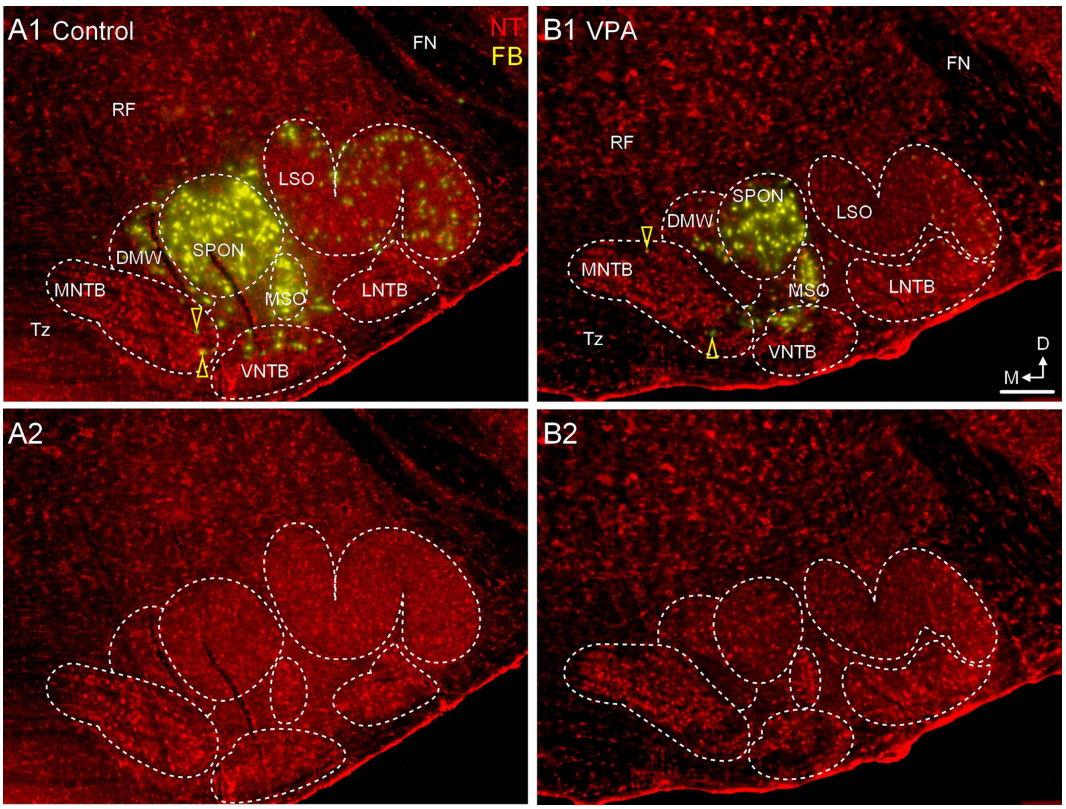


FIGURE 5
Only occasional MNTB neurons project to the CNIC. Panels **(A1,B1)** show sections through the same rostrocaudal level of the SOC from a control **(A1,A2)** and VPA-exposed animal **(B1,B2)** after tracer injection in the CNIC. Retrogradely-labeled neurons are pseudocolored yellow and Neurotrace counter-stained cells are shown in red (NT). Retrogradely labeled MNTB neurons are indicated with yellow arrowheads. Panels **(A2,B2)** show the Neurotrace counter-stained sections from panels **(A1,B1)** but without the tracer label for reference. The scale bar is equal to 500μm. D, Dorsal; FN, Facial nerve; LNTB, Lateral nucleus of the trapezoid body; M, Medial; RF, Reticular formation; Tz, Trapezoid body; VNTB, Ventral nucleus of the trapezoid body.

2014b), but in this species appears to originate from non-principal MNTB neurons. In rats, deposits of retrograde tracers in the vMG and dMG result in robust labeling in the ipsilateral MNTB (Burchell et al., 2022). Our injections in the MG resulted in labeling across the auditory brainstem, consistent with previous reports of thalamic projections from the CNIC, NLL, SOC, and VCN from other species (ferrets: Angelucci et al., 1998; guinea pig: Schofield et al., 2014a,b; rat: Mansour et al., 2021b). It should be emphasized that in control animals, focal injections of FG restricted to the vMG resulted in labeling of up to 84% of MNTB neurons (Burchell et al., 2022). Approximately 87% of MNTB neurons retrogradely labeled from the vMG are CB immunoreactive, confirming that at least in the rat, the thalamic projection from the MNTB is derived from principal neurons (Burchell et al., 2022). Deposits of an anterograde tracer in the MNTB resulted in labeled axons and terminals in the SPON, LSO, VNLL, (consistent with previous reports; see above) but also the ipsilateral nucleus of the brachium of the inferior colliculus and vMG (Burchell et al., 2022). Consistent with a glycinergic projection to the auditory thalamus, there is dense somatic immunolabeling for the glycine receptor in the dMG and vMG, with only scant labeling in the mMG (Burchell et al., 2022). Together, these results support the presence of a prominent projection from MNTB principal neurons in rats providing a fast, glycinergic input to the vMG.

Functions of the MNTB projection to the auditory thalamus

The role of direct projections from the cochlear nuclei and SOC to the MG are unclear. Specifically, there is a direct projection from stellate neurons in the VCN to the contralateral CNIC and MG (Malmierca et al., 2002; Schofield et al., 2014a; Zimmerman et al., 2020). Our results show that 13,913 neurons in the rat VCN project to the contralateral CNIC (Zimmerman et al., 2020) and 7,164 neurons in the VCN project to the contralateral MG (Mansour et al., 2021b). In the current study, we show that 2,419 MNTB neurons project to the ipsilateral MG. Outside of the VNLL, whose thalamic projection has not yet been examined in rats, the VCN appears to be the largest single subcollicular source of input to the MG, followed by the MNTB (Table 1; Mansour et al., 2021b). The stellate neuron input from the VCN is most likely excitatory based on the nature of VCN projections to the CNIC (Ito and Oliver, 2010) and seems to be most heavily directed to the contralateral mMG (Malmierca et al., 2002; Schofield et al., 2014a). The mMG receives input from the inferior colliculus, CN, SOC, NLL (Schofield et al., 2014a,b; Malmierca et al., 2002; Anderson et al., 2006) and several non-auditory sources. The mMG also receives input from the vestibular system (Roucoux-Hanus and Boisacq-Schepens, 1977) and spinothalamic tract relaying pain and thermal sense (LeDoux et al., 1987). The mMG projects to auditory, somatosensory and prefrontal

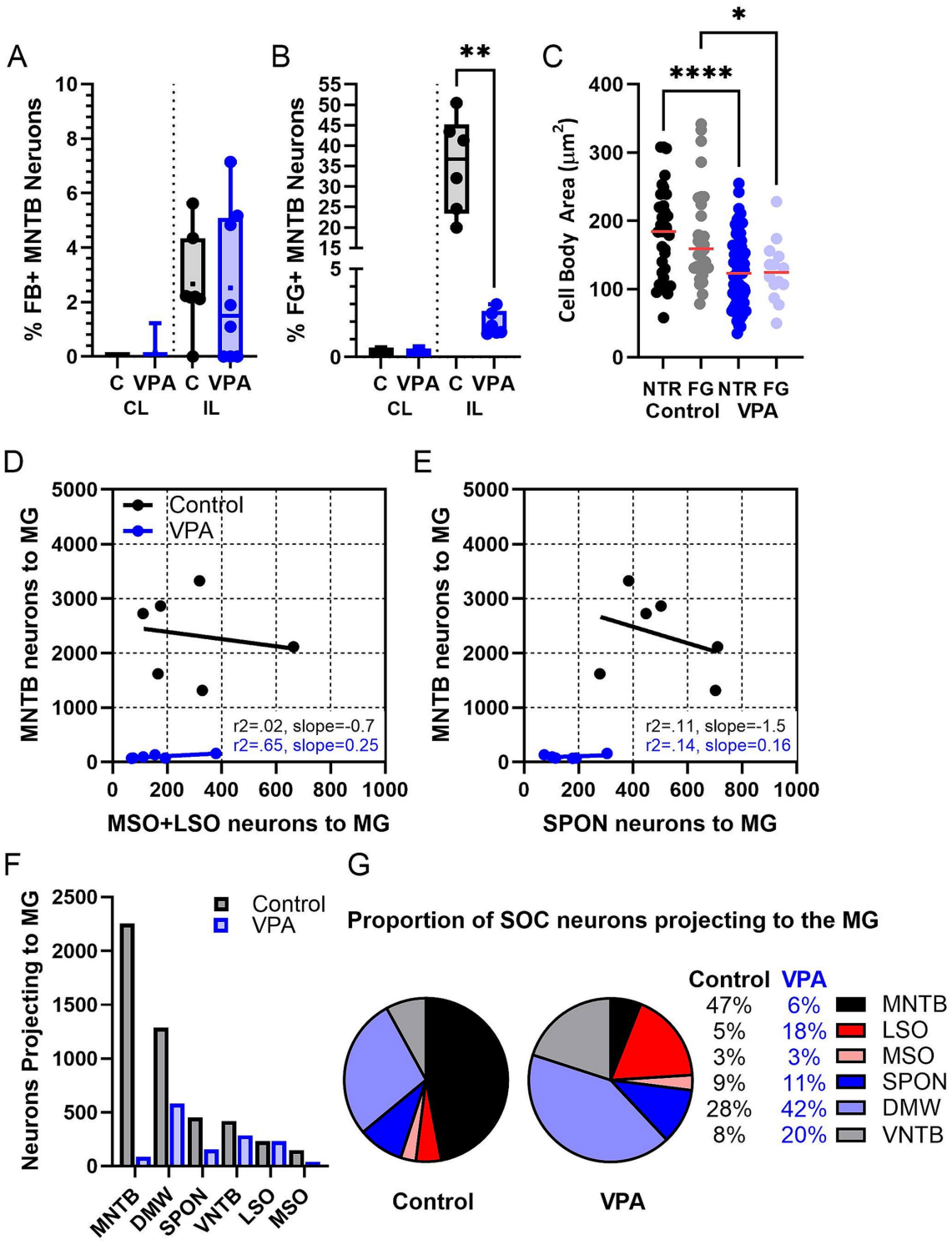


FIGURE 6
Quantification of the MNTB projection. Panel **(A)** shows the percentage of MNTB neurons that were retrogradely labeled from the CNIC (Mann–Whitney). Panel **(B)** shows the percentage of MNTB neurons retrogradely labeled from the MG (Mann–Whitney). Each data point is averaged data from one animal. Panel **(C)** shows the cross-sectional area of MNTB neurons in control and VPA-exposed animals comparing counterstained (NTR) and retrogradely labeled (FG) neurons (ANOVA). Panel **(D)** shows linear correlation comparing the number of neurons projecting to the MG from the MSO and LSO to the number of neurons projecting to the MG from the MNTB. Panel **(E)** shows linear correlation comparing the number of neurons projecting to the MG from the SPON to the number of neurons projecting to the MG from the MNTB. In Panel **(D,E)**, each data point corresponds to one animal. Panel **(F)** shows the mean number of SOC neurons projecting to the MG in control and VPA-exposed animals. Panel **(G)** shows the distribution of neurons participating in the olivogeniculate projection. The control chart is based on distribution of 7,166 neurons and the VPA chart is based on distribution of 825 neurons. C, Control; CL, Contralateral; DMW, Dorsal medial wedge; FG, Fluorogold; IL, Ipsilateral; LSO, Lateral superior olive; MSO, Medial superior olive; NTR, Neurotrace red; SPON, Superior paraolivary nucleus. Key to symbols: $*p < 0.05$; $**p < 0.01$, and $****p < 0.0001$.

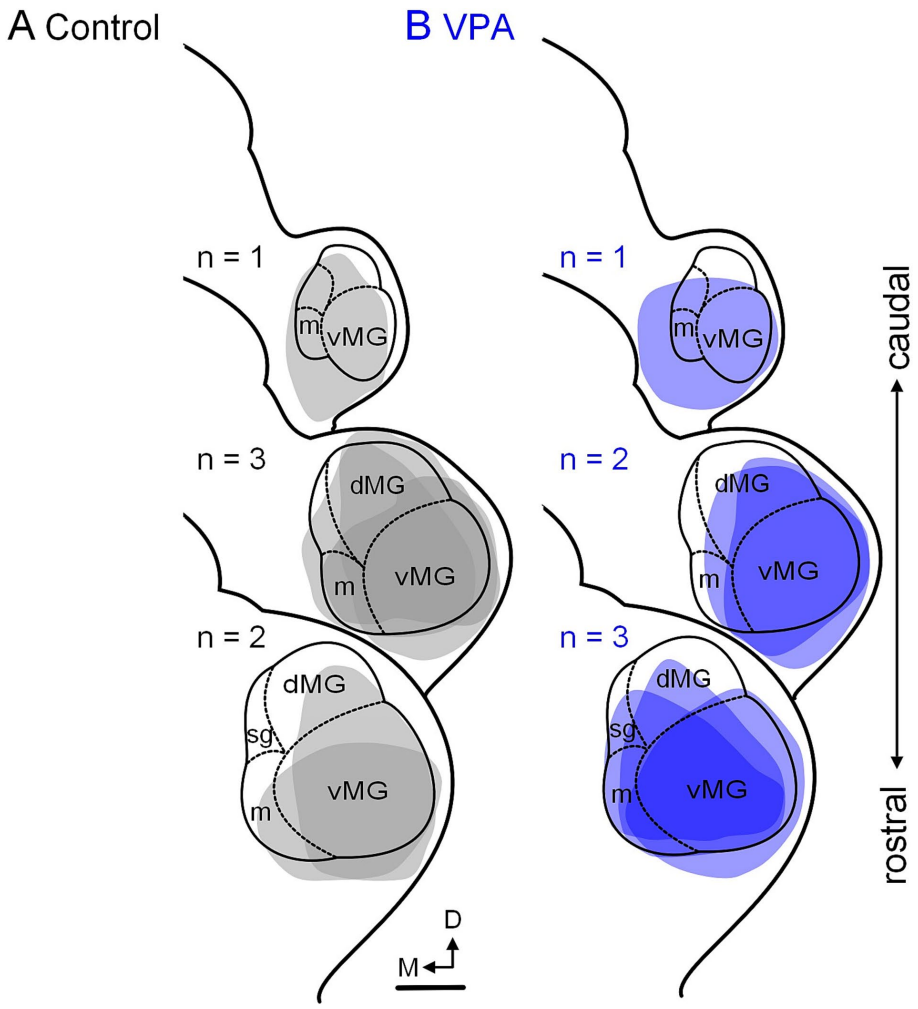


FIGURE 7
Tracer injection sites in the MG. Injection sites for the six control animals are shown in panel **(A)** and those for the six VPA-exposed animals are shown in panel **(B)**. These cases were selected to match injections site size and rostrocaudal distribution of injections between control and VPA-exposed animals. The scale bar is equal to 200 µm. D, Dorsal; dMG, Dorsal nucleus of the medial geniculate; m, Medial nucleus of the medial geniculate; M, Medial; vMG, Ventral nucleus of the medial geniculate.

cortex (Spreafico et al., 1981; Avedaño and Llamas, 1984; Winer, 1985), amygdala (Ottersen and Ben-Ari, 1979; LeDoux et al., 1985; Doron and LeDoux, 1999) and provides descending input to the auditory brainstem (Whitley and Henkel, 1984). Together, these features of the mMG illustrate its possible role in integration across several sensory modalities. The MNTB input is most likely glycinergic and mainly targets the vMG (Burchell et al., 2022). The vMG is the main relay of ascending auditory information from the CNIC to the auditory cortex (Ryugo and Killackey, 1974; LeDoux et al., 1987; Winer and Larue, 1987; González-Hernández et al., 1991; Clerici and Coleman, 1990; Winer et al., 1999; Kimura et al., 2003; Hazama et al., 2004; Ito and Oliver, 2012; Smith et al., 2012) and therefore its functions are likely focused on hearing. The roles these inputs from the VCN and MNTB play in shaping responses of neurons across the MG subdivision are unclear, but they clearly provide fast and precise input to the auditory thalamus (Schofield et al., 2014b). It is important to emphasize that based on tract tracing studies in rat and guinea pig (Malmierca et al., 2002; Schofield et al., 2014a,b; Burchell et al., 2022), the VCN and MNTB projections are targeting different regions of the MG and would appear to be functionally independent. As such, we will only discuss the MNTB projection further.

Within the SOC, glycinergic input from the MNTB to the MSO arrives before excitatory, glutamatergic inputs from the ipsilateral VCN, despite a longer axon distance and extra synapse (Grothe, 1994; Grothe and Sanes, 1993; Roberts et al., 2014). In the rat, MNTB principal neurons have spontaneous discharge rates of 20–30 spikes/s and respond to pure tone-pips with precise temporal patterns of action potentials; shortly following the stimulus offset, MNTB neurons have a brief window of quiescence and then gradually resume their spontaneous discharge rate (Kulesza et al., 2003; Kulesza, 2007; Kadner et al., 2006; Kadner and Berrebi, 2008; Kopp-Scheinpflug et al., 2008). This post-stimulus interruption in MNTB responses to pure tone-pips is essential in the formation of offset responses in the SPON (Kulesza et al., 2003; Kadner et al., 2006). Together, these findings suggest that glycinergic input from the MNTB likely reaches the vMG before any other lemniscal inputs, but more importantly provides fast and temporally precise inhibition. Additionally, based on our tracer injections in the IC and MG, it appears that the MNTB projection to the vMG has very few if any

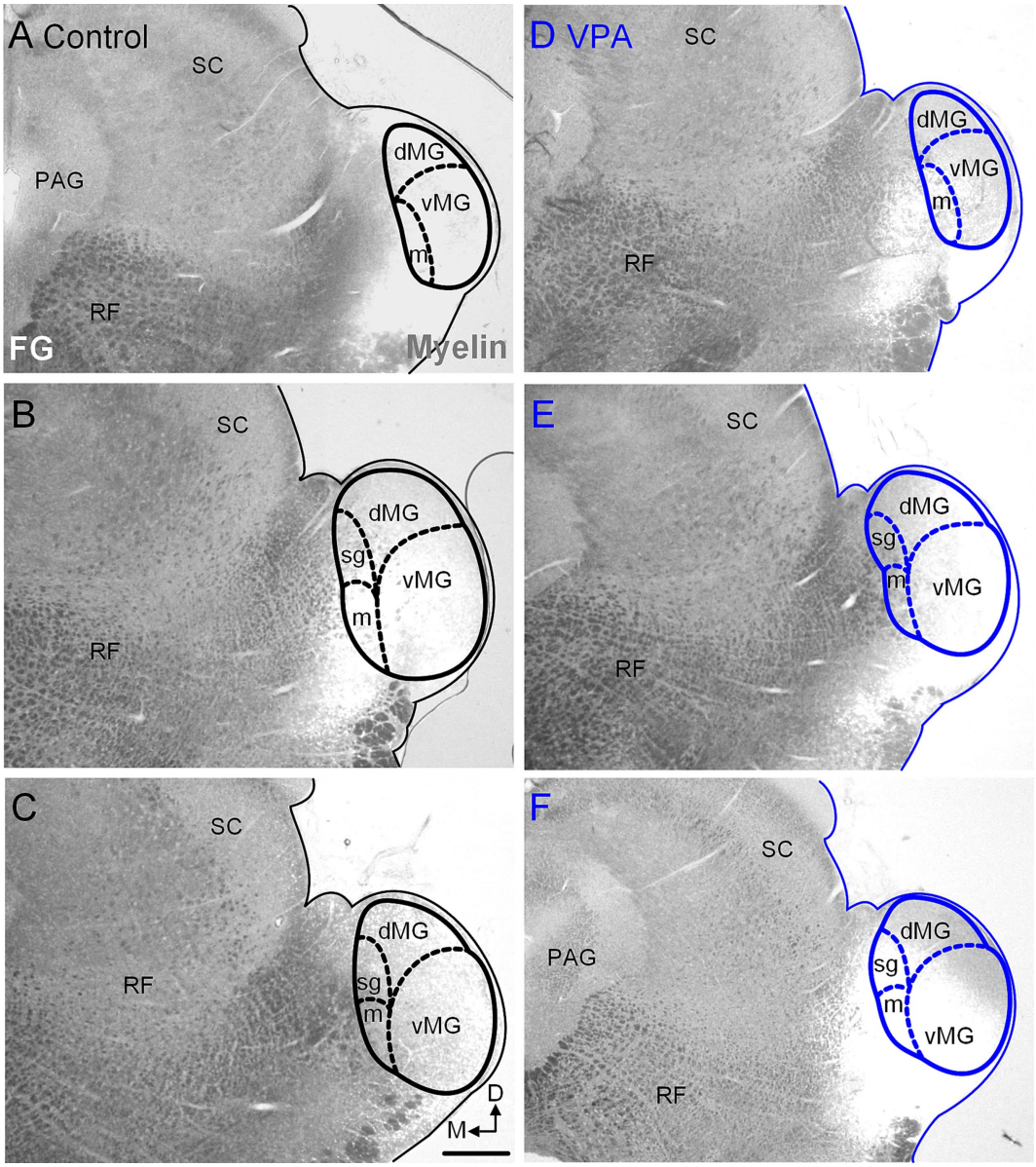


FIGURE 8
Injection sites in the MG. Representative examples of recovered injections sites in the MG are provided for control **(A–C)** and VPA-exposed animals **(D–F)**. The images were taken with simultaneous illumination with white light and a mercury lamp with a UV filter cube. Myeloarchitecture is shown in gray and the tracer injection in white. The scale bar is equal to 200 µm. D, Dorsal; dMG, Dorsal nucleus of the medial geniculate; m, Medial nucleus of the medial geniculate; M, Medial; vMG, Ventral nucleus of the medial geniculate.

collaterals to the CNIC (Figure 8)—this is unique among nuclei in the CN, SOC and NLL projecting to the thalamus. The reason for this projection pattern is unclear but we propose that maintenance of the timing and integration of this glycinergic input is functionally important for at least a subset of functionally distinct vMG neurons (see below).

In vivo recordings in rabbits reveal that about 8% of neurons in the rabbit vMG respond to pure tones with offset responses and about 3% of neurons respond to pure tone-pips with on/off responses (Cetas et al., 2002). Similar offset-type responses have been found in and around the vMG of other species (guinea pig: Yu et al., 2004; cat: Aitkin and Prain, 1974, mouse: Anderson and Linden, 2016). Our immunolabeling for the glycine receptors in the dMG and vMG is largely somatic, similar to what is found in the SPON (Kulesza and Berrebi, 2000), where glycinergic inputs play an essential role in forming offset responses (Kulesza, 2007; Burchell et al., 2022). Based on the role of the MNTB in forming offset responses in the SPON and the distribution of glycine receptor positive puncta in the vMG, we hypothesize that the MNTB input to this region functions, at least in part, to create responses timed to the stimulus offset.

Impact of VPA exposure on connectivity in the auditory brainstem

In control animals, we estimate about 20,326 total neurons in the SOC (LSO, MSO, MNTB, SPON, VNTB, LNTB and DMW). However, in VPA-exposed animals, there are only 15,136 total

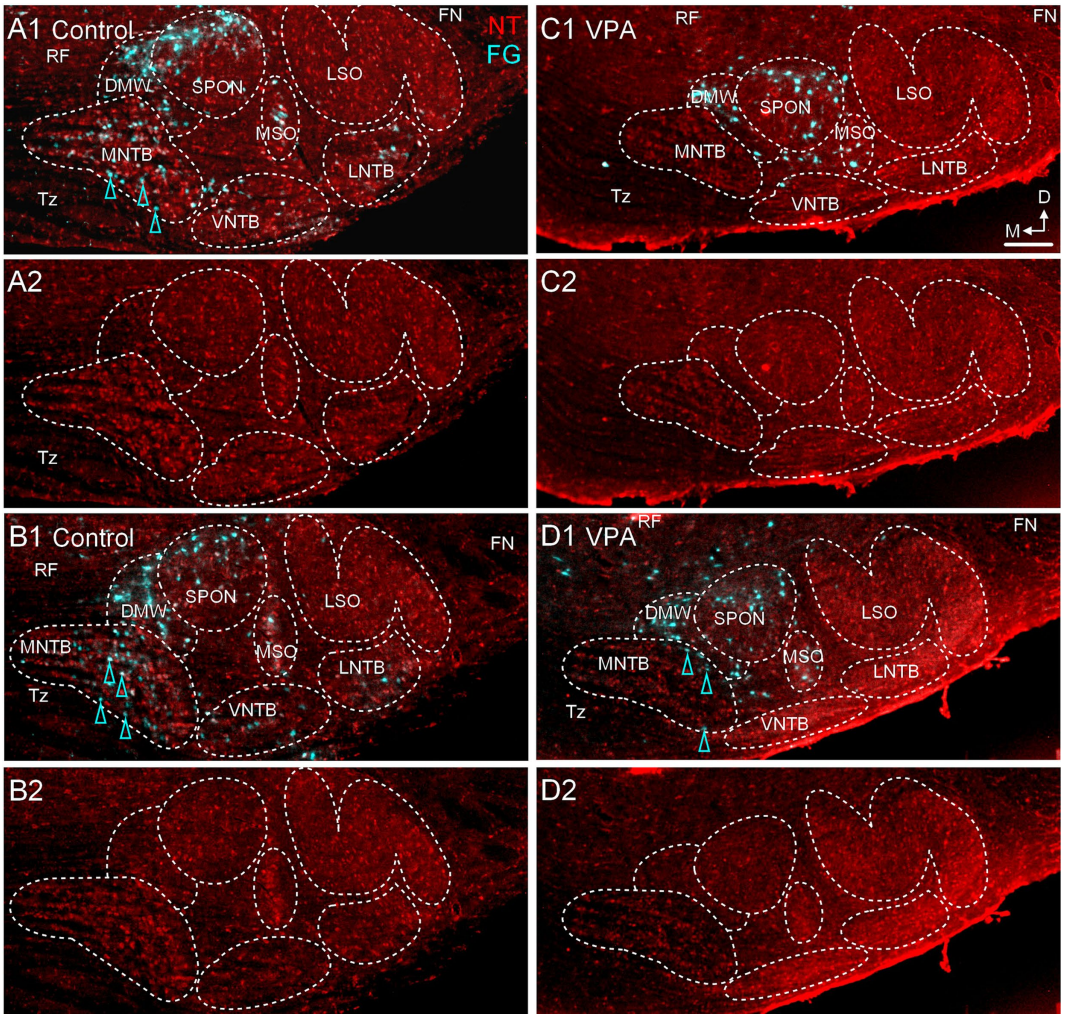


FIGURE 9
VPA exposure abolishes the projection from the MNTB to the MG. Retrograde labeling from a deposit of FG in the MG is shown for control **(A1, B1)** and VPA-exposed animals **(C1,D1)**. Panels **(A1,A2,B1,B2)** are from two different control animals; panels **(C1,C2,D1,D2)** are from two different VPA-exposed animals. Retrogradely labeled neurons are pseudocolored cyan and Neurotrace counter-stained cells are shown in red (NT). Retrogradely labeled neurons are indicated with cyan arrowheads. Panels **(A2,B2,C2,D2)** show Neurotrace counter-stained sections without the tracer label for reference. The scale bar in panel **(C1)** is equal to 200 μm and applies to all images. D, Dorsal; FN, Facial nerve; LNTB, Lateral nucleus of the trapezoid body; M, Medial; RF, Reticular formation; Tz, Trapezoid body; VNTB, Ventral nucleus of the trapezoid body.

neurons in these nuclei—this equates to a 26% decrease in the total number of neurons in the SOC. However, VPA exposure results in approximately a 49% decrease in the SOC projection to the CNIC (Zimmerman et al., 2020) and a 73% decrease in the SOC projection to the MG (Mansour et al., 2021b; Mansour and Kulesza, 2021). Additionally, VPA exposure appears to result in a significant reorganization of the olivogeniculate projection in rats. VPA exposure results in a 20% decrease in the total number of MNTB neurons (Zimmerman et al., 2018) but a 96% decrease in the total number of MNTB neurons projecting to the MG (Mansour et al., 2021b). VPA exposure results in a 25% decrease in the total number of LSO neurons (Zimmerman et al., 2018). The ascending projection from the LSO to the ipsilateral CNIC is inhibitory and likely glycinergic, while the projection to the contralateral CNIC is glutamatergic (Ito and Oliver, 2010). VPA exposure results in a 34% decrease in the ipsilateral projection and a 47% decrease in the contralateral projection from the LSO to the CNIC (Zimmerman et al., 2020). However, VPA exposure resulted in a 57% decrease in the ipsilateral projection (glycine) but a 172% increase in the contralateral projection to the MG from the LSO (Mansour et al., 2021b). The MSO projection to the MG is likely glutamatergic. VPA exposure results in a 57% decrease in the total number of MSO neurons (Zimmerman et al., 2018), a 74% decrease in the number of MSO neurons projecting to the CNIC (Zimmerman et al., 2020) and 74% decrease in the number of neurons projecting to the MG (Mansour et al., 2021b). The SPON projection to the MG is most likely GABAergic (Kulesza and Berrebi, 2000). VPA exposure results in a 43% decrease in the total number of SPON neurons (Zimmerman et al., 2018), a 61% decrease in the number of SPON neurons projecting to the CNIC and a 66% decrease in the total number of SPON neurons projecting to the MG (Mansour et al., 2021b). While VPA exposure results in significant reorganization of the olivogeniculate projection (Figure 5G), there is still a net reduction in the number of SOC neurons projecting to the thalamus. Specifically, the proportion of VNTB and DMW neurons

projecting to the MG increases (Figure 5G), but there is an overall reduction in the number of neurons projecting to the MG from these nuclei (Table 1, column K). The only exception to this pattern is from the contralateral LSO (Table 1, column K). There are glycinergic neurons in the rat LSO, VNTB and LNTB (Wenthold et al., 1987; Rampon et al., 1996) and changes in projections from these nuclei may compensate for the loss of glycinergic input from the MNTB, although they likely cannot provide the same temporal precision. Besides the MNTB, these results do not currently provide a clear pattern for the impact of *in utero* VPA exposure on projections of specific nuclei or neurotransmitter systems in the auditory brainstem. VPA has been shown to inhibit neurite outgrowth (Qian et al., 2009), and we propose that the drastic reduction in the thalamic projection of the MNTB is due to the impact of VPA on developing axons. Nonetheless, these results emphasize two important points. First, our findings are consistent with loss of projections to both the CNIC and MG beyond what is predicted from neuron loss alone (Table 1, column K). Second, VPA exposure seems to have a preferential impact on longer axonal projections and the MNTB projection to the thalamus in particular.

As we have previously shown, the number of neurons from the VCN and most SOC nuclei projecting to the MG are fewer than those projecting to the CNIC. There are however two exceptions to this: the DMW and MNTB (Burchell et al., 2022). In control animals, we estimate that only about 810 DMW neurons (combined ipsilateral and contralateral) project to the CNIC but 1,286 neurons project to the vMG (1.6-fold larger thalamic projection). In VPA-exposed animals we estimate that 174 DMW neurons project to the CNIC and about 583 neurons project to the vMG (3.3-fold larger thalamic projection). This is mainly attributable to a nearly 10-fold decrease in the projection from the ipsilateral DMW to the vMG after VPA exposure. In control animals, we estimate that only about 145 MNTB neurons project to the CNIC but 2,256 neurons project to the vMG (16-fold larger thalamic projection). In VPA-exposed animals we estimate that approximately 80 MNTB neurons project to the CNIC and only about 85 neurons project to the vMG. This difference in the number of MNTB neurons projecting to the MG compared to the CNIC in VPA-exposed animals is essentially 0 and is consistent with abolishment of the thalamic projection from the MNTB (Figure 1). This finding is based on injections of the retrograde tracer FG into the MG. Anterograde tracing experiments will undoubtably provide additional insight into course, collaterals and distribution of MNTB axons beyond the SOC. It is not clear to what degree MNTB projections to the CN, SPON, MSO, LSO and NLL are impacted by *in utero* VPA exposure, but we will explore these projections in future studies.

Impact of loss of MNTB input to the vMG

The role of glycinergic input to the VNLL, INLL or vMG from the MNTB is not well characterized, so we can only speculate on the impact of losing this projection. Again, we propose that at least in the vMG, the MNTB input contributes to formation of offset responses. VPA exposure appears to abolish this projection to the vMG and so we hypothesize that VPA-exposed animals have significantly fewer offset responding neurons in the vMG. While there are significantly fewer MNTB and SPON neurons in VPA-exposed animals, we have not examined the distribution of glycine receptors or glycine-immunoreactive puncta in the SPON. MNTB principal neurons are characteristically CB+, but VPA exposure results in reduced CB immunolabeling in the MNTB, and many MNTB neurons have CB immunoreactivity restricted to the nucleus (Zimmerman et al., 2018), so counting CB+ puncta may not be a viable metric to quantify this projection to the SPON, VNLL or INLL. Regardless, VPA exposure results in near complete loss of MNTB input to the vMG. Since the MNTB input would provide a fast, glycinergic input to vMG neurons we hypothesize that VPA-exposed animals have reduced coding of temporal information in the auditory thalamus. This most likely impairs coding of complex sounds such as vocalizations.

Interestingly, the physiological impact of abolishing the thalamic projection from the MNTB may not be so clear cut. Mice with deletion of the transcription factor *En1*, lack MNTB and VNTB neurons but neurons in the LSO and SPON still receive glycinergic innervation (Jalabi et al., 2013; Altieri et al., 2014). Mice lacking an MNTB had normal sound-evoked startle responses, but elevated thresholds to pure tones, significantly reduced amplitude of wave III, which is attributed largely to the MNTB and reduced sound localization abilities (Jalabi et al., 2013). However, these mice have fewer GlyT2+ puncta in the LSO but no change in the SPON. The development of these GlyT2+ puncta in the LSO even followed a similar time course as control animals, but was delayed in the SPON (Altieri et al., 2014). In fact, strychnine-sensitive offset responses could still be elicited in the SPON, despite there being no MNTB neurons (Jalabi et al., 2013). The origin of these glycinergic inputs to the SPON and LSO in the absence of MNTB neurons has not been resolved, but likely arise from the contralateral VCN (Jalabi et al., 2013).

Our tract tracing studies show that the projection to the MG from the contralateral VCN is greatly reduced in VPA-exposed animals (Table 1). Specifically, deposits of retrograde tracers in the MG results in labeling of about 7,166 VCN neurons in control animals but only 825 neurons in VPA-exposed animals (Mansour et al., 2021b)—this equates to a 88% decrease. While the VCN may reprogram to compensate for loss of local glycinergic projections in *En1* deficit animals, this does not appear likely for long-range projections in VPA-exposed animals. Therefore, we hypothesize significant loss of glycinergic innervation of the vMG and dMG in VPA-exposed animals. Regardless, our results are consistent with significantly reduced and disproportionate ascending thalamic projections in VPA-exposed animals. These changes likely translate into impaired temporal and spectral coding of auditory information in the MG and auditory cortex and provide evidence that certain projections may be preferentially impacted in animal models of ASD.

Data availability statement

The raw data supporting the conclusions of this article will be made available by the authors, without undue reservation.

Ethics statement

The animal study was approved by Lake Erie College of Osteopathic Medicine IACUC. The study was

conducted in accordance with the local legislation and institutional requirements.

Author contributions

YM: Data curation, Investigation, Methodology, Writing – review & editing. RK: Conceptualization, Data curation, Formal analysis, Funding acquisition, Investigation, Methodology, Project administration, Resources, Software, Supervision, Validation, Visualization, Writing – original draft, Writing – review & editing.

Funding

The author(s) declare that no financial support was received for the research, authorship, and/or publication of this article.

Conflict of interest

The authors declare that the research was conducted in the absence of any commercial or financial relationships that could be construed as a potential conflict of interest.

The author(s) declared that they were an editorial board member of Frontiers, at the time of submission. This had no impact on the peer review process and the final decision.

Publisher's note

All claims expressed in this article are solely those of the authors and do not necessarily represent those of their affiliated organizations, or those of the publisher, the editors and the reviewers. Any product that may be evaluated in this article, or claim that may be made by its manufacturer, is not guaranteed or endorsed by the publisher.

References

Adams, J. C. (1979). Ascending projections to the inferior colliculus. *J. Comp. Neurol.* 183, 519–538. doi: 10.1002/cne.901830305

Aitkin, L. M., and Prain, S. M. (1974). Medial geniculate body: unit responses in the awake cat. *J. Neurophysiol.* 37, 512–521. doi: 10.1152/jn.1974.37.3.512

Alcántara, J. I., Weisblatt, E. J., Moore, B. C., and Bolton, P. F. (2004). Speech-in-noise perception in high-functioning individuals with autism or Asperger's syndrome. *J. Child Psychol. Psychiatry* 45, 1107–1114. doi: 10.1111/j.1469-7610.2004.t01-1-00303.x

Alhelo, H., and Kulesza, R. J. (2022). Brainstem motor neuron dysmorphology and excitatory/inhibitory imbalance in an animal model of autism. *Folia Morphol. (Warsz)* 81, 863–873. doi: 10.5603/FM.a2021.0098

Allen, D. A. (1988). Austistic Spectrum disorders: clinical presentation in preschool children. *J. Child Neurol.* 3, S48–S56. doi: 10.1177/088307388003001S10

Altieri, S. C., Zhao, T., Jalabi, W., and Maricich, S. M. (2014). Development of glycinergic innervation to the murine LSO and SPN in the presence and absence of the MNTB. *Front. Neural Circuits* 8:109. doi: 10.3389/fncir.2014.00109

American Psychiatric Association (2013). Diagnostic and Statistical Manual of Mental Disorders. Washington, DC.

Anderson, L. A., and Linden, J. F. (2016). Mind the gap: two dissociable mechanisms of temporal processing in the auditory system. *J. Neurosci.* 36, 1977–1995. doi: 10.1523/JNEUROSCI.1652-15.2016

Anderson, L. A., Malmierca, M. S., Wallace, M. N., and Palmer, A. R. (2006). Evidence for a direct, short latency projection from the dorsal cochlear nucleus to the auditory thalamus in the guinea pig. *Eur J Neurosci.* 24, 491–8.

Angelucci, A., Clascá, F., and Sur, M. (1998). Brainstem inputs to the ferret medial geniculate nucleus and the effect of early deafferentation on novel retinal projections to the auditory thalamus. *J. Comp. Neurol.* 400, 417–439. doi: 10.1002/(SICI)1096-9861(19981026)400:3<417::AID-CNE10>3.0.CO;2-O

Arai, R., Winsky, L., Arai, M., and Jacobowitz, D. M. (1991). Immunohistochemical localization of calretinin in the rat hindbrain. *J. Comp. Neurol.* 310, 21–44. doi: 10.1002/cne.903100105

Avedafio, C., and Llamas, A. (1984). "Thalamic and nonthalamic projections to association areas of the cat's cerebral cortex" in Cortical Integration. eds. F. Reinoso-Suarez and C. Ajmone-Marsan (New York: Raven Press), 195–211.

Azouz, H. G., Kozou, H., Khalil, M., Abdou, R. M., and Sakr, M. (2014). The correlation between central auditory processing in autistic children and their language processing abilities. *Int. J. Pediatr. Otorhinolaryngol.* 78, 2297–2300. doi: 10.1016/j.ijporl.2014.10.039

Banks, M. I., and Smith, P. H. (1992). Intracellular recordings from neurobiotin-labeled cells in brain slices of the rat medial nucleus of the trapezoid body. *J. Neurosci.* 12, 2819–2837. doi: 10.1523/JNEUROSCI.12-07-02819.1992

Beyerl, B. D. (1978). Afferent projections to the central nucleus of the inferior colliculus in the rat. *Brain Res.* 145, 209–223. doi: 10.1016/0006-8993(78)90858-2

Bolton, P. F., Golding, J., Emond, A., and Steer, C. D. (2012). Autism spectrum disorder and autistic traits in the Avon longitudinal study of parents and children: precursors and early signs. *J. Am. Acad. Child Adolesc. Psychiatry* 51, 249–260.e25. doi: 10.1016/j.jaac.2011.12.009

Bromley, R. L., Mawer, G. E., Briggs, M., Cheyne, C., Clayton-Smith, J., Garcia-Finana, M., et al. (2013). The prevalence of neurodevelopmental disorders in children prenatally exposed to antiepileptic drugs. *J. Neurol. Neurosurg. Psychiatry* 84, 637–643. doi: 10.1136/jnnp-2012-304270

Brunso-Bechtold, J. K., Thompson, G. C., and Masterton, R. B. (1981). HRP study of the organization of auditory afferents ascending to central nucleus of inferior colliculus in cat. *J. Comp. Neurol.* 197, 705–722. doi: 10.1002/cne.901970410

Burchell, A., Mansour, Y., and Kulesza, R. (2022). Leveling up: a long-range olivary projection to the medial geniculate without collaterals to the central nucleus of the inferior colliculus in rats. *Exp. Brain Res.* 240, 3217–3235. doi: 10.1007/s00221-022-06489-2

Cant, N. B., and Benson, C. G. (2006). Organization of the inferior colliculus of the gerbil (*Meriones unguiculatus*): differences in distribution of projections from the cochlear nuclei and the superior olivary complex. *J. Comp. Neurol.* 495, 511–528. doi: 10.1002/cne.20888

CDC.gov (2024). Available online at: http://www.cdc.gov/ncbddd/autism/index.html (Accessed Jan 8, 2023).

Cetas, J. S., Price, R. O., Velenovsky, D. S., Crowe, J. J., Sinex, D. G., and McMullen, N. T. (2002). Cell types and response properties of neurons in the ventral division of the medial geniculate body of the rabbit. *J. Comp. Neurol.* 445, 78–96. doi: 10.1002/cne.10164

Christensen, J., Grønborg, T. K., Sørensen, M. J., Schendel, D., Parner, E. T., Pedersen, L. H., et al. (2013). Prenatal valproate exposure and risk of autism spectrum disorders and childhood autism. *JAMA* 309, 1696–1703. doi: 10.1001/jama.2013.2270

Clerici, W. J., and Coleman, J. R. (1990). Anatomy of the rat medial geniculate body: I. Cytoarchitecture, myeloarchitecture, and neocortical connectivity. *J. Comp. Neurol.* 297, 14–31. doi: 10.1002/cne.902970103

Coleman, J. R., and Clerici, W. J. (1987). Sources of projections to subdivisions of the inferior colliculus in the rat. *J. Comp. Neurol.* 262, 215–226. doi: 10.1002/cne.902620204

Delgado, C. F., Simpson, E. A., Zeng, G., Delgado, R. E., and Miron, O. (2023). Newborn auditory brainstem responses in children with developmental disabilities. *J. Autism Dev. Disord.* 53, 776–788. doi: 10.1007/s10803-021-05126-1

Doron, N. N., and Ledoux, J. E. (1999). Organization of projections to the lateral amygdala from auditory and visual areas of the thalamus in the rat. *J Comp Neurol.* 412:383–409.

Druga, R., and Syka, J. (1984). Ascending and descending projections to the inferior colliculus in the rat. *Physiol. Bohemoslov.* 33, 31–42

Dubiel, A., and Kulesza, R. J. Jr. (2016). Prenatal valproic acid exposure disrupts tonotopic c-Fos expression in the rat brainstem. *Neuroscience* 324, 511–523. doi: 10.1016/j.neuroscience.2016.01.030

Friauf, E., and Ostwald, J. (1988). Divergent projections of physiologically characterized rat ventral cochlear nucleus neurons as shown by intra-axonal injection of horseradish peroxidase. *Exp. Brain Res.* 73, 263–284. doi: 10.1007/BF00248219

Gillberg, C., Rosenhall, U., and Johansson, E. (1983). Auditory brainstem responses in childhood psychosis. *J. Autism Dev. Disord.* 13, 181–195. doi: 10.1007/BF01531818

González-Hernández, T. H., Galindo-Mireles, D., Castaneyra-Perdomo, A., and Ferres-Torres, R. (1991). Divergent projections of projecting neurons of the inferior colliculus to the medial geniculate body and the contralateral inferior colliculus in the rat. *Hear. Res.* 52, 17–21. doi: 10.1016/0378-5955(91)90184-B

Gravel, J. S., Dunn, M., Lee, W. W., and Ellis, M. A. (2006). Peripheral audition of children on the autistic spectrum. *Ear Hear.* 27, 299–312. doi: 10.1097/01.aud.0000215979.65645.22

Greenspan, S. I., and Wieder, S. (1997). Developmental patterns and outcomes in infants and children with disorders in relating and communicating: a chart review of 200 cases of children with autistic spectrum diagnoses. *J. Dev. Learn. Disord.* 1, 87–141.

Grothe, B. (1994). Interaction of excitation and inhibition in processing of pure tone and amplitude-modulated stimuli in the medial superior olive of the mustached bat. *J. Neurophysiol.* 71, 706–721. doi: 10.1152/jn.1994.71.2.706

Grothe, B., and Sanes, D. H. (1993). Bilateral inhibition by glycinergic afferents in the medial superior olive. *J. Neurophysiol.* 69, 1192–1196. doi: 10.1152/jn.1993.69.4.1192

Harrison, J. M., and Irving, R. (1964). Nucleus of the trapezoid body: dual afferent innervation. *Science* 143, 473–474. doi: 10.1126/science.143.3605.473

Hazama, M., Kimura, A., Donishi, T., Sakoda, T., and Tamai, Y. (2004). Topography of corticothalamic projections from the auditory cortex of the rat. *Neuroscience* 124, 655–667. doi: 10.1016/j.neuroscience.2003.12.027

Helfert, R. H., Bonneau, J. M., Wenthold, R. J., and Altschuler, R. A. (1989). GABA and glycine immunoreactivity in the guinea pig superior olivary complex. *Brain Res.* 501, 269–286. doi: 10.1016/0006-8993(89)90644-6

Hernández-Díaz, S., Straub, L., Bateman, B. T., Zhu, Y., Mogun, H., Wisner, K. L., et al. (2024). Risk of autism after prenatal Topiramate, valproate, or lamotrigine exposure. *N. Engl. J. Med.* 390, 1069–1079. doi: 10.1056/NEJMoa2309359

Ito, T., and Oliver, D. L. (2010). Origins of glutamatergic terminals in the inferior colliculus identified by retrograde transport and expression of VGLUT1 and VGLUT2 genes. *Front. Neuroanat.* 4:135.

Ito, T., and Oliver, D. L. (2012). The basic circuit of the IC: tectothalamic neurons with different patterns of synaptic organization send different messages to the thalamus. *Front. Neural Circuits* 6:48. doi: 10.3389/fncir.2012.00048

Jalabi, W., Kopp-Scheinpflug, C., Allen, P. D., Schiavon, E., DiGiacomo, R. R., Forsythe, I. D., et al. (2013). Sound localization ability and glycinergic innervation of the superior olivary complex persist after genetic deletion of the medial nucleus of the trapezoid body. *J. Neurosci.* 33, 15044–15049. doi: 10.1523/JNEUROSCI.2604-13.2013

Kadner, A., and Berrebi, A. S. (2008). Encoding of temporal features of auditory stimuli in the medial nucleus of the trapezoid body and superior paraolivary nucleus of the rat. *Neuroscience* 151, 868–887. doi: 10.1016/j.neuroscience.2007.11.008

Kadner, A., Kulesza, R. J. Jr., and Berrebi, A. S. (2006). Neurons in the medial nucleus of the trapezoid body and superior paraolivary nucleus of the rat may play a role in sound duration coding. *J. Neurophysiol.* 95, 1499–1508. doi: 10.1152/jn.00902.2005

Kapfer, C., Seidl, A. H., Schweizer, H., and Grothe, B. (2002). Experience-dependent refinement of inhibitory inputs to auditory coincidence-detector neurons. *Nat. Neurosci.* 5, 247–253. doi: 10.1038/nn810

Kelly, J. B., Liscum, A., van Adel, B., and Ito, M. (1998). Projections from the superior olive and lateral lemniscus to tonotopic regions of the rat's inferior colliculus. *Hear. Res.* 116, 43–54. doi: 10.1016/S0378-5955(97)00195-0

Kelly, J. B., van Adel, B. A., and Ito, M. (2009). Anatomical projections of the nuclei of the lateral lemniscus in the albino rat (*Rattus norvegicus*). *J. Comp. Neurol.* 512, 573–593. doi: 10.1002/cne.21929

Khalfa, S., Bruneau, N., Rogé, B., Georgieff, N., Veuillet, E., Adrien, J. L., et al. (2001). Peripheral auditory asymmetry in infantile autism. *Eur. J. Neurosci.* 13, 628–632. doi: 10.1046/j.1460-9568.2001.01423.x

Kimura, A., Donishi, T., Sakoda, T., Hazama, M., and Tamai, Y. (2003). Auditory thalamic nuclei projections to the temporal cortex in the rat. *Neuroscience* 117, 1003–1016. doi: 10.1016/S0306-4522(02)00949-1

Kopp-Scheinpflug, C., Tolnai, S., Malmierca, M. S., and Rübsamen, R. (2008). The medial nucleus of the trapezoid body: comparative physiology. *Neuroscience* 154, 160–170. doi: 10.1016/j.neuroscience.2008.01.088

Koren, G., Nava-Ocampo, A. A., Moretti, M. E., Sussman, R., and Nulman, I. (2006). Major malformations with valproic acid. *Can. Fam. Physician* 52, 444–447.

Kosmer, K, and Kulesza, RJ. Cortical dysmorphology and reduced cortico-collicular projections in an animal model of autism spectrum disorder. Cereb. Cortex (2024) *34*, 146–160. doi: 10.1093/cercor/bhad501

Kudo, M., Nakamura, Y., Tokuno, H., and Kitao, Y. (1990). Auditory brainstem in the mole (Mogera): nuclear configurations and the projections to the inferior colliculus. *J. Comp. Neurol.* 298, 400–412. doi: 10.1002/cne.902980403

Kulesza, R. J. Jr. (2007). Cytoarchitecture of the human superior olivary complex: medial and lateral superior olive. *Hear. Res.* 225, 80–90. doi: 10.1016/j.heares.2006.12.006

Kulesza, R. J. Jr., and Berrebi, A. S. (2000). Superior paraolivary nucleus of the rat is a GABAergic nucleus. *J. Assoc. Res. Otolaryngol.* 1, 255–269. doi: 10.1007/s101620010054

Kulesza, R. J. Jr., Spirou, G. A., and Berrebi, A. S. (2003). Physiological response properties of neurons in the superior paraolivary nucleus of the rat. *J. Neurophysiol.* 89, 2299–2312. doi: 10.1152/jn.00547.2002

Kulesza, R. J., Lukose, R., and Stevens, L. V. (2011). Malformation of the human superior olive in autistic spectrum disorders. *Brain Res.* 1367, 360–371. doi: 10.1016/j.brainres.2010.10.015

Kulesza, R. J., and Mangunay, K. (2008). Morphological features of the medial superior olive in autism. *Brain Res.* 1200, 132–137. doi: 10.1016/j.brainres.2008.01.009

Kulesza, R. J., Viñuela, A., Saldaña, E., and Berrebi, A. S. (2002). Unbiased stereological estimates of neuron number in subcortical auditory nuclei of the rat. *Hear. Res.* 168, 12–24. doi: 10.1016/S0378-5955(02)00374-X

Kuwabara, N., DiCaprio, R. A., and Zook, J. M. (1991). Afferents to the medial nucleus of the trapezoid body and their collateral projections. *J. Comp. Neurol.* 314, 684–706. doi: 10.1002/cne.903140405

Kuwabara, N., and Zook, J. M. (1992). Projections to the medial superior olive from the medial and lateral nuclei of the trapezoid body in rodents and bats. *J. Comp. Neurol.* 324, 522–538. doi: 10.1002/cne.903240406

Kwon, S., Kim, J., Choe, B. H., Ko, C., and Park, S. (2007). Electrophysiologic assessment of central auditory processing by auditory brainstem responses in children with autism spectrum disorders. *J. Korean Med. Sci.* 22, 656–659. doi: 10.3346/jkms.2007.22.4.656

LeDoux, J. E., Ruggiero, D. A., Forest, R., Stornetta, R., and Reis, D. J. (1987). Topographic organization of convergent projections to the thalamus from the inferior colliculus and spinal cord in the rat. *J. Comp. Neurol.* 264, 123–146. doi: 10.1002/cne.902640110

LeDoux, J. E., Sakaguchi, A., Iwata, J., and Reis, D. J. (1985). Auditory emotional memories, establishment by projections from the medial geniculate nucleus to the posterior neostriatum and/or dorsal amygdala. *Ann. N. Y. Acad. Sci.* 444, 463–464. doi: 10.1111/j.1749-6632.1985.tb37611.x

Lohmann, C., and Friauf, E. (1996). Distribution of the calcium-binding proteins parvalbumin and calretinin in the auditory brainstem of adult and developing rats. *J. Comp. Neurol.* 367, 90–109. doi: 10.1002/(SICI)1096-9861(19960325)367:1<90::AID-CNE7>3.0.CO;2-E

Lukose, R., Beebe, K., and Kulesza, R. J. (2015). Organization of the human superior olivary complex in 15q duplication syndromes and autism spectrum disorders. *Neuroscience* 286, 216–230. doi: 10.1016/j.neuroscience.2014.11.033

Lukose, R., Schmidt, E., Wolski, T. P. Jr., Murawski, N. J., and Kulesza, R. J. (2011). Malformation of the superior olivary complex in an animal model of autism. *Brain Res.* 1398, 102–112. doi: 10.1016/j.brainres.2011.05.013

Mabunga, D. F., Gonzales, E. L., Kim, J. W., Kim, K. C., and Shin, C. Y. (2015). Exploring the validity of valproic acid animal model of autism. *Exp. Neurobiol.* 24, 285–300. doi: 10.5607/en.2015.24.4.285

Main, S., and Kulesza, R. J. (2017). Repeated prenatal exposure to valproic acid results in cerebellar hypoplasia and ataxia. *Neuroscience* 340, 34–47. doi: 10.1016/j.neuroscience.2016.10.052

Malhotra, A. S., and Kulesza, R. (2023). Abnormal auditory brainstem responses in an animal model of autism spectrum disorder. *Hear. Res.* 436:108816. doi: 10.1016/j.heares.2023.108816

Malmierca, M. S., Merchan, M. A., Henkel, C. K., and Oliver, D. L. (2002). Direct projections from cochlear nuclear complex to auditory thalamus in the rat. *J. Neurosci.* 22, 10891–10897. doi: 10.1523/JNEUROSCI.22-24-10891.2002

Mansour, Y., Ahmed, S. N., and Kulesza, R. (2021b). Abnormal morphology and subcortical projections to the medial geniculate in an animal model of autism. *Exp. Brain Res.* 239, 381–400. doi: 10.1007/s00221-020-05982-w

Mansour, Y., Burchell, A., and Kulesza, R. J. (2021a). Central auditory and vestibular dysfunction are key features of autism spectrum disorder. *Front. Integr. Neurosci.* 15:743561. doi: 10.3389/fnint.2021.743561

Mansour, Y., Burchell, A., and Kulesza, R. (2022). Abnormal vestibular brainstem structure and function in an animal model of autism spectrum disorder. *Brain Res.* 1793:148056. doi: 10.1016/j.brainres.2022.148056

Mansour, Y., and Kulesza, R. (2020). Three dimensional reconstructions of the superior olivary complex from children with autism spectrum disorder. *Hear. Res.* 393:107974. doi: 10.1016/j.heares.2020.107974

Mansour, Y., and Kulesza, R. J. (2021). The untouchable ventral nucleus of the trapezoid body: preservation of a nucleus in an animal model of autism spectrum disorder. *Front. Integr. Neurosci.* 15:730439. doi: 10.3389/fnint.2021.730439

Mansour, Y., Mangold, S., Chosky, D., and Kulesza, R. J. (2019). Auditory midbrain hypoplasia and Dysmorphology after prenatal Valproic acid exposure. *Neuroscience* 396, 79–93. doi: 10.1016/j.neuroscience.2018.11.016

Maziade, M., Mérette, C., Cayer, M., Roy, M. A., Szatmari, P., Côté, R., et al. (2000). Prolongation of brainstem auditory-evoked responses in autistic probands and their unaffected relatives. *Arch. Gen. Psychiatry* 57, 1077–1083. doi: 10.1001/archpsyc.57.11.1077

Miron, O., Beam, A. L., and Kohane, I. S. (2018). Auditory brainstem response in infants and children with autism spectrum disorder: a meta-analysis of wave V. *Autism Res.* 11, 355–363. doi: 10.1002/aur.1886

Moore, M. J., and Caspary, D. M. (1983). Strychnine blocks binaural inhibition in lateral superior olivary neurons. *J. Neurosci.* 3, 237–242. doi: 10.1523/JNEUROSCI.03-01-00237.1983

Moore, S. J., Turnpenny, P., Quinn, A., Glover, S., Lloyd, D. J., Montgomery, T., et al. (2000). A clinical study of 57 children with fetal anticonvulsant syndromes. *J. Med. Genet.* 37, 489–497. doi: 10.1136/jmg.37.7.489

Morest, D. K. (1968a). The collateral system of the medial nucleus of the trapezoid body of the cat, its neuronal architecture and relation to the olivo-cochlear bundle. *Brain Res.* 9, 288–311. doi: 10.1016/0006-8993(68)90235-7

Morest, D. K. (1968b). The growth of synaptic endings in the mammalian brain: a study of the calyces of the trapezoid body. *Z. Anat. Entwicklungsgesch.* 127, 201–220. doi: 10.1007/BF00526129

Nordeen, K. W., Killackey, H. P., and Kitzes, L. M. (1983). Ascending auditory projections to the inferior colliculus in the adult gerbil,*Meriones unguiculatus*. *J. Comp. Neurol. Psychol.* 214, 131–143. doi: 10.1002/cne.902140203

Ornitz, E. M. (1969). Disorders of perception common to early infantile autism and schizophrenia. *Compr Psychiatry.* 10:259–74.

Ottersen, O. P., and Ben-Ari, Y. (1979). Afferent connections to the amygdaloid complex of the rat and cat.I.Projections from the thalamus. *J. Comp. Neurol.* 187, 401–424. doi: 10.1002/cne.901870209

Ottersen, O. P., and Storm-Mathisen, J. (1984). Glutamate- and GABA-containing neurons in the mouse and rat brain, as demonstrated with a new immunocytochemical technique. *J. Comp. Neurol.* 229, 374–392. doi: 10.1002/cne.902290308

Pack, A. M., Oskoui, M., Williams Roberson, S., Donley, D. K., French, J., Gerard, E. E., et al. (2024). Teratogenesis, perinatal, and neurodevelopmental outcomes after in utero exposure to Antiseizure medication: practice guideline from the AAN, AES, and SMFM. *Neurology* 102:e209279. doi: 10.1212/WNL.0000000000209279

Paxinos, G., and Watson, C. (2007). The Rat Brain in Stereotaxic Coordinates. London: Academic Press.

Qian, Y., Zheng, Y., and Tiffany-Castiglioni, E. (2009). Valproate reversibly reduces neurite outgrowth by human SY5Y neuroblastoma cells. *Brain Res.* 1302, 21–33. doi: 10.1016/j.brainres.2009.09.051

Ramezani, M., Lotfi, Y., Moossavi, A., and Bakhshi, E. (2019). Auditory brainstem response to speech in children with high functional autism spectrum disorder. *Neurol. Sci.* 40, 121–125. doi: 10.1007/s10072-018-3594-9

Rampon, C., Luppi, P. H., Fort, P., Peyron, C., and Jouvet, M. (1996). Distribution of glycine-immunoreactive cell bodies and fibers in the rat brain. *Neuroscience.* 75:737–55.

Rasalam, A. D., Hailey, H., Williams, J. H., Moore, S. J., Turnpenny, P. D., Lloyd, D. J., et al. (2005). Characteristics of fetal anticonvulsant syndrome associated autistic disorder. *Dev. Med. Child Neurol.* 47, 551–555. doi: 10.1017/S0012162205001076

Résibois, A., and Rogers, J. H. (1992). Calretinin in rat brain: an immunohistochemical study. *Neuroscience* 46, 101–134. doi: 10.1016/0306-4522(92)90012-Q

Roberts, M. T., Seeman, S. C., and Golding, N. L. (2014). The relative contributions of MNTB and LNTB neurons to inhibition in the medial superior olive assessed through single and paired recordings. *Front. Neural Circuits* 8:49. doi: 10.3389/fncir.2014.00049

Rodier, P. M., Ingram, J. L., Tisdale, B., Nelson, S., and Romano, J. (1996). Embryological origin for autism: developmental anomalies of the cranial nerve motor nuclei. *J. Comp. Neurol.* 370, 247–261. doi: 10.1002/(SICI)1096-9861(19960624)370:2<247::AID-CNE8>3.0.CO;2-2

Roper, L., Arnold, P., and Monteiro, B. (2003). Co-occurrence of autism and deafness: diagnostic considerations. *Autism* 7, 245–253. doi: 10.1177/13623613030073002

Rosenblum, S. M., Arick, J. R., Krug, D. A., Stubbs, E. G., Young, N. B., and Pelson, R. O. (1980). Auditory brainstem evoked responses in autistic children. *J. Autism Dev. Disord.* 10, 215–225. doi: 10.1007/BF02408472

ROTH, D. A. E., MUCHNIK, C., SHABTAI, E., HILDESHEIMER, M., and HENKIN, Y. (2012). Evidence for atypical auditory brainstem responses in young children with suspected autism spectrum disorders. *Dev. Med. Child Neurol.* 54, 23–29. doi: 10.1111/j.1469-8749.2011.04149.x

Roucoux-Hanus, M., and Boisacq-Schepens, N. (1977). Ascending vestibular projections, further results at cortical and thalamic levels in the cat. *Exp. Brain Res.* 29, 283–292. doi: 10.1007/BF00237048

Russo, N., Zecker, S., Trommer, B., Chen, J., and Kraus, N. (2009). Effects of background noise on cortical encoding of speech in autism spectrum disorders. *J. Autism Dev. Disord.* 39, 1185–1196. doi: 10.1007/s10803-009-0737-0

Ryugo, D. K., and Killackey, H. P. (1974). Differential telencephalic projections of the medial and ventral divisions of the medial geniculate body of the rat. *Brain Res.* 82, 173–177. doi: 10.1016/0006-8993(74)90903-2

Saldaña, E., Aparicio, M. A., Fuentes-Santamaría, V., and Berrebi, A. S. (2009). Connections of the superior paraolivary nucleus of the rat: projections to the inferior colliculus. *Neuroscience* 163, 372–387. doi: 10.1016/j.neuroscience.2009.06.030

Schindelin, J., Arganda-Carreras, I., Frise, E., Kaynig, V., Longair, M., Pietzsch, T., et al. (2012). Fiji: an open-source platform for biological-image analysis. *Nat. Methods* 9, 676–682. doi: 10.1038/nmeth.2019

Schneider, T., Roman, A., Basta-Kaim, A., Kubera, M., Budziszewska, B., Schneider, K., et al. (2008). Gender-specific behavioral and immunological alterations in an animal model of autism induced by prenatal exposure to valproic acid. *Psychoneuroendocrinology* 33, 728–740. doi: 10.1016/j.psyneuen.2008.02.011

Schofield, B. R. (1994). Projections to the cochlear nuclei from principal cells in the medial nucleus of the trapezoid body in guinea pigs. *J. Comp. Neurol.* 344, 83–100. doi: 10.1002/cne.903440107

Schofield, B. R., and Cant, N. B. (1992). Organization of the superior olivary complex in the guinea pig: II. Patterns of projection from the periolivary nuclei to the inferior colliculus. *J. Comp. Neurol.* 317, 438–455. doi: 10.1002/cne.903170409

Schofield, B. R., Mellott, J. G., and Motts, S. D. (2014a). Subcollicular projections to the auditory thalamus and collateral projections to the inferior colliculus. *Front. Neuroanat.* 8:70. doi: 10.3389/fnana.2014.00070

Schofield, B. R., Motts, S. D., Mellott, J. G., and Foster, N. L. (2014b). Projections from the dorsal and ventral cochlear nuclei to the medial geniculate body. *Front. Neuroanat.* 8:10. doi: 10.3389/fnana.2014.00010

Sersen, E. A., Heaney, G., Clausen, J., Belser, R., and Rainbow, S. (1990). Brainstem auditory-evoked responses with and without sedation in autism and Down's syndrome. *Biol. Psychiatry* 27, 834–840. doi: 10.1016/0006-3223(90)90464-D

Smith, P. H., Joris, P. X., Carney, L. H., and Yin, T. C. (1991). Projections of physiologically characterized globular bushy cell axons from the cochlear nucleus of the cat. *J. Comp. Neurol.* 304, 387–407. doi: 10.1002/cne.903040305

Smith, P. H., Joris, P. X., and Yin, T. C. (1998). Anatomy and physiology of principal cells of the medial nucleus of the trapezoid body (MNTB) of the cat. *J. Neurophysiol.* 79, 3127–3142. doi: 10.1152/jn.1998.79.6.3127

Smith, P. H., Uhlrich, D. J., Manning, K. A., and Banks, M. I. (2012). Thalamocortical projections to rat auditory cortex from the ventral and dorsal divisions of the medial geniculate nucleus. *J. Comp. Neurol.* 520, 34–51. doi: 10.1002/cne.22682

Sohmer, H. (1982). Auditory nerve-brain stem responses (ABR) in children with developmental brain disorders and in high risk neonates. *Electroencephalogr. Clin. Neurophysiol. Suppl.* 36, 315–327

Sommer, I., Lingenhöhl, K., and Friauf, E. (1993). Principal cells of the rat medial nucleus of the trapezoid body: an intracellular in vivo study of their physiology and morphology. *Exp. Brain Res.* 95, 223–239. doi: 10.1007/BF00229781

Spangler, K. M., Warr, W. B., and Henkel, C. K. (1985). The projections of principal cells of the medial nucleus of the trapezoid body in the cat. *J. Comp. Neurol.* 238, 249–262. doi: 10.1002/cne.902380302

Spreafico, R., Hayes, N. L., and Rustioni, A. (1981). Thalamic projections to the primary and secondary somatosensory cortices in cat, single and double retrograde tracer studies. *J. Comp. Neurol.* 203, 67–90. doi: 10.1002/cne.902030107

Student, M., and Sohmer, H. (1978). Evidence from auditory nerve and brainstem evoked responses for an organic brain lesion in children with autistic traits. *J. Autism Child. Schizophr.* 8, 13–20. doi: 10.1007/BF01550274

Szelag, E., Kowalska, J., Galkowski, T., and Pöppel, E. (2004). Temporal processing deficits in high-functioning children with autism. *Br. J. Psychol.* 95, 269–282. doi: 10.1348/0007126041528167

Tanguay, P. E., Edwards, R. M., Buchwald, J., Schwafel, J., and Allen, V. (1982). Auditory brainstem evoked responses in autistic children. *Arch. Gen. Psychiatry* 39, 174–180. doi: 10.1001/archpsyc.1982.04290020040008

Tas, A., Yagiz, R., Tas, M., Esme, M., Uzun, C., and Karasalihoglu, A. R. (2007). Evaluation of hearing in children with autism by using TEOAE and ABR. *Autism* 11, 73–79. doi: 10.1177/1362361307070908

Teder-Sälejärvi, W. A., Pierce, K. L., Courchesne, E., and Hillyard, S. A. (2005). Auditory spatial localization and attention deficits in autistic adults. *Brain Res. Cogn. Brain Res.* 23, 221–234. doi: 10.1016/j.cogbrainres.2004.10.021

Tharpe, A. M., Bess, F. H., Sladen, D. P., Schissel, H., Couch, S., and Schery, T. (2006). Auditory characteristics of children with autism. *Ear Hear.* 27, 430–441. doi: 10.1097/01.aud.0000224981.60575.d8

Thivierge, J., Bédard, C., Côté, R., and Maziade, M. (1990). Brainstem auditory evoked response and subcortical abnormalities in autism. *Am. J. Psychiatry* 147, 1609–1613

Tomchek, S. D., and Dunn, W. (2007). Sensory processing in children with and without autism: a comparative study using the short sensory profile. *Am. J. Occup. Ther.* 61, 190–200. doi: 10.5014/ajot.61.2.190

Wenthold, R. J., Huie, D., Altschuler, R. A., and Reeks, K. A. (1987). Glycine immunoreactivity localized in the cochlear nucleus and superior olivary complex. *Neuroscience* 22, 897–912. doi: 10.1016/0306-4522(87)92968-X

Whitley, J. M., and Henkel, C. K. (1984). Topographical organization of the inferior collicular projection and other connections of the ventral nucleus of the lateral lemniscus in the cat. *J. Comp. Neurol.* 229, 257–270. doi: 10.1002/cne.902290210

Williams, G., King, J., Cunningham, M., Stephan, M., Kerr, B., and Hersh, J. H. (2001). Fetal valproate syndrome and autism: additional evidence of an association. *Dev. Med. Child Neurol.* 43, 202–206. doi: 10.1111/j.1469-8749.2001.tb00188.x

Winer, J. A. (1985). The medial geniculate body of the cat. *Adv. Anat. Embryol. Cell Biol.* 86, 1–97. doi: 10.1007/978-3-642-69634-3_1

Winer, J. A., and Larue, D. T. (1987). Patterns of reciprocity in auditory thalamocortical and corticothalamic connections, study with horseradish peroxidase and autoradiographic methods in the rat medial geniculate body. *J. Comp. Neurol.* 257, 282–315. doi: 10.1002/cne.902570212

Winer, J. A., Sally, L. S., Larue, D. T., and Kelly, J. B. (1999). Origins of medial geniculate body projections to physiologically defined zones of rat primary auditory cortex. *Hear. Res.* 130, 42–61. doi: 10.1016/S0378-5955(98)00217-2

Wing, L. (1997). The autistic spectrum. *Lancet* 350, 1761–1766. doi: 10.1016/S0140-6736(97)09218-0

Wong, V., and Wong, S. N. (1991). Brainstem auditory evoked potential study in children with autistic disorder. *J. Autism Dev. Disord.* 21, 329–340. doi: 10.1007/BF02207329

Yu, Y. Q., Xiong, Y., Chan, Y. S., and He, J. (2004). In vivo intracellular responses of the medial geniculate neurones to acoustic stimuli in anaesthetized guinea pigs. *J. Physiol.* 560, 191–205. doi: 10.1113/jphysiol.2004.067678

Zarbin, M. A., Wamsley, J. K., and Kuhar, M. J. (1981). Glycine receptor: light microscopic autoradiographic localization with [3H]strychnine. *J. Neurosci.* 1, 532–547. doi: 10.1523/JNEUROSCI.01-05-00532.1981

Zhao, H., Wang, Q., Yan, T., Zhang, Y., Xu, H. J., Yu, H. P., et al. (2019). Maternal valproic acid exposure leads to neurogenesis defects and autism-like behaviors in non-human primates. *Transl. Psychiatry* 9:267. doi: 10.1038/s41398-019-0608-1

Zimmerman, R., Patel, R., Smith, A., Pasos, J., and Kulesza, R. J. (2018). Repeated prenatal exposure to valproic acid results in auditory brainstem hypoplasia and reduced calcium binding protein immunolabeling. *Neuroscience* 377, 53–68. doi: 10.1016/j.neuroscience.2018.02.030

Zimmerman, R., Smith, A., Fech, T., Mansour, Y., and Kulesza, R. J. Jr. (2020). In utero exposure to valproic acid disrupts ascending projections to the central nucleus of the inferior colliculus from the auditory brainstem. *Exp. Brain Res.* 238, 551–563. doi: 10.1007/s00221-020-05729-7

frontiers | Frontiers in Cellular Neuroscience

TYPE Original Research
PUBLISHED 08 November 2024
DOI 10.3389/fncel.2024.1424773

Check for updates

OPEN ACCESS

EDITED BY
Christian Keine,
University of Oldenburg, Germany

REVIEWED BY
Kristen Rak,
Comprehensive Hearing Center, Germany
Kelsey L. Anbuhl,
New York University, United States

*CORRESPONDENCE
Nicole Rosskothen-Kuhl
✉ nicole.rosskothen-kuhl@uniklinik-freiburg.de

†PRESENT ADDRESS
Sarah Green,
Max Delbrück Center for Molecular Medicine (MDC),
Berlin, Germany

RECEIVED 28 April 2024
ACCEPTED 08 October 2024
PUBLISHED 08 November 2024

CITATION
Rosskothen-Kuhl N, Green S and Jakob TF (2024) Does age protect against loss of tonotopy after acute deafness in adulthood?.
Front. Cell. Neurosci. 18:1424773.
doi: 10.3389/fncel.2024.1424773

COPYRIGHT
© 2024 Rosskothen-Kuhl, Green and Jakob. This is an open-access article distributed under the terms of the Creative Commons Attribution License (CC BY). The use, distribution or reproduction in other forums is permitted, provided the original author(s) and the copyright owner(s) are credited and that the original publication in this journal is cited, in accordance with accepted academic practice. No use, distribution or reproduction is permitted which does not comply with these terms.

Does age protect against loss of tonotopy after acute deafness in adulthood?

Nicole Rosskothen-Kuhl[1,2]*, Sarah Green[1†] and Till F. Jakob[1,3]

[1]Neurobiological Research Laboratory, Section for Experimental and Clinical Otology, Department of Oto-Rhino-Laryngology, Faculty of Medicine, Medical Center – University of Freiburg, Freiburg, Germany, [2]Faculty of Biology, Bernstein Center Freiburg, University of Freiburg, Freiburg, Germany, [3]Department of Otorhinolaryngology, Faculty of Medicine, Medical Center – University of Freiburg, University of Freiburg, Freiburg, Germany

The mammalian auditory system develops a topographical representation of sound frequencies along its pathways, also called tonotopy. In contrast, sensory deprivation during early development results in no or only rudimentary tonotopic organization. This study addresses two questions: (1) How robust is the central tonotopy when hearing fails in adulthood? (2) What role does age play at time of deafness? To address these questions, we deafened young and old adult rats with previously normal hearing. One month after deafening, both groups were unilaterally supplied with cochlear implants and electrically stimulated for 2 h. The central auditory neurons, which were activated as a result of the local electrical intracochlear stimulation, were visualized using Fos staining. While the auditory system of young rats lost the tonotopic organization throughout the brainstem, the auditory system of the older rats mainly sustained its tonotopy. It can be proposed that plasticity prevails in the central auditory system of young adult rats, while network stability prevails in the brains of aging rats. Consequently, age may be an important factor in protecting a hearing-experienced adult auditory system from a rapid loss of tonotopy when suffering from acute hearing loss. Furthermore, the study provides compelling evidence that acute deafness in young adult patients should be diagnosed as early as possible to prevent maladaptation of the central auditory system and thus achieve the optimal hearing outcome with a hearing prosthesis.

KEYWORDS

aging, adult hearing loss, auditory brainstem, tonotopy, cochlear implant, cochlear nucleus, lateral superior olive, inferior colliculus

1 Introduction

Around 5% of the world's population (~430 million people) suffer from disabling hearing loss (WHO, 2024) making it the most common sensory impairment of our age. The majority of these are adults (~396 million). The prevalence of hearing loss increases with age, reaching approximately 25% for the population over 60 years of age, with an upward trend for higher age (Roth et al., 2011; Von Gablenz et al., 2017; WHO, 2024). Age-related hearing loss in humans is mostly attributed to the loss of cochlear outer hair cells and is often associated with changes in the auditory nerve and the central auditory system, among other factors (Willott, 1984; Palombi and Caspary, 1996; McFadden et al., 1997; Ingham et al., 1998; Syka, 2002; Ouda et al., 2015). Currently, this form of hearing loss is not reversible. Nevertheless, following the diagnosis of hearing loss patients can be (re)integrated into an acoustic environment through the use of hearing aids or neuroprostheses such as the cochlear implant (CI). For people with severe to profound sensorineural hearing loss, CIs can be highly beneficial, allowing for near-normal

spoken language acquisition. For prelingually deaf patients best performances can be observed when CI implantation takes place during early development, specifically within the first 3 years of life (Kral and Sharma, 2012). Postlingually deaf CI patients who had normal hearing in early development can still achieve good hearing performances in adulthood, even after more than 10 to 30 years of deafness (Moon et al., 2014; Hiel et al., 2016; Medina et al., 2017; Kim et al., 2018) although they show better speech understanding with a duration of deafness less than 10 years and younger age at implantation (Kim et al., 2018). Various studies indicate that age does not influence or limit the outcome with CI in postlingual deafness (Moon et al., 2014; Hiel et al., 2016; Garcia-Iza et al., 2018). To the best of our knowledge, it is still unclear why older CI patients with reduced or altered plasticity (Burke and Barnes, 2006; Apple et al., 2017; Foscarin et al., 2017) can achieve similar or even better hearing performance than younger CI patients with presumably more plastic brains. For example, adult-deafened CI patients demonstrate enhanced performances in sound source localization in comparison to prelingually deafened, early fitted CI patients (Litovsky et al., 2012; Ehlers et al., 2017). Although one possible reason for better directional hearing in older CI patients may be the hearing experience during an early critical period resulting in the development of central binaural circuits, recent studies in an early-deafened, adult CI-fitted animal model provide important evidence that the adult, hearing-inexperienced auditory system can still develop very good directional hearing if it receives informative directional cues via the bilateral CIs from the onset of stimulation (Rosskothen-Kuhl et al., 2021; Buck et al., 2023).

The normal hearing central auditory system, from the cochlear nucleus to the auditory cortex, is organized tonotopically. This means that groups of neurons have the greatest sensitivity to a particular frequency and are arranged in a frequency-specific manner. While the traditional developmental picture assumed a predefined, hard-wired auditory brainstem that forms its tonotopy even without sensory input, more recent studies provide evidence that the precise tonotopy in the auditory system is based on the refinement of neural circuits as a result of activity-dependent synaptic plasticity and/or afferent input after the onset of hearing (Kandler et al., 2009; Mann and Kelley, 2011; Akter et al., 2018). In the case of normal hearing, an organization of the auditory system can be observed already early in life (Kandler et al., 2009). In rats, an adult-like tonotopic arrangement matures before the third week of life (Friauf, 1992). However, previous studies have shown that tonotopy is altered in the absence of auditory input. In various model organisms, early bilateral hearing loss results in the reduction or even complete loss of tonotopic order in subcortical and cortical regions (Raggio and Schreiner, 1999; Leake et al., 2008; Fallon et al., 2009; Rosskothen-Kuhl and Illing, 2012; Jakob et al., 2015; Rauch et al., 2016; Jakob et al., 2019). In rats, we have demonstrated that unilateral or bilateral neonatal deafness results in the absence of tonotopic organization along the deprived auditory pathway (Rosskothen-Kuhl and Illing, 2012; Jakob et al., 2015; Rauch et al., 2016; Rosskothen-Kuhl et al., 2018; Jakob et al., 2019).

Aim of this study was to investigate on the neuronal level why the deafened auditory system of elderly might be still able to benefit from CI supply despite an altered level of plasticity. We focused on the effect of deafness on the mature auditory brainstem and addressed two key questions: firstly, how stable is the tonotopic organization of a hearing-experienced auditory system after 1 month of deafness in adulthood? and secondly, what role does age play at the time of deafness? To address these questions, we investigated the tonotopic organization of the auditory brainstem after 1 month of deafness in adult rats of different ages. The auditory system of deafened rats was re-activated by electrical intracochlear stimulation (EIS), and the stimulation-induced neuronal activity pattern was visualized by staining the plasticity and activity marker Fos in brain sections (Ehret and Fischer, 1991; Friauf, 1992; Guzowski et al., 2001; Jakob and Illing, 2008; Rapanelli et al., 2010; Rosskothen-Kuhl and Illing, 2010, 2012; Rauch et al., 2016; Rosskothen-Kuhl et al., 2018). In many studies on different brain areas and neuronal phenotypes, Fos mRNA and Fos protein have been used as a marker for neuronal activity (Morgan and Curran, 1991; Cohen and Greenberg, 2008; Cruz et al., 2013). Fos belongs to the Immediate-Early-Gene family associated with activity dependent gene expression and its promoter is rapidly switched on in strongly activated neurons (Cohen and Greenberg, 2008; Cruz et al., 2013). In the auditory system, Fos expression requires at least 30–45 min of acoustic or electrical stimulation (Rosskothen-Kuhl and Illing, 2012; Rauch et al., 2016). As shown by Reisch et al. (2007) and Rosskothen-Kuhl et al. (2018), stimulation induced Fos expression in the auditory brainstem occurred only in neurons and not in glial cells. While previous studies have demonstrated that local EIS of hearing-experienced rats results in a tonotopic activation of neurons along the auditory pathway according to the stimulation position, our work in hearing-inexperienced, deaf rats has shown that a comparable intracochlear stimulation leads to a significantly increased number of activated neurons and a broader spread of excitation over almost the entire auditory brainstem (Rosskothen-Kuhl and Illing, 2010, 2012; Jakob et al., 2015; Rauch et al., 2016; Rosskothen-Kuhl et al., 2018; Jakob et al., 2019). Building on our previous work, we were able to show here that the activity pattern of a hearing-experienced, adult-deafened auditory system varies greatly depending on the duration of hearing prior to onset of deafness and thus the age at which deafness occurred. A reduction in tonotopic organization in the auditory system was associated with a younger age at onset of deafness.

2 Materials and methods

2.1 Experimental groups

Forty-seven female Wistar rats were divided into four groups: (1) young (y) or old (o) adult, normal hearing (NH = yNH + oNH) rats ($n = 15$), (2) neonatally-deafened (ND), young adult rats ($n = 9$), (3) young adult-deafened (YAD) rats ($n = 12$), and (4) old adult-deafened (OAD) rats ($n = 11$). The left cochlea of each rat was electrically stimulated with a CI for 2 h (for details see section 2.5). Additionally, two YAD rats and two OAD rats underwent cochlear implantation on their left side for 2 h without stimulation and served as adult-deafened (AD) "implanted" controls. Further, four adult-deafened rats served as "pure" controls (YAD: $n = 2$; OAD: $n = 2$). At the time of perfusion, all rats in the "young" adult group were approximately

Abbreviations: ABR, Auditory brainstem response; AD, Adult-deafened; AVCN, Anteroventral cochlear nucleus; CI, Cochlear implant; CIC, Central inferior colliculus; cp, Corresponding; dB, Dezibel; EA, Ethacrynic acid; EABR, Electrically evoked ABR; EIS, Electrical intracochlear stimulation; KM, Kanamycin; LSO, Lateral superior olive; ND, Neonatally-deafened; NH, Normal hearing; o, Old; OAD, Old adult-deafened; oNH, Old normal hearing; ROI, Regions of interest; SL, Sensation level; SPL, Sound pressure level; stim, Stimulation; y, Young; YAD, Young adult-deafened; yNH, Young normal hearing.

16 weeks (=4 months) old, whereas all rats in the "old" adult group were around 13 months old (Figure 1). ND animals and portions of the NH animals have already been utilized in previous studies and served as reference groups (Rosskothen-Kuhl and Illing, 2010, 2012). For an overview of the timeline and experimental treatment of each experimental cohort (see Figure 1). All procedures involving a total 55 rats were approved by the Regierungspräsidium Freiburg (permission number G-10/83) and followed the guidelines of the EU directive 2010/63/EU for animal experiments.

2.2 Induction of adult deafness

Corresponding to Liu et al. (2011) three or 12 months old rats were systemically deafened by a single intravenous injection of ethacrynic acid solution (EA, 75 mg/kg body weight, 25 mg/mL solution, e.g., 945 µL EA solution for a 315 g rat, REOMAX, Bioindustrial L.I.M. S.P.A., Italy,) followed by intramuscular injections of kanamycin solution (KM, 500 mg/kg body weight, e.g., 985 µL KM solution for a 315 g rat, K4000, Sigma-Aldrich, Germany). Anesthesia was initiated under 5% isoflurane (Forene 100% [V/V], Abbott GmbH & Co. KG, Germany) in an inhalation chamber and maintained with ~1.5% isoflurane while the rats were kept warm on a heating pad. Before placing a tail vein catheter, the tail of the rats was heated in 38°C warm water for vasodilatation. After rinsing the lateral tail vein with *ca.* 0.1 mL sterile 0.9% NaCl solution, freshly prepared EA solution was slowly injected into the tail vein. Afterwards, the tail vein was rinsed again with *ca.* 0.1–0.2 mL 0.9% NaCl solution. In a second step, KM solution was injected intramuscularly. To ensure a sufficient supply of liquid and electrolytes, 1–2 mL Ringer's solution was injected subcutaneously followed by subcutaneous Carprofen (4–5 mg/kg body weight, 50 mg/mL solution, Carprieve, Norbrook Laboratories Ltd., Northern Ireland) injection for pain relief. The co-administration of EA and KM results in a rapid and permanent hearing loss induced by irreversible lesion of outer and inner hair cells (Figure 5 in Liu et al., 2011).

2.3 Induction of neonatal deafness

Neonatal rats were deafened by daily intraperitoneal injections of kanamycin (400 mg/kg body weight, 50–60 mg/mL in 0.9% NaCl solution, e.g., 320 µL KM solution for a 40 g rat, K0254, Sigma-Aldrich, Germany), from postnatal day 10 to 20 inclusively (Osako et al., 1979; Rosskothen-Kuhl and Illing, 2012). This is known to cause widespread death of inner and outer hair cells (Osako et al., 1979; Matsuda et al., 1999; Argence et al., 2008) while keeping the number of spiral ganglion cells comparable to that in untreated control rats (Osako et al., 1979; Argence et al., 2008).

2.4 Verification of hearing function or hearing loss

Normal hearing or hearing loss due to pharmacological treatment was verified by measuring auditory brainstem responses (ABRs) as described in Jakob et al. (2015), Jakob et al. (2016), Rosskothen-Kuhl et al. (2018), Buck et al. (2021), Buck et al. (2023). In short, under ketamine (80 mg/kg body weight, 10% solution of Ketanest S (25 mg/mL), e.g., 160 µL for a 200 g rat, Medistar Arzneimittelvertrieb GmbH, Germany) and xylazine (12 mg/kg body weight, 50 mg/mL solution, e.g., 120 µL for a 200 g rat, Rompun, Bayer, Germany) anesthesia each ear was stimulated separately through hollow ear bars with 0.5 ms clicks (0.1–3 kHz) with peak amplitudes up to 95 dB SL (SL = individual sensation level per rat). ABRs were recorded by averaging scalp potentials measured with subcutaneous needle electrodes between mastoids and the vertex of the rat's head over 300 click presentations. While normal hearing rats typically exhibited click ABR thresholds near 0 dB SL, deafened rats showed increased hearing thresholds ≥95 dB SL to broadband click stimuli as well as pure tones (Rosskothen-Kuhl et al., 2021; Buck et al., 2023). Figures 2A,B show ABRs of an adult-deafened rat 1 week before and half a week after deafening by EA and KM injection. Additionally, all kanamycin treated rats consistently failed to show a motor response to a handclap. The absence of this so-called Preyer's reflex indicates a sustained increase of ABR threshold above 81 dB SPL (Jero et al., 2001).

2.5 Electrical intracochlear stimulation

Two hours of EIS were applied under urethane anesthesia (intraperitoneal, 1.5 g/kg body weight, 0.25 g/mL urethan in 0.9% NaCl solution, e.g., 1.5 mL urethan solution for a 250 g rat, Fluka AG, Switzerland). In case of adult-deafened rats, unilateral EIS occurred on average 46 days after deafening. The stimulation set-up and cochlear implantation is described in detail in (Rosskothen-Kuhl and Illing, 2010, 2012, 2014; Jakob et al., 2015; Jakob et al., 2019). In short, two rings of an electrode array (CI24RE, Cochlear®, Australia) were inserted through a cochleostomy in a medio-dorsal direction (pointing to apex) into the middle turn of the rat cochlea corresponding to the 8–12 kHz region. The CI was connected to a Nucleus Implant Communicator kindly provided by Cochlear Germany GmbH and Co. KG. Electrically evoked ABRs (EABRs) were recorded to corroborate for the correct placement of stimulation electrodes and to determine an appropriate current level. Current levels for EIS were set to match an EABR amplitude of 9 µV ± 10%. This was achieved by a mean current level of ~340 µA, corresponding to acoustic stimuli of 80–85 dB above hearing threshold of NH rats. Corresponding to Rosskothen-Kuhl and Illing (2012), this stimulation intensity triggers tonotopic activation in the auditory system of NH rats.

2.6 Animal perfusion and preparation of brain sections

Following completion of the post-deafening survival time with or without 2 h of stimulation (see Figure 1 for details), rats were sacrificed by a lethal dose of sodium-thiopental (intraperitoneal, 50 mg/mL per 200 g body weight of Trapanal 2.5 g, Nycomed, Germany) and perfused transcardially for 60 min. For perfusion, 4°C cold fixative containing 4% paraformaldehyde in 0.1 M phosphate buffer at pH 7.4 was used. Brains were removed from the skull and stored overnight in a phosphate buffer containing 20% sucrose. Before preparing brain slices, the brains were frozen in −40°C cold 2-methylbutane (≥99%, Roth, Germany) on dry ice for 2 min.

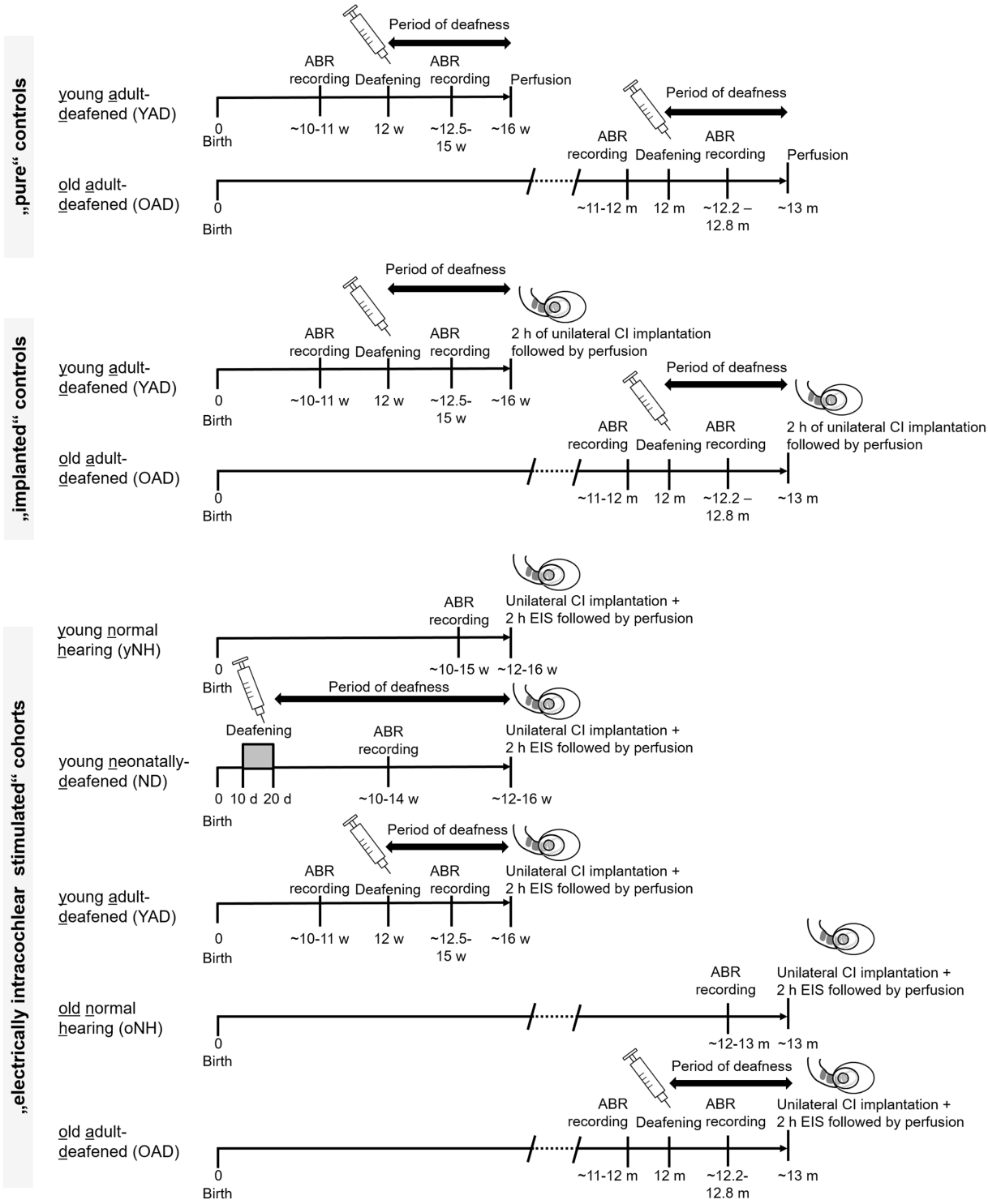


FIGURE 1
Timeline and experimental treatment of each experimental cohort. Young and old adult-deafened (YAD/OAD) rats were both deafened by a single injection of kanamycin in combination with ethacrynic acid at an age of 12 weeks or 12 months, respectively. Normal hearing and loss of hearing function were verified by ABR measurements before and after the treatment. In contrast, neonatally-deafened (ND) rats were hearing impaired by daily injection of kanamycin from postnatal day 10–20, inclusively, while the young and old normal hearing (yNH/oNH) cohorts remained untreated. All rats of the electrically intracochlear stimulated cohort underwent unilateral cochlear implantation at around 16 weeks of age (young adult cohort) or 13 months of age (old adult cohort), immediately followed by sustained electrical intracochlear stimulation (EIS) for 2 h (h) and subsequent perfusion. m: months, w: weeks; d: days.

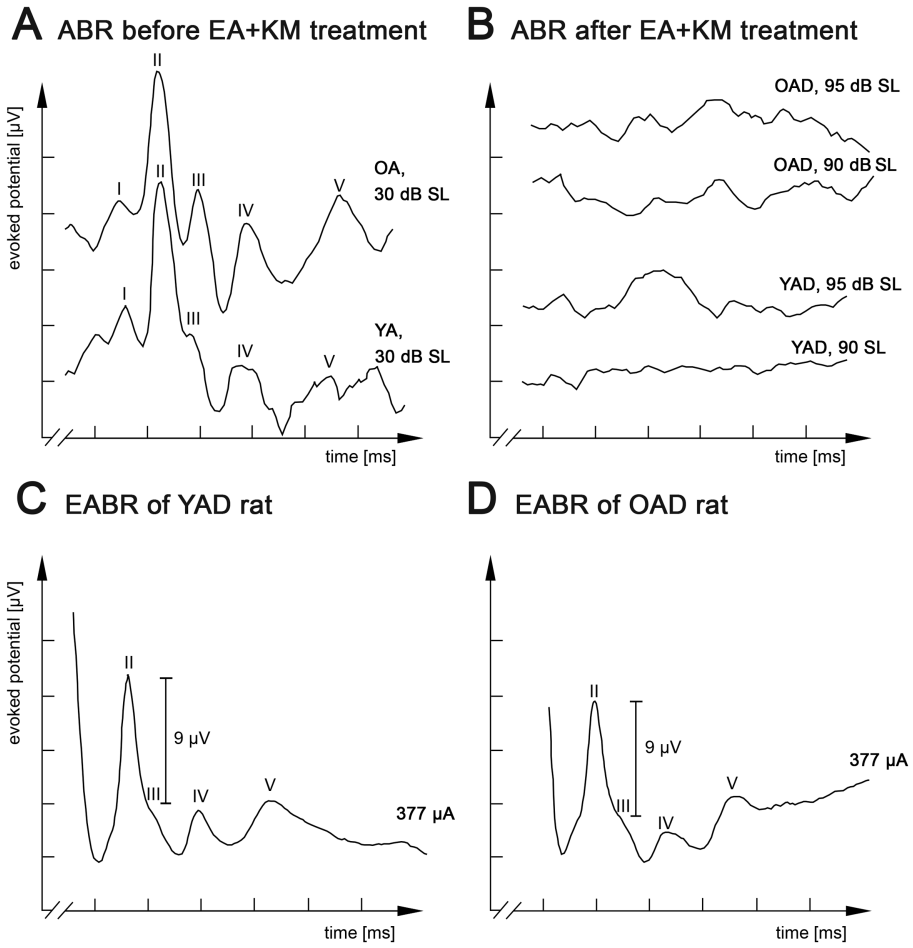


FIGURE 2
Kanamycin treatment in adult rats results in loss of auditory brainstem responses (ABR) and restored responses by electrical intracochlear stimulation. **(A)** Acoustic stimulation with broadband click stimuli at 30 dB SL induced comparable ABRs in normally hearing old adult (OA) and young adult (YA) rats. **(B)** Click-evoked ABR measurements of the same young adult-deafened rat (YAD) and one old adult-deafened (OAD) rat 3 days after treatment with ethacrynic acid (EA) and kanamycin (KM). Electrical intracochlear stimulation at a current level of ~377 µA induced comparable electrically evoked ABRs (EABRs) in YAD **(C)** and OAD **(D)** rats. I-V: recorded positive waves of acoustically **(A,B)** or electrically **(C,D)** evoked auditory brainstem potentials. x-axis: 2 ms per unit, y-axis: 4 µV per unit.

Frontal plane brain sections of 30 µm thickness containing anteroventral cochlear nucleus (AVCN), lateral superior olive (LSO), and central inferior colliculus (CIC) were cut using a cryostat.

2.7 Immunohistochemistry

Here, brain sections were exposed to a primary antibody raised in goat against Fos (SC-52-G, 1:2000, lot. no. L1406/K1808/F1109, Santa Cruz Biotechnology Inc., United States) (Rosskothen-Kuhl and Illing, 2010, 2012; Rosskothen-Kuhl et al., 2018). Visualization of primary antibody binding sites was based on the avidin–biotin technique (Cat. No. PK-6100, Vector Laboratories, United States), followed by staining with 0.05% 3.3-diaminobenzidine tetrahydrochloride (Cat. No. 32750, Sigma, Germany), 0.3% ammonium nickel (II) sulfate hexahydrate (Cat. No. A1827, Sigma, Germany) and 0.0015% H_2O_2 in 50 mM Tris buffer. A very detailed description of the immunostaining protocol used can be found in our previous studies (Illing et al., 2002; Rosskothen-Kuhl and Illing, 2010, 2012, 2014; Jakob et al., 2015; Jakob et al., 2019).

2.8 Quantification of Fos-positive (+) nuclei

Photographs were taken from ipsilateral AVCN (side of implantation or stimulation), ipsilateral LSO, and contralateral CIC (opposite to implantation or stimulation) of unilaterally stimulated rats using a 10x objective (for AVCN and LSO) or a 5x objective (for CIC) and a digital camera (Axiocam, Zeiss, Germany) at an 8-bit gray tone scale for quantitative evaluation of the staining results. Prior to the automated counting of Fos(+) nuclei, the color information of each image was removed by using Adobe Photoshop CS (Adobe Systems Inc., United States). As shown in Figure 7, two identically sized and equally positioned regions of interest (ROI) were selected in AVCN, LSO, and CIC to determine differences in the spatial Fos expression pattern between the experimental groups (red rectangles).

10.3389/fncel.2024.1424773

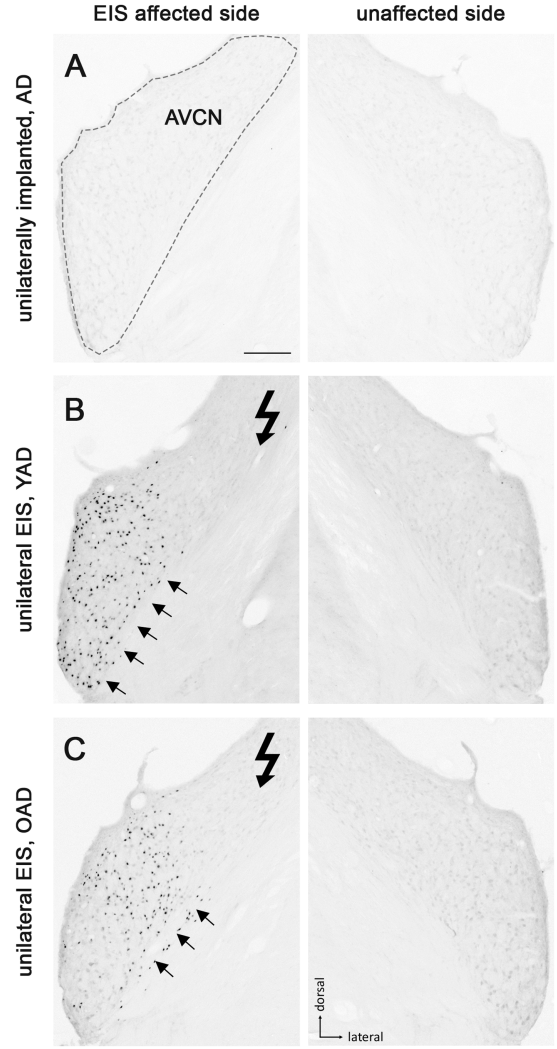


FIGURE 3
Patterns of Fos expression in the anteroventral cochlear nucleus (AVCN) of adult-deafened rats (AD, representative for the YAD and OAD cohort). **(A)** No Fos expression was found in unstimulated but unilaterally implanted AD rats in both AVCNs. Dashed line shows the border of AVCN. **(B)** Unilateral electrical intracochlear stimulation (EIS) of young adult-deafened (YAD) rats resulted in a large number of Fos expressing neurons (black dots) in the middle to ventral region of the ipsilateral AVCN (arrows), affected by EIS. **(C)** Corresponding to the intracochlear electrode position, old adult-deafened (OAD) rats showed a Fos expression limited to the central region of the ipsilateral AVCN (arrows). Flash symbol: side affected by EIS. All sections are at the level of Bregma −9.8 to −9.68 mm (Paxinos and Watson, 1986). Scale bar for A–C = 200 µm.

A fixed pair of ROIs (ROI 1, ROI 2) was used per auditory brainstem region of interest (AVCN, LSO, CIC; Figure 7, left).

While ROI 1 was placed in the mid-frequency range of NH rats, corresponding to the intracochlear stimulation position, ROI 2 covered the low frequency region of NH rats corresponding to an unstimulated intracochlear position (Ryan et al., 1988; see Figure 7A, left). Within the defined ROIs, gray value information was spread to the full 8-bit range (from 0 to 256). For automated counting of Fos(+) nuclei, photographs of three to five adjacent sections per rat through the anterior-to-posterior axis of AVCN, LSO, and CIC were chosen in the center of the strongest Fos appearance, after we had qualitatively checked all AVCN, LSO, and CIC sections of each animal for Fos expression. All photographs were imported into the image analysis program iTEM (Olympus, Germany) where detection threshold for gray tone values was set to 145 for AVCN, 165 for LSO, and 200 for CIC. Following the definition of ROIs, detection of the stained nuclei was performed under the settings for ratio (1–4), mean diameter (2–15), elongation (1–5), area (8–100), gray value minimum (200) and roundness (0.1–1). The ratio of ROI 2/ROI 1 was calculated for each brain section to identify differences in the stimulation-induced Fos expression pattern between the four different experimental groups (NH, ND, YAD, and OAD; Figure 7). To avoid a possible zero in the division calculation in the numerator, the number of Fos positive cells in ROI 1 and ROI 2 were each added with plus one. Ratios around 1 indicate a loss of tonotopy, while ratios closer to 0 indicate a more tonotopic organization of the corresponding auditory region.

2.9 Statistical analysis

Statistical analysis was performed using Prism software (GraphPad Software, Inc., United States). We tested our data for normal distributions (using the Kolmogorov–Smirnov test) and equal variances (using the Brown–Forsythe and Bartlett tests). As our data did not consistently fulfill both criteria, we used the non-parametric Kruskal–Wallis and Mann–Whitney tests for statistical analysis. For both, significance level was set to $p < 0.05$. In case of multiple comparisons, p-values were corrected using Dunn's multiple comparisons test. All adjusted p-values as well as the number of values per group are reported in Table 2. In addition, we indicate the results of Kruskal–Wallis statistics (H) for each test. Significances were differentiated into (***) for $p < 0.001$, (**) for $p < 0.01$, and (*) for $p < 0.05$ (Table 1). Stereological corrections for counting particles in the sectioned material were not made as particle size was small compared to section thickness and comparisons are based on numerical relationships among objects of similar size rather than on absolute densities. The Fos analysis for AVCN, LSO, and CIC was based on a total of 47 rats.

3 Results

3.1 Effect of kanamycin treatment in adult rats on auditory brainstem responses

Two cohorts of adult-deafened rats were studied: young adult-deafened (YAD) and old adult-deafened (OAD) rats. Before pharmacological treatment with kanamycin both cohorts showed normal hearing thresholds [young rats ($n = 12$): $\bar{x} = 14.3$ dB SL; old rats ($n = 11$): $\bar{x} = 14.7$ dB SL] and ABR responses with five distinguishable peaks (I–V, Figure 2A). Three days after EA + KM treatment, hearing thresholds increased by an average of 92 dB SL for young rats ($n = 16$ rats) and 93 dB SL for old rats ($n = 15$ rats; Figure 2B). Despite loss of outer and inner hair cells as previously described by Liu et al. (2011), the functionality of the auditory nerve has been preserved in both groups, which was verified by measuring EABRs with four differentiated peaks (II-V) under identical EIS. For both YAD and OAD rats, a peak II mean amplitude of 9 µV ± 10% was achieved by applying a current of in mean ~ 340 µA (Figures 2C,D).

10.3389/fncel.2024.1424773

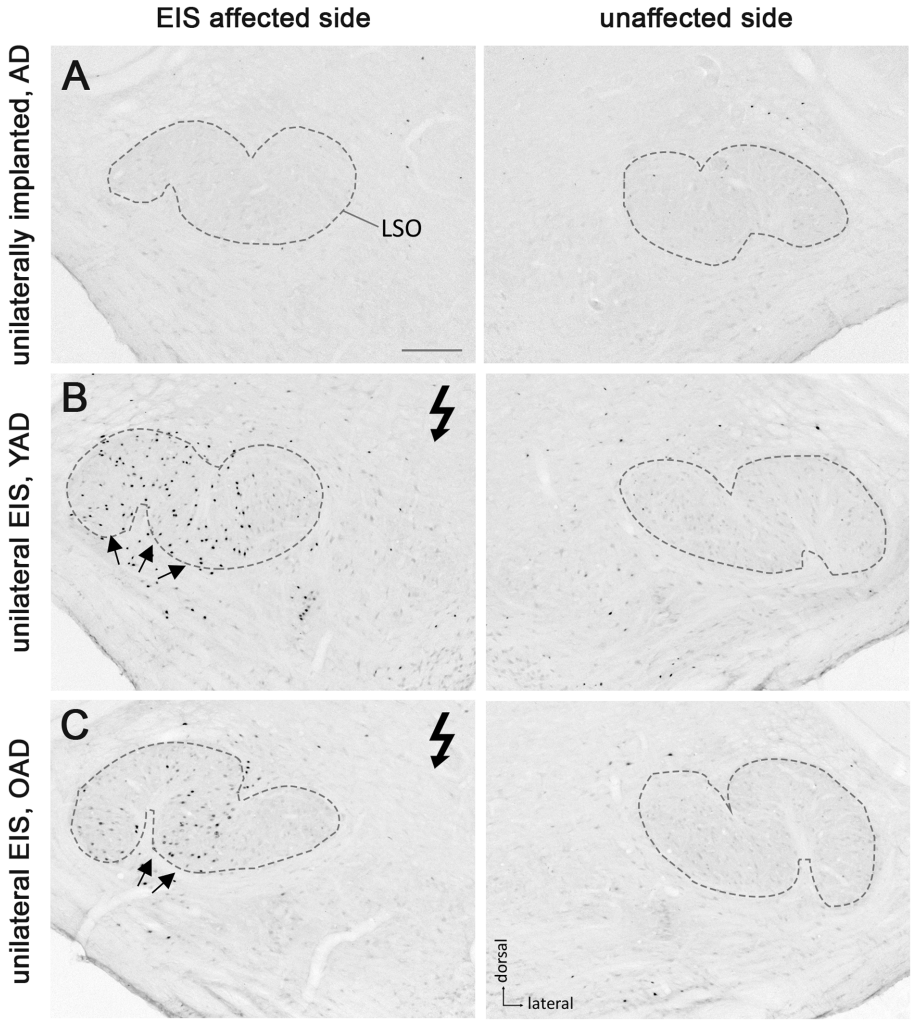


FIGURE 4
Patterns of Fos expression in the lateral superior olives (LSO) of adult-deafened rats (AD, representative for the YAD and OAD cohort). **(A)** Marginal Fos expression was found in unstimulated but unilaterally implanted AD rats in both LSOs (dashed lines). **(B)** Electrical intracochlear stimulation (EIS) of young adult-deafened (YAD) rats resulted in a large number of Fos expressing neurons (black dots) spread over nearly two-thirds of the EIS affected, ipsilateral LSO (arrows). **(C)** Corresponding to the intracochlear electrode position, old adult-deafened (OAD) rats showed a Fos expression limited to the central region of the ipsilateral LSO (arrows). Flash symbol: side affected by EIS. All sections are at the level of Bregma –9.8 to –9.3 mm (Paxinos and Watson, 1986). Scale bar for A–C = 200 µm.

3.2 Deafening of young but not of old adult rats results in reduction of tonotopic organization

Deafness-induced changes in the tonotopic organization along the auditory brainstem were studied by staining brain sections containing AVCN (Figure 3), LSO (Figure 4), and CIC (Figure 5) for the activity and plasticity marker Fos. Previous studies have demonstrated that Fos is a suitable marker for mapping changes in the activity pattern of the central auditory system (Rosskothen-Kuhl and Illing, 2010, 2012, 2014; Jakob et al., 2015; Jakob et al., 2016; Rosskothen-Kuhl et al., 2018; Jakob et al., 2019). However, its expression in auditory neurons requires at least 30–45 min of acoustic or electrical stimulation (Rosskothen-Kuhl and Illing, 2012).

One month after bilateral deafening of YAD and OAD rats, the mid-frequency region of their left cochlea was electrically stimulated for 2 h. As a result, only the neurons of the stimulated auditory pathway (EIS affected side ≙ ipsilateral AVCN, ipsilateral LSO and contralateral CIC) expressed the Fos protein, although differences in the expression pattern were observed between the two cohorts. In YAD rats, a broadly distributed neuronal expression of Fos was observed over more than half of the ipsilateral AVCN (Figure 3B, arrows), the ipsilateral LSO (Figure 4B, arrows), and the contralateral CIC (Figure 5B, arrows) without clear boundaries indicating a tonotopic correspondence with the intracochlear stimulation position. Contralateral to stimulation (unaffected side ≙ contralateral AVCN, contralateral LSO and ipsilateral CIC), no Fos expression was observed in the AVCN, LSO, and CIC of this cohort (Figures 3–5B), which was consistent with the Fos expression pattern of implanted, non-stimulated controls (Figures 3–5A). In contrast, OAD rats showed a lower and more focused tonotopic Fos expression in the ipsilateral AVCN and LSO as well as in the contralateral CIC, corresponding to the position of intracochlear stimulation and indicated by Fos(+) neurons in the middle area of these auditory regions (Figures 3–5C, arrows). Contralateral to the electrical stimulation (unaffected side), OAD rats also showed no Fos expression (Figures 3–5C), corresponding to controls.

TABLE 1 Overview of all experimental groups and the interventions.

Group	1		2	3	4	Additional control groups			
Name	Young NH (yNH) control	Old NH (oNH) control	ND	YAD	OAD	YAD control	YAD impl.	OAD control	OAD impl.
Number (*n*)	15		9	12	11	2	2	2	2
Age at deafening	–		10–20 days	3 months	12 months	3 months	3 months	12 months	12 months
Duration of deafness	–		4 months	1 month	1 month	1 month	1 month	1 month	1 month
Intervention	EIS		EIS	EIS	EIS	–	Impl.	–	Impl.
Age at stimulation	4 months	13 months	4 months	4 months	13 months	–	–	–	–

yNH, young normal hearing; oNH, old normal hearing; ND, neonatally-deafened; YAD, young adult-deafened; OAD, old adult-deafened; Impl., Implantation of electrode without stimulation; EIS, electrical intracochlear stimulation.

TABLE 2 Statistical data of Fos quantification in three auditory brainstem regions of all four experimental groups: normally hearing (NH), neonatally-deafened (ND), young adult-deafened (YAD), old adult-deafened (OAD).

	AVCN (H = 106.7)	LSO (H = 88.71)	CIC (H = 61.37)
NH vs. OAD	$p = 0.017$ (**), $n_{NH} = 56$, $n_{OAD} = 49$	$p = 0.9378$ (n.s.), $n_{NH} = 51$, $n_{OAD} = 43$	$p = 0.0042$ (**), $n_{NH} = 55$, $n_{OAD} = 47$
NH vs. YAD	$p < 0.0001$ (***), $n_{NH} = 56$, $n_{YAD} = 47$	$p < 0.0001$ (***), $n_{NH} = 51$, $n_{YAD} = 445$	$p < 0.0001$ (***), $n_{NH} = 55$, $n_{YAD} = 46$
NH vs. ND	$p < 0.0001$ (***), $n_{NH} = 56$, $n_{ND} = 34$	$p < 0.0001$ (***), $n_{NH} = 51$, $n_{ND} = 31$	$p < 0.0001$ (***), $n_{NH} = 55$, $n_{ND} = 24$
OAD vs. YAD	$p = 0.0083$ (**), $n_{OAD} = 49$, $n_{YAD} = 47$	$p = 0.0002$ (***), $n_{OAD} = 43$, $n_{YAD} = 45$	$p = 0.1203$ (n.s.), $n_{OAD} = 47$, $n_{YAD} = 46$
OAD vs. ND	$p < 0.0001$ (***), $n_{OAD} = 49$, $n_{ND} = 34$	$p < 0.0001$ (***), $n_{OAD} = 43$, $n_{ND} = 31$	$p = 0.0003$ (***), $n_{OAD} = 47$, $n_{ND} = 24$
YAD vs. ND	$p = 0.0685$ (n.s.), $n_{YAD} = 47$, $n_{ND} = 34$	$p = 0.0624$ (n.s.), $n_{YAD} = 45$, $n_{ND} = 31$	$p = 0.2104$ (n.s.), $n_{YAD} = 46$, $n_{ND} = 24$

H = Kruskal–Wallis statistics, n = number (n) of analyzed sections.

3.3 The age at onset of deafness affects the tonotopic organization of the auditory system

Figure 6 shows the neuronal Fos expression in the auditory brainstem (AVCN, LSO, and CIC) of young and old NH (yNH, oNH), OAD, YAD, and ND rats after 2 h of EIS. In previous studies we have demonstrated that the expression pattern of Fos and thus the stimulation-induced activity in the central auditory brainstem massively changes when hearing fails in early development (Rosskothen-Kuhl and Illing, 2010, 2012; Jakob et al., 2015; Rauch et al., 2016; Rosskothen-Kuhl et al., 2018; Jakob et al., 2019). While local intracochlear stimulation of young and old NH (yNH, oNH) rats induces a tonotopic Fos expression in auditory brainstem nuclei (Ryan et al., 1988; Rosskothen et al., 2008; Jakob and Illing, 2008; Rosskothen-Kuhl and Illing, 2010; Rauch et al., 2016) (Figures 6A–F, arrow(s)), local EIS of ND rats results in a spread of neuronal activity beyond the "normal" frequency borders, which is shown by a massive increase and dispersion of Fos-positive nuclei (Rosskothen-Kuhl and Illing, 2012; Jakob et al., 2015; Rauch et al., 2016; Rosskothen-Kuhl et al., 2018; Jakob et al., 2019) (Figures 6G–I, arrows). Neonatally-deafened brains thus show a lack of tonotopic organization along the auditory pathway, which is most likely a result of missing sensory input during early development. When comparing the stimulation-induced Fos expression patterns of NH rats (Figures 6A–F) and ND rats (Figures 6G–I) with the expression patterns observed in young and old adult-deafened animals (Figures 6G–L), it becomes clear that: first, the neuronal activity pattern of YAD rats (Figures 6J–L) is similar if not identical to the pattern of ND rats, and second, OAD rats (Figures 6G–I) show a more tonotopic Fos expression which is similar to the expression pattern of NH animals.

3.4 The shorter the hearing experience before deafness, the less the development or preservation of tonotopic organization in the auditory brainstem

To identify a correlation between tonotopic organization of the auditory system and hearing experience prior to deafness, the topography of stimulation-induced Fos expression in AVCN (Figure 7A, dashed line), LSO (Figure 7B, dashed line), and CIC (Figure 7C, dashed line) was determined for all four experimental groups: (1) young and old NH rats, (2) OAD rats, (3) YAD rats, and (4) ND rats. Defining two regions of interest (ROIs), with ROI 1 lying in the core region of mid-frequency sensitivity of NH rats (corresponding to our intracochlear stimulation position) and ROI 2 positioned in the region of lower frequency sensitivity of NH rats and thus corresponding to an unstimulated intracochlear site (Figure 7, red rectangles), the change of the local distribution of Fos(+) neurons was quantified by calculating the ratio of ROI 2 divided by ROI 1 (ROI 2/ROI 1). As a result, all three brainstem regions showed a significant increase of the ratio (ROI 2/ROI 1) with decrease of the hearing experience (Figure 7; for *p*-values of statistical analysis, see Table 1). Comparing all four experimental groups (Figure 7), it becomes clear that NH rats (young and old NH rats, which were combined into one cohort due to comparable Fos expression) showed the lowest ratio (median for AVCN = 0.075, LSO = 0.14, and CIC = 0.4), indicating the

10.3389/fncel.2024.1424773

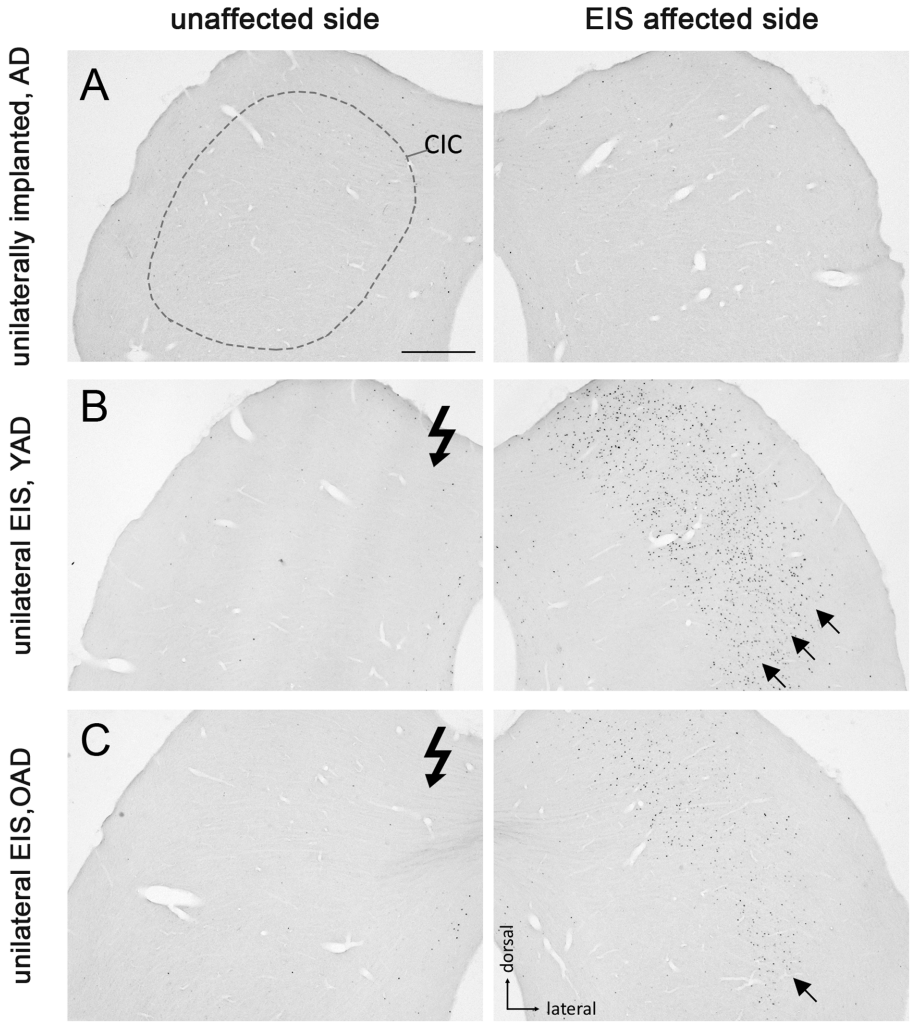


FIGURE 5
Fos expression pattern in the central inferior colliculus (CIC) of adult-deafened rats (AD, representative for the YAD and OAD cohort). **(A)** Marginal Fos expression was found in unstimulated but unilaterally implanted AD rats in both CICs. Dashed line shows the border of CIC. **(B)** Electrical intracochlear stimulation (EIS) of young adult-deafened (YAD) rats resulted in a large number of Fos expressing neurons (black dots) in the middle to lateral area of the contralateral CIC (arrows), side affected by EIS. **(C)** Corresponding to intracochlear electrode position, old adult-deafened (OAD) rats showed a Fos expression limited to the central region of the contralateral CIC (arrow). EIS affected side: CIC contralateral to EIS. Unaffected side: CIC ipsilateral to EIS. Flash symbol: side affected by EIS. All sections are at the level of Bregma −9.16 to −8.8 mm (Paxinos and Watson, 1986). Scale bar for A–C = 500 μm.

highest degree of tonotopic order along their auditory brainstem followed by somewhat higher ratios for OAD rats (median for AVCN = 0.34, LSO = 0.4, and CIC = 0.7). For all three auditory regions, the ratios of YAD rats were in median between 0.67 and 0.79 and thus higher than for the NH and OAD cohorts, which points out a massively reduced tonotopic order. The highest ROI 2/ROI 1 ratio with values close to 1 (Figure 7, dashed line in statistical panels) were detected for the ND cohort with the shortest hearing experience (median for AVCN = 0.82, LSO = 1, and CIC = 0.87), meaning that the distribution of Fos(+) neurons in both ROIs was almost equal and thus indicating a loss of tonotopy. In detail, for AVCN, we found significant differences between all groups, except for YAD and ND rats (Figure 6A; Table 1). In the LSO, we detected significant differences between groups, excluding NH vs. OAD rats and YAD vs. ND rats (Figure 6B; Table 2). For CIC, all groups showed significant differences between each other except YAD vs. OAD and YAD vs. ND rats (Figure 6C; Table 1). The detailed statistical results, including *p*-values, Kruskal–Wallis statistics (H), and number (n) of analyzed sections, are presented in Table 1. Overall, our quantification provides strong evidence that the preservation of tonotopic organization after adult-onset deafness correlates with the duration of hearing experience and thus with the age at deafness. Although they differed significantly from NHs rats in AVCN and CIC, OAD rats (~12 months hearing +1 month deaf) more or less maintained their tonotopy, whereas YAD rats (~3 months hearing +1 month deaf) interestingly lost their established organization already 1 month after deafness.

4 Discussion

A better understanding of the age-dependent plastic changes that occur in the mature auditory system following acute deafness is an

10.3389/fncel.2024.1424773

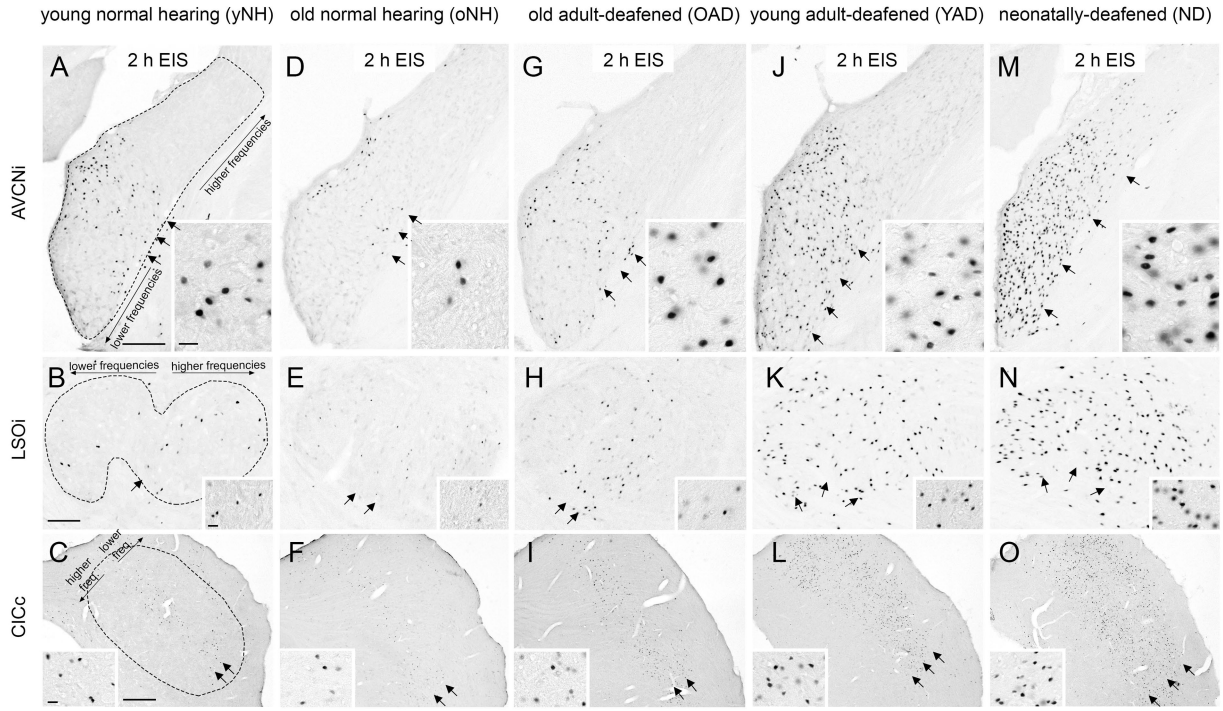


FIGURE 6
Stimulation-induced Fos expression patterns in neurons of the auditory brainstem of five experimental groups, young and old normal hearing (yNH/oNH), old adult-deafened (OAD), young adult-deafened (YAD), and neonatally-deafened (ND) rats. (A–F) In young (A–C) and old (D–F) NH rats stimulation-induced Fos expression is found in a tonotopic order corresponding to the intracochlear stimulation position of ~8–12 kHz (arrows) in AVCNi (A+D), LSOi (B+E), and CICc (C+F). (G–I) Similar to NH rats, OAD rats showed a Fos expression with a tonotopic distribution (arrows) in the auditory brainstem. (J–L) In contrast, YAD rats showed an increased and spread Fos expression pattern (arrows) indicating a degraded tonotopic organization. (M–O) In the auditory brainstem of ND rats, Fos expression pattern (arrows) was similar if not identical to the pattern of YAD rats, recognizable by an increased number of widely spread Fos-positive neurons in the auditory brainstem regions. Insets show Fos-positive nuclei at 100× magnification. Scale bar = 20 µm. AVCNi: anteroventral cochlear nucleus ipsilateral to electrical stimulation; CICc: central inferior colliculus contralateral to electrical stimulation; LSOi: lateral superior olive ipsilateral to electrical stimulation. Scale bars in A,B = 200 µm, and in C = 500 µm. Scale bars are valid for the entire row. Sub panels (A–C) represent the tontotopic axes for the three different auditory regions.

essential step toward improved rehabilitation of hearing-impaired patients and could contribute to improved auditory perception after the fitting with hearing prostheses. IThe present study investigated the impact of deafness on the tonotopic organization of the mature auditory brainstem as a function of age at onset of deafness. One of the most important findings was that the central auditory system of younger and older adult rats differently respond to sudden and severe deafness. Using histological staining of the neuronal activity and plasticity marker Fos, we demonstrated for the first time that just 1 month of bilateral deafness results in a loss of tonotopic order in the auditory brainstem of younger rats, whereas the auditory system of older rats showed not such marked changes in the stimulation-induced Fos expression pattern. This suggests that the tonotopic order, as observed in normal hearing peers, is more or less preserved in older rats despite acute deafness.

4.1 Hearing function and induction of deafness in adulthood

Regardless of age, all of our rats (only female) showed normal hearing thresholds prior to pharmacological deafening in adulthood. This observation coincides with a study on female Wistar rats by Möhrle et al. (2016), in which significant hearing threshold loss could only be detected at the age of 19 months or older. Our 12-month-old animals showed hearing thresholds similar to the thresholds of middle-aged animals (6–10 months) observed by Möhrle et al. (2016). This is different from the observations made for male Wistar rats, where an increase in hearing threshold is already observed at an age of 12 months and even earlier in noise exposed animals (Alvarado et al., 2014; Alvarado et al., 2019). But even if the hearing threshold of our older rats was still unaffected, the hearing function at suprathreshold levels could be different in young and old animals, e.g., due to the loss of spiral ganglion neurons or synaptic contacts of the spiral ganglion cells to the inner hairs cells (Kujawa and Liberman, 2009; Sergeyenko et al., 2013; Möhrle et al., 2016).

In addition to Liu et al. (2011), we were able to demonstrate ototoxic efficacy of the combined compounds EA and KM not only for young adult rats (~3 months old) but also for older rats (~12 months old), as evidenced by the loss of the Preyer's reflex (see Jero et al., 2001) and a strong increase in hearing thresholds by ~92–93 dB SL, indicating the efficacy of this systemic deafness method regardless of the age of the animals. Despite pharmacologically induced deafness, which according to Liu et al. (2011) is mainly caused by irreversible degeneration of outer and

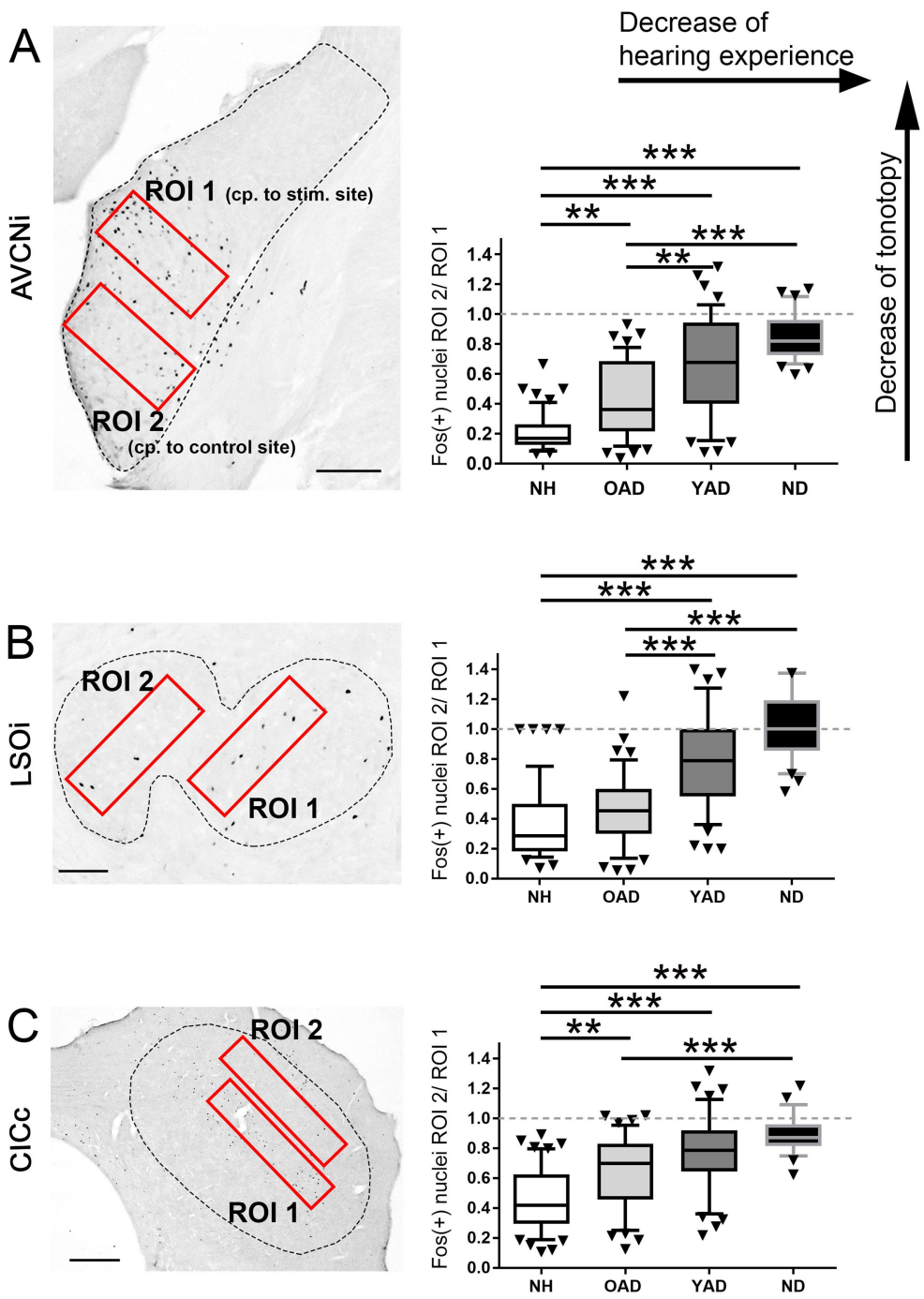


FIGURE 7
Quantification of the spatial distribution of the stimulation-induced Fos expression in the auditory brainstem of the four experimental groups, normal hearing (NH), old adult-deafened (OAD), young adult-deafened (YAD), and neonatally-deafened (ND) rats. (A–C) Left figures show the two regions of interest (ROIs in red) in AVCNi **(A)**, LSOi **(B)**, and CICc **(C)** and the figures on the right show the results of the ratio calculation presented as box plots for each of the four cohorts. ROI 1 is placed in the mid-frequency range of a NH rat corresponding (cp.) to the intracochlear stimulation (stim.) position, ROI 2 covers the low frequency region of a NH rat corresponding to an unstimulated intracochlear position. For statistics, the quotient of ROI 2 divided by ROI 1 (ROI 2/ROI 1) was calculated (right figures A–C). A small ratio corresponds to a good tonotopic order; a value of 1 means a Fos expression beyond the mid-frequency range of NH rats and thus a degradation of tonotopic order. Significant differences are shown by asterisks with * for $p < 0.05$, **for $p < 0.01$, *** for $p < 0.001$. Box plots show distribution-based metrics of the 10th and 90th percentile and the median. AVCNi: anteroventral cochlear nucleus ipsilateral to electrical stimulation; CICc: central inferior colliculus contralateral to electrical stimulation; LSOi: lateral superior olive ipsilateral to electrical stimulation. Scale bars in A,B = 200 µm, and in C = 500 µm.

inner hair cells, both groups of EA and KM treated animals showed well differentiated EABRs following cochlear implantation. Under identical stimulation conditions and parameters, these EABRs were comparable to the EABRs of our normal hearing rats (see also Rosskothen-Kuhl et al., 2018; Jakob et al., 2019), indicating good and sufficient preservation of spiral ganglion neurons after 1 month of deafness. However, to our knowledge, it is still unclear whether at all and if so which classes of spiral ganglion fibers are affected by EA and KM treatment in rats and whether they differ depending on age at deafness, which could result in different fiber sensitivity between the two cohorts.

4.2 Loss of tonotopy in younger but not in older auditory systems after acute deafness in adulthood

Fos (also known as c-Fos) belongs to the Immediate Early-Gene family associated with activity-dependent gene expression. The Fos promoter becomes rapidly induced in strongly activated neurons (Morgan and Curran, 1986; Cohen and Greenberg, 2008; Cruz et al., 2013). In the auditory system, Fos mRNA and protein expression can be induced by acoustic (Ehret and Fischer, 1991; Jakob et al., 2019) or electric stimulation (Vischer et al., 1994; Rosskothen et al., 2008; Rauch et al., 2016; Rosskothen-Kuhl et al., 2018).

Thirty to forty-five minutes of sustained electrical stimulation of the cochlea is sufficient to induce neuronal Fos expression along the auditory pathway of both NH as well as ND animals (Rosskothen-Kuhl and Illing, 2010, 2012). While frequency-specific stimulation of the cochlea of NH rats results in a local Fos expression pattern corresponding to the intracochlear stimulation position and thus reveals a tonotopic organization of the auditory pathway (Rosskothen et al., 2008; Rosskothen-Kuhl and Illing, 2010; Jakob, 2011; Jakob et al., 2019), comparable stimulation of ND rats leads to a massively increased number of activated neurons, which are spread over almost the entire frequency range of the different auditory brainstem regions and thus indicates a loss of tonotopy (Rosskothen-Kuhl and Illing, 2012; Jakob et al., 2015; Rauch et al., 2016; Rosskothen-Kuhl et al., 2018; Jakob et al., 2019).

In this study, we could demonstrate that not only neonatal deafness but also acute deafness in young adulthood can result in a degraded tonotopic organization (Figures 3–6). An auditory deprivation of 1 month, which corresponded to a quarter of the animal's lifetime, was sufficient to degenerate the frequency mapping of the auditory pathway developed in the first 3 months of life as indicated by a spread of Fos(+) neurons beyond the "normal" frequency borders. By directly comparing the stimulation-induced Fos expression levels and patterns of all four cohorts, NH, OAD, YAD, and ND rats, we derived two main conclusions: First, the shorter the duration of deafness, the better the tonotopy of the auditory pathway, and second, with identical duration of deafness in adulthood, as in our YAD vs. OAD cohorts, age at onset of deafness and/or hearing experience appears to influence the preservation of tonotopy. In accordance with our results of the Fos quantification shown in Figure 7, a higher age at onset of deafness and thus a longer period of auditory experience, as in the case of our OAD cohort, seems to have a positive effect on the preservation of the tonotopic organization in the adult auditory system. In contrast to the older animals, the auditory system of younger animals seems to react quickly to the sudden absence of sensory input.

4.2.1 Preservation of tonotopy in the older auditory system

Several studies have already shown that the plasticity level is higher in younger than in older brains (Berardi et al., 2004; Bavelier et al., 2010; Kwok et al., 2011; Sorg et al., 2016; Foscarin et al., 2017). An important role is attributed to the perineuronal nets (PNNs) in the central nervous system. PNNs are part of the extracellular matrix and play an important role in neuronal protection (Suttkus et al., 2012), the stabilization of synaptic contacts (Hockfield et al., 1990) as well as the inhibition of structural and functional plasticity (Frischknecht et al., 2009). In principle, the brain's extracellular matrix mediates structural stability by enwrapping synaptic contacts fundamental, for example, for long-term memory storage (Happel et al., 2014). In the aging auditory system of rats, Mafi et al. (2020) have shown that the density of PNNs is massively increasing. Especially in the central and dorsal inferior colliculus a strong increase of PNNs on GABAergic and non-GABAergic cells could be identified. In addition, Foscarin et al. (2017) have demonstrated in rats that brain aging changes the sulfation of proteoglycans in PNNs, making the perineuronal nets more inhibitory and thus leading to a decrease in plasticity. Among others, a lower plasticity potential in the auditory system of our OAD cohort could be a reason why the tonotopic organization is still preserved after 1 month of deafness. Presumably, PNN-mediated inhibition of plasticity slows down or even prevents disinhibition of the auditory network in older rats, which can normally be triggered within hours after both juvenile and adult hearing loss (Browne et al., 2012; Llano et al., 2012; Resnik and Polley, 2017; Balaram et al., 2019). This hypothesis is in line with a study by Bavelier et al. (2010) who claim that "… a reduction in plasticity as development proceeds is likely to allow greater adaptability of the organism to variable conditions early in life, while ensuring an efficient neural architecture for known conditions by adulthood." Whether the tonotopic organization in the OAD rats is still maintained even after a longer period of deafness or is lost with a delay cannot yet be answered and requires a follow-up study on OAD rats with a longer period of deafness.

An altered structural plasticity level discussed here might be one possible explanation for the changes we have identified in the auditory system. Alternatively or in addition, functional plasticity could also play a role here (Irvine, 2018; Kim et al., 2019). Thus, the altered local expression of Fos in the normally tonotopically organized auditory brainstem regions could be a consequence of functional remodeling of the tonotopic representation of the cochlear input to the respective brain region. In contrast to the widespread and accepted hypothesis that aging can be associated with a reduced or even complete loss of plasticity (Kwok et al., 2011; Sorg et al., 2016; Foscarin et al., 2017; Persic et al., 2020), a study by Cisneros-Franco et al. (2018) has shown that passive sound exposure can result in a plastic reorganization of the tonotopic map in the auditory cortex of older (age 22–24 months) but not younger adult rats (age 6–8 months). The increased but dysregulated plasticity was associated with a reduced inhibition of the aging auditory system. However, it should be noted that Cisneros-Franco et al. (2018) refer to cortical and not

to subcortical structures and performed the experiments on hearing and not on deafened animals, thus limiting the applicability of these results to our study.

4.2.2 Loss of tonotopy in the young adult auditory system

In addition to the hypothesis that older auditory networks may have a lower plasticity potential, Heusinger et al. (2019) demonstrated a rapid degradation of the extracellular matrix after acute unilateral deafness in young adult rats (age 2–5 months). This was accompanied by an ingrowth of immature synapses into the AVCN of the deaf side. Furthermore, a modulation of the extracellular matrix in the CIC contralateral to deafness was observed already 1 day after deafness. This study thus provides important evidence that the young adult-deafened auditory system has a high plasticity potential and undergoes a remodeling of synaptic connections within only a few days after deafness due to short-term degradation of the extracellular matrix. According to these observations, it can be assumed that the auditory system of our YAD cohort was also plastic and underwent structural and/or functional remodeling as a result of acute hearing loss. A well-described consequence of adult deafness is changes in inhibitory networks. While studies on the auditory brainstem have identified inhibitory changes within days (Bledsoe et al., 1995; Abbott et al., 1999; Vale and Sanes, 2002; Vale et al., 2003), cortical networks undergo disinhibition within a few hours, as indicated by a reduced expression of GABAergic markers (Kotak et al., 2005; Sarro et al., 2008; Takesian et al., 2010; Browne et al., 2012; Llano et al., 2012; Takesian et al., 2012; Mowery et al., 2015; Resnik and Polley, 2017; Balaram et al., 2019). This could be one reason for the dramatic increase in neuronal activity and the accompanying degraded tonotopy in the auditory brainstem of our electrically stimulated YAD rats. In support of this hypothesis, a study by Gallinaro and Rotter (2018) on structural plasticity based on firing rate homeostasis in recurrent neuronal networks provide evidence that connectivity in sensory networks changes depending on stimulation and that a disturbance of the steady state could result in the degradation of connections, for example due to the loss of sensory input.

In agreement with our observations on young-adult rats, studies on other animal models and humans have shown that adult deafness can affect the tonotopic organization of the auditory pathway. Using fMRI on young to middle aged human patients, Wolak et al. (2017) demonstrate that postlingual sensorineural hearing loss affects the tonotopic organization of the auditory cortex. Significant differences in the cortical tonotopic map compared to normal hearing controls were also found in patients with bilateral high-frequency hearing loss (Koops et al., 2020). In line with this, the study by Robertson and Irvine (1989) demonstrates a plasticity of frequency organization in the auditory cortex of adult guinea pigs as early as 35 days after unilateral deafness. In addition, mild noise-induced hearing loss in adulthood leads to a broader frequency tuning in the primary auditory cortex of cats (Seki and Eggermont, 2002). According to Pienkowski and Eggermont (2011), deafness caused by damage to the auditory periphery induces plasticity in the adult auditory cortex, which is reflected in changes in the topographic map, among other things. In addition to the cortex, the auditory thalamus also shows plasticity of the tonotopic organization after unilateral deafness of adult cats (Kamke et al., 2003). In contrast to the auditory cortex and the medial geniculate body in the thalamus, no or only limited and non-permanent reorganization of the tonotopic map has been observed in regions of the auditory brainstem such as the dorsal cochlear nucleus or the CIC after deafness in adulthood (Rajan and Irvine, 1998; Irvine et al., 2003; Pienkowski and Eggermont, 2011). The previous observations for the auditory brainstem thus contrast with the results of our study in young adult-deafened rats, which for the first time demonstrated a deterioration of the tonotopy from the ventral cochlear nucleus via the LSO to the CIC of the auditory brainstem (even) after 4 weeks of auditory deprivation. Although the tonotopy of the auditory system has long been considered resistant to changes, e.g., hearing loss, after completion of a critical developmental phase, the above studies as well as our own results show that plasticity is preserved in the young adult brain and occurs at both cortical and subcortical levels.

4.3 Clinical relevance

As shown by Hiel et al. (2016), age is not a limiting factor for the CI fitting of patients. Even after a long period of deafness of 10–30 years a CI can still be of great benefit (Moon et al., 2014; Hiel et al., 2016; Medina et al., 2017). One possible explanation could be an increased stability of the hearing-experienced, mature auditory network in old age. Despite a possibly reduced plasticity, a better preservation of network organization after deafness could help older patients to analyze sensory input via CI in a meaningful way. Provided that the data from the animal experiments can be transferred to human patients, our study provides evidence that elderly patients might be very suitable for reactivation of their auditory system by CIs due to a higher stability of their mature sensory networks even after a longer period of deafness. This hypothesis is supported, for example, by the better preservation of tonotopic organization after acute deafness in the old auditory system of mammals. This is in contrast to the auditory networks of younger patients, which are probably more plastic and therefore adapt more quickly to changes in sensory input. To date, the performance and benefit of older patients supplied with CI is still discussed controversially. While some studies show a better outcome for the younger adult CI patients (Chatelin et al., 2004; Vermeire et al., 2005; Lundin et al., 2013), others could not identify any differences (Labadie et al., 2000; Haensel et al., 2005; Mosnier et al., 2020; Bourn et al., 2022) or even demonstrate better performances for the elderly (Leung et al., 2005). For example, Leung et al. (2005) show that the age at implantation is only a low predictive value for postoperative performance. Elderly even performed better when the duration of deafness exceeded 25 years compared to their younger counterparts.

Based on our data, we suppose that patients who become deaf at an advanced age might have a larger time window to benefit from CI supply in contrast to young adult patients who should be treated as soon as possible after deafening in order to counteract the degeneration of trained network organizations at an early stage. However, it is very likely that the latter, with appropriate training and rehabilitation, can compensate for a potential loss of network organization in the long term due to their higher level of plasticity.

5 Conclusion

The central auditory system of young and old adult rats adapts differentially to acute deafness in adulthood. Our study, in which the auditory system was (re)activated by electrical stimulation of the cochlea, demonstrated that the auditory pathway of young adult rats after acute deafness exhibits a loss of tonotopy partly resembling that of neonatally-deafened rats. In contrast, after acute deafness in older animals, the auditory system retains its tonotopic order, similar to that of normal hearing animals. We conclude that plasticity predominates in the central auditory system of young adult rats. This is evidenced by the observation that acute deafness results in a degradation of frequency mapping along the auditory pathway after only a short period of deafness. In contrast, network stability seems to prevail in the older auditory system. This could explain the preservation of frequency mapping in the auditory system even after a period of severe deafness and could be an optimal prerequisite for enabling a good hearing outcome after CI supply in older deaf patients.

Data availability statement

The original contributions presented in the study are included in the article/supplementary material, further inquiries can be directed to the corresponding author.

Ethics statement

The animal study was approved by Regierungspräsidium Freiburg, 79083 Freiburg im Breisgau, Permission number G-10/83. The study was conducted in accordance with the local legislation and institutional requirements and followed the guidelines of the EU directive 2010/63/EU for animal experiments.

Author contributions

NR-K: Conceptualization, Data curation, Formal analysis, Funding acquisition, Investigation, Methodology, Project administration, Resources, Software, Supervision, Validation, Visualization, Writing – original draft, Writing – review & editing. SG: Data curation, Formal analysis, Investigation, Methodology, Validation, Writing – review & editing. TJ: Data curation, Formal analysis, Investigation, Visualization, Writing – original draft, Writing – review & editing, Validation.

Funding

The author(s) declare that financial support was received for the research, authorship, and/or publication of this article. This research was supported by a research grant from Cochlear Germany GmbH and Co. KG, Hannover, Germany (Research Agreement IIR-1498).

Acknowledgments

We thank H. Hildebrandt for technical assistance, proofreading, and helpful discussions and R.-B. Illing for continuous support and helpful discussion. Stimulation electrodes, programming software, and hardware components were kindly provided by Cochlear Germany GmbH & Co. KG, Hannover, Germany. We acknowledge support by the Open Access Publication Fund of the University of Freiburg.

Conflict of interest

The authors declare that the research was conducted in the absence of any commercial or financial relationships that could be construed as a potential conflict of interest.

Publisher's note

All claims expressed in this article are solely those of the authors and do not necessarily represent those of their affiliated organizations, or those of the publisher, the editors and the reviewers. Any product that may be evaluated in this article, or claim that may be made by its manufacturer, is not guaranteed or endorsed by the publisher.

References

Abbott, S. D., Hughes, L. F., Bauer, C. A., Salvi, R., and Caspary, D. M. (1999). Detection of glutamate decarboxylase isoforms in rat inferior colliculus following acoustic exposure. *Neuroscience* 93, 1375–1381. doi: 10.1016/s0306-4522(99)00300-0

Akter, N., Adachi, R., Kato, A., Fukaya, R., and Kuba, H. (2018). Auditory input shapes Tonotopic differentiation of Kv1.1 expression in avian Cochlear nucleus during late development. *J. Neurosci.* 38, 2967–2980. doi: 10.1523/JNEUROSCI.2472-17.2018

Alvarado, J. C., Fuentes-SantamarÃa, V. Ã., Gabaldón-Ull, M. C., Blanco, J. L., and Juiz, J. M. (2014). Wistar rats: a forgotten model of age-related hearing loss. *Front. Aging Neurosci.* 6:29. doi: 10.3389/fnagi.2014.00029

Alvarado, J. C., Fuentes-Santamaría, V., Gabaldón-Ull, M. C., and Juiz, J. M. (2019). Age-related hearing loss is accelerated by repeated short-duration loud sound stimulation. *Front. Neurosci.* 13:77. doi: 10.3389/fnins.2019.00077

Apple, D. M., Solano-Fonseca, R., and Kokovay, E. (2017). Neurogenesis in the aging brain. *Biochem. Pharmacol.* 141, 77–85. doi: 10.1016/j.bcp.2017.06.116

Argence, M., Vassias, I., Kerhuel, L., Vidal, P.-P., and De Waele, C. (2008). Stimulation by cochlear implant in unilaterally deaf rats reverses the decrease of inhibitory transmission in the inferior colliculus. *Eur. J. Neurosci.* 28, 1589–1602. doi: 10.1111/j.1460-9568.2008.06454.x

Balaram, P., Hackett, T. A., and Polley, D. B. (2019). Synergistic transcriptional changes in AMPA and GABAA receptor genes support compensatory plasticity following unilateral hearing loss. *Neuroscience* 407, 108–119. doi: 10.1016/j.neuroscience.2018.08.023

Bavelier, D., Levi, D. M., Li, R. W., Dan, Y., and Hensch, T. K. (2010). Removing brakes on adult brain plasticity: from molecular to behavioral interventions. *J. Neurosci.* 30, 14964–14971. doi: 10.1523/JNEUROSCI.4812-10.2010

Berardi, N., Pizzorusso, T., and Maffei, L. (2004). Extracellular matrix and visual cortical plasticity: freeing the synapse. *Neuron* 44, 905–908. doi: 10.1016/j.neuron.2004.12.008

Bledsoe, S. C., Nagase, S., Miller, J. M., and Altschuler, R. A. (1995). Deafness-induced plasticity in the mature central auditory system. *Neuroreport* 7, 225–229. doi: 10.1097/00001756-199512000-00054

Bourn, S. S., Goldstein, M. R., Morris, S. A., and Jacob, A. (2022). Cochlear implant outcomes in the very elderly. *Am. J. Otolaryngol.* 43:103200. doi: 10.1016/j.amjoto.2021.103200

Browne, C. J., Morley, J. W., and Parsons, C. H. (2012). Tracking the expression of excitatory and inhibitory neurotransmission-related proteins and neuroplasticity markers after noise induced hearing loss. *PLoS One* 7:e33272. doi: 10.1371/journal.pone.0033272

Buck, A. N., Buchholz, S., Schnupp, J. W., and Rosskothen-Kuhl, N. (2023). Interaural time difference sensitivity under binaural cochlear implant stimulation persists at high pulse rates up to 900 pps. *Sci. Rep.* 13:3785. doi: 10.1038/s41598-023-30569-0

Buck, A. N., Rosskothen-Kuhl, N., and Schnupp, J. W. (2021). Sensitivity to interaural time differences in the inferior colliculus of cochlear implanted rats with or without hearing experience. *Hear. Res.* 408:108305. doi: 10.1016/j.heares.2021.108305

Burke, S. N., and Barnes, C. A. (2006). Neural plasticity in the ageing brain. *Nat. Rev. Neurosci.* 7, 30–40. doi: 10.1038/nrn1809

Chatelin, V., Kim, E. J., Driscoll, C., Larky, J., Polite, C., Price, L., et al. (2004). Cochlear implant outcomes in the elderly. *Otol. Neurotol.* 25, 298–301. doi: 10.1097/00129492-200405000-00017

Cisneros-Franco, J. M., Ouellet, L., Kamal, B., and de Villers-Sidani, E. (2018). A brain without brakes: reduced inhibition is associated with enhanced but dysregulated plasticity in the aged rat auditory cortex. *eNeuro* 5:ENEURO.0051-18.2018. doi: 10.1523/ENEURO.0051-18.2018

Cohen, S., and Greenberg, M. E. (2008). Communication between the synapse and the nucleus in neuronal development, plasticity, and disease. *Annu. Rev. Cell Dev. Biol.* 24, 183–209. doi: 10.1146/annurev.cellbio.24.110707.175235

Cruz, F. C., Koya, E., Guez-Barber, D. H., Bossert, J. M., Lupica, C. R., Shaham, Y., et al. (2013). New technologies for examining neuronal ensembles in drug addiction and fear. *Nat. Rev. Neurosci.* 14, 743–754. doi: 10.1038/nrn3597

Ehlers, E., Goupell, M. J., Zheng, Y., Godar, S. P., and Litovsky, R. Y. (2017). Binaural sensitivity in children who use bilateral cochlear implants. *J. Acoust. Soc. Am.* 141, 4264–4277. doi: 10.1121/1.4983824

Ehret, G., and Fischer, R. (1991). Neuronal activity and tonotopy in the auditory system visualized by c-fos gene expression. *Brain Res.* 567, 350–354. doi: 10.1016/0006-8993(91)90819-h

Fallon, J. B., Irvine, D. R. F., and Shepherd, R. K. (2009). Cochlear implant use following neonatal deafness influences the cochleotopic organization of the primary auditory cortex in cats. *J. Comp. Neurol.* 512, 101–114. doi: 10.1002/cne.21886

Foscarin, S., Raha-Chowdhury, R., Fawcett, J. W., and Kwok, J. C. F. (2017). Brain ageing changes proteoglycan sulfation, rendering perineuronal nets more inhibitory. *Aging (Albany NY)* 9, 1607–1622. doi: 10.18632/aging.101256

Friauf, E. (1992). Tonotopic order in the adult and developing auditory system of the rat as shown by c-fos immunocytochemistry. *Eur. J. Neurosci.* 4, 798–812. doi: 10.1111/j.1460-9568.1992.tb00190.x

Frischknecht, R., Heine, M., Perrais, D., Seidenbecher, C. I., Choquet, D., and Gundelfinger, E. D. (2009). Brain extracellular matrix affects AMPA receptor lateral mobility and short-term synaptic plasticity. *Nat. Neurosci.* 12, 897–904. doi: 10.1038/nn.2338

Gallinaro, J. V., and Rotter, S. (2018). Associative properties of structural plasticity based on firing rate homeostasis in recurrent neuronal networks. *Sci. Rep.* 8:3754. doi: 10.1038/s41598-018-22077-3

Garcia-Iza, L., Martinez, Z., Ugarte, A., Fernandez, M., and Altuna, X. (2018). Cochlear implantation in the elderly: outcomes, long-term evolution, and predictive factors. *Eur. Arch. Otorrinolaringol.* 275, 913–922. doi: 10.1007/s00405-018-4910-y

Guzowski, J. F., Setlow, B., Wagner, E. K., and McGaugh, J. L. (2001). Experience-dependent gene expression in the rat hippocampus after spatial learning: a comparison of the immediate-early genes arc, c-fos, and zif268. *J. Neurosci.* 21, 5089–5098. doi: 10.1523/JNEUROSCI.21-14-05089.2001

Haensel, J., Ilgner, J., Chen, Y.-S., Thuermer, C., and Westhofen, M. (2005). Speech perception in elderly patients following cochlear implantation. *Acta Otolaryngol.* 125, 1272–1276. doi: 10.1080/00016480510044214

Happel, M. F. K., Niekisch, H., Castiblanco Rivera, L. L., Ohl, F. W., Deliano, M., and Frischknecht, R. (2014). Enhanced cognitive flexibility in reversal learning induced by removal of the extracellular matrix in auditory cortex. *Proc. Natl. Acad. Sci. USA* 111, 2800–2805. doi: 10.1073/pnas.1310272111

Heusinger, J., Hildebrandt, H., and Illing, R.-B. (2019). Sensory deafferentation modulates and redistributes neurocan in the rat auditory brainstem. *Brain Behav.* 9:e01353. doi: 10.1002/brb3.1353

Hiel, A.-L., Gerard, J.-M., Decat, M., and Deggouj, N. (2016). Is age a limiting factor for adaptation to cochlear implant? *Eur. Arch. Otorrinolaringol.* 273, 2495–2502. doi: 10.1007/s00405-015-3849-5

Hockfield, S., Kalb, R. G., Zaremba, S., and Fryer, H. (1990). Expression of neural proteoglycans correlates with the acquisition of mature neuronal properties in the mammalian brain. *Cold Spring Harb. Symp. Quant. Biol.* 55, 505–514. doi: 10.1101/sqb.1990.055.01.049

Illing, R.-B., Michler, S. A., Kraus, K. S., and Laszig, R. (2002). Transcription factor modulation and expression in the rat auditory brainstem following electrical intracochlear stimulation. *Exp. Neurol.* 175, 226–244. doi: 10.1006/exnr.2002.7895

Ingham, N. J., Thornton, S. K., Comis, S. D., and Withington, D. J. (1998). The auditory brainstem response of aged guinea pigs. *Acta Otolaryngol.* 118, 673–680. doi: 10.1080/00016489850183160

Irvine, D. R. F. (2018). Plasticity in the auditory system. *Hear. Res.* 362, 61–73. doi: 10.1016/j.heares.2017.10.011

Irvine, D. R. F., Rajan, R., and Smith, S. (2003). Effects of restricted cochlear lesions in adult cats on the frequency organization of the inferior colliculus. *J. Comp. Neurol.* 467, 354–374. doi: 10.1002/cne.10921

Jakob, T. F. (2011). Stimulationsabhängige Genexpression im zentralen auditorischen System. *HNO* 59, 230–238. doi: 10.1007/s00106-010-2250-3

Jakob, T. F., Döring, U., and Illing, R.-B. (2015). The pattern of Fos expression in the rat auditory brainstem changes with the temporal structure of binaural electrical intracochlear stimulation. *Exp. Neurol.* 266, 55–67. doi: 10.1016/j.expneurol.2015.02.015

Jakob, T., and Illing, R.-B. (2008). Laterality, intensity, and frequency of electrical intracochlear stimulation are differentially mapped into specific patterns of gene expression in the rat auditory brainstem. *Audiol. Med.* 6, 215–227. doi: 10.1080/16513860701875521

Jakob, T. F., Illing, R.-B., and Rosskothen-Kuhl, N. (2019). Monaural neonatal deafness induces inhibition among bilateral auditory networks under binaural activation. *Neuroscience* 400, 1–16. doi: 10.1016/j.neuroscience.2018.12.033

Jakob, T. F., Rosskothen-Kuhl, N., and Illing, R.-B. (2016). Induction of single-sided deafness in the newborn rat and its consequence for cochlear nucleus volume development. *Hear. Res.* 333, 210–215. doi: 10.1016/j.heares.2015.09.002

Jero, J., Coling, D. E., and Lalwani, A. K. (2001). The use of Preyer's reflex in evaluation of hearing in mice. *Acta Otolaryngol.* 121, 585–589. doi: 10.1080/000164801316878863

Kamke, M. R., Brown, M., and Irvine, D. R. F. (2003). Plasticity in the tonotopic organization of the medial geniculate body in adult cats following restricted unilateral cochlear lesions. *J. Comp. Neurol.* 459, 355–367. doi: 10.1002/cne.10586

Kandler, K., Clause, A., and Noh, J. (2009). Tonotopic reorganization of developing auditory brainstem circuits. *Nat. Neurosci.* 12, 711–717. doi: 10.1038/nn.2332

Kim, E. J., Feng, C., Santamaria, F., and Kim, J. H. (2019). Impact of auditory experience on the structural plasticity of the AIS in the mouse brainstem throughout the lifespan. *Front. Cell. Neurosci.* 13:456. doi: 10.3389/fncel.2019.00456

Kim, H., Kang, W. S., Park, H. J., Lee, J. Y., Park, J. W., Kim, Y., et al. (2018). Cochlear implantation in Postlingually deaf adults is time-sensitive towards positive outcome: prediction using advanced machine learning techniques. *Sci. Rep.* 8:18004. doi: 10.1038/s41598-018-36404-1

Koops, E. A., Renken, R. J., Lanting, C. P., and van Dijk, P. (2020). Cortical Tonotopic map changes in humans are larger in hearing loss than in additional tinnitus. *J. Neurosci.* 40, 3178–3185. doi: 10.1523/JNEUROSCI.2083-19.2020

Kotak, V. C., Fujisawa, S., Lee, F. A., Karthikeyan, O., Aoki, C., and Sanes, D. H. (2005). Hearing loss raises excitability in the auditory cortex. *J. Neurosci.* 25, 3908–3918. doi: 10.1523/JNEUROSCI.5169-04.2005

Kral, A., and Sharma, A. (2012). Developmental neuroplasticity after cochlear implantation. *Trends Neurosci.* 35, 111–122. doi: 10.1016/j.tins.2011.09.004

Kujawa, S. G., and Liberman, M. C. (2009). Adding insult to injury: cochlear nerve degeneration after "temporary" noise-induced hearing loss. *J. Neurosci.* 29, 14077–14085. doi: 10.1523/JNEUROSCI.2845-09.2009

Kwok, J. C. F., Dick, G., Wang, D., and Fawcett, J. W. (2011). Extracellular matrix and perineuronal nets in CNS repair. *Dev. Neurobiol.* 71, 1073–1089. doi: 10.1002/dneu.20974

Labadie, R. F., Carrasco, V. N., Gilmer, C. H., and Pillsbury, H. C. (2000). Cochlear implant performance in senior citizens. *Otolaryngol. Head Neck Surg.* 123, 419–424. doi: 10.1067/mhn.2000.109759

Leake, P. A., Hradek, G. T., Bonham, B. H., and Snyder, R. L. (2008). Topography of auditory nerve projections to the cochlear nucleus in cats after neonatal deafness and electrical stimulation by a cochlear implant. *J. Assoc. Res. Otolaryngol.* 9, 349–372. doi: 10.1007/s10162-008-0127-x

Leung, J., Wang, N.-Y., Yeagle, J. D., Chinnici, J., Bowditch, S., Francis, H. W., et al. (2005). Predictive models for cochlear implantation in elderly candidates. *Arch. Otolaryngol. Head Neck Surg.* 131, 1049–1054. doi: 10.1001/archotol.131.12.1049

Litovsky, R. Y., Goupell, M. J., Godar, S., Grieco-Calub, T., Jones, G. L., Garadat, S. N., et al. (2012). Studies on bilateral cochlear implants at the University of Wisconsin's binaural hearing and speech laboratory. *J. Am. Acad. Audiol.* 23, 476–494. doi: 10.3766/jaaa.23.6.9

Liu, H., Ding, D., Jiang, H., Wu, X., Salvi, R., and Sun, H. (2011). Ototoxic destruction by co-administration of kanamycin and ethacrynic acid in rats. *J Zhejiang Univ Sci B* 12, 853–861. doi: 10.1631/jzus.B1100040

Llano, D. A., Turner, J., and Caspary, D. M. (2012). Diminished cortical inhibition in an aging mouse model of chronic tinnitus. *J. Neurosci.* 32, 16141–16148. doi: 10.1523/JNEUROSCI.2499-12.2012

Lundin, K., Näsvall, A., Köbler, S., Linde, G., and Rask-Andersen, H. (2013). Cochlear implantation in the elderly. *Cochlear Implants Int.* 14, 92–97. doi: 10.1179/1754762812Y.0000000006

Mafi, A. M., Hofer, L. N., Russ, M. G., Young, J. W., and Mellott, J. G. (2020). The density of Perineuronal nets increases with age in the inferior colliculus in the Fischer Brown Norway rat. *Front. Aging Neurosci.* 12:27. doi: 10.3389/fnagi.2020.00027

Mann, Z. F., and Kelley, M. W. (2011). Development of tonotopy in the auditory periphery. *Hear. Res.* 276, 2–15. doi: 10.1016/j.heares.2011.01.011

Matsuda, K., Ueda, Y., Doi, T., Tono, T., Haruta, A., Toyama, K., et al. (1999). Increase in glutamate-aspartate transporter (GLAST) mRNA during kanamycin-induced cochlear insult in rats. *Hear. Res.* 133, 10–16. doi: 10.1016/s0378-5955(99)00050-7

McFadden, S. L., Campo, P., Quaranta, N., and Henderson, D. (1997). Age-related decline of auditory function in the chinchilla (Chinchilla laniger). *Hear. Res.* 111, 114–126. doi: 10.1016/s0378-5955(97)00099-3

Medina, M. D. M., Polo, R., Gutierrez, A., Muriel, A., Vaca, M., Perez, C., et al. (2017). Cochlear implantation in Postlingual adult patients with long-term auditory deprivation. *Otol. Neurotol.* 38, e248–e252. doi: 10.1097/MAO.0000000000001257

Möhrle, D., Ni, K., Varakina, K., Bing, D., Lee, S. C., Zimmermann, U., et al. (2016). Loss of auditory sensitivity from inner hair cell synaptopathy can be centrally compensated in the young but not old brain. *Neurobiol. Aging* 44, 173–184. doi: 10.1016/j.neurobiolaging.2016.05.001

Moon, I. S., Park, S., Kim, H.-N., Lee, W.-S., Kim, S. H., Kim, J.-H., et al. (2014). Is there a deafness duration limit for cochlear implants in post-lingual deaf adults? *Acta Otolaryngol.* 134, 173–180. doi: 10.3109/00016489.2013.850175

Morgan, J. I., and Curran, T. (1986). Role of ion flux in the control of c-fos expression. *Nature* 322, 552–555. doi: 10.1038/322552a0

Morgan, J. I., and Curran, T. (1991). Stimulus-transcription coupling in the nervous system: involvement of the inducible proto-oncogenes fos and Jun. *Annu. Rev. Neurosci.* 14, 421–451. doi: 10.1146/annurev.ne.14.030191.002225

Mosnier, I., Ferrary, E., Aubry, K., Bordure, P., Bozorg-Grayeli, A., Deguine, O., et al. (2020). The French National Cochlear Implant Registry (EPIIC): Cochlear implantation in adults over 65years old. *Eur. Ann. Otorhinolaryngol. Head Neck Dis.* 137, S19–S25. doi: 10.1016/j.anorl.2020.07.011

Mowery, T. M., Kotak, V. C., and Sanes, D. H. (2015). Transient hearing loss within a critical period causes persistent changes to cellular properties in adult auditory cortex. *Cereb. Cortex* 25, 2083–2094. doi: 10.1093/cercor/bhu013

Osako, S., Tokimoto, T., and Matsuura, S. (1979). Effects of kanamycin on the auditory evoked responses during postnatal development of the hearing of the rat. *Acta Otolaryngol.* 88, 359–368. doi: 10.3109/00016487909137180

Ouda, L., Profant, O., and Syka, J. (2015). Age-related changes in the central auditory system. *Cell Tissue Res.* 361, 337–358. doi: 10.1007/s00441-014-2107-2

Palombi, P. S., and Caspary, D. M. (1996). Physiology of the aged Fischer 344 rat inferior colliculus: responses to contralateral monaural stimuli. *J. Neurophysiol.* 76, 3114–3125. doi: 10.1152/jn.1996.76.5.3114

Paxinos, G., and Watson, C. (1986). RAT BRAIN. Burlington: Elsevier Science.

Persic, D., Thomas, M. E., Pelekanos, V., Ryugo, D. K., Takesian, A. E., Krumbholz, K., et al. (2020). Regulation of auditory plasticity during critical periods and following hearing loss. *Hear. Res.* 397:107976. doi: 10.1016/j.heares.2020.107976

Pienkowski, M., and Eggermont, J. J. (2011). Cortical tonotopic map plasticity and behavior. *Neurosci. Biobehav. Rev.* 35, 2117–2128. doi: 10.1016/j.neubiorev.2011.02.002

Raggio, M. W., and Schreiner, C. E. (1999). Neuronal responses in cat primary auditory cortex to electrical cochlear stimulation. III. Activation patterns in short- and long-term deafness. *J. Neurophysiol.* 82, 3506–3526. doi: 10.1152/jn.1999.82.6.3506

Rajan, R., and Irvine, D. (1998). Absence of plasticity of the frequency map in dorsal cochlear nucleus of adult cats after unilateral partial cochlear lesions. *J. Comp. Neurol.* 399, 35–46. doi: 10.1002/(SICI)1096-9861(19980914)399:1<35::AID-CNE3>3.0.CO;2-B

Rapanelli, M., Lew, S. E., Frick, L. R., and Zanutto, B. S. (2010). Plasticity in the rat prefrontal cortex: linking gene expression and an operant learning with a computational theory. *PLoS One* 5:e8656. doi: 10.1371/journal.pone.0008656

Rauch, A.-K., Rosskothen-Kuhl, N., and Illing, R.-B. (2016). Counter-regulation of the AP-1 monomers pATF2 and Fos: molecular readjustment of brainstem neurons in hearing and deaf adult rats after electrical intracochlear stimulation. *Neuroscience* 313, 184–198. doi: 10.1016/j.neuroscience.2015.11.025

Reisch, A., Illing, R.-B., and Laszig, R. (2007). Immediate early gene expression invoked by electrical intracochlear stimulation in some but not all types of neurons in the rat auditory brainstem. *Exp. Neurol.* 208, 193–206. doi: 10.1016/j.expneurol.2007.06.016

Resnik, J., and Polley, D. B. (2017). Fast-spiking GABA circuit dynamics in the auditory cortex predict recovery of sensory processing following peripheral nerve damage. *eLife* 6:e21452. doi: 10.7554/eLife.21452

Robertson, D., and Irvine, D. R. (1989). Plasticity of frequency organization in auditory cortex of guinea pigs with partial unilateral deafness. *J. Comp. Neurol.* 282, 456–471. doi: 10.1002/cne.902820311

Rosskothen, N., Hirschmüller-Ohmes, I., and Illing, R.-B. (2008). AP-1 activity rises by stimulation-dependent c-Fos expression in auditory neurons. *Neuroreport* 19, 1091–1093. doi: 10.1097/WNR.0b013e328303bbeb

Rosskothen-Kuhl, N., Buck, A. N., Li, K., and Schnupp, J. W. (2021). Microsecond interaural time difference discrimination restored by cochlear implants after neonatal deafness. *eLife* 10:e59300. doi: 10.7554/eLife.59300

Rosskothen-Kuhl, N., Hildebrandt, H., Birkenhäger, R., and Illing, R.-B. (2018). Astrocyte hypertrophy and microglia activation in the rat auditory midbrain is induced by electrical Intracochlear stimulation. *Front. Cell. Neurosci.* 12:43. doi: 10.3389/fncel.2018.00043

Rosskothen-Kuhl, N., and Illing, R.-B. (2010). Nonlinear development of the populations of neurons expressing c-Fos under sustained electrical intracochlear stimulation in the rat auditory brainstem. *Brain Res.* 1347, 33–41. doi: 10.1016/j.brainres.2010.05.089

Rosskothen-Kuhl, N., and Illing, R.-B. (2012). The impact of hearing experience on signal integration in the auditory brainstem: a c-Fos study of the rat. *Brain Res.* 1435, 40–55. doi: 10.1016/j.brainres.2011.11.046

Rosskothen-Kuhl, N., and Illing, R.-B. (2014). Gap43 transcription modulation in the adult brain depends on sensory activity and synaptic cooperation. *PLoS One* 9:e92624. doi: 10.1371/journal.pone.0092624

Roth, T. N., Hanebuth, D., and Probst, R. (2011). Prevalence of age-related hearing loss in Europe: a review. *Eur. Arch. Otorrinolaringol.* 268, 1101–1107. doi: 10.1007/s00405-011-1597-8

Ryan, A. F., Furlow, Z., Woolf, N. K., and Keithley, E. M. (1988). The spatial representation of frequency in the rat dorsal cochlear nucleus and inferior colliculus. *Hear. Res.* 36, 181–189. doi: 10.1016/0378-5955(88)90060-3

Sarro, E. C., Kotak, V. C., Sanes, D. H., and Aoki, C. (2008). Hearing loss alters the subcellular distribution of presynaptic GAD and postsynaptic GABAA receptors in the auditory cortex. *Cereb. Cortex* 18, 2855–2867. doi: 10.1093/cercor/bhn044

Seki, S., and Eggermont, J. J. (2002). Changes in cat primary auditory cortex after minor-to-moderate pure-tone induced hearing loss. *Hear. Res.* 173, 172–186. doi: 10.1016/s0378-5955(02)00518-x

Sergeyenko, Y., Lall, K., Liberman, M. C., and Kujawa, S. G. (2013). Age-related cochlear synaptopathy: an early-onset contributor to auditory functional decline. *J. Neurosci.* 33, 13686–13694. doi: 10.1523/JNEUROSCI.1783-13.2013

Sorg, B. A., Berretta, S., Blacktop, J. M., Fawcett, J. W., Kitagawa, H., Kwok, J. C. F., et al. (2016). Casting a wide net: role of Perineuronal nets in neural plasticity. *J. Neurosci.* 36, 11459–11468. doi: 10.1523/JNEUROSCI.2351-16.2016

Suttkus, A., Rohn, S., Jäger, C., Arendt, T., and Morawski, M. (2012). Neuroprotection against iron-induced cell death by perineuronal nets - an *in vivo* analysis of oxidative stress. *Am. J. Neurodegener. Dis.* 1, 122–129

Syka, J. (2002). Plastic changes in the central auditory system after hearing loss, restoration of function, and during learning. *Physiol. Rev.* 82, 601–636. doi: 10.1152/physrev.00002.2002

Takesian, A. E., Kotak, V. C., and Sanes, D. H. (2010). Presynaptic GABA(B) receptors regulate experience-dependent development of inhibitory short-term plasticity. *J. Neurosci.* 30, 2716–2727. doi: 10.1523/JNEUROSCI.3903-09.2010

Takesian, A. E., Kotak, V. C., and Sanes, D. H. (2012). Age-dependent effect of hearing loss on cortical inhibitory synapse function. *J. Neurophysiol.* 107, 937–947. doi: 10.1152/jn.00515.2011

Vale, C., and Sanes, D. H. (2002). The effect of bilateral deafness on excitatory and inhibitory synaptic strength in the inferior colliculus. *Eur. J. Neurosci.* 16, 2394–2404. doi: 10.1046/j.1460-9568.2002.02302.x

Vale, C., Schoorlemmer, J., and Sanes, D. H. (2003). Deafness disrupts chloride transporter function and inhibitory synaptic transmission. *J. Neurosci.* 23, 7516–7524. doi: 10.1523/JNEUROSCI.23-20-07516.2003

Vermeire, K., Brokx, J. P. L., Wuyts, F. L., Cochet, E., Hofkens, A., and van de Heyning, P. H. (2005). Quality-of-life benefit from cochlear implantation in the elderly. *Otol. Neurotol.* 26, 188–195. doi: 10.1097/00129492-200503000-00010

Vischer, M. W., Häusler, R., and Rouiller, E. M. (1994). Distribution of Fos-like immunoreactivity in the auditory pathway of the Sprague-Dawley rat elicited by cochlear electrical stimulation. *Neurosci. Res.* 19, 175–185. doi: 10.1016/0168-0102(94)90141-4

Von Gablenz, P., Hoffmann, E., and Holube, I. (2017). Prävalenz von Schwerhörigkeit in Nord- und Süd-Deutschland. *HNO* 65, 130–135. doi: 10.1007/s00106-016-0318-4

WHO (2024). Deafness and hearing loss. Available at: https://www.who.int/news-room/fact-sheets/detail/deafness-and-hearing-loss.

Willott, J. F. (1984). Changes in frequency representation in the auditory system of mice with age-related hearing impairment. *Brain Res.* 309, 159–162. doi: 10.1016/0006-8993(84)91022-9

Wolak, T., Cieśla, K., Lorens, A., Kochanek, K., Lewandowska, M., Rusiniak, M., et al. (2017). Tonotopic organisation of the auditory cortex in sloping sensorineural hearing loss. Hear. Res. 355, 81–96. doi: 10.1016/j.heares.2017.09.012

frontiers | Frontiers in Cellular Neuroscience

TYPE Original Research
PUBLISHED 18 November 2024
DOI 10.3389/fncel.2024.1404206

Check for updates

OPEN ACCESS

EDITED BY
Bernhard Englitz,
Radboud University, Netherlands

REVIEWED BY
André Dagostin,
Oregon Health & Science University, United States
Igor Delvendahl,
University of Freiburg, Germany

*CORRESPONDENCE
Christoph Körber
✉ koerber@uni-heidelberg.de

†PRESENT ADDRESS
Christoph Körber,
Institute of Neuroanatomy, University Medical Center Göttingen, Göttingen, Germany

‡These authors have contributed equally to this work

RECEIVED 20 March 2024
ACCEPTED 04 November 2024
PUBLISHED 18 November 2024

CITATION
Lessle S, Ebbers L, Dörflinger Y, Hoppe S, Kaiser M, Nothwang HG and Körber C (2024) Maintenance of a central high frequency synapse in the absence of synaptic activity. *Front. Cell. Neurosci.* 18:1404206. doi: 10.3389/fncel.2024.1404206

COPYRIGHT
© 2024 Lessle, Ebbers, Dörflinger, Hoppe, Kaiser, Nothwang and Körber. This is an open-access article distributed under the terms of the Creative Commons Attribution License (CC BY). The use, distribution or reproduction in other forums is permitted, provided the original author(s) and the copyright owner(s) are credited and that the original publication in this journal is cited, in accordance with accepted academic practice. No use, distribution or reproduction is permitted which does not comply with these terms.

Maintenance of a central high frequency synapse in the absence of synaptic activity

Sascha Lessle[1‡], Lena Ebbers[2‡], Yvette Dörflinger[1], Simone Hoppe[1], Michaela Kaiser[1], Hans Gerd Nothwang[2,3] and Christoph Körber[1*†]

[1]Department of Functional Neuroanatomy, Institute of Anatomy and Cell Biology, Heidelberg University, Heidelberg, Germany, [2]Division of Neurogenetics, Center of Excellence Hearing4All, School of Medicine and Health Sciences, Carl von Ossietzky University Oldenburg, Oldenburg, Germany, [3]Research Center for Neurosensory Science, Carl von Ossietzky University Oldenburg, Oldenburg, Germany

Activity has long been considered essential for circuit formation and maintenance. This view has recently been challenged by proper synaptogenesis and only mildly affected synapse maintenance in the absence of synaptic activity in forebrain neurons. Here, we investigated whether synaptic activity is necessary for the development and maintenance of the calyx of Held synapse. This giant synapse located in the auditory brainstem is highly specialized to maintain high frequency, high-fidelity synaptic transmission for prolonged times and thus shows particularly high synaptic activity. We expressed the protease tetanus toxin light chain (TeNT) exclusively in bushy cells of the ventral cochlear nucleus (VCN) of juvenile mice. Since globular bushy cells give rise to the calyx of Held, expression of TeNT in these cells specifically abolished synaptic transmission at the calyx without impairing general functionality of the central auditory system. Calyces lacked synaptic activity after two weeks of TeNT expression. However, this did not lead to major changes in presynaptic morphology, the number of active zones (AZs) or the composition of postsynaptic AMPA-type glutamate receptors (GluAs). Moreover, the fenestration of the calyx of Held, a hallmark of structural maturation, occurred normally. We thus show that the maintenance of a specialized high frequency synapse in the auditory brainstem occurs in a hardwired, probably genetically encoded, manner with little dependence on synaptic activity.

KEYWORDS

calyx of Held, tetanus toxin, VCN, MNTB, Math5

Introduction

Ever since the pioneering work of Hubel and Wiesel in the visual system, neuronal activity has been recognized as a key determinant for proper development and maturation of neuronal circuits (Hubel and Wiesel, 1964, 1965; Katz and Shatz, 1996; Blankenship and Feller, 2010; Kirkby et al., 2013; Wang and Bergles, 2015). Recent findings in circuits of the forebrain and neuronal cultures, however, questioned this long-standing theory.

The absence of Munc13 or Munc18, both crucial for neurotransmitter release, or cleavage of the SNARE protein VAMP2 (a.k.a. synaptobrevin2) by the expression of TeNT caused only a moderate reduction in synapse numbers (Verhage et al., 2000; Varoqueaux et al., 2002; Sando et al., 2017; Sigler et al., 2017; Quinn et al., 2019). Thus, synapse assembly and maintenance appear to be only partially dependent on neuronal activity but rather rely on cell intrinsic programs. These intriguing findings in forebrain neurons, which are active at moderate frequencies, raise the question whether assembly and maintenance of specialized high frequency synapses is also controlled by cell intrinsic genetic programs rather than by synaptic activity.

A prime high frequency brain area is the auditory brainstem, as the processing of sound features relies on ultrafast and ultraprecise timing of synaptic signals (Grothe et al., 2010). Moreover, spontaneous synaptic activity in the auditory system has been described long before the onset of hearing, suggesting a role in auditory circuit development (Wang and Bergles, 2015; Babola et al., 2018). High frequency, high-fidelity synaptic transmission is achieved by various synaptic specializations, including giant synapses such as the calyx of Held. This glutamatergic axo-somatic synapse arises from globular bushy cells (GBCs) in the ventral cochlear nucleus (VCN) and terminates on principal neurons of the contralateral medial nucleus of the trapezoid body (MNTB) (Borst and Soria van Hoeve, 2012). The calyx undergoes profound morphological and functional maturations, as it develops from a bouton-type synapse [postnatal day 2 (P2)] to its cup-shaped juvenile form (P6) and later, after the onset of hearing, into the fenestrated, mature synapse (P14) (Kandler and Friauf, 1993; Hoffpauir et al., 2006; Ford et al., 2009; Borst and Soria van Hoeve, 2012; Holcomb et al., 2013). The role of synaptic activity for the development and maturation of the calyx of Held as well as MNTB principal neurons has so far been investigated in congenitally deaf or cochlea ablated mice and gerbils. Altered synaptic activity due to a lack of neurotransmitter release from inner hair cells of the cochlea during circuit development resulted in the loss of tonotopic organization in the MNTB (Leao et al., 2006; Ford et al., 2009), action potential broadening, increased NMDA receptor expression (Erazo-Fischer et al., 2007) and considerable cell death of MNTB neurons (Hirtz et al., 2011; Satheesh et al., 2012). Moreover, conductive hearing loss caused changes in calyceal morphology as well as in pre- and postsynaptic function (Grande et al., 2014).

However, in deaf or deafened animal models the auditory system is affected as a whole with auditory brainstem neurons generating abnormal spontaneous activity by themselves (Youssoufian et al., 2008). In order to overcome this limitation, we selectively expressed TeNT in the bushy cells of the VCN using Math5-Cre mice, which express Cre-recombinase specifically in these cells. This strategy blocks neurotransmitter release in the calyx of Held without disrupting the complete auditory brainstem circuitry. Electrophysiological analysis revealed a lack of neurotransmitter release from the calyx of Held after 14 days of TeNT expression. Yet, even after another 7 days of synaptic silence, the calyx was not retracted, degraded or altered with respect to AZ number or postsynaptic AMPA receptor composition. We rather observed minor changes in synapse morphology. These findings suggest that the maintenance of the calyx of Held giant synapse is largely independent of synaptic activity but may rather be controlled by cell intrinsic, genetic means.

Materials and methods

Animals

All experiments were conducted in accordance with the German federal law and the EU directive 2010/63 for the care and use of laboratory animals. Protocols were approved by the local authorities (Regierungspräsidium Karlsruhe). All experiments were conducted in heterozygous Math5-Cre mice in which the coding sequence of the transcription factor Math5 (a.k.a. Atoh7) is replaced by Cre-recombinase on one allele (Yang et al., 2003). Heterozygous mice were chosen for the experiments since the lack of both Math5 alleles results in latency shifts in auditory brain stem responses and thus an impairment of auditory processing. However, these shifts have not been reported for mice lacking only one Math5 allele (Saul et al., 2008). Mice were stereotactically injected at P6/7 with AAVs encoding either TeNT fused to EGFP or EGFP alone in a Cre-dependent manner. Injected mice were returned to their mothers and kept there until further use. Mice were sacrificed at P20/21 (electrophysiology) or P27/28 (immunohistochemistry, electron microscopy).

AAV constructs

The coding sequence of tetanus toxin light chain was N-terminally fused to EGFP as described before (Nakashiba et al., 2008), to allow identification of synapses expressing the construct. The fusion protein was cloned between two loxP-sites to render its expression Cre-dependent. EGFP alone, cloned between two loxP-sites served as a control. Cre-dependent expression of both constructs was under the control of the CAG or the hsyn promotor. The constructs were packed in chimeric AAV particles of the serotypes 1 and 2, as described previously (Körber et al., 2015). The functionality of EGFP-TeNT was assessed by Western Blot and immunocytochemistry (Figure 1). Co-expression of the EGFP-TeNT construct and EGFP-tagged VAMP2 in HEK293 cells resulted in an apparently complete cleavage of VAMP2, judged by the shift of the VAMP2 signal from 40 kDa (VAMP2: 13 kDa, EGFP: 27 kDa) to 32 kDa (Figure 1A, VAMP2 amino acids 1–76: ~8 kDa). To ensure that functionality of the tagged, Cre-dependent TeNT was not limited to HEK293 cells, we examined the effect of TeNT-expression on VAMP2 levels in cultured cortical neurons by immunocytochemistry, using an anti-VAMP2 antibody that does not recognize the cleaved form (Figures 1B, C; Sando et al., 2017). We observed a marked reduction in VAMP2 signal in TeNT-expressing neurons already 3 days after transduction (Figure 1C). VAMP2 levels plateaued 6 days after transduction with no further reduction for the next 6 days (Figure 1B). The remaining VAMP2 signal originated mostly from structures in the somata of the neurons, e.g., the ER, in which VAMP2 is shielded from TeNT (Figure 1C). In accordance with previous reports (Hoogstraaten et al., 2020), TeNT-expressing synapses, identified by immunostaining against Piccolo, were apparently devoid of VAMP2 signal by P6 (Figure 1C).

10.3389/fncel.2024.1404206

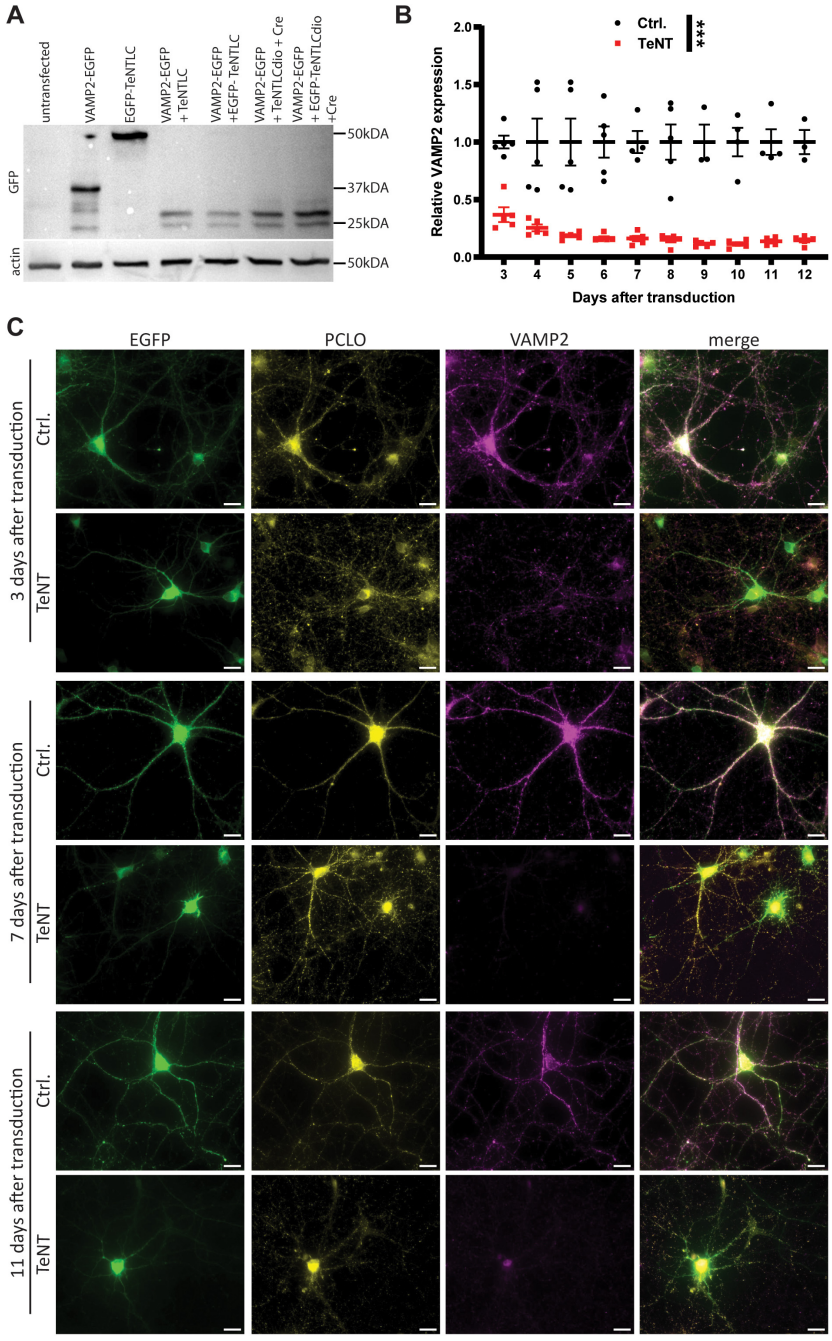


FIGURE 1
EGFP-TeNT is functional in HEK293 cells and cultured cortical neurons. **(A)** Western Blot analysis of untransfected HEK293 cells (lane 1) and HEK293 cells expressing VAMP2-EGFP (lane 2), EGFP-TeNT (lane 3), VAMP2-EGFP and untagged TeNT (lane 4), VAMP2-EGFP and EGFP-TeNT (lane 5), VAMP2-EGFP, untagged, Cre-dependent TeNT and Cre-recombinase (lane 6) and VAMP2-EGFP, Cre-dependent EGFP-TeNT and Cre-recombinase (lane 7), probed against EGFP. Co-expression of VAMP2-EGFP with any of the TeNT constructs results in a band shift of 8 kDa, which corresponds to the molecular weight of VAMP2 amino acids 1 to 76 which are cleaved of by TeNT. Of note, EGFP tagged versions of TeNT are barely detectable, as soon as VAMP2-EGFP is co-expressed. This is due to a reduction in the amount of TeNT present in the samples. **(B)** Quantification of VAMP2 fluorescence signal in cultured cortical neurons expressing either EGFP only or EGFP-TeNT, normalized to control (5 independent neuronal cultures, for each culture: average of 5 neurons per condition, $p < 0.001$, two-way ANOVA, $p < 0.05$ for each time point, Sidak's post-hoc test). **(C)** Representative images of cultured cortical neurons expressing either Cre-dependent EGFP or Cre-dependent EFGP-TeNT and Cre-recombinase stained for VAMP2 and Piccolo at 3, 7 and 11 days after transduction. Scale bars are 20 μm. *** = $p < 0.001$.

Western blotting

HEK293 cells were transfected with plasmids encoding EGFP-tagged VAMP2 and various versions of TeNT (tagged or untagged, Cre-dependent or Cre-independent) using the polyethylenimine method. Three days after transfection, cells were lysed in RIPA buffer supplemented with protease inhibitor. Membranes were pelleted and the supernatant was subjected to SDS-PAGE and

semi-dry Western Blotting. Proteins were probed with a primary antibody against EGFP (rabbit polyclonal, target species: species independent, dilution 1:2000, Cat. no.: PABG1; Proteintech, Martinsried, Germany). β-actin served as a loading control (mouse monoclonal, target species: mouse, rat, zebrafish, human, dilution 1:5000, Cat. no.: 251011, Synaptic Systems). Appropriate secondary antibodies conjugated to HRP (Biorad or Proteintech) were used at dilutions of 1:3000 (EGFP) or 1:15000 (β-actin). Protein signal was visualized using SuperSignal West Pico Plus Chemoluminescent Substrate (Cat. no. 34577, ThermoFischer) and an iBright Imaging System (ThermoFischer).

Immunocytochemistry

Cultured cortical neurons transduced with AAVs encoding either membrane-bound EGFP or Cre-dependent EGFP-TeNT and Cre-recombinase (separate AAVs) were fixed (4% PFA in PBS) for 5 min, 3 to 12 days after transduction. Cells were washed three times in PBS and stored at 4°C until further use. Blocking and permeabilization were performed in blocking buffer (1% normal goat serum, 0,2% Triton-X-100 in PBS) for 90 min. Incubation with primary antibodies against GFP (chicken polyclonal; dilution 1:1000; target species: species independent, Cat. no. ab13970, Abcam), Piccolo (guinea pig polyclonal, dilution 1:1000; target species: rat, mouse; Cat. no.: 142104; Synaptic Systems) and VAMP2/Synaptobrevin2 (mouse monoclonal; dilution 1:1000; target species: human, rat, mouse, hamster; Cat. no. 104211, Synaptic Systems) was performed in blocking buffer for 2 h. After washing with PBS (three times, 10 min), appropriate secondary antibodies coupled to Alexa-dyes (dilution 1:1000; Thermo Fischer) were applied for 45 min in blocking buffer. Thereafter, cells were washed 3 times in PBS and mounted in Mowiol. All incubation steps were performed at room temperature under gentle agitation. Images were acquired using a widefield fluorescence microscope (DM6000, Leica) equipped with a 63× HCX PL APO (1.45 NA) objective. Relative VAMP2 fluorescence signal was analyzed with ImageJ.

Stereotaxic injections

AAV particles were stereotactically injected into the VCN of anesthetized Math5-Cre mice of either sex at P6/7 as described earlier (Vasileva et al., 2012). In brief, mice were deeply anesthetized using isoflurane and aligned in the stereotactic apparatus (Kopf Instruments, Tujunga, CA, USA). A craniectomy was performed and ∼2 μl of virus solution were evenly distributed to the following coordinates relative to bregma and midline (*x*, *y*, in mm): 0.5, –4.5; 0.55, –4.5; 0.6, –4.5; 0.45, –5.1; 0.45, –5.2 using a custom build manipulator (Wimmer et al., 2004). Z- and A-positions were kept constant at 0.45 mm and 6.5 mm, respectively. After the surgery, mice recovered within minutes and were returned to their mothers.

Preparation of fixed brain slices

Mice were deeply anesthetized with Pentobarbital (500 mg/kg bodyweight) at P27/28 and transcardially perfused with 15 ml of PBS followed by 15 ml of Zamboni's solution (2% PFA, 15% picric acid in 0.15 M phosphate buffer). Brains were removed from the skull, post-fixed at 4°C for 2–4 h (immunohistochemistry) or over night (electron microscopy) and stored in 30% sucrose/PBS at −20°C until further usage.

Immunohistochemistry

Coronal sections of 60–80 μm thickness were cut on a vibratome (VT1000S, Leica) and antibody staining was performed as described previously (Ebbers et al., 2015). Briefly, slices were washed three times in PBS before incubation in blocking solution (3% bovine serum albumin, 10% goat serum and 0.3% Triton in PBS) for 1 h at room temperature. The following primary antibodies were applied in carrier solution (1% bovine serum albumin, 1% normal goat serum, and 0.3% Triton X-100 in PBS) and incubated over night at 4°C: anti-Piccolo (guinea pig polyclonal, dilution 1:200; target species: rat, mouse; Cat. no.: 142104; Synaptic Systems), anti-GFP (chicken polyclonal; dilution 1:1000; target species: species independent; Cat. no.: ab13970, Abcam), anti-NeuN (mouse monoclonal, dilution 1:250, target species: avian, chicken, ferret, human, mouse, pig, rat, salamander, Cat. no: mab377, Sigma-Aldrich), anti-vGlut1 (guinea pig polyclonal, dilution 1:1000, target species: rat, Cat. no.: ab5905, Sigma-Aldrich), anti-GluA1 (mouse monoclonal; dilution 1:500; target species: rat, mouse, human; Cat. no.: 182011; Synaptic Systems) and anti-GluA4 (rabbit polyclonal; dilution 1:500; target species: rat, mouse, chicken, human, chimpanzee; Cat. no.: AB1508; Merck). Subsequently, slices were washed in PBS and incubated with appropriate Alexa-coupled secondary antibodies in carrier solution (dilution 1:1000; 1.5 h; room temperature). Slices were again rinsed with PBS and mounted.

Stained brainstem sections were examined by confocal microscopy using a Leica TCS SP8 microscope equipped with a 63× HCX PL APO (1.45 NA) objective. Overview images were acquired on an Olympus BX63 microscope with a 20× UPlanSApo (0.75 NA) objective. Fluorescence signals of EGFP and immunolabeled structures were automatically detected and segmented using trained classifiers in ilastik software (Berg et al., 2019). Quantitative structural 3D analysis, cell counting and colocalization analysis were performed using arivis Vision 4D software (Zeiss).

Preparation of acute brainstem slices

Mice were rapidly decapitated at P20/21. Brains were removed in ice-cold slicing solution containing (in mM): 125 NaCl, 25 $NaHCO_3$, 2.5 KCl, 1.25 NaH_2PO_4, 3 myoinositol, 2 Na-pyruvate, 0.4 ascorbic acid, 0.1 $CaCl_2$, 3 $MgCl_2$ and 25 glucose aerated with carbogen (5% CO_2 in O_2). Brainstem slices of 200 μm thickness were prepared on a vibratome (VT1200S, Leica) and stored in artificial cerebrospinal fluid (ACSF) (in mM: 125 NaCl, 25 $NaHCO_3$, 2.5 KCl, 1.25 NaH_2PO_4, 2 $CaCl_2$, 1 $MgCl_2$ and 25 glucose aerated with carbogen, pH 7.3) at 37°C for 45 min and at room temperature (22 ± 1°C) thereafter.

Electrophysiology

Whole-cell patch-clamp recordings were established from MNTB principal neurons contacted by fluorescently labeled calyces, using an EPC-10/2 amplifier controlled by PatchMaster software (HEKA, Reutlingen, Germany). Recordings were performed in ACSF supplemented with 2 μM strychnine (Sigma Aldrich) using pipettes pulled from thick-walled borosilicate glass (Cat. no.: 1807515, Hilgenberg, Malsfeld, Germany) which had open tip resistances of 2–3 MΩ. The pipette solution contained (in mM): 130 Cs gluconate, 10 CsCl, 10 HEPES, 10 TEA-Cl, 5 Na_2-phosphocreatine, 5 EGTA, 4 Mg-ATP and 0.3 GTP (pH 7.2). The holding potential was −70 mV. Series resistances ranged from 3 to 6 MΩ and were compensated for by > 90%. Currents were digitized at 100 kHz and Bessel-filtered at 2.9 kHz. All experiments were performed at room temperature. Synaptic responses were elicited by bipolar pulses (100 μs, 50 V) applied via a bipolar stimulation pipette (Θ-barrel, open tip diameter ∼3 μm) filled with ACSF that was positioned in the immediate vicinity of the labeled calyx hemi-node. Data were analyzed using custom-written IGOR (Wavemetrics, Lake Oswego, OR, USA) routines.

Correlated light and electron microscopy

Fixed brain slices were prepared as described above. MNTBs containing fluorescently labeled calyces were excised from coronal brainstem sections and stained with DAPI. Confocal image stacks were obtained from both sides of the tissue blocks using a Leica TCS SP8 microscope equipped with a 20× HC PL APO CS2 (0.75 NA) objective and denoised.

Afterward, the tissue blocks were prepared for scanning electron microscopy as described previously (Horstmann et al., 2012). In brief, tissue blocks were incubated in cacodylic acid (100 mM) for 30 min and post-fixed in 1.5% potassium ferricyanide and 2% osmium tetroxide (1 h, on ice). Samples were washed with water, dehydrated in an ascending series of alcohol, incubated in propylene oxide/epoxy (1:1) over night and embedded in epoxy resin (polymerization: 36 h, 60°C). Ribbons of ultrathin sections (40 nm, ∼150 sections/ribbon) were cut through the MNTB on an Ultracut S microtome (Leica) equipped with a diamond knife angled at 45° (Diatome, Biel, Switzerland) and collected on clean, glow discharged silicon wafers (SiMat Silicon Materials, Landsberg, Germany). The sections were exposed to chloroform vapor to neutralize tissue compression due to sectioning, dried and stained using a modified Reynolds-procedure [saturated uranyl acetate (16 min) followed by lead citrate (8 min)]. Scanning electron microscopy was performed using a LEO Gemini 1530 equipped with a field emission gun and an ATLAS scanning generator (Zeiss). Calyces that showed fluorescent labeling in confocal image stacks were identified in EM sections based on their position relative to characteristic groups of nuclei. Electron micrographs of identified synapses were taken at a pixel size of 3.8 nm using the InLens detector at the following settings: 3.6 mm working distance, 30 μm aperture and 2 keV acceleration voltage.

Electron microscopy experiments and analysis were performed in a double-blind manner. AZs and synaptic vesicles (SVs) were manually traced using OpenCAR software (Sätzler et al., 2002). AZs were identified by the presence of an opposing postsynaptic density and of SVs in the vicinity, thereby avoiding confusion with puncta adherentia (Sätzler et al., 2002). The perpendicular distance between individual SVs and the AZ was calculated using OpenCARe (Sätzler et al., 2002).

Statistical analysis

Statistical significance was assigned by unpaired, two-tailed Student's *t*-test or two-way ANOVA followed by Sidak's post-hoc test using Prism 10 software (Graphpad software, La Jolla, CA). Significant differences are marked by asterisks (* = $p < 0.05$, ** = $p < 0.01$, *** = $p < 0.001$). Data are presented as mean ± SEM.

Results

To investigate how the absence of synaptic activity affects the calyx of Held, we used TeNT to abolish synaptic transmission selectively at this synapse. TeNT cleaves the SNARE proteins synaptobrevin 1 and synaptobrevin 2 (a.k.a. VAMP1 and VAMP2, respectively), thereby preventing the formation of the SNARE complex and thus synaptic vesicle (SV) fusion (Link et al., 1992; Humeau et al., 2000). Specific silencing of the calyx was achieved by Cre-dependent TeNT expression in the bushy cells of the VCN of Math5-Cre mice (Yang et al., 2003; Saul et al., 2008). Therefore, AAV particles coding either for EGFP-tagged TeNT or EGFP only were stereotactically injected into the VCN at P6/7. Effectivity of functional silencing of the calyx was assessed at P20/21, after 14 days of TeNT expression, while structural changes were examined at P27/28, 21 days after AAV injection and at least 7 days after the cessation of synaptic transmission. At P28, numerous cells expressing EGFP or TeNT were detected throughout the VCN, in accordance with the distribution of bushy cells (Figure 2; Saul et al., 2008). Moreover, projections of fluorescently labeled TeNT-expressing VCN cells were consistent with those of Math5-expressing spherical bushy cells [ipsilateral lateral superior olive (LSO)] and globular bushy cells (contralateral MNTB) (Figure 2, arrow heads; Saul et al., 2008). We next examined, if transduction of either AAV was more effective and if expression of TeNT led to neuronal cell death. Therefore, we stained neurons in the VCN with the pan-neuronal marker NeuN and determined the total number of neurons in the VCN and the number of neurons expressing either EGFP alone or TeNT (Figures 3A, B). VCNs of mice expressing TeNT contained fewer neurons compared to mice expressing only EGFP (Figure 3C, control: 432 ± 16 cells/VCN, average of 3–4 slices per mouse, 3 mice; TeNT: 256 ± 27 cells/VCN, average of 2–4 slices per mouse, 5 mice, $p = 0.0037$, student's *t*-test). Interestingly, we found higher transduction rates in mice injected with TeNT-encoding AAVs (Figures 3A–C, control: 5% ± 1%, average of 3–4 slices per mouse, 3 mice; TeNT: 16% ± 4%, average of 2–4 slices per mouse, 5 mice, $p = 0.083$, student's *t*-test). Next, we examined if the neuron loss in the VCN also results in a loss of calyces in the contralateral MNTB. Therefore, we labeled calyces with the presynaptic marker vGlut1 and determined the number of calyces per MNTB and the number of NeuN-labeled

cells that were not contacted by a calyx synapse (Figures 3A', B', C). We did not find a reduction in the number of labeled calyces in the MNTB of mice injected with TeNT, as compared to control (control: 298 ± 13 calyces/MNTB, average of 2 slices per mouse, 3 mice; TeNT: 261 ± 33 calyces/MNTB, average of 2 slices per mouse, 5 mice, $p = 0.45$, student's t-test). However, when we counted the number of MNTB neurons that were not contacted by a large, calyx-like vGlut1-expressing synapse, we observed more such neurons in MNTBs of TeNT-expressing mice, although this trend did not reach significance (Figures 3A', B', C; control: 8 ± 3 cells/MNTB, average of 2 slices per mouse, 3 mice; TeNT: 19 ± 5 calyces/MNTB, average of 2 slices per mouse, 5 mice, $p = 0.17$, student's t-test). Of note, we observed multiple calyces that were contacting MNTB principal neurons not labeled by NeuN. We thus conclude that TeNT expression in the VCN results in cell loss in the VCN of TeNT expressing mice, but not in a loss of calyces under our experimental conditions. TeNT thus provides a suitable tool to assess the effects of synaptic silence on the structure of the calyx.

TeNT practically abolishes synaptic transmission at the calyx of Held

Synaptic silencing by TeNT was assessed by recording spontaneous and evoked EPSCs (sEPSCs and eEPSCs, respectively). First, we recorded sEPSCs from MNTB principal neurons contacted by fluorescently labeled TeNT or EGFP-control calyces at P20/21. sEPSC frequency was greatly diminished in MNTB neurons contacted by TeNT-expressing calyces as compared to controls (control: 1.57 ± 0.40 Hz, $n = 15$ calyces from 7 mice, TeNT: 0.23 ± 0.07 Hz, $n = 10$ calyces from 7 mice, $p = 0.013$, student's t-test) (Figures 4A, D). Nevertheless, we still observed some residual sEPSCs in MNTB neurons contacted by TeNT calyces. These sEPSCs were significantly smaller and had a tendency toward slower kinetics than those obtained from MNTB cells contacted by control calyces (amplitude: control: 69 ± 4 pA, $n = 15$ calyces from 7 mice, TeNT: 51 ± 6 pA, $n = 10$ calyces from 7 mice, $p = 0.012$; risetime: control: 149 ± 9 µs, $n = 15$ calyces from 7 mice, TeNT: 179 ± 12 µs, $n = 10$ calyces from 7 mice, $p = 0.05$; decay time constant: control: 0.323 ± 0.012 ms, $n = 15$ calyces from 7 mice, TeNT: 0.351 ± 0.012 ms, $n = 10$ calyces from 7 mice, $p = 0.14$, student's t-tests) (Figure 4). This would be consistent with a non-calyceal origin as described previously (Hamann et al., 2003). However, this previous study has not examined the properties of non-calyceal sEPSCs explicitly. Recordings of evoked non-calyceal EPSCs suggest that the rise time of these inputs is ~3 times slower than that of calyceal EPSCs (rise time extra-calyceal EPSCs: 616 ± 85 µs; Hamann et al., 2003). Since the difference in sEPSC rise time observed here is only a trend and not as pronounced as that previously described for non-calyceal inputs, we cannot exclude that some spontaneous release from the calyx remains in TeNT expressing calyces (see discussion).

Based on the sEPSC recordings, we cannot formally rule out that some neurotransmitter release occurs from the calyx in the presence of TeNT. To demonstrate synaptic silencing of the calyx of Held, we performed a second set of experiments and examined evoked neurotransmitter release in response to direct electrical stimulation. At P20/21, typical calyceal EPSCs in the nA-range with fast kinetics (Borst and Soria van Hoeve, 2012) were recorded from 8 out of 8 control calyces, but none of the 10 TeNT-expressing ones (EPSC amplitude: control: 6.45 ± 1.0 nA, $n = 8$ calyces from 7 mice, TeNT: 0.11 ± 0.02 nA, $n = 10$ calyces from 9 mice, $p < 0.0001$, student's t-test) (Figure 5). Occasionally observed small inward currents had waveforms that did not resemble EPSCs and may be artifacts of the close-by stimulation (Figure 5A, inset). Although TeNT-expressing calyces did not show typical EPSCs in response to a single electric stimulus, high frequency stimulation, which resembles the physiological activity pattern during sound perception (Kopp-Scheinpflug et al., 2008), could result in a build-up of presynaptic calcium which in turn could lead to fusion of more release-reluctant SVs. We therefore applied 100 Hz stimulus trains (50 stimuli) to calyces expressing either TeNT or EGFP and recorded the postsynaptic EPSCs at P20/21. Train-elicited EPSC from MNTB principal cells contacted by control calyces showed typical short-term depression (STD) with steady state EPSCs that were still in the nA-range (Figure 5C, $n = 10$ calyces from 6 mice). Application of 100 Hz stimulus trains to TeNT-expressing calyces did not result in detectable EPSCs (Figure 5C, $n = 8$ calyces from 4 mice). Finally, we investigated whether TeNT expression also abolished asynchronous release. Therefore, we determined the number of miniature-like EPSCs in the 100 ms after the ending of the 100 Hz stimulus trains. Control synapses showed variable degrees of asynchronous release while it was virtually absent from TeNT-expressing calyces (Figure 5C inset and Figure 5D, # of miniature-like events: control: 11.2 ± 3.4 events, $n = 10$ calyces from 6 mice, TeNT: 0.4 ± 0.2 events, $n = 8$ calyces from 4 mice, $p = 0.012$, student's t-test). MNTB principal neurons contacted by TeNT-expressing synapses occasionally showed a single miniature-like event during these 100 ms. However, this could also represent spontaneous release from non-calyceal inputs to the MNTB principal cell (see discussion). The lack of evoked as well as asynchronous neurotransmitter release from the calyx thus confirms its silence and thereby the effectiveness of TeNT after 14 days of expression.

Prolonged synaptic silence induces only minor changes in synapse morphology

Having established synaptic silence at the calyx of Held after 14 days of TeNT expression, we next examined whether prolonged absence of synaptic transmission causes structural changes or degradation of the calyx. Therefore, we performed confocal imaging of TeNT and control (EGFP only) calyces that were immunolabelled for the AZ marker Piccolo (Gundelfinger et al., 2016) at P27/28, after at least 7 days of synaptic silence. Calyces were 3D reconstructed based on the EGFP signal. We did not observe grossly changed calyces even after 21 days of TeNT expression. However, TeNT calyces showed a slight increase in synaptic volume as compared to controls (control: 816 ± 40 μm^3, $n = 36$ calyces from 3 mice, TeNT: 1030 ± 78 μm^3, $n = 30$ calyces from 3 mice; $p = 0.013$, student's t-test) while the surface of the calyx remained constant (control: 2847 ± 122 μm^2, $n = 36$ calyces from 3 mice, TeNT: 3103 ± 267 μm^2, $n = 30$ calyces from 3 mice; $p = 0.36$, student's t-test). This resulted in a thickening of

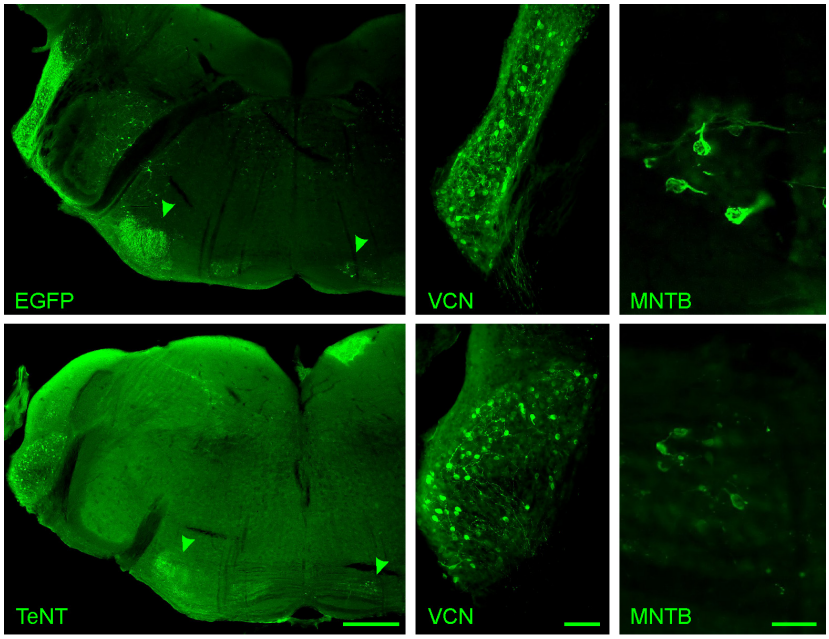


FIGURE 2
Tetanus toxin is expressed in bushy cells of the VCN. Cre-dependent expression of EGFP-tagged TeNT and EGFP control in the auditory brainstem of a Math5-Cre mouse are visualized at P28 by EGFP fluorescence. Top row: EGFP control, bottom row: EGFP-tagged TeNT. Left: overview of the auditory brainstem including the VCN and the superior olivary complex. Green arrowheads indicate the projection areas of spherical and globular bushy cells, the ipsilateral LSO and the contralateral MNTB, respectively. Middle: Close-up of the VCN showing fluorescent, tagged TeNT- or EGFP-expressing cells. The pattern of fluorescently labeled cells is consistent with Math5-expressing bushy cells (Saul et al., 2008). Right: Close-up of the contralateral MNTB showing calyces expressing either tagged TeNT or EGFP only. Scale bars are 500 μm (left) and 100 μm (middle, right).

the calyx of Held, as indicated by the decrease in surface/volume-ratio (control: 3.6 ± 0.12 μm^{-1}, n = 36 calyces from 3 mice, TeNT: 3.09 ± 0.16 μm^{-1}, n = 30 calyces from 3 mice; p = 0.01, student's t-test) (Figures 6A–C). These minor changes in synaptic morphology were not accompanied by a change in AZ number as the number of Piccolo-labeled immunoreactive clusters remained constant (control: 368 ± 33 clusters/calyx, n = 36 calyces from 3 mice, TeNT: 315 ± 28 clusters/calyx, n = 30 calyces from 3 mice; p = 0.24, student's t-test) (Figure 6D). Our results thus indicate that the morphology of the calyx of Held as well as the number of AZs are largely independent of synaptic activity.

The AMPA receptor composition at the calyx of Held synapse is independent of synaptic activity

The lack of major morphological changes at the calyx prompted us to examine if the absence of synaptic activity leads to alterations on the postsynaptic side of the synapse. Therefore, we investigated the composition of the postsynaptic AMPA receptors by staining for the subunits GluA1 and GluA4 in TeNT and control synapses. GluA4 is highly expressed at the mature calyx of Held (Yang et al., 2011), while the juvenile synapses also possess GluA1 receptors (Borst and Soria van Hoeve, 2012). Synaptic localization of GluA clusters was determined by partial overlap of immunoreactive signals for the GluA subunit and Piccolo. We did not observe differences in the number or size of synaptic GluA4 clusters in TeNT and control synapses (number: control: 83 ± 11 clusters/calyx, n = 17 calyces from 3 mice, TeNT: 69 ± 11 clusters/calyx, n = 15 calyces from 3 mice, p = 0.36, student's t-test; size: control: 184 ± 28 μm^2, n = 17 calyces from 3 mice, TeNT: 178 ± 32 μm^2, n = 15 calyces from 3 mice, p = 0.89, student's t-test) (Figures 7B, C). Likewise, synaptic AMPA receptor clusters containing the juvenile subunit GluA1 in MNTB neurons contacted by TeNT-expressing calyces remained constant in number and size compared to control synapses. Notably, GluA1 clusters in TeNT synapses tended to be bigger than those in control ones, although this trend did not reach significance (number: control: 48 ± 9 clusters/calyx, n = 18 calyces from 3 mice, TeNT: 64 ± 11 clusters/calyx, n = 15 calyces from 3 mice, p = 0.27, student's t-test; size: control: 104 ± 21 μm^2, n = 18 calyces from 3 mice, TeNT: 181 ± 38 μm^2, n = 15 calyces from 3 mice, p = 0.07, student's t-test) (Figures 7A, C). The lack of synaptic transmission thus did not result in a pronounced compensatory incorporation of the juvenile GluA1 subunit into the calyx of Held synapse.

TeNT expression leads to a loss of SVs close to the AZ without affecting AZ length

Although our results so far suggest that the structure of the calyx is largely independent of synaptic transmission, we next examined the ultrastructure of AZ in calyces expressing TeNT. Therefore, we performed corelative light and electron microscopy (CLEM) of identified TeNT and control calyces.

10.3389/fncel.2024.1404206

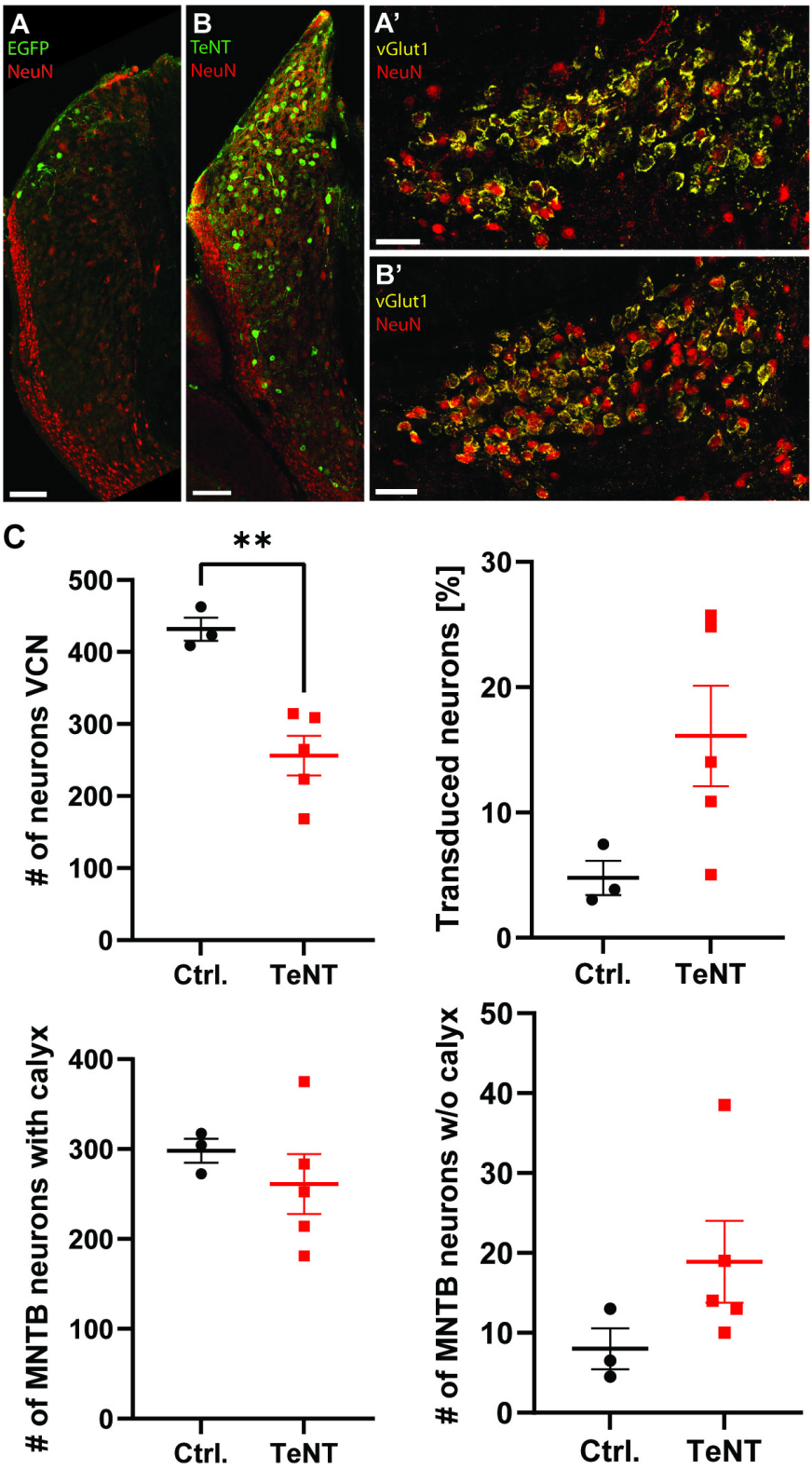


FIGURE 3
Tetanus toxin expression leads to a reduction in bushy cell number in the VCN without affecting calyx numbers in the VCN. **(A,B)** Representative images of the VCN of Math5-Cre mice expressing either EGFP or TeNT stained for the pan-neuronal marker NeuN. **(A',B')** Representative images of the MNTB of Math5-Cre mice expressing either EGFP **(A')** or TeNT **(B')** stained for the pan-neuronal marker NeuN and the calyceal marker vGlut1. Images represent maximal projections of confocal stacks spanning 20 μm in depth. **(C)** Quantification of the number of neurons in the VCN, the transduction efficiency of both AAV constructs, the number of calyces in the contralateral MNTB and the number of MNTB neurons not contacted by a vGlut1-labeled calyx. (n = 2–5 slices per animal, 3–5 mice, student's t-test). $^{**}p < 0.01$.

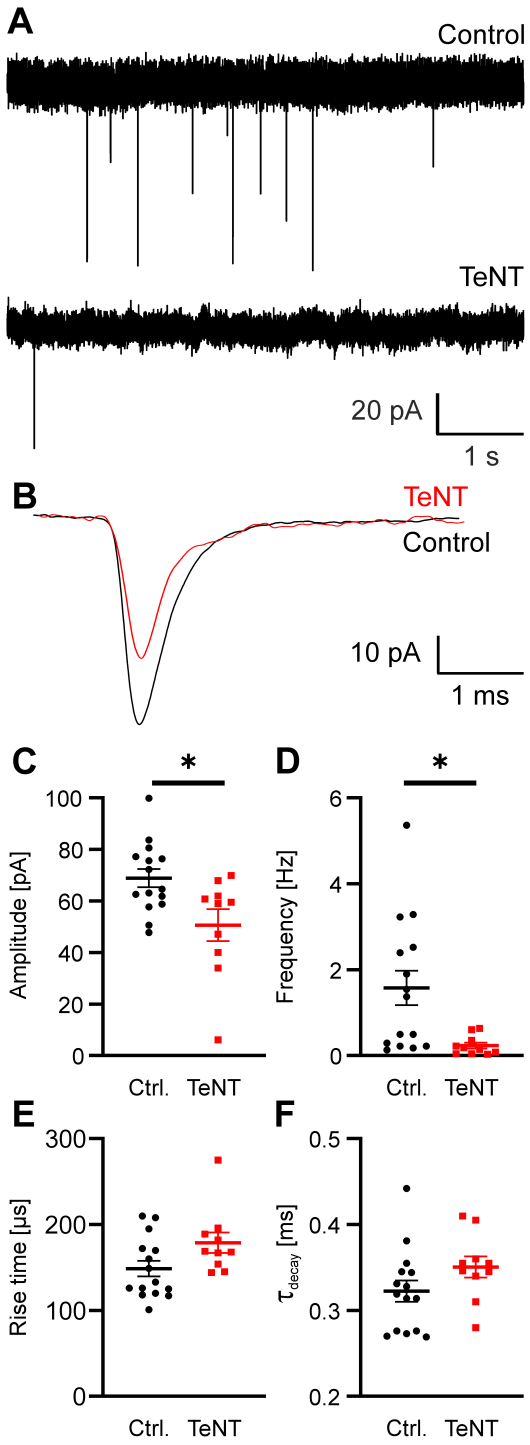


FIGURE 4
Expression of TeNT impairs spontaneous neurotransmitter release at the calyx of Held. **(A)** Representative sample current traces obtained from MNTB neurons at P21 show a drastic reduction in sEPSC frequency. **(B)** Overlay of averaged sEPSCs obtained from the same cells as in **(A)**. **(C–F)** Quantification of sEPSC properties (amplitude, frequency, rise time and decay time constant, n = 10–15, student's t-test). * = $p < 0.05$.

In line with results presented above, we did not observe alterations in the gross morphology of TeNT-expressing calyces, as indicated by the number of calyx stalks (control: 12.4 ± 0.8 stalks/calyx, n = 14 calyces from 3 mice, TeNT: 11.7 ± 1.3 stalks/calyx, n = 10 calyces from 3 mice; p = 0.65, student's t-test, Figure 8E). Analysis of the ultrastructure of AZs showed no difference in AZ length after TeNT expression (control: 273 ± 21 nm, n = 14 calyces from 3 mice, TeNT: 281 ± 11 nm, n = 10 calyces from 3 mice, p = 0.78, student's t-test) (Figures 8A, C), but a greatly reduced number of SVs (Figures 8A, B). Consistent with our electrophysiological results, the AZs of TeNT calyces showed a prominent loss of the membrane-proximal SVs (0–20 nm from plasma membrane: control: 0.21 ± 0.08 SVs/100 nm AZ, n = 14 calyces from 3 mice, TeNT: 0.05 ± 0.01 SVs/100 nm AZ, n = 11 calyces from 3 mice, p = 0.026, two way ANOVA followed by Sidak's post-hoc test) (Figures 8A, B), which constitute the ready-releasable pool of SVs (Imig et al., 2014). Additionally, we found a significant increase in the diameter of SVs in TeNT calyces (control: 25 ± 2 nm, n = 14 calyces from 3 mice, TeNT: 40 ± 3 nm, n = 10 calyces from 3 mice, p = 0.0002, student's t-test) (Figure 8D), which may be caused by a higher fraction of slightly bigger SV-like endocytic compartments (Heuser and Reese, 1973) in the potential SVs analyzed. Another surprising finding of our EM analysis was a general reduction in the number of SVs within a distance of ~100 nm from the presynaptic plasma membrane in TeNT-expressing calyces (Figure 8B). This could either be caused by defects in local SV recycling or by a reduction in the cells ability to supply new SVs to the synapse and thus an excess in SV degradation (see Discussion).

Discussion

In the present study, we demonstrate that even prolonged absence of synaptic transmission has only minor effects on the morphology and AMPA receptor composition of the calyx of Held synapse. The silencing of the calyx did not interfere with the maintenance and maturation of the calyx, since fenestration, a hallmark of structural maturation, apparently occurred/proceeded regularly in TeNT synapses. Thus, the structural integrity of this specialized high frequency, high-fidelity synapse is largely independent of synaptic activity.

TeNT expression efficiently prevents neurotransmitter release without affecting calyx survival

Prolonged expression of TeNT in bushy cells resulted in a decrease in neuronal number in the VCN. However, this loss in neurons was not accompanied by a reduction in the number of calyces in the contralateral MNTB, suggesting that the reduction in the number of VCN neurons could be due to a loss of spherical but not globular bushy cells. Spherical bushy cells (SBCs) also express Math5 and therefore Cre-recombinase in the mouse line used. It could be that, for an unknown reason, SBCs are more sensitive to TeNT expression than GBCs and prolonged TeNT expression therefore leads to a loss of SBCs. The viability of GBCs in turn seems to be unaffected by TeNT expression, as we did not observe a reduction in calyx numbers in the contralateral MNTB, even after 21 days of TeNT expression. This apparent lack of effect

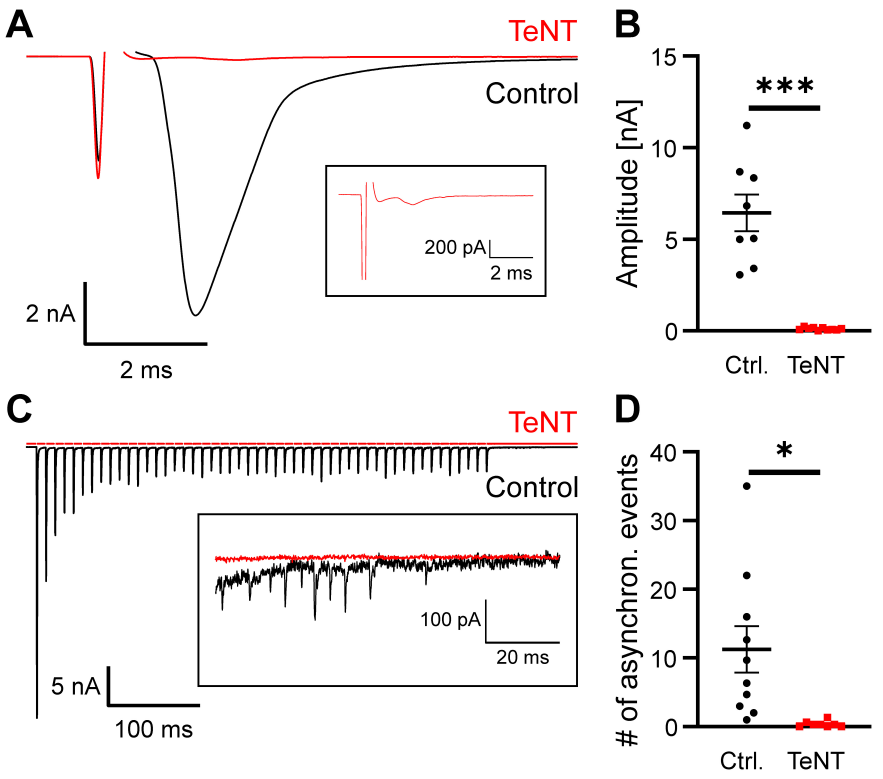


FIGURE 5
Expression of TeNT abolishes evoked neurotransmitter release at the calyx of Held. **(A)** Representative sample current traces obtained from MNTB neurons at P21 demonstrating the absence of calyceal EPSC in response to direct electrical stimulation of a TeNT-expressing axon. Inset: Detail of the recording from the TeNT-expressing calyx. **(B)** Quantification of evoked EPSC amplitude (n = 8–10, student's t-test). **(C)** Representative sample current traces obtained from MNTB neurons at P20/21 in response to trains of 50 electrical stimuli at 100 Hz delivered directly to TeNT- or EGFP-expressing axons. Inset: Detail of the 100 ms after the cessation of the stimulus trains of the recordings shown at higher scale. **(D)** Quantification of the number of miniature-like, asynchronous events in the 100 ms after the cessation of a 100 Hz stimulus train (n = 8–10, student's t-test). * = $p < 0.05$, *** = $p < 0.001$.

of TeNT on GBC survival is in accordance with previous results from neuronal cultures and hippocampal CA1 neurons which are resistant to TeNT expression, too (Santos et al., 2017; Hoogstraaten et al., 2020; Adaikkan et al., 2024). In the MNTB, we did observe a number of NeuN-labeled neurons that were not contacted by vGlut1-labeled calyces. Although the number of these calyx-less MNTB neurons is higher in TeNT expressing mice, the effect did not reach significance and the number is far lower than the 30–40% of cells that have been reported previously (Jackson, 2020). The discrepancy to the previous study could be due to the reference (NeuN vs. MAP2), virus system (AAV vs. helper-dependent adenovirus) or, most likely, the day of virus injection (P6/7 vs. P0). Expression of TeNT from P0 will likely interfere with the expansion of the calyx from a bouton type synapse to the juvenile, cup-shaped terminal (Hoffpauir et al., 2006, Holcomb et al., 2013) while TeNT expression under our experimental conditions only becomes effective at a much later stage. In accordance with this assumption, expression of TeNT from P0 results in a large number of abnormally formed calyces (Jackson, 2020), which we did not observe under our experimental conditions. Of note, we also observed vGlut1-labeled calyceal structures that contacted MNTB neurons devoid of NeuN signal, which is probably due to an insufficient NeuN labeling by the primary antibody and occurs independent of the construct expressed in the bushy cells. Taken together, under our experimental conditions, we observe neuronal TeNT-dependent cell death in the VCN that is not accompanied by a loss of calyces in the contralateral MNTB, suggesting that GBCs are rather insensitive to TeNT-expression. However, we cannot formally exclude that a minor fraction of calyces is indeed lost upon prolonged TeNT expression. Nevertheless, our conclusions on the remaining calyces remain unaffected by this potential loss of a few calyces.

TeNT affects synaptic transmission within minutes, when directly applied to the presynapse via a patch pipette at high concentrations (Sakaba et al., 2005). However, prolonged expression is required under our experimental conditions due to the comparatively slow build-up of efficient TeNT concentrations at the synapse, the sheer amounts of VAMP2 copies that needed to be cleaved at the calyx (~70 copies/SV, ~70,000 SVs/calyx, Takamori et al., 2006; Sätzler et al., 2002, respectively) and the need to accumulate sufficient amounts of fluorescently labeled TeNT to be detected in acute slices. Effective synaptobrevin cleavage by TeNT after 14 days of *in vivo* incubation was shown by electrophysiology. TeNT expression drastically reduced the frequency of sEPSCs in MNTB principal neurons. However, we still detected some remaining sEPSCs in MNTB cells contacted by TeNT expressing calyces. These sEPSCs can either represent spontaneous release from non-calyceal inputs, or they originate

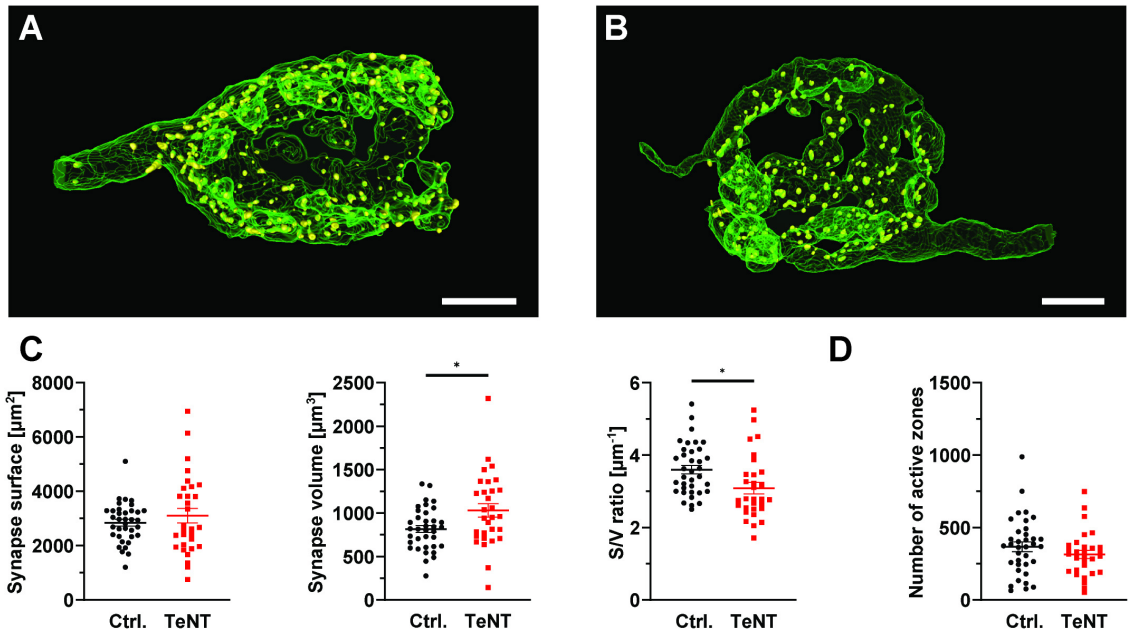


FIGURE 6
Prolonged expression of TeNT in the calyx of Held has minor impact on synapse morphology. **(A,B)** Representative 3D reconstructions of control **(A)** and TeNT-expressing **(B)** calyces, obtained from confocal image stacks using the fluorescent signal of EGFP-labeled TeNT or cytosolic EGFP (control) at P28. Yellow structures represent AZs identified by immunostainings against Piccolo. **(C)** Quantification of synapse morphology (synapse surface, synapse volume, surface-to-volume ratio, n = 30–36, student's t-test). **(D)** Quantification AZ numbers at P27/28 (n = 30–36, student's t-test). *$p < 0.05$; Scale bars in **(A,B)**: 5 µm.

from the calyx, despite TeNT expression. Excitatory inputs to MNTB neurons independent of the calyx of Held have been demonstrated both structurally and functionally (Holcomb et al., 2013; Hamann et al., 2003, respectively). Evoked EPSCs from these inputs have been shown to be smaller in amplitude and about three times slower in rise time than calyceal evoked EPSCs (Hamann et al., 2003). The properties of spontaneous EPSCs from those inputs are not known but it can be assumed that their rise time is somewhat slower than that of calyceal sEPSCs, too. Although we found a tendency toward such a slowing (Figures 4B, E) this trend did reach significance, suggesting that non-calyceal inputs may represent a higher portion of sEPSCs in MNTB neurons contacted by TeNT-expressing calyces as compared to controls. The origin of the non-calyceal inputs is unknown, but it is highly unlikely that they originate from the contralateral VCN (Kandler and Friauf, 1993; Borst and Soria van Hoeve, 2012) or express Math5 (Saul et al., 2008). Therefore, neurotransmitter release from these terminals is not affected in our experimental paradigm. Alternatively, the remaining sEPSCs could still originate from the calyx of Held, despite the expression of TeNT, in line with the knock-out of VAMP2 not abolishing synaptic release completely (Schoch et al., 2001, Deák et al., 2004). However, the knock-out of VAMP2 leads to the upregulation of VAMP1, resulting in a partial functional compensation (Imig et al., 2014). Under our experimental conditions, an upregulation of VAMP1 is unlikely to account for the remaining sEPSCs, as TeNT also cleaves VAMP1 in mice (Humeau et al., 2000). Nevertheless, sEPSC could be mediated by other v-SNAREs such as VAMP4, VAMP7 and Vti1a that are insensitive to TeNT and could thus compensate for the loss of VAMP1 and VAMP2. Spontaneous SV release depending on one of these v-SNAREs has not yet been reported at the calyx of Held, but in various other synapses including the neuromuscular junction and bouton-type synapses in hippocampal cultured neurons (Hua et al., 2011; Raingo et al., 2012; Ramirez et al., 2012; Bal et al., 2013; Liu et al., 2019). It is thus conceivable that the remaining sEPSCs recorded in MNTB neurons contacted by TeNT-expressing calyces represent a mixture of non-calyceal inputs and calyceal sEPSCs mediated by TeNT-insensitive v-SNAREs.

Despite some residual sEPSCs recorded in MNTB neurons contacted by TeNT-expressing calyces, we are confident that neurotransmitter release from the calyx is indeed virtually abolished by TeNT for two reasons. First, we were unable to electrically induce synchronous or asynchronous neurotransmitter release from TeNT calyces, not even by trains of high frequency stimulation, although this was possible in all WT synapses tested. Second, our EM results show a close to complete lack of SVs in close proximity to the AZ in TeNT-expressing calyces. Since these membrane-near SVs constitute the ready releasable pool (Imig et al., 2014), we conclude, in accordance with our electrophysiological results, that TeNT-expressing calyces are basically devoid of release-ready SVs and thus - most likely - practically silent. Of note, we still observed rather small, slow inward currents in some of the TeNT-expressing calyces (e.g., Figure 5A inset). Such a slow SV release that is apparently insensitive to acutely applied TeNT has been described at the neuromuscular junction and calyx of Held (Dreyer and Schmitt, 1983; Bevan and Wendon, 1984; Sakaba et al., 2005). At the calyx of Held, upon acute application of TeNT via a patch pipette a slow component of SV release has been shown to persist for 9 min in response to prolonged presynaptic depolarization

10.3389/fncel.2024.1404206

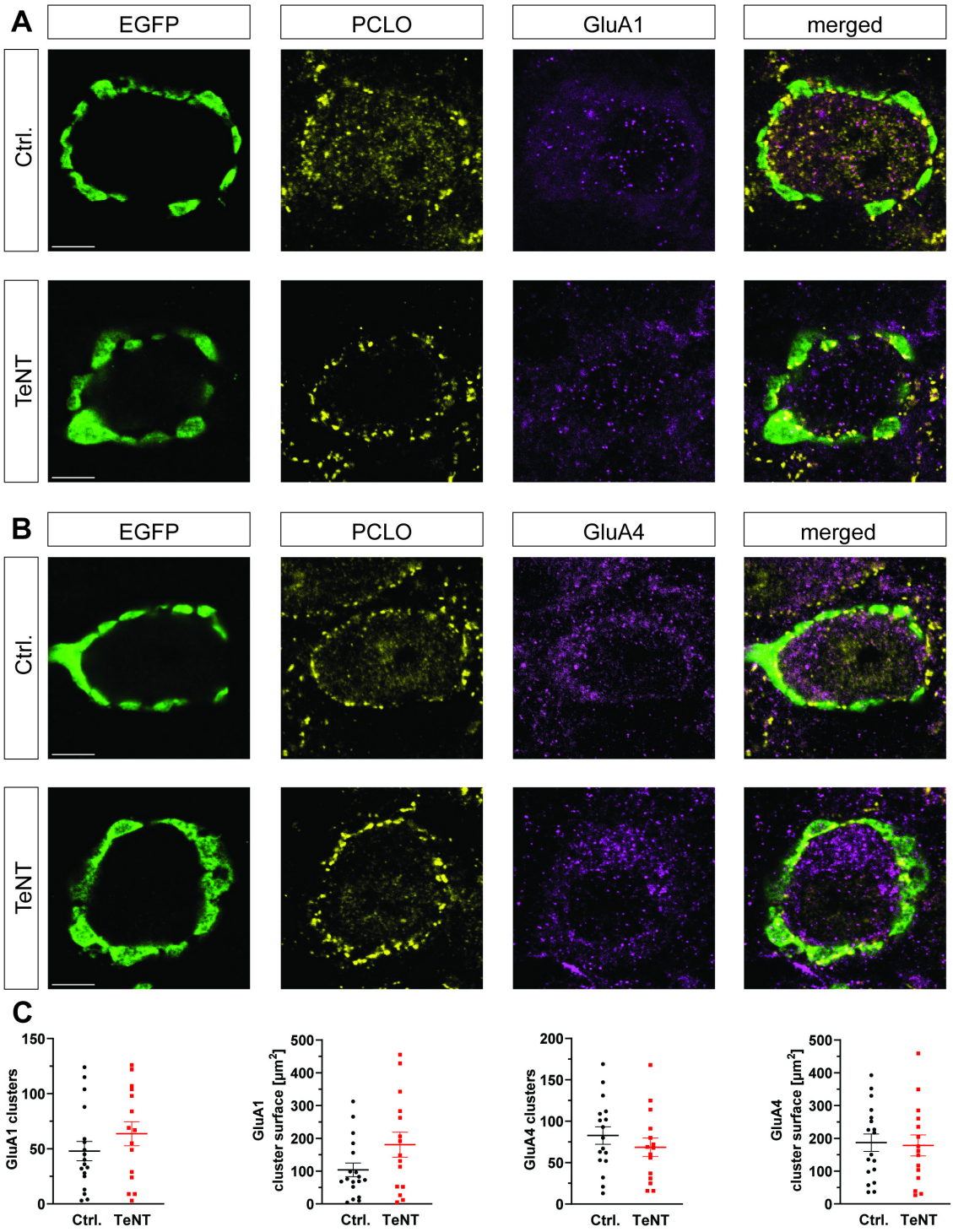


FIGURE 7
TeNT expression does not change postsynaptic AMPA receptor composition. **(A,B)** Representative confocal images (single plane) of calyces expressing TeNT or EGFP stained for Piccolo and either GluA1 **(A)** or GluA4 **(B)** at P28. The immunoreactive signal inside the MNTB principal neurons represents ongoing protein synthesis/processing. It is not used for quantification. **(C)** Quantification of number and size of synaptically localized GluA clusters (n = 15–18, student's t-test). Scale bars: 5 µm.

(Sakaba et al., 2005). The slow inward currents obtained here may thus represent a slow component release employing TeNT-insensitive SVs which would involve an alternative v-SNARE protein (see above), although they have not been implicated in evoked SV release, yet. However, it also seems rather unlikely that the slow inward current is carried by SVs that rely on VAMP1 or 2, for two reasons: first, the published acute TeNT application is limited to minutes, 9 min in the case of the calyx, while we express TeNT for 14 days prior to recordings. It seems unlikely that a fraction of VAMP1 or 2 molecules is guarded

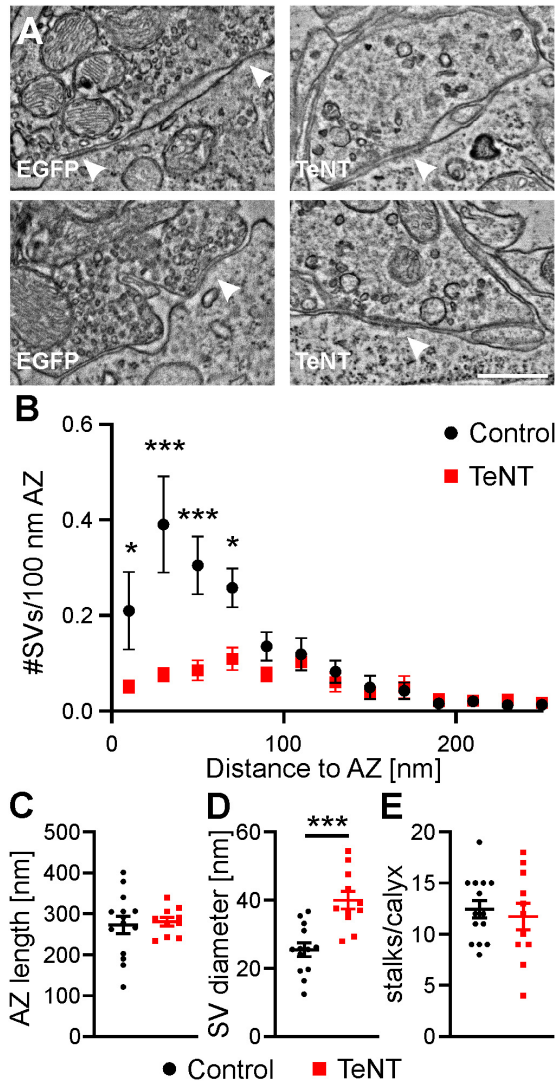


FIGURE 8
TeNT expression depletes membrane proximal SVs but does not change AZ length. **(A)** Representative electron micrographs of AZs from control and TeNT-expressing calyces, as identified by CLEM. Arrow heads indicate AZs. **(B)** Distribution of SV to AZ distances at AZs from control and TeNT-expressing calyces (n = 10–14 calyces, two-way ANOVA followed by Sidak's post-hoc test). **(C–E)** Quantification of AZ length, SV diameter and the number of stalks per calyx (n = 10–14 calyces, student's t-test). Scale bar in **(A)**: 500 nm. * = $p < 0.05$; *** = $p < 0.001$.

from TeNT by an assembled SNARE complex for such extended periods. Second, prolonged presynaptic depolarizations result in far higher presynaptic calcium concentrations than those induced by trains of action potentials, which did not result in synchronous or asynchronous SV release in TeNT-expressing calyces (Figures 5C, D). Prolonged depolarization thus induces the release of SVs that are not available upon action potential-induced SV fusion and more release reluctant, although they possess an at least partially assembled SNARE complex (Sakaba, 2006).

Interestingly, we not only observed a marked decrease in SVs in the immediate vicinity of the presynaptic plasma membrane, but in AZ-associated SVs in general. The numbers of SVs were reduced for ~100 nm into the presynaptic volume. This could be due to two reasons: a deficiency in local SV recycling or the impairment of SV supply from the soma. VAMP2 has been reported to be involved in synaptic endocytosis at the calyx of Held and hippocampal synapses (Xu et al., 2013; Zhang et al., 2013, respectively). However, newly supplied SVs are of course equipped with VAMP2, too. Since TeNT is not specifically localized to the calyx, but broadly expressed throughout the bushy cell soma, it is conceivable that the entire VAMP2 content of the newly generated SVs is cleaved before the arrival at the calyx, therefore not functional, and thus marked for degradation. We consider the former case more likely for two reasons: first, we should have observed an accumulation of newly supplied, release-incompetent SVs associated with the AZ, which we did not. Second, we observed an increase in synapse volume in TeNT-expressing calyces (Figure 6), which could indicate an impairment in membrane handling in these synapses, although the synaptic surface area was unchanged. The clarification of the exact mechanism causing the observed decrease in SV number provides an interesting topic for future studies.

Synaptic silence does not affect synapse maturation or the survival of MNTB neurons

Silencing of synaptic transmission by abolishing neurotransmitter release has been achieved by a number of genetic manipulations, including the knock-out of essential presynaptic proteins, without precluding synaptogenesis (Verhage et al., 2000; Varoqueaux et al., 2002; Deák et al., 2004). Formation of the calyx of Held occurs before E17 as a bouton-shaped contact (Marrs and Spirou, 2012) that expands to its juvenile, cup-shaped form between P4 and P6, concomitant with the establishment of a one-to-one connectivity (Hoffpauir et al., 2006; Holcomb et al., 2013). The mature, fenestrated shape of the calyx is reached by P14-16, shortly after the onset of hearing (Kandler and Friauf, 1993; Ford et al., 2009, Borst and Soria van Hoeve, 2012). We only injected the TeNT-encoding AAVs at P6/7, at a time when the calyx has reached the juvenile stage. Our experimental conditions thus do not interfere with initial synapse formation, synapse expansion and synaptic pruning. However, TeNT was already expressed at the start of fenestration, although only for ~4 days. Since this expression time is short, and TeNT may not have reached effective concentrations, yet, it is difficult to draw conclusions on whether the start of the fenestration process depends on synaptic activity. Nevertheless, fenestration is only close to complete by P14, 8 days after the start of TeNT expression. At this time, it is likely that a considerable amount of TeNT is present at the synapse and it is thus tempting to speculate that fenestration proceeds even under conditions of reduced or abolished neurotransmitter release. This is surprising because fenestration has been suggested to assist in efficient glutamate clearance from the synaptic cleft (Renden et al., 2005) and thus represent a morphological adjustment necessary to sustain the high frequency synaptic activity of the mature calyx (Crins et al., 2011; Sonntag et al., 2011). Notably, unspecific silencing of the calyx by unilateral denervation even resulted in a more complex fenestration of the calyx (Grande et al., 2014), while reducing synaptic activity by ear occlusion leads to smaller endbulbs of Held in the VCN (Zhuang et al., 2017;

Wong and Xu-Friedman, 2022). In the present study, we did not observe differences in synapse size or complexity. This apparent discrepancy may be due to the broad impairment of the auditory system by denervation and the fact that synapses are still capable of adjusting neurotransmitter release under both of these experimental conditions.

The lack of neurotransmitter release from inner hair cells in mice lacking the L-type channel $Ca_v1.3$ has been shown to result in pronounced cell death throughout the auditory brainstem (Hirtz et al., 2011; Satheesh et al., 2012). However, although $Ca_v1.3$ is highly expressed in auditory brainstem neurons, the lack of it does not abolish neurotransmitter release, but changes action potential properties (Hirtz et al., 2011). Therefore, we consider it likely that the observed loss of neurons in $Ca_v1.3$ knock-out mice is not due to the lack of neurotransmitter release, but rather impaired calcium signaling pathways at the soma. Under our experimental conditions, we neither observed a loss of calyces from the MNTB, nor a decrease in MNTB principal neurons. This allowed us to specifically examine the maintenance of the calyx of Held in the absence of calyceal neurotransmitter release.

Synaptic maintenance of the calyx of Held is largely independent of neurotransmitter release

TeNT expression has been performed in various regions of the central nervous system with variable results, ranging from the failure to establish specific synaptic connections (Kerschensteiner et al., 2009) via defects in synaptic refinement and pruning (Yu et al., 2004; Wang et al., 2007; Lopez et al., 2012) to the loss of a fraction of synapses with no further impact on the remaining ones (Sando et al., 2017; Sigler et al., 2017; Quinn et al., 2019). Under our experimental conditions, we do not interfere with synaptic formation, refinement or pruning, since these events take place before TeNT reaches an effective concentration at the calyx (see above). However, we found only a minor morphological adaptation of the mature calyx of Held to the absence of synaptic activity with a thickening of the calyx being the sole significant effect. Interestingly, we did not observe a reduction in AZ number that would resemble the loss of synapses reported after silencing of the forebrain or neuronal cultures (Sando et al., 2017; Sigler et al., 2017; Quinn et al., 2019). This may be explained by the finding that TeNT expression mainly interferes with the formation of synapses in cultured neurons (Quinn et al., 2019), a process that is probably completed before TeNT expression becomes effective in our study (Borst and Soria van Hoeve, 2012). Additionally, and perhaps even more surprisingly, we neither observed a significant difference in the number or size of postsynaptic AMPA receptor clusters nor in their subtypes in silent synapses. MNTB neurons contacted by TeNT-expressing, silent calyces only tended to incorporate more of the juvenile GluA1 subunit into their synapses, which is particularly surprising, since the mature calyx of Held reaches synaptic transmission rates of up to ~350 Hz during sound perception (Kopp-Scheinpflug et al., 2008) and its silencing thus induces a particularly drastic decrease in synaptic activity. Further experiments will be needed to investigate if the high frequency auditory brainstem synapses are generally maintained during synaptic silence or if this applies only to the calyx and possibly other giant synapses.

Limitations

Although the data presented here imply that the expression of TeNT and the resulting absence of synaptic transmission does not result in the degradation of the calyx of Held but has only minor effects on synapse morphology, our study has certain limitations. Most importantly, we still recorded some few sEPSCs at the MNTB principal cell after 14 days of TeNT expression that are of unknown origin but can result from calyceal SV release mediated by TeNT-insensitive v-SNAREs (see above). We can also not formally exclude that the remaining sEPSCs are due to a misalignment of the pre- and postsynaptic compartments. SV fusion outside the AZ would result in prolonged diffusion times till the glutamate reaches the receptors and thus slower rise times (see Budisantoso et al., 2013 for details on glutamate diffusion kinetics). However, neither our immunohistochemical data nor our ultrastructural analysis show evidence for a misalignment of the synaptic compartments. A technical limitation of our study is the direct stimulation of TeNT-expressing axons giving rise to the calyx of Held in the terminal's immediate vicinity. We cannot guarantee that TeNT-expression does not hamper the efficient invasion of the AP into the calyx, although we are not aware of any reports or mechanisms that would suggest such an effect of TeNT. Additionally, our study does not determine the exact timepoint at which the calyx is silent. The determination of this is hampered by the fact that we require approximately 10 days of expression to accumulate enough fluorescent protein at the calyx to identify transduced synapses, under our experimental conditions (Vasileva et al., 2012; Körber et al., 2015).

Conclusion

Taken together, our results show that synaptic activity of the calyx of Held is dispensable for maintenance and supposedly also for the later stages of synaptic maturation. The calyx may thus be regarded essential for the system and therefore maintained independent of synaptic activity. Interestingly, we did not even observe changes in the number of AZs or in the postsynaptic AMPA receptor composition. The functional importance of the calyx in the sound source localization circuit is evident by its specialized morphology and the presence of several hundreds of AZs (Joris and Trussell, 2018). It thus seems that the brain maintains such a central relay station in an activity-independent, hardwired and probably genetically encoded manner. Future studies, using a more broadly, systemic expression of TeNT in the auditory brainstem, may provide further insights into the mechanisms of synaptic maintenance in the absence of synaptic transmission in this high frequency signaling brain area.

Data availability statement

The raw data supporting the conclusions of this article will be made available by the authors, without undue reservation.

Ethics statement

The animal study was approved by the Regierungspräsidium Karlsruhe Abteilung 3. The study was conducted in accordance with the local legislation and institutional requirements.

Author contributions

SL: Formal analysis, Investigation, Visualization, Writing – original draft, Writing – review and editing. LE: Formal analysis, Investigation, Visualization, Writing – original draft, Writing – review and editing. YD: Investigation, Writing – review and editing. SH: Investigation, Writing – review and editing. MK: Methodology, Resources, Writing – review and editing. HGN: Conceptualization, Funding acquisition, Supervision, Writing – original draft, Writing – review and editing. CK: Conceptualization, Formal analysis, Funding acquisition, Investigation, Supervision, Visualization, Writing – original draft, Writing – review and editing.

Funding

This work was supported by the DFG via NO428/7-1 to HGN and SPP 1608 to CK. The publication of this article was supported by the DFG and Heidelberg University within the "Open Access Publishing" funding program.

Acknowledgments

We are grateful to Marion Schmitt, Franziska Gleiche, Annette Herold, and Martina Reents for excellent technical support, Heinz Horstmann for help with electron microscopy, Dr. Carlo Beretta for help with immunohistochemistry analysis, and Dr. Gan for providing the Math5-Cre mouse line.

Conflict of interest

The authors declare that the research was conducted in the absence of any commercial or financial relationships that could be construed as a potential conflict of interest.

The authors declared that they were an editorial board member of Frontiers, at the time of submission. This had no impact on the peer review process and the final decision.

Publisher's note

All claims expressed in this article are solely those of the authors and do not necessarily represent those of their affiliated organizations, or those of the publisher, the editors and the reviewers. Any product that may be evaluated in this article, or claim that may be made by its manufacturer, is not guaranteed or endorsed by the publisher.

References

Adaikkan, C., Joseph, J., Foustoukos, G., Wang, J., Polygalov, D., Boehringer, R., et al. (2024). Silencing CA1 pyramidal cells output reveals the role of feedback inhibition in hippocampal oscillations. *Nat. Commun.* 15:2190. doi: 10.1038/s41467-024-46478-3

Babola, T. A., Li, S., Gribizis, A., Lee, B. J., Issa, J. B., Wang, H. C., et al. (2018). Homeostatic control of spontaneous activity in the developing auditory system. *Neuron* 99, 511–524.

Bal, M., Leitz, J., Reese, A. L., Ramirez, D. M., Durakoglugil, M., Herz, J., et al. (2013). Reelin mobilizes a VAMP7-dependent synaptic vesicle pool and selectively augments spontaneous neurotransmission. *Neuron* 80, 936–946. doi: 10.1016/j.neuron.2013.08.024

Berg, S., Kutra, D., Kroeger, T., Straehle, C. N., Kausler, B. X., Haubold, C., et al. (2019). ilastik: Interactive machine learning for (bio)image analysis. *Nat. Methods* 16, 1226–1232. doi: 10.1038/s41592-019-0582-9

Bevan, S., and Wendon, L. M. (1984). A study of the action of tetanus toxin at rat soleus neuromuscular junctions. *J. Physiol.* 348, 1–17. doi: 10.1113/jphysiol.1984.sp015095

Blankenship, A. G., and Feller, M. B. (2010). Mechanisms underlying spontaneous patterned activity in developing neural circuits. *Nat. Rev. Neurosci.* 11, 18–29.

Borst, J. G., and Soria van Hoeve, J. (2012). The calyx of held synapse: From model synapse to auditory relay. *Annu. Rev. Physiol.* 74, 199–224.

Budisantoso, T., Harada, H., Kamasawa, N., Fukazawa, Y., Shigemoto, R., and Matsui, K. (2013). Evaluation of glutamate concentration transient in the synaptic cleft of the rat calyx of Held. *J. Physiol.* 591, 219–239. doi: 10.1113/jphysiol.2012.241398

Crins, T. T., Rusu, S. I., Rodríguez-Contreras, A., and Borst, J. G. (2011). Developmental changes in short-term plasticity at the rat calyx of held synapse. *J. Neurosci.* 31, 11706–11717.

Deák, F., Schoch, S., Liu, X., Südhof, T. C., and Kavalali, E. T. (2004). Synaptobrevin is essential for fast synaptic-vesicle endocytosis. *Nat. Cell Biol.* 6, 1102–1108.

Dreyer, F., and Schmitt, A. (1983). Transmitter release in tetanus and botulinum A toxin-poisoned mammalian motor endplates and its dependence on nerve stimulation and temperature. *Pflugers Arch.* 399, 228–234. doi: 10.1007/BF00656720

Ebbers, L., Satheesh, S. V., Janz, K., Rüttiger, L., Blosa, M., Hofmann, F., et al. (2015). L-type calcium channel Cav1.2 is required for maintenance of auditory brainstem nuclei. *J. Biol. Chem.* 290, 23692–23710. doi: 10.1074/jbc.M115.672675

Erazo-Fischer, E., Striessnig, J., and Taschenberger, H. (2007). The role of physiological afferent nerve activity during in vivo maturation of the calyx of Held synapse. *J. Neurosci.* 27, 1725–1737. doi: 10.1523/JNEUROSCI.4116-06.2007

Ford, M. C., Grothe, B., and Klug, A. (2009). Fenestration of the calyx of Held occurs sequentially along the tonotopic axis, is influenced by afferent activity, and facilitates glutamate clearance. *J. Comp. Neurol.* 514, 92–106. doi: 10.1002/cne.21998

Grande, G., Negandhi, J., Harrison, R. V., and Wang, L. Y. (2014). Remodelling at the calyx of Held-MNTB synapse in mice developing with unilateral conductive hearing loss. *J. Physiol.* 592, 1581–1600. doi: 10.1113/jphysiol.2013.268839

Grothe, B., Pecka, M., and McAlpine, D. (2010). Mechanisms of sound localization in mammals. *Physiol. Rev.* 90, 983–1012.

Gundelfinger, E. D., Reissner, C., and Garner, C. C. (2016). Role of bassoon and piccolo in assembly and molecular organization of the active zone. *Front. Synaptic Neurosci.* 7:19. doi: 10.3389/fnsyn.2015.00019

Hamann, M., Billups, B., and Forsythe, I. D. (2003). Non-calyceal excitatory inputs mediate low fidelity synaptic transmission in rat auditory brainstem slices. *Eur. J. Neurosci.* 18, 2899–2902. doi: 10.1111/j.1460-9568.2003.03017.x

Heuser, J. E., and Reese, T. S. (1973). Evidence for recycling of synaptic vesicle membrane during transmitter release at the frog neuromuscular junction. *J. Cell Biol.* 57, 315–344.

Hirtz, J. J., Boesen, M., Braun, N., Deitmer, J. W., Kramer, F., Lohr, C., et al. (2011). Cav1.3 calcium channels are required for normal development of the auditory brainstem. *J. Neurosci.* 31, 8280–8294. doi: 10.1523/JNEUROSCI.5098-10.2011

Hoffpauir, B. K., Grimes, J. L., Mathers, P. H., and Spirou, G. A. (2006). Synaptogenesis of the calyx of Held: Rapid onset of function and one-to-one morphological innervation. *J. Neurosci.* 26, 5511–5523. doi: 10.1523/JNEUROSCI.5525-05.2006

Holcomb, P. S., Hoffpauir, B. K., Hoyson, M. C., Jackson, D. R., Deerinck, T. J., Marrs, G. S., et al. (2013). Synaptic inputs compete during rapid formation of the calyx of held: A new model system for neural development. *J. Neurosci.* 33, 12954–12969. doi: 10.1523/JNEUROSCI.1087-13.2013

Hoogstraaten, R. I., van Keimpema, L., Toonen, R. F., and Verhage, M. (2020). Tetanus insensitive VAMP2 differentially restores synaptic and dense core vesicle fusion in tetanus neurotoxin treated neurons. *Sci. Rep.* 10:10913. doi: 10.1038/s41598-020-67988-2

Horstmann, H., Körber, C., Sätzler, K., Aydin, D., and Kuner, T. (2012). Serial section scanning electron microscopy (S3EM) on silicon wafers for ultra-structural volume imaging of cells and tissues. *PLoS One* 7:e35172. doi: 10.1371/journal.pone.0035172

Hua, Z., Leal-Ortiz, S., Foss, S. M., Waites, C. L., Garner, C. C., Voglmaier, S. M., et al. (2011). v-SNARE composition distinguishes synaptic vesicle pools. *Neuron* 71, 474–487. doi: 10.1016/j.neuron.2011.06.010

Hubel, D. H., and Wiesel, T. N. (1964). Effects of monocular deprivation in kittens. *Naunyn Schmiedebergs Arch. Exp. Pathol. Pharmakol.* 248, 492–497.

Hubel, D. H., and Wiesel, T. N. (1965). Receptive fields and functional architecture in two nonstriate visual areas (18 and 19) of the cat. *J. Neurophysiol.* 28, 229–289. doi: 10.1152/jn.1965.28.2.229

Humeau, Y., Doussau, F., Grant, N. J., and Poulain, B. (2000). How botulinum and tetanus neurotoxins block neurotransmitter release. *Biochimie* 82, 427–446.

Imig, C., Min, S. W., Krinner, S., Arancillo, M., Rosenmund, C., Südhof, T. C., et al. (2014). The morphological and molecular nature of synaptic vesicle priming at presynaptic active zones. *Neuron* 84, 416–431. doi: 10.1016/j.neuron.2014.10.009

Jackson, D. R. (2020). *Structural Transformations of Synaptic Partners During Growth and Competition of the Giant Nerve Terminal, the Calyx of Held, in the Medial Nucleus of the Trapezoid Body in the Developing Postnatal Mouse*. Morgantown, WV: West Virginia.

Joris, P. X., and Trussell, L. O. (2018). The calyx of held: A hypothesis on the need for reliable timing in an intensity-difference encoder. *Neuron* 100, 534–549. doi: 10.1016/j.neuron.2018.10.026

Kandler, K., and Friauf, E. (1993). Pre- and postnatal development of efferent connections of the cochlear nucleus in the rat. *J. Comp. Neurol.* 328, 161–184. doi: 10.1002/cne.903280202

Katz, L. C., and Shatz, C. J. (1996). Synaptic activity and the construction of cortical circuits. *Science* 274, 1133–1138.

Kerschensteiner, D., Morgan, J. L., Parker, E. D., Lewis, R. M., and Wong, R. O. L. (2009). Neurotransmission selectively regulates synapse formation in parallel circuits in vivo. *Nature* 460, 1016–1020.

Kirkby, L. A., Sack, G. S., Firl, A., and Feller, M. B. (2013). A role for correlated spontaneous activity in the assembly of neural circuits. *Neuron* 80, 1129–1144.

Kopp-Scheinpflug, C., Tolnai, S., Malmierca, M. S., and Rübsamen, R. (2008). The medial nucleus of the trapezoid body: Comparative physiology. *Neuroscience* 154, 160–170.

Körber, C., Horstmann, H., Venkataramani, V., Herrmannsdörfer, F., Kremer, T., Kaiser, M., et al. (2015). Modulation of presynaptic release probability by the vertebrate-specific protein mover. *Neuron* 87, 521–533. doi: 10.1016/j.neuron.2015.07.001

Leao, R. N., Sun, H., Svahn, K., Berntson, A., Youssoufian, M., Paolini, A. G., et al. (2006). Topographic organization in the auditory brainstem of juvenile mice is disrupted in congenital deafness. *J. Physiol.* 571, 563–578. doi: 10.1113/jphysiol.2005.098780

Link, E., Edelmann, L., Chou, J. H., Binz, T., Yamasaki, S., Eisel, U., et al. (1992). Tetanus toxin action: Inhibition of neurotransmitter release linked to synaptobrevin proteolysis. *Biochem. Biophys. Res. Commun.* 189, 1017–1023. doi: 10.1016/0006-291x(92)92305-h

Liu, Y., Sugiura, Y., Südhof, T. C., and Lin, W. (2019). Ablation of all synaptobrevin vSNAREs blocks evoked but not spontaneous neurotransmitter release at neuromuscular synapses. *J. Neurosci.* 39, 6049–6066. doi: 10.1523/JNEUROSCI.0403-19.2019

Lopez, C. M., Pelkey, K. A., Chittajallu, R., Nakashiba, T., Tóth, K., Tonegawa, S., et al. (2012). Competition from newborn granule cells does not drive axonal retraction of silenced old granule cells in the adult hippocampus. *Front. Neural Circuits* 6:85. doi: 10.3389/fncir.2012.00085

Marrs, G. S., and Spirou, G. A. (2012). Embryonic assembly of auditory circuits: Spiral ganglion and brainstem. *J. Physiol.* 590, 2391–2408. doi: 10.1113/jphysiol.2011.226886

Nakashiba, T., Young, J. Z., McHugh, T. J., Buhl, D. L., and Tonegawa, S. (2008). Transgenic inhibition of synaptic transmission reveals role of CA3 output in hippocampal learning. *Science* 319, 1260–1264. doi: 10.1126/science.1151120

Quinn, D. P., Kolar, A., Harris, S. A., Wigerius, M., Fawcett, J. P., and Krueger, S. R. (2019). The stability of glutamatergic synapses is independent of activity level, but predicted by synapse size. *Front. Cell. Neurosci.* 13:291. doi: 10.3389/fncel.2019.00291

Raingo, J., Khvotchev, M., Liu, P., Darios, F., Li, Y. C., Ramirez, D. M., et al. (2012). VAMP4 directs synaptic vesicles to a pool that selectively maintains asynchronous neurotransmission. *Nat. Neurosci.* 15, 738–745. doi: 10.1038/nn.3067

Ramirez, D. M., Khvotchev, M., Trauterman, B., and Kavalali, E. T. (2012). Vti1a identifies a vesicle pool that preferentially recycles at rest and maintains spontaneous neurotransmission. *Neuron* 73, 121–134. doi: 10.1016/j.neuron.2011.10.034

Renden, R., Taschenberger, H., Puente, N., Rusakov, D. A., Duvoisin, R., Wang, L. Y., et al. (2005). Glutamate transporter studies reveal the pruning of metabotropic glutamate receptors and absence of AMPA receptor desensitization at mature calyx of held synapses. *J. Neurosci.* 25, 8482–8497. doi: 10.1523/JNEUROSCI.1848-05.2005

Sakaba, T., Stein, A., Jahn, R., and Neher, E. (2005). Distinct kinetic changes in neurotransmitter release after SNARE protein cleavage. *Science* 309, 491–494. doi: 10.1126/science.1112645

Sakaba, T. (2006). Roles of the fast-releasing and the slowly releasing vesicles in synaptic transmission at the calyx of Held. *J. Neurosci.* 26, 5863–5871. doi: 10.1523/JNEUROSCI.0182-06.2006

Sando, R., Bushong, E., Zhu, Y., Huang, M., Considine, C., Phan, S., et al. (2017). Assembly of excitatory synapses in the absence of glutamatergic neurotransmission. *Neuron* 94, 312–321.

Santos, T. C., Wierda, K., Broeke, J. H., Toonen, R. F., and Verhage, M. (2017). Early golgi abnormalities and neurodegeneration upon loss of presynaptic proteins Munc18-1. *Syntaxin-1, or SNAP-25. J. Neurosci.* 37, 4525–4539. doi: 10.1523/JNEUROSCI.3352-16.2017

Satheesh, S. V., Kunert, K., Rüttiger, L., Zuccotti, A., Schönig, K., Friauf, E., et al. (2012). Retrocochlear function of the peripheral deafness gene Cacna1d. *Hum. Mol. Genet.* 21, 3896–3909. doi: 10.1093/hmg/dds217

Sätzler, K., Söhl, L. F., Bollmann, J. H., Borst, J. G., Frotscher, M., Sakmann, B., et al. (2002). Three-dimensional reconstruction of a calyx of Held and its postsynaptic principal neuron in the medial nucleus of the trapezoid body. *J. Neurosci.* 22, 10567–10579. doi: 10.1523/JNEUROSCI.22-24-10567.2002

Saul, S. M., Brzezinski, J. A., Altschuler, R. A., Shore, S. E., Rudolph, D. D., Kabara, L. L., et al. (2008). Math5 expression and function in the central auditory system. *Mol. Cell. Neurosci.* 37, 153–169. doi: 10.1016/j.mcn.2007.09.006

Schoch, S., Deák, F., Königstorfer, A., Mozhayeva, M., Sara, Y., Südhof, T. C., et al. (2001). SNARE function analyzed in synaptobrevin/VAMP knockout mice. *Science* 294, 1117–1122.

Sigler, A., Oh, W. C., Imig, C., Altas, B., Kawabe, H., Cooper, B. H., et al. (2017). Formation and maintenance of functional spines in the absence of presynaptic glutamate release. *Neuron* 94, 304–311.

Sonntag, M., Englitz, B., Typlt, M., and Rübsamen, R. (2011). The calyx of held develops adult-like dynamics and reliability by hearing onset in the mouse in vivo. *J. Neurosci.* 31, 6699–6709. doi: 10.1523/JNEUROSCI.0575-11.2011

Takamori, S., Holt, M., Stenius, K., Lemke, E. A., Grønborg, M., Riedel, D., et al. (2006). Molecular anatomy of a trafficking organelle. *Cell* 127, 831–846.

Varoqueaux, F., Sigler, A., Rhee, J. S., Brose, N., Enk, C., Reim, K., et al. (2002). Total arrest of spontaneous and evoked synaptic transmission but normal synaptogenesis in the absence of Munc13-mediated vesicle priming. *Proc. Natl. Acad. Sci. U S A.* 99, 9037–9042. doi: 10.1073/pnas.122623799

Vasileva, M., Horstmann, H., Geumann, C., Gitler, D., and Kuner, T. (2012). Synapsin-dependent reserveo pool of synaptic vesicles supports replenishment of the readily releasable pool under intense synaptic transmission. *Eur. J. Neurosci.* 36, 3005–3020. doi: 10.1111/j.1460-9568.2012.08225.x

Verhage, M., Maia, A. S., Plomp, J. J., Brussaard, A. B., Heeroma, J. H., Vermeer, H., et al. (2000). Synaptic assembly of the brain in the absence of neurotransmitter secretion. *Science* 287, 864–869.

Wang, C. L., Zhang, L., Zhou, Y., Zhou, J., Yang, X. J., Duan, S. M., et al. (2007). Activity-dependent development of callosal projections in the somatosensory cortex. *J. Neurosci.* 27, 11334–11342.

Wang, H. C., and Bergles, D. E. (2015). Spontaneous activity in the developing auditory system. *Cell Tissue Res.* 361, 65–75.

Wimmer, V. C., Nevian, T., and Kuner, T. (2004). Targeted in vivo expression of proteins in the calyx of Held. *Pflugers Arch.* 449, 319–333.

Wong, N. F., and Xu-Friedman, M. A. (2022). Time course of activity-dependent changes in auditory nerve synapses reveals multiple underlying cellular mechanisms. *J. Neurosci.* 42, 2492–2502. doi: 10.1523/JNEUROSCI.1583-21.2022

Xu, J., Luo, F., Zhang, Z., Xue, L., Wu, X. S., Chiang, H. C., et al. (2013). SNARE proteins synaptobrevin, SNAP-25, and Syntaxin are involved in rapid and slow endocytosis at synapses. *Cell Rep.* 3, 1414–1421. doi: 10.1016/j.celrep.2013.03.010

Yang, Y. M., Aitoubah, J., Lauer, A. M., Nuriya, M., Takamiya, K., Jia, Z., et al. (2011). GluA4 is indispensable for driving fast neurotransmission across a high-fidelity central synapse. *J. Physiol.* 589, 4209–4227. doi: 10.1113/jphysiol.2011.208066

Yang, Z., Ding, K., Pan, L., Deng, M., and Gan, L. (2003). Math5 determines the competence state of retinal ganglion cell progenitors. *Dev. Biol.* 264, 240–254.

Youssoufian, M., Couchman, K., Shivdasani, M. N., Paolini, A. G., and Walmsley, B. (2008). Maturation of auditory brainstem projections and calyces in the congenitally deaf (dn/dn) mouse. *J. Comp. Neurol* 506, 442–451. doi: 10.1002/cne.21566

Yu, C. R., Power, J., Barnea, G., O'Donnell, S., Brown, H. E. V., Osborne, J., et al. (2004). Spontaneous neural activity is required for the establishment and maintenance of the olfactory sensory map. *Neuron* 42, 553–566. doi: 10.1016/s0896-6273(04)00224-7

Zhang, Z., Wang, D., Sun, T., Xu, J., Chiang, H. C., Shin, W., et al. (2013). The SNARE proteins SNAP25 and synaptobrevin are involved in endocytosis at hippocampal synapses. *J. Neurosci.* 33, 9169–9175.

Zhuang, X., Sun, W., and Xu-Friedman, M. A. (2017). Changes in properties of auditory nerve synapses following conductive hearing loss. *J. Neurosci.* 37, 323-332.

frontiers | Frontiers in Cellular Neuroscience

TYPE Original Research
PUBLISHED 07 January 2025
DOI 10.3389/fncel.2024.1523978

Check for updates

OPEN ACCESS

EDITED BY
Christian Keine,
University of Oldenburg, Germany

REVIEWED BY
Pankaj Bhatia,
Wayne State University, United States
Lavinia Sheets,
Washington University in St. Louis, United States
Juan D. Goutman,
CONICET Instituto de Investigaciones en Ingeniería Genética y Biología Molecular "Dr. Héctor N. Torres" (INGEBI), Argentina

*CORRESPONDENCE
Tina Pangrsic
✉ tpangrs@gwdg.de

RECEIVED 06 November 2024
ACCEPTED 20 December 2024
PUBLISHED 07 January 2025

CITATION
Oestreicher D, Malpede AM, Reitmeier A, Bräuer CP, Schoch L, Strenzke N and Pangrsic T (2025) Noise-induced ribbon synapse loss in the mouse basal cochlear region does not reduce inner hair cell exocytosis.
Front. Cell. Neurosci. 18:1523978.
doi: 10.3389/fncel.2024.1523978

COPYRIGHT
© 2025 Oestreicher, Malpede, Reitmeier, Bräuer, Schoch, Strenzke and Pangrsic. This is an open-access article distributed under the terms of the Creative Commons Attribution License (CC BY). The use, distribution or reproduction in other forums is permitted, provided the original author(s) and the copyright owner(s) are credited and that the original publication in this journal is cited, in accordance with accepted academic practice. No use, distribution or reproduction is permitted which does not comply with these terms.

Noise-induced ribbon synapse loss in the mouse basal cochlear region does not reduce inner hair cell exocytosis

David Oestreicher[1,2], Alfonso Mauro Malpede[1,2], Annalena Reitmeier[1,2], Carolin Paula Bräuer[1,2], Laura Schoch[1,2], Nicola Strenzke[3,4] and Tina Pangrsic[1,2,4]*

[1]Experimental Otology Group, InnerEarLab, Department of Otolaryngology, University Medical Center Göttingen, Göttingen, Germany, [2]Auditory Neuroscience Group, Max Planck Institute for Multidisciplinary Sciences, Göttingen, Germany, [3]Auditory Systems Physiology Group, Institute for Auditory Neuroscience, InnerEarLab, University Medical Center Göttingen, Göttingen, Germany, [4]Collaborative Research Center 889, University of Göttingen, Göttingen, Germany

Noise-induced hearing loss is one of the most common forms of hearing loss in adults and also one of the most common occupational diseases. Extensive previous work has shown that the highly sensitive synapses of the inner hair cells (IHCs) may be the first target for irreparable damage and permanent loss in the noise-exposed cochlea, more precisely in the cochlear base. However, how such synaptic loss affects the synaptic physiology of the IHCs in this particularly vulnerable part of the cochlea has not yet been investigated. To address this question, we exposed 3–4-week-old C57BL/6J mice to 8–16 kHz noise for 2 h under isoflurane anesthesia. We then employed hearing measurements, immunohistochemistry and patch-clamp to assess IHC synaptic function. Two noise sound pressure levels (SPLs) were used to evoke acute hearing threshold elevations with different levels of recovery 2 weeks post-exposure. Regardless of noise intensity, the exposure resulted in a loss of approximately 25–36% of ribbon synapses in the basal portions of the cochlea that persisted 2 weeks after exposure. Perforated patch-clamp recordings were made in the IHCs of the basal regions of the cochlea where the greatest synaptic losses were observed. Depolarization-evoked calcium currents in IHCs 2 weeks after exposure were slightly but not significantly smaller as compared to controls from age-matched non-exposed animals. Exocytic changes monitored as changes in membrane capacitance did not follow that trend and remained similar to controls despite significant loss of ribbons, likely reflecting increased exocytosis at the remaining synapses. Additionally, we report for the first time that acute application of isoflurane reduces IHC calcium currents, which may have implications for noise-induced IHC synaptic loss.

KEYWORDS

inner hair cell, noise trauma, ribbon synapse, isoflurane, calcium channel

Introduction

Disabling hearing loss is one of the most relevant common diseases, affecting more than 5% of the world's population, with the number expected to rise continuously (World Health Organization, 2021). Sensorineural hearing impairment (HI) is caused by pathological changes in the auditory system or the vestibulocochlear nerve and can be either genetic or acquired. The latter may result from age-related degeneration, ototoxic drug exposure and noise-induced

damage (Cunningham and Tucci, 2017). Noise-induced hearing loss (NIHL) is primarily linked to chronic exposure to high noise levels, commonly associated with noisy occupational environments, gunshots and blasts, the use of personal audio devices, and exposure during social settings such as nightclubs and concerts (Fink, 2024).

Excessive noise stimulation damages delicate structures in the inner ear, which can lead to temporary (e.g., minor stereociliar damage) or permanent changes (e.g., hair cell loss). Hair cell ribbon synapses have been recognized as very vulnerable elements of the cochlea (Kujawa and Liberman, 2009; reviewed in Liberman and Kujawa, 2017). Numerous animal models have shown that upon noise trauma, the number of ribbon synapses can remain permanently reduced without loss of hair cells and even after full recovery of elevated hearing thresholds (Furman et al., 2013; Hickman et al., 2020; Hickox et al., 2017; Kujawa and Liberman, 2009; Lin et al., 2011). Similar degeneration pathways with progressive neural deterioration in the aging cochlea that precedes hair cell loss were observed in animal-models studying age-dependent hearing loss (Fernandez et al., 2015; Parthasarathy and Kujawa, 2018; Sergeyenko et al., 2013) and in human temporal bone studies (Wu et al., 2019). It was furthermore shown that these degeneration processes are accelerated by noise exposure (Wu et al., 2021). The loss of synaptic ribbons leads to the loss of the associated spiral ganglion neurons (SGN) after months to years (Kujawa and Liberman, 2015). As a correlate, a permanent reduction in the amplitude of suprathreshold auditory brainstem response (ABR) wave I can be observed in the synaptopathic regions (Kujawa and Liberman, 2009). The neuronal loss is thought to primarily affect the low-spontaneous-rate fibers with high thresholds, as this would explain the recovered thresholds and the typical impairments associated with NIHL (Bourien et al., 2014; Furman et al., 2013; Liberman and Kujawa, 2017). Alternatively, a recent study in gerbils suggested that the initial loss of auditory fibers is not subtype-specific; rather, low-spontaneous-rate fibers may be less prone to recover as compared to high-spontaneous-rate fibers, effectively resulting in chronic loss of primarily low-spontaneous-rate fibers (Jeffers et al., 2021). Another study in CBA/CaJ mice did not find evidence for increased vulnerability of low-spontaneous rate fibers but revealed a new "hyperactive" subtype of auditory fibers with higher peak- and sustained rates after noise exposure (Suthakar and Liberman, 2021).

The mechanism underlying the loss of IHC ribbons is linked to neurotransmission at the IHC synapses, which are glutamatergic. Excessive glutamate release, as a result of acoustic overstimulation, can induce excitotoxic damage to the postsynaptic nerve terminals. In pharmacological experiments, perfusion with kainic acid leads to swelling and retraction of afferent cochlear nerve fibers (Pujol et al., 1985; Wan et al., 2014) and the genetically-induced absence of glutamatergic transmission or pharmacological blockade of Ca^{2+}-permeable postsynaptic glutamate AMPA receptors prevents noise-induced loss of synaptic elements (Hu et al., 2020; Kim et al., 2019; Pujol et al., 1985; Sebe et al., 2017; Wan et al., 2014).

While two studies addressed early effects of noise exposure in the IHCs with temporary noise-induced synaptopathy in the apical turn of the cochlea with partially contradictory results on the effect of noise trauma on IHC synaptic function (Boero et al., 2021; Liu et al., 2019), it remains to be shown how the loss of ribbon synapses affects the notoriously more vulnerable basal IHCs of the organ of Corti. In our study, we established a mouse model of noise exposure under isoflurane gas anesthesia using two noise levels and recorded IHC synaptic activity in the basal turn of 5–6-week-old mice exposed 2 weeks prior to this measurement. We observed a moderate and delayed presynaptic ribbon and synapse loss that was not accompanied by reduced whole-cell exocytic activity, possibly suggesting upregulation of the synaptic activity at the remaining ribbons. Noise exposure under isoflurane anesthesia resulted in moderate temporary to mild permanent hearing loss. As previous studies described protective effects of isoflurane against noise trauma (Chung et al., 2007; Kim et al., 2005), but toxicity for ribbons in neonatal mice (Li et al., 2022), we tested its effects on the systems level, synapse density and also synaptic hair cell function in our experimental conditions. Prolonged isoflurane exposure resulted in a 5–8 dB shift of ABR thresholds, but left auditory synapse density unperturbed 2 weeks after exposure. This is in contrast to a prior study that detected a loss of SGNs after repeated isoflurane anesthesia in neonatal mice (Li et al., 2022). Using whole-cell patch clamp recordings of IHCs we observed an 18% reduction of voltage-gated calcium currents upon acute exposure to isoflurane. Reduced presynaptic calcium signaling and consequently glutamate transmission in the presence of isoflurane anesthesia might offer some protection of hair cells and ribbon synapses against noise-induced damage, but cannot completely prevent it.

Materials and methods

Animals

Male C57BL/6J mice at the age of 3–4 (D0) and 5–6 (D14) weeks were used for electro-physiological, immunohistochemical and systems physiology experiments. All experiments complied with the national animal care guidelines and were approved by the University of Göttingen Board for animal welfare and the animal welfare office of the state of Lower Saxony.

Systems physiology recordings: auditory brainstem responses (ABRs) and distortion product otoacoustic emissions (DPOAEs)

Mice were anesthetized using isoflurane (5% Induction/2% Maintenance). Recordings were obtained in a custom-made soundproof box (IAC GmbH, Germany) with a Tucker-Davis (TDT) BioSig System III/BioSig software (Tucker-Davis Technologies, Alachua, FL). Body temperature was maintained using a heating pad (37°C) and ECG was monitored continuously. For ABR recordings, subcutaneous needles were placed at the vertex, the ipsilateral pinna and at the lower back. Using a JBL2402 speaker in free-field configuration, tone bursts (10-ms plateau, 1-ms cos2 rise/fall) were ipsilaterally presented at 19 Hz. ABR traces were amplified 10.000 times and filtered from 400 to 4.000 Hz, to obtain two separate mean ABR traces and averaged from 1,000 repetitions. Thresholds were defined in stacked waveforms as the lowest stimulus intensity (dB SPL) at which a reproducible waveform could be visually detected with a 5 dB precision. Data from animals where fewer than four frequencies were measured reliably were excluded from the analysis. DPOAEs were measured using a custom-written MATLAB (MathWorks) routine. Two primary tones f1 and f2 (ratio f1/f2 = 1.2, level difference f2 = f1 + 10 dB) were presented via two speakers (MF-1, TDT) and a custom-made ear probe containing an MKE-2 microphone (Sennheiser). Stimulus duration was 16 ms and f2 levels varied from 10 to 70 dB SPL in 5 dB steps. For higher intensities, we extrapolated a threshold. The microphone signal was amplified (UAC-2; Zoom) and

digitized (TDT System). DPOAE amplitude was analyzed at 2 × f2-f1 using custom-written MATLAB software with fast Fourier transformation. DPOAE thresholds were determined as the interpolated f1 intensity at which the DPOAE intensity exceeded −5 dB SPL.

Noise exposure

The animals were exposed to an 8–16 kHz band noise for 2 h at 92 or 96 dB (SPL). Noise exposure was performed in a custom-made soundproof box (IAC GmbH, Germany) under isoflurane gas anesthesia (5% Induction/2% Maintenance) for the sake of animal welfare and refinement of animal experiments. The noise waveform was created digitally using a TDT System III controlled by a custom-written Matlab routine that was driving a JBL2402 speaker to generate an 8–16 kHz noise band with a flat frequency spectrum.

Patch-clamp

For patch-clamp recordings, the basal turn of the cochleae was dissected in Modified Ringer's solution (MRS) containing (in mM): 111 NaCl, 35 TEA-Cl, 2.8 KCl, 1 $MgCl_2$, 1 CsCl, 10 NaOH-HEPES, 1.3 $CaCl_2$, and 11.3 D-glucose (pH 7.2, 305 mOsm/L). IHCs of the ~48 kHz tonotopical region were investigated using the perforated patch configuration. The pipette solution contained (in mM): 130 Cs-gluconate, 10 TEA-Cl, 10 4-AP, 1 $MgCl_2$, 10 HEPES, 300 mg/mL amphotericin B, pH 7.2 ~ 290 mOsm. MRS was also used for the bath perfusion. Recordings were performed at room temperature using an EPC-10 amplifier (Heka-Germany) controlled by Patchmaster software. Currents were leak-corrected using a p/10 protocol, sampled at 50 kHz and corrected offline for the liquid junction potential (−14 mV). Only recordings showing leak currents lower than 50 pA were included in the final analysis.

For *in vitro* isoflurane experiments a 0.6 mM isoflurane solution [close to 2 MAC (the minimum alveolar concentration required to suppress movement in response to noxious stimulation in 50% of subjects) for isoflurane in mice (Sonner et al., 2007); 0.31 mM corresponds to 1 MAC for isoflurane in mice] was prepared from a saturated stock solution in gas-tight containers as described earlier (Baumgart et al., 2015). Superfusion of 0.6 mM isoflurane was carried out with a perfusion system connected to a manifold tip with a diameter of 200 µm (ALA QTP-200, ALA Scientific Instruments, United States). Recordings were initiated 3–5 min after perfusion initiation. These were compared to the recordings prior to isoflurane application and during wash-out.

Immunohistochemistry and confocal microscopy

Cochleae were fixed in 4% formaldehyde (FA) for 10 min on ice and decalcified overnight in EDTA (0.5 M, pH 8) at 4°C. After permeabilization in 1% Triton X-100, cochleae were blocked in goat serum dilution buffer (GSDB; 16% normal goat serum, 450 mM NaCl, 0.3% Triton X-100, and 20 mM phosphate buffer at pH 7.4) for 1 h on ice and incubated in primary antibodies in GSDB with chicken anti-Homer1 (Synaptic Systems, 160,006), mouse anti-CtBP2 (BD Transduction Laboratories, 612,044) and rabbit anti-Myo6 (Proteus Biosciences, 25–6,791) at 4°C overnight. This was followed by a second fixation of 2 h in 4% FA. After that, organs of Corti were dissected into 3–4 pieces and incubated with matching Alexa-fluorophore conjugated secondary antibodies for 1 h at room temperature. Explants were then mounted in Mowiol mounting medium.

Synapse counts: Images to determine regions of interest were acquired with a Zeiss LSM 510 META confocal microscope and a 10× air objective. A tonotopic map for each individual organ of Corti was calculated using a custom-made Matlab (Mathworks) routine based on the mouseline-specific total length of the organ of Corti (Müller et al., 2005). For the areas of interest (8, 16, 24, 32, and 48 kHz) z-stacks were acquired with an Abberior Expert Line confocal microscope using a 1.4 NA 100× oil-immersion objective, 80 × 80 nm pixel size and a z-step size of 200 nm.

Hair cell counts: For hair cell counts images were acquired with a Leica SP8 confocal microscope using a 1.4 NA 20× oil-immersion objective, 378.8 × 378.8 nm pixel size and a z-step size of 0.65 µm. Images were taken from the apical (8–12 kHz) and the basal turn (32 kHz region) of each analyzed organ. OHCs were counted and divided by the length of the analyzed region (222 ± 10 µm).

Ribbon counts

Confocal immunofluorescence images were adjusted for brightness and contrast using ImageJ (NIH) and analyzed using Imaris (Bitplane) software. Pre- and postsynaptic immunofluorescent spots were detected by the spot detection tool of Imaris in a region of interest of about 6–10 IHCs. The number of synapses was analyzed by counting juxtaposed immunofluorescent spots labeling presynaptic ribbon constituent CtBP2 and a postsynaptic density constituent Homer1.

Data analysis

Electrophysiological data were analyzed using custom analysis routines written in Igor Pro Software (Wavemetrics). ABR and DPOAE recordings were analyzed by custom-written Matlab (Mathworks) scripts. All data are presented as mean ± SEM. Data were tested for significance using ANOVA with Dunnett's multicomparisons test to detect possible statistically significant differences to the respective control. In case of *in vitro* isoflurane effects, Tukey's multicomparisons test was chosen to allow comparisons between data acquired before and upon isoflurane application as well as during the wash-out phase.

Results

Noise exposure under isoflurane anesthesia results in moderate acute increase of ABR and DPOAE thresholds with almost complete or partial recovery at two noise levels

To investigate the effects of a two-hour exposure to 8–16 kHz noise band under isoflurane anesthesia at 92 and 96 dB SPL, we assessed auditory function immediately after (D0) and 14 days

post-exposure (D14) by measuring auditory brainstem responses (ABR) and distortion product otoacoustic emissions (DPOAE) (Figure 1). We observed an acute ABR threshold shift of around 20 dB following an exposure to 92 dB SPL and 40 dB upon exposure to 96 dB SPL noise (Supplementary Figures S1A,B). Since gas anesthesia through isoflurane was shown to elevate hearing thresholds (Kim et al., 2012; Sheppard et al., 2018) and protect hair cells against noise-induced permanent auditory damage accompanied by hair cell loss (Kim et al., 2005) we evaluated a possible influence of isoflurane on the recorded hearing thresholds and noise exposure. For this, we performed an additional set of experiments, in which animals were kept under identical isoflurane anesthesia conditions but in the absence of noise and similarly recorded hearing threshold before and immediately after 2-h isoflurane exposure (Isoflurane 2 h D0) as well as 2 weeks afterwards (Isoflurane 2 h D14). Under these experimental conditions, we observed an acute ABR threshold shift of on average 5–8.5 dB SPL across the measured frequencies (Figure 1B; Isoflurane 2 h D0), while DPOAE amplitudes remained unaffected by prolonged isoflurane exposure (Supplementary Figure S1C). We then calculated the threshold shifts of ABR measurements conducted before and after noise exposure and compared them to threshold shifts of the Isoflurane 2 h D0 group. This revealed significantly larger ABR threshold shifts upon exposure to 92- and 96-dB noise bands as compared to the shifts observed with isoflurane exposure alone [Figure 1B; Dunnett's test; $p < 0.05$ (see also figure legends): Δ92 dB D0 vs. ΔIsoflurane 2 h D0 at 16–32 kHz; Δ96 dB D0 vs. ΔIsoflurane 2 h D0 at 12–32 kHz; ΔIsoflurane 2 h D0 $N = 7$, Δ92dB D0 $N = 32$, Δ96dB D0 $N = 17$]. Two weeks after exposure, ABR thresholds largely recovered in the 92-dB group, but remained elevated at 32 kHz in the 96-dB group (Figure 1C; Dunnett's multiple comparisons test; $p = 0.0001$ for Δ96 dB D14 vs. ΔIsoflurane 2 h D14 at 32 kHz; ΔIsoflurane 2 h D14 $N = 7$, Δ92 dB D14 $N = 26$, Δ96 dB D14 $N = 6$).

A smaller but also significant effect was observed in DPOAE thresholds, which were similarly raised in both exposure groups and report outer hair cell (OHC) malfunction likely related to acute damage of stereocilia [Figure 1D; Dunnett's multiple comparisons test; $p < 0.05$: 92 dB D0 vs. Control D0 at 16–32 kHz; 96 dB D0 vs. Control D0 at 11.3–32 kHz (see also figure legends); Control D0 $N = 16$, 92 dB D0 $N = 14$, 96 dB D0 $N = 13$]. Two weeks later, DPOAEs of exposed animals were undistinguishable from age-matched control animals in both groups except at 16 and 22.7 kHz for 96-dB (Figure 1E; Dunnett's multiple comparisons test; $p < 0.02$: 96 dB D14 vs. Control D14 for 16 kHz and 22.7 kHz; Control D14 $N = 9$, 92 dB D14 $N = 13$; 96 dB D14 $N = 6$).

Increased DPOAE (and concomitantly ABR) thresholds 2 weeks post-exposure could be related to persistent stereocilia damage or hair cell loss (Kurabi et al., 2017). To test for potential cell loss, we performed immunohistochemistry of the organs of Corti and counted the number of OHCs in the basal part of the cochlea (32 kHz area) of exposed and age-matched control animals 2 weeks after exposure (Figures 2A,B). We detected decreased OHC density in the animals exposed to 96-dB, but not 92-dB noise band (Figure 2B; Dunnett's multiple comparisons test, $p < 0.05$). A partial loss of the OHCs in the 96-dB group can explain the reduction of high frequency hearing sensitivity (increased DPOAE and ABR thresholds) 2 weeks post-exposure. Increased threshold at 16 kHz in the 96-dB group at 2 weeks after exposure, on the other hand, is hard to reconcile with the observation of no significant increase in the ABR threshold in this frequency region. We postulate that due to the nature of the underlying stimulus the effect in the DPOAE may be detected more precisely. With this respect, it is worth noting that a discrepancy between the DPOAE and ABR thresholds was observed in the past in clinical studies, where DPOAEs proved superior to pure tone audiometry as a screening tool to detect hair cell malfunction: DPOAE amplitudes first decreased before threshold changes were detected at the corresponding frequencies in pure tone audiometry in patients that received cisplatin treatment or in a cohort of hemodialyzed patients. Reduced emissions with normal hearing could therefore indicate an underlying pathological condition that may later lead to significant hearing loss (Bendo et al., 2015; Knight et al., 2007; Ress et al., 1999).

Permanent loss of hair cell ribbon synapses after moderate noise trauma under isoflurane anesthesia

We assessed synapse density of specific tonotopic regions by counting ribbons and postsynaptic boutons through colocalizing anti-CtBP2 and anti-Homer 1 immunospots per IHC, respectively (Figures 2C–E′). In control, non-exposed ears, the mean counts showed a broad peak of around 19 ribbons/IHC in mid-cochlear regions, slightly declining toward the apical and basal ends (Figures 2D–E′). These values are consistent with previously reported data (Kim et al., 2019; Kujawa and Liberman, 2009; Meyer et al., 2009).

D0 organs of Corti were fixed immediately after a hearing test following the two-hour noise exposure and immunostained in the following days. Within 2 h of noise trauma and shortly thereafter there were no evident signs of synaptic loss in either the pre-synaptic or post-synaptic elements (Dunnett's multiple comparisons test; see Supplementary Table S1), suggesting that in our recording conditions the synaptic degeneration (e.g., disassembly of the ribbons or loss of boutons or postsynaptic density proteins) does not occur during noise exposure or immediately thereafter but develops over the next days following exposure. In a subset of experiments, cochleae of the 92-dB-noise group were harvested 1 day post-exposure (D1). These revealed a significant loss of 17–19% of ribbons and 25–30% of ribbon synapses (t.i. juxtaposed CtBP2/Homer1 immunospots) in the high-frequency regions (32–48 kHz) (Supplementary Figure S2; Dunnett's test; Control D0 vs. 92 dB D1: $p < 0.01$ for 32 and 44 kHz; 92 dB D1 $N = 5$). Synaptopathy at D1 however was not yet fully developed. Two weeks after exposure, a synaptic loss of an approximately 20–23% of ribbons and 25–36% of ribbon synapses was observed in the high-frequency regions (≥32 kHz) of the noise-exposed ears for both noise intensities examined (92- and 96-dB SPL) and to a lesser extent at 24 kHz 2 weeks after exposure (Figures 2E,E′). Furthermore, in the high-frequency regions on average one to two more orphan ribbons were observed per IHC of exposed animals 2 weeks after exposure, which is comparably higher to studies exposing CBA or C57Bl/6J mice in awake state (Fernandez et al., 2015; Kim et al., 2019; Liberman et al., 2015). Interestingly, the stronger noise exposure did not cause significantly more synaptic loss as compared to the lower sound intensity, but lead to larger "permanent" shift in the ABR and DPOAE thresholds (Figure 1). In the high-frequency (32–48 kHz) regions of the noise-exposed ears, the ribbon density was observed to decrease to approximately 13/IHC 2 weeks after exposure. Conversely, in the lower-frequency (≤24 kHz) regions, no alterations in the ribbon

10.3389/fncel.2024.1523978

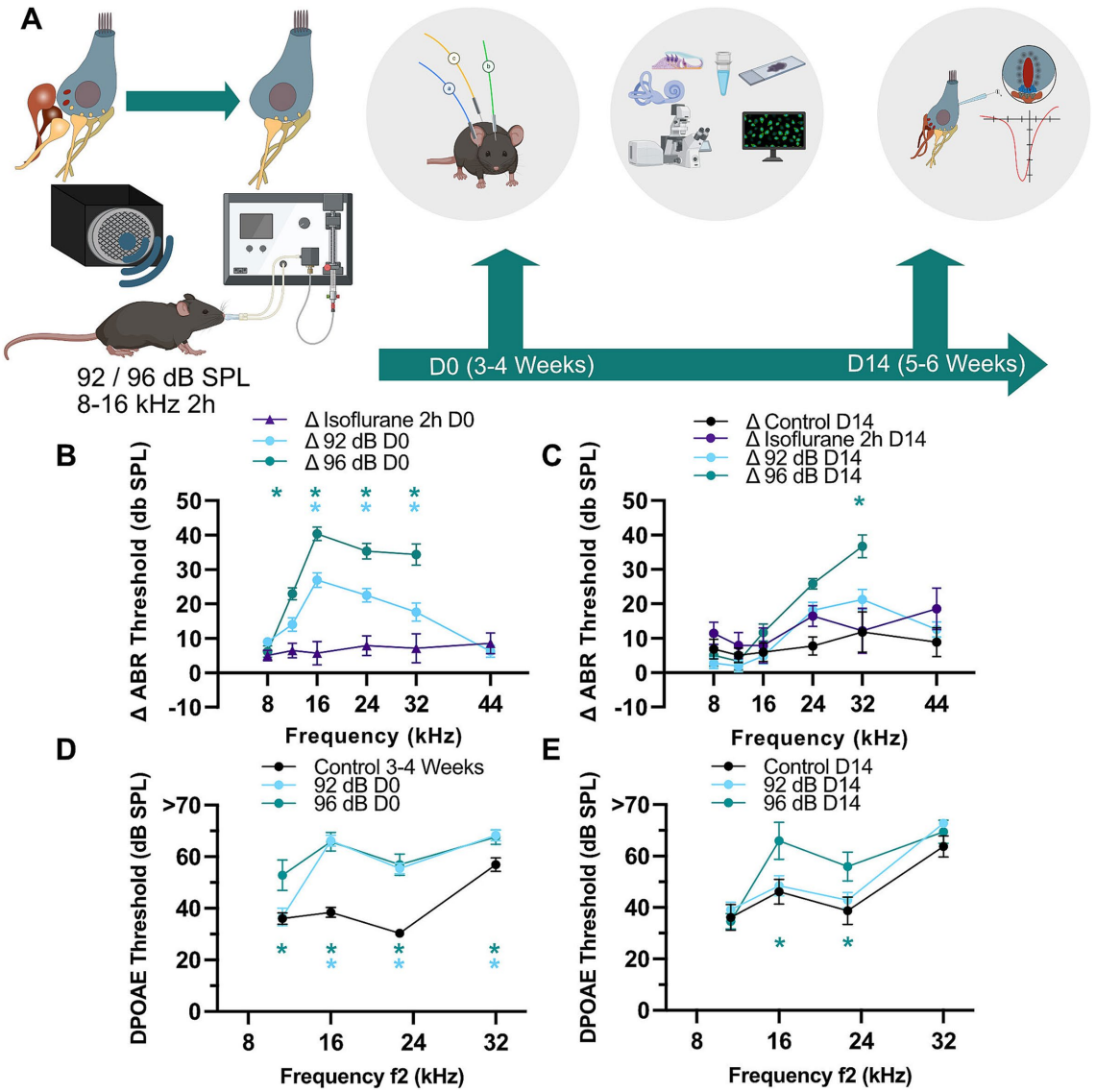


FIGURE 1
Partial recovery of threshold shifts and otoacoustic emissions after moderate noise trauma. **(A)** To establish a noise-induced auditory synaptopathy in the basal turn of the cochlea male C57/Bl6 mice of 3–4 weeks of age (D0) were exposed to a white noise from 8 to 16 kHz with 92 or 96 dB SPL for 2 h under isoflurane gas anesthesia. Hearing was tested (ABR, DPOAE) before and after exposure and in a subset of animals 2 weeks after exposure. The final hearing measurement was followed by histological and/or cell physiological assessment of IHC synapses. Partially created with BioRender. **(B)** ABR threshold shifts immediately after exposure as compared to pre-exposure values obtained in the same animals. Immediately after noise exposure to either sound pressure level (D0; 92- and 96-dB) the ABR shifts were significantly higher as compared to the shift caused by isoflurane anesthesia alone (asterisks: Dunnett's multiple comparisons test; $p < 0.001$ for 96-dB at 12 kHz, <0.002 and <0.03 for 92-dB at 24 and 32 kHz, respectively; <0.0001 for other asterisks). $N = 31, 32, 31, 32, 32, 25$ for the 92-dB D0 group at 8–44 kHz frequencies, respectively. $N = 7$ for the D0 Isoflurane 2 h group at all tested frequencies. $N = 17, 17, 15, 15, 15$ for the 96-dB D0 group tested at 8–32 kHz. **(C)** ABR thresholds showed better recovery in the 92- as compared to 96-dB group (asterisk: Dunnett's multiple comparisons test; $p = 0.0001$). $N = 25, 26, 25, 26, 25, 18$ for the 92-dB D14 group. $N = 7$ for the D14 Isoflurane 2 h group at all tested frequencies. $N = 11, 11, 11, 11, 11, 8$ for the non-exposed control. $N = 6$ for the 96-dB D14 group tested at frequencies 8–32 kHz. **(D,E)** DPOAE thresholds remained significantly elevated at 16 and 22.7 kHz for 96 dB after 14 days (D14) (Dunnett's multiple comparisons test; $p < 0.02$). $N = 16$ for Control D0; $N = 14$ for 92-dB D0 group; $N = 13$ for 96-dB D0 group. $N = 9$ for Control D14; $N = 13$ for 92-dB D14 group; $N = 6$ for 96-dB D14 group at all tested frequencies. p-values for asterisks in **(D)**: <0.0001 at 16 and 24 kHz for both noise levels, 0.0002 (96-dB group at 8 kHz), 0.01 and 0.02 at 32 kHz for 92- and 96-dB group, respectively.

density were observed (Figure 2E′). Previous studies suggested that prolonged exposure to volatile gas anesthetics alone can result in loss of a fraction of ribbon synapses in the cochleae of newborn mice (Li et al., 2022). To test whether the observed loss of synapses in our exposed animals may have been caused by isoflurane exposure, ribbon synapse density was assessed in the organs of Corti of animals under prolonged isoflurane anesthesia (Figures 2E,E′). We observed no difference to the control group (organs of Corti from non-exposed animals that did not undergo prolonged isoflurane anesthesia). This suggests that the observed synaptic loss in the noise-exposed groups is indeed caused by noise exposure and a single prolonged exposure of 3-week-old mice to low levels of isoflurane (2% vol.) does not cause obvious cochlear synaptic loss within 2 weeks after exposure to the anesthetic.

10.3389/fncel.2024.1523978

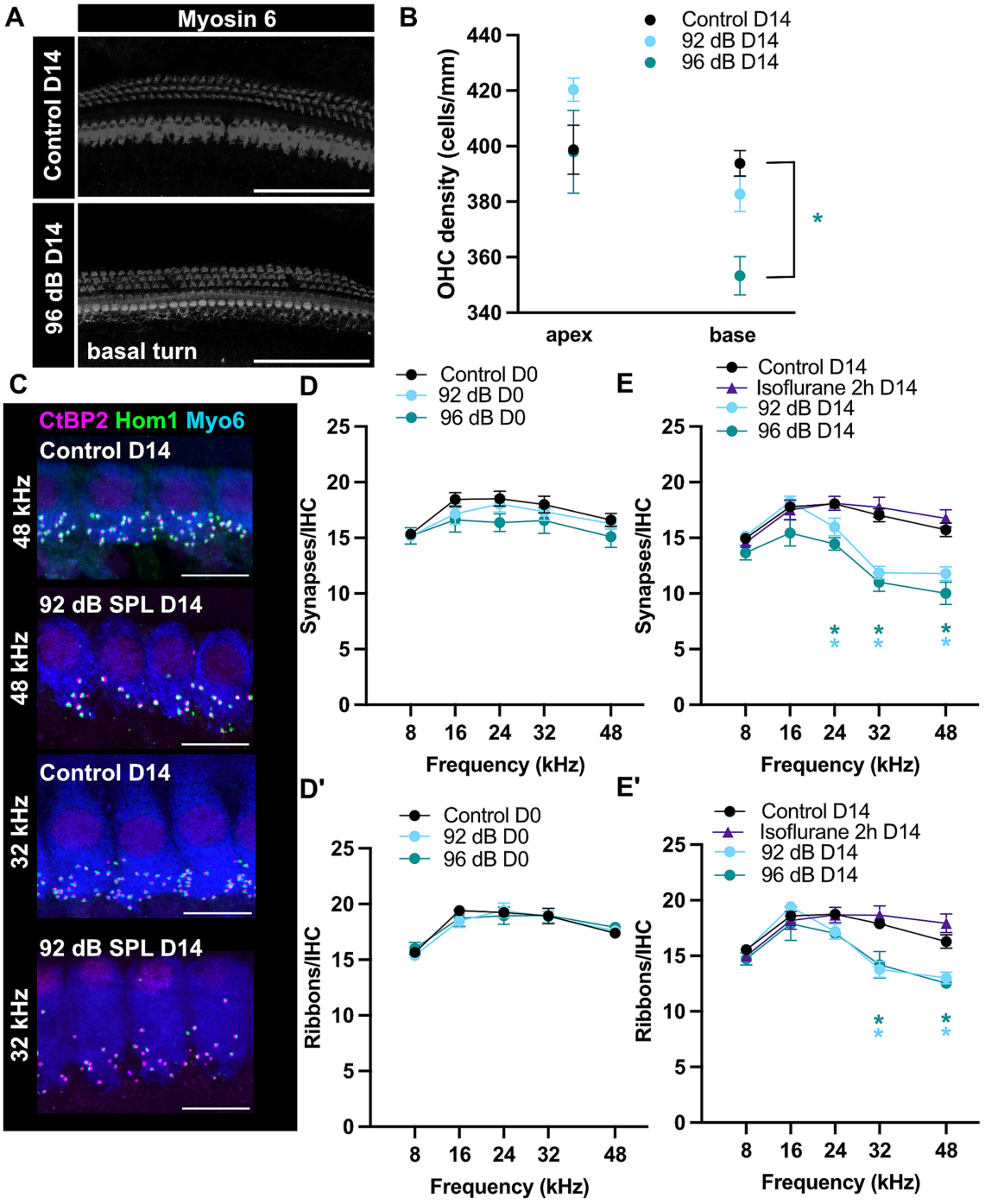


FIGURE 2
Ribbon-synapse loss is persistent but delayed. **(A)** Examples of maximum-projections of confocal z-stacks showing myosin 6-immunostained hair cells 2 weeks after 96-dB noise-trauma and in age-matched controls. Scale bars: 100 µm. **(B)** Reduced OHC-density was detected in the cochlear base of the 96-dB (Dunnett's test; $p < 0.05$), but not 92-dB group (apex: $N = 6, 3, 6$; base: $N = 6, 7, 5$ for Control D14, 92 dB D14 and 96 dB D14, respectively). **(C)** Maximum-projections of confocal z-stacks depicting IHCs from a noise-traumatized and control animal in the 48- and 32-kHz-region. Scale bars: 10 µm. Acutely after noise-exposure there was no significant change in either synapse **(D)** or ribbon **(D')** density (Control D0 $N = 13, 13, 12, 11, 12$ for the respective frequencies; 92 dB D0 $N = 8, 8, 8, 7, 6$; 96 dB D0 $N = 7, 7, 7, 6, 6$ for the frequencies 8–48 kHz). However, note a trend to reduced numbers of IHC synapses. **(E)** Fourteen days after noise exposure ribbon density was significantly reduced at 32–48 kHz and **(E')** synapse density at 24–48 kHz (Dunnett's test; $p < 0.05$; see Supplementary Table S1; Control D14 $N = 17, 18, 17, 18, 12$; 92 dB D14 $N = 11, 11, 14, 18, 15$; 96 dB D14 $N = 5, 5, 3, 6, 2$; Isoflurane 2 h D14 $N = 4, 6, 6, 6, 5$). Prolonged isoflurane exposure in the absence of noise trauma caused no synaptic loss.

Noise-induced ribbon loss does not result in decreased IHC exocytosis

Patch-clamp measurements from noise-exposed apical IHCs revealed mostly comparable levels of presynaptic activity upon short to mid-long depolarization steps to age-matched non-exposed controls despite temporary loss of synaptic ribbons (Boero et al., 2021). However, a prior study published conflicting results demonstrating significantly reduced exocytosis after temporary ribbon loss in 4-week-old mice (Liu et al., 2019). To directly test the effects of noise exposure in the IHCs of the most vulnerable, basal part of the cochlea (Figure 3A), we performed these challenging recordings from a subset of our exposed organs of Corti. Whenever possible, the same animals were used to assess the synaptic density as well as IHC synaptic physiology to obtain most comparable results. Current–voltage relationships in the basal IHCs of 5–6-week-old mice revealed similar maximal currents (Figure 3B) but slightly larger membrane capacitance responses as previously observed in the adult basal IHCs of the gerbils or mice (Johnson and Marcotti, 2008; Zuccotti et al., 2012). Surprisingly, patch-clamp recordings 2 weeks after noise exposure showed no significant changes in IHC synaptic function on the whole-cell level (Figure 3C, upper panel; Dunnett's multicomparison test; example traces in Figure 3D) despite a moderate but significant decrease in ribbon density at high-frequency tonotopic positions (20–23%), as identified by immunofluorescence (Figure 2). The relative amount of membrane capacitance change upon a 100-ms depolarization step thus increased from approx. 2.1 fF/ribbon in control to 3.7 fF/ribbon (by 81%) and to 4.0 fF/ribbon (by 97%) in the IHCs exposed to 92- and 96-dB, respectively. Calcium charge transfer was slightly but not significantly reduced upon noise exposure (Figure 3C, lower panel; apart from the 100-ms depolarization pulse in the 96-dB group; $p < 0.03$), which is consistent with the observation of no significant reduction in the maximal calcium current amplitudes at short depolarization pulses (Figure 3B). Observation of a modest decrease in the calcium charge transfer together with the slight (but non-significant) increase in the whole-cell membrane capacitance jumps prompted us to test the efficiency of sustained component (≥20-ms pulse duration) of exocytosis (Figure 3C′). A trend toward an increased efficiency of exocytosis upon noise exposure was observed (two-way ANOVA; $p = 0.0505$), which however did not reach statistical significance at any of the individual observation points (Dunnett's multicomparison test, $p > 0.05$). Together, these observations suggest that the remaining (ca. 80%) ribbon synapses may undergo compensatory mechanisms to maintain overall synaptic functionality. This is consistent with the study of Boero et al. (2021), in which maintained exocytosis for shorter- and a significant increase in IHC exocytosis for very long depolarization durations was observed 1 day after exposure of pre-weaning animals. This potentiation of exocytosis was suggested to be driven by glutamate-dependent mechanisms (Boero et al., 2021).

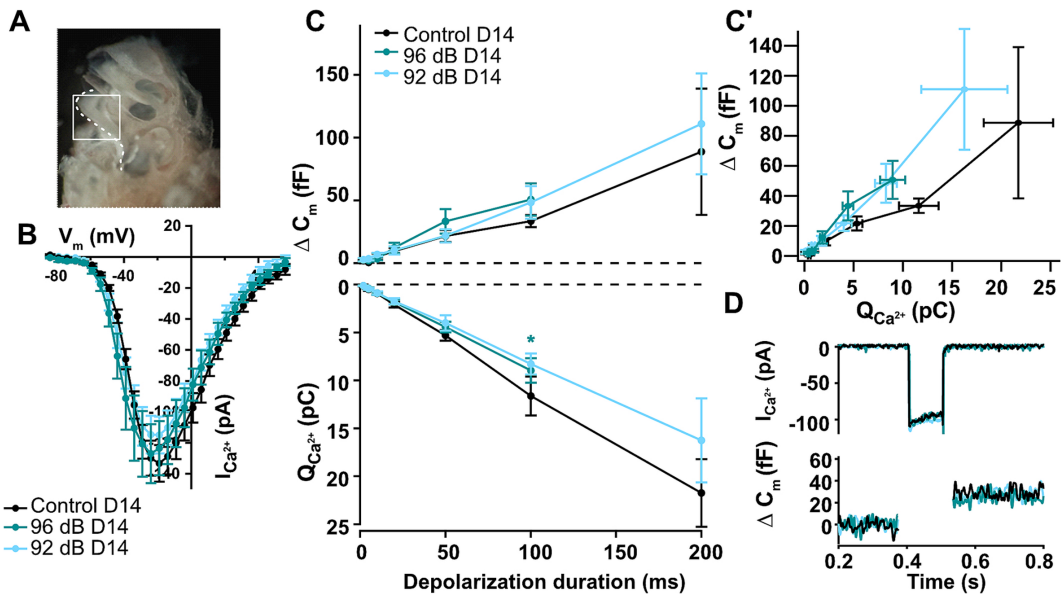


FIGURE 3
Noise-induced auditory synaptopathy in the basal turn of the cochlea leaves overall IHC synaptic activity largely unchanged. **(A)** An image of the mouse cochlea with exposed cochlear turns and region that was extracted (white) with the basal turn that was used for the patch-clamp measurements of high-frequency IHCs after noise-trauma. **(B)** Current–voltage-relationships recorded 2 weeks after noise exposure show comparable Ca^{2+} current amplitudes between noise-exposed and unexposed controls (Control D14 $n = 9$, 96 dB D14 $n = 5$, 92 dB D14 $n = 9$). **(C,C′)** Calcium-dependent exocytosis as measured by increments of membrane capacitance was not significantly different from control hair cells 14 days after noise trauma for any of the noise intensities, but a slight trend toward increased efficiency of exocytosis was detected (Control D14 $n = 3, 4, 6, 7, 9, 13, 5$; 96 dB D14 $n = 3, 4, 5, 5, 8$; 92 dB D14 $n = 6, 9, 9, 10, 10, 13, 6$). Asterisk: $p < 0.03$; none of the other points showed significant differences (Dunnett's tests for dCm and QCa; $p > 0.05$). The efficiency of the sustained exocytosis (dCm/QCa at 20–100 ms) showed a trend toward increased values for the noise-exposed IHCs (two-way ANOVA: $p = 0.0505$; but none of the individual points reached statistical significance). **(D)** Representative calcium-current and capacitance traces upon a 100-ms long depolarization to maximal calcium current potential.

Acute effects of isoflurane on IHC physiology

As shown in this and previous studies, acute exposure to isoflurane increases ABR thresholds (Figure 1) and reduces ABR wave I amplitudes, likely due to recruitment of fewer auditory nerve fibers (Cederholm et al., 2012). The exact action of isoflurane on cochlear function is not entirely understood, but may involve direct effects on hair cell function. For example, isoflurane was shown to inhibit neurotransmitter release in hippocampal neurons (Herring et al., 2009; Li et al., 2022) and modulate the function of voltage-gated Na^+ and Ca^{2+} channels (Baumgart et al., 2015; Herold et al., 2017; Herring et al., 2009; Westphalen et al., 2011). To understand the extent of putative acute isoflurane exposure effects on IHC synaptic physiology, we employed bath perfusion of 0.6 mM isoflurane [corresponding to 1.935 MAC for isoflurane in mice (Sonner et al., 2007; see methods)] and performed patch-clamp experiments in IHCs of acutely isolated organs of Corti. Here, IHCs from the apical turns of the organs were used due to much better accessibility to electrophysiological recordings. Calcium currents upon short depolarizations to different potentials as well as membrane capacitance changes upon 100-ms long depolarization steps to the maximal calcium current potential were recorded during perfusion of normal saline containing 1.3 mM [Ca^{2+}], upon application of isoflurane and consequent wash-out (Figure 4). In our recording conditions, the perfusion of 0.6 mM isoflurane typically took maximal effects within 3–5 min and caused an approximately 18% reduction in the maximal calcium currents (Figure 4D; one-way ANOVA with Tukey's multiple comparison: Control vs. Isoflurane and Isoflurane vs. Wash out $p < 0.01$; Control vs. Wash out $p > 0.05$; $n = 8$). Similarly, we observed a significant reduction in the calcium charge transfer upon 100-ms long depolarization steps (Figures 4A,C; one-way ANOVA with Tukey's multiple comparison: Control vs. Isoflurane $p < 0.0001$; Control vs. Wash out $p > 0.05$; Isoflurane vs. Wash out $p < 0.05$; $n = 5$). This resulted in modestly reduced membrane capacitance jumps, which however did not reach statistical significance, likely due to larger variability (Figure 4B; one-way ANOVA with Tukey's multiple comparison, $p > 0.05$ for all comparisons, Control vs. Isoflurane; Control vs. Wash out; Isoflurane vs. Wash out; $n = 5$). *In vivo*, reduced IHC presynaptic calcium signaling and consequently glutamate transmission in the presence of isoflurane anesthesia might offer some protection of hair cells and ribbon synapses against noise-induced damage, but as demonstrated in the current study, cannot completely prevent it.

Discussion

In this study we show delayed moderate auditory synaptopathy with acute moderate ABR threshold shift that largely recovers upon noise exposure (2-h, 8–16 kHz noise band) under isoflurane anesthesia in young weaned C57Bl/6J male mice. Increasing the sound pressure level from 92 to 96 dB led to a permanent threshold shift at high frequencies, but no further increase in synaptic loss, which amounted to about (11-) 25–36% in the (mid to) basal tonotopic regions of the cochlea. The loss of paired pre- and post-synaptic structures scaled with the loss of presynaptic ribbons, with few orphan ribbons detected throughout analyzed organs. The loss of ribbons was accompanied by slightly, but not significantly reduced IHC whole-cell calcium currents and no reduction in IHC exocytosis, possibly suggesting long lasting compensatory mechanisms on the whole-cell level. Our data also suggests that isoflurane reduces IHC synaptic calcium currents. Hence, reduced hair cell synaptic activity in the presence of isoflurane anesthesia may partially protect ribbon synapses from noise exposure possibly explaining the relatively modest synapse loss and modest permanent ABR threshold shift upon 96-dB noise trauma.

Noise-induced ABR and DPOAE thresholds measured under isoflurane anesthesia

Immediately after noise exposure, the mice showed 10–40 dB SPL threshold shift in the ABRs at frequencies ≥16 kHz. To account for

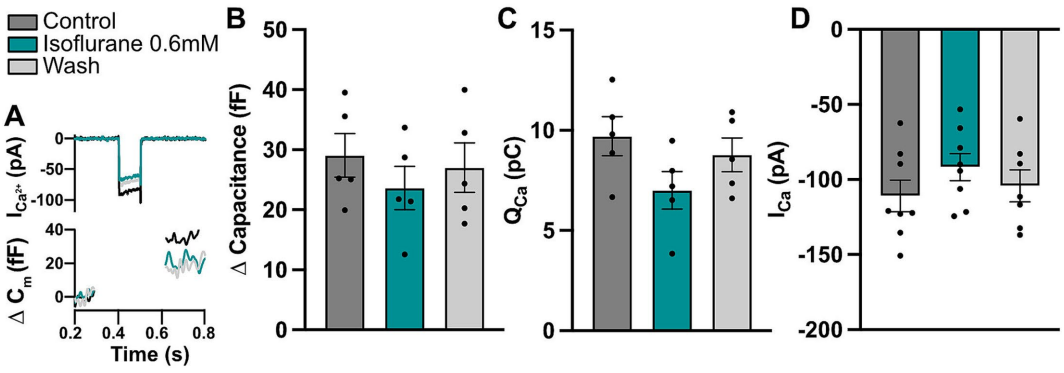


FIGURE 4
Isoflurane affects IHC calcium currents. **(A)** Representative calcium current and capacitance traces upon a 100-ms step depolarization step to maximal current potential for the different conditions. **(B)** A trend toward decreased exocytosis upon a 100-ms step depolarization could be observed in acutely-exposed IHCs (one-way ANOVA with Tukey's multiple comparison, $p > 0.05$; $n = 5$). **(C)** Calcium charge transfer was significantly reduced during isoflurane perfusion, but recovered after wash-out (one-way ANOVA with Tukey's multiple comparison, for p values see text; $n = 5$). **(D)** Calcium current amplitudes upon 10-ms long step depolarizations to the maximum calcium current potential were significantly reduced upon isoflurane application and recovered during wash-out (one-way ANOVA with Tukey's multiple comparison, for p-values see text; $n = 8$).

the threshold shift caused by anesthesia alone, we compared the ABR threshold shifts upon 2-h noise exposure under anesthesia to the shifts produced by 2-h isoflurane anesthesia alone, in the absence of acoustic overstimulation. Based on these comparisons, we conclude that a 2-h noise exposure at 92 dB SPL caused a transient threshold shift with an almost complete recovery within the following 2 weeks. Acute elevation of ABR hearing thresholds was relatively modest, which we ascribe to protective effects of isoflurane, effectively reducing the amount of cochlear activation. Increasing noise exposure to 96 dB SPL resulted in more extensive temporary loss of hearing sensitivity and mild permanent threshold shift, as observed 2 weeks after exposure at high frequencies. Traditionally, OHCs were considered the most vulnerable cochlear elements that may become damaged and lost upon noise trauma resulting in a permanent hearing threshold shift (Kurabi et al., 2017). To assess the functionality of OHCs in our system, we measured DPOAE thresholds. Immediately post-exposure, we observed a significant DPOAE threshold shift, which completely recovered for the 92-dB but not 96-dB group 2 weeks after exposure. Thus, mild permanent threshold shifts as detected in the ABRs upon 96-dB noise exposure was likely connected to OHC damage, as also suggested by the observation of partial loss of basal OHCs.

Isoflurane elevates ABR thresholds as demonstrated across various species (Cederholm et al., 2012; Ruebhausen et al., 2012; Stronks et al., 2010). In mice, the strongest effect was described for the most sensitive tonotopic frequency region (16 kHz) with approx. 16-dB baseline hearing threshold shift between measurements performed under ketamine/xylazine vs. isoflurane anesthesia (Cederholm et al., 2012). A further (10-dB) increase in the hearing thresholds was observed during a 1-h long exposure to low levels of isoflurane. Similarly, an approximately 27-dB hearing threshold shift was observed in rats upon prolonged isoflurane anesthesia (Ruebhausen et al., 2012). In our experimental conditions, we also observed a rise in ABR thresholds during a 2-h exposure to isoflurane, which however was less pronounced (approx. 5–8 dB SPL) and similar across all measured frequencies (Figure 1B). It has to be noted that hearing thresholds under isoflurane anesthesia may be very sensitive to small perturbations in local anesthetic concentrations determined by the isoflurane % vol. settings and the flow of anesthetics through the system (t.i. the speed of isoflurane delivery and removal from the mask), which, in addition to animal age or deviations in other parameters can account for some of the differences observed across studies. Compared to data acquired in mice of matching ages and background, the ABR thresholds under ketamine/xylazine anesthesia are typically approx. 10 dB lower in the 8–16 kHz range as compared to pre-exposure controls in the present study, measured right after isoflurane induction (see, e.g., WT controls in Oestreicher et al., 2024 vs. controls in the current study). As demonstrated, noise exposure under isoflurane anesthesia evokes smaller hearing threshold shifts with more recovery and lower hair cell loss (Kim et al., 2005) as compared to exposure in awake animals. While we do not have data from awake exposures under otherwise identical experimental conditions, based on our data of *in vitro* isoflurane experiments and afore mentioned *in vivo* data, we believe that isoflurane anesthesia resulted in partial protection against hearing loss.

Delayed and moderate auditory synaptopathy not accompanied by whole-cell membrane capacitance changes

Previous reports in awake exposed CBA mice demonstrated that noise-induced loss of ribbons and synapses occurs very quickly and is detected to almost full extent immediately after exposure (e.g., Liberman et al., 2015). Similarly, some immediate loss of ribbons or ribbon synapses was also detected immediately after noise-exposure in C57Bl/6J mice (Kim et al., 2019). In contrast, our data showed no loss of ribbons or ribbon synapses immediately after noise exposure apart from a slight tendency toward reduced synapses numbers for 96-dB group. The differences in the postsynaptic immunosignal could potentially be explained by the use of different immunohistochemical markers: while postsynaptic glutamate receptors may undergo internalization, an antibody against a scaffold protein Homer1, as used in the present study, may more faithfully report the presence and location of the postsynaptic boutons. However, this cannot account for the discrepancy observed presynaptically. In this aspect, our data are consistent with the observations in 6-week-old C57Bl/6J mice (of both sexes) exposed un-anesthetized to 90-dB 8-16 kHz noise band for 2-h, also detecting no ribbon loss immediately after exposure (Kaur et al., 2019). Several factors may affect the outcome of noise trauma, including noise paradigm, species, strain, age, sex, anesthesia (reviewed in Hickox et al., 2017), likely also dictating the speed of initial and likely very dynamic changes in the first hours following noise exposure.

In our experimental conditions, increasing noise levels from 92 to 96 dB did not further increase synaptopathic loss. This is consistent with recent data obtained in C57Bl/N mice exposed under reversible anesthetic (Blum et al., 2024). It is possible that larger (and possibly faster) acute damage (e.g., to stereocilia) upon higher noise levels effectively reduces the amount of hair cell activation during noise exposure and thus prevents further, more extensive excitotoxicity and there may be conditions, where this effect prevails. The idea that OHC damage may protect the IHC synapses has also been introduced in earlier studies (e.g., Fernandez et al., 2015; Liberman et al., 2015). Interestingly, while in the study by Blum et al. (2024) a larger loss of ribbons as compared to post-synapses was observed, in our experimental conditions the loss of ribbons scaled with the loss of ribbon synapses.

While IHC active zones are reportedly heterogeneous (Frank et al., 2009; Moser et al., 2023; Neef et al., 2018; Ohn et al., 2016; Özçete and Moser, 2021) and possibly a mixed (Jeffers et al., 2021; Suthakar and Liberman, 2021) rather than homogeneous subpopulation of active zones (with primarily large ribbons and large exocytic responses; Kujawa and Liberman, 2009; Özçete and Moser, 2021) may be initially lost upon noise trauma, a loss of approx. 20–23% of ribbons would still be expected to manifest as significant exocytic loss. However, this was not observed in our data. In fact, we detected a slight tendency toward increased exocytic efficiency in the basal IHCs of noise-traumatized mice. Our finding in the basal IHCs 2 weeks after noise exposure is consistent with the results obtained in young apical IHCs a day after exposure to noise evoking a transient ribbon loss (Boero et al., 2021), thus suggesting long-term effects of noise trauma on presynaptic IHC function. While we can at

present not exclude further (partial) recovery of ribbons at later time points in our experimental conditions, ribbons and ribbon synapses typically do not recover considerably beyond 2 weeks post-exposure (e.g., Jeffers et al., 2021; Kujawa and Liberman, 2009; Wu et al., 2019). The observed adaptive presynaptic IHC changes might very well fit into the observation of an overall increase in ribbon size after noise trauma (Blum et al., 2024; Boero et al., 2021; Kim et al., 2019; Liberman et al., 2015; Paquette et al., 2016; Wu et al., 2019) or multiplication of ribbons in a subpopulation of active zones not distinguishable under confocal microscopy (Lu et al., 2024; Moverman et al., 2023) as well as the observation of "hyperactive" auditory nerve fibers with higher peak- and also steady-state spiking rates in the synaptopathic regions of noise-traumatized CBA-mice (Suthakar and Liberman, 2021). Ribbon multiplication and hypertrophy is expected to result in an increase in the available synaptic vesicles per active zone, which would increase IHC membrane capacitance responses, but possibly also underlie noise-induced hyperactivity of a subpopulation of auditory nerve fibers (Moverman et al., 2023; Suthakar and Liberman, 2021). Ribbon reorganization upon noise trauma was shown to be very dynamic and complex (Moverman et al., 2023; Paquette et al., 2016); in addition to ribbon size, noise trauma further affects the exact positioning of synapses within the IHCs (Liberman et al., 2015; Paquette et al., 2016). Whereas the loss of ribbons was shown to require glutamatergic neurotransmission (Hu et al., 2020; e.g., Kim et al., 2019), noise-induced remodeling of ribbons seems to be glutamate-independent (Boero et al., 2021; Kim et al., 2019). Ribbon hypertrophy may represent a form of presynaptic homeostatic plasticity and was also observed in synaptic mutants with reduced synaptic release or (local) presynaptic calcium signal (Eckrich et al., 2019; Oestreicher et al., 2024). Further work is required to understand the mechanisms that drive ribbon dynamics upon noise exposure and beyond, possibly utilizing live imaging of ribbons in various conditions (Ismail Mohamad et al., 2024; Voorn et al., 2024).

The observations of this and prior studies suggest that the hyperactivity observed in higher centers of the auditory pathways may at least partially be related to changes in the auditory periphery, particularly at the first auditory synapse. These peripheral changes could contribute to the development of hyperacusis and tinnitus in noise-exposed ears by increasing central gain in the auditory pathway (Chambers et al., 2016; Mulders and Robertson, 2013; Salvi et al., 1990). However, the adaption processes may be insufficient to fully compensate for deficits in precise sound encoding in noisy environments (Bakay et al., 2018; Monaghan et al., 2020).

In the future, noise-induced alterations in synaptic function at the level of individual IHC synapses need to be investigated to understand how heterogeneous synapses (mal-)adapt to noise-induced damage of the IHC release machinery and which of the changes observed in SGN firing may originate presynaptically.

Acute effects of isoflurane on HC physiology and beyond

Isoflurane as a volatile gas anesthetic has many advantages compared to other commonly used anesthetics that need to be administered peritoneally, e.g., the ease of administration, consistency in the level of anesthesia and less animal handling during experiments. Isoflurane affects hearing function by increasing ABR thresholds and latencies and decreasing compound action potentials (Bielefeld, 2014; Stronks et al., 2010). In line with data from Cederholm et al. (2012), we suggest that this is not due to isoflurane effects on cochlear amplification but due to its action on synaptic calcium channels.

Traumatic noise exposure under isoflurane anesthesia leads firstly to less hearing loss and also to less damage to hair cells compared to the same noise exposure in awake animals (Chung et al., 2007; Kim et al., 2005). One proposed mechanism for this protective effect is the antagonistic effect of isoflurane on *N*-methyl-D-aspartate (NMDA) receptors, which may reduce the production of reactive oxygen species (ROS) associated with hearing loss (Chung et al., 2007; Kim et al., 2005). This hypothesis is supported by evidence of similar protective effects with other NMDA receptor antagonists (Chen et al., 2001; Ohinata et al., 2003). On the other hand, there is no evidence that ketamine can elicit such a protective effect although the drug mainly acts as an NMDA antagonist (Harada et al., 1999; Zorumski et al., 2016).

While different mechanisms of isoflurane action on various receptor types, e.g., Glycine-, GABA-, Kainate-, and NMDA-receptors are known (Dildy-Mayfield et al., 1996; Downie et al., 1996; Franks, 2008; Harrison et al., 1993), *in vitro* studies demonstrated an inhibition of the release machinery in hippocampal neurons with 1 mM isoflurane (Herring et al., 2009), and attenuation of voltage-gated sodium and calcium channels (Hemmings, 2009; Westphalen et al., 2011). Additionally, isoflurane inhibited glutamate release by reducing calcium influx and not by interfering with stimulus-vesicle-secretion coupling in hippocampal neurons (Baumgart et al., 2015; Herold et al., 2017). To investigate the effect on the calcium channels of inner hair cells, we performed patch clamp experiments on isolated hair cells treated with a clinically relevant concentration of 0.6 mM isoflurane. In the experiments we measured a reduction in calcium current amplitude and a trend toward reduced calcium-dependent exocytosis, analogous to the experiments with hippocampal neurons (Baumgart et al., 2015). Although we lack a direct comparison, reduced calcium currents and reduced glutamate transmission could be another factor how isoflurane could protect against excessive noise damage, a notion that should be tested in the future.

Conclusion

In this study we report for the first time how a noise-induced synaptopathy affects hair cell synaptic function in the most vulnerable part of the cochlea, typically affected by noise trauma. While we did not observe an immediate loss of synapses, this was significant and amounted to approximately 25–36% 2 weeks after exposure in the high-frequency regions of the cochlea (and 11–20% in the mid-cochlea). Given the expectation that the amount of synaptic exocytosis should scale with the number of presynaptic ribbons but in line with the results recently observed in a different study that probed the presynaptic function early after noise exposure, calcium current amplitudes and calcium-dependent exocytosis remained unaffected up to 200-ms depolarizations. These results suggest compensatory presynaptic mechanisms that enhance IHC exocytosis at the remaining ribbon synapses.

While our noise exposure recordings cannot be directly compared to experiments performed in awake animals, there might be a protective effect of isoflurane on the amount of damage inflicted by noise as shown in earlier studies. The finding of an 18% decrease in IHC calcium currents due to clinically-relevant isoflurane concentration may suggest an advantage for isoflurane and similar inhalation anesthetics during otological and neurosurgical procedures involving drilling of the skull and in particular the temporal bone, as they may provide some, but not complete, protection from acoustic trauma. While drilling of the skull is typically significantly shorter (20–45 min, longer in case of more complicated cases), it may be louder than noise levels used in this study and can easily exceed 100 dB SPL (Kylén et al., 1977; Yin et al., 2011), in particular when drilling on the ossicular chain or during cochleostomy in temporal bone studies (Jiang et al., 2007; Pau et al., 2007; Yu et al., 2014), and even when drilling cortical bone (Yin et al., 2011). The amount of noise exposure may vary between ear surgeries, depending on the location of drilling, the type of and the pressure applied to the drill, nevertheless, possible noise damage to the ear should always be taken into consideration (Banakis Hartl et al., 2017; Kylén et al., 1977; Parkin et al., 1980). The choice of anesthesia may influence the risk of noise-induced damage, with inhalation anesthesia possibly offering some protection.

Data availability statement

The raw data supporting the conclusions of this article will be made available by the authors, without undue reservation.

Ethics statement

The animal study was approved by University of Göttingen Board for animal welfare and the animal welfare office of the state of Lower Saxony. The study was conducted in accordance with the local legislation and institutional requirements.

Author contributions

DO: Conceptualization, Formal analysis, Funding acquisition, Investigation, Methodology, Supervision, Visualization, Writing – original draft, Writing – review & editing. AM: Formal analysis, Investigation, Methodology, Visualization, Writing – review & editing. AR: Formal analysis, Investigation, Writing – review & editing. CB: Formal analysis, Investigation, Writing – review & editing. LS: Formal analysis, Investigation, Writing – review & editing. NS: Data curation, Formal analysis, Methodology, Software, Writing – review & editing. TP: Conceptualization, Data curation, Formal analysis, Funding acquisition, Project administration, Resources, Supervision, Validation, Writing – original draft, Writing – review & editing.

Funding

The author(s) declare that financial support was received for the research, authorship, and/or publication of this article. This work was supported by grants of the German Research Foundation through the collaborative research center 889 (B09 to TP), and the Clinician Scientist Program "Cell Dynamics in Disease and Therapy" at the University Medical Center Göttingen (project number 413501650 to DO).

Acknowledgments

We would like to thank Ina Preuss, Sandra Gerke, and Sina Langer for excellent technical support. We would further like to thank Karl Herold from the Department of Anesthesiology at Cornell University New York, who provided expertise for designing the *in vitro* experiments with isoflurane.

Conflict of interest

The authors declare that the research was conducted in the absence of any commercial or financial relationships that could be construed as a potential conflict of interest.

Generative AI statement

The authors declare that no Generative AI was used in the creation of this manuscript.

Publisher's note

All claims expressed in this article are solely those of the authors and do not necessarily represent those of their affiliated organizations, or those of the publisher, the editors and the reviewers. Any product that may be evaluated in this article, or claim that may be made by its manufacturer, is not guaranteed or endorsed by the publisher.

Supplementary material

The Supplementary material for this article can be found online at: https://www.frontiersin.org/articles/10.3389/fncel.2024.1523978/full#supplementary-material

References

Bakay, W. M. H., Anderson, L. A., Garcia-Lazaro, J. A., McAlpine, D., and Schaette, R. (2018). Hidden hearing loss selectively impairs neural adaptation to loud sound environments. *Nat. Commun.* 9:4298. doi: 10.1038/s41467-018-06777-y

Banakis Hartl, R. M., Mattingly, J. K., Greene, N. T., Farrell, N. F., Gubbels, S. P., and Tollin, D. J. (2017). Drill-induced Cochlear injury during Otologic surgery: Intracochlear pressure evidence of acoustic trauma. *Otol. Neurotol.* 38, 938–947. doi: 10.1097/MAO.0000000000001474

Baumgart, J. P., Zhou, Z.-Y., Hara, M., Cook, D. C., Hoppa, M. B., Ryan, T. A., et al. (2015). Isoflurane inhibits synaptic vesicle exocytosis through reduced Ca2+ influx, not Ca2+− exocytosis coupling. *Proc. Natl. Acad. Sci.* 112, 11959–11964. doi: 10.1073/pnas.1500525112

Bendo, E., Resuli, M., and Metaxas, S. (2015). DPOAE measurements in comparison to audiometric measurements in hemodialyzed patients. *J. Acute Dis.* 4, 226–229. doi: 10.1016/j.joad.2015.04.009

Bielefeld, E. C. (2014). Influence of dose and duration of isoflurane anesthesia on the auditory brainstem response in the rat. *Int. J. Audiol.* 53, 250–258. doi: 10.3109/14992027.2013.858280

Blum, K., Schepsky, P., Derleder, P., Schätzle, P., Nasri, F., Fischer, P., et al. (2024). Noise-induced cochlear synaptopathy in C57BL/6 N mice as a function of trauma strength: ribbons are more vulnerable than postsynapses. *Front. Cell. Neurosci.* 18:5216. doi: 10.3389/fncel.2024.1465216

Boero, L. E., Payne, S., Gómez-Casati, M. E., Rutherford, M. A., and Goutman, J. D. (2021). Noise exposure potentiates exocytosis from Cochlear inner hair cells. *Front. Synaptic Neurosci.* 13:740368. doi: 10.3389/fnsyn.2021.740368

Bourien, J., Tang, Y., Batrel, C., Huet, A., Lenoir, M., Ladrech, S., et al. (2014). Contribution of auditory nerve fibers to compound action potential of the auditory nerve. *J. Neurophysiol.* 112, 1025–1039. doi: 10.1152/jn.00738.2013

Cederholm, J. M. E., Froud, K. E., Wong, A. C. Y., Ko, M., Ryan, A. F., and Housley, G. D. (2012). Differential actions of isoflurane and ketamine-based anaesthetics on cochlear function in the mouse. *Hear. Res.* 292, 71–79. doi: 10.1016/j.heares.2012.08.010

Chambers, A. R., Resnik, J., Yuan, Y., Whitton, J. P., Edge, A. S., Liberman, M. C., et al. (2016). Central gain restores auditory processing following near-complete Cochlear denervation. *Neuron* 89, 867–879. doi: 10.1016/j.neuron.2015.12.041

Chen, G.-D., Kong, J., Reinhard, K., and Fechter, L. D. (2001). NMDA receptor blockage protects against permanent noise-induced hearing loss but not its potentiation by carbon monoxide. *Hear. Res.* 154, 108–115. doi: 10.1016/S0378-5955(01)00228-3

Chung, J. W., Ahn, J. H., Kim, J. Y., Lee, H. J., Kang, H. H., Lee, Y. K., et al. (2007). The effect of isoflurane, halothane and pentobarbital on noise-induced hearing loss in mice. *Anesth. Analg.* 104, 1404–1408. doi: 10.1213/01.ane.0000261508.24083.6c

Cunningham, L. L., and Tucci, D. L. (2017). Hearing loss in adults. *N. Engl. J. Med.* 377, 2465–2473. doi: 10.1056/NEJMra1616601

Dildy-Mayfield, J. E., Eger, E. I., and Harris, R. A. (1996). Anesthetics produce subunit-selective actions on glutamate receptors. *J. Pharmacol. Exp. Ther.* 276, 1058–1065

Downie, D. L., Hall, A. C., Lieb, W. R., and Franks, N. P. (1996). Effects of inhalational general anaesthetics on native glycine receptors in rat medullary neurones and recombinant glycine receptors in Xenopus oocytes. *Br. J. Pharmacol.* 118, 493–502. doi: 10.1111/j.1476-5381.1996.tb15430.x

Eckrich, S., Hecker, D., Sorg, K., Blum, K., Fischer, K., Münkner, S., et al. (2019). Cochlea-specific deletion of Cav1.3 calcium channels arrests inner hair cell differentiation and unravels pitfalls of conditional mouse models. *Front. Cell. Neurosci.* 13:225. doi: 10.3389/fncel.2019.00225

Fernandez, K. A., Jeffers, P. W. C., Lall, K., Liberman, M. C., and Kujawa, S. G. (2015). Aging after noise exposure: acceleration of Cochlear synaptopathy in "recovered" ears. *J. Neurosci.* 35, 7509–7520. doi: 10.1523/JNEUROSCI.5138-14.2015

Fink, D. (2024). What is the safe noise exposure level to prevent noise-induced hearing loss? *J. Expo. Sci. Environ. Epidemiol.* 1–5. doi: 10.1038/s41370-024-00660-3 [Epub ahead of print].

Frank, T., Khimich, D., Neef, A., and Moser, T. (2009). Mechanisms contributing to synaptic Ca2+ signals and their heterogeneity in hair cells. *Proc. Natl. Acad. Sci. USA* 106, 4483–4488. doi: 10.1073/pnas.0813213106

Franks, N. P. (2008). General anaesthesia: from molecular targets to neuronal pathways of sleep and arousal. *Nat. Rev. Neurosci.* 9, 370–386. doi: 10.1038/nrn2372

Furman, A. C., Kujawa, S. G., and Liberman, M. C. (2013). Noise-induced cochlear neuropathy is selective for fibers with low spontaneous rates. *J. Neurophysiol.* 110, 577–586. doi: 10.1152/jn.00164.2013

Harada, H., Kelly, P. J., Cole, D. J., Drummond, J. C., and Patel, P. M. (1999). Isoflurane reduces N-methyl-D-aspartate toxicity in vivo in the rat cerebral cortex. *Anesth. Analg.* 89, 1442–1447. doi: 10.1213/00000539-199912000-00022

Harrison, N. L., Kugler, J. L., Jones, M. V., Greenblatt, E. P., and Pritchett, D. B. (1993). Positive modulation of human gamma-aminobutyric acid type a and glycine receptors by the inhalation anesthetic isoflurane. *Mol. Pharmacol.* 44, 628–632

Hemmings, H. C. (2009). Sodium channels and the synaptic mechanisms of inhaled anaesthetics. *Br. J. Anaesth.* 103, 61–69. doi: 10.1093/bja/aep144

Herold, K. F., Sanford, R. L., Lee, W., Andersen, O. S., and Hemmings, H. C. (2017). Clinical concentrations of chemically diverse general anesthetics minimally affect lipid bilayer properties. *Proc. Natl. Acad. Sci.* 114, 3109–3114. doi: 10.1073/pnas.1611717114

Herring, B. E., Xie, Z., Marks, J., and Fox, A. P. (2009). Isoflurane inhibits the neurotransmitter release machinery. *J. Neurophysiol.* 102, 1265–1273. doi: 10.1152/jn.00252.2009

Hickman, T. T., Hashimoto, K., Liberman, L. D., and Liberman, M. C. (2020). Synaptic migration and reorganization after noise exposure suggests regeneration in a mature mammalian cochlea. *Sci. Rep.* 10:19945. doi: 10.1038/s41598-020-76553-w

Hickox, A. E., Larsen, E., Heinz, M. G., Shinobu, L., and Whitton, J. P. (2017). Translational issues in cochlear synaptopathy. *Hear. Res.* 349, 164–171. doi: 10.1016/j.heares.2016.12.010

Hu, N., Rutherford, M. A., and Green, S. H. (2020). Protection of cochlear synapses from noise-induced excitotoxic trauma by blockade of Ca^{2+}—permeable AMPA receptors. *Proc. Natl. Acad. Sci.* 117, 3828–3838. doi: 10.1073/pnas.1914247117

Ismail Mohamad, N., Santra, P., Park, Y., Matthews, I. R., Taketa, E., and Chan, D. K. (2024). Synaptic ribbon dynamics after noise exposure in the hearing cochlea. *Commun. Biol.* 7, 421–413. doi: 10.1038/s42003-024-06067-y

Jeffers, P. W. C., Bourien, J., Diuba, A., Puel, J.-L., and Kujawa, S. G. (2021). Noise-induced hearing loss in gerbil: round window assays of synapse loss. *Front. Cell. Neurosci.* 15:9978. doi: 10.3389/fncel.2021.699978

Jiang, D., Bibas, A., Santuli, C., Donnelly, N., Jeronimidis, G., and O'Connor, A. F. (2007). Equivalent noise level generated by drilling onto the Ossicular chain as measured by laser Doppler Vibrometry: a temporal bone study. *Laryngoscope* 117, 1040–1045. doi: 10.1097/MLG.0b013e3180459a10

Johnson, S. L., and Marcotti, W. (2008). Biophysical properties of CaV1.3 calcium channels in gerbil inner hair cells. *J. Physiol.* 586, 1029–1042. doi: 10.1113/jphysiol.2007.145219

Kaur, T., Clayman, A. C., Nash, A. J., Schrader, A. D., Warchol, M. E., and Ohlemiller, K. K. (2019). Lack of Fractalkine receptor on macrophages impairs spontaneous recovery of ribbon synapses after moderate noise trauma in C57BL/6 mice. *Front. Neurosci.* 13:620. doi: 10.3389/fnins.2019.00620

Kim, J. U., Ahn, Y. S., Suh, J. K., and Chung, J. W. (2012). Effect of isoflurane on the hearing in mice. *Korean J. Audiol.* 16:14. doi: 10.7874/kja.2012.16.1.14

Kim, J. U., Lee, H. J., Kang, H. H., Shin, J. W., Ku, S. W., Ahn, J. H., et al. (2005). Protective effect of isoflurane anesthesia on noise-induced hearing loss in mice. *Laryngoscope* 115, 1996–1999. doi: 10.1097/01.mlg.0000180173.81034.4d

Kim, K. X., Payne, S., Yang-Hood, A., Li, S.-Z., Davis, B., Carlquist, J., et al. (2019). Vesicular glutamatergic transmission in noise-induced loss and repair of Cochlear ribbon synapses. *J. Neurosci.* 39, 4434–4447. doi: 10.1523/JNEUROSCI.2228-18.2019

Knight, K. R., Kraemer, D. F., Winter, C., and Neuwelt, E. A. (2007). Early changes in auditory function as a result of platinum chemotherapy: use of extended high-frequency audiometry and evoked distortion product Otoacoustic emissions. *J. Clin. Oncol.* 25, 1190–1195. doi: 10.1200/JCO.2006.07.9723

Kujawa, S. G., and Liberman, M. C. (2009). Adding insult to injury: cochlear nerve degeneration after "temporary" noise-induced hearing loss. *J. Neurosci.* 29, 14077–14085. doi: 10.1523/JNEUROSCI.2845-09.2009

Kujawa, S. G., and Liberman, M. C. (2015). Synaptopathy in the noise-exposed and aging cochlea: primary neural degeneration in acquired sensorineural hearing loss. *Hear. Res.* 330, 191–199. doi: 10.1016/j.heares.2015.02.009

Kurabi, A., Keithley, E. M., Housley, G. D., Ryan, A. F., and Wong, A. C.-Y. (2017). Cellular mechanisms of noise-induced hearing loss. *Hear. Res.* 349, 129–137. doi: 10.1016/j.heares.2016.11.013

Kylén, P., Stjernvall, J.-E., and Arlinger, S. (1977). Variables affecting the Drill-generated noise levels in ear surgery. *Acta Otolaryngol.* 84, 252–259. doi: 10.3109/00016487709123964

Li, Y., Yu, H., Zhou, X., Jin, L., Li, W., Li, G.-L., et al. (2022). Multiple sevoflurane exposures during the neonatal period cause hearing impairment and loss of hair cell ribbon synapses in adult mice. *Front. Neurosci.* 16:945277. doi: 10.3389/fnins.2022.945277

Liberman, M. C., and Kujawa, S. G. (2017). Cochlear synaptopathy in acquired sensorineural hearing loss: manifestations and mechanisms. *Hear. Res.* 349, 138–147. doi: 10.1016/j.heares.2017.01.003

Liberman, L. D., Suzuki, J., and Liberman, M. C. (2015). Erratum to: dynamics of cochlear synaptopathy after acoustic overexposure. *JARO J. Assoc. Res. Otolaryngol.* 16:221. doi: 10.1007/s10162-015-0514-z

Lin, H. W., Furman, A. C., Kujawa, S. G., and Liberman, M. C. (2011). Primary neural degeneration in the Guinea pig cochlea after reversible noise-induced threshold shift. *JARO J. Assoc. Res. Otolaryngol.* 12, 605–616. doi: 10.1007/s10162-011-0277-0

Liu, H., Lu, J., Wang, Z., Song, L., Wang, X., Li, G.-L., et al. (2019). Functional alteration of ribbon synapses in inner hair cells by noise exposure causing hidden hearing loss. *Neurosci. Lett.* 707:134268. doi: 10.1016/j.neulet.2019.05.022

Lu, Y., Liu, J., Li, B., Wang, H., Wang, F., Wang, S., et al. (2024). Spatial patterns of noise-induced inner hair cell ribbon loss in the mouse mid-cochlea. *iScience* 27:27. doi: 10.1016/j.isci.2024.108825

Meyer, A. C., Frank, T., Khimich, D., Hoch, G., Riedel, D., Chapochnikov, N. M., et al. (2009). Tuning of synapse number, structure and function in the cochlea. *Nat. Neurosci.* 12, 444–453. doi: 10.1038/nn.2293

Monaghan, J. J. M., Garcia-Lazaro, J. A., McAlpine, D., and Schaette, R. (2020). Hidden hearing loss impacts the neural representation of speech in background noise. *Curr. Biol.* 30, 4710–4721.e4. doi: 10.1016/j.cub.2020.09.046

Moser, T., Karagulyan, N., Neef, J., and Jaime Tobón, L. M. (2023). Diversity matters — extending sound intensity coding by inner hair cells via heterogeneous synapses. *EMBO J.* 42:e114587. doi: 10.15252/embj.2023114587

Moverman, D. J., Liberman, L. D., Kraemer, S., Corfas, G., and Liberman, M. C. (2023). Ultrastructure of noise-induced cochlear synaptopathy. *Sci. Rep.* 13:19456. doi: 10.1038/s41598-023-46859-6

Mulders, W. H. A. M., and Robertson, D. (2013). Development of hyperactivity after acoustic trauma in the guinea pig inferior colliculus. *Hear. Res.* 298, 104–108. doi: 10.1016/j.heares.2012.12.008

Müller, M., Hünerbein, K., von Hoidis, S., and Smolders, J. W. T. (2005). A physiological place–frequency map of the cochlea in the CBA/J mouse. *Hear. Res.* 202, 63–73. doi: 10.1016/j.heares.2004.08.011

Neef, J., Urban, N. T., Ohn, T.-L., Frank, T., Jean, P., Hell, S. W., et al. (2018). Quantitative optical nanophysiology of Ca2+ signaling at inner hair cell active zones. *Nat. Commun.* 9:290. doi: 10.1038/s41467-017-02612-y

Oestreicher, D., Chepurwar, S., Kusch, K., Rankovic, V., Jung, S., Strenzke, N., et al. (2024). CaBP1 and 2 enable sustained CaV1.3 calcium currents and synaptic transmission in inner hair cells. *eLife* 13:RP93646. doi: 10.7554/eLife.93646.3

Ohinata, Y., Miller, J. M., and Schacht, J. (2003). Protection from noise-induced lipid peroxidation and hair cell loss in the cochlea. *Brain Res.* 966, 265–273. doi: 10.1016/S0006-8993(02)04205-1

Ohn, T.-L., Rutherford, M. A., Jing, Z., Jung, S., Duque-Afonso, C. J., Hoch, G., et al. (2016). Hair cells use active zones with different voltage dependence of Ca2+ influx to decompose sounds into complementary neural codes. *Proc. Natl. Acad. Sci. USA* 113, E4716–E4725. doi: 10.1073/pnas.1605737113

Özçete, Ö. D., and Moser, T. (2021). A sensory cell diversifies its output by varying Ca2+ influx-release coupling among active zones. *EMBO J.* 40:e106010. doi: 10.15252/embj.2020106010

Paquette, S. T., Gilels, F., and White, P. M. (2016). Noise exposure modulates cochlear inner hair cell ribbon volumes, correlating with changes in auditory measures in the FVB/nJ mouse. *Sci. Rep.* 6:25056. doi: 10.1038/srep25056

Parkin, J. L., Wood, G. S., Wood, R. D., and McCandless, G. A. (1980). Drill- and suction-generated noise in mastoid surgery. *Arch. Otolaryngol. Chic. Ill* 106, 92–96. doi: 10.1001/archotol.1980.00790260024008

Parthasarathy, A., and Kujawa, S. G. (2018). Synaptopathy in the aging cochlea: characterizing early-neural deficits in auditory temporal envelope processing. *J. Neurosci.* 38, 7108–7119. doi: 10.1523/JNEUROSCI.3240-17.2018

Pau, H. W., Just, T., Bornitz, M., Lasurashvilli, N., and Zahnert, T. (2007). Noise exposure of the inner ear during drilling a Cochleostomy for Cochlear implantation. *Laryngoscope* 117, 535–540. doi: 10.1097/MLG.0b013e31802f4169

Pujol, R., Lenoir, M., Robertson, D., Eybalin, M., and Johnstone, B. M. (1985). Kainic acid selectively alters auditory dendrites connected with cochlear inner hair cells. *Hear. Res.* 18, 145–151. doi: 10.1016/0378-5955(85)90006-1

Ress, B. D., Sridhar, K. S., Balkany, T. J., Waxman, G. M., Stagner, B. B., and Lonsbury-martin, B. L. (1999). Effects of *cis*-platinum chemotherapy on otoacoustic emissions: the development of an objective screening protocol. *Otolaryngol. Head Neck Surg.* 121, 693–701. doi: 10.1053/hn.1999.v121.a101567

Ruebhausen, M. R., Brozoski, T. J., and Bauer, C. A. (2012). A comparison of the effects of isoflurane and ketamine anesthesia on auditory brainstem response (ABR) thresholds in rats. *Hear. Res.* 287, 25–29. doi: 10.1016/j.heares.2012.04.005

Salvi, R. J., Saunders, S. S., Gratton, M. A., Arehole, S., and Powers, N. (1990). Enhanced evoked response amplitudes in the inferior colliculus of the chinchilla following acoustic trauma. *Hear. Res.* 50, 245–257. doi: 10.1016/0378-5955(90)90049-U

Sebe, J. Y., Cho, S., Sheets, L., Rutherford, M. A., Gersdorff, H.Von, and Raible, D. W.. (2017). Ca2+-permeable AMPARs mediate glutamatergic transmission and excitotoxic damage at the hair cell ribbon synapse. *J. Neurosci.* 37, 6162–6175. doi: 10.1523/JNEUROSCI.3644-16.2017

Sergeyenko, Y., Lall, K., Liberman, M. C., and Kujawa, S. G. (2013). Age-related Cochlear Synaptopathy: an early-onset contributor to auditory functional decline. *J. Neurosci.* 33, 13686–13694. doi: 10.1523/JNEUROSCI.1783-13.2013

Sheppard, A. M., Zhao, D.-L., and Salvi, R. (2018). Isoflurane anesthesia suppresses distortion product otoacoustic emissions in rats. *J. Otol.* 13, 59–64. doi: 10.1016/j.joto.2018.03.002

Sonner, J. M., Werner, D. F., Elsen, F. P., Xing, Y., Liao, M., Harris, R. A., et al. (2007). Effect of isoflurane and other potent inhaled anesthetics on minimum alveolar concentration, learning, and the righting reflex in mice engineered to express alpha1 gamma-aminobutyric acid type a receptors unresponsive to isoflurane. *Anesthesiology* 106, 107–113. doi: 10.1097/00000542-200701000-00019

Stronks, H. C., Aarts, M. C. J., and Klis, S. F. L. (2010). Effects of isoflurane on auditory evoked potentials in the cochlea and brainstem of guinea pigs. *Hear. Res.* 260, 20–29. doi: 10.1016/j.heares.2009.10.015

Suthakar, K., and Liberman, M. C. (2021). Auditory-nerve responses in mice with noise-induced cochlear synaptopathy. *J. Neurophysiol.* 126, 2027–2038. doi: 10.1152/jn.00342.2021

Voorn, R. A., Sternbach, M., Jarysta, A., Rankovic, V., Tarchini, B., Wolf, F., et al. (2024). Slow kinesin-dependent microtubular transport facilitates ribbon synapse assembly in developing cochlear inner hair cells. *eLife* 13:RP98145. doi: 10.7554/eLife.98145.1

Wan, G., Gómez-Casati, M. E., Gigliello, A. R., Liberman, M. C., and Corfas, G. (2014). Neurotrophin-3 regulates ribbon synapse density in the cochlea and induces synapse regeneration after acoustic trauma. *eLife* 3:e03564. doi: 10.7554/eLife.03564

Westphalen, R. I., Kwak, N.-B., Daniels, K., and Hemmings, H. C. (2011). Regional differences in the effects of isoflurane on neurotransmitter release. *Neuropharmacology* 61, 699–706. doi: 10.1016/j.neuropharm.2011.05.013

World Health Organization (2021). World report on hearing. Geneva: World Health Organization. Avilable at: https://www.who.int/publications/i/item/9789240020481

Wu, P. Z., Liberman, L. D., Bennett, K., de Gruttola, V., O'Malley, J. T., and Liberman, M. C. (2019). Primary neural degeneration in the human cochlea: evidence for hidden hearing loss in the aging ear. *Neuroscience* 407, 8–20. doi: 10.1016/j.neuroscience.2018.07.053

Wu, P.-Z., O'Malley, J., de, V., and Liberman, M. C. (2021). Primary neural degeneration in noise-exposed human cochleas: correlations with outer hair cell loss and word-discrimination scores. *J. Neurosci.* 41, 4439–4447. doi: 10.1523/JNEUROSCI.3238-20.2021

Yin, X., Strömberg, A.-K., and Duan, M. (2011). Evaluation of the noise generated by otological electrical drills and suction during cadaver surgery. *Acta Otolaryngol.* 131, 1132–1135. doi: 10.3109/00016489.2011.600725

Yu, H., Tong, B., Zhang, Q., Zhu, W., and Duan, M. (2014). Drill-induced noise level during cochleostomy. *Acta Otolaryngol.* 134, 943–946. doi: 10.3109/00016489.2014.927591

Zorumski, C. F., Izumi, Y., and Mennerick, S. (2016). Ketamine: NMDA receptors and beyond. *J. Neurosci.* 36, 11158–11164. doi: 10.1523/JNEUROSCI.1547-16.2016

Zuccotti, A., Kuhn, S., Johnson, S. L., Franz, C., Singer, W., Hecker, D., et al. (2012). Lack of brain-derived neurotrophic factor hampers inner hair cell synapse physiology, but protects against noise-induced hearing loss. *J. Neurosci.* 32, 8545–8553. doi: 10.1523/JNEUROSCI.1247-12.2012

frontiers | Frontiers in Cellular Neuroscience

TYPE Original Research
PUBLISHED 29 January 2025
DOI 10.3389/fncel.2024.1450115

Check for updates

OPEN ACCESS

EDITED BY
Christian Keine,
University of Oldenburg, Germany

REVIEWED BY
Sunil Puria,
Harvard Medical School, United States
Alessandro Altoe,
University of Southern California, United States
Anders Fridberger,
Linköping University, Sweden

*CORRESPONDENCE
Marcel van der Heijden
✉ marcel.vdh.work@gmail.com

RECEIVED 16 June 2024
ACCEPTED 16 December 2024
PUBLISHED 29 January 2025

CITATION
Kondylidis K, Vavakou A and van der Heijden M (2025) The spatial buildup of nonlinear compression in the cochlea. *Front. Cell. Neurosci.* 18:1450115. doi: 10.3389/fncel.2024.1450115

COPYRIGHT
© 2025 Kondylidis, Vavakou and van der Heijden. This is an open-access article distributed under the terms of the Creative Commons Attribution License (CC BY). The use, distribution or reproduction in other forums is permitted, provided the original author(s) and the copyright owner(s) are credited and that the original publication in this journal is cited, in accordance with accepted academic practice. No use, distribution or reproduction is permitted which does not comply with these terms.

The spatial buildup of nonlinear compression in the cochlea

Kostas Kondylidis[1,2], Anna Vavakou[1,3] and Marcel van der Heijden[1]*

[1]Dept. Neuroscience, Erasmus MC, Rotterdam, Netherlands, [2]GERS-GeoEND, IFSTTAR, Université Gustave Eiffel, Nantes, France, [3]Institute for Auditory Neuroscience, University Medical Center, Göttingen, Germany

In the mammalian cochlea, the transduction from vibrations to inner hair cell receptor currents is preceded by a stage of mechanical pre-processing that involves a rapid, strongly nonlinear compression. The mechanisms by which the cochlea realizes this dynamic compression are still poorly understood. Previous work by our group suggested that compression does not occur locally, but is realized by a cascade of weakly nonlinear elements along the cochlear partition. The resulting progressive accumulation of nonlinearity was termed the spatial buildup of compression. Here we studied mechanical compression in the basal turn of the sensitive gerbil cochlea using optical coherence tomography. We recorded vibrations at multiple positions along the length of the cochlear partition. Such longitudinal studies were virtually impossible with previous techniques. Using a tailored two-tone stimulus we quantified the spatial profile of compression. We found that the amount of compression grew gradually in an intensity-dependent fashion along our measurement stretch, as we moved apically toward the place of maximum vibration. This gradual buildup of compression was not mirrored by a gradual reduction beyond the peak. In fact the amount of compression accumulated even beyond the peak. This asymmetric pattern supports the view that mechanical compression is realized in a cascaded, distributed fashion which hinges on the traveling wave nature of cochlear vibrations.

KEYWORDS

cochlear mechanics, basilar membrane, compression, traveling wave, distortion products

1 Introduction

In the mammalian ear, the huge (>100-dB) dynamic range of audible sounds is compressed to less than 40 dB to fit the much smaller dynamic range of inner hair cell transduction. The exact mechanisms underlying this mechanical sensitivity control are unknown, but outer hair cells play a crucial role; their loss causes a linearization of the cochlear response (Patuzzi et al., 1989; Ruggero and Rich, 1991).

Experimentally, nonlinear compression in the cochlea has been quantified by the slopes of input–output functions of basilar membrane vibrations. In a sensitive cochlea, the slopes observed at a single position can vary from linearity (1 dB/dB) well below the best frequency to values as low as 0.1 dB/dB above best frequency (e.g., Rhode, 2007). The strong frequency dependence also shows up in the nonlinear interaction between different frequency components. The response to one tone (probe) is suppressed by the introduction of another tone (suppressor), On the basilar membrane (BM), the amount of suppression depends in a nontrivial way on the frequencies of both the probe and the suppressor (e.g., Cooper, 1996).

Mechanical compression and its strong frequency dependence have a prominent effect on subsequent stages of the auditory pathway. Auditory nerve responses to single tones show frequency dependent growth rates consistent with single-tone BM responses

(Cooper and Yates, 1994), and two-tone suppression in auditory nerve responses (Abbas and Sachs, 1976; Delgutte, 1990) is generally consistent with two-tone suppression on the BM, including its complex frequency dependence. The classical psychoacoustic study of Wegel and Lane (1924) reported how the audibility of one tone (signal) is affected by the introduction of a second tone (masker). The frequency dependence of these masking data and later refinements (e.g., Zwicker and Jaroszewski, 1982) is again consistent with the suppression data on the BM, suggesting a strong role of cochlear nonlinearity in auditory off-frequency masking.

Most of the BM data described above were obtained in the base of the cochlea, but the corresponding effects in the auditory nerve data and psychoacoustics span a large range of frequencies. The entanglement of compression and frequency analysis thus appears to be a universal feature of mammalian hearing, and it is desirable to try and capture the complexity in terms of a limited number of unifying principles. This may be a first step toward understanding the physiological mechanisms. To be sure, several detailed cochlear models reproduce the basic frequency dependence of compression and suppression; early examples include Lyon (1982), Kanis and de Boer (1994), and Geisler and Sang (1995), but these models differ among them in many basic aspects. In our view it is helpful to transcend the realm of detailed models and rather try to formulate an overarching framework to explain the universal features of cochlear compression and suppression.

The basic features of compression are as follows (see also Robles and Ruggero, 2001; Cooper, 2004). At a given cochlear location the amount of compression, quantified by the slopes of input-out functions, depends strongly on stimulus frequency. The frequency dependent growth is observed not only when single tones are presented, but also when multiple frequencies are presented simultaneously (Versteegh and Van der Heijden, 2012). When viewed in the frequency domain, the entanglement is reflected by a strong intensity dependence of frequency selectivity (Rhode, 2007). Cochlear nonlinearity has been most extensively studied from recordings of basilar membrane (BM) vibrations in the basal turns, but more recently a similar frequency dependence of compression was reported in BM vibration in the second turn of the gerbil cochlea (2.5-kHz region; Meenderink et al., 2022). The main characteristics of cochlear compression at the level of the BM can be summarized as follows.

- Cochlear compression is very fast but not instantaneous (Cooper and Van der Heijden, 2016).
- It approximates a multiband gain control, meaning that sensitivity is more or less independently regulated in different frequency bands (Cooper, 2004; Robles and Ruggero, 2001).
- At high intensities the independence of frequency bands breaks down asymmetrically. Low-frequency components start to suppress the sensitivity to sounds at much higher frequencies (upward spread of masking; Wegel and Lane, 1924).
- At a given BM location the degree of compression, expressed as the slope in dB/dB of I/O functions, is strongly frequency dependent. Components more than ~1/2 octave below the best frequency show linear growth (1 dB/dB). With increasing frequency the slopes become increasingly more compressive (<1 dB/dB), and this trend continues beyond the best frequency (Rhode, 2007; Cooper et al., 2018).

Thus the nonlinear character of BM responses is largely restricted to a narrow band of frequencies around the best frequency, often called the "tip" of the tuning curve. When studying cochlear structures other than the BM, additional complexities are encountered. Superimposed onto the type of narrowband compression observed in the BM, mechanical responses inside the organ of Corti also show a wideband compression (Rhode and Cooper, 1996; Cooper and Dong, 2003; Gao et al., 2014; Cooper et al., 2018) that seems to have a different origin and is physiologically more robust (Strimbu et al., 2020). In the present study this wideband nonlinearity is only briefly touched upon and we will mainly restrict the analysis to the "classical," narrowly tuned, compression of BM vibrations.

A previous experimental study from our lab (Versteegh and Van der Heijden, 2013) analyzed the entanglement of frequency selectivity and compression by assessing the mutual suppression of different frequency components. The independent variation of the suppressor frequency and probe frequency resulted in a rich data set that was not easy to summarize. A large number of systematic effects were observed which at first glance lacked an obvious relationship. Further analysis, however, revealed that a marked simplification and unification of the bewildering set of observations could be achieved when invoking arguments based on cochlear tonotopy, i.e., the systematic dependence of frequency tuning on cochlear location. By invoking tonotopy, the frequency dependent effects could be interpreted in terms of the *spatial* distribution of nonlinear effects along the length of the BM. The analysis underscored the essential role of traveling waves in the explanation of the complexities of cochlear compression, an ingredient that had rarely been systematically discussed before, with the exception of a very early nonlinear model by Kim et al. (1973). Versteegh and Van der Heijden (2013) argued that "many seemingly unrelated aspects of compression and suppression are in fact consequences of the gradual accumulation of nonlinearity along the travel direction. Likewise, the complex phase effects were found to reflect systematic changes in the local propagation speed of traveling waves." They called this the *spatial buildup* of cochlear compression. A more recent analysis by Altoè et al. (2021) elaborates on these ideas.

The key feature of this conceptual framework is the concept of forward gain. At each point along the traveling wave, the gain with which the vibrations are conveyed to the next segment is variable, and depends on the local vibration amplitude. This is a form of negative feedback: larger local vibrations cause a reduction in the local forward gain and vice versa. From a functional perspective, the local character of the feedback allows it to be very fast—in principle as fast as the ability of single outer hair cells to convert their sensory input to a mechanical response. At the same time, the cascaded configuration allows the nonlinear contribution of each single outer hair cell to be very modest. Instead of burdening a single local structure with realizing an enormous (>50 dB) variation in sensitivity, a cascaded configuration distributes the work among a large number of hair cells, each of which need to adjust its gain by a small faction. For instance, a chain of 100 elements, each of which varies its gain by just 0.5 dB, results in a total gain variation of 50 dB. A cascaded configuration is in marked contrast to a set of discrete nonlinear oscillators (e.g., Jülicher et al., 2001), each of which would have to realize the large amount of gain variation observed in the sensitive cochlea.

One of the complexities of cochlear compression that finds a natural explanation in the conceptual framework of spatial buildup is the frequency dependence of the growth of compression. This is

illustrated in Figure 1 by comparing the normalized spatial vibration patterns for different sound intensities.

If compression is indeed achieved by a regulation of local forward gain (e.g., through variable damping) the amount of compression for a single tone is seen to gradually accumulate from base to apex. A simple "scaling" (tonotopy) argument then concludes the explanation of the frequency dependence of the slopes of I/O function at single BM positions. A key aspect is the continued accumulation of compression beyond the peak.

The experimental data that underpinned the spatial buildup of compression in the study of Versteegh and Van der Heijden (2013) existed of single-point vibration recordings on the BM. The spatial aspect was analyzed indirectly, by invoking "scaling." Specifically, uniform changes in stimulus frequency were used as a proxy for changing the longitudinal recording position. Likewise, recent experimental studies designed to test the spatial buildup of cochlear nonlinearity (Charaziak et al., 2020; Altoè and Charaziak, 2023) used "scaling" to extrapolate single-point BM data to spatial excitation patterns. The use of scaling is understandably popular among modelers, but its experimental basis is feeble. Neither its quantitative accuracy nor the scope of its validity has been subjected to dedicated tests. For this reason, Versteegh and Van der Heijden (2013) stressed the need for multipoint data to explore the spatial buildup of cochlear compression more directly. The present study presents such a spatial test.

We studied mechanical compression in the basal turn of the sensitive gerbil cochlea. The novelty in this work lies in the recording of vibration patterns at multiple longitudinal positions along the cochlear partition. The use of optical coherence vibrometry (OCT) for our experiments made these longitudinal recording series relatively straightforward; such spatial studies were extremely difficult with previous techniques (Ren, 2002). Using a tailored two-tone stimulus we accurately quantified the spatial profile of compression. We found the amount of compression to grow gradually in an intensity-dependent fashion along our measurement stretch, as we move apically toward the place of maximum vibration. Our results confirm and quantify the spatial buildup of compression, suggesting that outer hair cells realize mechanical compression in a cascaded, distributed fashion. This process of gradual accumulation critically depends on the traveling wave nature of cochlear vibrations.

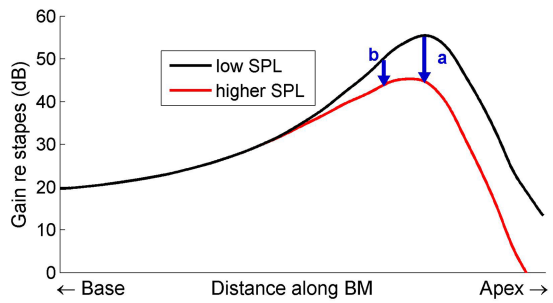


FIGURE 1
Schematic diagram illustrating how compressive growth of BM vibrations depends on longitudinal location. The curves represent the displacement patterns on the BM, normalized to middle-ear motion, evoked by a single tone presented at two intensities. The upper curve represents a low-intensity, linear, response. Increasing the intensity decreases the local forward gain of the traveling wave (e.g., by increased damping), resulting in a progressively smaller gain (lower curve). The arrows mark the amount of compression at two positions (b basal to a). The gradual divergence of the two curves causes the amount of compression to increase from base to apex.

A preliminary version of this work was presented at the 14th International Mechanics of Hearing Workshop in Helsingør, Denmark, July 2022.

2 Methods

2.1 General idea

Effective I/O functions were obtained by presenting a pair of equal-amplitude tones differing in frequency by 20 Hz. The resulting 20-Hz "beating" pattern affords a quasistatic variation of the sound pressure level (SPL). This dynamic method of obtaining I/O functions is efficient and robust, and 20 Hz is slow enough for the BM response to be free of hysteresis (Cooper and Van der Heijden, 2016). By recording BM responses along a longitudinal stretch (up to 700 µm long), we assessed how the nonlinear compression developed along the propagation direction of the traveling wave.

2.2 Animal preparation

Experiments were performed in accordance with the guidelines of the Animal Care and Use Committee at Erasmus MC. Sound evoked vibrations were recorded from the stapes and cochlear partition of healthy young gerbils ($n = 18$, aged 49–190 days, weight range 57–88 g). This includes experiments used for optimizing the stimulus and recording protocols. Animals were anesthetized using intraperitoneal injections of ketamine (80 mg/kg) and xylazine (12 mg/kg), with no recovery allowed at the end of the experiments. Maintenance (¼) doses of the anesthetic were given at intervals of between 10 and 60 min, as required to abolish pedal withdrawal reflexes. Animals were tracheotomized, but self-ventilating. Core temperatures were maintained at 38 degrees Celsius using a thermostatically controlled heating pad. The pinna and external meatus of the left ear was retracted and a 4×6 mm wide opening was made into the postero-lateral bulla to expose the basal aspects of the cochlea, including the stapes and the round window. A paper wick was used to prevent any buildup of fluid in the round window recess.

Experiments took place in a sound-proof chamber, with the animals supported in a goniometric cradle mounted on a vibration isolated table. Imaging and vibration measurements were made in the first turn of the cochlea, as viewed through the intact round window membrane. All measurements were made under open-bulla conditions, but the cochlea itself was intact.

2.3 OCT vibrometry

For a detailed description of the OCT recording system (see Cooper et al., 2018). An externally-triggered spectral domain optical coherence tomography system (ThorLabs Telesto III; central wavelength,

1,300 nm) was used for imaging and vibrometry. The system provided cross-sectional (B-scan) and axial images (A- scans and M-scans) phase-locked to an acoustic stimulation system (Tucker Davies Technologies system III) with a sampling rate of 111.6 kHz. Parallel series of intra-cochlear images (B-scans) were used to identify the anatomical structures of interest and to aim the beam for the recording of time series (M-scan) during acoustic stimulation. For the majority of recordings reported here, we aimed at the portion of the BM near the feet of the Deiters' cells, which is the point of largest motion of the BM (Cooper and Van der Heijden, 2018). An exception are the recordings shown in Figure 9, which were obtained from the junction of Deiters' cells and outer hair cells, near the center of the "hotspot" in Cooper et al. (2018). Figure 2 illustrates the targets of the vibration recordings.

For each animal, we recorded motion responses along one longitudinal stretch on the cochlea. The length of longitudinal stretches varied across experiments (290–695 μm), as the viewing angle through the round window was not identical. Consequently, the distance between recording positions (60–100 μm; 10 positions per cochlear stretch) also varied. Having the anatomical information from the B-scan images (radial and depth direction), and the distance between adjacent B-scans (longitudinal direction), we determined the Euclidian distance between neighboring measurement positions. Acoustic stimuli were subsequently presented, and vibration measurements (M-scans) were obtained for each position.

The acquisition of complete longitudinal series in a single cochlea required near-perfect mechanical and physiological stability. Buildup of fluid on the round window membrane, for instance, changes the optical path of the recording beam and disrupts the measurement series. Such artifacts were identified based on the comparison of pre- and pos-recording B-scans. Any deterioration in sensitivity was tested by a similar comparison of responses to low-SPL tone complexes. Data from 4 animals are shown in this study; they were selected for mechanical and physiological stability during complete recording series.

2.4 Acoustic stimulus and analysis of the vibrations

Stimuli generated by a personal computer with custom MATLAB-software were fed through a 24-bit D/A-channel (RX6; Tucker-Davis Technologies (TDT)) at 111.6 kHz. A programmable attenuator (PA5; TDT) followed by an amplifier (SA1; TDT) conditioned the signal before a speaker (CF1; TDT) played the stimuli. The speaker was connected to a sound delivery probe sealed to the ear canal with Vaseline. The sound system varied less than 4 dB in the 5–25 kHz range after correcting for the acoustic transfer of the probe.

To determine the best frequency of the recording locations, we used 41-component irregularly spaced (Zwuis) tone complexes presented at 20–70 dB SPL per tone. The best frequency of each recording position was determined by peak fitting of the magnitude-versus-frequency curve at the lowest SPL at which the data permitted such curve fitting (typically, 30 dB SPL). For the main recordings of the experiment we used 11.5-s long, equal amplitude tone pairs presented at 70 dB SPL per tone. The two simultaneous tones were spaced 20 Hz apart. The center frequency was typically chosen to match the best frequency of the most apical BM location within the longitudinal stretch available. The same stimulus was repeated while visiting each of the locations along the longitudinal stretch. If time permitted, the center frequency was varied in 1-kHz steps, repeating the longitudinal recording series for each frequency.

The basic analysis of the OCT vibrometry data is described in our previous work (Cooper et al., 2018). The cochlear vibrations in response to the tone pairs were first analyzed in the spectral domain: response components at the primary frequencies f_1 and f_2 of the stimulus as well as the odd intermodulation components at frequencies $f_1 \pm n\,(f_2\text{-}f_1)$, with $n = 1,2,\ldots$, were subjected to a Rayleigh test for significance of phase locking to the stimulus (Versteegh and Van der Heijden, 2012). Only

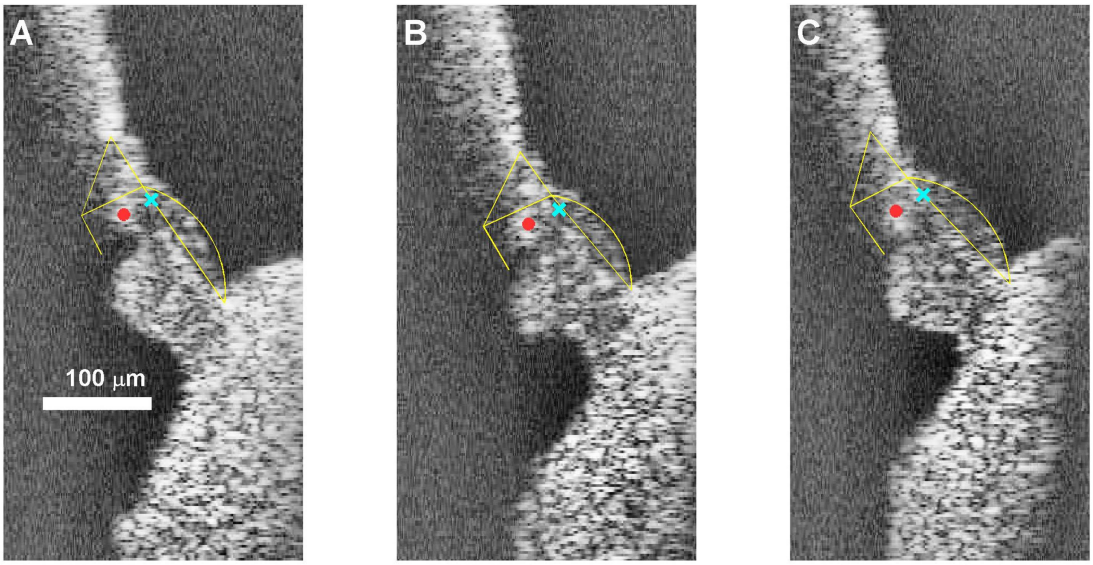


FIGURE 2
B-scans illustrating the targets of the vibration recordings in this study. **(A)** Most basal position in cochlea RG211043. **(B)** Near-middle (#6/10) position **(C)** most apical position. In all three panels, Yellow frames mark the location of the two zones of the basilar membrane, the pillar cells and the reticular lamina. The cyan X marks the recording position for basilar membrane recording, which constitute the majority of our data (Figures 4–8). The red dot shows the "hotspot" location (see text) that was used for the data in Figure 9. The scale bar applies to all three panels.

components with a confidence level $p < 0.001$ were admitted to the analysis. From the multi-tone response thus obtained, further analysis was performed in both the spectral and temporal domains as described in the Results section (see Figure 3).

2.5 Numerical simulation of compression

For the illustration of the data analysis in Results (Figure 3) we used a numerical simulation of a compressed two-tone response $y(t)$, equal to

$$y(t) = \frac{x(t)}{\sqrt[4]{E^2(t) + E_0^2}}, \quad (1)$$

where $x(t)$ is the two-tone stimulus

$$x(t) = \cos\omega_1 t + \cos\omega_2 t, \quad (2)$$

$E(t)$ is the envelope of the stimulus:

$$E(t) = 2\left|\cos\frac{1}{2}(\omega_2 - \omega_1)t\right| \quad (3)$$

and E_0 is a constant. This nonlinear map realizes an instantaneous power-law compression of 0.5 dB/dB, with a linear behavior at small ($<<E_0$) amplitudes (Van der Heijden, 2005).

3 Results

3.1 Analysis of a numerically compressed waveform

In order to explain the analysis of the two-tone responses, we illustrate the analysis steps using artificial data obtained by

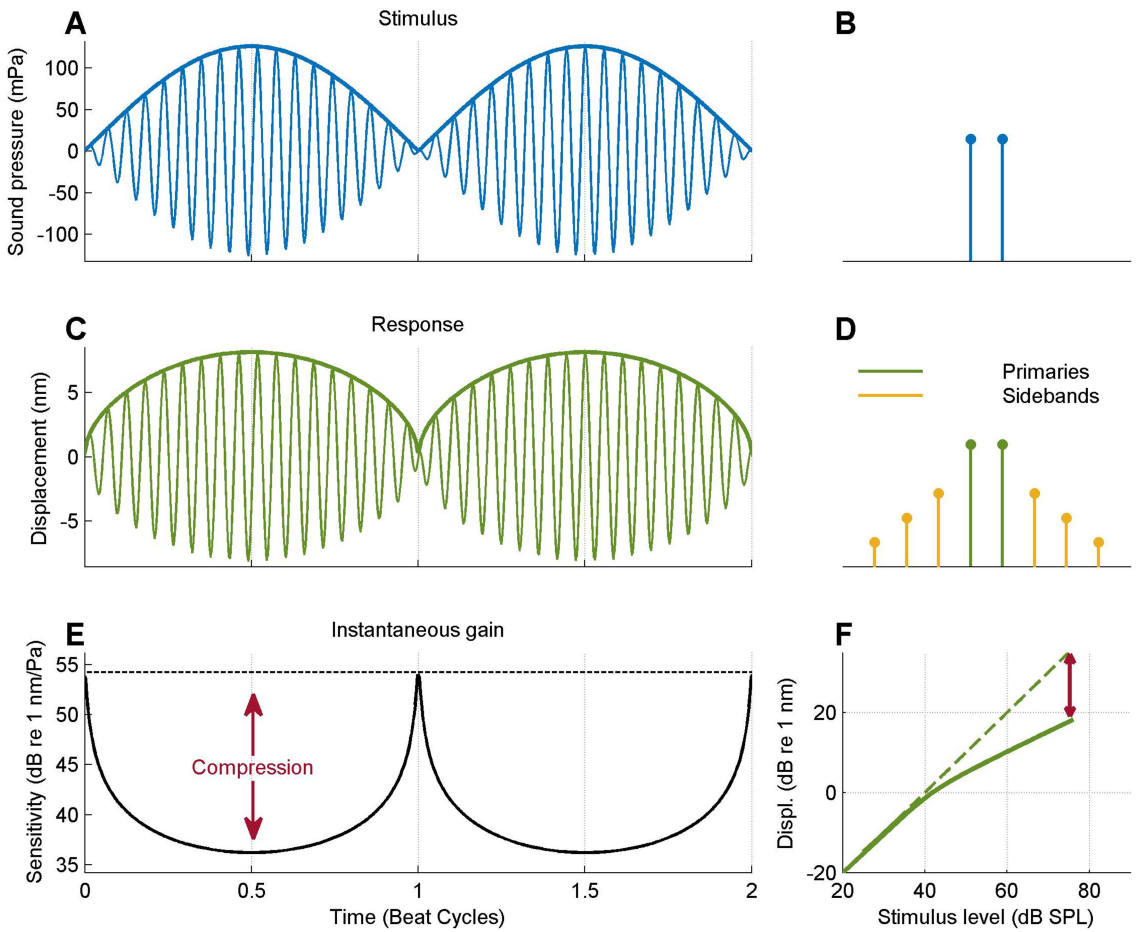


FIGURE 3
Data analysis illustrated using a model response. **(A)** Two-tone stimulus waveform (thin line) and envelope (thick line). The equal amplitude tones cause a periodic perfect cancelation. **(B)** Frequency spectrum of the stimulus, showing the two equal-amplitude primaries. **(C)** Simulated response waveform obtained by numerically compressing the waveform (0.5 dB/dB; see text) and response envelope (thick line). Note the flat-topped envelope compared to the stimulus. **(D)** Spectrum of the compressed waveform, consisting of the primary tones plus odd-order intermodulation products ("sidebands"). **(E)** Instantaneous gain or sensitivity, obtained by computing the ratio of response envelope and stimulus envelope. Red arrow, amount of instantaneous compression. **(F)** I/O curve obtained by plotting the response envelope against the stimulus envelope. Dashed line shows the extrapolation of the low-SPL linear I/O to higher SPLS; red arrow shows the amount of compression at the highest instantaneous SPL.

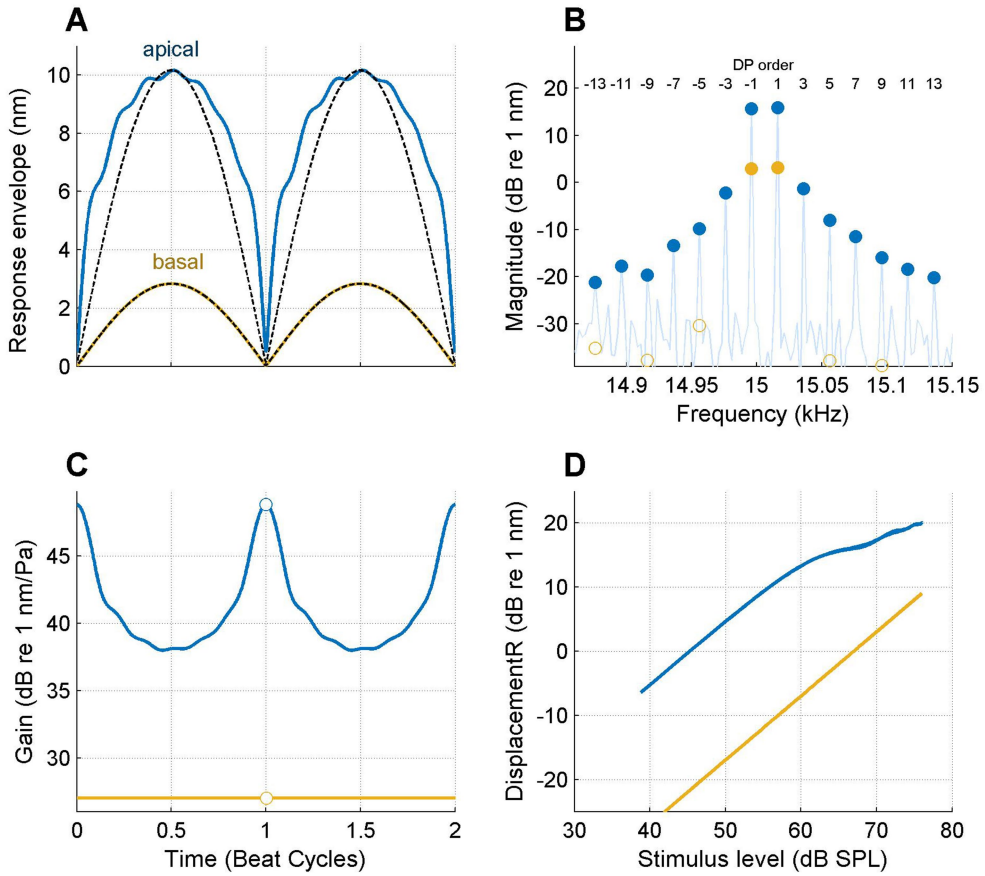


FIGURE 4
Longitudinal variation of nonlinear compression on the BM. Responses to the same 15-kHz tone pair are shown for two locations separated by 601 μm. **(A)** Response envelopes at the two locations as indicated in the graph. Black dashed lines: sinusoidal shapes for comparison. **(B)** Response spectrum. Filled symbols are stimulus or DP components that passed the $p = 0.001$ Rayleigh tests for significant phase locking to the stimulus (see text). Open symbols indicate components at the same frequencies that failed the test. **(C)** Instantaneous gain. **(D)** I/O curves. Best frequencies: 21.6 kHz (basal; ochre lines and symbols) and 15.4 kHz (apical; blue lines and symbols). Experiment RG211043.

subjecting an equal-amplitude tone pair to an instantaneous power-law compression with linear behavior at small amplitudes (see Methods, 2.4).

3.2 Buildup of compression toward the traveling wave peak

The two-tone stimulus (Figure 3A) shows a 20-Hz, beating pattern with sharp minima due to perfect periodic cancelation. The stimulus envelope is sinusoidal. The stimulus spectrum (Figure 3B)consists of the two stimulus components. The compressive transformation (see Methods, Equation 1) results in a response waveform (Figure 3C) with flattened envelope peaks; the envelope minima are undistorted as the transformation is linear at low amplitudes. The nonlinear transformation creates intermodulation products that occur as sidebands flanking the primaries in the response spectrum (Figure 3D). The instantaneous gain, expressed as the ratio of response envelope and stimulus envelope various in a periodic fashion (Figure 3E). The gain peaks at the stimulus minima and is maximally reduced at the envelope maxima. Instantaneous compression is defined as the difference between the time-varying gain and its peak value (red arrows in Figure 3E). I/O curves are obtained by plotting response envelope directly against stimulus envelope (Figure 3F) on a double logarithmic scale. This brings out the linear growth at low SPLs and the compressive (here, 0.5-dB/dB) growth at higher SPLs. Compression is indicated in Figure 3E (red arrow) as the difference in dB between the actual response magnitude and the value derived from linear extrapolation of the low-SPL I/O curve (dashed line in Figure 3E).

Figure 4 shows the analysis of vibrations recorded on the BM in the basal turn of a sensitive gerbil cochlea in response to a tone pair centered at 15 kHz. Each panel compares the responses to the same stimulus recorded at two longitudinal locations of the same cochlea separated by 601 μm. The response at the basal location (ochre curves in Figure 4) is linear, as reflected by the sinusoidal response envelope (Figure 4A), the absence of sidebands (Figure 4B), the constant gain (Figure 4C) and the linear, 1-dB/dB slope of the I/O curve

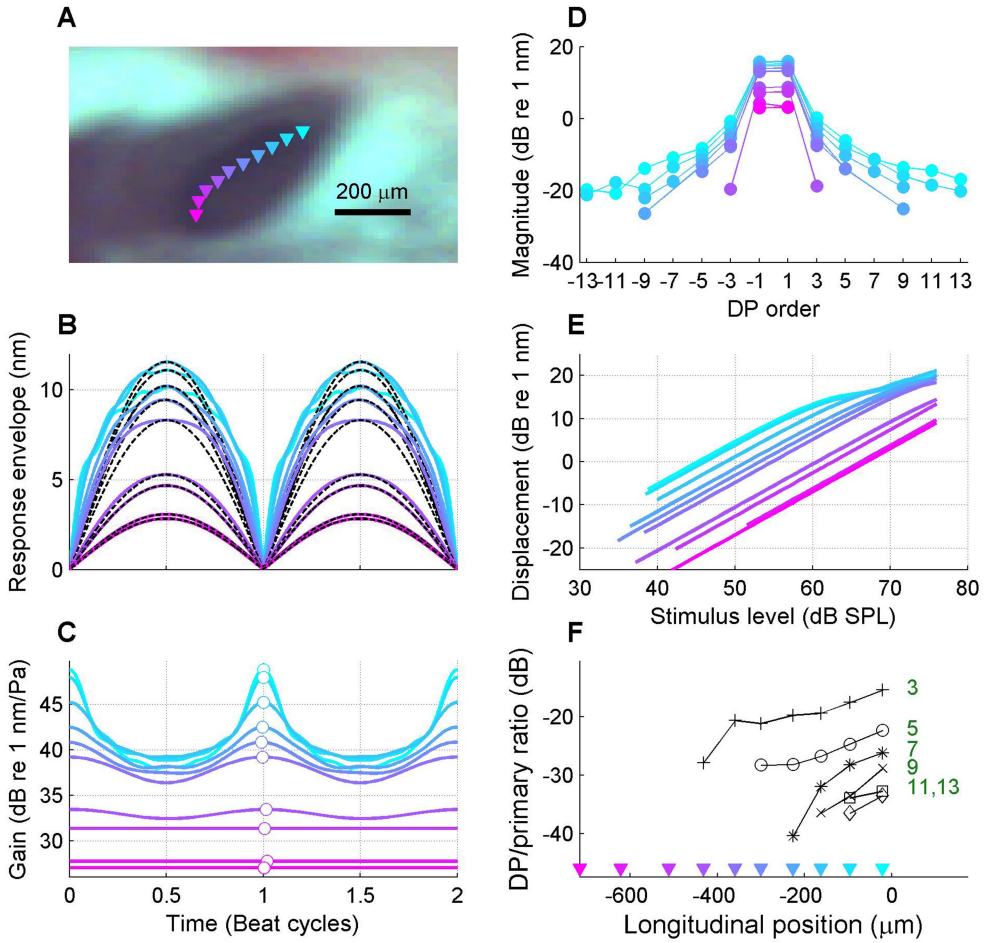


FIGURE 5
Gradual transition from linear to compressive responses along the length of the cochlea. **(A)** Video image of round window region with the OCT beam positions of the recording series superimposed (colored triangles). Best frequencies ranged from 23.8 down to 15.4 kHz. **(B)** Collection of BM response envelopes; stimulus frequency 15 kHz. Each curve shows data from a single location; the colors of the curves correspond to the beam positions indicated in panel **(A)**. **(C)** Corresponding time-varying gain curves. **(D)** Corresponding response spectra. **(E)** Corresponding I/O curves. **(F)** Magnitude ratio of distortion (sideband) components to primary components for each order of distortion, plotted as a function of longitudinal location from base to apex. This ratio serves as a metric for the local amount of compression (see text). The best place of the 15-kHz stimulus frequency is 0 μm by convention. Experiment RG211043.

(Figure 4D). In marked contrast, the recordings from the apical location show a flattened envelope (blue curves in Figure 4A); a large family of distortion products of order 3–13 (Figure 4B), a time-varying gain with a range of ~10 dB (Figure 4C) and an I/O function with a clear compressive segment at the higher SPLs (Figure 4D).

In order to illustrate the transition from a linear response to a strongly compressive response in more spatial detail, Figure 5 shows data obtained from a series of BM locations spanning a longitudinal stretch of 695 μm.

The data in Figure 5 confirm that the nonlinear compression of the response to the stimulus is gradually accumulating from the most basal location (0 μm), where the response is linear to the peak location of the 15-kHz stimulus (~700 μm), where the response is strongly compressive. In addition to the response envelopes, instantaneous gain curves, spectra and I/O curves (Figures 5B–E), a spectral metric of compression is shown in Figure 5F, namely the magnitude ratio of the sidebands to the primary components. The idea is that the sidebands reflect the nonlinear distortion that comes with the compression; the stronger the compression, the stronger the sideband-to-primary ratio. This holds for sidebands of all orders (Van der Heijden, 2005). This correlation is not only expected from theoretical considerations; it is also clearly visible in the data when comparing the response spectra (Figure 5D) to the amount of compression shown by the gain curves (Figure 5C). The sideband-to-primary ratio quantifies this correlation and provides a simple metric whose spatial variation can be assessed in a straightforward way.

A spatial depiction of the accumulation of compression can be realized by treating the different time points of the magnitude and gain curves as independent, "quasistatic" responses to single tones presented at different SPL values as they occur at consecutive time points. Specifically, the SPL values are extracted from the stimulus envelope (Figure 3A). The resulting spatial profiles are shown in

10.3389/fncel.2024.1450115

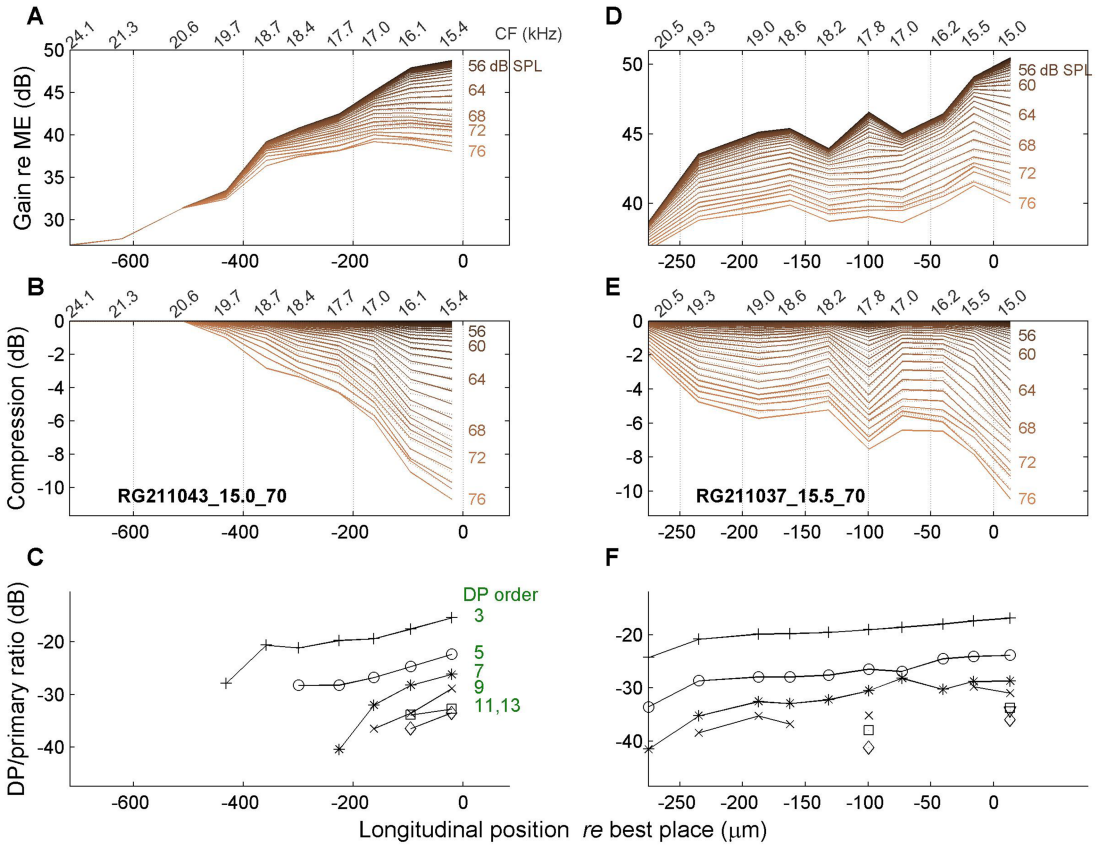


FIGURE 6
Spatial profiles of vibration magnitude, amount of compression and degree of distortion. In all panels, 0 μm corresponds to the best place of the stimulus frequency. **(A,D)** Magnitude of BM vibration, normalized to stapes motion, as a function of longitudinal location. Each curve represents a different SPL value (see text). **(B,E)** Corresponding spatial profiles of compression, i.e., the difference between gain at different SPL values and its maximum value occurring at the lowest SPL values. **(C,F)** Magnitude ratio of sidebands to primary components in the BM response as a function of longitudinal location. The order of the distortion is indicated in the graph. The two columns present data from different animals as indicated in panels **(B,E)**. Stimulus frequency, 15 kHz (left column); 15.5 kHz (right column).

Figures 6, 7 for four different cochleas. The upper rows (Figures 6A,D, 7A,D) show the magnitude of BM vibrations (normalized to stapes motion) as a function of longitudinal location. Each curve corresponds to a different SPL as indicated in the graphs.

The second row (Figures 6B,E, 7B,E) shows the amount of compression, i.e., the reduction of gain re the maximum value, as a function of longitudinal location. The spatial compression profiles in all four animals clearly show the systematic accumulation of compression along the direction of the traveling wave. The third row (Figures 6C,F, 7C,F) shows the corresponding sideband to primary ratio. This spectral metric of compression confirms the spatial buildup of nonlinear compression up to the peak of the traveling wave.

3.3 Nonlinear compression beyond the peak

The data of Figures 4–7 cover the growing flank of the traveling wave, i.e., the portion on the basal side of the peak. The observed growth of nonlinear compression from base to apex is consistent with the hypothesis of the spatial buildup of compression described in the Introduction, i.e., a framework in which the nonlinear compression at the peak is the result of a cascade of weakly compressive elements. On the other hand, the same data are also consistent with a very different mode of explanation in which compression reflects the operation of local nonlinear oscillators (e.g., Jülicher et al., 2001). The two modes of explanation, however, differ markedly in their prediction of the portion of the wave beyond the peak, at the apical flank. A cascade of nonlinear elements predicts that the amount of compression continues to accumulate beyond the peak. In contrast, a collection of uncoupled nonlinear oscillators predicts a gradual reduction of the amount of nonlinear compression beyond the peak. The latter, more symmetric pattern of compression is a direct consequence of the symmetric behavior of nonlinear oscillators: their response is maximally compressive at the best frequency and becomes more linear on both sides of the peak. To distinguish between the two scenarios, it is therefore necessary to study the spatial profile of compression at the apical flank of the peak of traveling wave.

In one experiment we managed to record responses to many stimulus frequencies at the same series of longitudinal locations on the BM. This allowed us to study nonlinear compression in both flanks of

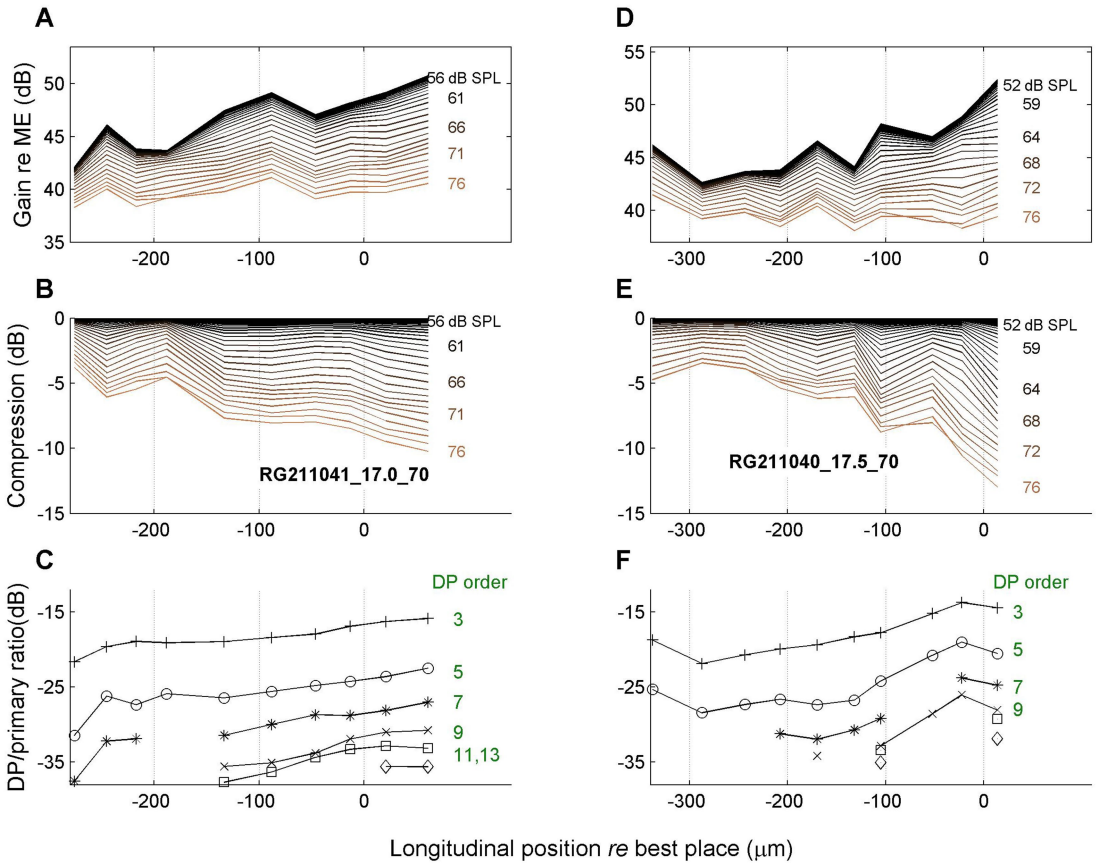


FIGURE 7
Spatial profiles as in Figure 7. Data of two more animals as indicated in panels **(B,E)**. Stimulus frequency, 17 kHz (left column); 17.5 kHz (right column).

the peak of the traveling wave. A representative set of results is shown in Figure 8.

The data in Figure 8 show that the spatial range over which compression occurred was ~800 μm, which is consistent with the longitudinal BM patterns of Ren (2002) and Fisher et al. (2012). With decreasing stimulus frequency (lower rows) the spatial peak and the compressive region shift toward the apex. The data in Figure 8 show a clear spatial asymmetry. The accumulation of nonlinear compression is gradual on the basal side of the peak (Figures 8F–H). Although the apical side of the peak also shows a return to linearity (zero compression in Figures 8E,F), this return to nonlinearity is much more abrupt. At first glance the abrupt disappearance of compression seems to contradict the hypothesis of a spatial buildup: in a cascade of compressive elements, the amount of compression can only accumulate. Any abrupt return to linearity ("plateau region," e.g., Rhode, 2007) can be explained by an independent propagation mode (e.g., a pressure wave; Olson, 1998) that becomes dominant in the region beyond the peak where the slow traveling wave has decayed. But a gradual return to linearity would require a cascade of expansive elements that undo the compression that the wave has accumulated so far. This appears like a very unlikely scenario. Alternatively, such a gradual return to linearity may be evidence against the spatial buildup of compression and point toward a collection of uncoupled nonlinear oscillators.

The return to linearity in Figures 8E,F, however, may also be a spurious effect caused by the data analysis, which starts in the spectral domain (see Methods, 2.4). The gain and compression profiles are ultimately derived from the set of primary and sideband components that pass the Rayleigh test. Now the steep decay of the wave beyond its peak (Figures 8A,B) causes the sidebands to disappear in the noise floor just before the primaries themselves disappear. By construction, the disappearance of sidebands shows up in the analysis as a return to linearity, even though it is really more of a measurement problem. It is here that the spectral metric of compression, the sideband-to-primary ratio (Figures 8I–L) comes to the rescue. First of all it confirms that the apparent return to linearity in Figures 8E,F is indeed caused by a sudden disappearance of the sidebands, caused by their failure to pass the Rayleigh test. Furthermore, the sideband-to-primary confirms the spatial asymmetry of the compression. The systematic growth in the basal flank (Figures 8G,H) is not mirrored by a systematic decline in the apical flank (Figures 8I,J). In the apical flank the sideband-to-primary ratio keeps growing or saturates, eventually followed by a sudden disappearance of the sidebands.

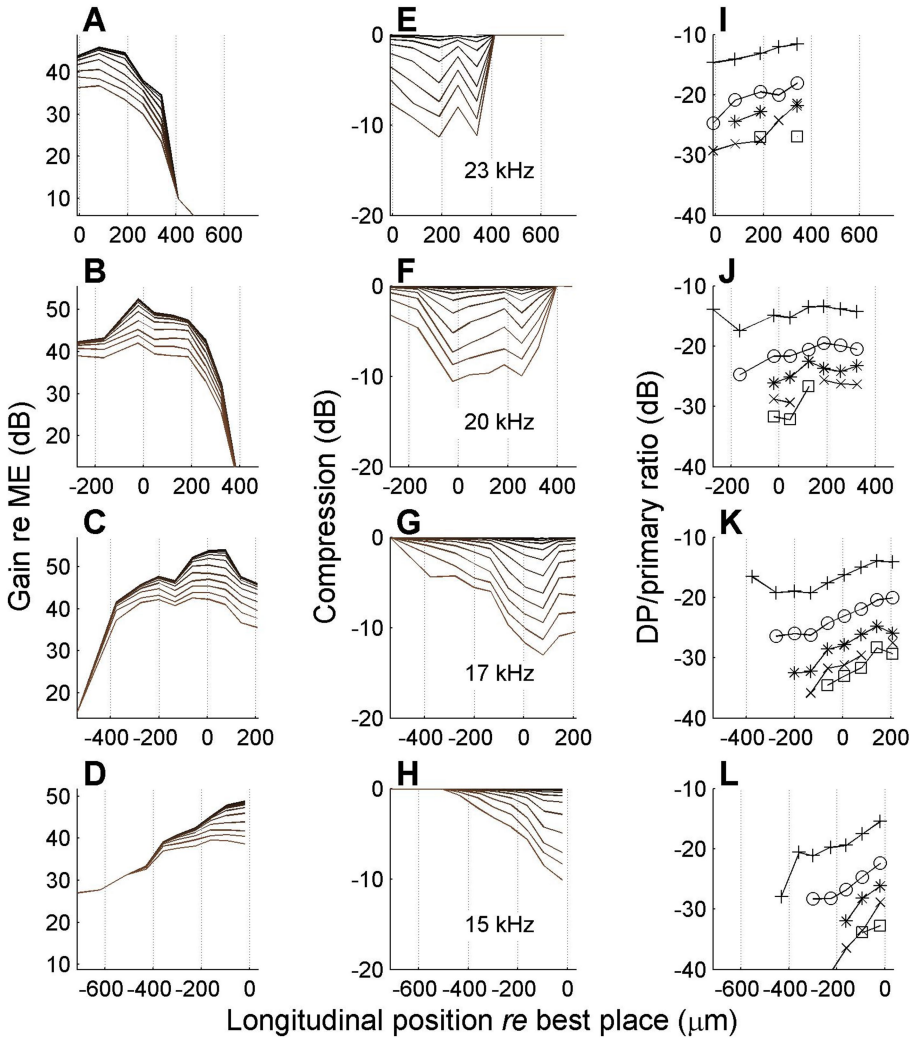


FIGURE 8
Spatial profiles of vibration magnitude, amount of compression and degree of distortion for different frequencies. Each row shows data obtained with a different stimulus frequency as indicated in the middle column. **(A–D)** Magnitude of BM vibration, normalized to stapes motion, as a function of longitudinal location. Different curves correspond to different SPLs as in Figure 6. **(E–H)** Corresponding spatial profiles of compression, i.e., the difference between gain at different SPL values and its maximum value occurring at the lowest SPL values. **(I,L)** Magnitude ratio of sidebands to primary components in the BM response as a function of longitudinal location. Animal RG211043. The physical range of longitudinal positions is identical in all panels, but, consistent with previous figures, 0 μm always corresponds to the best place of the stimulus frequency.

3.4 Nonlinear compression inside the organ of Corti

Figure 9 shows the same analysis as Figure 8, but now based on data recorded near the Deiters' cell / outer hair cell junction ("hotspot" in Cooper et al., 2018) of the same animal (see Figure 2). There are several differences with the BM data of Figure 8. The amount of compression is larger in the hotspot than in the BM; this is consistent with data in the literature (e.g., Gao et al., 2014; Cooper et al., 2018; Strimbu et al., 2020). The decline of compression on the apical side is more gradual in the hotspot than in the BM (compare Figures 9E,F to Figures 8E,F), causing the spatial compression profiles to be more symmetric (Figure 9F). The more gradual decline of compression is also reflected in the profiles of the sideband-to-primary ratio (Figures 9I–L): instead of saturating and disappearing toward the apex, they show a mild reduction before disappearing (Figures 9K,L).

4 Discussion

Overall, the nonlinear longitudinal patterns of BM vibration confirm the spatial buildup of compression inferred from single-point recordings by Versteegh and van der Heijden (2013). Nonlinear growth at best place is indeed the culmination of a gradual buildup of compressive nonlinearity during wave propagation. In the base of the gerbil the nonlinear region starts ~0.5 mm basal to the best place. This coincides with the slow part of the traveling wave, and is consistent with a framework in which the slow wave propagation is exploited as a means to regulate sensitivity, most likely by controlling the amount of local damping based on local vibration amplitude.

As discussed more comprehensively in Cooper et al. (2018) and Van der Heijden and Vavakou (2022), an attractive feature of this framework is the clear functional role of traveling waves in the

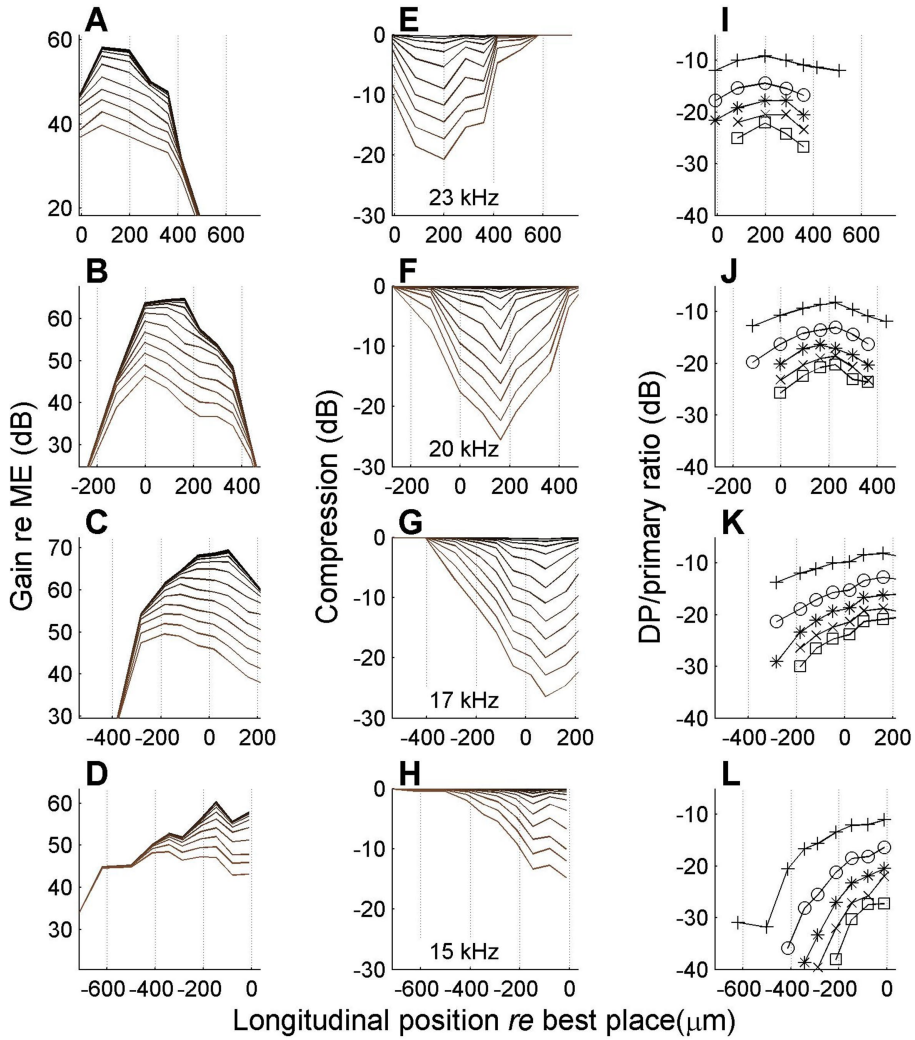


FIGURE 9
Spatial profiles of vibration magnitude, amount of compression and degree of distortion for different frequencies. Data obtained from the junction of Deiters' cells and outer hair cells. Layout identical to Figure 8, same cochlea.

cochlea. In an alternative scheme, a parallel or "filterbank" design, each local filter or oscillator would need to be strongly compressive by itself over a huge dynamic range, and without abrupt saturation (hard clipping). This is a nontrivial engineering feat to achieve in a local circuit. In contrast, in a series or "cascade" design the workload of dynamic compression is neatly shared among a spatially distributed collection of regulators. The cumulative operation of a cascade ensures that each local link has only a modest role in the final result. Mathematically speaking, the effect of a cascade is characterized by exponential behavior (as a function of place), and small variations of the exponential coefficient (local damping) suffice to realize a considerable regulation of net gain. This is both simple and efficient, but the cascade design comes with a price, namely a potential interference across frequency bands in the form of suppression (physiology) and masking (psychophysics). This is the breakdown of the independence of sensitivity control across frequency bands mentioned in the Introduction: high-intensity, lower-frequency sounds interfere with the audibility of sound at (much) higher frequencies, an effect known in psychoacoustics as "upward spread of masking" (Wegel and Lane, 1924).

Beyond the peak of the traveling wave, at its apical flank, the BM vibrations showed a continued accumulation of nonlinear compression. In our view this spatial asymmetry is the strongest indication of the inherent directionality of the dynamic range compression in the cochlea. It is clearly inconsistent with the view of the cochlea as a set of uncoupled oscillators. In fact it is not obvious that adapting such a "filterbank" framework by incorporating a coupling between adjacent oscillators (Duifhuis et al., 1986) would correctly reproduce the unidirectional character of compression observed in our data. On the other hand, the unidirectionality of the nonlinear compression as reported in this study does not necessarily imply the unidirectionality of the compressive mechanism itself. Two broad classes of models are both compatible with our findings. In the first class, the variable forward gain stems from a local regulation of damping; either negative (Neely and Kim, 1983; de Boer 1983) or positive (van der Heijden and Vavakou, 2022). Damping itself is not directional: it equally affects waves forward and reverse traveling

waves. In this class of models the unidirectional buildup stems from the unidirectional context in which damping does its job, namely, the traveling wave. In the second class of models, directionality is an inherent property of the compressive mechanism; it is built into the system in the sense that each segment passes its excitation only to its apical neighbor. Such a nonreciprocal transfer of excitation is not a waveguide in the classical sense. It is more properly described as a cascade. Cochlear models of this inherently unidirectional type include Kim et al. (1973), Lyon (1982), Geisler and Sang (1995), and experimental support for unidirectional coupling includes Ren (2004), and Ren et al. (2014). The findings of the current study, however, cannot be used to decide between the two classes of models.

The nonlinear compression profiles inside the organ of Corti (Figure 9) were also spatially asymmetric, but could not be characterized by a purely unidirectional accumulation of nonlinearity. This difference in the longitudinal compression profiles between BM and structures inside the organ of Corti is not easy to interpret, but it should be noted that the organ of Corti vibrations have a number of other features that present qualitative differences with the BM: compression over a much wider frequency range down to frequencies many octaves below the best frequency; the higher "threshold SPL" needed for the responses to become compressive over a wide frequency range; large phase leads *re* the BM in the low-frequency tail; the suppressibility of low-frequency responses by higher frequency tones (Gao et al., 2014; Cooper et al., 2018; Dewey et al., 2019). Importantly, the wideband compression, even though it disappears post mortem, is physiologically much more robust than the tuned, BM-like compression (Strimbu et al., 2020). These qualitative differences have led to the proposal that the wideband compression observed in the organ of Corti has a different origin than the "classical" narrowband BM nonlinearity and is more locally generated (Cooper et al., 2018; Dewey et al., 2019). The data in Figure 9 are consistent with such a local contribution to the nonlinearity. In this interpretation, the observed pattern of compression is a superposition of a propagating, tuned, nonlinearity and a local, untuned nonlinearity. The decay of the traveling wave beyond its peak causes its amplitude to fall below the threshold for the wideband compression, and this explains the slight reduction of compression beyond the peak, where only the propagating, tuned compression persists.

Our data are restricted to the high-frequency, basal region of the cochlea, and one may question whether our conclusions equally apply to other cochlear regions. It is sometimes argued that the mechanics in the apex is qualitatively different (e.g., Burwood et al., 2022; for a recent discussion of this "apical exceptionalism," see Recio-Spinoso et al., 2023). Although we have only presented basal data in this study, we believe that the spatial buildup of compression, and in particular the crucial role in cochlear nonlinearity played by the traveling wave, reflect generic cochlear mechanisms. The nonlinear phenomena naturally explained by the spatial buildup (Versteegh and van der Heijden, 2013) have been found throughout the cochlea. The systematic decrease of I/O slopes with frequency has been reported in the 2–3-kHz region (middle turn) of the gerbil BM (Meenderink et al., 2022) and in the 400-Hz region of the chinchilla tectorial membrane (Rhode and Cooper, 1996). Systematic decrease of the rate of suppression with increasing suppressor frequency has been found for the vibrations in the chinchilla apex for probe frequencies ranging from 200 to 800 Hz (Cooper and Rhode, 1996). The systematic effect of suppressor frequency on the rate of suppression in auditory nerve fibers has been found over a large range of characteristic frequencies, e.g., 17.8 kHz (Abbas and Sachs, 1976); 540 Hz (Delgutte, 1990). Its psychoacoustic counterpart, the effect of masker frequency on the growth of masking has been reported for a wide range of signal frequencies, as low as 600 Hz (Wegel and Lane, 1924) and 250 Hz (Glasberg and Moore, 1994). Many of these data suggest that the degree of nonlinearity is lower in the apex than in the base, but all of the data share the consistent feature that the slopes of I/O curves and the rate of suppression decrease with increasing frequency. Thus there appears to be no compelling reason to invoke qualitative differences in the mechanisms of compression between base and apex; they seem to share the same buildup of compression along the traveling wave.

Data availability statement

The raw data supporting the conclusions of this article will be made available by the authors, without undue reservation. Data underlying the figures in this article can be found at https://doi.org/10.6084/m9.figshare.28079705.

Ethics statement

The animal study was approved by the Ethische Commissie Dierproeven van het Erasmus MC. The study was conducted in accordance with the local legislation and institutional requirements.

Author contributions

KK: Methodology, Software, Visualization, Writing – original draft, Data curation, Investigation. AV: Data curation, Investigation, Methodology, Writing – review & editing. MH: Methodology, Conceptualization, Funding acquisition, Resources, Software, Supervision, Validation, Visualization, Writing – original draft.

Funding

The author(s) declare financial support was received for the research, authorship, and/or publication of this article. This work was supported by the Netherlands Organization for Scientific Research, ALW 823.02.018. AV was supported by a HORIZON TMA MSCA Postdoctoral Fellowship (OPTOCODE, grant agreement No. 101107675).

Acknowledgments

The authors thank Johan Pel for suggesting this collaboration.

Conflict of interest

The authors declare that the research was conducted in the absence of any commercial or financial relationships that could be construed as a potential conflict of interest.

Publisher's note

All claims expressed in this article are solely those of the authors and do not necessarily represent those of their affiliated organizations, or those of the publisher, the editors and the reviewers. Any product that may be evaluated in this article, or claim that may be made by its manufacturer, is not guaranteed or endorsed by the publisher.

References

Abbas, P. J., and Sachs, M. B. (1976). Two-tone suppression in auditory-nerve fibers: extension of a stimulus-response relationship. *J. Acoust. Soc. Am.* 59, 112–122. doi: 10.1121/1.380841

Altoè, A., and Charaziak, K. K. (2023). Intracochlear overdrive: characterizing nonlinear wave amplification in the mouse apex. *J. Acoust. Soc. Am.* 154, 3414–3428. doi: 10.1121/10.0022446

Altoè, A., Charaziak, K. K., Dewey, J. B., Moleti, A., Sisto, R., Oghalai, J. S., et al. (2021). The elusive cochlear filter: wave origin of cochlear cross-frequency masking. *J. Assoc. Res. Otolaryngol.* 22, 623–640. doi: 10.1007/s10162-021-00814-2

Burwood, G., Hakizimana, P., Nuttall, A. L., and Fridberger, A. (2022). Best frequencies and temporal delays are similar across the low-frequency regions of the guinea pig cochlea. *Sci. Adv.* 8:eabq2773. doi: 10.1126/sciadv.abq2773

Charaziak, K. K., Dong, W., Altoè, A., and Shera, C. A. (2020). Asymmetry and microstructure of temporal-suppression patterns in basilar-membrane responses to clicks: relation to tonal suppression and traveling-wave dispersion. *J. Assoc. Res. Otolaryngol.* 21, 151–170. doi: 10.1007/s10162-020-00747-2

Cooper, N. P. (1996). Two-tone suppression in cochlear mechanics. *J. Acoust. Soc. Am.* 99, 3087–3098. doi: 10.1121/1.414795

Cooper, N. P. (2004). "Compression in the peripheral auditory system" in Compression: from cochlea to cochlear implants. eds. S. P. Bacon, R. R. Fay and A. N. Popper (New York: Springer), 18–61.

Cooper, N. P., and Dong, W. (2003). "Baseline position shifts and mechanical compression in the apical turns of the cochlea" in Biophysics of the cochlea: from molecules to models, eds. Gumme, A. W., Dahlhof, E., Nowotny, M., Sherer, M. P. (Singapore:World Scientific). 261–270.

Cooper, N. P., and Rhode, W. S. (1996). Two-tone suppression in apical cochlear mechanics. *Audit. Neurosci.* 3, 123–134.

Cooper, N. P., and Van der Heijden, M. (2016). "Dynamics of Cochlear nonlinearity" in Physiology, psychoacoustics and cognition in normal and impaired hearing (Cham: Springer), 267–273.

Cooper, N. P., and Van der Heijden, M. (2018). Spatial profiles of sound-evoked vibration in the gerbil cochlea. AIP Conference Proceedings, vol. 1965, no. 1. eds.Başkent, D., Gaudrain, E., De Kleine, E., Wagner, A. and Lanting, C. Singapore: AIP Publishing.

Cooper, N. P., Vavakou, A., and Van der Heijden, M. (2018). Vibrationa hotspots reveal longitudinal funneling of sound-evoked motion in the mammalian cochlea. *Nat. Commun.* 9, 1–12. doi: 10.1038/s41467-018-05483-z

Cooper, N. P., and Yates, G. K. (1994). Nonlinear input-output functions derived from the responses of guinea-pig cochlear nerve fibres: variations with characteristic frequency. *Hear. Res.* 78, 221–234. doi: 10.1016/0378-5955(94)90028-0

De Boer, E. (1983). No sharpening? A challenge for cochlear mechanics. *The Journal of the Acoustical Society of America*, 73, 567–573.

Delgutte, B. (1990). Two-tone rate suppression in auditory-nerve fibers: dependence on suppressor frequency and level. *Hear. Res.* 49, 225–246. doi: 10.1016/0378-5955(90)90106-Y

Dewey, J. B., Applegate, B. E., and Oghalai, J. S. (2019). Amplification and suppression of traveling waves along the mouse organ of Corti: evidence for spatial variation in the longitudinal coupling of outer hair cell-generated forces. *J. Neurosci.* 39, 1805–1816. doi: 10.1523/JNEUROSCI.2608-18.2019

Duifhuis, H., Hoogstraten, H. W., Van Netten, S. M., Diependaal, R. J., and Bialek, W. (1986). Modelling the cochlear partition with coupled Van der pol oscillators. Peripheral auditory mechanisms: Proceedings of a conference held at Boston University, Boston, MA, August 13–16, 1985 (pp. 290–297). Springer: Berlin, Heidelberg.

Fisher, J. A., Nin, F., Reichenbach, T., Uthaiah, R. C., and Hudspeth, A. J. (2012). The spatial pattern of cochlear amplification. *Neuron* 76, 989–997. doi: 10.1016/j.neuron.2012.09.031

Gao, S. S., Wang, R., Raphael, P. D., Moayedi, Y., Groves, A. K., Zuo, J., et al. (2014). Vibration of the organ of Corti within the cochlear apex in mice. *J. Neurophysiol.* 112, 1192–1204. doi: 10.1152/jn.00306.2014

Geisler, C. D., and Sang, C. (1995). A cochlear model using feed-forward outer-hair-cell forces. *Hear. Res.* 86, 132–146. doi: 10.1016/0378-5955(95)00064-B

Glasberg, B. R., and Moore, B. C. (1994). Growth-of-masking functions for several types of maskers. *J. Acoust. Soc. Am.* 96, 134–144. doi: 10.1121/1.410473

Jülicher, F., Andor, D., and Duke, T. (2001). Physical basis of two-tone interference in hearing. *Proc. Natl. Acad. Sci.* 98, 9080–9085. doi: 10.1073/pnas.151257898

Kanis, L. J., and de Boer, E. (1994). Two-tone suppression in a locally active nonlinear model of the cochlea. *J. Acoust. Soc. Am.* 96, 2156–2165. doi: 10.1121/1.410157

Kim, D. O., Molnar, C. E., and Pfeiffer, R. R. (1973). A system of nonlinear differential equations modeling basilar-membrane motion. *J. Acoust. Soc. Am.* 54, 1517–1529. doi: 10.1121/1.1914449

Lyon, R. F. (1982). A computational model of filtering, detection, and compression in the cochlea. In ICASSP'82. IEEE International Conference on Acoustics, Speech, and Signal Processing, p. 1282–1285, IEEE.

Meenderink, S. W., Lin, X., Park, B. H., and Dong, W. (2022). Sound induced vibrations deform the organ of Corti complex in the low-frequency apical region of the gerbil cochlea for normal hearing: sound induced vibrations deform the organ of Corti complex. *J. Assoc. Res. Otolaryngol.* 23, 579–591. doi: 10.1007/s10162-022-00856-0

Neely, S. T., and Kim, D. O. (1983). An active cochlear model showing sharp tuning and high sensitivity. *Hear. Res.* 9, 123–130. doi: 10.1016/0378-5955(83)90022-9

Olson, E. S. (1998). Observing middle and inner ear mechanics with novel intracochlear pressure sensors. *J. Acoust. Soc. Am.* 103, 3445–3463. doi: 10.1121/1.423083

Patuzzi, R. B., Yates, G. K., and Johnstone, B. M. (1989). Outer hair cell receptor current and sensorineural hearing loss. *Hear. Res.* 42, 47–72. doi: 10.1016/0378-5955(89)90117-2

Recio-Spinoso, A., Dong, W., and Oghalai, J. S. (2023). On the tonotopy of the low-frequency region of the cochlea. *J. Neurosci.* 43, 5172–5179. doi: 10.1523/JNEUROSCI.0249-23.2023

Ren, T. (2002). Longitudinal pattern of basilar membrane vibration in the sensitive cochlea. *Proc. Natl. Acad. Sci.* 99, 17101–17106. doi: 10.1073/pnas.262663699

Ren, T. (2004). Reverse propagation of sound in the gerbil cochlea. *Nature Neuroscience*, 7, 333–334. doi: 10.1038/nn1216

Ren, T., He, W., Li, Y., Grosh, K., and Fridberger, A. (2014). Light-induced vibration in the hearing organ. *Sci. Rep.* 4:5941. doi: 10.1038/srep05941

Rhode, W. S. (2007). Basilar membrane mechanics in the 6–9 kHz region of sensitive chinchilla cochleae. *J. Acoust. Soc. Am.* 121, 2792–2804. doi: 10.1121/1.2718397

Rhode, W. S., and Cooper, N. P. (1996). Nonlinear mechanics in the apex of the chinchilla cochlea in vivo. *Audit. Neurosci.* 3, 101–121.

Robles, L., and Ruggero, M. A. (2001). Mechanics of the mammalian cochlea. *Physiol. Rev.* 81, 1305–1352. doi: 10.1152/physrev.2001.81.3.1305

Ruggero, M. A., and Rich, N. C. (1991). Furosemide alters organ of corti mechanics: evidence for feedback of outer hair cells upon the basilar membrane. *J. Neurosci.* 11, 1057–1067. doi: 10.1523/JNEUROSCI.11-04-01057.1991

Strimbu, C. E., Wang, Y., and Olson, E. S. (2020). Manipulation of the endocochlear potential reveals two distinct types of cochlear nonlinearity. *Biophys. J.* 119, 2087–2101. doi: 10.1016/j.bpj.2020.10.005

Van der Heijden, M. (2005). Cochlear gain control. *J. Acoust. Soc. Am.* 117, 1223–1233. doi: 10.1121/1.1856375

Van der Heijden, M., and Vavakou, A. (2022). Rectifying and sluggish: outer hair cells as regulators rather than amplifiers. *Hear. Res.* 423:108367. doi: 10.1016/j.heares.2021.108367

Versteegh, C. P., and van der Heijden, M. (2012). Basilar membrane responses to tones and tone complexes: nonlinear effects of stimulus intensity. *J. Assoc. Res. Otolaryngol.* 13, 785–798. doi: 10.1007/s10162-012-0345-0

Versteegh, C. P., and van der Heijden, M. (2013). The spatial buildup of compression and suppression in the mammalian cochlea. *J. Assoc. Res. Otolaryngol.* 14, 523–545. doi: 10.1007/s10162-013-0393-0

Wegel, R. L. F., and Lane, C. E. (1924). The auditory masking of one pure tone by another and its probable relation to the dynamics of the inner ear. *Phys. Rev.* 23, 266–285. doi: 10.1103/PhysRev.23.266

Zwicker, E., and Jaroszewski, A. (1982). Inverse frequency dependence of simultaneous tone-on-tone masking patterns at low levels. *J. Acoust. Soc. Am.* 71, 1508–1512. doi: 10.1121/1.387850

frontiers | Frontiers in Cellular Neuroscience

TYPE Review
PUBLISHED 19 May 2025
DOI 10.3389/fncel.2025.1568506

Check for updates

OPEN ACCESS

EDITED BY
Riccardo Fesce,
Humanitas University, Italy

REVIEWED BY
Ruili Xie,
The Ohio State University, United States
Hui Hong,
Creighton University, United States

*CORRESPONDENCE
Christian Keine
✉ christian.keine@uol.de

RECEIVED 29 January 2025
ACCEPTED 17 April 2025
PUBLISHED 19 May 2025

CITATION
Keine C and Englitz B (2025) Cellular and synaptic specializations for sub-millisecond precision in the mammalian auditory brainstem. *Front. Cell. Neurosci.* 19:1568506. doi: 10.3389/fncel.2025.1568506

COPYRIGHT
© 2025 Keine and Englitz. This is an open-access article distributed under the terms of the Creative Commons Attribution License (CC BY). The use, distribution or reproduction in other forums is permitted, provided the original author(s) and the copyright owner(s) are credited and that the original publication in this journal is cited, in accordance with accepted academic practice. No use, distribution or reproduction is permitted which does not comply with these terms.

Cellular and synaptic specializations for sub-millisecond precision in the mammalian auditory brainstem

Christian Keine[1,2]* and Bernhard Englitz[3]

[1]Carl von Ossietzky Universität Oldenburg, School of Medicine and Health Sciences, Division of Physiology, Oldenburg, Germany, [2]Research Center Neurosensory Science, Carl von Ossietzky Universität, Oldenburg, Germany, [3]Computational Neuroscience Lab, Donders Center for Neuroscience, Radboud University, Nijmegen, Netherlands

Audition in all animals relies on delicate sound pressure variations arriving at the ears, and these sound waves are intertwined representations of the complex auditory environment. The process of auditory perception and behavior is fundamentally based on reconstructive analysis, starting at the auditory nerve and culminating in the segregation of auditory sources through the extraction of spatial, spectral, and temporal cues. This analysis is made possible by specialized structures in the auditory brainstem that accurately represent and process incoming signals, preparing them for various downstream analyses. Decades of research have provided substantial insight into the morphological and physiological adaptations of specific auditory synapses, which we present and compare in the context of their presumed functions. Here, we focus on two parallel pathways originating from the auditory nerve and converging in the midbrain, featuring several well-studied synapses across multiple nuclei (cochlear nucleus, medial nucleus of the trapezoid body, ventral nucleus of the lateral lemniscus, and medial and lateral superior olivary nuclei). These synapses form the backbone of the high temporal precision of auditory representation, which is crucial for sound localization, speech comprehension, and speaker identification, each relying on subtle monaural or binaural cues. Finally, we highlight the similarities and differences with other brain areas that face challenges comparable to those of the auditory system.

KEYWORDS

synaptic transmission, auditory brainstem, specialization, cochlear nucleus (CN), medial nucleus of the trapezoid body (MNTB), ventral nucleus of the lateral lemniscus (VNLL), medial superior olive (MSO), lateral superior olive (LSO)

Introduction

The auditory system has the remarkable ability to effortlessly decode the complex mixture of sounds around us, locating a person's voice in a noisy room, appreciating the nuances of music, or reacting instantly to warning sounds. This ability hinges on the capacity to process information with extraordinary speed and precision, resolving details on a sub-millisecond timescale. Here, the principle of "form follows function" is illustrated at multiple levels across different species and brain structures. The neuronal processing architecture and cellular components of the system have been shaped by the specific requirements for speed, temporal precision, and faithful reconstruction. This process starts in the cochlea, where low-dimensional, high-sampling-rate sound pressure

fluctuations are converted into a high-dimensional, lower-sampling-rate representation of the electrical signals. The electrical information is then transmitted via the auditory nerve to the brainstem, where it is processed and relayed through various ascending pathways, beginning with the cochlear nucleus. Complex computations essential for sound localization and understanding intricate patterns, such as speech, must occur at these early stations, as microsecond accuracy cannot be maintained for long in a complex, constantly varying system, such as the brain. Maintaining a tight temporal relationship between spike times and the temporal features of sound is required to address these challenges. To meet these demands, several parallel pathways have evolved to extract specific sound features and serve complementary roles in sound processing, each with intriguing specializations. Failure to develop or maintain these extraordinary properties may lead to deficiencies such as auditory processing disorders, delayed language development in children, and deficiencies in sound localization, binaural hearing, speech perception in noise, and tinnitus (Whitton et al., 2011; Gourévitch et al., 2014; Kopp-Scheinpflug and Tempel, 2015; Kaplan et al., 2016; Shore and Wu, 2019; Jacxsens et al., 2022; Knipper et al., 2022).

In this review, we focus on the cellular and synaptic specializations of two parallel pathways: the binaural localization pathway starting from the bushy cells of the cochlear nucleus (CN), including the medial nucleus of the trapezoid body (MNTB), and the two primary binaural computation centers in the superior olivary complex (SOC), the medial and lateral superior olivary nuclei (MSO and LSO). Second, we highlight the specializations in a monaural "spectral feature extraction pathway," starting from the octopus cells in the CN and including globular cells in the ventral nucleus of the lateral lemniscus (VNLL). Both pathways start by receiving input from the auditory nerve and constitute major inputs to the inferior colliculus (IC), a midbrain integration center. We aimed to examine the current understanding of specializations at various levels, including morphological and physiological adaptations, and interpret them in light of their neuronal circuit function. We conclude this review by discussing the functional implications and significance of comparable specializations in other sensory systems.

Anatomical overview and present focus

Sound processing begins in the cochlea, where sound frequencies are spatially mapped along the basilar membrane. This low-dimensional representation of sound information at the sensory epithelium required the evolution of separate specialized pathways to reconstruct and analyze different aspects of the auditory environment, resulting in parallel streams of information. Frequency-specific information from the cochlea is relayed to the central auditory system via spiral ganglion neurons (SGNs), whose axons collectively form the auditory nerve (AN; Figure 1). These thick, myelinated axons are excitatory (glutamatergic) and make contact with various cell types in the CN (Ryugo and Fekete, 1982; Gómez-Nieto and Rubio, 2011), the starting point of multiple parallel processing pathways, each extracting different features of the auditory scene.

The two pathways selected in this review, both starting from the AN and converging in the IC, share the presence of giant axosomatic terminals, alongside more conventional synaptic boutons. The primary binaural pathway begins with the endbulb of the Held terminal onto CN bushy cells and includes the calyx of the Held—MNTB synapse, as well as the two binaural nuclei MSO and LSO for computing interaural time and level differences (ITDs and ILDs, respectively). This information is then used to localize sound sources in the horizontal plane and enables us to turn our eyes, head, and body toward a sound, which is fundamental to identifying threats, finding resources, and focusing attention. In parallel, a distinct monaural pathway specialized for processing spectrotemporal sound features is critical for detecting temporal gaps and onsets, which is critical for speech understanding and listening in noise (Verhey et al., 2003). This circuit includes octopus cells in the CN and endbulb-like synapses on globular cells in the VNLL (see Figure 2 and Table 1 for an overview). Its ability to precisely encode transient events also provides cues for segregating competing sounds in auditory scene analysis.

For each synapse, we analyze three core aspects that underpin their specialized functions. First, we investigate the general structure and morphology and compare the prevalence of these structures across species. Second, we focus on the organization and structure of synaptic inputs, as their number and location on the post-synaptic cell are critical in shaping the output. Third, we examine pre- and post-synaptic physiology, since regulating neurotransmitter release is essential for synaptic function and, together with the intrinsic properties of post-synaptic cells, provides the basis for information processing throughout the ascending auditory pathway. By comparing these features across different cell types and nuclei, we aim to illustrate the strategies employed by the auditory brainstem to achieve its remarkable processing capabilities.

The bushy cell—superior olive pathway

Sound localization relies on the computation of interaural differences and depends on the temporal acuity of signal transmission. The bushy cell—superior olive pathway is critical for preprocessing acoustic information and transmitting it to the centers of binaural integration. At the beginning of this pathway, bushy cells in the CN receive excitatory inputs from auditory nerve fibers via giant axosomatic terminals called the endbulbs of Held (Held, 1891; Brawer et al., 1974; Lorente de Nó, 1981; Ramon y Cajal, 1995). Bushy cells are excitatory (glutamatergic) and project to nuclei in the SOC including the MNTB, LSO, and MSO (Cant and Casseday, 1986). The MNTB features a second giant axosomatic terminal, the calyx of Held, which is perhaps the largest and best-studied synapse in the central nervous system. The two binaural nuclei, the MSO and LSO, compute ITDs and ILDs, respectively. Despite differences in axonal length and an additional chemical synapse in the MNTB, this pathway operates with astonishing accuracy and allows the detection of ILDs of <1 dB and ITDs as small as 10 μs, which is approximately 100 times faster than the average duration of an action potential

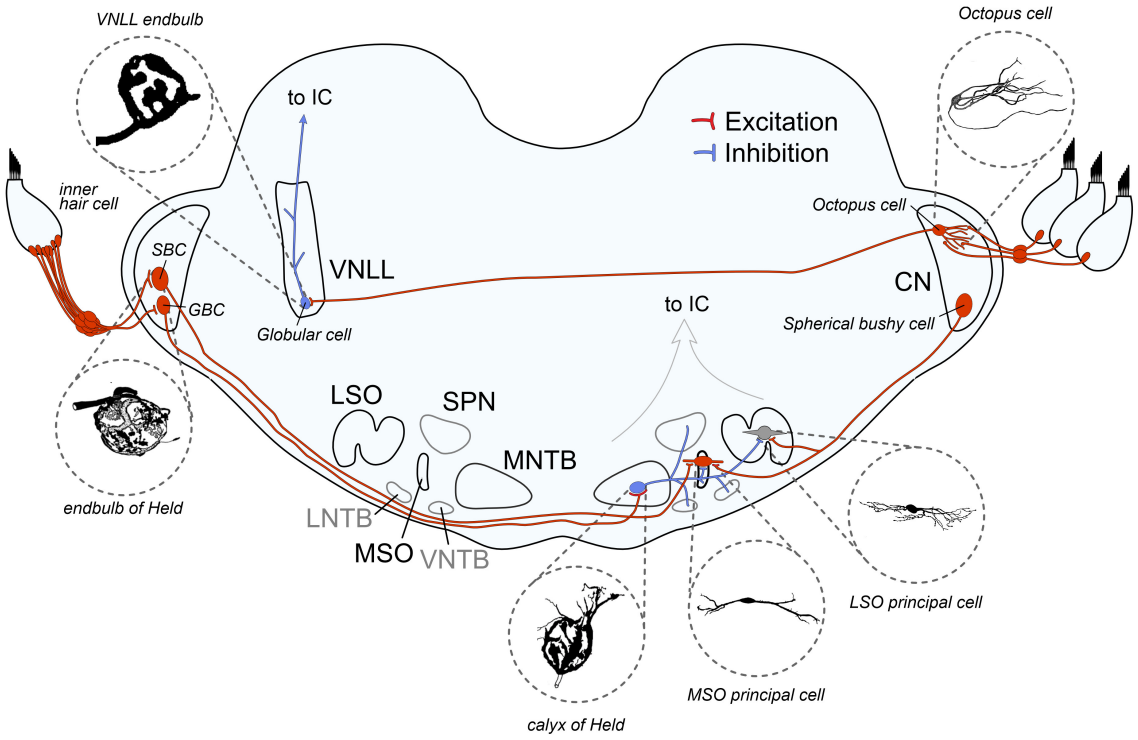


FIGURE 1
Schematic overview of auditory brainstem pathways discussed in this review. The binaural pathway includes two giant axosomatic terminals in the cochlear nucleus (CN) and the medial nucleus of the trapezoid body (MNTB) before making contact onto the binaural coincidence detector neurons that calculate interaural time and level differences in the medial and lateral superior olive (MSO and LSO, respectively). The monaural pathway to detect spectral sound features includes the octopus cells in the CN as monaural coincidence detectors and the giant axosomatic endbulb onto globular cells in the ventral nucleus of the lateral lemniscus (VNLL). LNTB, lateral nucleus of the trapezoid body; VNTB, ventral nucleus of the trapezoid body; SPN, superior olivary nucleus; IC, inferior colliculus; SBC, spherical bushy cell; GBC, globular bushy cell. Image sources: endbulb of Held: modified from Ryugo et al. (1998) with permission (John Wiley and Sons), calyx of Held: modified from Morest (1968) with permission (Copyright 1968 Springer-Verlag), VNLL endbulb: modified from Vater and Feng (1990) with permission (John Wiley and Sons), MSO principal cell: modified from Scott et al. (2005) (Copyright 2005 Society for Neuroscience), LSO principal cell: modified from Rietzel and Friauf (1998) with permission (John Wiley and Sons), Octopus cell: modified from Oertel et al. (2000) (Copyright 2000 National Academy of Sciences).

(Klumpp and Eady, 1956; Mills, 1958; Thavam and Dietz, 2019). Achieving this precision requires exceptional timing across several synapses, which has been achieved through cellular and synaptic specializations in this pathway.

The endbulb of Held

Structure and morphology

The first central synapse in this pathway is established between the auditory nerve (AN) and bushy cells in the CN. This specialized connection, known as the endbulb of Held, is conserved across the animal kingdom, including reptiles (Browner and Marbey, 1988; Szpir et al., 1990), birds (Carr and Boudreau, 1991; Köppl, 1994), and mammals such as mice (Limb and Ryugo, 2000), cats (Sento and Ryugo, 1989; Ryugo et al., 1998), dolphins (Malkemper et al., 2012), primates (Gómez-Nieto and Rubio, 2011), and humans (Adams, 1986) (see Ryugo and Parks, 2003 for review). Bushy cells are large, round cells characterized by one, or occasionally two, short, bushy dendritic trees (Brawer et al., 1974). In species with extended low-frequency hearing, such as cats and gerbils, bushy cells are classified into two types based on the distribution of endoplasmic reticulum when viewed under an electron microscope: spherical (SBC) and globular bushy cells (GBC) (Cant and Morest, 1979b; Tolbert and Morest, 1982). Although this morphological distinction is less evident in species like mice with limited low-frequency hearing (Lauer et al., 2013), a recent study confirmed the presence of distinct bushy cell types based on transcriptome analysis (Jing et al., 2025). In cats, SBCs are further subdivided into small and large cells based on their soma sizes, with distinct projection patterns to the LSO and MSO, respectively (Osen, 1969b; Cant and Casseday, 1986). This classification into small and large SBCs also appears in humans (Wagoner and Kulesza, 2009) but has not been observed in gerbils (Gleich et al., 1998; Bazwinsky et al., 2008) or guinea pigs (Hackney et al., 1990). SBCs and GBCs occupy different regions in the CN: SBCs are located rostrally in the anteroventral CN (AVCN), with the largest cells occupying the most rostral and ventral portion, where they respond to low-frequency sounds (Osen, 1969b; Brawer et al., 1974; Sento and Ryugo, 1989; Liberman, 1991). GBCs are clustered around the auditory nerve root, the caudal AVCN, and the posteroventral CN (PVCN) (Osen, 1969a; Cant and Morest, 1979a; Tolbert et al., 1982; Wagoner and Kulesza, 2009).

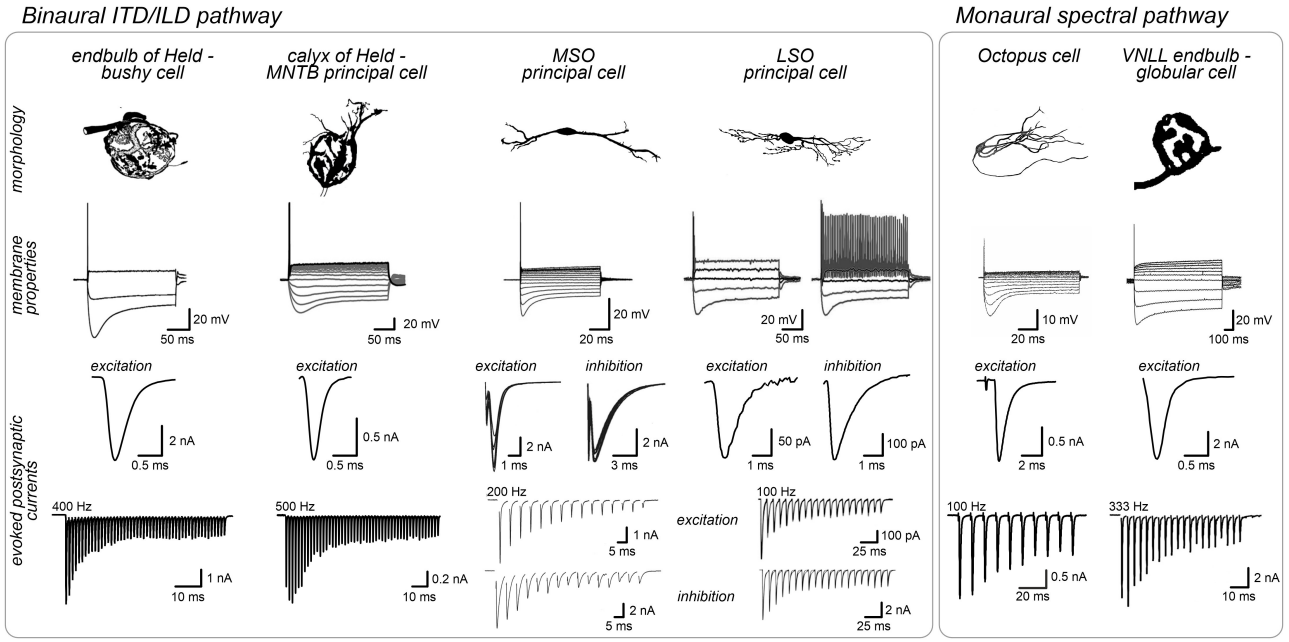


FIGURE 2
Shared structural and physiological adaptations facilitate rapid signal processing across auditory brainstem pathways. Neurons specialized for high-fidelity synaptic transmission such as bushy cells, MNTB neurons and VNLL globular cells often feature large round cell bodies targeted by giant axosomatic terminals (endbulbs/calyces) that evoked strong and rapid synaptic currents. These cells typically have moderate input resistance. In contrast, neurons acting as coincidence detectors, like MSO and LSO principal neurons (binaural pathway) or octopus cells (monaural pathway) tend to have more complex cell morphologies, integrate multiple smaller inputs along their dendrites and exhibit exceptionally fast membrane properties (low input resistance, fast time constant) ideally suited for precise temporal integration of fast synaptic currents. Post-synaptic current amplitudes are illustrative and depend on experimental conditions, thus limiting a direct comparison between studies. Image sources: endbulb of Held: morphology modified from Ryugo et al. (1998) with permission (John Wiley and Sons), membrane properties modified from Nerlich et al. (2014b), synaptic currents modified from Xie and Manis (2017); calyx of Held: morphology modified from Morest (1968) with permission (Copyright 1968 Springer-Verlag), membrane properties modified from Weimann et al. (2024), synaptic currents modified from Keine et al. (2022); MSO, morphology and membrane properties modified from Scott et al. (2005) (Copyright 2005 Society for Neuroscience), synaptic currents modified from Couchman et al. (2010); LSO, morphology modified from Rietzel and Friauf (1998) with permission (John Wiley and Sons), membrane properties modified from Haragopal and Winters (2023) (CC BY 4.0), synaptic currents modified from Pilati et al. (2016) and Garcia-Pino et al. (2017). Octopus cell: modified from Oertel et al. (2000) (Copyright 2000 National Academy of Sciences), membrane properties: modified from Golding et al. (1999) (Copyright 1999 Society for Neuroscience), synaptic currents modified from Cao and Oertel (2010) (Copyright 2010 The American Physiological Society); VNLL: morphology modified from Vater and Feng (1990) with permission (John Wiley and Sons), membrane properties modified from Caspari et al. (2015), synaptic currents modified from Kladisios et al. (2022).

Despite being part of the same neuronal circuit, SBCs and GBCs have distinct projection targets. SBCs project to the MSO (bilaterally) and the ipsilateral LSO (Osen, 1969b; Cant and Casseday, 1986). In contrast, GBCs primarily target the contralateral MNTB, via the large calyx of Held, while also sending projections to the ipsilateral LSO (Harrison and Warr, 1962; Tolbert et al., 1982; Smith et al., 1991).

Organization of synaptic inputs

The number, strength, and distribution of synaptic inputs on the post-synaptic cell are critical for shaping the post-synaptic output. Specifically, the probability of spike generation depends on these properties and generally increases with the number, strength, and proximity of synaptic inputs to each other and the soma.

The number of endbulb inputs on bushy cells can vary significantly depending on the cell type, species, and location within the CN. In cats, the largest SBCs, which are tuned to low frequencies and located in the rostral pole of the AVCN, receive input from only 1–2 large endbulbs (Brawer and Morest, 1975; Rouiller et al., 1986; Sento and Ryugo, 1989; Ryugo and Sento, 1991; Jones et al., 1992), whereas in mice, SBCs are contacted by approximately 2–4 endbulbs (Cao and Oertel, 2010; Wright et al., 2014). In contrast, GBCs receive substantially more endbulb inputs, ranging from 5–12 in mice (Cao and Oertel, 2010; Spirou et al., 2023) to approximately 20 in cats, although some cells can receive up to 60 endbulb inputs (Liberman, 1991; Ostapoff and Morest, 1991; Spirou et al., 2005). Further complexity exists in mice, where multiple endbulbs contacting an individual BC can originate from different SGN subtypes (Wang et al., 2021; Wong et al., 2025) and vary significantly in size and synaptic strength, resulting in 1–2 dominant suprathreshold inputs alongside multiple smaller endbulb inputs (Spirou et al., 2023). However, in cats, individual bushy cells receive inputs with similar morphologies, presumably from the same SGN subtype (Sento and Ryugo, 1989; Ryugo and Sento, 1991). Despite being a large axosomatic synapse, the endbulb's intricate morphology allows individual swellings to form connections with the somata and dendrites of nearby neurons, creating neuronal clusters; however, their physiological role remains unclear (Cant and Morest, 1979b; Smith and Rhode,

1987; Ostapoff and Morest, 1991; Ryugo and Sento, 1991; Ryugo et al., 1996; Spirou et al., 2005; Gómez-Nieto and Rubio, 2009). The endbulb's exceptional size accommodates many individual release sites (active zones, AZ), ranging from 150 in rats (Nicol and Walmsley, 2002) to 500–2,000 in cats (Cant and Morest, 1979b; Ryugo and Fekete, 1982; Ryugo et al., 1996). Despite the large morphological scale of the terminal, the ultrastructure of individual AZs resembles that found in conventional bouton synapses, containing approximately 2–4 "docked" vesicles ready for release (Ryugo et al., 1996; Nicol and Walmsley, 2002; Ryugo et al., 2006; Lin et al., 2011; Mendoza Schulz et al., 2014). Consequently, the endbulb possesses a substantial readily-releasable pool (RRP) of several hundred synaptic vesicles (Nicol and Walmsley, 2002; Lin et al., 2011; Taruno et al., 2012; Butola et al., 2021; Hintze et al., 2021). Another distinguishing feature to conventional synapses is that endbulbs contain a dense network of mitochondria (Lenn and Reese, 1966; Tolbert and Morest, 1982; Lauer et al., 2013; Hintze et al., 2024). The abundance of pre-synaptic mitochondria is thought to meet the high metabolic demands of sustained firing and potentially help buffer calcium within the terminal (Rowland et al., 2000; Billups and Forsythe, 2002; Kim et al., 2005; Verstreken et al., 2005; Perkins et al., 2010; Lucas et al., 2018).

Pre- and post-synaptic physiology

Beyond organization and morphology, synaptic function relies on the finely tuned interplay between pre- and post-synaptic terminals, where many adaptations are observed at the physiological level. Ion channels and receptors on both sides ultimately shape the input-output function and determine the computational capacity of the neuronal circuits. As one of the largest pre-synaptic terminals, the endbulb of Held is accessible to whole-cell patch-clamp recordings, allowing measurement of action potential (AP) properties and calcium currents, both of which influence synaptic vesicle release (Lin et al., 2011; Butola et al., 2021). Pre-synaptic APs in the endbulb are brief (half-width: 200–300 μs), and this brevity limits the duration of calcium influx into the pre-synaptic terminal, thus effectively regulating synaptic vesicle (SV) release (Lin et al., 2011).

Calcium enters the pre-synaptic terminal through voltage-gated calcium channels (VGCC), which triggers the release of SV in response to a pre-synaptic AP (Nanou and Catterall, 2018; Young and Veeraraghavan, 2021). In the mature endbulb, the dominant VGCC subtype is $Ca_V2.1$ (P/Q-type) (Doughty et al., 1998; Lin et al., 2011; Zhuang et al., 2020), which opens during short APs and triggers efficient SV release (Scheuber et al., 2004; Eggermann et al., 2011; Dolphin and Lee, 2020). Although physiological estimates suggest that the total number of VGCC in the endbulb is lower than that in the calyx (Lin et al., 2011), the VGCC density per AZ is comparable (endbulb: ~40 VGCC/AZ, calyx of Held: ~50 VGCC/AZ) when adjusted for terminal size and AZ number (Lin et al., 2011; Nakamura et al., 2015; Lübbert et al., 2019).

The arrangement of VGCC relative to SVs dictates the speed and efficiency of transmitter release (Wang and Augustine, 2014; Stanley, 2016; Nusser, 2018). In the endbulb, SVs are positioned close to VGCC, resulting in tight coupling that enables rapid and efficient "nanodomain" release upon the arrival of the pre-synaptic AP (Lin et al., 2011). This fast and synchronous SV release is further supported by the expression of the fast calcium sensor protein, synaptotagmin (Syt) 2 (MacLeod and Pandya, 2022). Despite the primarily fast and synchronous SV release, pre-synaptic modulation can still affect the amount and time course of neurotransmitter release. At the endbulb, the activation of pre-synaptic $GABA_B$ receptors reduces SV release, thereby influencing information transfer across the synapse (Brenowitz et al., 1998; Brenowitz and Trussell, 2001b; Chanda and Xu-Friedman, 2010).

Specializations for fast and temporally precise signal transmission in the pre-synaptic terminal are complemented by adaptations in the post-synaptic cell to maintain high temporal precision. Several post-synaptic properties are shared between the cells discussed in this review and contribute to efficient encoding of temporal information.

Fast excitatory currents (EPSCs) are primarily mediated by AMPA-type glutamate receptors. Bushy cells express AMPA receptors containing GluA3 and GluA4 subunits (Wang et al., 1998b; Petralia et al., 2000; Ravindranathan et al., 2000; Schmid et al., 2001), with GluA3 subunits clustered at the center of the synapse (Rubio et al., 2017). GluA1 is absent, whereas GluA2 is expressed at low levels (Hunter et al., 1993; Rubio and Wenthold, 1997; Wang et al., 1998b; Gardner et al., 1999, 2001). In mature animals, AMPA receptor subunits are expressed in the *flop splice* variant, which renders them rapidly desensitizing with a fast recovery from desensitization (Sommer et al., 1990; Mosbacher et al., 1994; Geiger et al., 1995; Koike et al., 2000; Gardner et al., 2001; Schmid et al., 2001; Krampfl et al., 2002; Pei et al., 2009). Furthermore, NMDA receptors are present at moderate levels (Watanabe et al., 1994; Gómez-Nieto and Rubio, 2011). The expression of fast-gating AMPA receptors combined with highly synchronous SV release results in very brief EPSCs (<0.5 ms), enabling the synapse to follow high firing rates (Otis and Trussell, 1996; Brenowitz and Trussell, 2001a; Xie and Manis, 2013; Antunes et al., 2020; Zhang et al., 2022).

When stimulated at high frequencies in brain slices, endbulb EPSCs show considerable short-term depression (STD) (Oleskevich et al., 2000; Oleskevich and Walmsley, 2002; Wang and Manis, 2005; Ngodup et al., 2015). This suggests either a high SV release probability, which rapidly depletes the RRP, or post-synaptic receptor desensitization, with the latter having little contribution at the mature endbulb (Brenowitz and Trussell, 2001b; Wang and Manis, 2008). Importantly, under near-physiological low calcium (1–1.5 mM) conditions, short-term depression is reduced and has minimal impact on EPSC amplitudes during ongoing activity (Wang and Manis, 2008; Yang and Xu-Friedman, 2015). These findings align with *in vivo* observations, where the EPSP amplitude remains largely unaffected by preceding events in the presence of spontaneous activity (Kuenzel et al., 2011; Keine et al., 2016; Stasiak et al., 2018). Although EPSC depression levels vary among cells, they are similar across endbulbs that contact the same bushy cell, despite originating from different SGN subtypes (Yang and Xu-Friedman, 2009; Zhang et al., 2022; Wong et al., 2025).

While the generation of APs is controlled by voltage-gated sodium and potassium channels, the cell's intrinsic electrical properties, including input resistance, resting membrane potential,

TABLE 1 Cellular and synaptic properties of auditory brainstem neurons in two parallel pathways.

	Structure	Interaural ITD/ILD pathway						Monaural spectral pathway	
		Endbulb of Held – bushy cell	Calyx of Held - MNTB	MSO		LSO		Octopus cell	VNLL endbulb – globular cell
	Synapse type	Excitatory (glutamate)	Excitatory (glutamate)	Excitatory (glutamate)	Inhibitory glycine)	Excitatory (glutamate)	Inhibitory (glycine)	Excitatory (glutamate)	Excitatory (glutamate)
Pre-synaptic	Morphology	Large, cup-like or finger-like, complex	Giant, cup-like or finger-like, complex	Bouton-type with multiple varicosities	Bouton-type with multiple varicosities	Bouton-type with few varicosities	Large bouton-type with multiple varicosities	Bouton-type	Large, cup-like, simple
	Number of inputs	1–4 (SBC) 5–60 (GBC)	1	4–8	2–4	20–40	5–8	>60	1–3
	Active zone number	150–2,000	500–1,000	∼5 per bouton	-	1–3 per input	6–60 per input	-	-
	Dominant VGCC subtype	CaV2.1	CaV2.1	CaV2.1/CaV2.2	CaV2.1	CaV2.1	CaV2.1	-	-
Post-synaptic	Morphology	Globular with 1–2 tufted dendrites	Globular with tufted dendrites	Bipolar with thick dendrites		Bipolar with intricately branched dendrites		Globular with 4–6 thick undirectional dendrites	Globular with profuse dendrites
	Membrane time constant	<2 ms	2–4 ms	0.3–0.5 ms		1–3 ms		∼0.2 ms	2–4 ms
	Input resistance	∼100 MΩ	∼100 MΩ	<10 MΩ		∼50 MΩ		<10 MΩ	100–150 MΩ
	AP half-width	200–500 µs	∼200 µs	∼300 µs		∼200 µs		∼300 µs	200–500 µs
	HCN expression	HCN1,2,4	HCN2	HCN1		HCN1,2		HCN1	HCN1,2

10.3389/fncel.2025.1568506

and membrane time constant are influenced by the presence of hyperpolarization-activated cyclic nucleotide–gated (HCN) channels and low-voltage-activated potassium channels (Kv1). In mature animals, bushy cells typically fire one or a few APs at stimulus onset in response to depolarizing square-pulse current injections (Wu and Oertel, 1984; Schwarz and Puil, 1997). This phasic response is due to the expression of dendrotoxin-sensitive, low-threshold, voltage-activated Kv1 channels (Manis and Marx, 1991; Cao et al., 2007), which renders bushy cells suitable for preserving the timing of endbulb inputs (Wu and Oertel, 1984).

Kv1 channels are often expressed alongside HCN channels, which are open at or near the cell's resting membrane potential, thereby reducing the cell's input resistance and shortening the membrane time constant. HCN channels can also enhance temporal precision by facilitating rapid recovery from hyperpolarization (Hassfurth et al., 2009; Cao and Oertel, 2011; Khurana et al., 2011; Golding and Oertel, 2012). Bushy cells express several HCN subtypes (HCN1, HCN2, and HCN4) (Schwarz and Puil, 1997; Leao et al., 2006; Cao et al., 2007; Oertel et al., 2008). HCN1 activates the fastest, rendering it ideally suited to support the demand for high temporal precision (Magee, 1998, 1999; Chen et al., 2001; Moosmang et al., 2001; Khurana et al., 2012; Oertel et al., 2017). Conversely, HCN2 and HCN4 activate more slowly but have a greater potential for modulation via intracellular cAMP (Ludwig et al., 1998, 1999; Santoro et al., 1998; Santoro and Tibbs, 1999).

The combined expression of Kv1 and HCN channels in bushy cells determines their characteristic membrane properties, featuring low input resistance (<100 MΩ) (Wu and Oertel, 1984; Schwarz and Puil, 1997) and fast membrane time constant (<2 ms) (Wang and Manis, 2006; Cao et al., 2007). These properties result in brief EPSPs that minimize temporal summation, allowing only the largest and most synchronous EPSPs to evoke APs (Manis and Marx, 1991; McGinley and Oertel, 2006; Cao et al., 2007).

Finally, rapid repolarization after an AP, which is crucial for enabling high firing rates, is facilitated by high-threshold voltage-activated potassium channels, particularly the Kv3 subfamily (Manis and Marx, 1991; Brew and Forsythe, 1995; Du et al., 1996; Rathouz and Trussell, 1998; Wang and Kaczmarek, 1998; Coetzee et al., 1999; Brown et al., 2016). Bushy cells express Kv3.1, Kv3.3, and Kv3.4, contributing to their brief AP duration (200–500 µs) (Weiser et al., 1995; Li et al., 2001; Pál et al., 2005).

In response to sound, bushy cell firing resembles that of the AN input, displaying a "primary-like" response. Bushy cells exhibit narrow frequency tuning, sharp onsets, and precise encoding of temporal fine structure (Rhode et al., 1983; Rhode and Smith, 1986; Kopp-Scheinpflug et al., 2002). Notably, bushy cells, particularly GBCs, can follow the fine structure of sounds with higher precision than their AN input (Joris et al., 1994a,b; Keine et al., 2016, 2017). Bushy cells are therefore well-suited to preserve and even enhance the temporal precision of the auditory nerve input, enabling them to deliver the fast and temporally precise excitation required by downstream nuclei.

In summary, the first central synapse in the binaural sound localization pathway is formed by a large axosomatic terminal connecting the AN to bushy cells in the cochlear nucleus, which is conserved across many vertebrate species. The large pre-synaptic terminal with multiple AZ and rapid neurotransmitter release, in combination with post-synaptic specializations, such as fast-gating AMPA receptors and intrinsic membrane properties, support rapid and temporally precise action potential generation. These adaptations are fundamental for supporting downstream processing of sound localization.

The calyx of Held

The MNTB serves as a crucial inhibitory hub within the auditory brainstem. It provides precisely timed glycinergic inhibition to several SOC nuclei, including the LSO, MSO, and superior olivary nucleus (SPN) (Spangler et al., 1985; Banks and Smith, 1992; Kuwabara and Zook, 1992; Wu and Kelly, 1992; Sommer et al., 1993; Srinivasan et al., 2004). This function relies heavily on the calyx of Held—MNTB synapse, which acts as a high-fidelity relay, converting precisely timed excitation from GBCs to an equally precise inhibitory output.

Structure and morphology

The GBC-MNTB pathway showcases numerous morphological and physiological specializations designed for fast and reliable information transfer, with the calyx of Held pre-synaptic terminal being the most prominent. This giant excitatory (glutamatergic) terminal is formed by the axons of GBCs located in the contralateral CN and is considered one of the largest pre-synaptic terminals in the mammalian central nervous system (Harrison and Warr, 1962; Morest, 1968). The axons that form the calyx of Held are among the thickest and most heavily myelinated axons in the auditory system, ensuring fast signal conduction (Morest, 1968; Ford et al., 2015). Its exceptional size and experimental accessibility have made the calyx of Held uniquely accessible for electrophysiological experiments, allowing simultaneous patch-clamp recordings from both the pre-synaptic terminal and post-synaptic cell (Forsythe, 1994; Borst et al., 1995), a feat that is currently impossible at smaller conventional synapses. Consequently, the calyx of Held has become the primary model system for studying fundamental processes, such as synaptic transmission, plasticity, and neuronal development (von Gersdorff and Borst, 2002; Schneggenburger and Forsythe, 2006; Borst and Soria van Hoeve, 2012; Yu and Goodrich, 2014; Baydyuk et al., 2016; Neher, 2017; Joris and Trussell, 2018; Sakaba, 2018).

Notably, the size of the MNTB varies between species. It is easily recognizable in rodents and contains a relatively uniform population of large globular cells with tufted dendrites. However, in primates, including humans, the MNTB is poorly developed and appears as a loose collection of cells (Richter et al., 1983; Moore, 1987; Bazwinsky et al., 2003; Kulesza, 2008, 2014; Hilbig et al., 2009; Schmidt et al., 2010; Kulesza et al., 2011; Kulesza and Grothe, 2015). Despite this difference, calyx-type terminals have been identified in both rhesus monkeys and humans, suggesting that this striking morphological specialization offers unique benefits across diverse acoustic environments and is perhaps independent of the prominence or spatial organization of the MNTB (Richter et al., 1983; Bazwinsky et al., 2005; Kulesza, 2014).

Organization of synaptic inputs

In contrast to bushy cells, which can receive multiple endbulb inputs, MNTB principal cells are typically contacted by a single glutamatergic calyx terminal, with the occasional occurrence of two or three calyces per MNTB cell (Held, 1893; Vater and Feng, 1990; Rodríguez-Contreras et al., 2006, 2008). This single calyx terminal can engulf more than half of the MNTB cell soma. Similar to endbulbs, calyx axons sprout collateral branches that form conventional boutons on nearby MNTB cells (Lenn and Reese, 1966; Casey and Feldman, 1982; Rodríguez-Contreras et al., 2008; Thomas et al., 2019). In mice, which exhibit a well-developed MNTB, calyx terminals vary in complexity. Larger terminals often exhibit more intricate branching and are highly fenestrated (Grande and Wang, 2011; Grande et al., 2014; Wang et al., 2015; Fekete et al., 2019), presumably to facilitate transmitter diffusion during high-frequency stimulation (Ford et al., 2015). The complex morphology of the calyx includes second- and third-order branches consisting of swellings and finger-like stalks. These structures may comprise distinct biochemical compartments (Rowland et al., 2000; Taschenberger et al., 2002; Wimmer et al., 2006; Spirou et al., 2008) with different synaptic vesicle release probabilities; however, their physiological functions are currently poorly understood (Grande and Wang, 2011; Fekete et al., 2019).

Similar to the endbulb, the calyx harbors hundreds (500–1,000) of AZs (Sätzler et al., 2002; Taschenberger et al., 2002; Wimmer et al., 2006; Dondzillo et al., 2010). Although large overall, each individual AZ is morphologically similar to conventional bouton synapses (Rowland et al., 2000; Sätzler et al., 2002; Taschenberger et al., 2002; Lin et al., 2011; Schneggenburger et al., 2012; Thomas et al., 2019). The sheer size of the pre-synaptic terminal and the number of release sites result in an enormous RRP, exceeding 1,000 SVs (Schneggenburger et al., 1999; Wu and Borst, 1999; Bollmann et al., 2000; Sun and Wu, 2001; Sätzler et al., 2002; de Lange et al., 2003; Wimmer et al., 2006; Lin et al., 2011). Mirroring the endbulb, a dense network of mitochondria has been described for the calyx, presumably serving a similar function in supporting the metabolic demand and acting as an additional calcium buffer (Lenn and Reese, 1966; Nakajima, 1971; Rowland et al., 2000; Wimmer et al., 2006; Thomas et al., 2019).

Pre- and post-synaptic physiology

As perhaps the largest pre-synaptic terminal in the mammalian central nervous system (CNS), the calyx of Held has been instrumental in deciphering much of what we know about neurotransmitter release. Similar to the endbulb of Held, pre-synaptic APs are brief (~200 μs halfwidth) (Taschenberger et al., 2002). This brevity is supported by the exclusion of sodium channels from the calyx terminal. Instead, they are densely clustered at the last elongated axonal heminode (Leão et al., 2005). The calyx expresses various potassium channels: Low-threshold channels are mainly composed of Kv1.2 homomers, with some Kv1.3. Kv1.3 is located at the calyx terminal (Gazula et al., 2010), whereas Kv1.1 and Kv1.2 are excluded from the terminal and concentrated at the axon-terminal transition zone, likely to reduce nerve terminal excitability (Dodson et al., 2003; Ishikawa et al., 2003). High-threshold Kv3 potassium channels help rapidly repolarize the membrane, shortening AP duration, thereby regulating transmitter release and enabling high firing rates (Taschenberger and von Gersdorff, 2000; Joshi and Wang, 2002; Chao and Yang, 2019; Richardson et al., 2022). This specific arrangement of sodium and potassium channels ensures that the pre-synaptic AP remains remarkably stable, even during high firing rates exceeding several hundred Hertz (Wang and Kaczmarek, 1998; Taschenberger and von Gersdorff, 2000; Sierksma and Borst, 2017).

Similar to the endbulb, calcium entry into the mature calyx is exclusively mediated by $Ca_V2.1$ channels (Doughty et al., 1998; Iwasaki and Takahashi, 1998; Lin et al., 2011). Calcium currents in the calyx seem to inactivate more strongly during step-like depolarization than those in the endbulb (Forsythe et al., 1998; Lin et al., 2011). However, during AP-like depolarizations, VGCC inactivation may be negligible, and calcium current facilitation may play a dominant role, especially in the endbulb (Wang and Kaczmarek, 1998; Felmy et al., 2003; Inchauspe et al., 2007; Müller et al., 2008, 2010; Lin et al., 2011).

In the mature calyx, SVs are positioned closely (~20 nm) to VGCCs, enabling rapid and efficient nanodomain release upon the arrival of the pre-synaptic AP (Taschenberger and von Gersdorff, 2000; Taschenberger et al., 2002; Fedchyshyn and Wang, 2005; Renden and von Gersdorff, 2007; Wang et al., 2008; Kochubey et al., 2009; Eggermann et al., 2011; Chen et al., 2015; Stanley, 2016). The expression of the fast calcium sensor Syt2 further supports rapid SV release (Pang et al., 2006; Cooper and Gillespie, 2011; Kochubey et al., 2016). Recently, Syt3 was identified as the calcium sensor responsible for efficient SV replenishment at the calyx of Held (Weingarten et al., 2022), enabling fast and indefatigable synaptic transmission.

Early slice studies suggested a high SV release probability at the calyx, given the large post-synaptic currents (Borst and Sakmann, 1996). However, studies performed under more physiological conditions (body temperature, low calcium) indicate that the release probability at the calyx is low (Lorteije et al., 2009; Borst, 2010; Keine et al., 2022). Adding to this complexity, some findings suggest that SV release probabilities can differ between calyces and even between AZ within the same calyx, indicating functional heterogeneity (Grande and Wang, 2011; Fekete et al., 2019). Explaining the diverse forms of short-term plasticity observed under different conditions requires models containing multiple SV pools with sequential priming processes and distinct release probabilities (Sakaba, 2006, 2018; Wölfel et al., 2007; Guo et al., 2015; Neher, 2015; Lin et al., 2022, 2025). However, during physiological spontaneous activity, relatively simple models are often sufficient to approximate the calyx' short-term plasticity (Hermann et al., 2007, 2009).

Although SV release is primarily fast and synchronous, it can be modulated by the activation of pre-synaptic receptors, including $GABA_B$ and glycine receptors (Turecek and Trussell, 2001; Price and Trussell, 2006), as well as intracellular signaling molecules such as cAMP (Kaneko and Takahashi, 2004).

On the post-synaptic side, AMPA receptors are evenly distributed throughout the post-synaptic density (Budisantoso et al., 2013), similar to other glutamatergic synapses (Budisantoso et al., 2012). These receptors primarily consist of GluA4 in the

fast *flop* variant (Geiger et al., 1995; Hermida et al., 2010; Yang et al., 2011). Most AMPA receptors also include at least one GluA2 subunit, rendering them impermeable to calcium (Koike-Tani et al., 2005; Lujan et al., 2019). Similar to bushy cells, NMDA receptors are expressed at moderate levels in adult animals but contribute little to the large and fast synaptic currents at this synapse (Barnes-Davies and Forsythe, 1995; Wang and Kaczmarek, 1998; Sato et al., 1999; Nakagawa et al., 2000; Futai et al., 2001).

The resulting EPSCs in MNTB neurons are fast (<0.5 ms) and display mature characteristics immediately after hearing onset (∼P12 in mice) (Taschenberger and von Gersdorff, 2000; Futai et al., 2001; Joshi and Wang, 2002; Fedchyshyn and Wang, 2005; Keine et al., 2022). Under near-physiological conditions, high-frequency electrical stimulation of the calyx axon causes initial EPSC facilitation, followed by depression, consistent with a low release probability *in vivo* (von Gersdorff and Borst, 2002; Lorteije et al., 2009; Borst, 2010; Keine et al., 2022; Kladisios et al., 2023). Similar to the endbulb-bushy cell synapse, the impact of synaptic short-term plasticity appears to be subtle *in vivo*, with only modest EPSP facilitation at brief intervals (Lorteije et al., 2009; Crins et al., 2011; Sonntag et al., 2011; Stasiak et al., 2018). Receptor desensitization contributes little to short-term depression because of the low SV release probability and rapid glutamate clearance from the highly fenestrated calyx (Joshi and Wang, 2002; Taschenberger et al., 2002, 2005; Koike-Tani et al., 2008). Notably, short-term depression in mice is inversely correlated with calyx complexity: simple calyces with higher release probability show strong EPSC depression and reduced AP firing reliability compared to more complex calyces (Grande and Wang, 2011; Fekete et al., 2019).

The combination of an elaborate pre-synaptic terminal, large SV pools, and efficient release mechanisms ensures strong excitation of the MNTB cell, leading to reliable AP generation even during prolonged activity. Although the delay between the pre-synaptic and post-synaptic AP can increase considerably during sustained high-frequency stimulation, most of this added delay occurs between the EPSP and AP (Guinan and Li, 1990; Elezgarai et al., 2003; Fedchyshyn and Wang, 2007; Mc Laughlin et al., 2008; Tolnai et al., 2009). The delay between the pre-synaptic AP and EPSP remains remarkably stable in mature animals, emphasizing the efficiency of SV release and replenishment in the calyx (Mc Laughlin et al., 2008; Sonntag et al., 2011). Notably, neurons tuned to low sound frequencies tend to exhibit more stable transmission delays, suggesting a specialization for activity-invariant timing of synaptic transmission (Stange-Marten et al., 2017).

Post-synaptic intrinsic properties further shape the MNTB output. Unlike bushy cells, which predominantly express HCN1, MNTB neurons mainly express HCN2 but not HCN1 (Koch et al., 2004; Leao et al., 2006; Khurana et al., 2012; Baumann et al., 2013; Kopp-Scheinpflug et al., 2015). This difference in HCN subtype expression might be related to the cell's function: bushy cells might benefit from the fast HCN1 dynamics to enhance temporal precision for coincidence detection, whereas MNTB neurons, receiving input from a single suprathreshold calyx terminal, do not require coincident inputs to generate APs.

The combined expression of Kv1 channels (Brew and Forsythe, 1995; Dodson et al., 2002; Kladisios et al., 2023) and HCN channels results in an input resistance (∼100 MΩ) (Banks and Smith, 1992; Hassfurth et al., 2009; Kladisios et al., 2020, 2023) and membrane time constant (2–4 ms) (Scott et al., 2005; Roberts et al., 2014; Kladisios et al., 2020, 2023) comparable to bushy cells. Consequently, depolarizing square-pulse current injections result in a single AP in adult MNTB cells. This phasic firing is important for limiting the number of APs and preserving temporal precision in response to the large EPSCs generated by the calyx terminal. Fast repetitive firing of MNTB neurons is supported by the expression of Kv3.1 and Kv3.3 channels (Wang et al., 1998a; Choudhury et al., 2020).

The single suprathreshold calyx in combination with an MNTB cell that responds with a single, well-timed AP leads to MNTB activity that is a faithful representation of its GBC input. Consequently, MNTB responses to sound are mostly indistinguishable from their GBC input (Mc Laughlin et al., 2008; Englitz et al., 2009; Sonntag et al., 2011) (but see *Functional consequences in relation to synaptic specializations*).

In summary, the calyx of Held—MNTB synapse combines several morphological and physiological specializations, rendering it an ideal relay station to provide well-timed and sustained inhibition to several nuclei in the auditory brainstem, including the two binaural nuclei involved in sound localization, the MSO and LSO.

Medial superior olive

The MSO is the first station in the auditory system where differences between the arrival times of sounds at both ears (interaural time differences, ITD) are computed. Cellular and synaptic specializations enable MSO neurons to detect these time differences with sub-millisecond precision (Goldberg and Brown, 1969; Yin and Chan, 1990). While it is generally accepted that MSO neurons act as coincidence detectors, the exact mechanisms underlying their extraordinary precision, including the origin of internal delays and the role of inhibition, are still actively debated.

Structure and morphology

The MSO has been described in many mammals, but its size and cellular organization vary considerably across species. Generally, it tends to be larger and more organized in animals with large heads and sensitive low-frequency hearing, which rely on ITDs for sound localization (Harrison and Irving, 1966a; Irving and Harrison, 1967; Moore and Moore, 1971; Glendenning and Masterton, 1998; Grothe, 2000; Grothe and Pecka, 2014). Various studies have identified up to four distinct cell types in the MSO of different animals, but the most common are bipolar cells, often referred to as principal cells (Schwartz, 1977; Kiss and Majorossy, 1983; Henkel and Brunso-Bechtold, 1990; Smith, 1995; Kulesza, 2007). These cells have a characteristic spindle-like shape, with thick, tapered dendrites (∼4 μm diameter, 100–200 μm length) extending from the medial and lateral poles of the cell soma (Stotler, 1953; Kiss and Majorossy, 1983; Henkel and Brunso-Bechtold, 1990; Kudo et al., 1990; Smith, 1995; Rautenberg et al., 2009). In species with sensitive low-frequency hearing that effectively use ITDs for sound

localization (e.g., gerbils, cats, and humans), these bipolar cells are arranged in a single column and aligned in the parasagittal plane, with their dendrites extending medially and laterally (Schwartz, 1977; Kulesza, 2007; Rautenberg et al., 2009; Bondy et al., 2021). Conversely, in animals that do not rely heavily on ITDs (e.g., bats, mice, rats, and opossums), the MSO is still present, but the organization of cell bodies, dendrites, and synaptic inputs is less strictly defined, suggesting that it might serve functions other than primary ITD processing in these species (Ollo and Schwartz, 1979; Grothe and Park, 2000; Kapfer et al., 2002; Fischl et al., 2016; Rincón et al., 2024).

MSO neurons are excitatory and project primarily to the auditory midbrain, the ipsilateral IC, and the dorsal and intermediate nuclei of the lateral lemnicus (DNLL and INLL, respectively) (Glendenning et al., 1981; Henkel and Spangler, 1983; Casseday et al., 1988; Vater et al., 1995; Henkel, 1997; Oliver et al., 2003; Loftus et al., 2004; Cant, 2013; Rincón et al., 2024).

Organization of synaptic inputs

In contrast to the giant endbulb and calyx terminals discussed earlier, synaptic inputs onto MSO neurons are smaller conventional bouton-type terminals. Nevertheless, the soma and proximal dendrites of MSO neurons are densely covered with these inputs (Perkins, 1973; Lindsey, 1975; Schwartz, 1977).

MSO cells receive both excitatory (glutamatergic) inputs originating from SBCs in the ipsi- and contralateral CN (Stotler, 1953; Warr, 1966; Osen, 1969b; Lindsey, 1975; Grothe and Sanes, 1993; Kitzes et al., 1995; Smith, 1995; Magnusson et al., 2005; Scott et al., 2005; Chirila et al., 2007) and inhibitory (glycinergic) inputs primarily from the MNTB, with a smaller contribution from the LNTB, relaying information reflecting the activity from the contralateral ear (Adams and Mugnaini, 1990; Cant and Hyson, 1992; Kuwabara and Zook, 1992; Spirou and Berrebi, 1997; Spirou et al., 1998; Roberts et al., 2014). Morphological and electrophysiological evidence suggests that the number of individual fiber inputs is surprisingly low for a coincidence detector, ranging between 2–4 fibers for inhibition and 4–8 fibers for excitation (Couchman et al., 2010).

A key feature in animals that use ITDs is the precise spatial segregation of these inputs (Stotler, 1953; Clark, 1969a; Kuwabara and Zook, 1992; Kapfer et al., 2002). Excitatory inputs are distributed along the dendrites (Clark, 1969b; Callan et al., 2021), with ipsilateral and contralateral inputs confined to the lateral and medial dendrites, respectively (Stotler, 1953; Clark, 1969b; Lindsey, 1975; Smith et al., 1993). Despite their small size, a single excitatory axon forms multiple points of contact along its target dendrite, each containing multiple active zones (Clark, 1969b; Lindsey, 1975; Kiss and Majorossy, 1983; Brunso-Bechtold et al., 1990; Kapfer et al., 2002; Callan et al., 2021). In contrast, inhibitory inputs are small and confined to the soma and proximal dendrites (Stotler, 1953; Clark, 1969b; Perkins, 1973; Kuwabara and Zook, 1992; Grothe and Sanes, 1993, 1994; Kapfer et al., 2002; Werthat et al., 2008; Grothe et al., 2010; Couchman et al., 2012). Importantly, this strict segregation of dendritic excitation and somatic inhibition is less apparent or absent in species with poor low-frequency hearing that do not use ITDs. This suggests that the spatial arrangement of synaptic inputs is a crucial adaptation for enhancing ITD detection in the sub-millisecond range required for sound localization (Kapfer et al., 2002; Seidl and Grothe, 2005).

Pre- and post-synaptic physiology

Owing to their small size and relative inaccessibility for direct patch-clamp recordings, the calcium dynamics and SV release mechanisms in these bouton inputs remain largely unexplored. However, some key features have been uncovered: glycine release is mediated by $Ca_V2.1$ channels with some contribution from $Ca_V2.2$ (N-type), whereas glutamate release is mediated by both $Ca_V2.1$ and $Ca_V2.2$, at least in young rats around hearing onset (Barnes-Davies et al., 2001). Consistent with the MSO's need for precise timing, pre-synaptic terminals on MSO neurons express Syt2, enabling fast and synchronous SV release, similar to the endbulb and calyx (Cooper and Gillespie, 2011). Both excitatory and inhibitory inputs can be modulated by the activation of pre-synaptic $GABA_B$ receptors, at least in the juvenile MSO (Hassfurth et al., 2010; Stange et al., 2013). Post-synaptically, MSO principal cells are equipped with AMPA receptors that are distributed across the soma and dendrites, apparently with little subunit preference (Caicedo and Eybalin, 1999), whereas glycine receptors are concentrated primarily on the soma (Couchman et al., 2012). NMDA receptors are expressed at moderate levels during adulthood; however, their functional role remains unclear (Smith et al., 2000; Couchman et al., 2012). Despite originating from smaller pre-synaptic terminals, both excitatory and inhibitory synaptic currents are surprisingly large, comparable in amplitude to those evoked by the much larger endbulb (Couchman et al., 2010; Franzen et al., 2015), and show comparable short-term depression during high-frequency stimulation (Couchman et al., 2010; Fischl et al., 2016). Crucially, their kinetics are dramatically different: EPSCs are extremely fast, with decay times of approximately 250 μs, whereas IPSCs are several-fold slower (~1.5 ms decay) (Magnusson et al., 2005; Couchman et al., 2010; Myoga et al., 2014; Franzen et al., 2020).

While the pre-synaptic physiology and synaptic currents share some features with the larger endbulb and calyx terminals, the intrinsic membrane properties of MSO neurons are exceptionally tuned for microsecond coincidence detection and set them apart from most other auditory brainstem neurons. MSO neurons exhibit a remarkably low input resistances (<10 MΩ) and extraordinarily fast membrane time constants (<300 μs)—about 10 times faster than those of MNTB neurons (Magnusson et al., 2005; Scott et al., 2005; Chirila et al., 2007; Couchman et al., 2010; Fischl et al., 2016; Nabel et al., 2019; Franzen et al., 2020; Kladisios et al., 2020; Siveke et al., 2021). These rapid membrane dynamics ensure that EPSPs are very brief (<1 ms) (Kullmann et al., 2005; Mathews et al., 2010; Winters et al., 2017), minimizing the time window for input summation and enhancing sensitivity to coincident events. These extraordinary membrane properties arise largely from the expression of Kv1 and HCN1 channels (Svirskis et al., 2002; Koch et al., 2004; Scott et al., 2005; Mathews et al., 2010; Khurana et al., 2012; Baumann et al., 2013; Kopp-Scheinpflug et al., 2015; Fischl et al., 2016; Winters et al., 2017). In

addition to contributing to the fast membrane time constant, the expression of Kv1 channels may also facilitate resonance behavior up to several hundred Hertz, potentially further enhancing ITD detection (Remme et al., 2014; Mikiel-Hunter et al., 2016; Fischer et al., 2018). Notably, Kv1 channels are gradually expressed along the dendrites, ensuring that EPSPs arriving at different dendritic locations produce similar voltage changes at the soma. Consequently, inputs from all over the dendritic tree can contribute effectively to ITD computation (Mathews et al., 2010; Winters et al., 2017).

In MSO neurons, the integration of synaptic inputs is finely tuned to detect ITDs. Despite individual EPSCs being relatively large, the cell's low input resistance limits EPSP amplitudes, often rendering them insufficient to evoke APs. Consequently, triggering APs requires the near-simultaneous arrival of multiple excitatory inputs (van der Heijden et al., 2013; Franken et al., 2015; Plauška et al., 2016; Kladisios et al., 2020).

Although these EPSPs sum largely linearly (Roberts et al., 2013; van der Heijden et al., 2013; Franken et al., 2015; Plauška et al., 2016), the generation of an AP depends non-linearly on the resulting EPSP amplitude (van der Heijden et al., 2013). A notable consequence of their extremely low input resistance is that MSO neurons typically generate small somatic APs (often $<$10 mV), rendering *in vivo* recordings with high signal-to-noise ratios particularly challenging (Yin and Chan, 1990; Scott et al., 2005; Chirila et al., 2007; Couchman et al., 2010; van der Heijden et al., 2013; Franken et al., 2015).

MSO responses *in vivo* are based on the coincidence detection of binaural inputs; thus, firing rates vary with ITD (Goldberg and Brown, 1969; Yin and Chan, 1990; Pecka et al., 2008; van der Heijden et al., 2013; Franken et al., 2015; Plauška et al., 2016). Principal cells in the MSO favor low-frequency sounds, and their fast membrane time constant and rapid EPSCs allow them to detect microsecond differences in the arrival time between inputs from both ears. Notably, MSO neurons are generally broadly tuned, and their firing rates are modulated over ITD ranges that exceed the "physiological ITD" based on the physical difference between the two ears (Brand et al., 2002; Pecka et al., 2008).

In summary, MSO neurons are highly specialized coincidence detectors, fine-tuned for temporal precision, supported by their bipolar morphology, rapid synaptic signaling, and exceptionally fast membrane properties. These adaptations allow them to calculate ITDs with the microsecond accuracy required for sound localization.

Lateral superior olive

The LSO is a key component of the ILD pathway. The auditory system can distinguish ILDs as small as 1 dB, which corresponds to a difference in sound location of 1° in the horizontal plane (Mills, 1958). This remarkable acuity arises primarily from LSO neurons that compare ipsilateral excitation with contralateral inhibition. LSO neurons then provide ascending projections to regions in the IC similar to those targeted by the MSO, but with excitatory neurons targeting the IC bilaterally and inhibitory neurons projecting ipsilaterally (Oliver et al., 1995; Loftus et al., 2004; Haragopal and Winters, 2023).

Structure and morphology

Similar to the MSO, the LSO is a common structure observed in all terrestrial mammals studied to date (Glendenning and Masterton, 1998; Tollin, 2003; Grothe et al., 2010; Grothe and Pecka, 2014). However, its overall shape and number of neurons can differ significantly across species (Irving and Harrison, 1967; Willard and Martin, 1983; Sanes et al., 1989; Casey, 1990; Moore et al., 1995; Moore, 2000; Kulesza, 2007; Hilbig et al., 2009; Reuss et al., 2009; Sterenborg et al., 2010; Hirtz et al., 2011; 2012; Rosengauer et al., 2012; Bazwinsky-Wutschke et al., 2016; Nothwang, 2016). Up to seven different cell types have been identified in the LSO, with principal cells being the most abundant, comprising approximately 75% of the neuronal population (Ollo and Schwartz, 1979; Helfert and Schwartz, 1986, 1987; Rietzel and Friauf, 1998; Kulesza, 2007; Franken et al., 2018). For the remainder of this review, we will focus on LSO principal cells, which possess a spindle-shaped soma with two prominent primary dendrites emerging from opposite somatic poles (Cant, 1984; Helfert and Schwartz, 1986, 1987; Schofield and Cant, 1991; Rietzel and Friauf, 1998), resembling MSO principal neurons. In contrast to the thick MSO dendrites, LSO dendrites are more intricate and branch extensively, spreading across a considerable rostrocaudal distance (Scheibel and Scheibel, 1974; Helfert and Schwartz, 1986).

Organization of synaptic inputs

LSO principal neurons receive their main excitatory inputs from SBCs in the ipsilateral CN and their primary inhibitory inputs from the contralateral CN via GBCs relayed through the MNTB (Moore and Caspary, 1983; Smith et al., 1993; Sommer et al., 1993). Additionally, excitatory inputs from GBCs and planar multipolar neurons in the ipsilateral VCN have been reported (Friauf and Ostwald, 1988; Smith et al., 1991; Doucet and Ryugo, 2003).

Similar to the MSO, a substantial portion of the LSO principal cell soma is covered with synaptic inputs (Helfert and Schwartz, 1986; Franken et al., 2018), which are predominantly inhibitory (Cant, 1984; Wenthold et al., 1987; Helfert et al., 1989; Friauf, 1992; Helfert et al., 1992; Brunso-Bechtold et al., 1994; Cooper and Gillespie, 2011; Hirtz et al., 2012; Gjoni et al., 2018a). Inhibitory and excitatory inputs are somewhat spatially segregated; inhibitory terminals tend to cluster on or near the soma, whereas excitatory terminals are located more distally on thin dendrites (Cant, 1984; Helfert et al., 1992; Smith et al., 1998). Inhibitory dominance is also reflected in synaptic morphology. Although both inputs form conventional boutons, the inhibitory terminals are notably larger and more complex. Specifically, individual inhibitory axons form multiple large swellings or varicosities (~6, range 1–13), each typically containing several AZs (~3, range 1–11). This structural arrangement provides the basis for strong unitary inhibition from an estimated 4–8 converging fibers, totaling hundreds of AZs (Noh et al., 2010; Gjoni et al., 2018a,b). In contrast, the more numerous excitatory fibers (~20–40 fibers) primarily target dendrites and form smaller terminals with few varicosities (1–3) that usually contain only a single AZ (Gjoni et al., 2018a,b).

Pre- and post-synaptic physiology

While direct electrophysiological recordings of LSO pre-synaptic terminals are currently lacking, several studies have revealed similarities with other auditory brainstem synapses. Synaptic transmission at both excitatory (glutamatergic) and inhibitory (glycinergic) terminals appears to rely predominantly on $Ca_V2.1$ calcium channels and Syt1/2, ensuring rapid and synchronous SV release (Alamilla and Gillespie, 2011; Giugovaz-Tropper et al., 2011; Bouhours et al., 2017), similar to the endbulb and calyx of Held.

Pre-synaptic modulation mirrors the patterns observed elsewhere in the circuit. Activation of pre-synaptic $GABA_B$ receptors reduces SV release from both excitatory and inhibitory inputs. Notably, this modulation appears to have a stronger effect on excitatory inputs, suggesting a potential mechanism for dynamically adjusting ILD sensitivity by preferentially dampening excitation (Magnusson et al., 2008).

On the post-synaptic side, glutamatergic transmission is mediated by AMPA receptors containing primarily GluA2/3 and GluA4 subunits, following the general pattern observed in the auditory brainstem (Caicedo and Eybalin, 1999; Schwartz and Eager, 1999; Schmid et al., 2001). Similar to other SOC nuclei, mature LSO neurons express moderate levels of NMDA receptors, but their functional role remains unclear (Munemoto et al., 1998; Sato et al., 1999; Nakagawa et al., 2000).

Inhibition is mediated by abundant glycine receptors clustered on the soma and proximal dendrites (Friauf et al., 1997; Sato et al., 2000; Kapfer et al., 2002). A unique feature of inhibition in the LSO is its remarkable speed: inhibitory currents decay rapidly (~0.7 ms), essentially matching the speed of excitatory currents (Moore and Caspary, 1983; Wu and Kelly, 1991, 1992; Kandler and Friauf, 1995; Wu and Kelly, 1995; Kotak et al., 1998; Pilati et al., 2016). This contrasts with most other brainstem nuclei, where inhibition is typically several times slower than excitation (Smith et al., 2000; Couchman et al., 2010; Xie and Manis, 2013; Mayer et al., 2014; Nerlich et al., 2014a,b; Rajaram et al., 2019).

The combination of large inhibitory terminals with multiple release sites and abundant post-synaptic glycine receptors generates strong inhibition (Gjoni et al., 2018a) with only moderate short-term depression over several seconds (Giugovaz-Tropper et al., 2011; Walcher et al., 2011; Kramer et al., 2014; Krächan et al., 2017). This sustained SV release is supported by rapid and efficient SV recovery mechanisms, rendering these synapses fatigue-resistant and capable of maintaining high temporal precision during ongoing activity (Kramer et al., 2014; Krächan et al., 2017; Brill et al., 2019). Excitatory inputs, while producing smaller EPSCs, match this reliability with comparable SV replenishment rates (Case et al., 2011; Garcia-Pino et al., 2017; Gjoni et al., 2018b; Brill et al., 2019).

Post-synaptic specializations further enhance temporal precision in the LSO. Principal neurons exhibit low input resistance (~50 MΩ) and a fast membrane time constant (1–3 ms) (Hassfurth et al., 2009; Sterenborg et al., 2010; Walcher et al., 2011; Haragopal and Winters, 2023; Maraslioglu-Sperber et al., 2024), supported by the expression of Kv1 (Barnes-Davies et al., 2004) and HCN1/2 channels (Koch et al., 2004; Leao et al., 2006; Kopp-Scheinpflug et al., 2015). While not as "leaky" as MSO neurons, LSO principal neurons have significantly faster membrane dynamics than bushy cells and MNTB neurons. The specific placement of HCN channels along the dendrites can further modulate EPSP integration by locally decreasing input resistance (Leão et al., 2011).

While other neurons discussed in this review typically respond to depolarizing square-pulse current injections with one or a few APs at the onset (Wu and Oertel, 1984; Wu and Kelly, 1991; Brew and Forsythe, 1995; Smith, 1995; Scott et al., 2005; Caspari et al., 2015; Franzen et al., 2015; Kladisios et al., 2020), LSO can either fire single APs or exhibit sustained AP firing (Tsuchitani, 1988; Finlayson and Caspary, 1991; Wu and Kelly, 1991; Barnes-Davies et al., 2004; Sterenborg et al., 2010; Winters et al., 2017; Maraslioglu-Sperber et al., 2024). The physiological roles of these different types of principal neurons and their contributions to ILD coding are not yet fully understood.

As coincidence detectors integrating ipsilateral excitation and contralateral inhibition (relayed via the MNTB), LSO neurons crucially depend on the precise relative timing between these opposing inputs. *In vivo*, this timing is remarkably matched: excitatory and inhibitory signals arrive at the LSO nearly simultaneously, despite the inhibitory pathway being longer and including an additional synapse (Finlayson and Caspary, 1989; Joris and Yin, 1998; Tollin and Yin, 2005). This latency matching is achieved through the specializations of the GBC-MNTB pathway discussed previously, namely the large diameter of GBC axons and the exceptionally fast synaptic transmission at the calyx of Held—MNTB junction. LSO principal neurons favor high-frequency sounds, and the integration of ipsilateral excitation and contralateral inhibition results in firing rates that vary with ILD. Responses to ipsilateral ("excitatory") sounds have long been characterized as "chopper"-type (Guinan et al., 1972; Tsuchitani, 1977; Finlayson and Caspary, 1989; Joris and Yin, 1995; Tollin et al., 2008; Tsai et al., 2010; Greene and Davis, 2012). However, this characterization has recently been challenged by *in vivo* patch-clamp recordings, suggesting that LSO principal cells, at least in the ventral LSO of the Mongolian gerbil, are similar to MSO cells, exhibiting onset responses (Franken et al., 2018). Further highlighting the significance of timing, the same study found that changing ILDs affects the latency of the inhibitory input more profoundly than its amplitude (Franken et al., 2018). Intriguingly, LSO neuron firing seems to be facilitated when inhibition slightly precedes excitation (Irvine et al., 2001; Beiderbeck et al., 2018), underscoring the notion that precise temporal integration is vital even within this nominal intensity-processing pathway.

The octopus cell—VNLL pathway

While the bushy cell—superior olive pathway is primarily associated with binaural computation and detection of interaural time and level differences, the parallel octopus cell—VNLL pathway is thought to be crucial for monaural spectrotemporal cues. These include the detection of onsets and gaps, which are important features for vocalization, speech understanding, and auditory scene analysis.

Octopus cells located in the caudal and ventral portion of the VCN receive auditory nerve input and project to several targets, including the VNLL. The VNLL, an elongated nucleus between the SOC and the dorsal NLL, receives major inputs from the CN, MNTB, and periolivary nuclei (Glendenning et al., 1981; Spangler et al., 1985). Functionally, VNLL neurons are predominantly inhibitory (glycine and/or GABA) and provide a major source of inhibition to the contralateral inferior colliculus (IC) and other targets in the NLL and SOC (Brunso-Bechtold et al., 1981; Zook and Casseday, 1982, 1987; Willard and Martin, 1983; Whitley and Henkel, 1984; Tanaka et al., 1985; Vater et al., 1992; Sommer et al., 1993; Saint Marie et al., 1997; Schofield and Cant, 1997; Ueyama et al., 1999; Riquelme et al., 2001; Kelly et al., 2009; Moore and Trussell, 2017). Similar to bushy cells and MNTB cells, globular cells in the VNLL's ventral pole receive large axosomatic presynaptic terminals ("VNLL endbulbs") originating from octopus cells of the contralateral CN (Friauf and Ostwald, 1988; Vater and Feng, 1990; Schofield, 1995; Adams, 1997; Schofield and Cant, 1997; Vater et al., 1997; Smith et al., 2005).

Octopus cells

Octopus cells within the CN are specialized neurons that detect the precise timing of complex acoustic events, particularly those with broad frequency content occurring simultaneously. By integrating information across many auditory nerve fibers from a wide range of frequencies on a sub-millisecond timescale, they can signal the precise timing of these events to higher auditory centers.

Structure and morphology

Located in the most posterior and dorsal part of the VCN, most octopus cells possess a defining anatomical feature: several thick dendrites emerge primarily from one side of the cell body and extend across the frequency axis of auditory nerve fibers, resembling the tentacles of an octopus (Harrison and Irving, 1966b; Osen, 1969b). This distinct morphology is conserved across species with diverse hearing ranges, including cats (Osen, 1969b; Kane, 1973), gerbils (Cant and Benson, 2006; Bazwinsky et al., 2008), rats (Alibardi, 2003), chinchillas (Feng et al., 1994; Ostapoff et al., 1994), mice (Felix et al., 2017), bats (Vater and Feng, 1990), and humans (Adams, 1986, 1997; Kulesza, 2014). A crucial aspect of their morphology is the orientation of their dendrites, which stretch perpendicular to the tonotopically organized AN endings. This arrangement allows a single octopus cell to receive inputs from numerous auditory nerve fibers carrying a wide band of frequencies, covering approximately 1/3 of the animal's hearing range (Harrison and Warr, 1962; Harrison and Irving, 1966b; Golding et al., 1995; Oertel et al., 2000). Similar to GBCs, octopus cells are excitatory (glutamatergic) and possess exceptionally large-diameter axons, ensuring the rapid conduction of their output signals (Rhode et al., 1983; Oertel et al., 1990; Schofield, 1995; Schofield and Cant, 1997). In some species, such as mice and cats, octopus cells cluster together to form a sharply defined "octopus cell area" that is almost exclusively populated by these neurons (Osen, 1969b; Wickesberg et al., 1994; Golding et al., 1995, 1999).

Organization of synaptic inputs

Octopus cells receive their primary excitatory input directly from the AN (Harrison and Irving, 1966b; Kane, 1973). Unlike the giant endbulb terminals on bushy cells, these inputs are smaller, more numerous bouton-type synapses (Alibardi, 2003). A single octopus cell integrates inputs from many (>60) individual AN fibers (De No, 1933; Brown and Ledwith, 1990; Cao and Oertel, 2010), primarily originating from low-threshold type 1a SGNs with short latency and low temporal jitter (Kreeger et al., 2025). These inputs appear to be spatially organized along the dendrites: ANFs sensitive to low sound frequencies tend to synapse closer to the soma and proximal dendrites, whereas fibers sensitive to higher sound frequencies target more distal dendritic regions (Harrison and Irving, 1966b; Golding et al., 1995; Oertel et al., 2000).

Although some larger boutons make contact with the cell soma (Kane, 1973; Alibardi, 2003), the vast majority (>80%) of excitatory synapses are located on the dendrites, highlighting the importance of dendritic integration for octopus cell computation (Kreeger et al., 2025). Anatomical evidence and data obtained from *in vivo* whole-cell recordings suggest that excitatory inputs are of different sizes, creating a bias toward certain frequencies (Kane, 1973; Alibardi, 2003; Lu et al., 2022).

In addition to this massive excitatory drive, octopus cells receive inhibitory inputs that primarily target dendrites, which may shape the timing and magnitude of incoming excitatory signals and thus influence neuronal computation (Adams and Mugnaini, 1987; Saint Marie et al., 1989; Juiz et al., 1996; Alibardi, 2003; Kreeger et al., 2025). However, the origin, tonotopic arrangement, and physiological role of these inhibitory inputs remain largely unknown (Kreeger et al., 2025).

Pre- and post-synaptic physiology

The unique structure and input organization dictate the specialized function of octopus cells, enabling them to act as monaural coincidence and sweep detectors with sub-millisecond precision (Oertel, 1983; Golding et al., 1995; Golding and Oertel, 2012; Lu et al., 2022). Their extraordinary temporal acuity arises from several key biophysical adaptations. Similar to MSO neurons, octopus cells possess a very "leaky" membrane, resulting in an extremely low input resistance (<10 MΩ) and a remarkably fast membrane time constant (~200 μs). This leakiness is primarily due to the dense expression of Kv1 and HCN channels (Golding et al., 1999; Bal and Oertel, 2000, 2001; Cao and Oertel, 2005; Oertel et al., 2008). The HCN-mediated current is particularly large in octopus cells and activated at more depolarized membrane potentials than in other brainstem neurons, leaving a substantial number of these channels open at rest (Golding et al., 1995, 1999; Cao and Oertel, 2011).

Post-synaptically, octopus cells express fast-gating AMPA receptors (Golding et al., 1995; Hackney et al., 1996) that lack the GluA2 subunit, making them permeable to calcium, and resulting in large synaptic currents (Gardner et al., 1999, 2001). The combination of the fast membrane time constant and these fast-gating AMPA receptors leads to very brief EPSPs, effectively preventing temporal summation unless events arrive in near-perfect synchrony (Oertel, 1983; Golding et al., 1995, 1999;

McGinley and Oertel, 2006; Cao and Oertel, 2011, 2017). Similar to other auditory brainstem neurons, octopus cells express Kv3.1 potassium channels, which minimize AP duration (~300 μs) and support high firing rates (Perney and Kaczmarek, 1997; Golding et al., 1999).

These intrinsic and synaptic properties shape the *in vivo* responses of octopus cells. They typically respond weakly to sustained pure tones because of their broad frequency tuning and fast membrane time constant (Godfrey et al., 1975; Rhode and Smith, 1986). However, when multiple AN inputs are activated near simultaneously, such as during transient broadband sounds like clicks, they fire with exceptional temporal precision, often phase-locking with exactly one spike per stimulus up to hundreds of Hertz (McGinley and Oertel, 2006; Recio-Spinoso and Rhode, 2020; Lu et al., 2022) Beyond simple sound onsets, octopus cells respond robustly to complex spectrotemporal patterns, including frequency modulations and appear sensitive to the direction and speed of frequency sweeps—features characteristic of speech and other natural sounds (Young and Sachs, 1979; Shannon et al., 1995; Pressnitzer et al., 2011; Shamma et al., 2011; Lu et al., 2022).

In summary, octopus cells are biophysically similar to MSO principal neurons, featuring an extraordinarily low input resistance and a fast membrane time constant. Combined with their broadband AN inputs, they are ideally suited to detect monaural coincidences across a wide frequency range. Thus, octopus cells may be involved in binding co-occurring frequency information and detecting monaural spectral patterns on a sub-millisecond timescale and rapidly transmitting this information to ascending brain centers, including the VNLL.

Globular cells of the ventral nucleus of the lateral lemniscus

Within the VNLL, a key relay station in the ascending auditory pathway, globular cells are particularly crucial for temporal processing. While perhaps less prominent than nuclei in the SOC or IC, the VNLL is essential for processing precise auditory timing and is a key structure for integrating the spectral information of sounds. Primarily receiving contralateral monaural inputs, VNLL globular cells are typically inhibitory and rely on fast and reliable signal transmission to preserve the temporal features encoded in the CN (Oertel, 1999). These cells subsequently provide broadband onset inhibition to neurons within the VNLL, the SOC, and the ipsilateral IC, which might help to reduce spectral splatter and sharpen temporal responses (Adams, 1979; Brunso-Bechtold et al., 1981; Whitley and Henkel, 1984; Nayagam et al., 2005; Spencer et al., 2015; Gómez-Martínez et al., 2023).

Structure and morphology

Globular cells are predominantly found in the ventral portion of the VNLL in most mammals (Adams, 1979, 1997; Covey and Casseday, 1986; Merchán et al., 1994; Schofield and Cant, 1997; Zhao and Wu, 2001; Mylius et al., 2013; Zacher and Felmy, 2024). In bats, these cells are arranged in a distinct columnar area, perhaps representing a structural adaptation linked to echolocation (Zook and Casseday, 1985; Covey and Casseday, 1986). Morphologically, globular cells feature round to oval cell bodies with extensive dendritic trees, bearing some resemblance to bushy cells in the CN and MNTB principal neurons (Adams, 1979, 1997; Covey and Casseday, 1986; Kudo et al., 1990; Vater and Feng, 1990; Merchán et al., 1994; Schofield and Cant, 1997; Vater et al., 1997; Zhao and Wu, 2001; Mylius et al., 2013). Similar to those related cell types, a defining characteristic of VNLL cells is their primary input from a giant axosomatic pre-synaptic terminal. These VNLL endbulbs are glutamatergic terminals originating from the thick axons of octopus cells located in the contralateral CN (Friauf and Ostwald, 1988; Vater and Feng, 1990; Schofield, 1995; Adams, 1997; Schofield and Cant, 1997; Vater et al., 1997; Smith et al., 2005).

Like the endbulbs in the CN and the calyx in the MNTB, VNLL endbulbs represent a conserved anatomical adaptation found in several mammals, including cats (Stotler, 1953; Adams, 1997; Smith et al., 2005), rodents (rat: Friauf and Ostwald, 1988; gerbil: Berger et al., 2014; mouse: Caspari et al., 2015), guinea pigs (Schofield and Cant, 1997), bats (Covey and Casseday, 1986; Vater and Feng, 1990; Huffman and Covey, 1995; Vater et al., 1997), and humans (Adams, 1997). Intriguingly, these large terminals are present even in primates and humans, where the VNLL is considered relatively poorly developed compared to other species. Notably, although VNLL endbulbs have been found in several mammalian species, the percentage of VNLL cells receiving endbulbs is significantly higher in humans than in cats, despite an overall less developed nucleus (Adams, 1997). Although comprehensive data on the presence and size of VNLL inputs across species are currently lacking, the high proportion of endbulb-receiving VNLL neurons in humans may indicate an adaptation to low-frequency hearing.

Organization of synaptic inputs

While morphologically similar to CN endbulb and calyx terminals, VNLL endbulbs are less extensively studied. Most globular cells receive input from a small number of endbulb inputs, with estimates ranging between 1–3 (Covey and Casseday, 1986; Vater and Feng, 1990; Adams, 1997; Berger et al., 2014; Baumann and Koch, 2017; Kladisios et al., 2020). In terms of convergence, this places them between bushy cells (often receiving multiple endbulbs) and MNTB cells (typically receiving a single calyx). Correspondingly, VNLL endbulbs are approximately half the size of the calyx terminal (Berger et al., 2014). Unlike the intricate branching observed at the CN endbulb and the calyx, VNLL endbulbs are morphologically simpler, with less complex branching and fewer processes, essentially clasping the globular cell soma (Adams, 1997). Ultrastructurally, VNLL endbulbs contain multiple AZs (Smith et al., 2005), rendering them a smaller and simpler version of the calyx (Berger et al., 2014).

Pre- and Post-synaptic physiology

Physiologically, VNLL endbulbs share key features with their CN and MNTB counterparts. Pre-synaptic APs are brief (~200 μs halfwidth), although smaller in amplitude than those in the calyx (Berger et al., 2014). However, the smaller AP is offset by changes in VGCC activation and deactivation, resulting in comparable

pre-synaptic calcium influx and SV release kinetics (Berger et al., 2014).

Post-synaptically, VNLL globular cells express fast-gating AMPA receptors composed of GluA2 and GluA4 subunits (Caicedo and Eybalin, 1999) and only a minor NMDA component (Kladisios et al., 2022). This composition generates large and rapid EPSCs (<0.5 ms), similar to those in CN bushy cells and MNTB neurons (Caspari et al., 2015; Baumann and Koch, 2017; Kladisios et al., 2020). Under physiological conditions, synaptic short-term plasticity is characterized by initial facilitation followed by depression (Caspari et al., 2015; Kladisios et al., 2022), similar to the calyx of Held—MNTB synapse.

VNLL globular cells express Kv1.1 channels (Rosenberger et al., 2003; Zacher and Felmy, 2024) and moderate levels of HCN1/2 channels (Koch et al., 2004; Caspari et al., 2015; Gessele et al., 2016; Zacher and Felmy, 2024). These contribute to membrane properties closely resembling those of MNTB neurons, with an input resistance of 100–150 MΩ, a membrane time constant of approximately 5 ms, and the generation of a single or a few APs in response to depolarizing current injection (Zhao and Wu, 2001; Caspari et al., 2015; Franzen et al., 2015; Baumann and Koch, 2017; Fischer et al., 2018; Kladisios et al., 2020).

Considering the large pre-synaptic terminal together with morphological and physiological properties comparable to MNTB neurons, it is unsurprising that *in vivo* responses of VNLL globular cells to sound generally resemble those of their primary excitatory input, the octopus cells. To pure tones, these cells respond with sharply timed onset spikes independent of sound intensity and can entrain to high-frequency click trains up to 1 kHz (Covey and Casseday, 1991; Adams, 1997; Zhang and Kelly, 2006; Recio-Spinoso and Joris, 2014; Recio-Spinoso and Rhode, 2020).

In summary, VNLL globular cells exhibit morphological and physiological features similar to those of other fast-processing auditory brainstem neurons, such as bushy cells and MNTB neurons. The presence of such features outside the canonical sound localization pathway indicates that they are not unique to the pathways of binaural integration but rather represent a fundamental biological toolkit optimized to preserve or enhance temporal fidelity with sub-millisecond precision. Consequently, VNLL globular cells play a crucial role in faithfully relaying the precise temporal patterns encoded by their octopus cell inputs. This reliable relay is critical for processing sound onsets and complex temporal structures relevant for speech and other environmental sounds. Therefore, the existence of these "high-fidelity" features in a predominantly monaural pathway underscores the importance of rapid temporal processing across multiple auditory streams beyond binaural spatial hearing.

Functional consequences in relation to synaptic specializations

To fully appreciate the morphological and physiological specializations discussed here, they must be viewed within their functional context. The widespread existence of these features across various species suggests strong evolutionary pressure favoring rapid, precise, and reliable neuronal signaling, which is largely invariant to the acoustic environment. Large axosomatic terminals, as seen in the CN, MNTB, and VNLL, provide a structural basis for delivering strong and rapid excitation suitable for high firing rates. As detailed above, this capability is underpinned by large SV pools and efficient VGCC-SV coupling. This pre-synaptic capacity is complemented post-synaptically by features such as fast-gating AMPA receptors, electrotonic compactness, and the expression of Kv1 and Kv3 potassium channels, all of which support fast post-synaptic responses.

However, how these specializations translate into the neuron's response to sound can vary significantly between synapses. The neuronal code containing acoustic information can be modified through selective AP transmission across the synaptic junction, creating vastly different input–output functions. Therefore, studying this relationship is crucial for understanding a neuron's computational role within its neuronal circuit. However, obtaining such input–output functions for single neurons is challenging, particularly *in vivo*.

Fortunately, the large axosomatic terminals in the CN, MNTB, and VNLL offer a unique opportunity to assess synaptic reliability *in vivo*, as extracellular recordings from these neurons often reveal complex waveforms, as noted in some of the earliest recordings (Pfeiffer, 1966; Guinan and Li, 1990; Adams, 1997). This composite signal arises from the proximity of the recording electrode to both the giant pre-synaptic terminal and the post-synaptic soma (Lorteije et al., 2009; Typlt et al., 2010). It typically starts with a small voltage deflection, the "pre-potential," which reflects the pre-synaptic AP. A few hundred microseconds later, a second potential appears, generated by the EPSP, which may or may not be large enough to trigger a post-synaptic AP. When transmission fails (i.e., no post-synaptic AP is triggered), the isolated EPSP becomes clearly visible, as seen in recordings from the mature endbulb or pre-hearing calyx terminals (Lorteije et al., 2009; Typlt et al., 2010; Crins et al., 2011; Kuenzel et al., 2011; Sonntag et al., 2011; Keine and Rübsamen, 2015; Keine et al., 2016; Stasiak et al., 2018). When transmission succeeds, the EPSP typically merges into the rising phase of a much larger post-synaptic AP, often remaining as a discernible *bump*. Statistical analysis of their temporal relationships combined with pharmacological studies to isolate the origin of these components provides robust evidence for this interpretation of the complex waveform (Mc Laughlin et al., 2008; Englitz et al., 2009; Lorteije et al., 2009; Typlt et al., 2010; Sonntag et al., 2011; Keine and Rübsamen, 2015; Keine et al., 2016; Stasiak et al., 2018). These recordings thus provide a powerful tool for assessing input–output functions *in vivo* and help elucidate how AP failures affect sound encoding.

Despite sharing many structural and morphological features, the endbulb-BC and calyx-MNTB synapses display markedly different synaptic reliability and input-output functions. In mature animals, the calyx of Held-MNTB synapse is renowned for its high fidelity. MNTB neurons are among the few cells in the central nervous system in which the output is typically a one-to-one representation of its calyceal input, allowing the synapse to act as a reliable relay for auditory information. While some studies found occasional transmission failures *in vivo* (Guinan and Li, 1990; Kopp-Scheinpflug et al., 2003; Lorteije et al., 2009; Crins et al., 2011; Wang et al., 2015), others reported reliable synaptic

transmission (Green and Sanes, 2005; Mc Laughlin et al., 2008; Englitz et al., 2009; Sonntag et al., 2009, 2011; Tolnai et al., 2009; Stasiak et al., 2018). In some cases, statistical analysis suggests that post-synaptic APs from another, more distant cell were mistakenly interpreted as isolated pre-potentials (Mc Laughlin et al., 2008; Englitz et al., 2009). Nonetheless, discrepancies might also arise from methodological factors, including potential cell damage from the recording electrode, differences in recording conditions, and the impact of anesthesia. Under most conditions, however, synaptic transmission at the calyx-MNTB synapse appears to be highly secure. Consequently, the *in vivo* response of MNTB neurons to sound is virtually identical to that of their corresponding GBC inputs, characterized by a primary-like response pattern with a more or less prominent "notch" in the peristimulus-time histogram (Smith et al., 1998; Rhode, 2008; Sonntag et al., 2009). Although MNTB neurons receive strong inhibitory inputs with fast kinetics, their functional impact remains unclear (Albrecht et al., 2014; Mayer et al., 2014).

This high fidelity stands in stark contrast to the endbulb of Held—BC synapses, which frequently fails to trigger post-synaptic APs. These failures, characterized by the presence of the pre-potential and an isolated EPSP but lacking the post-synaptic AP, are observed across species even during spontaneous activity and are particularly recognizable in SBCs that receive large endbulb inputs (Englitz et al., 2009; Kuenzel et al., 2011; Nerlich et al., 2014b; Keine and Rübsamen, 2015; Keine et al., 2016, 2017; Stasiak et al., 2018). This indicates that, unlike the calyx, the endbulb operates near the bushy cell's AP threshold, rendering signal transmission and, thus, the neuron's input–output function highly sensitive to modulation, especially by inhibition (Englitz et al., 2009; Dehmel et al., 2010; Kuenzel et al., 2011; Keine and Rübsamen, 2015; Keine et al., 2016, 2017; Stasiak et al., 2018). While bushy cell responses to pure tones often resemble the primary-like pattern of their AN input (Blackburn and Sachs, 1989; Rhode, 2008; Typlt et al., 2012), the interplay between strong endbulb-evoked excitation, local inhibition, and convergence of multiple inputs enhances temporal precision and aids in encoding the temporal aspects of sound (Dehmel et al., 2010; Kuenzel et al., 2011; Keine and Rübsamen, 2015; Keine et al., 2016, 2017; Koert and Kuenzel, 2021; Spirou et al., 2023).

Data on the synaptic reliability of VNLL endbulbs are limited. *In vitro* studies suggest that while a single endbulb might be insufficient to reliably trigger post-synaptic APs before hearing onset (Berger et al., 2014), a developmental increase in EPSC size (Baumann and Koch, 2017; Kladisios et al., 2020) leads to a reliable one-to-one connection in mature animals, although it may be less robust than the calyx at high stimulation frequencies (Caspari et al., 2015; Kladisios et al., 2020). Consistent with this, *in vivo* recordings in mature cats have found no evidence of isolated pre-potentials, suggesting reliable transmission (Adams, 1997). Whether the reliability of the mature VNLL endbulb is modulated during ongoing activity and whether species-dependent differences exist remains to be investigated.

These differences in reliability likely reflect the different functions within the neuronal circuit. It is conceivable that the computational roles diverge when large excitatory inputs target inhibitory vs. excitatory neurons. In sign-inverting synapses, such as those in the MNTB and VNLL, excitatory input is inverted into an inhibitory output to multiple brain areas. If the inversion of sign is the main purpose of these synapses, it is perhaps unsurprising that they exhibit high reliability with little to no modulation of the input-output function. Conversely, at the CN endbulb-bushy cell synapses, where both the auditory nerve input and bushy cell output are excitatory, the junction allows for more complex synaptic integration and signal modulation. This modulation can manifest as an increase in temporal precision, reproducibility, and sparsity of the bushy cell output compared to the auditory nerve (Dehmel et al., 2010; Kuenzel et al., 2011; Keine and Rübsamen, 2015; Keine et al., 2016, 2017).

Comparison to other brain areas

Although the specializations that enable rapid and precise signaling in the auditory brainstem are remarkable adaptations, they are not unique to the auditory system. Similar adaptations can be observed in other brain areas facing comparable challenges. Many of these specializations are widespread across different neuronal populations and species, suggesting common solutions to universal problems in high-frequency neurotransmission.

Generally, achieving high-frequency synaptic transmission requires several key elements: fast and efficient SV release, rapid gating of post-synaptic receptors, and brief action potentials that allow the neuron to generate them in quick succession. For instance, the tight nanodomain coupling between VGCC and SV that ensures rapid nanodomain release has been observed far beyond mammalian auditory synapses, including the frog neuromuscular junction (Harlow et al., 2001; Shahrezaei et al., 2006), the squid giant synapse (Augustine, 1990; Adler et al., 1991), and the ciliary ganglion of the chick (Stanley, 1993). Efficient coupling between SV and VGCC is not limited to excitatory synapses but also found in inhibitory neurons of the cerebellum and cortex (Bucurenciu et al., 2008; Arai and Jonas, 2014). Similarly, the expression of fast calcium sensors Syt1 or Syt2 is a common feature of synapses requiring fast exocytosis, appearing in both excitatory and inhibitory synapses across various brain regions, including the brainstem, cerebellum, hippocampus, and neocortex (Geppert et al., 1994; Fernández-Chacón et al., 2001; Pang et al., 2006; Xu et al., 2007; Kochubey et al., 2016).

Post-synaptically, fast-gating AMPA receptors are crucial for generating rapid excitatory synaptic currents, minimizing spike time jitter, and maintaining high temporal precision (Cathala et al., 2005; Takahashi, 2005). Such receptors are expressed in various brain areas, including the olfactory bulb (Schoppa, 2006), the vestibular calyx synapse (Kirk et al., 2017), and fast-spiking cortical interneurons (Hull et al., 2009). Furthermore, high-threshold, voltage-gated potassium channels of the Kv3 type support the ability to fire rapidly and are found in fast-spiking neurons across different brain regions, such as the neocortex, hippocampus, subthalamus, amygdala, the vestibular nucleus, and even the electrosensory system of weakly electric fish (Weiser et al., 1995; Du et al., 1996; Massengill et al., 1997; Sekirnjak et al., 1997; Martina et al., 1998; Chow et al., 1999; Erisir et al., 1999; Wigmore and Lacey, 2000; Rashid et al., 2001; Tansey et al.,

2002; McDonald and Mascagni, 2006; Gittis et al., 2010). These channels are activated only briefly near the peak of an AP, due to their high voltage threshold, causing rapid repolarization and prominent after-hyperpolarization. This shortens the AP duration and facilitates the recovery of voltage-gated sodium channels, enabling neurons to sustain high firing rates without compromising AP amplitudes.

A compelling example of specialization for high-frequency signaling occurs in the cerebellum, specifically at the synapse between cerebellar mossy fiber boutons (cMFB) and granule cells (GC). Granule cells can maintain extraordinarily high firing rates, exceeding 1000 spikes/second (Garwicz et al., 1998; Rancz et al., 2007; Prsa et al., 2009; Ritzau-Jost et al., 2014). Although cMFB are morphologically conventional bouton-type synapses, they are significantly enlarged (3–12 μm) (Hámori and Somogyi, 1983; Rothman et al., 2016), making them accessible for direct pre-synaptic patch-clamp recordings both *in vitro* and *in vivo* (Rancz et al., 2007; Powell et al., 2015). Unlike bushy cells and MNTB neurons that receive one or a few large axosomatic terminals, GCs integrate inputs from many cMFBs (12–50) (Jakab and Hámori, 1988; Billings et al., 2014). Each input contains multiple AZs, totaling 150–300 AZs per GC (Jakab and Hámori, 1988; Xu-Friedman and Regehr, 2003; Kim et al., 2013).

Mirroring the auditory synapses described earlier, SV release in the cMFB is triggered by extremely brief pre-synaptic APs (Ritzau-Jost et al., 2014). Pre-synaptic calcium entry is predominantly mediated by $Ca_V2.1$ channels tightly coupled to SVs, leading to fast nanodomain release, similar to many synapses in the auditory brainstem (Sargent, 2005; Delvendahl et al., 2015a). Reliable high-frequency transmission is sustained by a large RRP and efficient SV replenishment (Saviane and Silver, 2006; Hallermann et al., 2010; Ritzau-Jost et al., 2014). Furthermore, pre-synaptic calcium-buffer dynamics are similar to those observed in the calyx of Held (Helmchen et al., 1997; Jackson and Redman, 2003; Müller et al., 2007).

Post-synaptically, GCs are smaller than bushy cells or MNTB cells (5–7 μm in diameter) but display a similar electrotonic compactness due to their short dendrites, which minimize dendritic filtering (Silver et al., 1992; D'Angelo et al., 1993; Delvendahl et al., 2015b), and thus resemble the adaptations observed in bushy cells, MNTB cells, and MSO principal cells.

Similar to auditory brainstem neurons, GCs use fast-gating AMPA receptors composed of GluA2 and GluA4 subunits, which enable rapid synaptic currents and efficient recovery from desensitization (Silver et al., 1992; Cathala et al., 2005; DiGregorio et al., 2007). The ability to fire rapidly is also supported by the expression of Kv1 and Kv3-type potassium channels (Ritzau-Jost et al., 2014). Notably, unlike in most mature auditory brainstem neurons, where NMDA receptor expression is low, these receptors are substantially expressed in GCs (D'Angelo et al., 1990; Silver et al., 1992). Additionally, GCs exhibit a slow component of their AMPA receptor currents, which may contribute to sustaining elevated firing rates by producing tonic depolarization (Digregorio et al., 2002; Xu-Friedman and Regehr, 2003; Nielsen et al., 2004; Sargent, 2005; Rancz et al., 2007; Powell et al., 2015).

In summary, the specializations observed in the auditory brainstem are not isolated phenomena. Similar structural and physiological adaptations appear in other brain regions that face comparable computational demands. This suggests that mechanisms such as nanodomain coupling, specific calcium sensors and specialized receptors and ion channels represent a fundamental molecular toolkit that evolution has employed and refined repeatedly to meet the diverse functional demands of neural circuits throughout the brain.

Discussion

A core principle in neuroscience is that distinct neural circuits have evolved with specialized properties to perform specific computations (Luo, 2021). The auditory system is inherently temporal, requiring the extraction of relevant features from rapidly varying sound pressure waves; thus, it faces unique challenges compared with other sensory systems. Consequently, the importance of the temporal dimension has resulted in several structural and functional specializations along the auditory pathway. While the cochlea encodes basic features such as sound intensity and frequency, more complex features such as sound localization, source segregation, and auditory object identity emerge from computations performed along the auditory pathway, starting in the auditory brainstem. The fundamental computations (localization, timing, and spectral analysis) performed at the auditory brainstem then act as building blocks for further processing in higher auditory centers to achieve complex perception.

Perhaps the most widely recognized function requiring exquisite temporal precision is the localization of sound sources in the horizontal plane based on ITDs and ILDs. Human listeners can detect ITDs as small as 10–20 μs (Klumpp and Eady, 1956; Mills, 1958), requiring neuronal computations to operate at sub-millisecond precision. Beyond spatial hearing, understanding complex sounds, such as speech, relies on this temporal acuity to encode rapid transients (e.g., consonant bursts), periodic fine structure (pitch), and slower envelope modulations (syllables) (Russo et al., 2004; Akhoun et al., 2008). Octopus cells in the PVCN, with their rapid membrane properties and broadband AN inputs, are ideally suited to detect the coincident firing of many AN with exceptional temporal precision. This precise temporal information is then relayed via the VNLL globular cells, which provide fast and reliable inhibition, perhaps crucial for segmenting speech streams, identifying consonants, and reducing spectral splatter (Nayagam et al., 2005; Spencer et al., 2015). Furthermore, the ability to encode temporal fine structure is vital for pitch perception and contributes significantly to vowel identification and understanding speech in noisy or reverberant environments (Lorenzi et al., 2006; Moore, 2008; Hopkins and Moore, 2011). Ultimately, auditory scene analysis, the ability to segregate sound sources in the environment ("cocktail-party" problem), depends on the high-resolution spatial and temporal information encoded by the brainstem (Shamma et al., 2011; Yao et al., 2015).

The perception of acoustic stimuli is modulated by the temporal and spectral relationships between sound components,

and these interactions can be used to segregate sound sources, such as multiple speakers in a room (Palmer, 1990; de Cheveigné, 2021). The octopus cell—VNLL pathway appears to be particularly sensitive to such interactions (Recio-Spinoso and Rhode, 2020; Lu et al., 2022). This manifold use of temporally precise auditory information underscores the critical importance of the brainstem's specialized machinery in preserving the fine temporal details necessary for hearing in naturalistic settings.

In conclusion, the specialized cellular and synaptic properties found within auditory brainstem pathways, including giant synapses, cellular morphology, and ion channel expression patterns, constitute a highly optimized biological framework designed for computations that demand extraordinary temporal precision. Understanding the molecular and cellular basis of this temporal precision is crucial for deciphering the neural basis of hearing in both normal and pathological states. Future studies that use cell-type-specific optogenetics (Mattis et al., 2011), transcriptomics (Jing et al., 2025), and population recording techniques, such as high-density electrode arrays (Steinmetz et al., 2021), will be essential for advancing our understanding of the circuits formed by neurons and synapses discussed in this review.

Author contributions

CK: Conceptualization, Project administration, Writing – original draft, Writing – review & editing. BE: Writing – original draft, Writing – review & editing.

Funding

The author(s) declare that financial support was received for the research and/or publication of this article. This work was supported by intramural funds to CK (FP 2024-099) and the Open Access Publication Funding from the German Research Foundation. The funding sources had no role in conception and design, preparation of the manuscript, or the decision to submit for publication.

Conflict of interest

The authors declare that the research was conducted in the absence of any commercial or financial relationships that could be construed as a potential conflict of interest.

Generative AI statement

The author(s) declare that no Gen AI was used in the creation of this manuscript.

Publisher's note

All claims expressed in this article are solely those of the authors and do not necessarily represent those of their affiliated organizations, or those of the publisher, the editors and the reviewers. Any product that may be evaluated in this article, or claim that may be made by its manufacturer, is not guaranteed or endorsed by the publisher.

References

Adams, J. C. (1979). Ascending projections to the inferior colliculus. *J. Comp. Neurol.* 183, 519–538. doi: 10.1002/cne.901830305

Adams, J. C. (1986). Neuronal morphology in the human cochlear nucleus. *Arch. Otolaryngol. Head. Neck Surg.* 112, 1253–1261. doi: 10.1001/archotol.1986.03780120017003

Adams, J. C. (1997). Projections from octopus cells of the posteroventral cochlear nucleus to the ventral nucleus of the lateral lemniscus in cat and human. *Aud. Neurosci.* 3, 335–350.

Adams, J. C., and Mugnaini, E. (1987). Patterns of glutamate decarboxylase immunostaining in the feline cochlear nuclear complex studied with silver enhancement and electron microscopy. *J. Comp. Neurol.* 262, 375–401. doi: 10.1002/cne.902620305

Adams, J. C., and Mugnaini, E. (1990). Immunocytochemical evidence for inhibitory and disinhibitory circuits in the superior olive. *Hear. Res.* 49, 281–298. doi: 10.1016/0378-5955(90)90109-3

Adler, E. M., Augustine, G. J., Duffy, S. N., and Charlton, M. P. (1991). Alien intracellular calcium chelators attenuate neurotransmitter release at the squid giant synapse. *J. Neurosci.* 11, 1496–1507. doi: 10.1523/JNEUROSCI.11-06-01496.1991

Akhoun, I., Gallégo, S., Moulin, A., Ménard, M., Veuillet, E., Berger-Vachon, C., et al. (2008). The temporal relationship between speech auditory brainstem responses and the acoustic pattern of the phoneme/ba/in normal-hearing adults. *Clin. Neurophysiol.* 119, 922–933. doi: 10.1016/j.clinph.2007.12.010

Alamilla, J., and Gillespie, D. C. (2011). Glutamatergic inputs and glutamate-releasing immature inhibitory inputs activate a shared post-synaptic receptor population in lateral superior olive. *Neuroscience* 196, 285–296. doi: 10.1016/j.neuroscience.2011.08.060

Albrecht, O., Dondzillo, A., Mayer, F., Thompson, J. A., and Klug, A. (2014). Inhibitory projections from the ventral nucleus of the trapezoid body to the medial nucleus of the trapezoid body in the mouse. *Front. Neural Circ.* 8:83. doi: 10.3389/fncir.2014.00083

Alibardi, L. (2003). Ultrastructure and immunocytochemical characteristics of cells in the octopus cell area of the rat cochlear nucleus: comparison with multipolar cells. *Ann. Anat.* 185, 21–33. doi: 10.1016/S0940-9602(03)80003-1

Antunes, F. M., Rubio, M. E., and Kandler, K. (2020). Role of GluA3 AMPA receptor subunits in the pre-synaptic and post-synaptic maturation of synaptic transmission and plasticity of endbulb-bushy cell synapses in the cochlear nucleus. *J. Neurosci.* 40, 2471–2484. doi: 10.1523/JNEUROSCI.2573-19.2020

Arai, I., and Jonas, P. (2014). Nanodomain coupling explains Ca^{2+} independence of transmitter release time course at a fast central synapse. *Elife* 3, 1–13. doi: 10.7554/eLife.04057

Augustine, G. J. (1990). Regulation of transmitter release at the squid giant synapse by pre-synaptic delayed rectifier potassium current. *J. Physiol.* 431, 343–364. doi: 10.1113/jphysiol.1990.sp018333

Bal, R., and Oertel, D. (2000). Hyperpolarization-activated, mixed-cation current (I(h)) in octopus cells of the mammalian cochlear nucleus. *J. Neurophysiol.* 84, 806–817. doi: 10.1152/jn.2000.84.2.806

Bal, R., and Oertel, D. (2001). Potassium currents in octopus cells of the mammalian cochlear nucleus. *J. Neurophysiol.* 86, 2299–2311. doi: 10.1152/jn.2001.86.5.2299

Banks, M. I., and Smith, P. H. (1992). Intracellular recordings from neurobiotin-labeled cells in brain slices of the rat medial nucleus of the trapezoid body. *J. Neurosci.* 12, 2819–2837. doi: 10.1523/JNEUROSCI.12-07-02819.1992

Barnes-Davies, M., Barker, M. C., Osmani, F., and Forsythe, I. D. (2004). Kv1 currents mediate a gradient of principal neuron excitability across the tonotopic axis in the rat lateral superior olive. *Eur. J. Neurosci.* 19, 325–333. doi: 10.1111/j.0953-816X.2003.03133.x

Barnes-Davies, M., and Forsythe, I. D. (1995). Pre- and post-synaptic glutamate receptors at a giant excitatory synapse in rat auditory brainstem slices. *J. Physiol.* 488, 387–406. doi: 10.1113/jphysiol.1995.sp020974

Barnes-Davies, M., Owens, S., and Forsythe, I. D. (2001). Calcium channels triggering transmitter release in the rat medial superior olive. *Hear. Res.* 162, 134–145. doi: 10.1016/S0378-5955(01)00378-1

Baumann, V. J., and Koch, U. (2017). Perinatal nicotine exposure impairs the maturation of glutamatergic inputs in the auditory brainstem. *J. Physiol.* 12:12. doi: 10.1113/JP274059

Baumann, V. J., Lehnert, S., Leibold, C., and Koch, U. (2013). Tonotopic organization of the hyperpolarization-activated current (Ih) in the mammalian medial superior olive. *Front. Neural Circuits* 7:117. doi: 10.3389/fncir.2013.00117

Baydyuk, M., Xu, J., and Wu, L.-G. (2016). The calyx of Held in the auditory system: structure, function, and development. *Hear. Res.* 338, 22–31. doi: 10.1016/j.heares.2016.03.009

Bazwinsky, I., Bidmon, H. J., Zilles, K., and Hilbig, H. (2005). Characterization of the rhesus monkey superior olivary complex by calcium binding proteins and synaptophysin. *J. Anat.* 207, 745–761. doi: 10.1111/j.1469-7580.2005.00491.x

Bazwinsky, I., Härtig, W., and Rübsamen, R. (2008). Characterization of cochlear nucleus principal cells of Meriones unguiculatus and *Monodelphis domestica* by use of calcium-binding protein immunolabeling. *J. Chem. Neuroanat.* 35, 158–174. doi: 10.1016/j.jchemneu.2007.10.003

Bazwinsky, I., Hilbig, H., Bidmon, H. J., and Rübsamen, R. (2003). Characterization of the human superior olivary complex by calcium binding proteins and neurofilament H (SMI-32). *J. Comp. Neurol.* 456, 292–303. doi: 10.1002/cne.10526

Bazwinsky-Wutschke, I., Härtig, W., Kretzschmar, R., and Rübsamen, R. (2016). Differential morphology of the superior olivary complex of *Meriones unguiculatus* and *Monodelphis domestica* revealed by calcium-binding proteins. *Brain Struct. Funct.* 221, 4505–4523. doi: 10.1007/s00429-015-1181-x

Beiderbeck, B., Myoga, M. H., Müller, N. I. C., Callan, A. R., Friauf, E., Grothe, B., et al. (2018). Precisely timed inhibition facilitates action potential firing for spatial coding in the auditory brainstem. *Nat. Commun.* 9:1771. doi: 10.1038/s41467-018-04210-y

Berger, C., Meyer, E. M. M., Ammer, J. J., and Felmy, F. (2014). Large somatic synapses on neurons in the ventral lateral lemniscus work in pairs. *J. Neurosci.* 34, 3237–3246. doi: 10.1523/JNEUROSCI.3664-13.2014

Billings, G., Piasini, E., Lorincz, A., Nusser, Z., and Silver, R. A. (2014). Network structure within the cerebellar input layer enables lossless sparse encoding. *Neuron* 83, 960–974. doi: 10.1016/j.neuron.2014.07.020

Billups, B., and Forsythe, I. D. (2002). Pre-synaptic mitochondrial calcium sequestration influences transmission at mammalian central synapses. *J. Neurosci.* 22, 5840–5847. doi: 10.1523/JNEUROSCI.22-14-05840.2002

Blackburn, C. C., and Sachs, M. B. (1989). Classification of unit types in the anteroventral cochlear nucleus: PST histograms and regularity analysis. *J. Neurophysiol.* 62, 1303–1329. doi: 10.1152/jn.1989.62.6.1303

Bollmann, J. H., Sakmann, B., and Borst, J. G. (2000). Calcium sensitivity of glutamate release in a calyx-type terminal. *Science* 289, 953–957. doi: 10.1126/science.289.5481.953

Bondy, B. J., Haimes, D. B., and Golding, N. L. (2021). Physiological diversity influences detection of stimulus envelope and fine structure in neurons of the medial superior olive. *J. Neurosci.* 41, 6234–6245. doi: 10.1523/JNEUROSCI.2354-20.2021

Borst, J. G., Helmchen, F., and Sakmann, B. (1995). Pre- and post-synaptic whole-cell recordings in the medial nucleus of the trapezoid body of the rat. *J. Physiol.* 489, 825–840. doi: 10.1113/jphysiol.1995.sp021095

Borst, J. G., and Sakmann, B. (1996). Calcium influx and transmitter release in a fast CNS synapse. *Nature* 383, 431–434. doi: 10.1038/383431a0

Borst, J. G. G. (2010). The low synaptic release probability *in vivo*. *Trends Neurosci.* 33, 259–266. doi: 10.1016/j.tins.2010.03.003

Borst, J. G. G., and Soria van Hoeve, J. (2012). The calyx of Held synapse: from model synapse to auditory relay. *Annu. Rev. Physiol.* 74, 199–224. doi: 10.1146/annurev-physiol-020911-153236

Bouhours, B., Gjoni, E., Kochubey, O., and Schneggenburger, R. (2017). Synaptotagmin2 (Syt2) drives fast release redundantly with syt1 at the output synapses of parvalbumin-expressing inhibitory neurons. *J. Neurosci.* 37, 4604–4617. doi: 10.1523/JNEUROSCI.3736-16.2017

Brand, A., Behrend, O., Marquardt, T., McAlpine, D., and Grothe, B. (2002). Precise inhibition is essential for microsecond interaural time difference coding. *Nature* 417, 543–547. doi: 10.1038/417543a

Brawer, J. R., and Morest, D. K. (1975). Relations between auditory nerve endings and cell types in the cat's anteroventral cochlear nucleus seen with the Golgi method and Nomarski optics. *J. Comp. Neurol.* 160, 491–506. doi: 10.1002/cne.901600406

Brawer, J. R., Morest, D. K., and Kane, E. C. (1974). The neuronal architecture of the cochlear nucleus of the cat. *J. Comp. Neurol.* 155, 251–299. doi: 10.1002/cne.901550302

Brenowitz, S., David, J., and Trussell, L. (1998). Enhancement of synaptic efficacy by pre-synaptic GABA(B) receptors. *Neuron* 20, 135–141. doi: 10.1016/S0896-6273(00)80441-9

Brenowitz, S., and Trussell, L. O. (2001a). Maturation of synaptic transmission at end-bulb synapses of the cochlear nucleus. *J. Neurosci.* 21, 9487–9498. doi: 10.1523/JNEUROSCI.21-23-09487.2001

Brenowitz, S., and Trussell, L. O. (2001b). Minimizing synaptic depression by control of release probability. *J. Neurosci.* 21, 1857–1867. doi: 10.1523/JNEUROSCI.21-06-01857.2001

Brew, H. M., and Forsythe, I. D. (1995). Two voltage-dependent K+ conductances with complementary functions in post-synaptic integration at a central auditory synapse. *J. Neurosci.* 15, 8011–8022. doi: 10.1523/JNEUROSCI.15-12-08011.1995

Brill, S. E., Janz, K., Singh, A., and Friauf, E. (2019). Considerable differences between auditory medulla, auditory midbrain, and hippocampal synapses during sustained high-frequency stimulation: Exceptional vesicle replenishment restricted to sound localization circuit. *Hear. Res.* 381:107771. doi: 10.1016/j.heares.2019.07.008

Brown, M. C., and Ledwith, J. V. 3rd (1990). Projections of thin (type-II) and thick (type-I) auditory-nerve fibers into the cochlear nucleus of the mouse. *Hear. Res.* 49, 105–118. doi: 10.1016/0378-5955(90)90098-A

Brown, M. R., El-Hassar, L., Zhang, Y., Alvaro, G., Large, C. H., and Kaczmarek, L. K. (2016). Physiological modulators of Kv3.1 channels adjust firing patterns of auditory brain stem neurons. *J. Neurophysiol.* 116, 106–121. doi: 10.1152/jn.00174.2016

Browner, R. H., and Marbey, D. (1988). The nucleus magnocellularis in the red-eared turtle, Chrysemys scripta elegans: eighth nerve endings and neuronal types. *Hear. Res.* 33, 257–271. doi: 10.1016/0378-5955(88)90156-6

Brunso-Bechtold, J. K., Henkel, C. K., and Linville, C. (1990). Synaptic organization in the adult ferret medial superior olive. *J. Comp. Neurol.* 294, 389–398. doi: 10.1002/cne.902940308

Brunso-Bechtold, J. K., Linville, M. C., and Henkel, C. K. (1994). Terminal types on ipsilaterally and contralaterally projecting lateral superior olive cells. *Hear. Res.* 77, 99–104. doi: 10.1016/0378-5955(94)90257-7

Brunso-Bechtold, J. K., Thompson, G. C., and Masterton, R. B. (1981). HRP study of the organization of auditory afferents ascending to central nucleus of inferior colliculus in cat. *J. Comp. Neurol.* 197, 705–722. doi: 10.1002/cne.901970410

Bucurenciu, I., Kulik, A., Schwaller, B., Frotscher, M., and Jonas, P. (2008). Nanodomain coupling between Ca2+ channels and Ca2+ sensors promotes fast and efficient transmitter release at a cortical GABAergic synapse. *Neuron* 57, 536–545. doi: 10.1016/j.neuron.2007.12.026

Budisantoso, T., Harada, H., Kamasawa, N., Fukazawa, Y., Shigemoto, R., and Matsui, K. (2013). Evaluation of glutamate concentration transient in the synaptic cleft of the rat calyx of Held: glutamate concentration in synapse. *J. Physiol.* 591, 219–239. doi: 10.1113/jphysiol.2012.241398

Budisantoso, T., Matsui, K., Kamasawa, N., Fukazawa, Y., and Shigemoto, R. (2012). Mechanisms underlying signal filtering at a multisynapse contact. *J. Neurosci.* 32, 2357–2376. doi: 10.1523/JNEUROSCI.5243-11.2012

Butola, T., Alvanos, T., Hintze, A., Koppensteiner, P., Kleindienst, D., Shigemoto, R., et al. (2021). RIM-binding protein 2 organizes Ca21 channel topography and regulates release probability and vesicle replenishment at a fast central synapse. *J. Neurosci.* 41, 7742–7767. doi: 10.1523/JNEUROSCI.0586-21.2021

Caicedo, A., and Eybalin, M. (1999). Glutamate receptor phenotypes in the auditory brainstem and mid-brain of the developing rat. *Eur. J. Neurosci.* 11, 51–74. doi: 10.1046/j.1460-9568.1999.00410.x

Callan, A. R., He,ß, M., Felmy, F., and Leibold, C. (2021). Arrangement of excitatory synaptic inputs on dendrites of the medial superior Olive. *J. Neurosci.* 41, 269–283. doi: 10.1523/JNEUROSCI.1055-20.2020

Cant, N. B. (1984). The fine structure of the lateral superior olivary nucleus of the cat. *J. Comp. Neurol.* 227, 63–77. doi: 10.1002/cne.902270108

Cant, N. B. (2013). Patterns of convergence in the central nucleus of the inferior colliculus of the Mongolian gerbil: Organization of inputs from the superior olivary complex in the low frequency representation. *Front. Neural Circuits* 7:29. doi: 10.3389/fncir.2013.00029

Cant, N. B., and Benson, C. G. (2006). Wisteria floribunda lectin is associated with specific cell types in the ventral cochlear nucleus of the gerbil, Meriones unguiculatus. *Hear. Res. 216–217* 64–72. doi: 10.1016/j.heares.2006.01.008

Cant, N. B., and Casseday, J. H. (1986). Projections from the anteroventral cochlear nucleus to the lateral and medial superior olivary nuclei. *J. Comp. Neurol.* 247, 457–476. doi: 10.1002/cne.902470406

Cant, N. B., and Hyson, R. L. (1992). Projections from the lateral nucleus of the trapezoid body to the medial superior olivary nucleus in the gerbil. *Hear. Res.* 58, 26–34. doi: 10.1016/0378-5955(92)90005-8

Cant, N. B., and Morest, D. K. (1979a). Organization of the neurons in the anterior division of the anteroventral cochlear nucleus of the cat. Light-microscopic observations. *Neuroscience* 4, 1909–1923. doi: 10.1016/0306-4522(79)90065-4

Cant, N. B., and Morest, D. K. (1979b). The bushy cells in the anteroventral cochlear nucleus of the cat. A study with the electron microscope. *Neuroscience* 4, 1925–1945. doi: 10.1016/0306-4522(79)90066-6

Cao, X.-J., and Oertel, D. (2005). Temperature affects voltage-sensitive conductances differentially in octopus cells of the mammalian cochlear nucleus. *J. Neurophysiol.* 94, 821–832. doi: 10.1152/jn.01049.2004

Cao, X.-J., and Oertel, D. (2010). Auditory nerve fibers excite targets through synapses that vary in convergence, strength, and short-term plasticity. *J. Neurophysiol.* 104, 2308–2320. doi: 10.1152/jn.00451.2010

Cao, X.-J., and Oertel, D. (2011). The magnitudes of hyperpolarization-activated and low-voltage-activated potassium currents co-vary in neurons of the ventral cochlear nucleus. *J. Neurophysiol.* 106, 630–640. doi: 10.1152/jn.00015.2010

Cao, X.-J., and Oertel, D. (2017). Genetic perturbations suggest a role of the resting potential in regulating the expression of the ion channels of the KCNA and HCN families in octopus cells of the ventral cochlear nucleus. *Hear. Res.* 345, 57–68. doi: 10.1016/j.heares.2017.01.001

Cao, X.-J., Shatadal, S., and Oertel, D. (2007). Voltage-sensitive conductances of bushy cells of the Mammalian ventral cochlear nucleus. *J. Neurophysiol.* 97, 3961–3975. doi: 10.1152/jn.00052.2007

Carr, C. E., and Boudreau, R. E. (1991). Central projections of auditory nerve fibers in the barn owl. *J. Comp. Neurol.* 314, 306–318. doi: 10.1002/cne.903140208

Case, D. T., Zhao, X., and Gillespie, D. C. (2011). Functional refinement in the projection from ventral cochlear nucleus to lateral superior olive precedes hearing onset in rat. *PLoS ONE* 6:e20756. doi: 10.1371/journal.pone.0020756

Casey, M. A. (1990). The effects of aging on neuron number in the rat superior olivary complex. *Neurobiol. Aging* 11, 391–394. doi: 10.1016/0197-4580(90)90004-J

Casey, M. A., and Feldman, M. L. (1982). Aging in the rat medial nucleus of the trapezoid body I. Light microscopy. *Neurobiol. Aging* 3, 187–195. doi: 10.1016/0197-4580(82)90039-2

Caspari, F., Baumann, V. J., Garcia-Pino, E., and Koch, U. (2015). Heterogeneity of intrinsic and synaptic properties of neurons in the ventral and dorsal parts of the ventral nucleus of the lateral lemniscus. *Front. Neural Circuits* 9:74. doi: 10.3389/fncir.2015.00074

Casseday, J. H., Covey, E., and Vater, M. (1988). Connections of the superior olivary complex in the rufous horseshoe bat Rhinolophus rouxi. *J. Comp. Neurol.* 278, 313–329. doi: 10.1002/cne.902780302

Cathala, L., Holderith, N. B., Nusser, Z., DiGregorio, D. A., and Cull-Candy, S. G. (2005). Changes in synaptic structure underlie the developmental speeding of AMPA receptor-mediated EPSCs. *Nat. Neurosci.* 8, 1310–1318. doi: 10.1038/nn1534

Chanda, S., and Xu-Friedman, M. A. (2010). Neuromodulation by GABA converts a relay into a coincidence detector. *J. Neurophysiol.* 104, 2063–2074. doi: 10.1152/jn.00474.2010

Chao, O. Y., and Yang, Y.-M. (2019). Timing constraints of action potential evoked Ca2+ current and transmitter release at a central nerve terminal. *Sci. Rep.* 9:4448. doi: 10.1038/s41598-019-41120-5

Chen, S., Wang, J., and Siegelbaum, S. A. (2001). Properties of hyperpolarization-activated pacemaker current defined by coassembly of HCN1 and HCN2 subunits and basal modulation by cyclic nucleotide. *J. Gen. Physiol.* 117, 491–503. doi: 10.1085/jgp.117.5.491

Chen, Z., Das, B., Nakamura, Y., DiGregorio, D. A., and Young, S. M. Jr (2015). Ca2+ channel to synaptic vesicle distance accounts for the readily releasable pool kinetics at a functionally mature auditory synapse. *J. Neurosci.* 35, 2083–2100. doi: 10.1523/JNEUROSCI.2753-14.2015

Chirila, F. V., Rowland, K. C., Thompson, J. M., and Spirou, G. A. (2007). Development of gerbil medial superior olive: integration of temporally delayed excitation and inhibition at physiological temperature. *J. Physiol.* 584, 167–190. doi: 10.1113/jphysiol.2007.137976

Choudhury, N., Linley, D., Richardson, A., Anderson, M., Robinson, S. W., Marra, V., et al. (2020). Kv3.1 and Kv3.3 subunits differentially contribute to Kv3 channels and action potential repolarization in principal neurons of the auditory brainstem. *J. Physiol.* 598, 2199–2222. doi: 10.1113/JP279668

Chow, A., Erisir, A., Farb, C., Nadal, M. S., Ozaita, A., Lau, D., et al. (1999). K(+) channel expression distinguishes subpopulations of parvalbumin- and somatostatin-containing neocortical interneurons. *J. Neurosci.* 19, 9332–9345. doi: 10.1523/JNEUROSCI.19-21-09332.1999

Clark, G. M. (1969a). The ultrastructure of nerve endings in the medial superior olive of the cat. *Brain Res.* 14, 293–305. doi: 10.1016/0006-8993(69)90111-5

Clark, G. M. (1969b). Vesicle shape versus type of synapse in the nerve endings of the cat medial superior olive. *Brain Res.* 15, 548–551. doi: 10.1016/0006-8993(69)90181-4

Coetzee, W. A., Amarillo, Y., Chiu, J., Chow, A., Lau, D., McCormack, T., et al. (1999). Molecular diversity of K+ channels. *Ann. N. Y. Acad. Sci.* 868, 233–285. doi: 10.1111/j.1749-6632.1999.tb11293.x

Cooper, A. P., and Gillespie, D. C. (2011). Synaptotagmins I and II in the developing rat auditory brainstem: Synaptotagmin I is transiently expressed in glutamate-releasing immature inhibitory terminals. *J. Comp. Neurol.* 519, 2417–2433. doi: 10.1002/cne.22634

Couchman, K., Grothe, B., and Felmy, F. (2010). Medial superior olivary neurons receive surprisingly few excitatory and inhibitory inputs with balanced strength and short-term dynamics. *J. Neurosci.* 30, 17111–17121. doi: 10.1523/JNEUROSCI.1760-10.2010

Couchman, K., Grothe, B., and Felmy, F. (2012). Functional localization of neurotransmitter receptors and synaptic inputs to mature neurons of the medial superior olive. *J. Neurophysiol.* 107, 1186–1198. doi: 10.1152/jn.00586.2011

Covey, E., and Casseday, J. H. (1986). Connectional basis for frequency representation in the nuclei of the lateral lemniscus of the bat Eptesicus fuscus. *J. Neurosci.* 6, 2926–2940. doi: 10.1523/JNEUROSCI.06-10-02926.1986

Covey, E., and Casseday, J. H. (1991). The monaural nuclei of the lateral lemniscus in an echolocating bat: parallel pathways for analyzing temporal features of sound. *J. Neurosci.* 11, 3456–3470. doi: 10.1523/JNEUROSCI.11-11-03456.1991

Crins, T. T. H., Rusu, S. I., Rodríguez-Contreras, A., and Borst, J. G. G. (2011). Developmental changes in short-term plasticity at the rat calyx of Held synapse. *J. Neurosci.* 31, 11706–11717. doi: 10.1523/JNEUROSCI.1995-11.2011

D'Angelo, E., Rossi, P., and Garthwaite, J. (1990). Dual-component NMDA receptor currents at a single central synapse. *Nature* 346, 467–470. doi: 10.1038/346467a0

D'Angelo, E., Rossi, P., and Taglietti, V. (1993). Different proportions of N-methyl-d-aspartate and non-N-methyl-d-aspartate receptor currents at the mossy fibre-granule cell synapse of developing rat cerebellum. *Neuroscience* 53, 121–130. doi: 10.1016/0306-4522(93)90290-V

de Cheveigné, A. (2021). Harmonic cancellation-A fundamental of Auditory Scene Analysis. *Trends Hear.* 25:23312165211041424. doi: 10.1177/23312165211041422

de Lange, R. P. J., de Roos, A. D. G., and Borst, J. G. G. (2003). Two modes of vesicle recycling in the rat calyx of Held. *J. Neurosci.* 23, 10164–10173. doi: 10.1523/JNEUROSCI.23-31-10164.2003

De No, R. L. (1933). Anatomy of the eighth nerve: III.—General plan of structure of the primary cochlear nuclei. *Laryngoscope* 43, 327–350. doi: 10.1288/00005537-193304000-00014

Dehmel, S., Kopp-Scheinpflug, C., Weick, M., Dörrscheidt, G. J. G. J., and Rübsamen, R. (2010). Transmission of phase-coupling accuracy from the auditory nerve to spherical bushy cells in the Mongolian gerbil. *Hear. Res.* 268, 234–249. doi: 10.1016/j.heares.2010.06.005

Delvendahl, I., Jablonski, L., Baade, C., Matveev, V., Neher, E., and Hallermann, S. (2015a). Reduced endogenous Ca2+ buffering speeds active zone Ca2+ signaling. *Proc. Natl. Acad. Sci. U. S. A.* 112, E3075–3084. doi: 10.1073/pnas.1508419112

Delvendahl, I., Straub, I., and Hallermann, S. (2015b). Dendritic patch-clamp recordings from cerebellar granule cells demonstrate electrotonic compactness. *Front. Cell. Neurosci.* 9:93. doi: 10.3389/fncel.2015.00093

Digregorio, D. A., Nusser, Z., and Silver, R. A. (2002). Spillover of Glutamate onto Synaptic AMPA Receptors Enhances Fast Transmission at a Cerebellar Synapse the presence of slowly decaying components in some synaptic currents indicates that significant levels of glu. *Neuron* 35, 521–533. doi: 10.1016/S0896-6273(02)00787-0

DiGregorio, D. A., Rothman, J. S., Nielsen, T. A., and Silver, R. A. (2007). Desensitization properties of AMPA receptors at the cerebellar mossy fiber-granule cell synapse. *J. Neurosci.* 27, 8344–8357. doi: 10.1523/JNEUROSCI.2399-07.2007

Dodson, P. D., Barker, M. C., and Forsythe, I. D. (2002). Two heteromeric Kv1 potassium channels differentially regulate action potential firing. *J. Neurosci.* 22, 6953–6961. doi: 10.1523/JNEUROSCI.22-16-06953.2002

Dodson, P. D., Billups, B., Rusznák, Z., Szûcs, G., Barker, M. C., and Forsythe, I. D. (2003). Pre-synaptic rat Kv1.2 channels suppress synaptic terminal hyperexcitability following action potential invasion. *J. Physiol.* 550, 27–33. doi: 10.1113/jphysiol.2003.046250

Dolphin, A. C., and Lee, A. (2020). Pre-synaptic calcium channels: specialized control of synaptic neurotransmitter release. *Nat. Rev. Neurosci.* 21, 213–229. doi: 10.1038/s41583-020-0278-2

Dondzillo, A., Sätzler, K., Horstmann, H., Altrock, W. D., Gundelfinger, E. D., and Kuner, T. (2010). Targeted three-dimensional immunohistochemistry reveals localization of pre-synaptic proteins Bassoon and Piccolo in the rat calyx of held before and after the onset of hearing. *J. Comp. Neurol.* 518, 1008–1029. doi: 10.1002/cne.22260

Doucet, J. R., and Ryugo, D. K. (2003). Axonal pathways to the lateral superior olive labeled with biotinylated dextran amine injections in the dorsal cochlear nucleus of rats. *J. Comp. Neurol.* 461, 452–465. doi: 10.1002/cne.10722

Doughty, J. M., Barnes-Davies, M., Rusznák, Z., Harasztosi, C., and Forsythe, I. D. (1998). Contrasting Ca2+ channel subtypes at cell bodies and synaptic terminals of rat anterioventral cochlear bushy neurones. *J. Physiol.* 512, 365–376. doi: 10.1111/j.1469-7793.1998.365be.x

Du, J., Zhang, L., Weiser, M., Rudy, B., and McBain, C. J. (1996). Developmental expression and functional characterization of the potassium-channel subunit Kv3.1b in parvalbumin-containing interneurons of the rat hippocampus. *J. Neurosci.* 16, 506–518. doi: 10.1523/JNEUROSCI.16-02-00506.1996

Eggermann, E., Bucurenciu, I., Goswami, S. P., and Jonas, P. (2011). Nanodomain coupling between Ca^{2+} channels and sensors of exocytosis at fast mammalian synapses. *Nat. Rev. Neurosci.* 13, 7–21. doi: 10.1038/nrn3125

Elezgarai, I., Díez, J., Puente, N., Azkue, J. J., Benítez, R., Bilbao, A., et al. (2003). Subcellular localization of the voltage-dependent potassium channel Kv3.1b in postnatal and adult rat medial nucleus of the trapezoid body. *Neuroscience* 118, 889–898. doi: 10.1016/S0306-4522(03)00068-X

Englitz, B., Tolnai, S., Typlt, M., Jost, J., and Rübsamen, R. (2009). Reliability of synaptic transmission at the synapses of held in vivo under acoustic stimulation. *PLoS ONE* 4:e7014. doi: 10.1371/journal.pone.0007014

Erisir, A., Lau, D., Rudy, B., and Leonard, C. S. (1999). Function of specific K+ channels in sustained high-frequency firing of fast-spiking neocortical interneurons. *J. Neurophysiol.* 82, 2476–2489. doi: 10.1152/jn.1999.82.5.2476

Fedchyshyn, M. J., and Wang, L.-Y. (2005). Developmental transformation of the release modality at the calyx of Held synapse. *J. Neurosci.* 25, 4131–4140. doi: 10.1523/JNEUROSCI.0350-05.2005

Fedchyshyn, M. J., and Wang, L.-Y. (2007). Activity-dependent changes in temporal components of neurotransmission at the juvenile mouse calyx of Held synapse: modulation of synaptic delay and neurotransmission. *J. Physiol.* 581, 581–602. doi: 10.1113/jphysiol.2007.129833

Fekete, A., Nakamura, Y., Yang, Y.-M., Herlitze, S., Mark, M. D., DiGregorio, D. A., et al. (2019). Underpinning heterogeneity in synaptic transmission by pre-synaptic ensembles of distinct morphological modules. *Nat. Commun.* 10:826. doi: 10.1038/s41467-019-08452-2

Felix, R. A., Ii, Gourévitch, B., Gómez-Álvarez, M., Leijon, S. C. M., Saldaña, E., and Magnusson, A. K. (2017). Octopus cells in the posteroventral cochlear nucleus provide the main excitatory input to the superior paraolivary nucleus. *Front. Neural Circuits* 11:37. doi: 10.3389/fncir.2017.00037

Felmy, F., Neher, E., and Schneggenburger, R. (2003). Probing the intracellular calcium sensitivity of transmitter release during synaptic facilitation. *Neuron* 37, 801–811. doi: 10.1016/S0896-6273(03)00085-0

Feng, J. J., Kuwada, S., Ostapoff, E. M., Batra, R., and Morest, D. K. (1994). A physiological and structural study of neuron types in the cochlear nucleus. I. Intracellular responses to acoustic stimulation and current injection. *J. Comp. Neurol.* 346, 1–18. doi: 10.1002/cne.903460102

Fernández-Chacón, R., Königstorfer, A., Gerber, S. H., García, J., Matos, M. F., Stevens, C. F., et al. (2001). Synaptotagmin I functions as a calcium regulator of release probability. *Nature* 410, 41–49. doi: 10.1038/35065004

Finlayson, P. G., and Caspary, D. M. (1989). Synaptic potentials of chinchilla lateral superior olivary neurons. *Hear. Res.* 38, 221–228. doi: 10.1016/0378-5955(89)90067-1

Finlayson, P. G., and Caspary, D. M. (1991). Low-frequency neurons in the lateral superior olive exhibit phase-sensitive binaural inhibition. *J. Neurophysiol.* 65, 598–605. doi: 10.1152/jn.1991.65.3.598

Fischer, L., Leibold, C., and Felmy, F. (2018). Resonance properties in auditory brainstem neurons. *Front. Cell. Neurosci.* 12:8. doi: 10.3389/fncel.2018.00008

Fischl, M. J., Burger, R. M., Schmidt-Pauly, M., Alexandrova, O., Sinclair, J. L., Grothe, B., et al. (2016). Physiology and anatomy of neurons in the medial superior olive of the mouse. *J. Neurophysiol.* 116, 2676–2688. doi: 10.1152/jn.00523.2016

Ford, M. C., Alexandrova, O., Cossell, L., Stange-Marten, A., Sinclair, J., Kopp-Scheinpflug, C., et al. (2015). Tuning of Ranvier node and internode properties in myelinated axons to adjust action potential timing. *Nat. Commun.* 6:8073. doi: 10.1038/ncomms9073

Forsythe, I. D. (1994). Direct patch recording from identified pre-synaptic terminals mediating glutamatergic EPSCs in the rat CNS, in vitro. *J. Physiol.* 479, 381–387. doi: 10.1113/jphysiol.1994.sp020303

Forsythe, I. D., Tsujimoto, T., Barnes-Davies, M., Cuttle, M. F., and Takahashi, T. (1998). Inactivation of pre-synaptic calcium current contributes to synaptic depression at a fast central synapse. *Neuron* 20, 797–807. doi: 10.1016/S0896-6273(00)81017-X

Franken, T. P., Joris, P. X., and Smith, P. H. (2018). Principal cells of the brainstem's interaural sound level detector are temporal differentiators rather than integrators. *Elife* 7, 1–25. doi: 10.7554/eLife.33854

Franken, T. P., Roberts, M. T., Wei, L., Golding, N. L., and Joris, P. X. (2015). In vivo coincidence detection in mammalian sound localization generates phase delays. *Nat. Neurosci.* 18, 444–452. doi: 10.1038/nn.3948

Franzen, D. L., Gleiss, S. A., Berger, C., Kümpfbeck, F. S., Ammer, J. J., and Felmy, F. (2015). Development and modulation of intrinsic membrane properties control the temporal precision of auditory brain stem neurons. *J. Neurophysiol.* 113, 524–536. doi: 10.1152/jn.00601.2014

Franzen, D. L., Gleiss, S. A., Kellner, C. J., Kladisios, N., and Felmy, F. (2020). Activity-dependent calcium signaling in neurons of the medial superior Olive during late postnatal development. *J. Neurosci.* 40, 1689–1700. doi: 10.1523/JNEUROSCI.1545-19.2020

Friauf, E. (1992). Tonotopic order in the adult and developing auditory system of the rat as shown by c-fos immunocytochemistry. *Eur. J. Neurosci.* 4, 798–812. doi: 10.1111/j.1460-9568.1992.tb00190.x

Friauf, E., Hammerschmidt, B., and Kirsch, J. (1997). Development of adult-type inhibitory glycine receptors in the central auditory system of rats. *J. Comp. Neurol.* 385, 117–134. doi: 10.1002/(SICI)1096-9861(19970818)385:1<117::AID-CNE7>3.0.CO;2-5

Friauf, E., and Ostwald, J. (1988). Divergent projections of physiologically characterized rat ventral cochlear nucleus neurons as shown by intra-axonal injection of horseradish peroxidase. *Exp. Brain Res.* 73, 263–284. doi: 10.1007/BF00248219

Futai, K., Okada, M., Matsuyama, K., and Takahashi, T. (2001). High-fidelity transmission acquired via a developmental decrease in NMDA receptor expression at an auditory synapse. *J. Neurosci.* 21, 3342–3349. doi: 10.1523/JNEUROSCI.21-10-03342.2001

Garcia-Pino, E., Gessele, N., and Koch, U. (2017). Enhanced excitatory connectivity and disturbed sound processing in the auditory brainstem of Fragile X mice. *J. Neurosci.* 37, 7403–7419. doi: 10.1523/JNEUROSCI.2310-16.2017

Gardner, S. M., Trussell, L. O., and Oertel, D. (1999). Time course and permeation of synaptic AMPA receptors in cochlear nuclear neurons correlate with input. *J. Neurosci.* 19, 8721–8729. doi: 10.1523/JNEUROSCI.19-20-08721.1999

Gardner, S. M., Trussell, L. O., and Oertel, D. (2001). Correlation of AMPA receptor subunit composition with synaptic input in the mammalian cochlear nuclei. *J. Neurosci.* 21, 7428–7437. doi: 10.1523/JNEUROSCI.21-18-07428.2001

Garwicz, M., Jörntell, H., and Ekerot, C. F. (1998). Cutaneous receptive fields and topography of mossy fibres and climbing fibres projecting to cat cerebellar C3 zone. *J. Physiol.* 512, 277–293. doi: 10.1111/j.1469-7793.1998.277bf.x

Gazula, V.-R., Strumbos, J. G., Mei, X., Chen, H., Rahner, C., and Kaczmarek, L. K. (2010). Localization of Kv1.3 channels in pre-synaptic terminals of brainstem auditory neurons. *J. Comp. Neurol.* 518, 3205–3220. doi: 10.1002/cne.22393

Geiger, J. R. P., Melcher, T., Koh, D. S., Sakmann, B., Seeburg, P. H., Jonas, P., et al. (1995). Relative abundance of subunit mRNAs determines gating and Ca2+ permeability of AMPA receptors in principal neurons and interneurons in rat CNS. *Neuron* 15, 193–204. doi: 10.1016/0896-6273(95)90076-4

Geppert, M., Goda, Y., Hammer, R. E., Li, C., Rosahl, T. W., Stevens, C. F., et al. (1994). Synaptotagmin I: A major Ca2+ sensor for transmitter release at a central synapse. *Cell* 79, 717–727. doi: 10.1016/0092-8674(94)90556-8

Gessele, N., Garcia-Pino, E., Omerbaši,ć, D., Park, T. J., and Koch, U. (2016). Structural changes and lack of HCN1 channels in the binaural auditory brainstem of the naked mole-rat (*Heterocephalus glaber*). *PLoS ONE* 11:e0146428. doi: 10.1371/journal.pone.0146428

Gittis, A. H., Moghadam, S. H., and du Lac, S. (2010). Mechanisms of sustained high firing rates in two classes of vestibular nucleus neurons: differential contributions of resurgent Na, Kv3, and BK currents. *J. Neurophysiol.* 104, 1625–1634. doi: 10.1152/jn.00378.2010

Giugovaz-Tropper, B., González-Inchauspe, C., Di Guilmi, M. N., Urbano, F. J., Forsythe, I. D., and Uchitel, O. D. (2011). P/Q-type calcium channel ablation in a mice glycinergic synapse mediated by multiple types of Ca 2+ channels alters transmitter release and short term plasticity. *Neuroscience* 192, 219–230. doi: 10.1016/j.neuroscience.2011.06.021

Gjoni, E., Aguet, C., Sahlender, D. A., Knott, G., and Schneggenburger, R. (2018a). Ultrastructural basis of strong unitary inhibition in a binaural neuron. *J. Physiol.* 596, 4969–4982. doi: 10.1113/JP276015

Gjoni, E., Zenke, F., Bouhours, B., and Schneggenburger, R. (2018b). Specific synaptic input strengths determine the computational properties of excitation-inhibition integration in a sound localization circuit. *J. Physiol.* 596, 4945–4967. doi: 10.1113/JP276012

Gleich, O., Kadow, C., and Strutz, J. (1998). The postnatal growth of cochlear nucleus subdivisions and neuronal somata of the anteroventral cochlear nucleus in the *Mongolian gerbil* (*Meriones unguiculatus*). *Audiol. Neurootol.* 3, 1–20. doi: 10.1159/000013775

Glendenning, K. K., Brusno-Bechtold, J. K., Thompson, G. C., and Masterton, R. B. (1981). Ascending auditory afferents to the nuclei of the lateral leminscus. *J. Comp. Neurol.* 197, 673–703. doi: 10.1002/cne.901970409

Glendenning, K. K., and Masterton, R. B. (1998). Comparative morphometry of mammalian central auditory systems: variation in nuclei and form of the ascending system. *Brain Behav. Evol.* 51, 59–89. doi: 10.1159/000006530

Godfrey, D. A., Kiang, N. Y., and Norris, B. E. (1975). Single unit activity in the posteroventral cochlear nucleus of the cat. *J. Comp. Neurol.* 162, 247–268. doi: 10.1002/cne.901620206

Goldberg, J. M., and Brown, P. B. (1969). Response of binaural neurons of dog superior olivary complex to dichotic tonal stimuli: some physiological mechanisms of sound localization. *J. Neurophysiol.* 32, 613–636. doi: 10.1152/jn.1969.32.4.613

Golding, N. L., Ferragamo, M. J., and Oertel, D. (1999). Role of intrinsic conductances underlying responses to transients in octopus cells of the cochlear nucleus. *J. Neurosci.* 19, 2897–2905. doi: 10.1523/JNEUROSCI.19-08-02897.1999

Golding, N. L., and Oertel, D. (2012). Synaptic integration in dendrites: exceptional need for speed: Need for speed in auditory neurons. *J. Physiol.* 590, 5563–5569. doi: 10.1113/jphysiol.2012.229328

Golding, N. L., Robertson, D., and Oertel, D. (1995). Recordings from slices indicate that octopus cells of the cochlear nucleus detect coincident firing of auditory nerve fibers with temporal precision. *J. Neurosci.* 15, 3138–3153. doi: 10.1523/JNEUROSCI.15-04-03138.1995

Gómez-Martínez, M., Rincón, H., Gómez-Álvarez, M., Gómez-Nieto, R., and Saldaña, E. (2023). The nuclei of the lateral lemniscus: unexpected players in the descending auditory pathway. *Front. Neuroanat.* 17:1242245. doi: 10.3389/fnana.2023.1242245

Gómez-Nieto, R., and Rubio, M. E. (2009). A bushy cell network in the rat ventral cochlear nucleus. *J. Comp. Neurol.* 516, 241–263. doi: 10.1002/cne.22139

Gómez-Nieto, R., and Rubio, M. E. (2011). Ultrastructure, synaptic organization, and molecular components of bushy cell networks in the anteroventral cochlear nucleus of the rhesus monkey. *Neuroscience* 179, 188–207. doi: 10.1016/j.neuroscience.2011.01.058

Gourévitch, B., Edeline, J. M., Occelli, F., and Eggermont, J. J. (2014). Is the din really harmless? Long-term effects of non-traumatic noise on the adult auditory system. *Nat. Rev. Neurosci.* 15, 483–491. doi: 10.1038/nrn3744

Grande, G., Negandhi, J., Harrison, R. V., and Wang, L.-Y. (2014). Remodeling at the calyx of Held-MNTB synapse in mice developing with unilateral conductive hearing loss. *J. Physiol.* 592, 1581–1600. doi: 10.1113/jphysiol.2013.268839

Grande, G., and Wang, L.-Y. (2011). Morphological and functional continuum underlying heterogeneity in the spiking fidelity at the calyx of Held synapse in vitro. *J. Neurosci.* 31, 13386–13399. doi: 10.1523/JNEUROSCI.0400-11.2011

Green, J. S., and Sanes, D. H. (2005). Early appearance of inhibitory input to the MNTB supports binaural processing during development. *J. Neurophysiol.* 94, 3826–3835. doi: 10.1152/jn.00601.2005

Greene, N. T., and Davis, K. A. (2012). Discharge patterns in the lateral superior olive of decerebrate cats. *J. Neurophysiol.* 108, 1942–1953. doi: 10.1152/jn.00908.2011

Grothe, B. (2000). The evolution of temporal processing in the medial superior olive, an auditory brainstem structure. *Prog. Neurobiol.* 61, 581–610. doi: 10.1016/S0301-0082(99)00068-4

Grothe, B., and Park, T. J. (2000). Structure and function of the bat superior olivary complex. *Microsc. Res. Tech.* 51, 382–402. doi: 10.1002/1097-0029(20001115)51:4<382::AID-JEMT7>3.0.CO;2-7

Grothe, B., and Pecka, M. (2014). The natural history of sound localization in mammals–a story of neuronal inhibition. *Front. Neural Circuits* 8:116. doi: 10.3389/fncir.2014.00116

Grothe, B., Pecka, M., and McAlpine, D. (2010). Mechanisms of sound localization in mammals. *Physiol. Rev.* 90, 983–1012. doi: 10.1152/physrev.00026.2009

Grothe, B., and Sanes, D. H. (1993). Bilateral inhibition by glycinergic afferents in the medial superior olive. *J. Neurophysiol.* 69, 1192–1196. doi: 10.1152/jn.1993.69.4.1192

Grothe, B., and Sanes, D. H. (1994). Synaptic inhibition influences the temporal coding properties of medial superior olivary neurons: an in vitro study. *J. Neurosci.* 14, 1701–1709. doi: 10.1523/JNEUROSCI.14-03-01701.1994

Guinan, J. J., Guinan, S. S., and Norris, B. E. (1972). Single auditory units in the superior olivary complex: I: responses to sounds and classifications based on physiological properties. *Int. J. Neurosci.* 4, 101–120. doi: 10.3109/00207457209147165

Guinan, J. J., and Li, R. Y. (1990). Signal processing in brainstem auditory neurons which receive giant endings (calyces of Held) in the medial nucleus of the trapezoid body of the cat. *Hear. Res.* 49, 321–334. doi: 10.1016/0378-5955(90)90111-2

Guo, J., Ge, J.-L., Hao, M., Sun, Z.-C., Wu, X.-S., Zhu, J.-B., et al. (2015). A three-pool model dissecting readily releasable pool replenishment at the calyx of held. *Sci. Rep.* 5:9517. doi: 10.1038/srep09517

Hackney, C. M., Osen, K. K., Ottersen, O. P., Storm-Mathisen, J., and Manjaly, G. (1996). Immunocytochemical evidence that glutamate is a neurotransmitter in the cochlear nerve: a quantitative study in the guinea-pig anteroventral cochlear nucleus. *Eur. J. Neurosci.* 8, 79–91. doi: 10.1111/j.1460-9568.1996.tb01169.x

Hackney, C. M. C. M., Osen, K. K. K. K., and Kolston, J. (1990). Anatomy and Embryology Anatomy of the cochlear nuclear complex of guinea pig. *Anat. Embryol. (Berl.)* 182, 123–149. doi: 10.1007/BF00174013

Hallermann, S., Fejtova, A., Schmidt, H., Weyhersmüller, A., Silver, R. A., Gundelfinger, E. D., et al. (2010). Bassoon speeds vesicle reloading at a central excitatory synapse. *Neuron* 68, 710–723. doi: 10.1016/j.neuron.2010.10.026

Hámori, J., and Somogyi, J. (1983). Differentiation of cerebellar mossy fiber synapses in the rat: a quantitative electron microscope study. *J. Comp. Neurol.* 220, 365–377. doi: 10.1002/cne.902200402

Haragopal, H., and Winters, B. D. (2023). Principal neuron diversity in the murine lateral superior olive supports multiple sound localization strategies and segregation of information in higher processing centers. *Commun. Biol.* 6:432. doi: 10.1038/s42003-023-04802-5

Harlow, M. L., Ress, D., Stoschek, A., Marshall, R. M., and McMahan, U. J. (2001). The architecture of active zone material at the frog's neuromuscular junction. *Nature* 409, 479–484. doi: 10.1038/35054000

Harrison, J. M., and Irving, R. (1966a). Ascending connections of the anterior ventral cochlear nucleus in the rat. *J. Comp. Neurol.* 126, 51–63. doi: 10.1002/cne.901260105

Harrison, J. M., and Irving, R. (1966b). The organization of the posterior ventral cochlear nucleus in the rat. *J. Comp. Neurol.* 126, 391–401. doi: 10.1002/cne.901260303

Harrison, J. M., and Warr, W. B. (1962). A study of the cochlear nuclei and ascending auditory pathways of the medulla. *J. Comp. Neurol.* 119, 341–379. doi: 10.1002/cne.901190306

Hassfurth, B., Grothe, B., and Koch, U. (2010). The mammalian interaural time difference detection circuit is differentially controlled by GABAB receptors during development. *J. Neurosci.* 30, 9715–9727. doi: 10.1523/JNEUROSCI.1552-10.2010

Hassfurth, B., Magnusson, A. K., Grothe, B., and Koch, U. (2009). Sensory deprivation regulates the development of the hyperpolarization-activated current in auditory brainstem neurons: Regulation of Ih in the auditory brainstem. *Eur. J. Neurosci.* 30, 1227–1238. doi: 10.1111/j.1460-9568.2009.06925.x

Held, H. (1891). Die zentralen Bahnen des Nervus aeusticus bei der Katze. *Arch. f. Anat. u. Physiol. Anat. Abt* 15, 271–291.

Held, H. (1893). Die centrale Gehörleitung. *Arch. Anat. Physiol. Anat. Abt.* 17, 201–248.

Helfert, R. H., Juiz, J. M., Bledsoe, S. C., Bonneau, J. M., Wenthold, R. J., and Altschuler, R. A. (1992). Patterns of glutamate, glycine, and GABA immunolabeling in four synaptic terminal classes in the lateral superior olive of the guinea pig. *J. Comp. Neurol.* 323, 305–325. doi: 10.1002/cne.903230302

Helfert, R. H., and Schwartz, I. R. (1986). Morphological evidence for the existence of multiple neuronal classes in the cat lateral superior olivary nucleus. *J. Comp. Neurol.* 244, 533–549. doi: 10.1002/cne.902440409

Helfert, R. H., and Schwartz, I. R. (1987). Morphological features of five neuronal classes in the gerbil lateral superior olive. *Am. J. Anat.* 179, 55–69. doi: 10.1002/aja.1001790108

Helfert, R. H., Wenthold, R. J., Altschuler, R. A., and Bonneau, J. M. (1989). GABA and glycine imunoreactivity in the guinea pig superior olivary complex. *Brain Res.* 501, 269–286. doi: 10.1016/0006-8993(89)90644-6

Helmchen, F., Borst, J. G. G., and Sakmann, B. (1997). Calcium dynamics associated with a single action potential in a CNS pre-synaptic terminal. *Biophys. J.* 72, 1458–1471. doi: 10.1016/S0006-3495(97)78792-7

Henkel, C. K. (1997). Axonal morphology in fibrodendritic laminae of the dorsal nucleus of the lateral lemniscus: Afferent projections from the medial superior olivary nucleus. *J. Comp. Neurol.* 380, 136–144. doi: 10.1002/(SICI)1096-9861(19970331)380:1<136::AID-CNE10>3.0.CO;2-Y

Henkel, C. K., and Brunso-Bechtold, J. K. (1990). Dendritic morphology and development in the ferret medial superior olivary nucleus. *J. Comp. Neurol.* 294, 377–388. doi: 10.1002/cne.902940307

Henkel, C. K., and Spangler, K. M. (1983). Organization of the efferent projections of the medial superior olivary nucleus in the cat as revealed by HRP and autoradiographic tracing methods. *J. Comp. Neurol.* 221, 416–428. doi: 10.1002/cne.902210405

Hermann, J., Grothe, B., and Klug, A. (2009). Modeling short-term synaptic plasticity at the calyx of Held using in vivo-like stimulation patterns. *J. Neurophysiol.* 101, 20–30. doi: 10.1152/jn.90243.2008

Hermann, J., Pecka, M., Von Gersdorff, H., Grothe, B., and Klug, A. (2007). Synaptic transmission at the calyx of held under in vivo-like activity levels. *J. Neurophysiol.* 98, 807–820. doi: 10.1152/jn.00355.2007

Hermida, D., Mateos, J. M., Elezgarai, I., Puente, N., Bilbao, A., Bueno-López, J. L., et al. (2010). Spatial compartmentalization of AMPA glutamate receptor subunits at the calyx of Held synapse. *J. Comp. Neurol.* 518, 163–174. doi: 10.1002/cne.22189

Hilbig, H., Beil, B., Hilbig, H., Call, J., and Bidmon, H. J. (2009). Superior olivary complex organization and cytoarchitecture may be correlated with function and catarrhine primate phylogeny. *Brain Struct. Funct.* 213, 489–497. doi: 10.1007/s00429-008-0201-5

Hintze, A., Gültas, M., Semmelhack, E. A., and Wichmann, C. (2021). Ultrastructural maturation of the endbulb of Held active zones comparing wild-type and otoferlin-deficient mice. *iScience* 24:102282. doi: 10.1016/j.isci.2021.102282

Hintze, A., Lange, F., Steyer, A. M., Anstatt, J., Möbius, W., Jakobs, S., et al. (2024). Developmental changes of the mitochondria in the murine anteroventral cochlear nucleus. *iScience* 27:108700. doi: 10.1016/j.isci.2023.108700

Hirtz, J. J., Boesen, M., Braun, N., Deitmer, J. W., Kramer, F., Lohr, C., et al. (2011). $Ca_v1.3$ calcium channels are required for normal development of the auditory brainstem. *J. Neurosci.* 31, 8280–8294. doi: 10.1523/JNEUROSCI.5098-10.2011

Hirtz, J. J., Braun, N., Griesemer, D., Hannes, C., Janz, K., Löhrke, S., et al. (2012). Synaptic refinement of an inhibitory topographic map in the auditory brainstem requires functional Cav1.3 calcium channels. *J. Neurosci.* 32, 14602–14616. doi: 10.1523/JNEUROSCI.0765-12.2012

Hopkins, K., and Moore, B. C. J. (2011). The effects of age and cochlear hearing loss on temporal fine structure sensitivity, frequency selectivity, and speech reception in noise. *J. Acoust. Soc. Am.* 130, 334–349. doi: 10.1121/1.3585848

Huffman, R. F., and Covey, E. (1995). Origin of ascending projections to the nuclei of the lateral lemniscus in the big brown bat, Eptesicus fuscus. *J. Comp. Neurol.* 357, 532–545. doi: 10.1002/cne.903570405

Hull, C., Isaacson, J. S., and Scanziani, M. (2009). Post-synaptic mechanisms govern the differential excitation of cortical neurons by thalamic inputs. *J. Neurosci.* 29, 9127–9136. doi: 10.1523/JNEUROSCI.5971-08.2009

Hunter, C., Petralia, R. S., Vu, T., and Wenthold, R. J. (1993). Expression of AMPA-selective glutamate receptor subunits in morphologically defined neurons of the mammalian cochlear nucleus. *J. Neurosci.* 13, 1932–1946. doi: 10.1523/JNEUROSCI.13-05-01932.1993

Inchauspe, C. G., Forsythe, I. D., and Uchitel, O. D. (2007). Changes in synaptic transmission properties due to the expression of N-type calcium channels at the calyx of Held synapse of mice lacking P/Q-type calcium channels. *J. Physiol.* 584, 835–851. doi: 10.1113/jphysiol.2007.139683

Irvine, D. R., Park, V. N., and McCormick, L. (2001). Mechanisms underlying the sensitivity of neurons in the lateral superior olive to interaural intensity differences. *J. Neurophysiol.* 86, 2647–2666. doi: 10.1152/jn.2001.86.6.2647

Irving, R., and Harrison, J. M. (1967). The superior olivary complex and audition: a comparative study. *J. Comp. Neurol.* 130, 77–86. doi: 10.1002/cne.901300105

Ishikawa, T., Nakamura, Y., Saitoh, N., Li, W.-B., Iwasaki, S., and Takahashi, T. (2003). Distinct roles of Kv1 and Kv3 potassium channels at the calyx of Held pre-synaptic terminal. *J. Neurosci.* 23, 10445–10453. doi: 10.1523/JNEUROSCI.23-32-10445.2003

Iwasaki, S., and Takahashi, T. (1998). Developmental changes in calcium channel types mediating synaptic transmission in rat auditory brainstem. *J. Physiol.* 509, 419–423. doi: 10.1111/j.1469-7793.1998.419bn.x

Jackson, M. B., and Redman, S. J. (2003). Calcium dynamics, buffering, and buffer saturation in the boutons of dentate granule-cell axons in the hilus. *J. Neurosci.* 23, 1612–1621. doi: 10.1523/JNEUROSCI.23-05-01612.2003

Jacxsens, L., De Pauw, J., Cardon, E., van der Wal, A., Jacquemin, L., Gilles, A., et al. (2022). Brainstem evoked auditory potentials in tinnitus: a best-evidence synthesis and meta-analysis. *Front. Neurol.* 13:941876. doi: 10.3389/fneur.2022.941876

Jakab, R. L., and Hámori, J. (1988). Quantitative morphology and synaptology of cerebellar glomeruli in the rat. *Anat. Embryol.* 179, 81–88. doi: 10.1007/BF00305102

Jing, J., Hu, M., Ngodup, T., Ma, Q., Lau, S.-N. N., Ljungberg, M. C., et al. (2025). Molecular logic for cellular specializations that initiate the auditory parallel processing pathways. *Nat. Commun.* 16:489. doi: 10.1038/s41467-024-55257-z

Jones, D. R., Hutson, K. A., and Morest, D. K. (1992). Growth cones and structural variation of synaptic end-bulbs in the cochlear nucleus of the adult cat brain. *Synapse* 10, 291–309. doi: 10.1002/syn.890100404

Joris, P. X., Carney, L. H., Smith, P. H., and Yin, T. C. (1994a). Enhancement of neural synchronization in the anteroventral cochlear nucleus. I. Responses to tones at the characteristic frequency. *J. Neurophysiol.* 71, 1022–1036. doi: 10.1152/jn.1994.71.3.1022

Joris, P. X., Smith, P. H., and Yin, T. C. (1994b). Enhancement of neural synchronization in the anteroventral cochlear nucleus. II. Responses in the tuning curve tail. *J. Neurophysiol.* 71, 1037–1051. doi: 10.1152/jn.1994.71.3.1037

Joris, P. X., and Trussell, L. O. (2018). The calyx of Held: a hypothesis on the need for reliable timing in an intensity-difference encoder. *Neuron* 100, 534–549. doi: 10.1016/j.neuron.2018.10.026

Joris, P. X., and Yin, T. C. (1995). Envelope coding in the lateral superior olive. I. Sensitivity to interaural time differences. *J. Neurophysiol.* 73, 1043–1062. doi: 10.1152/jn.1995.73.3.1043

Joris, P. X., and Yin, T. C. T. (1998). Envelope coding in the lateral superior olive. III. Comparison with afferent pathways. *J. Neurophysiol.* 79, 253–269. doi: 10.1152/jn.1998.79.1.253

Joshi, I., and Wang, L.-Y. (2002). Developmental profiles of glutamate receptors and synaptic transmission at a single synapse in the mouse auditory brainstem. *J. Physiol.* 540, 861–873. doi: 10.1113/jphysiol.2001.013506

Juiz, J. M., Helfert, R. H., Bonneau, J. M., Wenthold, R. J., and Altschuler, R. A. (1996). Three classes of inhibitory amino acid terminals in the cochlear nucleus of the guinea pig. *J. Comp. Neurol.* 373, 11–26. doi: 10.1002/(SICI)1096-9861(19960909)373:1<11::AID-CNE2>3.0.CO;2-G

Kandler, K., and Friauf, E. (1995). Development of glycinergic and glutamatergic synaptic transmission in the auditory brainstem of perinatal rats. *J. Neurosci.* 15, 6890–6904. doi: 10.1523/JNEUROSCI.15-10-06890.1995

Kane, E. C. (1973). Octopus cells in the cochlear nucleus of the cat: heterotypic synapses upon homeotypic neurons. *Int. J. Neurosci.* 5, 251–279. doi: 10.3109/00207457309149485

Kaneko, M., and Takahashi, T. (2004). Pre-synaptic mechanism underlying cAMP-dependent synaptic potentiation. *J. Neurosci.* 24, 5202–5208. doi: 10.1523/JNEUROSCI.0999-04.2004

Kapfer, C., Seidl, A. H., Schweizer, H., and Grothe, B. (2002). Experience-dependent refinement of inhibitory inputs to auditory coincidence-detector neurons. *Nat. Neurosci.* 5, 247–253. doi: 10.1038/nn810

Kaplan, A. B., Kozin, E. D., Remenschneider, A., Eftekhari, K., Jung, D. H., Polley, D. B., et al. (2016). Amblyaudia: review of pathophysiology, clinical presentation, and treatment of a new diagnosis. *Otolaryngol. Head Neck Surg.* 154, 247–255. doi: 10.1177/0194599815615871

Keine, C., Al-Yaari, M., Radulovic, T., Thomas, C. I., Valino Ramos, P., Guerrero-Given, D., et al. (2022). Pre-synaptic Rac1 controls synaptic strength through the regulation of synaptic vesicle priming. *Elife* 11:e1505. doi: 10.7554/eLife.81505

Keine, C., and Rübsamen, R. (2015). Inhibition shapes acoustic responsiveness in spherical bushy cells. *J. Neurosci.* 35, 8579–8592. doi: 10.1523/JNEUROSCI.0133-15.2015

Keine, C., Rübsamen, R., and Englitz, B. (2016). Inhibition in the auditory brainstem enhances signal representation and regulates gain in complex acoustic environments. *Elife* 5:19295. doi: 10.7554/eLife.19295.029

Keine, C., Rübsamen, R., and Englitz, B. (2017). Signal integration at spherical bushy cells enhances representation of temporal structure but limits its range. *Elife* 6:29639. doi: 10.7554/eLife.29639.021

Kelly, J. B., Van Adel, B. A., and Ito, M. (2009). Anatomical projections of the nuclei of the lateral lemniscus in the Albino rat (Rattus norvegicus). *J. Comp. Neurol.* 512, 573–593. doi: 10.1002/cne.21929

Khurana, S., Liu, Z., Lewis, A. S., Rosa, K., Chetkovich, D., and Golding, N. L. (2012). An essential role for modulation of hyperpolarization-activated current in the development of binaural temporal precision. *J. Neurosci.* 32, 2814–2823. doi: 10.1523/JNEUROSCI.3882-11.2012

Khurana, S., Remme, M. W. H., Rinzel, J., and Golding, N. L. (2011). Dynamic interaction of Ih and IK-LVA during trains of synaptic potentials in principal neurons of the medial superior olive. *J. Neurosci.* 31, 8936–8947. doi: 10.1523/JNEUROSCI.1079-11.2011

Kim, H. W., Kim, N., Kim, K. W., and Rhyu, I. J. (2013). Three-dimensional imaging of cerebellar mossy fiber rosettes by ion-abrasion scanning electron microscopy. *Microsc. Microanal.* 19, 172–177. doi: 10.1017/S1431927613012609

Kim, M.-H., Korogod, N., Schneggenburger, R., Ho, W.-K., and Lee, S.-H. (2005). Interplay between Na^{1}/ca^{2}+ exchangers and mitochondria in ca^{2}+ clearance at the calyx of Held. *J. Neurosci.* 25, 6057–6065. doi: 10.1523/JNEUROSCI.0454-05.2005

Kirk, M. E., Meredith, F. L., Benke, T. A., and Rennie, K. J. (2017). AMPA receptor-mediated rapid EPSCs in vestibular calyx afferents. *J. Neurophysiol.* 117, 2312–2323. doi: 10.1152/jn.00394.2016

Kiss, A., and Majorossy, K. (1983). Neuron morphology and synaptic architecture in the medial superior olivary nucleus. Light- and electron microscope studies in the cat. *Exp. Brain Res.* 52, 315–327. doi: 10.1007/BF00238026

Kitzes, L. M., Kageyama, G. H., Semple, M. N., and Kil, J. (1995). Development of ectopic projections from the ventral cochlear nucleus to the superior olivary complex induced by neonatal ablation of the contralateral cochlea. *J. Comp. Neurol.* 353, 341–363. doi: 10.1002/cne.903530303

Kladisios, N., Fischer, L., and Felmy, F. (2020). Minimal number of required inputs for temporally precise action potential generation in auditory brainstem nuclei. *Front. Cell. Neurosci.* 14:592213. doi: 10.3389/fncel.2020.592213

Kladisios, N., Fischer, L., Jenzen, F., Rebhan, M., Leibold, C., and Felmy, F. (2022). Synaptic mechanisms underlying temporally precise information processing in the VNLL, an auditory brainstem nucleus. *J. Neurosci.* 42, 6536–6550. doi: 10.1523/JNEUROSCI.0948-22.2022

Kladisios, N., Wicke, K. D., Pätz-Warncke, C., and Felmy, F. (2023). Species-specific adaptation for ongoing high-frequency action potential generation in MNTB neurons. *J. Neurosci.* 43, 2714–2729. doi: 10.1523/JNEUROSCI.2320-22.2023

Klumpp, R. G., and Eady, H. R. (1956). Some measurements of interaural time difference thresholds. *J. Acoust. Soc. Am.* 28, 859–860. doi: 10.1121/1.1908493

Knipper, M., Singer, W., Schwabe, K., Hagberg, G. E., Li Hegner, Y., Rüttiger, L., et al. (2022). Disturbed balance of inhibitory signaling links hearing loss and cognition. *Front. Neural Circuits* 15:785603. doi: 10.3389/fncir.2021.785603

Koch, U., Braun, M., Kapfer, C., and Grothe, B. (2004). Distribution of HCN1 and HCN2 in rat auditory brainstem nuclei. *Eur. J. Neurosci.* 20, 79–91. doi: 10.1111/j.0953-816X.2004.03456.x

Kochubey, O., Babai, N., and Schneggenburger, R. (2016). A Synaptotagmin isoform switch during the development of an identified CNS synapse. *Neuron* 90, 984–999. doi: 10.1016/j.neuron.2016.04.038

Kochubey, O., Han, Y., and Schneggenburger, R. (2009). Developmental regulation of the intracellular Ca2+ sensitivity of vesicle fusion and Ca2+-secretion coupling at the rat calyx of Held: Developmental regulation of Ca2+sensitivity of vesicle fusion. *J. Physiol.* 587, 3009–3023. doi: 10.1113/jphysiol.2009.172387

Koert, E., and Kuenzel, T. (2021). Small dendritic synapses enhance temporal coding in a model of cochlear nucleus bushy cells. *J. Neurophysiol.* 125, 915–937. doi: 10.1152/jn.00331.2020

Koike, M., Tsukada, S., Tsuzuki, K., Kijima, H., and Ozawa, S. (2000). Regulation of kinetic properties of GluR2 AMPA receptor channels by alternative splicing. *J. Neurosci.* 20, 2166–2174. doi: 10.1523/JNEUROSCI.20-06-02166.2000

Koike-Tani, M., Kanda, T., Saitoh, N., Yamashita, T., and Takahashi, T. (2008). Involvement of AMPA receptor desensitization in short-term synaptic depression at the calyx of Held in developing rats: desensitization involved in synaptic depression. *J. Physiol.* 586, 2263–2275. doi: 10.1113/jphysiol.2007.142547

Koike-Tani, M., Saitoh, N., and Takahashi, T. (2005). Mechanisms underlying developmental speeding in AMPA-EPSC decay time at the calyx of Held. *J. Neurosci.* 25, 199–207. doi: 10.1523/JNEUROSCI.3861-04.2005

Köppl, C. (1994). Auditory nerve terminals in the cochlear nucleus magnocellularis: differences between low and high frequencies: auditory nerve terminals in *N. magnocellularis*. *J. Comp. Neurol.* 339, 438–446. doi: 10.1002/cne.903390310

Kopp-Scheinpflug, C., Dehmel, S., Dörrscheidt, G. J., and Rübsamen, R. (2002). Interaction of excitation and inhibition in anteroventral cochlear nucleus neurons that receive large endbulb synaptic endings. *J. Neurosci.* 22, 11004–11018. doi: 10.1523/JNEUROSCI.22-24-11004.2002

Kopp-Scheinpflug, C., Lippe, W. R., Dörrscheidt, G. J., and Rübsamen, R. (2003). The medial nucleus of the trapezoid body in the gerbil is more than a relay: comparison of pre- and post-synaptic activity. *J. Assoc. Res. Otolaryngol.* 4, 1–23. doi: 10.1007/s10162-002-2010-5

Kopp-Scheinpflug, C., Pigott, B. M., and Forsythe, I. D. (2015). Nitric oxide selectively suppresses IH currents mediated by HCN1-containing channels: NO suppresses HCN1. *J. Physiol.* 593, 1685–1700. doi: 10.1113/jphysiol.2014.282194

Kopp-Scheinpflug, C., and Tempel, B. L. (2015). Decreased temporal precision of neuronal signaling as a candidate mechanism of auditory processing disorder. *Hear. Res.* 330, 213–220. doi: 10.1016/j.heares.2015.06.014

Kotak, V. C., Korada, S., Schwartz, I. R., and Sanes, D. H. (1998). A developmental shift from GABAergic to glycinergic transmission in the central auditory system. *J. Neurosci.* 18, 4646–4655. doi: 10.1523/JNEUROSCI.18-12-04646.1998

Krächan, E. G., Fischer, A. U., Franke, J., and Friauf, E. (2017). Synaptic reliability and temporal precision are achieved via high quantal content and effective replenishment: auditory brainstem versus hippocampus. *J. Physiol.* 595, 839–864. doi: 10.1113/JP272799

Kramer, F., Griesemer, D., Bakker, D., Brill, S., Franke, J., Frotscher, E., et al. (2014). Inhibitory glycinergic neurotransmission in the mammalian auditory brainstem upon prolonged stimulation: short-term plasticity and synaptic reliability. *Front. Neural Circuits* 8:14. doi: 10.3389/fncir.2014.00014

Krampfl, K., Schlesinger, F., Zörner, A., Kappler, M., Dengler, R., and Bufler, J. (2002). Control of kinetic properties of GluR2 flop AMPA-type channels: impact of R/G nuclear editing: R/G nuclear editing and GluR2 flop channels. *Eur. J. Neurosci.* 15, 51–62. doi: 10.1046/j.0953-816x.2001.01841.x

Kreeger, L. J., Honnuraiah, S., Maeker, S., Shea, S., Fishell, G., and Goodrich, L. V. (2025). An anatomical and physiological basis for flexible coincidence detection in the auditory system. *eLife* 13:RP100492. doi: 10.7554/eLife.100492.2

Kudo, M., Nakamura, Y., Tokuno, H., and Kitao, Y. (1990). Auditory brainstem in the mole (Mogera): nuclear configurations and the projections to the inferior colliculus. *J. Comp. Neurol.* 298, 400–412. doi: 10.1002/cne.902980403

Kuenzel, T., Borst, J. G. G., and van der Heijden, M. (2011). Factors controlling the input-output relationship of spherical bushy cells in the gerbil cochlear nucleus. *J. Neurosci.* 31, 4260–4273. doi: 10.1523/JNEUROSCI.5433-10.2011

Kulesza, R. J. (2007). Cytoarchitecture of the human superior olivary complex: medial and lateral superior olive. *Hear. Res.* 225, 80–90. doi: 10.1016/j.heares.2006.12.006

Kulesza, R. J. (2014). Characterization of human auditory brainstem circuits by calcium-binding protein immunohistochemistry. *Neuroscience* 258, 318–331. doi: 10.1016/j.neuroscience.2013.11.035

Kulesza, R. J., Lukose, R., and Stevens, L. V. (2011). Malformation of the human superior olive in autistic spectrum disorders. *Brain Res.* 1367, 360–371. doi: 10.1016/j.brainres.2010.10.015

Kulesza, R. J. Jr (2008). Cytoarchitecture of the human superior olivary complex: nuclei of the trapezoid body and posterior tier. *Hear. Res.* 241, 52–63. doi: 10.1016/j.heares.2008.04.010

Kulesza, R. J. Jr, and Grothe, B. (2015). Yes, there is a medial nucleus of the trapezoid body in humans. *Front. Neuroanat.* 9:35. doi: 10.3389/fnana.2015.00035

Kullmann, D. M., Ruiz, A., Rusakov, D. M., Scott, R., Semyanov, A., and Walker, M. C. (2005). Pre-synaptic, extrasynaptic and axonal GABAA receptors in the CNS: where and why? *Prog. Biophys. Mol. Biol.* 87, 33–46. doi: 10.1016/j.pbiomolbio.2004.06.003

Kuwabara, N., and Zook, J. M. (1992). Projections to the medial superior olive from the medial and lateral nuclei of the trapezoid body in rodents and bats. *J. Comp. Neurol.* 324, 522–538. doi: 10.1002/cne.903240406

Lauer, A. M., Connelly, C. J., Graham, H., and Ryugo, D. K. (2013). Morphological characterization of bushy cells and their inputs in the laboratory mouse (Mus musculus) anteroventral cochlear nucleus. *PLoS ONE* 8:e73308. doi: 10.1371/journal.pone.0073308

Leao, K. E., Leao, R. N., Sun, H., Fyffe, R. E. W., and Walmsley, B. (2006). Hyperpolarization-activated currents are differentially expressed in mice brainstem auditory nuclei: varied expression ofIhin brainstem auditory nuclei. *J. Physiol.* 576, 849–864. doi: 10.1113/jphysiol.2006.114702

Leão, K. E., Leão, R. N., and Walmsley, B. (2011). Modulation of dendritic synaptic processing in the lateral superior olive by hyperpolarization-activated currents: Ih in LSO dendrite. *Eur. J. Neurosci.* 33, 1462–1470. doi: 10.1111/j.1460-9568.2011.07627.x

Leão, R. M., Kushmerick, C., Pinaud, R., Renden, R., Li, G.-L., Taschenberger, H., et al. (2005). Pre-synaptic Na+ channels: locus, development, and recovery from inactivation at a high-fidelity synapse. *J. Neurosci.* 25, 3724–3738. doi: 10.1523/JNEUROSCI.3983-04.2005

Lenn, N. J., and Reese, T. S. (1966). The fine structure of nerve endings in hte nucleus of the trapezoid body and the ventral cochlear nucleus. *Am. J. Anat.* 118, 375–390. doi: 10.1002/aja.1001180205

Li, W., Kaczmarek, L. K., and Perney, T. M. (2001). Localization of two high-threshold potassium channel subunits in the rat central auditory system. *J. Compar. Neurol.* 437, 196–218. doi: 10.1002/cne.1279

Liberman, M. C. (1991). Central projections of auditory-nerve fibers of differing spontaneous rate. I. Anteroventral cochlear nucleus. *J. Comp. Neurol.* 313, 240–258. doi: 10.1002/cne.903130205

Limb, C. J., and Ryugo, D. K. (2000). Development of primary axosomatic endings in the anteroventral cochlear nucleus of mice. *J. Assoc. Res. Otolaryngol.* 1, 103–119. doi: 10.1007/s101620010032

Lin, K.-H., Oleskevich, S., and Taschenberger, H. (2011). Pre-synaptic Ca2+ influx and vesicle exocytosis at the mouse endbulb of Held: a comparison of two auditory nerve terminals: Ca2+influx and vesicle exocytosis at the mouse endbulb of Held. *J. Physiol.* 589, 4301–4320. doi: 10.1113/jphysiol.2011.209189

Lin, K.-H., Ranjan, M., Lipstein, N., Brose, N., Neher, E., and Taschenberger, H. (2025). Number and relative abundance of synaptic vesicles in functionally distinct priming states determine synaptic strength and short-term plasticity. *J. Physiol.* doi: 10.1113/JP286282. [Epub ahead of print].

Lin, K.-H., Taschenberger, H., and Neher, E. (2022). A sequential two-step priming scheme reproduces diversity in synaptic strength and short-term plasticity. *Proc. Natl. Acad. Sci. U. S. A.* 119:e2207987119. doi: 10.1073/pnas.2207987119

Lindsey, B. G. (1975). Fine structure and distribution of axon terminals from cochlear nucleus on neurons in the medial superior olivary nucleus of the cat. *J. Comp. Neurol.* 160, 81–103. doi: 10.1002/cne.901600106

Loftus, W. C., Bishop, D. C., Saint Marie, R. L., and Oliver, D. L. (2004). Organization of binaural excitatory and inhibitory inputs to the inferior colliculus from the superior olive. *J. Comp. Neurol.* 472, 330–344. doi: 10.1002/cne.20070

Lorente de Nó, R. (1981). *The Primary Acoustic Nuclei*. New York, NY: Raven Press.

Lorenzi, C., Gilbert, G., Carn, H., Garnier, S., and Moore, B. C. J. (2006). Speech perception problems of the hearing impaired reflect inability to use temporal fine structure. *Proc. Natl. Acad. Sci. U. S. A.* 103, 18866–18869. doi: 10.1073/pnas.0607364103

Lorteije, J. A. M., Rusu, S. I., Kushmerick, C., and Borst, J. G. G. (2009). Reliability and precision of the mouse calyx of Held synapse. *J. Neurosci.* 29, 13770–13784. doi: 10.1523/JNEUROSCI.3285-09.2009

Lu, H.-W., Smith, P. H., and Joris, P. X. (2022). Mammalian octopus cells are direction selective to frequency sweeps by excitatory synaptic sequence detection. *Proc. Natl. Acad. Sci. U. S. A.* 119 e2203748119. doi: 10.1073/pnas.2203748119

Lübbert, M., Goral, R. O., Keine, C., Thomas, C., Guerrero-Given, D., Putzke, T., et al. (2019). CaV2.1 α1 subunit expression regulates pre-synaptic CaV2.1 abundance and synaptic strength at a central synapse. *Neuron* 101, 260–273.e6. doi: 10.1016/j.neuron.2018.11.028

Lucas, S. J., Michel, C. B., Marra, V., Smalley, J. L., Hennig, M. H., Graham, B. P., et al. (2018). Glucose and lactate as metabolic constraints on pre-synaptic transmission at an excitatory synapse. *J. Physiol.* 596, 1699–1721. doi: 10.1113/JP275107

Ludwig, A., Zong, X., Jeglitsch, M., Hofmann, F., and Biel, M. (1998). A family of hyperpolarization-activated mammalian cation channels. *Nature* 393, 587–591. doi: 10.1038/31255

Ludwig, A., Zong, X., Stieber, J., Hullin, R., Hofmann, F., and Biel, M. (1999). Two pacemaker channels from human heart with profoundly different activation kinetics. *EMBO J.* 18, 2323–2329. doi: 10.1093/emboj/18.9.2323

Lujan, B., Dagostin, A., and von Gersdorff, H. (2019). Pre-synaptic diversity revealed by Ca2+-permeable AMPA receptors at the calyx of Held synapse. *J. Neurosci.* 39, 2981–2994. doi: 10.1523/JNEUROSCI.2565-18.2019

Luo, L. (2021). Architectures of neuronal circuits. *Science* 373:eabg7285. doi: 10.1126/science.abg7285

MacLeod, K. M., and Pandya, S. (2022). Expression and neurotransmitter association of the synaptic calcium sensor synaptotagmin in the avian auditory brain stem. *J. Assoc. Res. Otolaryngol.* 23, 701–720. doi: 10.1007/s10162-022-00863-1

Magee, J. C. (1998). Dendritic hyperpolarization-activated currents modify the integrative properties of hippocampal CA1 pyramidal neurons. *J. Neurosci.* 18, 7613–7624. doi: 10.1523/JNEUROSCI.18-19-07613.1998

Magee, J. C. (1999). Dendritic I(h) normalizes temporal summation in hippocampal CA1 neurons. *Nat. Neurosci.* 2, 508–514. doi: 10.1038/9158

Magnusson, A. K., Kapfer, C., Grothe, B., and Koch, U. (2005). Maturation of glycinergic inhibition in the gerbil medial superior olive after hearing onset: glycinergic inhibition in the gerbil MSO. *J. Physiol.* 568, 497–512. doi: 10.1113/jphysiol.2005.094763

Magnusson, A. K., Park, T. J., Pecka, M., Grothe, B., and Koch, U. (2008). Retrograde GABA signaling adjusts sound localization by balancing excitation and inhibition in the brainstem. *Neuron* 59, 125–137. doi: 10.1016/j.neuron.2008.05.011

Malkemper, E. P., Oelschläger, H. H. A., and Huggenberger, S. (2012). The dolphin cochlear nucleus: Topography, histology and functional implications. *J. Morphol.* 273, 173–185. doi: 10.1002/jmor.11013

Manis, P. B., and Marx, S. O. (1991). Outward currents in isolated ventral cochlear nucleus neurons. *J. Neurosci.* 11, 2865–2880. doi: 10.1523/JNEUROSCI.11-09-02865.1991

Maraslioglu-Sperber, A., Pizzi, E., Fisch, J. O., Kattler, K., Ritter, T., and Friauf, E. (2024). Molecular and functional profiling of cell diversity and identity in the lateral superior olive, an auditory brainstem center with ascending and descending projections. *Front. Cell. Neurosci.* 18:1354520. doi: 10.3389/fncel.2024.1354520

Martina, M., Schultz, J. H., Ehmke, H., Monyer, H., and Jonas, P. (1998). Functional and molecular differences between voltage-gated K+ channels of fast-spiking interneurons and pyramidal neurons of rat hippocampus. *J. Neurosci.* 18, 8111–8125. doi: 10.1523/JNEUROSCI.18-20-08111.1998

Massengill, J. L., Smith, M. A., Son, D. I., and O'Dowd, D. K. (1997). Differential expression of K4-AP currents and Kv3.1 potassium channel transcripts in cortical neurons that develop distinct firing phenotypes. *J. Neurosci.* 17, 3136–3147. doi: 10.1523/JNEUROSCI.17-09-03136.1997

Mathews, P. J., Jercog, P. E., Rinzel, J., Scott, L. L., and Golding, N. L. (2010). Control of submillisecond synaptic timing in binaural coincidence detectors by K(v)1 channels. *Nat. Neurosci.* 13, 601–609. doi: 10.1038/nn.2530

Mattis, J., Tye, K. M., Ferenczi, E. A., Ramakrishnan, C., O'Shea, D. J., Prakash, R., et al. (2011). Principles for applying optogenetic tools derived from direct comparative analysis of microbial opsins. *Nat. Methods* 9, 159–172. doi: 10.1038/nmeth.1808

Mayer, F., Albrecht, O., Dondzillo, A., and Klug, A. (2014). Glycinergic inhibition to the medial nucleus of the trapezoid body shows prominent facilitation and can sustain high levels of ongoing activity. *J. Neurophysiol.* 112, 2901–2915. doi: 10.1152/jn.00864.2013

Mc Laughlin, M., van der Heijden, M., and Joris, P. X. (2008). How secure is in vivo synaptic transmission at the calyx of Held? *J. Neurosci.* 28, 10206–10219. doi: 10.1523/JNEUROSCI.2735-08.2008

McDonald, A. J., and Mascagni, F. (2006). Differential expression of Kv3.1b and Kv3.2 potassium channel subunits in interneurons of the basolateral amygdala. *Neuroscience* 138, 537–547. doi: 10.1016/j.neuroscience.2005.11.047

McGinley, M. J., and Oertel, D. (2006). Rate thresholds determine the precision of temporal integration in principal cells of the ventral cochlear nucleus. *Hear. Res. 216–217* 52–63. doi: 10.1016/j.heares.2006.02.006

Mendoza Schulz, A., Jing, Z., María Sánchez Caro, J., Wetzel, F., Dresbach, T., Strenzke, N., et al. (2014). Bassoon-disruption slows vesicle replenishment and induces homeostatic plasticity at a CNS synapse. *EMBO J.* 33, 512–527. doi: 10.1002/embj.201385887

Merchán, M. A., Saldaña, E., and Plaza, I. (1994). Dorsal nucleus of the lateral lemniscus in the rat: concentric organization and tonotopic projection to the inferior colliculus. *J. Comp. Neurol.* 342, 259–278. doi: 10.1002/cne.903420209

Mikiel-Hunter, J., Kotak, V., and Rinzel, J. (2016). High-frequency resonance in the gerbil medial superior olive. *PLoS Comput. Biol.* 12, 1–23. doi: 10.1371/journal.pcbi.1005166

Mills, A. W. (1958). On the minimum audible angle. *J. Acoust. Soc. Am.* 30, 237–246. doi: 10.1121/1.1909553

Moore, B. C. J. (2008). The role of temporal fine structure processing in pitch perception, masking, and speech perception for normal-hearing and hearing-impaired people. *J. Assoc. Res. Otolaryngol.* 9, 399–406. doi: 10.1007/s10162-008-0143-x

Moore, D. R., Russell, F. A., and Cathcart, N. C. (1995). Lateral superior olive projections to the inferior colliculus in normal and unilaterally deafened ferrets. *J. Comp. Neurol.* 357, 204–216. doi: 10.1002/cne.903570203

Moore, J. K. (1987). The human auditory brain stem: a comparative view. *Hear. Res.* 29, 1–32. doi: 10.1016/0378-5955(87)90202-4

Moore, J. K. (2000). Organization of the human superior olivary complex. *Microsc. Res. Tech.* 51, 403–412. doi: 10.1002/1097-0029(20001115)51:4<403::AID-JEMT8>3.0.CO;2-Q

Moore, J. K., and Moore, R. Y. (1971). A comparative study of the superior olivary complex in the primate brain. *Folia Primatol.* 16, 35–51. doi: 10.1159/000155390

Moore, L. A., and Trussell, L. O. (2017). Corelease of inhibitory neurotransmitters in the mouse auditory midbrain. *J. Neurosci.* 37, 9453–9464. doi: 10.1523/JNEUROSCI.1125-17.2017

Moore, M. J., and Caspary, D. M. (1983). Strychnine blocks binaural inhibition in lateral superior olivary neurons. *J. Neurosci.* 3, 237–242. doi: 10.1523/JNEUROSCI.03-01-00237.1983

Moosmang, S., Stieber, J., Zong, X., Biel, M., Hofmann, F., and Ludwig, A. (2001). Cellular expression and functional characterization of four hyperpolarization-activated pacemaker channels in cardiac and neuronal tissues. *Eur. J. Biochem.* 268, 1646–1652. doi: 10.1046/j.1432-1327.2001.02036.x

Morest, D. K. (1968). The growth of synaptic endings in the mammalian brain: a study of the calyces of the trapezoid body. *Z. Anat. Entwicklungsgesch.* 127, 201–220. doi: 10.1007/BF00526129

Mosbacher, J., Schoepfer, R., Monyer, H., Burnashev, N., Seeburg, P. H., and Ruppersberg, J. P. (1994). A molecular determinant for submillisecond desensitization in glutamate receptors. *Science* 266, 1059–1062. doi: 10.1126/science.7973663

Müller, M., Felmy, F., and Schneggenburger, R. (2008). A limited contribution of Ca2+ current facilitation to paired-pulse facilitation of transmitter release at the rat calyx of Held: Ca2+current facilitation during paired-pulse facilitation. *J. Physiol.* 586, 5503–5520. doi: 10.1113/jphysiol.2008.155838

Müller, M., Felmy, F., Schwaller, B., and Schneggenburger, R. (2007). Parvalbumin is a mobile pre-synaptic ca^{2+}buffer in the calyx of Held that accelerates the decay of $ca^{2+}$and short-term facilitation. *J. Neurosci.* 27, 2261–2271. doi: 10.1523/JNEUROSCI.5582-06.2007

Müller, M., Goutman, J. D., Kochubey, O., and Schneggenburger, R. (2010). Interaction between facilitation and depression at a large CNS synapse reveals mechanisms of short-term plasticity. *J. Neurosci.* 30, 2007–2016. doi: 10.1523/JNEUROSCI.4378-09.2010

Munemoto, Y., Kuriyama, H., Doi, T., Sato, K., Matsumoto, A., Sugatani, J., et al. (1998). Auditory pathway and auditory brainstem response in mice lacking NMDA receptor ε1 and ε4 subunits. *Neurosci. Lett.* 251, 101–104. doi: 10.1016/S0304-3940(98)00509-6

Mylius, J., Brosch, M., Scheich, H., and Budinger, E. (2013). Subcortical auditory structures in the Mongolian gerbil: I. Golgi architecture. *J. Comp. Neurol.* 521, 1289–1321. doi: 10.1002/cne.23232

Myoga, M. H., Lehnert, S., Leibold, C., Felmy, F., and Grothe, B. (2014). Glycinergic inhibition tunes coincidence detection in the auditory brainstem. *Nat. Commun.* 5:3790. doi: 10.1038/ncomms4790

Nabel, A. L., Callan, A. R., Gleiss, S. A., Kladisios, N., Leibold, C., and Felmy, F. (2019). Distinct distribution patterns of potassium channel sub-units in somato-dendritic compartments of neurons of the medial superior Olive. *Front. Cell. Neurosci.* 13:38. doi: 10.3389/fncel.2019.00038

Nakagawa, H., Sato, K., Shiraishi, Y., Kuriyama, H., and Altschuler, R. A. (2000). NMDAR1 isoforms in the rat superior olivary complex and changes after unilateral cochlear ablation. *Brain Res. Mol. Brain Res.* 77, 246–257. doi: 10.1016/S0169-328X(00)00059-0

Nakajima, Y. (1971). Fine structure of the medial nucleus of the trapezoid body of the bat with special reference to two types of synaptic endings. *J. Cell Biol.* 50, 121–134. doi: 10.1083/jcb.50.1.121

Nakamura, Y., Harada, H., Kamasawa, N., Matsui, K., Rothman, J. S., Shigemoto, R., et al. (2015). Nanoscale distribution of pre-synaptic Ca(2+) channels and its impact on vesicular release during development. *Neuron* 85, 145–158. doi: 10.1016/j.neuron.2014.11.019

Nanou, E., and Catterall, W. A. (2018). Calcium Channels, Synaptic Plasticity, and Neuropsychiatric Disease. *Neuron* 98, 466–481. doi: 10.1016/j.neuron.2018.03.017

Nayagam, D. A. X. X., Clarey, J. C., and Paolini, A. G. (2005). Powerful, onset inhibition in the ventral nucleus of the lateral lemniscus. *J. Neurophysiol.* 94, 1651–1654. doi: 10.1152/jn.00167.2005

Neher, E. (2015). Merits and limitations of vesicle pool models in view of heterogeneous populations of synaptic vesicles. *Neuron* 87, 1131–1142. doi: 10.1016/j.neuron.2015.08.038

Neher, E. (2017). Some subtle lessons from the calyx of Held synapse. *Biophys. J.* 112, 215–223. doi: 10.1016/j.bpj.2016.12.017

Nerlich, J., Keine, C., Rübsamen, R., Burger, R. M., and Milenkovic, I. (2014a). Activity-dependent modulation of inhibitory synaptic kinetics in the cochlear nucleus. *Front. Neural Circuits* 8:145. doi: 10.3389/fncir.2014.00145

Nerlich, J., Kuenzel, T., Keine, C., Korenic, A., Rübsamen, R., and Milenkovic, I. (2014b). Dynamic fidelity control to the central auditory system: synergistic glycine/GABAergic inhibition in the cochlear nucleus. *J. Neurosci.* 34, 11604–11620. doi: 10.1523/JNEUROSCI.0719-14.2014

Ngodup, T., Goetz, J. A., McGuire, B. C., Sun, W., Lauer, A. M., and Xu-Friedman, M. A. (2015). Activity-dependent, homeostatic regulation of neurotransmitter release from auditory nerve fibers. *Proc. Natl. Acad. Sci. U. S. A.* 112, 6479–6484. doi: 10.1073/pnas.1420885112

Nicol, M. J., and Walmsley, B. (2002). Ultrastructural basis of synaptic transmission between endbulbs of Held and bushy cells in the rat cochlear nucleus. *J. Physiol.* 539, 713–723. doi: 10.1113/jphysiol.2001.012972

Nielsen, T. A., DiGregorio, D. A., and Silver, R. A. (2004). Modulation of glutamate mobility reveals the mechanism underlying slow-rising AMPAR EPSCs and the diffusion coefficient in the synaptic cleft. *Neuron* 42, 757–771. doi: 10.1016/j.neuron.2004.04.003

Noh, J., Seal, R. P., Garver, J. A., Edwards, R. H., and Kandler, K. (2010). Glutamate co-release at GABA/glycinergic synapses is crucial for the refinement of an inhibitory map. *Nat. Neurosci.* 13, 232–238. doi: 10.1038/nn.2478

Nothwang, H. G. (2016). Evolution of mammalian sound localization circuits: A developmental perspective. *Prog. Neurobiol.* 141, 1–24. doi: 10.1016/j.pneurobio.2016.02.003

Nusser, Z. (2018). Creating diverse synapses from the same molecules. *Curr. Opin. Neurobiol.* 51, 8–15. doi: 10.1016/j.conb.2018.01.001

Oertel, D. (1983). Synaptic responses and electrical properties of cells in brain slices of the mouse anteroventral cochlear nucleus. *J. Neurosci.* 3, 2043–2053. doi: 10.1523/JNEUROSCI.03-10-02043.1983

Oertel, D. (1999). The role of timing in the brain stem auditory nuclei of vertebrates. *Annu. Rev. Physiol.* 61, 497–519. doi: 10.1146/annurev.physiol.61.1.497

Oertel, D., Bal, R., Gardner, S. M., Smith, P. H., and Joris, P. X. (2000). Detection of synchrony in the activity of auditory nerve fibers by octopus cells of the mammalian cochlear nucleus. *Proc. Natl. Acad. Sci. U. S. A.* 97, 11773–11779. doi: 10.1073/pnas.97.22.11773

Oertel, D., Cao, X.-J., Ison, J. R., and Allen, P. D. (2017). Cellular computations underlying detection of gaps in sounds and lateralizing sound sources. *Trends Neurosci.* 40, 613–624. doi: 10.1016/j.tins.2017.08.001

Oertel, D., Shatadal, S., and Cao, X.-J. (2008). In the ventral cochlear nucleus Kv1.1 and subunits of HCN1 are colocalized at surfaces of neurons that have low-voltage-activated and hyperpolarization-activated conductances. *Neuroscience* 154, 77–86. doi: 10.1016/j.neuroscience.2008.01.085

Oertel, D., Wu, S. H., Garb, M. W., and Dizack, C. (1990). Morphology and physiology of cells in slice preparations of the posteroventral cochlear nucleus of mice. *J. Comp. Neurol.* 295, 136–154. doi: 10.1002/cne.902950112

Oleskevich, S., Clements, J., and Walmsley, B. (2000). Release probability modulates short-term plasticity at a rat giant terminal. *J. Physiol.* 524, 513–523. doi: 10.1111/j.1469-7793.2000.00513.x

Oleskevich, S., and Walmsley, B. (2002). Synaptic transmission in the auditory brainstem of normal and congenitally deaf mice. *J. Physiol.* 540, 447–455. doi: 10.1113/jphysiol.2001.013821

Oliver, D. L., Beckius, G. E., Bishop, D. C., Loftus, W. C., and Batra, R. (2003). Topography of interaural temporal disparity coding in projections of medial superior olive to inferior colliculus. *J. Neurosci.* 23, 7438–7449. doi: 10.1523/JNEUROSCI.23-19-07438.2003

Oliver, D. L., Beckius, G. E., and Shneiderman, A. (1995). Axonal projections from the lateral and medial superior olive to the inferior colliculus of the cat: a study using electron microscopic autoradiography. *J. Comp. Neurol.* 360, 17–32. doi: 10.1002/cne.903600103

Ollo, C., and Schwartz, I. R. (1979). The superior olivary complex in C57BL/6 mice. *Am. J. Anat.* 155, 349–373. doi: 10.1002/aja.1001550306

Osen, K. K. (1969a). Cytoarchitecture of the cochlear nuclei in the cat. *J. Comp. Neurol.* 136, 453–484. doi: 10.1002/cne.901360407

Osen, K. K. (1969b). The intrinsic organization of the cochlear nuclei in the cat. *Acta Otolaryngol.* 67, 352–359. doi: 10.3109/00016486909125462

Ostapoff, E. M., Feng, J. J., and Morest, D. K. (1994). A physiological and structural study of neuron types in the cochlear nucleus. II. Neuron types and their structural correlation with response properties. *J. Comp. Neurol.* 346, 19–42. doi: 10.1002/cne.903460103

Ostapoff, E. M., and Morest, D. K. (1991). Synaptic organization of globular bushy cells in the ventral cochlear nucleus of the cat: a quantitative study. *J. Comp. Neurol.* 314, 598–613. doi: 10.1002/cne.903140314

Otis, T. S., and Trussell, L. O. (1996). Inhibition of transmitter release shortens the duration of the excitatory synaptic current at a calyceal synapse. *J. Neurophysiol.* 76, 3584–3588. doi: 10.1152/jn.1996.76.5.3584

Pál, B., Pór, Á., Pocsai, K., Szücs, G., and Rusznák, Z. (2005). Voltage-gated and background K + channel subunits expressed by the bushy cells of the rat cochlear nucleus. *Hear. Res.* 199, 57–70. doi: 10.1016/j.heares.2004.07.020

Palmer, A. R. (1990). The representation of the spectra and fundamental frequencies of steady-state single- and double-vowel sounds in the temporal discharge patterns of guinea pig cochlear-nerve fibers. *J. Acoust. Soc. Am.* 88, 1412–1426. doi: 10.1121/1.400329

Pang, Z. P., Melicoff, E., Padgett, D., Liu, Y., Teich, A. F., Dickey, B. F., et al. (2006). Synaptotagmin-2 is essential for survival and contributes to Ca 2+ triggering of neurotransmitter release in central and neuromuscular synapses. *J. Neurosci.* 26, 13493–13504. doi: 10.1523/JNEUROSCI.3519-06.2006

Pecka, M., Brand, A., Behrend, O., and Grothe, B. (2008). Interaural time difference processing in the mammalian medial superior olive: the role of glycinergic inhibition. *J. Neurosci.* 28, 6914–6924. doi: 10.1523/JNEUROSCI.1660-08.2008

Pei, W., Huang, Z., Wang, C., Han, Y., Jae, S. P., and Niu, L. (2009). Flip and flop: a molecular determinant for AMPA receptor channel opening. *Biochemistry* 48, 3767–3777. doi: 10.1021/bi8015907

Perkins, G. A., Tjong, J., Brown, J. M., Poquiz, P. H., Scott, R. T., Kolson, D. R., et al. (2010). The micro-architecture of mitochondria at active zones: electron tomography reveals novel anchoring scaffolds and cristae structured for high-rate metabolism. *J. Neurosci.* 30, 1015–1026. doi: 10.1523/JNEUROSCI.1517-09.2010

Perkins, R. E. (1973). An electron microscopic study of synaptic organization in the medial superior olive of normal and experimental chinchillas. *J. Comp. Neurol.* 148, 387–415. doi: 10.1002/cne.901480306

Perney, T. M., and Kaczmarek, L. K. (1997). Localization of a high threshold potassium channel in the rat cochlear nucleus. *J. Comp. Neurol.* 386, 178–202. doi: 10.1002/(SICI)1096-9861(19970922)386:2<178::AID-CNE2>;3.0.CO;2-Z

Petralia, R. S., Rubio, M. E., Wang, Y. X., and Wenthold, R. J. (2000). Differential distribution of glutamate receptors in the cochlear nuclei. *Hear. Res.* 147, 59–69. doi: 10.1016/S0378-5955(00)00120-9

Pfeiffer, R. R. R. (1966). Anteroventral cochlear nucleus: wave forms of extracellularly recorded spike potentials. *Science* 154, 667–668. doi: 10.1126/science.154.3749.667

Pilati, N., Linley, D. M., Selvaskandan, H., Uchitel, O., Hennig, M. H., Kopp-Scheinpflug, C., et al. (2016). Acoustic trauma slows AMPA receptor-mediated EPSCs in the auditory brainstem, reducing GluA4 subunit expression as a mechanism to rescue binaural function. *J. Physiol.* 594, 3683–3703. doi: 10.1113/JP271929

Plauška, A., Borst, J. G., and van der Heijden, M. (2016). Predicting binaural responses from monaural responses in the gerbil medial superior olive. *J. Neurophysiol.* 115, 2950–2963. doi: 10.1152/jn.01146.2015

Powell, K., Mathy, A., Duguid, I., and Häusser, M. (2015). Synaptic representation of locomotion in single cerebellar granule cells. *Elife* 4, 1–18. doi: 10.7554/eLife.07290

Pressnitzer, D., Suied, C., and Shamma, S. A. (2011). Auditory scene analysis: the sweet music of ambiguity. *Front. Hum. Neurosci.* 5:158. doi: 10.3389/fnhum.2011.00158

Price, G. D., and Trussell, L. O. (2006). Estimate of the chloride concentration in a central glutamatergic terminal: a gramicidin perforated-patch study on the calyx of Held. *J. Neurosci.* 26, 11432–11436. doi: 10.1523/JNEUROSCI.1660-06.2006

Prsa, M., Dash, S., Catz, N., Dicke, P. W., and Thier, P. (2009). Characteristics of responses of Golgi cells and mossy fibers to eye saccades and saccadic adaptation recorded from the posterior vermis of the cerebellum. *J. Neurosci.* 29, 250–262. doi: 10.1523/JNEUROSCI.4791-08.2009

Rajaram, E., Kaltenbach, C., Fischl, M. J., Mrowka, L., Alexandrova, O., Grothe, B., et al. (2019). Slow NMDA-mediated excitation accelerates offset-response latencies generated via a post-inhibitory rebound mechanism. *eNeuro* 6:ENEURO.0106-19.2019. doi: 10.1523/ENEURO.0106-19.2019

Ramon y Cajal, S. (1995). *Histology of the Nervous System of Man and Vertebrates (trans. Swanson, N., & Swanson, L.)*. New York, NY: Oxford University Press.

Rancz, E. A., Ishikawa, T., Duguid, I., Chadderton, P., Mahon, S., and Häusser, M. (2007). High-fidelity transmission of sensory information by single cerebellar mossy fibre boutons. *Nature* 450, 1245–1248. doi: 10.1038/nature05995

Rashid, A. J., Morales, E., Turner, R. W., and Dunn, R. J. (2001). The contribution of dendritic Kv3 K+ channels to burst threshold in a sensory neuron. *J. Neurosci.* 21, 125–135. doi: 10.1523/JNEUROSCI.21-01-00125.2001

Rathouz, M., and Trussell, L. (1998). Characterization of outward currents in neurons of the avian nucleus magnocellularis. *J. Neurophysiol.* 80, 2824–2835. doi: 10.1152/jn.1998.80.6.2824

Rautenberg, P. L., Grothe, B., and Felmy, F. (2009). Quantification of the three-dimensional morphology of coincidence detector neurons in the medial superior olive of gerbils during late postnatal development. *J. Comp. Neurol.* 517, 385–396. doi: 10.1002/cne.22166

Ravindranathan, A., Donevan, S. D., Sugden, S. G., Greig, A., Rao, M. S., and Parks, T. N. (2000). Contrasting molecular composition and channel properties of AMPA receptors on chick auditory and brainstem motor neurons. *J. Physiol.* 523, 667–684. doi: 10.1111/j.1469-7793.2000.00667.x

Recio-Spinoso, A., and Joris, P. X. (2014). Temporal properties of responses to sound in the ventral nucleus of the lateral lemniscus. *J. Neurophysiol.* 111, 817–835. doi: 10.1152/jn.00971.2011

Recio-Spinoso, A., and Rhode, W. S. (2020). Information processing by onset neurons in the cat auditory brainstem. *J. Assoc. Res. Otolaryngol.* 21, 201–224. doi: 10.1007/s10162-020-00757-0

Remme, M. W. H., Donato, R., Mikiel-Hunter, J., Ballestero, J. A., Foster, S., Rinzel, J., et al. (2014). Subthreshold resonance properties contribute to the efficient coding of auditory spatial cues. *Proc. Natl. Acad. Sci. U. S. A.* 111, E2339–E2348. doi: 10.1073/pnas.1316216111

Renden, R., and von Gersdorff, H. (2007). Synaptic vesicle endocytosis at a CNS nerve terminal: faster kinetics at physiological temperatures and increased endocytotic capacity during maturation. *J. Neurophysiol.* 98, 3349–3359. doi: 10.1152/jn.00898.2007

Reuss, S., Disque-Kaiser, U., Antoniou-Lipfert, P., Gholi, M. N., Riemann, E., and Riemann, R. (2009). Neurochemistry of olivocochlear neurons in the hamster. *Anat. Rec.* 292, 461–471. doi: 10.1002/ar.20881

Rhode, W. S. (2008). Response patterns to sound associated with labeled globular/bushy cells in cat. *Neuroscience* 154, 87–98. doi: 10.1016/j.neuroscience.2008.03.013

Rhode, W. S., and Smith, P. H. (1986). Encoding timing and intensity in the ventral cochlear nucleus of the cat. *J. Neurophysiol.* 56, 261–286. doi: 10.1152/jn.1986.56.2.261

Rhode, W. S., Smith, P. H., Oertel, D., and Smith, P. H. (1983). Physiological response properties of cells labeled intracellularly with horseradish peroxidase in cat ventral cochlear nucleus. *J. Comp. Neurol.* 213, 448–463. doi: 10.1002/cne.902130408

Richardson, A., Ciampani, V., Stancu, M., Bondarenko, K., Newton, S., Steinert, J. R., et al. (2022). Kv3.3 subunits control pre-synaptic action potential waveform and neurotransmitter release at a central excitatory synapse. *Elife* 11:75219. doi: 10.7554/eLife.75219

Richter, E. A., Norris, B. E., Fullerton, B. C., Levine, R. A., and Kiang, N. Y. S. (1983). Is there a medial nucleus of the trapezoid body in humans? *Am. J. Anat.* 168, 157–166. doi: 10.1002/aja.1001680205

Rietzel, H. J., and Friauf, E. (1998). Neuron types in the rat lateral superior olive and developmental changes in the complexity of their dendritic arbors. *J. Comp. Neurol.* 390, 20–40. doi: 10.1002/(SICI)1096-9861(19980105)390:1<20::AID-CNE3>3.0.CO;2-S

Rincón, H., Gómez-Martínez, M., Gómez-Álvarez, M., and Saldaña, E. (2024). Medial superior olive in the rat: anatomy, sources of input and axonal projections. *Hear. Res.* 449:109036. doi: 10.1016/j.heares.2024.109036

Riquelme, R., Saldaña, E., Osen, K. K., Ottersen, O. P., and Merchán, M. A. (2001). Colocalization of GABA and glycine in the ventral nucleus of the lateral lemniscus in rat: An in situ hybridization and semiquantitative immunocytochemical study. *J. Comp. Neurol.* 432, 409–424. doi: 10.1002/cne.1111

Ritzau-Jost, A., Delvendahl, I., Rings, A., Byczkowicz, N., Harada, H., Shigemoto, R., et al. (2014). Ultrafast action potentials mediate kilohertz signaling at a central synapse. *Neuron* 84, 152–163. doi: 10.1016/j.neuron.2014.08.036

Roberts, M. T., Seeman, S. C., and Golding, N. L. (2013). A mechanistic understanding of the role of feedforward inhibition in the mammalian sound localization circuitry. *Neuron* 78, 923–935. doi: 10.1016/j.neuron.2013.04.022

Roberts, M. T., Seeman, S. C., and Golding, N. L. (2014). The relative contributions of MNTB and LNTB neurons to inhibition in the medial superior olive assessed through single and paired recordings. *Front. Neural Circuits* 8:49. doi: 10.3389/fncir.2014.00049

Rodríguez-Contreras, A., de Lange, R. P. J., Lucassen, P. J., and Borst, J. G. G. (2006). Branching of calyceal afferents during postnatal development in the rat auditory brainstem. *J. Comp. Neurol.* 496, 214–228. doi: 10.1002/cne.20918

Rodríguez-Contreras, A., van Hoeve, J. S. S., Habets, R. L. P., Locher, H., and Borst, J. G. G. (2008). Dynamic development of the calyx of Held synapse. *Proc. Natl. Acad. Sci. U. S. A.* 105, 5603–5608. doi: 10.1073/pnas.0801395105

Rosenberger, M. H., Fremouw, T., Casseday, J. H., and Covey, E. (2003). Expression of the Kv1.1 Ion channel subunit in the auditory brainstem of the big brown bat, *Eptesicus fuscus*. *J. Comp. Neurol.* 462, 101–120. doi: 10.1002/cne.10713

Rosengauer, E., Hartwich, H., Hartmann, A. M., Rudnicki, A., Satheesh, S. V., Avraham, K. B., et al. (2012). Egr2::cre mediated conditional ablation of dicer disrupts histogenesis of mammalian central auditory nuclei. *PLoS ONE* 7:e49503. doi: 10.1371/journal.pone.0049503

Rothman, J. S., Kocsis, L., Herzog, E., Nusser, Z., and Silver, R. A. (2016). Physical determinants of vesicle mobility and supply at a central synapse. *Elife* 5, 1–30. doi: 10.7554/eLife.15133

Rouiller, E. M., Cronin-Schreiber, R., Fekete, D. M., and Ryugo, D. K. (1986). The central projections of intracellularly labeled auditory nerve fibers in cats: an analysis of terminal morphology. *J. Comp. Neurol.* 249, 261–278. doi: 10.1002/cne.902490210

Rowland, K. C., Irby, N. K., and Spirou, G. A. (2000). Specialized synapse-associated structures within the calyx of Held. *J. Neurosci.* 20, 9135–9144. doi: 10.1523/JNEUROSCI.20-24-09135.2000

Rubio, M. E., Matsui, K., Fukazawa, Y., Kamasawa, N., Harada, H., Itakura, M., et al. (2017). The number and distribution of AMPA receptor channels containing fast kinetic GluA3 and GluA4 subunits at auditory nerve synapses depend on the target cells. *Brain Struct. Funct.* 222, 3375–3393. doi: 10.1007/s00429-017-1408-0

Rubio, M. E., and Wenthold, R. J. (1997). Glutamate receptors are selectively targeted to post-synaptic sites in neurons. *Neuron* 18, 939–950. doi: 10.1016/S0896-6273(00)80333-5

Russo, N., Nicol, T., Musacchia, G., and Kraus, N. (2004). Brainstem responses to speech syllables. *Clin. Neurophysiol.* 115, 2021–2030. doi: 10.1016/j.clinph.2004.04.003

Ryugo, D. K., and Fekete, D. M. (1982). Morphology of primary axosomatic endings in the anteroventral cochlear nucleus of the cat: a study of the endbulbs of Held. *J. Comp. Neurol.* 210, 239–257. doi: 10.1002/cne.902100304

Ryugo, D. K., Montey, K. L., Wright, a,. L., Bennett, M. L., and Pongstaporn, T. (2006). Postnatal development of a large auditory nerve terminal: the endbulb of Held in cats. *Hear. Res.* 216–217, 100–115. doi: 10.1016/j.heares.2006.01.007

Ryugo, D. K., and Parks, T. N. (2003). Primary innervation of the avian and mammalian cochlear nucleus. *Brain Res. Bull.* 60, 435–456. doi: 10.1016/S0361-9230(03)00049-2

Ryugo, D. K., Rosenbaum, B. T., Kim, P. J., Niparko, J. K., and Saada, A. A. (1998). Single unit recordings in the auditory nerve of congenitally deaf white cats: morphological correlates in the cochlea and cochlear nucleus. *J. Comp. Neurol.* 397, 532–548. doi: 10.1002/(SICI)1096-9861(19980810)397:4<532::AID-CNE6>3.0.CO;2-2

Ryugo, D. K., and Sento, S. (1991). Synaptic connections of the auditory nerve in cats: relationship between endbulbs of held and spherical bushy cells. *J. Comp. Neurol.* 305, 35–48. doi: 10.1002/cne.903050105

Ryugo, D. K., Wu, M. M., and Pongstaporn, T. (1996). Activity-related features of synapse morphology: a study of endbulbs of held. *J. Comp. Neurol.* 365, 141–158. doi: 10.1002/(SICI)1096-9861(19960129)365:1<141::AID-CNE11>3.0.CO;2-T

Saint Marie, R. L., Morest, D. K., and Brandon, C. J. (1989). The form and distribution of GABAergic synapses on the principal cell types of the ventral cochlear nucleus of the cat. *Hear. Res.* 42, 97–112. doi: 10.1016/0378-5955(89)90120-2

Saint Marie, R. L., Shneiderman, A., and Stanforth, D. A. (1997). Patterns of γ-aminobutyric acid and glycine immunoreactivities reflect structural and functional differences of the cat lateral lemniscal nuclei. *J. Comp. Neurol.* 389, 264–276. doi: 10.1002/(SICI)1096-9861(19971215)389:2<264::AID-CNE6>3.0.CO;2-#

Sakaba, T. (2006). Roles of the fast-releasing and the slowly releasing vesicles in synaptic transmission at the calyx of Held. *J. Neurosci.* 26, 5863–5871. doi: 10.1523/JNEUROSCI.0182-06.2006

Sakaba, T. (2018). Kinetics of transmitter release at the calyx of Held synapse. *Proc. Jpn. Acad. Ser. B Phys. Biol. Sci.* 94, 139–152. doi: 10.2183/pjab.94.010

Sanes, D. H., Merickel, M., and Rubel, E. W. (1989). Evidence for an alteration of the tonotopic map in the gerbil cochlea during development. *J. Comp. Neurol.* 279, 436–444. doi: 10.1002/cne.902790308

Santoro, B., Liu, D. T., Yao, H., Bartsch, D., Kandel, E. R., Siegelbaum, S. A., et al. (1998). Identification of a gene encoding a hyperpolarization-activated pacemaker channel of brain. *Cell* 93, 717–729. doi: 10.1016/S0092-8674(00)81434-8

Santoro, B., and Tibbs, G. R. (1999). The HCN gene family: molecular basis of the hyperpolarization-activated pacemaker channels. *Ann. N. Y. Acad. Sci.* 868, 741–764. doi: 10.1111/j.1749-6632.1999.tb11353.x

Sargent, P. B. (2005). Rapid vesicular release, quantal variability, and spillover contribute to the precision and reliability of transmission at a glomerular synapse. *J. Neurosci.* 25, 8173–8187. doi: 10.1523/JNEUROSCI.2051-05.2005

Sato, K., Kuriyama, H., and Altschuler, R., a. (2000). Expression of glycine receptor subunit mRNAs in the rat cochlear nucleus. *Hear. Res.* 144, 47–52. doi: 10.1016/S0378-5955(00)00044-7

Sato, K., Nakayama, H., Kuriyama, H., and Altschuler, R. A. (1999). Differential distribution of N-methyl-D-aspartate receptor-2 subunit messenger RNA in the rat superior olivary complex. *Neuroscience* 89, 839–853. doi: 10.1016/S0306-4522(98)00350-9

Sätzler, K., Söhl, L. F., Bollmann, J. H., Borst, J. G. G., Frotscher, M., Sakmann, B., et al. (2002). Three-dimensional reconstruction of a calyx of Held and its post-synaptic principal neuron in the medial nucleus of the trapezoid body. *J. Neurosci.* 22, 10567–10579. doi: 10.1523/JNEUROSCI.22-24-10567.2002

Saviane, C., and Silver, R. A. (2006). Fast vesicle reloading and a large pool sustain high bandwidth transmission at a central synapse. *Nature* 439, 983–987. doi: 10.1038/nature04509

Scheibel, M. E., and Scheibel, A. B. (1974). Neuropil organization in the superior olive of the cat. *Exp. Neurol.* 43, 339–348. doi: 10.1016/0014-4886(74)90175-7

Scheuber, A., Miles, R., and Poncer, J. C. (2004). Pre-synaptic Cav2.1 and Cav2.2 differentially influence release dynamics at hippocampal excitatory synapses. *J. Neurosci.* 24, 10402–10409. doi: 10.1523/JNEUROSCI.1664-04.2004

Schmid, S., Guthmann, A., Ruppersberg, J. P., and Herbert, H. (2001). Expression of AMPA receptor subunit flip/flop splice variants in the rat auditory brainstem and inferior colliculus. *J. Comp. Neurol.* 430, 160–171. doi: 10.1002/1096-9861(20010205)430:2<160::AID-CNE1022>3.0.CO;2-3

Schmidt, E., Wolski, T. P., and Kulesza, R. J. (2010). Distribution of perineuronal nets in the human superior olivary complex. *Hear. Res.* 265, 15–24. doi: 10.1016/j.heares.2010.03.077

Schneggenburger, R., and Forsythe, I. D. (2006). The calyx of Held. *Cell Tissue Res.* 326, 311–337. doi: 10.1007/s00441-006-0272-7

Schneggenburger, R., Han, Y., and Kochubey, O. (2012). Ca(2+) channels and transmitter release at the active zone. *Cell Calcium* 52, 199–207. doi: 10.1016/j.ceca.2012.04.011

Schneggenburger, R., Meyer, A. C., and Neher, E. (1999). Released fraction and total size of a pool of immediately available transmitter quanta at a calyx synapse. *Neuron* 23, 399–409. doi: 10.1016/S0896-6273(00)80789-8

Schofield, B. R. (1995). Projections from the cochlear nucleus to the superior paraolivary nucleus in guinea pigs. *J. Comp. Neurol.* 360, 135–149. doi: 10.1002/cne.903600110

Schofield, B. R., and Cant, N. B. (1991). Organization of the superior olivary complex in the guinea pig. I. Cytoarchitecture, cytochrome oxidase histochemistry, and dendritic morphology. *J. Comp. Neurol.* 314, 645–670. doi: 10.1002/cne.903140403

Schofield, B. R., and Cant, N. B. (1997). Ventral nucleus of the lateral lemniscus in guinea pigs: cytoarchitecture and inputs from the cochlear nucleus. *J. Comp. Neurol.* 379, 363–385. doi: 10.1002/(SICI)1096-9861(19970317)379:3<363::AID-CNE4>3.0.CO;2-1

Schoppa, N. E. (2006). AMPA/kainate receptors drive rapid output and precise synchrony in olfactory bulb granule cells. *J. Neurosci.* 26, 12996–13006. doi: 10.1523/JNEUROSCI.3503-06.2006

Schwartz, I. R. (1977). Dendritic arrangements in the cat medial superior olive. *Neuroscience* 2, 81–101. doi: 10.1016/0306-4522(77)90070-7

Schwartz, I. R., and Eager, P. R. (1999). Glutamate receptor subunits in neuronal populations of the gerbil lateral superior olive. *Hear. Res.* 137, 77–90. doi: 10.1016/S0378-5955(99)00140-9

Schwarz, D. W., and Puil, E. (1997). Firing properties of spherical bushy cells in the anteroventral cochlear nucleus of the gerbil. *Hear. Res.* 114, 127–138. doi: 10.1016/S0378-5955(97)00162-7

Scott, L. L., Mathews, P. J., and Golding, N. L. (2005). Posthearing developmental refinement of temporal processing in principal neurons of the medial superior olive. *J. Neurosci.* 25, 7887–7895. doi: 10.1523/JNEUROSCI.1016-05.2005

Seidl, A. H., and Grothe, B. (2005). Development of sound localization mechanisms in the Mongolian gerbil is shaped by early acoustic experience. *J. Neurophysiol.* 94, 1028–1036. doi: 10.1152/jn.01143.2004

Sekirnjak, C., Martone, M. E., Weiser, M., Deerinck, T., Bueno, E., Rudy, B., et al. (1997). Subcellular localization of the K+ channel subunit Kv3.1b in selected rat CNS neurons. *Brain Res.* 766, 173–187. doi: 10.1016/S0006-8993(97)00527-1

Sento, S., and Ryugo, D. K. (1989). Endbulbs of held and spherical bushy cells in cats: morphological correlates with physiological properties. *J. Comp. Neurol.* 280, 553–562. doi: 10.1002/cne.902800406

Shahrezaei, V., Cao, A., and Delaney, K. R. (2006). Ca2+ from one or two channels controls fusion of a single vesicle at the frog neuromuscular junction. *J. Neurosci.* 26, 13240–13249. doi: 10.1523/JNEUROSCI.1418-06.2006

Shamma, S. A., Elhilali, M., and Micheyl, C. (2011). Temporal coherence and attention in auditory scene analysis. *Trends Neurosci.* 34, 114–123. doi: 10.1016/j.tins.2010.11.002

Shannon, R. V., Zeng, F. G., Kamath, V., Wygonski, J., and Ekelid, M. (1995). Speech recognition with primarily temporal cues. *Science* 270, 303–304. doi: 10.1126/science.270.5234.303

Shore, S. E., and Wu, C. (2019). Mechanisms of Noise-Induced Tinnitus: Insights from Cellular Studies. *Neuron* 103, 8–20. doi: 10.1016/j.neuron.2019.05.008

Sierksma, M. C., and Borst, J. G. G. (2017). Resistance to action potential depression of a rat axon terminal in vivo. *Proc. Natl. Acad. Sci. U. S. A.* 114, 4249–4254. doi: 10.1073/pnas.1619433114

Silver, R. A., Traynelis, S. F., and Cull-Candy, S. G. (1992). Rapid-time-course miniature and evoked excitatory currents at cerebellar synapses in situ. *Nature* 355, 163–166. doi: 10.1038/355163a0

Siveke, I., Myoga, M. H., Grothe, B., and Felmy, F. (2021). Ambient noise exposure induces long-term adaptations in adult brainstem neurons. *Sci. Rep.* 11:5139. doi: 10.1038/s41598-021-84230-9

Smith, A. J., Owens, S., and Forsythe, I. D. (2000). Characterisation of inhibitory and excitatory post-synaptic currents of the rat medial superior olive. *J. Physiol.* 529, 681–698. doi: 10.1111/j.1469-7793.2000.00681.x

Smith, P. H. (1995). Structural and functional differences distinguish principal from nonprincipal cells in the guinea pig MSO slice. *J. Neurophysiol.* 73, 1653–1667. doi: 10.1152/jn.1995.73.4.1653

Smith, P. H., J.oris, P. X., Carney, L. H., Yin, T. C. T., and Joris, P. X. (1991). Projections of physiologically characterized globular bushy cell axons from the cochlear nucleus of the cat. *J. Comp. Neurol.* 304, 387–407. doi: 10.1002/cne.903040305

Smith, P. H., Joris, P. X., and Yin, T. C. (1993). Projections of physiologically characterized spherical bushy cell axons from the cochlear nucleus of the cat: evidence for delay lines to the medial superior olive. *J. Comp. Neurol.* 331, 245–260. doi: 10.1002/cne.903310208

Smith, P. H., Joris, P. X., Yin, T. C., and Joris, P. X. (1998). Anatomy and physiology of principal cells of the medial nucleus of the trapezoid body (MNTB) of the cat. *J. Neurophysiol.* 79, 3127–3142. doi: 10.1152/jn.1998.79.6.3127

Smith, P. H., Massie, A., and Joris, P. X. (2005). Acoustic stria: Anatomy of physiologically characterized cells and their axonal projection patterns. *J. Comp. Neurol.* 482, 349–371. doi: 10.1002/cne.20407

Smith, P. H., and Rhode, W. S. (1987). Characterization of HRP-labeled globular bushy cells in the cat anteroventral cochlear nucleus. *J. Comp. Neurol.* 266, 360–375. doi: 10.1002/cne.902660305

Sommer, B., Keinänen, K., Verdoorn, T. A., Wisden, W., Burnashev, N., Herb, A., et al. (1990). Flip and flop: a cell-specific functional switch in glutamate-operated channels of the CNS. *Science* 249, 1580–1585. doi: 10.1126/science.1699275

Sommer, I., Lingenhöhl, K., and Friauf, E. (1993). Principal cells of the rat medial nucleus of the trapezoid body: an intracellular in vivo study of their physiology and morphology. *Exp. Brain Res.* 223–239. doi: 10.1007/BF00229781

Sonntag, M., Englitz, B., Kopp-Scheinpflug, C., and Rübsamen, R. (2009). Early postnatal development of spontaneous and acoustically evoked discharge activity of principal cells of the medial nucleus of the trapezoid body: an in vivo study in mice. *J. Neurosci.* 29, 9510–9520. doi: 10.1523/JNEUROSCI.1377-09.2009

Sonntag, M., Englitz, B., Typlt, M., and Rübsamen, R. (2011). The calyx of Held develops adult-like dynamics and reliability by hearing onset in the mouse in vivo. *J. Neurosci.* 31, 6699–6709. doi: 10.1523/JNEUROSCI.0575-11.2011

Spangler, K. M., Warr, W. B., and Henkel, C. K. (1985). The projections of principal cells of the medial nucleus of the trapezoid body in the cat. *J. Comp. Neurol.* 238, 249–262. doi: 10.1002/cne.902380302

Spencer, M. J., Nayagam, D. A. X., Clarey, J. C., Paolini, A. G., Meffin, H., Burkitt, A. N., et al. (2015). Broadband onset inhibition can suppress spectral splatter in the auditory brainstem. *PLoS ONE* 10:e0126500. doi: 10.1371/journal.pone.0126500

Spirou, G. A., and Berrebi, A. S. (1997). Glycine immunoreactivity in the lateral nucleus of the trapezoid body of the cat. *J. Comp. Neurol.* 383, 473–488. doi: 10.1002/(SICI)1096-9861(19970714)383:4<473::AID-CNE6>3.0.CO;2-#

Spirou, G. A., Chirila, F. V., von Gersdorff, H., and Manis, P. B. (2008). Heterogeneous Ca2+ influx along the adult calyx of Held: a structural and computational study. *Neuroscience* 154, 171–185. doi: 10.1016/j.neuroscience.2008.04.002

Spirou, G. A., Kersting, M. G., Carr, S., Razzaq, B., Alves-Pinto, C. Y., Dawson, M., et al. (2023). High-resolution volumetric imaging constrains compartmental models to explore synaptic integration and temporal processing by cochlear nucleus globular bushy cells. *Elife* 12, 1–44. doi: 10.7554/eLife.83393

Spirou, G. A., Rager, J., and Manis, P. B. (2005). Convergence of auditory-nerve fiber projections onto globular bushy cells. *Neuroscience* 136, 843–863. doi: 10.1016/j.neuroscience.2005.08.068

Spirou, G. A., Rowland, K. C., and Berrebi, A. S. (1998). Ultrastructure of neurons and large synaptic terminals in the lateral nucleus of the trapezoid body of the cat. *J. Comp. Neurol.* 398, 257–272. doi: 10.1002/(SICI)1096-9861(19980824)398:2<257::AID-CNE7>3.0.CO;2-#

Srinivasan, G., Friauf, E., and Löhrke, S. (2004). Functional glutamatergic and glycinergic inputs to several superior olivary nuclei of the rat revealed by optical imaging. *Neuroscience* 128, 617–634. doi: 10.1016/j.neuroscience.2004.06.012

Stange, A., Myoga, M. H., Lingner, A., Ford, M. C., Alexandrova, O., Felmy, F., et al. (2013). Adaptation in sound localization: from GABA(B) receptor-mediated synaptic modulation to perception. *Nat. Neurosci.* 16, 1840–1847. doi: 10.1038/nn.3548

Stange-Marten, A., Nabel, A. L., Sinclair, J. L., Fischl, M., Alexandrova, O., Wohlfrom, H., et al. (2017). Input timing for spatial processing is precisely tuned via constant synaptic delays and myelination patterns in the auditory brainstem. *Proc. Natl. Acad. Sci. U. S. A.* 2017:02290. doi: 10.1073/pnas.1702290114

Stanley, E. F. (1993). Single calcium channels and acetylcholine release at a presynaptic nerve terminal. *Neuron* 11, 1007–1011. doi: 10.1016/0896-6273(93)90214-C

Stanley, E. F. (2016). The nanophysiology of fast transmitter release. *Trends Neurosci.* 39, 183–197. doi: 10.1016/j.tins.2016.01.005

Stasiak, A., Sayles, M., and Winter, I. M. (2018). Perfidious synaptic transmission in the guinea-pig auditory brainstem. *PLoS ONE* 13:e0203712. doi: 10.1371/journal.pone.0203712

Steinmetz, N. A., Aydin, C., Lebedeva, A., Okun, M., Pachitariu, M., Bauza, M., et al. (2021). Neuropixels 2.0: A miniaturized high-density probe for stable, long-term brain recordings. *Science* 372:eabf4588. doi: 10.1126/science.abf4588

Sterenborg, J. C., Pilati, N., Sheridan, C. J., Uchitel, O. D., Forsythe, I. D., and Barnes-Davies, M. (2010). Lateral olivocochlear (LOC) neurons of the mouse LSO receive excitatory and inhibitory synaptic inputs with slower kinetics than LSO principal neurons. *Hear. Res.* 270, 119–126. doi: 10.1016/j.heares.2010.08.013

Stotler, W. A. (1953). An experimental study of the cells and connections of the superior olivary complex of the cat. *J. Comp. Neurol.* 98, 401–431. doi: 10.1002/cne.900980303

Sun, J. Y., and Wu, L. G. (2001). Fast kinetics of exocytosis revealed by simultaneous measurements of pre-synaptic capacitance and post-synaptic currents at a central synapse. *Neuron* 30, 171–182. doi: 10.1016/S0896-6273(01)00271-9

Svirskis, G., Kotak, V., Sanes, D. H., and Rinzel, J. (2002). Enhancement of signal-to-noise ratio and phase locking for small inputs by a low-threshold outward current in auditory neurons. *J. Neurosci.* 22, 11019–11025. doi: 10.1523/JNEUROSCI.22-24-11019.2002

Szpir, M. R., Sento, S., and Ryugo, D. K. (1990). Central projections of cochlear nerve fibers in the alligator lizard. *J. Comp. Neurol.* 295, 530–547. doi: 10.1002/cne.902950403

Takahashi, T. (2005). Post-synaptic receptor mechanisms underlying developmental speeding of synaptic transmission. *Neurosci. Res.* 53, 229–240. doi: 10.1016/j.neures.2005.07.005

Tanaka, K., Otani, K., Tokunaga, A., and Sugita, S. (1985). The organization of neurons in the nucleus of the lateral lemniscus projecting to the superior and inferior colliculi in the rat. *Brain Res.* 341, 252–260. doi: 10.1016/0006-8993(85)91064-9

Tansey, E. P., Chow, A., Rudy, B., and McBain, C. J. (2002). Developmental expression of potassium-channel subunit Kv3.2 within subpopulations of mouse hippocampal inhibitory interneurons. *Hippocampus* 12, 137–148. doi: 10.1002/hipo.1104

Taruno, A., Ohmori, H., and Kuba, H. (2012). Inhibition of pre-synaptic Na(+)/K(+)-ATPase reduces readily releasable pool size at the avian end-bulb of Held synapse. *Neurosci. Res.* 72, 117–128. doi: 10.1016/j.neures.2011.11.003

Taschenberger, H., Leão, R. M., Rowland, K. C., Spirou, G. A., and von Gersdorff, H. (2002). Optimizing synaptic architecture and efficiency for high-frequency transmission. *Neuron* 36, 1127–1143. doi: 10.1016/S0896-6273(02)01137-6

Taschenberger, H., Scheuss, V., and Neher, E. (2005). Release kinetics, quantal parameters and their modulation during short-term depression at a developing synapse in the rat CNS: Fluctuation analysis at the developing calyx of Held. *J. Physiol.* 568, 513–537. doi: 10.1113/jphysiol.2005.093468

Taschenberger, H., and von Gersdorff, H. (2000). Fine-tuning an auditory synapse for speed and fidelity: developmental changes in pre-synaptic waveform, EPSC kinetics, and synaptic plasticity. *J. Neurosci.* 20, 9162–9173. doi: 10.1523/JNEUROSCI.20-24-09162.2000

Thavam, S., and Dietz, M. (2019). Smallest perceivable interaural time differences. *J. Acoust. Soc. Am.* 145:458. doi: 10.1121/1.5087566

Thomas, C. I., Keine, C., Okayama, S., Satterfield, R., Musgrove, M., Guerrero-Given, D., et al. (2019). Pre-synaptic mitochondria volume and abundance increase during development of a high-fidelity synapse. *J. Neurosci.* 39, 7994–8012. doi: 10.1523/JNEUROSCI.0363-19.2019

Tolbert, L. P., Morest, D. K., and Yurgelun-Todd, D. A. (1982). The neuronal architecture of the anteroventral cochlear nucleus of the cat in the region of the cochlear nerve root: horseradish peroxidase labelling of identified cell types. *Neuroscience* 7, 3031–3052. doi: 10.1016/0306-4522(82)90228-7

Tolbert, L. P., and Morest, D. K. K. (1982). The neuronal architecture of the anteroventral cochlear nucleus of the cat in the region of the cochlear nerve root: Golgi and Nissl methods. *Neuroscience* 7, 3013–3030. doi: 10.1016/0306-4522(82)90227-5

Tollin, D. J. (2003). The Lateral Superior Olive: A Functional Role in Sound Source Localization. *Neuroscientist* 9, 127–143. doi: 10.1177/1073858403252228

Tollin, D. J., Koka, K., and Tsai, J. J. (2008). Interaural level difference discrimination thresholds for single neurons in the lateral superior olive. *J. Neurosci.* 28, 4848–4860. doi: 10.1523/JNEUROSCI.5421-07.2008

Tollin, D. J., and Yin, T. C. T. (2005). Interaural phase and level difference sensitivity in low-frequency neurons in the lateral superior olive. *J. Neurosci.* 25, 10648–10657. doi: 10.1523/JNEUROSCI.1609-05.2005

Tolnai, S., Englitz, B., Scholbach, J., Jost, J., and Rübsamen, R. (2009). Spike transmission delay at the calyx of Held in vivo: rate dependence, phenomenological modeling, and relevance for sound localization. *J. Neurophysiol.* 102, 1206–1217. doi: 10.1152/jn.00275.2009

Tsai, J. J., Koka, K., and Tollin, D. J. (2010). Varying overall sound intensity to the two ears impacts interaural level difference discrimination thresholds by single neurons in the lateral superior olive. *J. Neurophysiol.* 103, 875–886. doi: 10.1152/jn.00911.2009

Tsuchitani, C. (1977). Functional organization of lateral cell groups of cat superior olivary complex. *J. Neurophysiol.* 40, 296–318. doi: 10.1152/jn.1977.40.2.296

Tsuchitani, C. (1988). The inhibition of cat lateral superior olive unit excitatory responses to binaural tone bursts. II. The sustained discharges. *J. Neurophysiol.* 59, 184–211. doi: 10.1152/jn.1988.59.1.184

Turecek, R., and Trussell, L. O. (2001). Pre-synaptic glycine receptors enhance transmitter release at a mammalian central synapse. *Nature* 411, 587–590. doi: 10.1038/35079084

Typlt, M., Englitz, B., Sonntag, M., Dehmel, S., Kopp-Scheinpflug, C., Rübsamen, R., et al. (2012). Multidimensional characterization and differentiation of neurons in the anteroventral cochlear nucleus. *PLoS ONE* 7:e29965. doi: 10.1371/journal.pone.0029965

Typlt, M., Haustein, M. D., Dietz, B., Steinert, J. R., Witte, M., Englitz, B., et al. (2010). Pre-synaptic and post-synaptic origin of multicomponent extracellular waveforms at the endbulb of Held-spherical bushy cell synapse. *Eur. J. Neurosci.* 31, 1574–1581. doi: 10.1111/j.1460-9568.2010.07188.x

Ueyama, T., Sato, K., Kakimoto, S., Houtani, T., Sakuma, S., Ohishi, H., et al. (1999). Comparative distribution of GABAergic and peptide-containing neurons in the lateral lemniscal nuclei of the rat. *Brain Res.* 849, 220–225. doi: 10.1016/S0006-8993(99)02079-X

van der Heijden, M., Lorteije, J. A. M., Plauška, A., Roberts, M. T., Golding, N. L., and Borst, J. G. G. (2013). Directional hearing by linear summation of binaural inputs at the medial superior olive. *Neuron* 78, 936–948. doi: 10.1016/j.neuron.2013.04.028

Vater, M., Casseday, J. H., and Covey, E. (1995). Convergence and divergence of ascending binaural and monaural pathways from the superior olives of the mustached bat. *J. Comp. Neurol.* 351, 632–646. doi: 10.1002/cne.903510411

Vater, M., Covey, E., and Casseday, J. H. (1997). The columnar region of the ventral nucleus of the lateral lemniscus in the big brown bat (*Eptesicus fuscus*): synaptic arrangements and structural correlates of feedforward inhibitory function. *Cell Tissue Res.* 289, 223–233. doi: 10.1007/s004410050869

Vater, M., and Feng, A. S. (1990). Functional organization of ascending and descending connections of the cochlear nucleus of horseshoe bats. *J. Comp. Neurol.* 292, 373–395. doi: 10.1002/cne.902920305

Vater, M., Kössl, M., and Horn, A. K. E. (1992). GAD- and GABA-immunoreactivity in the ascending auditory pathway of horseshoe and mustached bats. *J. Comp. Neurol.* 325, 183–206. doi: 10.1002/cne.903250205

Verhey, J. L., Pressnitzer, D., and Winter, I. M. (2003). The psychophysics and physiology of comodulation masking release. *Exp. Brain Res.* 153, 405–417. doi: 10.1007/s00221-003-1607-1

Verstreken, P., Ly, C. V., Venken, K. J. T., Koh, T.-W., Zhou, Y., and Bellen, H. J. (2005). Synaptic mitochondria are critical for mobilization of reserve pool vesicles at Drosophila neuromuscular junctions. *Neuron* 47, 365–378. doi: 10.1016/j.neuron.2005.06.018

von Gersdorff, H., and Borst, J. G. G. (2002). Short-term plasticity at the calyx of Held. *Nat. Rev. Neurosci.* 3, 53–64. doi: 10.1038/nrn705

Wagoner, J. L., and Kulesza, R. J. (2009). Topographical and cellular distribution of perineuronal nets in the human cochlear nucleus. *Hear. Res.* 254, 42–53. doi: 10.1016/j.heares.2009.04.008

Walcher, J., Hassfurth, B., Grothe, B., and Koch, U. (2011). Comparative posthearing development of inhibitory inputs to the lateral superior olive in gerbils and mice. *J. Neurophysiol.* 106, 1443–1453. doi: 10.1152/jn.01087.2010

Wang, L.-Y., and Augustine, G. J. (2014). Pre-synaptic nanodomains: a tale of two synapses. *Front. Cell. Neurosci.* 8:455. doi: 10.3389/fncel.2014.00455

Wang, L.-Y., Neher, E., and Taschenberger, H. (2008). Synaptic vesicles in mature calyx of Held synapses sense higher nanodomain calcium concentrations during action potential-evoked glutamate release. *J. Neurosci.* 28, 14450–14458. doi: 10.1523/JNEUROSCI.4245-08.2008

Wang, L. Y., Gan, L., Forsythe, I. D., and Kaczmarek, L. K. (1998a). Contribution of the Kv3.1 potassium channel to high frequency firing in mouse auditory neurones. *J. Physiol.* 509, 183–194. doi: 10.1111/j.1469-7793.1998.183bo.x

Wang, L. Y., and Kaczmarek, L. K. (1998). High-frequency firing helps replenish the readily releasable pool of synaptic vesicles. *Nature* 394, 384–388. doi: 10.1038/28645

Wang, M., Zhang, C., Lin, S., Wang, Y., Seicol, B. J., Ariss, R. W., et al. (2021). Biased auditory nerve central synaptopathy is associated with age-related hearing loss. *J. Physiol.* 599, 1833–1854. doi: 10.1113/JP281014

Wang, T., de Kok, L., Willemsen, R., Elgersma, Y., and Borst, J. G. G. (2015). In vivo synaptic transmission and morphology in mouse models of Tuberous sclerosis, Fragile X syndrome, Neurofibromatosis type 1, and Costello syndrome. *Front. Cell. Neurosci.* 9:234. doi: 10.3389/fncel.2015.00234

Wang, Y., and Manis, P. B. (2005). Synaptic transmission at the cochlear nucleus endbulb synapse during age-related hearing loss in mice. *J. Neurophysiol.* 94, 1814–1824. doi: 10.1152/jn.00374.2005

Wang, Y., and Manis, P. B. (2006). Temporal coding by cochlear nucleus bushy cells in DBA/2J mice with early onset hearing loss. *J. Assoc. Res. Otolaryngol.* 7, 412–424. doi: 10.1007/s10162-006-0052-9

Wang, Y., and Manis, P. B. (2008). Short-term synaptic depression and recovery at the mature mammalian endbulb of Held synapse in mice. *J. Neurophysiol.* 100, 1255–1264. doi: 10.1152/jn.90715.2008

Wang, Y. X., Wenthold, R. J., Ottersen, O. P., and Petralia, R. S. (1998b). Endbulb synapses in the anteroventral cochlear nucleus express a specific subset of AMPA-type glutamate receptor subunits. *J. Neurosci.* 18, 1148–1160. doi: 10.1523/JNEUROSCI.18-03-01148.1998

Warr, W. B. (1966). Fiber degeneration following lesions in the anterior ventral cochlear nucleus of the cat. *Exp. Neurol.* 14, 453–474. doi: 10.1016/0014-4886(66)90130-0

Watanabe, M., Mishina, M., and Inoue, Y. (1994). Distinct distributions of five NMDA receptor channel subunit mRNAs in the brainstem. *J. Comp. Neurol.* 343, 520–531. doi: 10.1002/cne.903430403

Weimann, S. R., Zhang, C., and Burger, R. M. (2024). A developmental switch in cholinergic mechanisms of modulation in the medial nucleus of the trapezoid body. *J. Neurosci.* 44, 1–16. doi: 10.1523/JNEUROSCI.0356-23.2023

Weingarten, D. J., Shrestha, A., Juda-Nelson, K., Kissiwaa, S. A., Spruston, E., and Jackman, S. L. (2022). Fast resupply of synaptic vesicles requires synaptotagmin-3. *Nature* 611, 320–325. doi: 10.1038/s41586-022-05337-1

Weiser, M., Bueno, E., Sekirnjak, C., Marione, M. E., Baker, H., Hillman, D., et al. (1995). The potassium channel subunit KV3.1b is localized to somatic and axonal membranes of specific populations of CNS neurons. *J. Neurosci.* 15, 4298–4314. doi: 10.1523/JNEUROSCI.15-06-04298.1995

Wenthold, R. J., Huie, D., Altschuler, R., a., and Reeks, K., a. (1987). Glycine immunoreactivity localized in the cochlear nucleus and superior olivary complex. *Neuroscience* 22, 897–912. doi: 10.1016/0306-4522(87)92968-X

Werthat, F., Alexandrova, O., Grothe, B., and Koch, U. (2008). Experience-dependent refinement of the inhibitory axons projecting to the medial superior olive. *J. Neurobiol.* 68, 1454–1462. doi: 10.1002/dneu.20660

Whitley, J. M., and Henkel, C. K. (1984). Topographical organization of the inferior collicular projection and other connections of the ventral nucleus of the lateral lemniscus in the cat. *J. Comp. Neurol.* 229, 257–270. doi: 10.1002/cne.902290210

Whitton, J. P., Polley, D. B., Jp, W., Db, P., Whitton, J. P., and Polley, D. B. (2011). Evaluating the perceptual and pathophysiological consequences of auditory deprivation in early postnatal life: A comparison of basic and clinical studies. *J. Assoc. Res. Otolaryngol.* 12, 535–546. doi: 10.1007/s10162-011-0271-6

Wickesberg, R. E., Whitlon, D., and Oertel, D. (1994). In vitro modulation of somatic glycine-like immunoreactivity in presumed glycinergic neurons. *J. Comp. Neurol.* 339, 311–327. doi: 10.1002/cne.903390302

Wigmore, M. A., and Lacey, M. G. (2000). A Kv3-like persistent, outwardly rectifying, Cs+-permeable, K+ current in rat subthalamic nucleus neurones. *J. Physiol.* 527, 493–506. doi: 10.1111/j.1469-7793.2000.t01-1-00493.x

Willard, F. H., and Martin, G. F. (1983). The auditory brainstem nuclei and some of their projections to the inferior colliculus in the North American opossum. *Neuroscience* 10, 1203–1232. doi: 10.1016/0306-4522(83)90109-4

Wimmer, V. C., Horstmann, H., Groh, A., and Kuner, T. (2006). Donut-like topology of synaptic vesicles with a central cluster of mitochondria wrapped into membrane protrusions: a novel structure-function module of the adult calyx of Held. *J. Neurosci.* 26, 109–116. doi: 10.1523/JNEUROSCI.3268-05.2006

Winters, B. D., Jin, S.-X., Ledford, K. R., and Golding, N. L. (2017). Amplitude normalization of dendritic EPSPs at the Soma of binaural coincidence detector neurons of the medial superior Olive. *J. Neurosci.* 37, 3138–3149. doi: 10.1523/JNEUROSCI.3110-16.2017

Wölfel, M., Lou, X., and Schneggenburger, R. (2007). A Mechanism Intrinsic to the Vesicle Fusion Machinery Determines Fast and Slow Transmitter Release at a Large CNS Synapse. *J. Neurosci.* 27, 3198–3210. doi: 10.1523/JNEUROSCI.4471-06.2007

Wong, N. F., Brongo, S. E., Forero, E. A., Sun, S., Cook, C. J., Lauer, A. M., et al. (2025). Convergence of type 1 spiral ganglion neuron subtypes onto principal neurons of the anteroventral cochlear nucleus. *J. Neurosci.* 45:e1507242024. doi: 10.1523/JNEUROSCI.1507-24.2024

Wright, S., Hwang, Y., and Oertel, D. (2014). Synaptic transmission between end bulbs of Held and bushy cells in the cochlear nucleus of mice with a mutation in Otoferlin. *J. Neurophysiol.* 112, 3173–3188. doi: 10.1152/jn.00522.2014

Wu, L. G., and Borst, J. G. G. (1999). The reduced release probability of releasable vesicles during recovery from short-term synaptic depression. *Neuron* 23, 821–832. doi: 10.1016/S0896-6273(01)80039-8

Wu, S. H., and Kelly, J. B. (1991). Physiological properties of neurons in the mouse superior olive: membrane characteristics and post-synaptic responses studied in vitro. *J. Neurophysiol.* 65, 230–246. doi: 10.1152/jn.1991.65.2.230

Wu, S. H., and Kelly, J. B. (1992). Synaptic pharmacology of the superior olivary complex studied in mouse brain slice. *J. Neurosci.* 12, 3084–3097. doi: 10.1523/JNEUROSCI.12-08-03084.1992

Wu, S. H., and Kelly, J. B. (1995). Inhibition in the superior olivary complex: pharmacological evidence from mouse brain slice. *J. Neurophysiol.* 73, 256–269. doi: 10.1152/jn.1995.73.1.256

Wu, S. H., and Oertel, D. (1984). Intracellular injection with horseradish peroxidase of physiologically characterized stellate and bushy cells in slices of mouse anteroventral cochlear nucleus. *J. Neurosci.* 4, 1577–1588. doi: 10.1523/JNEUROSCI.04-06-01577.1984

Xie, R., and Manis, P. B. (2013). Target-specific IPSC kinetics promote temporal processing in auditory parallel pathways. *J. Neurosci.* 33, 1598–1614. doi: 10.1523/JNEUROSCI.2541-12.2013

Xie, R., and Manis, P. B. (2017). Synaptic transmission at the endbulb of Held deteriorates during age-related hearing loss. *J. Physiol.* 595, 919–934. doi: 10.1113/JP272683

Xu, J., Mashimo, T., and Südhof, T. C. (2007). Synaptotagmin-1,−2, and−9: Ca(2+) sensors for fast release that specify distinct pre-synaptic properties in subsets of neurons. *Neuron* 54, 567–581. doi: 10.1016/j.neuron.2007.05.004

Xu-Friedman, M. A., and Regehr, W. G. (2003). Ultrastructural contributions to desensitization at cerebellar mossy fiber to granule cell synapses. *J. Neurosci.* 23, 2182–2192. doi: 10.1523/JNEUROSCI.23-06-02182.2003

Yang, H., and Xu-Friedman, M. A. (2009). Impact of synaptic depression on spike timing at the endbulb of Held. *J. Neurophysiol.* 102, 1699–1710. doi: 10.1152/jn.00072.2009

Yang, H., and Xu-Friedman, M. A. (2015). Skipped-stimulus approach reveals that short-term plasticity dominates synaptic strength during ongoing activity. *J. Neurosci.* 35, 8297–8307. doi: 10.1523/JNEUROSCI.4299-14.2015

Yang, Y.-M., Aitoubah, J., Lauer, A. M., Nuriya, M., Takamiya, K., Jia, Z., et al. (2011). GluA4 is indispensable for driving fast neurotransmission across a high-fidelity central synapse: GluA4 and high-frequency auditory neurotransmission. *J. Physiol.* 589, 4209–4227. doi: 10.1113/jphysiol.2011.208066

Yao, J. D., Bremen, P., and Middlebrooks, J. C. (2015). Emergence of spatial stream segregation in the ascending auditory pathway. *J. Neurosci.* 35, 16199–16212. doi: 10.1523/JNEUROSCI.3116-15.2015

Yin, T. C., and Chan, J. C. (1990). Interaural time sensitivity in medial superior olive of cat. *J. Neurophysiol.* 64, 465–488. doi: 10.1152/jn.1990.64.2.465

Young, E. D., and Sachs, M. B. (1979). Representation of steady-state vowels in the temporal aspects of the discharge patterns of populations of auditory-nerve fibers. *J. Acoust. Soc. Am.* 66, 1381–1403. doi: 10.1121/1.383532

Young, S. M. Jr, and Veeraraghavan, P. (2021). Pre-synaptic voltage-gated calcium channels in the auditory brainstem. *Mol. Cell. Neurosci.* 112:103609. doi: 10.1016/j.mcn.2021.103609

Yu, W.-M. M., and Goodrich, L. V. (2014). Morphological and physiological development of auditory synapses. *Hear. Res.* 311, 3–16. doi: 10.1016/j.heares.2014.01.007

Zacher, A. C., and Felmy, F. (2024). Anatomy of superior olivary complex and lateral lemniscus in Etruscan shrew. *Sci. Rep.* 14:14734. doi: 10.1038/s41598-024-65451-0

Zhang, C., Wang, M., Lin, S., and Xie, R. (2022). Calretinin-expressing synapses show improved synaptic efficacy with reduced asynchronous release during high-rate activity. *J. Neurosci.* 42, 2729–2742. doi: 10.1523/JNEUROSCI.1773-21.2022

Zhang, H., and Kelly, J. B. (2006). Responses of neurons in the rat's ventral nucleus of the lateral lemniscus to monaural and binaural tone bursts. *J. Neurophysiol.* 95, 2501–2512. doi: 10.1152/jn.01215.2005

Zhao, M., and Wu, S. H. (2001). Morphology and physiology of neurons in the ventral nucleus of the lateral lemniscus in rat brain slices. *J. Comp. Neurol.* 433, 255–271. doi: 10.1002/cne.1139

Zhuang, X., Wong, N. F., Sun, W., and Xu-Friedman, M. A. (2020). Mechanisms and functional consequences of pre-synaptic homeostatic plasticity at auditory nerve synapses. *J. Neurosci.* 40, 6896–6909. doi: 10.1523/JNEUROSCI.1175-19.2020

Zook, J. M., and Casseday, J. H. (1982). Cytoarchitecture of auditory system in lower brainstem of the mustache bat, *Pteronotus parnellii*. *J. Comp. Neurol.* 207, 1–13. doi: 10.1002/cne.902070102

Zook, J. M., and Casseday, J. H. (1985). Projections from the cochlear nuclei in the mustache bat, *Pteronotus parnellii*. *J. Comp. Neurol.* 237, 307–324. doi: 10.1002/cne.902370303

Zook, J. M., and Casseday, J. H. (1987). Convergence of ascending pathways at the inferior colliculus of the mustache bat, *Pteronotus parnellii*. *J. Comp. Neurol.* 261, 347–361. doi: 10.1002/cne.902610303

frontiers | Frontiers in Cellular Neuroscience

TYPE Original Research
PUBLISHED 15 October 2025
DOI 10.3389/fncel.2025.1625868

Check for updates

OPEN ACCESS

EDITED BY
Christian Keine,
University of Oldenburg, Germany

REVIEWED BY
Enrico Castroflorio,
Laminar Pharma SL, Spain
Shigeo Takamori,
Doshisha University, Japan

*CORRESPONDENCE
Eckhard Friauf
✉ eckhard.friauf@bio.uni-kl.de

†These authors have contributed equally to this work and share first authorship

RECEIVED 09 May 2025
ACCEPTED 01 September 2025
PUBLISHED 15 October 2025

CITATION
Pizzi E, Hofmann LN, Singh A and Friauf E (2025) Robust inhibitory glycinergic transmission and the effect of bafilomycin, folimycin and EIPA: lessons from the auditory brainstem.
Front. Cell. Neurosci. 19:1625868.
doi: 10.3389/fncel.2025.1625868

COPYRIGHT
© 2025 Pizzi, Hofmann, Singh and Friauf. This is an open-access article distributed under the terms of the Creative Commons Attribution License (CC BY). The use, distribution or reproduction in other forums is permitted, provided the original author(s) and the copyright owner(s) are credited and that the original publication in this journal is cited, in accordance with accepted academic practice. No use, distribution or reproduction is permitted which does not comply with these terms.

Robust inhibitory glycinergic transmission and the effect of bafilomycin, folimycin and EIPA: lessons from the auditory brainstem

Erika Pizzi[1†], Lina N. Hofmann[1†], Abhyudai Singh[2] and Eckhard Friauf[1*]

[1]Animal Physiology Group, Department of Biology, University of Kaiserslautern-Landau, Kaiserslautern, Germany, [2]Department of Electrical and Computer Engineering, Biomedical Engineering, Mathematical Sciences, Interdisciplinary Neuroscience Program, University of Delaware, Newark, DE, United States

Sustained synaptic transmission requires the continuous replenishment of released synaptic vesicles (SVs). This process is particularly critical in neuronal circuits that operate at high rates and with high temporal precision, such as those in the auditory brainstem. Here, we investigated the effect of SV (re-)filling on inhibitory synapses between the medial nucleus of the trapezoid body (MNTB) and the lateral superior olive (LSO). These synapses transmit information with high speed and fidelity, properties essential for auditory computations such as sound localization. We specifically examined the role of the vacuolar ATPase (V-ATPase), a proton pump that acidifies the SV lumen to enable neurotransmitter loading. Using patch-clamp recordings in acute mouse slices, we assessed synaptic function under control conditions and during continuous V-ATPase inhibition with bafilomycin or folimycin. Contrary to our initial hypothesis, pharmacological inhibition caused only moderate impairment of sustained transmission. Even under high drug concentrations and intense stimulation (e.g., 100 Hz for 4 min), steady-state responses declined only to ~33% of control. Similar reductions were observed in the replenishment rate, the size of the readily releasable pool, and the cumulative eIPSC amplitude. Quantal size decreased gradually, reaching ~70% of control. Recovery from synaptic depression persisted in the presence of V-ATPase blockade, although it was less efficient. Together, these findings indicate that MNTB-LSO synapses are relatively resistant to V-ATPase inhibition, suggesting that SV replenishment does not rely solely on V-ATPase activity. Alternative acidification mechanisms may contribute, and among potential candidates, the Na^+/H^+ exchanger isoform NHE6 showed strong immunoreactivity in glycinergic MNTB axon terminals contacting LSO somata. This identifies NHE6 as a promising target for future investigation.

KEYWORDS

synaptic vesicle cycle, patch-clamp recordings, V-ATPase, Na^+/H^+ exchanger, inhibitory synapses

Introduction

Synaptic transmission, the primary means of interneuronal information transfer, is a complex process involving several pre- and postsynaptic components. On the presynaptic side, dozens to thousands of spherical synaptic vesicles (SVs) are packed into axon terminals. Only a fraction of these is morphologically docked and functionally primed, thus forming the readily releasable pool (RRP). The remaining SVs form the reserve pool and the recycling pool (Rizzoli and Betz, 2005; Alabi and Tsien, 2012; Neher, 2015).

An action potential (AP) entering an axon terminal provides the depolarization necessary to open voltage-gated Ca^{2+} channels, triggering a rapid rise in local $[Ca^{2+}]_i$. As a result, a fraction of release-competent SVs fuse with the plasma membrane and release their transmitter cargo into the synaptic cleft via regulated rapid exocytosis (Katz, 1969; Südhof, 2013; Silva et al., 2021). The outer and inner diameters of most SVs are ~40 nm and ~25 nm, respectively (Schikorski and Stevens, 1997; Neef et al., 2007); for further references see (Clements, 1996). For the intravesicular volume, values of ~10^{-5} µm^3 (10^{-20} L; Schikorski and Stevens, 1997), ~40 zL ($4*10^{-20}$ L; Clarkson et al., 2016) and ~$2*10^{-20}$ L (Takamori et al., 2006) have been reported. At excitatory axon terminals, the intravesicular glutamate concentrations are 60–100 mM (Burger et al., 1989; Bruns and Jahn, 1995), corresponding to 3,000–6,000 transmitter molecules per SV (Danbolt, 2001; Freche et al., 2011). Inhibitory synapses have been much less studied than their excitatory counterparts.

Both the *de novo* filling of SVs and the reloading of recycled SVs with transmitter molecules are achieved by a cascade of active transport processes. The acidification of the SV lumen is generated by a multi-subunit, primary active vacuolar (H^+)-ATPase (H^+ pump) in the SV membrane (V-ATPase; Figure 1A). This V-ATPase couples the hydrolysis of ATP with the transport of H^+ into the vesicle lumen. Results from the *Torpedo marmorata* electric organ and glutamatergic neurons show that V-ATPase activity generates a pH value in the SV lumen that is 1.4–1.7 units more acidic than the pH of ~7.2 in the cytosol (Harlos et al., 1984; Chaudhry et al., 2008; Ruffin et al., 2014). Scant evidence from GABAergic SVs suggests a less acidic luminal pH of ~6.4 (Egashira et al., 2016). The electrochemical H^+ gradient generated by the V-ATPase is used by secondary-active neurotransmitter transporters to drive the transport of transmitter molecules from the cytosol into the SV lumen via an exchange mechanism (Edwards, 2007; Anne and Gasnier, 2014). While the cytosolic transmitter concentration is ~10 mM, the luminal concentration is ~10-fold higher.

In the case of GABA and glycine, the two major inhibitory transmitters in the CNS, the secondary-active transporter is VIAAT (vesicular inhibitory amino acid transporter, also known as vesicular GABA transporter VGAT) (McIntire et al., 1997; Sagné et al., 1997; Wojcik et al., 2006; Zafra and Giménez, 2008; Figure 1A). Glycine, the transmitter at fast inhibitory synapses, is primarily supplied to VIAAT by the glycine transporter GlyT2 via reuptake of released glycine from the extracellular space (Aubrey et al., 2007; Rousseau et al., 2008; Apostolides and Trussell, 2013; Brill et al., 2021). Endogenous glycine concentrations in presynaptic boutons were reported at 20–40 mM or at ~5 mM (Supplisson and Roux, 2002; Apostolides and Trussell, 2013). Together, the reliable and sustained cooperativity of multiple transporters is required to ensure proper SV (re-)filling and to dynamically regulate inhibitory synaptic strength.

In the auditory system, especially in the brainstem nuclei, synaptic transmission occurs with remarkable robustness, even during sustained high-frequency stimulation at 100 Hz and above (Lujan and von Gersdorff, 2017). A microcircuit and an established model system for the analysis of inhibitory synapses is formed by glycinergic neurons in the medial nucleus of the trapezoid body and postsynaptic neurons in the lateral superior olive (MNTB and LSO; Brill et al., 2019; Figure 1B). The high resilience, reliability and temporal precision of the MNTB-LSO connection is achieved through a high quantal content (*m*, number of SVs released by an AP) and effective replenishment mechanisms (Krächan et al., 2017). During sustained 100-Hz trains, 6,000 release events can occur within 60 s, involving the exocytosis of ~24,000 SVs from the axon terminals of a single MNTB neuron terminating on an LSO neuron (minimal stimulation; young adult mice; Müller et al., 2022). At the end of the 60-s challenge period (s_{50-60}), when synaptic depression is maximal, steady-state release is still ~350 SVs/s. One must hypothesize that the synaptic indefatigability requires efficient replenishment, as all SVs, including those from the reserve pool, are used in this severe challenge conditions (Rizzoli, 2014). At steady state, SV fusion and SV replenishment are in equilibrium.

To assess the efficacy of SV replenishment and the underlying molecular mechanisms at a high-fidelity inhibitory synapse, we here performed electrophysiological experiments in mouse brain slices and generated presynaptic AP trains at the MNTB-LSO inputs to deplete the RRP and to assess sustained neurotransmission. Long-lasting and high-frequency stimulation was used (up to 4 min and 200 Hz; Figure 1C). We pharmacologically interfered with SV transmitter loading by adding the plecomacrolide antibiotic bafilomycin (Bafi), a high-affinity inhibitor of V-ATPase-mediated H^+ transport (Bowman et al., 1988; Dröse and Altendorf, 1997; Zhou et al., 2000; Forgac, 2007). Bafi blocks the reacidification of newly endocytosed SVs. In complementary experiments, we used folimycin (Foli; Muroi et al., 1993; Sara et al., 2005; Groemer and Klingauf, 2007). Unexpectedly, the pharmacological treatments had only moderate effects on SV replenishment and did not abolish synaptic transmission, despite the high drug concentrations and very intense stimulation conditions used. The resistance to pharmacological treatment suggests effective SV (re-)filling mechanisms at MNTB-LSO synapses that are not solely dependent on V-ATPase activity. Rather, another mechanism appears to coexist that provides an H^+ source for VIAAT and thus helps to generate SVs with a sufficiently high glycine content. In the Discussion section, we provide some thoughts on the nature of this source.

Materials and methods

Animals and ethical approval

Animal breeding and experiments were approved by the regional councils of Rhineland-Palatinate according to the German Animal Welfare Act (TSchG §4/3) and followed the guidelines for the protection and welfare of laboratory animals. C57BL/6 J mice were bred in the animal facilities of the University of Kaiserslautern-Landau, and both sexes were analyzed at postnatal days (P) 11 ± 1.

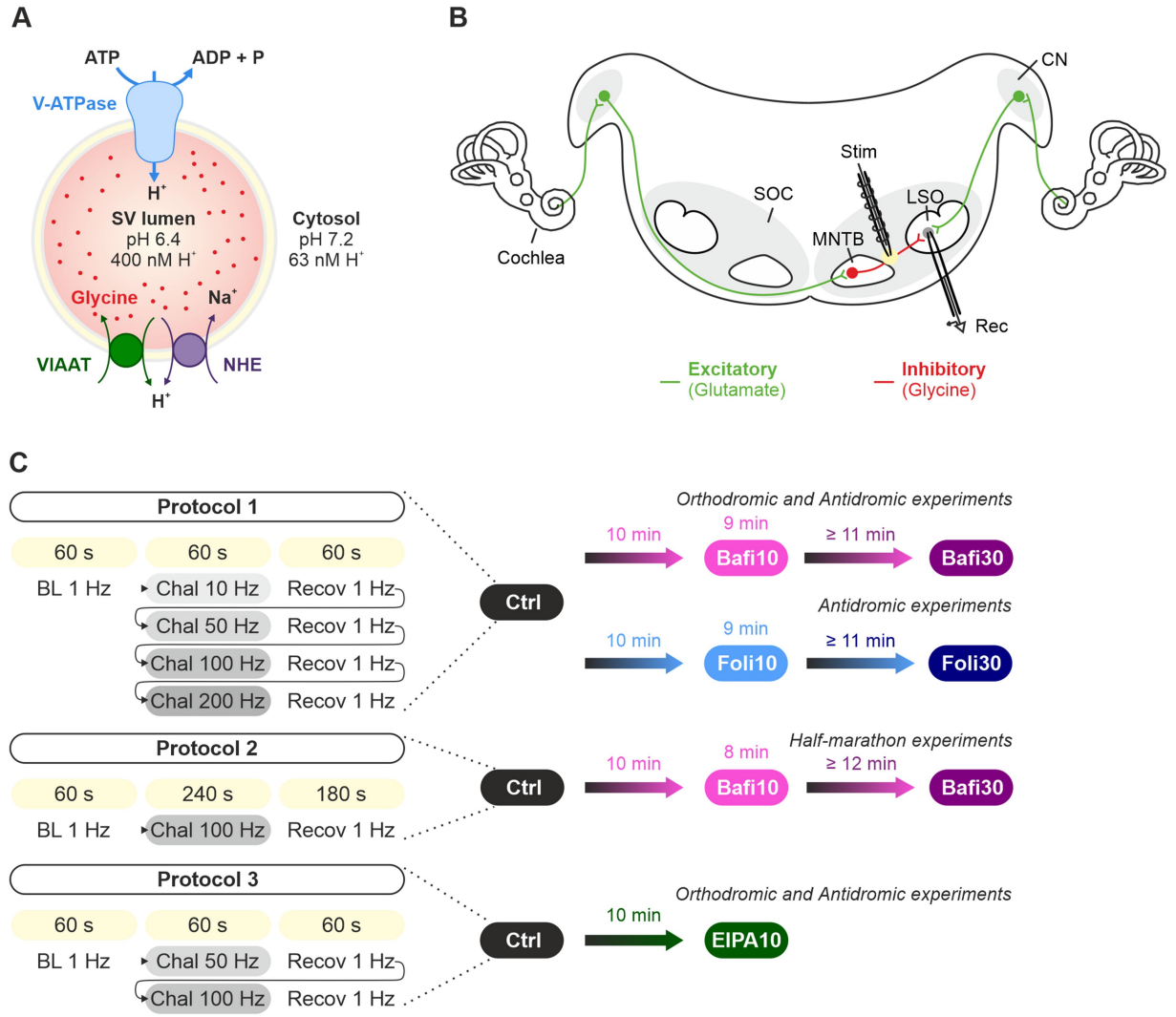


FIGURE 1
Analysis of synaptic transmission at glycinergic MNTB-LSO inputs under control conditions and upon pharmacological treatment with the V-ATPase blockers Bafi and Foli and the NHE blocker EIPA. **(A)** Schematic of the vacuolar transporters involved in proton pumping and thus in VIAAT-mediated filling of SVs with the inhibitory neurotransmitter glycine. **(B)** Schematic of the MNTB-LSO circuit in a mouse coronal brainstem slice. **(C)** Schematic of the three stimulation protocols used. All protocols started with a 1-Hz|60-s stimulation period to establish a baseline (BL, average peak amplitude = 100%). Protocol 1 included four challenge periods at 10, 50, 100 and 200 Hz, each followed by a recovery period at 1 Hz. Protocol 1 was used to assess the effect of Bafi (2 μM), Foli (1 μM) and EtOH (0.1%; sham control experiments, Supplementary Figures S1–S4). Protocol 2 (half-marathon experiments) consisted of a 100-Hz challenge period lasting 240 s which was followed by a 180-s recovery period; it was used to evaluate Bafi effects at a concentration of 5 μM. Protocol 3 consisted of two challenge periods (50 and 100 Hz) and two recovery periods; it was used to evaluate the effects of the NHE inhibitor EIPA (100 μM) on synaptic transmission and on AP fidelity in antidromic stimulation experiments. A 6-s long pause was introduced after the BL and each 60-s recovery.

Electrophysiology

Coronal brainstem slices containing the MNTB and the LSO were prepared in accordance with the methodology previously described by Hirtz et al. (2012). Slices were stored at room temperature (RT) in carbonated artificial cerebrospinal fluid (ACSF), which consisted of the following components (in mM): 125 NaCl, 2.5 KCl, 1.25 NaH_2PO_4, 2 sodium pyruvate, 3 myo–inositol, 0.44 L (+) ascorbic acid, 25 $NaHCO_3$, 10 glucose, 1 $MgCl_2$, 2 $CaCl_2$. The solution had an osmolality of 290 ± 10 mOsm/L and was bubbled with carbogen to achieve a pH of 7.4. Individual slices were transferred into the recording chamber on an upright microscope (Nikon Eclipse E60FN, Minato, Japan) equipped with infrared-differential interference contrast optics (Nikon 4x CFI Achromat, 0.1 ∞; 60x CFI Fluor W, 1.00 W ∞; Zeiss Fluar CFI 5x/0.25 ∞/0.17; Olympus LUMPlanFL N 60x/1.00 W ∞/0/FN26.5) and an Orca-05G camera (Hamamatsu, Hamamatsu City, Japan). Whole-cell recordings were performed at 35 ± 1°C (Slice Mini Chamber I equipped with temperature controller TC07, Luigs & Neumann, Ratingen, Germany). LSO principal neurons were identified by their fusiform somata, and this identification was subsequently confirmed through an examination of their electrophysiological properties (Sterenborg et al., 2010). Patch pipettes and stimulation pipettes (GB150F-8P with filament, Science Products, Hofheim am Taunus, Germany) were constructed with a P-1000

horizontal puller (Sutter Instruments, Novato, CA, United States). The input resistance of the patch pipettes ranged from 2.5 to 4.5 MΩ when filled with an internal solution containing the following components (in mM): 140 K-gluconate, 10 HEPES, 5 EGTA, 1 MgCl, 2 $CaCl_2$, 2 Na_2ATP, 0.3 Na_2GTP. The pH was 7.3 and the osmolality was 280 ± 10 mOsm/L. The recordings were conducted using an EPC10 amplifier and controlled with PatchMaster software (HEKA, Lambrecht/Pfalz, Germany). Recordings were sampled at 20 kHz and low-pass filtered at 2.9 kHz. The liquid junction potential (15.4 mV) was corrected online. Series resistance amounted up to 20 MΩ and compensated between 40 and 60%. If the input resistance changed by >30%, the recording was discarded. Stimulation pipettes (tip diameter ~10 µm), filled with ACSF and connected to a stimulus isolator (STG4002; MultiChannel Systems; Reutlingen; Germany), were placed either at the lateral edge of the MNTB (orthodromic stimulation) or at the medial edge of the LSO (antidromic stimulation). In both cases, 100-µs long electrical current pulses were applied to evoke inhibitory postsynaptic currents (eIPSCs) or APs, respectively. At a holding potential of −70 mV, eIPSCs were outward currents. Stimulus amplitudes were adjusted to values which yielded stable maximal eIPSCs during low-frequency stimulation (0.5 Hz to avoid synaptic depression). For APs, once the rheobase was reached, the stimulus amplitude was doubled. We employed three different stimulation protocols (Figure 1): Protocol 1 started with a 1-Hz|60-s stimulation period to establish a baseline value (BL, average eIPSC peak amplitude = 100%). Thereafter, MNTB-LSO synapses were electrically stimulated for 60-s at various frequencies in ascending order (Challenge period: Chal 1-4; 10, 50, 100, 200-Hz). Each challenge period was immediately followed by a 60-s period at 1-Hz (Recovery period: Recov1-4). A total of 21,900 stimuli were applied. A 6-s pause was introduced for data storing after BL and between the last stimulus of the recovery period and the 1st stimulus of the subsequent challenge period. Protocol 2 started with a 1-Hz|60-s BL, followed by a 4-min | 100-Hz stimulation (Chal 1-4). The challenge period was followed by a 180-s period at 1-Hz (Recov1-3). A total of 24,240 stimuli were applied. A 6-s pause was introduced for data storing after BL and between the last stimulus of the recovery period and the 1st stimulus of the subsequent challenge period. Protocol 3 consisted of a 1-Hz|60-s period to assess the BL, followed by 60-s challenging periods at 50-Hz and 100-Hz stimulation (Chal1-2). Each challenge period was followed by a 60-s period at 1-Hz to assess recovery from depression (Recov1-2). Thus, a total of 9,180 stimuli were applied. A 6-s pause was introduced for data storing after the BL period and between the last stimulus pulse of Recov1 and the 1st stimulus pulse of Chal2.

Immunohistochemistry

Lethally anesthetized mice (10% ketamine, 220 µg/g body weight plus 2% xylazine, 24 µg/g body weight, intraperitoneal) were transcardially perfused with 100 mM phosphate-buffered saline (PBS, pH 7.4) at RT, followed by ice-cold 4% paraformaldehyde (PFA) for 20 min (Ecoline VC-360 pump, IsmaTec, Chicago, United States). Brains were removed from the skull, postfixed for 1 h in 4% PFA (4°C) and stored in 30% sucrose-PBS at 6°C overnight. 30-µm-thick coronal brainstem slices were cut with a sliding microtome (HM 400 R, MICROM) and transferred to 15% sucrose-PBS, followed by three rinses in PBS (30 min, RT). For NHE6, a heat-induced epitope retrieval protocol was used prior to antibody treatment. For this, slices were immersed in 10 mM sodium citrate buffer (pH 6.0) plus 0.05% Tween 20 (Roth, Karlsruhe, Germany) and heated at 95°C for 20–40 min. They were then returned to RT, followed by three rinses in PBS (5 min, RT). Slides were applied free-floating at 4°C for 1 in blocking solution (0.3% Triton-X-100, 10% goat serum, 2% bovine serum albumin (BSA) in PBS). Antibodies against GlyT2 (1:200, host: mouse, Synaptic Systems, Göttingen, Germany) and NHE6 (1:200, host: rabbit, Sigma Aldrich, St. Louis, United States) were applied free-floating at 4°C overnight in carrier solution (0.3% Triton-X-100, 1% goat serum, 1% BSA in PBS), followed by three rinses in PBS (30 min, RT). Slices were then incubated in the dark for 2 h in carrier solution and secondary antibody (1,1,000; goat-anti-mouse, Alexa Fluor 488; goat-anti-rabbit, Alexa Fluor 647, Thermo Fisher Scientific, Waltham, United States), followed by three rinses in PBS (30 min, RT). Slices were mounted on gelatin-coated glass slides and covered with mounting medium containing 2.5% DABCO (1,4-diazabicyclo[2.2.2] octane; Sigma-Aldrich, St. Louis, MO, United States). Images were acquired with a TCS SP5 X confocal microscope equipped with an HCX PL APO 63 × oil objective (Leica Microsystems, Wetzlar, Germany). For quantitative analysis, intensity profiles at inhibitory synapses were analyzed using Fiji ImageJ 1.54 as described previously (Fischer et al., 2019). Line scans were drawn from the center of the soma across membrane-associated GlyT2 signals. Eight intensity profiles were obtained per cell. In total, two P11 animals, 16 cells and 128 intensity profiles were determined. The position of maximum GlyT2 signal was set to zero, with negative and positive scan positions representing intracellular and extracellular locations, respectively. A rolling ball background subtraction (radius 20) was applied to images in Fiji ImageJ 1.54 (Schindelin et al., 2012), followed by brightness adjustment. To assess colocalization of the immunosignals, Fiji's Coloc2 plugin was used to determine the Pearson correlation coefficient and the Costes' test (P_{Costes}), a measure of reliability (Costes et al., 2004). $P_{Costes} = 1$ indicates >95% certainty that colocalization exists.

Pharmacology

Application of bafilomycin or folimycin to inhibit V-ATPase

Bafilomycin A1 (Bafi; Abcam, Cambridge, United Kingdom or Thermo Fisher Scientific, Waltham, United States) was dissolved in ethanol (EtOH) to reach a stock concentration of 2 mM. Folimycin (Foli; a.k.a. concanamycin A) was dissolved in dimethyl sulfoxide (DMSO) to a stock concentration of 2 mM (Abcam, Cambridge, United Kingdom). Notably, the IC_{50} of Bafi and the K_i of Foli are in the (sub-)nanomolar range. The stock solutions were stored at −20°C. On the day of the experiment, the stock solutions were diluted in ACSF such that the final concentration was 2 or 5 µM for Bafi and 1 µM for Foli. The pharmacological analysis began after a 10-min wash-in period (referred to as Bafi10 and Foli10). A third recording session was conducted after waiting at least 11 and up to 41 min (referred to as Bafi30 or Foli30). To maximize their effects, the drugs were continuously perfused during the recording sessions. This strategy differed drastically from the 3-min Bafi exposure period used in a

study on glutamatergic calyx of Held synapses (Hori and Takahashi, 2012). It also differed considerably from the <2-min application via a picospritzer used in a study on isolated and cultured hippocampal neurons that had formed autapses (Ikeda and Bekkers, 2009).

Application of EIPA to inhibit Na^+/H^+ exchangers (NHEs)

The amiloride derivative EIPA was dissolved in DMSO at 100 mM and stored at −20°C (ethylisopropylamiloride; Tocris, Bristol, United Kingdom). Because EIPA is hydrophobic, it permeates cells. EIPA reportedly blocks NHEs, the electroneutral Na^+/H^+ exchangers (Alexander et al., 2011; Li et al., 2020). On the day of the experiment, EIPA was diluted in ACSF to a final concentration of 100 µM (same concentration as in Goh et al., 2011; Huang and Trussell, 2014; Li et al., 2020) and bath-applied for 10 min before recording commenced (referred to as EIPA10).

Data analysis

Foot-to-peak eIPSC amplitudes were analyzed with a custom-written plugin (Dr. Alexander Fischer, University of Kaiserslautern-Landau) implemented in IGOR Pro 6.37 or 9.01 (WaveMetrics Inc., Lake Oswego, OR, United States). Negative eIPSC amplitudes were set to zero. Data were then normalized to BL (mean eIPSC peak amplitude = 100%; Galarreta and Hestrin, 1998).

Recovery behavior was calculated by three means: (a) RecovA: last 10 eIPSCs recovery vs. BL (= 100%); (b) RecovB: last 10 eIPSC recovery vs. last 10 eIPSC of previous challenge; (c) Fractional recovery (FR):

$$FR = \frac{last\ 10\ eIPSC\ recovery - last\ 10\ eIPSC\ challenge}{baseline\ (=100\%) - last\ 10\ eIPSC\ challenge}$$

sIPSCs were analyzed during 1-Hz|60-s stimulus periods (BL and recovery periods) and manually detected using Clampfit 10.2.0.14 (Molecular Devices, CA, United States). Histograms of the sIPSCs peak amplitudes were generated and fitted with Gaussian curves. The quantal size (q) was determined by a Gaussian fit from 0 pA to the bin after the first local maximum (see Krächan et al., 2017; bin width 5 pA, in some cases 3 pA). The cumulative current evoked through complete release of the *RRP* (I_{RRP}) was assessed by forward extrapolation of a linear fit through $eIPSC_{1\text{-}5}$ obtained at 100 Hz (Elmqvist and Quastel, 1965). The number of SVs in the *RRP* (N_{RRP}) was determined as the ratio I_{RRP}/q. The quantal content (m) was obtained as $eIPSC_1/q_{Recov2}$. The release probability (Pv) was calculated as $I_{RRP}/eIPSC_1$. The transfer rate (TR) was evaluated as described (Müller et al.). Briefly, TR was assessed from the slope of a line fit through the last 10 s ($s_{50\text{-}60}$) of the cumulative eIPSC curve in a challenge period.

Statistics

Statistical analysis was performed with GraphPad Prism 9 (GraphPad Software). Data are presented as mean ± SEM. For distribution analysis, the Kolmógorov–Smirnov test was used. Normally distributed data were compared using paired or unpaired two-tailed t-tests. If the distribution was not normal, the Wilcoxon rank-sum test or the Mann–Whitney U test was used. Details on the specific tests used are provided in the Supplementary Tables S1–S12. The *post hoc* tests were corrected using Bonferroni's adjustments where applicable ($\alpha_{adjusted} = \alpha/k$, where α is the significance level and k the number of comparisons). Since k was maximally 2, the adjusted significance levels are as follows:

α	$\alpha_{adjusted}$	Notation p-value < α or $\alpha_{adjusted}$
0.05	0.025	*
0.01	0.005	**
0.001	0.0005	***

Results

The stimulus regime for the first series of experiments (named "Protocol 1") consisted of an initial 60-s|1-Hz period to assess the baseline level (BL) of eIPSC peak amplitudes, followed by four 60-s challenge interposed by 60-s recovery periods. Challenge frequencies were offered in ascending order (10, 50, 100, 200 Hz; Figure 1C). In total, Protocol 1 lasted 9 min and included 21,900 stimulus pulses. In a first round, the synaptic behavior was assessed in ASCF (Ctrl). Then the V-ATPase inhibitor Bafi (2 µM) was bath-applied for 10 min before a second round was performed on the same neuron (Bafi10). Finally, another neuron was patch clamped in the same slice and analyzed in a third round (≥ 30 min drug treatment named "Bafi30").

The synaptic performance of an example neuron in the Ctrl situation is illustrated in Figure 2A1. The synaptic depression, the sustained performance, and the recovery behavior are evident, and the results are consistent with previous findings (e.g., Kramer et al., 2014; Krächan et al., 2017). The mean BL eIPSC peak amplitude was calculated to be 951 pA, and BL $eIPSC_1$ was 1,189 pA, thus showing an overshoot of 25%. We have previously referred to such an overshooting *in vitro* behavior as "manic." It occurs after "long" rest intervals of several seconds (Friauf et al., 2015). During the 10-Hz challenge, the peak amplitudes decreased to 629 pA. During the subsequent recovery period, they quickly and reliably returned to BL (942 pA or 99%). As expected, synaptic depression was greater during the 50-Hz challenge, reaching a final level of 178 pA. Recovery was again rapid and robust, even exceeding BL (1,199 pA = 126%). During the 100-Hz challenge, amplitudes dropped massively to 63 pA. Again, recovery was robust, with the mean amplitude of the last 10 s ($s_{50\text{-}60}$) reaching 1,023 pA (108% of BL). The final 200-Hz challenge resulted in virtually complete abolition of transmission (13 pA), but recovery returned values to 1,080 pA (114% of BL).

During the subsequent 10-min wash-in of Bafi, a new BL of 865 pA was achieved (Figure 2A2). This value was 9% lower than the Ctrl value. A decrease in steady-state amplitudes ($s_{50\text{-}60}$) was evident during 10-Hz and 50-Hz challenge (550 and 229 pA, respectively). At 100-Hz, there was a plateau after the initial rapid decline, as in Ctrl, and

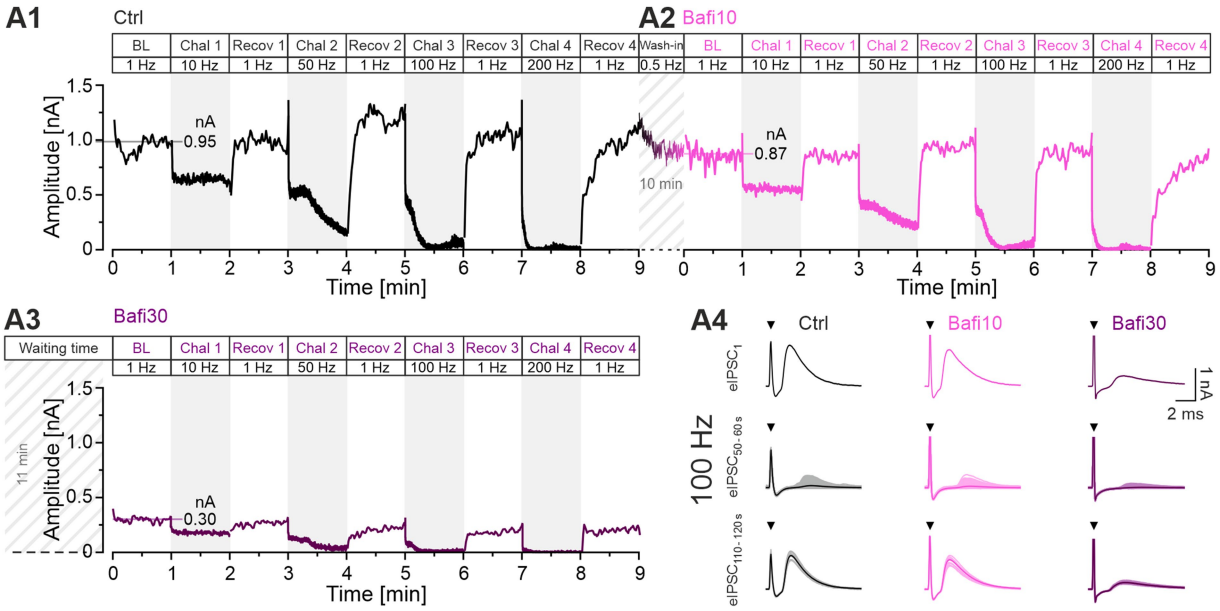


FIGURE 2
MNTB-LSO inputs function reliably during sustained high-frequency stimulation and recover robustly and precisely from synaptic depression. Inhibition of V-ATPase activity with 2 μM Bafi does not completely abolish information transfer. **(A1)** Time course of absolute peak eIPSC amplitudes obtained with Protocol 1 from a P11 LSO neuron under Ctrl conditions (black, ACSF): BL (0–1 min; dotted horizontal line indicates mean peak amplitude), four periods of 60-s challenge (Chal; gray regions) and 1 Hz|60-s recovery (Recov; white regions; 1–9 min), four challenge frequencies in ascending order (10, 50, 100, 200 Hz, see Figure 1C) **(A2,A3)**. Same as **(A1)**, but for Bafi10 (2 μM, 10-min wash-in, magenta) **(A2)** and Bafi30 (2 μM, ≥ 30-min treatment, purple) **(A3)**. A 6-s pause was introduced after the BL and each 60-s recovery period. Diagonally striped regions indicate perfusion periods of 2 μM Bafi (time indicated in the figure; after perfusion, the drug was maintained in the bath throughout the entire recording period). Time courses are simple moving averages over three (1 Hz) or nine (10–200 Hz) data points to smooth out short-term fluctuations and highlight longer-term trends. Data in **(A1,A2)** are from the same neuron, whereas **(A3)** is from a different neuron. The number of stimulus pulses in each panel is 21,900. **(A4)** Representative eIPSCs for the three cohorts during Chal 3 and Recov 3, showing $eIPSC_1$ and the overlay of individual eIPSCs and graphical means for $eIPSC_{s50\text{-}60}$ and $eIPSC_{s110\text{-}120}$ (lightly and darkly shaded). Arrows indicate stimulation artifacts. Note transmission failures in the 100-Hz traces for eIPSCs during $s_{50\text{-}60}$ (for AP fidelity aspects, see Figures 10, 11; Müller et al., 2022).

amplitudes were 49 pA during $s_{50\text{-}60}$. The final 200-Hz challenge resulted in a massive depression to 12 pA, again implying virtually completely abolished transmission. As in the Ctrl scenario, amplitudes returned very close to BL levels during recovery periods (10 Hz: 867 pA = 100%; 50 Hz: 977 pA = 113%, 100 Hz: 899 pA = 104%; 200 Hz: 827 pA = 96%).

The ability to recover from depression after the severe challenge during Protocol 1 suggests that the 10-min|2-μM Bafi treatment may have been insufficient to strongly inhibit transmission at MNTB-LSO synapses. To address this issue, we assessed the synaptic performance in a second neuron after Bafi was washed in for ≥ 30 min to increase the chance of efficient V-ATPase inhibition. The example neuron showed drastically smaller eIPSCs than the Ctrl/Bafi10 neuron (Figure 2A3). For example, the BL was 300 pA, only 32% of the Ctrl. This implies a smaller RRP and/or a lower q, most likely due to efficient V-ATPase inhibition. $s_{50\text{-}60}$ depression levels during the four challenge periods were 175, 37, 13 and 3 pA, respectively. Although these values indicate a complete collapse of synaptic transmission at the two highest frequencies, especially at 200 Hz, Bafi30 synapses managed to recover partially in each case (Figure 2A4 shows individual eIPSCs at 100 Hz). Recovery after the 100-Hz and 200-Hz challenge reached 206 and 221 pA, respectively, (69 and 74% of the 300 pA BL). These single-cell results provide some preliminary evidence that V-ATPase inhibition was incomplete or that there may be another source of H^+ ions fueling VIAAT.

Cohort data confirm that sustained transmission is not affected upon 10-min wash-in of bafilomycin (Bafi10), yet it is reduced after 30-min treatment (Bafi30)

To corroborate the anecdotal evidence derived from the two example neurons shown in Figure 2, we proceeded to examine the cohort behavior (n = 11, 11, 9; Figure 3). The BL values were found to be similar between the Ctrl and Bafi10 cohort (mean: 1,023 vs. 914 pA or 100:89; Figures 3A1,A2,A4,A5). In contrast, Bafi30 values were significantly reduced, reaching only 35% of the Ctrl (354 pA; Figure 3A3). Furthermore, the time courses of depression and subsequent recovery to the four challenge frequencies were in accordance with those observed for the example neurons (Figures 3A1–A3; compare with Figure 2).

Subsequently, statistical analyses were conducted across the four 60-s challenge periods ($eIPSC_1$, $s_{0.9\text{-}1}$, $s_{9\text{-}10}$, $s_{50\text{-}60}$; Figures 3B2–E5; Supplementary Table S1). Only one of the 17 Ctrl_vs_Bafi10 comparisons yielded a statistically distinguishable result (Figures 3A4,B2–B4,C2–C4,D2–D4,E2–E4). In contrast, Bafi30 amplitudes were observed to be significantly lower than those of the Ctrl in 15 out of the 17 comparisons. For example, at $s_{50\text{-}60}$ of the 50-Hz challenge, Ctrl amplitudes were ~3-fold higher than Bafi30 amplitudes (267 vs. 88 pA, Figures 3C1,C5). With the harshest 200-Hz challenge, peak amplitudes declined markedly in each of the three cohorts

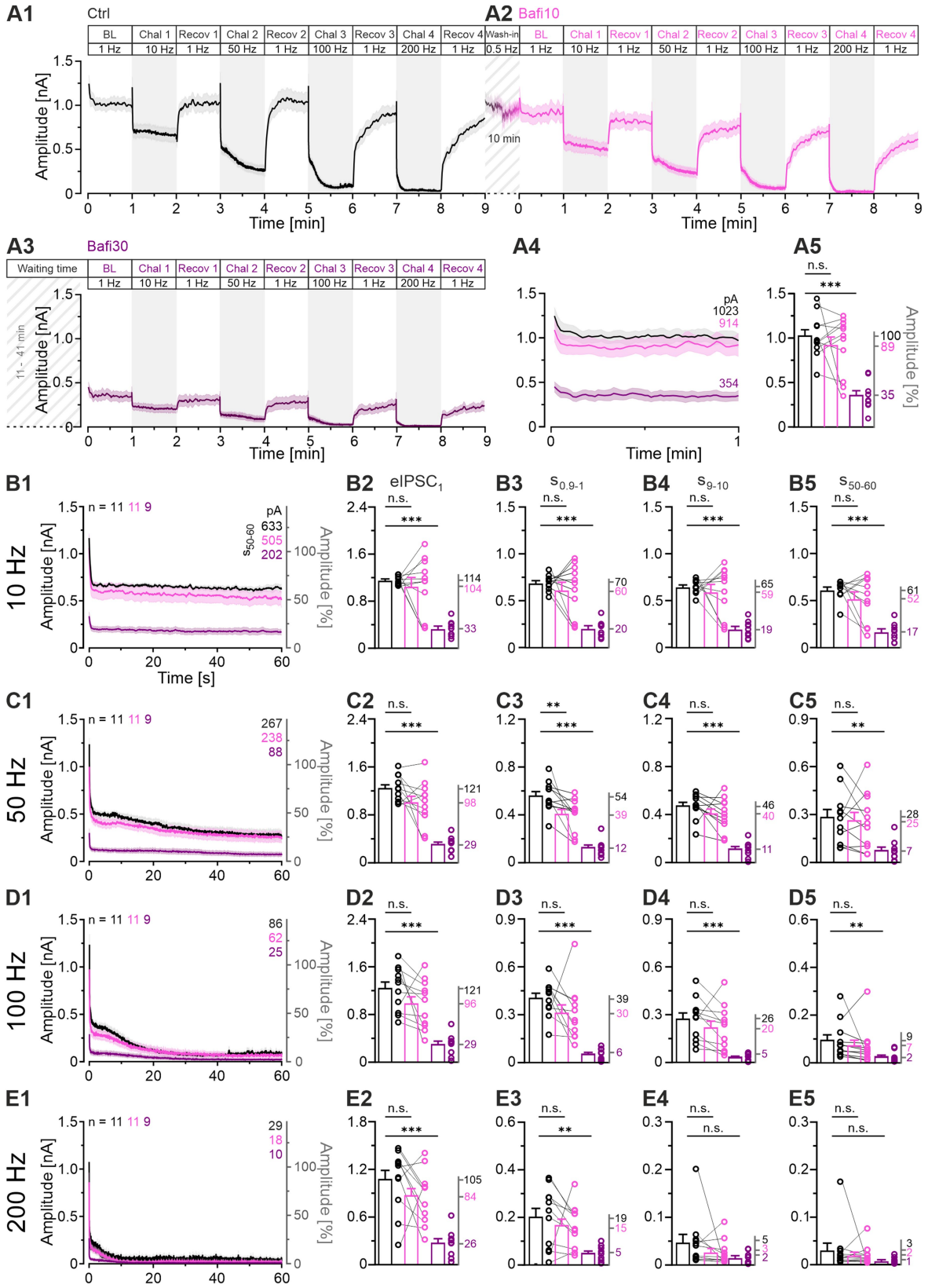


FIGURE 3
Ongoing synaptic transmission is not affected by 10-min wash-in of 2 μM Bafi (Bafi10) at MNTB-LSO inputs. In contrast, treatment for ≥30 min (Bafi30) leads to reduced amplitudes. **(A1,A2)** Time course of eIPSC mean ± SEM peak amplitudes for Ctrl (black) and Bafi10 (magenta) obtained from paired recordings with Protocol 1 (see Figure 1C). **(A3)** Time course for Bafi30 (purple). Data in **(A3)** are from a different neuron than in **(A1,A2)**. The BL mean

(Continued)

FIGURE 3 (Continued)
of the Ctrl was set to 100%. Diagonally striped regions indicate perfusion periods of 2 μM Bafi. A 6-s pause was introduced after the BL and each 60-s recovery period. **(A4)** Close-up of the BL traces. Mean values are shown on the right. **(A5)** Statistics for BL analysis (mean: Ctrl: 1,023 pA = 100%, Bafi10: 914 pA = 89%; Bafi30: 354 pA = 35%). **(B1)** Time course of absolute and normalized eIPSC peak amplitudes during 10-Hz|60-s challenge. Upper right numbers indicate the mean amplitudes during $s_{50\text{-}60}$. **(B2–B5)** Statistics at four time points ($eIPSC_1$, $s_{0.9\text{-}1}$, $s_{9\text{-}10}$, $s_{50\text{-}60}$). Mean percentages are shown on the right y-axis. **(C–E)** Same as B, but for 50 Hz **(C1–C5)**, 100 Hz **(D1–D5)** and 200 Hz **(E1–E5)**. Note the different amplitude scaling in **(B2–E5)**; the variables on the left and right y-axes are the same as in **(B1)**. Time courses are simple moving averages over three (1 Hz) or nine (10–200 Hz) data points, with SEM lightly shaded. Ctrl and Bafi10, n = 11; Bafi30, n = 9. See Supplementary Table S1 for details, including statistics.

(Figures 3E1–E5). By $s_{50\text{-}60}$, they were down to 29, 18 and 10 pA (equivalent to 2.8, 1.8 and 1.0%; Figure 3E5), indicating a near-complete depletion of transmitter release, particularly in the presence of the drug. This may explain the lack of statistical significance shown in panels E4 and E5. To further assess the near-complete collapse of synaptic transmission during the 200-Hz challenge in the two Bafi cohorts, the latest time at which the response amplitude reached ≥ 100 pA/pulse was determined. The values were 4.45, 3.58 and 0.05 s for Ctrl, Bafi10 and Bafi30, respectively (Figure 3E1). This further highlights the drastic difference observed in the Ctrl_vs_Bafi30 comparison, but not for Ctrl_vs_Bafi10 (numbers refer to 890, 716 and 10 stimulus events, respectively). To evaluate the resilience of the synapses, it is noteworthy that each cohort could maintain synaptic transmission for a considerably longer duration during the 100-Hz challenge. The last response exceeding 100 pA was observed at 59.27, 23.78 and 5.75 s for the Ctrl, Bafi10 and Bafi30 cohort, respectively (Figures 3D1–D5).

The sample results confirm that treating the brainstem slices with 2 μM Bafi for 10 min is insufficient to substantially reduce transmission at MNTB-LSO synapses. The postulated drug effect becomes evident only after a longer application time of ≥ 30 min. As a caveat it is also necessary to consider the possibility of a more severe stimulation history and/or rundown effects after this time. The issue is addressed below (see Supplementary Figures S1, S2A1–A3). In any case, the results obtained with Protocol 1 demonstrate that synaptic transmission persists for thousands of stimulus pulses, even in the Bafi30 scenario. It can thus be argued that the pharmacological blockade of V-ATPase, as conducted here, results in an incomplete cessation of SV (re)filling, thus leading to only partial synaptic fatigue. As demonstrated in the section "Recovery from depression is reduced but not abolished by Bafi treatment," the resilience of the MNTB-LSO synapses is also evidenced by their ability to recover from depression, even in the presence of Bafi.

Sustained neurotransmission capacity is reduced by bafilomycin but persists

The above analysis included only some aspects of the synaptic performance, namely windows with a total duration of 11.1 s. To assess the transmission capacity during the entire 60 s for each challenge period, we determined the cumulative eIPSC amplitude (Müller et al., 2022). Each cohort showed the highest value at 50 Hz, indicating that this is the "best transmission frequency" (Figures 4A1,B1,C1,D1,E1,E3). Ctrl synapses generated a cumulative amplitude of 1,077 nA at this frequency, whereas Bafi10 and Bafi30 values were 899 and 343 nA, respectively (83 and 32% of Ctrl; Figures 4B1,B2). No statistically significant difference occurred in any of the four Ctrl_vs_Bafi10 comparisons, whereas significance was evident in each Ctrl_vs_Bafi30 comparison (Figures 4A2,B2,C2,D2; Supplementary Table S2). Notably, synapses treated with Bafi30 performed at ~1/3 of the Ctrl level at each challenge frequency.

To quantify neurotransmission during the steady-state phase of the challenge periods, and thus the continuous replenishment rate, we analyzed the transmission rate during the last 10 s of the challenge period ($TR_{50\text{-}60}$, [nA/s]). The results confirmed those obtained for the entire 60-s periods, namely a statistically significant difference for Ctrl_vs_Bafi30 at each frequency, but no difference for Ctrl_vs_Bafi10 (Figures 4A3,B3,C3,D3). For example, the Ctrl had a mean $TR_{50\text{-}60}$ of 17.3 nA/s at 50-Hz challenge, compared to Bafi10 and Bafi30 values of 14.6 and 5.7 nA/s, respectively (ratios: 100:84:33; Figure 4B3). Very similar ratios were obtained at the three other challenging frequencies (10 Hz: 100:82:32; 100 Hz: 100:88:34; 200 Hz: 100:60:32).

We also analyzed the overall transmission by determining the cumulative eIPSC amplitude over all four challenge periods, thereby assessing the response strength to 21,600 pulses. On average, the Ctrl cohort was able to elicit 2,842 nA (on average 132 pA/event), whereas the Bafi10 and Bafi30 values were reduced to 79 and 33%, respectively (2,256 and 927 nA; Figure 4E2). Again, the difference was statistically significant for Ctrl_vs_Bafi30, but not for Ctrl_vs_Bafi10.

Taken together, the results obtained from the analysis of overall transmission further support our conclusion that synaptic transmission at MNTB-LSO synapses is substantially reduced only after prolonged Bafi application (≥ 30 min).

Normalized data show similar performance across cohorts

Since the Bafi30 BL was ~3-fold lower than the Ctrl BL (354 vs. 1,023 pA; Figures 3A4,A5), we wondered whether this initial difference alone, present before the first challenge period, could explain the transmission differences described so far. To address this question, we set the BL of each neuron to 100% (BL = 1), allowing us to assess its relative performance. For the 10-Hz challenge, the mean final cumulative value was 381 for the Ctrl, very close to the Bafi10 and Bafi30 values of 348 and 344, respectively (Figure 4E3). Thus, the relative performance was remarkably similar between cohorts (100: 91: 90). Values for the 50-Hz challenge were 1,079, 1,009 and 854 BL (100: 94: 79), and confirming results were obtained at 100 Hz (847, 783 and 659 BL; 100: 92: 78) and 200 Hz (575, 419 and 449 BL; 100: 73: 78). None of the eight comparisons reached statistical significance (Figure 4E3). Finally, the normalized current integrals across 4-min challenging also showed statistically indistinguishable performances (Figure 4E4). Together, these results imply a weaker transmission strength with prolonged Bafi treatment (Bafi30), but similar transmission kinetics.

10.3389/fncel.2025.1625868

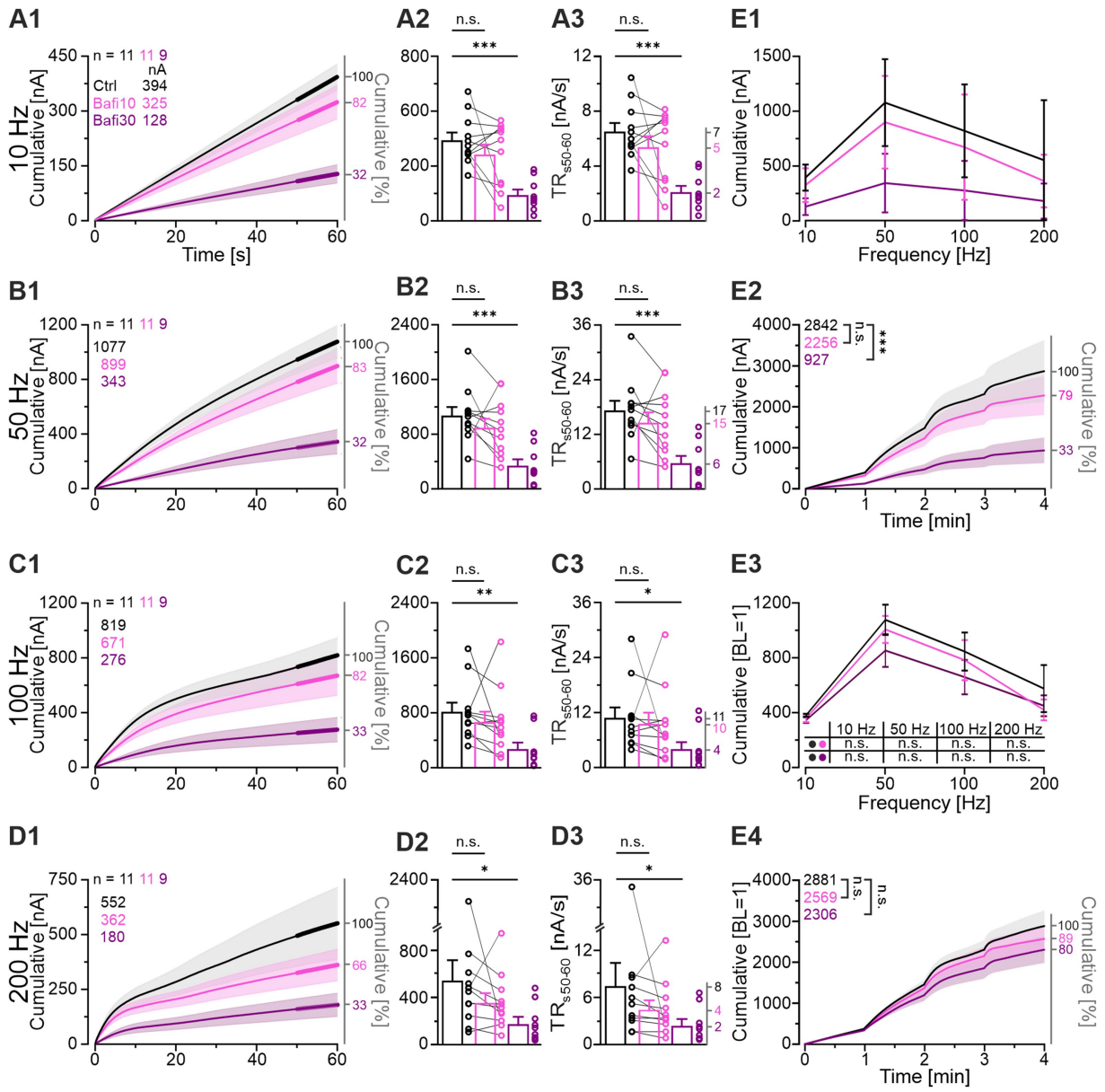


FIGURE 4
Bafi30 reduces transmission capacity by >60% at MNTB-LSO synapses, but transmission kinetics remain similar. **(A1–D1)** Cumulative current integrals as a function of time at the four challenge frequencies in Ctrl (black), Bafi10 (magenta) and Bafi30 (purple) during Protocol 1 (see Figure 1C). Traces show the incremental increase, and a linear slope corresponds to a steady-state release of constant synaptic strength. Thick lines mark periods when the transmission rate (TR) was quantified ($s_{50\text{-}60}$). Upper left numbers indicate the cumulative current amplitudes at $eIPSC_{60s}$. **(A2–D2)** Statistics of $eIPSC_{60s}$ at the four challenge frequencies. Variables on the left y-axis are the same as in **(A1)**. **(A3–D3)** TR during $s_{50\text{-}60}$. Mean values are shown on right y-axis. **(E1)** Comparison of the transmission performance between the three cohorts over the four challenge frequencies. **(E2)** Cumulative current integrals summarized over the entire 4 min of challenge (21,600 stimulus pulses). The numbers in the upper left indicate the cumulative absolute current amplitudes at 4 min. **(E3)** As **(E1)**, but normalized so that the BL of each neuron equals 100% (BL = 1). **(E4)** As **(E2)**, but after normalization. Time courses are mean cumulative amplitudes (SEM lightly shaded). Ctrl and Bafi10, n = 11; Bafi30, n = 9. See Supplementary Table S2 for details, including statistics.

Recovery from depression is reduced but not abolished by Bafi treatment

Effective SV (re-)filling is of great importance, not only for the robustness of neurotransmission during ongoing activation, but also for the recovery from synaptic depression. Accordingly, we examined the recovery behavior in the context of V-ATPase inhibition and compared it to the Ctrl situation (Figure 5; Protocol 1). After normalization of the eIPSC peak amplitudes of each neuron to its own baseline (BL = 100%), considerable overlap of the challenge-related traces was observed across cohorts, whereas the recovery traces showed greater divergence (Figure 5A1). In particular, the Bafi30 cohort exhibited lower values (Figures 5B1,C1,D1,E1).

Recovery was quantified in three ways (Figures 5A2,B2,C2,D2,E2; cf. Brill et al., 2019; Brill et al., 2021). The *RecovA* metric assesses the ability of the system to accurately return to the BL level. The Ctrls were

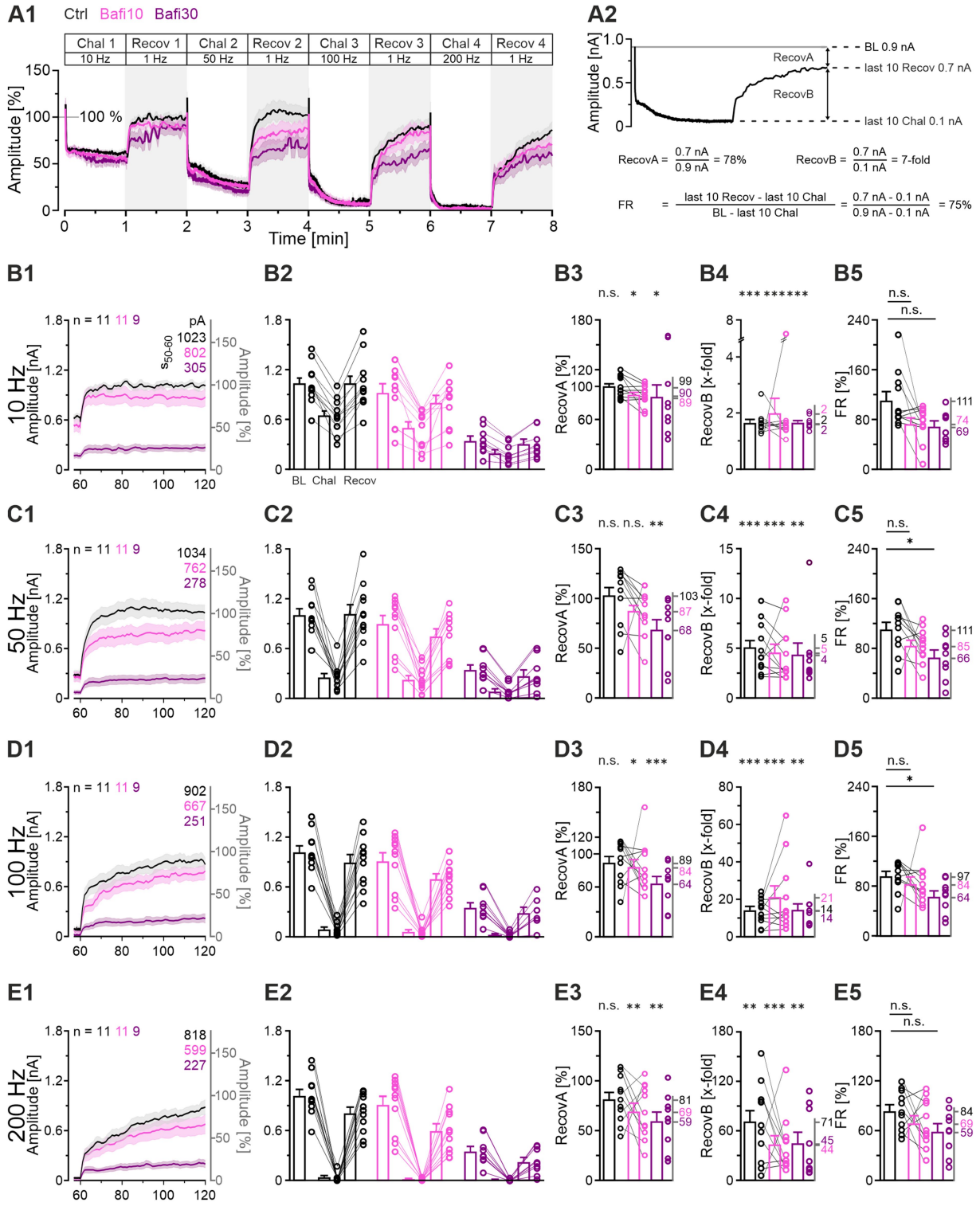


FIGURE 5
Recovery from depression is very efficient at Ctrl and Bafi10 synapses but reduced in Bafi30. **(A1)** Time course of normalized eIPSC amplitudes (mean ± SEM) in Ctrl (black), Bafi10 (magenta) and Bafi30 (purple) during Protocol 1 (see Figure 1C). The BL mean of the Ctrl, Bafi10 and Bafi30 was set to 100% (gray horizontal line). A 6-s pause was introduced after BL and after each 60-s recovery period for data storage. **(A2)** Recovery behavior was evaluated using three methods: (1) RecovA: last 10 eIPSCs of recovery vs. BL (= 100%); (2) RecovB: last 10 eIPSCs of recovery vs. last 10 eIPSCs of previous challenge; (3) FR: $\frac{last10\,eIPSCs\ Recov - last10\,eIPSCs\ Chal}{BL(=100\%) - last10\,eIPSCs\ Chal}$. Example calculations are provided for clarity. **(B1)** Time course of absolute and normalized amplitudes during 1-Hz|60-s recovery after 10-Hz challenge. Numbers in the upper right indicate absolute mean amplitudes during $s_{50\text{-}60}$. **(B2)** Quantification at the end of the BL, challenge, and recovery periods (last 10 eIPSCs). Variables on the left y-axis are the same as in **(B1)**. **(B3–B5)** Statistics for RecovA **(B3)**, RecovB **(B4)**, and FR **(B5)**. Means are shown on the right y-axis. **(C–E)** Same as **(B)**, but for recovery after 50-Hz **(C1–C5)**, 100-Hz **(D1–D5)**, and 200-Hz challenge **(E1–E5)**. Variables on the left y-axis in **(C2–E2)** are the same as in **(C1)**. Note the different amplitude scaling in **(B3–E5)**. Time courses are simple moving averages over three (1 Hz) or nine (10–200 Hz) data points (SEM lightly shaded). Ctrl and Bafi10, n = 11; Bafi30, n = 9. See Supplementary Table S3 for details, including statistics.

able to do so after each challenge period (Figures 5B3,C3,D3,E3; end values 99, 103, 89 and 81%). Bafi10 was successful in three of four instances (Figures 5B3,C3,D3) and thus only slightly inferior. In contrast, Bafi30 was unsuccessful in three instances (Figures 5C3,D3,E3), implying replenishment impairment.

The *RecovB* metric focuses on the fold increase from the steady-state depression level (the last 10 challenge events), and thus does not consider the BL. For each cohort, the *RecovB* behavior was statistically significant (Figures 5B4,C4,D4,E4). The results demonstrate the ability of MNTB-LSO synapses to recover from depression, even after a ≥ 30-min treatment with the V-ATPase blocker.

We also determined the fractional recovery (*FR*). The Bafi30 cohort showed significantly lower *FR* values than the Ctrl at two frequencies (Figures 5C5,D5; Supplementary Table S3). In contrast, no statistically significant difference was observed between Bafi10 and Ctrl at any frequency (Figures 5B5–E5). Collectively, these findings provide further evidence that the effects of 2 μM Bafi were relatively subtle and became effective only after prolonged treatment (≥ 30 min) and challenge frequencies ≥ 50 Hz.

As a final step, we compared the time courses of recovery between cohorts. For this purpose, we calculated the weighted time constant τ_w after fitting the curves with a biexponential function. During recovery after the 10-Hz challenge, τ_w values were low, implying fast replenishment (Ctrl: 2.1, Bafi10: 2.1, Bafi30: 2.1 s; ratios 100:100:100). They were substantially higher for the recovery after 100-Hz (Ctrl: 23.7, Bafi10: 23.8, Bafi30: 34.4 s; ratios 100:100:145) and 200-Hz challenge (Ctrl: 35.2, Bafi10: 34.9, Bafi30: 39.5 s; ratios 100:99:112). The observation that the ratios differed less than 1.5-fold in each comparison suggests that blocking the V-ATPase activity did not affect the recovery kinetics.

Delayed and gradual reduction of the quantal size (*q*) in the presence of Bafi

Impaired (re-)filling of SVs upon V-ATPase blockade should result in a smaller quantal size (*q*). A complete absence of (re-)filling should even abolish the transmission completely. To test these hypotheses, we determined the peak amplitude of spontaneous IPSCs (sIPSCs) during the baseline and the four recovery periods after challenge (BL and *Recov1-Recov4*). Example current traces for the three cohorts during the BL and the *Recov4* periods are shown in Figures 6A1–A6. For each neuron, *q* was determined from the Gaussian distribution of its sIPSC peak amplitudes (Figures 6B1–B6; see Krächan et al., 2017). In the Ctrl_vs_Bafi10 comparison, we found no significant change in *q* (Figure 6C3; Supplementary Table S4). In contrast, a significantly lower *q* value was observed in the Ctrl_vs_Bafi30 comparison (Figure 6C3). The *q* values averaged 26 pA in Ctrl, 27 pA in Bafi10 and 20 pA in Bafi30, corresponding to ratios of 100:104:77 (Figure 6C3). We consider the 23% reduction in Bafi30 to be moderate. The frequency of sIPSCs was determined across the BL and *Recov1-4* periods. Values were 5.7, 5.4 and 3.4 events per second for the Ctrl, Bafi10 and Bafi30 cohorts, respectively (not shown). They correspond to ratios of 100:95:63 and provide further evidence that Bafi treatment did not abolish the (re-)filling process.

After determining the *q* values, we reanalyzed the $TR_{50\text{-}60}$ results (cf. Figures 4A3,B3,C3,D3) in order to obtain a vesicle-oriented value of the replenishment rate (SV fusion and SV replenishment are balanced in steady state). At the end of the 50-Hz challenge period, 642 SVs per second were replenished in the Ctrl. The corresponding values for Bafi10 and Bafi30 were 542 and 302 SVs/s, respectively. These results refer to ratios of 100:84:47, and similar ratios were obtained at the other challenge frequencies (10 Hz: 100:82:42; 100 Hz: 100:91:51; 200 Hz: 100:64:44).

Taken together, these results show a delayed and gradual appearance of incompletely filled SVs upon V-ATPase blockade. The moderate reductions in *q* and replenishment rate demonstrate that MNTB axon terminals still maintain a pool of readily releasable SVs whose glycine content is high enough to evoke a postsynaptic current of ~20 pA per SV, i.e., about 70% of the Ctrl level. Thus, refilling of SVs is maintained despite inhibition of V-ATPase activity.

Bafi application results in reduced readily releasable pool (*RRP*), reduced quantal content (*m*) and increased release probability (P_v)

To analyze synaptic parameters in more detail, we examined *RRP*, *m* and P_v. The forward extrapolation method was used to determine the RRP (Elmqvist and Quastel, 1965) and the 100-Hz challenge period was analyzed (Figure 6D1). Mean values for I_{RRP} were 11.3, 8.5 and 2.4 nA for Ctrl, Bafi10, and Bafi30, respectively (Figure 6D2). With the *q* values shown above, these numbers correspond to an N_{RRP} of 434, 389, and 125 SVs, respectively (100:90:29), thus demonstrating a 3.5-fold and statistically significant reduction in Bafi30.

We also determined the quantal content *m* for $eIPSC_1$ of the 100-Hz challenge period ($m_1 = eIPSC_1/q$; *q* was determined from the preceding *Recov2* period). Again, the Ctrl_vs_Bafi30 comparison showed a statistically significant difference (47 vs. 21 SVs, i.e., ratio of 100:45; Figure 6D3). Finally, we observed a statistically significant difference for the release probability P_v in the Ctrl_vs_Bafi30 comparison ($P_v = m_1/I_{RRP}$). While P_v was 11% in the Ctrl, it was significantly increased to 16% in Bafi30 (~1.5-fold; Figure 6D4).

The 3.5-fold reduction in N_{RRP} was confirmed by means of a fluctuation analysis assuming a binomial release of SVs (not shown). We have recently used this analysis to evaluate statistical fluctuations of *m* at MNTB-LSO synapses (Vahdat et al., 2025) and found a P_v value of 93%, which is considerably higher than the value found in the present study.

Collectively, the reduction in *q* and *m* values (down to 70 and 45%, respectively; in combination down to 32%) underlies the >3-fold variation in $eIPSC_1$ values in the Ctrl_vs_Bafi30 comparison at the onset of the 100-Hz challenge (cf. Figure 3D2).

"Half-marathon" experiments (4-min|100-Hz challenge; 5 μM Bafi) confirm staggering emergence of pharmacological V-ATPase inhibition

The above results demonstrated diminished yet persistent activity at MNTB-LSO synapses even after prolonged treatment with 2 μM Bafi (≥30 min; Figures 2–5). We thus sought to determine whether a higher Bafi concentration (5 μM) and more intense stimulation conditions would result in a greater reduction in neurotransmission, or even its complete abolition. The underlying procedure, designated "Protocol 2" or "half-marathon" (Figure 1C) comprised a Ctrl episode (4-min|100-Hz challenge followed by 3-min|1-Hz recovery, totaling 24,180 stimulus pulses) which was followed by a Bafi10 episode (paired recordings) and a

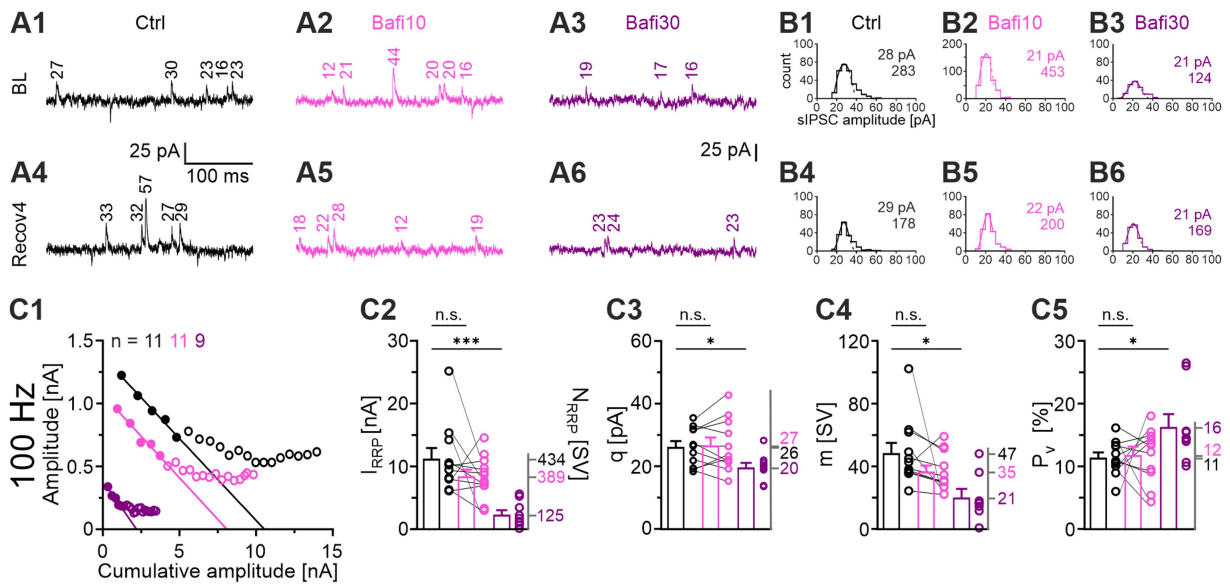


FIGURE 6
Synaptic parameters are altered by Bafi30: *q*, I_{RRP}, and *m* are reduced, whereas P_v is increased. **(A)** Original sIPSC traces for Ctrl (black), Bafi10 (magenta), and Bafi30 (purple). **(A1)** sIPSC amplitudes during BL **(A1)** and Recov4 **(A4)** for Ctrl. Same as **(A1,A4)**, but for Bafi10 **(A2,A5)**, and Bafi30 **(A3,A6)**. Numbers indicate the sIPSC amplitudes. **(B)** Estimation of *q*. **(B1,B4)** Distribution histograms of sIPSC amplitudes from current traces in **(A)** during BL **(B1)** and Recov4 **(B4)** for Ctrl. **(B2–B6)** Same as **(B1,B4)**, but for Bafi10 **(B2,B5)** and Bafi30, respectively **(B3,B6)**. A Gaussian curve was fitted from 0 pA to the bin after the first local maximum (dashed curves). Numbers in panels represent *q* values and number of sIPSCs for BL **(B1–B3)** and Recov4 **(B4–B6)** (see Materials and Methods for details). Data for Ctrl and Bafi10 are from one neuron, while data for Bafi30 are from another neuron. **(C)** Analysis of synaptic parameters. **(C1)** Elmqvist & Quastel plots used to determine I_{RRP}. The stimulation frequency was 100 Hz and a linear fit was applied to eIPSCs$_{1\text{-}5}$ of the cohort mean values (see Materials and Methods). **(C2)** Statistics for I_{RRP}. Means of N_{RRP} on the right y-axis. **(C3)** Statistics for *q* (obtained from a 300 s period over BL and Recov1-Recov4). Means on the right y-axis. Statistics for *m* **(C4)**, and P_v **(C5)**. Mean values on right y-axis. Note that $N_{RRP} = I_{RRP}/q$. Variables on the left y-axis in **(B2–B6)** are the same as in **(B1)**. Ctrl and Bafi10, $n = 11$; Bafi30, $n = 9$. See Supplementary Table S4 for details, including statistics.

final Bafi30 episode (from a different neuron). The stimulus conditions for each Bafi episode were identical to those employed for the Ctrl episode. The results are summarized in Figure 7, in which panel A1 illustrates the time course of the eIPSC amplitudes for the three cohorts. From the third challenge period onwards, that is not before 12,000 – 18,000 stimulus pulses, a significant reduction in steady-state eIPSC amplitudes was observed in the Bafi10 cohort (Figure 7A2, $s_{170\text{-}180}$). This finding differs from the results obtained with Protocol 1 (see Figure 3). By the conclusion of the 4-min challenge period ($s_{230\text{-}240}$), the steady-state amplitudes had decreased to 51, 25, and 17 pA (Figures 7A1,A2). The ~2-fold lower performance in Bafi10 and the 3-fold lower performance in Bafi30, in both cases statistically proven, unambiguously demonstrate the presence of a drug effect.

A more detailed examination of the time course of eIPSCs revealed that the largest amplitude differences occurred during the initial 20 s between the Ctrl and Bafi10 cohorts on one hand and the Bafi30 cohort on the other (left inset in Figure 7A1). This suggests that Bafi30 may experience significantly accelerated synaptic fatigue, whereas Ctrl and Bafi10 can draw from an intact RRP. However, the kinetics of depression remain largely indistinguishable (right inset in Figure 7A1).

Analysis of the cumulative eIPSC amplitudes corroborated the observation that a higher drug concentration and a more severe stimulation condition yielded had a greater effect on synaptic transmission (Figure 7B1). The Ctrl cohort was observed to elicit 1,567 nA, whereas the Bafi10 and the Bafi30 cohorts achieved only 66 and 33%, respectively (1,027 and 524 nA). For the Ctrl_vs_Bafi30 comparison, a statistically significant difference was observed (Figure 7B2; Supplementary Table S5). The results indicate that the inhibition of V-ATPase considerably impacts SV (re)filling when three conditions are met: first, a highly concentrated solution of Bafi is administered; second, the application time is considerable; third, the stimulation conditions are harsh. The results for the $TRs_{230\text{-}240}$ corroborate this conclusion (Figure 7B3; Ctrl: 6; Bafi10: 3; Bafi30: 2 nA/s; ratio 100:50:33).

Our subsequent investigation focused on the recovery behavior following the half-marathon challenge, with particular attention paid to $s_{230\text{-}240}$ (Figures 7C1–C4). Regarding *RecovA*, the Ctrl cohort exhibited complete recovery, reaching 107% of BL. In contrast, the Bafi10 and Bafi30 cohorts showed incomplete recovery, reaching only 63 and 68% of the BL level, respectively, and these values were significantly different from the BL (Figure 7C2). The ability of each cohort to reach higher eIPSC amplitudes after exhibiting very low levels at the end of the 4-min|100-Hz challenge was evaluated by assessing *RecovB*. The Ctrl and Bafi10 cohorts exhibited significantly higher amplitudes (24- and 23-fold, respectively; Figure 7C3, see also panel A2, $s_{230\text{-}240}$). In contrast, *RecovB* did not reach statistical significance for Bafi30 (16-fold). Finally, there was a significant difference in *FR* between the Ctrl and Bafi30 cohorts, but not between the Ctrl and the Bafi10 cohorts (Figure 7C4; Ctrl: 107%; Bafi10: 61%; Bafi30: 46%).

During the harsh 4-min|100-Hz challenge, we made an intriguing observation following the 6-s pauses required for data storage at

10.3389/fncel.2025.1625868

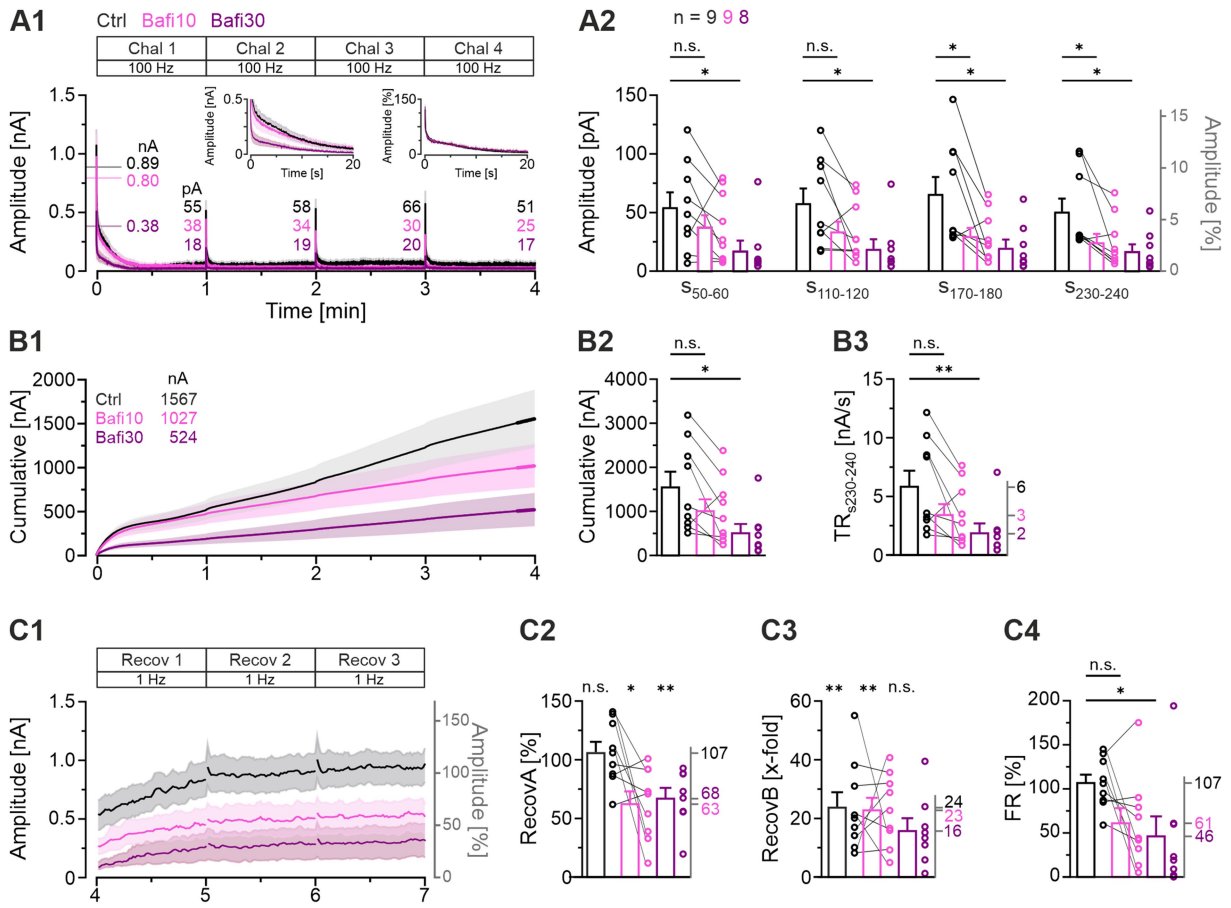


FIGURE 7
A higher Bafi concentration (5 μM) and harsher stimulation conditions further reduce synaptic strength. **(A1)** Time course of absolute eIPSC amplitudes (mean ± SEM) obtained during the 100-Hz|240-s challenge ("half-marathon"; Protocol 2; see Figure 1C) for Ctrl (black), Bafi10 (5 μM, magenta), and Bafi30 (5 μM, purple). The Ctrl and Bafi10 data are from a different neuron than the Bafi30 data. A 6-s pause was introduced after each challenge period for data storage. The BL mean of the Ctrl was set to 100%. Horizontal lines indicate the mean BL amplitude for each cohort (numbers are also given). Numbers indicate absolute mean amplitudes during $s_{50\text{-}60}$. The left inset shows a close-up of the first 20 s; the right inset shows the same, but for normalized amplitudes. **(A2)** Statistics at four different time intervals ($s_{50\text{-}60}$, $s_{110\text{-}120}$, $s_{170\text{-}180}$, $s_{230\text{-}240}$). **(B1)** Time course of cumulative amplitudes (same x-axis as in **A1**). Thick lines mark the 10-s periods in which TR was quantified ($s_{230\text{-}240}$). Numbers in the upper left indicate the cumulative current after 4 min. **(B2)** Statistics for cumulative amplitudes. **(B3)** Statistics for TR. Mean values on right y-axis. **(C1)** Time course of absolute and normalized eIPSC amplitudes during the 1-Hz|180-s recovery after the 4-min challenge. A 6-s pause was introduced after each 60-s period for data storage. **(C2–C4)** Statistics for RecovA **(C2)**, RecovB **(C3)** and FR **(C4)**. Mean percentages on the right y-axis. Time courses are simple moving averages over three (1 Hz) or nine (100 Hz) data points (SEM lightly shaded). Ctrl and Bafi10, n = 9; Bafi30, n = 8. See Supplementary Table S5 for details, including statistics.

minutes 1, 2, and 3, namely short-term recovery (Figure 7A1; NB: a similar observation was made by Qiu et al. (2015) at Calyx-of Held – MNTB synapses). As the stimulation was terminated during these three pauses, we were able to assess and quantify this short-term recovery without interference. To achieve this, we applied a variant of the *FR* formula

$$\left(\frac{eIPSC_1\ of\ Chal2 - mean\ amplitude_{s50-60}of\ Chal1}{BL - mean\ amplitude_{s50-60}of\ Chal1}\right.$$ etc.)

and found lower values in the Bafi cohorts compared to Ctrl, but still ongoing recovery (Figure 7A1). The Ctrl: Bafi10: Bafi30 ratios were: min_1: 100:95:89; min_2: 100:71:64; min_3: 100:59:48. This implies that the presence of Bafi did not abolish SV replenishment, even when a brief time domain of just a few seconds and the harsh half-marathon conditions are considered. The results confirm those obtained for the recovery periods lasting 60 s.

Taken together, the results from the half-marathon experiments show that a 10-min application time of Bafi at an extraordinarily high concentration (5 μM) is sufficient to elicit blocking effects on synaptic transmission. However, the effects do not become evident before at least 12,000 stimulus pulses are given within ~2 min. Moreover, they still enable eIPSC amplitudes of sufficient height (~50% of Ctrl) during sustained activation, resulting in statistically indistinguishable cumulative eIPSC amplitudes. Recovery from depression is impaired but still reaches about two third of the BL level, implying ongoing SV (re)filling. As expected, the Bafi30 effects are generally more severe.

Reduction of synaptic strength is drug-specific and not time-dependent (sham control experiments)

One potential pitfall of the experiments discussed above is that the observed decrease in eIPSC amplitudes cannot be unambiguously attributed to a drug effect. Rather, the decrease may be time-dependent.

To address this concern, we performed sham control experiments essentially identical to Protocol 1 (see Figure 3), except that only the solvent for Bafi was washed in (0.1% EtOH). We observed an almost perfect superposition of the current traces (Supplementary Figures S1A1–A3,B1,C1,D1,E1; Supplementary Table S6). In essence, these results impressively demonstrate that there was no time dependence. In both EtOH10 and EtOH30, the synaptic performance was statistically indistinguishable from Ctrl (in ACSF) for BL analysis (Supplementary Figures S1A4,A5), for challenge periods (Supplementary Figures S1B1,B2,C1,C2,D1,D2,E1,E2), and for robust recovery (Supplementary Figures S1F1–F3,G1–G3,H1–H3,I1–I3).

Taken together, the data show no effect of EtOH on synaptic transmission, suggesting that the impairment is solely due to the drug (Bafi) and not due to the solvent or the time.

We also compared EtOH effects with Bafi effects (Supplementary Figure S2; Supplementary Table S7; see also Figure 3) and found significantly impaired transmission in Bafi30_vs_EtOH30 (Supplementary Figures S2C1–C3) but neither in $Ctrl_{Bafi}$_vs_$Ctrl_{EtOH}$ (Supplementary Figures S2A1–A3) nor in Bafi10_vs_EtOH10 (Supplementary Figures S2B1–B3). Impaired transmission was evident during the last 10 s at each challenge frequency (Supplementary Figure S2C2) and during each recovery period (Supplementary Figure S2C3). Collectively, the results from the sham control experiments confirm that the reduced synaptic strength observed in the presence of bafilomycin is caused by V-ATPase inhibition. Time-dependent or solvent-dependent effects can be excluded.

Bafi effects are reproduced by folimycin

In a complementary set of experiments, we assessed the effects of inhibited V-ATPase activity by repeating the experiments with Protocol 1, except that Bafi was replaced by folimycin (Foli, 1 μM). The results are shown in Supplementary Figures S3, S4. Foli essentially recapitulated the effects of Bafi in direction and magnitude (Supplementary Tables S8, S9). For 86% (67/78) of the parameters that we quantified in both the Bafi and Foli cohorts, the statistics were congruent, thus demonstrating that both drugs affected V-ATPase activity in a very similar manner (Supplementary Table S9). For example, the BL was significantly reduced in Foli30 compared to the Ctrl (49%; 633 vs. 1,321 pA), but not in the Foli10 (87%; 1,151 pA; Supplementary Figures S3A4,A5). A consistent observation was made for the Bafi cohort, namely 38 and 89%, respectively (Supplementary Table S9; cf. Figures 3A4,A5). Furthermore, the Foli30 cohort showed increased synaptic depression compared to the Ctrl at each challenge frequency and in each time window (16 parameters), whereas the Foli10 cohort was statistically indistinguishable from the Ctrl for each of those 16 parameters (Supplementary Figures S3B1–B5,C1–C5,D1–D5,E1–E5). A similar scenario had been found for Bafi (Supplementary Table S9; cf. Figure 3). Finally, application of Foli did not result in significantly lower q values in Foli10, but it did so in Foli30 (Supplementary Figure S4E3), consistent with the previous findings on Bafi.

Treatment with Foli30 also resulted in impaired recovery after each challenge period (Supplementary Figures S4A1,A2,B1,B2,C1,C2,D1,D2; Supplementary Table S10). For Foli10, however, such an impairment was only detectable after a 200-Hz exposure (Supplementary Figures S4A2,B2,C2,D2). *RecovB* reached statistical significance in each case (Supplementary Figures S4A3,B3,C3,D3), suggesting that refilling mechanisms are still functional, albeit significantly reduced. *FR* values showed a significant difference in each comparison of Ctrl_vs_Foli30 (Supplementary Figures S4A4,B4,C4,D4).

The I_{RRP} of Foli10 was statistically indistinguishable from the Ctrl, but it was drastically reduced in Ctrl_vs_Foli30 (~4-fold; Supplementary Figures S4E1,E2). The N_{RRP} in the Ctrl, Foli10, and Foli30 contained 832, 620 and 374 SVs, respectively (Supplementary Figure S4E2). Thus, the N_{RRP} differed only 2.2-fold between Ctrl and Foli30. The lower N_{RRP} ratio compared to I_{RRP} is explained by the finding that q values were almost 2-fold lower in Foli30 than in Ctrl (13 vs. 23 pA; Supplementary Figure S4E3). Notably, this reduction was greater than that shown for Bafi30 in Figure 6C3. The Foli30 cohort also showed a statistically significant reduction in m, similar to the Bafi30 results (64 SVs/38 SVs = 1.7-fold; Supplementary Figure S4E4). In contrast, P_v values were not altered by Foli (10, 11, 9%; Supplementary Figure S4E5; different from Bafi30).

The similar results obtained with Bafi or Foli, when considered together, underscore the need for prolonged drug treatment to impair synaptic transmission. Statistically significant differences occurred in 39 out of 46 Ctrl_vs_Bafi30 comparisons and in 39 out of 39 Ctrl_vs_Foli30 comparisons, representing 85 and 97%, respectively (Supplementary Table S9). In contrast, with shorter drug treatment, only 3 out of 46 comparisons in Ctrl_vs_Bafi10 and 0 out of 39 in Ctrl_vs_Foli10 showed statistical significance (7 and 0%, respectively). These results impressively highlight the delayed onset of impaired transmission in the presence of V-ATPase blockers. In conclusion, the effects of Foli essentially recapitulated those of Bafi in direction and magnitude. They provide consistent evidence that V-ATPase activity is necessary to generate glycine-filled SVs and ensure robust synaptic transmission at MNTB-LSO synapses. However, SV (re)filling does not appear to depend on V-ATPase activity alone.

The Na^+/H^+ exchanger NHE6 is highly abundant in presynaptic axon terminals around LSO neurons and in MNTB neurons

Because our Bafi and Foli analyses had revealed an only incomplete blockade of transmission, despite severe treatment conditions, we wondered whether there might be another proton pump besides the V-ATPase that could acidify the SVs, thereby creating a favorable proton gradient for VIAAT-mediated glycine import. One candidate is the Na^+/H^+ exchanger (NHE; see Figure 1C). Thirteen isoforms have been identified (Pedersen and Counillon, 2019), of which NHE6-NHE9 are located in the membranes of intracellular organelles (Alexander et al., 2017).

In order to assess the distribution of NHE proteins in the LSO and other superior olivary complex (SOC) nuclei, we used immunohistochemistry, thereby focusing on the NHE6 isoform. Our approach was motivated by mRNA sequencing results obtained in our group from laser-dissected tissues (Maraslioglu-Sperber, 2021). These results demonstrated high expression of *Slc9A6*, the gene encoding NHE6, in the LSO and MNTB of juvenile mice, among nine NHE isoforms analyzed. *Slc9A6* expression was the most pronounced, with a level of 11 transcripts per million in the LSO and 12 in the MNTB. Interestingly, NHE6 belongs to the subset of Na^+/H^+ exchangers that are found in recycling endosomes (Brett et al.,

2002; Masereel et al., 2003; Orlowski and Grinstein, 2004; Nakamura et al., 2005) and secretory organelles (Miyazaki et al., 2001; Kondapalli et al., 2014). Consistent with this, NHE6 has been identified in SVs (Preobraschenski et al., 2014; Taoufiq et al., 2020). Finally, NHE6 has been implicated in luminal pH regulation (Ohgaki et al., 2010; Ohgaki et al., 2011). Taken together, these findings identified NHE6 as an interesting candidate for our MNTB-LSO study.

To assign NHE6 signals to glycinergic neurons, our immunohistochemical analysis included a double-labeling strategy for NHE6 and GlyT2, which is a marker protein for glycinergic neurons (Friauf et al., 1999; Eulenburg et al., 2005). We found strong NHE6 immunofluorescence in the MNTB, the SPN and the LSO (Figure 8A1). At the cellular level, the cytoplasm of virtually every glycinergic MNTB soma was NHE6 positive (Figures 8A2,A3). This pattern stood in contrast to that observed in the LSO, where neuronal somata exhibited almost complete absence of NHE immunoreactivity, yet were decorated with double-labeled puncta in a perisomatic fashion (Figures 8A4–A6). We attribute these puncta to axon terminals of MNTB neurons. Quantification of NHE6 and GlyT2 co-localization confirmed the close proximity of the immunosignals (Figures 8B1–B3). Taken together, these results suggest that terminals of MNTB axons that contact LSO somata contain substantial amounts of NHE6.

Application of EIPA to brainstem slices with the aim to block Na^+/H^+ exchangers results in severely impaired transmission, yet recovery still occurs

No selective antagonist for NHE6 has been identified to our knowledge. Nevertheless, NHE-mediated Na^+/H^+ exchange in general is reportedly suppressed by the "broadband" antagonist ethyl-isopropyl-amiloride (EIPA; Vigne et al., 1983; Masereel et al., 2003; Hori and Takamori, 2021). We therefore characterized transmission at MNTB-LSO synapses in the presence of EIPA (100 µM). The procedure is illustrated in Figure 1C and outlined in Protocol 3. It consists of a Ctrl episode performed in ACSF and comprised a 1-min|50-Hz challenge, a 1-min|100-Hz challenge and two 1-min|1-Hz recovery periods, corresponding to 9,120 stimulus pulses in total. Subsequently, an EIPA10 episode was initiated that was identical in structure to the preceding Ctrl episode (paired recordings).

In the Ctrl, the synaptic depression during each challenge period, along with the subsequent recovery, occurred in a manner consistent with our expectations (Figure 9A1). However, we made an unanticipated observation during the 10-min wash-in period of EIPA, during which MNTB axons were stimulated at a low frequency of 0.5 Hz. The eIPSC amplitudes decreased from 1,619 pA at the end Ctrl-Recov2 to 799 pA at the beginning of EIPA-BL (Figures 9A1,A2).

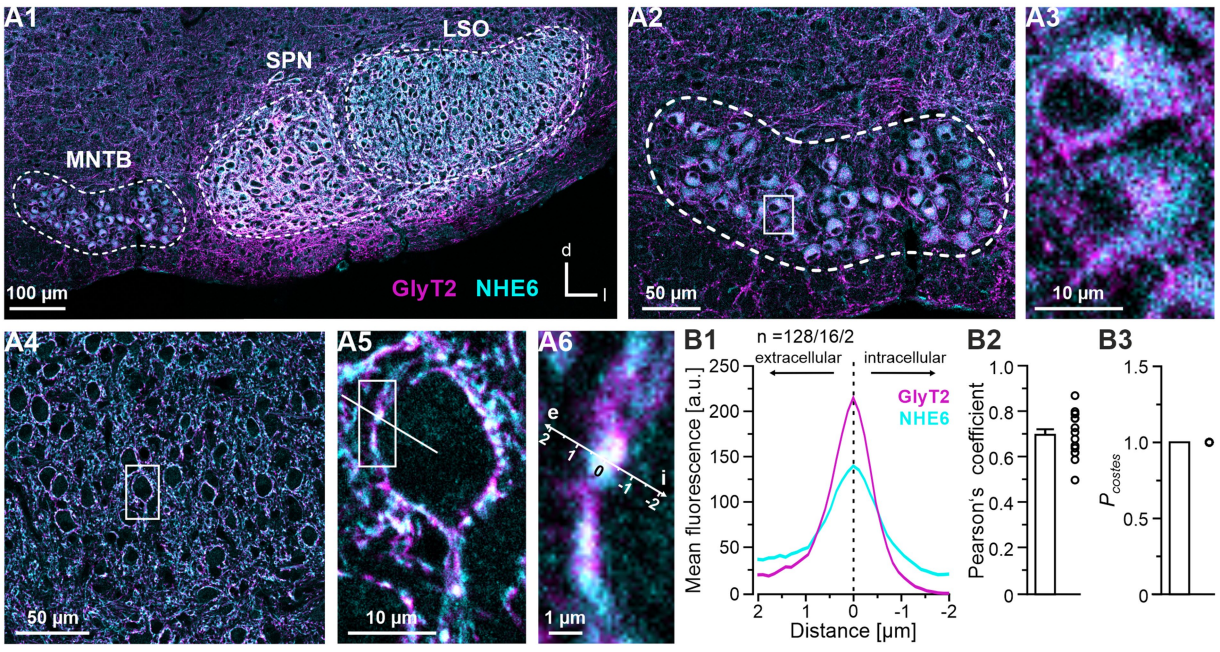


FIGURE 8
Co-distribution of NHE6 and GlyT2 in the superior olivary complex (SOC). **(A)** Immunohistochemical analysis of NHE6 and GlyT2 in a coronal brainstem section at P11. **(A1)** Double-labeling for NHE6 (cyan) and GlyT2 (magenta) in the SOC. MNTB, SPN and LSO are outlined by dotted lines. **(A2)** NHE6 and GlyT2 immunosignals in the MNTB. **(A3)** Close-up of two representative MNTB neurons from the framed area in **(A2)**. **(A4)** Double-labeling in the LSO. **(A5)** Close-up of a representative LSO neuron in the framed area in **(A4)**. A representative line scan is shown. **(A6)** Close-up of the framed area in **(A5)**. The spatial axis is also used in **(B1)**. **(B)** Quantification of NHE6 and GlyT2 co-distribution. **(B1)** Averaged intensity profiles for NHE6 (magenta) and GlyT2 (cyan). Prior to averaging, each profile was aligned to the position of the maximum GlyT2 signal. See Materials and Methods for details. Negative and positive µm values indicate intracellular and extracellular signals, respectively. *n*, number of profiles/cells/animals. **(B2)** Pearson's coefficients and **(B3)** corresponding P_{Costes} values. The Pearson's coefficient was 0.70 ± 0.02 (16 cells) and the P_{Costes} value was 1.00 ± 0.00 (16 cells; NB: co-distribution is indicated by P_{Costes} > 0.95). Optical thickness: 1 µm. d, dorsal; e, extracellular; i, intracellular; l, lateral; LSO, lateral superior olive; MNTB, medial nucleus of the trapezoid body; SPN, superior paraolivary nucleus.

This resulted in a markedly reduced BL of 55% (Figures 9A3,A4), suggesting an initial inhibitory effect of EIPA on transmission that cannot be attributed to challenge-induced SV depletion. During each challenge period, the transmission in EIPA10 exhibited a ~ 4-fold reduction compared to the Ctrl (Figures 9B1,B2,D1,D2; Supplementary Table S11). *RecovA* showed no statistically significant difference from the preceding BL in each cohort following 50-Hz challenge (Figures 9C1,C2), indicating that the efficacy of recovery remained unchanged. However, after 100-Hz challenge, *RecovA* was insufficient (Figures 9E1,E2). Furthermore, the *FR* was significantly lower than that for the Ctrl after each challenge period (Figures 9C3,E3; 50 Hz: 119 vs. 68%, 100 Hz: 106 vs. 56%), suggesting that EIPA may indeed inhibit SV (re)filling. The observation that the synaptic strength exceeded 500 pA during each recovery period, however, indicates that SV (re)filling is not completely abolished by the drug (Figures 9C1,E1).

As before, we determined the readily releasable pool (I_{RRP}) at the begin of the 100-Hz challenge period (Figure 9F1). We found a severe reduction in the presence of EIPA10 (~4-fold, from 30.9 to 7.3 nA; Figure 9F2). These I_{RRP} values relate to N_{RRP} values of 930 and 254 SVs, respectively. The quantal size *q* remained unaltered (Figure 9F3), while the quantal content *m* was almost 3-fold lower (Figure 9F4), in line with the diminished N_{RRP}. Finally, the release probability *Pv* was found to be unaltered (Figure 9F5). In summary, the EIPA10 experiments yielded some surprising results, including the extraordinary time course of eIPSC amplitudes during the drug wash-in period (Figure 9A2), which ultimately resulted in an almost 2-fold lower BL compared to the Ctrl (Figure 9A3). Therefore, a word of caution is warranted regarding the interpretation of the EIPA10 results. This issue will be further discussed in the following section.

EIPA has adverse effects on AP generation that require careful interpretation of the results on synaptic effects

While performing the EIPA experiments, we noticed that the drug affected the AP behavior of LSO neurons. In the absence of EIPA, Ctrl neurons fired an onset AP in response to a 200-ms depolarizing current pulse, which is typical for LSO principal neurons (Sterenborg et al., 2010; Friauf et al., 2019). This onset AP was not elicited in the presence of EIPA (Figure 10A1), where each of the eight neurons analyzed exhibited a complete cessation in firing (Figure 10A2). This unanticipated outcome prompted us to be concerned about the activation efficiency of the MNTB neurons in the synaptic stimulation experiments. To address this concern, we performed antidromic stimulation experiments on MNTB neurons as previously described (Müller et al., 2022). The stimulation regime was according to Protocol 3, and APs with peak amplitudes <1 mV were considered as failures. The Ctrl MNTB neurons showed mild failure behavior at the end of the 50-Hz and the 100-Hz challenge period, but the amplitudes of their APs remained largely unaltered (example traces in Figure 10B1 and the 60-s time courses for the cohort in Figure 10C1). In contrast, EIPA10 MNTB neurons exhibited a high failure rate and a drastic reduction in AP peak amplitude, resulting in the emergence of mini spikes (spikelets) whose amplitude was only ~3 mV (Figure 10B2; time course in panels C2 and D). The AP fidelity of the Ctrl during $s_{0\text{-}10}$ was 99 and 89% at 50-Hz and 100-Hz challenge, respectively (Figure 10C1). The corresponding values for EIPA10 were only 45 and 20% (Figure 10C2). By $s_{50\text{-}60}$, the fidelity values were 86 and 74% for the Ctrls and 24 and 11% for EIPA10 (Figure 10E). The Ctrls demonstrated the ability to regain perfect fidelity values of 100% during each recovery period. In contrast, the corresponding values for EIPA10 were only 60 and 49% (Figure 10C2). As mentioned above, the AP fidelity was only 45% during $s_{0\text{-}10}$ of the 50-Hz challenge (Figures 10B2,C2). It is noteworthy that a similarly low level (56%) was already present during the BL period, and it emerged during the 2nd half of the 10-min wash-in period of EIPA at 0.5-Hz stimulation (Figure 10C2). In sum, the results illustrate considerable and deleterious effects of EIPA10 on AP generation and/or AP conduction.

In a next step, we conducted antidromic stimulation experiments in the presence of the V-ATPase inhibitor Bafi (2 μM) to ascertain whether the drug might also exert any deleterious effects on AP generation, as we had demonstrated for EIPA. Protocol 1 was employed to emulate the synaptic stimulation scenario previously utilized for Bafi (cf. Figures 1, 2). Detailed results are presented in Figures 10F1–F3,G1–G4 and in Supplementary Table S12. For the Ctrl, the $s_{50\text{-}60}$ fidelity values were 100, 84, 70 and 33%, respectively, at challenge frequencies of 10, 50, 100 and 200 Hz. The corresponding values for Bafi10 were 89, 82, 61 and 35% (Figures 10G1–G4). None of these values was statistically different from the Ctrl. Finally, the Bafi30 values were 88, 66, 44 and 19%, respectively, and again, no value was statistically different from the Ctrl. Furthermore, the recovery from depression was robust in each case, ranging from 86 to 100% (Figure 10F3). Collectively, these findings imply that Bafi elicits no considerable aversive side effects on AP behavior, in clear contrast to EIPA.

When corrected for AP failures, the blocking effect of Bafi on SV replenishment is confirmed. In contrast, EIPA does not appear to impair replenishment

To consider the influence of AP failures on the overall transmission efficiency of MNTB-LSO synapses, we performed a mathematical analysis. This analysis aimed to separate effects on AP generation and/or AP conduction from those caused by drug-induced synaptic fatigue. For this purpose, mean eIPSC values from the challenge periods were corrected by assuming 100% AP fidelity. This allows to conservatively attribute the changes in eIPSC amplitude to changes in the presynaptic release machinery. The following example illustrates the procedure: If the AP fidelity rate was 40% at a given time point and the corresponding eIPSC amplitude was 210 pA, the latter value was multiplied by 2.5, thereby obtaining a "failure-corrected" value of 525 pA. The procedure was employed to correct the EIPA10, Bafi10 and Bafi30 means presented in Figures 3, 9, respectively. The results from 50- and 100-Hz challenge are shown in Figure 11 and Supplementary Table S13 provides a detailed quantification of the findings for the $s_{50\text{-}60}$ periods. Two arbitrary thresholds were set (50 and 200%), and they revealed no effect on synaptic transmission in the Bafi10 experiments upon failure corrections, thus confirming the aforementioned results (Figures 11A1,A2,C1,C2). In contrast, synaptic transmission was affected in Bafi30 upon correction, as described before. However, there was no complete abolishment, because eIPSC amplitudes were only moderately decreased, as documented by $\frac{drug}{Ctrl}$

10.3389/fncel.2025.1625868

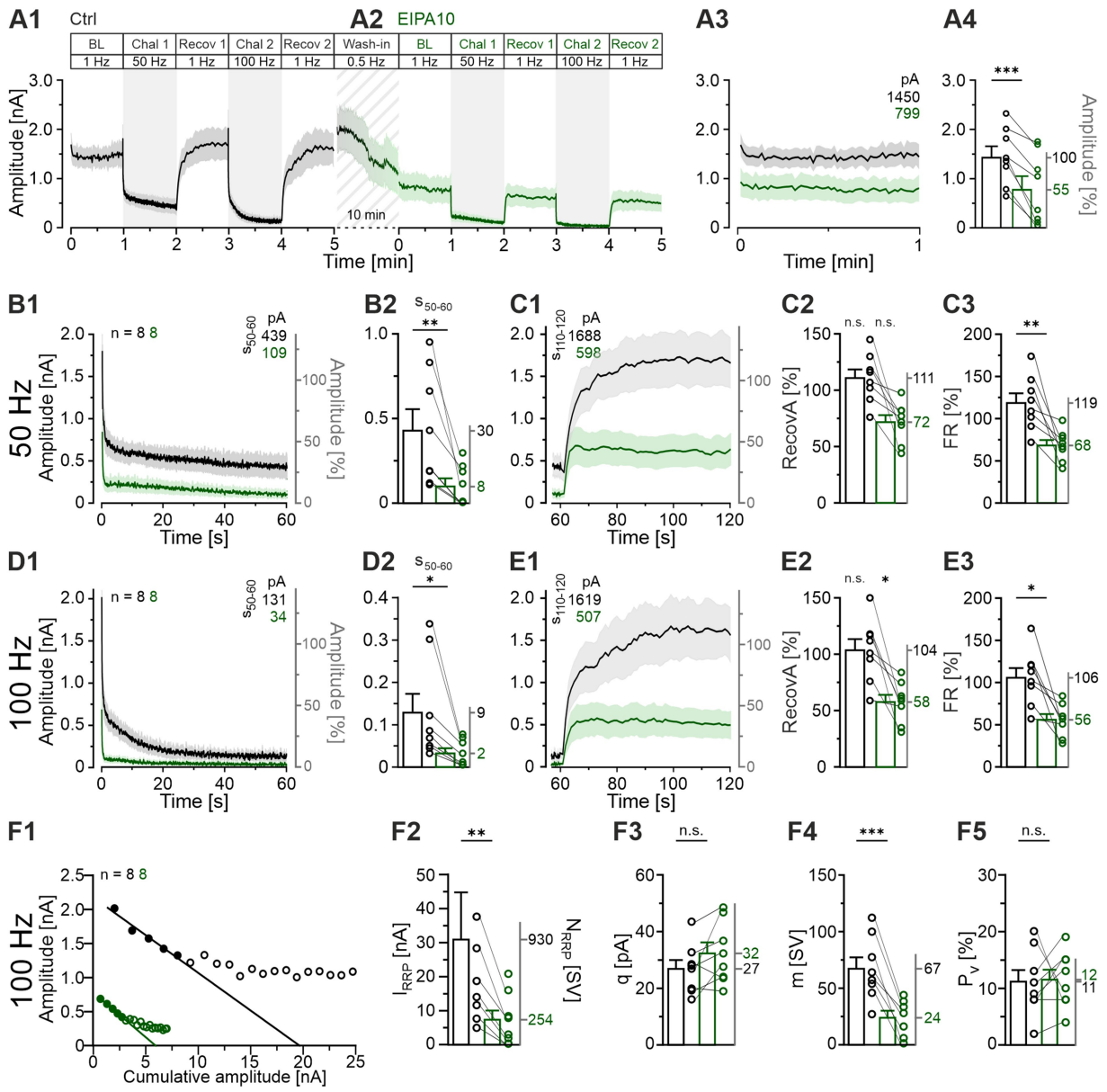


FIGURE 9
Application of EIPA with the intention of blocking NHE activity results in a markedly reduced sustained transmission but does not prevent recovery. **(A1,A2)** Time course of eIPSC amplitudes (mean ± SEM) for Ctrl (black) and EIPA10 (100 μM, green), obtained from paired recordings (Protocol 3, see Figure 1C). Diagonally striped region represents the wash-in period for EIPA. **(A3)** Close-up of the BL traces. The numbers in the upper right indicate the absolute mean amplitudes. **(A4)** Statistical analysis for the BL periods (mean Ctrl = 100%, EIPA10: 55%). **(B1)** Time course of absolute and normalized eIPSC peak amplitudes during the 50-Hz|60-s challenge. The numbers in the upper right indicate the absolute mean amplitudes during $s_{50\text{-}60}$. **(B2)** Statistical analysis during $s_{50\text{-}60}$. **(C1)** Time course of absolute and normalized eIPSC peak amplitudes during a 1-Hz|60-s recovery period following the 50-Hz challenge. The numbers in the upper left indicate the mean amplitudes during $s_{110\text{-}120}$. **(C2,C3)** Statistical analysis for RecovA **(C2)** and FR **(C3)**. Mean percentages on the right y-axis. **(D1–E3)** Same as **(B1–E3)**, but for 100 Hz. **(F)** Analysis of synaptic parameters. **(F1)** Elmqvist and Quastel plots were used to determine I_{RRP}; forward extrapolation was applied to the linear fit through eIPSCs$_{1\text{-}5}$ evoked at 100 Hz. Cohort values (see Materials and Methods for details). **(F2)** Statistical analysis for I_{RRP} Mean values of N_{RRP} on the right y-axis. **(F3–F5)** Statistics for q (obtained from a 300 s period over BL and Recov1-Recov4). **(F3)**, m **(F4)**, and P_v **(F5)**. Means on the right y-axis. Variables on the left y-axis in **(B2–D2)** are the same as in **(B1)**. Note the different amplitude scaling in **(B2,D2)**. Time courses are simple moving averages over three (1 Hz) or nine (50-100 Hz) data points (SEM lightly shaded). Ctrl, n = 8; EIPA10, n = 8. See Supplementary Table S11 for details, including statistics.

ratios in the range of 42-46%. For the EIPA experiments, our failure-correction revealed that this drug appears to leave SV (re-)filling unaffected (Figures 11B1,B2,D1,D2). An unchanged q value upon EIPA treatment (Figure 9F3) provides further evidence that EIPA does not appear to affect SV (re)filling.

Summary of the major results

The main findings of the present study are as follows: (1) In the absence of any V-ATPase blocker, synaptic transmission at inhibitory MNTB-LSO synapses is robust and remarkably resistant to fatigue,

10.3389/fncel.2025.1625868

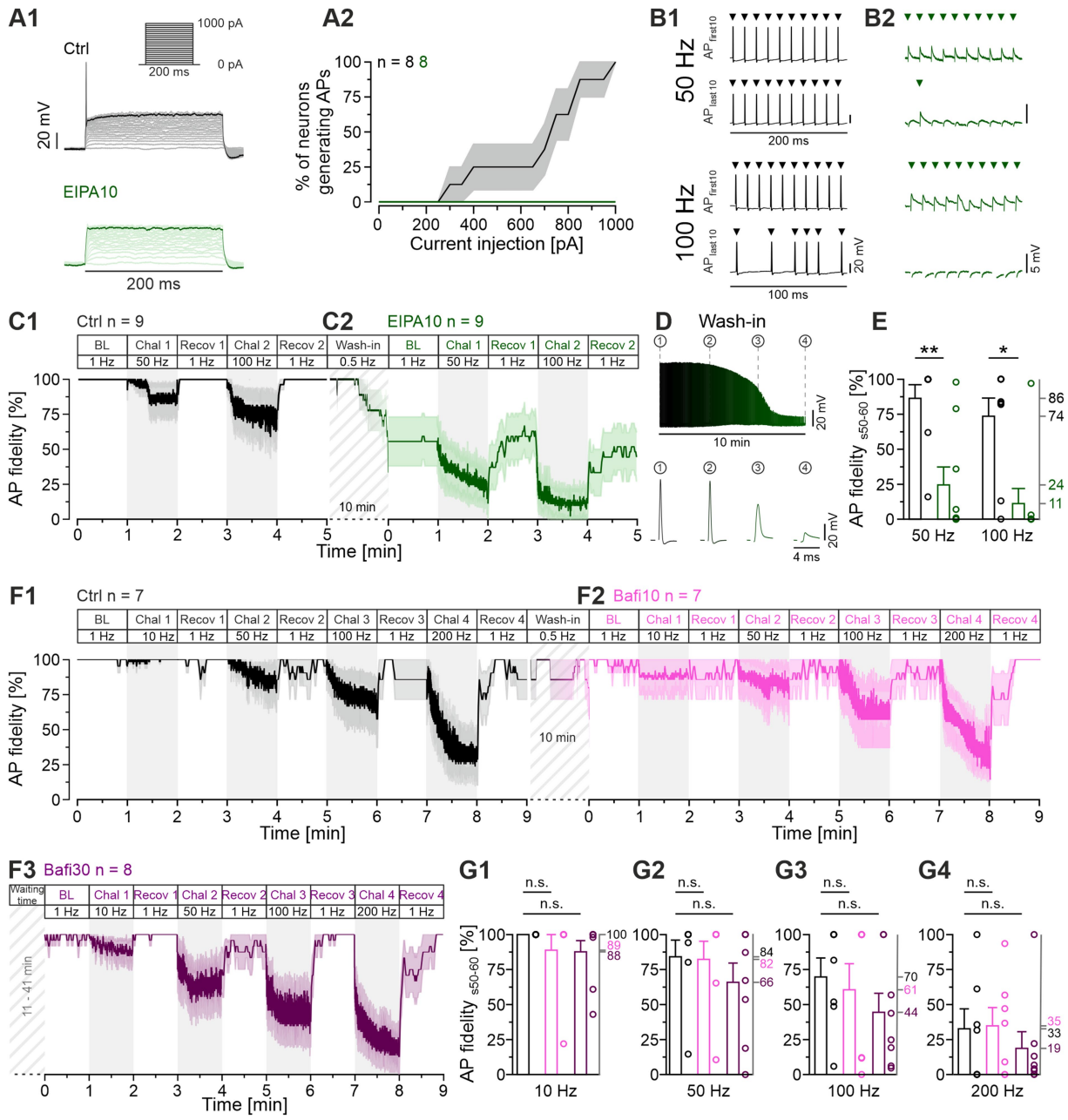


FIGURE 10
Application of EIPA reduces the reliability of AP firing, whereas Bafi does not. **(A1)** Representative voltage traces from a Ctrl MNTB neuron (black, top) and after application of EIPA10 (100 µM; green, bottom) at rheobase 850 pA. The traces show voltage responses to rectangular current pulses (inset: 0 to 1,000 pA; 50 pA increments; 200 ms duration). **(A2)** Percentage of neurons generating APs (mean ± SEM) as a function of the current amplitude. Note the absence of APs upon EIPA treatment. Same neurons as shown in Figure 9. **(B)** Representative antidromic APs during Chal 1 and Chal 2 periods, showing the first and last 10 APs for Ctrl **(B1)** and EIPA10 **(B2)**. Each arrow marks an AP. Note the different amplitude scaling in **(B1,B2)**. **(C1,C2)** Time course of AP fidelity (mean ± SEM) for Ctrl **(C1)** and EIPA10 **(C2)** obtained with protocol 3 (see Figure 1C, antidromic stimulation). Diagonally striped regions represent the wash-in period of EIPA. A 6-s long pause was introduced after the BL and each 60-s recovery period. Ctrl, n = 9; EIPA10, n = 9. **(D)** AP amplitudes during the 10-min wash-in period (top), and magnification of four representative APs at different time points (bottom). **(E)** Statistical analysis for AP fidelity during $s_{50\text{-}60}$. **(F)** Time course of AP fidelity (mean ± SEM) for Ctrl (black) **(F1)** and Bafi10 (magenta) **(F2)** obtained from paired recordings with protocol 1 (see Figure 1C, antidromic stimulation). **(F3)** Time course for Bafi30 (purple). Data in **(F3)** are from a different neuron than in **(F1,F2)**. Diagonally striped regions indicate perfusion periods of 2 µM Bafi. A 6-s pause was introduced after the BL and each 60-s recovery period. **(G)** Statistics for AP fidelity during $s_{50\text{-}60}$ for 10 Hz **(G1)**, 50 Hz **(G2)**, 100 Hz **(G3)**, and 200 Hz **(G4)**. Variables on the left y-axis in **(G2–G4)** are the same as in **(G1)**. Mean percentages on the right y-axis. Ctrl, n = 7; Bafi10, n = 7; Bafi30, n = 8. See Supplementary Table S12 for details, including statistics.

even under severe high-frequency stimulation conditions in the minute range and beyond (the half-marathon experiments included 24,000 stimulus pulses in 4 min; Figure 7). Furthermore, recovery from synaptic depression is rapid and complete, demonstrating great resilience. (2) Interfering with SV refilling by pharmacologically blocking V-ATPase activity with Bafi or Foli reduces steady-state

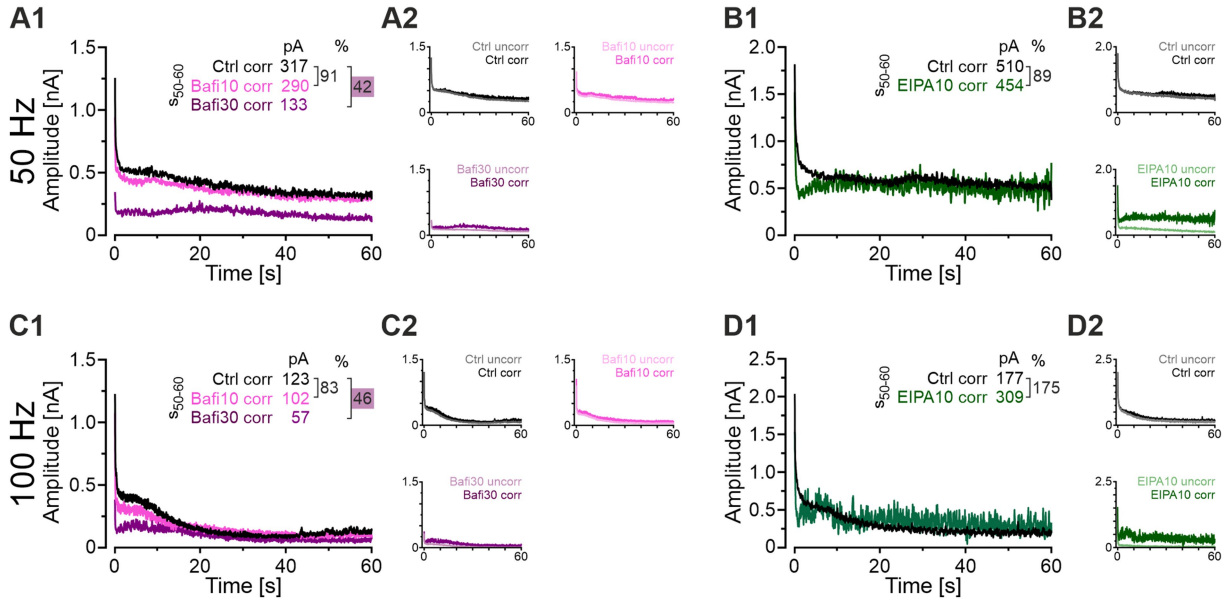


FIGURE 11
When AP failures are corrected, EIPA no longer affects synaptic transmission. **(A1)** Time course of eIPSC mean peak amplitudes upon AP correction for Ctrl (black), Bafi10 (magenta), and Bafi30 (purple) during 50-Hz|60-s challenge. Upper right numbers indicate the mean corrected amplitudes during $s_{50\text{-}60}$ and the percentages (e.g., $\frac{133}{317}$ = 42%). Ratios < 50% are highlighted in purple. **(A2)** Time course of corrected amplitudes (dark color) and uncorrected amplitudes (light color) for Ctrl (upper left), Bafi10 (upper right), and Bafi30 (lower left). **(B1)** Same as **(A1)**, but for EIPA10 (green). **(B2)** Same as **(A2)**, but for Ctrl (top) and EIPA (bottom). **(C1–D2)** Same as **(A1–B2)**, but for 100 Hz. Variables on the left y-axis in **(A2,B2,C2,D2)** are the same as in **(A1)**. Note the different amplitude scaling in **(B1,B2,D1,D2)**. See Supplementary Table S13 for details.

eIPSCs only after prolonged drug application (≥30 min; Figures 3, 4; Supplementary Figures S3, S4). (3) However, the amplitude reduction is only moderate, so that transmission remains at a level of ~30%. (4) In line with the amplitude reduction, the quantal size *q* is reduced, but only to ~70% and only after prolonged blocker use (Figure 6; Supplementary Figure S4E3). (5) The ability to recover from synaptic depression is maintained in the presence of any V-ATPase blocker (Figure 5; Supplementary Figure S4). (6) Even when the drug concentration is increased and the stimulus conditions are most severe (half-marathon), Bafi10 effects are only evident after > 12,000 stimulus pulses (Figure 7). This further demonstrates the resistance of MNTB-LSO synapses to pharmacological treatment. (7) Application of EIPA to block NHE activity greatly reduces AP fidelity and thus affects neurotransmission (Figure 9). However, after correction of the AP failures, the hypothesis that EIPA affects SV refilling cannot be maintained (Figures 10, 11). Collectively, these major results suggest that effective SV refilling at MNTB-LSO synapses, especially under harsh stimulus conditions, does not depend solely on V-ATPase activity. Rather, another mechanism likely coexists that provides an H^+ source for VIAAT and thus helps to generate SVs with a sufficiently high glycine content.

Discussion

In the present study, we investigated the robustness of sustained synaptic transmission at inhibitory glycinergic synapses in the auditory brainstem, thereby emphasizing the role of SV refilling. To this end, we applied the drugs Bafi, Foli and EIPA to acute mouse brainstem slices and performed whole-cell patch-clamp experiments with long-lasting high-frequency stimulation (minute range, up to 200 Hz). The major results are summarized at the end of the Results section. They demonstrate an important role for the V-ATPase blockers Bafi and Foli, thereby confirming the importance of this pump in generating the H^+ gradient that VIAAT utilizes to (re-)fill SVs. However, despite rigorous treatment and stimulation conditions, the blocking effects were only moderate, an unexpected outcome. The incomplete block suggests that proper V-ATPase activity at MNTB-LSO inputs is necessary but not sufficient for maintaining transmission. When examining the effects of EIPA on NHE(6) activity, we observed adverse side effects, namely profound blockade of APs. This indicates that EIPA is unsuitable for specifically targeting vacuolar NHE transport activity. These findings prompt further investigation into the potential contribution of other H^+ transporters, beyond the V-ATPase, in supplying H^+ ions to fuel VIAAT and thereby ensuring adequate loading of SVs with neurotransmitter molecules.

Incomplete blocking of V-ATPase is unlikely to explain the moderate impairment at MNTB-LSO synapses

We argue that an incomplete pharmacological block of V-ATPase activity does not satisfactorily explain the persistence of transmission at MNTB-LSO synapses. Persistence was evident from substantial steady-state amplitudes, preserved quantal size, and recovery from depression. Notably, Bafi had to be applied for >30 min before its effect reached statistical significance (Figures 3–6; Protocol 1). Furthermore, relatively high concentrations of Bafi were required to elicit an effect (2 μM in Protocol 1; 5 μM in Protocol 2). Similar results were obtained with Foli (1 μM in Protocol 1; Supplementary Figure S3). The available literature supports this view. *In vitro* studies on dissociated cells,

including primary neuron cultures, have used Bafi concentrations ranging from 0.25–4 μM (Granseth and Lagnado, 2008; Li et al., 2011; Peng et al., 2012; Ratnayaka et al., 2012; Santos et al., 2013; Siksou et al., 2013; Vargas et al., 2014; Di Giovanni and Sheng, 2015; Tang et al., 2015; Tagliatti et al., 2020). Comparable concentrations were used in organotypic culture studies (0.2–2 μM; Rose et al., 2013; Allain et al., 2016), purified synaptosomes (1 μM; Geerlings et al., 2001), acute brain slices (1–6 μM; Zhou et al., 2000; Harrison and Jahr, 2003; Satake et al., 2012; Muller et al., 2013; Song et al., 2013), an *ex vivo* optic nerve preparation (4 μM; Micu et al., 2016), and whole-larvae Zebra fish neuroblasts (1 μM; Einhorn et al., 2012). These concentrations are ~1,000 times higher than the K_i values for Bafi, which lie in the (sub-)nanomolar range (reviewed in Dröse and Altendorf, 1997). In most of the 20 cited studies, pretreatment with Bafi lasted only 30 s or 1–10 min (when specified). The five acute brain slice studies reported longer incubation times of 1 to ≥2.5 h. Thus, our drug application protocols appear reasonably consistent with established experimental parameters. Further support for complete V-ATPase block by Bafi comes from preliminary results demonstrating a gradual decline of eIPSC amplitudes when MNTB-LSO synapses are continuously stimulated at 1 Hz for ~40 min. These results predict an eventual abolishment of transmission and complete exhaustion of the releasable SV pool after ~51 min (see Supplementary Information).

How do our results compare with those from other synaptic systems?

A comparison of our drug-related results with those obtained in other synaptic systems reveals both similarities and striking differences (Table 1). Regarding the effects of V-ATPase inhibition on spontaneously released SVs, only one study reported a complete loss of events (Song et al., 2013), whereas most found moderately reduced *q* values. This suggests that across synaptic systems, transmitter-filled SVs remain available when V-ATPase activity is inhibited. Notably, drug-treated MNTB-LSO synapses displayed much smaller effects on sPSC frequency than other synapse types.

Far fewer studies have investigated evoked transmission during sustained high-frequency stimulation. At calyx of Held-MNTB synapses, V-ATPase inhibition did not completely abolish responses but reduced them to 10% of control during intense stimulation at 20 Hz for 400 s (Qiu et al., 2015). Thus, it appears that these auditory synapses also exhibit partial resistance to V-ATPase blockade, though less so than MNTB-LSO synapses, where steady-state transmission remained at ~25%. Taken together, we conclude that SV replenishment relies on both common and system-specific mechanisms. The persistence of transmission at both auditory synapse types, even under strong stimulation, points to an additional mechanism that ensures reliable SV (re-)filling at these high-fidelity synapses.

MNTB-LSO synapses are unlikely to use a large reserve pool to efficiently replenish the RRP

During Protocol 1, we delivered 21,600 stimulus pulses. In the absence of Bafi, MNTB-LSO synapses reached a cumulative eIPSC amplitude of 2,842 nA (Figure 4E2). Combined with a mean *q* value of 26 pA (Figure 6C3), this corresponds to ~109,000 released SVs. Given that N_{RRP} comprised 434 SVs (Figure 6D2), the RRP was turned over ~250 times. Analysis of the Foli experiments yielded similar results, with ~190,000 released SVs and ~230 RRP turnovers. Sustaining neurotransmission at such levels requires highly efficient replenishment mechanisms, with candidate resources being the recycling pool and the reserve pool. The recycling pool is generally thought to contain ~5–20% of all SVs, whereas the reserve pool forms the largest reservoir (~80–90%; Rizzoli and Betz, 2005). The RRP typically accounts for only ~1–2%. For MNTB-LSO synapses, specific pool sizes have not been determined. However, estimates from calyx of Held-MNTB synapses suggest ~180,000 SVs in the reserve pool, ~7,000 in the recycling pool, and ~3,000 in the RRP (95, 3.5, and 1.5% of the total pool, respectively; Rizzoli and Betz, 2005). If a similar distribution applies to MNTB-LSO synapses, the total SV pool would contain only ~29,000 SVs. Consequently, the release of 109,000 or more SVs cannot be explained by consumption of a pre-existing reserve. Instead, replenishment must exceed the size of the total pool nearly 4-fold during the four minutes. In this context, it is noteworthy that the entire recycling pool of hippocampal synapses is exocytosed within ~20 s during 10-Hz stimulation (200 stimulus pulses; Fernández-Alfonso and Ryan, 2004), and ~40% of the total SV pool participates in recycling (Fernández-Alfonso and Ryan, 2006).

In our Bafi and Foli experiments, we aimed to block V-ATPase to prevent the reacidification of SVs in the recycling pool. In this scenario, endocytosed SVs remain trapped in an alkaline state, thereby preventing neurotransmitter reloading and rendering them unable to replenishment the RRP (Sankaranarayanan and Ryan, 2001). Results from the Bafi30 experiments showed a cumulative eIPSC amplitude of 927 nA, 33% of the Ctrl value (Figure 4E2). With a *q* value of 19 pA and an N_{RRP} of 125 SVs (Figures 6C1–C5,D2), this corresponds to ~49,000 released SVs and a 392-fold RRP turnover (compared to a 250-fold turnover in the Ctrl). Again, we conclude that such robust replenishment cannot be explained by recruitment from the reserve pool alone, nor by *de novo* synthesis. Transport of SVs from the soma to the axon terminal would occur on a time scale of hours, far too slow to sustain transmission under acute synaptic stress. In the following section, we will discuss an alternative scenario.

An additional H^+ pump system besides the V-ATPase is likely at MNTB-LSO synapses

We propose that SVs are reacidified by additional H^+ transporters besides the V-ATPases, and we suggest that NHEs are strong candidates (Figure 12). *Slc9a6*, the gene encoding NHE6, exhibited the highest expression level, similarly high as that of *Slc32a1* (VIAAT). Prominent immunoreactivity in MNTB axon terminals targeting LSO somata provides further support (Figure 8). Since NHE2–NHE5 expression was not detected in either region, NHE6 appears to be the most likely candidate. However, pharmacological attempts to block NHE activity with the antagonist EIPA were confounded by adverse effects on AP generation, preventing specific assessment. We acknowledge that functional evidence for NHE6's role in SV acidification is lacking, and our immunohistochemical and gene expression data alone are insufficient to confirm its involvement.

TABLE 1 Synaptic transmission upon pharmacological blockade of the H^+ pump V-ATPase with Bafi or Foli.

Synaptic system	Drug conditions	Analysis of spontaneous events		Analysis of evoked responses					Reference
		q (mPSC amplitude)	sPSC frequency	Stimulus conditions	Steady-state ePSC amplitude	TR (transmission rate)	FR (fractional recovery)	N_{RRP} (readily releasable pool)	
MNTB – LSO acute slices	2 µM Bafi, > 30 min	**100:77** Ctrl 26 pA, Drug 20 pA	**100:60** Ctrl 5.7 s^{-1}, Drug 3.4 s^{-1}	50 Hz | 60 s	**100:25** Ctrl 267 pA, Drug 88 pA	**100:35** Ctrl 17 nA/s, Drug 6 nA/s	**100:87** Ctrl 111%, Drug 66%	**100:29** Ctrl 434 SV, Drug 125 SV	Current study
MNTB – LSO acute slices	1 µM Foli, > 30 min	**100:54** Ctrl 24 pA, Drug 13 pA	**100:85** Ctrl 5.9 s^{-1}, Drug 5.0 s^{-1}	50 Hz | 60 s	**100:26** Ctrl 504 pA, Drug 126 pA	**100:29** Ctrl 29 nA/s, Drug 8 nA/s	**100:39** Ctrl 103%, Drug 40%	**100:45** Ctrl 832 SV, Drug 374 SV	Current study
Hippocampal neurons acute slices	4 µM Bafi, ≥ 2.5 h	**100:0** Ctrl 3 pA, Drug 0 pA	**100:0** Ctrl 1 s^{-1}, Drug 0 s^{-1}						Song et al. (2013)
Cerebellar neurons acute slices	1 µM Bafi, > 1 h	**100:55** Ctrl 55 pA, Drug 30 pA							Satake et al. (2012)
Cerebellar Purkinje cells acute slices	2 µM Bafi, ≥ 1 h		**100:9** Ctrl 4.9 s^{-1}, Drug 0.43 s^{-1}						Harrison and Jahr (2003)
Calyx of Held – MNTB acute slices	2 µM Foli, > 2.5 h			20 Hz | 400 s	**100:10** Ctrl 971 pA, Drug 99 pA	Ctrl 860 SVs/s Drug not available		Ctrl 2,196 SVs Drug not available	Qiu et al. (2015)
Hippocampal neurons primary cell culture	67 nM Foli, 15-20 min 2 min in 46 mM K^+	**100:92** Ctrl 26 pA, Drug 24 pA	**100:10** Ctrl 7.8 s^{-1}, Drug 0.8 s^{-1}						Groemer and Klingauf (2007)
Hippocampal neurons acute slices	1 µM Bafi, > 2 h	**100:80** Ctrl 13.7 pA, Drug 11.0 pA	**100:6** Ctrl 1.7 s^{-1}, Drug 0.1 s^{-1}						Zhou et al. (2000)
Hippocampal neurons autapses	1 µM Bafi, 1 h	**100:59** Ctrl 21.0 pA, Drug 12.3 pA	**100:11** Ctrl 12.7 s^{-1}, Drug 1.4 s^{-1}						
Hippocampal neurons dissociated cultures	67 nM Foli, 10 min	**100:80** Ctrl 13 pA, Drug 10 pA	**100:17** Ctrl 6 s^{-1}, Drug 1 s^{-1}	low frequency no details	**100:75** Ctrl 1.6 nA, Drug 1.2 nA				Sara et al. (2005)

The table confronts the results of the present study to those of seven previous reports. All parameters ($n = 7$) were assessed via electrophysiological recordings. Notice the paucity of evoked response analyses in the literature. For simplicity reasons, data presentation for MNTB-LSO synapses is restricted to 50 Hz | 60 s and to long drug treatment (> 30 min). Ratios (in bold, Ctrl = 100%) are given to facilitate direct comparisons.

10.3389/fncel.2025.1625868

We therefore propose the following hypothetical scenario, which aligns with existing literature across various synaptic systems (Kononenko and Haucke, 2015). After AP-triggered SV fusion and rapid transmitter release, SV membranes are retrieved and SVs via either classical clathrin-mediated endocytosis or clathrin-independent ultrafast endocytosis (Brockmann and Rosenmund, 2016; Eddings and Watanabe, 2025). The former occurs with a time constant of ~10 s, while the latter can proceed within hundreds of milliseconds (Dittman and Ryan, 2009; Soykan et al., 2017; Watanabe and Boucrot, 2017) or even faster (<100 ms; Watanabe et al., 2013; Delvendahl and Hallermann, 2016). In addition, activity-dependent bulk endocytosis, similar to micropinocytosis, can occur (Camblor-Perujo and Kononenko, 2021). Subsequently, reacidification takes place locally with time constants of 4–40 s (Atluri and Ryan, 2006; Egashira et al., 2015). NHEs could mediate rapid reacidification, particularly during heavy synaptic activity. In hippocampal synapses, a full exo-endocytosis cycle ~30 s (Fernández-Alfonso and Ryan, 2006), but can be as short as 15 s (Ryan and Smith, 1995; Hori and Takahashi, 2012). In the auditory brainstem, it may be faster. A recent article by Gallimore et al. (2025) provides further insight into the complete SV cycle.

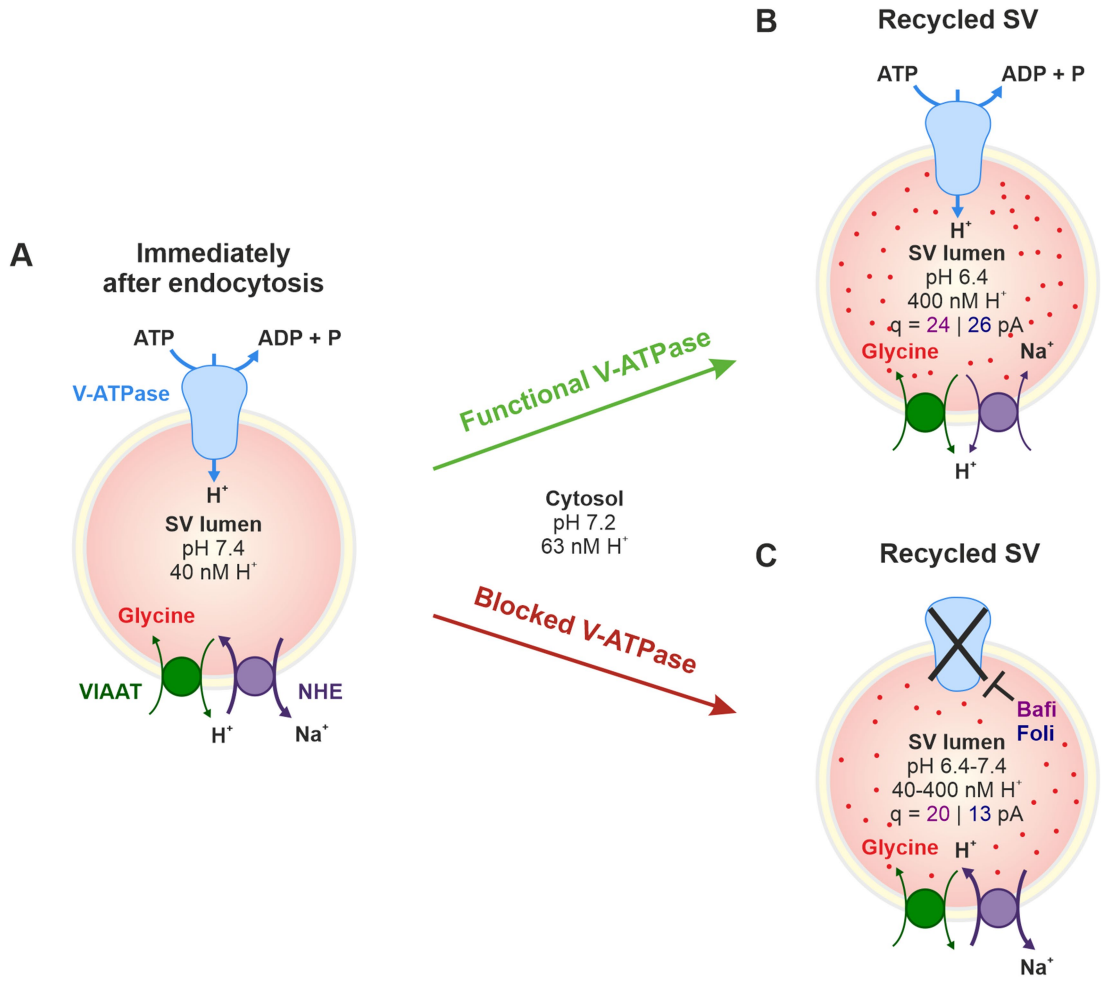


FIGURE 12
Schematic of the SV acidification mechanism proposed in the present study. **(A)** Immediately after endocytosis, the lumen of a recycling SV is filled with extracellular fluid (~150 mM Na^+; pH = 7.4, corresponding to 40 nM H^+). In addition, the SV is virtually free of glycine (no red dots). Key components for SV acidification and neurotransmitter filling are the V-ATPase (blue) and the VIAAT (green). By pumping H^+ into the lumen, the V-ATPase generates an electrochemical gradient across the SV membrane which provides the driving force that is used by the VIAAT to load the SV with glycine, which is a zwitter ion. To regulate the electrochemical gradient, additional transport mechanisms are involved, such as H^+/Na^+ exchangers (NHE, purple). An interesting candidate is NHE6, which is highly immunopositive in glycinergic MNTB axon terminals (see Figure 8). We propose that NHE(6) operates in reverse mode immediately after endocytosis. Expelling Na^+ from the SV while importing H^+ promotes H^+-coupled glycine antiport by VIAAT and thus glycine loading. **(B)** Under normal SV refilling conditions, V-ATPase-mediated H^+ pumping results in an intraluminal pH of 6.4 (400 nM H^+, Egashira et al., 2016). The present study revealed quantal sizes q of 24 pA in the $Ctrl_{Bafi}$ cohort and of 26 pA in the $Ctrl_{Foli}$ cohort (see Figure 6C3; Supplementary Figure S4E3). **(C)** The present study also revealed that blockade of V-ATPase activity with Bafi or Foli reduces, but does not abolish, sustained high-frequency transmission at MNTB-LSO synapses. Therefore, SV replenishment is not solely dependent on V-ATPase. V-ATPase blockade resulted in a ~ 20% lower q value in Bafi30 ($\frac{20\,pA\,Bafi30}{24\,pA\,Ctrl_{Bafi}}$ = 83%; see Figure 6C3) and a 50% lower q value in Foli30 ($\frac{13\,pA\,Foli30}{26\,pA\,Ctrl_{Foli}}$ = 50%; see Supplementary Figure S4E3). The scenario evaluates a hypothetical role for NHE(6) in intraluminal H^+ transport. It provides an alternative mechanism for SV acidification that partially compensates for the blockade of V-ATPase function.

As noted above, SVs refilling takes tens of seconds. One might argue that the rapid recovery observed after high-frequency stimulation in Bafi-treated synapses (within a few seconds; Figure 5) is inconsistent with this time course. However, steady-state amplitudes during challenge were determined in the $s_{50\text{-}60}$ window. Therefore, SVs endocytosed early (e.g., at $s_{5\text{-}25}$) could have recycled within 25–55 s, consistent with published data.

In our proposed dual-transporter model, vacuolar NHEs operate under highly favorable conditions for transporting H^+ into the SV lumen. Immediately after endocytosis, the lumen contains extracellular fluid. Hence, luminal [Na^+] (which was 153 mM in our ACSF) is ~30-fold higher than in the cytosol, driving Na^+ efflux from the SVs. Because NHEs are antiporters, this drives H^+ influx into the lumen, promoting reacidification. In addition, the luminal pH immediately after endocytosis is 7.4, compared to a cytosolic pH of 7.2, corresponding to a ~ 1.6-fold lower luminal [H^+] (40 vs. 63 nM). This gradient also favors H^+ entry into the lumen, an effect even more pronounced when V-ATPase activity is absent. Interestingly and perhaps surprisingly, a luminal pH of 7.4 corresponds to only 0.000275 free H^+ ions per SV. A single free H^+ ion in the SV lumen would result in pH 4 (Preobraschenski et al., 2014). However, the SV lumen has a buffer capacity of ~57 mM/pH, provided by vesicle proteins, ATP, and transmitter molecules (Edwards, 2007), which allows storage of ~1,200 H^+ ions per SV (Egashira et al., 2015).

The equilibrium situation illustrated in Figure 1 is also relevant for NHE-mediated ion transport at rest. At a luminal pH of 6.4 versus a cytosolic pH of 7.2, the H^+ gradient favors efflux from the SV. NHE activity under these conditions would dissipate the H^+ gradient, counteract V-ATPase activity, and regulate alkalinization (Ouyang et al., 2013; Takamori, 2016). Further studies are needed to clarify the role of additional H^+ transporters beyond V-ATPase in supplying protons to VIAAT, thereby ensuring sufficient SV filling, particularly during prolonged high-frequency activity. This issue applies to both inhibitory and excitatory synapses (Goh et al., 2011; Huang and Trussell, 2014; Lee et al., 2021).

Finally, in addition to NHE6, neurotransmitter transporter 4 (NTT4, also known as XT1 or B0AT3), might also contribute to SV refilling with glycine when the proton-motive force generated by the V-ATPase is diminished or absent. NTT4, encoded by *Slc6A17,* is exclusively expressed in the nervous system and associated with neuronal SVs (El Mestikawy et al., 1997; Fischer et al., 1999; Masson et al., 1999; Zaia and Reimer, 2009). Immunoreactivity has been demonstrated in both excitatory and inhibitory neurons (Hägglund et al., 2013). NTT4 catalyzes the transport of neutral amino acids, including glycine (Parra et al., 2008; Nicoli et al., 2025). Importantly, NTT4 is a sodium-dependent symporter that is inhibited by low pH (Zaia and Reimer, 2009), making it ideally suited for the initial stages of SV refilling (see Figure 12).

Outlook

Several important questions remain open, leaving ample room for future experimentation. First, does sustained high-frequency stimulation after pharmacological inactivation of V-ATPase completely abolish neurotransmission in systems other than the MNTB-LSO synapses described here? Is the resilience in SV refilling unique to the auditory system, or does it extend to other robust, high-frequency synapses such as cerebellar mossy fiber-granule cell synapses (Delvendahl and Hallermann, 2016)? Could it even represent a more general property of synapses? Second, does NHE(6) directly contribute to refilling? This question requires functional evidence from assays employing specific NHE(6) antagonists or gene silencing. Third, are there additional vesicular transporters that maintain transmitter supply during high-frequency synaptic activity? Finally, can the robustness and resilience of neurotransmission at MNTB-LSO synapses be substantiated at the ultrastructural level using functional electron microscopy? Answering this question will require technically demanding "flash and freeze" or "zap and freeze" methods (Vandael and Jonas, 2024; Eddings and Watanabe, 2025).

Data availability statement

The original contributions presented in the study are included in the article/Supplementary material, further inquiries can be directed to the corresponding author.

Ethics statement

The animal study was approved by German Animal Welfare Act (TSchG §4/3) of Rhineland-Palatinate. The study was conducted in accordance with the local legislation and institutional requirements.

Author contributions

EP: Validation, Formal analysis, Visualization, Writing – review & editing, Conceptualization, Investigation. LH: Investigation, Validation, Formal analysis, Writing – review & editing, Visualization. AS: Formal analysis, Methodology, Writing – review & editing. EF: Writing – review & editing, Project administration, Supervision, Writing – original draft, Funding acquisition, Conceptualization, Resources.

Funding

The author(s) declare that financial support was received for the research and/or publication of this article. The project has received funding from the BMBF/NIDCD grant 01GQ2001 (ModSynTrans) to EF. Support by NIH/NIDCD grant R01DC019268 is acknowledged by AS.

Acknowledgments

The authors thank Jennifer Klein and Tina Kehrwald for excellent technical support and Ekkehard Neuhaus for granting us access to a TCS SP5 X confocal microscope. They further thank Jonas Fisch for helpful comments on a late version of the manuscript.

Conflict of interest

The authors declare that the research was conducted in the absence of any commercial or financial relationships that could be construed as a potential conflict of interest.

Generative AI statement

The authors declare that no Gen AI was used in the creation of this manuscript.

Any alternative text (alt text) provided alongside figures in this article has been generated by Frontiers with the support of artificial intelligence and reasonable efforts have been made to ensure accuracy, including review by the authors wherever possible. If you identify any issues, please contact us.

Publisher's note

All claims expressed in this article are solely those of the authors and do not necessarily represent those of their affiliated organizations, or those of the publisher, the editors and the reviewers. Any product that may be evaluated in this article, or claim that may be made by its manufacturer, is not guaranteed or endorsed by the publisher.

Supplementary material

The Supplementary material for this article can be found online at: https://www.frontiersin.org/articles/10.3389/fncel.2025.1625868/full#supplementary-material

References

Alabi, A. A., and Tsien, R. W. (2012). Synaptic vesicle pools and dynamics. *Cold Spring Harb. Perspect. Biol.* 4:a013680. doi: 10.1101/cshperspect.a013680

Alexander, S. P., Kelly, E., Marrion, N. V., Peters, J. A., Faccenda, E., Harding, S. D., et al. (2017). The concise guide to pharmacology 2017/18: transporters. *Br. J. Pharmacol.* 174, S360–S446. doi: 10.1111/bph.13883

Alexander, S. P., Mathie, A., and Peters, J. A. (2011). Guide to receptors and channels (GRAC), 5th edition. *Br. J. Pharmacol.* 164, S1–S324. doi: 10.1111/j.1476-5381.2011.01649_1.x

Allain, A. E., Cazenave, W., Delpy, A., Exertier, P., Barthe, C., Meyrand, P., et al. (2016). Nonsynaptic glycine release is involved in the early KCC2 expression. *Dev. Neurobiol.* 76, 764–779. doi: 10.1002/dneu.22358

Anne, C., and Gasnier, B. (2014). Vesicular neurotransmitter transporters: mechanistic aspects. *Curr. Top. Membr.* 73, 149–174. doi: 10.1016/b978-0-12-800223-0.00003-7

Apostolides, P. F., and Trussell, L. O. (2013). Rapid, activity-independent turnover of vesicular transmitter content at a mixed glycine/GABA synapse. *J. Neurosci.* 33, 4768–4781. doi: 10.1523/JNEUROSCI.5555-12.2013

Atluri, P. P., and Ryan, T. A. (2006). The kinetics of synaptic vesicle reacidification at hippocampal nerve terminals. *J. Neurosci.* 26, 2313–2320. doi: 10.1523/JNEUROSCI.4425-05.2006

Aubrey, K. R., Rossi, F. M., Ruivo, R., Alboni, S., Bellenchi, G. C., Le Goff, A., et al. (2007). The transporters GlyT2 and VIAAT cooperate to determine the vesicular glycinergic phenotype. *J. Neurosci.* 27, 6273–6281. doi: 10.1523/JNEUROSCI.1024-07.2007

Bowman, E. J., Siebers, A., and Altendorf, K. (1988). Bafilomycins: a class of inhibitors of membrane ATPases from microorganisms, animal cells, and plant cells. *Proc. Natl. Acad. Sci. USA* 85, 7972–7976. doi: 10.1073/pnas.85.21.7972

Brett, C. L., Wei, Y., Donowitz, M., and Rao, R. (2002). Human Na^+/H^+ exchanger isoform 6 is found in recycling endosomes of cells, not in mitochondria. *Am. J. Physiol. Cell Physiol.* 282, C1031–C1041. doi: 10.1152/ajpcell.00420.2001

Brill, S. E., Janz, K., Singh, A., and Friauf, E. (2019). Considerable differences between auditory medulla, auditory midbrain, and hippocampal synapses during sustained high-frequency stimulation: exceptional vesicle replenishment restricted to sound localization circuit. *Hear. Res.* 381:107771. doi: 10.1016/j.heares.2019.07.008

Brill, S. E., Maraslioglu, A., Kurz, C., Kramer, F., Fuhr, M. F., Singh, A., et al. (2021). Glycinergic transmission in the presence and absence of functional GlyT2: lessons from the auditory brainstem. *Front. Synaptic Neurosci.* 12:560008. doi: 10.3389/fnsyn.2020.560008

Brockmann, M. M., and Rosenmund, C. (2016). Catching up with ultrafast endocytosis. *Neuron* 90, 423–424. doi: 10.1016/j.neuron.2016.04.027

Bruns, D., and Jahn, R. (1995). Real-time measurement of transmitter release from single synaptic vesicles. *Nature* 377, 62–65. doi: 10.1038/377062a0

Burger, P. M., Mehl, E., Cameron, P. L., Maycox, P. R., Baumert, M., Lottspeich, F., et al. (1989). Synaptic vesicles immunoisolated from rat cerebral cortex contain high levels of glutamate. *Neuron* 3, 715–720. doi: 10.1016/0896-6273(89)90240-7

Camblor-Perujo, S., and Kononenko, N. L. (2021). Brain-specific functions of the endocytic machinery. *FEBS J.* 289, 2219–2246. doi: 10.1111/febs.15897

Chaudhry, F. A., Boulland, J.-L., Jenstad, M., Bredahl, M. K. L., and Edwards, R. H. (2008). "Pharmacology of neurotransmitter transport into secretory vesicles" in Pharmacology of neurotransmitter release. Handbook of experimental pharmacology. eds. T. C. Südhof and K. Starke (Berlin Heidelberg: Springer-Verlag).

Clarkson, C., Antunes, F. M., and Rubio, M. E. (2016). Conductive hearing loss has long-lasting structural and molecular effects on presynaptic and postsynaptic structures of auditory nerve synapses in the cochlear nucleus. *J. Neurosci.* 36, 10214–10227. doi: 10.1523/JNEUROSCI.0226-16.2016

Clements, J. D. (1996). Transmitter timecourse in the synaptic cleft: its role in central synaptic function. *TINS* 19, 163–171. doi: 10.1016/s0166-2236(96)10024-2

Costes, S. V., Daelemans, D., Cho, E. H., Dobbin, Z., Pavlakis, G., and Lockett, S. (2004). Automatic and quantitative measurement of protein-protein colocalization in live cells. *Biophys. J.* 86, 3993–4003. doi: 10.1529/biophysj.103.038422

Danbolt, N. C. (2001). Glutamate uptake. *Prog. Neurobiol.* 65, 1–105. doi: 10.1016/s0301-0082(00)00067-8

Delvendahl, I., and Hallermann, S. (2016). The cerebellar mossy fiber synapse as a model for high-frequency transmission in the mammalian CNS. *TINS* 39, 722–737. doi: 10.1016/j.tins.2016.09.006

Di Giovanni, J., and Sheng, Z. H. (2015). Regulation of synaptic activity by snapin-mediated endolysosomal transport and sorting. *EMBO J.* 34, 2059–2077. doi: 10.15252/embj.201591125

Dittman, J., and Ryan, T. A. (2009). Molecular circuitry of endocytosis at nerve terminals. *Annu. Rev. Cell Biol.* 25, 133–160. doi: 10.1146/annurev.cellbio.042308.113302

Dröse, S., and Altendorf, K. (1997). Bafilomycins and concanamycins as inhibitors of V-ATPases and P-ATPases. *J. Exp. Biol.* 200, 1–8. doi: 10.1242/jeb.200.1.1

Eddings, C. R., and Watanabe, S. (2025). Ultrafast endocytosis in mouse cortical inhibitory synapses. *bioRxiv*. doi: 10.1101/2025.06.06.658279

Edwards, R. H. (2007). The neurotransmitter cycle and quantal size. *Neuron* 55, 835–858. doi: 10.1016/j.neuron.2007.09.001

Egashira, Y., Takase, M., and Takamori, S. (2015). Monitoring of vacuolar-type H^+ ATPase-mediated proton influx into synaptic vesicles. *J. Neurosci.* 35, 3701–3710. doi: 10.1523/jneurosci.4160-14.2015

Egashira, Y., Takase, M., Watanabe, S., Ishida, J., Fukamizu, A., Kaneko, R., et al. (2016). Unique pH dynamics in GABAergic synaptic vesicles illuminates the mechanism and kinetics of GABA loading. *Proc. Natl. Acad. Sci. USA* 113, 10702–10707. doi: 10.1073/pnas.1604527113

Einhorn, Z., Trapani, J. G., Liu, Q., and Nicolson, T. (2012). Rabconnectin3alpha promotes stable activity of the H+ pump on synaptic vesicles in hair cells. *J. Neurosci.* 32, 11144–11156. doi: 10.1523/jneurosci.1705-12.2012

El Mestikawy, S., Wehrlé, R., Masson, J., Lombard, M. C., Hamon, M., and Sotelo, C. (1997). Distribution pattern and ultrastructural localization of Rxt1, an orphan Na^+/cl^--dependent transporter, in the central nervous system of rats and mice. *Neuroscience* 77, 319–333. doi: 10.1016/s0306-4522(96)00466-6

Elmqvist, D., and Quastel, D. M. (1965). A quantitative study of end-plate potentials in isolated human muscle. *J. Physiol.* 178, 505–529. doi: 10.1113/jphysiol.1965.sp007639

Eulenburg, V., Armsen, W., Betz, H., and Gomeza, J. (2005). Glycine transporters: essential regulators of neurotransmission. *Trends Biochem. Sci.* 30, 325–333. doi: 10.1016/j.tibs.2005.04.004

Fernández-Alfonso, T., and Ryan, T. A. (2004). The kinetics of synaptic vesicle pool depletion at CNS synaptic terminals. *Neuron* 41, 943–953. doi: 10.1016/S0896-6273(04)00113-8

Fernández-Alfonso, T., and Ryan, T. A. (2006). The efficiency of the synaptic vesicle cycle at central nervous system synapses. *Trends Cell Biol.* 16, 413–420. doi: 10.1016/j.tcb.2006.06.007

Fischer, J., Bancila, V., Mailly, P., Masson, J., Hamon, M., El Mestikawy, S., et al. (1999). Immunocytochemical evidence of vesicular localization of the orphan transporter RXT1 in the rat spinal cord. *Neuroscience* 92, 729–743. doi: 10.1016/s0306-4522(99)00017-2

Fischer, A. U., Müller, N. I. C., Deller, T., Del Turco, D., Fisch, J. O., Griesemer, D., et al. (2019). GABA is a modulator, rather than a classical transmitter, in the medial nucleus of the trapezoid body-lateral superior olive sound localization circuit. *J. Physiol.* 597, 2269–2295. doi: 10.1113/jp277566

Forgac, M. (2007). Vacuolar ATPases: rotary proton pumps in physiology and pathophysiology. *Nat. Rev. Mol. Cell Biol.* 8, 917–929. doi: 10.1038/nrm2272

Freche, D., Pannasch, U., Rouach, N., and Holcman, D. (2011). Synapse geometry and receptor dynamics modulate synaptic strength. *PLoS One* 6:e25122. doi: 10.1371/journal.pone.0025122

Friauf, E., Aragon, C., Löhrke, S., Westenfelder, B., and Zafra, F. (1999). Developmental expression of the glycine transporter GLYT2 in the auditory system of rats suggests involvement in synapse maturation. *J. Comp. Neurol.* 412, 17–37. doi: 10.1002/(SICI)1096-9861(19990913)412:1%3C17::AID-CNE2%3E3.0.CO;2-E

Friauf, E., Fischer, A. U., and Fuhr, M. F. (2015). Synaptic plasticity in the auditory system: a review. *Cell Tissue Res.* 361, 177–213. doi: 10.1007/s00441-015-2176-x

Friauf, E., Krächan, E. G., and Müller, N. I. C. (2019). "Lateral superior olive" in The Oxford handbook of the auditory brainstem. ed. K. Kandler (New York: Oxford University Press).

Galarreta, M., and Hestrin, S. (1998). Frequency-dependent synaptic depression and the balance of excitation and inhibition in the neocortex. *Nat. Neurosci.* 1, 587–594. doi: 10.1038/2822

Gallimore, A. R., Hepburn, I., Georgiev, S. V., Rizzoli, S. O., and De Schutter, E. (2025). Dynamic regulation of vesicle pools in a detailed spatial model of the complete synaptic vesicle cycle. *Sci. Adv.* 11:eadq6477. doi: 10.1126/sciadv.adq6477

Geerlings, A., Núñez, E., López-Corcuera, B., and Aragón, C. (2001). Calcium- and syntaxin 1-mediated trafficking of the neuronal glycine transporter GLYT2. *J. Biol. Chem.* 276, 17584–17590. doi: 10.1074/jbc.M010602200

Goh, G. Y., Huang, H., Ullman, J., Borre, L., Hnasko, T. S., Trussell, L. O., et al. (2011). Presynaptic regulation of quantal size: K^+/H^+ exchange stimulates vesicular glutamate transport. *Nat. Neurosci.* 14, 1285–1292. doi: 10.1038/nn.2898

Granseth, B., and Lagnado, L. (2008). The role of endocytosis in regulating the strength of hippocampal synapses. *J. Physiol.* 586, 5969–5982. doi: 10.1113/jphysiol.2008.159715

Groemer, T. W., and Klingauf, J. (2007). Synaptic vesicles recycling spontaneously and during activity belong to the same vesicle pool. *Nat. Neurosci.* 10, 145–147. doi: 10.1038/nn1831

Hägglund, M. G., Hellsten, S. V., Bagchi, S., Ljungdahl, A., Nilsson, V. C., Winnergren, S., et al. (2013). Characterization of the transporterB^0AT3 (Slc6a17) in the rodent central nervous system. *BMC Neurosci.* 14:54. doi: 10.1186/1471-2202-14-54

Harlos, P., Lee, D. A., and Stadler, H. (1984). Characterization of a Mg^{2+}-ATPase and a proton pump in cholinergic synaptic vesicles from the electric organ of *Torpedo marmorata*. *Eur. J. Biochem.* 144, 441–446. doi: 10.1111/j.1432-1033.1984.tb08485.x

Harrison, J., and Jahr, C. E. (2003). Receptor occupancy limits synaptic depression at climbing fiber synapses. *J. Neurosci.* 23, 377–383. doi: 10.1523/jneurosci.23-02-00377.2003

Hirtz, J. J., Braun, N., Griesemer, D., Hannes, C., Janz, K., Löhrke, S., et al. (2012). Synaptic refinement of an inhibitory topographic map in the auditory brainstem requires functional $Ca_v1.3$ calcium channels. *J. Neurosci.* 32, 14602–14616. doi: 10.1523/JNEUROSCI.0765-12.2012

Hori, T., and Takahashi, T. (2012). Kinetics of synaptic vesicle refilling with neurotransmitter glutamate. *Neuron* 76, 511–517. doi: 10.1016/j.neuron.2012.08.013

Hori, T., and Takamori, S. (2021). Physiological perspectives on molecular mechanisms and regulation of vesicular glutamate transport: lessons from calyx of held synapses. *Front. Cell. Neurosci.* 15:811892. doi: 10.3389/fncel.2021.811892

Huang, H., and Trussell, L. O. (2014). Presynaptic HCN channels regulate vesicular glutamate transport. *Neuron* 84, 340–346. doi: 10.1016/j.neuron.2014.08.046

Ikeda, K., and Bekkers, J. M. (2009). Counting the number of releasable synaptic vesicles in a presynaptic terminal. *Proc. Natl. Acad. Sci. USA* 106, 2945–2950. doi: 10.1073/pnas.0811017106

Katz, B. (1969). The release of neural transmitter substances. Liverpool: Liverpool University Press.

Kondapalli, K. C., Prasad, H., and Rao, R. (2014). An inside job: how endosomal Na^+/H^+ exchangers link to autism and neurological disease. *Front. Cell. Neurosci.* 8:172. doi: 10.3389/fncel.2014.00172

Kononenko, N. L., and Haucke, V. (2015). Molecular mechanisms of presynaptic membrane retrieval and synaptic vesicle reformation. *Neuron* 85, 484–496. doi: 10.1016/j.neuron.2014.12.016

Krächan, E. G., Fischer, A. U., Franke, J., and Friauf, E. (2017). Synaptic reliability and temporal precision are achieved via high quantal content and effective replenishment: auditory brainstem versus hippocampus. *J. Physiol.* 595, 839–864. doi: 10.1113/JP272799

Kramer, F., Griesemer, D., Bakker, D., Brill, S., Franke, J., Frotscher, E., et al. (2014). Inhibitory glycinergic neurotransmission in the mammalian auditory brainstem upon prolonged stimulation: short-term plasticity and synaptic reliability. *Front. Neural Circuits* 8:14. doi: 10.3389/fncir.2014.00014

Lee, U., Ryu, S. H., and Chang, S. (2021). SCAMP5 mediates activity-dependent enhancement of NHE6 recruitment to synaptic vesicles during synaptic plasticity. *Mol. Brain* 14:47. doi: 10.1186/s13041-021-00763-0

Li, H., Foss, S. M., Dobryy, Y. L., Park, C. K., Hires, S. A., Shaner, N. C., et al. (2011). Concurrent imaging of synaptic vesicle recycling and calcium dynamics. *Front. Mol. Neurosci.* 4:34. doi: 10.3389/fnmol.2011.00034

Li, D., Zhu, Y., and Huang, H. (2020). Spike activity regulates vesicle filling at a glutamatergic synapse. *J. Neurosci.* 40, 4972–4980. doi: 10.1523/jneurosci.2945-19.2020

Lujan, B., and Von Gersdorff, H. (2017). Tuning auditory synapses for resilience, reliability and precision. *J. Physiol.* 595, 621–622. doi: 10.1113/JP273496

Marasli oglu-Sperber, A. (2021). Transcriptional and functional profiling of murine auditory brainstem cells. Doctoral dissertation, University of Kaiserslautern-Landau, Kaiserslautern, Germany.

Masereel, B., Pochet, L., and Laeckmann, D. (2003). An overview of inhibitors of Na^+/H^+ exchanger. *Eur. J. Med. Chem.* 38, 547–554. doi: 10.1016/s0223-5234(03)00100-4

Masson, J., Riad, M., Chaudhry, F., Darmon, M., Aïdouni, Z., Conrath, M., et al. (1999). Unexpected localization of the Na^+/Cl^--dependent-like orphan transporter, Rxt1, on synaptic vesicles in the rat central nervous system. *Eur. J. Neurosci.* 11, 1349–1361. doi: 10.1046/j.1460-9568.1999.00540.x

Mcintire, S. L., Reimer, R. J., Schuske, K., Edwards, R. H., and Jorgensen, E. M. (1997). Identification and characterization of the vesicular GABA transporter. *Nature* 389, 870–876. doi: 10.1038/39908

Micu, I., Plemel, J. R., Lachance, C., Proft, J., Jansen, A. J., Cummins, K., et al. (2016). The molecular physiology of the axo-myelinic synapse. *Exp. Neurol.* 276, 41–50. doi: 10.1016/j.expneurol.2015.10.006

Miyazaki, E., Sakaguchi, M., Wakabayashi, S., Shigekawa, M., and Mihara, K. (2001). NHE6 protein possesses a signal peptide destined for endoplasmic reticulum membrane and localizes in secretory organelles of the cell. *J. Biol. Chem.* 276, 49221–49227. doi: 10.1074/jbc.M106267200

Muller, E., Bakkar, W., Martina, M., Sokolovski, A., Wong, A. Y., Legendre, P., et al. (2013). Vesicular storage of glycine in glutamatergic terminals in mouse hippocampus. *Neuroscience* 242, 110–127. doi: 10.1016/j.neuroscience.2013.03.007

Müller, N. I. C., Paulussen, I., Hofmann, L. N., Fisch, J. O., Singh, A., and Friauf, E. (2022). Development of synaptic fidelity and action potential robustness at an inhibitory sound localization circuit: effects of otoferlin-related deafness. *J. Physiol.* 600, 2461–2497. doi: 10.1113/JP280403

Muroi, M., Shiragami, N., Nagao, K., Yamasaki, M., and Takatsuki, A. (1993). Folimycin (concanamycin a), a specific inhibitor of V-ATPase, blocks intracellular translocation of the glycoprotein of vesicular stomatitis virus before arrival to the Golgi apparatus. *Cell Struct. Funct.* 18, 139–149. doi: 10.1247/csf.18.139

Nakamura, N., Tanaka, S., Teko, Y., Mitsui, K., and Kanazawa, H. (2005). Four Na^+/H^+ exchanger isoforms are distributed to Golgi and post-Golgi compartments and are involved in organelle pH regulation. *J. Biol. Chem.* 280, 1561–1572. doi: 10.1074/jbc.M410041200

Neef, A., Khimich, D., Pirih, P., Riedel, D., Wolf, F., and Moser, T. (2007). Probing the mechanism of exocytosis at the hair cell ribbon synapse. *J. Neurosci.* 27, 12933–12944. doi: 10.1523/JNEUROSCI.1996-07.2007

Neher, E. (2015). Merits and limitations of vesicle pool models in view of heterogeneous populations of synaptic vesicles. *Neuron* 87, 1131–1142. doi: 10.1016/j.neuron.2015.08.038

Nicoli, A. L., Al Abed, A. S., Hulme, S. R., Das, A., Gauthier-Coles, G., Bröer, A., et al. (2025). Glutamine transport via amino acid transporter NTT4 (SLC6A17) maintains presynaptic glutamate supply at excitatory synapses in the CNS. *Prog. Neurobiol.* 250:102785. doi: 10.1016/j.pneurobio.2025.102785

Ohgaki, R., Matsushita, M., Kanazawa, H., Ogihara, S., Hoekstra, D., and Van Ijzendoorn, S. C. (2010). The Na^+/H^+ exchanger NHE6 in the endosomal recycling system is involved in the development of apical bile canalicular surface domains in HepG2 cells. *Mol. Biol. Cell* 21, 1293–1304. doi: 10.1091/mbc.e09-09-0767

Ohgaki, R., Van Ijzendoorn, S. C., Matsushita, M., Hoekstra, D., and Kanazawa, H. (2011). Organellar Na^+/H^+ exchangers: novel players in organelle pH regulation and their emerging functions. *Biochemist* 50, 443–450. doi: 10.1021/bi101082e

Orlowski, J., and Grinstein, S. (2004). Diversity of the mammalian sodium/proton exchanger SLC9 gene family. *Pflugers Arch.* 447, 549–565. doi: 10.1007/s00424-003-1110-3

Ouyang, Q., Lizarraga, S. B., Schmidt, M., Yang, U., Gong, J., Ellisor, D., et al. (2013). Christianson syndrome protein NHE6 modulates TrkB endosomal signaling required for neuronal circuit development. *Neuron* 80, 97–112. doi: 10.1016/j.neuron.2013.07.043

Parra, L. A., Baust, T., El Mestikawy, S., Quiroz, M., Hoffman, B., Haflett, J. M., et al. (2008). The orphan transporter Rxt1/NTT4 (SLC6A17) functions as a synaptic vesicle amino acid transporter selective for proline, glycine, leucine, and alanine. *Mol. Pharmacol.* 74, 1521–1532. doi: 10.1124/mol.108.050005

Pedersen, S. F., and Counillon, L. (2019). The SLC9A-C mammalian Na^+/H^+ exchanger family: molecules, mechanisms, and physiology. *Physiol. Rev.* 99, 2015–2113. doi: 10.1152/physrev.00028.2018

Peng, X., Parsons, T. D., and Balice-Gordon, R. J. (2012). Determinants of synaptic strength vary across an axon arbor. *J. Neurophysiol.* 107, 2430–2441. doi: 10.1152/jn.00615.2011

Preobraschenski, J., Zander, J. F., Suzuki, T., Ahnert-Hilger, G., and Jahn, R. (2014). Vesicular glutamate transporters use flexible anion and cation binding sites for efficient accumulation of neurotransmitter. *Neuron* 84, 1287–1301. doi: 10.1016/j.neuron.2014.11.008

Qiu, X., Zhu, Q., and Sun, J. (2015). Quantitative analysis of vesicle recycling at the calyx of held synapse. *Proc. Natl. Acad. Sci. USA* 112, 4779–4784. doi: 10.1073/pnas.1424597112

Ratnayaka, A., Marrakchi, N., Bush, D., Burden, J. J., Branco, T., and Staras, K. (2012). Recruitment of resting vesicles into recycling pools supports NMDA receptor-dependent synaptic potentiation in cultured hippocampal neurons. *J. Physiol.* 590, 1585–1597. doi: 10.1113/jphysiol.2011.226688

Rizzoli, S. O. (2014). Synaptic vesicle recycling: steps and principles. *EMBO J.* 33, 788–822. doi: 10.1002/embj.201386357

Rizzoli, S. O., and Betz, W. J. (2005). Synaptic vesicle pools. *Nat. Rev. Neurosci.* 6, 57–69. doi: 10.1038/nrn1583

Rose, T., Schoenenberger, P., Jezek, K., and Oertner, T. G. (2013). Developmental refinement of vesicle cycling at Schaffer collateral synapses. *Neuron* 77, 1109–1121. doi: 10.1016/j.neuron.2013.01.021

Rousseau, F., Aubrey, K. R., and Supplisson, S. (2008). The glycine transporter GlyT2 controls the dynamics of synaptic vesicle refilling in inhibitory spinal cord neurons. *J. Neurosci.* 28, 9755–9768. doi: 10.1523/JNEUROSCI.0509-08.2008

Ruffin, V. A., Salameh, A. I., Boron, W. F., and Parker, M. D. (2014). Intracellular pH regulation by acid-base transporters in mammalian neurons. *Front. Physiol.* 5:43. doi: 10.3389/fphys.2014.00043

Ryan, T. A., and Smith, S. J. (1995). Vesicle pool mobilization during action potential firing at hippocampal synapses. *Neuron* 14, 983–989. doi: 10.1016/0896-6273(95)90336-4

Sagné, C., El Mestikawy, S., Isambert, M. F., Hamon, M., Henry, J. P., Giros, B., et al. (1997). Cloning of a functional vesicular GABA and glycine transporter by screening of genome databases. *FEBS Lett.* 417, 177–183. doi: 10.1016/s0014-5793(97)01279-9

Sankaranarayanan, S., and Ryan, T. A. (2001). Calcium accelerates endocytosis of vSNAREs at hippocampal synapses. *Nat. Neurosci.* 4, 129–136. doi: 10.1038/83949

Santos, M. S., Park, C. K., Foss, S. M., Li, H., and Voglmaier, S. M. (2013). Sorting of the vesicular GABA transporter to functional vesicle pools by an atypical dileucine-like motif. *J. Neurosci.* 33, 10634–10646. doi: 10.1523/jneurosci.0329-13.2013

Sara, Y., Virmani, T., Deak, F., Liu, X., and Kavalali, E. T. (2005). An isolated pool of vesicles recycles at rest and drives spontaneous neurotransmission. *Neuron* 45, 563–573. doi: 10.1016/j.neuron.2004.12.056

Satake, S., Inoue, T., and Imoto, K. (2012). Paired-pulse facilitation of multivesicular release and intersynaptic spillover of glutamate at rat cerebellar granule cell-interneurone synapses. *J. Physiol.* 590, 5653–5675. doi: 10.1113/jphysiol.2012.234070

Schikorski, T., and Stevens, C. F. (1997). Quantitative ultrastructural analysis of hippocampal excitatory synapses. *J. Neurosci.* 17, 5858–5867. doi: 10.1523/JNEUROSCI.17-15-05858.1997

Schindelin, J., Arganda-Carreras, I., Frise, E., Kaynig, V., Longair, M., Pietzsch, T., et al. (2012). Fiji: an open-source platform for biological-image analysis. *Nat. Methods* 9, 676–682. doi: 10.1038/nmeth.2019

Siksou, L., Silm, K., Biesemann, C., Nehring, R. B., Wojcik, S. M., Triller, A., et al. (2013). A role for vesicular glutamate transporter 1 in synaptic vesicle clustering and mobility. *Eur. J. Neurosci.* 37, 1631–1642. doi: 10.1111/ejn.12199

Silva, M., Tran, V., and Marty, A. (2021). Calcium-dependent docking of synaptic vesicles. *TINS* 44, 579–592. doi: 10.1016/j.tins.2021.04.003

Song, I., Volynski, K., Brenner, T., Ushkaryov, Y., Walker, M., and Semyanov, A. (2013). Different transporter systems regulate extracellular GABA from vesicular and non-vesicular sources. *Front. Cell. Neurosci.* 7:23. doi: 10.3389/fncel.2013.00023

Soykan, T., Kaempf, N., Sakaba, T., Vollweiter, D., Goerdeler, F., Puchkov, D., et al. (2017). Synaptic vesicle endocytosis occurs on multiple timescales and is mediated by formin-dependent actin assembly. *Neuron* 93, 854–866.e4. doi: 10.1016/j.neuron.2017.02.011

Sterenborg, J. C., Pilati, N., Sheridan, C. J., Uchitel, O. D., Forsythe, I. D., and Barnes-Davies, M. (2010). Lateral olivocochlear (LOC) neurons of the mouse LSO receive excitatory and inhibitory synaptic inputs with slower kinetics than LSO principal neurons. *Hear. Res.* 270, 119–126. doi: 10.1016/j.heares.2010.08.013

Südhof, T. C. (2013). Neurotransmitter release: the last millisecond in the life of a synaptic vesicle. *Neuron* 80, 675–690. doi: 10.1016/j.neuron.2013.10.022

Supplisson, S., and Roux, M. J. (2002). Why glycine transporters have different stoichiometries. *FEBS Lett.* 529, 93–101. doi: 10.1016/s0014-5793(02)03251-9

Tagliatti, E., Bello, O. D., Mendonca, P. R. F., Kotzadimitriou, D., Nicholson, E., Coleman, J., et al. (2020). Synaptotagmin 1 oligomers clamp and regulate different modes of neurotransmitter release. *Proc. Natl. Acad. Sci. USA* 117, 3819–3827. doi: 10.1073/pnas.1920403117

Takamori, S. (2016). Presynaptic molecular determinants of quantal size. *Front. Synaptic Neurosci.* 8:2. doi: 10.3389/fnsyn.2016.00002

Takamori, S., Holt, M., Stenius, K., Lemke, E. A., Gronborg, M., Riedel, D., et al. (2006). Molecular anatomy of a trafficking organelle. *Cell* 127, 831–846. doi: 10.1016/j.cell.2006.10.030

Tang, L. T. H., Craig, T. J., and Henley, J. M. (2015). SUMOylation of synapsin Ia maintains synaptic vesicle availability and is reduced in an autism mutation. *Nat. Commun.* 6:7728. doi: 10.1038/ncomms8728

Taoufiq, Z., Ninov, M., Villar-Briones, A., Wang, H. Y., Sasaki, T., Roy, M. C., et al. (2020). Hidden proteome of synaptic vesicles in the mammalian brain. *Proc. Natl. Acad. Sci. USA* 117, 33586–33596. doi: 10.1073/pnas.2011870117

Vahdat, Z., Gambrell, O., Fisch, J. O., Friauf, E., and Singh, A. (2025). Inferring synaptic transmission from the stochastic dynamics of the quantal content: an analytical approach. *PLoS Comput. Biol.* 21:e1013067. doi: 10.1371/journal.pcbi.1013067

Vandael, D., and Jonas, P. (2024). Structure, biophysics, and circuit function of a "giant" cortical presynaptic terminal. *Science* 383:eadg6757. doi: 10.1126/science.adg6757

Vargas, K. J., Makani, S., Davis, T., Westphal, C. H., Castillo, P. E., and Chandra, S. S. (2014). Synucleins regulate the kinetics of synaptic vesicle endocytosis. *J. Neurosci.* 34, 9364–9376. doi: 10.1523/jneurosci.4787-13.2014

Vigne, P., Frelin, C., Cragoe, E. J. Jr., and Lazdunski, M. (1983). Ethylisopropyl-amiloride: a new and highly potent derivative of amiloride for the inhibition of the Na^+/H^+ exchange system in various cell types. *Biochem. Biophys. Res. Commun.* 116, 86–90. doi: 10.1016/0006-291x(83)90384-4

Watanabe, S., and Boucrot, E. (2017). Fast and ultrafast endocytosis. *Curr. Opin. Cell Biol.* 47, 64–71. doi: 10.1016/j.ceb.2017.02.013

Watanabe, S., Rost, B. R., Camacho-Perez, M., Davis, M. W., Sohl-Kielczynski, B., Rosenmund, C., et al. (2013). Ultrafast endocytosis at mouse hippocampal synapses. *Nature* 504, 242–247. doi: 10.1038/nature12809

Wojcik, S. M., Katsurabayashi, S., Guillemin, I., Friauf, E., Rosenmund, C., Brose, N., et al. (2006). A shared vesicular carrier allows synaptic corelease of GABA and glycine. *Neuron* 50, 575–587. doi: 10.1016/j.neuron.2006.04.016

Zafra, F., and Giménez, C. (2008). Glycine transporters and synaptic function. *IUBMB Life* 60, 810–817. doi: 10.1002/iub.128

Zaia, K. A., and Reimer, R. J. (2009). Synaptic vesicle protein NTT4/XT1 (SLC6A17) catalyzes Na^+-coupled neutral amino acid transport. *J. Biol. Chem.* 284, 8439–8448. doi: 10.1074/jbc.M806407200

Zhou, Q., Petersen, C. C., and Nicoll, R. A. (2000). Effects of reduced vesicular filling on synaptic transmission in rat hippocampal neurones. *J. Physiol.* 525, 195–206. doi: 10.1111/j.1469-7793.2000.t01-1-00195.x

10.3389/fncel.2025.1625868

Glossary

α - significance level

ACSF - artificial cerebrospinal fluid

AP - action potential

Bafi - bafilomycin

BL - baseline

BSA - bovine serum albumin

Chal - challenge

CN - cochlear nucleus

CNS - central nervous system

Ctrl - Control condition (ACSF)

d - dorsal

DABCO - 1,4-diazabicyclo[2.2.2]octane

DMSO - dimethyl sulfoxide

EIPA - ethylisopropylamiloride

EtOH - ethanol

eIPSC$_1$ - evoked inhibitory postsynaptic current evoked by first stimulus

eIPSC - evoked inhibitory postsynaptic current

Foli - folimycin

FR - fractional recovery

GABA - γ-aminobutyric acid

GlyT2 - glycine transporter 2

I_{RRP} - cumulative eIPSC amplitude upon complete depletion of RRP

k - number of comparisons

l - lateral

LSO - lateral superior olive

m - quantal content

MNTB - medial nucleus of the trapezoid body

NHE - Na^+/H^+ exchanger

NTT4 - sodium-dependent neutral amino acid transporter

N_{RRP} - number of SVs in RRP

P - postnatal

PBS - phosphate-buffered saline

PFA - paraformaldehyde

Pv - release probability

q - quantal size

Rec - recording

Recov - recovery

RRP - readily releasable pool

RT - room temperature

SOC - superior olivary complex

SPN - superior paraolivary nucleus

Stim - stimulation

SV - synaptic vesicle

TR - transfer rate

V-ATPase - vacuolar (H^+)-ATPase (H^+ pump)

VGAT - vesicular GABA transporter

VIAAT - vesicular inhibitory amino acid transporter

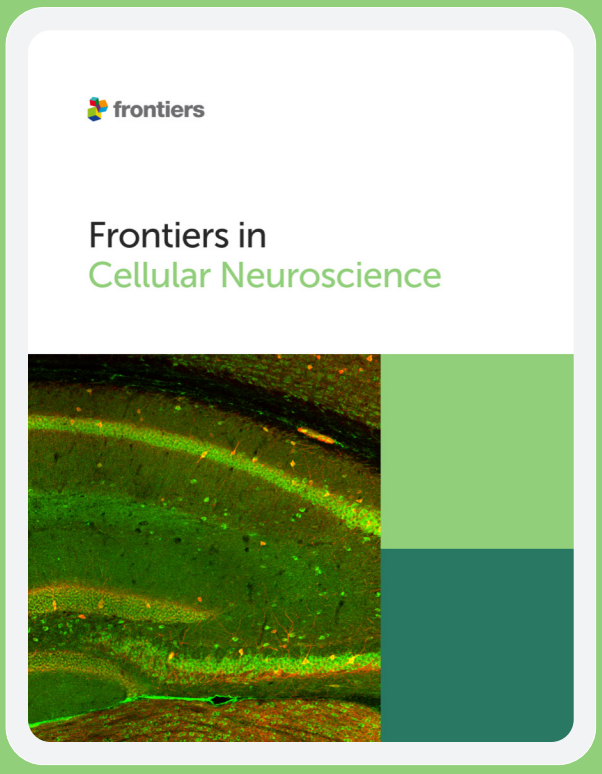
Frontiers in
Cellular Neuroscience

Leading research in cellular mechanisms underlying brain function and development

Part of the world's most cited neuroscience journal series that advances our understanding of the cellular mechanisms underlying cell function in the nervous system across all species.

Discover the latest Research Topics

See more →



Frontiers

Avenue du Tribunal-Fédéral 34
1005 Lausanne, Switzerland
frontiersin.org

Contact us

+41 (0)21 510 17 00
frontiersin.org/about/contact